LOW-SPEED WIND TUNNEL TESTING

THIRD EDITION

Jewel B. Barlow
William H. Rae, Jr.
Alan Pope

CONTENTS

PREFACE

The practice of low-speed experimental aerodynamics has continued to evolve and continues to be a cornerstone in the development for a wide range of vehicles and other devices that must perform their functions in the face of forces imposed by strong flows of air or water. In the 1970s and continuing into the early 1980s a sizable group of experts predicted that the need for aerodynamic experiments, particularly in the subsonic regime, would rapidly disappear as computational fluid dynamics would in a rather short time become sufficiently capable so that all needed information would be available from computational simulations at a cost-effectiveness superior to that of experiments. It is true that computational capability has continued to improve at a substantial pace, but it has not come close to reaching a level sufficient to replace the need for experimental data in development projects. There are now no credible predictions that computational simulation will replace the need for all data from physical experiments in any significant development projects. Turbulence continues to confound us in many respects.

Increasing capability of computing equipment has contributed greatly to changes in the practice of experimental aerodynamics by increasing dramatically the rate at which measurements can be obtained, by making additional measurement methods such as pressure-sensitive paint feasible, and by making it possible to share the results of experiments in practically real time with people at widely separated geographic locations. There is also a need to integrate directly the outcomes of experiments with the outcomes of computational simulations as each progresses. This is a capability that continues to be a work in progress at many laboratories.

Nevertheless, as stated in the preface to the previous edition, the basic methods and theory have remained unchanged over several decades. The scope of the book remains the same: to help students taking a course in wind tunnel experimentation and to furnish a reference source to wind tunnel engineers and others who use wind tunnels to solve problems of fluid flow or vehicle development. Considerable new material has been added in this edition. Some material has been added to the treatment of fundamental issues, including a more extensive theoretical introduction to help relate experimental work to computational simulations and a chapter on the design of experiments and data quality. The most obvious additions are separate chapters on ground vehicle experiments, marine vehicle experiments, and wind engineering, with the material on aircraft divided into two chapters. Because of the wide scope, we continue to include material on tunnel design, calibration, and simple as well as more sophisticated instrumentation. All the material in the book is directed to low-speed experiments. The subject of high-speed wind tunnel testing is covered

in *High-speed Wind Tunnel Testing* by A. Pope and K.L. Goin (John Wiley & Sons, New York, 1965).

We note the absence of a table of wind tunnel facilities that has appeared in previous editions. The substantial additions of material have resulted in a rather large book. The Subsonic Aerodynamic Testing Association (SATA) now has a site on the World Wide Web that includes facility descriptions and operational capabilities. The URL is *http://hww.nial:twsu.edu/sata/sata.h&* A list of members of the SATA is provided in Appendix 1. We believe this represents a readily available resource and that it is likely to be maintained with up-to-date information.

The untimely death of Bill Rae in 1992 cut short his work on this edition. Jewel Barlow and Alan Pope wish to acknowledge his early contributions to planning for the revisions leading to the current form. Jewel Barlow is pleased that Alan Pope saw fit to substantially entrust this endeavor to him and hopes that the result is worthy of that trust. Several students at the University of Maryland have made substantial contributions. First among those is Daniel "Rick" Harris, who drafted the chapter on marine vehicles, with Rui Guterres, who drafted the chapter on ground vehicles, and Molly Simmons, who did yeoman duty in many ways in close array. Robert Ranzenbach, Ahmad Kassaee, and Mark Dresser as leaders of the technical staff along with June Kirkley as the right-hand person in the office and her able assistant, Zenith Nicholas, have done much to keep the Glenn L. Martin Wind Tunnel laboratory on an even keel while allowing Jewel Barlow to focus on preparation of the manuscript. Jewel Barlow also wishes to express his gratitude to the many representatives of member facilities of the SATA with whom he has had the privilege and pleasure of sharing meetings, information, and experiences that have enriched his knowledge of wind tunnel experiments and more.

Very special thanks from Jewel Barlow are expressed to Diane Barlow, his wife, who has given unwavering support as well as good advice.

1 Introduction

This book concerns low-speed wind tunnels. The common usage of this classification includes wind tunnels with maximum speed capability up to about 300 mph (440 ft/sec, Mach $\cong$ 0.4, 134 m/s, 261 knots). The concepts to be treated are applicable to higher speed tunnels and to water tunnels as well. However, before launching into the main topics, it is worthwhile to set the stage for wind tunnels in general by asking the question: *What has motivated the invention, development, and continuing uses of wind tunnels?*

Our planet, Earth, is completely enveloped by oceans of air and water. Humans and almost all the other creatures spend their lives immersed in one or the other of these fluids. Naturally produced motions from gentle breezes and currents to storms and floods have profound impact on human existence. Winds and currents have been harnessed for moving about by boat and sail since before the earliest existing recorded history. And it seems certain that humans throughout their existence have marvelled at the agility of birds and fishes in their expositions of swimming and flying skills. Today, less than 100 years after the first successful airplane, there exists a vast array of aircraft tailored for many specific uses with corresponding variety in their shapes. The shapes of airplanes are determined by considerations of aerodynamics with varying degrees of attention to performance, agility, stealth, procurement cost, operational cost, time to delivery, and any other aspect that a customer may require for intended missions. There are millions of automobiles in routine use whose shapes attest to the influence of external aerodynamics on the decisions of the designers. The main focus for production automobiles has been on aerodynamic drag, although lift has received considerable attention as well. Aerodynamic down load is most often the main objective for racing automobiles. Automobile companies are also keenly interested in knowing how to choose details of external shapes to reduce exterior and interior noise. Racing yacht keels are the subject of intense investigations in efforts to achieve advantages of a few seconds per mile. Architects routinely require aerodynamic evaluations of any prominent building almost anywhere. Nearly every building component is being subjected to aerodynamic evaluation if it is to be accepted for use in hurricane-prone areas such as Florida. The shapes of submarines and the details of their propulsion systems are evaluated as designers attempt to maximize speed, minimize energy requirements, and minimize noise generation. Aerodynamic influences are substantial in the design of large bridges.

Yet the veil covering the secrets of the forces involved in the dynamic interactions of fluids and solid objects has only begun to be lifted and only in relatively recent times and continues to refuse all efforts to tear it cleanly away. The investigative

methods leading to quantitative predictions have been a combination of experiment and theory, with computational methods becoming a new tool of increasing consequence since the 1960s. The great advances in theory and computational capability notwithstanding, experimental explorations remain the mainstay for obtaining data for designers' refined and final decisions across a broad range of applications. A primary tool of experimental aerodynamics is the wind tunnel. The proper and productive use of experimental investigations in general and wind tunnels in particular requires applications of aerodynamic theory and computational methods in the planning of facilities, the planning of experiments, and the interpretation of resulting data. Those aspects of aerodynamics will be drawn upon heavily in the course of this book.

To answer the question posed above: The invention, use, and ongoing evolution of the wind tunnel has been, and is now, motivated first by a wide interest in practical problems in aerodynamics and second by the fact that theoretical and computational methods have not been. are not now. and will not in the foreseeable future be capable of providing the full range of results needed to guide detailed design decisions for many practical problems.

The most successful attack on virtually any aerodynamic design problem will be based on application of a combination of results from experimental, theoretical, and computational methods appropriately combined and leavened by experience.

1.1 AERODYNAMICS

Readers of this book will find many parts where it will be helpful to have a prior knowledge of aerodynamics[1] to the level represented in texts such as Anderson[2] or Shames[3] or to have such a reference readily available. Included in those and other texts are discussions of flow similarity in which definitions of *similar flows* are given. This is a very important concept that leads to significant advantages in experimental work and in theoretical and computational work as well. The most common approach to the concept of similarity is through dimensional analysis using some variation of the Buckingham Pi theorem.[4] Knowledge, of a detailed mathematical model of the processes involved is not required to apply the Pi theorem. A reduction in the number of independent parameters to be manipulated in an investigation is obtained based on the requirement of dimensional homogeneity for any equation expressing a valid relationship among physical variables. Introductory treatments of dimensional analysis are given by Anderson[2] and by Shames.[3] A very useful discussion based on dimensional analysis is given by Karamcheti.[5] More extensive treatments of background and applications of similitude methods in engineering are given by Sedov,[6] David and Nolle,[7] and Baker, Westine, and Dodge? Some of the most important results are those associated with "distorted" models, that is, models in which complete similarity cannot be achieved but that nevertheless are very useful. Such models are the norm rather than the exception, as becomes apparent when almost any specific wind tunnel program is being planned.

Although the application of dimensional analysis has been of great importance in studies in aerodynamics, that approach will not be elaborated at this point.

Motivated by the need to bring theoretical, computational, and experimental methods into closer proximity, dimensionless similarity parameters will be obtained directly from the equations for which solutions are sought in theoretical and computational studies.

Principal Equations of Aerodynamics

The fundamental principles from which the equations used to model "low-speed" aerodynamic flows are derived **are** only three in number. These **are (1)** mass is conserved, (2) force and motion **are** related by Newton's Second Law, and (3) energy exchanges are governed by the First Law of **Thermodynamics.** In addition to these three principles, certain fluid properties and their variations with pressure and temperature must be described mathematically with sufficient accuracy for each application.

The equations expressing the three principles provide relationships among various quantities (such as density, velocity, pressure, rate of strain, internal energy, and viscosity) as they vary in space and time. The dependence for a particular quantity, say velocity, is indicated as $\mathbf{V}(\mathbf{r}, t)$ where $\mathbf{r}$ is a three-component position vector and t is time. The details of the function expressing the space and time dependence are strongly affected by the choice of reference frame while the physical phenomena cannot be affected by the choice of reference frame. It is desirable to choose reference frames that lead to relatively simple forms for the functional descriptions of the various quantities.

Two kinematic results of importance relate time derivatives from different perspectives. One relation is between "Lagrangian" and "Eulerian" descriptions of the motion of particles. The other relation is between the time derivatives of quantities when measurements are made from two reference frames that are moving relative to one another.

The Lagrangian and Eulerian perspectives of motion of a field of particles are described in almost every book on aerodynamics. The Lagrangian perspective is based on the idea of "tagging" every particle and subsequently describing the motion of each particle as a function of time with a space coordinate indicating the identity of the particle. The usual choice would be that the space coordinate indicates the position of the particle at time equal to zero. The Eulerian perspective is based on the idea of focusing on particular points in space and describing the motion of particles passing through each point in space as a function of time. The time derivatives are related by Equation **(1.1),** where the internal energy e has been used as an example. The derivative from the Lagrangian perspective is referred to as a "total derivative" or "material derivative" and is indicated by the capital D as the derivative symbol. The relation holds for all other such quantities including components of velocity:

$$\frac{De(\mathbf{r}, t)}{Dt} = \frac{\partial}{\partial t} e(\mathbf{r}, t) + (\mathbf{V} \cdot \nabla) e(\mathbf{r}, t) \tag{1.1}$$

The relationships that arise when two reference frames are moving relative to one another are important when "noninertial" reference frames become more convenient

for a problem than the alternatives. The equations for these situations are given by Shames.[3]

Conservation of Mass

The continuity equation follows from the principle of conservation of mass. It can be written as a partial differential equation as follows:

$$\frac{\partial \rho}{\partial t} + \nabla \cdot (\rho V) = 0 \tag{1.2}$$

In this equation and throughout the book ρ is the density of the fluid, t is the time, and V is the vector fluid velocity. The standard notations for divergence operator and dot product are used.

Newton's Second Law, $F = mu$

The application of Newton's second law to an elemental mass can be expressed quite generally as

$$\rho\left(\frac{DV}{Dt}\right) = \rho F_B + F_S \tag{1.3}$$

where F_B is the body force per unit mass and F_S the surface force per unit volume. The time derivative is the "total" derivative in the sense used in Equation (1.1)[1] with respect to an inertial reference frame and V is the velocity of the material element with respect to the same inertial frame. The left-hand side can be written as

$$\rho\left(\frac{DV}{Dt}\right) = \rho\left(\frac{\partial V}{\partial t} + (V \cdot \nabla)V\right) \tag{1.4}$$

or as

$$\rho\left(\frac{DV}{Dt}\right) = \rho\left(\frac{\partial V}{\partial t} + \nabla\frac{V^2}{2} - V \times (\nabla \times V)\right) \tag{1.5}$$

This last form is convenient for deriving the well-known Bernoulli equation when the appropriate conditions are applied.

The body force is frequently neglected in aerodynamic developments but rarely in hydrodynamic applications. In either case it is most commonly of gravitational origin and in that case is simply $F_B = g$, where g is the gravitational acceleration. Body forces will also arise in cases of noninertial reference frames.

The surface force for a material element is expressed in terms of the *state* of *stress* at the location of the element. For a particular material the state of stress is

related to the *state of strain,* including the possibility of memory effects. For any particular material, solid or fluid, the relationship between stress and strain must be obtained from experimental evaluation. The two most common forms of the relation are those for *elastic* bodies and for *Newtonian fluids.* For elastic bodies the relationship between stress and strain is given by Hooke's law, which can be stated in an oversimple form as "stress is proportional to strain." For Newtonian fluids the relationship between stress and strain is given by *Stokes' law of friction,* which is a generalization to three dimensions of the assumption made by Newton for the simpler case of two-dimensional parallel flow. Stokes' law of friction states that the "stress is proportional to the time rate of strain." Using Stokes' law to develop the surface force in Equation (1.3)[3] produces the equations of motion for a Newtonian fluid. These equations are known as the Navier–Stokes equations. Detailed derivations of these equations are given by Schlichting[9] and Loitsyanskii.[10] The surface force per unit volume that follows from Stokes' law of friction can be written as

$$\mathbf{F}_S = - \nabla\left(p + \tfrac{2}{3}\mu\nabla \cdot \mathbf{V}\right) + 2\nabla \cdot (\mu\dot{\mathbf{S}}) \tag{1.6}$$

New variables appearing in Equation (1.6) are pressure p, coefficient of viscosity μ, and rate of strain tensor $\dot{\mathbf{S}}$. The assumption that the bulk modulus is $-\tfrac{2}{3}$ times the coefficient of viscosity is incorporated in Equation **(1.6).** The elements of $\dot{\mathbf{S}}$ associated with a Cartesian reference frame are given by the equations

$$\dot{\mathbf{S}}_{xx} = \frac{\partial u}{\partial x} \tag{1.7}$$

$$\dot{\mathbf{S}}_{yy} = \frac{\partial v}{\partial y} \tag{1.8}$$

$$\dot{\mathbf{S}}_{zz} = \frac{\partial w}{\partial z} \tag{1.9}$$

$$\dot{\mathbf{S}}_{xy} = \dot{\mathbf{S}}_{yx} = \frac{1}{2}\left(\frac{\partial v}{\partial x} + \frac{\partial u}{\partial y}\right) \tag{1.10}$$

$$\dot{\mathbf{S}}_{xz} = \dot{\mathbf{S}}_{zx} = \frac{1}{2}\left(\frac{\partial u}{\partial z} + \frac{\partial w}{\partial x}\right) \tag{1.11}$$

$$\dot{\mathbf{S}}_{yz} = \dot{\mathbf{S}}_{zy} = \frac{1}{2}\left(\frac{\partial w}{\partial y} + \frac{\partial v}{\partial z}\right) \tag{1.12}$$

The Navier–Stokes equation for the case of a viscous compressible fluid with body force of gravitational origin can be written as

$$\rho\left(\frac{\partial \mathbf{V}}{\partial t} + (\mathbf{V} \cdot \nabla)\mathbf{V}\right) = \rho\mathbf{g} - \nabla\left(p + \frac{2}{3}\mu\nabla \cdot \mathbf{V}\right) + 2\nabla \cdot (\mu\dot{\mathbf{S}}) \tag{1.13}$$

The Navier–Stokes equation is considered to be an accurate representation of Newton's Second Law applied to water and air over wide ranges of temperature and pressure.

First Law of Thermodynamics: The Energy Equation

The energy equation is a mathematical representation of the principle of conservation of energy. A form is given here that is appropriate for flow of a fluid in which there may be heat transfer by conduction, transformation between mechanical energy and thermal energy by both reversible and irreversible processes, and energy contribution or absorption by body force of gravitational origin but no radiative transfer. The reader is referred to Anderson[2] and Loitsyanskii[10] for detailed derivations of the energy equation. The energy equation may be written as

$$\rho\frac{\partial}{\partial t}\left(C_v T + \frac{V^2}{2}\right) + \rho\mathbf{V} \cdot \nabla\left(C_v T + \frac{V^2}{2}\right) = \rho\mathbf{g} \cdot \mathbf{V} - \nabla \cdot p\mathbf{V}$$
$$+ \nabla \cdot \left[2\mu\nabla\left(\frac{V^2}{2}\right) + \mu(\nabla \times \mathbf{V}) \times \mathbf{V} - \frac{2}{3}\mu(\nabla \cdot \mathbf{V})\mathbf{V}\right] + \nabla \cdot k\,\nabla T \quad (1.14)$$

An additional variable, the temperature T, is present in the energy equation. Two additional parameters also are present. These are the specific heat at constant volume, C_v, and the thermal conductivity k. These parameters are considered to be constants throughout any flow considered in this book.

Equation of State and Other Considerations

Equations (1.2), (1.13), and **(1.14)** provide five equations relating the variables p, V, p, T, and μ. Since there are seven scalar variables, two additional relations are required to obtain a solvable set.

We consider typical cases of air and water because it is common to use low-speed wind tunnels to investigate hydrodynamic as well as aerodynamic problems.

In the case of water, the density varies very little with pressure so long as the pressure is greater than the vapor pressure, which in turn is a function of temperature. An assumption of constant density is invariably applied for flows of water. Viscosity is primarily a function of temperature in the cases of both air and water. In flows of water, if the initial and boundary conditions are isothermal, then negligible temperature variations will arise from the flow phenomena. In such circumstances both density and viscosity can be considered constant. Equations **(1.2)** and **(1.13)** then provide an equal number of equations and unknowns.

In the case of air, the processes are more complex even for "low-speed" flow as we use the term here. It is assumed that air in these regimes is a calorically perfect gas, which means that the specific heats are constant. As stated above, it is also assumed that the thermal conductivity is constant, in which case it can be factored to the leading position in the last term of Equation **(1.14).** The perfect gas equation

of state gives a good description of air over the range of conditions of interest here. Equation (1.15) is the sixth of seven needed relations among the seven variables:

$$p = \rho RT \tag{1.15}$$

The seventh relation is a specification of variation of viscosity with temperature. Equation (1.16), which is an expression of Sutherland's law, gives such a relationship for air:

$$\frac{\mu}{\mu_0} = \left(\frac{T_R}{T_0}\right)^{3/2} \frac{T_0 + 198.6}{T_R + 198.6} \tag{1.16}$$

where T_R is temperature in degrees Rankine. For $T_0 = 518.6°R$, the viscosity is $\mu_0 = 3.74 \times 10^{-7}$ lb − s/ft^2. The dependence of viscosity on temperature is frequently approximated by a power law, as discussed by Schlichting? For example Equation (1.17) is given in the National Advisory Committee for Aeronautics (NACA) Report 1135[11] for air:

$$\frac{\mu}{\mu_0} = \left(\frac{T}{T_0}\right)^{0.76} \tag{1.17}$$

For each problem to be investigated there will be an appropriate set of initial and boundary conditions that along with the set of equations (1.2), (1.13), (1.14), (1.15), and (1.16) approximately describe the subsequent spatial and temporal evolution of the seven variables.

1.2 PROPERTIES OF AIR AND WATER

The properties of the fluids involved in experiments and in operations of devices are critical. It is common to idealize their properties, but it is important to keep in mind the degree of approximation involved in the idealization. Jones'' has given a substantial summary of the models of properties of air, water, and some additional substances.

Properties of Air

Air is a mixture of nitrogen, oxygen, water vapor, and several other gases present in small quantities. The equation of state is written as Equation (1.18), where R is the universal gas constant and M is the apparent molecular weight of the mixture.

The apparent molecular weight for air is significantly affected by the presence of water vapor:

$$p = \frac{\rho R T}{M} \tag{1.18}$$

Jones" gives an extensive development and arrives at Equation (1.19) for density of air as a function of temperature ($^\circ$K), pressure (Pa), relative humidity, and effective saturation vapor pressure of water (Pa):

$$\rho_a = \left(\frac{0.0034847}{T}\right)(p - 0.003796 R_h e_s) \quad \text{kg/m}^3 \tag{1.19}$$

The saturation vapor pressure is related to temperature by

$$e_s = (1.7526 \times 10^{11})e^{(-5315.56/T)} \tag{1.20}$$

Equations (1.19) and (1.20) give density of 1.1992 kg/m^3 for $p = 101325$ Pa, T = 293.15°K, and relative humidity of 50%. Over plausible ranges of variation of relative humidity of say 30–75% the density varies by -0.5%. This is small but is definitely not negligible compared to the level of measurement accuracy sought in many wind tunnel experiments.

An equation for viscosity of air has previously been given as Equation (1.17). Table 1.1 summarizes some properties of air at the "standard" condition.

Properties of Water

The density of water is nearly constant over common ranges of pressure and temperature. The small variation with temperature at atmospheric pressure is modeled by Jones with Equation (1.21). This gives density in kilograms per cubic meter for temperature in degrees Celsius. The temperature should be in the range of 5-40:

$$\rho_w = 999.84847 + 0.06337563t - (8.523829 \times 10^{-3})t^2$$
$$+ (6.943248 \times 10^{-5})t^3 - (3.821216 \times 10^{-7})t^4 \tag{1.21}$$

TABLE 1.1. Air at "Standard" Condition

Temperature, T	59°F = 518.67°R = 15°C = 288.16°K	
Density, ρ	0.002378 slug/ft^3	1.225 kg/m^3
Pressure, p	2116 lb/ft^2	101,325 Pa (N/m^2)
Viscosity, μ	3.74 $\times$ 10^{-7} lb-sec/ft^2	1.791 $\times$ 10^{-6} kg/m-s
Kinematic viscosity, ν	1.55 $\times$ 10^{-4} ft^2/sec	1.44 $\times$ 10^{-5} m^2/s
Reciprocal of ν	6452 sec/ft^2	69,440 s/m^2
Gas constant, R	1714.9 ft-lb/slug-°R	287 N-m/kg-°K

TABLE 1.2. Fresh Water

Temperature	39.2°F = 498.87°R = 4°C = 277.16°K		15°C = 288.16°K
Density	1.940 slugs/ft³	1000 kg/m³	999.13 kg/m³
Viscosity	3.229 × 10⁻⁵ lb-sec/ft²	1.52 × 10⁻³ N-s/m²	1.105 × 10⁻³ N-s/m²
Kinematic viscosity	1.664 × 10⁻⁵ ft²/sec	1.52 × 10⁻⁶ m²/s	1.106 × 10⁻⁶ m²/s
Reciprocal of v	60,100 sec/ft²	657,900 s/m²	904,300 s/m²

The variation of viscosity of water with temperature for the range of 0–20°C is given by Equation (1.22),[12] where the viscosity is in centipoise (g/cm-s):

$$\log \mu = \frac{1301}{998.333 + 8.1855\,(T - 20) + 0.00585(T - 20)^2} - 3.30233 \quad (1.22)$$

This equation can be used for moderately higher water temperatures with little error. The density of water decreases about 1% for a temperature change from 4 to 45°C. The variation in kinematic viscosity of water with temperature is primarily due to change in the viscosity. In the case of air, kinematic viscosity changes with temperature are significantly affected by changes in both density and viscosity.

Table 1.2 gives some properties of water at two temperatures. A row showing the reciprocal of the kinematic viscosity is included as this is a value directly proportional to the Reynolds number for a given size of model or prototype and a given speed. By comparison of the data in the two tables it can be seen that the Reynolds number in water for a given size article and a given speed will be approximately 13 times the Reynolds number in air if both fluids are at a temperature of 15°C. This ratio will climb to about 15 if both fluids are at 20°C.

Sea water will be somewhat more dense and have slightly different viscosity.

1.3 flow SIMILARITY

To explore similarity for flows governed by the set of equations (1.2), (1.13). (1.14), (1.15), and (1.16), consider a problem of determining flow properties about a complete airplane, automobile, ship, or other body. In principle, it is necessary to find the appropriate solution to the system of partial differential equations with the associated boundary and initial conditions. The complete geometry of the body including any time-dependent motion is required to specify the boundary conditions at the body. For the present discussion, the body is considered to be rigid, in which case motion may be specified by the linear and angular velocities. Note that this would have to be treated more generally to include aeroelastic phenomena.

Attention is now turned to arriving at a corresponding set of nondimensional equations. The geometry can be nondimensionalized as a ratio to some reference length, which is usually chosen as the chord of the wing in the case of aircraft. Any

other length can be used, such as the overall airplane length for airplanes, the wheelbase in the case of automobiles, or the beam or overall length in the case of marine vehicles. The fluid speeds will be nondimensionalized by using the ratio to the speed at a selected point far away from the body. This is not a fundamental requirement, but it is the standard practice. In some experimental arrangements and in many computational problems-the question of whether there is an available point considered to be "far" from the body becomes an important issue. The density will also be nondimensionalized in terms of the ratio to the value at the selected point far from the body. Pressure will be nondimensionalized by introducing the standard pressure coefficient. The pressure coefficient is the ratio of the *change in pressure* due to the presence of the body (as compared to the pressure at the selected point far from the body) to the *dynamic pressure* at the selected point far from the body. Temperature will be nondimensionalized by its ratio to the value at the selected point far from the body. The time will be nondimensionalized as a ratio to the time for a fluid particle to travel the reference length at the speed of flow far from the body. To summarize, we will consider the variables in Equations (1.2), (1.13), (1.14), (1.15), and (1.16) to be given by $r = l\hat{r}$, $t = (l/V_\infty)\hat{t}$, $V = V_\infty\hat{V}$, $\rho = \rho_\infty\hat{\rho}$, $T = T_\infty\hat{T}$, $\mu = \mu_\infty\hat{\mu}$, and $p - p_\infty = \frac{1}{2}\rho_\infty V^2_\infty c_p$, where all the symbols with carets are dimensionless variables and c_p is the dimensionless form for pressure with the reference value shifted according to standard practice. Equation (1.2) becomes

$$\frac{\partial}{\partial \hat{t}}\hat{\rho} + \hat{\nabla} \cdot (\hat{\rho}\hat{V}) = 0 \qquad (1.23)$$

This is the same form as the dimensional equation. Equation (1.13) becomes

$$\hat{\rho}\frac{\partial}{\partial \hat{t}}\hat{V} + \hat{\rho}(\hat{V} \cdot \hat{\nabla})\hat{V} = \left(\frac{1}{F_r^2}\right)\hat{\rho}e_g - \frac{1}{2}\hat{\nabla} c_p + \frac{1}{R_e}\left(2\nabla \cdot \hat{\mu}\hat{\dot{S}} - \frac{2}{3}\hat{\nabla}(\hat{\mu}\nabla \cdot \hat{V})\right) \quad (1.24)$$

Two dimensionless coefficients appear in Equation (1.24). The first is

$$F_r \equiv \sqrt{\frac{V^2_\infty}{l_g}} \qquad (1.25)$$

which is the Froude number. Including the square root in the definition is not essential, but it is done here to be consistent with common usage. The symbol e_g is a unit vector in the direction of the gravitational field. Normally the coordinates would be chosen so that only one element would be nonzero. The Froude number is important for flows in which there is a free surface, such as will exist for surface ships. A Froude number will also arise as an important similarity parameter if there are unsteady boundary conditions. The acceleration of the boundaries will play a role similar to the gravitational acceleration. The Froude number is a significant parameter in some cases of dynamic systems such as towed bodies. A complete

similarity study of such systems requires inclusion of the equations of motion of the towed systems themselves as well as the fluid dynamic equations.

The Froude number will not appear if the fluid body forces are neglected. This is a common assumption introduced in aerodynamics texts. The Froude number will not be considered further in this introductory material.

The second coefficient appearing in Equation (1.24) is the most important parameter for most experiments conducted in low-speed wind tunnels. It is the Reynolds number,

$$R_e \equiv \frac{\rho_\infty V_\infty l}{\mu_\infty} \tag{1.26}$$

The Reynolds number is the primary similarity parameter of interest in planning experiments for Mach numbers less than -0.3 when the geometry is fixed.

The process of developing the nondimensional form of the energy equation leads to the introduction of some additional and some alternative parameters of the fluid. These are the specific heat at constant pressure, C_p; the ratio of specific heats, $\gamma \equiv C_p/C_v$; the speed of sound in the fluid, $a = \sqrt{\gamma RT}$; and the Prandtl number, $P_r \equiv \mu C_p/k$. To shorten the resulting equation, we also introduce the substitution $\Gamma \equiv \gamma(\gamma - 1)$. The nondimensional energy equation can be written as

$$\rho\frac{\partial}{\partial \hat{t}}\left(\hat{T} + \Gamma M_\infty^2 \frac{\hat{V}^2}{2}\right) + \rho\hat{\mathbf{V}} \cdot \nabla\left(\hat{T} + \Gamma M_\infty^2 \frac{\hat{V}^2}{2}\right) = \frac{\Gamma M_\infty^2}{F_r^2}\rho\hat{\mathbf{V}} \cdot \mathbf{e}_g - \frac{\Gamma M_\infty^2}{2}\nabla \cdot c_p\hat{\mathbf{V}}$$
$$+ \frac{\Gamma M_\infty^2}{R_e}\nabla \cdot \left[2\hat{\mu}\nabla\left(\frac{\hat{V}^2}{2}\right) + \hat{\mu}(\nabla \times \hat{\mathbf{V}}) \times \hat{\mathbf{V}} - \frac{2}{3}\hat{\mu}(\nabla \cdot \hat{\mathbf{V}})\hat{\mathbf{V}}\right] + \frac{\gamma}{P_{r\infty}R_e}\nabla^2\hat{T} \tag{1.27}$$

There are many terms in Equation (1.27), and finding solutions to it by mathematical or computational analysis is not the purpose here. The important result to be obtained here from this equation is that there are two dimensionless coefficients that did not appear in the nondimensional Navier–Stokes equation. These are the Mach number $M_\infty \equiv V_\infty/a_\infty$ and the Prandtl number $P_{r\infty}$. The Mach number is a flow parameter while the Prandtl number is a property of the fluid that is temperature dependent. The last term of Equation (1.27) is the term associated with transport of energy by heat conduction. For low-speed flows that do not have heated or cooled boundaries, there is seldom a significant contribution from this term. We will consider that this term is negligible for most circumstances with which we will be dealing in this book. This also implies that the Prandtl number will not be a consideration since it only appears in the heat conduction term. The net result is that the dimensionless energy equation provides the Mach number as an additional similarity parameter for our present class of problems.

Equations (1.23), (1.24), and (1.27) along with dimensionless forms of the equation of state and the variation of viscosity with temperature form a set of equations for the dimensionless flow variables. The associated boundary conditions for any particular case must also be obtained in nondimensional form.

For the moment consider only cases for which the boundary conditions are not functions of $\hat{t}$. This does not mean that the flow is steady throughout the domain

so this is not equivalent to an assumption of steady flow, which is a far more stringent assumption. Almost all flows of importance to vehicle aerodynamics are turbulent and therefore unsteady. Most wind tunnel studies involve steady "mean" flow. We can choose to use "wind axes," in which case the boundary conditions far upstream of our body would typically be $\hat{u}_\infty = 1$, $\hat{v}_\infty = 0$ $\hat{w}_\infty = 0$, $c_{p\infty} = 0$ $\hat{\rho}_\infty = 1$, $\hat{T}_\infty = 1$, and $\hat{\mu}_\infty = 1$ for-all $\hat{t}$. For a family of bodies of a particular shape the boundary conditions at the body surface, which can be represented as $\hat{S}(\hat{x}, \hat{y}, \hat{z}, a, \beta) = 0$, are $\hat{u}_s = \hat{v}_s = \hat{w}_s = 0$, plus given values for either $\hat{T}_s$ or $(\nabla \hat{T})_s$ for all $\hat{t}$. The angles can be given in terms of the components of $\hat{V}_\infty$ on a set of body-fixed axes. Let $\hat{u}_b$, $\hat{v}_b$, $\hat{w}_b$ be the components of $\hat{V}_\infty$ on body-fixed axes. Then tan a $\equiv$ $\hat{w}_b/\hat{u}_b$ and sin $\beta \equiv \hat{v}_b/\hat{V}_\infty$. If we could obtain solutions of the set of equations with the associated boundary conditions, we would have a set of functions:

$$\hat{u}(\hat{x}, \hat{y}, \hat{z}, \hat{t}, \alpha, \beta, R_e, M_\infty) \tag{1.28}$$

$$\hat{v}(\hat{x}, \hat{y}, \hat{z}, \hat{t}, \alpha, \beta, R_e, M_\infty) \tag{1.29}$$

$$\hat{w}(\hat{x}, \hat{y}, \hat{z}, \hat{t}, \alpha, \beta, R_e, M_\infty) \tag{1.30}$$

$$c_p(\hat{x}, \hat{y}, \hat{z}, \hat{t}, \alpha, \beta, R_e, M_\infty) \tag{1.31}$$

$$\hat{\rho}(\hat{x}, \hat{y}, \hat{z}, \hat{t}, \alpha, \beta, R_e, M_\infty) \tag{1.32}$$

$$\hat{\mu}(\hat{x}, \hat{y}, \hat{z}, \hat{t}, \alpha, \beta, R_e, M_\infty) \tag{1.33}$$

$$\hat{T}(\hat{x}, \hat{y}, \hat{z}, \hat{t}, \alpha, \beta, R_e, M_\infty) \tag{1.34}$$

which give the details of the nondimensional fluid velocity, pressure, density, viscosity, and temperature throughout the domain.

The values of the pressure coefficient and the shear stresses at the body surface would typically be of particular interest in the present context since the integrals of those quantities over the surface of the body provide the total force coefficients. To obtain these from the above set of functions, it is necessary to form the combinations representing expressions for the normal and tangential stress components on the body surface and integrate these over the entire body surface. This process provides dimensionless coefficients for force and moment components that can be represented by

$$C_L(\hat{t}, \alpha, \beta, R_e, M_\infty) \tag{1.35}$$

$$C_D(\hat{t}, \alpha, \beta, R_e, M_\infty) \tag{1.36}$$

$$C_S(\hat{t}, \alpha, \beta, R_e, M_\infty) \tag{1.37}$$

for "lift," "drag," and "side-force" coefficients and

$$C_l(\hat{t}, \alpha, \beta, R_e, M_\infty) \tag{1.38}$$

$$C_m(\hat{t}, \alpha, \beta, R_e, M_\infty) \tag{1.39}$$

$$C_n(\hat{t}, \alpha, \beta, R_e, M_\infty) \tag{1.40}$$

for "rolling moment," "pitching moment," and "yawing moment" coefficients. The force coefficients are related to the dimensional forces by the factor $\frac{1}{2}\rho_\infty V_\infty^2 l^2$, and the moment coefficients are related to the dimensional moments by the factor $\frac{1}{2}\rho_\infty V_\infty^2 l^3$. When the time dependence is averaged out or the actual circumstance of having steady boundary conditions yields steady results, these coefficients are functions only of the dimensionless similarity parameters Reynolds number and Mach number along with the attitude angles.

These are powerful results applying equally to experimental, analytical, and computational studies of fluid flows. Instead of separately varying the density, viscosity, flow speed, body size, and temperature, it is only necessary to vary the combinations represented by the similarity parameters. Each solution of the nondimensional system for a value of the Reynolds number provides a result that applies for every combination of the four involved quantities that give that particular Reynolds number. Of further significance is that the result shows that different fluids as well as different sizes of bodies in streams of differing speeds and differing coefficients of viscosity can be used when it is convenient to do so as long as the similarity parameters are matched.

For bodies completely immersed in a single fluid (as is always the case in wind tunnels) and that are rigid and held in a fixed position, the results will not be dependent on the Froude number, as has been stated previously. One interpretation of "low speed" as applied to wind tunnels is the speed below which the Mach number dependence is small enough to be neglected. In such cases, which are our primary concern, the results will be dependent on only one similarity parameter, the Reynolds number.

We find that for a body of fixed shape held rigidly in a "low-speed" stream, the time averages of the force and moment coefficients are functions of a single parameter, the Reynolds number, and two angles that are required to specify the body attitude relative to the free stream. This result holds for flows of water when cavitation is not present and for flows of air at speeds up to a Mach number of -0.3.

1.4 INCOMPRESSIBLE Π O W

In considering "low-speed" flows it is common to adopt the assumption that the density is constant, that is, $\hat{\rho} = 1$. With the assumption of constant density, Equation (1.23) reduces to the equation

$$\hat{\nabla} \cdot \hat{\mathbf{V}} = 0 \qquad (1.41)$$

and Equation (1.24) with some minor manipulation becomes

$$\frac{\partial}{\partial \hat{t}}\hat{\mathbf{V}} + \hat{\nabla}\left(\frac{1}{2}\,\hat{V}^2\right) + (\hat{\nabla} \times \hat{\mathbf{V}}) \times \hat{\mathbf{V}} = -\frac{1}{2}\,\hat{\nabla}c_p + \frac{1}{R_e}\left(2\hat{\nabla} \cdot \hat{\dot{\mathbf{S}}}\right) \qquad (1.42)$$

In cases in which dehsity is nearly constant, there are many situations in which the temperature variation is negligible. Such problems are entirely mechanical without any thennodynamic phenomena. Equations (1.41) and (1.42) are then a complete set for the three velocity components and the pressure coefficient. The force and moment coefficients in such cases will, of course, not be dependent on Mach number.

Classical Bernoulli Equation

For an idealized case of steady flow with viscosity equal to zero and a uniform velocity field far from any object that may be in the flow, we will have the time derivatives equal to zero, the Reynolds number will be infinity, and the curl of the velocity field must be everywhere equal to zero. Equation (1.42) then becomes

$$\hat{\nabla}\left(\frac{\hat{V}^2}{2}\right) = -\frac{1}{2}\hat{\nabla}c_p \quad \text{or} \quad \hat{\nabla}(\hat{V}^2 + c_p) = 0$$

Recalling the definitions $\hat{V}_\infty = 1$ and $c_{p\infty} = 0$, we have the result that

$$\hat{V}^2 + c_p = 1 \quad \text{or equivalently} \quad p + \tfrac{1}{2}\rho V^2 = p_\infty + \tfrac{1}{2}\rho V_\infty^2 \equiv p_{\text{tot}} \qquad (1.43)$$

which is the classical Bernoulli equation that is very important in low-speed wind tunnel work as it is the basis for most speed-setting systems.

Inviscid and Irrotational Flow

For inviscid, irrotational flow, a velocity potential ϕ exists so that we can write $\hat{V} = \hat{\nabla}\phi$, and the continuity equation (1.41) becomes

$$\hat{\nabla}^2\,\hat{\phi} = 0 \qquad (1.44)$$

This is the classical Laplace equation that arises in many applications in classical physics. The study of its solutions is sometimes called potential theory due to its application in determining the gravitational field potential associated with distributions of mass.

With the same assumptions as above for arriving at the Bemoulli equation except that time dependence is still allowed, Equation (1.42) becomes

$$\frac{\partial}{\partial\hat{t}}(\hat{\nabla}\hat{\phi}) + \hat{\nabla}\left(\frac{\hat{V}^2}{2}\right) + \frac{1}{2}\hat{\nabla}c_p = \nabla\left(\frac{\partial}{\partial\hat{t}}\hat{\phi} + \frac{\hat{V}^2}{2} + \frac{1}{2}c_p\right) = 0 \qquad (1.45)$$

or

$$2\frac{\partial}{\partial\hat{t}}\hat{\phi} + \hat{V}^2 + c_p = \text{const} \qquad (1.46)$$

Equation (1.46) is referred to as the unsteady Bemoulli equation.

1.5 TIME **DEPENDENCE OF THE SOLUTIONS**

Real flows in wind tunnels and elsewhere are always unsteady. For sufficiently small values of the Reynolds number, flows can be established that are very nearly steady based on observations. In a small set of circumstances, there are known solutions to the Navier–Stokes equations. None of these are of direct value to vehicle designers, although they serve as an aid to aerodynamicists in trying to understand basic issues in fluid flow.

A vast majority of aerodynamic problems associated with vehicle design and wind engineering efforts involve flows that can be considered to have an incoming free stream that can be characterized by a time-independent mean flow with a superimposed additive fluctuating contribution most often characterized in terms of a "turbulence level." For some applications, the description of the unsteadiness in the incoming flow may be much more detailed, but still will be based on statistical descriptors rather than detailed space–time functions. The interaction with the body of interest creates a spatial modification of the mean flow and in general creates fluctuating motions in the flow in addition to those present in the incoming stream. Landahl and Mollo-Christensen[14] give a good treatment of methods and summaries of aspects of turbulence. Issues associated with modeling effects of turbulence, both experimentally and computationally, are the most difficult issues with which aerodynamicists must grapple.

There are important classes of problems frequently studied in wind tunnels for which the assumption that the boundary conditions on the fluid are independent of time is not valid. Examples are studies that involve propellers or rotors, towed devices suspended on thin cables, significant elastic deflections such as occur for flutter models, fabric structures such as parachutes or sails, forced or "free" motion of complete models, and manipulation of the incoming flow. Incoming flow may be manipulated to produce essentially deterministic large-scale variations in the flow or, as in the case of wind engineering studies, the incoming stream may be passed over roughness elements or otherwise processed to produce high levels of large-scale turbulence. In addition, the presence of significant acoustic signals can in some situations produce significant macroscopic effects. Aeroacoustic effects in low-speed flows have been receiving increasing attention in the 1990s.

1.6 AEROACOUSTICS

The system of equations previously given for compressible flow with appropriate boundary conditions and with considerable reduction through appropriate assumptions can be reduced to the equations commonly applied to model acoustic phenomena. The most influential paper on this topic is that of Lighthill,[15] who derived an equation containing the same assumptions as those required in deriving the Navier–Stokes equations for compressible flow. It has become known as Lighthill's equation. We show it here and discuss some general properties because these proper-

ties provide some insight into aeroacoustics phenomena whether the investigations are to be carried out numerically or experimentally. Lighthill's equation is given as

$$\frac{1}{a_0^2}\frac{\partial^2}{\partial t^2}p' - \nabla^2 p' = \frac{\partial^2 \mathbf{T}_{ij}}{\partial r_i\, \partial r_j} \tag{1.47}$$

where p' $= p - p_\infty$ and a_0 is the speed of sound in the free stream. The right-hand side contains $\mathbf{T}_{ij}$, the celebrated **Lighthill** stress tensor. Direct solution of aeroacoustic problems using this formulation has not been achieved for technically important problems. But it is the basis for much understanding of aeroacoustics, especially generation and propagation of sound from jet engines. A subsequent development by Ffowcs-Williams and **Hawkings**[16] is most important to currently ongoing efforts to develop methods of direct solution to aeroacoustic problems and to understanding of mechanisms of generation. They derived what has become known as the **Ffowcs-Williams–Hawkings** equation, and a formal solution is given here as Equations (1.48)–(1.51):

$$p'(\mathbf{r}, t) = M + D + Q \tag{1.48}$$

where the right-hand side is made up of

$$(\text{Monopole})\; M = -\frac{1}{4\pi}\frac{\partial}{\partial t}\int_S \left[\frac{\rho_\infty V_i n_i}{|R|\, 1 - M\cos\phi|}\right]_{t_e} dS \tag{1.49}$$

$$(\text{Dipole})\; D = \frac{1}{4\pi}\frac{\partial}{\partial r_i}\int_S \left[\frac{(p - p_\infty)n_i}{|R|\, 1 - M\cos\phi|}\right]_{t_e} dS \tag{1.50}$$

$$(\text{Quadropole})\; Q = \frac{1}{4\pi}\frac{\partial^2}{\partial r_i\, \partial r_j}\int_V \left[\frac{\mathbf{T}_{ij}}{R\,|\,1 - M\cos\phi\,|}\right]_{t_e} d\mathbf{r}_s \tag{1.51}$$

There are a large number of variables. On the right-hand sides the variables are as follows: $(\mathbf{r}, t)$ gives the time and space location of the "observer." The spatial variables of integration are the coordinates of the sources as indicated by $\mathbf{r}_s$ and evaluated at the "retarded time" t_e. This is the time at each source element for which the emitted signal will reach the observer at time t The source–observer vector is given by $\mathbf{R} = \mathbf{r} - \mathbf{r}_s$, $R = |\mathbf{R}|$, ϕ is the angle between $\mathbf{r}$ and $\mathbf{r}_s$, n_i is the unit normal to the body surface enclosed by S, V_i are the fluid velocity components, M is the Mach number, and $\mathbf{T}_{ij}$ is Lighthill's stress tensor.

Very important descriptive interpretations have been given for the three terms, and they are found to scale very differently with flow speed. The "monopole" term is identified with a vibrating solid surface or an oscillating mass source. Examples are loudspeaker cones, vibrating sheet metal or glass, or the pulsating gas emitted from an automobile exhaust pipe. These are the most efficient generators of sound. The associated intensities increase as the fourth power of the fluid velocity.

The "dipole" term is identified with an oscillating pressure on a solid surface that then acts as a sound radiator. This will occur on a surface under a turbulent boundary layer or on the surface of a fixed circular cylinder that is undergoing the periodic shedding of the Karman vortex street phenomena. The efficiency of the dipole source type is intermediate between that of a monopole and a quadropole. The intensity increases as the sixth power of the velocity.

The "quadropole" term is a volume source associated with fluctuating gradients. It is more difficult to visualize but is associated with highly sheared turbulent flow volumes like the shear layers bounding rocket and jet engine exhausts. The intensity increases as the eighth power of the velocity. This can be the dominant type of source for jet and rocket engines.

For low-speed wind tunnel studies, there will be monopole-type sources if there are vibrating surfaces. Variations in noise generation due to shape changes are generally associated with the dipole type of source.

We will give some additional brief sections on aeroacoustics at other points in the book as it is being met at low-speed wind tunnels. Blake[11] has written one of the most useful technical treatments.

REFERENCES AND NOTES

1. The term *aerodynamics* as used here and throughout this book is intended in a broad sense as being synonymous with *fluid dynamics.*

2. Anderson, J. D., Jr., *Fundamentals of Aerodynamics,* 2nd ed., McGraw-Hill, New York, 1991.

3. Shames, I. H., *Fluid Mechanics,* 2nd ed., McGraw-Hill, New York, 1994.

4. Buckingham, E., "On Physically Similar Systems, Illustration of the Use of Dimensional Equations," *Phys. Rev.,* 4, 345–376, 1914. See also: "Model Experiments and the Forms of Empirical Equations," *Trans. ASME,* 37, 263–288, 1915.

5. Karamcheti, K., *Principles of Ideal Fluid Aerodynamics,* John Wiley & Sons, New York, 1966, Chapter 1.

6. Sedov, L. I., *Similarity and Dimensional Methods in Mechanics,* 10th ed., CRC Press, Boca Raton, FL, 1993.

7. David, F. W., and Nolle, H., *Experimental Modeling in Engineering,* Buttenvorths, London, 1982.

8. Baker, W. E., Westine, P. S., and Dodge, F. T., *Similarity Methods in Engineering Dynamics: Theory and Practice of Scale Modeling,* rev. ed., Elsevier, New York, 1991.

9. Schlichting, H. S., *Boundary Layer Theory,* McGraw-Hill, New York 1960.

10. Loitsyanskii, L. G., *Mechanics of Liquids and Gases,* Pergamon, New York, 1966.

11. Staff of Ames Research Center, "Equations, Tables, and Charts for Compressible Flow." NACA Report 1135, 1953.

12. Jones, F. E., *Techniques and Topics in Flow Measurements,* CRC Press, Boca Raton, FL, 1995.

13. *Handbook of Chemistry and Physics,* 61st ed., CRC Press, Boca Raton, FL, 1980–81, p. F-51.

14. Landahl, M. T., and Mollo-Christensen, E., Turbulence and Random Processes in Fluid Mechanics, 2nd ed., Cambridge University Press, Cambridge, 1992.

15. Lighthill, M. J., "On Sound Generated Aerodynamically: I General Theory," Proc. Roy. *Soc.,* 211, 564–587, 1952.

16. Ffowcs-Williams, J. E., and Hawkings, D. L., "Sound Generation by Turbulence and Surfaces in Arbitrary Motion." *Phil.* Trans. Roy. Society, 264 (1151), 301–346, 1969.

17. Blake, W. K., Mechanics of Flow-Induced Sound and Vibration, Academic, New York, 1986.

2 Wind Tunnels

Experimental information useful for solving aerodynamic and hydrodynamic problems may be obtained in a number of ways: from flight experiments; drop tests; rocket sleds; water tunnels; whirling arms; shock tubes; water tables; rocket flights; flying scale models; road tests; ballistic ranges; subsonic, near sonic, transonic, supersonic, and hypersonic wind tunnels; and other methods leading to an almost endless list. Each device has its own sphere of superiority, and no one device can be called "best."

This book considers only the design and use of low-speed wind tunnels. Because they make it possible to use models that can be prepared early in design cycles, because they include the full complexity of real fluid flow, and because they can provide large amounts of reliable data, wind tunnels are often the most rapid, economical, and accurate means for conducting aerodynamic research and obtaining aerodynamic data to support design decisions. Their use saves both money and lives.

The nations and industries of the world support aerodynamic research and development, of which conducting wind tunnel experiments is a major item, according to their needs, abilities, and desires. In many countries there is a separate national research organization that augments the activities of the armed services. A substantial amount of work is contracted from national agencies to universities and industry. There is a considerable and growing volume of aerodynamic research and development done by corporations for civil purposes in the development of aircraft, automobiles, marine vehicles, and architectural structures. A cross section of entities from all of these areas is represented by the membership of the Subsonic Aerodynamic Testing Association (SATA). The membership of the SATA in 1998 is given in Appendix 1.

2.1 IMPORTANT PARAMETERS FOR SIMILARITY

Since conducting experiments using scale models is the primary activity of most major wind tunnels, we pause now and consider aspects of experiments using scale models, the results of which may effectively be used to predict full-scale behavior. In Chapter 1 we have given the equations for fluid motion in nondimensional form. These equations provide a foundation for designing scale experiments and interpreting the resulting data. For present purposes, the results of principal interest are the dimensionless coefficients that appear in the nondimensional form of the fluid dynamics equations as derived in Chapter 1. The three coefficients are the

Reynolds number, the Mach number, and the Froude number. The coefficients as developed in Chapter 1 were obtained by introducing nondimensional variables into the conservation equations. We will now consider a more heuristic approach.

When a body moves through a fluid, forces arise that are due to the viscosity of the fluid, its inertia, its elasticity, and gravity. These forces are represented directly by the various terms in the Navier-Stokes equation. The inertia force, corresponding to the left-hand side of the Navier–Stokes equation, is proportional to the mass of air affected and the acceleration given that mass. Thus, while it is true that a very large amount of air is affected by a moving body (and each particle of air a different amount), we may say that the inertia force is the result of giving a constant acceleration to some "effective" volume of air. Let this effective volume of air he kl^3, where l is a characteristic length of the body and k is a constant for the particular body shape. Then we may write

$$\text{Inertia force} = \frac{\rho l^3 V}{t}$$

where ρ is the air density (slugs/ft^3), V is the velocity of the body (ft/sec), and t is time (sec).

Substituting l/V for t, we get

$$\text{Inertia force} = \frac{\rho l^3}{l/V} = \rho l^2 V^2 \tag{2.1}$$

The viscous force, according to its definition, may be written as

$$\text{Viscous force} \sim \mu V l \tag{2.2}$$

where μ is the coefficient of viscosity (slug/ft-sec).

The gravity force is proportional to the volume of the body, which in turn is proportional to the cube of the reference length. The gravity force may be written

$$\text{Gravity force} = \rho l^3 g \tag{2.3}$$

where g is the acceleration of gravity. Keep in mind that the gravity force term in the Navier–Stokes equation is the force on the fluid. It is not the gravity force on the body. As mentioned in Chapter I, it is necessary to introduce the equations of motion of the body along with the equations of motion of the fluid to carry out a formal nondimensionalization for the case of a fully coupled system of the motion of the body moving under the influence of the fluid and gravitational forces. However, in the present heuristic consideration, we may consider the gravity force on the body to have the same form as the gravity force on the fluid but with a different constant of proportionality.

The elastic force may be considered to be simply

$$\text{Elastic force} \sim pl^2 \qquad (2.4)$$

The speed of sound a in a fluid is related to pressure and density according to

$$a^2 \sim \frac{p}{\rho}$$

so that we may write

$$\text{Elastic force} = \rho a^2 l^2$$

Dividing the inertia force by each of the others gives three force ratios that, as can be seen in Equations (2.5)–(2.7), are the same forms as the dimensionless coefficients that appear in Chapter 1:

$$\text{Reynolds number} = \frac{\text{inertia force}}{\text{viscous force}} = \frac{\rho}{\mu} Vl \qquad (2.5)$$

$$\text{Mach number} = \frac{\text{inertia force}}{\text{elasticity force}} = \frac{V}{a} \qquad (2.6)$$

$$\text{Froude number} = \sqrt{\frac{\text{inertia force}}{\text{gravity force}}} = \sqrt{\frac{V^2}{lg}} \qquad (2.7)$$

The last equation, it will be noted, uses the square root of the ratio rather than the ratio itself. For wind tunnel experiments, the Froude number is an important similarity parameter only for dynamic tests in which model motion as well as the aerodynamic forces are involved. Although such experiments are very important, they constitute a minority of the experimental program in most wind tunnels. Such experiments will be treated in more detail later in the book.

For experiments in which the model is held stationary during data gathering, the Reynolds number and Mach number are the significant similarity parameters. If a model experiment has the same Reynolds and Mach numbers as the full-scale application, then the model and the full-scale flows will be dynamically similar. The nondimensional functions for fluid velocity components, pressure coefficient, density, viscosity, and temperature will then be the same for the model and the full-scale flows. In turn the force and moment coefficients will be the same for the model and full-scale flows.

Under these conditions, the forces developed by the model can be directly related to the forces on the full-scale article by multiplying the force coefficients obtained in the experiment using the model by the factor $\frac{1}{2}\rho_\infty V_\infty^2 l^2$ with the values of parameters in the factor corresponding to full scale. The moments developed by the model can

be directly related to the moments on the full-scale article by multiplying the moment coefficients obtained in the experiment using the model by the factor $\frac{1}{2}\rho_\infty V_\infty^2 l^3$ with the values in the factor corresponding to full scale.

In practice it is seldom possible to match both Reynolds number and Mach number to full scale in a model experiment. In fact, it is frequently the case that neither Reynolds number nor Mach number can be matched. Choices must then be made on the basis of which parameter is known to be most important for the type of flow situation under consideration.

The matching of Mach number usually applies only to flight vehicles in the high-speed flight region as Mach number effects predominate and the matching of Reynolds number effects is not as critical. In the low-speed flight region Reynolds number effects predominate and matching of Mach number is not as critical. However, for any experiment a careful evaluation of the effect of Reynolds and Mach numbers should be made to ensure that the results can be applied to the full-scale problem. Many wind tunnel experiments are seriously sensitive to Reynolds number effects, and no experiment should be attempted without knowledge of material like that found in Chapter 8 and a discussion with the experienced operators of the tunnel to be used.

Despite the fact that it is difficult, if not impossible, to match both Reynolds and Mach numbers in most wind tunnel experiments, the wind tunnel still is one of the most useful tools an aerodynamics engineer has available to him or her. Skillful use of the wind tunnel can make strong contributions to the aerodynamics engineer's goal of quickly and efficiently optimizing his or her design. The more complex the flow phenomena involved, the more important will be the role of the wind tunnel.

An interesting and useful fact that follows from the scaling relations is that the force on a body of a particular shape for which the flow characteristics are a function only of Reynolds number is the same regardless of the combination of size and speed that is used to produce the particular Reynolds number if the fluid, its temperature, and the free-stream pressure are unchanged. This can be seen by writing the expression for a particular force component. Choosing drag, we have

$$D = \frac{1}{2}\rho_\infty V_\infty^2 l^2 C_d(R_e) = \frac{1}{2}\frac{\rho_\infty^2 V_\infty^2 l^2}{\mu_\infty^2}\frac{\mu_\infty^2}{\rho_\infty^2} C_d(R_e)$$

or

$$D = \frac{\mu_\infty^2}{2\rho_\infty} R_e^2 C_d(R_e) = \frac{\mu_\infty^2 RT_\infty}{2p_\infty} R_e^2 C_d(R_e) \tag{2.8}$$

This indicates that the drag on a particular shape with length of 10 ft at 20 mph is the same as the drag on the same shape with a length of 1 ft at 200 mph if the fluid temperature and pressure are unchanged. Or the force on a $\frac{1}{8}$-scale truck model at 200 mph is the same as the force on the full-scale vehicle at 25 mph.

2.2   RESEARCH AND DEVELOPMENT PROGRAMS

Aerodynamic research and development programs should be based on available existing information from all pertinent sources. This would certainly start with a sound basis in the current state of aerodynamic theory. Appropriate results, if such exist, from previous experiments and from previous computational studies are typically of great value. The aerodynamics engineer must then choose approaches to develop the specific information required to meet the objectives of the immediate program. Three broad categories are commonly recognized: analytical, computational, and experimental. The analytical approach plays a vital role in the background studies and in gaining an appreciation for possibilities, but it never suffices for a vehicle development program. All development programs from the time of the Wright Brothers to the 1960s were based on a combination of analytical and experimental approaches. During the 1960s the evolution of the digital computer reached a point where solutions to approximate forms of the fluid dynamic equations could be obtained for vehiclelike geometries. The development of methods and computing machinery have advanced rapidly and have led to many predictions that "computers will replace wind tunnels.'" Hans Mark was the author of one of the more widely quoted such predictions. It has turned out, however, that the continuing dizzy pace of development of computers notwithstanding, the complexity of real flows has only partially been tamed by the computational approach. Practical computations for complete vehicles for the foreseeable future will require "turbulence models" that up to now at least must be tailored for specific types of flow. Hammond[1] presented a review of progress in application of computers to engineering development in both structural mechanics and fluid dynamics. In the case of fluid dynamics he gave three aspects of development as pacing items for increasing the effectiveness of applications of the computer: central processing speed, size of memory available, and turbulence models. The first two continue to advance at a rapid rate. In the case of turbulence models, Hammond asserted that while many have been developed it is not clear that there has been progress in terms of achieving generality or significantly improved performance in the period from 1964 to 1994. Ockendon and Ockendon[2] assert that "modeling turbulence is the major unsolved problem of fluid dynamics." This is the Achilles heel of current efforts to extend applications of computational aerodynamics.

The approaches to numerically solving the Navier–Stokes equations that are currently used and currently being investigated are discussed by Speziale.[3] The direct numerical solution (DNS) with no turbulence modeling is limited now and for the foreseeable future to simple geometries and low- to moderate-turbulence Reynolds numbers. According to Speziale, the direct numerical simulations of complex turbulent flows that are of technological importance could require the generation of databases with upward of 10^{20} numbers. This is unlikely to be possible in the near future, and even should it become feasible, it is not clear how this would result in a technologically useful result. The next line of attack that has been expected to minimize requirements for modeling turbulence is large eddy simulation (LES). Speziale discusses the failure of LES to live up to its earlier promise and is proposing

methods to blend the best of LES with Reynolds Averaged Navier–Stokes (RANS) methods in an effort to provide more technologically useful methods within capabilities of current and near-future computational machinery. Computational methods are now an important tool to be applied in aerodynamic development programs, but it should be recognized that they are best used in conjunction with analytical and experimental methods.

In addition, there is a lurking fundamental mathematical question concerning the Navier–Stokes equations. According to Doering and Gibbon! it remains uncertain whether the Navier–Stokes equations, even for incompressible cases, are actually a self-consistent system (pp. xi–xii):

> It has never been shown that the Navier–Stokes equations, in three spatial dimensions, possess smooth solutions starting from arbitrary initial conditions, even very smooth, physically reasonable initial conditions. It is possible that the equations produce solutions which exhibit finite-time singularities. If this occurs, then subsequent evolution may be nonunique, violating the fundamental tenets of Newtonian determinism for this model. Furthermore, finite-time singularities in the solutions signal that the equations are generating structures on arbitrarily small scales, contradicting the separation-of-scales assumption used to derive the hydrodynamic equations from microscopic models. It turns out that the nonlinear terms that can't be-controlled mathematically are precisely those describing what is presumed to be the basic physical mechanism for the generation of turbulence, namely vortex stretching. So what may appear to applied scientists to be mathematical formalities, i.e., questions of existence and uniqueness and regularity, are actually intimately tied up with the efficacy of the Navier–Stokes equations as a model for fluid turbulence. Whether or not the equations actually do display these pathologies remains an open problem: It's never been proved one way or the other.

This is an issue of far greater importance to analytical and computational efforts than to experimental work of the nature undertaken to support vehicle design.

Advances in computing power have contributed greatly to the capabilities and cost effectiveness of wind tunnels and other experimental facilities. Even small wind tunnels today will commonly have a dedicated computer to manage data gathering and presentation and possibly provide control of the experiment. This is true of all large wind tunnels. The time required to present the corrected data in graphical and/or tabulated form is typically of the order of milliseconds after the measurement is taken. It is now common to have the analytical and/or analytical predictions that have been used to design the experimental program available for direct graphical comparison as the experimental points are obtained. This enables the aerodynamics engineer both to check the predicted results and, based on the results of one tunnel run, to make an informed choice among the optional parameters that can be chosen for the next run. The most important parts of the matrix or conditions to be included in an experiment will be those parts that are most at variance with the analytical or computational predictions.

The availability of increased computing power has contributed in other ways to the effectiveness of wind tunnel programs. The process of model design and construc-

tion has been affected by the wide use of computer-based design, which provides numerical geometry specifications that are transmitted from designer to model maker electronically instead of by paper drawing. This can shorten the time required to prepare for an experiment provided the wind tunnel facility is intimately involved with the model design so that tunnel mounting features are included in the initial model realization.

There are new measurement methods that have been enabled by the availability of powerful dedicated computers and the potency of old methods has been amplified greatly. Many of these will be discussed later in this book.

Emerging communication technology such as the World Wide Web when linked to the highly computerized wind tunnel of today and tomorrow offers a possibility of the wind tunnel as a virtual laboratory for people for whom physical presence is not convenient or cost effective. This is a role that is likely to become more important as project teams are increasingly diversified and information must be delivered with the absolute minimum time delay to a cross section of the development team who may be geographically dispersed.

2.3   TYPES OF WIND TUNNELS

There are two basic types of wind tunnels and two basic test-section configurations. However, there are almost endless variations on the specific features of various tunnels. Virtually every wind tunnel with a test section larger than 2 s ft² is one of a kind. The two basic types are open circuit and closed circuit. The two basic test-section configurations are open test section and closed test section, although these must now be considered as the two ends of a spectrum since slotted wall test sections are now in use for low-speed as well as transonic wind tunnels.

The air flowing through an open circuit tunnel follows an essentially straight path from the entrance through a contraction to the test section, followed by a diffuser, a fan section, and an exhaust of the air. The tunnel may have a test section with no solid boundaries (open jet or Eiffel type) or solid boundaries (closed jet or National Physical Laboratory (NPL) type). Figure 2.1 shows a plan view of an open circuit tunnel with a closed jet.

The air flowing in a closed return wind tunnel, Prandtl, or Gottingen type, recirculates continuously with little or no exchange of air with the exterior. An example of a closed circuit tunnel is shown in Figure 2.2.

The great majority of the closed circuit tunnels have a single return, although tunnels with both double and annular returns have been built. Again, the closed circuit tunnel may have either a closed or open test section, and a number have been built that can be run with either an open or closed test section, as needed for a particular experimental program. As with any engineering design, there are advantages and disadvantages with both the open- and closed-circuit-type tunnels and with both open and closed jets. In general, the type of tunnel decided upon depends on funds available and purpose.
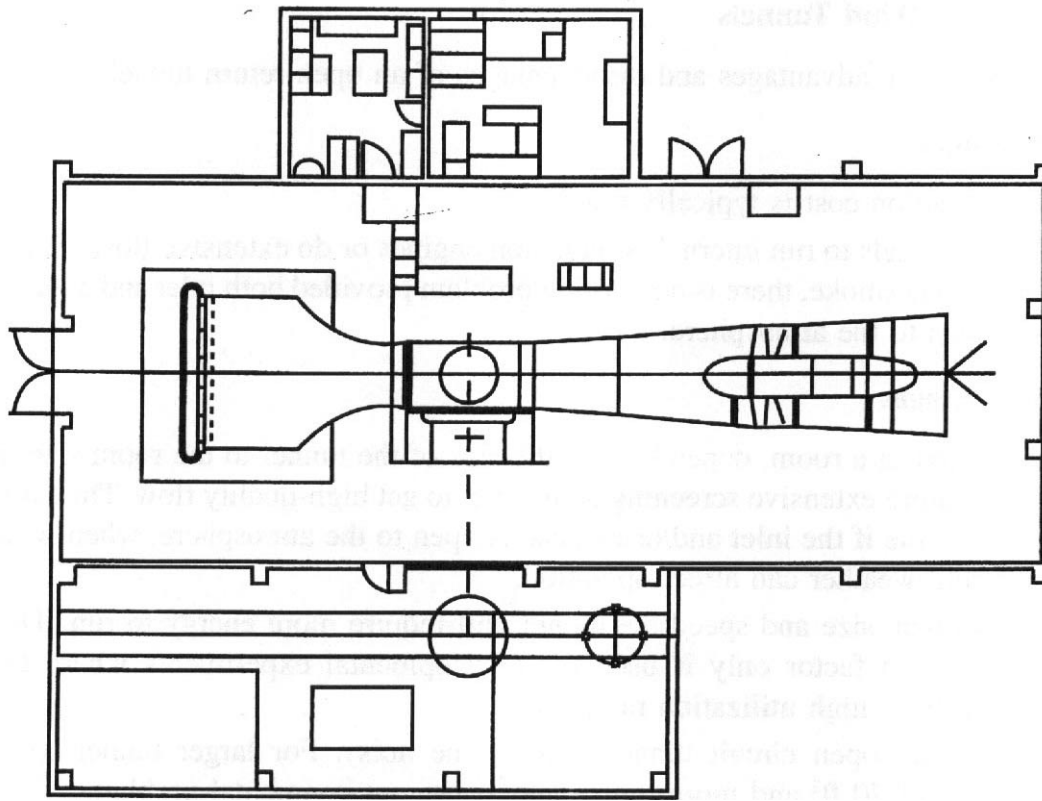
FIGURE 2.1   Plan view of an open circuit wind tunnel (Diamler-Benz Aerospace Airbus, Bremen, Germany).
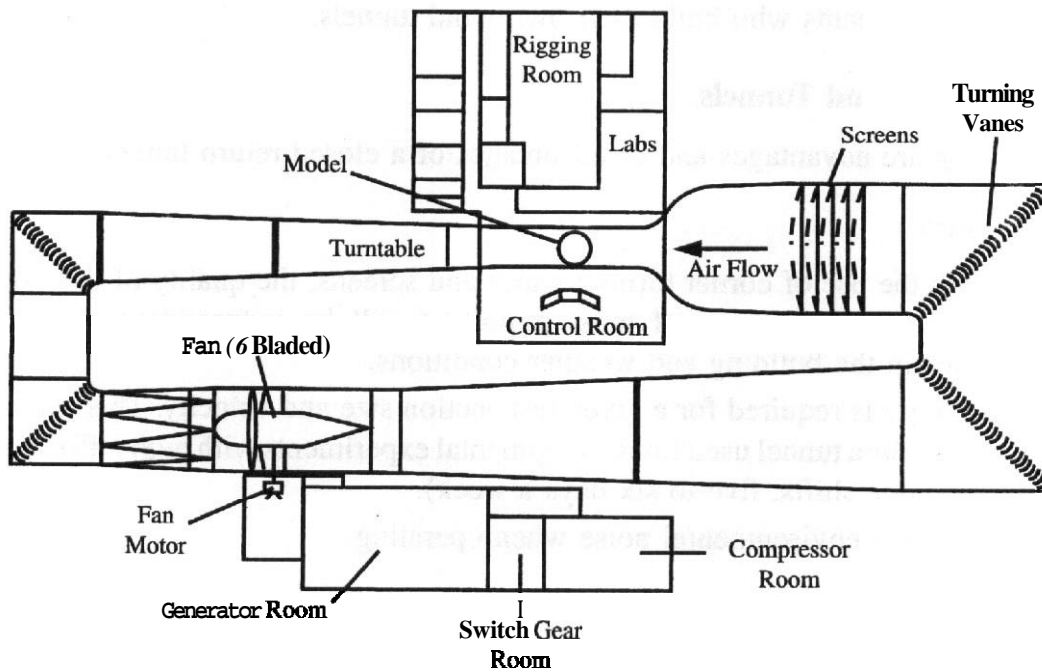
FIGURE 2.2   A closed circuit wind tunnel, Defense Establishment Research Agency (DERA), 13 × 9-ft tunnel in Bedford, England.

Open Return Wind Tunnels

The following are advantages and disadvantages of an open return tunnel:

Advantages

1. Construction cost is typically much less.
2. If one intends to run internal combustion engines or do extensive flow visualization via smoke, there is no purging problem provided both inlet and exhaust are open to the atmosphere.

Disadvantages

1. If located in a room, depending on the size of the tunnel to the room size, it may require extensive screening at the inlet to get high-quality flow. The same may be true if the inlet and/or exhaust is open to the atmosphere, when wind and cold weather can affect operation.
2. For a given size and speed the tunnel will require more energy to run. This is usually a factor only if used for developmental experiments where the tunnel has a high utilization rate.
3. In general, open circuit tunnels tend to be noisy. For larger tunnels (test sections of **70** ft^2 and more) noise may cause environmental problems, limit hours of operations, and/or require extensive noise treatment of the tunnel and surrounding room.

Because of the low initial cost, an open circuit tunnel is often ideal for schools and universities where a tunnel is required for classroom work and research and high utilization are not required. Open circuit designs are also frequently used by science fair participants who build their own wind tunnels.

Closed Return Wid Tunnels

The following are advantages and disadvantages of a closed return tunnel:

Advantages

1. Through the use of comer turning vanes and screens, the quality of the flow can be well controlled and most important will be independent of other activities in the building and weather conditions.
2. Less energy is required for a given test-section size and velocity. This can be important for a tunnel used for developmental experiments with high utilization (two or three shifts, five to six days a week).
3. There is less environmental noise when operating.

Disadvantages

1. The initial cost is higher due to return ducts and comer vanes.
2. If used extensively for smoke flow visualization experiments or running of internal combustion engines, there must be a way to purge tunnel.

3. If tunnel has high utilization, it may have to have an air exchanger or some other method of cooling.

Open or Closed Test Section?

An open test section in conjunction with an open circuit tunnel will require an enclosure around the test section to prevent air being drawn into the tunnel from the test section rather than the inlet.

For closed return tunnels of large size with an external balance, the open test section tends to have one solid boundary, since the balance must be shielded from the wind. This is an anomaly for aircraft experiments other than takeoff and landing, but it is a natural condition for exveriments on automobiles or surface-borne marine vehicles.

Many open test-section, closed circuit tunnels have experienced severe flow fluctuation problems that require extensive postconstruction diagnostics and corrective actions. One of the tunnels currently acknowledged to be one of the most useful tunnels in existence nevertheless has had substantial difficulties with unsteady flow and noise when running in the open test-section configuration.

The most common geometry is a closed test section, but a wide range of tunnel geometries have provided good experimental conditions once the tunnel idiosyncrasies have become known to the operators and users. Slotted wall test sections are becoming more common as are test sections that can be converted among two or more configurations.

It is also noted that in larger size tunnels a rectangular test section is preferable because it is easier to change a model when working off a flat surface. Further, if automobile or other ground vehicle experiments are to be conducted, a flat floor is a requirement.

Test-Section Size

In general it may be expected that the test section should have as large a cross-sectional area as possible. Ideally, a tunnel would be large enough to handle a full-scale vehicle. In fact, several tunnels were built in the 1920s through the 1940s to achieve this goal for aircraft. A number of tunnels are available in which full-scale automobiles are routinely used as test articles. However, since the World War II era, and presumably in the future, the size of aircraft have become such that wind tunnels to accommodate full-scale vehicles are not practical. If one uses the rule of thumb that the model span should be less than 0.8 of tunnel width, then Howard Hughes' *Hercules,* or as more popularly known, the "Spruce Goose," which was designed and built in the 1940s with a 320-ft wing span, would require a test section 400 ft wide. The cost of building and operating a tunnel of this size is staggering to contemplate. The cost of building a model, transporting it, and erecting it in the tunnel, as well as making changes during an experimental program, would also be an interesting, albeit expensive task. Thus, it is apparent that for the larger of modem aircraft, the concept of a tunnel to accommodate full-size aircraft is out of the

question based on costs. Recalling the earlier discussions of flow similarity, it is more important to seek to obtain Reynolds numbers for the model experiments that are as near as possible to the full-scale values than to be concerned with size alone. Consideration of this goal is given in the following. In practice most development experiments are done in tunnels with widths from 10 to 20 ft.

2.4 AERONAUTICAL WIND TUNNELS

A large fraction of wind tunnels have been designed and used for aeronautical purposes. For high-speed tunnels capable of sonic speeds or more, this is still the case. There are an increasing number of wind tunnels in use exclusively for other than aeronautical applications. We provide synopses of a number of specialized classes of facilities.

High-Reynolds-Number Tunnels

It is often not practicable to obtain full-scale Reynolds numbers by use of a full-scale vehicle in an experimental facility; however, there are methods of increasing the Reynolds number with smaller tunnels and models.

One of the oldest methods is to build a tunnel that can be pressurized. In fact, some of the earliest definitive work on Reynolds number effects was done in pressurized tunnels. The NACA variable-density tunnel (VDT)[5] that began operation in 1929 and the similar compressed-air tunnel at NPL in England were pressure tunnels (VDT up to 20 atm) and were used to simulate high Reynolds numbers. These tunnels used an annular return duct, because this design required the minimum amount of steel. The VDT, despite a high level of turbulence, yielded a good deal of insight into the effect of Reynolds numbers up to about 10 million on the characteristics of 78 airfoils.[6] The reason for pressurization can be seen by examination of the equation of state for a perfect gas and the equation for Reynolds number [Equation (2.5)]. If one increases the pressure by a factor of 20, the density, and hence the Reynolds number, for a given size and speed is increased by a factor of 20.

Some basic issues related to cost of construction and cost of operation of pressurized tunnels must be considered. The shell cost for a given size will be greater but the proper comparison is the shell cost for equal Reynolds number. Necessary compressor equipment will add to the cost for pressurized tunnels, and for larger facilities, the provision of access to the model test area without decompressing the entire tunnel will add to construction complexity and cost. Operation of pressurized facilities involves additional time to change the pressure condition and to access the model, which reduces productivity of the facility and thereby increases the cost to users. Despite these problems, there have been many tunnels built that can be pressurized to obtain higher Reynolds numbers.

A second approach is to change the working fluid. For a given power input the use of Freon 12 can increase the Mach number by a factor of 2.5 and the Reynolds

number by a factor of 3.6. Again, many of the problems of a pressure tunnel will exist, such as initial cost, cost of pumps, cost of the gas, and a method of making the test section habitable for model changes. The Transonic Dynamics Tunnel at the National Aeronautics and Space Administration (NASA) Langley is an example of a tunnel that used Freon 12 as the working fluid beginning in 1960. Recent recognition of detrimental effectson the environment from the use of Freon has led to plans to use a different heavy gas, referred to as R-134a.[7]

A third approach is that of a cryogenic tunnel. NASA has built such a facility at its Langley Research Center called the National Transonic Facility (NTF).[8] Although this tunnel is intended for transonic experiments, the same concept applies for a low-speed tunnel. The NTF tunnel combines the ability to operate at cryogenic temperatures with the ability to change pressure up to 9 atm. The working fluid is nitrogen, and by injecting liquid nitrogen upstream of the fan, the gas is cooled. By this technique it is possible to operate over a range of dynamic pressures and Reynolds numbers at a constant temperature to the tunnel's stagnation pressure limit, similar to any pressure tunnel. *Or,* the tunnel can be run at constant dynamic pressure, and by changing temperature, the Reynolds number can be changed. The range of unit Reynolds number and Mach number is impressive, varying from 1×10^6 to over 100×10^6 per foot. This sort of facility is very expensive both to build and to operate, but it does show what can be achieved in a wind tunnel. Low productivity of the NTF due to the long times required to cycle and stabilize the temperature has prevented it from being useful as a development facility. The European Transonic Facility at Cologne, Germany, is another high-Reynolds-number tunnel based on operation at cryogenic temperatures.

V/STOL Wind Tunnels

These tunnels require a much larger test section for a given size model owing to large downwash angles generated by powered lift systems in the transition flight region. Flight velocities in the transition region are low; thus tunnels with large test sections used for this purpose do not need high velocities, the maximum being in the 60–100-mph range, compared to the 200–300-mph range for a conventional low-speed wind tunnel. Since power varies with the cube of velocity, this reduces the installed power requirement. There will be, however, a demand to run the tunnel at higher speeds with conventional models; thus the tunnel will typically be powered for the higher speeds. This was the solution in both the Boeing Helicopter Co. tunnel[9] (test-section area 400 ft²) and the NASA Langley vertical/short takeoff and landing (V/STOL) tunnel (test-section area 300 ft²).

Another solution to the problem of building V/STOL tunnels is that taken for the Lockheed Martin Aeronautical Systems Co. tunnel. A drawing of the circuit is shown in Figure 2.3. The Lockheed low-speed wind tunnel has tandem test sections with two contractions. The first, and larger, test section is for V/STOL or powered lift models and has a cross-sectional area of 780 ft² with speeds from 23 to 115 mph. The second test section has a cross section of 378 ft² and speeds from 58 to 253 mph. This design avoids the high installed power required to drive the larger
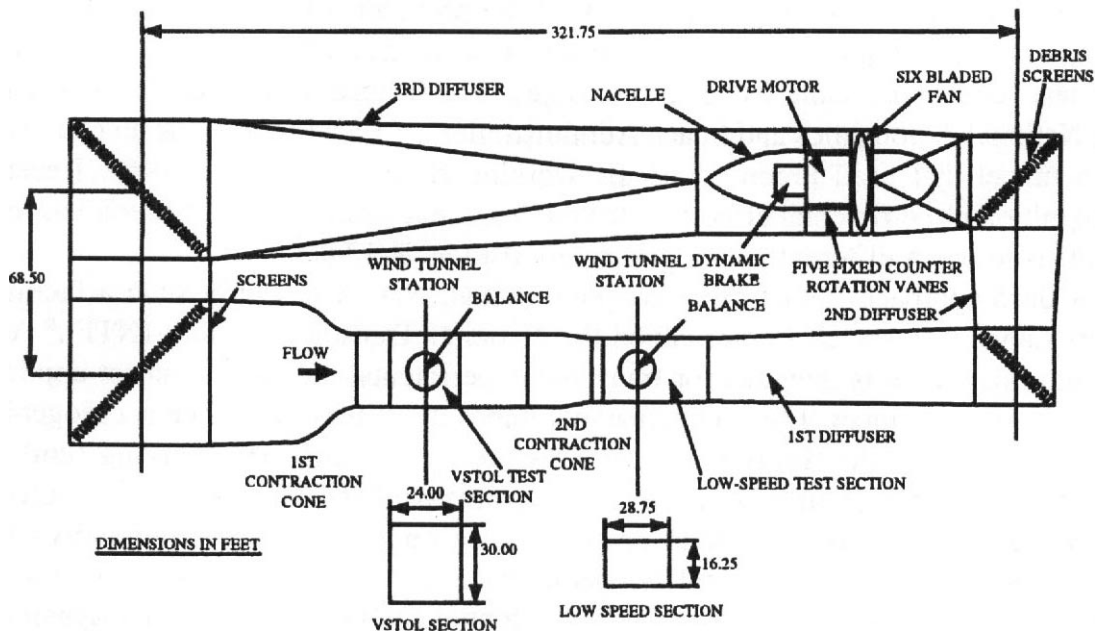
FIGURE 2.3 Tandem section design, Lockheed Martin Aeronautical Systems tunnel in Marietta, **Georgia.**

test section at high speeds. The length of the tunnel is increased by this solution, increasing the shell cost.

Another approach to a larger test section at low speeds for V/STOL and a smaller test section at higher speeds is to provide multiple interchangeable test sections. This is attractive, but the time required to install and remove the large inserts must be taken into account in the operational availability of the tunnel facility. The United Technologies Research Center has a large wind tunnel with interchangeable test sections.

The most economical approach to providing V/STOL tunnels has been to modify an existing wind tunnel. One of the least expensive methods of obtaining V/STOL capability is to use some portion of an existing tunnel **return** circuit for a V/STOL test section. This could be the settling area ahead of the contraction cone or, possibly, the end of the diffuser. These test sections may suffer from poorer flow quality than a tunnel built for the purpose, but this can be made acceptable by use of screens and honeycombs. The speed available will also be determined by the original tunnel dimensions. However, by using internal balances and a sting support, one can obtain V/STOL capabilities at an acceptable cost.

Another approach to modifying an existing tunnel for V/STOL experiments is to add another leg or legs to the tunnel. The McDonnell-Douglas low-speed tunnel actually has three legs. With this arrangement, they can operate with an 8 × 12-ft closed test section up to 200 mph or as a closed return tunnel with an open throat 15 × 20-ft V/STOL test section up to 80 mph. The V/STOL 15 × 20-ft open throat test section can also be operated as an open return tunnel up to 60 mph.

A second approach to adding another leg is the NASA Ames modification to the 40 × 80-ft closed throat tunnel, also known as the National Full Scale Facility.

The new leg forms basically an open circuit tunnel with a closed throat test section with dimensions of 80 X 120 ft. In this modification the tunnel was also repowered and new fans were built to increase the speed in both test sections.[10]

Another approach to an inexpensive V/STOL tunnel was the modification of an engine test cell by British Aerospace Aircraft. Again, this is an open circuit tunnel with a closed 18 X 18-ft test section. In the design and construction of the tunnel, many problems associated with large open circuit tunnels, such as the effect of gusts on the test-section flow and the effect of weather, were addressed.

These few examples show that there are many ingenious and practical solutions to adapting an existing facility for new experiments. The facilities of the SATA include other V/STOL capable tunnels.

Free-Flight Tunnels

In the 1930s several "free-flight" tunnels were built. These tunnels were of the open return type and were arranged so that dimensionally and dynamically scaled models could be flown under the influence of gravity. The tunnels could be tilted to set the angle of the air stream to match the glide path of the model. The dynamic behavior of the model could be studied in these tunnels, and often control surfaces could be deflected by command through a trailing wire. At present, none of these tunnels are in operation as a free-flight tunnel. NASA Langley has performed a considerable number of free-flight experiments in the 30 X 60-ft tunnel" with powered models. This facility has been used to study V/STOL transition, stalls, and loss of control of aircraft models.[12] The simulations in these tunnels are at very low Reynolds numbers, so care must be exercised in extrapolating the results to much higher Reynolds number conditions.

Spin Tunnels or Vertical Wind Tunnels

The tendency of some aircraft to enter a spin after a stall and the subsequent need to determine actions to achieve recovery from the spin have been perennial problems of the aircraft designer. The recovery from a spin is studied in a spin tunnel.[13] This is, in most cases, a vertical wind tunnel with the air drawn upward by a propeller near the top of the tunnel. An example is shown in Figure 2.4. Some spin tunnels use an annular return with turning vanes while others are open circuit with the air drawn in at the bottom and emitted at the top. A dynamically similar model is inserted into the tunnel by an operator in a spinning attitude. The tunnel air speed is adjusted to hold the model at a constant height and the model's motions recorded by movies and/or video for later analysis.[14] Spin tunnels are also equipped with six-component rotary balances so that direct force measurements can be made for the aircraft over a range of rotation rates at various attitudes. In this way spin modes can be predicted from the measurements without the restrictive requirement of dynamic scaling of the model,[15] and predictions for transient motions can be obtained by using the data in six-degree-of-freedom simulation programs. A number of spin
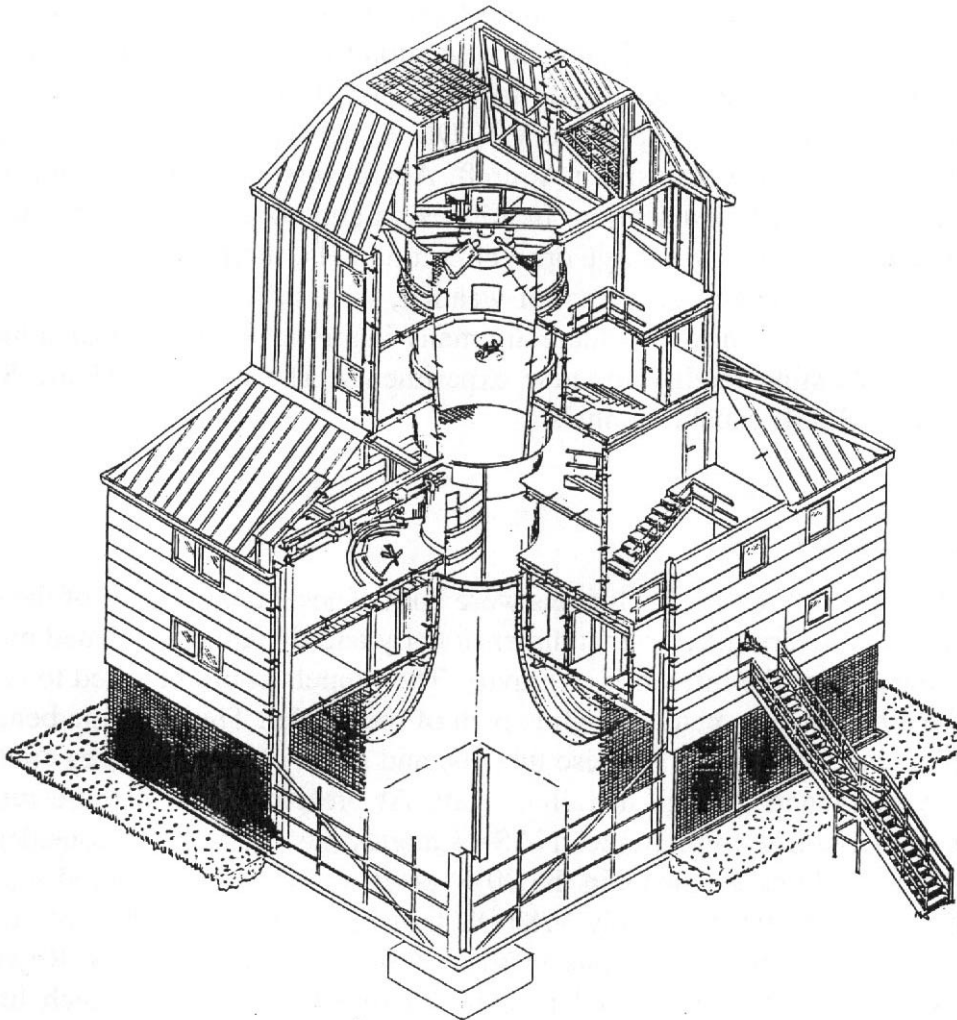
FIGURE 2.4   A vertical tunnel, Bihrle Applied Research Tunnel, Germany

tunnels have been built in several countries. Rotary balances have also been installed in horizontal wind tunnels to carry out similar experimental programs.[16]

Stability Tunnels

In 1941 a stability tunnel was built at NASA Langley. This tunnel had two inter-changeable test sections about 6 ft in size.[17] One test section had a set of rotating vanes that created a swirl in the airstream. The second test section was curved to simulate turning flight. This tunnel was moved to the Virginia Polytechnic Institute and State University in 1958 where it continues to serve as both a general- and a special-purpose wind tunnel. Similar results are obtained by using oscillating model techniques or free-flight experiments in conventional tunnels.

Propeller Tunnels

Propeller tunnels are similar to conventional tunnels with the exception that they usually have an open test section and a round cross section (see Chapter 3). One

of the earliest propeller tunnels was built at Stanford University in 1917 with a 5.5-ft-diameter test section. The propeller tunnel at NASA Langley with a 20-ft test section went into operation in 1922. Besides propeller experiments, this tunnel gave insight into the advantageous location of engine nacelles relative to the wing and the design of cowls (NASA cowl) for radial engines to reduce drag and increase cooling.[18]

Propulsion Tunnels

Experimental evaluation of aircraft engines, either reciprocating or jet, requires simulation of both flight velocity and the variation of atmospheric pressure and temperature. Since the engine must be operated in the tunnel, the exhaust gases must be removed from a closed circuit tunnel or an open circuit tunnel must be used. The altitude requirement necessitates pumps to provide the low density, and the lower temperature at altitudes requires a refrigeration system. Among the largest and most powerful experimental facilities in existence is the propulsion test facility at the U.S. Air Force's Arnold Engineering Development Center in Tullahouma, Tennessee.

Icing Tnnnels

The NASA 6 × 9-ft Icing Research Tunnel at Lewis Research Center near Cleveland, Ohio, is a conventional low-speed closed return tunnel with the addition of a refrigeration system to reduce the air temperature to $-40°F$ and atomizers upstream of the test section to produce water droplets that freeze. The shell of this tunnel is heavily insulated to help keep the tunnel cold. A novel aspect of this facility is that the fan must be run at idle speed during model changes to prevent it from freezing. The formation of ice on aircraft continues to be a serious safety problem for aircraft and helicopters that operate at low to medium altitudes.

Low-Turbulence Tunnels

These tunnels usually have a wide-angle diffuser just ahead of the settling chamber in order to increase the size of the settling chamber without a corresponding increase in the overall circuit dimensions. The large settling chamber has honeycombs and a larger than usual number of screens to damp out turbulence, and its size allows for a larger contraction ratio to further reduce turbulence. Some low-turbulence tunnels of the closed return type have used 180° curved corners rather than the usual two 90° turns. This type of comer has been used in the NASA Langley low-turbulence pressure tunnel (LTPT), a two-dimensional tunnel, and the Ames 12-ft high-speed pressure tunnel. The Langley LTPT uses a wide-angle diffuser ahead of the settling chamber, a 17.6 : 1 contraction ratio, and 11 screens.

Two-Dimensional Tnnnels

Two-dimensional tunnels are used primarily for evaluation of airfoil sections. They have been built both as open circuit and closed return types. These tunnels have

tall narrow test sections with height-to-width ratios of 2 or greater. The tunnels are usually of the low-turbulence type and may be pressurized to increase the Reynolds numbers. An example is the previously mentioned LTPT at Langley Research Center.

2.5   SMOKE TUNNELS

Smoke tunnels are used primarily for flow visualization. Usually these tunnels are of the nonreturn type, as photographs and video recording are the primary methods of data recording. Both two- and three-dimensional smoke tunnels have been built. For smoke sources current practice seems to favor vaporized light oils, kerosene, or propylene glycol although many other substances have been used. Smoke tunnels used for research rather than demonstration purposes tend to have very large contraction ratios (up to 24 : 1) and a large number of antiturbulence screens at the inlet to obtain smooth laminar flow.[19] In general, the speed of smoke tunnels tend to be low—around 30–60 ft/sec. Smoke has been injected both just before the model and at the tunnel inlet. For research tunnels, injecting ahead of the inlet and antiturbulence screens reduces the turbulence from the smoke-injector rake.

Smoke is used for flow visualization in many general-purpose tunnels, though rarely are the results as spectacular as can be obtained in a facility carefully tailored for the purpose.

2.6   AUTOMOBILE WIND TUNNELS

Experiments to obtain aerodynamic parameters that affect automobile performance, handling, engine cooling, brake cooling, and wind noise are made with either scale models or at full scale in larger tunnels. Unlike the case of aircraft, it is quite feasible and is common practice to build tunnels that accommodate the use of full-scale automobiles. It is also advantageous to use moderate scale such as 0.25–0.4 models and conduct experiments at full-scale Reynolds numbers.

External Flows

There are two distinct classes of wind tunnels involved in aerodynamic experiments on automobiles. The one that is the main focus of this book is concerned first and foremost with the external aerodynamic flow and with internal flow to the extent it has a significant interaction with the external flow characteristics. All of the major automobile manufacturers worldwide either own or have regular access to wind tunnels for such experiments of both model- and full-scale automobiles. In North America there are several wind tunnels used extensively for automobile aerodynamic experiments. The Lockheed low-speed wind tunnel in Marietta, Georgia, is used extensively for automobile work by several manufacturers and by a number of automobile racing teams, as is the National Research Council tunnel in Ottawa, Ontario. The General Motors Research Laboratory operates both model- and full-

scale tunnels. The Chrysler Corp. has recently completed a pilot tunnel that is serving as a working tunnel for experiments using scale models and as a pilot for a planned full-scale tunnel. The Glenn L. Martin wind tunnel (GLMWT) at the University of Maryland has worked extensively on automobile aerodynamics as well as heavy truck aerodynamics beginning in 1953. In Europe, the companies including Ford of Germany, Porsche, Opel, BMW, Volvo, Mercedes, Audi, Fiat, Pinninfarina, Volkswagen, and the Motor Industry Research Association (MIRA) of Great Britain all own and use wind tunnels extensively in aerodynamic development of automobiles. The primary manufacturers in Japan, including Nissan, Honda, Mazda, and Toyota, all have impressive aerodynamic experimental facilities. Figure 2.5 shows the Nissan full-scale wind tunnel.
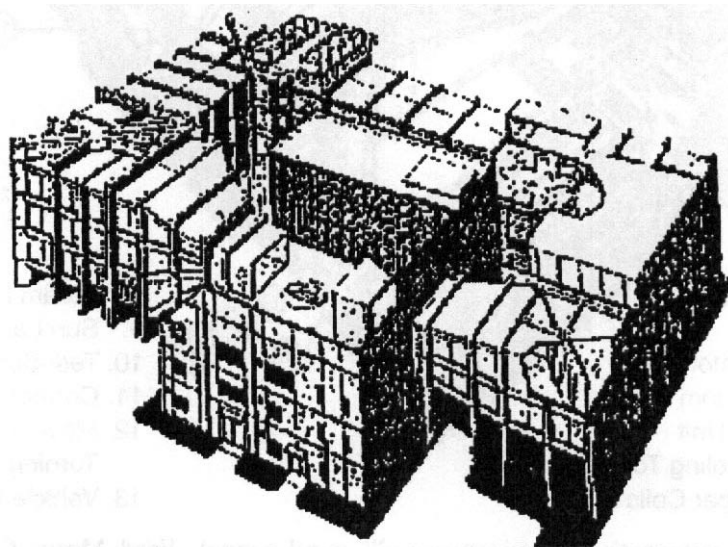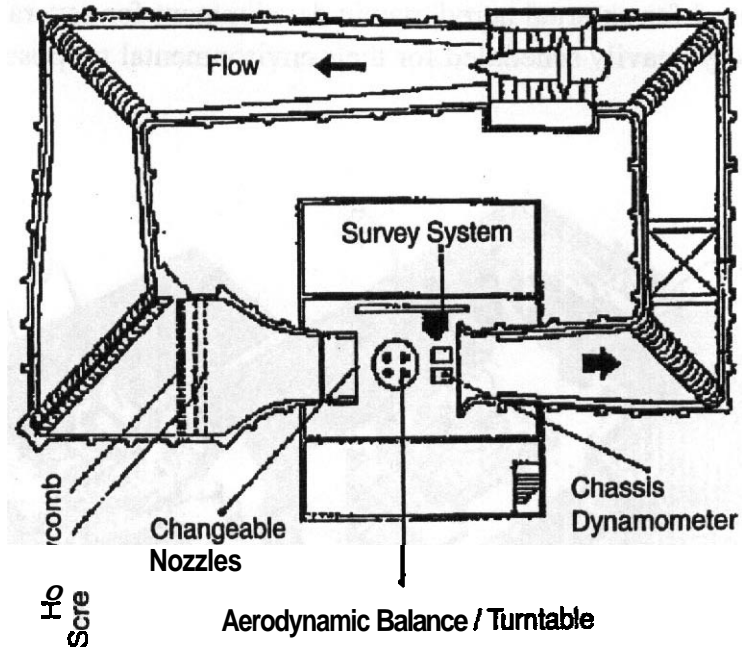
FIGURE 25   Full-scale facility at Nissan Motor Corp.

Climatic Wind Tunnels

The other class of wind tunnels are facilities that provide the capability to evaluate the drive systems, air conditioners, door, and window seals under simulated hot- and cold-weather environments and under arbitrarily chosen operating cycles. These facilities have capability to heat and cool the airstream, to simulate strong sun radiation conditions, to provide simulated rain, and to have the automobiles running on dynamometers around the clock for extended periods of time. An example of such a wind tunnel is shown in Figure 2.6. The auto industry frequently refers to these tunnels as "climatic" or "environmental"[20] wind tunnels. There are many more climatic wind tunnels in use by the automotive industry than of the class for external aerodynamic studies. Every manufacturer has several climatic wind tunnels, and there are some independent operators who sell such services. However, they have seldom been used for external aerodynamic development for several reasons. They are typically very heavily scheduled for their environmental purposes. The size that

1. Fire-bladed Fan	8. Steam Lances
2. D.C. Motor	9. Sun Lamps
3. Motor-Generator Set	10. Test Section
4. Equipment Room	11. Control Room
5. Refrigeration Unit	12. Movable Corner
6. Courtyard Cooling Tower	Turning Vane
7. Heat Exchanger Coils	13. Vehicle Entrance

FIGURE 2.6 An automotive "environmental" wind tunnel, Ford Motor Co., Dearborn, Michigan.

is quite adequate for the environmental work is not large enough to do external aerodynamic work on full-scale vehicles. And the flow quality is generally less than is thought proper for external aerodynamic studies.

Most automobiles are considered to be aerodynamically bluff bodies, which reflects the fact that there are almost always significant regions of separated flow on an automobile. This leads to interactions between the flow about the model and the wind tunnel walls or free jet boundary that are somewhat more complex than is the case for bodies with fully attached flow. One result is that understanding these types of flow in wind tunnels continues to engage research personnel.

A major point concerning wind tunnel experiments on automobiles is the question of ground simulation. To provide a strict simulation, the wind tunnel floor must move with the speed of the air. A considerable amount of work has been carried out to address the question of when this is necessary and when this condition can be relaxed. Generally speaking, it is the current practice to use a fixed floor with some treatment to produce a thin boundary layer for production car experiments and a moving floor for formula I or Championship Auto Racing Team (CART) race car experiments. The principal difference is the clearance between the bottom of the car and the ground. This and other issues will be addressed in more detail later in the book.

Wind tunnels for automotive experiments are increasingly required to have low-flow noise levels so that wind noise associated with flow around the vehicle can be measured with sufficient accuracy to allow assessment of proposed design variations.

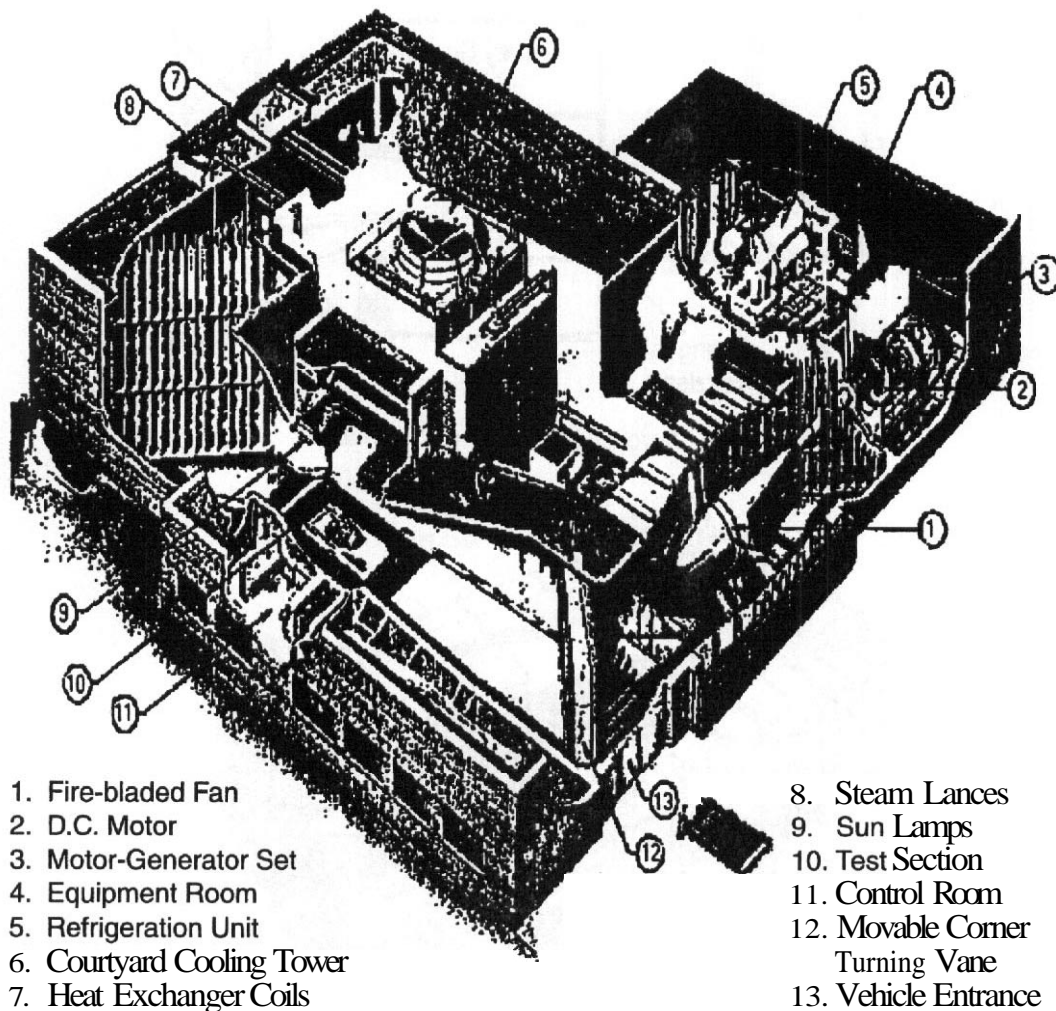## 2.7   AEROACOUSTIC WIND TUNNELS

Studies of flow-generated noise from submarines, ships, and other types of marine vehicles and appendages and their wake distributions have long been a problem in the military world, just as noise suppression for aircraft and land vehicles has been in the civilian area. Realizing the advantages of holding the model and the measuring instrumentation still and letting the fluid move, as well as the enormous cost of running full-scale experiments, and that noise suppression is more easily handled with air than with water, the David Taylor Research Center designed and built a unique wind tunnel known as the Anechoic Flow Facility. While basically a single-return wind tunnel with a closed test section upstream of an open one, its other features both as a wind tunnel and low-noise facility have made an enormous contribution to the world of wind tunnels for others to copy.

A sketch of the tunnel is shown in Figure 2.7. Special features include:

1. The use of a wide-angle diffuser to permit a contraction ratio of $10 : 1$ without a long diffuser and return path with corresponding high constructions costs.

2. The use of two $100°$ turns and two $80°$ turns instead of the more customary four 90" turns. This permitted the length needed for the fan noise suppressors, again with a shortened passage.
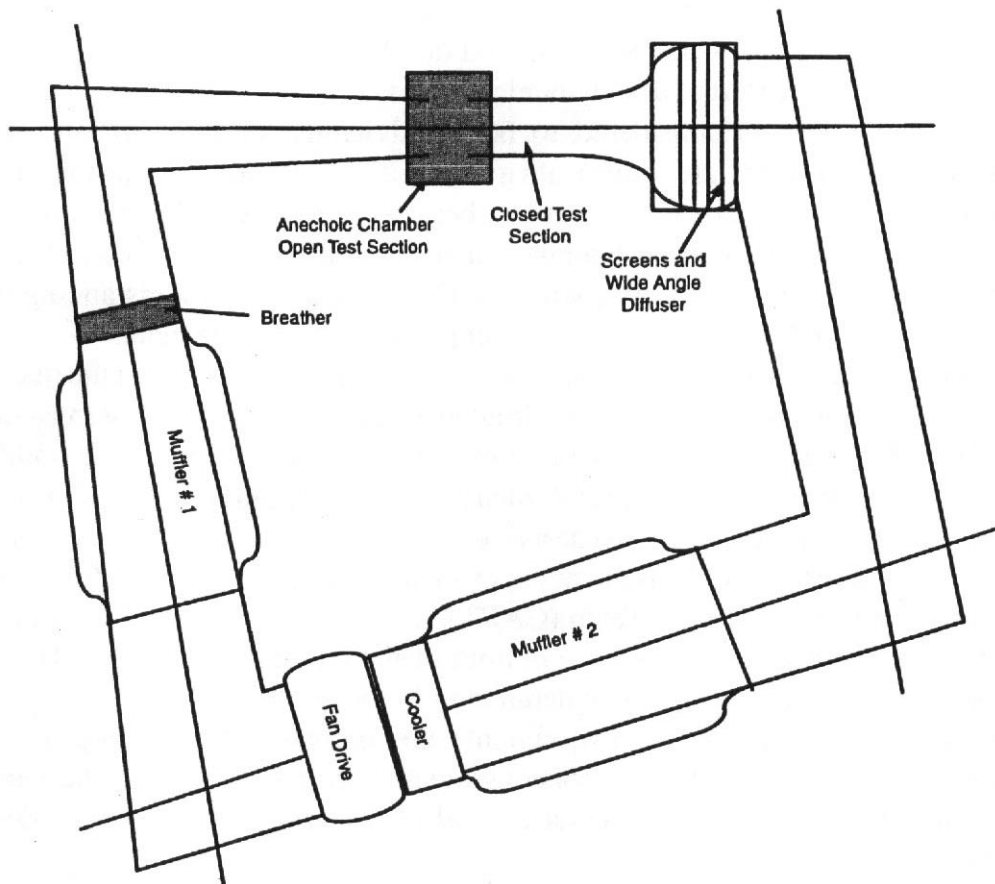
FIGURE 2.7   Layout of the Anechoic Flow Facility.

3. Extremely heavy concrete constructions plus the use of noise suppression materials on walls, ceilings, and turning vanes.

4. An anechoic chamber surrounding the open test section to yield by far the lowest noise levels achieved in a wind tunnel.

5. Section isolation is practiced throughout, as well as isolation of the entire tunnel from the ground through several feet of crushed rock.

Figure 2.8 shows a model in the anechoic facility of Figure 2.7. The wedges used for reflection cancellation are evident in the background.

Many general-purpose wind tunnels have been modified to include noise absorption materials and other features to provide quieter environments in which some aeroacoustic work can be carried out. Increased understanding of aeroacoustic principles, better material availability, and improved instrumentation that allows useful measurements in the presence of higher background noise have come together with increasing demands of users for quieter vehicles to stimulate an increasing level of activity in aeroacoustic studies in both special- and general-purpose wind tunnels. An example of a general-purpose facility that has received extensive acoustic treatment is the National Full Scale Facility.
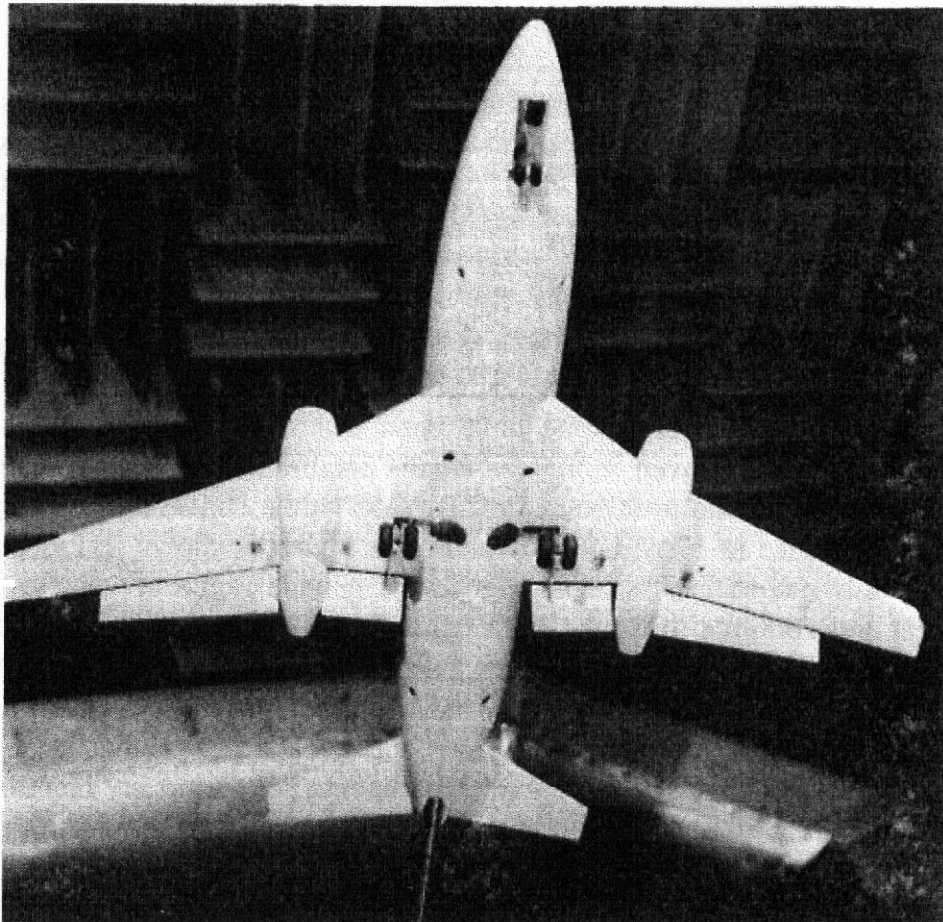
FIGURE 2.8   Airplane configuration for airframe noise study in the Anechoic Flow Facility. (Courtesy Naval Surface Warfare Center.)

2.8   WATER TUNNELS

Water tunnels are, of course, not wind tunnels. However, water tunnels are used in essentially the same way and under the same physical principles as low-speed wind tunnels. Water tunnels support direct investigation of cavitation phenomena that cannot be done in a wind tunnel. Water tunnels tend to be physically smaller than wind tunnels for achieving the same Reynolds numbers. However, this apparent advantage is more than offset by the greater difficulty in having water as the working fluid instead of air. There are few "large" water tunnels. There is a 48-in. tunnel at the Navy's Applied Physics Laboratory at State College, Pennsylvania. This tunnel is used for underwater vehicle development, including considerable work on torpedo design. Small water tunnels have been widely used for flow visualization studies. It has been possible to achieve low dispersion of die streaks, which combined with very low flow speeds has allowed more detailed observation and associated photographic and video recording than has been achieved in wind tunnels.

2.9 GENERAL-PURPOSE WIND TUNNELS

Many wind tunnels that have in practice become general-purpose facilities were originally designed based on requirements of experiments on aircraft of types common in the World War II era. The most common of these is the 7 X 10-ft class wind tunnel that have those approximate dimensions of their test sections. All of the NASA research centers that date from the days of the NACA have or had one or more of these: The U.S. Air Force has one, the U.S. Navy has two, five universities in the United States have tunnels of this class, and numerous other agencies and companies throughout the world have or had tunnels of this class. Many of these tunnels have been closed and some have been destroyed as work that had its origin in these tunnels moved more specialized facilities spawned by increasing understanding of particular problems. The GLMWT at the University of Maryland, which entered service in 1949, is one of these. **Its** layout is shown in Figure 2.9.

These facilities continue to be very good for a wide range of vehicle-related experiments and continue to be the best available for a range of special-purpose experiments that have not spawned their own specially designed aerodynamic facilities. For many purposes they are simply the most cost effective at carrying out exploratory investigations when no fully satisfactory capability is available.

A selection of subjects of aerodynamic experiments not previously mentioned is added here to further emphasize the broad range of applications that arise for low-speed wind tunnels.

People

Attention has been paid to people-drag of the type encountered by bike racers and skiers. The bicycles should ideally be arranged so that the biker can pedal and with

FIGURE 2.9 Layout of the Glenn L. Martin wind tunnel at the University of Maryland.

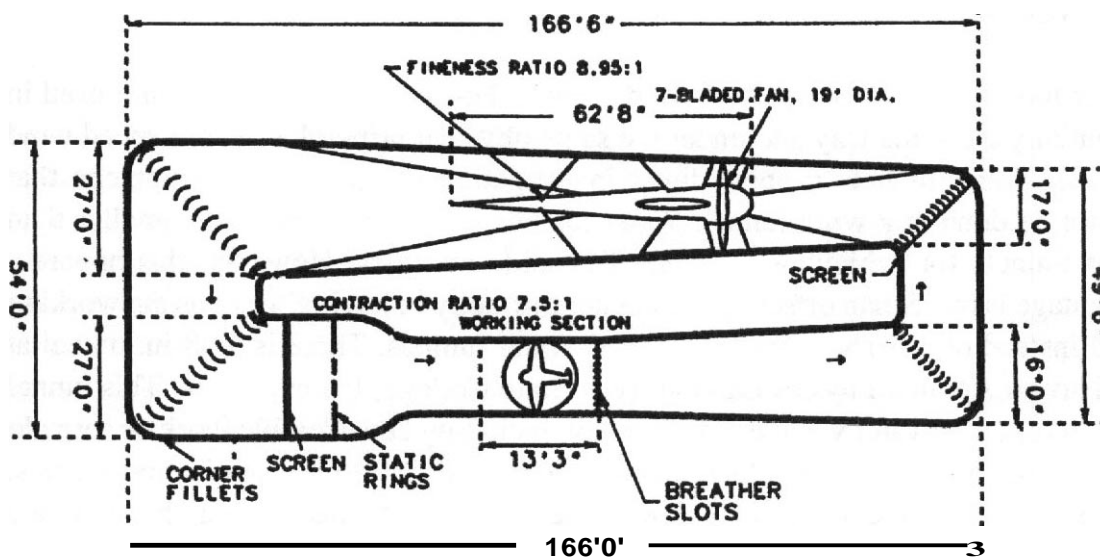a belt so that the front wheel rotates along with the back one. Experiments have shown a change of drag with the number of wheel spokes and other details. Wind tunnel entries have proven beneficial for showing bike riders their lowest drag posture. For skiers, the "model" is mounted in the tunnel and during a run at approximately 55 mph (which is close to full-scale "flight") assumes a series of positions endeavoring to learn Which minimizes his or her drag or possibly the lift-to-drag ratio in the case of ski jumpers. The fascinating part of these experiments, and they are not without hilarity despite the seriousness of the end results, is that the model corrects his or her own drag by watching a drag indicator. Position changes are shown on frontal and side TV projectors, and coaching suggestions sent in as needed. A programmed computation in real time can also be presented so the skier or biker can be shown how much each change helps in terms of race time or distance results. Substantial improvements in clothing have resulted from such programs. In some cases clothing has been evaluated to seek increases in drag when it is to be worn by an athlete seeking to increase load during training. Airborne troops have been trained in vertical wind tunnels so that they are familiar with the condition they will experience when jumping from aircraft. Figure 2.10 shows a skier suspended in a wind tunnel.

Birds and Insects

Over the years a number of wind tunnel experiments have been made of natural fliers, alive, frozen, and simulated. Initially experimenters were seeking mysterious and incredibly efficient devices that nature's creatures were supposed to have. No such things have been found; nor are they needed to explain natural flight. The high landing angles of some buds have been duplicated with highly latticed wings, and bud power has been estimated to be in line with demonstrated performance. Bird fat turns out to have a similar energy content to jet fuel. Differences that remain are of small magnitude and are within the uncertainty of experiments to date.

Live insects have been somewhat more cooperative than live birds and have flown more extensively in tunnels for close observation. In some cases, tunnels similar in concept to the "stability" tunnels described above have been used.

Wind Power Devices

Currently, and for the foreseeable future, there is a lot of interest in developing devices that will supply direct energy for pumping water for irrigation, to prevent pond freezing, or for the generation of electricity. Experiments are usually run at low tunnel speeds, but the tunnel engineer should satisfy himself or herself of the model integrity (and that it has a brake) and that damage to the tunnel is not likely to occur. Experiments will probably encompass runs under various power loadings and at different Reynolds numbers. It would be preferable to evaluate windmills in the wind gradient that they will eventually see, but this is rarely done. The tunnel engineer should encourage the windmill promoter to have siting experiments made in an environmental wind tunnel to get the best results in the field.[21,22] Prior
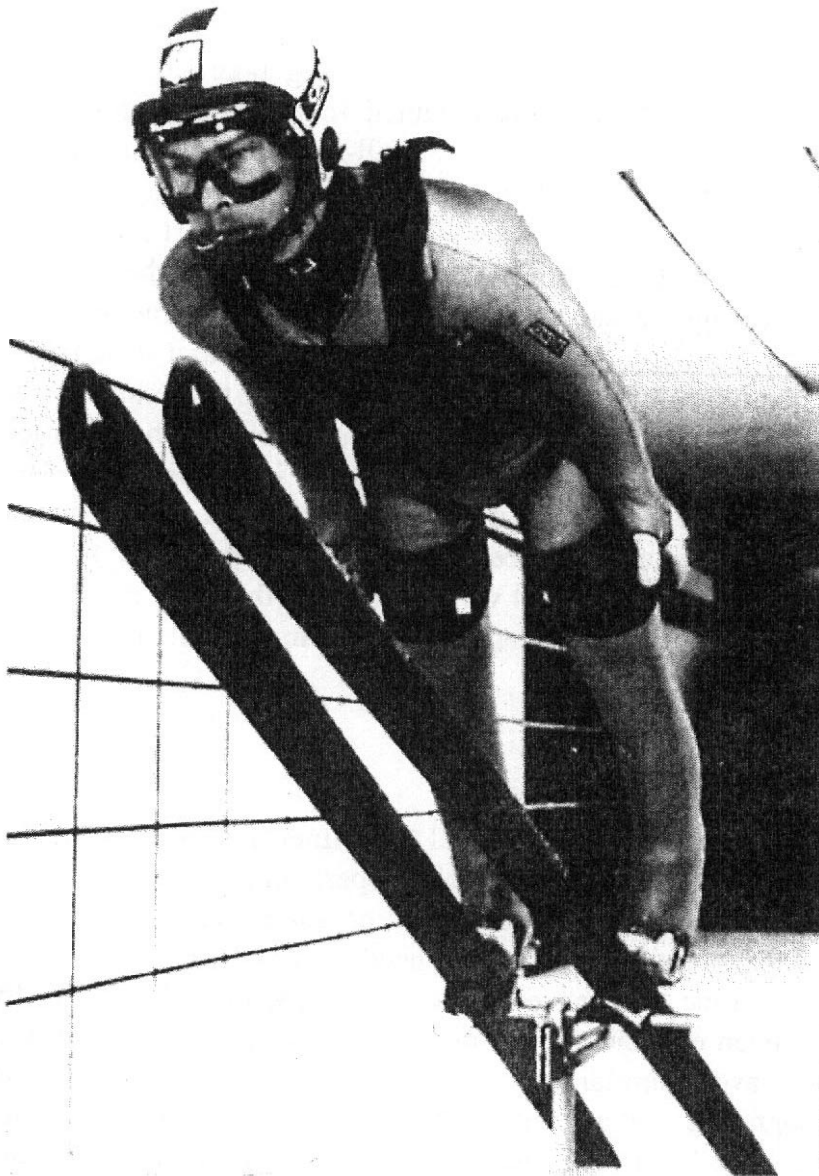
FIGURE 2.10 Skier in wind tunnel. (Courtesy Verdian-Calspan Operations.)

to siting studies, one may guess that the winds on a mountain top will run 80–100% higher than along a local plane. A long-term record cannot be established for the mountain location, but a ratio can be, and from this 50–100-year probabilities can be estimated.

At the moment, aside from several exotic but unproven designs, the types of windmills of most interest are the conventional or horizontal axis windmill, the Darrieus, and the Savonius, which is a bucket type. For estimating the maximum power coefficient one should use, respectively, 0.4, 0.4, and 0.3. The lower maximum power coefficient for the Savonius type is offset in practice by its lower manufacturing cost. Measurement of side force is not normally made but should be, as all types develop small to substantial lateral "lift" force, as does an airplane propeller.

Experiments on windmills in a wind tunnel require careful attention to wake-blocking corrections.

Large installations seem to suffer from making a disturbing buzzing sound, interrupting TV reception, and having instabilities, which lead to a short mechanical lifetime. Windmills should never be put on a rooftop, even to get a high local velocity. Natural winds have many times the total power needed for the entire electrical needs of humans, but the energy is very diffuse and therefore requires considerable ingenuity to harness economically. Windmills have, however, been a source of power that has been used successfully in certain locales for hundreds of years. It turns out that a maximum of 59.4% of the power as given by the rate of kinetic flowing through an area the size of the windmill disc is theoretically available.

Solar Collectors

Interest in solar energy has spawned a need for wind loads and moments on the various solar collectors, usually of parabolic cross section and of various aspect ratios and arranged in various arrays all the way from being in sheltered ground installations to being on rooftop locations subjected to all sorts of local wind concentrations. Since winds come from all directions, loads and moments must be measured for a full range of yaw. In particular, there is interest in drag (also called lateral load) and pitching moment and with the loads along the long axis. Yawing moments and roll moments are measured but are usually of lesser import. Besides needing loads for strength and preservation of the proper focal distance, the pitching moment is needed to size the drive motor that keeps the collector aimed at the sun and turns it over at night or in hail to reduce damage to the reflecting surface and reduce the collection of dust. Loads are reduced substantially by being shielded by a nearly solid fence around the array or other collectors, and this should be explored.

The experimental program usually consists of force, moment, and pressure data.[23] Obviously forces and moments are needed from the standpoint of foundation and structural design. Pressure data are needed for limiting local deflections of the reflector itself. The collector pitch angle is varied from $-180"$ to $+180°$ and yaw from $0°$ to $90°$. Array spacing and distance above ground are additional variables. Runs at several air speeds usually establish that there is little variation with Reynolds number. The tunnel speed range is chosen based on historical wind records at the proposed site. An example of an installation to evaluate the effect of wind screens is shown in Figure 2.11.

Radar Antennas and Satellite Television Receivers

The same type of experiments described above for solar collectors may be made for radar antennas or other dish-type receivers. A major difference is that one would not expect to find them in arrays, and more than likely radars will be placed on mountain tops where signals may be received from 360". As local winds may be quite high, it is not unusual to find them protected by radar-transparent domes.
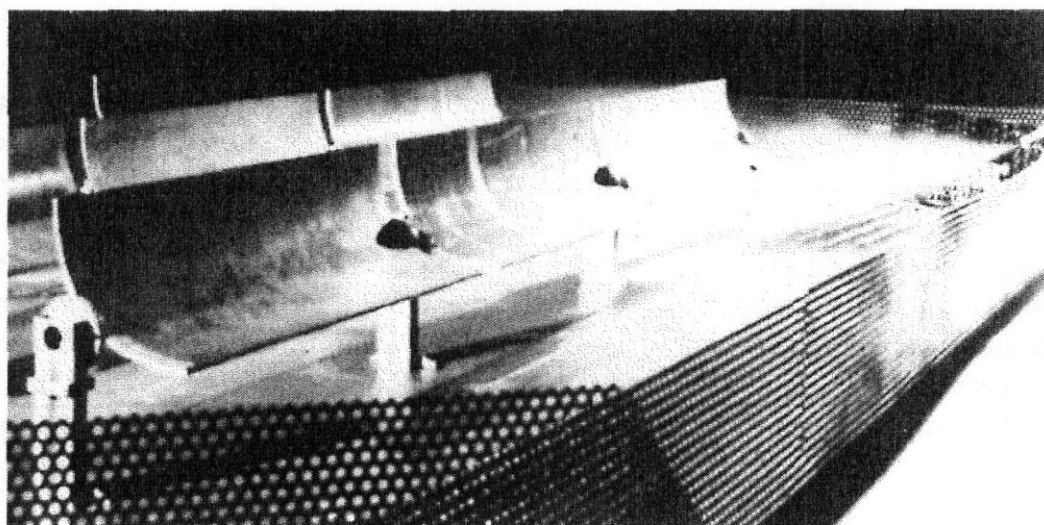
FIGURE 2.11   Effects of wind barriers on solar collectors being simulated in a wind tunnel.

Radar antennas are common on ships that may expect to encounter high-wind conditions and at those very times may be dependent on the radar for safety.

For wind tunnel experiments on exposed antennas the model should be mounted in the tunnel on top of the same structure it will see in the field–trailer, antenna stand, small house, and so on. Measurements of drag, side force, and torque should be made every $10°$ or so from $-10°$ to $+190°$. If there is any question at all about structural integrity, pressure measurements should be taken near corners, particularly on the dome, if one is to be used.

It is quite common to evaluate the actual hardware in the wind tunnel to obtain the actual structural integrity and the capability of the drive motors to operate the antenna in the specified wind conditions. Figure 2.12 shows a radar antenna undergoing direct evaluation of performance capability in a simulated wind condition. Figure 2.13 shows an example of data on the forces and torque for a different shaped antenna.

Sails and Above-Water Parts of Ships

The performance of sails have been evaluated in wind tunnels in limited numbers over the years. Marchaj[24,25] gives a good treatment of the subject. In general, sail experiments embrace measurements of side force, drag, yaw, and roll on a model mounted on the tunnel floor in an atmospheric tunnel where the boundary layer is properly simulated.

Sail material should be varied during an experiment to see what effect, if any, arises. Material roughness and porosity will probably be out of scale, and several variations of each should be tried for comparison.

Ship experiments have been somewhat more extensive. These usually embrace a floor or ground plane model cut off at the waterline, with measurements made of side force and drag only, although yaw and roll would be of interest. Again, a wind gradient should be provided as above.
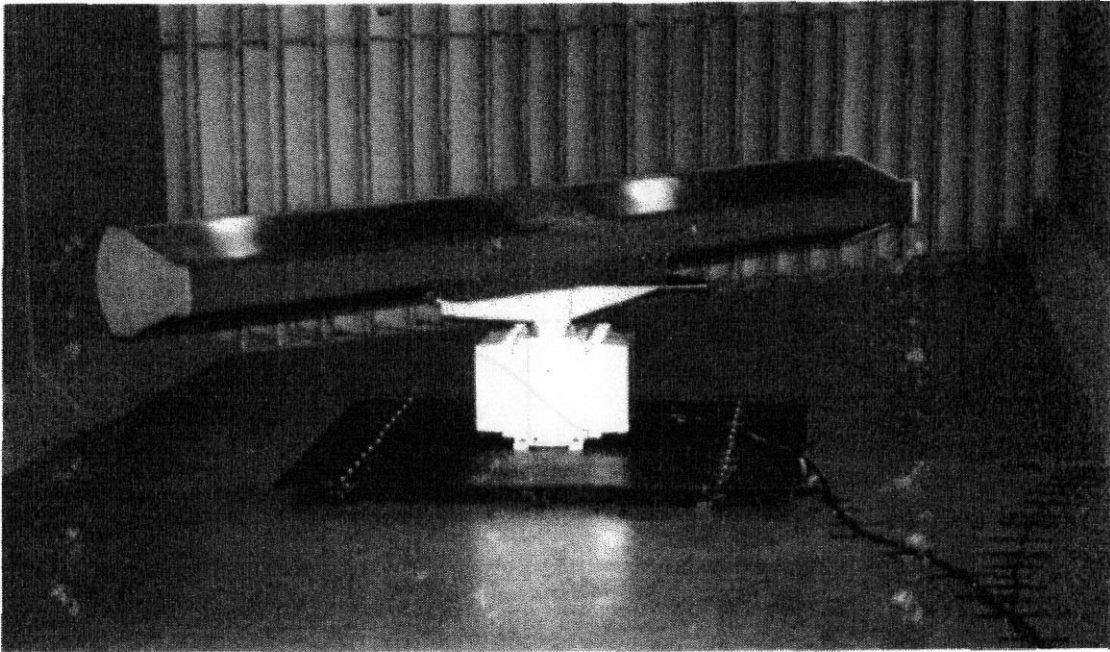
FIGURE 2.12   Air traffic control radar in wind tunnel simulation of service conditions. (Courtesy Glenn L. Martin Wind Tunnel.)

Both sail and ship model experiments should have their data corrected for wake and solid blockage. The models should be kept small enough so that at a yaw angle of 90° bow and stem remain no less than half a ship length from the tunnel walls. Extreme care to duplicate model detail, such as ships' railings, ventilators, and mast detail, are not warranted in studies to reduce aerodynamic drag.

Experiments on speed boats are primarily to find a body shape that has minimum nose-up characteristics. Here the model is set at a range of pitch angles about the stem, and the angle at which the aerodynamic moment overcomes the moment due to gravity and thrust about the stem is determined. The current wide, flat-bottomed speedboats can survive only a few degrees of nose up before they become unstable.

A relatively recent problem that arises with tankers carrying liquid natural gas is ascertaining that the vents needed as the gas boils off do not constitute a fire hazard.

Bridges

The effect of natural winds is important to the proper design of long or even intermediate bridge spans. There has been at least one case in which aerodynamic excitation at quite low wind speed led to fatigue cracking of high aspect ratio I beams in a bridge superstructure. Two wind instabilities must be studied: (1) vortex shedding, which causes limited vertical movement or torsional oscillations at generally low wind speeds; or (2) flutter instability, which can result in both vertical movement and torsional oscillation. Four types of experiments have been tried:
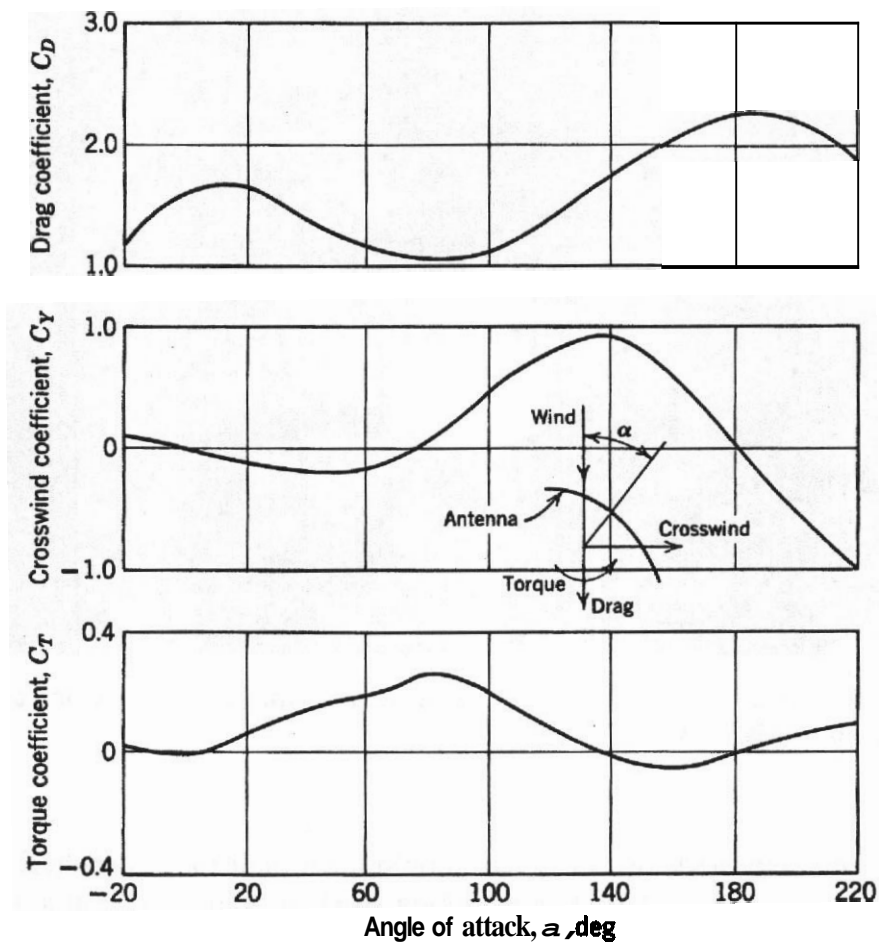
FIGURE 2.13 Data from elliptic **dish-type radar antenna. Drag component includes** support **drag.**

1. full models in smooth air,
2. section models in smooth air,
3. section models mounted on taut wires in smooth air, and
4. full elastic models in turbulent air.

Section models would of course be desirable for ease of construction, especially since the "final" design is frequently not available until well into the study, and the construction time (and cost) of a full elastic model are to be undertaken only if lesser cost methods are determined to be inadequate. When evaluated in smooth air, the section model does indicate changes that would reduce undesirable motions, and the section model data do agree fairly well with the full bridge model, both in smooth air, but they both have been found to give conservative results. Full models in turbulent **air** are the best. To be most useful, the turbulence properties must be scaled to the model size, and such real-air turbulence is very large. Whereas a typical general-purpose tunnel might have **a** u'/U of 0.5%, the **real** air might have a value of 10% or more [u' is the root-mean-square (RMS) variation in the horizontal

wind velocity, and U is the mean horizontal wind measured over a long time] Wardlaw[26] considers scaling laws for bridge experiments.

2.10   ENVIRONMENTAL WIND TUNNELS

These are tunnels designed to simulate Earth's natural boundary layer, which typically has a thickness of 1000–2000 ft. They are used to determine wind loads on buildings, air pollution dispersion patterns, soil erosion, snow drifts, flow patterns in the vicinity of building complexes, and so on. These are sometimes referred to as "meteorological wind tunnels." In contrast to most tunnels intended for vehicle development studies, the airstream in an environmental wind tunnel is not expected to be straight and smooth. Instead it is manipulated to obtain a flow distribution that is nonuniform in time and space to represent the atmospheric boundary layer.[27] The features of the atmospheric boundary layer are very different for various terrain characteristics so the tunnels must have ability to adjust the flow to simulate a variety of circumstances. This is accomplished by having adjustable roughness elements along the floor of the tunnel for as much as 10–15 test-section widths upstream of the zone in which the model is positioned. The Boundary Layer Wind Tunnel Facility at the University of Western Ontario even has an extended water pool to help in simulating flow in the marine boundary layer. Fortunately, the required flow speeds are typically quite low so the power requirements for environmental wind tunnels are not so high as for vehicle development wind tunnels.

The material in this section is complementary to material in Chapter 16 on wind engineering.

Experimental methods for environmental studies were done first in general-purpose wind tunnels, with considerable effort going into methods to develop appropriate simulation of the planetary boundary layer in the minimum possible streamwise distance. However, the methods have developed over the last two to three decades into quite specialized and sophisticated procedures that are required to deal with the highly nonuniform and unsteady flows and their effects. A new term has entered the technological lexicon. It is *wind engineering.* Wind engineering combines the fields of meteorology, fluid dynamics, structural mechanics, and statistical analysis to minimize the unfavorable effects of the wind and maximize the favorable ones. In general four separate areas are studied:

1. Wind Forces on Buildings and Structures. These problems are concerned with forces, moments, deflections, local pressures, and velocities.
2. Dynamics of Structures. This area includes buffet, flutter, swaying, and breathing.
3. Local Winds. These problems require measuring mean wind velocities, turbulence, and turbulence energy and scales.
4. Mass Transport by Winds. This covers soil erosion, pollution, blowing soil, efflux from smokestacks, and diffusion.

Research and practice in the field are very active and are reflected by the publications in the *Journal of Wind Engineering,* which was first published under the title of *Journal of Industrial Aerodynamics.*

Cermak[27,28] and Plate and Cermak[29] describe five requirements for experiments in meteorological or environmental wind tunnels:

1. proper scaling of buildings and topographic features;
2. matching Reynolds numbers, $\rho V w / \mu$;
3. matching Rossby numbers, $V / L \Omega$;
4. kinematic simulation of air flow, boundary layer velocity distribution, and turbulence; and
5. matching the zero pressure gradient found in the real world.

Reynolds number effects are usually small due to the sharp edges of most objects under study, but check runs should be made at varying speeds to make sure. If problems show up, they may usually be cured through the use of trip strips, as discussed in a later chapter. Reynolds numbers for buildings are commonly based on width w.

The Rossby number is concerned with the effect of the rotation of Earth on its winds. It accounts for a change of wind direction of perhaps 5" in 600 ft. This is of little significance and would be hard to simulate if it were necessary.

The velocity distributions in the natural boundary layer should be simulated as completely as possible. For example, at a scale 1 : 450 a 900-ft building will be 2 ft high. The boundary layer must be matched to at least 3 ft high, and preferably all the way to the test-section ceiling. The boundary layer velocity distribution and turbulence can be well duplicated by an installation of spires in the entrance cone followed by a roughness run of 10–15 test-section heights often made with small cubes on the floor. The building or locale to be evaluated and its environs are placed on a turntable, and rotations are then made such that the test area is subjected to winds from all directions. There is a small error in that the boundary layer and turbulence in the real world may be different according to the approach direction. Sometimes, especially when a building is on a lakeshore, a different wind structure is employed.

The longitudinal pressure gradient normally found in a wind tunnel and exacerbated by the very thick boundary layer needed can be made negligible by providing an adjustable test-section roof that may be adjusted to provide the extra cross-sectional area needed.

While it is necessary to provide cooled or heated air and test-section floor areas for some types of experiments on pollution, the tunnel engineer gets a break for force, pressure, and dynamic experiments, because when the wind blows bard, it is so well mixed that temperature gradients do not occur. For these experiments simulating the boundary layer structure and turbulence is adequate. Ground conditions influence the boundary layer [see Eq. (9.1)] and so no single boundary layer works for all experiments. Nor does the atmosphere have only one temperature gradient as both daily and seasonal changes occur.

There is an advantage in having a straight-through tunnel in this type of work (or a closed circuit tunnel that may be converted to open circuit) because tests are often made that could damage a closed circuit type. These include smoke, "snow material," erosion experiments with sand, when model failure is part of the experiment (roofing material or gravel), or when a water trough or structural failure may damage or rust balance components.

Air pollution experiments sometimes require that the tunnel be run at very low velocities. A direct-current drive motor plus a variable-pitch propeller is the best arrangement for this, but an alternating-current motor with a variable-pitch propeller is cheaper and usually adequate. Adjusting tunnel speed by rpm is less necessary with thick boundary layer flow because the flow pattern is adjusted by the spires and roughness. Atmospheric test engineers like to hold flow speeds to within 1–2%, which is on the high side for uncertainty for vehicle experimental work but is a challenge in the lower speed and unsteady environment of atmospheric boundary layer simulation.

Static Loads and Associated Experiments on Buildings

Wind tunnel engineers may be called upon to help correct buildings already built and in trouble or to guide the architect in a new design. "Trouble" can mean any of a long line of complaints, including building swaying, losing glass or cladding, losing roofing, people getting knocked down by wind,[30] whistling noises, smoke or other fumes coming in the ventilation system, and so on. These experiments are more tense than those on proposed buildings because the architect is usually very defensive. On proposed designs it is less costly to make changes. A full building experiment program encompasses the following:

1. Preliminary smoke experiments to search for possible trouble spots where pressure ports are needed.
2. Static wind loads, which may lead to dynamic experiments later.
3. Ventilation intake studies with smoke being emitted by nearby factories or efflux from the proposed building itself. (The high wind velocities near the top of a building result in a higher total pressure near the top and wind blowing downward. This can lead to a variety of unexpected intake problems.)
4. Local high-velocity areas that might cause problems for people.
5. Detailed smoke studies after force experiments have been made and the model painted a dull red to make the smoke show up better are used to convince the architect and his or her backers that the suggested changes are needed. Sometimes a location problem is identified so that simply moving the proposed building will solve the problem.[31]

Pressure measurements are needed in order to ensure the integrity of cladding and windows, and this requires high-bandwidth instrumentation to obtain in very turbulent flow. Current practice is to use transducers that have a flat frequency response

to say 150 Hz and then to average samples taken at rates of 50–150 s^{-1} for say 20 s. Locations for pressure ports are from item 1 above and from the tunnel engineer's experience.

A special case of wind loading occurs when one tall building is adjacent to another. Usually this produces shielding from winds in some directions and more serious buffeting in others. Buffeting from adjacent cylindrical or hexagonal structures can be reduced by fixing transition through added roughness.[32]

If the actual boundary layer is known at the location of a proposed site, the same boundary layer should be simulated. If not, the maximum speed at 30 ft altitude is measured or estimated and the boundary layer is structured according to the general properties of the local topology.

The dynamic pressure used for reducing the forces and moments to coefficient form may be taken as an average value over the model, the value noted at the middle of the model, or free stream q. It must be defined or the data are useless.

Dynamic Loads on Buildings

Buildings with more than a 6 : 1 ratio of height to width are apt to develop accelerations that are quite discomforting to the occupants. There are two approaches to solving this problem:

1. The building structural engineer knows the natural frequencies of the building, but not the buffet frequencies expected. Experiments using a rigid model on a high-response balance can obtain the needed information, and added stiffening can then be incorporated into the design.

2. An elastic model can be built and actual accelerations and displacements measured for the various wind speeds and wind directions, but a number of uncertainties remain. For example, the reference velocity is unknown, and there are some uncertainties as to the dynamic characteristics that should be built into the model. Dalgliesch, Cooper, and Templin[33] and the references therein consider the comparison between a model and a building that has already been built, noting a fair agreement with dynamic data from each but acknowledging that the experimental program was helped by having a building already constructed from which coefficient ranges could be determined. The model had 21 degrees of freedom, sensors that measured three displacements, and 15 accelerometers. Of interest was finding that torsional motion resulted in accelerations in some parts of the building that were 40% higher than in others.

Unsteady Aerodynamics in Wind Engineering

The wind can produce structural oscillations and other phenomena in several ways. Some typical cases are indicated .here.

Simple Oscillations   All natural and man-made structures have one or more natural frequencies at which they will readily oscillate unless critically or over damped. The natural frequencies of many items (trees, signposts, etc.) are close enough to

those of wind puffs that it is not unusual for a failure to result from successive puffs arriving in such a way as to amplify the motion to a failure condition. These are cases of forced response at a resonant frequency.

Aeolian Vibrations   Long, simply supported structures such as smokestacks and towers have a tendency to oscillate in a direction normal to a relatively smooth steady wind and at their natural frequency. This phenomena is a result of the combination of the structural tendency to vibrate at a natural frequency and aerodynamic phenomena of slender bodies shedding vortex streets. Vortex shedding from circular cylinders is one of the most studied problems in fluid dynamics. There is a range of Reynolds numbers over which there is an alternating shedding with corresponding unsteady side force and drag. Over a wide range of conditions the shedding frequency corresponds to a Strouhal number, fd/V, of about 0.2. As can be seen, there is likely to be some wind speed at which the shedding frequency and thus the side-force frequency will be equal to a natural frequency of the structure. When such a coincidence occurs, there is likely to be a significant vibration. Such an oscillation is called Aeolian, although sometimes the term is restricted to the case when the structure has a high natural frequency (10–100 **Hz)** and displacements are small. Such oscillations are the source of the tones in an "Aeolian Harp" produced by the wind.[34] Structures that are noncircular and elements of structures such as the individual beams in a tower or bridge may experience periodic shedding and corresponding aerodynamic excitation that can be damaging if any forcing frequency approaches a lowly damped natural frequency of the structure.

Galloping   A second type of motion arises when a body has a negative slope of the lift curve, and motion across the wind then produces a force in the direction of the wind. This is not unusual for buff bodies whose in-wind side becomes unstalled with a small angle of attack, and Bernoulli-type flow then is able to act. Galloping oscillations are usually violent and must be eliminated through design changes. For instance, twisting stranded wires or adding spiral wrappings has been found effective in many cases.

Breathing   Sometimes large-diameter stacks and other structures will distort at some natural frequency such that the flow pattern is changed toward that frequency. This is different from motion of the body in the absence of distortion.

Transmission lines exhibit both Aeolian and galloping oscillations. The Aeolian singing is understood, usually occurs at from 10 to 100 **Hz** full scale, and is suppressed by dampers. Galloping produced by wind loads is reasonably well understood, but unfortunately very large deflections (of say 100 diameters) are not uncommon and are hard to accommodate in a tunnel. Experiments have been made on spring-mounted sections employing a bare wire, stranded wire, and wires with simulated ice accretion. Here some galloping has been developed, but apparently only small deflections have occurred.

Agricultural/Windbreaks

Windbreaks can be used in connection with reducing the loads on structures. A second and important use is to reduce winter heating loads by reducing the convective cooling of a house, and a third is to increase the yield from some types of wheat that do not like being blown about. Instrumentation downstream of the windbreak should continue for at least six times its height, and data averaging should be employed to determine the windbreak efficiency.

Agricultural/Agronomy

Pollination for many agricultural products is by the wind, and thus plant distribution and planting patterns must be properly employed. Trees near the edge of the fields may need to be cut to improve the natural winds. On the other hand, some plants do better without a lot of buffering by the wind, and these need special attention. The area of wind engineering as applied to agriculture is only in its infancy.

Agricultural/Soil Erosion

Soil erosion caused by wind is of interest to the agronomist from the standpoint of losing topsoil. The road engineer, on the other hand, would like to see his or her roads stay clear. Another facet of soil erosion is the damage done to car windshields and paint by windbome particles.

The mechanism of natural soil pick-up is beginning to be understood.[35] Submicrometer particles will not erode from a smooth surface in a wind of gale velocities, but mixed with 5- to 50-μm grains they become highly erodible. Fundamental studies of large-scale grain loads have been made using strain-gage-mounted grains. Much of the correlation with full scale is encouraging.

Another type of erosion is the determination of the wind speed at which gravel begins to be eroded from the roof of a building,[36] damaging the roof, nearby parked cars, and passersby.

Snow Drifting

Many people in warmer regions do not realize the yearly cost of snow removal, and many in colder areas do not realize the savings possible by wind tunnel studies of ameliorating changes (preferably before but sometimes after construction) that reduce local drifting about access areas.

Drifting snow can block doorways and roads and may even inactivate a facility completely. Fortunately, the problem can be studied in a tunnel with good correlation to full scale. Snow patterns that might take years (in the Arctic) to accumulate may be duplicated in a few hours.

Kabayashi,[37] Strom et al.,[38] and Kind[39] present thorough discussions covering the snow-drifting phenomena. The basic parameters of snowdrift and erosion problems are discussed below.

When a stream of wind flows over a bed of loose particles, those higher than the others produce more drag until finally they roll and bump in the wind direction. This process is called "saltation" and is responsible for most of the motion (and end deposits) that form snowdrifts or soil erosion. When the wind velocity exceeds about five times the threshold speed, the particles bump hard enough to bounce into the stream when they are then said to be "in suspension." Saltation and suspension can occur at much lower speeds in the presence of falling particles. Modeling to match this phenomenon is by the following ratios:

Scale factor d/L, where d is the diameter of simulated snow particle and L is the length of a full-scale reference dimension.

Coefficient of restitution e. This concerns the rebound distance/drop distance and is 0.555 for ice.

Particle velocity V_p/V, where V_p is the velocity of simulated snow particle and V is the velocity of real snow particle.

Fall velocity V_f/V, where V_f is the free-fall velocity of simulated snow particle. Here we have one of the rare instances where we may "scale gravity"—at least to the extent that the fall velocity may be varied by changes in the particle density.

Particle Froude number V^2/gd, where g is acceleration of gravity.

Selecting a model scale of $\frac{1}{10}$, we find that the experiment velocity becomes 0.316 full-scale velocity. The fall ratio may be maintained by using borax ($Na_2B_2O_7$), whose density providentially yields the right value and whose coefficient of restitution is 0.334—lower than ice but possibly close to snow—and whose diameter may be controlled to be one-tenth that of snowflakes.

In a tunnel saltation has been found (for the above-simulated snow) to occur at 11 mph without snow falling and at lower velocities when snow is falling.

Data for snow experiments are obtained in the form of photographs and depth contours. One substantial contribution from tunnel experiments is the technique of reducing drifting by erecting a building on piles with a free space beneath. This has been applied in Arctic buildings with good results. Figure 2.14 is a from a wind tunnel study of snow drifting.

Evaporation and Related Issues

The growing need for studying transpiration from plants and evaporation from open bodies of water has resulted in the construction of wind tunnels in which the moisture content of the air and its temperature may be controlled. Tunnels of this type are in Japan, at the University of Nottingham in England, at the Colorado State University in the United States, and elsewhere. They are all low-speed tunnels employing controlled air exchange.

Transpiration experiments are full scale in that the weight of moisture removed from actual plants is studied. Electric lights or other heaters are used for temperature control.
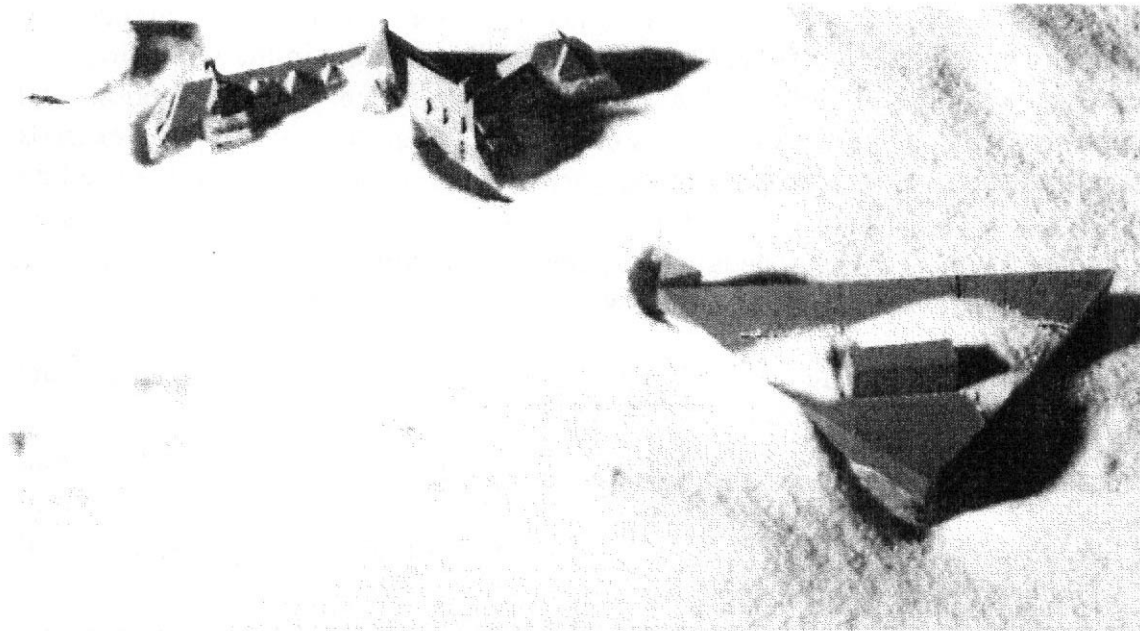
FIGURE 2.14 Snowdrift study for lodge, near building in photo, at a ski resort. Note the effect of tower at left rear, which provides self-removal of snow from entrance with prevailing wind from left.

Evaporation is of interest both to agronomists who **are** concerned with the loss of water from storage areas and channels and to process engineers who have drying problems. Both types of experiments have been explored in wind tunnels.

Evaporation experiments employ open bodies of water, and the surroundings are changed to study the increase or decrease of evaporation. Evaporation, as one might guess, depends on the surface area, the relative dryness of the air, and the effective wind velocity. This last term is the "catch," since the effective velocity may vary from a fraction of 1% to perhaps a few percent of the nominal velocity, depending on the type of boundary layer formed by the air over the water.

Pollution Dispersion

For all of the various types of pollutants being discharged into the air, it is important to know not only where they will go but also how far they must go before diffusion reduces their concentration sufficiently to render them harmless. The number and types of pollution problems are astounding. They include industrial smoke, throw-away gases from chemical processes, efflux from nuclear power plant holding tanks, using wind to carry silver iodide aloft to increase the probability of rain, the necessary distance from a liquefied petroleum gas (LPG) spill to obtain a noncombustible mixture, getting rid of hydrogen sulfide smell from a geothermal power plant, the dispersal of pesticides through trees, and so on. Furthermore, it is necessary to consider the wide range of 'weather conditions and assess the worst circumstance that is "likely" to occur.

Skinner and Ludwig[40-43] made a great contribution to methods for experimenting on dispersal in wind tunnels. They argue that (1) the dominant feature of plume

mixing is turbulent exchange and (2) fluid viscosity is not important. They also note that there is a minimum Reynolds number below which there will be a laminar sublayer in the tunnel that cannot be tolerated, or conversely, when experiments are done above that speed, a greater area can be examined by going to larger model-scale ratios as long as the tunnel speed is increased proportionately. Their conclusion, provided the stack flow is "reasonably turbulent," is that by exaggerating the buoyancy of the exit momentum of the stack effluent and compensating with an increase of tunnel speed, the same dispersion is obtained as when modeling the ratio of stack exit density to ambient density. Thus hot stack gases are not necessary for this type of experiment, permitting larger ground areas to be simulated by a model of fixed diameter. Having the plume in the tunnel, its dispersion rate may be measured, or a program of changes may be studied to move its location away from certain areas. Another type of pollution experiment employs a pollutant distributed at various locations to see how the dispersal is affected by changing conditions.

A few examples are given of smoke visualizations from pollution dispersal studies. Figure **2.15** and Figure **2.16** show the effect of a nearby building on plume height. Figure 2-17 shows how smoke (or pollutants) can blanket an entire factory under inversion conditions. Figure **2.18** shows the path of stack gases for a container ship. The objective is to keep the stack gases from impinging on the containers.

In addition to a need for studies of the above problems for engineering purposes, there is now a legal reason in the United States in that the Clean Air Act (Public Law **95-95**) describes "good engineering practice" as including pollution effects, and the U.S. Environmental Protection Agency reserves the right to require fluid modeling or field experiments for proposed installations.
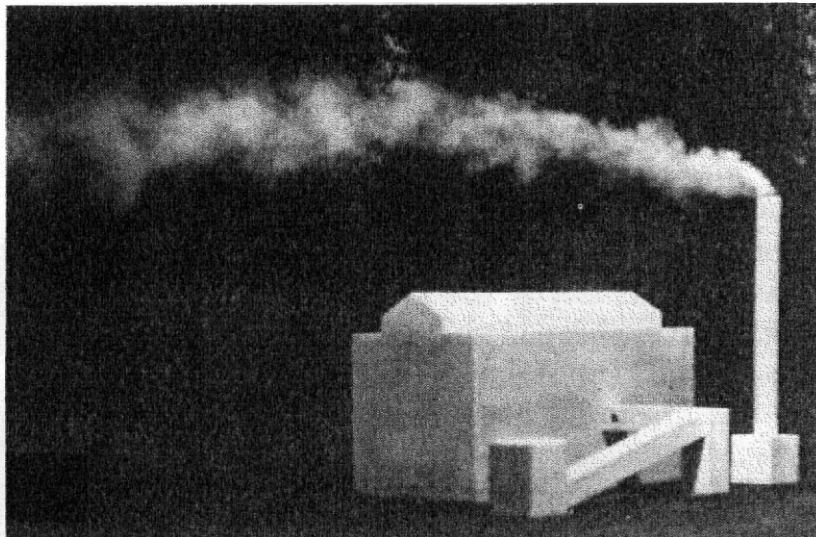
FIGURE 2.15 Efflux velocity is equal to wind speed and stack height is 1.5 times building height. Building is downstream of stack. (Courtesy National Physical Laboratory.)
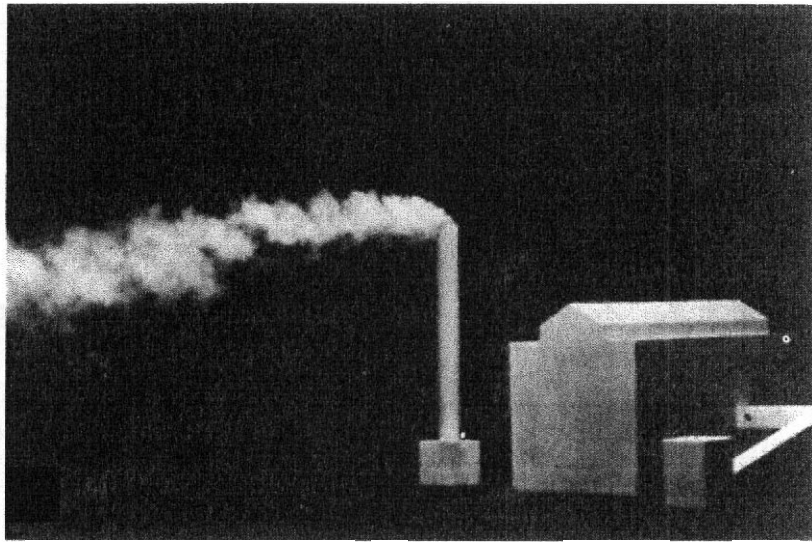
FIGURE 2.16 Same conditions as for Figure 2.10 except building is upstream or stack. (Courtesy National Physical Laboratory.)
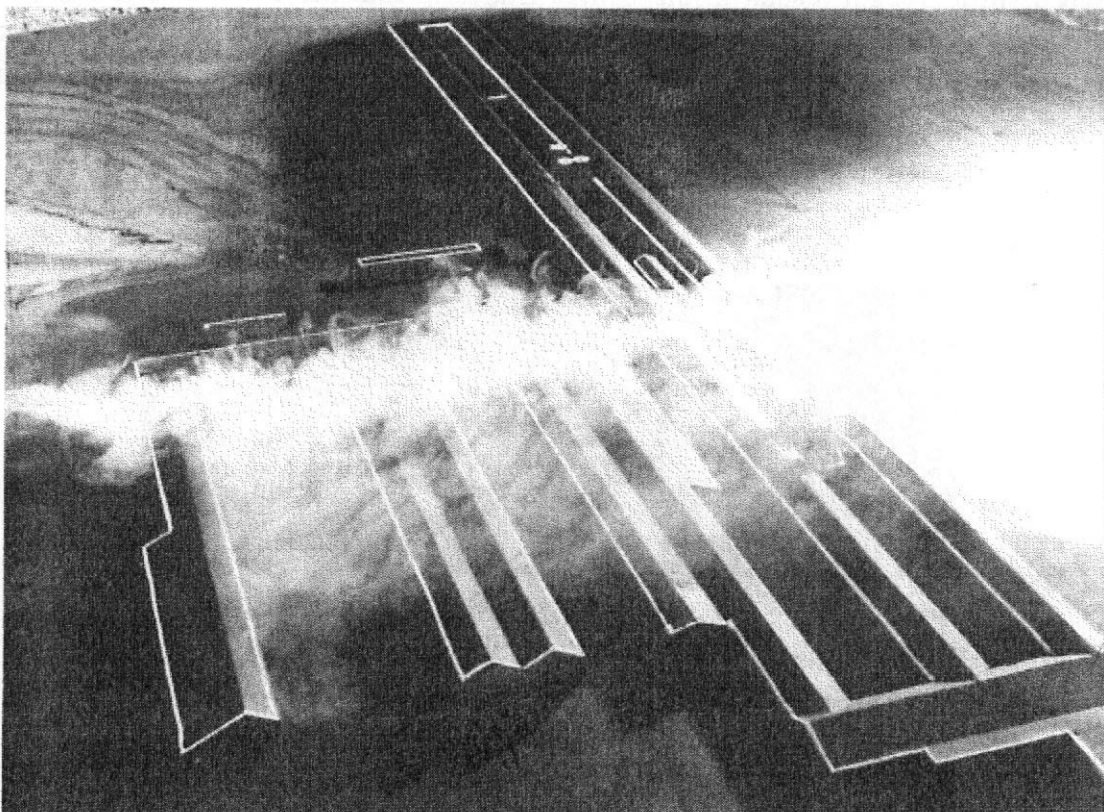
FIGURE 2.17 Smoke covering factory during an inversion simulation. (Courtesy Verdian-Calspan Operations.)
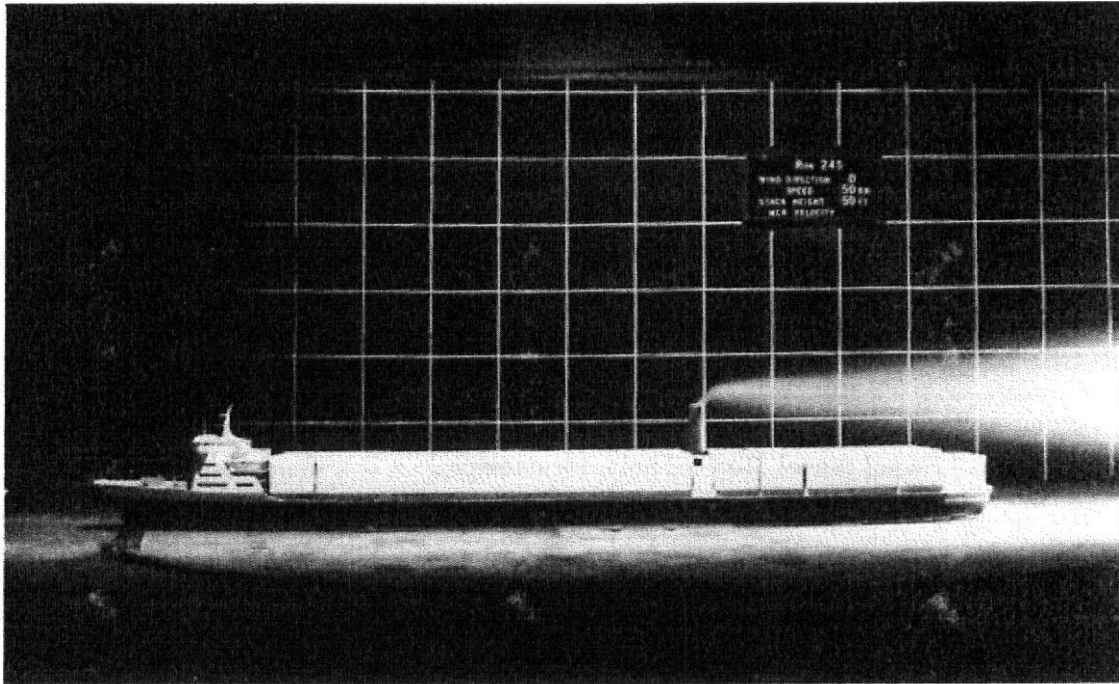
FIGURE 2.18   Measuring stack gas path. (Courtesy Colorado State University.)

REFERENCES AND NOTES

1. Hammond, D., AIAA Conference on Multidisciplinary Optimization, Panama City, FL, Sept. 1994.

2. Ockendon, H., and Ockendon, J. R., *Viscous Flow,* Cambridge University Press, Cambridge, 1995.

3. Speziale, C. G., "Turbulence Modeling for Time-Dependent RANS and VLES: A Review," *AIAA J.,* 36, (2), 173–184, 1998.

4. Doering, C. R., and Gibbon, J. D., *Applied Analysis of the Navier–Stokes Equations,* Cambridge University Press, Cambridge, 1995.

5. Jacobs, E. N., "The Variable Density Tunnel," NACA TR 416, 1932.

6. Abbott, I. H., and von Doenhoff, A. E., *Theory of Wing Sections. Including a Summary of Airfoil Data,* Dover, New York, 1959.

7. Cole, S. R., and Rivera, J. A., "The New Heavy Gas Testing Capability in the NASA Langley Transonic Dynamics Tunnel," Paper No. 4 presented at the Royal Aeronautical Society Forum on Wind Tunnels and Wind Tunnel Test Techniques, Cambridge, UK, April 14–16, 1997.

8. Nicks, O. W., and McKinney, L. W., "Status and Operational Characteristics of the National Transonic Facility," AIAA Paper 78-770, presented at the Tenth AIAA Aerodynamic Testing Conference, San Diego, CA, April, 1978.

9. See SATA web site referenced [in Appendix 1 for additional information on specific wind tunnels.]

10. Mort, K. W., Engelbert, D. F., and Dusterberry, J. C., "Status and Capabilities of the National Full Scale Facility," AIAA Paper 82-0607, paper presented at the Twelfth AIAA Aerodynamic Testing Conference, Williamsburg, VA, 1982.

11. DeFrance, S. J., "The NACA Full-Scale Wind Tunnel," NACA TR 459, 1933.

12. Chambers, R. J., Bowman, J. S., Jr., and Malcolm, G. N., "Stall/Spin Test Techniques Used by NASA," AGARD Flight Mechanics Panel Specialists Meeting on Stall/Spin Problems on Military Aircraft, Brussels, 1975.

13. Zimmerman, C. H., "Preliminary Tests in the NACA Free-Spinning Tunnel," NACA TR 557, 1936.

14. Niehouse, A. I., "Design and Operating Techniques of Vertical Spin Tunnels," AGARD Memorandum AG17/P7, 1954.

15. Discolor, M. B., and Barlow, J. B., "Determination of the Spin and Recovery Characteristics of a Typical Low-Wing General Aviation Design," AIAA Paper 80-0169, presented at the Eighteenth AIAA Aerospace Sciences Meeting, Los Angeles, CA, Jan. 1980.

16. Aero Machi wind tunnel, Torino, Italy, for example.

17. Bird, J. D., Jaquet, B. M., and Cowan, J. W., "Effect of Fuselage and Tail Surfaces on Low Speed Yawing Characteristics of a Swept Wing Model as Determined in Curved Flow Test Section of Langley Stability Tunnel," NACA TN 2483, 1951.

18. Stack, J., "The NACA High Speed Wind Tunnel and Tests of Six Propeller Sections," NACA TR 463, 1933.

19. Mueller, T. J., "On the Historical Development of Apparatus and Techniques for Smoke Visualization of Subsonic and Supersonic Flows," AIAA Paper 80-0420, presented at the Eleventh AIAA Aerodynamic Testing Conference, Colorado Springs, CO, March, 1980.

20. The use of the term *environmental wind tunnel* by the automotive industry indicates a very different type of facility from that described later in the section on Environmental Wind Tunnels, which describes facilities used to study problems associated with the natural wind.

21. R. N. Meroney, "Sites for Wind Power Installations," in Proceedings of the Workshop on Wind Energy Conversion Systems, Washington DC, June 9–11, Energy Research and Development Admin., 1975.

22. R. N. Meroney, "Prospecting for Wind: Windmills and Wind Characteristics," *Transport. Eng. J., ASCE, 107,* 413–426, 1981.

23. Randall, D. R., McBride, D., and Tate, R., "Steady State Wind Loading on Parabolic trough Solar Collectors," Sandia National Laboratories, Report No. 79-2134, 1980.

24. Marchaj, C. A., *Aero-Hydrodynamics of Sailing,* Adlard Coles Nautical and International Marine, Camden, 1979.

25. Marchaj, C. A., *Sail Performance, Techniques to Maximize Sail Power;* Adlard Coles Nautical and International Marine, Camden, 1996.

26. Wardlaw, R. L., "Sectional vs. Full Model Wind Tunnel Testing of Bridge Road Decks," DME/NAE Quarterly Bulletin No. 1978 (4), 1979.

27. Cermak, J. E., "Wind Tunnel Design for Physical Modeling of the Atmospheric Boundary Layer," *Proc. ASCE,* 107, 623–642, 1981.

28. Cermak, J. E., "Wind Tunnel Testing of Structures," *J. Eng. Mech. Div. ASCE,* 103, 1125–1140, 1977.

29. Plate, E. J., and Cermak, J. E., "Micrometeorological Wind Tunnel Facility, Description and Characteristics,"Colorado State University Civil Engineering Report, CER 63, 1963.

30. Local ground winds can be as much as four times those aloft.

31. If Candlestick Park had been built one playing field to the north, much of its wind problems could have been avoided. (J. E. Cermak, *Science Year: World Book Annual,* Field Enterprise Education Corp., Chicago, 1978.)

32. Peterka, J. A., and Cermak, J. E., "Adverse Wind Load Induced by Adjacent Buildings," ASCE Preprint 2456, 1976.

33. Dalgliesch, W. A., Cooper, K. R., and Templin, J. T., "Comparison of Model and Full-Scale Accelerations of a High Rise Building," NRC Presentation Paper, 1983.

34. Aeolus was the Greek God of the wind.

35. Cermak, J. E., "Note on the Determination of Snow Drift Locational Stability," Colorado State University Civil Engineering Report, CER 66, 1966.

36. Kind, R. J., "Further Wind Tunnel Tests on Building Models to Measure Wind Speeds at Which Gravel is Blown Off Roofs," NCR LTR LA-189, 1977.

37. Kabayashi, D., "Studies of Snow Transport in Low Level Drifting Snow, Institute of Low Temperature Science," Sapporo, Japan, Report A-31, 1958.

38. Strom, G., "Scale Model Studies of Snow Drifting," Research Report 73, U.S. Army Snow, Ice, and Permafrost Research Establishment, 1962.

39. Kind, R. J., A *Critical Examination of the Requirements for Model Simulation of Wind Induced Phenomena Such as Snow Drifting, Atmospheric Environment,* Vol. 10, Pergamon, New York, 1978, p. 219.

40. Ludwig, G. R., "Wind Tunnel Model Study of the Hot Exhaust Plume from the Compressor Research Facility at Wright Patterson Air Force Base," Report No. AFAPL TR 77-58, 1977.

41. Ludwig, G. R., and Skinner, G. T., "Wind Tunnel Modeling Study of the Dispersion of SO, in South Allegany County," EPA 903/9-75-019, 1976.

42. Skinner, G. T., and Ludwig, G. R., "Physical Modeling of Dispersion in the Atmospheric Boundary Layer," Calspan Report No. 201, Buffalo, NY, 1978.

43. Skinner, G. T., and Ludwig, G. R., "Experimental Studies of Carbon Monoxide Dispersion from a Highway Model in the Atmospheric Simulation Facility," Calspan NA 5411-A-1, Buffalo, NY, 1976.

3 Wind Tunnel Design

A considerable variety of wind tunnels have been designed and constructed to perform a wide range of aerodynamic tests. A number of special-purpose wind tunnels were mentioned in Chapter **2.** These included spin tunnels, icing tunnels, meteorological tunnels, tunnels designed for the testing of buildings, and others. Many low-speed tunnels, however, can be classified as general-purpose tunnels. These tunnels are equipped with mounting systems and instrumentation that can be readily adapted for many types of tests of air, ground, and marine vehicles, vehicle components, plus many other items including buildings, flutter, store separations, windmills, skiers, skydivers, and dynamic tests. **A** few of these tunnels have sufficiently large test sections to accommodate full-scale smaller aircraft and automobiles and are well suited for **V/STOL** testing. **A** growing number of tunnels have multiple test areas so that a wider range of tests can be readily accommodated. This type of arrangement leads to some compromises but is being found to be an overall advantage in some cases. In the medium-size tunnels with test-section area around 100 ft^2 large amounts of both research and vehicle development testing are accomplished. Tunnels with smaller size test sections are mostly used for research and instructional purposes. Ideally, the size of the tunnel is determined by its purpose. It is axiomatic that economics indicates that any given project should be carried out in the smallest size tunnel that will provide the needed simulation with the proviso that data from an improper and misunderstood simulation can be much worse than no data at all.

In this chapter, we present an approach to wind tunnel design that is appropriate for general-purpose wind tunnels. The principles are the same for other types of tunnels. **A** study of the basic aspects of wind tunnel design is useful to those who may be users or potential users of wind tunnels **as** well as those who may consider acquiring a wind tunnel. The material in this chapter will assist readers to gain an understanding of principal features of wind tunnels.

The first step in the design of a tunnel is to determine the size and shape of the test section based on the intended uses of the facility. **A** major part of the following discussions address tunnels for which the primary use is vehicle and vehicle component testing, since many tunnels **are** built for this purpose. It is also assumed that a major part of the testing will be force testing, where information is sought for performance, fuel efficiency, stability, or control of a vehicle that may be an aircraft, an automobile, a submarine, a racing yacht, or possibly others. Sections of this book addressing instrumentation **will,** however, consider a full range of measurement techniques for pressures, flow field variables, and other parameters.

The cross-sectional area of the test section basically determines the overall size of the facility. The test-section size, speed, and design will determine the required

power. The size of the facility will be the primary factor in determining the structural or shell costs, and the power and operating hours will **determine** the energy portion of the operational cost. Although the major cost of operation is the salaries of the tunnel personnel, the electrical energy cost to run the tunnel and its auxiliaries is not an insignificant cost, and it is doubtful that this cost will decrease in the long term. Thus, in the design there is a balance between initial costs and operating costs. In the past many tunnels have been built with short diffusers and related features to allow short circuit length to **hold down** initial costs while accepting higher energy costs of operation. This trade-off should be carefully examined with due consideration given to anticipated energy costs. The cost issues will not be treated further as they are too dependent on local circumstances both geographically and in time.

3.1   OVERALL AERODYNAMIC OBJECTIVE

The overall aerodynamic objective for most wind tunnels is to obtain a flow in the test section that is as near as possible to a parallel steady flow with uniform speed throughout the test section. Perfection is not possible so every design is bounded by constraints that include maximum cost, available space, available time, and available knowledge. It is almost always desired to obtain the largest size of the test section and the highest speed for the available funds. High speed and large size **are** of course competing demands.

Aeroacoustic evaluations and experiments have become of great importance in low-speed aerodynamics for a number of applications. The requirement for a facility to be a useful aeroacoustic facility is that the background noise level be **sufficiently** low. One very specialized tunnel for this purpose was described in the previous chapter. However, there are now many tunnels that have been modified to various degrees to reduce the background noise level. The specifications for many new tunnels include the requirements on background noise. It is also the case that more sophisticated measurement techniques and instrumentation are making it possible to obtain useful acoustic measurements in environments with higher background noise. We will not give a basic quantitative treatment of design for acoustic purposes as we will for aerodynamic performance. We will provide some descriptive information on the treatments that have been applied to some facilities.

There are some wind tunnels for which nonuniform and unsteady flow is desired. For **such** tunnels specifications on the spatial and time variations in the test section are given. The design of these tunnels is not treated here explicitly, although they will have many of the features of more conventional tunnels.

3.2   BASIC DECISIONS

Unit Reynolds Number

From the discussions in Chapters 1 and **2,** it can be concluded that a central issue in the sizing of a low-speed wind tunnel will be the achievable Reynolds number

for the models that can be accommodated. The same question arises for vehicle developers who must select from available wind tunnels one in which to carry out the tests in a development program. The equation for Reynolds number as given in both Chapters 1 and 2 is $R_e = \rho_\infty V_\infty l/\mu_\infty$. We will choose a Mach number of 0.3 as the upper limit of Mach number for the free stream beyond which we may be concerned about the effect of Mach number on a typical study. Considering sea level standard atmospheric conditions,' the maximum for V_∞ will be —330 ft/sec, or —100 m/s, and the "unit Reynolds number" will be —2.13 X 10^6 ft^{-1}, or 6.98 X 10^6 m^{-1}. These numbers and the appropriate characteristic length of the test article give a good approximation to the available Reynolds number in an atmospheric wind tunnel.

For vehicles including aircraft and racing automobiles that can operate at speeds of Mach 0.3 or greater in the atmosphere, test articles would have to be at least full scale to achieve operational Reynolds numbers in an atmospheric wind tunnel. This is either impossible or very costly for many vehicles. As a consequence there has been and continues to be much attention focused on obtaining effective results with less than full-scale test articles or with various separate component tests. An important example of the contribution of component testing is the development of airfoil profiles for various purposes that are then incorporated into three-dimensional wing designs. Another widely used method is to test half models since many vehicles have a plane of symmetry. Most important of all is the careful study of aerodynamic phenomena as they are affected by variation of Reynolds number so that useful conclusions can be obtained from tests that do not duplicate the operating Reynolds number.'

For many studies it is not necessary to produce the full-scale Reynolds number, but it must be of a "reasonable" value. Much low-speed testing involves aircraft takeoff and landing configurations where the Mach number is typically in the 0.15–0.3 range. Both the lift curve slope and maximum lift coefficient are affected by Mach numbers as low as 0.2. This tends to require a tunnel speed approximately equal to the full-scale landing speed. In an unpressurized tunnel using air, this means that the Reynolds number ratio of model to full scale is approximately equal to the size ratio between the scale model and the aircraft.

A primary decision is the choice of the minimum acceptable value of Reynolds number. Because much of low-speed testing is at high-lift conditions, the effect of Reynolds number on airfoils at high lift must be considered. Maximum lift and lift curve shape near stall for single-element airfoils vary considerably with Reynolds number up to at least one million. For multielement airfoils this range is much greater. The continuing need for testing facilities that allow near-full-scale Reynolds number testing of transport aircraft high-lift systems is a primary reason that the United States in the mid-1990s seriously considered construction of major new wind tunnels.[3]

In any case, the lower boundary for testing airfoils and wings for vehicles that will operate at higher full scale values is a Reynolds number in the range of 1,000,000–1,500,000 based on chord. At these values of Reynolds number, the model is likely to have an extensive region of laminar flow, and the possibility exists of poor simulation owing to separation of the model's laminar boundary layer.

It is assumed that laminar separations are unlikely to occur at full scale in the normal operating conditions. Therefore, flow similar to full scale is more likely to be achieved by fixing the transition location on the model? If the Mach number is taken as 0.2, then the tunnel velocity is about 150 mph. For this speed the unit Reynolds number is a little less than 1,500,000 ft^{-1}. Although the minimum Reynolds number cannot be rigidly defined, the above rationale has been used to define a minimum Reynolds number of between 1,500,000 and 2,500,000 based on wing chord for low-speed tunnels to be used for aeronautical development testing. There are some flight vehicles that operate at lower Reynolds numbers. There is, in fact, a whole series of airfoils for soaring gliders that are especially designed to operate at Reynolds numbers below 1,000,000. There are also an increasing number of small low-speed unmanned vehicles. Operational Reynolds numbers for these aircraft are often obtainable in a medium-sized wind tunnel.

For vehicles that operate in the atmosphere at speeds such that the Mach number is less than 0.3, the operational Reynolds number can be duplicated in an atmospheric wind tunnel with a scaled model. Consider a production automobile operating at 60 mph. The operating Reynolds number can be obtained using a three-eighths-scale model with an atmospheric tunnel test speed of 160 mph.

For marine vehicle testing, it is necessary to compare the properties of water and air and consider the differences in typical vehicle speeds. The ratio of the kinematic viscosity of air to the kinematic viscosity of water at a temperature of 15°C is about 13. A test of a marine vehicle in air at equal size would require an air flow speed 13 times greater than water flow speed to obtain equal Reynolds numbers. Or if a one-third-scale model is used, the air flow speed required would be 39 times the operational speed in water. In such a case the Reynolds number for an operational speed of 5 knots would be duplicated with an air flow speed of 195 knots. This approximate combination has proved to be quite useful in the development of keels for racing yachts. As with aircraft, the achievable Reynolds numbers are not as high as the development engineer would like. Great diligence in assessing the effect of Reynolds number is required. The kinematic viscosities of air and water vary significantly with temperature so the above ratio, taken at 15°C, must be adjusted according to expected operational conditions.

As reflected in the above discussions, it is not possible to give a rigid rule for the minimum acceptable Reynolds number. It has been suggested by Bradshaw and Pankhurst[5] that the laminar boundary layer momentum thickness Reynolds number, $\rho V \delta_2 / \mu$, at the minimum pressure point on the test body should be at least 320. This has been given by Preston[6] as the minimum at which a fully developed turbulent boundary layer can exist.

Test-Section Size

This is commonly the starting point in the design of a wind tunnel. The choice will follow from considerations of the desired Reynolds number capability, the budget for tunnel construction, and the costs for tunnel operation and tunnel users as reflected particularly in required model characteristics.

Airplane Models For a mean geometric chord of 1 ft and aspects ratio of 8–9 for an aircraft wing, the span is between 8 and 9 ft. The maximum span should be less than about 0.8 of the tunnel width due to effects of tunnel walls on the flow,' which leads to a width of 10–11.25 ft. For rectangular solid-wall tunnels, wall correction factors given in Chapter 10 show that for a small wing the wall correction factor will be minimum for a width-to-height ratio of about 1.5. The above considerations indicate why so many tunnels have been built in the 7 × 10- to 8 × 12-ft size range with maximum speed in the range of 200–300 knots. In addition to the consideration of flow properties, a model for a tunnel of this size is large enough so that the smaller parts are relatively easy to build.

Test-section lengths based on transport type aircraft testing or even fighter types of the World War II era were chosen to be −1–1.5 times the width based on the fact that span-to-length ratios tended to be greater than 1. Fighter aircraft and others for operation at transonic and higher speeds have much lower aspect ratios. Optimum test sections for these vehicles have greater lengths, perhaps on the order of 2 times the width.

V/STOL Aircraft For V/STOL models in a STOL descent case the speed will be near 70 knots due to model power limits or tip Mach number on propellers and rotors. The reduction in test speed will require a larger model to maintain reasonable Reynolds numbers. To minimize the wall corrections due to large downwash angles from these models, the model-span-to-tunnel-width ratio must be smaller, typically between 0.3 and 0.5. Thus the V/STOL tunnels built in the 1960s have test sections that are 20–30 ft wide.

Automobiles A key issue for automobile tunnels is the blockage based on frontal area. The flow around automobiles is often more characteristic of "bluff bodies" than of "streamlined bodies." This means that there is almost always a sizable region of separated flow. The wind tunnel test section needs to be sufficiently long so that these separated flow regions "close" before encountering the end of the test section and the entry of the diffuser. Otherwise the pressure in the separated region will not be correct and a large influence on drag will exist. In addition, the length-to-width ratio of automobiles is greater than for aircraft while the width-to-height ratio is much less. A wind tunnel test section sized for automobiles is therefore typically longer than a test section sized for aircraft and the width-to-height ratio approximates the width-to-height ratio of standard automobiles. Ideally the blockage, the ratio of model frontal area to test-section area, will be −5% or less. This is based on confidence (or rather lack of confidence) in blockage correction methods. Sufficient progress in correction methods has been made in recent years so that higher blockage factors are increasingly accepted as a trade against cost. At the same time, slotted-wall test sections have been found to provide good results with larger blockage than either completely open or completely closed test sections.

Keels, Submarines, and Sails Submarines and surface ships obviously have large length-to-width ratios. In addition, their operational range for "leeway" is smaller than that for angle of attack or sideslip for aircraft. A test section chosen for testing

these vehicles would have a length-to-width ratio of 2 or greater. Yacht keels are sufficiently similar to aircraft wings that they fit comfortably into conventional aircraft test sections. Test configurations that include both keels and rudders would be better accommodated in test sections with higher values of length-to-width ratio.

Sail testing for both main sails and spinnakers has difficulties associated with the variability of the shapes under load. There are no currently available "rules of the road" to guide such tests.

Instructional and Other Small Tunnels   For small research tunnels and student tunnels at universities and elsewhere, the prospect of achieving or even approaching operational Reynolds numbers is usually beyond the available budget. In many instances the problem of building models accurately may be a critical factor. Assuming that students can hold an airfoil dimension to 0.01 in. and that it is sufficient to hold the model to 1–2% tolerance, the following results can be reached. For a 12% thick airfoil with **2%** tolerance the minimum thickness equals 0.50 in., and the chord is 4.16 in. Using a mean chord of 4.0 in. and aspect ratio of 8, the span is 32.0 in. As the maximum span is 0.8 of the tunnel width, the width is 40 in. Using a width-to-height ratio of 1.5 for a minimum wall correction factor, the height is 26.7 in. The cross-sectional area is then —7.5 ft^2. A minimum test velocity would be about 100 ft/sec or a dynamic pressure of 12 lb/ft^2 because lower speeds and corresponding dynamic pressures would require instrumentation sensitivities that either are not readily available or **are** more costly than necessary.

Many demonstration tunnels and calibration tunnels have test-section areas of 1 ft^2 or less. These **are** very useful for observation of basic flow phenomena and calibration of instrumentation probes. However, they **are** of little use for doing vehicle component studies except in cases for which Reynolds numbers are quite low?

For a rectangular tunnel the width determines the model size and the Reynolds number at a fixed speed. The cost of the tunnel shell and its required power tend to vary with the square of the test-section width. Since funds for a tunnel are usually fixed, the largest tunnel that the funds will buy is generally built.

The size of smaller tunnels is frequently determined in the final analysis by the size of the room that will house the tunnel.

The Reynolds number per foot for a given size tunnel can be increased by building either a pressure tunnel or a cryogenic tunnel using a cold gas such as nitrogen. Other working fluids such as Freon and sulfur hexafluoride have been used to obtain desired conditions. These are special-purpose tunnels, and the need for their special capabilities must justify the cost as with any other tunnel. The time required for model changes will be long unless special provisions are made because the test section must be isolated before workers can enter to work on the model. Test productivity, as well as flow characteristics, is an important characteristic of a wind tunnel.

Open or Closed Return

Another basic design consideration is whether the tunnel will be of return or nonreturn (open circuit) type. Almost all of the small research tunnels are of the nonreturn

type, usually because of the lower construction costs. Power consumption for such tunnels is usually not a significant factor in overall cost. Although there exist some larger tunnels of nonreturn design, most of the larger tunnels are of the return type, the majority being single return. A few of the earlier tunnels were of double-return type. However, it has been more than 50 years since the double-return design has been chosen for a new wind tunnel.

Open or Closed Test Section

Open jet tunnels will have a lower energy ratio than a closed jet wind tunnel owing to the jet entraining stagnant air as it passes from the contraction cone exit to the collector inlet. If the tunnel has an external balance, the balance usually has to be shielded from the air jet and one of the boundaries tends to be closed. Open throats do not work for an open circuit tunnel with a propeller in the diffuser unless the test-section region is enclosed in an air-tight plenum or room. Open throat tunnels often suffer from pulsations similar to vibrations in organ pipes. An open throat gives easy access to the model in small tunnels. In large tunnels scaffold of some type is required to gain access to the model. The setting up and removal of the scaffold requires additional model change time. Since the jet length is usually kept short to reduce losses, there is the possibility that high-lift models may deflect the wake enough to miss the collector or that the wake of a bluff body will interact with the collector. An open jet provides easier access for traversing devices to move instrumentation to any point in the flow.

In general, the advantages appear to be with the closed throat tunnel for aeronautical testing. However, considerations of bluff body aerodynamics and overall size requirements have led to a number of open, partially open or slotted wall, and convertible jet tunnels built by automobile companies and others who engage in automobile test work or V/STOL development. These arrangements provide greater flexibility in uses of a tunnel provided the staff are sufficiently knowledgeable about the variety of wall effects that must be understood.

Closed throat tunnels that are vented to the atmosphere not at the test section but at another location will have the test section below atmospheric pressure. Thus they can suffer from leaks either through holes cut in walls for probes, wires, pipes, and so on, or through the struts required to mount the model. These tunnels usually have a sealed room or plenum around the test section. When running, the plenum will be at the same static pressure as the test section. Most small open circuit tunnels are not built this way and suffer from leaks. This makes wood an ideal material for such tunnels because it is easy to patch.

Aeroacoustic testing has become an important area of work in the development of a number of vehicles. Although such tests are done in both open and closed test-section facilities, an open test section provides the possibility for more complete test cell antireflection or anechoic treatment.

General Layout: Closed Return

The general layout for closed return tunnels has reached a form generally agreed upon for reasons of construction economy and tunnel efficiency. A thorough discussion of

design issues is given by Bradshaw and Pankhurst.[5] Starting with the test section and going downstream the common configuration includes the following elements:

(a) *The test section, which may be closed, open, partially open or convertible.* The test-section-length-to-hydraulic-diameter[9] ratio may typically be chosen to be 2 or more, in contrast to the shorter test sections of earlier era tunnels.

(b) *A diffuser of at least three or four test-section lengths.* The typical equivalent cone angle is in the range of 2–3.5° with the smaller angles being more desirable. The area ratio is typically 2–3, again with the smaller values being more desirable.

(c) *"First comer" incorporating turning vanes.*

(d) *Second leg that may continue the diffuser or may be constant area.*

(e) *Safety screen to prevent parts of failed models or other unintended flying objects from reaching the fan.* This screen is usually just ahead of the second-comer turning vanes.

(f) *"Second comer" incorporating tuming vanes that may be essentially copies of the first comer vanes solely to gain a small engineering and construction cost reduction.*

(g) *Transition from rectangular to circular cross section to take flow into the fan.*

(h) *Fan and straightener section.* Other drive devices such as ejectors have also been used.

(i) *Return or second diffuse]:*This will commonly incorporate a transition back to rectangular from the circular cross section at the fan. The transition will likely have begun in the straightener section. The second diffuser should follow similar design guides as the first diffuser.

(j) *"Third corner" incorporating turning vanes.*

(k) *Third leg that may be constant area.*

(l) *Heat exchanger.*

(m) *"Fourth comer" incorporating turning vanes that may be copies of the third-corner vanes.*

(n) *Wide-angle diffuser with separation control screens.* Typical properties are angles of about 45° and area ratios of 2–4.

(o) *Settling area.*

(p) *Flow conditioners typically including jlow straighteners and turbulence control screens.*

(q) *Contraction or nozzle.* Typical area ratios are in the range of 7–12, although lower and higher values are not uncommon.

The plane of the return passage is almost always horizontal to save cost and make the return passage easier to access. A vertical return is justified only when space is at a premium and has only been used for small-sized tunnels.
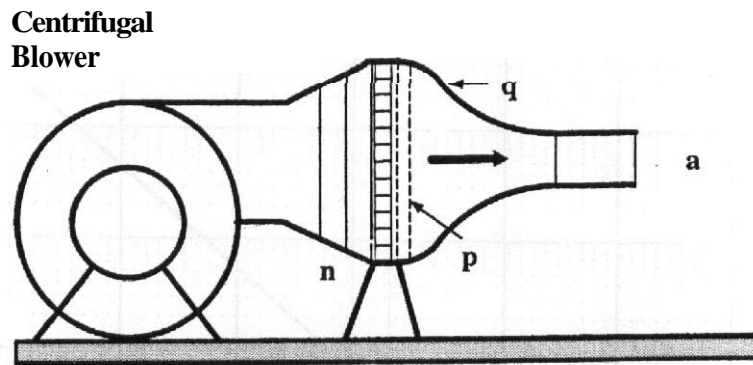
FIGURE **3.1** Layout of a closed single-return wind tunnel.

A representative layout of a closed return tunnel with notation for our analyses is given as Figure 3.1.

Ewald and co-authors[10] have presented a concept for obtaining economies in wind tunnel construction by producing a series of various sizes for which there are many common components. The first- and second-comer assemblies for one size would be the same as the third- and fourth-comer assemblies for the next larger size tunnel. The fan diffuser for one size would be the test-section diffuser for the next larger size. The engineering and construction drawings would be the same for all sizes except for the specified scale for each instance.

There are many very innovative configurations to accommodate particular needs that are quite different from the typical circuit described above. Planners of new facilities should consult more specialized literature for descriptions and discussions.

General Layout: Open Circuit

A typical layout of an open circuit tunnel is given in Figure 3.2, again with notation for reference in the analyses.

This type of tunnel is widely used for instructional purposes and for investigations of fundamental flow phenomena.

General Layout: Blower Tunnel

Another type of open circuit flow facility is the "blower tunnel" or "free-jet" facility. These are also widely used for instructional purposes and for calibration of flow

FIGURE **3.2** Elevation cross section of a typical small open circuit wind tunnel.

**Centrifugal
Blower**

FIGURE **3.3**   Typical layout of a blower driven free jet.

devices. A characteristic design problem for these facilities is choice of details of a wide-angle diffuser between the fan or blower and the settling area prior to the contraction. Mehta[11] gives a very useful discussion of the design of this class of flow facility. A typical facility layout is shown in Figure 3.3. The design guides for the wide-angle diffuser of a facility of this type are also applicable to a wide-angle diffuser to be a part of a closed return wind tunnel.

3.3   POWER CONSIDERATIONS

A measure of merit with regard to energy consumption and a framework for consideration of the energy consumption of various elements of a wind tunnel are developed in this section. **All** of the analyses given here are "one dimensional" in nature. The conditions at any cross section of a wind tunnel circuit are considered to be represented by the area-weighted average value of the flow parameters over the section. Consider the static pressure p at location c in a wind tunnel circuit that has cross-sectional area A_c. The static pressure p_c at c is characterized by the weighted average given by the equation

$$p_c \equiv \frac{1}{A_c} \iint_{A_c} p \, dA \tag{3.1}$$

Some ambiguity and inaccuracy is introduced by the assumption of one dimensionality, but the results are quite valuable in gaining an understanding of the behavior of flow in a wind tunnel circuit. It is likely that most existing wind tunnels have been configured using this assumption for the design calculations.

Jet Power

It is instructive to consider the power in a flowing jet to get **an** idea of the magnitudes involved. The power in a flowing jet, for example the flow in a wind tunnel test
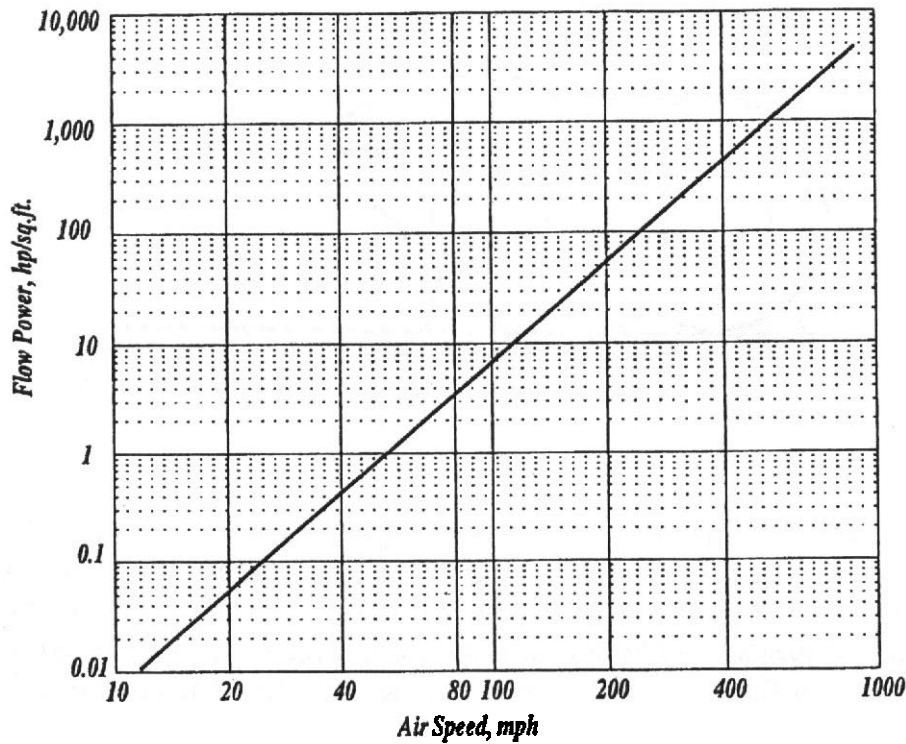
FIGURE 3.4   Jet power per unit area as a function of air speed for standard sea level density.

section, can be expressed in terms of density, test-section area, **and** test-section flow velocity **as** given in the equation

$$P_t = \tfrac{1}{2}\dot{m}_t V_t^2 = \tfrac{1}{2}\rho_t A_t V_t^3 \tag{3.2}$$

Figure 3.4 shows a plot of jet power per unit area for standard sea level air density as a function of jet speed.

Table 3.1 gives some specific values. The jet power for a tunnel with a test section of 100 ft^2 running at 200 mph is 5456 hp. Values are taken from the graph. The values of jet power are proportional to density so jet power at a given speed

TABLE 3.1. Jet Power per Unit Area at Selected Speeds

V (mph)	V (m/s)	Mach Number	hp/ft^2	kW/m^2
20	8.94	0.026	0.055	0.44
50	22.35	0.066	0.85	6.88
100	44.7	0.131	6.82	54.72
200	89.4	0.263	54.56	437.3
300	134.1	0.394	184.15	1476.2
400	178.8	0.525	436.51	3499.9

would vary accordingly if the density in the jet is different from the standard sea level value of 0.002378 slug/ft^3.

The data shown in Figure 3.4 and Table 3.1 are a good indication of the upper limits on flow speed obtainable from a known power source in a blower tunnel where all of the energy in the open jet is simply-dissipated in the surrounding air. This is also characteristic of simple heating and ventilating fans or blowers such as leaf blowers. Both closed return and open circuit configurations with diffusers can sustain test-section or jet flows with power greater than that of the power source, as will be developed in the following.

Energy Ratio

The ratio of the power in the test-section flow to the rate of "flow losses" around the circuit is a measure of the energy efficiency of a wind tunnel, although it is by no means a measure of the value of the tunnel for research and development. Other denominators in the definition of energy ratio are sometimes used. For example, the denominator might be chosen as the electrical power input to the motor or the mechanical power applied to the shaft of the fan. The definition chosen here provides a focus on the aerodynamic aspects of the energy budget and serves to separate clearly the circuit flow properties from the efficiency of the driving fan and the electrical or other driving equipment.

If we denote the rate of "flow losses" in the circuit by P_c, then the "energy ratio" can be expressed by

$$E_R = \frac{P_t}{P_c} \tag{3.3}$$

The energy ratio for closed return wind tunnels and open circuit tunnels other than free-jet facilities is nearly always greater than unity. It is typically in the range 3–7 for closed throat tunnels. The energy ratio for a free-jet facility is always less than 1, which is an important reason there are no large-size facilities using the free-jet configuration. We now turn to methods for estimating the energy balance in various parts of a wind tunnel so that the energy ratio for various wind tunnel configurations can be estimated.

Wind Tunnel Component Energy Losses

Wattendorf[12] considered the losses in a return-type wind tunnel by splitting the tunnel into component parts and analyzing the losses in each component in succession. Typical components are considered as (1) cylindrical sections, (2) corners, (3) expanding sections or diffusers, (4) contracting sections, (5) annular sections, (6) straightener section, and (7) fan. The fan is exceptional since energy is supplied to the airstream at that location. Wallis[13] provides a similar but much more extensive discussion. Eckert, Mort, and Jope[14] use the same approach and give an early

FORTRAN computer code along with results for several existing wind tunnels. These breakdowns can be compared to the typical layout given earlier for the closed return wind tunnel configuration.

In each of the sections except for the propeller or fan, it is commonly said that a loss of energy occurs. Actually there is an energy transformation from mechanical form to heat that results in raising the temperature of the flowing gas and the solid materials with which it is in contact. The energy transformation comes about due to the viscous action between the flowing gas and the solid boundaries.

We will refer to this transformation from mechanical energy to heat as a "loss" in the following discussion. Although the treatment later includes compressibility, the discussion given here is for incompressible flow.

If Bernoulli's equation, $p_{static} + \frac{1}{2}\rho V^2 = p_{total} = const$, were written between two locations in a duct, it would apply only if there were no losses between the sections. Naturally, in practice, there are always losses, and one or the other of the two terms at the second section must show a diminution corresponding to the loss in head. The law of continuity for an incompressible fluid, $A_1 V_1 = A_2 V_2$, where A and V are areas and velocities at the two stations, constrains the velocity, and hence the velocity head or dynamic pressure at the second location cannot decrease. But there will be equal drops in static head and in total head corresponding to the friction loss. Throughout the wind tunnel the losses that occur appear as successive pressure drops to be balanced by the pressure rise through the fan. The total pressure drop ΔH will be the pressure rise required of the fan.

The loss in a section is defined as the mean loss of total pressure sustained by the stream in passing through the particular section. The loss in a section is given in dimensionless form by the ratio of the pressure loss in the section to the dynamic pressure at the entrance to the section. For a typical "local" section this is given by

$$K_l = \frac{\Delta H_l}{(1/2)\rho_l V_l^2} = \frac{\Delta H_l}{q_l} \qquad (3.4)$$

This definition of loss coefficient is both important and convenient. It is convenient because the total pressure loss and the dynamic pressure are easily measurable quantities. We now consider further its importance. The time rate of energy loss in a section can be expressed as the product of the total pressure loss times the volume rate of flow through the section, $\Delta E_l = A_l V_l \Delta H_l$, which with ΔH_l from Equation (3.4) gives $\Delta E_l = A_l V_l K_l q_l$, and finally

$$\Delta E_l = K_l \left(\frac{1}{2} \dot{m} V_l^2 \right) \qquad (3.5)$$

Equation (3.5) shows that the loss coefficient defined by Equation (3.4) on the basis of total pressure loss and dynamic pressure also is the ratio of the rate of energy loss to the rate of flow of kinetic energy into the section.

Following Wattendorf these local losses are referred to the test-section dynamic

pressure, defining the coefficient of loss of the local section referred to the test-section dynamic pressure as

$$K_{lt} = \frac{\Delta H_l}{q_l} \frac{q_l}{q_t} = K_l \frac{q_l}{q_t} \tag{3.6}$$

Using the definition of P_t as given by Equation (3.3) with Equations (**3.5**) and (**3.6**) provides a test-section referenced result:

$$\Delta E_l = K_{lt} \left(\tfrac{1}{2}\dot{m}V_t^2\right) = K_{lt}P_t \tag{3.7}$$

The total rate of loss in the circuit is obtained by summing the rate of section losses for each of the individual sections:

$$P_c = \sum_l \Delta E_l = \sum_l K_{lt}P_t \tag{3.8}$$

The energy ratio as defined by Equation (3.3) can be expressed in terms of the loss coefficients of the various sections as

$$E_R = \frac{1}{\Sigma_l K_{lt}} \tag{3.9}$$

As noted previously, this definition of energy ratio excludes the energy losses associated with the **fan** and the motor. The total rate of loss in the circuit **as** represented by Equation (3.8) is the net power that the tunnel drive device must deliver to the airstream to maintain steady conditions.

Losses in a Constant-Area Section

Here we discuss an approximation for the loss in a constant-area section. It is usually the case that even the test section has a small variation in cross-sectional area with streamwise coordinate. But the relations for constant-area sections with fully developed flow are the basis for a number of loss estimates so that treatment is given here rather than in connection with a particular section analysis.

In the literature on hydraulics, there is a long history of expressing the flow losses in constant-area pipes in the form

$$\frac{\Delta p}{\rho} = f \frac{L}{D_h} \frac{\overline{U}^2}{2} \tag{3.10}$$

where Δp is the pressure drop over the length L of pipe of hydraulic diameter D_h, $\overline{U}$ is the mean speed of flow, and f is the "friction factor" or "friction coefficient". The parameter p is the density of the fluid as usual. The hydraulic diameter is

related to area by $D_h \equiv 2\sqrt{A/\pi}$. Comparing Equation (3.10) to Equation (3.4) shows that the local section loss coefficient is related to the friction factor by

$$K_l = f\frac{L}{D_h} \tag{3.11}$$

A relation to the wall shear stress can be given for constant-area sections. In a constant-area section the pressure drop is entirely balanced by the skin friction τ_w on the walls. In this case $L_{ca}\bar{\tau}_w C_{ca} = A_{,,} \times \Delta p_{ca}$, where L_{ca} is the length, C_{ca} is the circumference, and the overbar indicates an average of the wall shear stress. We obtain Equation (3.12) for a circular pipe with fully developed flow so that the wall shear stress is constant:

$$\tau_w = \tfrac{1}{4} f(\tfrac{1}{2}\rho\overline{U^2}) \tag{3.12}$$

The loss in a section is clearly dependent on cross-sectional shape since shapes other than circular will have circumferentially varying wall shear stress. The circumferential variation will be dependent on the geometric shape. That dependence will not be considered here as the range of cross sections that are suitable for wind tunnels is rather limited. Some discussion of cross sections is given by Shames.[15] Here the cross section will be considered to the characterized by the hydraulic diameter, which is defined above. For smooth pipes at high Reynolds number Shames[15] gives the *Prandtl universal law* of friction relating the Reynolds number and the friction factor:

$$\frac{1}{\sqrt{f}} = 2\,\log_{10}(R_e\sqrt{f}) - 0.8 \tag{3.13}$$

where

$$R_e = \frac{\rho V_{ca} D_h}{\mu}$$

where V_{ca} is the mean speed in the section. The friction factor f decreases with R_e. Here, f ranges from 0.013 at $R_e = 500{,}000$ to 0.010 at $R_e = 2{,}500{,}000$ to 0.007 at $R_e = 30{,}000{,}000$.

A convenient form of Equation (3.13) for an iterative solution algorithm is given by

$$f = [2\,\log_{10}(R_e\sqrt{f}) - 0.8]^{-2} \tag{3.14}$$

A starting value as far away as f $= 1$ will lead to convergence to four significant figures or better within four to six iterations.

Friction Factor and Skin Friction Coefficient

The skin friction coefficient for a flat plate in a uniform stream is defined by the relation $\tau_w = \tfrac{1}{2}\rho V_\infty^2 c_f$. The analogous expression for flow in a circular pipe would

be $\tau_w = \frac{1}{2}\rho U^2_{max} c_f$. Comparing this last expression to Equation (3.12) shows that $U^2_{max} c_f = \frac{1}{4} U^2 f$, or

$$c_f = \frac{1}{4} \frac{\overline{U}^2}{U^2_{max}} f \qquad (3.15)$$

These relations provide a framework within which to apply available theory and experimental data in an approximate way. There is no part of a wind tunnel circuit where the flow is actually close to fully developed pipe flow.

Dynamic Pressure Ratios and Reynolds Numbers

The task of finding the power required to drive a wind tunnel with a given P_t is now broken down into the subtasks of evaluating the K_{lt}'s for all subsections of the wind tunnel. In turn from Equation (3.6) it is seen that this task for each section can be subdivided into the evaluation of a loss coefficient based on local entry conditions and the ratio of local dynamic pressure to test-section dynamic pressure, q_l/q_t, which in turn can be rewritten as

$$\frac{q_l}{q_t} = \frac{A_t V_l}{A_l V_t} \qquad (3.16)$$

The factor represented by Equation (3.16) is evaluated using either an assumption of incompressible flow or an assumption of one-dimensional isentropic compressible flow. If the flow is assumed to be incompressible, then the condition of constant mass flow rate at each section yields

$$\frac{q_l}{q_t} = \frac{A_t^2}{A_l^2} \qquad (3.17)$$

The application of mass conservation including consideration of compressibility yields Equation (3.18), in which M is the Mach number at the location indicated by the subscript. In this equation, the areas and the test-section Mach number would be given but the local Mach number would not be known and must be determined:

$$\frac{q_l}{q_t} = \frac{A_t}{A_l} \frac{M_l}{M_t} \frac{\sqrt{1 + [(\gamma - 1)/2]M_t^2}}{\sqrt{1 + [(\gamma - 1)/2]M_l^2}} \qquad (3.18)$$

The local Mach number is a function of the test-section Mach number and the ratio of the local area to the test-section area. The equation is transcendental, which prevents the functional relation from being explicitly written down. The area–Mach number relation is often given in terms of the area A^* for choked flow and is shown here as Equation (3.19) (see Anderson[16] for development of these relations):

$$\left(\frac{A}{A^*}\right)^2 = \frac{1}{M^2}\left[\frac{2}{\gamma + 1}\left(1 + \frac{\gamma - 1}{2}M^2\right)\right]^{(\gamma+1)/(\gamma-1)} \tag{3.19}$$

If the ratio of Equation *(3.19)* applied to the test section is taken to the same equation applied to a local section, Equation *(3.20)* is obtained:

$$\left(\frac{A_l}{A_t}\right) = \left(\frac{M_t}{M_l}\right)^2 \left(\frac{1 + [(\gamma - 1)/2]M_l^2}{1 + [(\gamma - 1)/2]M_t^2}\right)^{(\gamma+1)/(\gamma-1)} \tag{3.20}$$

In the case of air as the working fluid for which the ratio of specific heats is *1.4,* Equation *(3.21)* is obtained:

$$\frac{A_l}{A_t} = \frac{M_t}{M_l}\left(\frac{1 + 0.2M_l^2}{1 + 0.2M_t^2}\right)^3 \tag{3.21}$$

This can be put in the form of Equation (3.22), which is convenient for an iterative algorithm to obtain the local Mach number when test-section Mach number, test-section area, and local **area** are given. A starting value of $M_l = 0$ can be used for subsonic wind tunnels:

$$M_l = \frac{M_t}{(1 + 0.2M_t^2)^3}\frac{A_t}{A_l}(1 + 0.2M_l^2)^3 \tag{3.22}$$

After obtaining the local Mach number, Equation *(3.18)* can then be used to obtain the ratio of local dynamic pressure to test-section dynamic pressure.

In the following discussion of losses in the various sections, the Reynolds number will be a needed parameter for each section. The test-section Reynolds number would usually be assumed given, which is $R_{et} = (\rho_t V_t D_t)/\mu_t$, where the test-section reference length is taken as the test-section hydraulic diameter. The local Reynolds number is related to the test-section Reynolds number by

$$R_{el} = R_{et}\frac{l}{D_t}\frac{\rho_l V_l}{\rho_t V_t}\frac{\mu_t}{\mu_l} = R_{et}\frac{l}{D_t}\frac{A_t}{A_l}\left(\frac{1 + [(\gamma - 1)/2]M_t^2}{1 + [(\gamma - 1)/2]M_l^2}\right)^{0.76} \tag{3.23}$$

3.4   SECTION LOSS COEFFICIENTS

The losses in various sections and components will not be considered. The treatment will be based on a typical closed return wind tunnel. Discussions of considerations in the design of typical wind tunnel sections will be given followed in each instance by the development of the loss analyses. We begin with the test section and proceed in the flow direction around the circuit. Three example wind tunnel designs are

considered at the end of the chapter. Figure 3.1 and the related description provides nomenclature for the various sections.

Test Section (a)[17]

Over the years many shapes have been used for test sections, including round, elliptical, square, rectangular, hexagonal, octagonal, rectangular with filleted comers, flat ceiling, and floor with half round ends. The cost and power are directly determined by the cross-sectional area and the length. The difference in losses in the test section due to the cross-sectional shape are negligible. Therefore, the shape of the test section should be based on the utility and considerations of the aerodynamics of the models to be tested.

For ease in installing models, changing models, installing ground planes, calibrating external balances, installing splitter plates for half models, or other modifications for nonstandard tests, no alternative can match a test section with flat walls. The flat ceiling and floor simplify the installation of yaw turn tables for a three-strut mounting system and its image. A flat floor is a major advantage if surface vehicles are to be tested. The walls, ceiling, and floor allow easy installation of windows to view and photograph the model when flow visualization is used. Some early wind tunnels had circular or elliptic shaped test sections due to availability of functional mathematical expressions for certain types of wall corrections for wings. This was of considerable importance when calculations were done by slide rule and by hand, but the currently available and growing computational power makes such considerations of little consequence today.

As the air proceeds along the test section, the boundary layer thickens. This action reduces the effective area of the jet from that of the geometric dimensions and causes an increase in the flow speed outside the wall boundary layers. If the geometric area is constant, the speed increase in turn produces a drop in local static pressure, tending to draw the model downstream. This added drag is commonly called "horizontal buoyancy"[18] as its action is analogous to the buoyancy due to the vertical pressure gradient in the atmosphere and the ocean. If the cross-sectional area of the jet is increased enough to allow for the thickening boundary layer, a constant value of the static pressure may be maintained throughout the test section. No exact design method is available that ensures the development of a constant static pressure. For a first approximation the walls of a closed jet should diverge about $\frac{1}{2}^{o}$ each; finer adjustments may be necessary after the tunnel is built and the longitudinal static pressure is measured. Some tunnels whose test sections have comer fillets have these fillets altered until a constant static pressure is obtained. The advantages of such a flow are enough to justify a moderate amount of work in obtaining it.

To minimize secondary flow problems in the comers of rectangular contractions, a $45°$ fillet is often installed at the *start* of the contraction to form an octagonal shape. These fillets are, in many tunnels, carried through the test section to prevent boundary layer growth in the comers of the test section and down the diffuser tapering out at the end of the diffuser.

The length of the test section in tunnels designed with aeronautical work as the primary focus varies from one to two times the major dimension of the section. The power losses in the test section are sizable, as will be seen shortly owing to the high speed; thus power can be saved by keeping it short. However, contractions do not deliver a uniform velocity distribution to the beginning of the test section. Therefore, a constant-area duct before the test section is usually employed. The lengths of test sections of wind tunnels that are expected to be used to test articles with large volumes of separated flow need to be sufficiently long so that all separated flow zones will close before the beginning of the diffuser.

A practical detail in the test-section design is the installation of sufficient windows for viewing the model. In the course of testing it will become necessary to see all parts of the model: top, sides, bottom, and as much of the front as is reasonably practical. For safety reasons, windows in the test section should be made of shatter resistant material. For many years the material of choice was plate safety glass. There are now plastics that can be used with lasers about as well as any glass short of optical flats. If propellers and rotors are to be tested, the manufacturers of the window material chosen should be consulted to determine the energy absorption capability and large safety factors should be applied. What used to be called bullet-proof glass (which never was bulletproof) is no longer sold under that name owing to product liability laws. It is a peculiar and interesting fact that despite the hazards of testing, more windows have been broken or otherwise damaged by overheating with photographer's lights than by model failure.

Adequate lighting is needed both to work on the model and for photographic purposes. It is very useful in tunnels with fillets in the test section to have lights built into them. Current developments in measurement methods such as pressure-sensitive paint and shear-sensitive liquid crystals will make the optical access of test sections even more critical than has been the case in the past.

Solid-Wall Jets   As mentioned above, test sections will normally have a slight divergence in an effort to obtain a constant static pressure. The analysis given here, however, is based on the relations for a constant-area duct given earlier. The subsequent section on the diffuser gives a treatment that can be adopted for the test section as well. Equations (3.11) and (3.14) are used to evaluate the test-section loss coefficient for a specified Reynolds number.

It is seen from the range of values given for f along with Equation (3.11) that the power loss in the test section of a closed-wall tunnel is of the order of 1% to several percent of the jet power with the test-section length that is chosen having an important part since the loss will be directly proportional to the length. Test sections for wind tunnels over many decades have tended to grow longer. Many tunnels built prior to 1960 have relatively short test sections of the order of 1–1.5 times the hydraulic diameter. The major test articles were expected to be high-aspect-ratio airplanes. In more recent times, tunnels tend to have somewhat longer test sections to accommodate many other test articles.
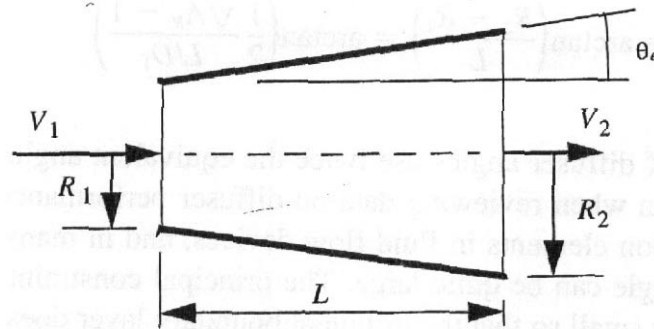
FIGURE 3.5   Diffuser geometry and notation.

Open Jets   For open cylindrical sections such as an open jet, a reasonable value for friction factor is $f = 0.08$. This is nearly an order of magnitude larger than the friction factor for a solid wall. This is a rather large penalty and will influence decisions for tunnels in which power consumption will be a significant factor in operating costs.

Diffusers (b), (d), and (i)

The diffuser" of a return wind tunnel typically extends from the downstream end of the test section to the third comer of the tunnel. It is divided into two parts by the tunnel fan. The second diffuser and fan section is often called the return duct or passage. The first diffuser usually extends to the first comer. Since the power losses at any point in the tunnel are expected to vary as the speed cubed, the purpose of the diffuser is to reduce the speed with as little energy loss as possible. Minimum energy loss corresponds to maximum pressure recovery. It is generally desirable to reduce the speed in the shortest possible distance without incurring flow separation. This will obtain good efficiency and will help to reduce construction costs by reducing the overall size of the tunnel shell. Obtaining good performance from the diffuser is critical to the success of the tunnel. Diffusers are sensitive to design errors that may cause either intermittent separation or steady separation. Such separations can be hard to localize but can cause vibrations, oscillating fan loading, oscillations in test-section velocities (often called surging), and increased losses in the tunnel downstream of their origin.

The primary parameters for a diffuser are the equivalent conical expansion angle and the area ratio. Consider a conical diffuser with a radius R_1 at the entrance, radius R_2 at the exit, and length L as indicated in Figure 3.5. Most wind tunnel diffusers are not conical.

Commonly used cross sections are rectangular or nearly rectangular with reasons closely paralleling the reasons given for choosing test sections with plane walls. The equivalent conical angle is defined as follows. Let R_1 be one-half the entrance hydraulic diameter D_1. Let R_2 be one-half the exit hydraulic diameter D_2 and A_R be A_2/A_1. Then the equivalent conical expansion angle is given by

$$\theta_e = \arctan\left(\frac{R_2 - R_1}{L}\right) = \arctan\left(\frac{1}{2}\frac{\sqrt{A_R} - 1}{L/D_1}\right) \qquad (3.24)$$

Some discussions of diffuser angles use twice the equivalent angle defined here so care should be taken when reviewing data on diffuser performance.

Diffusers are common elements in fluid flow devices, and in many applications the equivalent cone angle can be quite large. The principal constraint on the angle is that it be sufficiently small so that the turbulent boundary layer does not separate. Relatively large angles are possible for the case of uniform flow entering the upstream end of the diffuser. The flow leaving a wind tunnel test section, however, is anything but uniform. There can be wakes from model mounting struts and ground plane support struts; deflected wakes from the model, both laterally and vertically; large separated wakes when a model is stalled in pitch and yaw; or simply a large wake from bluff body models such as automobiles or parachutes. Also, the influence of the corner vanes in the first comer may have adverse effects. Current practice calls for an equivalent cone angle of $3.0°$ or less in conjunction with typical area ratios of around 3. The pressure recovery and pressure gradients and therefore the risk of separation are dependent on both the cone angle and the area ratio.[19] Thick boundary layers at the diffuser entrance will increase the risk of separation. If a very long 2.5" diffuser is used to obtain a large contraction ratio, there is danger of separation. Therefore, the total (both halves of the diffuser) tends to be limited to area ratios of $5:1$ or $6:1$, half of the area ratio in each half of the diffuser. This area ratio limits the tunnel contraction ratio. To achieve larger contraction ratios, a wide-angle diffuser is used before the settling chamber. These are typically diffusers with an area ratio in the range of 2–4 and an equivalent 22.5" cone angle. Screens may be used to smooth out the velocity variations and maintain satisfactory flow. More will be said about large angle diffusers in a subsequent subsection. In the present section, relations will be given for typical conditions for the first and second diffusers.

The return passage will need access doors and windows, usually near the fan. The doors and windows should be sealed and of adequate size to allow for installation and removal of the fan blades and the drive motor if it is placed in the fan nacelle. Built-in lights near the fan are most useful. Provisions for pressure rakes about a half-tunnel diameter ahead of the fan are very useful. The rake will be used to adjust the first- and second-comer vanes to obtain a uniform velocity front at the fan. Drains at the lowest point in the tunnel are also needed since the tunnel will have to be either washed or steam cleaned at intervals during its lifetime.

Diffuser Loss Coefficients In the divergent or diffuser sections, both wall friction and expansion losses occur. The fluid mechanics of diffusers is quite complex since the flow can depend on the details of the incoming flow profiles, which in turn will vary with the specific test model setups in a wind tunnel. For preliminary design purposes several assumptions are commonly made. The first is that the loss coeffi-

cient can be decomposed as a sum of a friction loss coefficient and an expansion loss coefficient, as indicated by

$$K_d = K_f + K_{ex} \tag{3.25}$$

Assuming the skin friction coefficient and density **are** constant along with the "one-dimensional" treatment yields a relation between the friction loss coefficient, conical angle, and diffuser area ratio. The result is given by Equation *(3.26)*. The friction factor is evaluated as in the case of the constant-area section using the entry Reynolds number:

$$K_f = \left(1 - \frac{1}{A_R^2}\right)\frac{f}{8 \sin \theta} \tag{3.26}$$

The expansion loss is more difficult and is obtained presently only by experimental correlation. The expansion loss coefficient is represented as a product of two factors. One factor is a function of the equivalent conical angle and the other is a function of diffuser area ratio. The result is

$$K_{ex} = K_e(\theta)\left(\frac{A_R - 1}{A_R}\right)^2 \tag{3.27}$$

The factor $K_e(\theta)$ depends significantly on the diffuser cross-sectional shape. The forms, based on experimental data and taken from Eckert et al.,[14] for circular and square cross sections are given here as Equations *(3.28)* and (3.29), respectively:

$$K_{e(circle)} = \begin{cases} 0.1033 - 0.02389\theta & \text{for } 0 < \theta < 1.5'' \\ 0.1709 - 0.1170\theta + 0.03260\theta^2 + 0.001078\theta^3 \\ \quad -0.0009076\theta^4 - 0.00001331\theta^5 + 0.00001345\theta^6 \\ \quad \text{for } 1.5° \leq \theta \leq 5° \\ -0.09661 + 0.04672\theta & \text{for } 5° < \theta \end{cases} \tag{3.28}$$

$$K_{e(square)} = \begin{cases} 0.09623 - 0.004152\theta & \text{for } 0 < \theta < 1.5° \\ 0.1222 - 0.04590\theta + 0.02203\theta^2 + 0.003269\theta^3 \\ \quad -0.0006145\theta^4 - 0.00002800\theta^5 + 0.00002337\theta^6 \\ \quad \text{for } 1.5'' \leq \theta \leq 5° \\ -0.01322 + 0.05866\theta & \text{for } 5° < \theta \end{cases} \tag{3.29}$$

Equations *(3.25)–(3.29)* may be used to estimate the local loss coefficient for circular and square cross-sectional diffusers.

Smaller expansions yield smaller losses up to the point where the skin friction of the added area becomes excessive. For reasonable values of λ the most efficient

divergence is about 5". However, as discussed elsewhere, space limitations for the tunnel as well as the cost of construction may dictate that a slightly larger divergence be employed at an increase in cost of operation.

It is found that the losses in a divergent section are two to three times greater than the corresponding losses in a cylindrical tube, although the progressively decreasing velocity would seem to indicate losses between that of a cylindrical section with the diameter of the smaller section and that of one with the diameter of the larger section. The reason for the added loss is that the energy exchange near the walls is of such a nature that the thrust expected from the walls is not fully realized. Effectively, a pressure force is thereby added to the skin friction forces.

The adverse pressure gradient in a diffuser will lead to separation if it is made too large. Since the return passage downstream of the fan will usually have a more uniform flow than the first diffuser just downstream of the test section, the expansion angle is sometimes larger. An additional argument for this type of design is that the disturbance caused by a model in the test section may limit satisfactory diffuser angles below smooth flow values. This is certainly the case for models that are bluff rather than streamlined.

Corners (c), (f), (j), and (m)

To avoid large losses and to maintain relatively straight flow throughout the circuit, the comers are equipped with turning vanes. Comers are usually, but not always, of constant area. The shape of turning vanes varies from bent plates to highly cambered airfoils. Provisions should be made to adjust the vanes either by pivoting the vanes or by trailing-edge tabs. If tabs are used, there should be some method of locking them to prevent their movement after the flow is acceptable. In the initial startup of a tunnel the vanes should be adjusted to ensure that the air is neither over- nor underturned. The first two corners are the most critical in terms of losses (owing to higher dynamic pressure) and the need for a uniform velocity entering the fan.

The losses in the comer vanes can be made small by selecting an efficient cross-sectional shape and by using an appropriate chord-to-gap ratio. Vanes using cambered airfoils and relatively blunt leading edges will be less sensitive to approaching air flow angularities than sharp leading-edge vanes.

The vane camber lines can be designed by cascade theory with good results. The geometry of a comer is indicated by Figure 3.6, which shows the flow between two. typical vanes. It is usually assumed that this flow can be adequately approximated as two dimensional. The exit velocity angle is exaggerated in the figure. The desired angle is usually $\psi = \frac{1}{2}\pi$, that is, $\theta = 0$. The mass flow per passage per unit depth is $\rho U_i h_i$. The local comer loss coefficient is denoted by

$$K_c = \frac{\Delta H_c}{q_c} \tag{3.30}$$

where $q_c = \frac{1}{2}\rho U_i^2$, $\Delta H_c = p_i + q_c - (p_0 + q_0)$, and $q_0 = \frac{1}{2}\rho U_0^2$ with all quantities being evaluated far enough away from the vanes so that the dividing streamlines
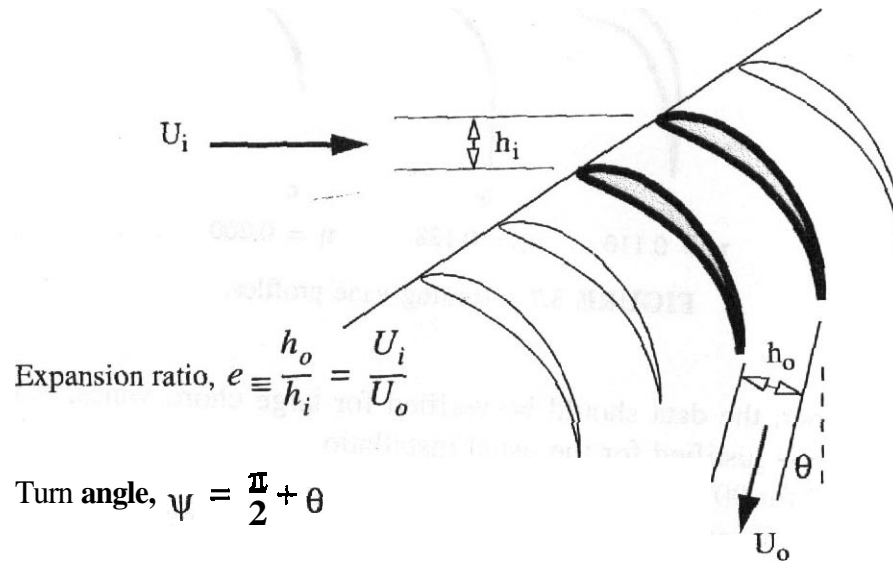
FIGURE 3.6   Geometry of cascade flow with area change from entrance to exit.

are straight and the flow is uniform. Measurements must actually be made much too close for these conditions to pertain, and therefore the quantities must be taken as area averages.

A corner without vanes may show a loss of 100% of the velocity head or more, that is, $K_c \geq 1.00$. With carefully designed vanes a K_c of 0.10 or less is achievable.

For a right-angle turn the component perpendicular to the incoming velocity of the rate of change of momentum through a constant-area corner is $\rho h_i U_i U_i$. This may be equated to the vane lift coefficient $\frac{1}{2}\rho c U_i^2 C_L$, where h is the vane gap and c is the vane chord, to determine that the vane lift coefficient is $2h_i/c$. Accordingly, to employ a reasonable C_l, the gap-to-chord ratio should be $1:3$ or smaller. The drag coefficient is equal to the lift coefficient for the constant-area and $90°$ turn. For the more general case of an expanding corner and general turn angle the expressions for "lift" and "drag" based on momentum relations are the following:

$$L = \rho U_i h_i U_0 \cos \ell = \rho U_i^2 h_i \frac{\cos \theta}{e} \tag{3.31}$$

$$C_l = 2\frac{h_i}{c} \frac{\cos \theta}{e} \tag{3.32}$$

$$D = \rho U_i h_i (U_i + U_0 \sin \theta) = \rho U_i^2 h_i \left(1 + \frac{\sin \theta}{e}\right) \tag{3.33}$$

$$C_d = 2\frac{h_i}{c}\left(1 + \frac{\sin \theta}{e}\right) \tag{3.34}$$

Several vane profiles are shown in Figure 3.7, and each is labeled with the loss experienced under test conditions by various early experimenters[20-23] at Reynolds numbers of about 40,000. Since these data are limited and are for relatively low

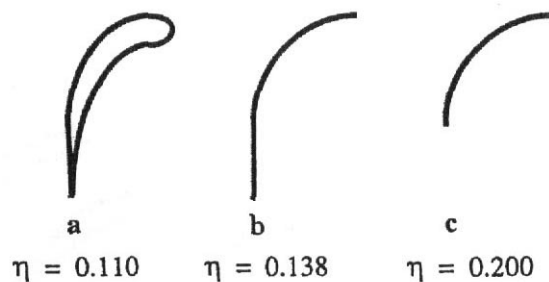$$\eta = 0.110 \qquad \eta = 0.138 \qquad \eta = 0.200$$

FIGURE 3.7   Turning vane **profiles.**

Reynolds number, the data should be verified for large chord vanes, but it is felt that an increase is justified for the usual installations. Salter[24] gives results of tests at $R_e = 500,000$ for $90°$ circular-arc vanes with a gap–chord ratio of $1 : 4$, a leading-edge angle of $4°$–$5°$, and a trailing-edge angle of $0°$ that show a loss coefficient of 0.06. This was certainly a good value. Winters[ZS] obtained additional data for the type of comer vane illustrated in Figure 3.7b indicating that it probably has a lower loss coefficient than the value given from the earlier data. Walls[13] provides a discussion of comer treatment with some additional data correlation. Sahlin and Johansson[26] provide a design of turning vanes for constant-area comers that are very efficient with loss coefficient as low as 0.036 at chord Reynolds number of $154,000$. Lindgren, Osterlund, and Johansson[27] extended that design to expanding comers and obtained a loss coefficient of 0.054 at a chord Reynolds number of $200,000$ and an expansion ratio $e = \frac{4}{3}$. Their results for $e = \frac{3}{2}$ and Reynolds number of $200,000$ give a loss coefficient as low as 0.08 and for $e = \frac{5}{3}$ as low as 0.14. These results point to new design possibilities for more compact circuits and/or simpler geometries for the diffuser walls with possible improvements in circuit efficiencies. We do not explore such possibilities in this book.

Estimating Corner Loss Coefficients   Early experiments at Gottingen[12] produced local loss coefficients of the order of 0.15 at a Reynolds number of about $500,000$. It was concluded there that skin friction on the vanes accounted for about one-third of the loss and that the remaining two-thirds is probably due to the creation of longitudinal vortices or eddies arising when three-dimensional flow is diverted around a comer. Wattendorf[12] made the assumption that the local comer loss coefficient could be decomposed into two parts: K_f due to skin friction and K_r due to flow rotation. The part due to skin friction was assumed to vary with the Reynolds number in a manner similar to skin friction on a flat plate. Based on these arguments and results, Equation (3.35) was used as a reasonable estimate of local loss coefficient for comers of the type shown in Figure 3.7. The Reynolds number to be used is the local comer value based on the vane chord:

$$K_c = 0.10 + \frac{4.55}{(\log_{10} R_{ec})^{2.58}} \tag{3.35}$$

Equation (3.35) is clearly a conservative estimate with regard to what is obtainable using the recent work on comer designs cited above.

Screens (e) and (n)

The safety screen is chosen to provide the necessary protection for the fan. It represents a significant loss element due to the fact that it is located in a relatively high speed part of the circuit. The other screens serve other purposes, including separation control for screens in the wide-angle diffuser and turbulence control for the flow conditioning screens at the nozzle entrance. Only the energy loss aspects of a screen will be discussed in this section.

Eckert et al.[14] give a relation for screen loss coefficient based on data given by Idel'chik.[28] Two basic parameters are used to characterize a screen. These are the "porosity" β_s and the wire Reynolds number $R_{ew} \equiv \rho V d_w / \mu$. A third parameter, the "mesh factor" K_{mesh} is used to differentiate among smooth and rough wire (or whatever the screen material may be).

Porosity is a function of wire diameter and weave density. It is also dependent on geometric factors, but it is rare for other than a square weave to be used. Let d_w be the wire diameter and w_m the width of one square mesh cell. Then the mesh density $p_, \equiv 1/W_m$ and the porosity is related to these by

$$\beta_s = (1 - d_w \rho_m)^2 \tag{3.36}$$

The complement of screen porosity, screen solidity $\sigma_s = 1 - \beta_s$, is sometimes used in the literature. Porosity would be zero for a solidly packed weave and one in the limit of a vanishing screen. Typical values for wind tunnel screens are in the range of 0.5–0.80. More discussions on details will follow in the later section on turbulence control screens.

The wire Reynolds number is typically very low compared to other Reynolds numbers encountered in wind tunnel work. For standard conditions in air, Reynolds number per foot at a flow speed of 1 ft/sec is 538 or Reynolds number per millimeter at 1 m/s is 69.1. Wire Reynolds numbers for safety screens may be up to a few thousand. For the turbulence control screens, values are likely to be only up to a few hundred.

Mesh factors are given by Idel'chik[28] as 1.0 for new metal wire, 1.3 for average circular metal wire, and 2.1 for silk thread. We will assume 1.3 for all example work here.

The expressions to approximate the local loss coefficient for a screen are

$$K_m = K_{mesh} K_{Rn} \sigma_s + \frac{\sigma_s^2}{\beta_s^2} \tag{3.37}$$

where the reference[14] gives, for $0 \le R_{ew} < 400$,

$$K_{Rn} = \left[0.785 \left(1 - \frac{R_{ew}}{354} \right) + 1.01 \right] \tag{3.38}$$

and, for $R_{ew} \ge 400$,

$$K_{Rn} = 1.0 \tag{3.39}$$

Other expressions **are** given in the literature for the screen Reynolds number sensitivity. Idel'chik[28] gives a plot that is only roughly matched by Equation (3.38). A much better fit to the given plot is obtained by Equation (3.40). The accuracy of predictions of screen loss coefficients is not good except on the basis of data taken on screens very nearly of the type to be used and in a very similar environment. More will be said in the next section on theoretical treatments of the effect of screens on flow passing through:

$$K_{Rn} = 0.785\left(\frac{R_{ew}}{241} + 1.0\right)^{-4} + 1.01 \tag{3.40}$$

Consider an expression for the drag of the wire screen and its implied loss coefficient. We might represent the drag as the product of the dynamic pressure of the incoming flow, the drag coefficient of the screen, and the area of the solid cylinders of wire. If this is done per unit area, we have

$$\frac{D_m}{A} = \tfrac{1}{2}\rho V^2 C_{dx}\sigma_s$$

and observing that the drag per unit area may be equated to the total pressure drop across the screen, this would give

$$K_m = C_{dw}\sigma_s \tag{3.41}$$

For screens used as safety screens, the porosity is quite high (and solidity correspondingly low), the wire Reynolds number is large, and the drag coefficient is nearly the same as an isolated wire cylinder. For more dense screens such as are used for turbulence management and similar purposes, the typical Reynolds numbers are lower and the interactions among the elements of the screen **are** much greater. These effects are reflected by the functions in Equations (3.37)–(3.39), which could be manipulated to obtain expressions for the drag coefficient of Equation (3.41).

Power Input Section

The most common device for driving the flow in subsonic wind tunnels is an axial flow fan. Axial flow fans, or propellers, will produce swirl in the flow they induce unless some combination of prerotation vanes and straightening vanes are provided. The fan itself is the source of power input while the vanes absorb some energy in the process of carrying out their function. However, in the present treatment, the fan and straighteners are considered together as the power input unit. Their combined function is to provide a rise in pressure as the flow passes through the section. The increase in pressure provided must be equal to the pressure losses throughout all
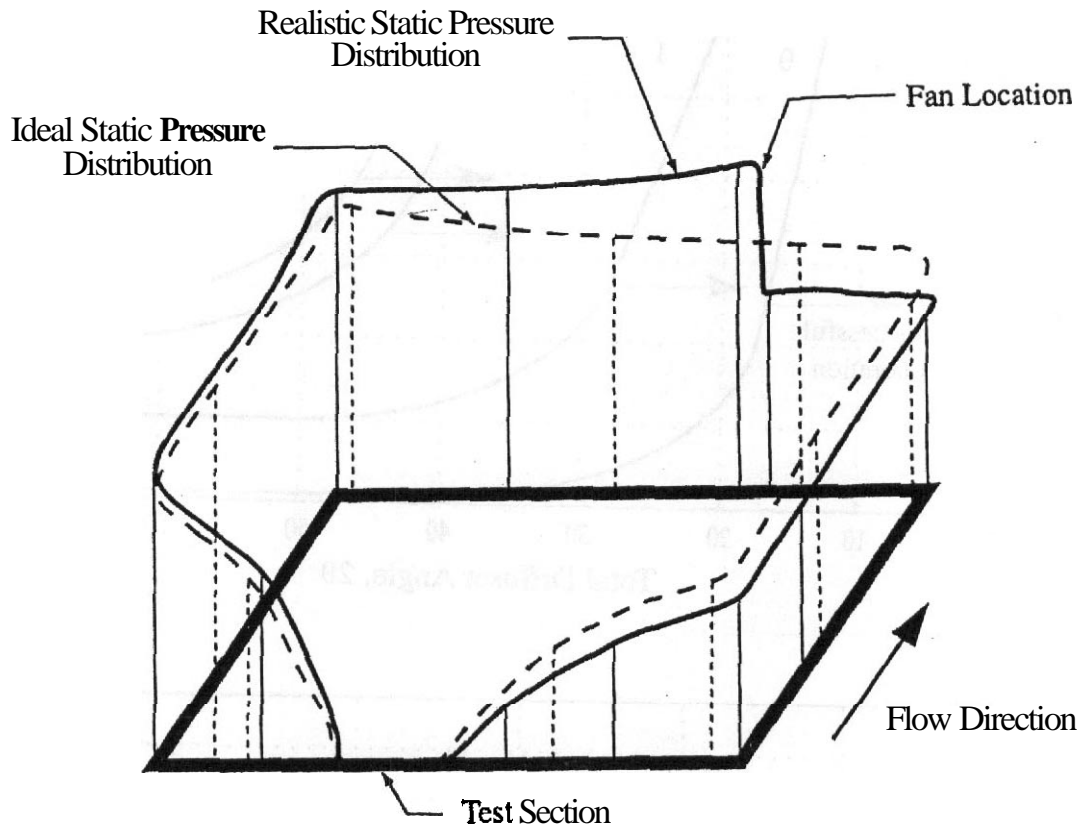
FIGURE 3.8   Schematic pressure variations around a circuit.

other sections of the tunnel at any given steady flow operating condition. A notional sketch is given as Figure **3.8** on which the variation of static pressure is shown as a function of location around a typical wind tunnel circuit. Two distributions are shown. The dashed line is the variation that would exist if there were no losses as is postulated for "ideal" nonviscous fluids. The solid line is an indication of the variation with losses. The scale of changes is exaggerated. The variation is taken from the pressure at the end of the test section, where many tunnels have their "breathers," which set the pressure there at ambient pressure. Some details of fan design will be addressed in a later section.

Wide-Angle Diffusers (m)

Wide-angle diffusers are used to obtain a higher overall area ratio for a given circuit length rather than for pressure recovery. Of course the pressure loss is to be minimized to the extent possible while achieving the other objectives. A diffuser is classed as "wide angle" when its cross section increases so quickly with axial distance that separation can be avoided only by use of boundary layer control. There are several means of boundary layer control, including suction, blowing, and insertion of fine mesh screens. The latter is the most common since it is usually the most economical. Mehta and Bradshaw[29] have given guidelines for wide-angle diffusers in terms of four parameters: area ratio A_R, diffuser angle 2θ, number of screens n, and total loss
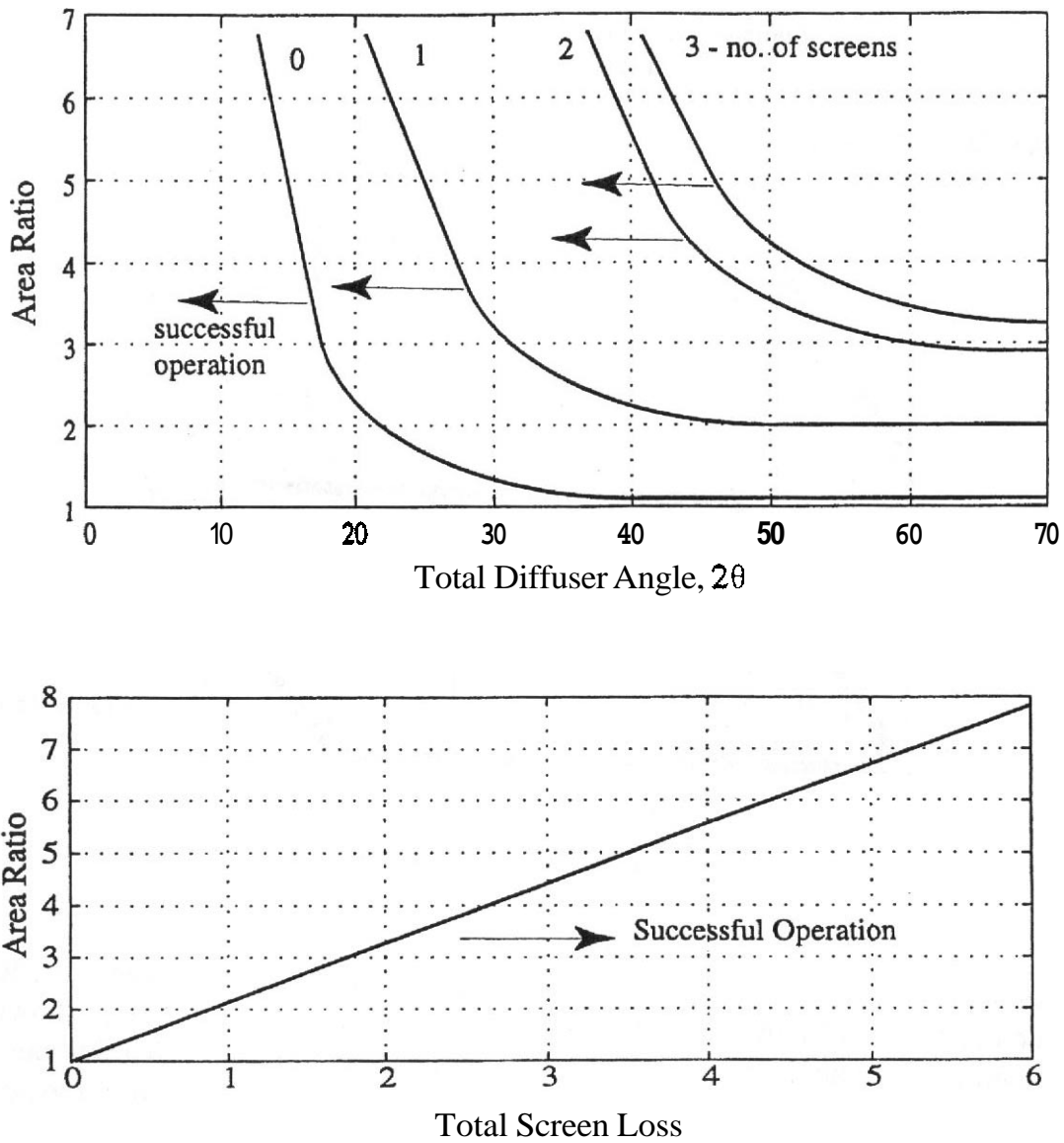
FIGURE 3.9   Design boundaries for diffusers with screens. (Based on Figures 3 and 4 from Mehta and Bradshaw.[29])

coefficient K_{sum}. For a tunnel that will be outfitted with a heat exchanger, it could be used as a loss element in the wide-angle diffuser. Figure 3.9 gives boundaries for number of screens as a function of diffuser area ratio and divergence angle. The total loss coefficient required of the screens is larger as the area ratio increases. The boundary is given as Equation (3.42), where $K_{sum} \equiv \Sigma \, \Delta p/q$:

$$K_{sum} > \frac{A_R - 1}{1.14} \qquad (3.42)$$

It is best if the screens are made perpendicular to the walls at their intersections so that the tendency of the screens to turn the flow toward the screen normal will not itself tend to induce separation.
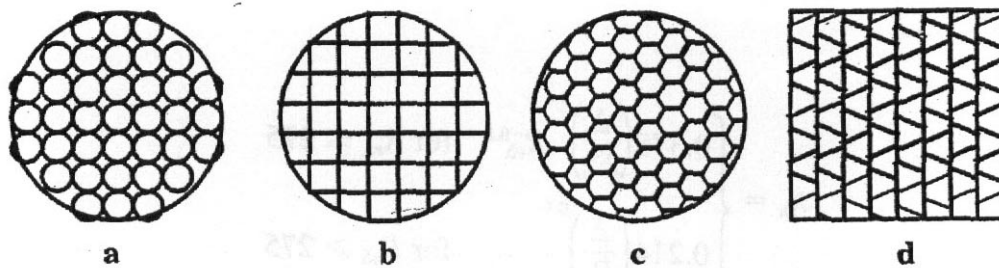
FIGURE **3.10**   Four types of honeycomb.

Honeycombs and Turbulence Screens (o)

The objective of obtaining a spatially uniform steady stream of air throughout the volume of a wind tunnel test section has been pursued for nearly a century. Over that time, as already indicated, a general arrangement of elements has been settled upon, but there remain problems in many details and the result is still not viewed as truly optimized. One area that continues to resist fully rational quantitative design treatment is the management and control of "turbulence" in the flow. To be sure, there exist some "design rules," but they have been obtained through observations of many arrangements and the corresponding theoretical bases rest on a considerable bed of assumptions that may or may not be applicable in a particular wind tunnel application. The problem is of such complexity, however, that all rational theoretical guidance, even though imprecise, is of very great value.

The story here will be started from Prandtl's discussion[30] of obtaining stream uniformity more than 60 years ago. The approach then, as now, was to use "honeycombs" to force the flow to all go in essentially the same direction and screens to bring the various parts of the flow closer to a constant speed.

Honeycombs   According to Prandtl,[30] "a honeycomb is a guiding device through which the individual air filaments are rendered parallel." (p. 11) Figure 3.10 shows some streamwise views of typical implementations of honeycomb as mentioned by Prandtl and that encompass the majority of honeycomb types in use today. The design parameters for honeycombs are the ratio of streamwise length to single-cell hydraulic diameter and the porosity or solidity defined as for screens. The operating state parameter is the Reynolds number with the characteristic length scale typically chosen to be the cell hydraulic diameter. Typical length-to-cell-diameter ratios are in the range of 6–8 and porosity is typically in the vicinity of 0.8. Such values lead to honeycomb loss coefficients of about 0.5. As will be seen, this means that such honeycombs, while effective as flow straighteners, are not so effective as typical screens in smoothing nonuniformities in flow speed.

Honeycomb Loss Coefficients   An expression for losses through honeycombs is given by Eckert, Mort, and Jope.[14] It is given here as

$$K_h = \lambda_h \left(\frac{L_h}{D_h} + 3 \right) \left(\frac{1}{\beta_h} \right)^2 + \left(\frac{1}{\beta_h} - 1 \right)^2 \tag{3.43}$$

where

$$\lambda_h = \begin{cases} 0.375\left(\dfrac{\Delta}{D_h}\right)^{0.4} R_{e\Delta}^{-0.1} & \text{for } R_{e\Delta} \leq 275 \\[2em] 0.214\left(\dfrac{\Delta}{D_h}\right)^{0.4} & \text{for } R_{e\Delta} > 275 \end{cases}$$

The parameters in these expressions **are** hydraulic diameter of a honeycomb cell, D_h; Reynolds number based on honeycomb material roughness and incoming flow speed, $R_{e\Delta}$; honeycomb porosity, β_h; and honeycomb thickness in flow direction, L_h.

Some specific data for losses in **honeycombs** are given by Scheiman and Brooks:[ ] by Loehrke and Nagib,[32] and by Roberts.[33] For honeycombs of the types shown in Figure *3.10* with $L_h/D_h = 6.0$ and equal tube areas, the values of K_h are found to be 0.30, 0.22, and *0.20* for *a, b,* and *c,* respectively. Loehrke and Nagib[32] give data specifically for flow straighteners made from packing ordinary drinking straws, which have the attraction of low cost and ready availability, although they are not suitable for large tunnels due to strength and long-term stability. Their cross section corresponds to Figure 3.10*a*. Roughly speaking, the loss in the honeycomb in a wind tunnel is usually less than *5%* of the total tunnel loss.

Mehta and Bradshaw[29] indicate that about *150* honeycomb cells per settling chamber diameter, or about *25,000* total cells, are adequate. This would lead to larger cells than are used in many of the larger tunnels.

Turbulence Screens There seems no better introduction to screens for flow control than that of Prandtl[30] (p. 14):

> **A** standard reference velocity is not obtained with the honeycomb, but can be achieved with screens. The flow resistance of a wire screen is approximately proportional to the square of the speed. Consequently, the resistance in a flow which locally manifests different speeds, is greater at the points of higher speed than at the points of lower speed. Together with the fact that the final pressure drop is about the same for all stream filaments the result is that the speedier filament expands upon striking the screen, the slower one contracts, and so the speeds become comparable upon passing through the screen. But this comparableness is always obtained at the expense of a great pressure drop in the screen. Putting the pressure drop in the screen at $\Delta p_s = K_s \cdot q_s$, where[34] K_s is a typical screen density factor, a previously existent moderate velocity difference is approximately lowered to $\dfrac{1}{1 + K_s}$. Disposing n screens, not too closely spaced, one behind the other, the pressure drop is $nK_s q_s$ and the discrepancies are reduced in the ratio of $\left(\dfrac{1}{1 + K_s}\right)^n$. It is readily proved that such an arrangement of n screens with moderate K_s factors, say with $K_s = 1$, is more promising than one single
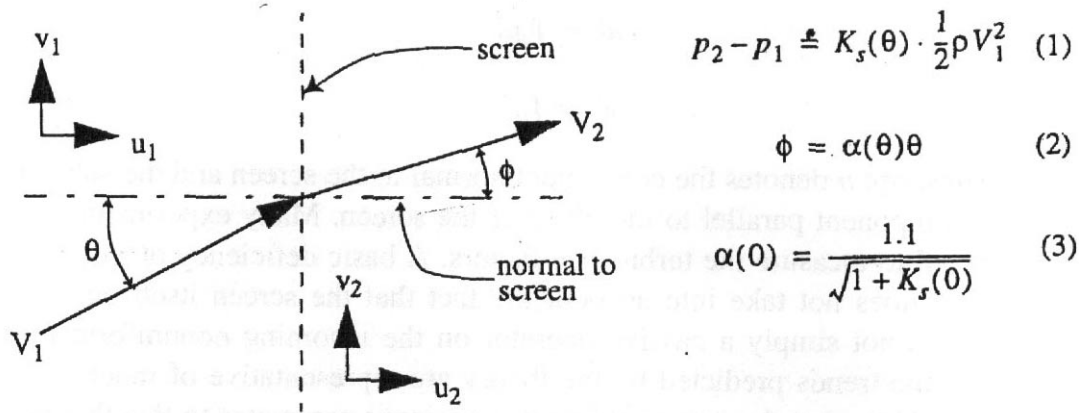
FIGURE **3.11**   Flow passing through a screen.

screen of very close mesh and a resistance figure of $K_s' = nK_s$. For reasons of energy conservation, the screens are as far as possible mounted in a section in which the stream manifests lower speed.

The above account by Prandtl has been elaborated by subsequent efforts, but his discussion is still a sound starting point. In the same article Prandtl went on to give a basic statement of the effect of contractions on flow nonuniformities. Those concepts will be included in a later section.

Batchelor[35] gives a theory of the effect of a screen modeled as an actuator sheet on the passage of an arbitrary velocity field subject to the assumption that the nonuniformities are small compared to the mean flow speed. The action of the screen is modeled by two parameters, the resistance coefficient and the deflection coefficient. Both parameters are in principle functions of the angle the incoming flow makes to the normal line to the screen. The notation is indicated in Figure 3.11. Although the basic theory assumed that K_s and a could be functions of the incoming angle θ, these parameters are taken to be constants viewed as the function values at $\theta = 0$. So the first two equations in **Figure** 3.11 are the assumed action rules for the screen at each point for all time. The third equation is a result obtained by Schubauer, Spangenberg, and Klebanoff[36] from experimental data. The results of Batchelor's theoretical analysis gives

$$u_2' = \left(\frac{1 + \alpha - \alpha K_s}{1 + \alpha + K_x} \right) u_1' \tag{3.44}$$

and

$$v_2' = \alpha v_1' = \frac{1.1}{\sqrt{1 + K_s}} v_1' \tag{3.45}$$

where the primed quantities are the deviation of the flow components from the mean values in their respective regions. The turbulence factors are defined by

$$u_2' = f_u u_1' \qquad\qquad (3.46)$$

$$v_2' = f_l v_1' \qquad\qquad (3.47)$$

where the subscript u denotes the component normal to the screen and the subscript I denotes a component parallel to the plane of the screen. Many experiments have been conducted to measure the turbulence factors. A basic deficiency of the theory cited is that it does not take into account the fact that the screen itself generates turbulence. It is not simply a passive operator on the incoming nonuniform flow. Nevertheless, the trends predicted by the theory are representative of much of the available data. Note that the loss coefficient is an input parameter to this theory. It must be obtained by additional theory or by experiment. We have previously given one approximation in Equation (3.37). The turbulence reduction factor f is defined for experimental purposes as the turbulence with manipulators installed divided by the turbulence without manipulators.

There **are** a number of papers in the literature that give summaries of work on flow through screens and other "turbulence manipulators." In addition to those already cited, useful discussions and results **are** given by Laws and Livesey,[37] by Bradshaw and Pankhurst,[5] by Loehrke and Nagib,[32] and others.

Scheiman and Brooks[3'] conducted a study in which they compared results of experiments and the available theories. The study included both screens and honeycombs. The porosity of the screens varied between 59 and 67% for mesh sizes from 4 to 42. The honeycombs had cell sizes from $\frac{1}{16}$ to $\frac{3}{8}$ in. and the length–cell size ratio varied between *6* and 8.

For the screens the values of loss coefficient calculated from theory differed from the experimental values by up to 50%.

The turbulence reduction factors (f) for both axial and lateral turbulence showed data scatter but no consistent pattern with velocity (i.e., screen Reynolds number). The range of screen Reynolds number based on wire diameter varied from 70 to 300. As there was no trend off with speed, the average value over the speed range was used.

The upstream turbulence for the screens was close to isentropic. The average measured values of f_u showed good agreement for axial turbulence with Prandtl's equation, which is obtained from Batchelor's result, Equation (3.44), by setting a = 0, and in the lateral direction with Dryden and Schubauer's result given previously as Equation (3.45).

When multiple screens are used, the turbulence reduction factors are the product of the individual screens. The pressure drop is the sum of the pressure drops of the individual screens. For two screens with spacing beyond the minimum either doubling the spacing or at the initial spacing, rotating one screen 45° had little effect on the turbulence reduction factor. Multiple screens must have a finite distance between them so that the turbulence induced by the first decays to a significant degree before the next screen is encountered. Spacing values based on mesh size of greater than 30 have been suggested as well as spacing based on a wire diameter of about 500.

When a honeycomb was used (data for the $\frac{1}{4}$-in. cell), the axial reduction was the same as the 20-mesh screen. The lateral reduction was equal to three 20-mesh screens. The pressure drop for the honeycomb at 50 ft/sec was slightly less than the calculated value at 50 ft/sec for the 20-mesh screen. The honeycomb plus one 20-mesh screen is equal to three 20-mesh screens for axial reduction and is about twice as effective in the lateral direction. The honeycomb was installed upstream of the screens, as suggested by various previous investigators.

The flow behind the honeycomb was not isentropic (see Loeherke and Nagib[32] for a discussion of upstream turbulence effects). When the screen turbulence reduction factors were based on the turbulence behind the honeycomb, the turbulence reduction predicted by Equation **(3.44)** with the value of α from Equation (3.45) gave the best match.

Scheiman and Brooks[3'] data for pairs of screens with different honeycombs illustrate an important problem that occurs when using hot-wire anemometers. Some of their data was taken with a 2-Hz bypass filter and other data was taken with a 100-Hz filter. The results of hot-wire anemometers depend strongly on the lower frequencies; thus the effect of the frequency cutoff should be determined and the cutoff frequency should be stated when the turbulence level is given. The likely variation of low-frequency cutoff filters chosen may explain some of the inconsistencies in published turbulence reduction data.

This low-frequency cutoff problem with hot wires makes it attractive to include parallel measurements using the classical turbulence sphere and critical Reynolds number as a method of comparing the turbulence of various flows. If spheres with different diameters are used, one has a measure of the relative scales of turbulence and turbulence intensity with tunnel speed.

Selection of honeycomb and screens for a wind tunnel is very much dependent on the purposes to which the tunnel is intended. It is also somewhat artful since some means of making adjustments after the tunnel is in operation is needed but very difficult to arrange for a large tunnel.

Screens used for turbulence reduction should have porosity greater than 0.57. Screens with smaller porosity suffer from a flow instability that appears in the test section.[36]

Most theoretical treatments of turbulence assume that the initial flow has isentropic turbulence. Most data for turbulence reduction are taken in flows that are either isentropic or very close to isentropic. This is done by inserting turbulence generators well upstream into a uniform flow (screens, an array of bars, or porous plates). After passing through this turbulence generator the turbulence approaches an isentropic state. In most cases the actual turbulent flow in a wind tunnel is not isentropic. In general, the mechanism of turbulence and its manipulation is very complex and not completely understood. These facts often lead to the unpleasant result that the predicted reduction of turbulence by screens or honeycombs does not agree with the measured results. Nonetheless, the theory combined with data can be used to compare various turbulence reduction schemes in a preliminary design trade-off. The difficulty is primarily related to obtaining an economic result. If a designer is not constrained by either construction cost or operating cost, then very

low levels of turbulence can readily be achieved by including sufficient straighteners and a large enough number of properly chosen screens. Bradshaw and Pankhurst[5] give a very concise and useful set of guidelines.

Practical Issues   An operational problem with screens is their amazing ability to accumulate dust. The dust **always** has a nonuniform distribution. Thus the screen's porosity and pressure drop will change, which in turn will change the velocity and angularity distribution in the test section in an unpredictable way with time. This problem will be aggravated when the tunnel is used for flow visualization studies using china clay, oil flow, or vaporized oil for smoke or when oil is used for seeding lasers. When screens **are** used, they must be installed so that they can be cleaned, and the quality of the test-section flow must be monitored.

For larger tunnels it is **difficult** to obtain either screens or honeycombs in widths adequate to span the tunnel ahead of the contraction cone. This means that screens must be spliced together. The splice is often accomplished by brazing widths of screens together, which must be done with extreme care. The individual screen mesh must be on top of each other and should not be filled with the brazing material. If the splice is semisolid, it will introduce turbulence. A poor splice can be detected in the test section as a band of higher turbulence and possibly lower velocity. The same problem can occur with cables across the screen's face, with tension cables to the fourth comer to **carry part** of the screen load. Honeycombs are often mounted in a shadow-box-type structure and this also can give the same effect.

Ideally a tunnel should be designed with screens in mind: with slots ahead of the contraction cone for mounting screens. Then the screens are mounted on a support frame and slid into the tunnel. This also facilitates cleaning the screens. The slot must be sealed, of course.

If screens are added to an existing tunnel, the screens can be brazed to a support ring that has radial screws to pull the screen tight. For multiple screens this type of installation can be difficult. Screens also have been attached to cables that **are** then attached to the tunnel walls. It is not unknown for a screen to tear loose from a tunnel.

The radial force per foot of perimeter due to the pressure drop will be $C_d q d^2/8\delta$, where δ is the screen sag in feet, and the wire tensile strength may then be computed using the total wire cross-sectional area per foot of perimeter.

Contraction "Cone" or Nozzle

The contraction "cone" or nozzle takes the flow from the settling chamber to the test section while increasing the average speed by factors up to 20 or more, although typical values are in the range of 6–10. The nozzle is in fact never conical in shape in spite of the term sometimes being used to refer to this section of a wind tunnel. A sketch indicating a typical arrangement is given in Figure 3.12. A one-dimensional analysis of the flow for such a segment actually misses entirely the main problems of design of a nozzle. The application of Bernoulli's equation and mass conservation in a one-dimensional sense indicates a continuously falling pressure as the flow
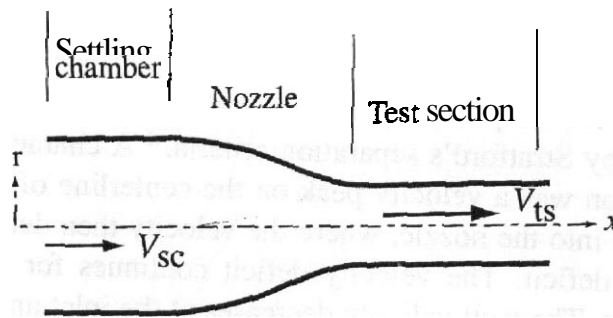
FIGURE 3.12   Contraction section.

moves from the entrance to the exit of the nozzle. If a pressure coefficient is defined as $C_{p_{ts}} = (p - p_{ts})/(1/2)\rho V_{ts}^2$, then the "one-dimensional" relation for pressure coefficient is

$$C_{p_{ts}} = 1 - \left[\frac{A_{ts}}{A(x)}\right]^2 \tag{3.48}$$

where A, is the area of the test section and $A(x)$ is the area as a function of the streamwise coordinate. The pressure coefficient is near 1 in the settling chamber and falls to 0 in the test section. At this level of analysis there would be no indicated problem of likely boundary layer instability since the pressure gradient would appear to be favorable throughout the nozzle.

However, a potential flow calculation for an axisymmetric nozzle shows that the flow along the wall at both the entrance and the exit to a typical smooth shape is slower (and the pressure higher) than the one-dimensional approximation. Morel[38] reports a study of axisymmetric nozzles in which these problems are discussed. If either of the adverse gradients at the beginning or the exit of the nozzle becomes severe enough for the boundary layer to separate, there will be degradation of the quality of the test-section flow, an increase in the power required, and an increase in the acoustic noise.

An additional problem arises for non-axisymmetric nozzles. For rectangular cross sections the surface streamlines intersect the side walls. This leads to secondary flow in the comers with attendant lower velocities and possibility of separation. This tendency has been alleviated in many tunnels by making the nozzle octagonal. This is done by beginning a 45° fillet at the start of the nozzle and carrying the fillet through the test section and first diffuser.

Until the advent of the digital computer there was no wholly satisfactory method of designing nozzles. The nozzle was designed either by eye or by adaptations of approximate methods. Experience has shown the radius of curvature should be less at the exit than at the entrance. Most of the early work on nozzles was based on potential theory.[39,40] Once the wall shape was determined, the regions of adverse pressure gradient were checked to make sure that they were not too sharp. The following paragraphs give brief discussions of nozzle design studies that reflect application of substantial computational effort.

Nozzle Design   Chmielewski[41] specified a distribution for a streamwise acceleration for a quasi-one-dimensional flow. Long constant-area ducts were used, one on each side of the nozzle, to ensure parallel flow. The velocities obtained from potential theory were checked by Stratford's separation criteria.[42] A characteristic feature of the velocity distribution was a velocity peak on the centerline of the constant-area inlet that persists well into the nozzle, where the velocity then decreases, ending in a centerline velocity deficit. The velocity deficit continues for about one radius beyond the nozzle exit. The wall velocity decreases at the inlet and increases at the exit. This leads to a cup-shaped velocity profile in the constant-area exit duct. This type of velocity profile has been measured in wind tunnels. The rapid growth in the boundary layer thickness in the constant-area inlet makes an inlet separation a possibility. For the contours used, the length of the nozzle decreased as the inlet radius was decreased and the exit radius increased. If, however, the area reduction is too gradual, the boundary layer will be subjected to a mild pressure gradient over a long distance, increasing the risk of separation.

Morel[38] considered uniform flow at the exit as being the basic requirement for a nozzle. He also pointed out that as the nozzle ratio decreases beyond 4 the length will decrease for fixed exit requirements. Borger[43] recommended a slight expansion near the nozzle exit to improve the exit flow uniformity.

Mikhail and Rainbird[44] were able to control the wall pressures and gradients and flow uniformity at the exit by controlling the distribution of wall curvature. The length of the exit section was defined on the basis of 0.25% flow uniformity at the centerline at one radius from the exit. The nozzle exit length (from the wall inflection point to constant-area duct) is sensitive to the required length in the test section for a uniform velocity profile. For an area ratio of 8 the inlet section length varied from 0.15 to 1.00 times the inlet radius, while the test-section settling length varied from 1.5 to 0.5 of the exit radius.

It is desirable to keep the length of the nozzle as short as possible, the length of the nozzle being defined as the sum of the settling chamber length plus the nozzle plus the settling length of the exit section. The settling chamber length is required for honeycombs and/or screens to reduce turbulence, if they are to be used. A settling chamber length of 0.5 times the inlet diameter is often used.

Quite often, for a new tunnel, either a complete model or models of parts of the tunnel are built to check the design. Although the model tunnel can duplicate the velocities of the full-scale tunnel, the Reynolds number will be reduced by the scale factor. Thus, the boundary layer will be thicker in the model tunnel than in the full-scale tunnel. Despite this problem, those facilities that have models of their tunnels have found them to be invaluable, both as a check of modifications to the full-scale tunnel and as a facility for experiments that would be too expensive to run in the large tunnel.

If a complete model tunnel is not built, often parts of the full-scale tunnel are simulated. Because the nozzle section is critical to the flow quality in the test section, quite often models of this part are built. The model may include the fourth corner. This model will need a bellmouth at its entrance and should include the test section to the first diffuser. The flow should be sucked through the model. This model type

can be used to check the test-section settling length. The nozzle's sensitivity to nonuniform flow can be checked also. The effect of honeycombs and/or screens in the settling chamber or turbulence both at the entrance to the nozzle and in the test section can be determined.

Nozzle Loss Coefficient   We give here a rudimentary method to estimate the nozzle loss coefficient. This level of analysis is sufficient for energy considerations since the nozzle will consume a small part of the drive power. The losses in the nozzle are considered to be from friction only so that the pressure drop is obtained by integrating the standard pipe friction law:

$$\Delta p_f = \int_0^{L_n} f \frac{\rho}{2} \frac{V_n^2}{D_n} dx \tag{3.49}$$

where L_n is the length of the nozzle, $D_n = D_n(x)$ the local nozzle hydraulic diameter, and V_n the local section mean speed. Continuity gives $V_n^2 = V_{sc}^2 \left(\dfrac{D_{sc}}{D_n}\right)^4$ where V_{sc} is the speed in the settling chamber and therefore at the entrance to the nozzle. The nozzle loss coefficient is $K_n \equiv \Delta p_f / q_{sc}$, which, using Equation (3.49), can be written as

$$K_n = f_{av} \left(\frac{L_n}{D_{sc}}\right) \int_0^1 \frac{D_{sc}^5}{D_n^5} d\left(\frac{x}{L_n}\right) \tag{3.50}$$

Since $K_{nt} = K_n(q_{sc}/q_{ts})$, we also have

$$K_{nt} = f_{av} \frac{L_n}{D_{ts}} \int_0^1 \frac{D_{ts}^5}{D_n^5} d\left(\frac{x}{L_n}\right) \tag{3.51}$$

Since the integrand of Equation (3.51) is always less than 1, it is seen that the nozzle loss coefficient based on test-section dynamic pressure is less than the test-section loss coefficient for equal length-to-hydraulic-diameter ratios. For a typical nozzle shape, the integral of Equation (3.51) has been found to be approximately 0.32. The friction factor can be retained inside the integral if a numerical integration is being evaluated. It is reasonable to take the friction factor as the average of the values for nozzle entrance and exit Reynolds numbers. A reasonable approximation for nozzle loss coefficient that was originally given by Wattendorf[12] is

$$K_{nt} = 0.32 f_{av} \frac{L_n}{D_{ts}} \tag{3.52}$$

Since the loss in the nozzle is typically of the order of 3% of total losses in the circuit, errors in estimating nozzle loss coefficient are much less important than errors in estimating losses in the high-speed part of the circuit.
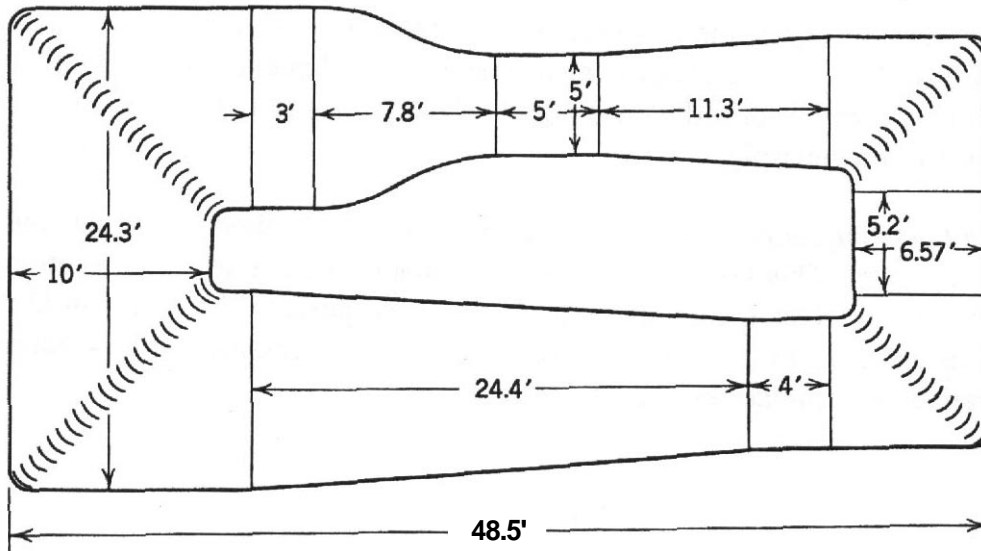
FIGURE 3.13   Example basic single-return circuit.

3.5   ENERGY RATIOS OF SOME TYPICAL CIRCUITS

We give results for selected wind tunnel circuit designs in this section. The first example is for a circuit of very conventional design, as shown in Figure 3.13. The details of the geometry are given for this example along with tabulated results. We then give a synopsis of results for several circuits by Eckert.[14]

The losses calculated for the single-return tunnel of Figure **3.13** based on a tunnel temperature of 100°F (ρ/μ = 5560) and a test-section speed of 100 mph (44.7 m/s) are shown in Table 3.2.

TABLE 3.2.   Section Loss Calculations for Example Circuit

Section	K_l	K_{lt}	Total Loss (%)
Jet	—	0.0093	5.10
Divergence	—	0.0391	21.3
Corner	—	0.0460	25.0
Cylinder	—	0.0026	1.40
Corner	—	0.0460	25.0
Cylinder	—	0.0020	1.10
Divergence	—	0.0160	8.90
Corner	—	0.0087	4.70
Corner	—	0.0087	4.70
Cylinder	—	0.0002	0.10
Cone	—	0.0048	2.70
Total	—	0.1834	100.0

$$E_R = 1/\Sigma K_{lt} = 5.45$$
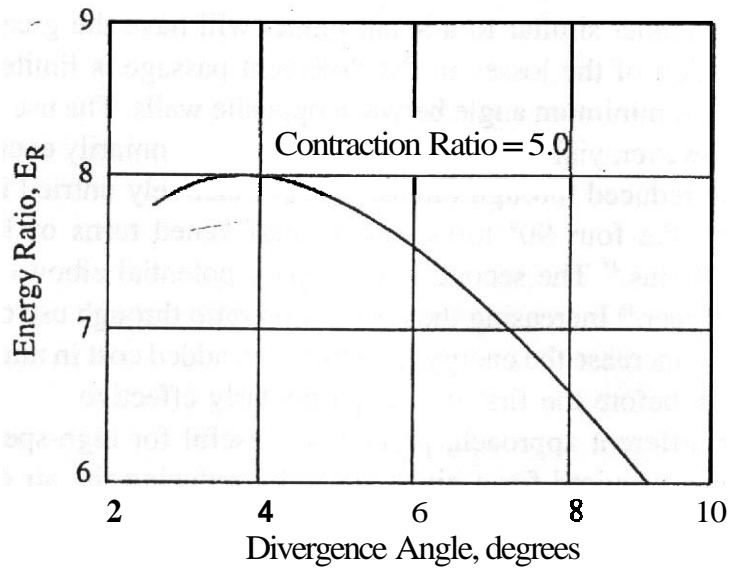
FIGURE 3.14   Effect of diffuser divergence angle on energy ratio.

This energy ratio estimate should probably be reduced about 10% for leaks and joints.

The effect of varying the angle of divergence or the contraction ratio for a family of tunnels similar to the one of Figure **3.13** may be seen in Figures **3.14** and **3.15.** The overall size of the tunnels is changing as the divergence angle varies with constant contraction ratio or as contraction ratio varies with constant divergence angle. There are several possibilities for attaining higher energy ratios. One fundamental effect is that an increase of efficiency accompanies larger Reynolds numbers.
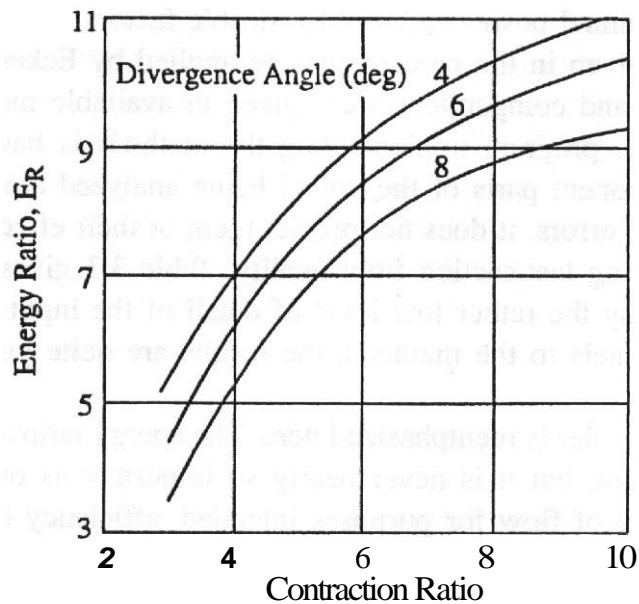
FIGURE 3.15   Effects of contraction ratio and divergence angle on energy ratio.

That is, a large tunnel similar to a small tunnel will have the greater efficiency of the two. Reduction of the losses in the divergent passage is limited, as previously stated, to a certain minimum angle between opposite walls. The use of this minimum angle would, however, yield smaller losses than are customarily encountered. Corner losses might be reduced through the use of two relatively untried innovations. The first is to break the four 90" turns into several vaned turns of less than 90°, as described by Darrius.[45] The second is to employ potential elbows for the turns, as described by Harper.[46] Increasing the contraction ratio through use of a longer return passage will also increase the energy ratio but at an added cost in tunnel construction. Increased length before the first turn is particularly effective.

An entirely different approach, particularly useful for high-speed tunnels, is to reduce the power required for a given speed by reducing the air density by partly evacuating the entire tunnel. This procedure greatly complicates model changes, since the tunnel pressure must be relieved before the tunnel crew can enter. (Pressure doors that seal off the test section from the rest of the tunnel can be used; this reduces the pumping between runs.) Since the power required is a function of pV^3, by reducing the pressure to one-fourth its former value, the speed may be increased by the ratio $\sqrt[3]{4}$ to 1 for the same power input. Stated differently, a 59% higher Mach number will be attained with the lower pressure.

When estimating power requirements for a proposed design, consideration must also be given to (a) the power required to overcome model drag under the most extreme cases and (b) the power required to overcome the increased tunnel losses due to stalling of parts of the diffuser from the effects of the model wake.

For (a) the power required to fly a model whose span is 0.8 tunnel diameter, AR = 5 and $C_D = 1.00$ is probably sufficient. Item (b) for conventional tests is covered in (a) above, but for wingtip mounting or section tests as much as 150% more power may be needed if the diffuser is seriously stalled and large rotational and diffusion losses are created. Bluff bodies such as truck models or parachutes can increase the tunnel power required by sizable factors.

The methods given in the preceding were applied by Eckert, Mort, and Jope[14] to seven tunnels, and comparisons were given to available measurements for the seven tunnels. The program implementing the methods is based on the assumption that all component parts of the tunnel being analyzed are properly designed. If there are design errors, it does not predict them or their effects on other parts of the tunnel, including test-section flow quality. Table 3.3 gives a summary of the results. Considering the rather low level of detail of the input parameters used in describing the tunnels to the methods, the results are quite good for the conventional designs.

A point made earlier is reemphasized here. The energy ratio achieved by a tunnel design is significant, but it is never nearly so important as other factors such as appropriate quality of flow for purposes intended, efficiency of available support equipment and people, quality and efficiency of instrumentation for acquiring data, and the effectiveness of the integrated environment in assisting users to plan and execute focused experimental programs.

TABLE 3.3. Measured and Computed Energy Ratios for Selected Facilities

Facility	Test-Section Speed (m/s)	Energy Ratio		
		Actual[a]	Computed	Difference (%)
NASA Ames, 40 x 80 ft	107.3	7.88	7.96	1.0
NASA Ames, 7 × 10 ft	133.0	7.85	8.07	2.8
Lockheed Martin low-speed wind tunnel	52.3	1.10	1.12	1.8
Indian Institute of Science, 14 x 9 ft	96.3	6.85	6.83	−0.3
Hawder Siddeley Aviation, 15-ft V/STOL	45.7	2.38	3.97	66.8
University of Washington, 8 x 12 ft	117.7	8.3	7.20	−13.3
NASA Langley, 30 x 60 ft	52.7	3.71	4.73	27.4

[a]**The quoted energy ratios are the best available and the best reported for each facility.**

3.6   FANSTRAIGHTENER SECTION

This section will deal with the fan nacelle, the fan, prerotation vanes, and flow–straightener vanes as a unit. The purpose of the fan–straightener combination is to take the incoming stream, usually assumed uniform, and produce an outgoing stream that is uniform with an increased total pressure. The increase in total pressure must match the integrated loss of total pressure throughout the other parts of the wind tunnel. Fan design will be considered in some detail in the next section.

There is now general agreement that the wind tunnel fan should be located downstream of the second comer. A fan position between the first and second comers is rarely used and a fan position between the test section and the first comer is even more rarely considered. Let us first rule out the positions that we may say are definitely undesirable. The fan develops its highest efficiency if it is located in a stream of a fairly high velocity, and its cost is at least partially proportional to its diameter squared. These two items rule out a fan in a very large part of the retum passage or in the settling chamber. Damage from a failing model and poor flow distribution make a position in the diffuser moderately risky. Attenuation of fan noise requires that the fan be as far from the test section as possible. This consideration eliminates at least the settling chamber and the diffuser to the first corner. The argument for a position just downstream of the second turn is that the flow has by then been in a section of constant or nearly constant area for a considerable time and therefore should be relatively smooth when it meets the fan, and at this location the velocity is desirably high. In addition, the location is as good as one can choose for noise considerations since the fan noise must propagate around two comers in either direction to reach the test section.

A number of configurations are in current use. Three basic systems are (1) a fan with straightener vanes behind it (see Figure 3.16); (2) a fan with prerotating vanes
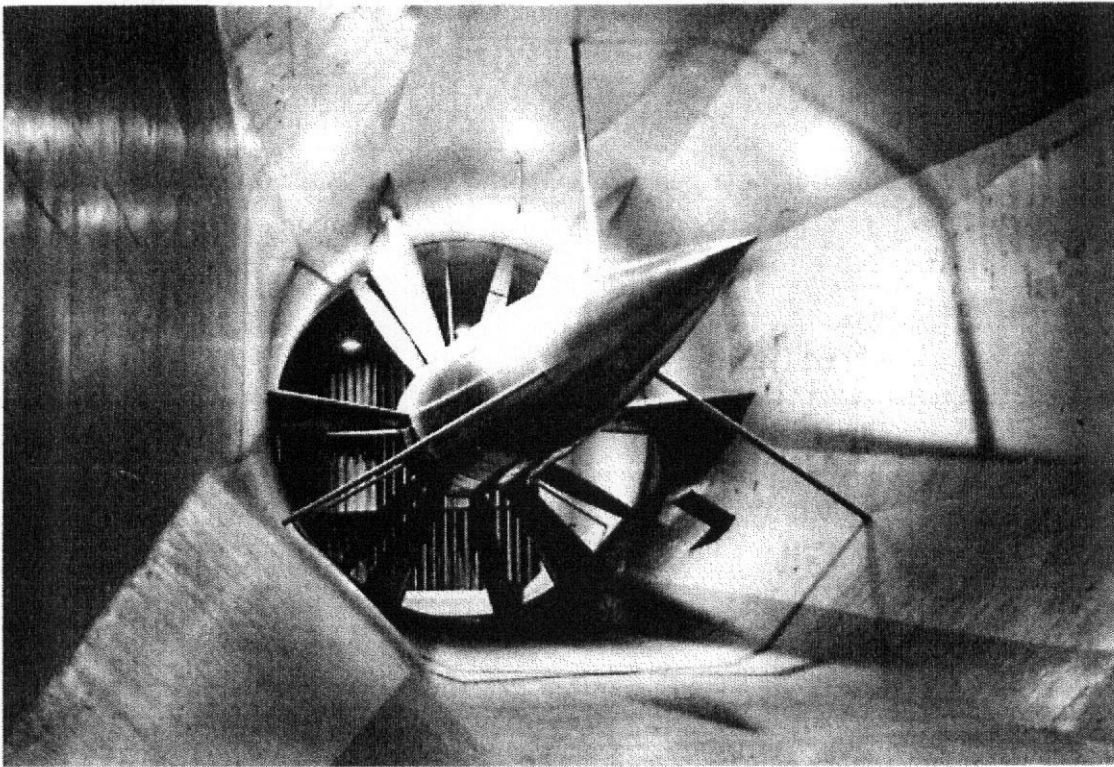
FIGURE 3.16   Nacelle–fan installation. The antitwist vanes are between us and the fan. (Courtesy of Glenn L. Martin Wind Tunnel.)

ahead of it as well as straightener vanes behind it; and (3) counterrotating fans in which the second fan removes the rotation imparted by the first. A fourth arrangement is to have multiple fans, each of which passes a part of the flow. Among more recent tunnels, 1 and **2** are by far the most prevalent.

The counterrotating fan can remove all the twist for all tunnels speeds and power inputs. Since two fans can obviously be designed to develop more thrust than one, counterrotating fans may become more competitive in high-power installations. The drive is more complicated, however, as equal torque needs to be applied to the airstream by both fans.

For tunnels of moderate size and power a single fan is usually quite satisfactory. If it is properly designed, a straightener system can **be** devised that will remove the twist for all power inputs and speeds. Such straighteners are discussed in the following paragraphs.

A variable-pitch fan is of great value even when a variable-rpm drive is available, since it gives much quicker speed control than varying the drive rpm. In tunnels with large contraction ratios the change in velocity distribution in the test section with change in fan-blade angle does not seem to be measurable. Also, when the the drive motor is of the synchronous type, the fan can be put in flat pitch for low pull-in torque and then opened out to develop the tunnel speed. This action may lead to greater power outputs from this type of motor, since the pull-in torque is often the limiting factor. For those tunnels that may be operated with two-dimensional

inserts, the variable-pitch fan is definitely advantageous in achieving optimum operation.

The area ratio between the fan and the test section is usually between 2 : 1 or 3 : 1. If the ratio is made larger, there is the risk of a poor velocity profile before the fan and an increase in cost due to size. If the area ratio is smaller, the incoming velocity will be higher and the fan rpm will be larger to maintain reasonable blade angles. However, the tip speed is limited by the practice of keeping the tip Mach number low enough to avoid formation of shock waves. The fan–nacelle diameter in large tunnels is about 30–50% of the fan section diameter.

The fan motor is either mounted in the nacelle or outside the tunnel.

When the motor is in the nacelle, this usually requires cooling for the motor. The cooling air can often be ducted through the nacelle supports. If the motor is outside the tunnel, it can drive the fan either through a gear box in the nacelle or the more usual method of a long shaft passing through the second comer. This shaft will **have** to be held in careful alignment by bearings and may or may not be enclosed in a fairing to reduce losses and the effects on the flow between the outside wall and second-comer turning vanes.

The fan may or may not have prerotation vanes upstream of the fan. The prerotation vanes **are** designed to produce a swirl opposite to the fan's swirl and hence zero swirl after the fan. This may not occur at all rpm. Thus, in most cases flow straighteners or antiswirl vanes are installed after the fan as a safety factor. The prerotation vanes are a stator and the fan spinner is attached to their inner end. These stators increase the velocity of the fan blade relative to the airstream. To avoid vibration between the prerotation vanes and the fan for N fan blades, do not use N, $3N/2$, or 2N prerotation blades. Similar constraints should be used between the fan blades and the nacelle supports. If prerotation vanes **are** not used, straightener vanes must be used downstream of the fan.

There are major structural design problems in the fan and nacelle regions, and the location of the motor will have a strong influence. As an example, if the motor is in the nacelle, then the nacelle struts must carry the torque and thrust of the fan to the tunnel shell, rather than only the thrust.

The nacelle should have a length-to-diameter ratio of about **3 with 30–40%** of its length of constant diameter. The equivalent closing cone angle should be $5°$ or less. An excessive adverse pressure gradient over the rear portion will lead to separation and a persistent wake that may show its shadow in the test section. Expansion of the walls over the rear of the nacelle should be avoided. The effective duct areas may yield an expansion angle of $10°–12°$ for short nacelles. If the nacelle does separate, a vortex generator installation may help. Their angle of attack should be relative to the local flow direction, which may change with fan speed. Extending the aft nacelle fairing may also help if flow problems occur in this area.

The wind tunnel fan is quite different from an airplane propeller. It is a ducted fan, and because it operates in a constant-area duct, continuity considerations enforce the condition that there is no increase in axial velocity across the fan. The fan in a wind tunnel "merely" replaces the total pressure losses of the tunnel and model.

Fan–Straightener Design

Collar[47] has given a considerable discussion of the design of wind tunnel fans. However, a method proposed by Patterson[48] and subsequently evolved and elaborated by Wallis[13] is presented here because it considers the fan–straightener system as a unit and does not concern itself merely with the fan. It uses assumptions referred to as the "free-vortex theory" for fan design. The assumptions will be elaborated in the following sections. The treatment is most advantageous for design studies in which the fan geometry is being sought for given flow conditions rather than addressing the problem of computing the performance of a given fan with given geometry and given rotational speed. The theory presented here assumes there is no radial flow and that there is a radial balance that corresponds to this assumption. Treatments that consider more general cases are given by Lewis[49] and others. It would be possible to do extremely detailed computational analyses today if the resources were available for a particular design project. Such high-cost approaches are not justified and are not needed to obtain quite good design results for most wind tunnel fan applications.

The present treatment neglects losses associated with the necessary tip clearance at the tunnel wall and is based on assumptions that lead to no radial flow. There are small tip clearance losses that contribute to efficiencies slightly lower than indicated by this theory. The loss due to tip clearance adds to both the friction and the expansion losses that occur at the walls of a wind tunnel and indicates that instead of constant thrust the wind tunnel fan should perhaps have a graded thrust loading curve, greatest at the walls in order to best develop a uniform velocity front. This refinement is beyond the scope of this presentation.

Flow Geometry   As detailed in the preceding sections, the losses that occur throughout the wind tunnel circuit appear as successive pressure drops to be balanced by the pressure rise through the fan. **The** total pressure drop *Ah* must be known for any desired operating condition to proceed with a design of the fan. The methods previously given may be used to obtain the needed results. Alternatively, if a physical model of the tunnel is available or can be produced, the necessary pressure rise may be measured across the fan and extrapolated to full-scale Reynolds number.

A schematic of a fan–straightener unit is shown in Figure 3.17. The incoming flow speed is u_1, defined as the test section speed times the ratio of test section area to fan area. Typically u_1 is of the order of one-third of the test-section speed for low-speed wind tunnels. The flow is analyzed based on the assumption that it proceeds in annuli, each of which can be treated independent of the others except that there is a balance of the radial pressure gradient and the centrifugal forces consistent with the assumption of no radial flow. **A** cut through a typical annulus is shown in Figure 3.17 along which three planes perpendicular to the tunnel axis are indicated. The flow variables at plane 1 are the incoming values. At plane 2 the flow values are the result of the fan acting on the incoming flow. At plane 3 the flow values are those resulting from the action of the straighteners on the flow
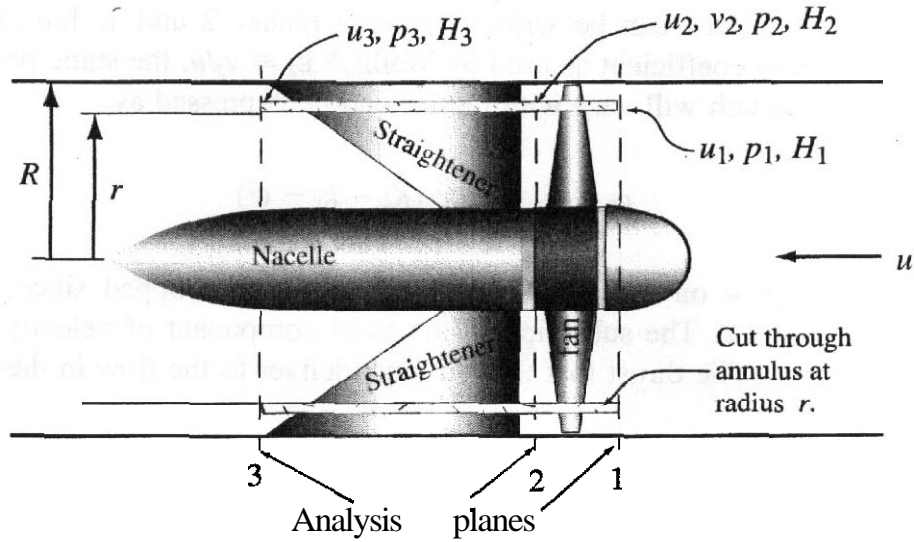
FIGURE 3.17   Schematic of fan–straightener unit.

with the properties at plane **2.** The incoming stream at plane 1 is assumed to be uniform with no tangential (swirl *v)* component. The fan acts on this incoming stream and produces a flow assumed to have a constant total pressure *H,* at every point in plane 2, and the values of u_2, p_2 **are** such that the radial static pressure variation and centrifugal acceleration associated with v_2 are balanced. This is the assumed "free-vortex" condition. The straighteners acting on the flow are assumed to remove the swirl component so that the flow at plane 3 is uniform and axial. Fan design by the present method consists of finding relations so that the fan geometry at a chosen operating condition is consistent with the above set of assumptions.

At each plane the standard Bernoulli relations **are** valid:

$$H_1 = p_1 + \tfrac{1}{2}\rho u_1^2 \tag{3.53}$$

$$H_2 = p_2 + \tfrac{1}{2}\rho(u_2^2 + v_2^2) \tag{3.54}$$

$$H_3 = p_3 + \tfrac{1}{2}\rho u_3^2 \tag{3.55}$$

The total pressure rise through the fan–straightener unit can be considered to be the "ideal" value minus the losses as the flow passes through the fan and then the straightener, with concepts being the same as the earlier analyses of various sections of the tunnel circuit. This can be expressed first dimensionally and then nondimensionally as follows. The subscript on *u* has been dropped since the axial component is constant under the assumptions of the analysis:

$$H_3 - H_1 = \Delta H_i - \Delta h_f - \Delta h, \tag{3.56}$$

$$\frac{H_3 - H_1}{(1/2)\rho u^2} = K_i - k_f - k_s \tag{3.57}$$

Analogous relations can be written between planes *2* and 1. Introducing the definition of swirl coefficient **as** used by Wallis,[50] $\varepsilon_2 \equiv v_2/u$, the static pressure rise across the fan, which will vary with radius, can be expressed as

$$p_2 - p_1 = \tfrac{1}{2}\rho u^2 \left(K_i - k_f - \varepsilon^2\right) \tag{3.58}$$

where the subscript on the swirl coefficient has been dropped since it is non-zero only at plane **2.** The subscript on the swirl component of velocity will similarly be dropped. The thrust that the fan must deliver to the flow in the elemental annulus is

$$dT_f = 2\pi r\, dr(p_2 - p_1) \tag{3.59}$$

The power that the fan must deliver to the flow in the elemental annulus is related to total pressure rise and flow rate by

$$dP_f = (2\pi r\, dr)u(H_3 - H_1 + \Delta h_f + \Delta h_s) = (2\pi r\, dr)u(\Delta H_i) \tag{3.60}$$

The torque that the fan must apply to the flow in the elemental annulus is given by the rate of change of angular momentum:

$$dG_f = \rho(2\pi r\, dr)uvr \tag{3.61}$$

The power and torque are related by the angular velocity of the fan:

$$dP_f = \Omega\, dG_f \tag{3.62}$$

We define the "flow coefficient"[51] as $\lambda \equiv u/\Omega r$ (also as used by Wallis[50]) and obtain the following relation between ideal total pressure rise coefficient, flow coefficient, and swirl coefficient:

$$K_i = \frac{2\varepsilon}{\lambda} \tag{3.63}$$

Equation (3.63) shows that the swirl coefficient and the swirl component of velocity will be inversely proportional to the radius if the ideal total pressure rise is uniform over the fan. This is assumed to be the case.

The useful power output from the fan–straightener unit in the elemental annulus may be expressed as

$$dP_0 = (2\pi r\, dr)u(H_3 - H_1) \tag{3.64}$$

The efficiency of the **fan–straightener** unit can usefully be defined as the ratio of the useful power output divided by the power input. We have two expressions for the power input: Equations *(3.60)* and *(3.62)*. *The efficiency* expressions are

$$\eta_{fs} = \frac{dP_0}{dP_f} = \frac{(2\pi r\, dr)\bar{u}(\Delta H_i - \Delta h_f - Ah_s)}{\Omega\rho(2\pi r\, dr)u\bar{v}r} = \frac{\lambda(K_i - k_f - k_s)}{2\varepsilon} = \frac{\lambda K_{fs}}{2\varepsilon} \quad (3.65)$$

where the overall pressure rise coefficient $K_{fs} \equiv K_i - k_f - k_s$ has been introduced. An expression for fan efficiency can be immediately produced in a similar way:

$$\eta_f = \frac{\lambda(K_i - k_f)}{2\varepsilon} = \frac{\lambda(K_{fs} + k_s)}{2\varepsilon} \quad (3.66)$$

and we also immediately obtain

$$\eta_f = \eta_{fs} + \eta_s \quad (3.67)$$

and

$$K_{fs} = \eta_{fs}K_i \quad (3.68)$$

and

$$\eta_s = \frac{\eta_{fs}k_s}{K_{fs}} \quad (3.69)$$

which will be key relations as they will be used in the fan design procedure to be outlined later.

It is very useful to consider another view of the fan operation and an alternative expression for the useful power output. The fan power output can be written as $dP_{f0} = (2\pi r\, dr)u(H_2 - H_1) = (2\pi r\, dr)u\, \Delta H_f$. The total pressure rise across the fan is the sum of the static pressure rise and the dynamic pressure associated with the swirl component of the flow just downstream of the fan indicated by plane 2 in Figure *3.17*. This amounts to a rearrangement of Equation (3.58), yielding

$$dP_{fo} = (2\pi r\, dr)u\left[(p_2 - p_1) + \frac{1}{2}\rho v^2\right] = u\, dT_f + \frac{1}{2}\frac{v}{r}dG_f \quad (3.70)$$

The fan power input is as given by Equation (3.62), which combined with Equation *(3.70)* gives

$$\eta_f = \frac{u\, dT_f + (1/2)(v/r)\, dG_f}{\Omega\, dG_f} = \lambda r\frac{dT_f}{dG_f} + \frac{1}{2}\varepsilon\lambda \quad (3.71)$$
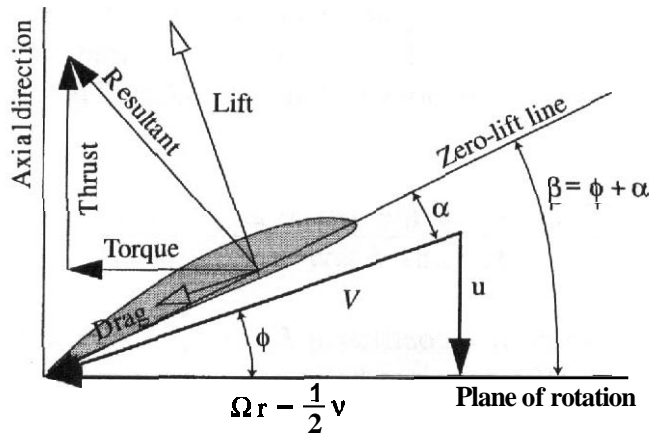
FIGURE 3.18   Typical fan blade element with velocity and force components.

The thrust and torque factors are now converted to coefficient form with the following conventions in which V is the resultant relative fluid speed at the fan plane, c is the blade chord, and N is the number of blades:

$$dT_f = (c\ dr)\left(\tfrac{1}{2}\rho V^2\right)NC_T \tag{3.72}$$

$$dG_f = (c\ dr)\left(\tfrac{1}{2}\rho V^2\right)rNC_G \tag{3.73}$$

in terms of which Equation (3.71) becomes

$$\eta_f = \lambda\frac{C_T}{C_G} + \tfrac{1}{2}\varepsilon\lambda \tag{3.74}$$

The required torque and power must be delivered to the flow through a finite number of blades. A typical low-speed wind tunnel will have a relatively low solidity fan so the present treatment will not consider cascade effects. A typical blade element is shown in Figure 3.18. The swirl component of velocity is taken as the average of the values incoming and the value at plane 2.

The thrust and torque coefficients appearing in Equations (3.72) and (3.73) can be written in terms of conventional airfoil parameters by reference to Figure 3.18:

$$C_T = c_l \cos\phi - c_d \sin\phi \tag{3.75}$$

$$C_G = c_l \sin\phi + c_d \cos\phi \tag{3.76}$$

Equations (3.74)–(3.76) can be combined to give

$$\eta_f = A\frac{(c_l/c_d - \tan\phi)}{(c_l/c_d \tan\phi + 1)} + \frac{1}{2}\varepsilon\lambda \tag{3.77}$$

which along with

$$\tan \phi = \frac{u}{\Omega r - (1/2)v} \quad \frac{A}{1 - (1/2)\varepsilon\lambda} \tag{3.78}$$

gives

$$\eta_f = \lambda \frac{(c_l/c_d) - \lambda + (1/2)\varepsilon[1 - (1/2)\varepsilon\lambda]}{(c_l/c_d)\lambda + 1 - (1/2)\varepsilon\lambda} \tag{3.79}$$

This equation is an important equation because it provides the sensitivity of fan efficiency to the lift-to-drag ratio of the fan airfoil sections. The other variables are the flow coefficient and the swirl coefficient. These are related to the fan–straightener pressure rise coefficient and fan–straightener system efficiency by Equation (3.65) for our assumed free-vortex design case. This can be used to obtain an alternative relation giving fan efficiency as a function of section lift-to-drag ratio, flow coefficient, fan–straightener system efficiency, and fan–straightener pressure rise coefficient. The result is

$$\eta_f = \lambda \frac{[c_l/c_d - \lambda + (K_{fs}\lambda/4\eta_{fs})(1 - K_{fs}\lambda^2/4\eta_{fs})]}{(c_l/c_d)\lambda + 1 - K_{fs}\lambda^2/4\eta_{fs}} \tag{3.80}$$

The fan–straightener pressure rise coefficient can be related to the circuit losses by noting that we must have

$$K_{fs} = \frac{q_t}{q_f}\frac{1}{E_R} = \frac{q_t}{q_f}\Sigma K_{lt} \tag{3.81}$$

which is the sum of circuit loss coefficients based on the fan dynamic pressure. This shows that the required value of K_{fs} is determined by the circuit properties. The value obtained from circuit analysis can be used in Equation (3.80) along with assumed values of efficiencies to obtain relationships between the flow coefficient and the section lii-to-drag ratios. For typical circuits the ratio of the test-section dynamic pressure to the dynamic pressure at the fan will be in the range of 2–10. For energy ratios in the range of 4–8, the resulting fan–straightener system pressure rise coefficient will be in the range of 0.25–2.5. The flow coefficient varies inversely with radius since the incoming flow is assumed to be uniform. It is largest at the fan root sections and smallest at the fan tip. It may range over 0.12–1.5 although this is not likely over that full range for a single fan. Figures 3.19 and 3.20 are based on Equation (3.80). The fan–straightener pressure rise coefficient has been chosen as 2.0 for these plots. The result is not very dependent on this choice. It is seen that increasing the section lift-to-drag ratio will increase the fan efficiency but not nearly in proportion to changes in the lift-to-drag ratio.
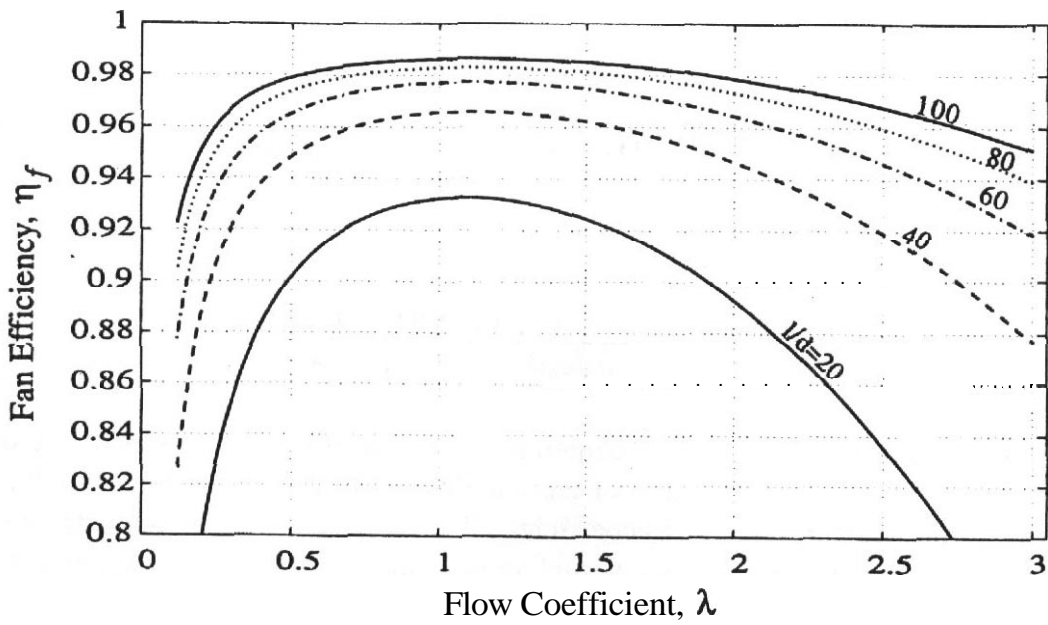
FIGURE 3.19 Approximate fan efficiency as a function of flow coefficient for a range of section lift-to-drag ratio.

It will be seen from Figures 3.19 and 3.20 that high fan efficiencies are largely determined by proper selection of the flow coefficient and utilization of section lift-to-drag ratios in the range of 60 and upward. The required pressure rise coefficient follows from the circuit properties and the location within the circuit at which the fan is located. It remains to demonstrate the methods for satisfying the criteria.
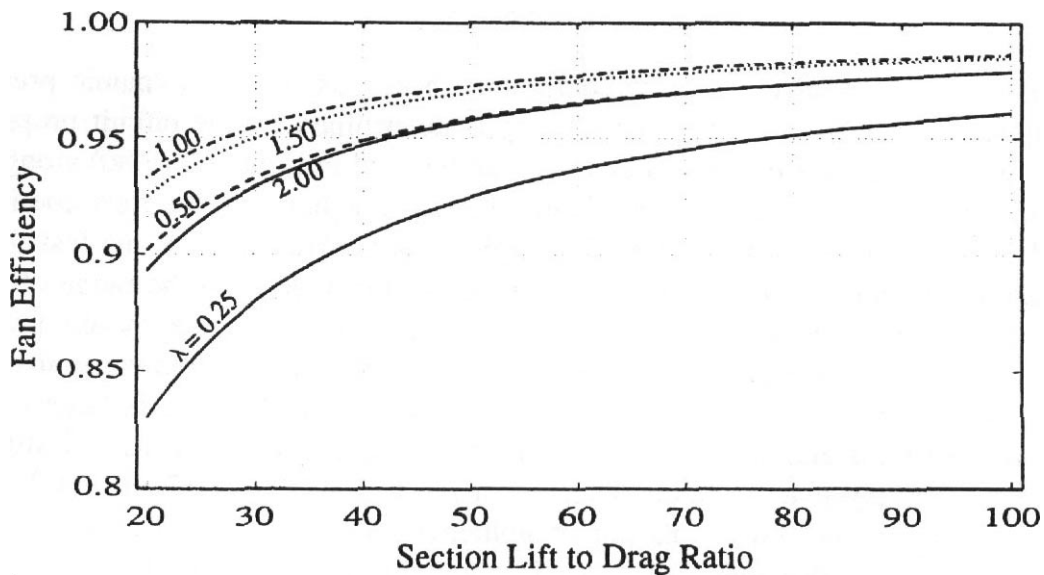
FIGURE 3.20 Approximate fan efficiency as a function of section lift-to-drag ratio at selected values of flow coefficient.

Equation (3.80) can also be put into the forms

$$\lambda = \frac{\eta_f}{(1 - \eta_f)\dfrac{c_l}{c_d}} + \left[\frac{1 - (1 + \eta_f)(K_{fs}/4\eta_{fs})}{(1 - \eta_f)(c_l/c_d)}\right]\lambda^2 + \left[\frac{(K_{fs}/(4\eta_{fs})^2}{(1 - \eta_f)(c_l/c_d)}\right]\lambda^4 \quad (3.82)$$

$$\frac{c_l}{c_d} = \frac{\eta_f}{(1 - \eta_f)\lambda} + \left[\frac{1 - (1 + \eta_f)(K_{fs}/4\eta_{fs})}{1 - \eta_f}\right]\lambda + \left[\frac{(K_{fs}/4\eta_{fs})^2}{1 - \eta_f}\right]\lambda^3 \quad (3.83)$$

These forms are useful depending on whether we assume we know the lift-to-drag ratio or the flow coefficient. Equation (3.82) can be used to solve for the flow coefficient in an iterative fashion when the section lift-to-drag ratio is assumed known.

Fan Blade Sections   The design of airfoils has received a large amount of attention since the beginning of aviation and has been advanced to substantial levels of rationality in the last 20 years. Eppler[52] has been a pioneer in airfoil design methods, and his work provides a good basis for studying the many others who have contributed to the area. Section lift-to-drag ratios of 60 and higher are readily obtainable. In fact, values of well over 100 have been demonstrated with modem airfoil design for carefully controlled conditions. A wind tunnel fan is likely to be required to operate over a range of conditions so it is probably not wise to choose a blade design that performs well only in a very narrow range of conditions.

In this presentation we consider a specific airfoil and its properties to illustrate the manner of doing a fan design. Type E of the RAF propeller sections has been found satisfactory, as has the slightly thicker type D (see Figure 3.21). The ordinates of these airfoils are shown in Table 3.4.

A set of data for RAF section D is given in Figure 3.22. Lift, drag, and lift-to-drag ratio are given as functions of chord angle of attack with Reynolds number
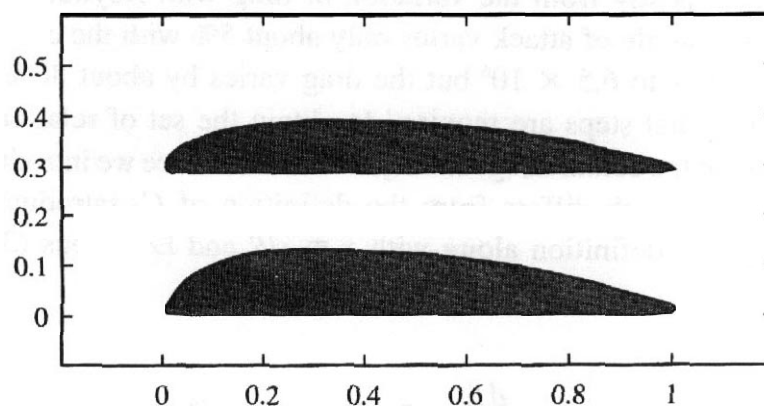
FIGURE 3.21   Typical early airfoils for fan sections.

TABLE 3.4. Ordinates of Fan Profiles D and E

Distance from Leading Edge"	Height above Flat Undersurface	
	D	E
0	0.0135	0.0115
0.0125	0.0370	0.0319
0.0250	0.0538	0.0442
0.0500	0.0780	0.0610
0.0750	0.0925	0.0724
0.1000	0.1030	0.0809
0.1500	0.1174	0.0928
0.2000	0.1250	0.0990
0.3000	0.1290	0.1030
0.4000	0.1269	0.1022
0.5000	0.1220	0.0980
0.6000	0.1120	0.0898
0.7000	0.0960	0.0770
0.8000	0.0740	0.0591
0.9000	0.0470	0.0379
0.9500	0.0326	0.0258
1.0000	0.0100	0.0076
L.E. rad	0.0135	0.0115
T.E. rad	0.0100	0.0076

"T.E. means Trailing Edge. L.E. means Leading Edge.

as a parameter. The effect of Mach number will also be significant for fan design and analysis. Application of the Prandtl–Glauert transformation will be satisfactory for preliminary designs.

Inspection of Figure *3.22* shows that the maximum values of lift-to-drag ratio occur for chord angle of attack of about $5°$ for the entire range of Reynolds numbers for which data are shown. The maximum lift-to-drag ratios range from *65* to 80 depending on the Reynolds number. The variation in life-to-drag ratio with Reynolds number comes mostly from the variation of drag with Reynolds number. The lift coefficient at $5°$ angle of attack varies only about *5%* with the changes in Reynolds number from *0.31* to 6.5 $\times$ 10^6 but the drag varies by about 80%.

A few additional steps are required to obtain the set of relations that allow the determination of the actual fan geometry. For convenience we introduce the definition $T_c \equiv T/(1/2)\rho u$, which differs from the definition of C_T introduction in Equation *(3.72)*. Using this definition along with $x \equiv r/R$ and Equations (3.58), (3.59), and (3.66), we obtain

$$\frac{dT_c}{dx} = 2x(K_{fs} + k_s - \varepsilon^2) \tag{3.84}$$
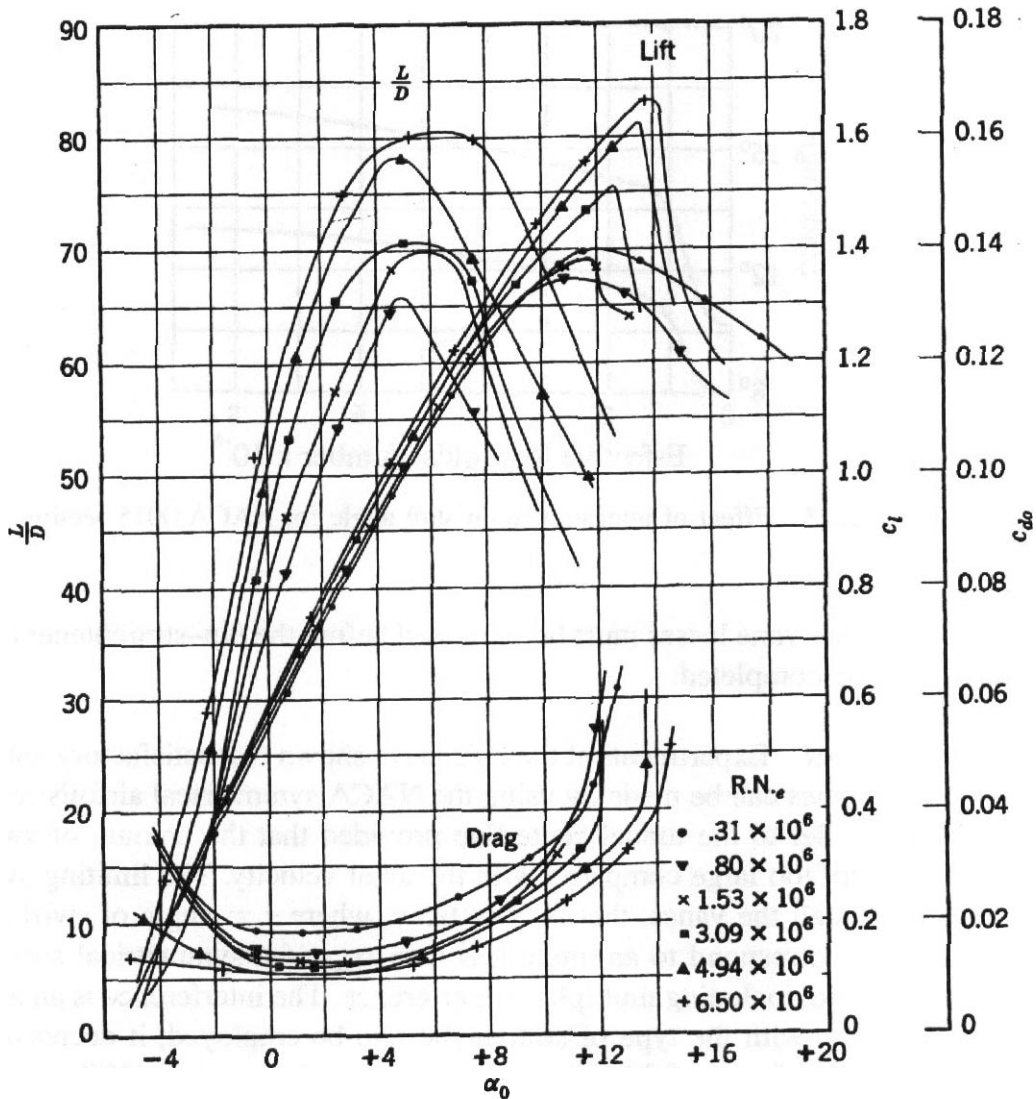
FIGURE 3.22   Characteristics of fan airfoil D, infinite aspect ratio.

If there are N blades, then each blade must carry $1/N$ of the required thrust, torque, and power. Let the following definitions be chosen for "sector length s_f and solidity σ_f:

$$s_f \equiv \frac{2\pi r}{N} \quad \text{and} \quad \sigma_f \equiv \frac{Nc}{2\pi r} = \frac{c}{s_f} \tag{3.85}$$

where c is the chord. Note that the sector length is determined simply by the number of blades and the radius of the annulus. The solidity depends on a detail of the blade, the chord. From Equation (3.72), Equation (3.75), and definitions of the variables, we can obtain

$$\frac{dT_c}{dx} = \frac{2\sigma_f C_T}{x(\sin \phi)^2} = \frac{cNC_T}{x^2(\sin \phi)^2 \pi R} \tag{3.86}$$

Equation (3.86) will be solved for c and used to compute the chord after the other variables have been determined.
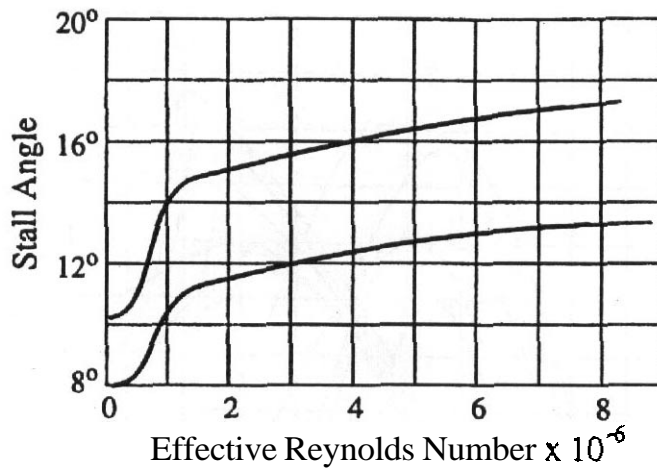
FIGURE 3.23 Effect of interference on stall angle for NACA 0015 section.

The straightener vane losses must be estimated before the fan–straightener design procedure can be completed.

Straightener Vanes Experiments at the NPL have shown that satisfactory antitwist or straightener vanes can be made by using the **NACA** symmetrical airfoils set with their chords parallel to the tunnel centerline provided that the amount of swirl to be removed is not too large compared with the axial velocity. The limiting swirl is that required to stall the vanes; that is, $\varepsilon = \tan \tau$, where τ = angle of swirl in the slipstream must correspond to an angle less than α_{stall} of a symmetrical section at infinite aspect ratio, including multiplane interference. The interference is an advantage here because, with the type of straighteners to be employed, it decreases the lift curve slope by a factor of 0.75. That is, α_{stall} with interference is 33% above the free-air stall angle, as shown in Figure 3.23 for an **NACA** 0015 section. The chord for the proposed straightener may be found from

$$c_s = \frac{2\pi r}{N_s} \tag{3.87}$$

where N_s is the number of straightener vanes and c_s is the chord of the vane at radius r.

If a constant-thickness ratio is assumed for the straightener vanes, the actual thickness at the wall would be large owing to the large chord. Hence it is advantageous to select a constant thickness (not thickness ratio). A reasonable value is that $t_s/c_s = 0.15$ at $x = r/R = 0.8$ (R = tunnel radius at propeller section). Hence from Equation (3.87),

$$\frac{t_s}{c_s} = \frac{N_s t_s}{2\pi R x} \tag{3.88}$$

The number of blades and number of vanes should be relatively prime. This avoids simultaneous multiple blade wakes striking straighteners, which will hap-

pen if there is a common multiplier between number of blades and number of vanes.

There will be a loss through the straightener, of course, and this loss will be greater than the skin friction of the vanes in free air, since the straightener is a diffuser, changing the swirl to static head. The pressure loss coefficient of a straightener composed of symmetrical NASA airfoil sections has been empirically determined as

$$k_s = 0.045 \left(\frac{t_s}{c_s}\right) + 0.003 \tag{3.89}$$

Substituting from Equation (3.87), we have

$$k_s = \left(\frac{0.045}{2\pi r}\right) t_s N_s + 0.003 \tag{3.90}$$

Factors influencing the General Layout   Large advance ratios (i.e., higher flow coefficients) imply lowered speeds of fan rotation, necessitating a drive motor of low rpm or a geared driving system. The size and cost of electric motors are more dependent on torque than on power so that a motor of specified power will be lower in cost for a higher specified rotation rate. The desire for higher rpm for the driving motor indicates that the higher speed regions of the wind tunnel are best suited for the location of the fan. Balancing that against the increase of nacelle drag as the local speed is increased, the best compromise usually locates the fan downstream of the second comer after the test section. If the fan is to be driven by a motor outside the tunnel, the comer location offers a short shaft length.

Maintaining a small tip clearance is important to prevent the development of tip losses. A small tip clearance leads to possibilities for structural damage from a small hard object, such as screws or bolts getting jammed between the blade tip and the tunnel wall. This can be prevented by making the blade ends frangible and easily repairable.

A large nacelle is advantageous from a number of considerations. By decreasing the tunnel cross-sectional area at the propeller, a higher velocity is achieved, and higher motor speeds are possible at the same advance ratio or flow coefficient. A large boss also encloses the fan root sections that must be thicker for structural reasons, leaving only thinner, more efficient sections exposed to the airstream. Frequently it is possible to use an airfoil of constant thickness in the exposed portion, thus facilitating the design. Relatively small gains are to be found from utilizing section lift-to-drag ratios greater than 60, so that the airfoil selection can accommodate some compromise with structural considerations. Although the optimum boss diameter increases with advance ratio and may be as large as 0.6–0.7 times the fan diameter, smaller values of 0.3–0.5 are frequently more practical for low-speed wind tunnel use. A larger boss requires a larger and longer nacelle for proper streamlining, which in tum involves increased cost, construction difficulties, and greater power

losses from the diffusing action as the area of the passage is increased. It would be possible to prevent the diffusing losses by shaping the tunnel so that the area throughout the fan nacelle region remains constant. This is sometimes done despite the added expense. Certainly the equivalent conical diffusion angle should be kept to 7° or less.

The number of blades on the fan is somewhat arbitrary from the point of view of aerodynamic performance, for the product of the number of blades and their chord represents the total area and must be aligned with the thrust requirements. Several factors influence the selection of the number of blades. The minimum number probably is 4, as the amplitude of pulsation at blade passage frequency increases as the number of blades is decreased. Aeroacoustic considerations therefore call for a large number of blades. The maximum number of blades will doubtless be limited by strength considerations. The maximum value of the sum of the blade chords Nc should not exceed the local circumference at the root if excessive interference is to be avoided. The Reynolds number of the blade chord should be above 700,000 in order to keep the section drag low, and the tip speed should be low enough to avoid compressibility problems. This means that the blade tips should not come too near the critical Mach number. Since the number of blades is not critical, a reasonable procedure is to estimate the number needed and examine the final design to see whether alterations are in order.

Design Procedure

Fan design is an iterative procedure, as is the case with all engineering systems. The starting point is some set of assumptions about the configuration and assumed values for a set of parameters. Other pertinent parameters can be determined from relations based on physical principles where possible or other considerations if there are no usable physically based relations available to the designer. The example that follows outlines a procedure.

Example Fan Design   A fan is required for a wind tunnel whose circuit has been analyzed and found to have an energy ratio equal to 5.0. The area of the test section is 56.4 ft², and the design test-section speed is 193 mph, or 283 ft/sec. The density and viscosity are taken to be standard sea level atmospheric values of p = 0.002378 slug/ft³ and μ = 3.74×10^{-7} lb-sec/ft². The wind tunnel duct diameter at the fan has been chosen to be 13 ft. A boss diameter of 0.60 and N = 12 blades are values selected for preliminary calculations. The airfoil section for the blade is chosen as the RAF section D, whose shape has been given in Table 3.4. The flow area is A_f − A_b = 133 − 47.8 = 85.2 ft², and u = 284 × 56.4/85.2 = 188 ft/sec. The ratio of dynamic pressure in the test section to dynamic pressure at the fan is 2.27 and the overall fan−straightener pressure coefficient must be K_{fs} = 0.454.

Step 0. We assume we can achieve a fan−straightener system efficiency η_{fs} = 0.93. This gives an ideal pressure rise coefficient K_i = 0.488.

Step 1. We assume a thickness-to-chord ratio for the straightener vanes of *0.12* at the tip and obtain k_s using Equation *(3.89)* and then obtain $\eta_s = 0.0172$ using Equation *(3.69)*. Finally we obtain $\eta_f = 0.947$ using Equation *(3.67)*.

Step *2.* If we assume a value for section lift-to-drag ratio, we can evaluate the coefficients in Equation *(3.82)*. In the present example we choose $L/D = 45$ and obtain $\lambda = 0.470$ as the solution. Note that the variation of the flow coefficient must be inversely proportional to radius so once it is chosen for any annulus, it is determined for all radii by the $1/r$ relation. We have computed it for the tip radius here. Also note that the assumed L/D will hold only at the tip. The assumptions of the free-vortex design procedure lead to a varying L/D with radius. The values of $U D$ for the other radii will be calculated later. Calculate the flow coefficient for the various radii.

Step *3.* We can now obtain the fan notation rate as $\Omega = (2u/\Omega D_f)\,(60/2\pi) = 587$ **rpm** and the rotational component of tip speed as $\Omega R = 400$ **ft/sec.** This gives a tip Mach number of about *0.38,* which is high enough to warrant applying a **Prandtl–Glauert** correction-to-lift curve, but this is not done in this example.

Step 4. The swirl coefficient at the tip is now computed using Equation *(3.65)*. obtaining $\varepsilon_{tip} = 0.115.$ As with the flow coefficient, the swirl coefficient varies inversely with radius so the values at other radii can be obtained. We check the value at the blade root to see if the straighteners will be stalled. The result is $\varepsilon_{root} = \varepsilon_{tip}(D_f/D_B) = 0.191$ or $\tau = 10.8°,$ which is well below the stall limit, as indicated by Figure *3.23* for any reasonable Reynolds number. Calculate the swirl coefficient for the various radii.

Step *5.* The straightener vane chords are summed to be given by Equation *(3.87)* and to have constant thickness. Equation *(3.90)* is used to calculate straightener pressure loss coefficient as a function of radius. Then the "straightener efficiency" for all radii can be calculated using Equation (3.69).

The values of all other parameters are to be calculated for the various radii assuming unchanging values for the fan–straightener pressure rise coefficient K_{fs} and the overall fan–straightener system efficiency $\eta_{fs}.$

Step *6.* Calculate the resulting fan efficiency values at the various radii.

Step *7.* Calculate the $U D$ values at the various radii using Equation *(3.83)*.

Step *8.* Calculate the inflow angle ϕ at the various radii using Equation *(3.78)*.

Step *9.* Calculate the approximate chord using Equation (3.86) with $C_T \approx c_{l,est}\cos\phi$ where $c_{l,est}$ is an estimated value for the section lift coefficient. This would be chosen consistent with the L/D values from step *6.*

Step *10.* Calculate the approximate Reynolds number using the approximate chord from step 8 and the known relative air speed as a function of radius.

Step 11. Using the approximate Reynolds numbers and the $W D$ values from steps *6* and 9 along with the airfoil section data as given by Figure *3.22,* find the angles of attack, the section lift coefficients, and the section drag coefficients.

Step 12. Using the inflow angles and the angles of attack, calculate the blade pitch distribution: $\beta = \phi + a.$

Step *13.* Calculate the chord values using Equation *(3.86)*.

A program that implements the above in the data processing language IDL is available from the authors.

A sample output for the example is:

```
************* Input Parameters *************
```

Test-section area   —   56.400 sq ft
Test-section speed   — 283.067 ft/sec
Circuit energy ratio   —   5.000
Fan diameter   —   13.000   ft
Boss diameter   —   7.800   ft
Number of blades   —   12
Number of straightener vanes   —   7
Straightener tip-thickness-to-chord ratio   =   0.120
Section lift-to-drag ratio   —   45.000
Fan-straightener target efficiency   —   0.930

```
++++++++++ Computed Results ++++++++++
```

Fan-straightener pressure rise coefficient =   0.4537
Ideal pressure rise coefficient   —   0.4878
Straightener loss   —   0.01721
Fan efficiency   —   0.9472
Flow coefficient   —   0.4700
Fan rotation rate   —   587.4   rpm
Tip speed due to rotation   —   399.8 ft/sec
Swirl coefficient at tip   —   0.1146
Swirl angle at tip   —   6.540   deg
Tip Mach number   —   0.3785
Swirl coefficient at root   —   0.1910
Swirl angle at root   —   10.81   deg

```
-------------- Radial Distributions --------------
```

x =	0.60	0.68	0.76	0.84	0.92	1.000
KS =	0.01200	0.01090	0.0101	0.00943	0.00887	0.00841
ETAF =	0.9545	0.9524	0.9507	0.9493	0.9481	0.9472
LAMA =	0.7833	0.6912	0.6184	0.5595	0.5108	0.4700
Output LoD =	40.1	40.	140.8	41.9	43.3	45.0
PHI (degrees) =	40.25	36.27	32.97	30.18	27.82	25.78
dTcdx =	0.5150	0.5932	0.6704	0.7467	0.8225	0.8979
yCt =	0.2150	0.2077	0.1985	0.1888	0.1791	0.1698
clapprox =	0.5017	0.5017	0.5102	0.5243	0.5421	0.5625
yapprox =	0.5617	0.513	50.4638	0.416	60.3736	0.3353
capprox =	0.9558	0.8739	0.7892	0.7089	0.6358	0.5707
RNaprx =	1.685e+6	1.694e+6	1.673e+6	1.635e+6	1.586e+6	1.532e+6
alpha =	0.1643	0.1622	0.2464	0.3858	0.5633	0.7681
cl =	0.5316	0.5314	0.5395	0.5530	0.5702	0.5899
cd =	0.01323	0.01322	0.01320	0.01316	0.01312	0.01309
cl/cd =	40.18	40.18	40.89	42.04	43.47	45.07
beta =	40.42	36.44	33.21	30.57	28.38	26.55
chord =	0.92	10.840	0.758	0.68	10.612	0.550

The usual requirement that propeller blade sections be thin (especially at the tips) does not rigidly hold in wind tunnel fans. The reasons are two: The air speed at the fan is often sufficiently low so that compressibility effects are not serious, and high enough L/D ratios are obtained easily so that straining for small increments through the use of thin sections is unnecessary. The thicker sections are stronger, too, but peculiar high-frequency vibrations that occur in many wind tunnel fans and the possibility of the propeller being struck by airborne objects make it advisable to incorporate margins of safety of the order of 5.0 into their design. An advantage accrues from having removable blades, since a damaged blade may then be replaced without rebuilding the entire fan. However, the replacement blade must be mass balanced to match the first moment of the other blades, as a minimum.

Tests of fans designed by the above method indicate that actual efficiencies will be from 3 to 5% less than theoretical, owing to tip clearance and boundary layer effects at the boss and tip.

If changes are made to the tunnel after it has been built, it may be necessary to make a fan revision. Though an entirely new fan would be best, flaps have been installed in several tunnels with satisfactory results and, of course, at much less cost than a whole new fan. The procedure is to rivet or screw a flat sheet at the desired flap angle until the chord is satisfactory to meet the new condition.

It is interesting to note that modified aircraft propellers have been used successfully in many tunnels. The remote-control variable-pitch feature that most of these have is most desirable.

3.7   RETURN (OR SECOND) DIFFUSER

The second diffuser usually extends from the fan section to the third comer. As indicated in the earlier discussion, in many tunnels this diffuser continues the expansion to the desired total area ratio. Again, the equivalent cone angle should be 5° or less. A favored design in recent facilities is to have a wide-angle diffuser following the third comer so the second diffuser may not provide the final expansion. The fan at the entrance gives an almost constant total pressure profile.

There are two likely sources of trouble in the second diffuser. The first is flow separation on the aft portion of the nacelle. The second in many rectangular tunnels is that the flow downstream of the fan may have nonuniform velocity distribution. In a flow improvement program at the University of Washington[S3] model tunnel studies showed very low velocities in the comers. The flow at the third comer was higher on the inside of the turn. However, the upflow-cross-flow distribution prior to the turn did not exhibit a discernable flow pattern similar to the test section. After the tum there were two distinct rotations in the upper and lower half of the duct. A model tunnel test section exhibited a similar cross-flow gradient to that present in the full-scale tunnel. Although this problem sounds like a secondary flow produced by the velocity gradients prior to the turn, in all cases the sense of the rotation was reversed.

It was discovered that when the antiswirl vanes were uniformly deflected either positively to reduce fan swirl or negatively to increase fan swirl the comers were filled and the cross-flow gradient was reduced but not eliminated. In the final tunnel modification the antiswirl vanes, which originally were simple flat plates hinged to the nacelle supports, were redesigned. The chord of the antiswirl vanes was increased. They were made into cambered airfoil sections using the nacelle struts for a leading edge. This modification filled the comers of the second diffuser and eliminated flow separation regions on the original flat-plate vanes. The new cambered vanes were deflected to $12°$ and resulted in a much more uniform velocity distribution with all four comers filled with higher energy flow. This flow improvement in the second diffuser and fourth comer also reduced the power consumption at all speeds by about 2.0%.

3.8   COOLING

All the energy supplied to the propeller driving a wind tunnel finally emerges as an increase of heat energy in the airstream. This increases the temperature of the tunnel air until heat losses balance the input. For low-power tunnels (and particularly those with open jets) this balance is realized at reasonable temperatures, the heat transfer through surface cooling and air exchange being sufficient. For tunnels with high-power inputs and high jet velocities this low-temperature balance no longer occurs. For example, the heat rise incurred by bringing air to rest at 450 mph is about 36°F. With an energy ratio of 8.0, the heat rise in the airstream would be 4.5°F per circuit, leading very shortly to prohibitive temperatures. Obviously, tunnels in this class require cooling arrangements to augment the inherent heat losses. It should be readily realized that steady-state operation with no net air temperature increase above ambient would require that there be a cooling apparatus absorbing energy at the same rate at which the fan is applying energy to the airstream.

Additional cooling may be accomplished by four means: (1) an increase in transfer of heat through the tunnel shell by external surface cooling, which at some facilities is obtained by running water over the tunnel exterior, (2) interior cooling by the addition of chilled turning vanes, (3) a heat exchanger in the largest tunnel section, or (4) a continual replacement of the heated tunnel air with cooler outside air by means of an air exchanger.

Some tunnels use an air exchanger to replace the lower energy boundary layer with cool outside air, having exchange towers to ensure adequate dispersion of the heated air and fresh air that is free from surface contamination. Assuming the previously mentioned rise of 4.5°F per circuit, a 10% exchange would limit the rise to 45°F, excluding heat losses elsewhere. (Ten percent is a lower than average amount of exchange.)

One difficulty associated with an air exchanger is that it puts the highest pressure section of the tunnel at atmospheric pressure, and hence the jet pressure is below atmospheric. This leads to troublesome but by no means insoluble problems of sealing off the balance room. (The same lower than ambient static pressure at the

test section is present in open circuit tunnels.) Another difficulty that must be considered is the possible effects of weather conditions on a tunnel with a large amount of air being exchanged.

It should be mentioned that a breather slot at the downstream end of the test section can be used in conjunction with the air exchanger to get the jet up to atmospheric pressure and hence avoid balance sealing troubles. However, this arrangement with the air going in the breather and out the exchanger requires as much as 20% of the total power input.

The internal heat exchanger needed for high-powered wind tunnels require an immense amount of surface, a great deal more than is offered by all four sets of guide vanes. Accordingly, a special installation is needed, and there is almost no way to avoid a very large amount of drag. In a preliminary study reported by Steinle[54] pressure drops of 8 to $18q$ were measured across exchangers; another design, unreported, bad $4q$. Thus the heat exchanger must be placed in the largest section of the tunnel where q is lowest. Fortunately the temperature of the stream is highest at this point and heat exchange, consequently, is most easily accomplished.

In view of its power cost a great deal of thought should go into the design of a heat exchanger, and it should be remembered that normal streamlining should be used here as well as elsewhere. The unknowns of internal and external boundary layer thicknesses make the problem of cooling through the walls quite difficult. In discussing internal cooling, Tifford[55] agrees that a radiator has possible advantages over cooled turning vanes.

The obvious disadvantages of high temperatures in the wind tunnel include added trouble cooling the drive motor (if it is in the tunnel and does not have separate cooling), the rapid softening of the materials commonly used for model temporary fillets, and increased personnel difficulties. Another deleterious effect is the drop in Reynolds number that occurs with increasing temperatures whether the tunnel is run at constant speed or at constant dynamic pressure. Figure 3.24 illustrates this effect.
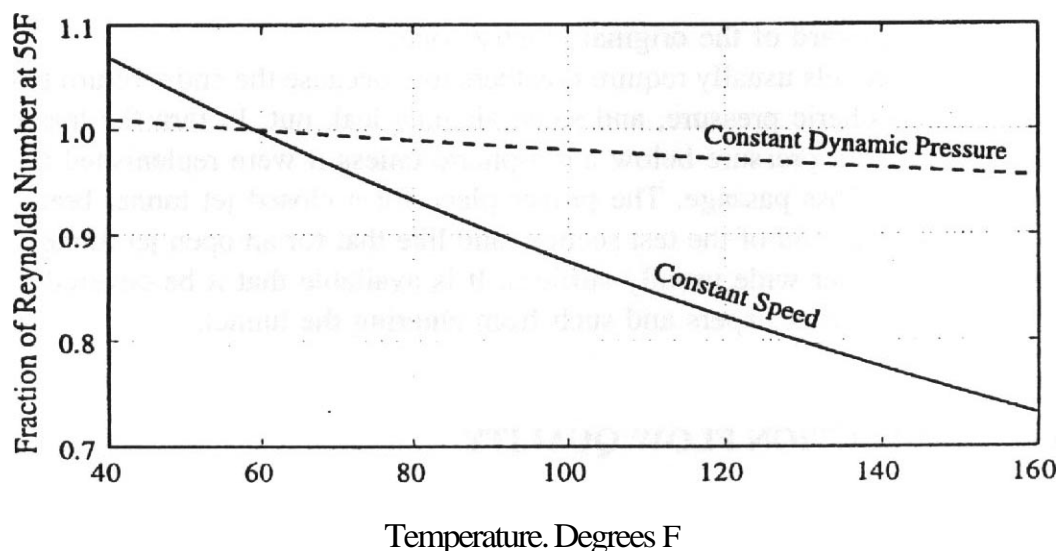
FIGURE 3.24   Effect of temperature on test Reynolds number.

Since most electric motors have high efficiencies, placing the motor outside the tunnel is probably not justified by the small amount of tunnel heating saved thereby, but the ease of motor repairs and tunnel repowering without a nacelle change are strong arguments for the external drive motor.

3.9   BREATHER: VIBRATIONS

If the tunnel is to be operated with an open jet, due consideration must be given to the possibility of pulsations similar to the vibrations in an organ pipe. Other oscillatory effects have been experienced that appear to be associated with unstable conditions as the open jet enters the diffuser collector. These phenomena, believed to be a function of jet length, can be quite serious. Some insight into these phenomena may be gleaned by studying the flow modeling discussed in the chapter on tunnel corrections.

A relatively simple solution that has proved successful in some cases consists of putting a slot (about 0.05 diameter wide) into the diffuser that connects it to the atmosphere. Such an arrangement is called a "breather." If the slot is properly made and adjusted so that it is just large enough to prevent organ piping, the losses can be kept low. In some open jet tunnels alterations to the exit cone proved sufficient to prevent the vibration, but in others no satisfactory exit cones or breathers have been found that would permit operation above 200 mph.

The NASA Langley 4 X 7-m tunnel, when run in a closed-on-bottom-only test-section configuration, has exhibited periodic flow pulsations in the axial direction at three dynamic pressures. The magnitude of the velocity peaks increased with the addition of flapped vanes between the first and second comers. The addition of triangular vanes with alternate deflections on the side walls and ceiling of the exit cone removed these pulsations at the higher dynamic pressures and reduced the width of the peak at the lowest dynamic pressures. The vanes are mounted inboard of the walls and ceiling. Model tunnel studies show that the remaining pulsation can be eliminated by modifying the reentry cone. The modification consists of a tapered cone forward of the original reentry cone.

Closed jet tunnels usually require breathers too, because the entire return passage is above atmospheric pressure, and some air may leak out. In turn the loss of air would drop the jet pressure below atmospheric unless it were replenished through a relatively low loss passage. The proper place for a closed jet tunnel breather is at the downstream end of the test section, and like that for an open jet tunnel a slot about 0.05 diameter wide usually suffices. It is available that it be covered with a fine screen to prevent papers and such from entering the tunnel.

3.10   TEST-SECTION FLOW QUALITY

For an empty test section the traditional view of the ideal flow outside the boundary layer would be the following. The velocity passing through each plane normal to the centerline would be uniformly parallel to the centerline and would have no

variation with time; that is, there would be no upflow or cross-flow and there would be no turbulence. Since it is doubtful that such flow can be obtained in a wind tunnel, the question then becomes what flow quality is acceptable at a reasonable tunnel performance level and operating cost. The tunnels constructed for wind engineering studies have quite different "ideal" flow requirements. They are designed to reproduce, insofar as possible, characteristics of Earth's boundary layer flow in some representative circumstances. This requires producing a nonuniform but specified mean flow and turbulence with specified integral scales and spectra.

Values for velocity variation across the test sections of general-purpose tunnels are often quoted in the range of 0.20–0.30% variation from average. This gives a dynamic pressure variation of 0.4–0.6%. Values for angular variation are often quoted in the range of 0.1" from the average flow angle. The upflow variation is the critical flow angle for most aeronautical tests. The drag data for lifting systems must be corrected for upflow, as is detailed in the chapter on tunnel corrections.

The first requirement is "steady flow," or sufficiently close to steady for the purposes of the facility, since it is not possible to achieve a flow of the magnitude envisioned without measurable unsteadiness. In general, unsteady flow is a result of flow separation(s) at one or more locations, either continuous or intermittent. The distinction between *separated unsteady flow* and *turbulence* is somewhat arbitrary, the latter term commonly applied to flow arising from wakes of vanes, noise, and so on. A specification is needed that is based on temporal and spatial frequency content.

Unsteady flow caused by a flow separation that either steadily or intermittently deflects the flow may be regarded as irrotational and inviscid outside the separated region. The only cure for these is to locate the source and eliminate it. This is not an easy task as the effects are usually detected a considerable distance from the source. Obvious locations to look for separation are the first diffuser, fust comer, fan nacelle, and contraction. If the tunnel has air leaks, the breather may cause separation. Usually leaks in a return tunnel will be near doors, drains, access holes for instrumentation, and so on, and they can be sealed given sufficient attention.

Other sources of unsteady flow can arise from the fan through nonuniform inflow. This will be at the blade frequency or possibly at harmonics. The number of fan blades, nacelle supports, and prerotation vanes should never be even multiples of each other so that interactions are not synchronous. Mechanical vibration of the fan will usually be at the fan rpm. Vibration of turning vanes due to turbulence or unsteady flow could occur over a wide frequency range. The vanes can be stiffened by horizontal plates, if required.

Nonuniform distribution of velocity can also occur by either poor vane design or improperly adjusted vanes that cause the flow to over- or underturn. Upflow and cross-flow distribution in the test section have occurred as a result of poor flow into the third comer and out of the fourth comer. In this region the turning vanes are quite long, and in a great many tunnels the trailing edges have a spanwise bow. Making sure that the flow is not over- or underturned and converting the fourth comer vanes to a large-grid adjustable honeycomb will almost certainly improve the upflow, cross-flow, velocity, and turbulence in the test section. There

also needs to be a settling length after the contraction to allow the velocity to become uniform.

Many tunnels suffer from one or more problems of various degrees of seriousness. The problems can likely be cured or reduced by the methods that have been discussed, but this takes persistence and time. In almost all cases the basic problem is time. A new wind tunnel represents a large investment. It usually is behind schedule when built, and thus the pressure to begin testing becomes irresistible. The down time for correcting problems can be large and, more important, somewhat unpredictable. Any time a change is made to a tunnel, a sufficient period of time must be set aside to allow for the complete recalibration of the test section. The authors cannot offer any solution to this part of the problem.

The modification[53] to the University of Washington tunnel that has been discussed to some extent already and is given more attention in the next section consumed about three months of double-shift work. This included the installation of new parts, adjustment, and calibration.

3.11 APPROACH TO FLOW IMPROVEMENT

The following paragraphs can provide a framework for any project undertaken to achieve improvement of flow in a tunnel.

The first task is to eliminate separation in the first diffuser. Make sure that the first two corners do not over- or underturn, that the flow is uniform approaching the fan, and that the nacelle flow is attached. The flow in the second diffuser should fill the duct. Using vane extensions and horizontal splitter plates, the fourth-corner turning vanes should be adjusted to yield uniform upflow and cross-flow and no large solid-body-type rotation in the test section. All of these should be done before honeycombs or screens are installed. The exception to the screens would be in a wide-angle diffuser if one is present. This then should yield a tunnel with the best test-section flow for the minimum power.

Using an axisymmetric contraction cone with a contraction ratio of 11, Ramjee and Hussain[56] have shown that the turbulence at the contraction cone exit is essentially independent of the screen Reynolds number based on either wire diameter or mesh size. For the longitudinal turbulence the values behind the screens ahead of the inlet vary from 0.029 to 0.052, while at the exit the variation was 0.0050–0.0054 for five different screens. The lateral variation at the inlet was 0.032–0.063 and 0.0060–0.0070 at the exit. The pressure loss coefficient for four of the screens varied from $K = 0.65$ to $K = 2.34$, based on the relations previously given, and the porosity varied from 0.62 to 0.75 (a screen with porosity of 0.25 has been excluded). The screen with $K = 2.34$, inlet turbulence of 0.29, and exit turbulence of 0.0051 gave the same results at the exit or test section as the one with $K = 0.65$, inlet turbulence of 0.052, and exit turbulence of 0.0050. These are the longitudinal values. This implies that one should use screens with the smallest pressure loss coefficient, and if multiple screens are used, again, screens with the smallest loss should be adopted.

Ramjee and Hussain[56] also determined that the ratio of rms exit to inlet turbulence as a function of contraction ratio (from Prandtl) is overpredicted in the longitudinal direction and underpredicted in the lateral direction. These predictions are

$$\text{u component turbulence reduction} = 1/c^2$$

$$\text{v component turbulence reduction} = 1/\sqrt{c}$$

The linear theory of turbulence reduction due to a contraction predicted an increase in the lateral component,[33] but this is not borne out by experiment, which shows a decrease. There does not at present appear to be a good method of predicting the effects of contraction ratio on turbulence reduction. The axial and lateral turbulence should be determined at several speeds, at the start of both the contraction and the test section. This will determine the turbulence reduction due to the contraction. The effect of filters on the turbulence measurements should be carefully evaluated. If the turbulence level is too high, then the installation of a honeycomb followed by a screen or screens must be considered. The reduction of axial and lateral turbulence and the pressure drops at the contraction can be estimated by published values. A better approach, using hot wires, would be to measure these values with the same filter settings that were used in the tunnel measurements.

If screens and/or honeycombs are installed, the reduction in turbulence should be checked as each device is installed. This will ensure that the minimum number of devices is used, thus holding losses to a minimum. The following values for turbulence are suggested. The ideal value would, of course, be zero. The final accepted values will be a trade-off between installation costs and reduction in tunnel performance and power costs.

For tunnels intended for research on boundary layers and boundary layer transition, the lateral values of the turbulence, which is usually the largest, must be kept sufficiently small. Values of about 0.05% have been suggested.

Tunnels used for developmental testing can have larger turbulence values, perhaps as high as 0.5% in the axial direction, although some large government tunnels try for 0.1%. However, there is no general agreement as to the required absolute value, and there are some who argue that tests of terrestrial vehicles should be done in streams with turbulence levels of up to 1%.

Another approach is as follows. The lower limit for the tunnel's Reynolds number range was on the order of 1.5 million based on instrumentation sensitivities and size of models. At these Reynolds numbers for a smooth model there will be an extensive region of laminar flow. Thus there is the possibility of poor flow simulation due to laminar separation on the model that does not occur at full scale. The usual practice to improve simulation is to use trip strips on the model to fix the transition along lines expected to occur on the full-scale article at some representative condition. Considering these practices the following suggestion is made. Test a smooth wing without flaps at lift coefficients around 0.2–0.5 without trip strips and check the natural transition using either oil flow or sublimation flow visualization. If the natural transition occurs, depending on the airfoil section, in the range of 30–60% of

the chord, the turbulence level in the tunnel is acceptable. If this can be accomplished without screens or honeycombs, the power consumption will be less and the dirt problem with screens changing flow characteristics will be avoided.

3.12   DRIVE SYSTEM

Since the thrust of the fan and the drag of the various tunnel components vary with the square of the fan rpm, it would appear that to maintain an even velocity front in the test section, speed adjustments should be made by varying fan rpm rather than fan pitch. Although this conclusion is justified in short tunnels of low contraction ratio, in the larger tunnels, particularly those with dust screens and internal coolers to act as flow dampers, it is certainly not essential. Indeed, many of the larger tunnels, which are equipped with both rpm and pitch change, use the latter as quicker and simpler. It does seem as though provision of both types of control is a good design procedure.

Various drive systems are described subsequently because they are still in use in various facilities. New facilities will almost certainly use solid-state controllers directly for DC machinery or more likely variable-frequency systems for **AC** machinery. The described drive systems are best thought of as basic concepts. The actual details of how the drive is accomplished has varied considerably from case to case. This field, like the electronics field, continues to change rapidly and solid-state devices continue to replace rotating equipment as the solid-state devices become less costly and more reliable.

Considering the drives capable of variable-speed control, we have the following:

1. *Solid State Controller for DC Motor.* **A** system of rectifiers takes the power line input and provides variable voltage and variable current to operate a **DC** motor. The system comes as an integrated package with RS 232 input and output so that a computer can send the commands for required speed.

2. *Generator and DC Motor* **A** direct-current generator run by a synchronous motor and used to drive a direct-current motor in the tunnel electrically is a satisfactory system below about 200 hp, the costs becoming excessive above that figure. It offers excellent speed control.

3. *Tandem Drive.* The combination of a **DC** motor for low powers and a single-speed induction motor for high powers is satisfactory for the range of 300–20,000 hp. With this arrangement the DC motor is used for low-power operation and for bringing the induction motor up to running speed.

4. *Variable Frequency.* The power range for this approach using solid-state variable-frequency systems is now up to at least 10,000 hp. This type of system is used at the Boeing Helicopter Company and was installed at the Lockheed Martin low-speed wind tunnel in the 1980s as part of a repowering project. The tunnel drive in these cases are in the 9000-hp range. The historic arrangement for variable-frequency systems involved a synchronous motor driving a DC generator whose

output was used to run a DC motor that in turn powered an alternator. The output of the alternator was provided to the fan motor, which could be either a synchronous or an induction motor. This is an excellent system but historically quite expensive. Solid-state systems are now cost competitive over a wide power range.

5. *Magnetic Coupling.* A synchronous motor can be used to drive a-fan through a variable-speed magnetic coupling. This is historically one of the least expensive setups as far as first cost is concerned and gives excellent speed control from zero to maximum velocity since it is virtually "stepless."

6. *Multispeed Squirrel Cage.* An induction motor arranged to have several operating speeds may be used in conjunction with a variable-pitch fan to get a satisfactory drive.

7. *Wound-Rotor Induction Motor.* In general, one cannot expect wide rpm changes, good control, or high efficiency from a wound-rotor induction motor, although such a motor has been used with reasonable success in combination with a variable-pitch fan. It does offer a low first cost and moderately small motor for tunnel installations.

8. *Double-Fed Induction Motor.* This arrangement requires a variable-frequency power source that is fed into the rotor of an induction motor. Its first cost is high, but it is probably the most widely used drive for very high power installations where efficiency is important.

9. *Internal-Combustion Drive.* The use of an internal-combustion engine is undesirable because of both high operating cost and lack of long-term reliability. In the few tunnels where they have been used the engineers invariably look forward to the day when the gasoline engine can be replaced by an electric drive. For reasons almost unknown (but surmised to be connected with the lack of a cooling airstream over the stationary engine and unskilled maintenance), reciprocating engines rarely deliver the life in tunnel use that they do on aircraft, 300 h being a fairly typical figure per engine. When an aircraft engine must be used, special care should be taken that the exhaust manifold be water jacketed or otherwise cooled. An annoying trouble with these engines (as if the above is not sufficient) is that their spark plugs foul up under the low-load operation frequently needed in a tunnel. For comparison, it is noted that many electric drive motors in wind tunnels operate for several decades between major rework. The drive motor of the Glenn L. Martin wind tunnel at the University of Maryland operated from **1949** to 1993 with only routine inspections and cleaning. Other facilities have had similar long life times. The electric motors usually outlast the fan systems by large margins.

3.13   WIND TUNNEL CONSTRUCTION

The structural loading on the various sections of a low-speed wind tunnel are usually less critical than the strength needed to avoid vibration, a significant exception being the assurance that the drive motor will stay in place should it lose one-half of its blades. The rest of the tunnel may be examined to withstand the maximum stagnation pressure with a safety factor of perhaps **4.0.**

Since vibration of parts of the wind tunnel contributes to noise, discomfort of the tunnel crew, and possible fatigue failures and usually adds to the turbulence in the wind stream, it is good practice to have the natural frequencies of all tunnel parts well above any exciting frequencies. Many of these parts of the tunnel are directly amenable to basic vibration theory; others must wait for treatment after the tunnel is built. At the time, for the small tunnels at least, flat panels can be checked with a simple shaker motor, and by means of a vibrometer or a similar device the natural frequencies can be determined. Any below the maximum fan **rpm** should be increased by stiffening the part. A special effort should be made to keep vibration out of the test section and balance supports.

All types of materials are used for tunnel construction: wood, plywood, thin metal, heavy metal (for pressure tunnels), cast concrete, **gunnite,** and plastics. Even though there is "general agreement" that low-speed wind tunnels require no cooling, heavy running in the summertime will usually make the tunnel operators wish they had some. It is highly advisable in fact that even 25-hp tunnels be cooled. Many tunnels have an opening where cooler outside air can be blown into the tunnel during model changes. Some large metal tunnels spray water over the outside to cool the tunnel.

Fan blades for low-speed tunnels are frequently made of wood, although modified aircraft propellers are sometimes used with trailing-edge flaps to provide a uniform pressure rise across the fan disk. Wood blades have excellent fatigue life. The wood for fan blades must be straight grained and knot free. Damage to wood blades can be repaired by scarfing in a piece of wood. To avoid abrasion, the leading edge at the tip can have a fiberglass insert. Often the last 2 or 3 in. of the tip are of balsa, as this will shatter when an unwanted object wedges between the tip and tunnel and can be easily replaced. There is no clear consensus on the matter of spare blades. Tunnels that use short-span, large-chord blades have used fiberglass and, more recently, composite materials such as carbon-fiber-reinforced epoxies. These blades may have spars and be filled with foam.

For small research and instruction tunnels plywood is possibly the best material. Particle board is another material used; however, it is not **as** stiff as plywood and can develop a sag when unsupported. A smooth surface finish is difficult to obtain on particle board; also, it chips easily and is difficult to patch. With wood, holes that inevitably get cut in the tunnel can be easily patched and epoxy fillers can be used to maintain a smooth interior surface. The plywood is normally placed inside a wood frame. The tunnel is often made in sections that bolt together. To prevent leaks, surgical tubing can be used as a gasket. The end of one section has a groove routed to receive the tubing. This is just a large O ring. The fan area can be metal, as it is easy to roll up round sections. The contraction can be laminated wood or could be built up with a fiberglass and foam sandwich. When student labor is used, the design must consider the skills available. A door in the floor in the plane of the fan will be necessary so that blades may be taken out of their hubs and replaced.

The detailed design, including selection of material, erection, and so on, of large tunnels is usually done by engineering firms that are familiar with all the building codes and have civil, mechanical, and electrical engineering expertise.

3.14   TEST-SECTION INSERTS

Many tunnels have an auxiliary two-dimensional test section that fits inside the normal test section in order to provide testing facilities for shorter span models at considerable savings in model cost. These jets are usually either endplate or contraction types.

The endplate jet insert consists of two flat plates sealed at the tunnel floor and ceiling with a space between them for mounting and testing a constant-chord two-dimensional airfoil model (Figure 3.25). In some installations the model supports come up inside the endplates, and the rear pitch strut is used to hold and move the wake survey rake. Since the drag of the model changes with many factors, and since drag changes can make more air pass *around* instead of through the test section, special provision must be made to control the test dynamic pressure. One
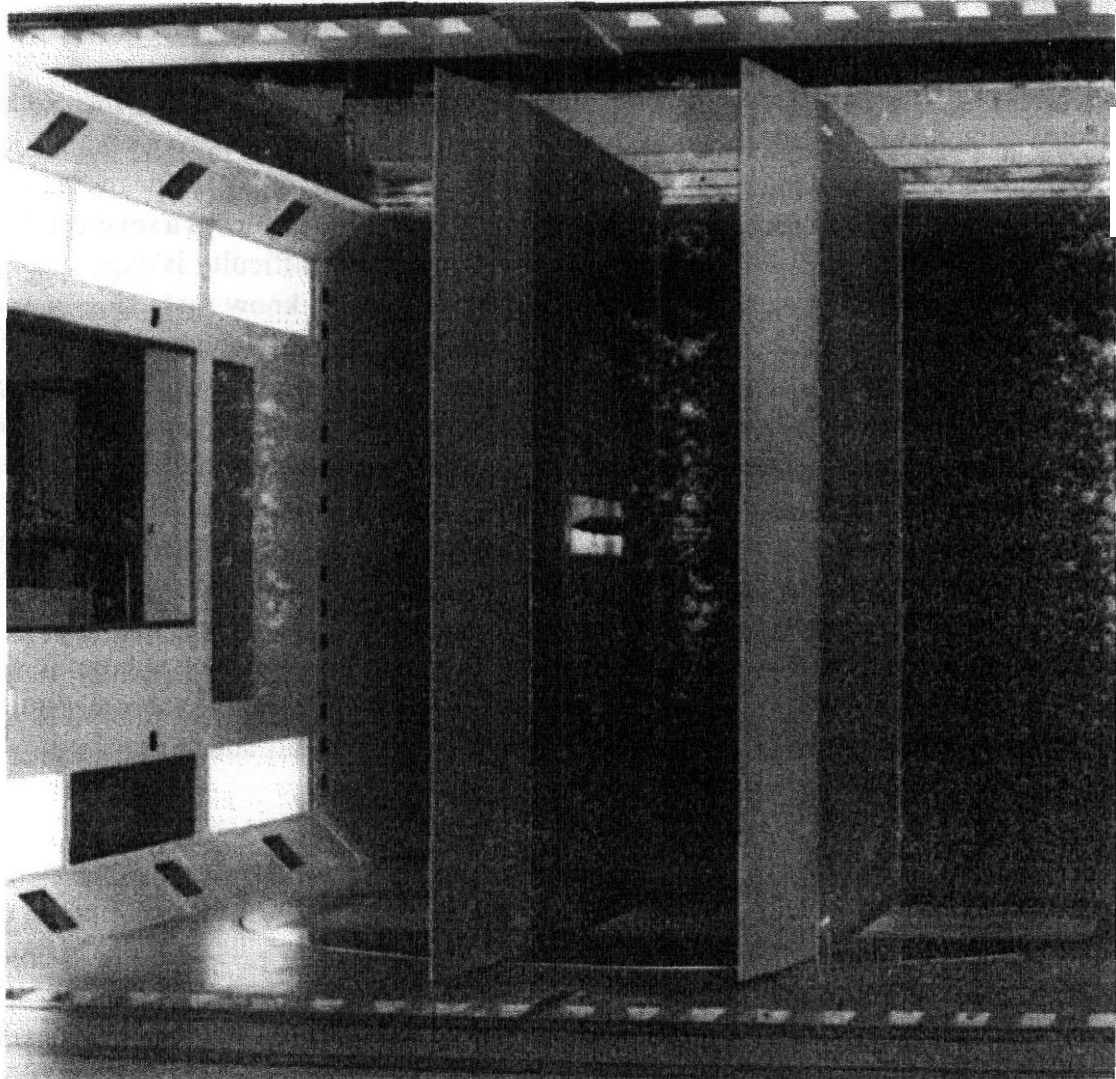
FIGURE 3.25   Two-dimensional insert for the Glenn L. Martin wind tunnel at the University of Maryland.

procedure is to use the customary double piezometer to hold constant the quantity of air that enters the original test section and ascertain that a constant fraction of *that* air passes through the new test section by reading pitot-static tubes placed outside it. Variations can be made by remotely movable trailing-edge flaps on the endplates.

A second approach is to contract the whole tunnel test section by an additional contraction section. This has the advantages of greatly increasing the contraction ratio, making the installation of turbulence screens easy, and providing sure and positive two-dimensional conditions. On the other hand, a much smaller quantity of air now passes through the tunnel for a particular test speed, since the test-section area is reduced, and in many cases the performance of the tunnel fan is greatly impaired. Still another source of trouble is the problem of diffusing the overcontracted passage. Somewhere some extremely rapid diffusion is going to have to take place, and the **task** is exceedingly difficult to do with even passable efficiency. In one installation a two-dimensional insert converted **a** 9-ft-diameter tunnel to a $2\frac{1}{2}$- $\times$ **9-ft** test section; the problem of the separated diffuser arose, but vortex generators on all four walls very nearly solved it.

Several other items are of interest when inserts are under consideration. One of these is the question of whether to mount the insert horizontal so that the model is vertical or vice versa. The horizontal insert offers the opportunity of using liquid seals around the model mounting endplates, but, on the other hand, the model is somewhat more difficult to get to for adjustments. In some instances a severe pressure differential will occur with this type of insert, and great difficulty is experienced in keeping any but the heaviest liquids in the seals. We now know that using mercury, as was common prior to 1970, was not a good idea due to its adverse health effects. Additional breather slots will usually alleviate this condition. Force measuring is also made more difficult by the large and indeterminable tares of the model mounting endplates, so much so that it is sometimes preferable to obtain the lift by pressure distribution on the model or on the floor and ceiling and drag by a momentum rake or to leave a small gap between model and walls. This, of course, then introduces some doubt about the "two dimensionality" of the flow so that additional flow investigations must be included in the test plans.

In conclusion, it does not appear possible to recommend one type of two-dimensional jet insert as clearly superior. As a final note, aerodynamics aside for a moment, the endplate type of insert is far easier to install and remove.

3.15   SAFETY

Though it may seem strange to the uninitiated to bring the question of safety into this discussion of wind tunnels, the long roster of injured indicates it is not to be overlooked. Accidents in tunnel use include fires, falls, injuries from sharp-edged models, and personnel being locked in a tunnel when it is started.

Starting with the last, anybody who enters a part of a wind tunnel not readily visible to the tunnel operators without firm understanding regarding the restart-

ing time is an idiot. But since it is not the practice to injure idiots, many tunnels preface a start with a blast on a horn, with a 5-sec wait for incumbents to punch stop switches installed in test sections, return passages, and near the fan blades. Another approach is to install an automobile ignition switch at the test-section entrance. The switch is in the tunnel start circuit. Still another approach is to use light beams (similar to burglar alarms) in various parts of the tunnel circuit that prevent the tunnel from starting when cut. When it is necessary for someone to be. in the tunnel while it is running, very clear signals and understanding must again be in place.

Falls are unfortunately frequent in wind tunnels. Their rounded surfaces, often coated with oil or other low-friction materials, including in some instances ice, and the precipitous slope of entrance cones have resulted in bruises and even broken arms and legs. The authors speak feelingly at this point. In view of the danger associated with the entrance cone and settling chamber, pitot-static tubes, thermocouples, and the like should be wall mounted, not floor mounted.

Fires in wind tunnels seem to be almost the rule rather than the exception. A broken propeller can spark a dust screen into fire; a trouble Light can make plenty of trouble; or building forms can in some way become ignited. Since the tunnel is closed, special care should be taken in selecting fire extinguishers. And special care should be taken also to see that fire extinguishers emitting poisonous vapors are not easily tripped. It may well be that the world's record for the hundred-yard dash rightfully belongs to be tunnel engineer who inadvertently activated the carbon dioxide system in one of the largest east coast tunnels.

Sharp edges on metal models are a potent hazard. The authors do not know a tunnel engineer or technician who has not suffered from this source. It is only good sense to protect the tunnel crew from these sharp edges using tape, wood, or plastic slats.

Safety may seem like a puerile subject, but it loses that appearance *afterward.*

REFERENCES AND NOTES

1. See Table 1.1.
2. For more on this topic see Chapter 8.
3. NWTC Project Office, National Wind Tunnel Complex, NASA CR-198491.
4. See Chapter 8.
5. Bradshaw, P., and Pankhurst, R. C., 'The Design of Low-Speed Wind Tunnels," Prog. Aeronaut. *Sci.,* 5, 1–59, 1964.
6. Preston, J. H., "The Minimum Reynolds Number for a Turbulent Boundary Layer and the Selection of a Transition Device:' *J. Fluid* Mech., 3, 373, 1958.
7. See Chapter 10.
8. See Chapter 8.
9. The hydraulic diameter of a duct is defined as the diameter of a circle having the same area as the cross section of the actual duct regardless of the shape.

10. Ewald, F. R., Holzdeppe, D., Cronauer, D., and Waudby-Smith, P., "Standardized Wind Tunnel Design and Construction for Aerodynamic Research and Development," ICAS Paper 94-3.1.4, presented at the Nineteenth Congress of the International Council of the Aeronautical Sciences, Anaheim, CA, Sept. 18–23, 1994.

11. Mehta, R. D., "The Aerodynamic Design of Blower Tunnels with Wide Angle Diffusers," *Prog. Aerospace Sci., 18,* 59–120, 1977.

12. Wattendorf, F. L., "Factors Influencing the Energy Ratio of Return Flow Wind Tunnels," paper presented at the Fifth International Congress for Applied Mechanics, Cambridge, Sept. 12–16, 1938, p. 52.

13. Wallis, R. A., *Axial Flow Fans and Ducts,* Krieger, Malabar, FL, 1993.

14. Eckert, W. T., Mort, K. W., and Jope, J., "Aerodynamic Design Guidelines and Computer Program for Estimation of Subsonic Wind Tunnel Performance," NASA TN D-8243, Oct. 1976.

15. Shames, I. H., *Mechanics of Fluids,* 3rd ed., McGraw-Hill, New York, 1992, Chapter 9.

16. Anderson, J. D., Jr., *Fundamentals of Aerodynamics,* McGraw-Hill, New York, 1991, Section 10.3.

17. See Figure 3.1 and the related discussion for the section designations.

18. See Chapter 9.

19. Robertson, J. M., and Fraser, H. R., "Separation Prediction for Conical Diffusers," *Trans. ASME, Series D82,* 201,201–209, 1960.

20. Krober, G., "Guide Vanes for Deflecting Fluid Currents with Small Loss of Energy," NACA TM 722, 1932.

21. Collar, A. R., "Some Experiments with Cascades of Airfoils," ARC R&M 1768, 1937.

22. Patterson, G. N., "Note on the Design of Corners in Duct Systems," ARC R&M 1773, 1937.

23. McPhail, D. C., "Experiments on Turning Vanes at an Expansion," ARC R&M 1876, 1939.

24. Salter, C., "Experiments on Thin Turning Vanes," ARC R&M 2469, Oct. 1946.

25. Winters, K. G., "Comparative Tests of Thin Turning Vanes in the RAE 4 × 3 Foot Wind Tunnel," ARC R&M 2589, 1947.

26. Sahlin, A., and Johansson, A. V., "Design of Guide Vanes for Minimizing the Pressure Loss in Sharp Bends," *Phys. Fluids A,* 3, 1934–1940, 1991.

27. Lindgren, B., Osterlund, J., and Johansson, A. V., "Measurement and Calculation of Guide Vane Performance in Expanding Bends for Wind Tunnels," Paper No. 7, presented at the CEAS Forum on Wind Tunnels and Wind Tunnel Test Techniques, Cambridge, United Kingdom, April 14–16, 1997.

28. Idel'chik, I. E., *Handbook of Hydraulic Resistance,* The Israel Program for Scientific Translations, Tel Aviv, 1966, AEC-TR-6630.

29. Mehta, R. D., and Bradshaw, P., "Design Rules for Small Low Speed Wind Tunnels," *Aeronaut. J.,* Nov. 1979, pp. 443–449.

30. Prandtl, L., "Attaining A Steady Stream in Wind Tunnels," NACA TM 726, Oct. 1933. At the time this was published, Prandtl had been involved in designing and building wind tunnels for his research in aerodynamics for more than 30 years. This memorandum contains descriptive material on some important wind tunnels of that era and earlier.

31. Scheiman, J., and Brooks, J. D., "Comparison of Experimental and Theoretical Turbulence Reduction from Screens, Honeycomb, and Honeycomb-Screen Combinations," *J. Aircraft,* **18(8), 638–643, 1981.**

32. Loehrke, R. I., and Nagib, H. M., "Experiments on Management of Free-Stream Turbulence," AGARD-R-598, Sept. **1972.**

33. Roberts, **H.** E., "Considerations in the Design of a Low-Cost Wind Tunnel," paper presented at the Fourteenth Annual Meeting of the Institute of Aeronautical Sciences, El Segundo, CA, Jan. **1946.**

34. The notation has been changed to be consistent with that in this book.

35. Batchelor, G. **K.,** *The Theory of Homogeneous Turbulence,* Cambridge University Press, **1967,** Cambridge, pp. **58–75.**

36. Schubauer, G. B., Spangenburg, W. G., and Klebanoff, P. S., "Aerodynamic Characteristics of Damping Screens," NACA TN **2001, 1950.**

37. Laws, E. **M.,** and Livesey, J. L., "Flow Through Screens," *Ann. Rev. Fluid Mech.,* **10, 247–266, 1978.**

38. Morel, T., "Comprehensive Design of Axisymmetric Wind Tunnel Contractions." *J. Fluids Eng., ASME,* **97,** 225–233, June **1975.**

39. Tsien, H. S., "On the Design of the Contraction Cone for a Wind Tunnel," *J. Aeronaut. Sci.,* **10, 68–70, 1943.**

40. Thwaites, B., "On the Design of Contractions for Wind Tunnels," ARC R&M **2278, 1946.**

41. Chmielewski, G. E., "Boundary Layer Considerations in the Design of Aerodynamic Contractions," *J. Aircraft,* **8,** 435–438, **1974.**

42. Stratford, G. S., "The Prediction of Separation of the Turbulent Boundary Layer," *J. Fluid Mech,* **51, 1–16, 1959.**

43. Borger, G. G., "The Optimization of Wind Tunnel Contractions for the Subsonic Range," NASA TTF **16899,** Mar. **1976.**

44. Mikhail, M. N., and Rainbird, W. J., "Optimum Design of Wind Tunnel Contractions," AIAA Paper **78-819,** presented at the AIAA Tenth Aerodynamic Testing Conference, **1978.**

45. Darrius, G., "Some Factors Influencing the Design of Wind Tunnels," *Brown-Boveri Rev.,* **30,** 168–176, July–Aug. **1943.**

46. Harper, J. J., "Tests on Elbows of a Special Design," *J. Aeronaut. Sci.,* **13, 1946.**

47. Collar, A. R., "The Design of Wind Tunnel Fans," ARC R&M **1889,** Aug. **1940.**

48. Patterson, G. N., "Ducted Fans: Design for High Efficiency," Australian Council for Aeronautics, ACA Vol. **7,** July **1944.**

49. Lewis, R. I., *Vortex Element Methods for Fluid Dynamic Analysis of Engineering Systems,* Cambridge University Press, Cambridge, **1991,** Chapters **4** and 5.

50. Wallis, R. A., *Axial Flow Fans and Ducts,* Krieger, Malabar, FL, **1993,** Section **8.3,** p. 188. The term *twist* or *rotation of the flow* was used in previous editions of this book and was denoted by *e.* The new terminology is being adopted here since Wallis's book has been kept current and is most useful as a reference for the current topic.

51. The flow coefficient λ is related to the "local advance ratio" $j \equiv u/nd = u\pi/\Omega r$ as used in previous editions of this book by $j = \pi\lambda$.

52. Eppler, R., *Airfoil Design and Data,* Springer-Verlag, Berlin, **1990.**

53. Shindo, S., Rae, W. H., Aoki, Y., and Hill, E. G., "Improvement of How Quality at the University of Washington Low Speed Wind Tunnel," AIAA Paper 78-815, presented at the AIAA Tenth Aerodynamic Testing Conference, San Diego, CA, April 1978, pp. 336-343.

54. Steinle, W. C., "The Experimental Determination of Aerodynamic Total Pressure Losses for Heat Exchanger Surfaces Considered for the 7 × 10 Foot Transonic Wind Tunnel," David Taylor Model Basin DTMB Aero Report 1951f, 1951.

55. Tifford, A. N., "Wind Tunnel Cooling," *J.* Aeronaut. *Sci.*, 10, 98–100, Mar. 1943.

56. Ramjee, V., and Hussain, A. K. M. F., "Influence of the Axisymmetric Contraction Ratio on Free Stream Turbulence," *J.* Fluids Eng., 98, 505–515, Sept. 1976.

4 Pressure, Flow, and Shear Stress Measurements

After a tunnel is constructed, the next step is to determine its flow characteristics and, of course, to change any that are not satisfactory for the purposes intended. First, however, it is necessary to discuss the quantities to be measured and the instruments that experience has shown are capable of useful results. We shall consider instruments needed for testing as well as for calibration.

The low-speed "steady" airstream is usually considered to be defined when we know its distribution of temperature, pressure, dynamic pressure, and "turbulence." There are several assumptions embedded in this statement. We admit that the airstream is expected to be turbulent and therefore not strictly steady or time invariant. The time variability of the airstream is to be characterized by its level of turbulence. Its pressure' and dynamic pressure are then the mean values for these quantities averaged over a time interval chosen according to the required precision of the mean. The stream temperature is similarly considered. Using the equation of state, we can then compute the density, and using the definitions of total pressure and total temperature, we can compute these quantities and flow speed as well. For atmospheric air, there is another variable that produces measurable effects. It is the water vapor content, which is usually indicated by relative humidity. The effect is reflected by a change in the effective gas constant in the equation of state.

We may also compute the Reynolds number for a particular model based on its chosen characteristic length. Much of our interest is centered on determining pressure, which can be measured most simply by use of liquid manometers but is more commonly measured by electronic devices so that the data stream can be manipulated by computing machinery. For our subsonic testing, the precision with which measurements of stream temperatures are made is usually less demanding than that of typical pressure measurements.

The role of acoustics in aerodynamics has increased steadily over several decades and has now become very important in a number of applications. The most prominent noise problem has been the noise associated with aircraft operation in the vicinity of airports. Dramatic reduction in noise produced by aircraft jet propulsion systems was achieved between 1960 and 1980. Advances in this area are continuing.

Other aerodynamic noise problems are receiving increasing attention. The "wind noise" perceived by drivers and passengers of automobiles is increasingly considered a measure of quality. Automobile and truck environmental noise is an important problem that is partly associated with the external aerodynamics of the vehicles. Helicopters have long had a characteristic signature associated with "blade slap."

136

The noise generated by helicopters has become a limiting factor in their acceptance for passenger transport in some areas, and it is a liability in military operations as it provides a means of detection by opponents. Acoustic radiation from wind turbine rotors has in some instances been sufficiently objectionable that local citizens have strenuously opposed the installation of additional units. A result is that subsonic aerodynamic facilities are now frequently called on to carry out acoustic measurements in addition to the more traditional measurements that focused on performance and control issues of vehicles and limits of operation or survivability of many other devices. Wind noise impinging on passengers of luxury yachts is of significant concern to naval architects. And finally, a closely related area is underwater acoustics, or hydroacoustics, which has been an area of intense activity for naval research in both offensive and defensive weaponry for decades.

Measurement of noise has become a common activity associated with low-speed wind tunnels. Microphones are simply pressure transducers with sufficiently high bandwidth frequency response.

4.1 PRESSURE

Concepts

We have previously discussed pressure and used it as a variable in our derivations of equations of motion of fluids. We have not however done this from basic physical principles as a physicist might wish. Although we have an inclination to include such a fundamental review, insufficient time and space preclude that endeavor. We instead refer the reader to Benedict[2] and sources cited therein for additional background and detail.

The basic notion of pressure that is implemented in measurement technology is force per unit area. Other concepts such as those embodied in various gas laws and kinetic theory are important in wind tunnel work but are necessary in relating pressure measurements to other ideas and results rather than directly in the measurement of pressure.

Manometers

One of the oldest devices for measuring pressures, and one of the easiest to build, is a manometer; a term normally applied to a device used to measure differential pressure. Common applications are measurements of the difference between a reference pressure such as atmospheric and a process pressure such as a port on a wing model and measurements of the difference between two pressures in a process, such as the pressures from the total and static ports of a pitot-static tube. A simple U-tube manometer (shown in Figure 4.1) can be made from two pieces of straight glass tubing made parallel and connected by tubing at the bottom or by bending glass tubing into a U shape. The tubing is filled with a liquid, and the difference in liquid heights in the two tubes is measured, usually by an attached scale. The
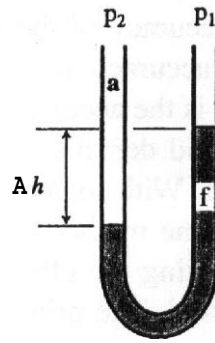
FIGURE 4.1   A U-tube-manometer.

plane defined by the centerlines of the two tubes may be inclined at varying angles to the horizontal, which provides varying sensitivity. Setting the tubes vertical is the most common case. The difference in pressures is related to the height difference and the parameters describing the manometer by the hydrostatic pressure equilibrium relation:

$$p_2 - p_1 = \Delta h \sin \beta g_l(\rho_f - \rho_a) \tag{4.1}$$

where Δh is the difference in extents of liquid columns in the two tubes and β is the angle between the horizontal and the plane of the parallel manometer tubes. The product $\Delta h \sin \beta$ is the vertical difference in the heights of the two columns. Using smaller values of β provides an increased sensitivity.

Here g_l is the weight per unit mass, also referred to as *acceleration of gravity.* The value needed here is the "local" value, which varies with location on Earth and with altitude. The largest variation at the surface is due to variation in latitude. The following equation was adopted by the International Association of Geodesy[3] in **1980:**

$$g = 978.0327[1.0 + 0.053024(\sin \phi)^2 - 0.0000058(\sin 2\phi)^2] \quad \text{dyn/g}$$

where ϕ is latitude. The adopted "standard" value[4] of g is **9.80665 N/kg,** or **32.17405 lbf/slug.** The variation from the equator to the north or south pole is about **0.5%.** Also, ρ_f is the density of liquid in the manometer (equivalently specific gravity times density of water) and ρ_a is the density of air in most wind tunnel applications but could be any fluid other than the manometer fluid that fills all the other spaces. (Note that a straightforward weighing of a volume of manometer fluid in the atmosphere to obtain the density will need to be corrected for buoyancy; otherwise the measurement will produce the difference in density of the manometer fluid and the density of the atmosphere. This difference in density is the quantity needed in the manometer equation.)

The manometer is the most fundamental instrument readily available for pressure measurement. Manometers are used frequently for calibrating and checking other devices, as it is difficult to obtain a more accurate or precise result in the range of differential pressures commonly of interest in subsonic aerodynamic testing.

The factors limiting the accuracy of the manometer can be considered to be in three categories. First is the accuracy with which the measurement of the heights can be accomplished. Second is the accuracy with which the liquid density is known and the uniformity of the liquid density. And third is the presence of forces other than the weight of the liquid. With regard to the first category, Brombacher[5] has given an account of some of the methods that have been devised to make precise height measurements. Minimizing the effects of the second category requires care in the monitoring materials used. The principal force other than weight that affects manometer readings is surface tension, which can directly lead to a pressure jump across the liquid–gas interfaces in the manometer as well as produce a nonplanar surface to make the precise determination of liquid column length more difficult. Benedict[2] and Adam[6] may be consulted for more detail.

The use of manometers has been so extensive that a number of units for pressure have been spawned, as noted by Soloukhin, Curtis, and Emrich,[7] from whom we have modeled Table **4.1.**

In the past, wind tunnels have used a wide array of manometers. These have ranged from the simple U-tube, similar to Figure **4.1,** using a ruler or strip of graph paper to measure fluid heights to large banks of 50–200 tube manometers with constant-level reservoirs to maintain the reference fluid height to manometers that

TABLE 4.1. Units Used for Indicating Pressure with Some Conversions

Name of Unit	Value[a]
1 atm	2116 lb/ft^2
1 atm	101.3 kPa
1 bar	100.0 kPa
1 kgf/cm^2	98.07 kPa
1 lb/in.^{2}	6.895 kPa
0 acoustic db[b]	10 Pa[c] or 20 μPa[d]
1 atm	14.7 lb/in.^{2}
1 in mercury	3.38 kPa
1 in water	249 Pa
1 mm mercury (Torr)	133.3 Pa
1 lb/ft^2	47.9 Pa
1 mm water	9.81 Pa

[a]The Système Internationale (SI) unit of pressure is the pascal (symbol is Pa) and is equal to one newton per square meter.

[b]Sound pressure level, in decibels (dB), is 20 times the logarithm to the base 10 of the ratio of the sound pressure level to the reference pressure value. The reference pressure should be explicitly stated in every document in which decibel units are used. In the absence of an explicit statement otherwise, sound pressure is the rms value.

[c]Reference value commonly used for transducers.

[d]Reference value commonly used for human hearing-related data. This is a nominal value for the threshold of human detection.

can be precisely read using some of the devices reviewed by Brombacher.[5] The U-tube and precision manometers could typically provide one or two pressures, and the large multitube manometers were used to determine pressure distributions over model surfaces. The simple, precision, and small multitube manometers usually were read and recorded by an individual. The large multitube manometers were photographed, and the films were read later by various techniques. The test-section total and static pressures were put on two of the manometer tubes. Then the pressure coefficients were merely the Ah of the desired pressure divided by the Ah of the dynamic pressure. To process data from large test programs, the photographs of the manometers were used with optical schemes arranged to scale the images so that the pressure coefficients could be ready directly using a microfilm machine. This could be considered a form of "optical data processing."

A number of fluids have been found useful in manometers. Characteristics that are of interest are visibility of the meniscus, density, stability to environmental changes, and possible material interactions with tubing over a long contact time. With the demise of large manometer systems, the more exotic fluids have become much less common. Today the most commonly used fluids are silicon oil or water with a small amount of dye. Both of these have well-known dependence of density with temperature and do not change density appreciably with other environmental variables such as relative humidity. Some information on the variation of density of water with temperature at atmospheric pressure has been given in Chapter 1. The variation of density for water and mercury with temperature in degrees Fahrenheit is given by the equations

$$\rho_{Hg} = \frac{26.3788}{1. + 0.000101\,(t_F - 32.)} \quad \text{slug/ft}^3 \tag{4.2}$$

$$\rho_{H_2O} = (1.93486 + 0.00030412t_F - 0.000451t_F^2 + 0.1 \times 10^{-7}t_F^3) \quad \text{slugs/ft}^3 \tag{4.3}$$

The variation of density for a particular batch of Dow Coming 1 centistoke DC-200 silicon oil as a function of temperature in degrees Celsius was found to be given by Equation (4.4). The calibration was obtained using a water bath, a precision hydrometer accurate to a specific gravity of 0.001, and a precision thermometer accurate to 0.1°C:

$$\rho_f = 1.640 + 0.00198t_C \quad \text{slugs/ft}^3 \tag{4.4}$$

We illustrate here two useful manometers that can be built in almost any laboratory. The first is a simple unit with a few tubes and adjustable slant angle (shown in Figure 4.2).[8] The second is a unit capable of very precise measurements with Ah readings of 0.0001 in. being possible if an appropriate micrometer or height gage is used in the construction. To achieve repeatability of such fine measurements, it is necessary that the thermal environment be quite stable. For example, if the room temperature is around 75°F, a thermal shield must be provided between the person observing the meniscus through the optics and the main part of the unit. Otherwise,
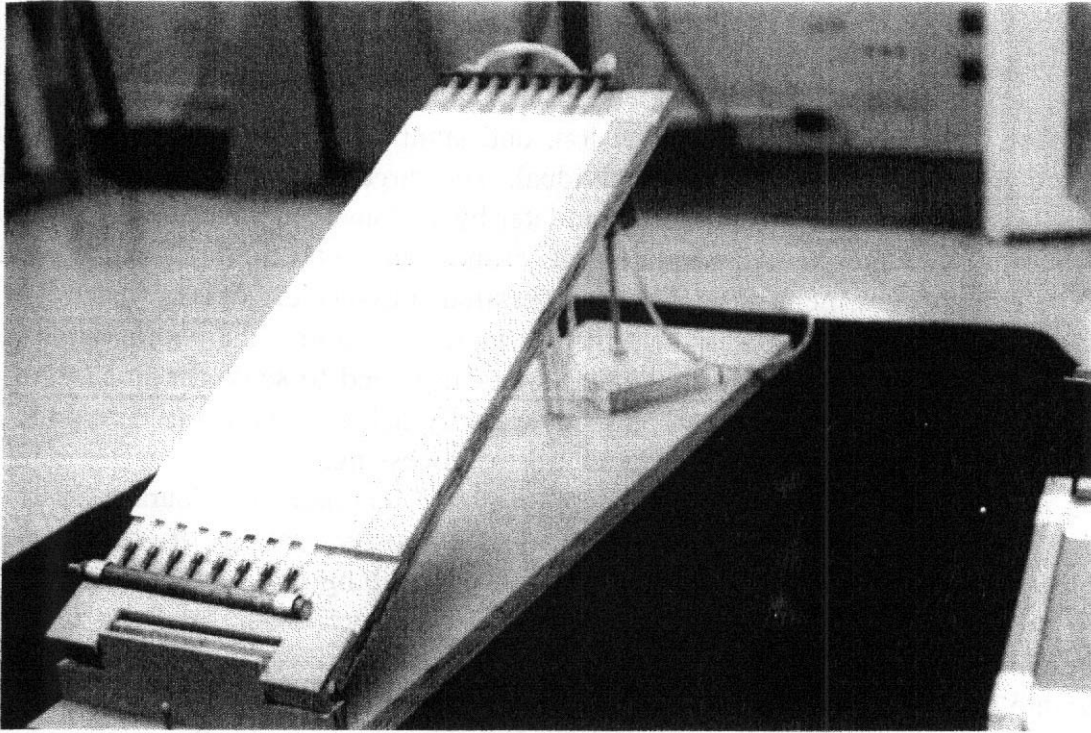
FIGURE 4.2 A multitube variable inclination manometer.

a steady drift will be observed due to the radiant heat from the person to the manometer unit and the corresponding expansion of the material. It is shown[9] in Figure **4.3** and is based on a design by Smith and Murphy.[10] Note that it is not claimed that an accuracy of 0.0001 in. of manometer fluid is readily achieved.

Finally we provide a note on the time response of a liquid manometer. According to Soloukhin et al., the response is that of a damped harmonic oscillator with natural frequency given by $\omega_n = \sqrt{2g/L - 16v^2 la^4}$ and a time constant given approximately by $a^2/4v$, where L is the length of the liquid column, a is its radius, and v is the kinematic viscosity of the liquid. These results do not include any effect of tubing that is necessary to connect a manometer to a pressure source of interest. The effect of tubing will be discussed later. More complete information on the time response of manometers is given by Holley and Bannister[11] and the subject is treated by Benedict[2] as well.

Pressure Transducers

The term *pressure* transducer is usually applied to a device that provides an electrical response to a pressure or change in pressure. There are many types of devices, a number of which are mentioned by Benedict[2] and Soloukhin et al.[7] In low-speed wind tunnel applications the transducers in common use may be considered in two classes. The first is the set of transducers used to monitor tunnel flow conditions. These units must be very accurate and very stable over the range of operating conditions of a particular tunnel. They can be put in thermally controlled enclosures
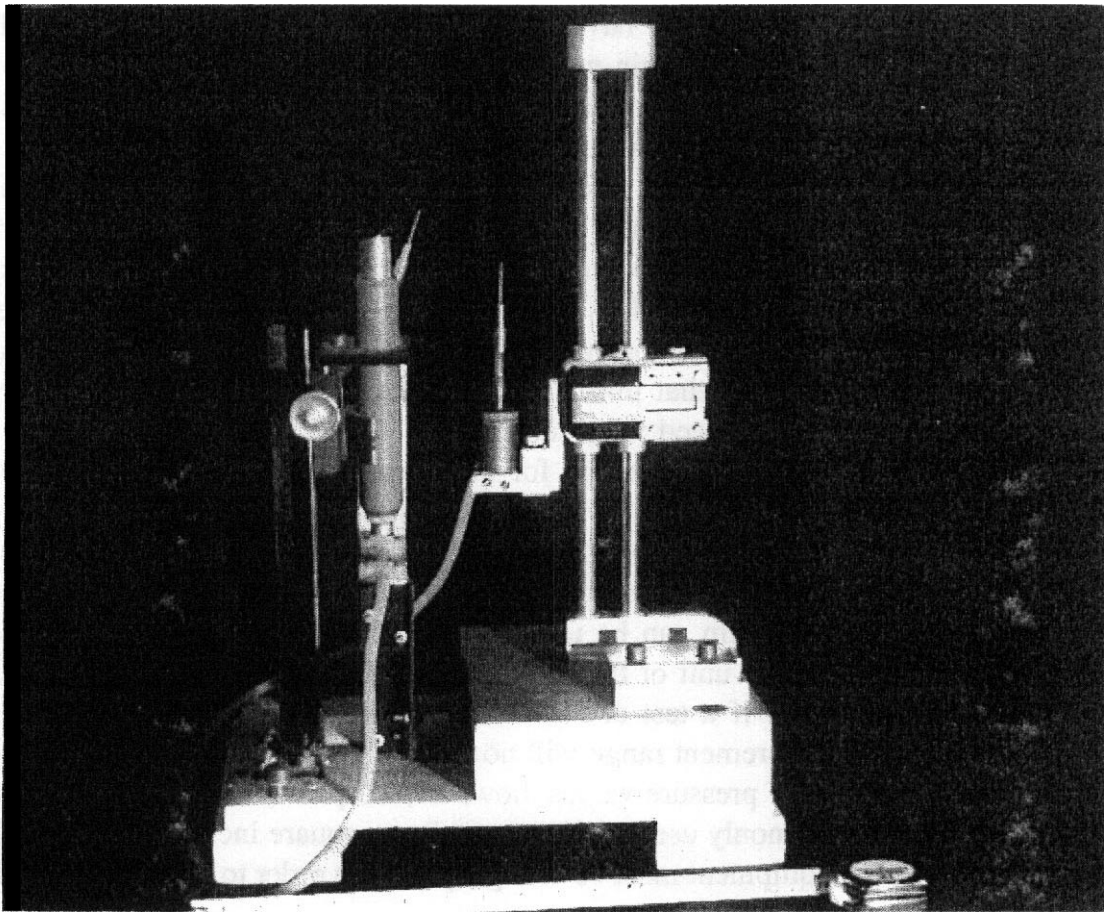
FIGURE 4.3   A high-precision micromanometer

to minimize drift due to temperature changes and their size is not critical. They are frequently units that are considered to be secondary standards and are commonly obtained with traceability to national standards laboratories.

The second class of transducers are used for measuring model pressures and perhaps wall or other surface pressures as needed for various tests. The cost per transducer for these units is more critical since a large number are frequently needed and their size is critical since they **are** often to be installed inside a model or in some other restricted space.

The most commonly used pressure transducers are of the diaphragm type, which simply means that the basic sensing mechanism is a thin sheet of material that deforms as the pressure across it changes. The methods of sensing the diaphragm deformation include strain gages directly attached to the diaphragm, circuits to sense the change in capacitance due to the geometric change, and circuits to sense the change in inductance due to the geometric change. The strain gage units **are** most numerous as they can be made smaller and with current solid-state electronic methods can be made for a few dollars. These units **are** remarkable for their economy, although they must be calibrated frequently against more stable standard units. There are many strain gage units with stainless steel diaphragms and even some with quartz diaphragms. Transducers using the capacitive sensing method tend to be in

the higher priced ranges and to have larger dynamic range capability as well as being more rugged than the strain-gage-based units. These are more likely to be found in the main tunnel condition sensing applications and for secondary calibration.

A majority of the pressure transducers used in subsonic wind tunnels are of the differential type, with a selected reference pressure applied to the reference side. Absolute pressure versions are almost always available. They differ from the differential units by having one side of the diaphragm permanently sealed to a fixed pressure chamber that is close to vacuum. This is necessary in order to avoid serious temperature sensitivity and leads to the absolute units having diaphragms that can withstand at least 1 atm. It turns out that this means they are not sufficiently sensitive for many applications in low-speed wind tunnels.

Consider the likely pressure range for an external aerodynamic test of some object in an atmospheric wind tunnel using test speeds of 100 m/s (—200 knots). The dynamic pressure will be about 0.055 atm and the likely range of pressures may be about 3 times the dynamic pressure. This means that a transducer with a full scale of around 0.2 atm can be used, which will be at least five times more sensitive than an absolute unit of the minimum available capacity. The conclusion becomes more dramatic if a test at 50 m/s (—100 knots) is considered since the required pressure measurement range will now be only —0.05 atm. The transducers come in a wide range of pressure values; however, 2.5 psid (—15 kPa) and 5.0 psid (30 kPa) are very commonly used (psid is pounds per square inch differential). The signal conditioning equipment must be of high quality in order to have the necessary signal-to-noise ratios.

The chosen reference pressure for a given test is manifolded to all the transducers and usually is led out of the tunnel with the electrical leads. In the case of mechanical scanning valves, Scanivalves, this tube is used to periodically check the transducer calibration and recalibrate if necessary, usually once a shift. This is done by removing the tube from the reference and applying a known pressure to the transducer. In pressure units the transducer output is compared to the applied pressure. The current generation of electronic scanners have the ability to switch all transducers to a calibration pressure source in situ so that periodic calibrations can be done automatically while the tunnel continues to operate if that is otherwise desirable. This has been provided because the silicon-based semiconductor strain gage units are at the same time cheaper per unit and more susceptible to drift than the typical stainless steel diaphragm transducers used in the Scanivalve systems. The in situ calibration processes have the major advantage of being an end-to-end calibration incorporating all of the signal conditioning, the digitizers, an even the curve fitting software almost precisely as it is used in the actual data gathering for the test. This was not generally the case for the Scanivalve systems, for which the process is described next. The electronic scanning modules coming into service in the mid-1990s frequently are accompanied by read-only memory modules that have calibration data including temperature dependence. This will reduce the frequency of required calibration.

Scanivalve transducers are usually calibrated against a secondary standard. When the transducer is calibrated outside the model, the bridge voltage used and the calibrated amplifier filter setting and gain are recorded. The same values are used

during the test. As an alternative, the bridge voltage can be recorded and the bridge output measured. The amplifier gain is then entered into the data reduction process. The bridge output is adjusted to zero for zero pressure or the voltage for zero pressure is recorded. Then a series of pressures are applied and the pressure and output voltage are recorded. These data are fed into a curve-fitting routine to determine the calibration curve. The transducers tend to be linear, but often a third-degree curve fit is used.

Often when a Scanivalve transducer is independently calibrated and then mounted in the model or Scanivalve, there are slight but measurable shifts of the calibration curve, apparently caused by clamping the transducer. When mounted, the transducer will repeat its calibration over a period of time. Thus, it appears that the pressure transducer should be calibrated mounted in the Scanivalve or the model. Calibration must be checked if the transducer clamp is loosened and then retightened. This could also occur for the newer electronic pressure scanners and should be kept in mind if the most precise results are required.

At the end of the discussion of manometers we gave an indication of the capability of the liquid manometer to respond to changing pressures. A comparative measure of a device to respond to a varying signal is its natural frequency. In the case of liquid manometers, the typical natural frequency is less than 1 Hz. In the pressure ranges most frequently used in low-speed wind tunnels the diaphragm-type transducers considered in this section will have natural frequencies in the range of a few hundred hertz. Some small units may have considerably higher natural frequencies. We repeat the cautionary note that the connecting pressure tubing will have a major dynamic effect on time-varying pressure measurements and must be considered carefully whenever a time-varying pressure signal is to be measured.

Piezoelectric Transducers

In addition to the diaphragm-type transducers discussed in the previous section, there is a type of transducer that uses a piezoelectric element that produces an electric field in response to applied pressures. These devices are discussed by Soloukhin, Curtis, and Emrich[7] and Blake[12] and the references therein. These pressure gages are able to measure higher frequency pressure fluctuations than the typical diaphragm-type transducers. They require associated electronics located near the gage to optimize their response. The transducers are mostly used for the measurement of time-varying pressures, but time-averaged pressures can also be obtained. They are made to have very small sensitive areas and in forms designed to be mounted flush in a model surface. This is consistent with their high-frequency response capabilities since the effect of connecting tubing on a pressure signal will make it difficult in any case to obtain measurements at frequencies more than a few hundred hertz.

These pressure gages also tend to be differential transducers, and the reference side can be connected to either a known pressure or a source of approximately time-averaged pressure, whose fluctuations are required. The units are sensitive to temperature and usually require attention to temperature compensation.

The natural frequencies of available piezoelectric pressure transducers extend upward to several thousand hertz, overlapping the domain of microphones.

Microphones

Microphones are widely used in the entertainment industry, so low-cost units are ubiquitous. Unfortunately, the units that are desirable for human communication processes do not have uniform response characteristics needed for physical measurement applications. The most common unit used for physical measurement has been the condenser microphone. The basic principles of these units are described by Blake.[12]

Pressure-Sensitive Paint (PSP)

Almost all of the preceding pressure-measuring devices require that the pressure at a point of interest be communicated to the sensing element from a pressure "tap" or "port" through a small tube to the sensor. There are two major problems with this method. The most important one is that it makes the models quite expensive to build. The second is that the time response of the pressure measurement is limited by the presence of the tubing as a transfer mechanism. There have been a number of important experiments using surface-mounted transducers, but these are by far the most expensive models and test programs. In any case, there can never be a large enough number of pressure taps to provide high accuracy for forces obtained by integration of measured surface pressure.

Pressure-sensitive paint offers the promise of very high spatial density of measurements with a moderate impact on model cost. There is, at present, a high capital cost for the cameras needed for high-quality results. This new method is being used extensively in transonic testing but has only recently been demonstrated to be capable of useful results for test speeds as low as 100 knots. We will provide an introduction to the basic aspects of PSP principles. Our presentation follows Crites and Benne.[13]

Basic Concepts Molecules of certain compounds, when exposed to radiation of certain wavelengths, will absorb photons and transition to a higher energy state, referred to as the "excited" condition. They will then return to ground state primarily by one of two paths. One path involves the emission of a photon at a wavelength less than the wavelength of the exciting radiation. The other is through interaction with an oxygen molecule and no photon emission. The likelihood of the second transition path increases with increasing density of oxygen molecules. Since the number density of oxygen molecules in air is a function of pressure, the balance between the two competing processes will shift as a function of pressure. The emitted radiation, termed luminescence, will be a function of the partial pressure of oxygen and therefore the pressure of the air in contact with the material. It is the luminescence that is to be measured and used as the indicator of the pressure of the air in contact with the material. The compounds used in this application have been referred to in the literature as luminiphors, lumiphors, and dye. This is early
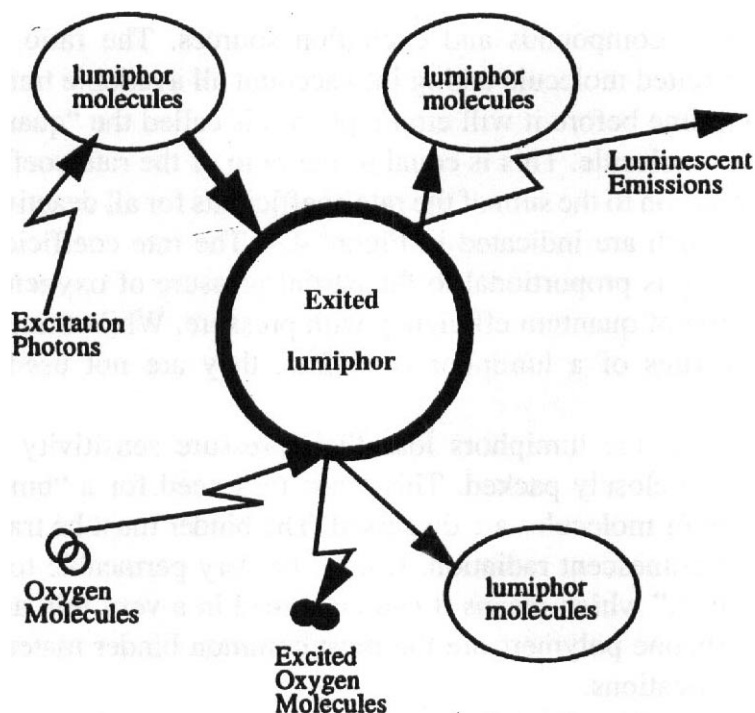
FIGURE 4.4   Oxygen-quenched photoluminescence process.

in the evolution of the aerodynamic applications of these materials so the terminology is not yet settled. We will use the term "lumiphor" for the sensor molecules. The phenomenon as described leads to the result that PSP is an absolute pressure sensor. It is to be expected, therefore, that obtaining resolution of the same order as is available from differential measurement techniques may be difficult.

A schematic representation of the oxygen-quenched photoluminescent process is given by Figure 4.4. To incorporate this process into an aerodynamic pressure measurement system, suitable lumiphor molecules are dispersed into an oxygen-permeable binder that has properties allowing it to be applied to the aerodynamic model as a paint. The model is mounted in the wind tunnel and illuminated with a radiation source of the appropriate frequency for the chosen lumiphor. The illumination source is filtered so that it is not emitting radiation in the luminescence wavelength band. One or more high-resolution charge-coupled device (CCD) video cameras collect the luminescent radiation through filters that remove all other wavelengths. An image is recorded with the wind off to obtain the distribution of intensity of luminescent radiation due to spatially varying illumination intensity, varying surface orientation, and other effects under uniform pressure conditions. The wind tunnel is turned on and a wind-on image is recorded. The recorded intensities with wind on and wind off are used along with calibration data on the PSP to compute the pressure distribution.

Lumiphor, Binder, and Primer   The processes indicated in Figure 4.4 occur with certain probabilities and corresponding time constants that are characteristic of the

specific lumiphor compounds and excitation sources. The ratio of the expected lifetime of an excited molecule taking into account all available transition processes to the expected time before it will emit a photon is called the "quantum efficiency" of the lumiphor molecule. This is equal to the ratio of the rate coefficient for decay by radiative emission to the sum of the rate coefficients for all deactivation processes, only some of which are indicated in Figure 4.4. The rate coefficient for decay by oxygen quenching is proportional to the partial pressure of oxygen, which leads in turn to a variation of quantum efficiency with pressure. While these coefficients are important properties of a lumiphor candidate, they are not used directly in the PSP process.

It turns out that the lumiphors lose their pressure sensitivity if the lumiphor molecules are too closely packed. This leads to a need for a "binder" material in which the lumiphor molecules **are** dispersed. The binder must be transparent to both excitation and luminescent radiation. It must be very permeable to oxygen. And it must be "paintlike," which means it can be spread in a very thin and smooth layer on a surface. Silicone polymers are the most common binder materials currently in use for PSP applications.

Finally a "primer" has been found to be essential to the success of PSP applications. The primer serves two major purposes. The first is to enhance adhesion of the binder–lumiphor mixture to the model surface. The second is as a diffuse reflector of radiation, which materially enhances the signal-to-noise ratio obtained by providing reflected excitation radiation in addition to the direct radiation from the sources as well as reflecting some of the luminescent radiation to the cameras that would otherwise not be collected.

The luminescence intensity i_e of the emitted radiation that is detectable by the cameras can be expressed as a product of three factors, the incident radiation i_i; the quantum efficiency of the lumiphor, ϕ; and the "paint efficiency" η_p:

$$i_e = i_i \eta_p \phi \tag{4.5}$$

The quantum efficiency is a function of pressure, with the form

$$\phi = \frac{k_F}{k_F + k_C + k_p p} \tag{4.6}$$

where k_F is the rate coefficient for the luminescent emission from an excited molecule, k_C is the rate coefficient for internal transition processes, and k_p is the coefficient for the oxygen extinction process, including the effect of binder permeability. But the incident radiation is not uniform and the paint efficiency varies over the surface, and neither are known. If the emitted radiation at zero pressure is denoted by i_{e0}, then

$$\frac{i_{e0}}{i_e} = \frac{\phi_0}{\phi} = \frac{\tau_0}{\tau} = 1 + ap \quad \text{where } a = \frac{k_p}{k_F + k_C} \tag{4.7}$$

If a reference image is recorded with wind off, in which case $p = p_r$, and the reference image data are divided by the wind-on image data, we obtain

$$\frac{i_{er}}{i_e} = A + B\frac{p}{p_r} \tag{4.8}$$

where

$$A = \frac{1}{1 + ap_r} \quad \text{and} \quad B = \frac{ap_r}{1 + ap_r} \tag{4.9}$$

Here A and B can be obtained from calibration of paint samples in a pressure chamber or by in situ calibration using pressure data from a few conventional pressure taps distributed on the surface. Inverting (4.8), we obtain

$$\frac{p}{p_r} = \frac{1}{B}\left(\frac{i_{er}}{i_e} - A\right) \tag{4.10}$$

This is known as the Stem–Volmer relation. According to Crites and Benne,[13] it is preferable in practice to use a least-squares fitted polynomial, typically of third order.

The coefficients A and B are generally functions of temperature. This dependence must be obtained from the calibration process, and the temperature on the model during testing must be monitored by some means. Current work on these paints includes an effort to obtain simultanwus optical measurement of temperature along with the pressure measurements. Presently, however, an independent temperature measurement is required.

There are two time responses of importance. One is the response of the paint to a change in pressure. This has been investigated by Carroll et al.[14] for a few formulations and by Baron et al.[15] for others. It is presently considered that the primary factor that leads to response times as long as the order of hundreds of milliseconds is permeability of the binder. This leads to an objective of putting the lumiphor molecules as close to the surface as possible in order to obtain fast response times. The second time response is the response to a change in the exitation source. This can vary considerably from one paint formulation to another.

There are many facets to the performance of lumiphors, binders, and primers. It is evident that there are a plethora of formulations that can be useful and that the exploration and refinement of these materials will proceed for a considerable time as efforts continue to discover the most useful combinations for various applications.

PSP Calibration   In order to obtain accurate pressure measurements using PSP, on the order of what can be obtained using differential transducers, a precise calibration procedure must be performed. Two methods of calibration are commonly used. One is in situ, with the model situated in the tunnel and a limited number of conventional taps installed to provide the "known" pressures. The second is a custom-designed calibration chamber, in which pressure and temperature can be precisely controlled.

In situ calibration is an effective and convenient method of determining the Stem–Volmer constants, but the model must be purpose built in order to do so. It must be equipped with a few conventional pressure taps and, ideally, a number of thermocouples. The Stem–Volmer constants A and B in **(4.10)** are derived by comparing the luminescence intensities from the reference and wind-on images to the measured pressures on the surface. The quantities i_e and p are known at each tap location during the test, and i_{er} and p_r are known from the wind-off measurements. So, A and B can be calculated on-line during a wind tunnel test.

The use of a custom calibration chamber allows more extensive and repetitive calibration data to be obtained. There must be a light source for excitation and a detection device, for example, a photomultiplier or CCD camera. Paint samples can be mounted directly to a thermoelectric cooler and sealed in a pressure chamber, so that complete temperature and pressure control can be achieved. By examining an extensive matrix of pressures and temperatures and the accompanying luminescence intensity, the Stem–Volmer constants may be derived as above.

The-two methods of calibration are **complementary**. Each has some advantages and disadvantages. In **situ** calibration reintroduces the main problem encountered with traditional pressure measurement. The models have to be built with a number of strategically placed pressure taps, and to ascertain temperature effects, thermocouples need to be installed on the model surface. There is one principal advantage, however. The paint employed in the calibration is the exact paint used in the test. If an external calibration chamber is used, the paint on a test sample may differ slightly from the paint used on the model, be it in composition, age, impurities, and so forth. Precautions must be taken to ensure paint consistency when not employing in situ calibration. It is best to do a pretest calibration in an environmental chamber and to provide a number of reference taps on the model so that in situ comparisons are available to check and monitor the paint performance as the test proceeds.

Data Systems for PSP   Pressure-sensitive paint is a distributed sensor and transducer system. The excitation source is the equivalent of the power supply voltage for a strain gage transducer. Assuming a reasonable distribution of the PSP over a model surface, there can be the equivalent of several million pressure transducers. A point at a time could be sampled by exciting a spot with a focused laser beam of the appropriate frequency and measuring the intensity of the luminescent radiation with a photomultiplier tube with appropriate lenses and filters. Obtaining the pressure at a point requires two measurements, first the emission intensity at the known reference pressure, i_{e0}, and then the emission intensity at the test condition, i_r. Assuming the values of A and B in the Stem–Volmer relation **(4.10)** have been obtained from a calibration system, the pressure can be computed. British Aerospace[16] has developed a system along these lines using a scanning laser. In such a system, it may be reasonable to expect the laser to provide a very nearly constant source intensity over a period between the reference and data measurement time frame. The variability in the pressure measurement will be determined by the signal-to-noise ratio for the intensity measurements from the photomultiplier. If the model moves under the load change that will occur between the wind-off and the

wind-on conditions, then there will be a change in the location of the point of focus that should be used to obtain the wind-on data. If this is ignored, then the wind-on data will be taken for a different portion of the paint system, which in general will have a different paint efficiency and so will introduce error into the pressure calculation. If the model motion under load is monitored by some means, then a correction of the focus can-be made. If the model shape deforms as well as shifts in a rigid-body fashion under load, then the problem is compounded. It is still possible to infer model deformation and to introduce a deformation correction if some set of points on the model are established with sufficient accuracy. If the shape deformation or movement involves significant rotation of the local surface normal relative to the direction of the excitation source or the axis of the collecting optics, then a method of correction for this effect is not available even if the particular paint spot can be located accurately. This is due to the fact that the effect of surface normal variation on the paint efficiency is not known.

The PSP system described by Crites and **Benne**[13] uses many source lamps for illumination and a CCD camera as the data-gathering device. This system in effect is operating as many parallel pressure transducers as there are pixel elements in the CCD camera. This would be 2^{18} for a **512 × 512** array and **4** times that many for a **1024 × 1024** array. Each effective transducer may have a distinct excitation strength, a distinct paint sensitivity, and a distinct pixel detector sensitivity. Each of the effective transducers will be subject to the errors due to model motion and distortion described above for the single laser spot system. The variation in the excitation source strength will be more troublesome since it will be more variable than is the case for the steerable laser beam.

It seems intuitive that both the excitation source and the optical axis of the measuring camera or photomultiplier are best aligned not too far from the normals to the surface elements on which measurements **are** being made. Therefore, if measurements are to be made over a substantial portion of a typical vehicle model, multiple cameras or multiple setups will be necessary. Then the different views will have some overlap and methods of registration from view to view will be required. This is reminiscent of the requirement for registration of various strips of aerial or satellite resource data. In order to utilize the pressure data to carry out integrations for total model forces and moments, methods **are** required to identify the orientation of the surface normal for each effective transducer, that is, for each pixel. Note that this is not required to create flow-visualization-type images. Such images carry considerably more information due to the quantitative pressure information.

The resulting data processing requirements are substantially greater than most historically associated with low-speed wind tunnel testing. There may be cases in which acoustic experiments or turbulence measurements produce such large data sets, although both cases will generate large amounts of data due to time histories rather than high spatial density of the measurements. In addition to sizable processing requirements for the data reduction, it is necessary to use data visualization methods that have been under development in the computational fluid dynamics arena in order to provide human users a means of "seeing" the results in a useful way. It is perhaps noteworthy that measurements with a spatial density of **—60,000** points per

square inch have been made. The limit in density would appear to be much higher, although this has not been addressed at this time. The available measurement density exceeds the plausible grid densities that can be applied for vehicle level Navier–Stokes solvers used in computational fluid dynamics, which are limited by the available computer speed and memory sizes. In fact, the practical measurement densities will be limited by the same resources due to limitations on handling and storing large data sets.

I t appears to the authors that PSP represents a paradigm shift in that it offers a clear possibility of measurement results that are more than competitive with projections of density and detail of computational methods for pressure distributions on complex surface geometries. The material given here is only an outline. Contemporary sources in the technical meeting and journal literature can be expected to contain a growing amount of detail on PSP systems and methods.

Evolution of Pressure Measurement

Wind tunnels have been in use for aerodynamic investigations since 1871, when Wenham conducted experiments under the aegis of the fledgling Aeronautical Society of Great Britain.'' Our present interest is in the reported use of a "water gauge" for measuring the speed of flow in Wenham's wind tunnel. This would be a pitot tube connected to a manometer with water as the liquid. In fact, this was the primary means of measuring pressure for many decades. Other fluids were used in addition to water, as mentioned earlier, with lighter fluids chosen to obtain slightly greater sensitivity for low pressures and heavier liquids such as mercury (quicksilver) being used to obtain higher pressure capability within reasonable tube lengths.

Finely constructed mechanical instruments using Bourdon tubes to drive dial gauges have been widely used for some purposes but are relatively expensive per pressure port.

By the 1950s electronic transducers became widely used with a variety of mechanisms as the basic sensing elements. The fundamental problem that had to be overcome by the transducers was the need for many channels at an acceptable cost. A 200-tube manometer could be constructed by a competent wind tunnel staff requiring a relatively small cash outlay. Purchasing 200 pressure transducers was beyond the budget of most wind tunnel laboratories. A device that provided an acceptable alternative was the mechanical scanner, the Scanivalve, which housed a single transducer and sequentially switched up to 48 diierent incoming pressure lines to be read by the transducer.

The use of these multistep, multiport valves that could usually be located inside the model had many advantages over banks of multitube manometers. When manometers were used to record a large number of pressures, a large amount of tunnel time was required to connect, phase out, and leak check the manometer. The large bundle of tubing from the model to the manometers outside the tunnel could modify the support tares and interference and thus affect the balance data. Using Scanivalves and pressure transducers allowed the pressure ports to be connected to the Scanivalves, phased out, and leak checked prior to the model entry into the tunnel, saving

large amounts of tunnel time. The small-diameter wires for stepping both the valves and the transducers were much easier to handle than the large bundles of plastic tubing, thus reducing the tare and interference problem.

Manometer data were recorded by photographing the manometer banks at each test condition. The manometers using photographs were faster in acquiring the data by orders of magnitude than the mechanical scanivalves. But the time required to develop film and read the tubes was also orders of magnitude longer than required by the digital data systems that were connected to the transducers in the Scanivalves by the 1960s.

Since the early 1980s pressure transducers have been manufactured using solid-state electronics. This new method along with a vastly expanded market for pressure transducers that has come from the computer feedback control of automobile engines has lowered the per-transducer cost to the point that electronic scanners with a separate solid-state transducer for each port are now the standard means of measuring large numbers of pressures in wind tunnel tests. These electronically scanned pressure modules, which came into wide use in the 1980s, can be practically as fast as photographing a manometer in acquisition of the data, and the processing is done immediately by current computer systems so that reduced data in large quantities are commonly available in a few seconds. Thus pressure transducers to measure pressures have replaced the large multitube manometers.

Major disadvantages, and in some cases risks, with the use of Scanivalves and other electronic data systems are a lack of data visibility and the possibility of either the transducer(s) slipping calibration or the valve leaking and being undetected. Strangely enough, these mishaps only occur on those units that measure critical pressures. These disadvantages are being addressed to a greater and greater degree as computer systems become capable of providing immediate visual feedback to the tunnel engineer for monitoring the performance of the systems. Up-to-date software systems take full care to provide system health monitoring so that malfunctions are made evident immediately.

There are still a few cases where a manometer is useful. One is in instruction where the properly set-up manometer will show the student or the uninitiated engineer the shape of a pressure distribution, such as the chordwise distribution of pressure on a wing or the momentum loss in the wake, with a more obvious physical connection between the pressure variation and the results shown by the manometer than is possible with more indirect devices. A second is during a test when it becomes useful to get a quick look at a few pressures at a few model conditions to guide further test direction. The most important is the use of a manometer as a calibration standard for the transducers.

All multitube systems—the manometer, the Scanivalve, and the electronic scanner—must be phased; that is, the engineer must know which pressure port on the model is connected to which manometer tube, Scanivalve port, or scanner port. This task requires meticulous bookkeeping and is very time consuming. After all the model ports are connected and phased, they must be checked for both plugs and leaks. A plug will show as a very slow response to a change in pressure. A leak will show as a change in pressure after a pressure is applied to the model pressure

port and held. If either of these occur and cannot be repaired, that model pressure port must be either eliminated from the data base or effectively marked as defective. This process has been improved greatly by using the computer system directly and interactively to check and record pressure port response and create a corresponding cross-reference table. This process eliminates the requirement to trace a large number of small tubes from ports to transducers and keep track of the corresponding identifying little tags that inevitably are oriented in the most awkward orientations.

4.2 TEMPERATURE

We refer the reader to Benedict[2] for information on details of temperature-measuring devices and theory. We assume that a choice of device such as a thermocouple, resistance thermometer, or glass thermometer will be guided by the specific installation requirements in a facility. Here we will mention the basic issues regarding the measurement of temperature in a low-speed flowing stream of air.

Similar to the case of pressure, the temperature of a flowing stream is called "static temperature" and is considered a measure of the average random translational kinetic energy of the gas molecules. The temperature will be sensed by an adiabatic probe in thermal equilibrium and at rest with respect to the gas. If observations are made from a frame in which the gas has a nonzero average velocity, then the thermal equivalent of the directed kinetic energy of the gas is termed the "dynamic temperature." Note that the dynamic temperature is dependent on the reference frame chosen. The dynamic temperature is conveniently expressed in terms of the Mach number and the ratio of specific heats:

$$T_{\mathrm{dyn}} = \left(\frac{\gamma - 1}{2}\right) M^2 T$$

The dynamic temperature is not large for subsonic flows but is quite measurable. For T near standard sea level atmospheric conditions it is $\sim 1\,^{\circ}\mathrm{F}$ for a Mach number of 0.1 and $\sim 10\,^{\circ}\mathrm{F}$ for a Mach number of 0.3.

The "total temperature" is the sum of the temperature and the dynamic temperature. The total temperature would be sensed by an idealized probe that "stagnates" an idealized gas. The relation between the total temperature and the temperature in the flowing gas is obtained from the First Law of Thermodynamics and can be expressed as

$$T_{\mathrm{tot}} = \left[1 + \left(\frac{\gamma - 1}{2}\right) M^2 \right] T \tag{4.11}$$

In a real gas the temperature at a stagnation point is not generally equal to the total temperature (see Benedict). However, for air at low Mach number and for pressures not too far different from atmospheric, the difference between "stagnation temperature" and total temperature is very small and can be neglected.

The temperature on a boundary that is essentially parallel to the flow velocity is related to the stream temperature through a "recovery factor" that is a function of the Prandtl number. For the cases we are considering the recovery factor is very nearly 1. In our case, then, the temperature is essentially constant through a boundary layer on the tunnel wall. Thus, an easy method of obtaining stream temperature is through the use of a flush, wall-mounted temperature probe. The probe should be located in the test section in a region where its chance of damage is minimal.

The test-section static temperature is required to determine the test-section velocity through the use of Bernoulli's incompressible equation after computing the density from the equation of state. The true velocity and viscosity are needed for the calculation of the Reynolds number, the velocity ratio in flutter model testing, to match the advance ratio in propeller power testing and helicopter rotor testing, and so forth. If the temperature probe is located in the settling chamber, then the appropriate correction should be applied to infer the test-section thermodynamic temperature.

4.3 FLOW INSTRUMENTATION

Pitot Tubes

A pitot tube is used to measure total pressure. The shape of the tube affects its sensitivity to flows inclined to the tube axis. Pitots with hemispherical noses begin to show errors in total pressure at very low angles of flow inclination. Pitot tubes with a sharp square nose begin to show errors near $8°$ flow inclination. This can be improved by chamfering the nose.

A Kiel tube[18] can provide accurate stagnation pressure for flow angles beyond $30°$. Other tip shapes provide various sensitivities, as indicated in Figure 4.5.
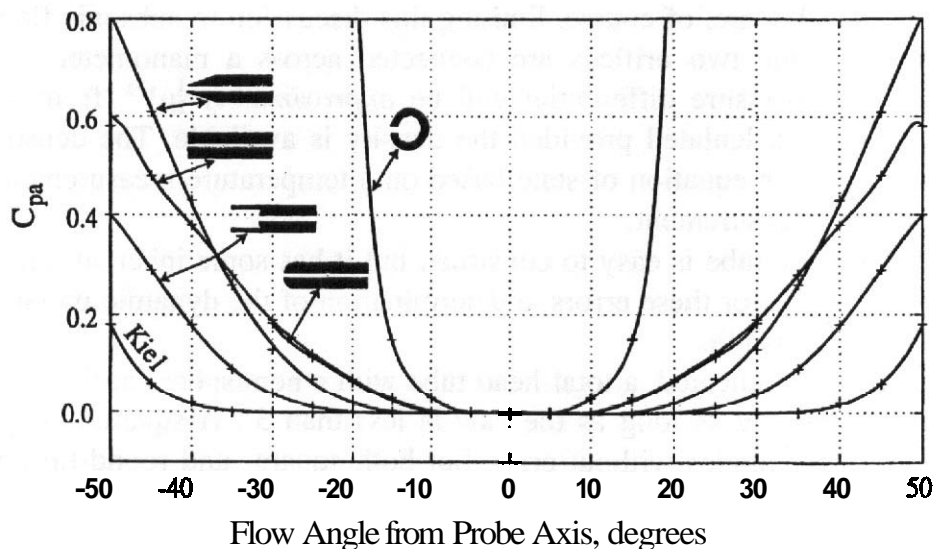
FIGURE 4 5   Variation of measured stagnation pressure with yaw for selected probe geometries: $C_{pa} = [p(\alpha) - p(0)]/(1/2pV^z)$.
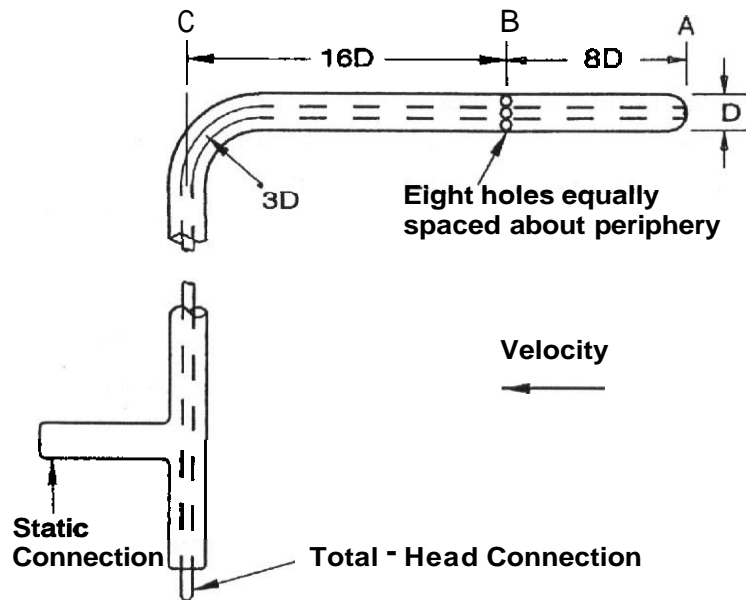
FIGURE 4.6   Standard pitot-static tube.

It is a relatively easy task to measure a pitot's sensitivity to flow angle by use of a flow of known angularity. The pitot is pitched or yawed depending on which is more convenient to determine its sensitivity to flow angularity. An excellent discussion of probe methods for measuring fluid velocity is given by Emrich.[19]

Pitot-Static Tubes

The most common device for determining the total pressure or total head and the static pressure of a stream is the pitot-static tube, an instrument that yields both the total head and the static pressure. A "standard" pitot-static tube is shown in Figure 4.6. The orifice at A senses total head $p + \frac{1}{2}\rho V^2$, and the orifices at B sense the static pressure. We are, of course, limiting this discussion to subsonic flows. If the pressures from the two orifices are connected across a manometer or pressure transducer, the pressure differential will be *approximately* $\frac{1}{2}\rho V^2$, from which the velocity may be calculated provided the density is available. The density can be calculated from the equation of state based on a temperature measurement and the static pressure measurement.

The pitot-static tube is easy to construct, but it has some inherent errors. If due allowance is made for these errors, a determination of the dynamic pressure within about 0.1% is possible.

As previously indicated, a total-head tube with a hemispherical tip will read the total head accurately as long as the yaw is less than $3°$. A squared-off pitot tube will go to higher angles without error, but both square- and round-tip pitot tubes suffer errors if they are used at too low Reynolds numbers or too close to a wall. At very low Reynolds numbers, the flow regime is referred to as "creeping flow." The difference between the pressure and stagnation pressure is not the dynamic pressure, $q = \frac{1}{2}\rho V^2$, which gives $c_{p(stag)} = 1$ for high-Reynolds-number flow. In this
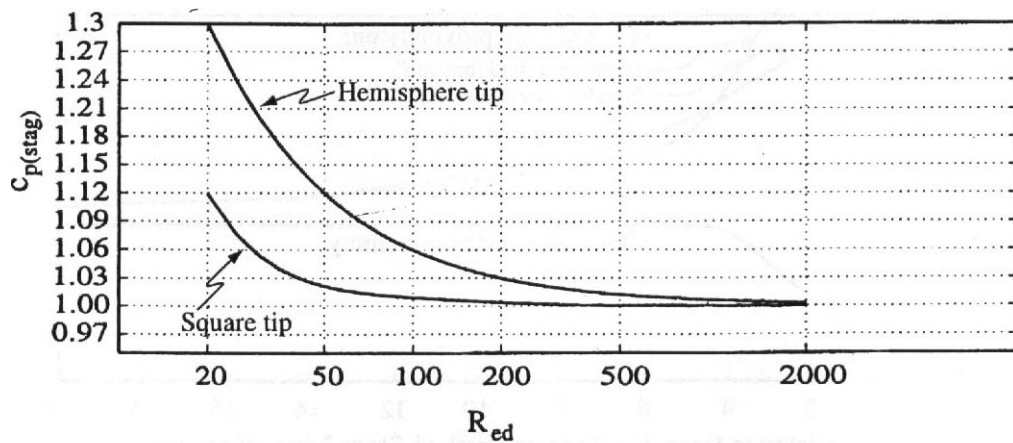
FIGURE 4.7   Performance of pitot tubes at low Reynolds number.

regime the stagnation pressure on a blunt-nosed body is given approximately in terms of the Reynolds number based on the body diameter by Barker[20] as

$$c_{p(\text{stag})} = \frac{p_{\text{stag}} - p}{q} = 1 + \frac{6}{R_{ed}} \tag{4.12}$$

Corrections for pitot tubes under these conditions are shown in Figures 4.7 and 4.8, as given by Spaulding and Merriam.[21]

The pressure sensed at the "static" holes differs from the stream static pressure due to two effects of the geometry. The first effect is generic for a semi-infinite axisymmetric body with flow approaching the "nose" of the body along the axis of symmetry. The nose of the probe has a region on the upstream surface where the flow stagnates and the pressure is above the stream pressure in the approaching
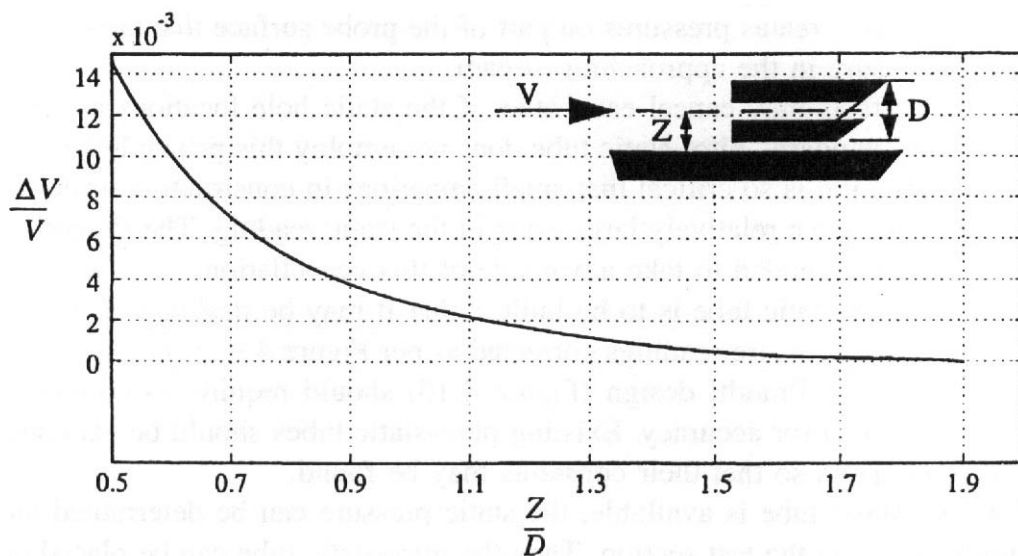
FIGURE 4.8   Velocity correction for a circular pitot tube near a wall.
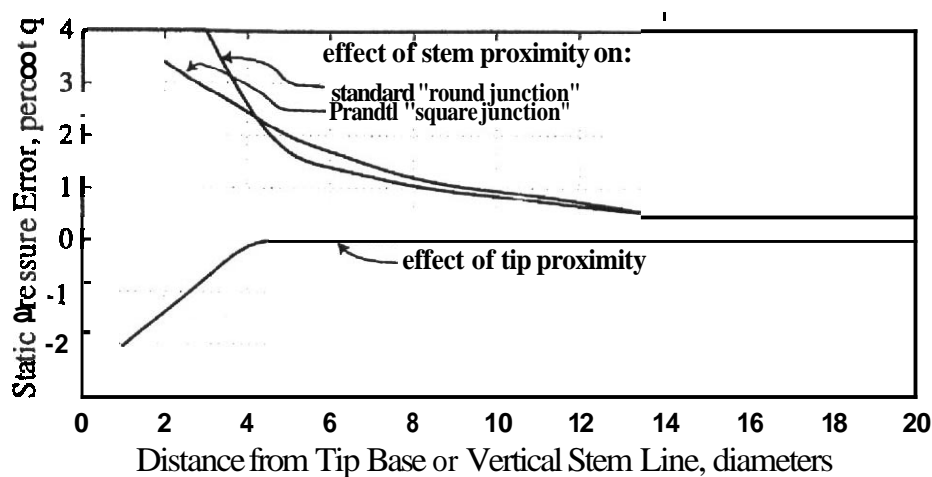
FIGURE 4.9   Effect of static orifice distance from tip or from stem: see Example 4.1.

flow. At the stagnation point, the pressure is the total pressure of the stream. The flow accelerates from the stagnation point around the **curved** surface and the local surface pressure rapidly falls through and below the stream or static pressure in the approaching flow. A minimum pressure is reached somewhere on the curved surface, and the pressure starts to "recover" toward the stream static pressure as one moves downstream along the surface parallel to the stream direction. If the probe were infinitely long and aligned with the flow, then the pressure on the tube surface would asymptotically approach the stream pressure with distance from the nose. This effect means that pressure taps on the probe's parallel surface a finite distance from the nose would produce a measurement that is lower than the local stream pressure. The amount of the difference in indicated in Figure 4.9.

The second effect is associated with the presence of the "stem," a cylinder whose axis is perpendicular to the approaching stream. A high-pressure region exists ahead of the stem, and that region includes the surface of the probe itself. In fact, the Prandtl design has a stagnation point near the intersection of the stem and the probe body. This effect creates pressures on part of the probe surface that are higher than the static pressure in the approaching stream.

The two effects may cancel each other if the static hole locations **are** properly chosen. The "standard" pitot-static tube does not employ this principle because the static hole location is so critical that small deviations in construction or damage to the tip can produce a relatively large error in the static reading. The Prandtl design (Figure **4.10)** is intended to take advantage of this cancellation.

If a new pitot-static tube is to be built, either it may be designed as per Figure **4.6** and its static pressure readings corrected as per Figure 4.9 or the Prandtl design may be used. The Prandtl design (Figure **4.10)** should require no correction but should be checked for accuracy. Existing pitot-static tubes should be examined for tip and stem errors so that their constants may be found.

If a long static tube is available, the static pressure can be determined along a longitudinal line in the test section. Then the pitot-static tube can be placed on this line and the static pressure orifices in a pitot-static tube can be calibrated.
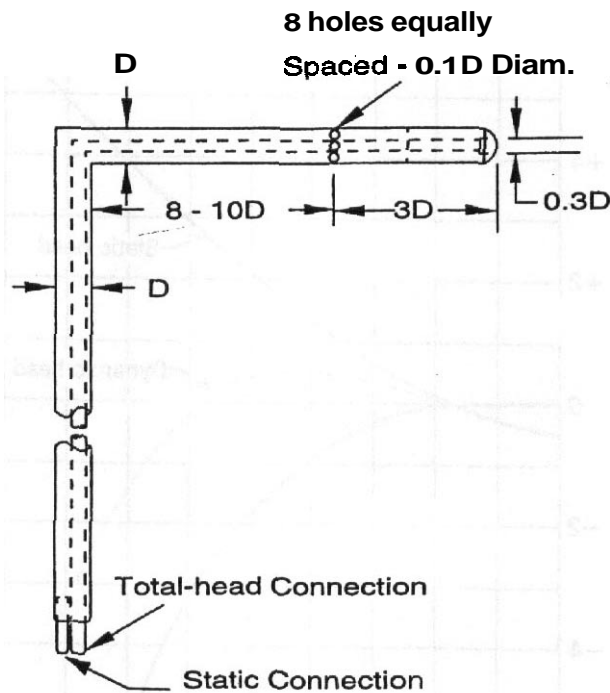
FIGURE 4.10   Prandtl's design for a pitot-static tube.

Example 4.1   A pitot-static tube whose static orifices are 3.20 from the base of the tip and 8.00 from the centerline of the stem reads 12.05 in. of water on a manometer for a particular setting of the tunnel. If the test section is at standard pressure as indicated by a barometer and at a temperature of 113°F as measured from a resistance thermometer, find (1) the dynamic pressure and (2) the true air speed.

First the pitot-static tube error must be found.

(a) lip Error. From Figure 4.9 it is seen that static orifices located $3.2D$ from the base of the tip will read 0.5% q too low.

(b) Stem *Error.* From Figure 4.9 it is seen that static orifices located $8.0D$ from the stem will read 1.13% q too high.

(c) Total *Error.* The static pressure therefore will be $1.13 - 0.5 = 0.63\%$ q too high, and hence the indicated dynamic pressure will be too low.

The data should be corrected as follows:

$$q_{true} = 1.0063 q_{indicated} \qquad V_{true} = 1.0031 V_{indicated}$$

1. Accordingly the dynamic pressure will be $1.0063 \times 12.05 = 12.13$ in, of water. Applying the conversion for units, this is $12.13 \times 5.204 = 63.12$ lb/ft².
2. The density is

$$\rho = 0.002378(518/572) = 0.002154 \text{ slug/ft}^3$$
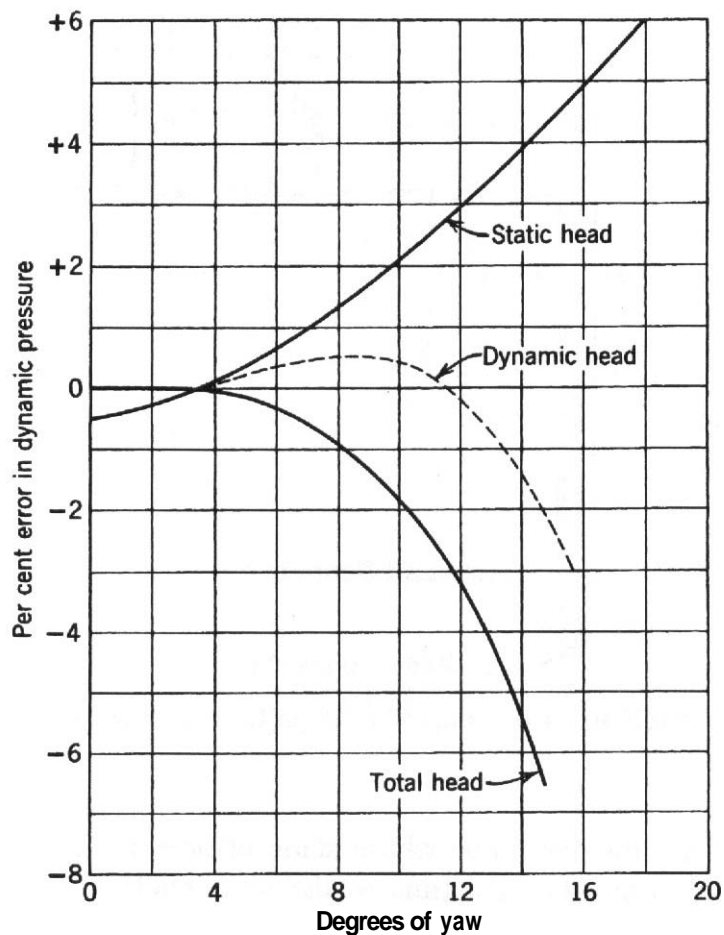
FIGURE 4.11   Performance of the standard pitot-static tube in yaw.

The true air speed is hence

$$V_t = \sqrt{\frac{2(63.12)}{0.002154}}$$

$$= 242.09 \text{ ft/sec} = 165.06 \text{ mph} = 143.34 \text{ knots}$$

The accuracy of a standard pitot-static tube when inclined to an airstream is shown in Figure **4.11.** If a pitot-static tube is placed near a model, the model's static pressure field will influence the pressure sensed by the static ports, and the reading will not be the free-stream velocity. This is why tunnel dynamic pressure calibrations are made without a model in the test section. The same problem exists on an aircraft, where great care has to be taken in the location of a static pressure source so as to find a location where the static pressure varies as little as possible with lift or aircraft attitude.

Pressure Probes for Velocity Measurement

Yawheads   A yawhead is a sphere that has two or more static ports on the forward face of the sphere (Figure **4.12).** If the ports are at exactly 45° to the centerline of
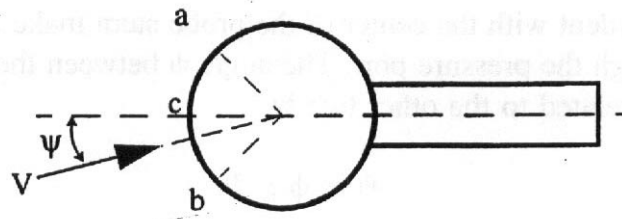
FIGURE 4.12   Yawhead.

the support and the flow is parallel to the support, then $(P_a - P_b)/q$ = APlq = 0. If there is flow angularity, then APlq $\neq$ 0, and the value of APlq will be a function of the flow angle. In practice, a **yawhead** must be calibrated. The probe is placed in a flow that has no angularity, and the probe is pitched or yawed about its center through an angle range both positive and negative. This is done for the **yawhead** in the "upright," or normally used, position, and then the **yawhead** is rotated 180" to an "inverted" position. This will result in two curves of APlq (upright and inverted) versus the angle for the **yawhead.** If the static ports **are** symmetrical to the support axis, the two curves will lie on top of each other. If there is an asymmetry in the static port locations or possibly in the conditions of the static ports themselves, the curve will be displaced by twice the error. The true curve lies halfway between the two measured curves. If the flow used to calibrate the **yawhead** is not parallel to the **yawhead** support axis at the zero angle, the true curve will not pass through the zero angle. It is normally desired to have the **yawhead** calibration independent of dynamic pressure and static pressure so the coefficient defined by (4.13) may be used:

$$C_\psi = \frac{p_b - p_a}{p_c - (1/2)(p_a + p_b)} \tag{4.13}$$

It is instructive to investigate the variation of C_ψ as if the pressure distribution on the spherical **yawhead** were accurately given by potential flow theory for a sphere in a uniform stream. Let the angle between the incoming stream direction and a line through the center of the sphere be 0. Then the pressure coefficient at the point where the line pierces the sphere is[ZZ]

$$c_p = \frac{p - p_\infty}{q_\infty} = 1 - \frac{9(\sin\theta)^2}{4} \tag{4.14}$$

If p_∞ and q, are otherwise known, then the angle is given in terms of the flow measurements by

$$\theta = \arcsin\left(\frac{2\sqrt{1 - c_p}}{3}\right) \tag{4.15}$$

Now let the line just envisioned pierce the sphere at the center of a pressure port,

and the line coincident with the center of the probe stem make an angle ϕ with the line passing through the pressure port. The angle ψ between the probe axis and the flow direction is related to the other two by

$$\psi = \phi - \theta \qquad (4.16)$$

In most cases of application, this is not the situation. It is frequently required to make measurements in parts of a model flow field where the static and dynamic pressures are not known. Therefore it is necessary to obtain the angle and possibly the static and dynamic pressures from the probe data alone. Equation (4.14) applied to a particular port (say port a) gives

$$p_a = [1 - \tfrac{9}{4}(\sin \theta_a)^2]q_\infty + p_\infty \qquad (4.17)$$

It can be seen that using the similar relations for the other two ports yields

$$c_\psi = \frac{(\sin \theta_b)^2 - (\sin \theta_a)^2}{(1/2)[(\sin \theta_b)^2 + (\sin \theta_a)^2] - (\sin \theta_c)^2} \qquad (4.18)$$

And using (4.16) we obtain

$$c_\psi = \frac{[\sin(\phi_b - \psi)]^2 - [\sin(\phi_a - \psi)]^2}{(1/2)\{[\sin(\phi_b - \psi)]^2 + [\sin(\phi_a - \psi)]^2\} - [\sin(\phi_c - \psi)]^2} \qquad (4.19)$$

For the case that $\phi_c = 0$ and $\phi_a = -\phi_b$, (4.19) reduces to

$$C_\psi = \frac{2 \tan(2\psi)}{\tan \phi_b} \qquad (4.20)$$

A calibration result would be expected to resemble (4.20). The result indicates that a singularity may be expected in the vicinity of $\pm 45°$ even for the case of ideal flow. For real flow, the singularity may occur at smaller values of the angle. Inverting (4.20) gives (4.21), which would be expected to resemble the relation required to obtain the yaw angle from the measurements of the three pressures:

$$\psi = \frac{1}{2} \arctan\left(\frac{C_\psi \tan \phi_b}{2}\right) \qquad (4.21)$$

Using the yaw angle ψ obtained from (4.21) along with (4.16), the angles from the flow vector to each port, θ_a, θ_b, θ_c, can be computed. Then the dynamic pressure and the static pressure can be obtained from two of the three equations represented by (4.17). One form of the results is as follows:

$$q_\infty = \frac{4(p_c - p_a)}{9[(\sin \theta_a)^2 - (\sin \theta_c)^2]} \qquad (4.22)$$

and

$$p_\infty = p_b - \left\{\frac{4(p_c - p_a)}{9[(\sin \theta_a)^2 - (\sin \theta_c)^2]}\right\}\left[1 - \frac{9(\sin \theta_b)^2}{4}\right] \qquad (4.23)$$

The last three equations are idealized and are not suggested for direct use. The process for a particular yaw probe consists of a calibration process in which the probe is placed into a stream of known dynamic and static pressures, the angle of yaw is varied over the range of interest, and the three port pressures p_a, p_b, p_c are recorded for the set of yaw angles. The four functions c_{pa}, c_{pb}, c_{pc}, C_ψ *are* formed from the port pressures, the dynamic pressure, and the static pressures. The probe can then be used to obtain the flow angle, dynamic pressure, and static pressure in an unknown flow by placing the probe into the flow of interest and recording the three port pressures. The yaw coefficient is computed directly according to (4.13). The yaw angle in the flow is then obtained by inverting the function $C_\psi(\psi)$ obtained during calibration. The dynamic and static pressures are obtained from (4.24) and (4.25):

$$q_\infty = \frac{p_c - p_a}{c_{pc}(\psi) - c_{pa}(\psi)} \qquad (4.24)$$

$$p_\infty = p_b - \left\{\frac{p_c - p_a}{c_{pc}(\psi) - c_{pa}(\psi)}\right\}c_{pb}(\psi) \qquad (4.25)$$

where the coefficient functions are from the calibration. The process must still be examined for effects of Reynolds number and Mach number.

Quite often a yawhead has five static ports rather than the three just described. With such an arrangement, the two flow angles required to define the three-dimensional flow vector may be obtained although the calibration is now over the two angles and a surface must be generated rather than a single curve. Pitot-static tubes that use a hemispherical nose can be made to have two yawheads built into the nose. In this case, one instrument at any place in the test section will measure total pressure, static pressure, dynamic pressure, upflow, and cross-flow. This is quite useful for determining flow conditions in a test section.

Claw   A claw will also measure flow angularity and is simple to build. In its simplest form a claw consists of two parallel pieces of tubing that are bent $45°$ away from their common axis and then bent back 90" toward their common axis (Figure 4.13). The two heads of the probe are cut off square about two diameters from the centerline. Often a third tube is added to measure total pressure, and the two claws can be made to simultaneously measure both cross-flow and upflow. The calibration technique for a claw is the same as that for a yawhead. Claws are more delicate than yawheads because the two tubes used to measure AP can be easily bent, thus changing the calibration.
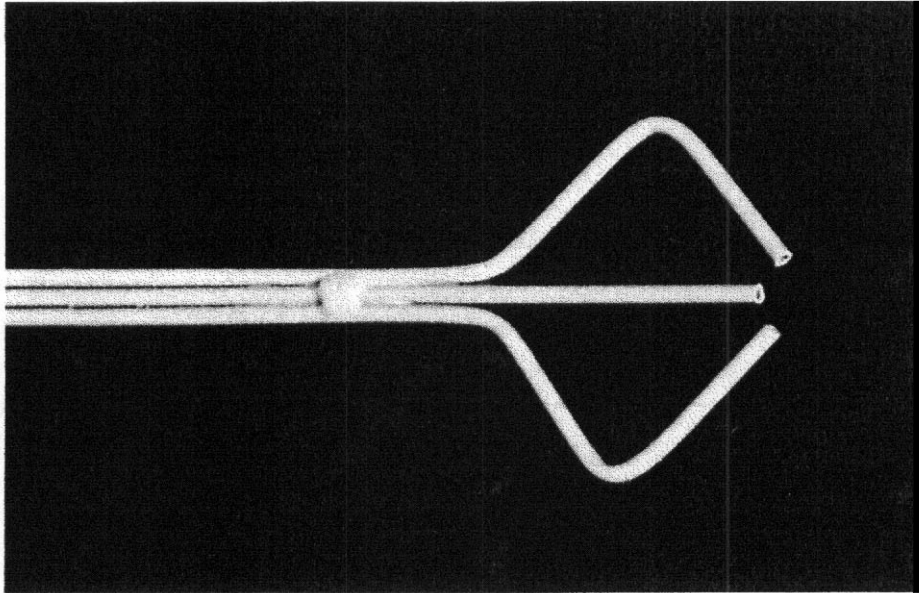
FIGURE 4.13   Claw probe.

Cone Probes   Cone probes with five or seven holes are widely used for flow vector measurements. They have the advantage of simplicity of construction and can be calibrated more readily to higher angles. Gupta[23] gives detailed treatment and examples of calibration results. Gallington[24] and Gerner et al.[25] give results that allow calibration for compressible flow.

Probes for Measurements in Reverse Flow   A number of developments have been carried out on probes to allow measurements to be made in flow with angles from almost any direction. Cogotti[26] describes and has used a 14-hole probe extensively. This probe is essentially two 7-hole cone probes in a back-to-back configuration. Yamaguchi et al.[''] and Rediniotis[28] have developed spherical probes with 13 holes arranged as multiple 5-hole yaw probes. Gupta[23] gave procedures for a spherical probe with 11 holes arranged in the pattern of the faces of a dodecahedron with the probe stem emerging from the location of the 12th face center.

Other Pressure Devices   Sometimes a simpler version of a yawhead is used. One device consists of five tubes arranged in a cross configuration with one tube in the center and two pairs of tubes attached to it at right angles. The center tube is cut off with its end approximately perpendicular to the flow. The other tubes are cut off at a $45°$ angle. A second device is similar but consists of two parallel tubes cut off at an angle. Both of these devices are calibrated in a manner similar to a yawhead or claw.

Devices Responding to Aerodynamic Forces

The devices described here are small airfoils, wedges, and vanes. They provide a response based on aerodynamic forces over surface areas larger than a typical pressure port.
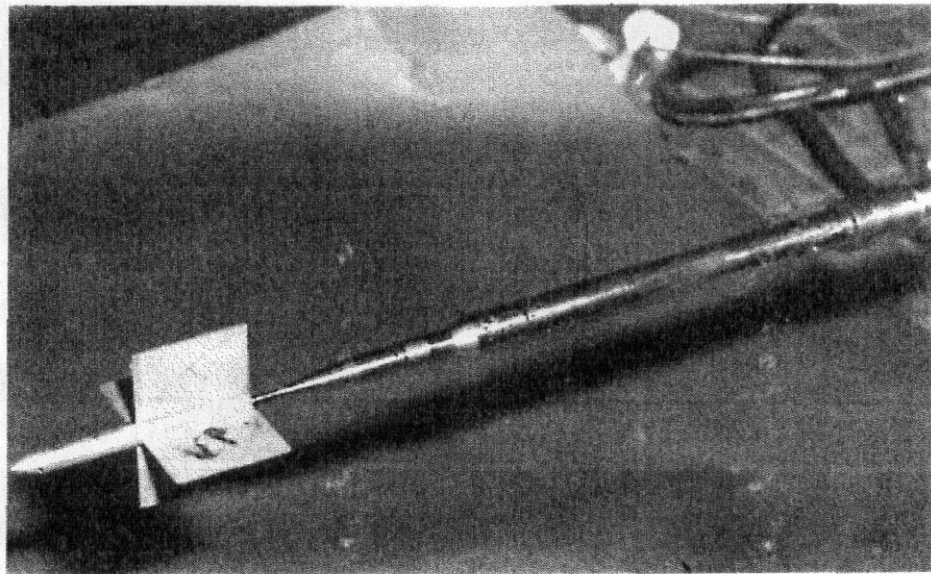
FIGURE 4.14   Vane-type flow angularity probe. Uses a five-component balance and can resolve about 0.006". Owing to its high natural frequency, probe can make continuous-motion surveys. (Photograph courtesy of Sverdrup Technology Inc.)

Airfoils and Vanes   Flow angles can be measured using small wings attached to sting balances. The flow angle calibration is obtained by the rotation of the drag polar. Small vanes of various configurations can also be used (Figure 4.14 from Luchuk, Anderson, and Homan[29]). Often these are attached to low-friction potentiometers to read the angle or to balances.

To measure velocities in highly deflected wakes, use has been made of an instrumentation rake that contains pitot tubes and static tubes and a devi'ce to measure flow angularity. This rake is then pitched to null the flow angle probes, thus aligning the rake with the flow. A potentiometer or digital shaft encoder can be used to record the angle and the velocity is obtained from the total and static pressures. These types of nulling devices are becoming less and less attractive as productivity is becoming a much more important element in wind tunnel activities. They **are** also becoming less needed since the computing power to handle increasingly complicated calibration functions is readily available.

Thermal Anemometers

Hot wires and hot films are used to obtain fast-response velocity measurements in turbulent flows as well **as** mean velocities and, with multiprobes, flow angularity. The probe or sensor is a fine wire (diameter of a few micrometers) or a coated **quartz** fiber attached between two supporting needles on the probe (Figure 4.15). Current passed through the wire or film raises its temperature above the adiabatic recovery temperature of the gas. The hot wire responds to changes in total temperature and mass flux (T_0 and ρU). In subsonic applications where the density is high and the fluid temperature is low and constant, the problem of heat transfer through the support needle (end losses) and radiation effects can be ignored, and the wire's
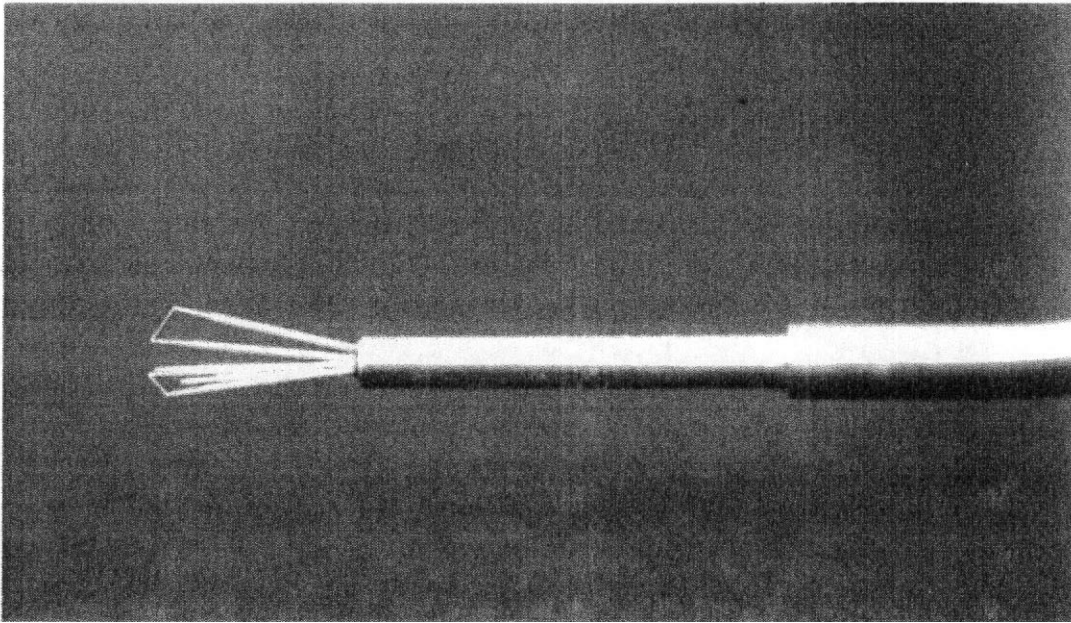
FIGURE 4.15   Three-element hot-film probe.

response basically is a function of velocity alone. Under these conditions and using appropriate calibration and measurement of the voltage across the bridge, both mean and turbulent velocities are obtained.

Electronic hot-wire circuits include a feedback system to maintain the wire at a constant wire resistance. This is a constant-temperature anemometer. Feedback can also be used to maintain a constant-current anemometer. Constant-temperature anemometers are easiest to use in subsonic or incompressible flow, while the constant-current anemometers are preferred in compressible flow. Frequency response to 50 kHz is easily obtained.[30]

In incompressible flows, the hot wire costs less and is easier to use than a laser anemometer. The hot wire does intrude into the flow and the laser does not. The hot wires are extremely fragile and often break, usually just after calibration and before use. If the flow field is dirty, the risk of the wire breaking is high.

If turbulence measurements are not required, a single or dual split film can be used. These units are more rugged and can be used to measure both mean velocities and flow angles. Units are available commercially with up to six elements so that flow direction can be determined with no ambiguity. Some research workers have constructed probes with as many as 18 elements to allow direct measurement of Reynolds stresses in turbulent flows.

Single or Dual Split Film   A single split film will be parallel to the axis of a small glass rod. A dual split film will have a second pair of split films at 90° to the first, aligned along the rod circumference. These devices, similar to hot wires, can be used to measure both velocity and flow angles. The split film is suitable for measuring mean velocities but does not have as high a bandwidth of frequency response as

hot wires for turbulence measurements. Thin-film sensors and the associated electronics are commercially available.

Laser Velocimeters

A laser velocimeter uses a tracer method, which depends on detection of an optical effect from a particle that is carried with the flow. The most common laser Doppler velocimeter (LDV) uses optics to split the laser beam into two parallel beams that are focused to cross at the point where measurements are to be made (a dual-beam system). Owing to wave interference, a fringe pattern in an ellipsoid-shaped volume at the beam intersection is formed. A second lens assembly (the receiver) with a small aperture is focused on this fringe region to collect light from seed particles crossing the fringes. This light is fed to a photodetector that is used as the input to the sophisticated electronic signal processor that measures modulated frequency.

In a dual-beam system the frequency from the scattered light from the two beams are superposed on the photodetector's surface. The mixing process in the photodetector then gives the difference in the frequency from the two beams. All other frequencies are too high to detect (this is called an optical heterodyne). If β is the angle between one of the beams and the bisector of the two beams and λ is the wavelength of the laser light, then it can be shown that when the particle velocity is much less than the speed of light the modulator frequency is

$$f_D = \frac{2u_x \sin \beta}{\lambda} \tag{4.26}$$

where u_x is the velocity parallel to the plane of the two beams and perpendicular to the bisector of the beams. Thus the relationship between the flow velocity and f_D is linear and a function of half the beam angle and the wavelength of the laser light. Perhaps it is easier to think of the system working in the following manner: When a particle moving with the flow passes through each fringe, it is illuminated, which causes a series of pulses from the photomultiplier. As the distance between the fringes is known, the time to cross the fringes is measured, and this yields the particle velocity. It should be noted that the fringe spacing in micrometers is equal to the calibration constant in meters per second per megahertz. When a large number of samples are taken, the signal processor and computer calculates both the average velocity and instantaneous velocity, which can be used to obtain the turbulence or velocity variation.

To calibrate the LDV, the wavelength of the laser is required. This is known to an accuracy better than 0.01%; thus only the beam crossing angle is required. As an alternate calibration method the velocity of the edge of a rotating disk at constant speed can be measured by the LDV for a direct calibration. This also can check the extent to which the fringes are parallel by varying the point along the optical axis where the wheel intercepts the measuring volume.

Two- and three-component LDV systems are formed by using laser systems that produce two or three different wavelengths, each of which can be treated as described above. The fringe patterns created by the different wavelengths must be formed

within a common volume and must have their planes oriented so that the desired velocity components can be sensed. A second component is relatively easy to add to a one-component system because the transmitting and collecting optics can have a common axis with the first component and in fact can use the same transmitting and collecting lens. Adding a third component is more complex since the optical axis for the beams to form the interference pattern for the third component cannot be coincident or parallel to the axis used for the first two components. It would be ideal if the optical axis for the third component could be perpendicular to the axis used for the first two. In practice, it is usually at a much smaller angle. The manufacturers of LDV systems are the best sources of information for the available features.

There are two basic modes that can be used for a LDV, the forward-scatter mode and the back-scatter mode. In the forward-scatter mode the receiving optics and photodetector would be on the opposite side of the test section from the transmitting optics. In the back-scatter mode both the transmitter and receiver are on the same side of the tunnel. The advantages/disadvantages of both modes are listed below.

Forward-Scatter Mode

Advantages

1. Low-power lasers can be used, such as helium neon, output 0.5–30 mV. These units have a high level of reliability.
2. The laser does not need cooling.
3. The signal-to-noise ratio is large.
4. Higher air speeds can be measured, but more laser output at higher speeds may be required.

Disadvantages

1. Windows on both sides of the test section are needed that are relatively flat optically to avoid beam misalignment.
2. When making traverses through the test section, the receiver must track the measuring volume. This may require both the transmitter and receiver to be on a steady base. In many tunnels the test section is elevated above the ground and the floors at the test-section level often vibrate with the tunnel.
3. Often the model will block the transmitted beam. This occurs, for example, when measuring downwash in the tail region.

In general, forward-scatter systems are good for small tunnels and measuring flow in the jet without a model.

Back-Scatter Mode

Advantages

1. The transmitter and receiver can be placed on the mount that is used to traverse the flow and there is no problem tracking the measurement volume. The entire LDV system can be packaged much more compactly.

2. Only one **window** is needed that is relatively flat optically to avoid beam scatter.
3. There are fewer problems with the model blocking signals, although in certain cases problems will occur.

Disadvantages

1. **A** much higher power laser is needed (continuous-wave argon), up to 20 W output. The higher power requires water cooling with associated plumbing problems.
2. The higher power increases the danger from the beams and their reflections. Usually it is necessary to have the laser operation site inspected and approved by laser or environmental safety personnel. An output of over 0.5 W is defined as high power.
3. The signal-to-noise ratio is much lower, which may increase the time required to make measurements. The signal-to-noise ratio is a function of laser power.

The output of the photodetector is a frequency, and this must be converted to a voltage or some number proportional to velocity. There are many ways that this can be done, but there is no apparent universally accepted optimum method. There is a strong tendency to use a dedicated computer of adequate size and speed for LDV data reduction. It is common to package the computer and software with an LDV system since the LDV system typically costs many times the cost of an appropriate computer.

A particle generator is usually needed for adding particles of a specific size (usually 0.1–10 μm) and density into the flow. Particle parameters must be controlled to get acceptable data rates and to ensure that particles travel at instantaneous local velocity. At low speeds natural dust may provide needed particles. Particle seeders are commercially available.

Problems in turbulent flow may occur when (1) intensity is large with respect to mean flow and (2) mean flow velocity changes rapidly with either time or location. Particles may not be able to maintain instantaneous velocity of flow (worse at low air density).

A typical seeding method is atomization, the process of generating liquid droplets with compressed air. Usually light oils are used. The resulting aerosols will contain some large droplets (10–15 μm). These probably do not follow the flow field, but they do tend to deposit themselves on the walls and windows, thus adding a cleaning chore for the tunnel crew.

Small-size solid particles can also be used. There are problems with keeping the original particle size and feeding the powder into the air at a constant rate. There are obvious questions regarding human exposure to such particles that must be investigated by any potential user. As with oil, there is a cleanup problem.

Laser velocimeters are used to measure momentum losses in wakes to obtain drag, measure circulation to obtain lift, map flow fields, trace vortex paths, measure turbulence, and so on. If the **LDV** is to be used as a flow-visualization-type diagnostic tool, the precision usually obtained in locating both the measured flow volume and

the velocity can be relaxed. This is possible because the relative magnitudes of changes are required rather than absolute values. The LDV itself, if not permanently mounted at the tunnel, must be capable of being installed and operational in a short time. The LDV traversing system must move the measurement volume quickly even at the expense of some degradation in the accuracy of the location. The measurement accuracy of velocities can often advantageously be relaxed in a trade-off for rapid acquisition of a larger number of samples.

The data system and computer should give the results, usually in plotted form for traverses, during or immediately after the run. In essence, when used in this manner, the LDV is competing with other flow visualization techniques such as china clay and tufts, and to be useful, it must operate within their typical required time frames. This continues to be difficult to achieve for systems in larger tunnels. As a result LDV systems are used as very special purpose measurement systems to obtain data that are nearly impossible to obtain by other means and in which the value of the data is sufficient to justify the high cost of both the LDV system and the relatively long tunnel occupancy times that are necessary.

Particle Image Velocimeters

Particle image velocimeters are another example of a tracer method. The basic idea is very straightforward. Take two pictures of a large number of particles with a known time interval between exposures and measure the distance traveled by each particle during that time interval. Many variations on practical implementations are being explored. At the present time there are excellent results being obtained for relatively low volumes and relatively low speeds. Very good results are obtained in water flow facilities. Moderately good results are obtained in small wind tunnels at low speed. But it is still difficult to apply PIV methods in large wind tunnels at speeds of the order of 100 m/sec.

Rakes

Total Head Rake   Airfoil profile drag has often been measured by the use of a drag wake rake. In this technique the momentum loss in the wake is determined by measurements with a bank of total head tubes. (See Section 4.5 for further discussion of the method.) The rake also should have two or more static tubes offset from the total head tubes to obtain the local static pressure. The rake size must be adequate to encompass more than the width of the wake. Often, the tube spacing is greater at both ends of the rake than in the center by a factor of 2. The spacing of the tubes must be known with precision so that the momentum profile can be accurately determined. Generally, the total tubes are made of 0.0625-in. thin-wall tubing (Figure 4.16). The static tubes must be offset from the plane of the total tubes to avoid interference effects on the static pressure. Their purpose is to determine the static pressure in the wake. Because the static pressure can be affected by both the total head tubes and the base of the rake, they must be carefully calibrated so that the error in static pressure is known. Since the static tubes must have a hemispherical
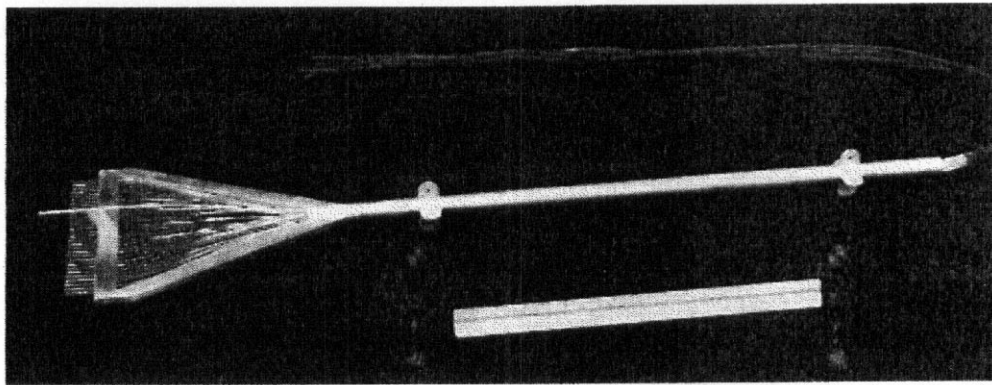
FIGURE 4.16   Total head rake. Note single static pressure tube. (Courtesy Aerolab Development Co., Laurel, Maryland.)

nose shape, **Krause**[31] has shown that it is possible to adjust this shape to reduce the error to zero.

As an alternative to a wake rake, a mechanical traversing mechanism can be used. Using various encoders, the location of a probe can be determined with a high degree of accuracy. The sensor can be a pitot and, preferably, a static tube, a multihole probe, a hot wire, or a thin film or even a fiber-optic laser velocimeter head.

When measuring the momentum loss in the wake by any method, **care** must be taken to ensure that the whole width of the wake is measured.

4.4   BOUNDARY LAYERS AND SURFACE SHEAR STRESS

Boundary Layer Mouse

Measurements in the boundary layer are often made to detect the transition between laminar and turbulent flow or to find the local skin-friction coefficient. Obtaining knowledge of the velocity profile in the boundary layer is important in attempts to determine these quantities. Within an attached boundary layer the static pressure is essentially constant while the total pressure varies. There are several ways in which the velocity profile can be obtained.

The oldest method is by use of a boundary layer mouse[31] (Figure 4.17). This device is a series of total head tubes, often with oval or flat inlets. To obtain the velocity profile with adequate resolution at the surface requires the total head tubes to be spaced closer together than their diameters. Thus, the total head tubes are placed on an inclined plane to obtain the required close vertical spacing. The boundary layer mouse often has a static orifice to measure the static pressure or the static pressure can be measured by a surface port. During use the mouse is attached to the model. The boundary layer mouse measures the velocity profile over a finite span of the model, rather than a single spanwise station.

The velocity profile can also be measured by using a traversing mechanism whose position off the surface can be quite accurately determined by a digital optical encoder. The traverse mechanism can carry a single total head probe, a hot wire,
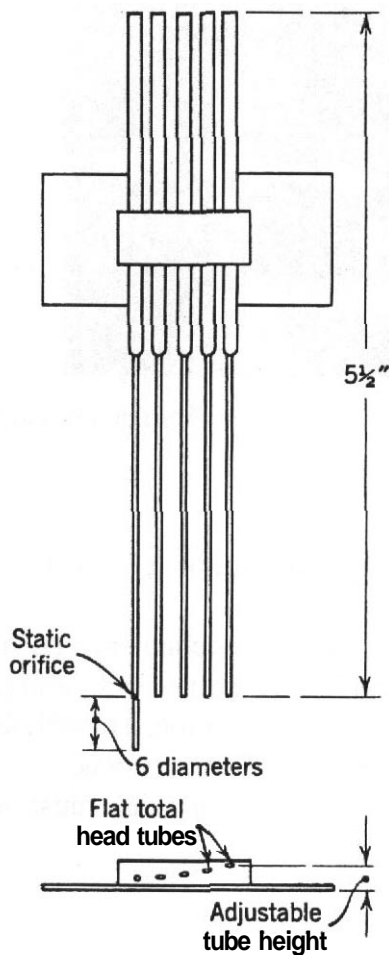
FIGURE 4.17   Boundary layer **mouse.**

or a split film. Very good agreement has been shown between pitot probes, hot wires, and thin films when supported'' by a traverse mechanism.

In general, it is better to support the boundary layer mouse or the traverse mechanism from the model rather than the tunnel walls. This avoids two problems. First, when the walls are used for support, the probes must be moved when the model is pitched and then reset to obtain a very close and accurately known proximity to the surface. The second problem with a wall support is that most models tend to move slightly and often oscillate when under loads owing to balance deflections or simply structural flexibility.

If the probes are being used to detect transition between laminar and turbulent flow, extreme care must be taken to ensure that the probe itself is not causing transition prematurely.

Many methods are in use to determine the location of the transition region. They include the following:

1. Plot the velocity gradient in the boundary layer and determine whether the flow is laminar or turbulent by the slope of the gradient, **as** illustrated in Figures 4.18 and 4.19.
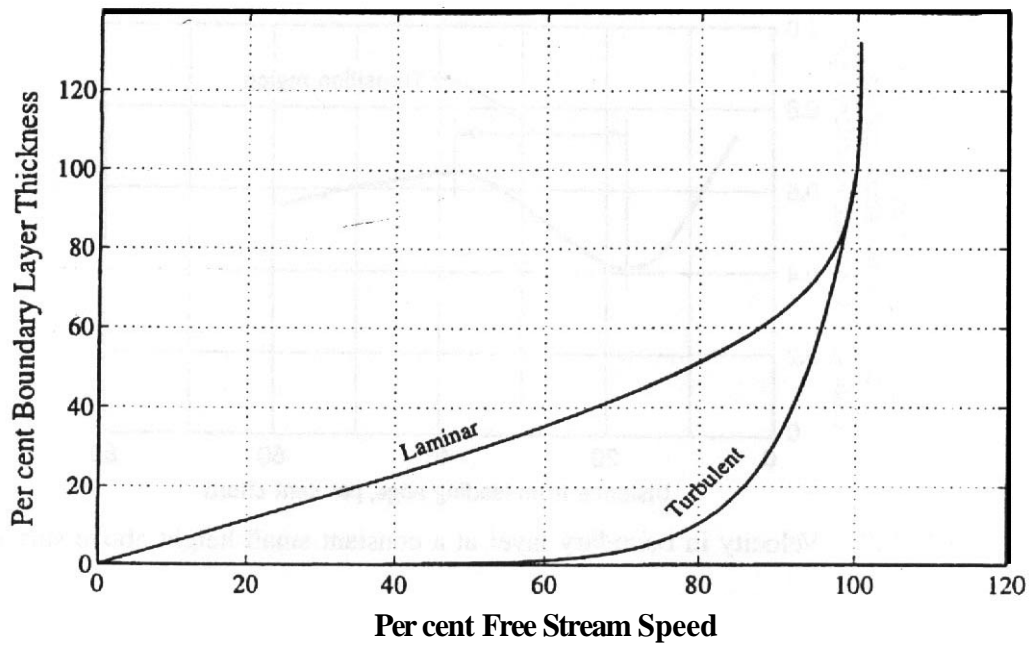
FIGURE 4.18   Velocity distribution in laminar and turbulent boundary layers.
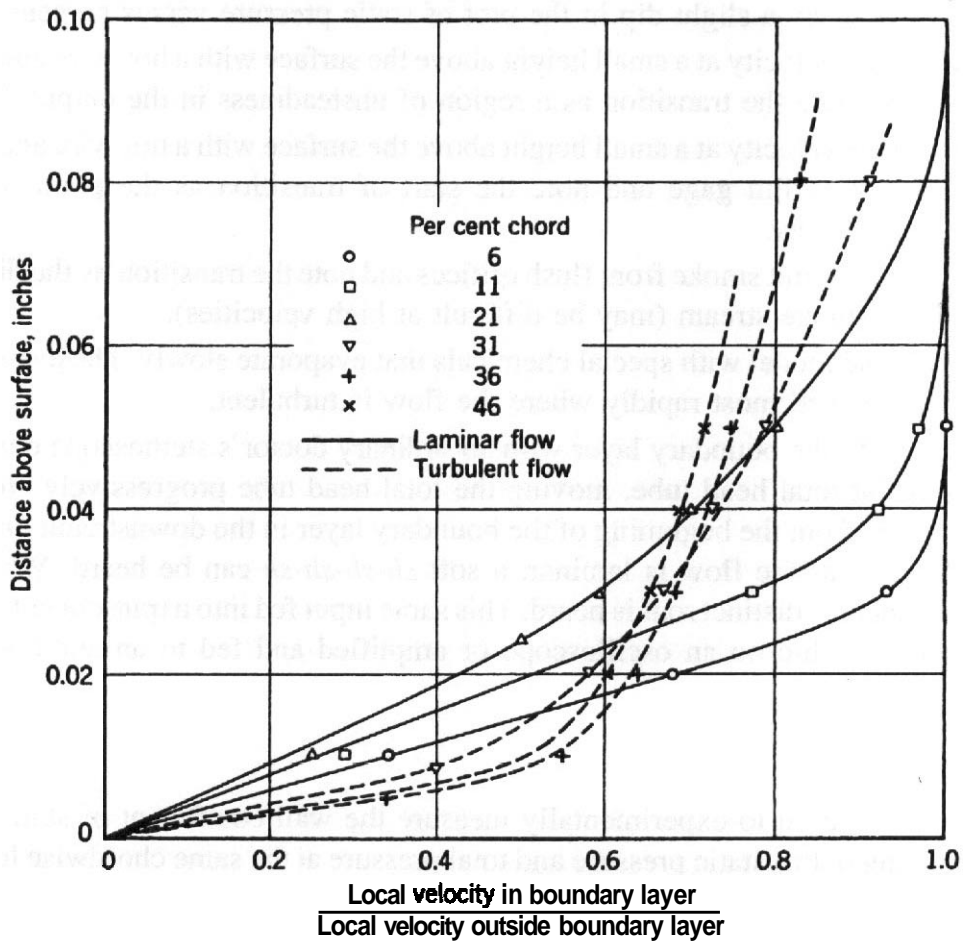
FIGURE 4.19   Boundary layer velocity profiles at six chordwise stations along an airfoil.
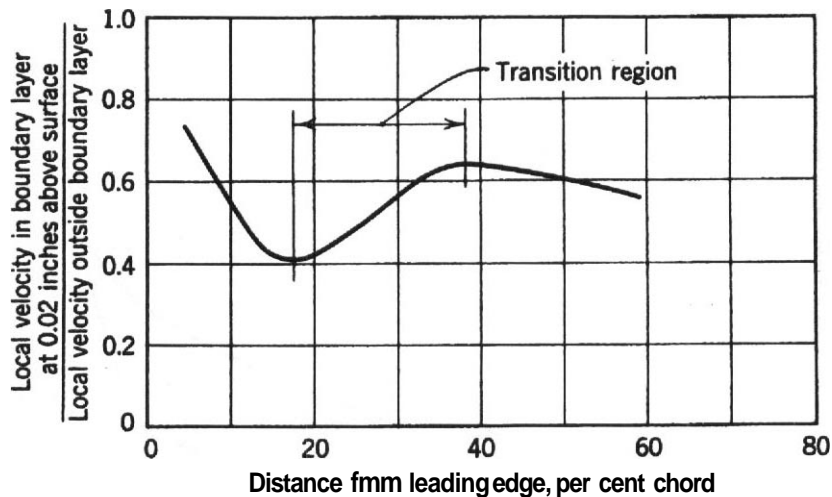
FIGURE 4.20   Velocity in boundary layer at a constant small height above surface.

2. Determine the beginning of transition as the point where the velocity as a function of **streamwise** distance at a fixed small height above the body surface is a minimum, as illustrated in Figure 4.20.

3. Read the static pressure at a small height above the surface, determine the transition by a slight dip in the plot of static pressure versus percent chord.

4. Read the velocity at a small height above the surface with a hot-wire anemometer and note the transition as a region of unsteadiness in the output.

5. Read the velocity at a small height above the surface with a hot-wire anemometer or thin-film gage and note the start of transition as the point of minimum velocity.

6. Carefully emit smoke from flush orifices and note the transition by the dispersal of the smoke stream (may be difficult at high velocities).

7. Paint the model with special chemicals that evaporate slowly. The evaporation will proceed most rapidly where the flow is turbulent.

8. Listen to the boundary layer with **an** ordinary doctor's stethoscope connected to a flat total head tube, moving the total head tube progressively along the surface from the beginning of the boundary layer in the downstream direction. As long as the flow is laminar, a soft *sh-sh-sh-sh* can be heard. When it is turbulent, a distinct roar is heard. This same input fed into a transducer becomes quite graphic on an oscilloscope or amplified and fed to an audio speaker.

Preston Tube

This device is used to experimentally measure the wall coefficient of skin friction by measuring both a static pressure and total pressure at the same chordwise location. The total pressure is measured by a **pitot** tube that touches the surface. This can be done because for unseparated turbulent flow there is a region near the wall on the order of 10% of the boundary layer thickness in which the flow depends on the

local wall skin friction τ_w, the density ρ, the kinematic viscosity ν, and a length. Preston[34] took one-half of the pitot-tube diameter as the length. Dimensional analysis leads to the equation

$$\frac{\tau_w d^2}{4\rho\nu^2} = f\left(\frac{(P_0 - P_w)d^2}{4\rho\nu^2}\right) \tag{4.27}$$

where P_0 is the pitot pressure and P_w is the wall static pressure at the same point in flow.

The value of f must be found from a calibration experiment. In a pipe flow using four pitots with inside-to-outside-diameter ratios of 0.006 (the outside diameters varied), the value of f was found. The wall skin friction τ_0 is found from $\tau_w = (P_1 - P_2)D/4L$. Here P_1 and P_2 are wall static pressures separated by length L in a pipe of inside diameter D. Preston found that $y^* = f(x^*)$, or

$$y^* = \log_{10}\left(\frac{\tau_w d^2}{4\rho\nu^2}\right) = -2.628 + \frac{7}{8}\log_{10}\left[\frac{(P_0 - P_w)d^2}{4\rho\nu^2}\right] \tag{4.28}$$

where y^* is a dimensionless shear stress for incompressible, isothermal flow and x^* is a dimensionless pressure difference for incompressible isothermal flow.

In 1964 Patel[35] published the results of tests with 14 different circular pitot probes using three different pipe diameters. The limits on pressure gradients for the calibration are also given. Patel obtained empirical equations for

$$y^* = \log^{10}\left(\frac{\tau_w d^2}{4\rho\nu^2}\right) = f\log^{10}\left[\frac{(P_0 - P_w)d^2}{4\rho\nu^2}\right] = f(x^*) \tag{4.29}$$

over three ranges of y^*:

1. $3.5 < y^* < 5.3$,
2. $1.5 < y^* < 3.5$, and
3. $y^* < 1.5$.

These ranges correspond to fully turbulent flow, transition flow, and the viscous sublayer, respectively.

For transition flow (2), or $1.5 < y^* < 5.3$,

$$y^* = 0.8287 - 0.1381x^* + 0.1437(x^*)^2 - 0.0060(x^*)^3 \tag{4.30}$$

In the viscous sublayer (3), or $y^* < 1.5$,

$$y^* = 0.37 + 0.50x^* \tag{4.31}$$

using the classical law of the wall in the viscous sublayers and by defining an effective center of the pitot as

$$y_{\text{eff}} = K_{\text{eff}}(\tfrac{1}{2}d) \qquad (4.32)$$

Patel obtained a value of $K_{\text{eff}} = 1.3$ for a round pitot tube. The velocity calculated from Preston tube data U_p is the true velocity in the undisturbed boundary layer at y_{eff}.

The work of Preston and Patel is for round pitot tubes. There are other calibrations for oval or flat Preston tubes in the literature. For example see Quarmby and Das,[36,37] MacMillan,[38,39] and Allen.[40]

Liquid Crystals for Shear Measurement

The use of liquid crystal coatings to obtain indications of transition locations has been studied for several decades. These coatings have continued to be studied and developed due to their promise for reducing the negative aspects of the two most widely used methods: sublimation and oil flow visualization. Both methods have the characteristic that each time the material is spread onto the surface one obtains a single result for which transition is to be observed. This means that for a typical determination of which transition is to be mapped as a function of angle of attack, the tunnel must be stopped and material redistributed on the surface between each change of angle of attack. Liquid crystals, on the other hand, offer the possibility of a single application to the surface providing data continuously as the angle of attack is changed.

Holmes and Obara[41] gave a state-of-the-art review of the use of liquid crystals in transition detection. They report on their use both in wind tunnels and for flight test applications. Reda and Muratore[42] and Reda et al." have recently reported significant new capabilities in the use of liquid crystals, not only for the detection of transition but also for the quantitative measurement of the magnitude and direction of surface shear stress. Two patents*," have been granted on the technology.

When a liquid crystal coating is illuminated from roughly the normal to the surface by white light and observed from an oblique angle, it has a color change response to shear that is dependent on both the direction and magnitude of the shear. It turns out that the color change is a maximum when the shear vector is directly away from the observer. Reda and co-worked[6] have been able to provide a calibration procedure that provides quantitative shear measurements over an entire surface that are similar in accuracy to available point measurement techniques when the method is applied to a planar surface. The method provides excellent transition detection on curved surfaces.

Liquid crystals are sensitive to temperature as well as shear. They must be formulated for specific temperature and shear ranges, just as a force transducer must be chosen with the appropriate sensitivity for a particular application. The references should be consulted for details.
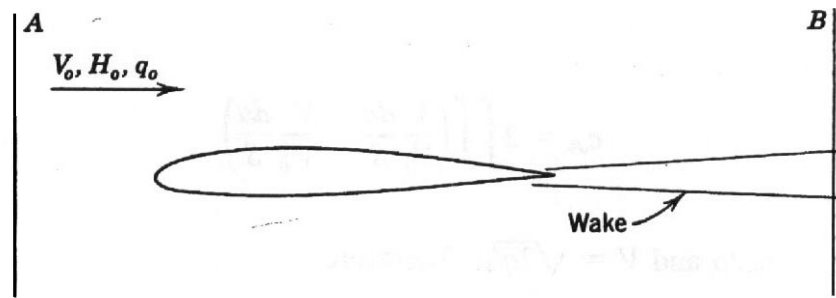
FIGURE 4.21   Notation for momentum analysis.

4.5   FLOW FIELD AND SURFACE ANALYSES

Obtaining the total force on a device in a wind tunnel usually involves the use of a balance. However, this is not always required and the methods described here provide more detail about the aerodynamic characteristics of a device than is obtained from balance measurements.

Control Volume Methods: Two Dimensions

The drag may be obtained by comparing the momentum in the air ahead of the model with the momentum behind the model (assuming the walls **are** parallel and that shear stress on the walls is neglected), and the lift may be found by integration of the pressure on the tunnel ceiling and floor. This approach is most often employed in airfoil section research in a two-dimensional tunnel.

The basic theory of wake survey measurement is discussed in the following. Consider the flow past an airfoil (Figure 4.21). It may be seen that the part of the air that passes over the model suffers a loss of momentum, and this loss is shown by and equals the profile drag of the airfoil, or

$$D = \frac{\text{mass}}{\text{sec}} \times \text{change in velocity}$$

$$= \int\!\!\int \rho V \, da (V_0 - V)$$

where D is drag, V_0 is the initial air speed (at **A),** V is the final air, speed in the wake (at B), and **da** is the small area of the wake perpendicular to the airstream. Hence

$$D = \int\!\!\int (\rho V V_0 \, da - \rho V^2 \, da)$$

and

$$c_{d0} = 2 \iint \left(\frac{V}{V_0} \frac{da}{S} - \frac{V^2}{V_0^2} \frac{da}{S} \right)$$

Also, $V_0 = \sqrt{2q_0/\rho}$ and $V = \sqrt{2q/\rho}$. Therefore

$$c_{d0} = 2 \iint \left(\sqrt{\frac{q}{q_0}} - \frac{q}{q_0} \right) \frac{da}{S} \tag{4.33}$$

For a unit section of the airfoil, $S = c \times 1$, and the area da is equal to $dy \times 1$, where y is measured perpendicular to the plane of the wing. Finally,

$$c_{d0} = 2 \int \left(\sqrt{\frac{q}{q_0}} - \frac{q}{q_0} \right) \frac{dy}{c} \tag{4.34}$$

From Bernoulli's equation

$$H_0 - p_0 = \tfrac{1}{2}\rho V_0^2 = q_0 \quad \text{and} \quad H - p = \tfrac{1}{2}\rho V^2 = q$$

where H and H_0 are the total head in the wake and free stream, respectively, and p and p_0 are the static head in the wake and free stream, respectively. Hence we have

$$c_{d0} = 2 \int \left(\sqrt{\frac{H - p}{H_0 - p_0}} - \frac{H - p}{H_0 - p_0} \right) \frac{dy}{c} \tag{4.35}$$

The ordinary pitot-static tube reads H − P directly, but practical difficulties usually prevent the construction of a bank of them. The customary method of obtaining values for Equation (4.35) is to use a wake survey rake. This is simply a bank of total head tubes spaced about a tube diameter apart with the total head orifice about one chord ahead of the rake body. The tubes are individually connected in order to the available pressure measurement system (PSP, multiple manometer, or scanivalve). If a manometer is used, only the ratio q/q_0 is needed; the readings are independent of the specific gravity of the fluid in the manometer and its angle, although the precision of measurement will be better for larger slant angles.

A traversing pitot tube can be used rather than a wake rake and is often used in conjunction with a data system. The data system measures the pitot-static position as well as the pressures. It is best to have the probe displacement and the total head
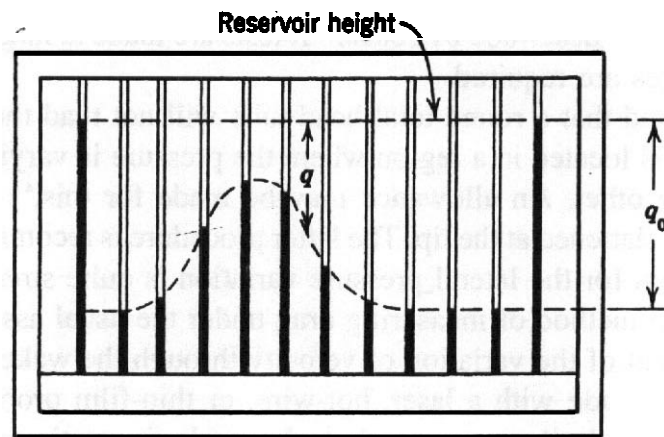
FIGURE 4.22   Wake as shown on a multitube manometer.

displayed on-line to ensure that the whole wake is traversed. A schematic of the appearance of a wake on a multitube manometer is shown in Figure 4.22.

In practice many more readings are usually obtained through shimming up the rake in small increments. A small amount of "splash" outside the wake proper may also appear, probably caused by the total pressure gradient present in the tunnel. The constant readings of the outside tubes indicate that they are out of the wake and hence may be used to determine q_0. Note that q_0 should be used from the wake rake reading, not from the tunnel q at the model location, because the longitudinal velocity gradient in the tunnel invalidates q calibrations made upstream. The other tubes read the values of q corresponding to their position on the rake.

It will be seen that the proper values of q can be obtained only if the rake is situated far enough behind the wing so that the wake has returned to tunnel static pressure, since a difference in static pressure across the wake will void the values for q. A solution to this problem is to locate the rake at least 0.7 chord behind the trailing edge of the wing. At this position the rake will be approximately at tunnel static pressure. A second solution is to equip the rake with static orifices, the usual practice being to employ three, one at each end and one in the middle, which are averaged. Since the measurement of free-stream static pressure close to a body is difficult at best, extreme caution must be exercised in locating the static holes. A satisfactory procedure is to locate them out of the plane of the rake body and calibrate them with a standard pitot-static tube, adjusting the tip length of each static tube until true static is read. If the tunnel is not at atmospheric static pressure normally, reference tubes on the multiple manometer or scanivalve should be connected to tunnel static pressure.

It has been said that the wake survey method cannot be used to measure the drag of stalled airfoils or of airfoils with flaps down. However, the problem is not with the theoretical basis but with the fact that stalled and very high lift conditions commonly produce a recirculating region and a wake that does not return to sufficiently parallel flow within the tunnel test section for the wake survey assumptions to be valid. If practical reasons prohibit the location of the rake far enough downstream so that the wake has not yet reached tunnel static pressure, additional correc-

tions are necessary, as described by Jones.[47] It tests are made at large Mach numbers, still further changes are required.

It has been found that a round total head tube will not read the true pressure at its centerline if it is located in a region where the pressure is varying from one side of the tube to the other. An allowance may be made for this,[47] or the total head tubes may each be flattened at the tip. The latter procedure is recommended, although the usual correction for the lateral-pressure variation is quite small.[48,49]

The momentum method of measuring drag under the usual assumptions is basically a measurement of the variation of velocity through the wake. These measurements can also be made with a laser, hot-wire, or thin-film probe. If the wake is not in equilibrium and allowance needs to be made for static pressure variation, then the velocity-only measurements are not sufficient.

It has been generally accepted that spanwise integration for profile drag is not necessary since the flow is two dimensional, other than a region near the wall. Several tunnels, however, have noted a spanwise variation of the profile drag coefficient when measured with wake rakes behind the airfoil. These spanwise variations are repeatable but can change with model configuration. Brune and co-workers,[50] Mueller and Jansen,[51] and Althaus[52] all show variations in profile drag across nominally two-dimensional sections. The spanwise variation of profile drag appears to decrease with increasing Reynolds number, but the variation is significant at all Reynolds numbers.

This problem is an area where further investigation appears warranted. Because the profile drag varies with span, how does one measure it? Obviously a measurement at a single spanwise station is suspect, and thus some average value should be determined. Should this be a mean or a weighted average? Furthermore, Mueller and Jansen[51] have shown that at low Reynolds numbers based on chord (below 100,000) there are large-scale vortices in the wake similar to a cylinder. Do these vortices persist at higher Reynolds numbers and thus make the use of wake surveys questionable due to rotational losses? It is well known that the wake survey is not valid in a stalled airfoil or where separation is present. Brune et al.[50] state that there was a good agreement of both streamwise velocities and turbulent intensity at a given chord location and different spanwise locations, which implies two-dimensional flow. Nonetheless, the profile drag varied with span. Based on the cited references, it is reasonable to raise the question of whether true two-dimensional flow exists, and if it does not, then does the approximation to two-dimensional flow typically vary as a function of Reynolds number?

Control Volume Methods: Three Dimensions

Three-dimensional applications of the control volume approach are also conceptually straightforward applications of the momentum equation. However, a much larger quantity of data is required in order to obtain usefully accurate integrations. And it is almost always the case that the measurement surfaces are close enough to the object so that uniformity of static pressure cannot be assumed. Three-dimensional wakes include considerable streamwise vorticity that must be accurately measured. The problem, while conceptually simple, is practically very difficult. Hacket[53] pro-

vides an example for the drag component. References in that paper provide additional sources on the methods required.

Lift and Drag by Pressure Distributions

Another method exists whereby the lift and drag may be measured: the integration of static pressures over the model surface. For this method the model is equipped with many flush orifices, each of which is connected to a pressure-measuring device. For lift determinations on a wing the pressures are plotted perpendicular to the chord, yielding the normal force coefficient C_N. When plotted parallel to the chord, they give the chord force coefficient C_C. The approximate C_L may be found from

$$C_L = C_N \cos \alpha \qquad (4.36)$$

A typical static-pressure distribution over a wing is shown in Figure 4.23a. The same pressure distribution plotted normal to the chord for the determination of normal force is shown in Figure 4.23b, and parallel to the chord for chord force determination in Figure 4.23c. Several of the pressure readings are labeled so that their relative positions may be followed in the various plots.

The growth of the pressure distribution with angle of attack is shown for a typical airfoil in Figure 4.24. In this figure may also be found a partial answer to the oft-repeated question: Which lifts more, the upper or the lower surface? At zero lift, both surfaces have both positive and negative lift. With increasing angle of attack the upper surface increases in proportion until it finally is lifting about 70% of the total.

Many interesting and useful observations may be made from pressure distributions:

1. the location of the minimum pressure point and its strength,
2. the load that the skin is to withstand and its distribution,
3. the location of the point of maximum velocity and its value (follows from item 1),
4. the location of the maximum pressure point and its strength,
5. the probable type of boundary layer flow and its extent,
6. the center of pressure location, and
7. the critical Mach number (follows from item 3).

An illustrative experiment for aerospace engineering students is to measure the lift curve and drag polar by recording pressures on manometers and using photographs. Students can see the change in width of the wake for all angles of attack as it increases and the change in pressures distribution on the wing (similar to Figure 4-24) as the manometers show them in real time.
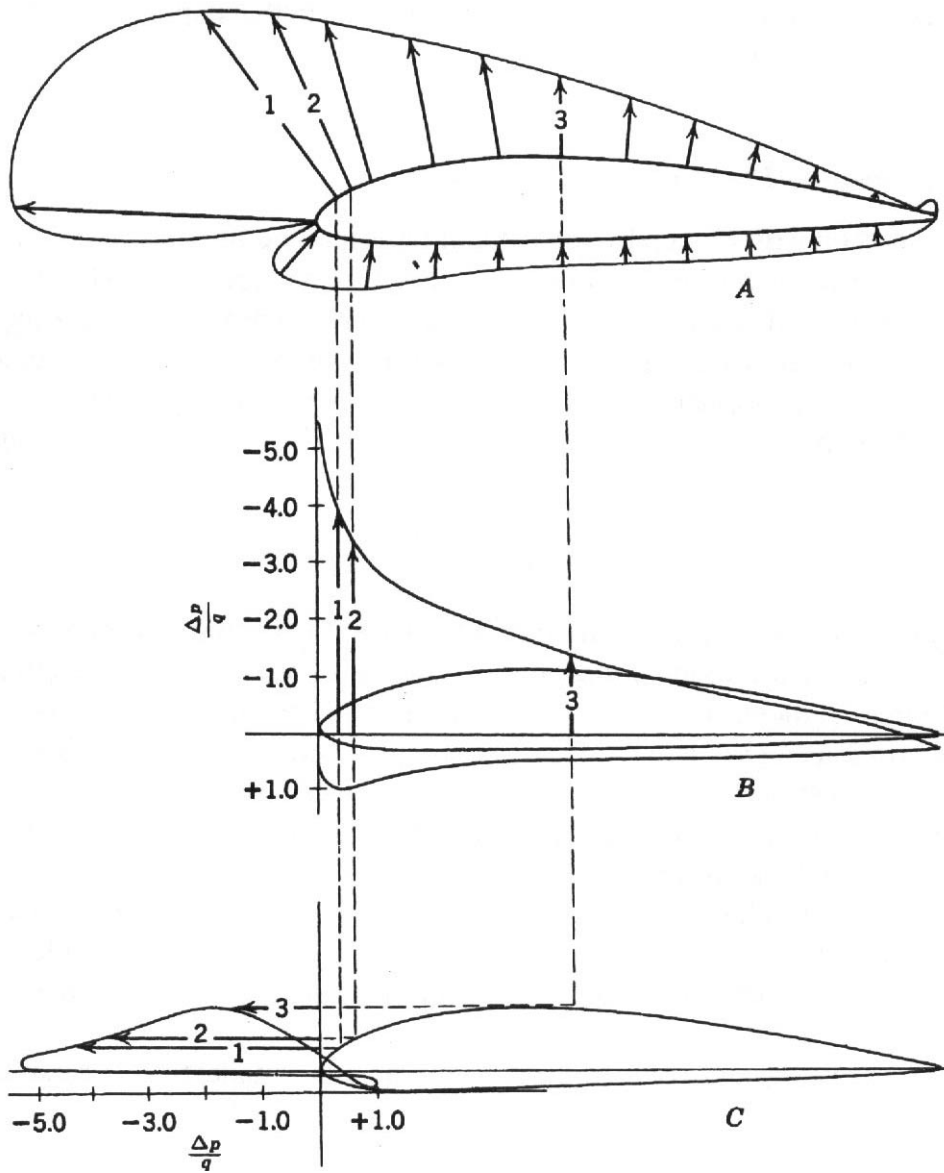
FIGURE 4.23   Example pressure distribution.

Two-dimensional tunnels often use ceiling and floor pressures to obtain lift and moment data. Pressure distributions are usually plotted as follows:

$$\text{Normal force } N = -\int Ap \; dS$$

where $Ap = p_u - p_l$, p_u is the pressure on the upper surface, p_l the pressure on the lower surface, and S the wing area.

For a unit depth of span,

$$N = -\int \Delta p \; dc$$
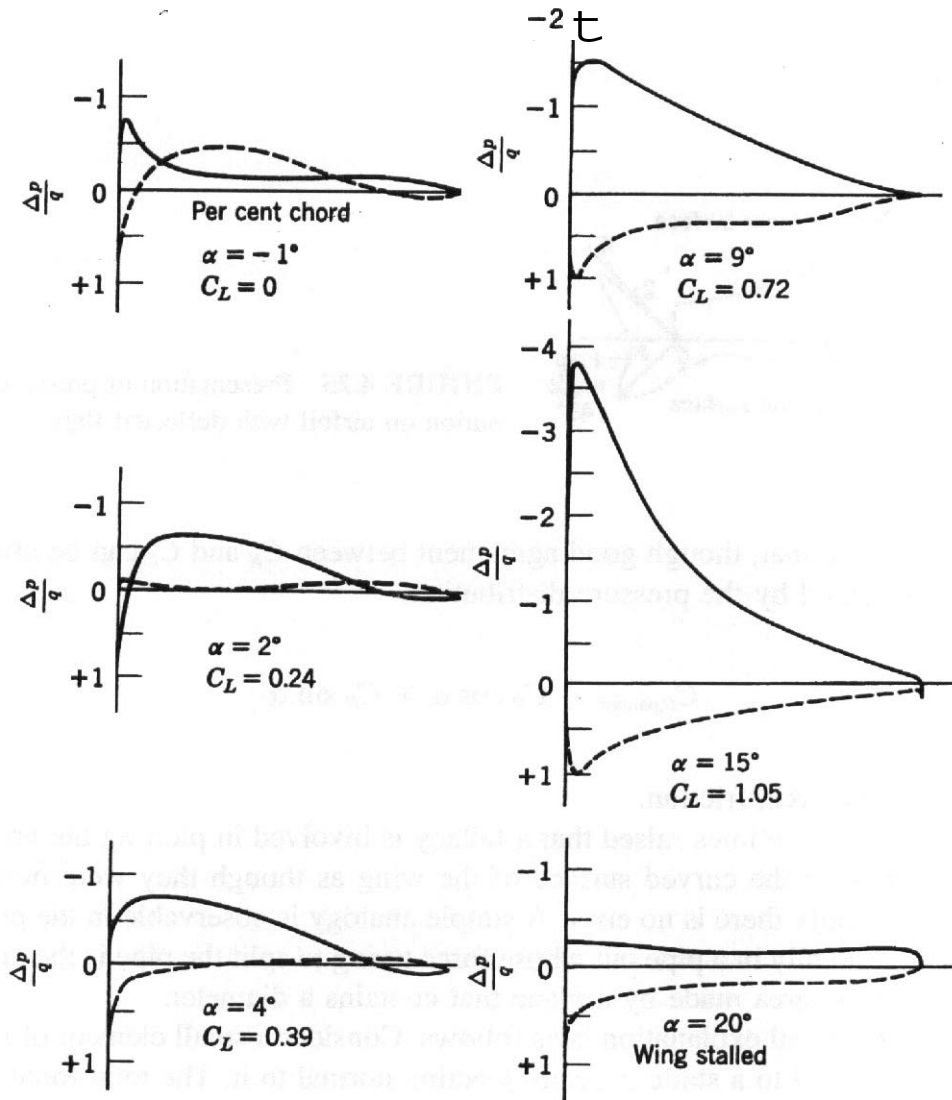
FIGURE 4.24   Growth of static pressure distribution with angle of attack for a typical airfoil.

where c is the wing chord. By definition, $N = (p/2)SV^2 C_N$, and hence

$$C_N = \frac{N}{qc} = -\frac{1}{c}\int \frac{\Delta p}{q} dc \qquad (4.37)$$

It follows that the pressures may be plotted in units of dynamic pressure against their respective locations on the chord. Furthermore, the area under such a curve divided by the chord is the normal force coefficient, and the moment of area about the leading edge divided by the area is the center of pressure.

When a trailing-edge flap is lowered, it is customary to show the flap pressures normal to the flap chord in its down position (see Figure 4.25). To find the total C_N due to the main wing and flap, we have

$$C_N = C_{N,\text{wing}} + C_{N,\text{flap}} \cos \delta_F \qquad (4.38)$$

where δ_F is the flap angle.
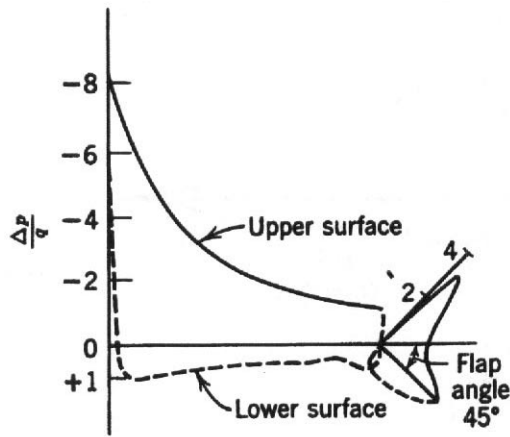
FIGURE 4.25   Presentation of pressure distribution on airfoil with deflected flap.

It is reiterated that, though good agreement between C_N and C_L can be obtained, the drag measured by the pressure distribution,

$$C_{D,\text{pressure}} = C_C \cos a + C_N \sin a \qquad (4.39)$$

does not include skin friction.

The point is sometimes raised that a fallacy is involved in plotting the pressures that act normal to the curved surface of the wing as though they were normal to the chord. Actually there is no error. A simple analogy is observable in the pressure that is acting radially in a pipe but whose force trying to split the pipe is the pressure times the section area made by a plane that contains a diameter.

The mathematical explanation is as follows. Consider a small element of surface **ds** that is subjected to a static pressure p acting normal to it. The total force on the element is $p\,ds$, directed along p, and the component of this force normal to the wing chord line is $p\,ds \cos a$. *(See* Figure 4.26.) But $ds \cos a = dc$, where dc is a short length of the chord, so that the total force normal to the wing chord line is $N = \int \Delta p\,dc$.

It will be noted in Figure 4.24 that a maximum stagnation pressure of $\Delta p/q = +1.0$ is usually developed near the leading edge of a wing. This may be accepted as the rule for section tests, but swept-back panels will show less than $\Delta p/q = +1.0$ at all stations except at the plane of symmetry.
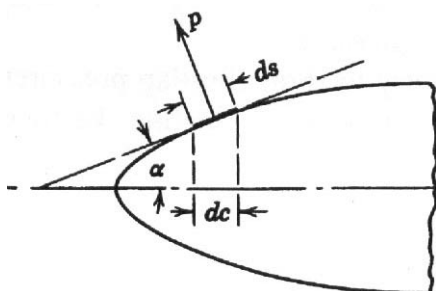
FIGURE 4.26   Pressure projection on an inclined surface.

The pitching mbment can also be obtained from the chordwise pressures by use of

$$C_{M_{LE}} = \frac{1}{C} \int \frac{\Delta P}{q}(x) \, dc \qquad (4.40)$$

where x is the distance from the leading edge to the AP.

(See Chapters 9 and 10 on data reduction of pressure data with blockage corrections for dynamic pressure and wall corrections for α.)

Since a laser can measure velocity, it is possible to measure the two-dimensional lift coefficient with a laser by using the relation between lift and circulation. This can be done on a three-dimensional wing as well by measuring the velocity around a closed path that encircles the wing (a line integral). The circulation Γ is given as

$$\Gamma = \oint_A^B V \, ds \qquad (4.41)$$

The Kutta–Joukowski theorem states that

$$\frac{L}{b} = \rho V \Gamma \qquad (4.42)$$

Thus the lift per unit span or the two-dimensional lift can be determined and easily converted to a two-dimensional lift coefficient. This method gives no information about the chordwise distribution of pressure.

This method can, however, be used to determine the distribution to the spanwise lift distribution of a wing caused by the tunnel walls in a three-dimensional test. The tunnel measured c_1 can be compared to the calculated values by a vortex lattice or other methods. Such information might be desired in the following circumstances. As stated in Chapter 6, the maximum model span should be about 0.8 times the tunnel width. Over the life, many aircraft are stretched and their gross weight increases, as does the wing loading. At some point it may be necessary to increase the wing area. This can be accomplished by extending the wing tips. If the original model's wing span was close to maximum, the span will now be too large. The tunnel walls induce an upwash at the wing that distorts the model span load and can distort the wing's stall near the tip. The method outlined can be used to check this distortion. If the tip stall pattern is greatly distorted, it may be necessary to build a new model.

Positioning Systems

The execution of aerodynamic experiments often requires the design and construction of equipment to accurately position either instrumentation or the test article. Engineers who work in aerodynamic laboratories must become knowledgeable about many aspects of mechanical design and electromechanical motion control. We cannot

provide details of such information here, but it is an area of great importance to successful aerodynamic experiments. The sets of measurements of surface stress, fluid velocity, fluid pressure, and the like are finite in number and may be distributed in various ways on the surfaces or within the fluid volume of the test area. In some cases interpretations are made in terms of the collection of point data, but often integrations over surfaces or volumes or both are performed as indicated in the preceding sections in order to extract desired information from the data. The accuracy of the outcomes of the integrations obviously depends directly on the accuracy of the position data.

REFERENCES AND NOTES

1. The terms *pressure* and *static pressure* are used interchangeably. They imply the pressure in a reference frame in which the mean molecular velocity is zero. *Temperature* and *static temperature* are similarly used. Additional detail in the definition is required if one considers the variation in dynamic pressure for parcels of fluid small enough to be participating in "turbulent" fluctuations but large compared to molecular dimensions.

2. Benedict, R. P., *Fundamentals of Temperature, Pressure, and Flow Measurements*, 3rd ed., John Wiley & Sons, New York, 1984.

3. Bray, A., Barbato, G., and Levi, R., *Theory and Practice of Force Measurement*, Academic, London, 1990.

4. Jones, F. E., *Flow Measurement*, CRC Press, Boca Raton, FL, 1995.

5. Brombacher, W. G., "Survey of Micromanometers," NBS Monogram 114, 1970.

6. Adam, N. K., The *Physics and Chemistry of Surfaces*, Dover, New York, 1984, p. 185.

7. Soloukhin, R. I., Curtis, C. W., and Emrich, R. J., "Measurement of Pressure," in *Methods of Experimental Physics*, Vol. 18, Part B, Academic Press, New York, 1981, Chapter 5.

8. The unit shown in Figure 4.2 was constructed by William Sekscienski, Project Engineer at the Glenn L. Martin wind tunnel.

9. The unit shown in Figure 4.3 was designed by Dr. Allen Winkelmann of the Aerospace Engineering Department at the University of Maryland.

10. Smith, A. M. O., and Murphy, J. S., "Micromanometer for Measuring Boundary Layer Profiles," *Rev. Sci. Instrum.*, 26(8), 775–781, 1955.

11. Holley, W. L., and Bannister, J. R., *J. Ind. Aerodyn.*, 1, 139–165, 1975.

12. Blake, W. K., "Differential Pressure Measurement," in Goldstein, R. J., Ed., *Fluid Mechanics Measurements*, Hemisphere, Washington, D.C., 1983, Chapter 3.

13. Crites, R. C., and Benne, M. E., "Emerging Technology for Pressure Measurement: Pressure Sensitive Paint," AIAA Paper 95-0106, presented at the Thirty-Third Aerospace Sciences Meeting and Exhibit, Reno, NV, Jan. 9–12, 1995.

14. Carroll, B. F., Abbitt, J. D., Lukas, E. W., and Moms, M. J., "Step Response of Pressure Sensitive Paint," *AIAA J.*, 34(3), 521–526, 1996.

15. Baron, A. E., Danielson, D. S., Gourterman, A. M., Wan, J. R., Callis, J. B., and McLachlan, B., "Submillisecond Response Times of Oxygen-Quenched Luminescent Coatings," *Rev. Sci. Instrum.*, 64(12), 3394–3402, 1993.

16. Davies, A. G., Bedwell, D., Dunleavy, M., and Brownjohn, N., "Recent Developments in Pressure Sensitive Paint Measurements Using the BAe System," Paper 28, in Proceed-

ings of Wind Tunnels and Wind Tunnel Test Techniques, Royal Aeronautical Establishment, Apr. 1997.

17. Randers-Pehrson, N. H., "Pioneer Wind Tunnels," *Smithsonian Miscellaneous Collections,* **93**(4), 1935.

18. Kiel, G., "A Total-Head Meter with Small Sensitivity to Yaw," NACA TM 775, 1935.

19. Emrich, R. J., "Probe Methods for Velocity Measurement," in *Methods of Experimental Physics,* Vol. 18, Part A, *Fluid Dynamics,* Academic, New York, 1981.

20. Barker, A., *Proc. Roy. Soc. Lond., 101,* 435, 1922.

21. Spaulding, E. R., and Merriam, K. G., "Comparative Tests of Pitot-Static Tubes," NACA TN 546, 1935.

22. Milne-Thomson, L. M., *Theoretical Hydrodynamics,* Dover, Mineola, 1996, Section 16.30, p. 489.

23. Gupta, M., "Comparative Study of the Spherical and Conical Head Pressure Probes for Use in Three Dimensional Flows," M.S. thesis, Department of Aerospace Engineering, University of Maryland, 1989.

24. Gallington, R. W., "Measurements of Very Large Flow Angles with Non-Nulling Seven Hole Probes," *Aeronautics Digest,* USAFA-TR-80-17, Spring/Summer 1980.

25. Gemer, A. A., Mauren, C. L., and Gallington, R. W., "Non-Nulling Seven-Hole Probes for High Angle Flow Measurement," *Exper. Fluids,* 2, 95–103, 1984.

26. Cogotti, A., "Flow-Field Surveys Behind Three Squareback Car Models Using a New Fourteen Hole Probe," SAE Paper 870243, 1987.

27. Yamaguchi, I., Takagi, M., Kurishima, K., and Mori, T., "Measurement of Wake Flow Fields, Including Reverse Flow, of Scale Vehicle Models Using a New 13-Hole Pitot Tube," SAE Paper 960676, in Vehicle Aerodynamics, SAE Paper SP-1145.

28. Kinser, E., and Rediniotis, O., "Development of a Nearly Omnidirectional Three Component Velocity Measurement Pressure Probe," AIAA Paper 96-0037, presented at the AIAA Aerospace Sciences Meeting, Reno, NV, Jan. 1996.

29. Luchuk, W., Anderson, C. F., & Homan, M. L., "1981 Calibration of the AEDC-PWT Aerodynamic Wind Tunnel (4T) at Mach Numbers from 0.1 to 1.3," Arnold Engineering Development Center, TR 82-10, 1982.

30. Bruun, H. H., *Hot Wire Anemometry, Principles and Signal Analysis,* Oxford University Press, Oxford, 1995.

31. Krause, L. N., "Effects of Pressure Rake Design Parameters on Static Pressure Measurements for Rakes Used in Subsonic Free Jets," NACA TN 2520, 1951.

32. Silverstein, A., "Determination of Boundary-Layer Transition on Three Symmetrical Airfoils in the NACA Full Scale Wind Tunnel," NACA TR 637, 1939.

33. Brune, G. W., Sikavi, D. A., Tran, E. T., and Doerzbacher, R. P., "Boundary Layer Instrumentation for High Lift Airfoil Models," AIAA Paper 82-0592, presented at the Twelfth Aerodynamic Testing Conference, Williamsburg, VA, March 1982, pp. 158–165.

34. Preston, J. H., "The Determination of Turbulent Skin Friction by Means of Pitot Tubes," *J. Roy. Aeronaut. Soc., 58,* 109–121, 1954.

35. Patel, V. C., "Calibration of the Preston Tube and Limitations on Its Use in Pressure Gradients," *J. Fluid Mech.,* 23, 288–330, 1969.

36. Quarmby, A., and Das, H. K., "Measurement of Skin Friction Using a Rectangular Mouthed Preston Tube," *J. Roy. Aeronaut. Soc., 73,* 288–330, 1969.

37. Quarmby, A., and Das, H. K., "Displacement Effects on Pitot Tubes with Rectangular Mouths," *Aeronaut. Quart.,* 20, 129–139, May 1969.

38. MacMillan, F. A., "Experiments on Pitot Tubes in Shear How," ARC R&M 3028, 1957.

39. MacMillan, J. M., "Evaluation of Compressible Flow Preston Tube Calibrations," NASA TN D-7190, 1973.

40. Allen, J. M., "Reevaluation of Compressible Flow Preston Tube Calibrations," NASA TM X-3488, 1977.

41. Holmes, B. J., and Obara, C. J., "Advances in Flow Visualization Using Liquid Crystal Coatings," Society of Automotive Engineers, SAE Paper 871017, General Aviation Aircraft Meeting and Exposition, Wichita, KS, Apr. 1987.

42. Reda, D. C., and Muratore, J. J., Jr., "Measurement of Surface Shear Stress Vectors Using Liquid Crystal Coatings," *AIAA J.,* 32(8), 1576–1582, 1994.

43. Reda, D. C., Wilder, M. C., Farina, D. J., Zilliac, G., McCabe, R. K., Lehman, J. R., Hu, K. C., Whitney, D. J., and Deardorff, D. G., "Areal Measurements of Surface Shear Stress Vector Distributions Using Liquid Crystal Coatings," AIAA Paper 96-0420, presented at the Thirty-Fourth Aerospace Sciences Meeting, Reno, NV, Jan. 1996.

44. Reda, D. C., "Methods for Determining Shear Direction Using Liquid Crystal Coatings," U.S. Patent No. 5,394,752, March 7, 1995.

45. Reda, D. C., "Method for Measuring Surface Shear Stress Magnitude and Direction Using Liquid Crystal Coatings," U.S. Patent No. 5,438,879, Aug. 8, 1995.

46. Reda, D. C., Wilder, M. C., and Crowder, J. P., "Simultaneous Full Surface Visualizations of Transition and Separation Using Liquid Crystal Coatings," AIAA Paper 96-2182, presented at the Nineteenth AIAA Advanced Measurement and Ground Testing Technology Conference, New Orleans, LA, June 1996.

47. Jones, B. M., "Measurement of Profile Drag by the Pitot-Traverse Method," ARC R&M 1688, 1936.

48. Bicknell, J., "Determination of the Profile Drag of an Airplane Wing in Flight at High Reynolds Numbers," NACA TR 667, 1939.

49. Silverstein, A., "A Simple Method for Determining Wing Profile Drag in Flight," *J. Aeronaut. Sci., 7,* 295–301, May 1940.

50. Brune, G. W., Sikavi, D. A., Tran, E. T., and Doerzbacher, R. P., "Boundary Layer Instrumentation for High-Lift Airfoil Models," AIAA Paper 82-0592, presented at the Twelfth Aerodynamic Testing Conference, Williamsburg, VA, 1982, p. 161.

51. Mueller, T. J., and Jansen, B. S., Jr., "Aerodynamic Measurements at Low Reynolds Number," AIAA Paper 82-0598, presented at the Twelfth Aerodynamic Testing Conference, Williamsburg, VA, 1982.

52. Althaus, D., "Drag Measurement on Airfoils," Organization Scientifique et Technique du Vol à Voile Congress, Paderborn, West Germany, 1981.

53. Hackett, J. H., "Effects of Moving Ground on Automobile Drag Measurement5 from Balance and from Wake Measurements," SAE Paper 850280, SAE International Congress, Detroit, 1985.

5 Flow Visualization

It is difficult to exaggerate the value of flow visualization. A reasonable mental image of a flow about a body is almost always necessary for a person to have a useful understanding of an aerodynamic or hydrodynamic problem. This is true whether the approach is strictly theoretical, mainly experimental, mainly computational, or some combination as is always the most effective. The ability to see flow patterns on and around a device under investigation often gives insight into a solution to an aerodynamic problem. This sometimes happens when the pattern of flow exhibited by the experiment or produced by a computation is in some significant way different from the mental image that the aerodynamicist had formulated. Or, perhaps, the aerodynamicist realized there were two or more possibilities and the experimental evidence resolved the uncertainty. **An** important reason for the wide appreciation of computational fluid dynamics is that the processes required to reach any solution, whether or not it is consistent with physical reality, also strongly support very visual presentations of very detailed results. These visual representations of detailed data sets **are** very memorable, as are many types of flow visualizations in physical experiments, and both are thereby quite useful for similar reasons.

In this chapter we will focus first on some relationships between the so-called primitive variables that describe a flow and quantities that have been found to be useful in visualization of the phenomena. We will then focus on physical flow visualization, which we have termed *direct visualization* as distinct from the newer *numericaljlow visualization,* which is also very important and which we will also discuss. Note that numerical flow visualization is frequently based on data obtained from experiment as well as from computations.

The equations of aerodynamics were presented in Chapter 1, and a list of functions was given that, if known, would constitute a complete mathematical specification of the flow in the domain of the known functions. For convenience we repeat these here in dimensional form. Equations (5.1)–(5.3) represent what **are** sometimes termed the "primitive variables" for a flow. The variables are velocity, a vector; pressure, a scalar; and temperature, a scalar. All are generally functions of a three-component position vector and time:

$$\mathbf{V}(\mathbf{r},\, t) = \begin{bmatrix} u(\mathbf{r},\, t) \\ v(\mathbf{r},\, t) \\ w(\mathbf{r},\, t) \end{bmatrix} \tag{5.1}$$

$$p = p(\mathbf{r},\, t) \tag{5.2}$$

$$T = T(\mathbf{r},\, t) \tag{5.3}$$

This is an Eulerian description of the flow. In addition to the primitive variables there are many derived variables that are frequently useful. Examples are "total pressure," density, vorticity, and **helicity** density. None of these flow variables are immediately evident as one experiences a flow of air, water, or other fluid. In Chapter 4 we have already discussed means of measuring certain quantities. Here, we are interested in how to "see" these and other useful functions in ways to help us "understand" the flow fields (or functions) for the purpose of evaluating the performance of vehicles and other devices, including incidentally the wind tunnel itself.

An alternative means of describing a flow is to "tag" each particle according to its position at some time and provide the variables for each particle as a function of time. This can be represented by Equations (5.4)–(5.6). There is no immediate way to know the properties at a particular point in space except at the key time t_0. This is termed a Lagrangian description of the flow':

$$\mathbf{V}(\mathbf{r}_0, t_0, t) = \begin{bmatrix} u(\mathbf{r}_0, t_0, t) \\ v(\mathbf{r}_0, t_0, t) \\ w(\mathbf{r}_0, t_0, t) \end{bmatrix} \qquad (5.4)$$

$$p = p(\mathbf{r}_0, t_0, t) \qquad (5.5)$$

$$T = T(\mathbf{r}_0, t_0, t) \qquad (5.6)$$

Classic flow visualization for low-speed flows is done by putting something that is visible into the flow at convenient locations and watching how the something, called a tracer, moves. The flow is inferred by the motion of the tracer. Tracer methods are the oldest and most commonly applied means of flow visualization. It seems likely that every human being has seen naturally occurring smoke or cloud formations being convected by movement of air and thereby conveying information about the motion of the air. We must, however, take care to relate how these "pictures" imprinted on our consciousness are related to our mathematical equations, which we use to quantify flow phenomena. In addition, it is necessary to investigate to what degree various sizes and types of tracer particles actually follow the flow. This question is addressed in detail by Somerscales.[2]

5.1 PATH-, STREAK-, STREAM-, AND TIMELINES

For the moment, assume that it is possible to put "tracer" particles into the flow at any desired location and that these particles are then convected perfectly along with the flow, or that we simply have the capability to "see" any small element in the flow that we choose. We have the following definitions.

Pathline

The path of a point or particle convected with the flow is called a pathline. If we could release a tracer particle at any selected point and record its subsequent path,

this would be a pathline. If we knew the functions indicated by (5.4), we could construct pathlines by the parametric relations

$$x(\mathbf{r}_0, t_0, t) = \int_{t_0}^{t} u(\mathbf{r}_0, t_0, t) \, dt + x_0$$

$$y(\mathbf{r}_0, t_0, t) = \int_{t_0}^{t} v(\mathbf{r}_0, t_0, t) \, dt + y_0 \qquad (5.7)$$

$$z(\mathbf{r}_0, t_0, t) = \int_{t_0}^{t} w(\mathbf{r}_0, t_0, t) \, dt + z_0$$

Approximations to pathlines can be obtained by releasing neutrally buoyant helium-filled soap bubbles into an air flow and taking "long" exposure photographs. In water flow facilities, the hydrogen bubble technique gives a similar but more robust result.

Streakline

Now consider the case of injecting tracer material continuously at a point in the flow. There are now many tracer particles being convected by the flow, each of which passed through a particular point in space but at different instants of time. A parametric representation of streaklines can be obtained in principle in a manner similar to (5.7):

$$x(\mathbf{r}_0, \tau, t) = \int_{(\tau < t)}^{t} u(\mathbf{r}_0, \tau, t) \, dt + x_0$$

$$y(\mathbf{r}_0, \tau, t) = \int_{(\tau < t)}^{t} v(\mathbf{r}_0, \tau, t) \, dt + y_0 \qquad (5.8)$$

$$z(\mathbf{r}_0, \tau, t) = \int_{(\tau < t)}^{t} w(\mathbf{r}_0, \tau, t) \, dt + z_0$$

A streakline is obtained by letting τ vary with t and holding $\mathbf{r}_0$ constant. The plume from a smoke source held in one place and constantly emitting provides an approximation to a streakline.

Streamline

A streamline through a point at an instant in time is the line whose tangent is the velocity at that point and that follows a path through the fluid such that the tangent at every point is the local instantaneous velocity. The mathematical construction of

a streamline is obtained from the Eulerian relations (5.1) by integrating the coupled system (5.9). Note that this produces a time-dependent result if the flow field varies with time:

$$\frac{dy}{dx} = \frac{v(\mathbf{r}, t)}{u(\mathbf{r}, t)} \qquad \frac{dz}{dx} = \frac{w(\mathbf{r}, t)}{u(\mathbf{r}, t)} \tag{5.9}$$

The streamline, streakline, and pathline through a point are coincident if the flow field is steady. This must be kept in mind when unsteady phenomena are under investigation. A direct method of producing a visualization of streamlines in an unsteady flow is not available.

Timeline

A timeline is generated by simultaneously emitting a short burst of tracers along a line perpendicular to the local flow. This marks a line of elements that are in a straight line at the initial time. The deformation of this line as the tracers are convected provides an indication of the velocity profile along the line. A mathematical construction of a timeline can be obtained by another modification of the Lagrangian expressions (5.7). The result is (5.10). This shows that a timeline is obtained by connecting the end points of a family of pathlines whose beginnings are along a line specified by choosing ρ to vary along a straight line:

$$x(\boldsymbol{\rho}, t_0, t) = \int_{t_0}^{t} u(\boldsymbol{\rho}, t_0, t) \, dt + x_0$$

$$y(\boldsymbol{\rho}, t_0, t) = \int_{t_0}^{t} v(\boldsymbol{\rho}, t_0, t) \, dt + y_0 \tag{5.10}$$

$$z(\boldsymbol{\rho}, t_0, t) = \int_{t_0}^{t} w(\boldsymbol{\rho}, t_0, t) \, dt + z_0$$

Timelines are rarely produced directly in air, although the hydrogen bubble technique can be used to do this very dramatically in water. An approximation in air could be obtained by observing the leading points of a smoke wire visualization.

5.2 DIRECT VISUALIZATION

We confine ourselves to techniques that have proved useful in low-speed flow. This excludes most optical techniques that depend on variations in index of refraction. There are some flows such as those for propellers and rotors in which the mean flow is at low Mach number but tip speeds approach sonic values for which shadow-

graph or Schlieren methods are useful. These techniques may also be useful when thermal gradients of significant magnitude are imposed on a low-speed flow. We refer the reader to literature on higher speed applications and more specialized publications for accounts of these techniques.

We consider two broad categories of flow visualization. The first is surface flow visualization and the second is flow field visualization. Strictly speaking, surface flow is also a flow field, but we will use these terms to distinguish between on-body and off-body fields. The methods considered for direct-surface flow visualization include tufts, oil flow, ink dot, china clay, and liquid crystals. The methods considered for off-body visualization include smoke injected in several ways, helium bubbles. and streamers.

Methods of Recording Direct Visualizations

There are basically four methods of recording direct visualizations. The first, historically most important but least permanent, method is for the engineer to observe with his or her eyes. Because of depth perception, one can see three-dimensional patterns and one always sees an evolution of the phenomena, not just the final average state. However, there is no direct permanent record in a form that can easily be put into a report or paper. It is possible, however, to sketch the patterns as they are observed. To do this efficiently, one needs to prepare in advance a basic drawing of the model on which streamlines or separated regions will be sketched when the tunnel is running. An advantage of doing sketches is that the mental process increases the likelihood of forming cognitive maps that capture the flow patterns. Other common methods of recording the results of flow visualizations are by film, either still or movie, by video recording using a standard VCR format, and by digital recording of digitized video, either still or movie. These methods produce a two-dimensional projection of a three-dimensional phenomenon. In principle, two or more cameras can be used to obtain multiple two-dimensional projections that contain sufficient information to reconstruct the three-dimensional image. In practice this has rarely been achieved and is not, at the present time, available for routine use. The state of the art in the needed technology indicates that such capabilities will be available in the near future. A situation in which such a system would be of great use would be when using smoke or helium bubbles to trace flow streamlines past a model. The photographic methods, while requiring more time for developing and printing, yield higher resolution. Video has the advantage of instant replay. The available resolution for video equipment is rapidly increasing and is adequate for most aerodynamic work today.

5.3 SURFACE FLOW VISUALIZATION

Information about the flow on the surface of an object being studied is usually most critical. Many times, the flow off the body is of interest primarily in order to understand the flow features on the surface. Key aspects of surface flows that may

be investigated using visualization techniques include stagnation point location, separation lines, location of boundary layer transition, characteristic unsteadiness, extent of separation zones, and types of critical points and their locations.

Tufts

The simplest and most frequently used method for surface flow visualization is to attach tufts to the surface of interest. The tufts must be of light, flexible material that will align itself with the local surface flow as a result of direct aerodynamic force. The most commonly used material is light yam with weights and lengths chosen according to model size and test speeds. Very small monofilament has also been used. There are also polyester and cotton sewing threads, such as **Clark's O.N.T.** mercerized cotton No. 60, which can be treated with a fluorescent material. The thread is a multiple-strand material and tends to unravel with time. Tufts do affect the aerodynamic forces to some extent as we will show, but there are many situations in which the method is so easy and economical that it is the first choice.

   Two basic methods of attaching tufts to a surface are by scotch tape or by glue. When tape is used, the tufts are usually made on a "tuft board." The tuft material is strung back and forth around pins, then the tape is applied to the tufts and the tuft material is cut at the edge of the tape. This gives a length of tape with tuft attached that is applied to the model (Figure 5.1). The model surface is cleaned with naphtha or other solvents to remove oil so that the tape will hold under the adverse conditions of high-speed flow.
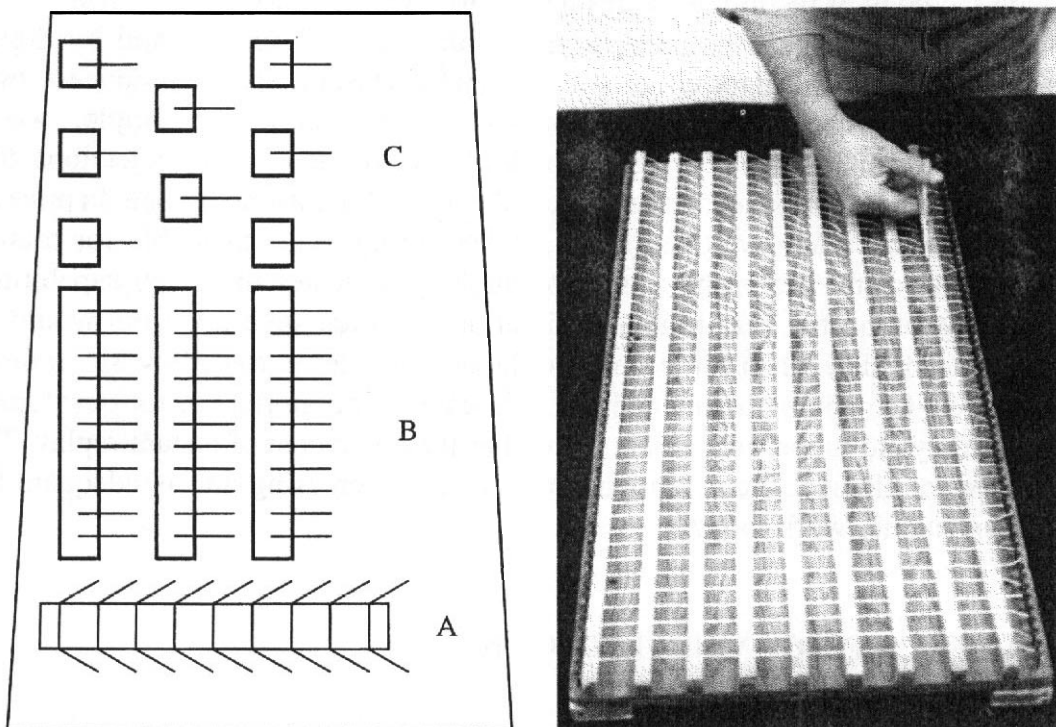
FIGURE 5.1   Methods of taping tufts to model (left figure) and a tuft board. The pattern shown as **A** is used for high-speed tests.
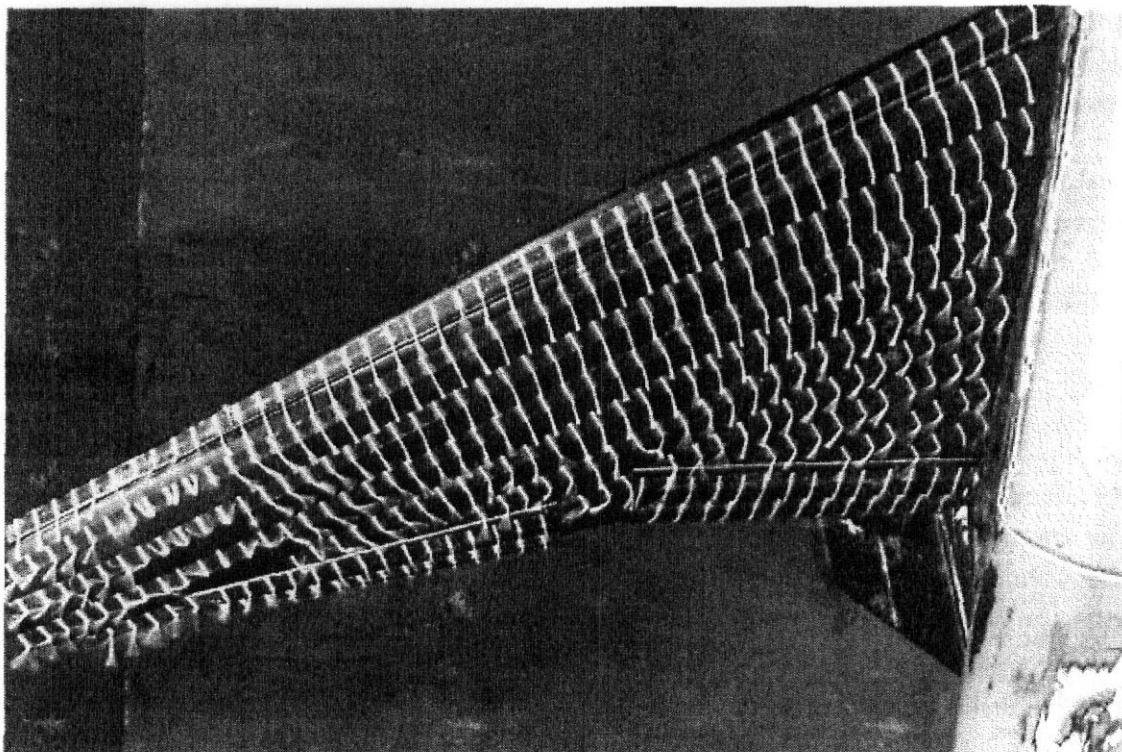
FIGURE 5.2   No. 6 floss (crochet yam), white light source; α = 27.3". Tufts taped to wing as in method B of Figure 5.1. (Photograph courtesy of University of Washington Aeronautical Laboratory.)

When tufts are glued to the model, a nitrocellulose cement such as Duco is used, thinned 50% with acetone or methyl ethyl ketone. Often 10% pigmented lacquer is added both to obscure the portion of the tuft under the glue and to make the glue dots visible by using a contrasting color. The glue dots are kept as small as possible.

Tufts readily show where flow is steady and where it is unsteady. Regions of complete separation and buffeting flow are readily identified. The resolution of the determination is of the order of the spacing of the tufts. The possibility of significant influence of the tufts themselves on the flow is very high and must always be kept in mind. This can be investigated by removing tufts upstream of indicated flow separation.

An example using No. 6 floss (crochet yarn) is shown in Figure 5.2.

An example using No. 60 thread tufts is shown in Figure 5.3 for a transport aircraft wing.

Minitufts

The glue technique is used for minitufts. These tufts have the least effect on the aerodynamic data and thus are often left on the model. The tuft material is monofilament nylon that has been treated with a fluorescent dye. Two sizes are used: 3 denier (diameter 0.02 mm, 0.0007 in.) and 15 denier (diameter 0.04 mm, 0.0017 in.). The dye used is Leucophor EFR liquid in a concentration of 1% in water with 2% acetic acid added. The tuft material is wound on an open wire reel and immersed
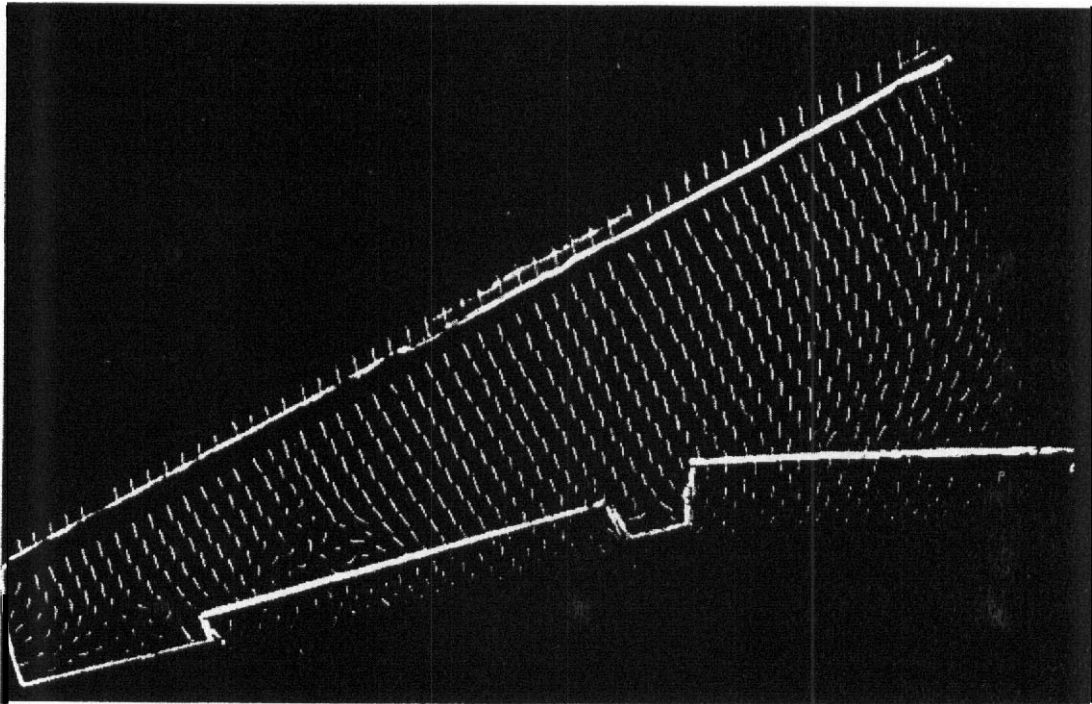
FJGURE 5.3   No. 60 thread tufts glued to wing, ultraviolet light source; $\alpha = 27.3''$. (Photograph courtesy of University of Washington Aeronautical Laboratory.)

in the dye for 15 min at 82.2°C (180°F) with frequent agitation. After drying for at least 1 hr the tuft material is wound onto small spools. During this step the material should be wiped with tissue pads to remove loose fluorescent powder that can transfer to the model surface in irregular patterns.

When gluing tufts to a model, a square grid is used (typically about 0.75 X 0.75 in.). The tuft material is taped to the wing undersurface and then wrapped around the wing in a chordwise direction. The material is in the chordwise direction on the top and moves diagonally across the wing on the bottom surface. As an alternate, the tuft material can be taped at both the leading and trailing edges. After the tuft material is applied, it is glued using a hypodermic syringe with a fine needle (a coarse needle can be partially closed with pliers). As the desired size drop of glue forms on the needle, touch it to the surface and pull away quickly. After the glue dries the tufts are cut just ahead of the glue spot of the next tuft. The model surface should be cleaned before the tufts and glue are applied using Freon or chlorinated hydrocarbons.[3] The monofilament nylon minitufts acquire static charges. These can be neutralized by the use of antistatic solutions or the antistatic material used in home dryers.

The minitufts are viewed and photographed in ultraviolet light as this is the way to make the small monofilament most visible. Threads can be similarly treated and can be photographed in either ultraviolet or white light. Minitufts provide the same type of information as larger tufts. They can provide greater resolution and have less influence on the flow.

An example of surface visualization using fluorescent minitufts is shown in Figure 5.4.
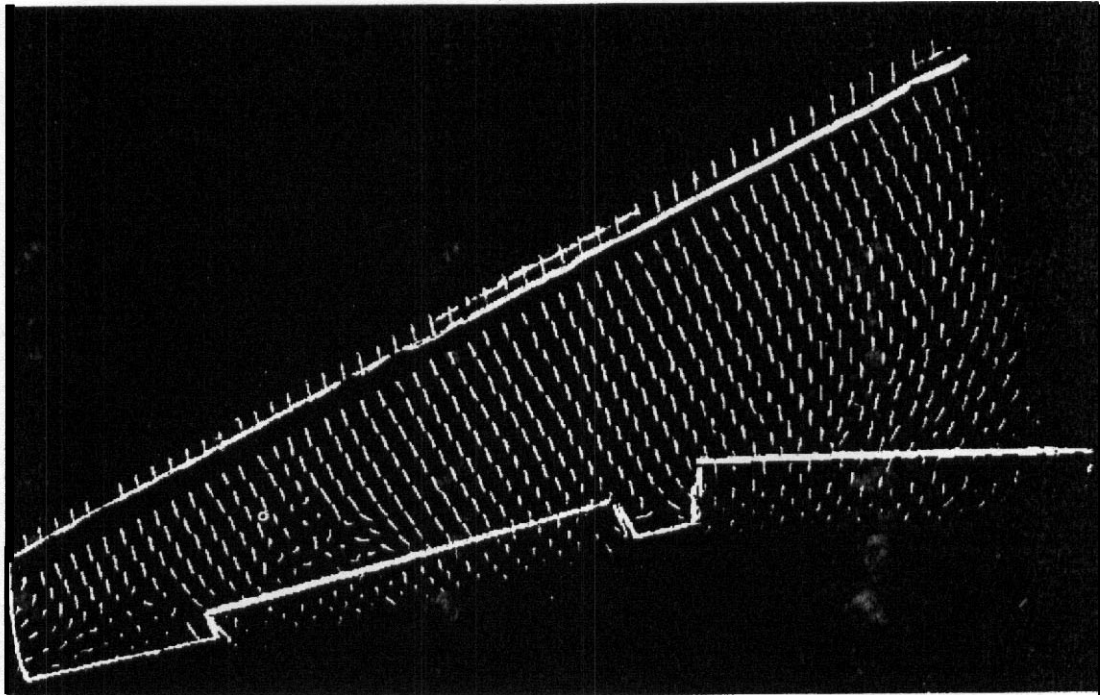
FIGURE 5.4   Fluorescent minitufts, ultraviolet light source; a = 27.3". Wing is outlined with a fluorescent felt marker pen. Compare stalled region near tip with Figures 5.3, 5.2, 5.5, and 5.8. (Photograph courtesy of University of Washington Aeronautical Laboratory.)

Oil

Oils and other viscous fluids are used to show the surface flow. The selected material is usually spread on the areas of interest with a paint brush. It will then flow under the influence of shear stress from the air stream and gravity. Since inclined surfaces are almost always of interest, the mixture needs to have viscosity sufficient so that it will not flow rapidly under the influence of gravity. The flow speed of the air must then be sufficient to impress shear stress large enough to cause the oil to flow and reveal the surface patterns within an acceptable time. This is typically of the order of 10's of seconds after the tunnel is brought to speed. It is difficult to use oil flow on vertical surfaces at air speeds less than 100 mph and 150 mph is much better. The most common material for oil flow is petroleum lubricating oils. These materials are messy to clean up afterward, both on the model and more so in the tunnel. Another material that works as well as oil when treated with a fluorescent dye is polyglycol.[4] At high C_L's or high surface velocities this material may have too low a viscosity, making it difficult to use. This material can be cleaned up with soap and hot water. When cleaning the tunnel after extensive oil flow runs, a portable set of ultraviolet fluorescent tubes is most useful. If the oil flows too slowly, it is thinned with naphtha, and if it is too thin, **60–70W** oil is added. The viscosity of the mixture is adjusted by trial and error for each application.

   The color of the oil needs to contrast with the color of the model surface. A widely used method is to add a fluorescent dye to the oil and illuminate it with ultraviolet lights, as is done for the fluorescent minitufts. In this case the model
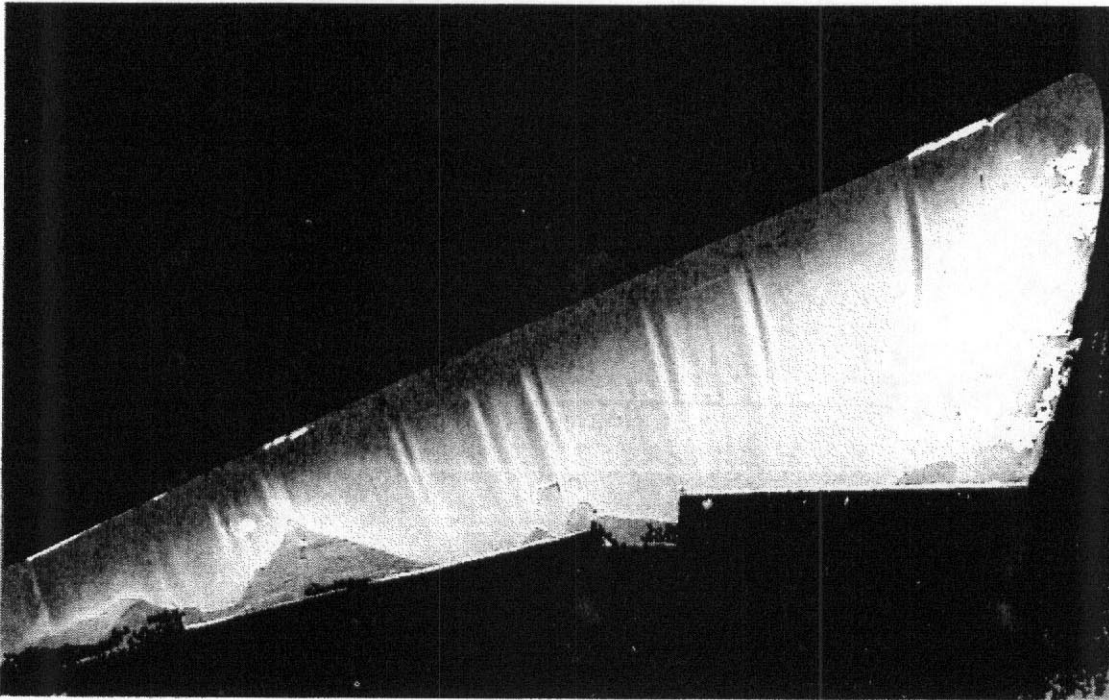
FIGURE 5.5 Oil applied at $\alpha = 0o$, tunnel started and brought close to speed, model pitched to a $= 27.3°$. (Photograph courtesy of University of Washington Aeronautical Laboratory.)

color is not too critical so long as it does not reflect strongly under the ultraviolet illumination. A light blue works very well with a dye that provides fluorescence in the yellow region of the spectrum. This is the most commonly used combination.

An example result of oil flow visualization using 40W motor oil treated with a very small amount of fluorescent dye is shown in Figure 5.5.

Oil can be made white by mixing titanium dioxide into it. This can be applied to a black model and ordinary light used for viewing and photography. This is sometimes preferable to the installation of black lights and the subsequent requirements on light management. We show two examples. Figure 5.6 shows a low-aspect-ratio wing at high angle of attack. Figure 5.7 shows the upper surface of an automobile.

Photographs can be taken after the tunnel is turned off, but the available time is short even on horizontal surfaces as the oil will flow under gravity.

China Clay

China clay is a suspension of kaolin in kerosene. The fluid is applied with a paint brush, usually with the model set at the desired attitude. The tunnel is started as quickly as possible after the model is painted. When the mixture has dried, photographs can be taken after the tunnel is shut down because the pattern does not change rapidly with time. This is similar to the Fales method with the kaolin substituted for lamp black.

An example of visualization using china clay is shown in Figure 5.8.
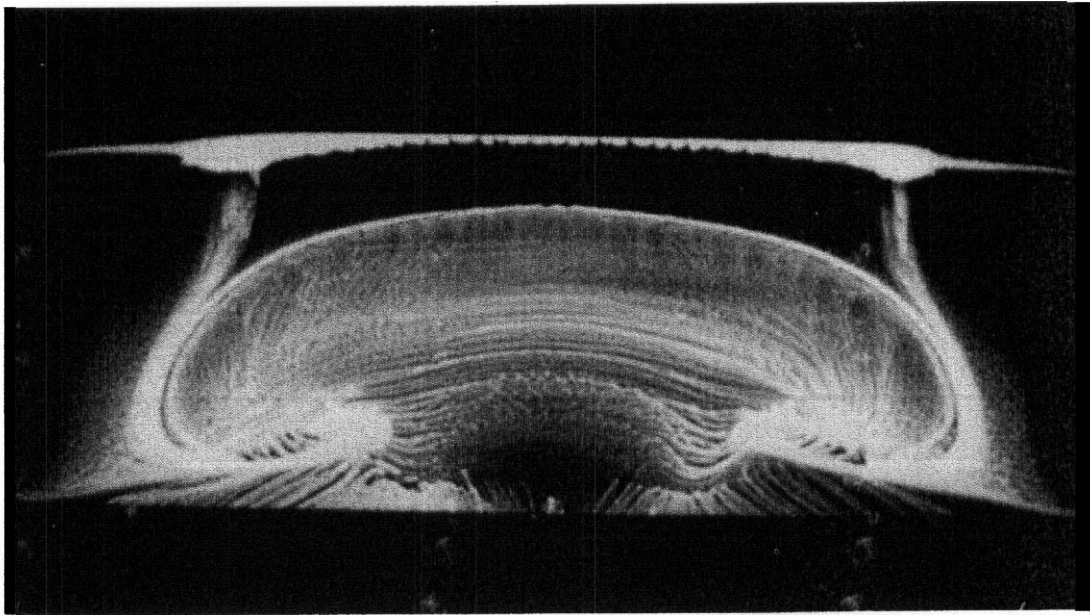
FIGURE 5.6 Oil flow on a low-aspect-ratio rectangular wing (Clark Y-14 airfoil, aspect ratio 4, $\alpha = 25.4°$, $R_{ec} = 360,000$).

Effects of Tufts, Minitufts, China Clay, and Oil

As previously mentioned tufts can affect the aerodynamic loads on a model. In Figure 5.9 a lift curve near stall shows the effects of various tufts on the data. The glued minitufts and No. 60 thread tufts consisted of about 900 tufts. The two taped tufts consisted of about 300 tufts. The data are an average of five runs for each set
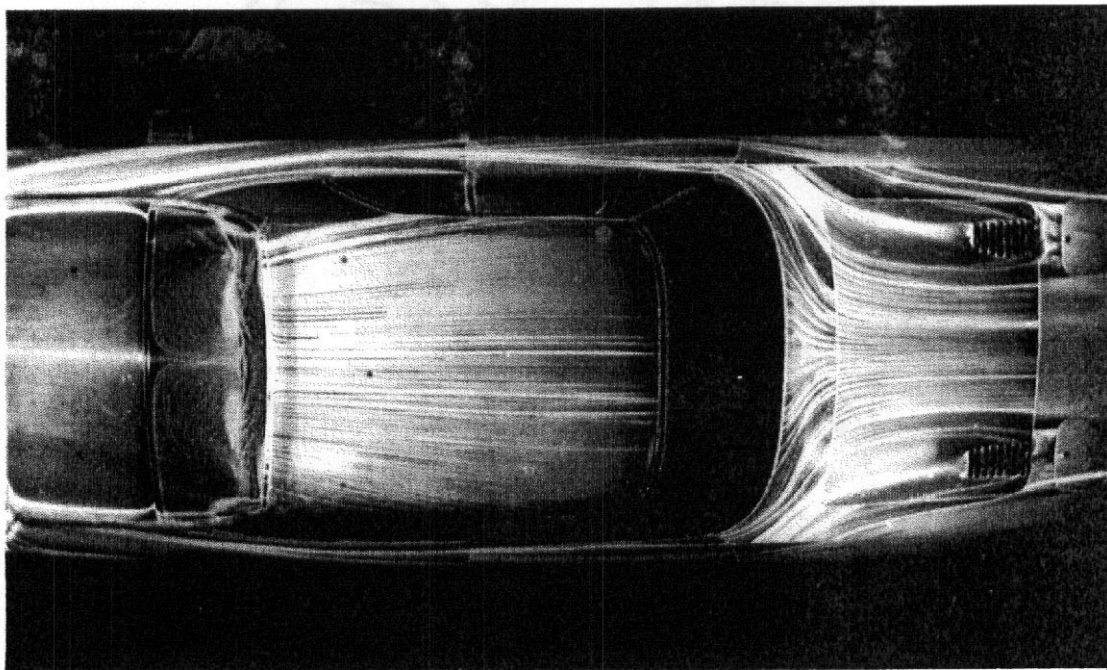
FIGURE 5.7   Oil flow on an automobile, yaw 0°.
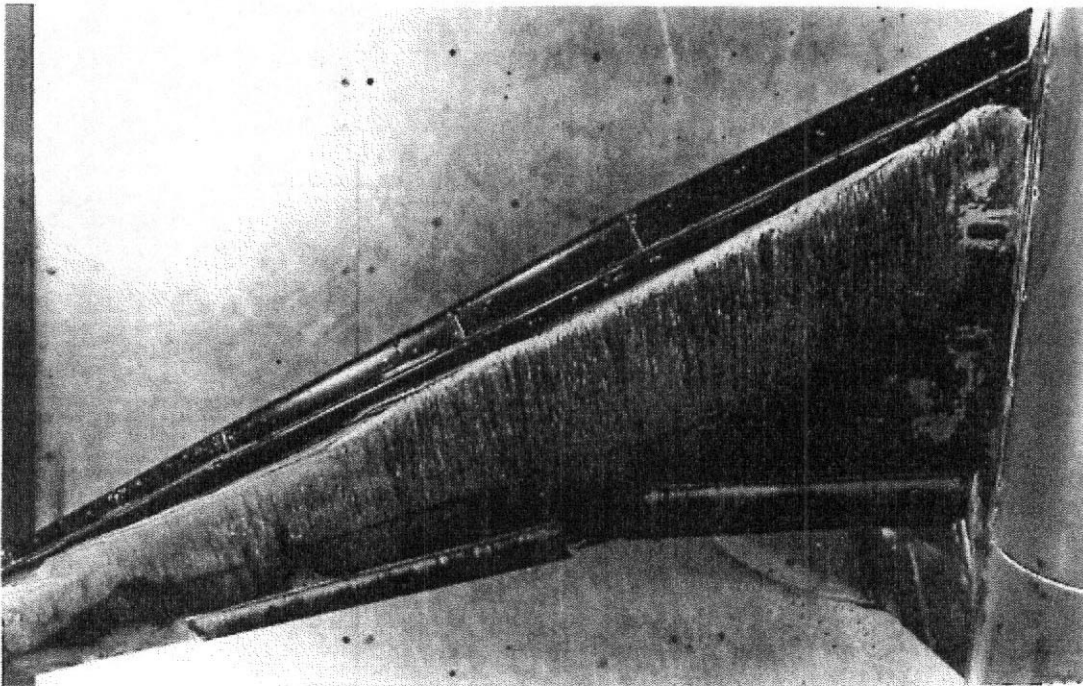
FIGURE 5.8 China clay applied at α = 0°, tunnel started and brought close to speed, model pitched to a = 27.3". (Photograph courtesy of University of Washington Aeronautical Laboratory.)
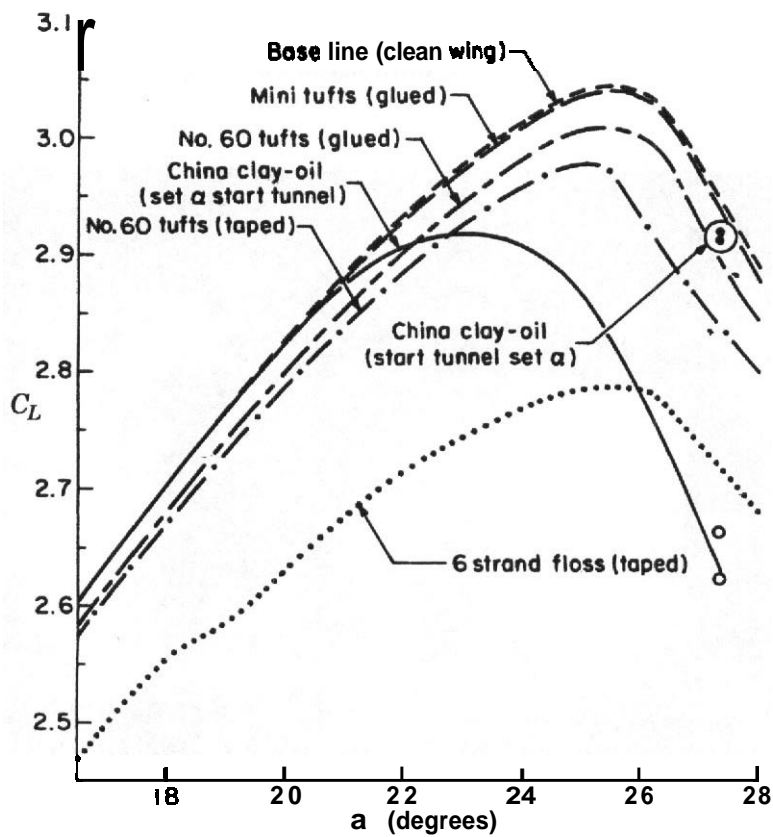
FIGURE **5.9** Effect of various tufts, china clay, and oil flow on lift curve near stall.

of tufts. The minitufts and the glued No. 60 thread have the minimum effect on lift. The effect of the tape can be seen by comparing the two sets of No. 60 thread tufts. The six-strand floss tufts are similar to the tufts made out of yam. The three different tuft types can be seen at $a = 27.3°$ in Figures 5.2–5.4.

Some Procedural Details

Correlation of Balance Data and Flow Visualization   The generally accepted practice when using the older, larger, six-strand floss for tufts is not to take balance measurements, or at least not to consider them to produce good data, when tufts are applied to the model. Figure 5.9 explains why this is the practice. Both the lift curve slope and maximum lift are greatly reduced. An advantage of minitufts is that their effect on the data is minimal; hence they can be left on the model. Oil and china clay also show minimum aerodynamic effects. During this comparison test of tufts at the model's minimum drag (a lift coefficient of about 1.0), the model drag decreased as tufts from the mini to No. 6 floss were added to the left wing with the horizontal tail on and the reverse happened with the tail off. The tufts apparently change the wing's span load distribution. However, old practices die slowly, so force data are often not taken during surface flow visualization. This, then, can lead to an improperly established flow field and the possibility of misleading flow visualization, especially near stall and, oddly enough, near minimum drag. If, however, force data are taken before and during the flow visualization run, the error may be detected and thereby possibly avoided.

Sequencing Attitude and Speed Setting   The usual procedure for china clay visualization is to set the model at the desired angle of attack and bring the tunnel up to speed. On a wing with a slotted leading-edge and/or trailing-edge flaps, this can result in erroneous aerodynamic data and flow visualization due to flow separation in the slots at low Reynolds numbers during the tunnel acceleration. This is shown by the oil flow and china clay data points beyond $a = 27.3"$ in Figure 5.9. Similar data were obtained on the clean wing. Figure 5.10 shows a china clay flow visualization for this test method. Similar results were obtained with oil flow.

Figures 5.8 and 5.5 were obtained by setting an α well below stall, starting the tunnel, and at 50–60 mph pitching the model to the desired a as the tunnel was accelerating to a dynamic pressure of 36 lb/ft^2. The force data corresponding to these figures agreed with the clean wing data and the flow is similar to Figures 5.4 and 5.3 for the minitufts and No. 60 thread tufts.

Symmetry and Hysteresis   An example of a very interesting flow phenomenon is given in Figures 5.11 and 5.12. Although it is common to assume that symmetric boundary conditions produce symmetric flows, there are many counterexamples. Any flow that includes large regions of separation may well exhibit asymmetry of the mean flow as well as asymmetry of the instantaneous flow even if the solid boundaries are sensibly symmetric. This can lead to results such as that illustrated here in which the integrated forces and moments exhibit random switching or it
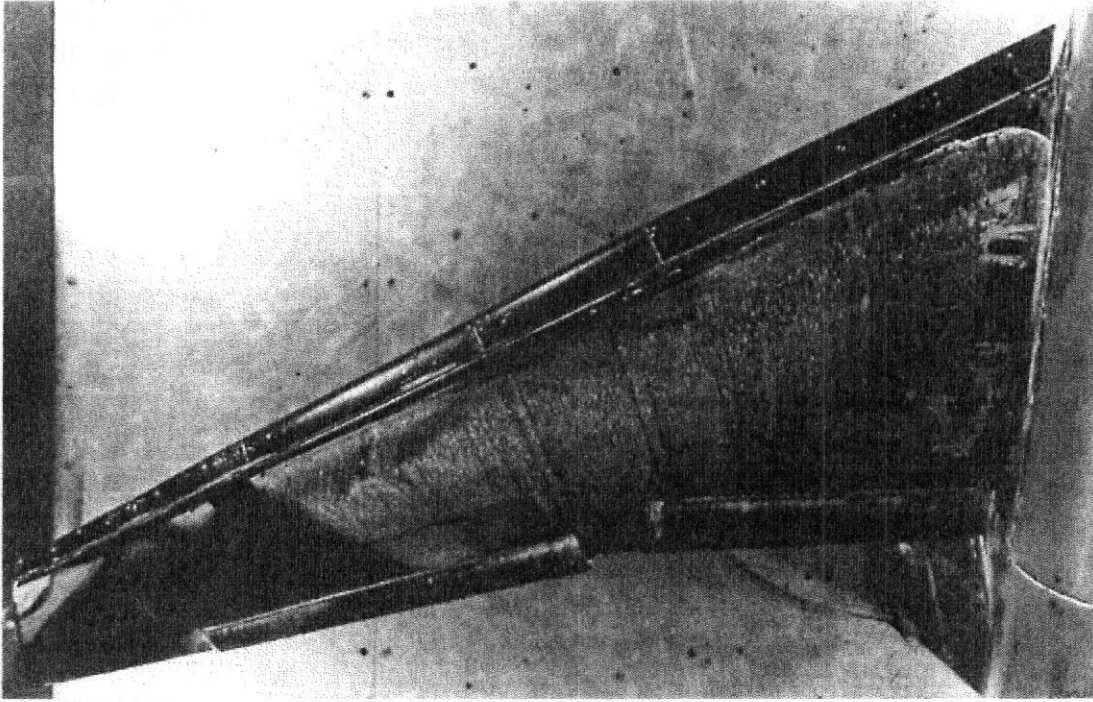
FIGURE 5.10 China clay applied at $a = 27.3°$, tunnel started and brought close to speed. Leading-edge slotted flap is stalled. Compare to Figures 5.4 and 5.8. (Photograph courtesy of University of Washington Aeronautical Laboratory.)
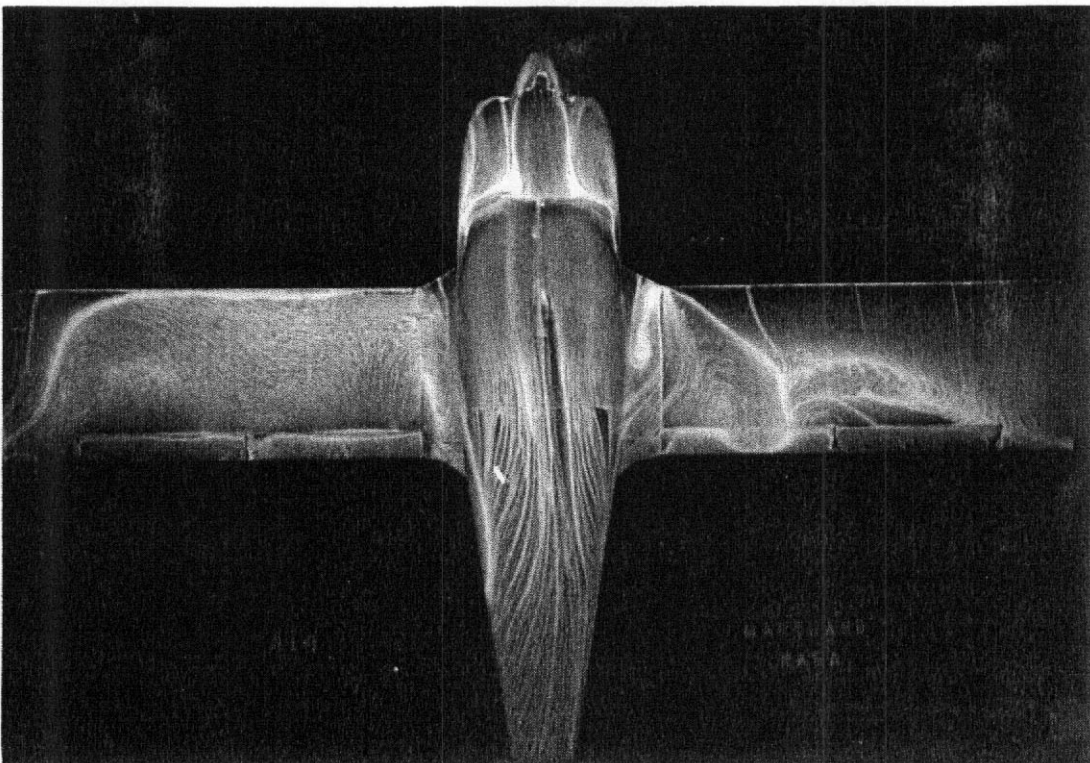
FIGURE 5.11 Oil visualization of flow on an airplane with $\alpha = 14''$ that has flow on the right wing attached and on the left wing separated.
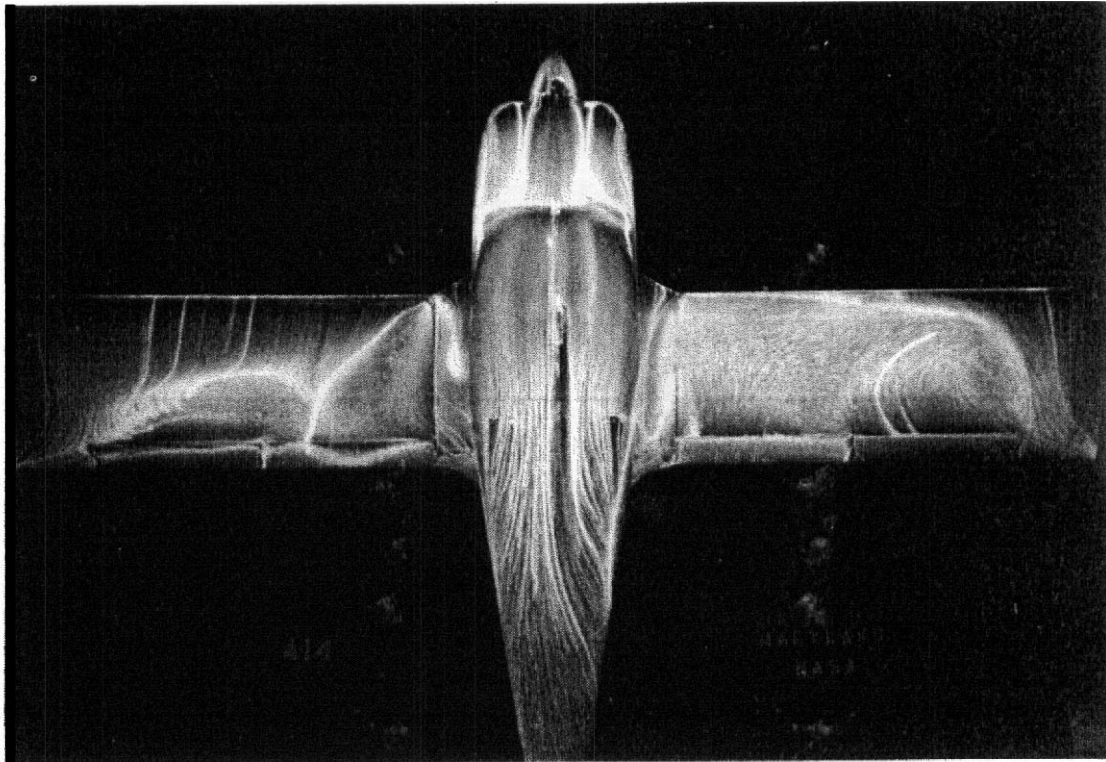
FIGURE 5.12   Here the left wing is attached and the right wing is separated. The model was not moved. The flow state alternated between the two conditions shown at random intervals in the range of a few seconds at a chord Reynolds number of about 2×10^6. This produces a very strong rolling moment that changes very abruptly and randomly.

can lead to hysteresis in which the forces and moments will be dependent on the time history of the attitude. Flow visualization methods are often important tools in identifying the flow structures associated with such events.

Flow Topology   Topological concepts are slowly gaining recognition as important to the study of complex flow phenomena such as bluff body flows and flows about wings and aircraft at high angles of attack. An early review was given by Tobak and Peake.[5] A later collection resulted from the IUTAM Symposium on Topological Fluid Mechanics.[6] The concepts are providing ways to understand the structure of flow fields and to tie the structure of a flow field to the topology of the surface flow on the test article. As oil flow techniques provide very fine detail of the surface flow, this is a preferred technique for studies of surface flow topology.

Relative Advantages of Tufts   Tufts have a great advantage in terms of productivity. Once the tufts are installed, the model can be repositioned and the indications studied visually and photographed for as long as desired. The model can then be simply moved to a new condition and the process continued. An example of a series of tuft photographs for a sequence of conditions for a powered tilt wing half model is shown in Figure 5.13.
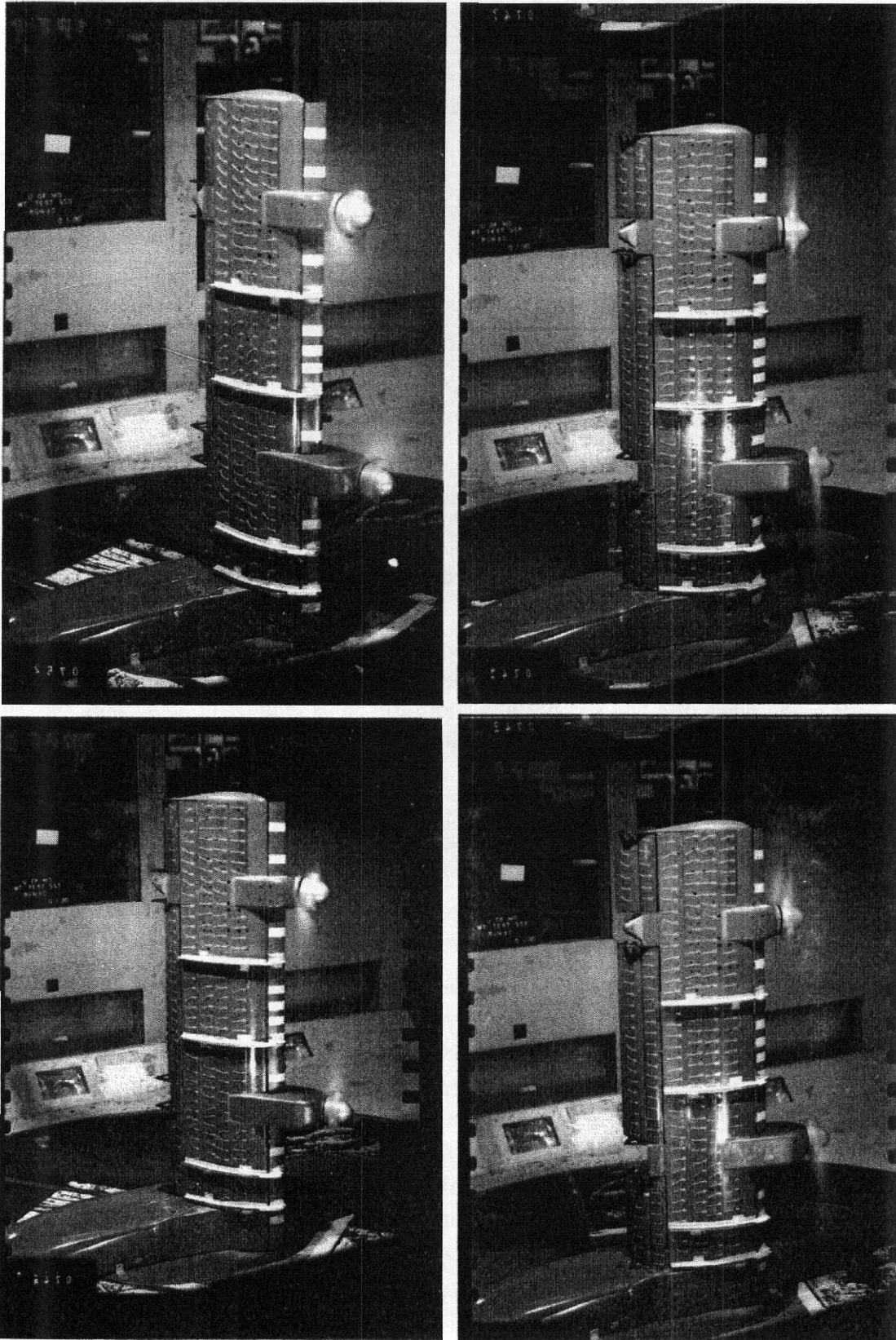
FIGURE 5.13 Visualization of flow on a powered tilt wing model in a series of conditions using tufts.

The oil and china clay methods produce patterns of limited duration in time for a single operating condition. Then the tunnel must be stopped and the material reapplied for each new condition to be visualized. Tufts are sometimes used for broad looks over a wide range of conditions with the more detailed techniques then applied for a smaller and selected set of conditions that have been found to be most critical.

Boundary Layers and Surface Shear Stress

Often the most important information being sought by flow visualization methods is a definition of the locations of transition from laminar to turbulent boundary layers and the locations of any separation regions. In the previous section, we have shown several results that illustrate separated flows. The location of transition between laminar and turbulent flow cannot be determined by tufts and is difficult with china clay. However, oil flow, sublimation methods, infrared images, and liquid crystals can be used to locate transition.

Oil Flow Detection of Transition   The basis for detecting boundary layer transition by viewing oil flow patterns is the increase in wall shear stress when a boundary layer transitions from laminar to turbulent. The result is that the oil is swept away faster in the region where the boundary layer is turbulent. Transition indicated by oil flow visualization is shown in Figure 5.14. The shear stress at the leading edge of a surface is high even under a laminar boundary layer so a typical pattern is that the oil is swept away rapidly at the leading edge with a gradual lessening of the scrubbing as the laminar layer thickens and then severe scrubbing downstream of transition. The oil pattern given by a laminar separation bubble with turbulent reattachment can be seen just downstream of the leading edge of the wing in Figure 5.6. In some cases a subcritical bump in the oil can cause a wake, which can confuse the transition location. This does not occur with sublimation.

Sublimation   In one sublimation technique a mixture of naphthalene and a carrier such as fluorine, acetone, or methyl ethyl ketone is sprayed on the model using a standard air spray gun. Note that the last two can remove many paints. The operator must wear a respirator mask when doing this. The mixture will leave the model surface white and therefore works best on a black or dark surface. The turbulent boundary layer will scrub the mixture off. A natural transition is shown on a wing using naphthalene in Figure 5.15.

Liquid Crystals   Liquid crystals that undergo changes in reflective properties as they are exposed to shear stress can be used as detectors of transition. This method has recently been developed[7] as a quantitative method as well as a method of visualization.

Infrared Thermography   The basis for this technique is that a surface at a temperature different from the tunnel stream will have faster heat transfer from the region under a turbulent boundary layer than from the region under a laminar layer. The
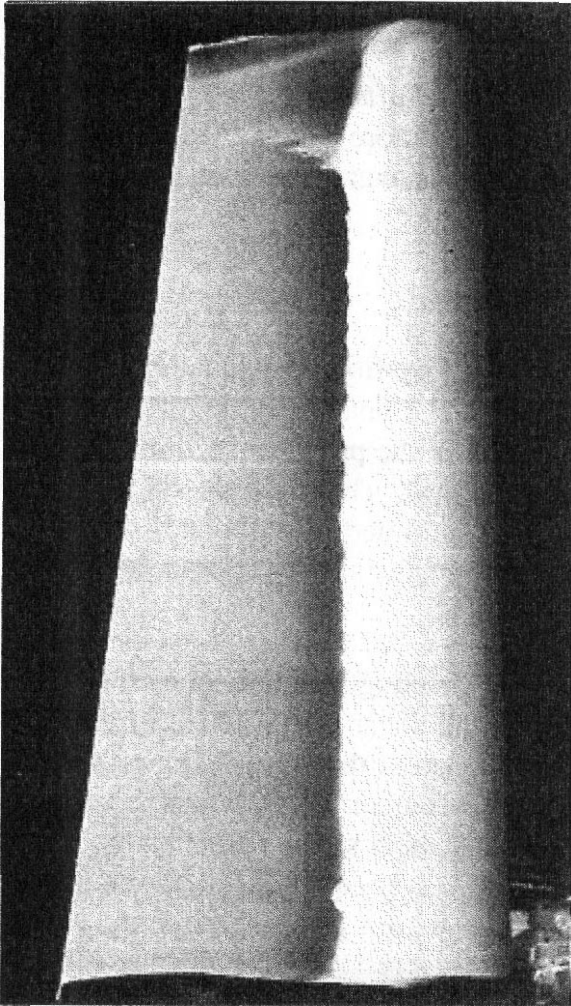
FIGURE 5.14   Oil flow visualization showing natural transition at approximately 40% chord; $C_L = 0.28$, $R_e = 1,260,000$ based on average chord. (Photograph courtesy of University of Washington Aeronautical Laboratory.)

resulting small temperature differences can be observed using commercially available infrared cameras. The results will vary with model structure and heat transfer characteristics so it is advisable to check results for a particular model type by observing artificially tripped layers. It should be kept in mind that it is the relative temperature, not the specific value of temperature, that gives the indication of transition.

Ultraviolet Fluorescence Photography

Ultraviolet fluorescence photography is used when the medium used for visualizing the flow has been treated with a dye that radiates in the visual spectrum when excited by ultraviolet light.[8] The two common caes already illustrated are the fluorescent minitufts and fluorescent oil.

The wavelength of the ultraviolet light is 320–400 mm, and it is transmitted by optical glass. There are three sources that are typically used to produce the ultraviolet light. There are special fluorescent tubes (black lights), mercury vapor lamps, and electronic photo flash units. In wind tunnel use, the first two light sources are used to enable the test engineer to observe the flow, and the flash units are used to take
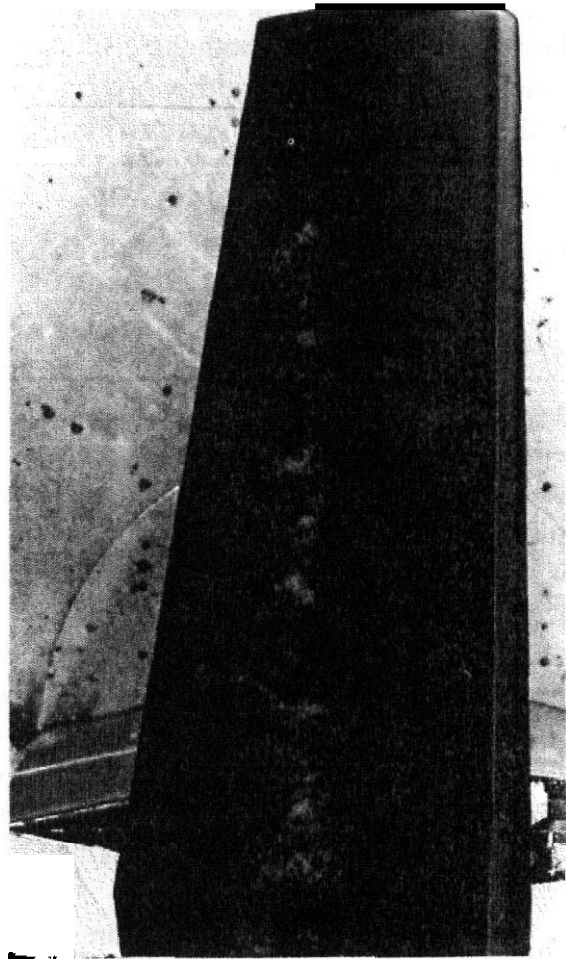
FIGURE 5.15 Naphthalene–fluorine flow visualization showing natural transition at approximately 40% chord; $C_L = 0.28$, $R_e = 1,260,000$ based on average chord. (Photograph courtesy of University of Washington Aeronautical Laboratory.)

still photographs of the flow when desired. Fluorescent tubes and mercury vapor lamps in general do not have a high enough light intensity to allow photographs without a very long exposure. Because fluorescent material emits light in the visual range, the tunnel test section must be shielded from visible light. Both the mercury vapor lamps and the flash units also emit visible light; thus they must be equipped with an exciter filter that will transmit ultraviolet light and absorb visible light. Two filters that accomplish this are Kodak Wrattan filter No. 18A or Coming Glass No. 5840.

For larger tunnels the flash lamps are usually studio units marketed for commercial photographers. The flash lamps should be able to handle 2000 W/s per flash as rated by photographers; the units come with power supplies that can store energy in capacitors and have the necessary trigger circuits. The reflectors for the flash units should be 10–14 in. in diameter to be efficient. The Coming glass exciter filter comes in 6.5-in. squares, four of which can be glued together and built into a frame to cover the reflector. As an alternative, one glass filter can be used with the flashbulb without a reflector. This would require approximately one additional f stop. For research tunnels where the camera-to-subject distances are small, standard flash units and a Wrattan 18A exciter, which can be obtained in a 3.5-in. square, can be used.

Photographic film is sensitive to blue and ultraviolet light. The light reaching the camera will contain both the visible fluorescent radiation and reflected ultraviolet radiation. To prevent the ultraviolet from exposing the film, a barrier filter is attached to the camera lens. The barrier filter can be a **Kodak** Wrattan filter No. **2A, 2B, 2C,** or **2E.** These can also be obtained in 3.0-in.-square gelatin sheets.

It is difficult to specify the filter combinations in advance as they depend on many factors that are specific to a given application. For large tunnels, which are expensive to operate, it is usually worth the time to make a mock-up of the tunnel and use this to determine the filters, exposure, and f stop for the film and fluorescent material. The mock-up should duplicate the distances from the light source or sources and from the camera to the model. Also, the mock-up should duplicate the glass or plastic windows that will be used in the wind tunnel. Some acrylic plastics and safety plate glass are designed to absorb ultraviolet radiation. The brightness of fluorescent dyes depends on the amount of ultraviolet radiation, and any loss through windows from the source should be minimized to avoid use of large apertures with their smaller depth of field.

In both the tunnel test section and mock-up, a series of exposures at various f stops should be made to determine the desired exposure. The negative that appears acceptable on proof prints plus the negative of at least one smaller aperture should be enlarged and used to determine final exposures. The negative is exposed to a **small** bright light source by the fluorescent dye; thus the size of the final image for a tuft will change with exposure. This effect cannot be seen on normal contact size proof prints.

Focusing the camera with a fluorescent light source is usually no problem because this can be done using either the black-light fluorescent lights or the mercury vapor lamp with an exciter filter as a light source. It should also be noted that black lights that can be fitted to standard **fixtures** are several orders of magnitude cheaper than the mercury vapor light with its power supply and exciter filter. It is also possible to photograph the fluorescent material with some video cameras during the flash from the light source.

5.4   ΠΟW FIELD VISUALIZATION

Tuft Wands and Tuft Grids

The least expensive **and** at the same time a very versatile method is using a tuft wand, a long tuft on a pole useful for tracing flow near the test article. If it is necessary that a person be in the tunnel, he or she must wear goggles to protect the eyes from dust. The person should disturb the flow in the vicinity of the test article as little as possible. Figure 5.16 shows a tuft wand in use.

To make the flow pattern downstream of the test article visible, a tufted wire grid is useful, as shown in Figure 5.17.

Helium-Filled Soap Bubbles

To trace **pathlines,** which are also streamlines if the flow is steady, helium-filled soap bubbles that have neutral buoyancy can be used. The bubbles **are** inserted
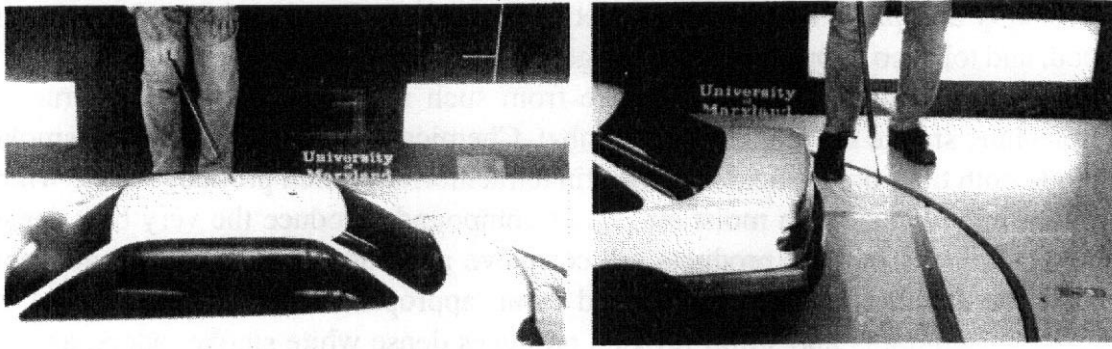
FIGURE 5.16   Investigating the flow structure of an automobile with a tuft wand.

ahead of the model and are photographed with a high-intensity light that passes through the tunnel as a plane of light. With proper photographic exposure time the bubbles appear as streaks. Maximum tunnel speed for use of helium bubbles is about 60 mph. The bubble generators are available commercially.

Smoke

Methods of Smoke Formation   The most common method of flow field visualization after tufts is smoke, which can be produced in a number of ways, although a
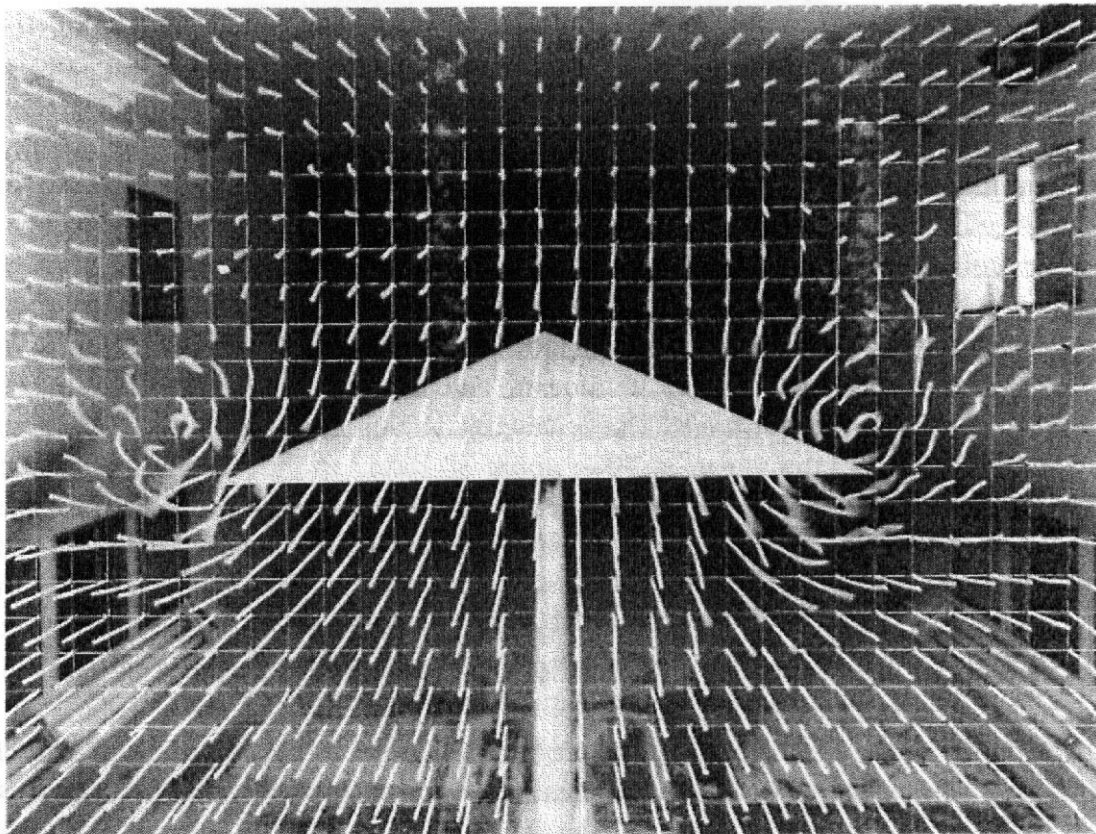
FIGURE 5.17   Flow visualization by the grid and tuft method, yawed delta wing.

universally accepted "best" way has yet to be devised. Burning damp straw, rotten wood, and tobacco to produce smoke is generally unsatisfactory, even though historic work[9,10] was accomplished with smoke from such materials. The same is true of pyrotechnic smoke devices (smoke bombs). Chemical methods of producing smoke include both titanium tetrachloride and tin tetrachloride, which produce smoke when brought into contact with moist air. These compounds produce the very best dense smoke filaments but the products are corrosive and can be used only in an open circuit facility that can be well vented to an appropriate location. A mixture of anhydrous ammonia and sulfur dioxide produces dense white smoke, odors, and, if the air is damp, sulfuric acid. A significant advantage of the system is the fact that the smoke can be started and stopped in a fraction of a second, which is not true of the alternatives. This allows the problems associated with it to be minimized if photographic records rather than real-time human visual inspection can be paramount. Steam and liquid nitrogen produce a good dense smoke with no aftereffects but are very difficult to control and therefore seldom used.

A method reported by Shindo and Brask[11] that works at velocities of over 100 mph is a vaporized petroleum product called Type 1962 Fog Juice, which is used in theatrical productions. The smoke generator consists of about 75 in. of 0.060-in.-outside-diameter (wall = 0.010 in.) stainless steel tubing. For a probe the tubing is placed inside a 0.375-in.-diameter steel tube and held by a collet about 8.0 in. from the end of the tubing, which is bent 90" about 3 in. from the end. Ceramic beads are used to insulate the stainless steel tubing from the outer tube. To vaporize the fluid, 10–15 A is applied to the stainless steel tubing from the collet to a point about 60.0 in. away inside a non-heat-conducting handle. This allows the stainless steel tube to expand. The power unit consists of a variac whose output is connected to the 230-V windings of a 1.5-kVA 115:230 transformer. The variac is used to control the temperature on the stainless steel tubing by applying 0–50 V. The tubing has about 3 Ω resistance, so the current is limited to a maximum of 15 A.

The fuel reservoir is airtight and has a pressure regulator used to set plant air pressure at about 30 lb/in.^{2} to feed the fuel to the probe and a needle valve to control the fuel flow. Plastic tubing connects the reservoir to the probe. It takes some experience to obtain the desired volume of smoke, which is affected by the air pressure, fuel flow, and voltage. The following values are approximate. With the power switch off, set the variac at 70%, apply 30 lb/in.^{2} to the reservoir, and crack open the needle valve. When a small stream of fluid comes out the end, turn on the power. When turning off, cut the power, and when a stream of fluid leaves the tube, shut the needle valve off. This is done to reduce carbon formation in the stainless steel tubing. If hot fluid is emitted, the temperature is too low; either increase the voltage or reduce the fuel flow. If the smoke pulsates, it is generally a sign that the air pressure is too low.

The most widely used method for producing smoke at the larger wind tunnels today is a wand system similar to that described above with polyethylene glycol as the "fuel." A useful alternative to air pressure to drive the fuel through the wand is a peristaltic pump. These are sold by suppliers to chemistry and life science
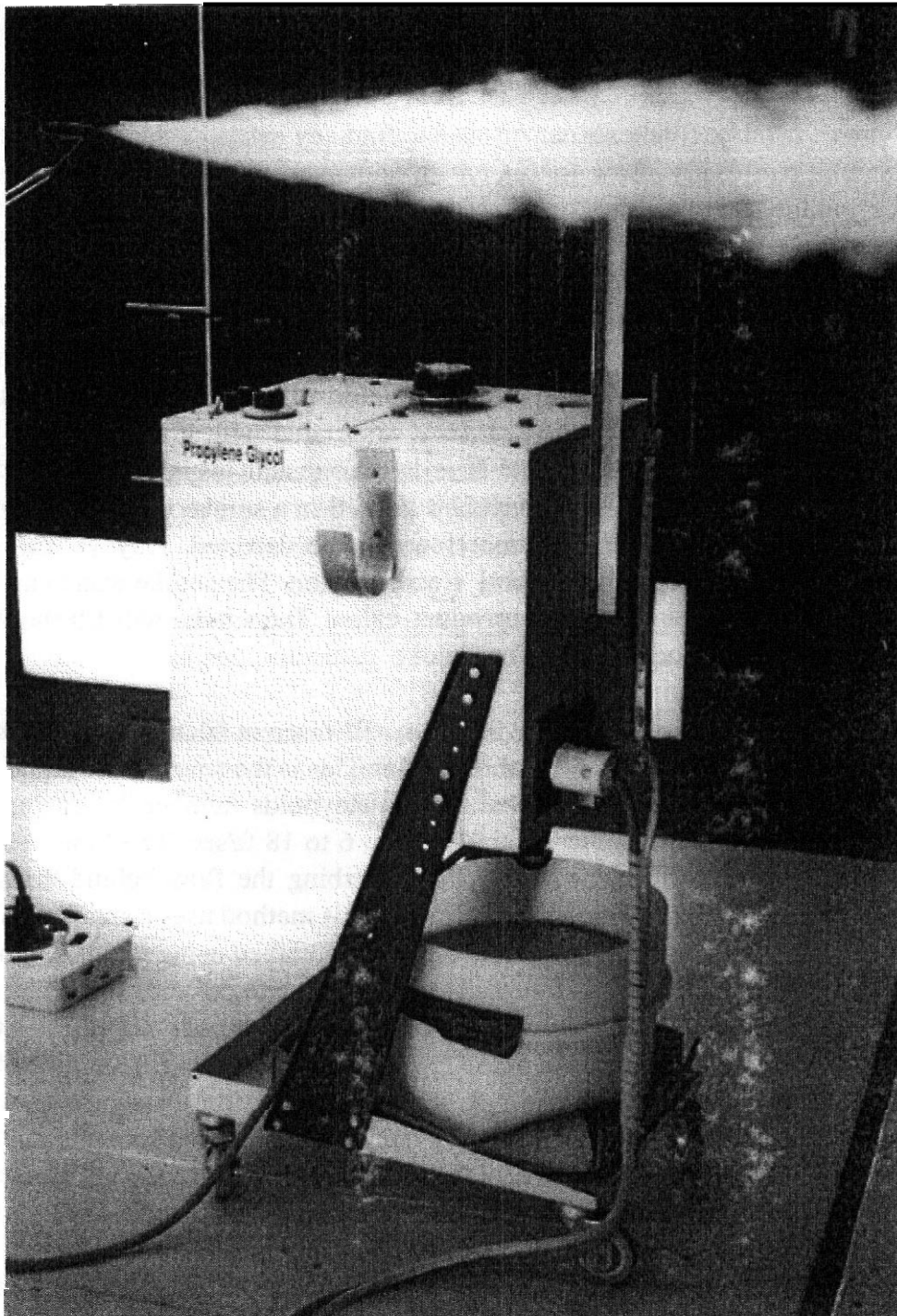
FIGURE 5.18   Smoke generator and delivery wand used at the Glenn L. Martin Wind Tunnel. (Designed and fabricated by Robert Wozniak.) (Photograph courtesy of Glenn L. Martin Wind Tunnel.)

laboratories and have very fine volume flow control. An example of such a system is shown in Figure 5.18.

F. N. M. Brown developed a system of smoke generation in which kerosene is vaporized and the vapor then cooled to the temperature of the airstream before being emitted into the stream.[12] The systems are designed to be used with special-purpose

flow visualization wind tunnels rather than in larger general-purpose wind tunnels. They have been used in many studies.[13]

Using Smoke   Smoke filaments can be used to find key locations such as stagnation points. Smoke can easily show the extent of separated regions and the size of a separation bubble. Smoke can also be used to show and track strong features such as tip or leading-edge vortices from lifting surfaces that may impinge on downstream parts of a vehicle with deleterious effects.

Strong stable light sources are required. If a periodic phenomenon is being investigated, then a stroboscope will be needed that can be synchronized to the period of the phenomenon being studied. Common subjects requiring such an arrangement are propellers and rotors.

Regions of separated flow can be detected in two opposite ways. Smoke filaments can be introduced upstream of the model and located in a series of positions so that the boundary of essentially undisturbed flow can be detected. Any volume into which smoke does not go readily is likely a wake region. The smoke wand can then be introduced directly into the apparent wake region. The smoke will fill the wake "bubble," thereby defining its extent.

Smoke Wire   Another method of producing small discrete filaments of smoke at low velocities is described by Batill and Mueller.[14] This is the smoke wire technique, and it appears to be limited to flows where the Reynolds number, based on wire diameter, does not exceed 20 or at velocities from 6 to 18 ft/sec. The limit is based on preventing the wake from the wire from disturbing the flow behind the wire, and the limit has been determined by experiment. This method uses a small-diameter wire that is coated with an oil. The best results were obtained using Life-Like model train smoke, which consists of a commercial-grade mineral oil with small amounts of oil of anise and blue dye added. The liquid-coated wire has 40–80 V AC or 4C–60 V DC impressed across it. As the wire is heated, fine smoke streaklines form at droplets on the wire (approximately 8 lines/cm for a 0.003-in.-diameter wire). As the wire is heated, it expands and thus sags. This can cause problems with the accurate placement of the streaklines. To avoid this, the wire was prestressed to about 1.5×10^5 lb/in.^{2}, which is near the yield point of type 302 stainless steel wire; thus the wire must be handled carefully.

As the oil-treated wire produces smoke for periods of up to 2 sec, a timing circuit was used for the lights and cameras used to photograph the smoke. Since the smoke wire is limited to low-Reynolds-number tests, it is probably best suited to use in small tunnels as it is difficult to run large tunnels at the required low velocities. An example of a smoke wire visualization is shown in Figure 5.19.

Shadowgraph

The shadowgraph method depends on the variation in refractive index of air due to density variation. It is well known and widely used for applications in high-speed flows in which substantial density variations are present. The technique has relatively
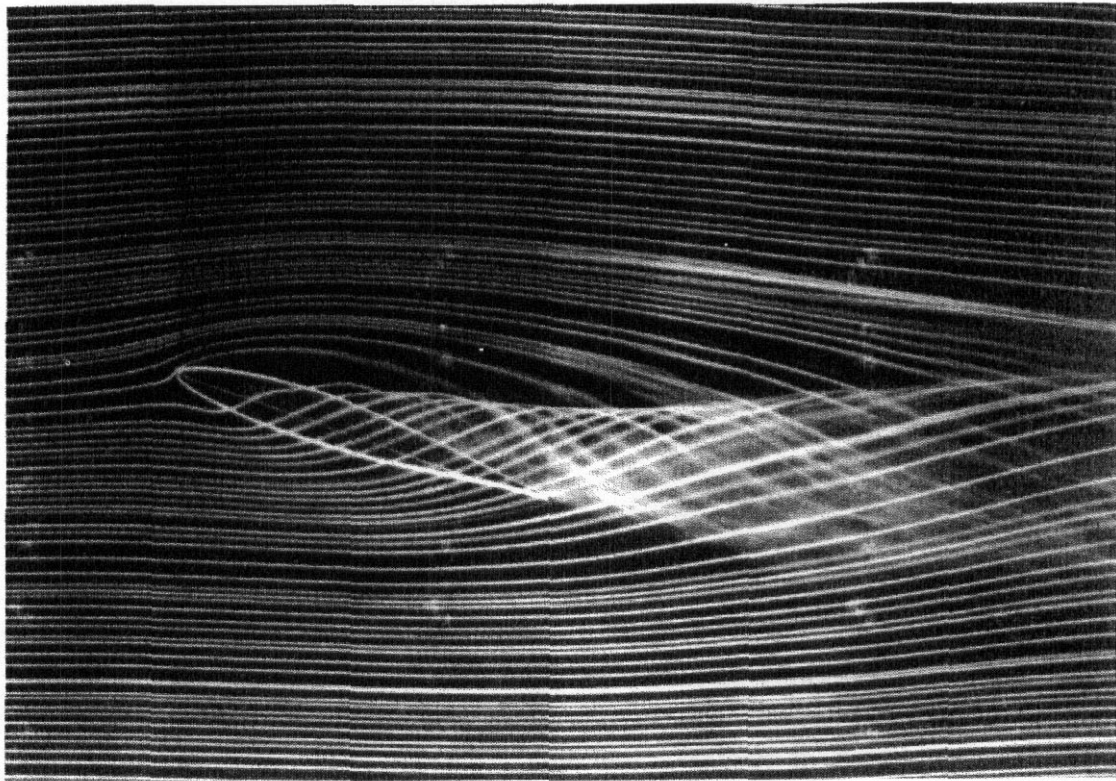
FIGURE 5.19   Streamlines past an airfoil **visualized by smoke** wire technique.

recently been applied to obtaining the paths of tip vortices of helicopter rotors and tracking their interaction with the fuselage in hovering and low-speed forward motion.

5.5   DATA-DRIVEN VISUALIZATION

In this category we place all the techniques in which information is processed by either analog or digital methods and produce flow images of some sort. The data may be a set of measurements such as the voltages from a set of pressure transducers attached to multihole probes along with the geometric data that give locations corresponding to each set of voltage data. Many other types of measurements are used in similar ways. Another example would be the luminosity data from a CCD camera recording the image of a model coated with pressure- or temperature-sensitive paint. The data may also come from a set of computations based on some flow model such as potential flow, Euler codes, or Navier–Stokes solvers.

The demarcation between the class of methods addressed here and those that have been termed "direct visualization" is rapidly blurring as every image shown earlier in this book already exists in digitized form and can be manipulated as a set of numerical data. The evolution is being driven by the continuing advance in our capability to acquire, manipulate, and present in various forms larger and larger data sets in smaller and smaller times.

We make no effort here to capture the many facets of this rapidly advancing collection of applications. However, anyone involved in aerodynamics in the next few years will have to deal with a variety of new developments. An indication of the high level of activity in this area is the series of international symposia on flow visualization that began in 1977 in Tokyo, the seventh[15] of which was held in 1995 and the eighth of which was held in 1997. The proceedings of the seventh contained more than 1000 pages.

For an account of a substantial cross section of methods, Yang[16] may be consulted. The few paragraphs that follow provide a brief introduction to a small sample of methods.

Data Presentation Methods

As data-gathering methods have become more capable, it has become common to obtain thousands or even millions of numerical values associated with various flow variables at various locations in space and time. The search for the most effective ways for an aerodynamicist to use such large volumes of data is ongoing. And it is a problem that is essentially the same for data sets obtained either experimentally or from computations. It is likely that this area will continue to change rather dramatically for some time to come. We give a few historically significant methods in the following, although they have been superseded by the advance of technology.

Color Display of Wake Flows—Analog Method   The first system by Crowder, Hill, and Pond" used a total pressure probe at the end of a swinging arm extending through the ceiling or wall of the tunnel. The probe was driven externally to the tunnel along a segment of an arc. At the end of each swing along the arc the length of the probe was changed (polar coordinate motion). Thus the probe surveyed an area of the tunnel. The pitot was connected to a pressure transducer. The output of the transducer, through suitable electronics, was fed to a light-emitting diode (LED) at the rear of the pitot. For three adjustable ranges of pressure the LED produced three colors. A camera was mounted downstream of the model. With the tunnel blacked out the camera, by remote control, took a time exposure of the probe sweeping out the area in the flow. With an adjustment of the test-section ambient light the model could be superimposed on the flow field photograph.

Other than the electronics to supply the proper current to the LED, this system required no additional data processing and the results were available when the film was developed, or after the run if instant film was used. The multicolored picture then showed the variation in total pressure from which wakes, vortices, and the like could easily be determined. The method trades off resolution in pressure for an increase in spatial resolution of the moving LED. The value of mapping the geometry of wake features was realized as this technique was applied.

Color Displays of Flow Fields—Digital Methods   Winkelmann and Tsao[18] obtained very detailed flow field surveys using several measurement techniques including pressure probes, hot-wire probes, and a laser velocimeter. The probe locations and

the output of the fransducers were recorded on magnetic tape with spatial data densities as high as 4000 measurements per inch of movement of the probe. The data were then processed through a program that applied color codes to the data. This program created three standard files for the white-light primary colors: red, green, and blue. These files were then used to drive a color video monitor to produce the color-coded flow field survey. Derived quantities such as vorticity were computed from the data sets and the resulting maps were produced in color-coded displays. The permanent record of the results were 35-mm photographs of the display.

Winkelmann's images based on data from single-element hot wire, pitot tube, and pitch probe are shown in Figure 5.20. These are from the flow field just

Fluorescent oil
Flow Test

location of
survey plane

Hot-Wire
dc

Ma>

Hot-Wire
rms

Pilot

Pitch

Min
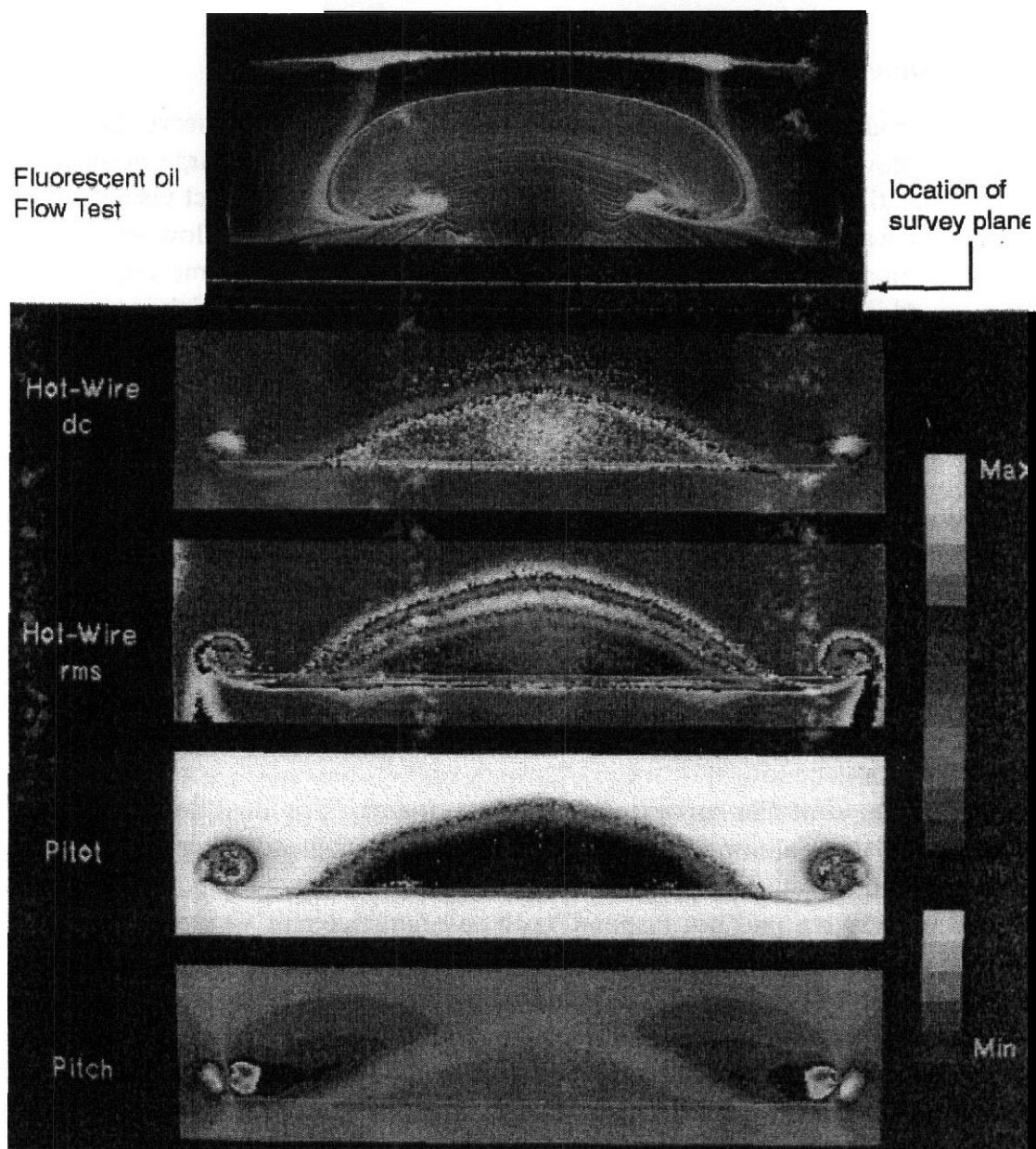
FIGURE 5.20   Images from surveys behind a rectangular wing; aspect ratio 4, Clark Y-14 airfoil, chord 15.2 cm, a $= 25.4°$, $R_{ec} = 360,000.$

downstream of the wing, for which a surface oil flow is shown in Figure 5.6. The processing for this work took considerable effort and time in **1983.** Today, similar amounts of data are routinely processed on the fly for both experimental and computational data sets. However, the amount of data gathered, all of which was obtained by point sampling techniques, was large and would still lead to long experimental runs. The time required to collect the data for each image in Winkelmann's work was about **90** min. This would have to be multiplied by each flow condition for which such an image is required. Much more time-effective methods are necessary for these types of data to be commonplace in development efforts. The particle image velocimetry methods hold promise but are still limited to relatively small spatial regions and relatively low speeds.

Flow Transducers **and Flow Imaging**

In order to produce an "image" of a flow in a usual sense and to serve the usual purposes of flow visualization, it is necessary to have data for a large number of geometric locations. This is obtained by the optical processes of direct visualization methods and was obtained by extensive surveying with standard flow sensors to produce the images in the preceding section. In the former, the time required to make a record is the exposure time for the film or digital camera, which is typically of the order of milliseconds to tens of milliseconds and may be much shorter in some instances. In the latter it is several tens of minutes or thousands of seconds. The ratio of times required to obtain a frame by these two types of methods can be 10^6 or more. In the first case, we get a "picture" very quickly but cannot easily extract as much detailed numerical information as we would like and not nearly as much as we get for each point at which we do a typical measurement with a device such as a hot **wire** or multihole pressure probe. In the second case, we can get very detailed numerical information for each measurement location that is related to a well-defined calibration process, but it takes too long and the measurements at the various locations are spread over a considerable time so the "image" can only be of an averaged type with respect to time.

Spatial and Temporal Characterization of Transducers   An ideal flow transducer would provide a signal simply proportional to the instantaneous value of the flow quantity of interest at a geometric point in space while imposing no influence whatever on the flow and not responding to any parameter or variable other than the flow quantity of interest. And for producing data-driven flow visualization, we would like to be able to operate as many of these ideal transducers in parallel **as** necessary to obtain sufficient resolution throughout the spatial domain of interest. It is obvious that we do not have available to us such capability. Even if we had ideal transducers, we would almost always be considering time-averaged, and possibly spatially averaged, results since most flows with which we work are turbulent and we would need to reduce the data to some manageable form from which a human could make decisions regarding the product under development.

Real transducers do require finite times to respond to stimuli and are influenced by interactions over finite spatial dimensions. Or, in other words, real transducers provide a response that represents an operational average over time and space. These characteristics are the basis for choosing one transducer over another for specific purposes.

Particle Image Velocimetry

Particle image velocimeters (**PIVs**) are discussed in Chapter 4. These systems provide one of the best available means of investigation of flow fields in a number of classes. Their primary forte is low speed and small spatial extent. Their use in larger tunnels is currently limited to local flow structures for model parts rather than full-field investigations around the test article.

Holography and Interferometry

Lasers with coherent light can be used to produce holographs that can be used for density measurements and flow visualization. Basically, the laser beam is split into collimated object and reference beams. The object beam passes through the flow and is combined with the reference beam on a photographic film. When the film is developed and illuminated by the reference beam, the information contained in the object beam is reconstructed.

If holographic information is desired, the interference fringe pattern is obtained on the film by exposing the film to the object beam twice. The interference pattern is reconstructed by illuminating the film with the reference beam. Density measurements require both calibration and careful optical alignment.

These systems have been used to Mach numbers as low as 0.20. This is still pushing the current limit for development projects, and these methods show no indication that they will reach a state of maturity and economic utility that will lead to their being widely used in the near future.

REFERENCES AND NOTES

1. Lamb, H., *Hydrodynamics,* 6th ed., Cambridge University Press, Cambridge, 1932, Article 13.

2. Somerscales, E. F. C., "Tracer Methods," in Emrich, R. J., Ed., *Methods of Experimental Physics,* Vol. 18, *Part A, Fluid Dynamics,* Academic, New York, 1981.

3. Crowder, J. P., "Add Fluorescent Mini-Tufts to the Aerodynamicists' Bag of Tricks," *Aeronaut. Astronaut.,* 18, 54–56, 1980.

4. Merzkirch, W., *Flow Visualization,* Academic, New York, 1974.

5. Tobak, M., & Peake, D. J., "Topology of Three Dimensional Separated Flows," *Ann. Rev. Fluid Mech., 14,* 61–85, 1982.

6. Moffan, H. K., and Tsinober, A., Ed. "Topological Fluid Mechanics," in *Proceedings of the IUTAM Symposium,* Cambridge University Press, Cambridge, 1989.

7. Reda, D. C., and Muratore, J. J., Jr., "A New Technique for the Measurement of Surface Shear Stress Vectors Using Liquid Crystal Coatings," AIAA Paper 94-0729, presented at the Thirty-Second AIAA Aerospace Sciences Meeting and Exhibit, Reno, NV, Jan. 10–13, 1994.

8. "Ultraviolet & Fluorescent Photography," M-27, Eastman Kodak Co., Rochester, NY.

9. Mach, L., "Uber die Sichtbarmachung von Luftstromlinien," *Aeitschrift fur Luftschiffahrt and Physik der Atmosphere,* **15**(6), 129–139, plates I-III, 1896.

10. Marey, E. J., "Changements de direction et de vitesse d'un courant d'air qui rencontre des corps de formes diverses," *Compt. Rend.,* **132,** 1291–1296, 1901.

11. Shindo, S., and Brask, O., "A Smoke Generator for Low Speed Wind Tunnels," Technical Note 69-1, University of Washington, Dept. of Aeronautics and Astronautics, 1969.

12. Merkyvirch, W., *Flow Visualization,* Academic, New York, 1974.

13. Mueller, T. J., "Smoke Flow Visualization in Wind Tunnels," *Astronaut. Aeronaut.* **21,** 50-62, Jan. 1983.

14. Batill, S., & Mueller, T., "Visualization of Transition in the Flow Over an Airfoil Using the Smoke Wire Technique," *AZAA J.,* **19,** 340–345, 1981.

15. Crowder, J. P., Ed., "Flow Visualization VII, Proceedings of the Seventh International Symposium on Flow Visualization," Seattle, WA, Sept. 11–14, 1995, Begell House, New York, 1995.

16. Yang, W. J., *Computer Assisted Flow Visualization: Second Generation Technology, CRC* Press, Boca Raton, FL. 1994.

17. Crowder, J. P., Hill, E. G., and Pond, C. R., "Selected Wind Tunnel Testing Developments at Boeing Aeronautical Laboratory," AIAA Paper 82-0458, 1982.

18. Winkelmann, A. W., and Tsao, C. P., "A Color Video Display Technique for Flow Field Surveys," AIAA Paper 83-0611, in *Proceedings of the AIAA Twelfth Aerodynamic Testing Conference,* AIAA, Washington, DC, 1983.

6 Calibration of the Test Section

After a tunnel is constructed, the next step is to determine its flow characteristics and, of course, to change any that are not satisfactory for the purposes intended. The types of measurements that will be required can be made with methods discussed in Chapters 4 and 5.

The low-speed "steady" airstream is usually considered to be defined when we know its distribution of temperature T, pressure p, dynamic pressure q, and "turbulence" η. There are several assumptions embedded in this statement. We admit that the airstream is expected to be turbulent and therefore not strictly steady or time invariant. The time variability of the airstream is to be characterized by its level of turbulence, which is commonly defined to be the rms of the variation of the longitudinal component from the mean value of air speed. The pressure' and dynamic pressure are the mean values for these quantities averaged over a time interval chosen as necessary to achieve the required precision of the mean. The stream temperature is similarly considered. Using the equation of state, we can then compute the density, and using the definitions of total pressure and total temperature, we can compute these quantities and flow speed as well. In the case of wind tunnels to be used for wind engineering, the temporal and spatial variations must be considered in considerably more detail and will include spectra and integral scales of the turbulent flow structures as well as a profile to match appropriate types of planetary boundary layers. We will not treat those issues in this chapter.

We may also compute the Reynolds number for a particular model based on its chosen characteristic length. Much of our interest is centered on determining pressure, which can be measured most simply by use of liquid manometers or more commonly by using electronic data systems, including various instrumentation elements and computer systems for data manipulation, storage, and presentation. For our subsonic testing, the precision with which measurements of stream temperatures are made are usually less demanding than the typical pressure measurements.

6.1 TEST-SECTION n 0 W CALIBRATION

Speed Setting

Setting the speed of a wind tunnel appears straightforward as we apply our basic understanding of fluid dynamics. However, it turns out that this basic question absorbs a considerable amount of attention even for experienced aerodynamicists. When there is no model in the test section, a measuring device, most commonly a

218
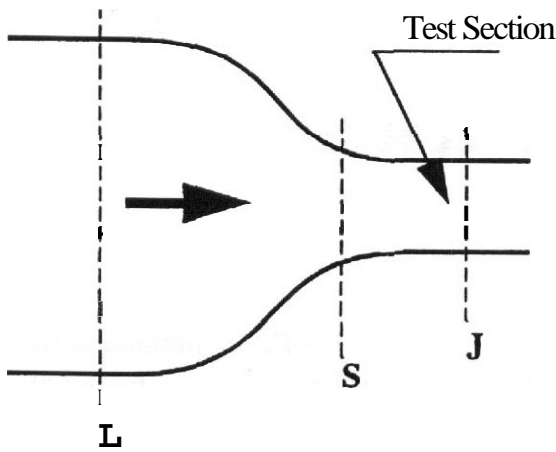
Test Section

FIGURE 6.1 Typical measurement stations for a wind tunnel **"q"** system.

pitot-static tube, can be put there to determine the air speed. One cannot, however, insert a pitot-static tube or other measuring device in the test section to measure dynamic pressure or speed along with an object under test because the test object will cause changes in the flow. These changes are referred to as "induced flow." Consider Figure 6.1, which gives a schematic indication of the settling chamber, contraction, and test section of a typical wind tunnel.

The tunnel speed is usually determined by measuring either static or total pressure in the settling chamber ahead of the contraction cone, as indicated by station L, and a static pressure ahead of the test section, as indicated by station S. If honeycomb or screens are used in the settling chamber, station L will be downstream of these devices. Using the subscripts L for the bellmouth or settling chamber and S for the region before the test section, Bernoulli's equation between the two stations will be

$$P_L + q_L = P_S + q_S - K_1 q_S \tag{6.1}$$

where $K_1 q_S$ represents an allowance for the small loss in total pressure between the bellmouth and station S. Here P is static pressure and q is dynamic pressure. Neglecting compressibility (6.2) follows from the continuity equation applied between the two stations (A is the area):

$$A_L V_L = A_S V_S \tag{6.2}$$

Squaring, multiplying by $\rho/2$, and solving for q_L,

$$\frac{\rho}{2} V_L^2 = q_L = \left(\frac{A_S}{A_L}\right)^2 \frac{\rho}{2} V_S^2 = \left(\frac{A_S}{A_L}\right)^2 q_S = K_2 q_S \tag{6.3}$$

Rewriting Bernoulli's equation and substituting for q_S above,

$$P_L - P_S = q_S(1 - K_1 - K_2) \tag{6.4}$$

If station S does not have the same cross-sectional area as the test section (station J), the continuity equation can be used to yield

$$q_S = \frac{\rho}{2} V_S^2 = \left(\frac{A_J}{A_S}\right)^2 \frac{\rho}{2} V_J^2 = K_3 q_J \tag{6.5}$$

Thus

$$P_L - P_S = (1 - K_1 - K_2)K_3 q_J \tag{6.6}$$

In this form the constant K_1 can be considered to include the small additional loss in total pressure from station S to the jet.

The actual calibration of the tunnel is accomplished by running the tunnel at various values of $P_L - P_S$ while measuring the dynamic pressure in the test section with a calibrated pitot-static tube. This evaluates $(1 - K_1 - K_2)K_3$. Because the velocity is not uniform throughout the test section, it is necessary to survey the test section. As a minimum, the area in the vertical plane of the model trunnion for aircraft models or other appropriate plane for other test objects should be surveyed. A better approach would be to survey a volume of the test section that is occupied by the model. If the pitot-static tube used has a hemispherical nose, it can be equipped with two yawheads at 90° to each other, and the distribution of the upflow and cross-flow can be obtained simultaneously.

The survey of the test section can be done with a simple pitot-static tube assuming there is a method to position it throughout the test section or a rake of pitot statics can be used. If there is no method of remotely positioning the pitot-static tube, the survey of the test section becomes a very tedious operation. In any event, this is a critical operation and the effects of the manner of holding and supporting any selected instrument must be carefully evaluated.

If a volume of the test section is surveyed and there are large variations in the dynamic pressure, it may be desirable to use a weighted average of the measured dynamic pressure. When the dynamic pressure calibration is completed, there is a relation established between the indicated dynamic pressure $(P_L - P_S)$ and the dynamic pressure q_J in the clean test section. There usually are a series of these calibrations for different test-section configurations. If the tunnel has an external balance, calibrations are often made with and without the balance struts and their fairings. If a ground plane is used often, calibrations are made for various heights of the ground plane.

It is desirable to obtain for each test-section configuration the distribution of the total pressure, static pressure, upflow, and cross-flow throughout the region occupied by the model. When the tunnel has an air exchanger or heat exchanger, the temperature distribution should also be measured.

The pressure sources for the tunnel speed control should be, ideally, either a ring around a tunnel station or at least a portion of a ring on the two side walls or the ceiling and floor. The possibility of the model pressure field directly affecting the nearer of the pressure sources at station S should always be kept in mind and

evaluated if a larger model than normal or an upstream mounting location is to be considered. The static source should consist of either a series of static sources or a sealed tube flush with the surface with many holes evenly spaced along its length. The tubes or multiple static sources of the ring should be manifolded together to yield an average static pressure at the station. If total pressure is used in the contraction cone, it is desirable to have multiple sources also.

The two pressure sources in the simplest case can be connected to a U-tube manometer that is used for setting the tunnel speed. It is more common to use a high-quality differential pressure transducer. Then the electrical output can be transmitted to any location convenient for the tunnel operator and to the data system.

One note of caution: Extreme care must be taken to make sure that there are no leaks in the tunnel dynamic pressure system. In large tunnels, the leak checking can be a time-consuming process. It is highly desirable and strongly suggested that the system should not be disturbed once it has been leak checked. It is often useful to record the pressures at each of the two tunnel stations as separate readings relative to atmospheric ambient pressure. Additional sources for this use should be provided rather than tapping into the tunnel dynamic pressure system.

It is also desirable to have a simple method of periodically checking the system for leaks. One way to do this is to use a calibration wing that can be installed easily. The wing can be run through a pitch series at several dynamic pressures. If the slope of the lift curve does not change, there is no change in the dynamic pressure calibration. This has the further advantage of also checking the tunnel upflow. If the drag polar does not rotate, the upflow has not changed.

Longitudinal Pressure Gradient

The static pressure gradient along the test section must be known in order to make necessary buoyancy corrections. It may be obtained by reading the local static pressure with a pitot-static tube that is progressively moved from entrance cone to exit cone. Care must be taken that the pitot tube is aligned directly into the wind and that no extraneous static pressure is created by the bracket holding the pitot tube. This last proviso is not possible to satisfy exactly.

Perhaps a more convenient method is to use a long static tube, as discussed in the next paragraph. The reader may reasonably ask why not measure the static pressure along the walls of the tunnel. It turns out that small variations in wall geometry associated with joints, mounting holes, and the like cause local variations in the static pressure that are typically too large to ignore and may change over time as various mounting installations are put in and taken out of a facility. Measuring wall pressures is a good adjunct to calibration and has become a common practice to obtain input for boundary corrections, but it is not a good idea to rely on wall pressure measurements for the baseline characterization.

Long Static Tube

As the name implies, this is a long tube that extends through the test section. The tube is often suspended on a series of wires that are used to align and tension the

tube. The tube is equipped with a number of static pressure rings. These rings have four or more static ports around the circumference that are manifolded together. If the flow angularity is small, then aft of the nose the flow will be practically parallel to the tube. This then yields a static pressure distribution along the length of the tube.

Dynamic Pressure Variation across Jet

The dynamic pressure is usually measured throughout selected regions of the test section by means of a pitot-static tube. The density is calculated from a barometric pressure measurement, a test-section static pressure measurement relative to the atmosphere, and a test-section temperature determination along with the equation of state. The local velocities are then obtained from

$$V = \sqrt{\frac{2q}{\rho}} \tag{6.7}$$

The velocities as calculated from the dynamic pressures or the pressures themselves are plotted, and the points are connected by "contour" lines of equal values. The variation of q in the working range of the jet should be less than 0.50% from the mean, which corresponds to a 0.25% variation in velocity. Some tunnels have been built to tighter specifications, but it is almost inevitable that custom tweaking of aspects of the tunnel circuit will be required to do better.

A plot of the dynamic pressure distribution in a rectangular test section is shown in Figure 6.2. Of interest is the asymmetry that is usually found, and the maximum variation in this example is well above satisfactory limits. The survey should have been carried to the walls.

The correction of an excessive velocity variation is not as serious a problem as the correction of excessive angular variation. There are more method of attack as well as less probability that the variation will change with tunnel speed. There are several minor adjustments that may be expected to improve a less than satisfactory speed distribution. There may be local flow separations that must be found and corrected or improperly set turning vanes. If the velocity variation is annular, the source may be the propeller load distribution. Such local problems in identifiable parts of the tunnel should be corrected. Finally screens may be added in the largest section of the tunnel with spatial mesh densities varied so that they are more dense in the sections that correspond to high-velocity regions in the jet. The improvement in velocity distribution by such screens is shown in Figure 6.3. The loss in energy ratio they cause is quite small and is far outweighed by the improvement in testing conditions.

Flow Angle Variation across Jet

The variation of flow angle in the jet can be measured by many devices. Regardless of the device used, it is desirable to map the upflow and cross-flow in a series of

Tunnel wall

Tunnel wall

▨ Less than 0.5 % from mean.	⧄ 1.0 to 1.5% from mean.
☐ 0.5 to 1.0% from mean.	▤ 1.5 to 2.0% from mean.
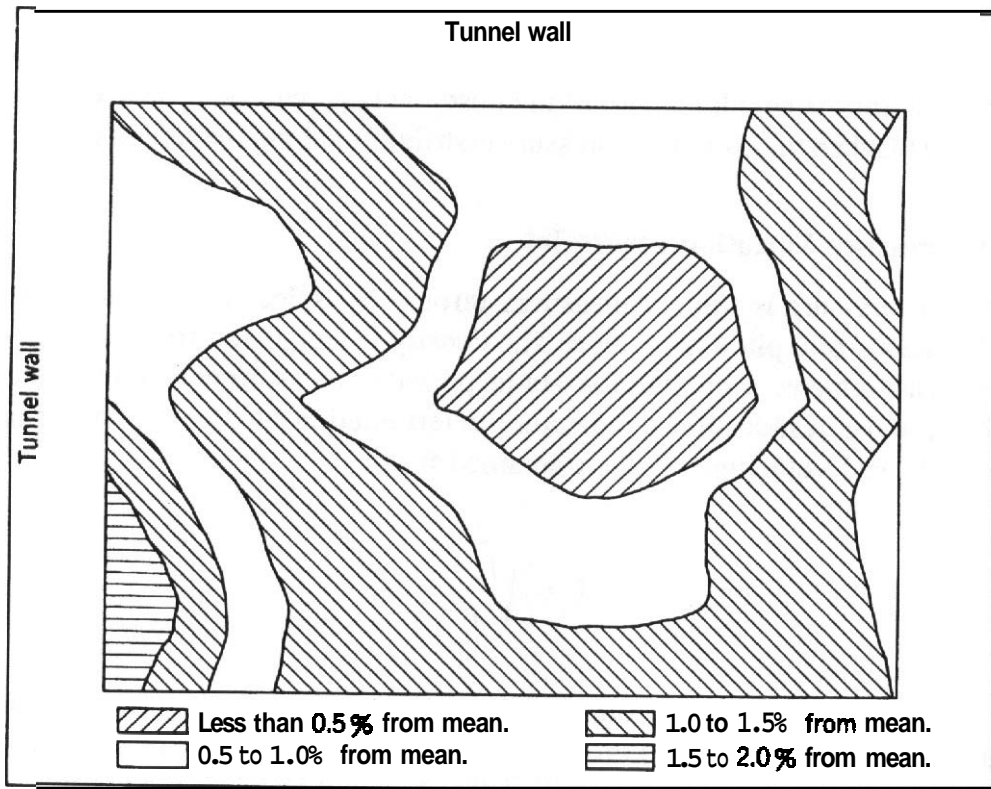
FIGURE 6.2   Example distribution of test-section dynamic pressure.

Distance from floor, inches

Without screens

With screens

Dynamic-pressure variation, per cent
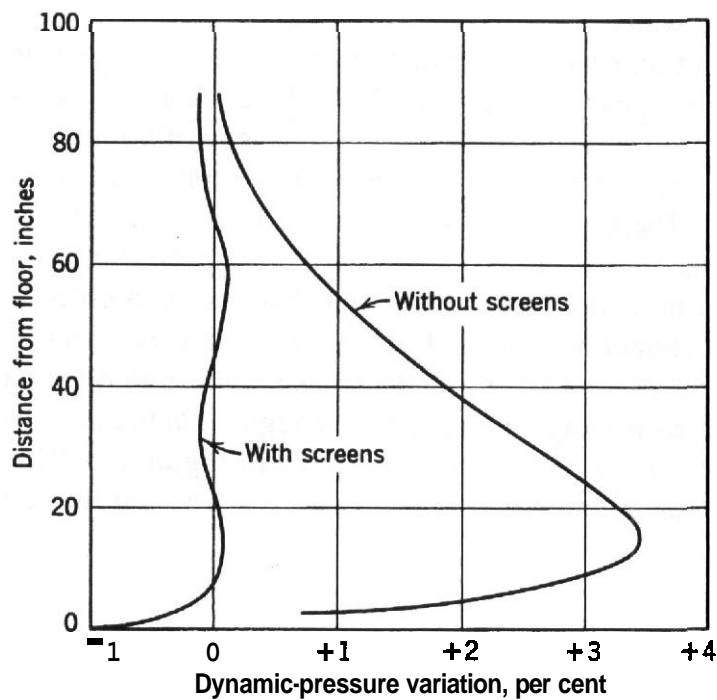
FIGURE 6.3   Effect of screens on velocity distribution in the test section.

transverse planes along the longitudinal axis in the region occupied by the model over the range of intended dynamic pressures. Often, when the upflow and cross-flow are plotted as flow direction vectors, regions of vortexlike flow can be seen in the test section. As indicated in Chapter 3, such flow is often the result of poor velocity distribution in the return duct before the third comer or the result of improperly set fourth-comer turning vanes.

A variation of upflow across the span of a wing results in an effective aerodynamic twist. A cross-flow gradient across the test section in the region of the vertical tail will change the slope of the yawing moment versus side slip or yaw angle. Thus it is desirable to have the upflow and cross-flow constant across the tunnel. This is difficult to achieve. It would be desirable to have the variation less than $\pm 0.10°$, but it is often necessary to accept the best values that can be achieved. The maximum variation should be held to $\pm 0.20°$.

Test-Section Turbulence Measurement

Variations between results of tests made in different wind tunnels at the same Reynolds number and between tests made in wind tunnels and in flight have indicated that some correction was needed for the effect of turbulence that exists in wind tunnels. It has been argued that this turbulence causes flow patterns in the tunnel to be similar to the flow pattern in free air at a higher Reynolds number. Hence the tunnel test Reynold number could be said to be a higher "effective Reynolds number." The physics of turbulent flow is far too complex to be captured by this simple concept. There are some phenomena for which it "works" to some extent and others for which it does not. We address first the historical use of this concept, which is dependent on the long-known fact that spheres (and circular cylinders) have quite well-defined critical Reynolds numbers near which the drag coefficient drops rather precipitously as the Reynolds number increases.

It has been experimentally verified that the Reynolds number at which the drag coefficient of a sphere decreases rapidly depends strongly on the degree of turbulence in the wind tunnel. The Reynolds number at which the reduction occurs decreases with increasing tunnel turbulence. There is also a strong effect of surface roughness. In this discussion, we are considering only aerodynamically smooth spheres. The decrease in drag coefficient with Reynolds number can be understood as the result of increasing the Reynolds number, producing earlier boundary layer transition from the laminar to turbulent state, which in turns leads to a downstream shift in the separation point and corresponding higher base pressure, a smaller wake, and less drag. Early flight measurements on spheres[Z] found that in the free atmosphere the critical Reynolds number for a sphere is 3.85 X 10^5. This value is larger than is achieved in wind tunnels, although many low-turbulence tunnels approach this value. In the atmosphere the turbulent eddies are so large relative to the sphere that they do not affect the thin boundary layer of the sphere.

Before the now common use of hot-wire anemometry, a turbulence sphere was the primary way to measure the relative turbulence of a wind tunnel. It remains a
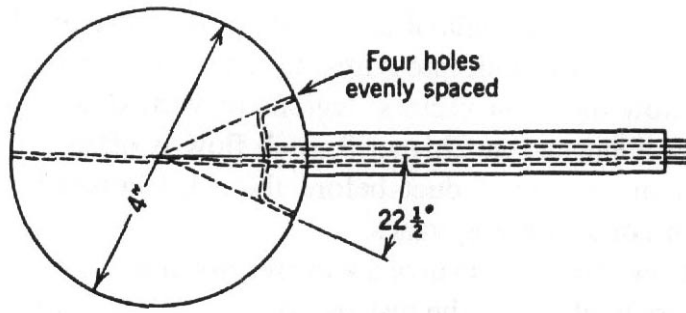
FIGURE 6.4   Turbulence sphere.

very useful and easy way to characterize the turbulent environment in a tunnel and to check if there is an indicated effect following changes in the tunnel configuration or special installations that might affect the flow quality. The configuration of a turbulence sphere is shown in Figure **6.4.** The critical Reynolds number for the sphere can be measured in two ways. One method is to plot the measured C_D based on cross-sectional area versus Reynolds number, as shown in Figure **6.5.** From the plot the Reynolds number in the tunnel for $C_D = 0.3000$ is read. The second method is to take the average of the four pressures on the aft surface of the sphere and subtract this value from the stagnation value at the leading edge of the sphere, yielding AP. A plot of $\Delta P/q$ versus Reynolds number is prepared for the sphere and the Reynolds number determined for $\Delta P/q = 1.220$, as indicated in Figure **6.6.** The pressure method has certain advantages. It needs no drag balance with the associated
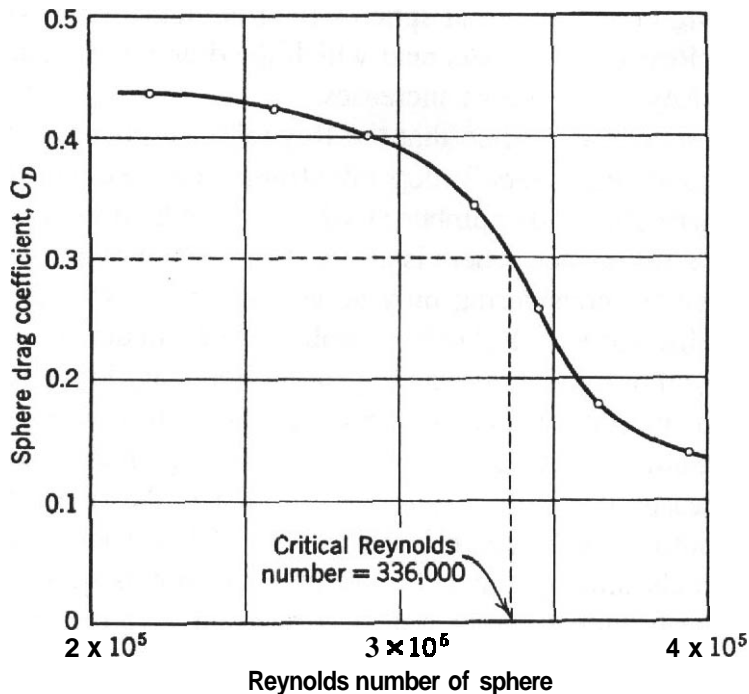
FIGURE 6.5   Drag coefficient for a sphere.

$$TF = 385,000/RN_{tunnel}$$
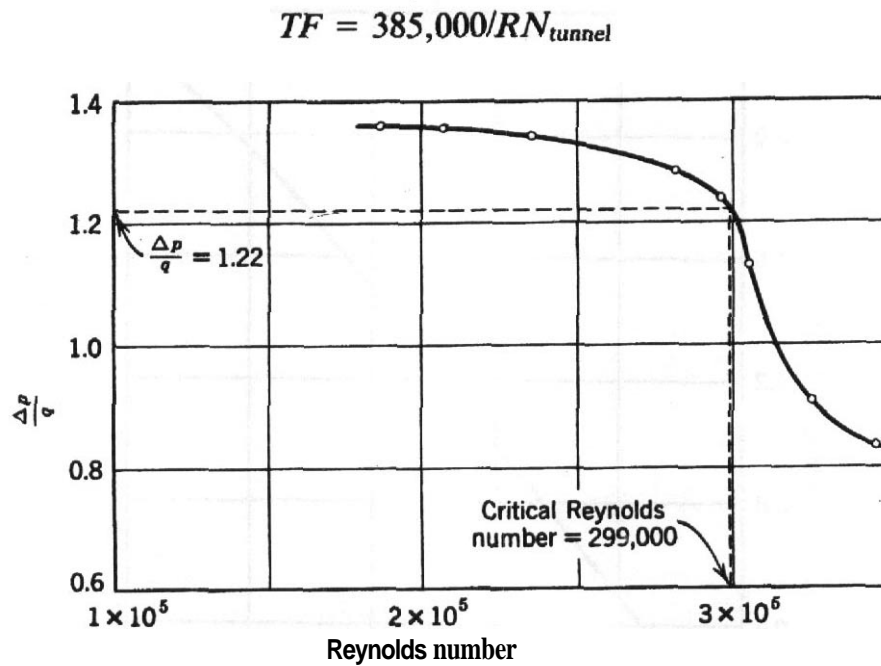
FIGURE 6.6   Variation of pressure coefficient as function of Reynolds number for a "turbulence sphere."

balance calibration and no evaluation of support tares for the portion of the support sting exposed to the airstream. Also, the sphere support sting can be stiffer as no deflection is needed by the drag balance.

The critical Reynolds number as defined by either force or pressure measurements is then used to define a turbulence factor for the tunnel by comparing the tunnel's critical Reynolds number to the atmospheric free-air Reynolds number:

$$TF = \frac{385,000}{RN_{tunnel}} \qquad (6.8)$$

Then the effective test Reynolds number is defined by

$$RN_e = TF \ X \ RN_{test} \qquad (6.9)$$

The use of a turbulence sphere yields what may be thought of as an average value of tunnel turbulence. It does not give any information on the magnitude of turbulence in either the axial or lateral direction. The use of a turbulence sphere may, however, prove to be a simple method of monitoring any change in tunnel turbulence. Its use requires no prior calibrations and the installation and running in a tunnel can be designed to be simple and quick.

The relation between the critical Reynolds number of a sphere and turbulence intensity as measured by a hot wire is shown in Figure 6.7. This is from the work of Dryden et al.[3] and Dryden and Kuethe.[4]
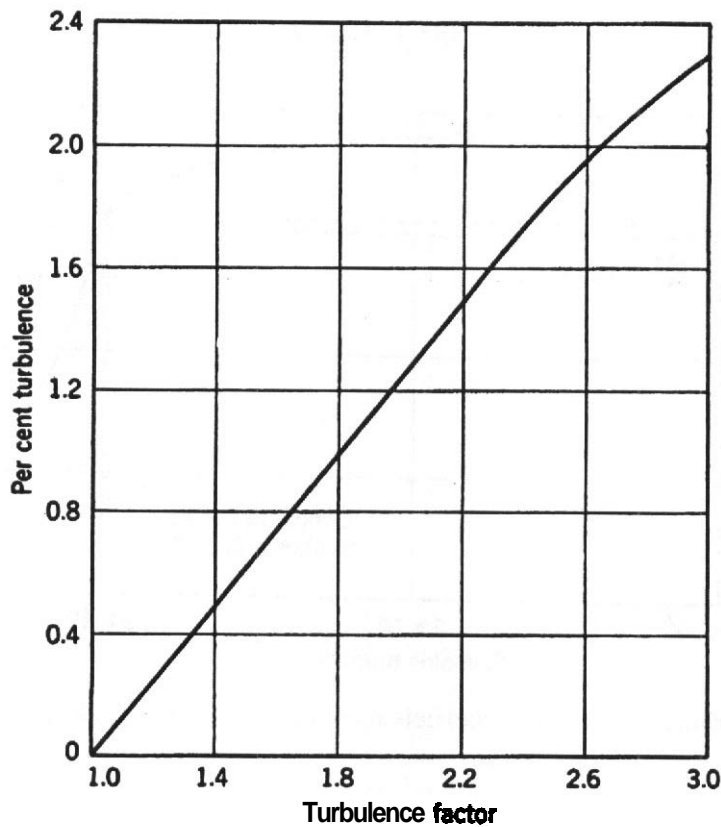
FIGURE 6.7   Variation of turbulence factor with turbulence intensity from hot-wire measurements.

Turbulence spheres can be made from cue, duck, and bowling balls. Several sizes are needed to enable the turbulence factor to be measured over a range of tunnel air speeds.

A brief examination of Figure 6.7 might lead to the conclusion that the higher the turbulence, the better the tunnel, as the effective Reynolds number of the test would be higher. This correction is not exact, and if the tunnel has excessive turbulence, the model may have a premature transition from laminar to turbulent flow, which can be critical for laminar flow airfoils. However, low-speed models are often equipped with trip strips that fix the transition point on the model and may reduce the requirement for extremely low turbulence. The need for low test-section turbulence is not as severe for small student tunnels as it would be for larger tunnels that are used for research and development tests. The effectiveness of screens and honeycomb elements for reducing turbulence in wind tunnels has been discussed in Chapter 3.

6.2   WIND TUNNEL BOUNDARY LAYERS

The boundary layers involved in tunnel calibration are generally much thicker than those encountered on a typical model. The tunnel boundary layers can be measured
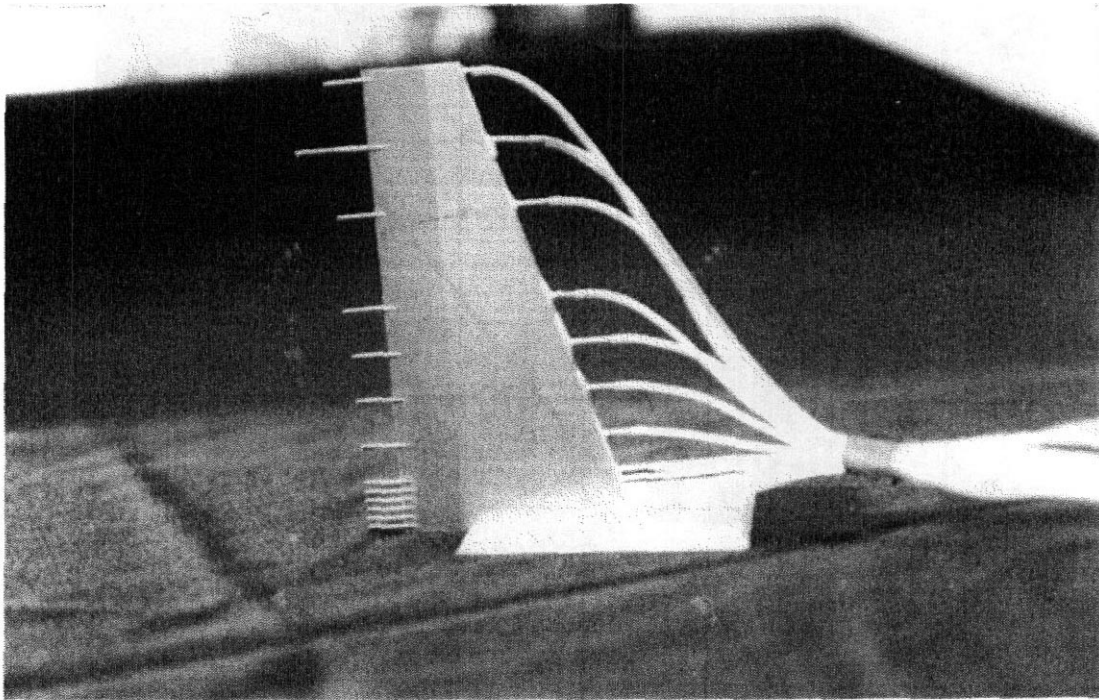
FIGURE 6.8   Boundary **layer rake.**

using rakes of pitot tubes (Figure 6.8), which are specially configured for the purpose. Or traversing devices (Figure 6.9) fitted with pitot tubes, static tubes, or hot wires can be used in places where a mechanism can be mounted on *the* outside of the flow surface. Other devices for boundary layer measurements will be discussed in a later chapter. The measurements of boundary layers for tunnel calibration purposes are generally needed to assess the presence of separation or tenaency to separation. All tunnel boundary layers will almost surely be turbulent, so there are few instances in which locations of transition on tunnel surfaces are sought. Methods for this purpose are discussed later in relation to model measurements.

Locating Points of Separation

If a tunnel has significant unsteady flow with low frequency compared to typical turbulence, it is likely that there are regions of separated flow. An exploratory investigation can be carried out with tuft wands, expecially in larger tunnels. More extensive investigations can be done with tufts on the tunnel surfaces and either visual or video monitoring for various tunnel operating conditions. Other methods of investigation are discussed in relation to model tests later, but they are seldom needed for direct investigation of tunnel surface layers.

The two basic methods of attaching tufts to a surface are by scotch tape or by glue. Tape is always used for attaching to tunnel walls. When tape is used, the tufts are usually made on a tuft board. (See Figure 5.1.) This gives a length of tape with tuft attached that is applied to the surface. The surface should be cleaned with naphtha or other solvents to remove oil to increase the length of time the tufts will remain attached under wind-on conditions.
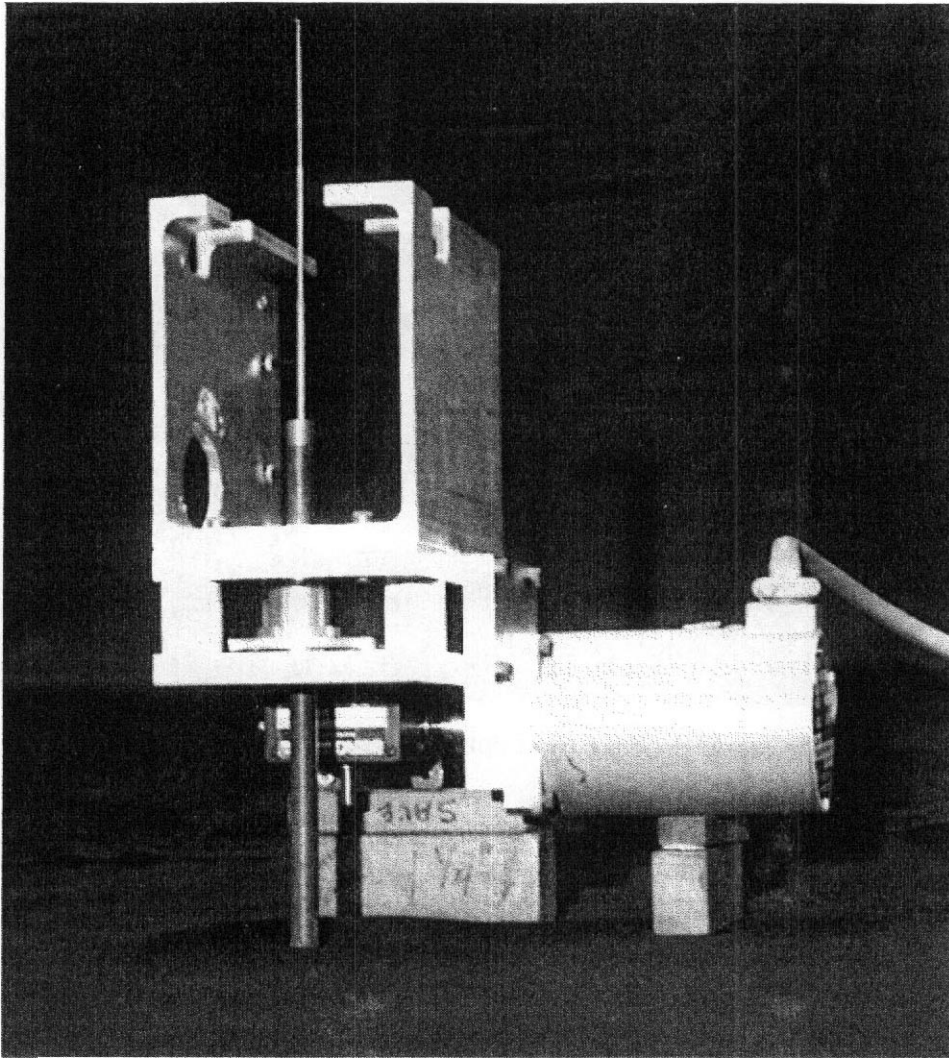
FIGURE 6.9 Typical traversing mechanism used for boundary layer surveys.

Off-Surface **Visualization**

The least expensive method for off-surface visualization is using a tuft wand, as previously mentioned. A long tuft on a pole, a tuft wand is useful for tracing flow near a model or to explore a tunnel circuit for regions of reversed flow. When it is necessary to put a person in the tunnel, he or she must wear goggles to protect the eyes from dust. It goes without saying that the person should take care to disturb the flow being investigated as little as is possible, although the human body is inevitably a large disturbance.

6.3 ACOUSTICS

As we have stated earlier, many low-speed wind tunnels will be utilized heavily for aeroacoustic investigations in the coming years. This is true for several converging reasons. There is a strong and increasing interest in managing aerodynamic noise.

There is an increasing store of knowledge that provides avenues for attacking problems directly and for intensifying research efforts with promise of even greater understanding. There has emerged a set of experimental methods that allow very useful aeroacoustic investigations to be undertaken in general-purpose wind tunnels with relatively moderate treatment, at least by comparison to the anechoic facilities that have been essential in the past.

6.4   WIND TUNNEL DATA SYSTEMS

The quality and features of the data system available for use at a wind tunnel have a large impact on the utility and potential productivity of the facility. The data system is becoming a more and more embedded element that determines the feasible data quality as well as potential efficiency of experiments that can be done at a laboratory.

The path from some physical parameter to a stored digital number will be followed. Initially we will look at these functions as they were carried out by hand and then follow the same process by an analog–digital system. Consider Example 4.1. Three measurements were needed to determine the velocity from a pitot-static tube: the test-section pressure, the test-section temperature, and the pressure difference across the pitot-static tube total and static ports. The hand process for obtaining air speed from the pitot-static tube measurements would be to (a) identify the manometer tubes that are connected to the pitot-static pressure ports, (b) read the heights of the fluid in the tubes with the proper signs, (c) write the signs and heights in the correct place on a data sheet, (d) do the calculations using whatever tool is preferred, (e) record intermediate results if considered useful for checking, and (f) record the final result in a way that allows it to be retrieved and utilized in conjunction with any other measurements that may be a function of air speed.

This is exactly the same process that a data system performs. First the desired parameter must be located. If five pressure modules of 32 ports are in use, then the data system must "know" the module and port position that is connected to the pitot-static pressures. This identification through appropriate program coding serves the same function as finding the manometer tube. The identification process can be tedious and error prone when large numbers of pressures are being recorded. The capabilities of the computer systems have been used at most laboratories to provide a program to assist in "port mapping."

The next item is to read the value and sign, which is not as simple as visually reading the height of the fluid in the manometer tube. In general, transducers produce electrical signals; the amplitude depends on the value of the physical parameter. The signal can have different forms, such as current variation, voltage variation, and resistance variation. The level of the signal is generally quite low and requires amplification. Amplifiers act only on input voltages; thus some transducers must have their output changed to a voltage. This is done with a signal conditioner appropriate to the particular device.

The electrical signal from the transducer consists of two parts: the part of the signal that is a direct function of the variable being measured and a part that is not a function of the variable being measured, which is considered "noise." The noise can have an electrical cause, a mechanical cause, or an aerodynamic cause. It is common to apply either analog or digital filters to improve the measurement results by removing the noise to varying extents. Extreme care must be taken to ensure that the required signal is in fact improved rather than damaged in this process. These issues will be considered further in Chapter 12.

The sign and amplitude or voltage of the analog signal that come out of the amplifier and/or filter represents the value of pressure. To use this value in calculations, it must be expressed as a number; that is, it must be in digital form. This is accomplished by an analog-to-digital converted (ADC), which produces a binary number that may take one of several forms, the details of which must be obtained from the specifications of the particular device as provided by the manufacturer. The binary number and sign are transferred to the computer where it may be stored directly or a computation may be performed to convert to "engineering units" before storage. The number representing pressure is stored in a file in a preselected order that corresponds to the sources. The file must contain additional information—frequently the test number, run number, angle of attack, and yaw angle plus some configuration identifiers. The data system has implemented the same functions that are done by hand: identify the manometer tube (address), read the sign and value in numeric form (sign plus voltage to ADC), write the value and sign in the proper place on the data sheet (store with correct address), convert raw readings to engineering units, and compute the speed and record in the proper place to correlate with any other measurements that may be dependent.

An additional important variable has not been mentioned—the time at which each measurement is taken. When recording is done by hand, this is only nominal. Many experiments require accurate time stamps for each data point so that the dynamics of events can be analyzed. This is much more demanding on the performance of data systems but is routinely done at frequencies up to hundreds of thousands of samples per second.

The data system will have multiple data channels, each of which can process data in a manner analogous to the above description. The number of channels in the system is determined by the estimated number of parameters that will have to be measured in a particular facility or, more likely, by the available funds. A system may have 20, 100, or more channels. It should be noted that the use of multiplexing devices such as a 32-port electronically scanned pressure module that allows 32 parameters to be measured on one analog-to-digital channel increases the number of parameters that can be acquired for a given number of electrical data system channels.

Multiplexers were also used in the days when things were done by hand using slide rules. They were either rotary switches or a series of switches that were used to connect different signals to an expensive device that allowed the signals to be read in digital units or often from a highly accurate analog indicator that had to be observed and the value recorded by hand on a data sheet. If the evolution of multiplexers is followed, it would go like this: very slow manual switches to faster

relays to reed relay Switches in a neutral gas to the current electronic multiplexers in a silicon chip. The reed switches could handle up to 10^3 switching operations per second. The current use of integrated circuits and semiconductor analog switches has increased the rate to 10^6 per second and even more for shorter word lengths.

Closely tied to the faster multiplexers has been the decrease in time required for the ADCs to read and convert the voltages. With the higher speeds of the converters and multiplexer switching it is possible to take an almost simultaneous sampling of all channels. This has led to systems that take a large number of samples over a very short time. The sets of samples are then summed and averaged, and a standard deviation is often determined.

It is now almost always possible for the data system to record data at a much higher rate than the typical time constants of the physical phenomena being investigated in a low-speed wind tunnel. It is important to explore the time variations of the time series and be sure that the chosen time frame over which data are taken is consistent with the objectives of the experiment. This will be explored further in Chapter 12.

Computers now typically used in wind tunnel data systems allow the setting of model attitude and acquisition of the data to be automated. There have been improvements also in electronic components required for each channel so that bridge voltage power supplies and bridge-balancing impedances are quite stable and are able to keep the electrical noise to a low level. Amplifiers can cover frequencies down to zero. They are more stable (less drift) and have better noise levels and improved common mode rejection. Programmable power supplies of secondary standard quality can be used to calibrate amplifiers periodically during test operations to check drift. The calibration is stored and used for all subsequent readings until the next calibration. The use of electronic analog filters or digital filters can reduce the effect of electrical noise to reasonable levels but keep in mind that these must be used carefully.

The measurement noise that arises from aerodynamic phenomena of the tunnel and model are more difficult to manage. The frequency of aerodynamic measurement noise is often quite low and simply extends the time over which a particular condition must be held and data averaged either by analog or digital means. This negates, to some degree, the advantages of the high-speed capabilities of digital acquisition systems. "Noise" as used in this paragraph is not referring to acoustic signals as detected by the human ear although there may be a direct physical relation in some instances.

REFERENCES AND NOTES

1. The terms *pressure* and *static pressure* are used interchangeably. They imply the pressure in a reference frame in which the mean molecular velocity is zero. *Temperature* and *static temperature* are similarly used. Additional detail in the definition is required if one considers the variation in dynamic pressure for parcels of fluid small enough to be participating in "turbulent" fluctuations but large compared to molecular dimensions.
2. Millikan, C. B., and Kline, A. L., "The Effect of Turbulence," *Aircraft Eng.,* Aug. *1933,* pp. 169–174.

3. Dryden, H. L., Schubauer, *G*. B., Mack, W. C., Jr., and Skramstad, H. K., "Measurements of Intensity and Scale of Wind Tunnel Turbulence and Their Relation to the Critical Reynolds Number of Spheres," NACA Report 581, 1937.

4. Dryden, H. L., and Kuethe, A. M., "Effect of Turbulence in Wind Tunnel Measurements," NACA Report 342, 1929.

7 Forces and Moments from Balance Measurements

The purpose of load measurements on the model is to make available the forces and moments so that they may be corrected for tunnel boundary and scale effects and utilized in predicting the performance of the full-scale vehicle or other device.

The loads may be obtained by at least the following four methods, which are listed in the order of frequency of use: (1) measuring the actual forces and moments on the complete model or on parts of the model with one or more balances; (2) measuring the stress distribution over the model by means of orifices connected to pressure-measuring devices or other means such as pressure- or shear-sensitive coatings; (3) measuring the effect that the model has on the airstream by wake surveys and tunnel wall pressures; and (4) measuring the motion of the model under the action of the aerodynamic forces and computing the forces from equations of motion.

In this chapter, we consider the first of these. The second and third will be considered in Chapter 7. The fourth will be considered in Chapter 18.

7.1 FORCES, MOMENTS, AND REFERENCE FRAMES

A reasonable concensus on definitions of standard reference frames for use in the study of vehicle dynamics in several subfields has been reached. We suggest consulting some standard references for more complete discussions. The American Institute of Aeronautics and Astronautics (AIAA)[1] has published a standard for aerospace applications. Etkin and Reid[z] can be consulted for examples of applications. The Society of Automotive Engineers (SAE)[3] has published a standard for automotive applications. Milliken and Milliken[4] can be consulted for examples of applications. Lewis[5] can be consulted for conventions and applications to marine vehicles. We include these references because it is common for a wind tunnel engineer to need an acquaintance with the terminology of a potential user of a facility and whose background may vary. We will be using the conventions from aeronautics in most of our discussions because those have tended to be adopted or adapted to a great extent for other applications.

The two most used reference frames are body axis frames and wind axis frames. A thii reference frame is referred to as stability axes. Any reference frame is determined by its orientation relative to some other frame or a basic physical reference and the location of the origin. A reference frame is a set of three orthogonal axes, by convention always labeled in a right-hand sequence.

234
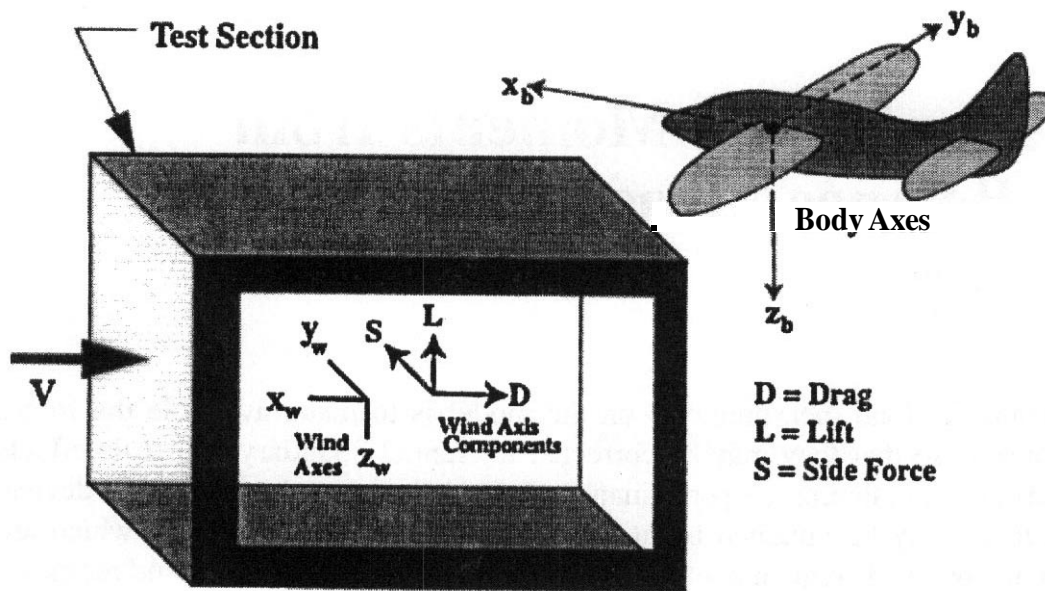
FIGURE 7.1   Wind and body reference frames.

Wind Axes

For wind tunnel applications, we first consider the wind axes. We illustrate this in Figure 7.1. The wind axes have x_w pointing into the wind, z_w pointing down, and y_w pointing to the right looking into the wind. If the test section is not horizontal, then an appropriate local convention must be adopted. We show vectors indicating components of forces that are used in wind axes. Note that drag is in the negative x_w direction and lift is in the negative z_w direction while the side force is in the positive y, direction.

We note that a perfectly aligned wind tunnel would have the wind axes exactly parallel to the wind tunnel axis. In reality, there are angularities, and these lead to the wind axes for any given model that may be angularly offset from the tunnel axes.

Body Axes

The body axes are fixed to the model and move with it. The exact alignment with any particular model must be specified as part of test planning. The x_b–z_b plane is frequently a plane of symmetry or approximately so. The force components on body axes are sometimes referred to as axial force, side force, and normal force for the x_b, y_b, z_b components, respectively, or sometimes as body drag, body lift, and body side force. This multiple terminology can lead to confusion and requires attention to avoid errors in communication. We will use the former set to refer to body axis components.

Moments and Reference Frame Origins

The moment components on the x, y, z axes are referred to as rolling moment, pitching moment, and yawing moment, respectively. If context is not sufficient to

distinguish between what is intended, then body roll, body pitch, and body yaw or wind roll, wind pitch, and wind yaw must be used. Note that the origins of the reference frames must be carefully specified in every case since the moments are directly and critically dependent on this choice and there is no universal standard.

Model Attitude

The standard way to specify model attitude is to use an **Euler** angle sequence going from wind axes to body axes of "yaw," ψ, about the z_w axis, "pitch," θ, about an intermediate y axis, and "roll," ϕ, about the x_b axis. **Etkin** and Reid[2] can be consulted for details. However, it is the aerodynamic angles, angle of attack α and sideslip β, that are the preferred independent variables for writing aerodynamic functions. The rotation sequence to go from wind axes to body axes for the aerodynamic angles is to rotate β in a negative sense about the z_w axis, then rotate a in a positive sense about the y_b axis. In the wind tunnel case for which the wind axes are aligned with what is taken as an **Earth** fixed frame in vehicle dynamics, yaw ψ is the negative of sideslip β provided roll is zero. This is the situation for many cases of tests using external balances. There are several opportunities to get signs mixed up so we will give a formal procedure.

Consider two reference frames F_1 and F_2, as sketched in Figure 7.2, where a vector A is shown along with expressions for its components on each of the two
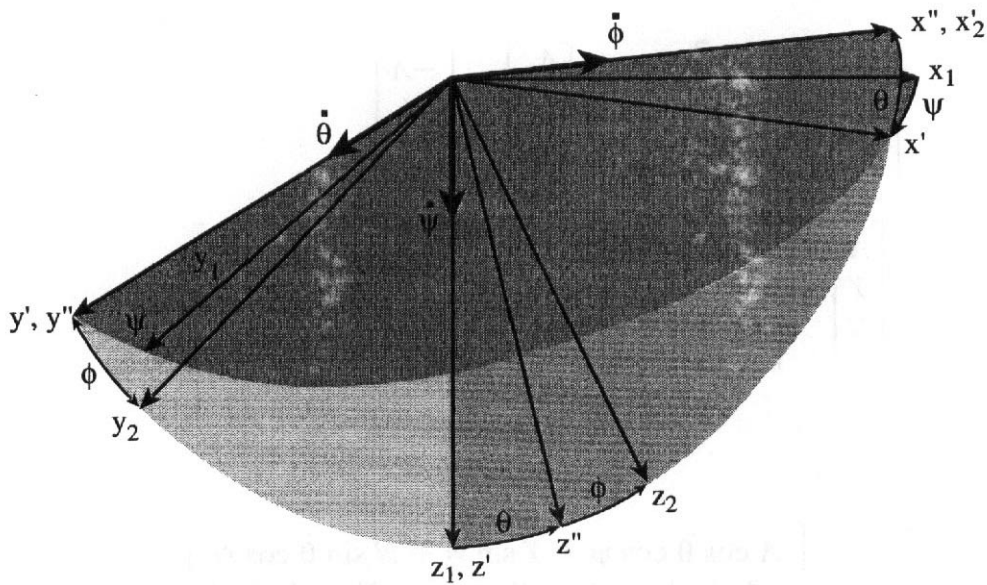
$$\mathbf{A_1} = \begin{bmatrix} A_{x_1} \\ A_{y_1} \\ A_{z_1} \end{bmatrix} \qquad \text{vector A} \qquad \mathbf{A_2} = \begin{bmatrix} A_{x_2} \\ A_{y_2} \\ A_{z_2} \end{bmatrix}$$

FIGURE 7.2   Transforming vectors from F_1 to F_2.

frames. The relationship between the components on the two frames in terms of the Euler angles as indicated in the sketch is as given by Equation (7.1), where we have identified frame 1 with the wind axes and frame 2 with the body axes:

$$
\begin{bmatrix} A_{x_b} \\ A_{y_b} \\ A_{z_b} \end{bmatrix} = \begin{bmatrix} 1 & 0 & 0 \\ 0 & \cos\phi & \sin\phi \\ 0 & -\sin\phi & \cos\phi \end{bmatrix} \begin{bmatrix} \cos\theta & 0 & -\sin\theta \\ 0 & 1 & 0 \\ \sin\theta & 0 & \cos\theta \end{bmatrix} \begin{bmatrix} \cos\psi & \sin\psi & 0 \\ -\sin\psi & \cos\psi & 0 \\ 0 & 0 & 1 \end{bmatrix} \begin{bmatrix} A_{x_w} \\ A_{y_w} \\ A_{z_w} \end{bmatrix}
$$

$$(7.1)$$

For the most common case arising in wind tunnel work for which roll ϕ is zero, the result is given by

$$
\begin{bmatrix} A_{x_b} \\ A_{y_b} \\ A_{z_b} \end{bmatrix} = \begin{bmatrix} \cos 0 \cos\psi & \sin\psi \cos 0 & -\sin\theta \\ \sin\psi & \cos\psi & 0 \\ \sin\theta \cos\psi & \sin 0 \sin\psi & \cos 0 \end{bmatrix} \begin{bmatrix} A_{x_w} \\ A_{y_w} \\ A_{z_w} \end{bmatrix}
$$

$$(7.2)$$

The conventions for positive aerodynamic force components are not in the positive directions for the axes. The relations are as follows, with Equation (7.4) giving the expressions for converting wind axis force components to **body** axes and Equation (7.5) giving the expressions for converting body axis force components to wind axes:

$$
\begin{bmatrix} A_{x_w} \\ A_{y_w} \\ A_{z_w} \end{bmatrix} = \begin{bmatrix} -D \\ S \\ -L \end{bmatrix} \quad \text{and} \quad \begin{bmatrix} A_{x_b} \\ A_{y_b} \\ A_{z_b} \end{bmatrix} = \begin{bmatrix} -A \\ Y \\ -N \end{bmatrix}
$$

$$(7.3)$$

$$
\begin{bmatrix} A \\ Y \\ N \end{bmatrix} = \begin{bmatrix} D\cos\theta\cos\psi - S\sin\psi\cos 0 - L\sin 0 \\ D\sin\psi + S\cos\psi \\ D\sin 0 \cos\psi - S\sin 0 \sin\psi + L\cos 0 \end{bmatrix}
$$

$$(7.4)$$

or

$$
\begin{bmatrix} D \\ S \\ L \end{bmatrix} = \begin{bmatrix} A\cos\theta\cos\psi + Y\sin\psi + N\sin\theta\cos\psi \\ -A\sin\psi\cos\theta + Y\cos\psi - N\sin\theta\sin\psi \\ -A\sin\theta + N\cos\theta \end{bmatrix}
$$

$$(7.5)$$

The moment components are consistent with the positive conventions on the axes so they follow directly from Equation (7.2). We use lowercase l, m, and **n** to denote moments with no subscript for the body axes and with subscript w for the wind

axis components. The results are given by Equation (7.6) for converting wind to body axes and Equation (7.7) for converting body to wind axes:

$$
\begin{bmatrix} l \\ m \\ n \end{bmatrix} = \begin{bmatrix} l_w \cos 0 \cos \psi + m_w \sin \psi \cos \theta - n_w \sin 0 \\ -l_w \sin \psi + m_w \cos \psi \\ l_w \sin \theta \cos \psi + m_w \sin \theta \sin \psi + n_w \cos \theta \end{bmatrix} \tag{7.6}
$$

$$
\begin{bmatrix} l_w \\ m_w \\ n_w \end{bmatrix} = \begin{bmatrix} l \cos \theta \cos \psi - m \sin \psi + n \sin 0 \cos \psi \\ 1 \sin \psi \cos 0 + m \cos \psi + n \sin \theta \sin \psi \\ -l \sin \theta + n \cos \theta \end{bmatrix} \tag{7.7}
$$

Conversions between "stability axes" and wind axes are obtained by putting $\theta = 0$ in Equations (7.4)–(7.7) and replacing the body axis components with stability axis components.

Other common expressions equivalent to these in terms of angle of attack and side slip are obtained by substituting $0 = \alpha$ and/or $\psi = -\beta$ directly into the above equations.

Moment Transfers

Frequent use is made of the relations from engineering statics which give the rules for transferring forces and moments from one reference point to another. The rule is simple, but again the non-right-hand rule conventions as treated above sometimes lead to errors. If a system of forces produces a resultant force $\mathbf{F}$ and a resultant moment $\mathbf{M}_1$ relative to point 1, then an equivalent system acting at another point, 2, is

$$
\mathbf{F}_2 = \mathbf{F}_1 \tag{7.8}
$$

$$
\mathbf{M}_2 = \mathbf{M}_1 - \mathbf{r}_{12} \times \mathbf{F}_1 \tag{7.9}
$$

where $\mathbf{r}_{12}$ is the vector from point 1 to point 2. The common use of this expression is to transfer moments from a "balance center" to a reference of choice for a particular model. Expanding Equation (7.9) for a case of obtaining the moment at the center-of-mass of a model (cm) from the force and moment measured at the balance center (bc) with all components in wind axes gives Equation (7.10), where $[x_{cm}\ y_{cm}\ z_{cm}]$ are the coordinates of the desired center of mass in the wind axis frame with origin at the balance center:

$$
\begin{bmatrix} l_{w_{cm}} \\ m_{w_{cm}} \\ n_{w_{cm}} \end{bmatrix} = \begin{bmatrix} l_{w_{bc}} \\ m_{w_{bc}} \\ n_{w_{bc}} \end{bmatrix} - \begin{bmatrix} 0 & -z_{cm} & y_{cm} \\ z_{cm} & 0 & -x_{cm} \\ -y_{cm} & x_{cm} & 0 \end{bmatrix} \begin{bmatrix} -D \\ S \\ -L \end{bmatrix}
$$

$$
\begin{bmatrix} l_{w_{cm}} \\ m_{w_{cm}} \\ n_{w_{cm}} \end{bmatrix} = \begin{bmatrix} l_{w_{bc}} + Sz_{cm} + Ly_{cm} \\ m_{w_{bc}} - Lx_{cm} + Dz_{cm} \\ n_{w_{bc}} - Dy_{cm} - Sx_{cm} \end{bmatrix} \tag{7.10}
$$

7.2 BALANCES

We have been treating relations between force and moment components on different reference frames. A wind tunnel balance is expected to separate these force and moment components and accurately resolve what is almost always small differences in large forces. A complicating factor is that the various force and moment components vary widely in value at any given air speed and each varies greatly over the speed range from minimum to maximum. Balance design and use are problems that should not be deprecated; in fact, it might truthfully be said that balance design is among the most trying problems in the field.

Concept of a **Six-Component** Balance

In an attempt to picture the situation most clearly, a conceptual but impractical wire balance based on spring scales is shown in Figure 7.3. The model, supposed to be too heavy to be raised by the aerodynamic lift, is held by six wires. Six forces are read by scales A, B, C, D, E, and F: The wires attached to A and B are parallel to the incoming air velocity vector and define a plane that can be taken as a reference plane for the balance. We will designate this the **x–y** plane. These wires point in the **x** direction. The wire attached to F is perpendicular to the A and B wires and is in the **x–y** plane. This wire points in the $-y$ direction. The wires attached to C and D are in a plane that is perpendicular to the **x–y** plane, which we designate the **y–z** plane. The C and D wires are perpendicular to the **x–y** plane. Wires **A** and C are attached at a common point on the right wing. Wires B, D, and F are attached to a common point on the left wing. Finally the wire attached to E is parallel to C and D and is in a plane parallel to C and D and halfway between them:
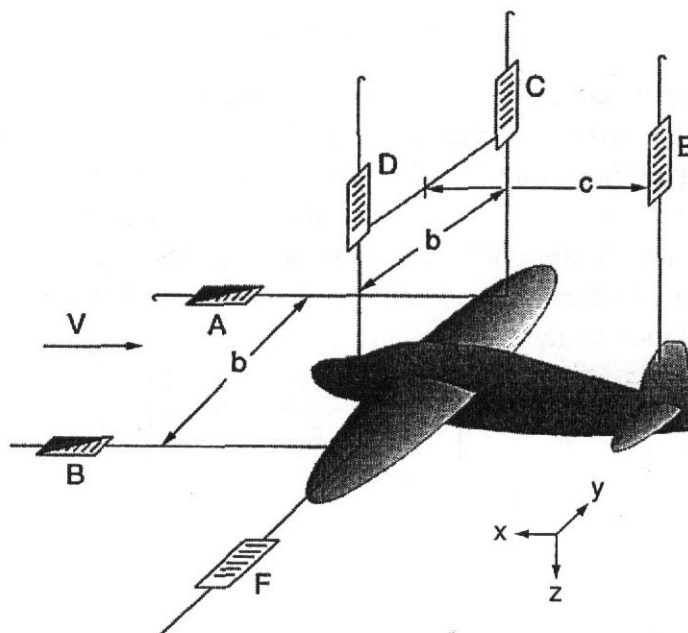
FIGURE 7.3 Diagrammatic wind tunnel balance.

1. Since the horizontal wires A, B, and F cannot transmit bending, the vertical force perpendicular to V, the lift, is obtained from the sum of the forces in the vertical wires: $L = C + D + E$.

2. The drag is the sum of the forces in the two horizontal wires parallel to the direction of V: $D = A + B$.

3. The side force is simply $\overline{Y} = F$.

4. If there is no rolling moment, that is, no moment component in the direction of the x axis, scales C and D will have equal readings. But more generally a rolling moment will appear as $l = (C - D) \times b/2$. Note carefully that this is with reference to a point halfway between the two wires C and D, through which the line of action of F passes, and in the plane defined as containing E.

5. Similarly, a yawing moment, that is, a moment component in the direction of the z axis, will result in nonequal forces in the wires A and B and the yawing moment will be given by $n = (A - B) \times b/2$. Here also note that this is a moment with reference to a point halfway between **A** and **B** and through which the line of F passes.

6. The pitching moment is given by $m = E \times c$. This is a moment about the line containing F.

Exact perpendicularity between the wires must be maintained. For instance, if the wire to scale F is not exactly perpendicular to wires A and B, a component of the drag will appear (improperly, of course) at scale F and will be interpreted as side force. A similar situation exists in regard to lift and drag and lift and side force. Since the lift is the largest force by far in typical aircraft complete model wind tunnel work, extreme care must be taken to ensure that it is orthogonal to the other components.

To illustrate the situation in more detail, consider a planar subset of lift, drag, and pitching moment, as indicated in Figure 7.4. We will assume that we can
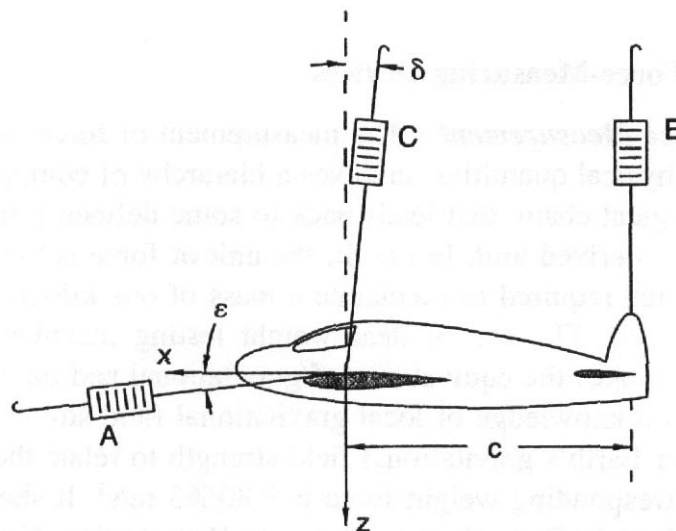
FIGURE 7.4 Effect of balance component skew.

determine precisely the direction of the x and z axes and apply loads along those axes in order to explore the reaction in the wires. The expressions for equilibrium in the X and Z directions are

$$Z + A \sin \varepsilon - C \cos \delta - E = 0$$

$$X + A \cos \varepsilon - C \sin \delta = 0 \qquad (7.11)$$

$$m + Ec = 0$$

Assume the actual loads are $m = 0$ and $Z = 10X$. What will our balance read with the improper alignment as indicated by Figure 7.4? Solving for A, C, and E gives

$$E = 0$$

$$C = \frac{Z \cos \varepsilon - X \sin \varepsilon}{\cos \varepsilon \cos 6 - \sin \varepsilon \sin 6} - \left[\frac{\cos \varepsilon - \sin \varepsilon/10}{\cos \varepsilon \cos \delta - \sin \varepsilon \sin \delta} \right] Z \qquad (7.12)$$

$$A = \frac{-X \cos \delta + Z \sin \delta}{\cos \varepsilon \cos 6 - \sin \varepsilon \sin 6} - \left[\frac{-\cos 6 + 10 \sin 6}{\cos \varepsilon \cos \delta - \sin \varepsilon \sin 6} \right] X$$

If the alignment is perfect, we of course get C $=$ Z and A $=$ $-$X. But if each of the angles is only 0.002 rads, or about $0.1°$, then C = 0.99982 and A = $-0.9800X$. This is a 2% error in the drag reading! This is not an artifact of our simple conceptual model of a balance. Alignments of multicomponent balances is very critical. And even after the best efforts, the result must be evaluated by calibration. We will discuss calibration in more detail later. It is advisable to thoroughly absorb the arrangement indicated by Figure 7.3 before proceeding to more complex balance arrangements.

Terminology for Force-Measuring Devices

Standards for Force Measurement The measurement of force, as with all other measurements of physical quantities, involves a hierarchy of comparisons, or more precisely a metrological chain, that leads back to some defined primary standards. Force, however, is a derived unit. In the SI, the unit of force is the newton, which is defined as the force required to accelerate a mass of one kilogram at one meter per second per second. The use of dead-weight testing machines as secondary transfer standards invokes the equivalence of gravitational and inertial acceleration effects and requires a knowledge of local gravitational field strength. The adopted "standard" value for Earth's gravitational field strength to relate the standard kilogram mass to a corresponding weight force is 9.80665 m/s^2. It should be realized that it varies significantly from place to place. At Hammerfest, Norway, the value has been measured as 9.82618 m/s^2 while in the United States, at Miami, Florida,

it has been measured as **9.79004 m/s²**. A model for the variation of acceleration of gravity g with latitude A has been given by Moritz[6] as

$$g = 978.0327[1 + 0.0053024(\sin \lambda)^2 - 0.0000058(\sin 2\lambda)^2] \qquad (7.13)$$

There is a systematic variation with altitude and measurable local variations associated with geological densities. Another standard correction required for dead-weight machines used as transfer standards for force measurement is the difference between the buoyancy force on the standard weight and the test article due to differences in density.

Load cells are widely used both for secondary standards and for measurement applications. Their output is not **directly** related to local gravitational field strength, but they are sensitive to other environmental and operational variables. If a load cell is checked against a "standard" weight, the result will, of course, be dependent on the local gravitational field strength.

For detailed discussions of issues of metrology for force measurement Bray, Barbato, and Levi[7] may be consulted. Standards organizations that maintain related documentation include the International Organization for Standardisation (ISO), Organisation Internationale de Métrologie Légale (OIML), Bureau International des Poids et Mesures (BIPM), American Society for Testing and Materials (ASTM), National Institute for Standards and Technology (NIST), and many others.

Terminology of Transducer Characterization   The historical definition of an "ideal" transducer has included that the output be proportional to the quantity being measured. An ideal transducer for a force component, say X, would provide an output, O, related to X by the equation $O = kX$, and ideally O would be insensitive to all other variables. Real transducers only approximate the linear relationship and **are** always sensitive to other variables to some degree. A notional calibration curve for a transducer is shown in Figure 7.5. The curves as shown have exaggerated curvature compared to a typical high-quality transducer. The tolerance is typically a fraction of a percent so the lines all collapse. It is easier to see the details of the characterization by plotting the difference between the calibration data and the linear fit plus the difference between the calibration data and a second-order fit. A result of this will often appear as shown in Figure 7.6. These plots are sometimes referred to as residual plots. With the available computational power today, there is little reason not to use whatever curve form is needed to reduce the residuals to have a mean of zero with random distribution. However, a majority of commercial transducers have their specifications given in terms of deviation from linearity. Each transducer specification should be carefully studied and the maker required to provide details on the calibration procedure and data processing. The usual situations in wind tunnel applications **are** such that **commercial** transducers will frequently be calibrated on site before being put into use. It is often possible to obtain better performance than the manufacturer quotes as nominal for a particular type.

Two fundamental types of balances for measuring total model forces and moments are in general use: external balances, which carry the loads outside the tunnel before
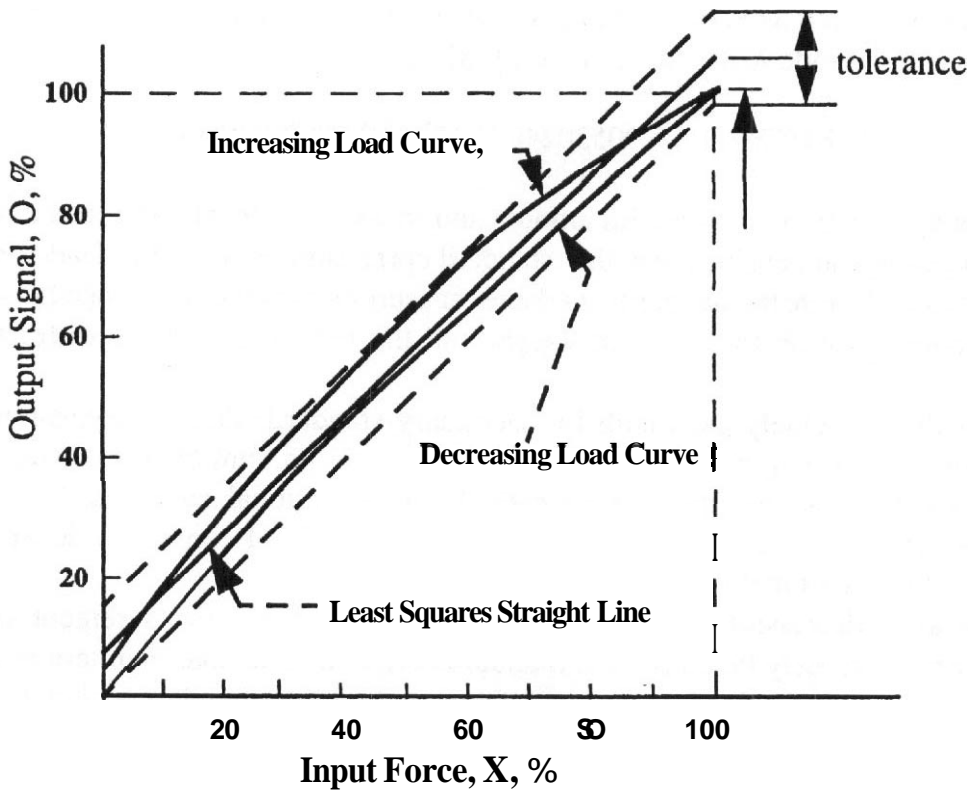
FIGURE 7.5   Typical calibration curve for a transducer to show terminology.
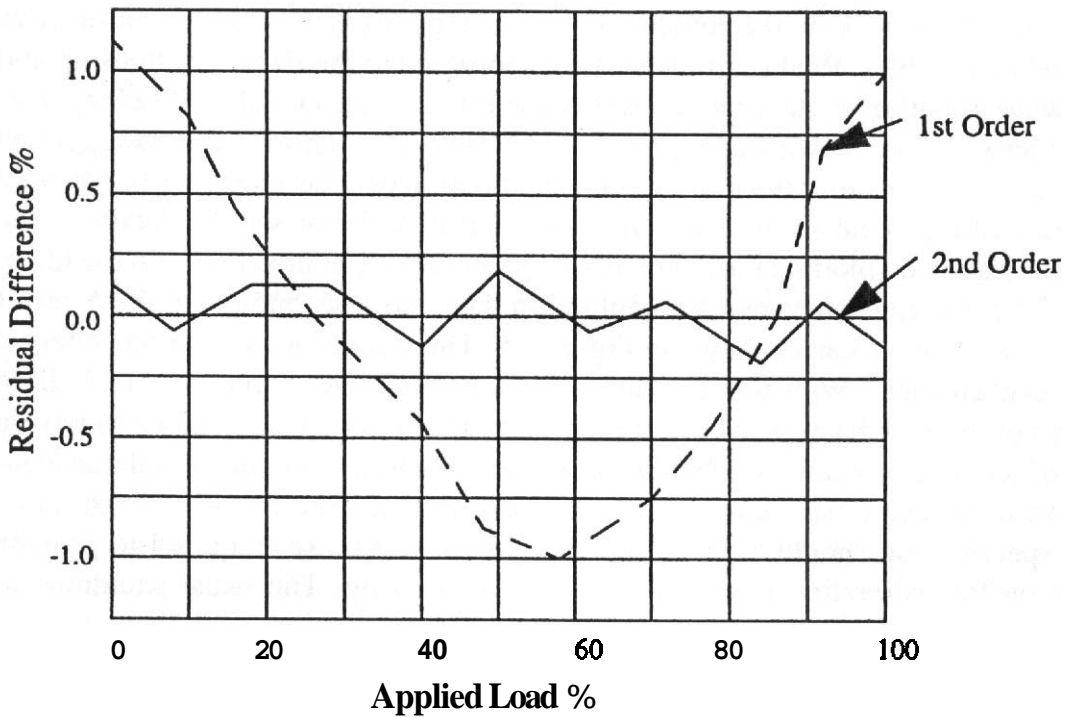
FIGURE 7.6   Characteristic variation of calibration of a transducer from linear and second-order fits.

they are measured, ãnd internal balances, which fit into the models and send data out through electrical signals. Both types have their advantages, and few tunnels can get along with either one alone. It is also common to design, fabricate, and calibrate special load-measuring units for model parts. These are usually similar to internal balances but almost always simpler in concept and execution.

Before proceeding further with considerations of various balance mechanisms, we will discuss aspects of the requirements on wind tunnel balances, with the main focus being on measurement of total model forces and moments.

7.3   BALANCE REQUIREMENTS AND SPECIFICATIONS

We have introduced some discussion of balance design and will follow with more, but we emphasize that it is our main purpose to impart some rudimentary knowledge about these systems so that a wind tunnel engineer can use them wisely. Actual balance design and construction require far more information than we can provide. We would like to issue a note of warning to those with little experience who might undertake the job. A wind tunnel balance is an immensely complicated apparatus, and its design and construction are much better left to balance engineers than to tunnel engineers. Scarcely a wind tunnel exists that has not been held back from use by long delays resulting from balance calibration, and sad indeed have been many tunnel engineers who found that they were saddled with research on balances rather than on airplanes. Buy the balance, then, if it is at all possible, and insist that it be set up and calibrated at the factory. If delays occur there, the tunnel is available for additional calibration, improvements to flow quality, and a host of other problems particularly besetting a new tunnel.

Any wind tunnel balance is of necessity a compromise between the required maximum load capability of all components and the accuracy required for minimum loads. The solution to this problem is much simpler for an internal balance, since several balances can be designed and built for different load ranges and one selected for the desired loads. A risk with an internal balance is that the model loads may inadvertently exceed the balance capacity. This may result in a failed balance. For an external balance a careful study must be used to try to account for every type of model and test for which the balance will be used over a period of years. In this type of study there is no substitution for wide and long experience in wind tunnel testing.

The expected loads that a balance must carry are primarily a function of the size of the tunnel test section and speed. If the size of a tunnel is doubled, the model size and the loads are increased fourfold for a fixed model-to-tunnel-size ratio, model attitude, and tunnel speed. It should be noted that in this case the Reynolds number goes up by factor of 2 and model volume by a factor of 8.

As a rule of thumb the maximum model span will be equal to or less than 0.8 of the tunnel width for a full model. For a half model, the model span will be equal to or less than 0.7 of the tunnel height.

A model of an aspect ratio of 9 and a span equal to 0.8 of the tunnel width in an 8 × 12-ft tunnel will lead to an area of 10.24 ft². If the model is tested at a dynamic pressure of 60.0 lb/ft², then qS = 614.4 lb. If one wishes to measure drag coefficient to ±0.0001 in cruise condition, or one drag count, the drag balance must be able to resolve 0.06 lb, which requires it to measure the drag to an accuracy of ±0.03 lb. If one assumes the model is a powered model of a propeller-driven airplane, the maximum dynamic pressure when power testing will be close to 15.0 lb/ft² and qS = 153.6 lb, and for one drag count the drag balance must be able to read 0.015 lb, or in other words be accurate to ±0.008 lb. The same model, power-off, past stall could have a C_D of 1.00 and at qS of 614.4 lb, which would yield a drag load of 614.4 lb. Thus, the drag balance should be able to resolve loads from 0.008 to 600 lb, a ratio of 75,000 : 1. Another way to look at the requirement is that the minimum reading should be 0.0012% of full scale. These values are typical of what is required for a general-purpose low-speed wind tunnel balance.

The ratio of maximum to minimum values of the drag balance also has implications for a computerized data system. If the desired ratio is 75,000 : 1, then 17 bits resolution is required (2^{16} = 65,536 and 2^{17} = 131,072). If a 14-bit (16,384) ADC is used, then the minimum drag value that can be detected for 600 lb full scale is 0.037 lb, or four times larger than required. This problem is relieved, as discussed in Section 3.9, by taking multiple passes at the data and averaging the value. However, the minimum detectable value is still 0.037 lb. The digitizing systems needed for external balances tend to be more akin, or actually identical, to five- to eight-digit integrating digital voltmeters than to high-speed ADCs used in signal processing or less demanding measurement systems.

Although in the previous example the requirement of one drag count C_D = 0.0001 was used, the authors do not want to leave the impression that measuring to this level is easy or routine. One drag count is the goal for cruise drag, but in most cases it is difficult to get model repeatability when configuration changes are made and then restored to supposedly the same configuration to better than two or three counts. Special attention must be given during model design to having the ability to return to any desired configuration with extreme precision. And of course it is necessary to take very special care during model changes. A very small geometric change can produce several counts of drag variation. And, of course, the tunnel conditions must be measured to the corresponding level of accuracy.

An external balance can be designed and built to obtain these ranges of load-resolving capability. This type of balance is quite large physically, and when designed to measure each of the six components separately, such a range of values is obtainable when the balance is carefully aligned, which is possible because of its size, corresponding rigidity, and robustness.

This range of resolution is much more difficult to obtain with an internal strain gage balance and in the previous example for a propeller-powered model might require the use of two internal balances: one for power-off and a second for power-on testing. Unfortunately, testing the same model on two balances is not efficient and would typically require two separate tunnel entries. The two advantages of an external balance are its great resolving power and its ability to hold its

TABLE 7.1. **Probable** Maximum Coefficients Developed by Full- and Half-Span Models

C_L	+4.0	−2.0	C_n	+0.20	−0.20
C_D	+1.0	−1.0	C_l	+0.20	−0.20
C_m	−1.0	+1.0	C_Y	+1.0	−1.0

calibration over very long periods of time. The disadvantages can be its size and often high initial cost and the time required to initially align or reduce the interactions between the six components. It is possible to calibrate the interactions and not align the balance. This option has become more attractive as calculations have become cheaper and faster. The computational algorithms have now become an essential complement to a balance.

The advantage of a sting or internal balance is a lower initial cost, although this may be negated by building several with overlapping load ranges to meet possible testing requirements over a period of time. A second advantage is that one balance may possibly be used in several tunnels, assuming that the balance can be adapted to different stings. With special stings, an internal balance can often be used to reach higher angles of attack than can be obtained with an external balance. This is most useful for tests of fighters that are required to operate at extreme angles of attack.

No single balance system will handle all possible tests for all possible vehicles. But an external balance proves to be the most versatile because of its large load range and adaptability to uses that were never thought of when it was designed.

Table 7.1 lists some suggested values in terms of maximum coefficients that would be desirable to achieve with a balance. For a half-span model it should be noted that the values given for the longitudinal components, that is, C_L, C_D, and C_m, apply, but the balance components are now $C_L = C_Y$, $C_D = C_D$, and $C_m = C_n$. This should not affect the yaw balance since the three moment components of external balances often have the same ranges. The requirement that the side-force component carry the full lift load may have an affect on the sensitivity of side force. A second problem with half models is that the center of lift of a half wing will not be at the balance moment center. In fact, it will be below the moment center, possibly one-half the distance from the centerline of the tunnel to the floor. This can lead to large rolling moments and can affect the load range of the roll balance. These comments apply to an external balance only. A sting balance for a half model would, in most cases, be designed for that purpose.

The maximum values in terms of forces and moments should be based on the smallest model expected at the lowest expected dynamic pressures and the maximum values from the largest model at the highest expected dynamic pressure and the maximum values given in Table 7.1. If a compromise must be made in the balance design, care must be taken to ensure that the balance is more than adequate for the ranges of model size and dynamic pressure at which most testing is expected to take place. This means that if one needs a higher resolution in side force for a full

model than is available when the side-force balance maximum load is equal to the lift load and half-model tests are not a primary requirement, then the half-model requirements can be relaxed. It should be noted that an 8 X 12-ft tunnel model span equal to 0.8 tunnel width and an aspect ratio of 9 yielded a wing area of 10.24 ft^2. A half model with a span equal to 0.70 of the tunnel height would have an area of 13.94 ft^2 for a full wing, since the Reynolds number will increase by the square root of the area ratio, or by 1.16. The main advantage of a half model lies in the reduction of model costs for the wing and, especially, the flap system.

Care should also be taken not to overemphasize a small model at low dynamic pressure in determining the minimum loads. Quite often the small models are for research purposes and are used to determine trends, not values, for a flight vehicle. It would be almost the height of absurdity to size the minimum values of the balance for the NASA 80 X 120 V/STOL test section (a part of the 40 X 80 tunnel), for a 6-ft^2 model at a dynamic pressure of 10 lb/ft^2.

The balance requirements previously discussed are for tunnels intended for research and development testing and would range in size from 7 X 10 ft (70 ft^2) and upward. Small tunnels intended for student use can have the tolerances relaxed. and they can be further relaxed for simple demonstration tunnels.

Tunnels designed for purposes other than aircraft testing will have an entirely different set of values. Terminology for a particular application area may vary. For example, a "drag count" for automobile applications is $\Delta C_d = 0.001$ and the reference area is the frontal area instead of the planform area, as is used for lifting surfaces. Table 7.2 lists the balance ranges for the General Motors automotive tunnel. It should be noted that automotive engineers are not as interested in developing large lift coefficients as are aeronautical engineers, at least for general-use production vehicles. Racing automobile designers do work very hard on managing aerodynamic down load.

In addition to the loading table, ranges for the pitch and yaw angles must be specified. Pitch angle range for two- and three-strut mounting systems will vary with the rearward distance of the pitch strut from the front struts but should in any event provide for $\pm 40°$. Usually yaw from $-40°$ to $+190°$ is provided. Two degrees per second is a good rate of change for both pitch and yaw, although much higher rates are being put into some systems so that dynamic testing can be explored. Current data systems can take data much faster than the aerodynamic forces respond

TABLE 7.2   Balance Load Ranges for General Motors Full-Scale Automotive Tunnel

Component	Low Range	High Range
Lift	517 lb	1506 lb
Drag	360 lb	1012 lb
Side force	517 lb	1506 lb
Pitching moment	2360 ft-lb	8114 ft-lb
Yawing moment	2360 ft-lb	8114 ft-lb
Rolling moment	2360 ft-lb	8114 ft-lb

TABLE 7.3. Permissible Measuring Errors in the Various Aerodynamic Coefficients[a]

	Low Angle of Attack	High Angle of Attack
Lift	$C_L = \pm 0.001$, or 0.1%	$C_L = \pm 0.002$, *or* 0.25%
Drag	$C_D = \pm 0.0001$, or 0.1%	$C_D = \pm 0.0020$, *or* 0.25%
Pitching moment	$C_m = \pm 0.001$, or 0.1%	$C_m = \pm 0.002$, or 0.25%
Yawing moment	$C_n = \pm 0.0001$, or 0.1%	$C_n = \pm 0.0010$, or 0.25%
Rolling moment	$C_l = \pm 0.001$, or 0.1%	$C_l = \pm 0.002$, or 0.25%
Side force	$C_Y = \pm 0.001$, or 0.1%	$C_Y = \pm 0.002$, or 0.25%

[a]For balance design requirements the actual loads should be figured using the smallest model expected to be tested and the lowest dynamic pressure. It is inevitable that the achievable uncertainty of the coefficients for the smallest models will be larger than for the largest models.

to rapid changes of condition. The temptation to run through operating states too fast to get repeatable data must be resisted. This may be possible in some cases only if the relationship between the achieved precisions and the mean values reported are explicitly shown as the test proceeds. Otherwise, there is great pressure to take data too fast since the data system can certainly log the numbers at a high rate.

The desired accuracies can be similarly attacked by first preparing a permissible error list from the aerodynamicist's viewpoint (Table 7.3). A critical maximum error condition may arise during powered testing of complete models because the dynamic pressure of the tunnel may then be unusually low.

7.4   EXTERNAL BALANCES

Four types of external balances have been in general use. These balances are named for their main load-carrying members—wire, platform, yoke, and pyramidal—and are discussed in the following paragraphs.

Wire Balances

One of the earliest types of wind tunnel balance was the wire balance, similar in principle to Figure 7.3. Spring scales were not used for the balance output since their deflections would change the model attitude. The model usually was mounted inverted so that aerodynamic lift added to the weight to prevent unloading the wires as the resulting tension can never be allowed to diminish to zero. With this type of balance there was a large tare drag on the wires that was difficult to assess accurately. The wires tended to break, which could lead to the loss of the model. Wire balances turned out to be much less robust and versatile than the alternatives and have not been used extensively since the very early days of aeronautics.

Platform, Yoke, and Pyramid Balances

Currently, most external balances provide strut-type mounting of models. These balances provide mechanisms for changing the angle of attack and yaw and transmit
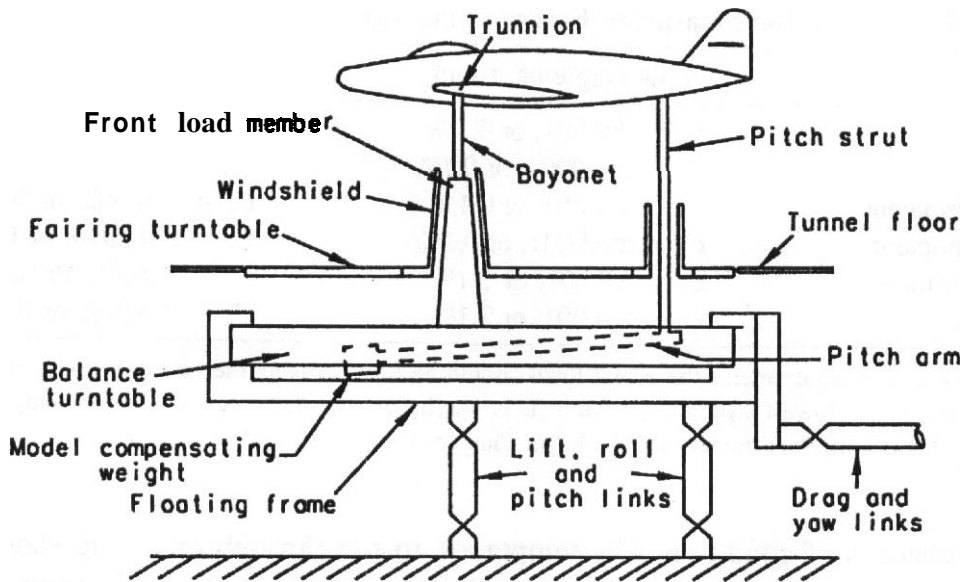
FIGURE 7.7   Greatly simplified diagrammatic sketch of some balance components.

the model loads down into a system of linkages that separate them into force and moment components. Such an apparatus is shown diagrammatically in Figure 7.7, and a linkage system is shown in Figure 7.8. The general massiveness of a balance structure may be seen in Figure 7.9.

Tracing the pathway followed by the loads from model to measuring unit (Figure 7.7), we see first that the model as illustrated is supported on two front-load members, or "struts," and a tail strut.' The struts, in turn, connect to the inner part of a floating
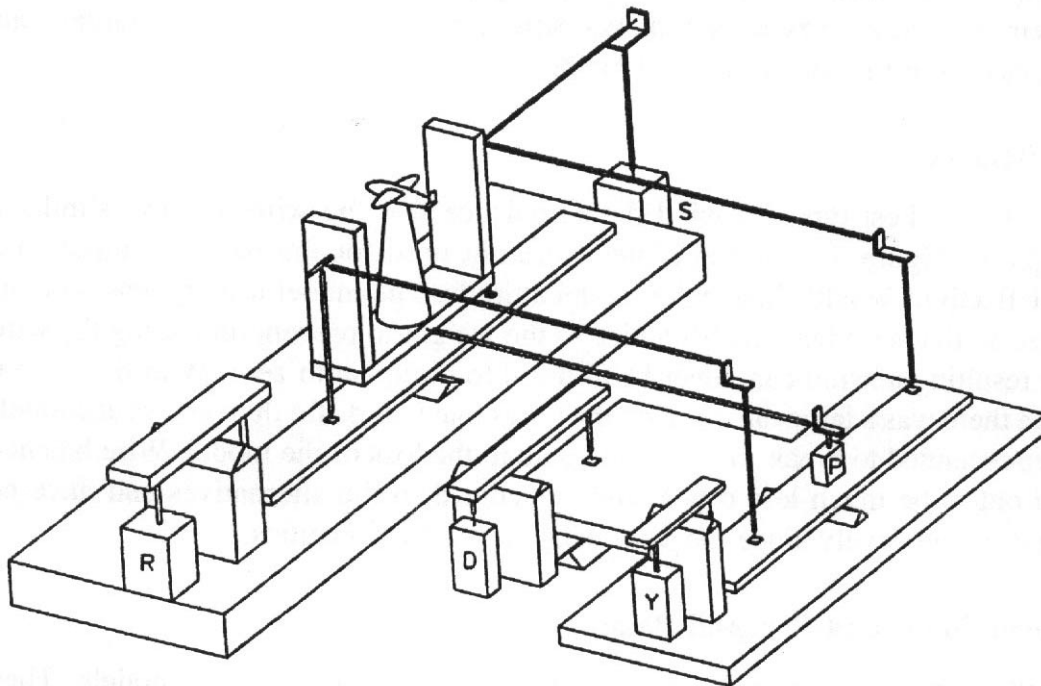
FIGURE 7.8   Balance linkage. Lift linkage (not shown) is beneath the roll table.
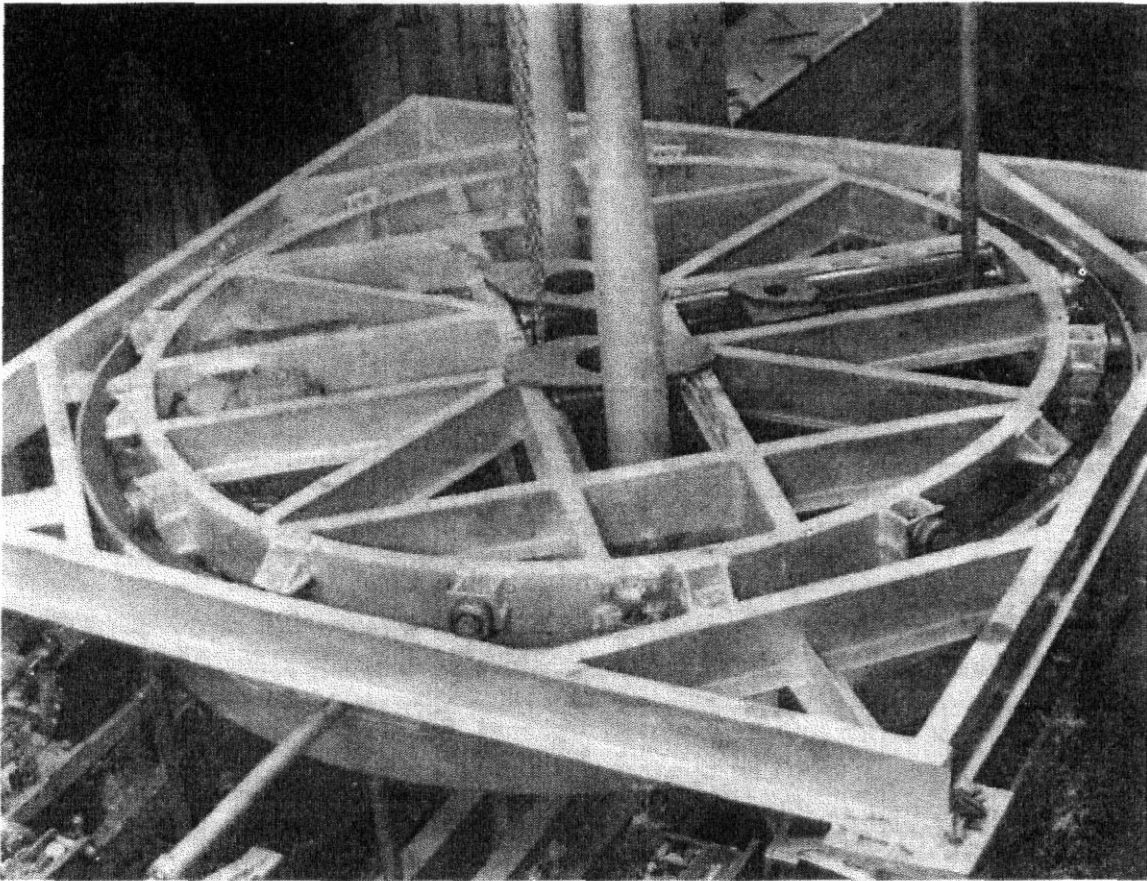
FIGURE **7.9** Massiveness of a wind tunnel balance is well illustrated by this photograph of a balance designed for a 150-mph wind tunnel with a 9-ft-diameter test section. During this early setup in the factory the load members have been dropped in place without going through their respective windshield support bases. **As** shown, the balance has approximately 45" negative **yaw.** (Courtesy Georgia Tech Research Corporation, 1998.)

ring frame that is free to turn (model yaw), and a mechanism is provided to raise or lower the tail strut to produce model pitch. The outer part of the floating frame is held in place by a system of struts that are specially designed to be strong in tension and compression but very weak in bending. These struts separate the components of the load by means of a linkage system and feed them into the measuring units or output transducers. Above the floating frame is a fairing turntable on which are mounted the windshields that minimize the direct aerodynamic forces on the support struts. The load turntable is tracked by the fairing turntable through the use of a servomechanism arrangement. And, as the fairing turntable rotates, the windshields are rotated in the opposite sense by a gear-driven mechanism so that they remain parallel to the airstream. In some balances the tail-strut fairing is moved up and down to keep the exposed length of tail strut constant as the angle of attack is changed. The windshields are connected electrically so that upon contact with the load members they activate fouling lights and/or audible signals so that the malfunction may be noted and corrected.

The linkage system by which the force and moment components are separated have gradually worked into three different fundamental types? These are named
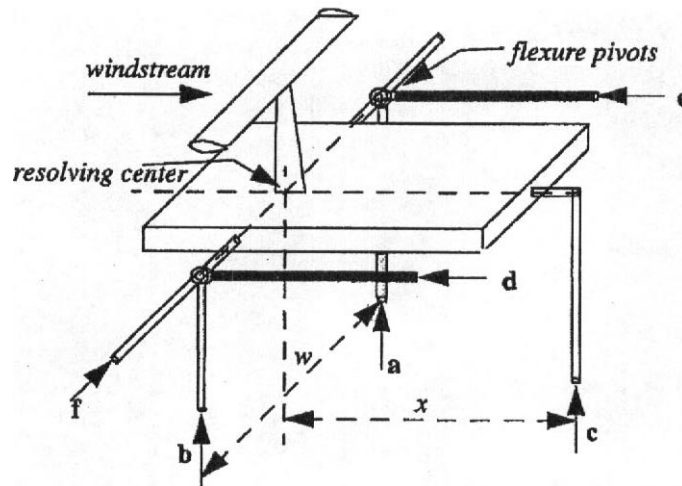
FIGURE 7.10 Basic layout of a platform balance.

platform, yoke, and *pyramidal,* according to the manner in which the main system is assembled.

Platform Balance The platform balance (Figure 7.10) utilizes either three or four legs to support the main frame. For the three-legged type, the forces and moments are

$$L = -(a + b + c) \qquad D = d + e \qquad S = -f$$

$$l = (a - b)(\tfrac{1}{2}w) \qquad n = (e - d)(\tfrac{1}{2}w) \qquad m = cx$$

Platform balances are widely used. Rugged and naturally orthogonal, they may be constructed and aligned with a minimum of difficulty. But they also have disadvantages: (1) the moments appear as small differences in large forces, an inherently undesirable arrangement; (2) the balance-resolving center is not at the center of the tunnel and the pitching moments must be transferred; and (3) the drag and side-force loads put pitching and rolling moments on the load ring. These interactions must be removed from the final data. Some of the disadvantages are ameliorated by the ease of computation today as compared to several decades ago. Also, applications such as automobiles and surface marine vehicles will be mounted on or near the floor, which is near the resolving center for a yoke balance.

Yoke Balance The yoke balance (Figure 7.11) offers an advantage over the platform balance in that the moment-resolving center is near the center of the tunnel. However. the inherent design of the yoke leads to bigger deflections than the platform balance, particularly in pitch and side force. Because the balance frame must span the test section in order to get the two upper drag arms in their positions, the yaw lever arm is exceptionally long. The high supporting pillars are subject to large deflections. Once again the final forces must be summed up: The drag is the addition of three forces, and the lift is the sum of two forces in the variant shown. The yoke balance
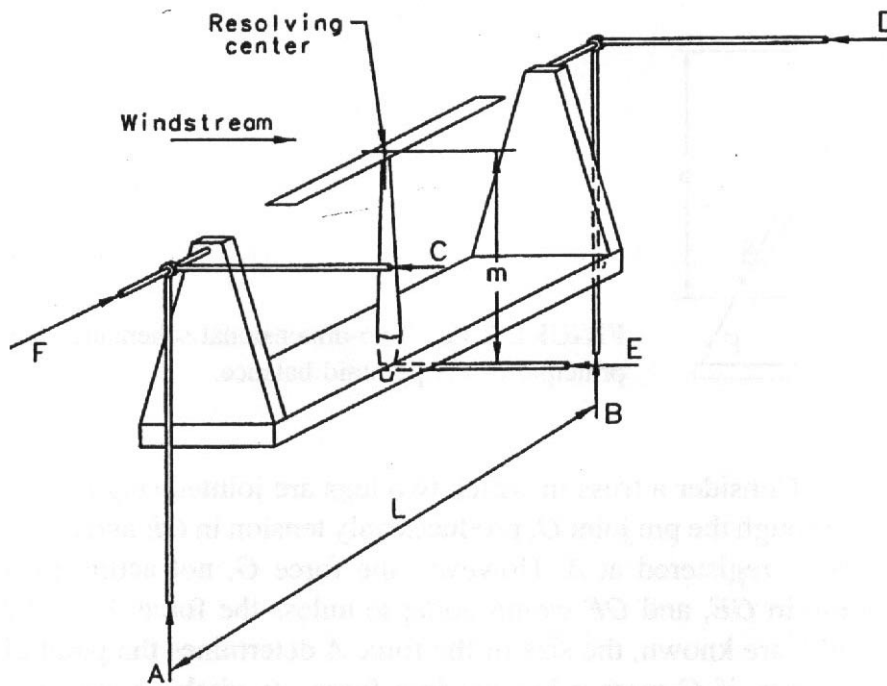
FIGURE 7.11 Basic layout of a yoke balance.

as shown here brings out the pitching moment in the drag system instead of in the lift. For the yoke balance, the forces and moments are

$$L = (a + b) \qquad D = c + d + e \qquad S = f$$

$$l = (b - a)(\tfrac{1}{2}w) \qquad m = -ex \qquad n = (d - c)(\tfrac{1}{2}w)$$

Pyramidal Balance The complaints usually heard about the platform and yoke balances are largely overcome by the ingenious engineering of the pyramidal type. However, as usually happens, additional difficulties are added.

These are the advantages: The pyramidal balance reads the moments about the resolving center, and the six components are inherently separated and read directly by six measuring units. No components need be added, subtracted, or multiplied. The difficulties involved in reading the small differences in large forces are eliminated, and direct reading of the forces and moments simplifies the calculations. Note that this is less of an advantage today than it was several decades ago when these systems were being intensively developed.

Several criticisms of the pyramidal balance are warranted. The alignment of the inclined struts is so critical that both the construction and the calibration of the balance are greatly complicated. Furthermore (and this appears quite serious), deflections of the inclined struts may so change their alignment that the moments are not accurate. This effect must be thoroughly investigated during the calibration of the balance.

The manner in which the pyramidal balance separates the moments is not simple, and it behooves the engineer and the student to approach the setup using an elemen-
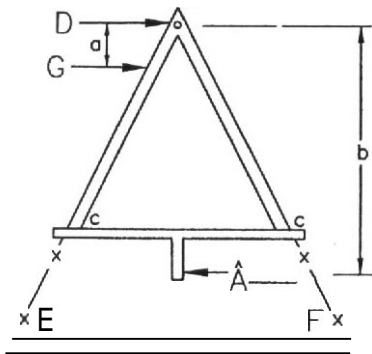
FIGURE 7.12 Two-dimensional schematic showing the principle of the pyramid balance.

tary truss system. Consider a truss in which two legs are jointed (Figure 7.12). The force D, acting through the pin joint O, produces only tension in OE and compression in OF. No force is registered at A. However, the force G, not acting through O, produces bending in OE, and OE would collapse unless the force A $= aG/b$ were present. If G and b **are** known, the size of the force A determines the point of action of G. In this manner, if G were a known drag force, its pitching moments about the resolving center O would be determined by the force A.

Though the previous example illustrates the principle of the pyramidal balance, in actual practice a considerable revision is required. In order to prevent the legs of the pyramid from being in the airstream, they **are** cut off at what would be c in Figure 7.12. The truncated legs **are** then carefully aligned so that their extensions pass through a common point. The complete setup is illustrated in Figure 7.13. The forces and moments **are**

$$\text{Lift} = \text{total weight on lowest table} \qquad \text{Drag} = D \qquad \text{Side force} = -C$$

$$\text{Pitching moment} = -P \times f \qquad \text{Rolling moment} = R \times f$$

$$\text{Yawing moment} = Y \times a$$

Deflections

One of the most troublesome problems of wind tunnel balances is rigidity, or to be more accurate, lack of rigidity. Deflections in the balance may move the model from the resolving center and invalidate the moment data or nullify the balance alignment so that part of the lift appears as drag or side force. The answer to the problem is obvious: Either the deflections must be kept down to where they are negligible or they must be evaluated and accounted for in the data reduction process. Of course, keeping them down is preferable.

The largest source of deflection is the mounting system. This must be long to reach out of the test section and thin to avoid excessive interference. Both requirements are in direct antithesis to the criterion of minimum deflection. The only way the wind tunnel engineer can meet this problem is to use materials of high modulus of elasticity for the strut. The desire for the shortest mounting strut possible is a strong argument for the selection of a rectangular or elliptic jet shape. Deflections in the
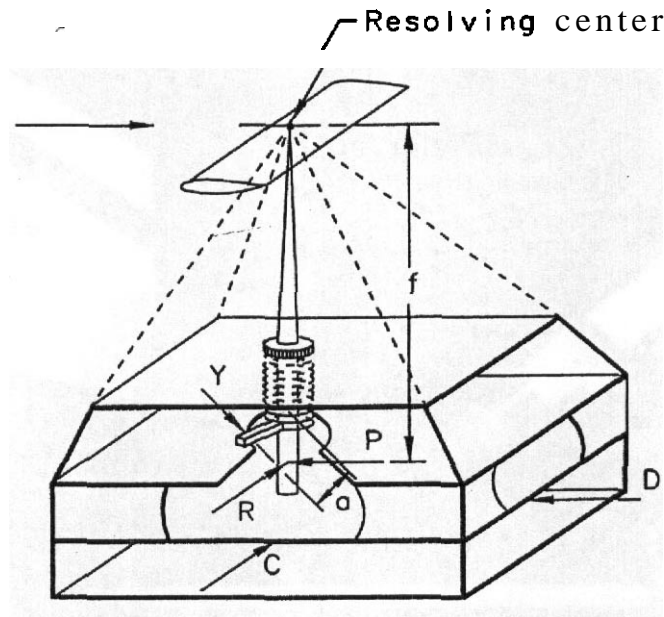
FIGURE 7.13 Pyramidal or virtual center balance.

balance frame may be diminished by having a deep and rigid framework. None of the common measuring units have deflections large enough to be serious, and so they rarely cause this type of trouble.

The effects of deflections are evaluated during the process of calibrating the balance, and corrections, if necessary, are given to the computing staff for inclusion in the data work-up. The model itself is a source of deflection.

Balance Linkages and Pivots

The principal components of an external balance consist of a large number of levers that are designed to have minimum deflection under maximum load. This increases their weight and often their size. The joints between the levers are usually pivots with very small angular motion. It is required that the pivots have very low friction (ideally zero friction) to avoid hysteresis in the balance when the directions of the loads are reversed. Early pivots in wind tunnel balances were knife edges. Because knife edges can be damaged by shock loads and can only carry loads in a compressive direction, they have been replaced by flexure pivots. It should be noted that ball and roller bearings make very poor pivots where the angular motion is very small and loads must be carried perpendicular to the shaft axis of the bearings. Under these conditions both the balls and their races can easily develop flat spots and a resulting large amount of friction when rotated.

The advantages of flexures are as follows:

1. They can be designed to withstand loads in any direction with no lost motion between the coupled members.
2. They are essentially frictionless, thus eliminating hysteresis effects.
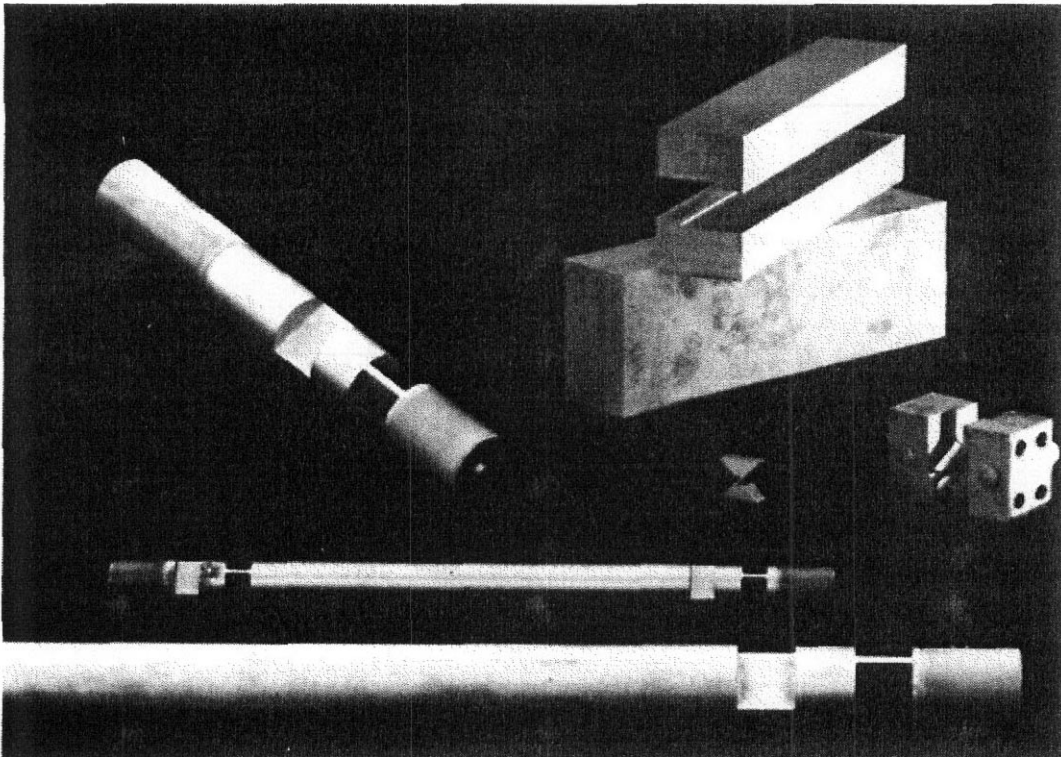
FIGURE 7.14 Flexures. Threads on rod flexure allow length adjustment. The Z flexure stock made on milling machine. Two halves of X flexure are cut from stock and pinned together. (Photograph courtesy of University of Washington Aeronautical Laboratory.)

3. They will withstand relatively rough treatment.
4. They are virtually wearproof; thus their characteristics remain constant over an indefinite period.

Flexures are usually one of two types. The first is a composite or rod flexure. These are used to transmit loads along their axis with small angular rotation and the critical design load is compressive. As the length of the rod often must be adjusted, the ends consist of fine right- and left-handed threads that can be clamped in a nut that is split in two and bolted together. These flexures are machined out of a solid bar stock. Examples are shown in Figure 7.14. The second is a restrained flexure, or X flexure. These are almost frictionless pivots, and if the rotation is small, the center of rotation is fixed. They can be made by machining a bar into a Z shape on a mill. The bar is cut into strips and then assembled in an X shape with tapped holes in the top and bottom for assembly to other parts. With electric discharges milling, they can be made from one piece. The X flexures are used in pairs.

The X flexure can be less than half as stiff as a rod flexure and allows twice the rotation angle. When the X flexure is loaded at right angles to its axis, two of the flexure strips are in compression and two are in tension when acting as a pivot. Thus the change in stiffness of the tension strips is compensated for by the opposite change in stiffness of the compression strips."

Balance Output Transducers

The external balance elements are arranged to transfer the loads that appear on a model to a set of output transducers. A principal objective of earlier designs was to kinematically separate the standard six components so that each output transducer provided a signal that would be directly proportional to one and only one force or moment component. With cheap and fast computation universally available, this objective is now traded off against simplicity, greater robustness, or even better performance.

The device used to measure the output of the balance should have the following characteristics:

1. The curve of the applied load versus the indicated load should be invariant. Assuming that the curve is linear and passes through zero, the slope should remain constant over time. If the slope of the curve changes (slips calibration), it is most difficult to detect. This problem can be serious with digital data systems. These systems use amplifiers with DC response, and the amplifiers are prone to drift. Each installation must determine the stability of its systems and perform checks at the appropriate intervals. It is desirable to make end-to-end checks by the use of check weights at regular scheduled intervals.

2. When the applied load is removed gradually, the measuring device should return to zero. The zero-shift problem is not as serious as slipping calibration. In most tunnels it is a standard policy to check the "balance zero" for shift at the end of each run or run series. If the zero shift is too large, the runs are repeated. Care must be taken with the end of run zero to make sure that the tunnel velocity is also zero.

3. The measuring device should display no hysteresis. In general, this is not a problem with typical measuring units. Often when hysteresis appears, it is due to some portion of the system being loose and therefore undergoing some slipping, or more commonly there is some slight contact or fouling that has not been found.

4. Every type must provide an appropriate interface to a data acquisition system.

The following are some types of measuring units that have been used as output devices on wind tunnel balances.

Automatic Beam Balance   A sketch of an automatic beam balance is shown in Figure 7.15. The version sketched shows the type of sensing used in the 1930s to 1970s. It consists of a "weigh beam" that has an electrically driven rider. When the beam drops down, a contact is made that causes the driving motor to move the rider in the direction that will balance the beam. A counter on the motor shaft locates the rider and may be calibrated to read the force weighed. The pendulum H (see Figure 7.15) can be adjusted to balance out the destabilizing component due to the weight of the beam. This type of force-measuring balance has the advantage that the measurement is always made in the balance null position and thus there is no
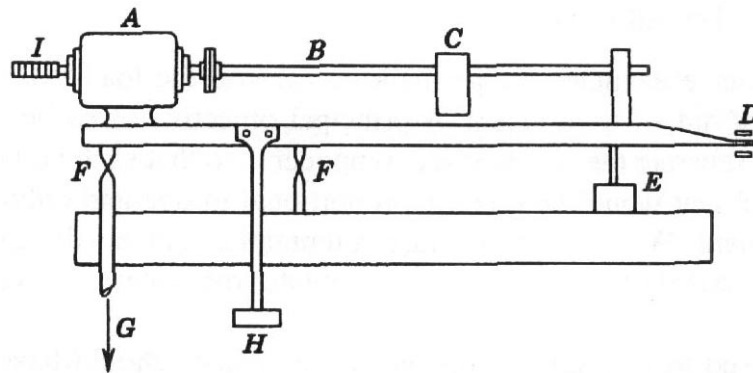
FIGURE 7.15   Beam balance: A, driving motor; *B*, threaded rod; *C*, rider; *D*, reversing contacts; *E*, dashpot; *F*, flexure pivot; *G*, applied load; H, pendulum weight; I, counter.

displacement of the system. The disadvantage is that they are relatively slow in reaching a balance condition, although it must be remembered that external balances can weigh several thousand pounds and cannot be expected to be highly responsive.

In some cases unit weights are used so that the weigh beam is required to resolve only part of the full-scale range of the system. A number of weigh beam systems have been constructed that are capable of routinely resolving 1 part in 100,000 and maintaining calibration for extensive periods.

Current designs for weigh beam systems use exactly the same principles as indicated by Figure 7.15 with two significant modifications. First, and most important, the method of sensing the equilibrium state is to provide a linear differential transformer at the end of the weigh beam instead of the mechanical contacts. This eliminates the hysteresis problem and can be made very reliable as well as very sensitive. Second, some quite advanced oil pot damping systems are included to manage the dynamic motion of the weigh beam under unsteady loading conditions.

Hydmulic Capsules   The hydraulic capsule is a device that measures forces through the pressures they exert on pistons of known area. They are not exactly null, but the amount of deflection of the piston is so small as to be negligible. The resulting pressure is a function of the size of the load and is measured through accurate pressure gages.

Electrical Measuring Devices   There are several methods for measuring forces or pressures electrically, most of them depending on amplifying the effect that tiny deflections have on the capacitance, inductance, or resistance of the unit. For example, the resistance of a carbon pack varies as the pressure on it, and the current it passes for a fixed voltage may be used as an index of the load. The amount of current needed to keep the core of a solenoid in a fixed location is an index of the load on it. The change in capacitance of a plate condenser with small deflections of the plates may again indicate a load. The resistance of a wire changes with the tension of the wire, and the current passed for a fixed voltage may indicate the tension. And so ad infinitum. A hundred different setups may be possible. It should

be borne in mind fiat through amplification the most minute changes may be noted and remarkable accuracy is possible.

Strain gages have been used as measuring devices in external balances with a satisfactory degree of success. One **major** manufacturer of balances has developed a special **high-voltage** unit for this application. The electromagnetic arrangement that measures the forces by **the amount** of current needed to maintain zero deflection in the unit has also been successful. This method is used in a majority of **high**-quality laboratory balances that are able to resolve 1 part in 10^6. These systems often have a unit weight addition setup in order to extend their range with maximum accuracy.

By far the most widely used electrical measuring device is the wire strain gage. The wire strain gage consists of very fine wire cemented to a flexure. The load, by deflecting the beam by a minute amount, stretches the wires glued to the beam and changes their resistance and the amount of current that will flow through them for a fixed applied voltage. The gages are almost always arranged in a bridge circuit to increase the sensitivity.

A wide range of commercial strain gages are available that vary widely in size, backing material, and sensitivity to temperature. The gages can be **affixed** to the flexure material with a variety of bonding agents, ranging from simple cellulose cement to more exotic adhesives, some of which require special curing techniques. Many commercially available signal conditioners supply bridge voltage and balancing impedance. There can be one, two, or four active gages in a bridge, but generally either two or four gages are used to minimize the effect of temperature. Four-gage bridges also increase the sensitivity and accuracy.

Strain gages are used more extensively for internal balances and for **special**-purpose component load measurement than for output devices on external balances. A typical resolving capability for a strain gage device is 1 part in 20,000 as compared so many times this for some other devices. This is, however, more than adequate if a device can be produced or obtained with just the right total range for a particular purpose.

Calibration of External Balances

External balances are usually attached very firmly to a large mass of concrete to obtain maximum stability and thus are calibrated in place, while internal balances are calibrated outside of the tunnel with only check loads applied to the model in place. Some tunnels built in the 1970s that are designed to use both external and sting balances have designed the external balance so that it can be removed from the tunnel for calibration in a laboratory. However, this is relatively rare.

Let us start by making clear the immensity of a wind tunnel balance calibration: With a competent crew the fust calibration of a new balance will take three months at least. This time frame supposes that adequate shop facilities for all sorts of changes are available and recognizes that the first "calibration" will almost inevitably involve many adjustments. Many balances have, however, subsequently served very well for decades with modest additional calibration efforts.
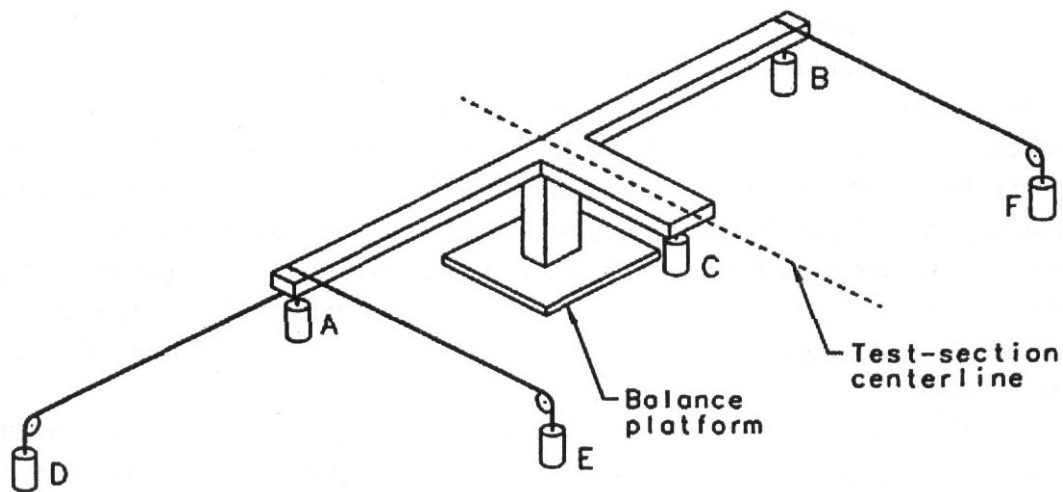
FIGURE 7.16   Balance loading tee. Weights added at A, *B,* or *C* should produce no drag or cross-wind force, and a weight moved from E to F should produce no indicated change in drag.

Calibration includes loading the elements of the balance to see whether they read what they should, ascertaining the deflections of the setup, loading the balance in combined cases that simulate the conglomeration of loads that various models will put on it, loading with the balance yawed, measuring the natural frequency of the balance so that resonance can be avoided, and applying fluctuating loads so that it can be determined that the time average of balance output provides an accurate mean value.

All the above requires considerable added equipment, and it is a good idea to make as much of it permanent as possible, since calibration checks will be needed many times during the life of the balance, although few if any of the same scale as the initial one. First in this list comes a loading tee, of which a schematic is shown in Figure 7.16 and a photograph is shown in Figure 7.17.

The calibration tee must provide a method to accurately attach cables for applying the loads. A reasonable tolerance is 0.005 in, on their location. The cable attachment can be knife edge hooks or ball and socket joints with the balls swaged onto aircraft cable for large balances. Piano wire can be used for smaller balances.

With any tee provisions have to be made to ensure that the loads applied by cables are parallel or perpendicular, as required in each case, to the tunnel centerlines for a wind axis balance. First the balance must be set at zero yaw. Then alignment lines are scribed on the floor using toolmaker's blue (or lines could be drawn on masking tape). A plumb bob can be used to align the pulleys. Next the cables are attached and an engineering level (optical) and 0.01 rulers can be used to level the cables, which must be loaded to about one-half of the full load. After leveling, the horizontal alignment could be checked. Pulleys should have a large radius, about 8 in. minimum, and should be built for this purpose. The groove for the cable should be cut so that the cable lies on the top edge of a groove narrower than the cable diameter for positive alignment. The pads holding the pulleys should be adjustable
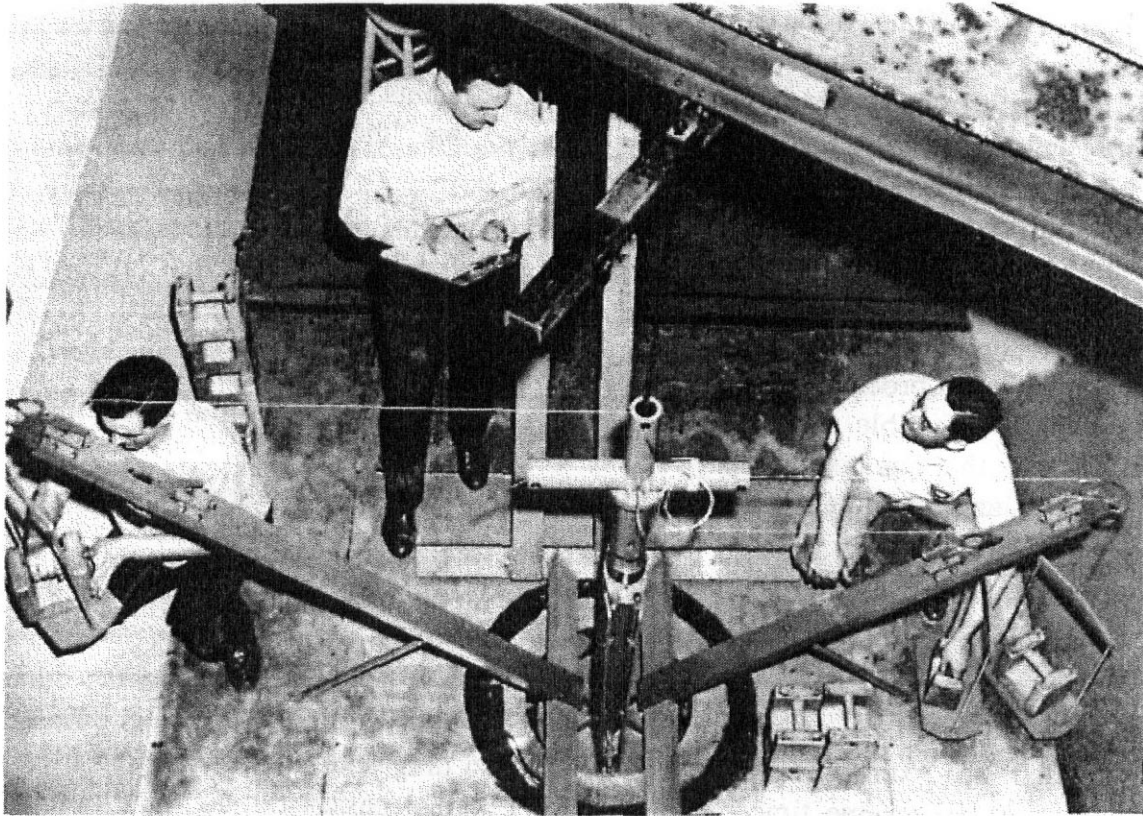
FIGURE 7.17   External balance loading tee. Each component can be independently loaded or combined loads can be applied. Shown are loads to side force and rolling moment. (Photograph courtesy of University of Washington Aeronautical Laboratory.)

in the vertical and horizontal planes. The most difficult load is positive lift. One approach is to lay a strong steel beam across the top fillets and use a pivoted lever to load lift. This reduces the weights and either a cable or rod with ball joints can be used. This can be plumbed optically or by use of a precision bubble level.

A set of calibrated weights will be needed. If it is decided not to buy a full set, they may usually be borrowed from the local state highway department. A half dozen or more dial gages for measuring deflections will also be needed.

The first step in calibration is a complete operational checkout of the measuring units and data read-out system. For a new balance each component should be loaded to the maximum load and balance deflections checked. The amount of deflection is a function of the balance design. These loads are also proof loads, although this usually is not a problem. Most balances have stops to protect the most sensitive and expensive parts in case of failure. These can be set at this time. A repaired balance should be put through the same loading cycle. It is common for **new** or repaired balances to require two or three full-load loading cycles before they settle in and give good repeatability.

The traditional method of calibrating external balances has been to adjust the balance to minimize the interactions. This was done to minimize the labor of reducing the data by hand. This practice resulted in direct balance readings very close to the

applied loads. Thus, when the coefficient data on repeat runs or between tests did not check, the raw balance readings proved useful in finding the source of the error. If balance readings agree in trends with the coefficients, then a check of the model configuration usually elicits from the customer that "the model is just the same, but" and the problem is solved.

With the ready availability of digital computers it is possible in the process of calibration of the balance to measure the interactions and, rather than commit extensive time to reducing or removing them, derive a computational algorithm that will provide the desired components. This can be implemented to produce results on line **as** a test proceeds. This latter method has been common for internal balances as it is not possible to obtain the degree of component separation under those constraints that has been routine for external balances.

The balance alignment procedure for obtaining minimum interaction is as follows:

1. For each component, load and adjust the component's slope to 1 : 1 or until output reading is equal to the load.

2. Load each component in sequence and reduce the interactions on the other five components (this assumes a six-component balance). The best way to proceed is to first make sure that lift is perpendicular to drag and side force using lift as the load. At the same time make sure the lift load passes through the moment center by checking pitching moment and rolling moment. Next, make sure drag is perpendicular to side force. This may require a recheck of lift, depending on the balance. This task is tedious on a new balance, but a feel for the balance is soon acquired that makes the job easier. When the interactions are minimized, the remainder may be due to deflections. Output devices that are nulling are advantageous in minimizing deflection.

3. During the work in 2, a plot of balance output similar to Figure 7.18 is useful to determine the error on each component due to its single-component loading. Balance loads should be applied from zero to full scale to zero. Plots of component loaded versus the other five components will show zero shifts and hysteresis. Depending on the balance design, it may be necessary to check the interactions with the balance yawed. This is to ensure that the balance-resolving center coincides with the model trunnion. The trunnion is the point about which the model is pitched and yawed. If these two points do not coincide, the data reduction will have to account for the discrepancy.

4. When minimum interactions have been achieved, repeated loadings should be made to check the balance repeatability. The setting of the safety stops should be rechecked. Combined loadings should also be applied to determine the magnitude of the second-degree interactions. These are treated in more detail in connection with internal balance calibrations later. It is also desirable to apply very small loads to check the balance sensitivity. At the University of Washington Aeronautical Laboratory **a** small aluminum bell crank mounted on a torsional flexure pivot was built for this purpose. The vertical arm was connected to the balance by fine piano wire. The horizontal arm contained the weight pan and a bubble level. This device
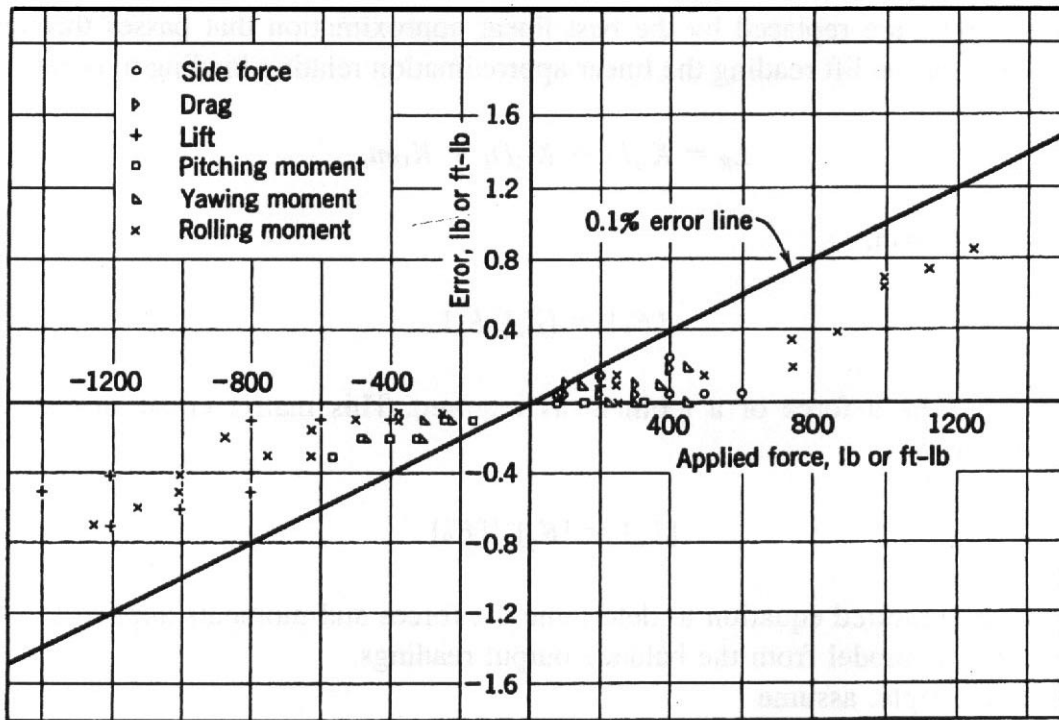
FIGURE 7.18   Plot of actual error versus applied load for the six force systems when each component is loaded separately. The straight line indicates the maximum permissible error of 0.01% of the applied load.

was supported on a scissor jack stand. The jack stand was used to level the wire to the balance and level the bell crank. Then loads of 0.01 lb were applied to drag and side force, and moments of 0.01 in.-lb were applied to the yawing moment. The pan and gravity were used for lift, pitching, and rolling moments. This indicates the difficulty of applying full-range loads with the precision in loading that many of these balances are capable of resolving. In fact, it seems that in many cases the limitation on the accuracy of external balance measurements is actually the precision and accuracy with which calibration loads can be applied.

5.   The natural frequency of the balance about the three axes should be determined along with the effect of the model weight on the frequencies. As mentioned earlier, the balance also should be checked with fluctuating loads to ensure that it measures the mean value.

Example 7.1   We consider a three-component balance to reduce the amount of data involved as compared to a six-component case. The balance is loaded as any balance and the outputs are plotted. It will be assumed that the balance can be adjusted. There are three components, *L, D,* and *m,* to be loaded over their respective ranges. The outputs from all three component output devices are recorded for each load applied, yielding nine functions, $L_R(L_L)$, $L_R(D_L)$, $L_R(m_L)$; $D_R(L_L)$, $D_R(D_L)$, $D_R(m_L)$; and $m_R(L_L)$, $m_R(D_L)$, $m_R(m_L)$. In this notation, the subscript L means applied load and the subscript R means the reading from the output device. It is assumed that there is an adjustment that allows the zeros to be made precise. If the curves are slightly

nonlinear, they are replaced by the best linear approximation that passes through zero. Thus, for the lift reading the linear approximation relating loading to output is

$$L_R = K_{11}L_L + K_{12}D_L + K_{13}m_L$$

or, in matrix form,

$$\{F_R\} = [K_{ij}]\{F_L\}$$

where $\mathbf{F}$ can be a force or a moment as required. This matrix equation can be inverted to give

$$\{F_L\} = [K_{ij}]^{-1}\{F_R\}$$

which is the required equation to determine the forces and moments applied to the balance by the model from the balance output readings.

As an example, assume

$$K = \begin{bmatrix} 1.000 & 0.00622 & -0.330 \\ 0.0221 & 1.000 & 0.0 \\ 0.162 & -0.00338 & 1.000 \end{bmatrix} = \begin{bmatrix} K_{L_R L_L} & K_{L_R D_L} & K_{L_R m_L} \\ K_{D_r L_L} & K_{D_R D_L} & K_{D_R m_L} \\ K_{m_R L_L} & K_{m_R D_L} & K_{m_R m_L} \end{bmatrix} \quad (7.14)$$

Then

$$K^{-1} = \begin{bmatrix} 0.949 & 0.00482 & 0.313 \\ -0.0212 & 1.000 & -0.00692 \\ -0.1536 & 0.00416 & 0.948 \end{bmatrix}$$

and the balance output equation is

$$\begin{bmatrix} L_L \\ D_L \\ m_L \end{bmatrix} = \begin{bmatrix} 0.949L_R - 0.00482D_R + 0.313m_R \\ -0.0212L_R + D_R - 0.00692m_R \\ -0.1536L_R + 0.00416D_R + 0.948m_R \end{bmatrix} \quad (7.15)$$

If one is trying to adjust the balance for minimum interactions, then from the $\Delta D_R/\Delta L_L$ term it can be seen that the lift and drag are not perpendicular. The K_{31} or the $\Delta m_R/\Delta L_L$ term shows that the balance moment center is aft of the geometric vertical centerline of the balance. Thus the curve can be used to provide information on the required adjustments. Of course, if the data system to be used is always available on line and the above results are sufficiently close, then these results can be used directly to relate output to loads during tests.

7.5   FUNDAMENTALS OF MODEL INSTALLATIONS

Any strut connecting a model to the balance can be considered to add three quantities to the balance output. The fust is the obvious result of the direct aerodynamic force on the exposed strut. The second is the effect of the strut's presence on the air flow pattern about the model. And the third is the effect of the model on the air flow about the strut. The last two items are usually lumped together under the term "interference," and their existence should make clear the impossibility of evaluating the total tare by the simple expedient of measuring the drag of the struts with the model out.

The earliest attachments were by means of wires or streamline struts. The ruling criterion was to add the smallest possible drag and then either estimate it or neglect it. Since the advent of the image system of evaluating the tare and interference, which we will discuss at some length, these effects have been evaluated by measurements rather than being estimated.

The mounting struts employed at first still tended toward the minimum drag criterion and had airfoil shapes. Later, however, many mounting struts of polygonal cross section were used. The idea behind this trend was that the Reynolds number of the mounting struts would always be quite low and the struts therefore might have not only a large drag but also a drag that varied widely for relatively small changes in shape or Reynolds number. The reason for such concern can be seen from the drag-versus-Reynolds-number plots for circular cylinders and spheres shown in Figure 7.19. To minimize the change in drag with Reynolds number, the transition point between laminar and turbulent flow should be fixed by some permanent method such as staking the transition point with a center punch. The main advantage of struts with a larger cross section, however, is that they will reduce the deflection of the model.

Only a minimum length of strut is exposed to the airstream, the remainder being shielded by fairings not attached to the balance. In this way the tare drag of the mounting is decreased, sometimes being only 50% of the minimum drag of an
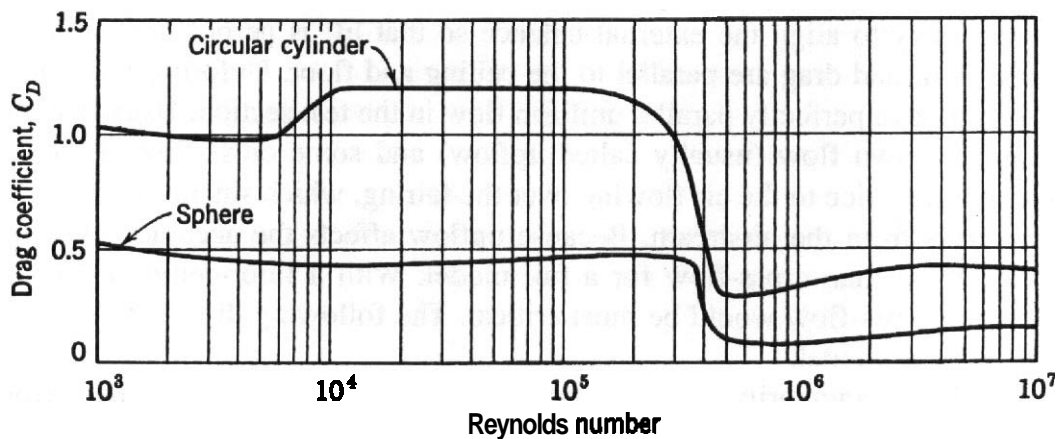
FIGURE 7.19   Variation of the drag coefficient of circular cylinders and spheres with Reynolds number.

average wing. It is not advisable to try to decrease the tare drag of the "bayonets" by continuing the windshields up close to the model because a fairing close to the model can increase the interference effects more than it decreases the tare. A proper balance between amount of exposed strut and proximity of the windshield to the model may be found by having adjustable sleeves at the windshield top. The sleeve location at which $C_{d0,min}$ for the model plus tare and interference is a minimum is the best, since this indicates that the tare plus interference is a minimum too.

Some balances yaw the model support struts oppositely to the model, so that the struts always remain parallel to the airstream and hence contribute the smallest possible effect when the model is yawed. Another useful arrangement is to have several sets of supports of varying size from which the smallest can be selected according to the load range.

One feature sometimes considered necessary for the ordinary support system is a diaphragm seal that prevents flow from around the balance up between the supports and shields into the tunnel. There are two types of pressures that may cause this flow. The first is due to the basic tunnel design, which not infrequently results in a test-section static pressure below the atmospheric pressure and hence in a pressure differential, sometimes quite large, between the balance chamber and the test section. The second pressure is that resulting from local flow induced by presence of the model. The flow can be eliminated by a light diaphragm seal. Closing off the balance room in no way changes the necessity for the support column seal.

The attachment fittings usually come into the wing at about the 30–50% chord point. In complete airplanes, the most rearward center-of-gravity location may be used to give maximum room for the fittings. If a model of a multiengine airplane is to be tested, the mounting strut interference will be smallest if the struts do not attach at a nacelle point.

Balance Aerodynamic Alignment

By definition, lift is perpendicular to the remote velocity and drag is parallel to it. In an ideal tunnel with the flow parallel to the test-section boundaries, it would only be necessary to align the external balance so that lift is perpendicular to the ceiling and floor and drag are parallel to the ceiling and floor. Unfortunately, most tunnels do not have perfectly parallel uniform flow in the test section. Usually there is some up or down flow (usually called upflow) and some cross-flow. There is also a local upflow due to the air flowing over the fairing, which shields the balance mounting struts from the airstream. Because upflow affects the accuracy of drag, it is more critical than cross-flow for a full model. With a floor-ceiling-mounted half model the cross-flow would be most critical. The following discussion will be for a full airplane model.

The tunnel flow angularity usually is not uniform across the tunnel in the region occupied by the wing, and it may vary with the dynamic pressure. For a given wing planform, an average value of the upflow can be obtained for a given dynamic pressure and the balance aligned so that drag is parallel and lift perpendicular to

the flow. But for any other wing or dynamic pressure the balance would not be properly aligned. Furthermore, the problem of applying loads during the balance calibration when the loads are not level will just make difficult tasks more difficult. The usual procedure is to align the balance so that lift is perpendicular to the test-section ceiling and floor and drag are parallel to them or to an internal balance reference surface. Then the upflow is measured and corrected for in the data reduction.

One thing simplifies the alignment. The lift for most tests is from 5 to 25 times larger than the drag, and it is usually sufficient to align so that no lift appears in the drag-reading apparatus without checking to see whether any drag appears in the lift-reading mechanism beyond ascertaining that the drag system is perpendicular to the lift.

The balance alignment to the tunnel flow is generally accomplished by running a wing both normal and inverted from zero lift to stall. To ensure equal support strut interference for both normal and inverted runs, dummy supports identical to the conventional ones are installed downward from the tunnel roof. The arrangement is shown in Figure 7.20. The data from both normal and downward lift are plotted as lift curves (C_L vs. a), polars (C_L vs. C_D), and moment curves (C_L vs. C_m). The negative lifts and moments are plotted as though they were positive, as shown in Figure 7.21. The angular variation between the lift curves is twice the error in setting the angle of attack and, as shown, indicates that the a is set too low. That is, when the balance angle indicator reads $-1°$, the model is really at $0°$ to the average wind. The polar (Figure 7.22) shows that the lift is not perpendicular to the relative wind, part of it appearing as drag. Here the balance is tipped aft in reference to the relative
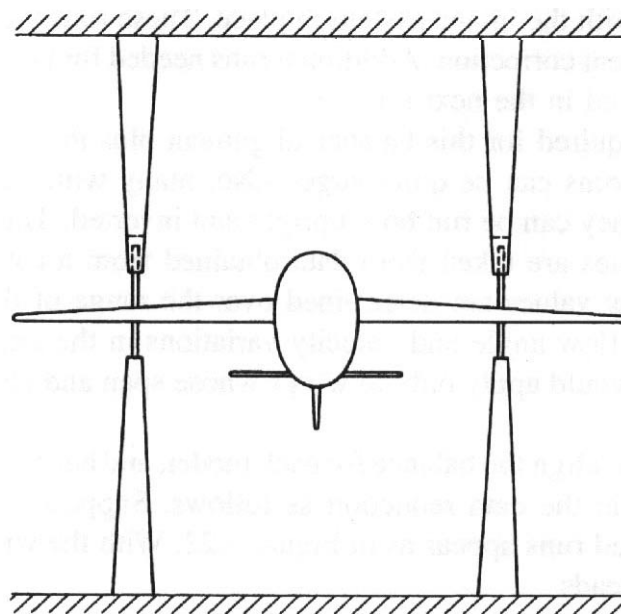
FIGURE 7.20   Arrangement for determining tare and interference simultaneously.
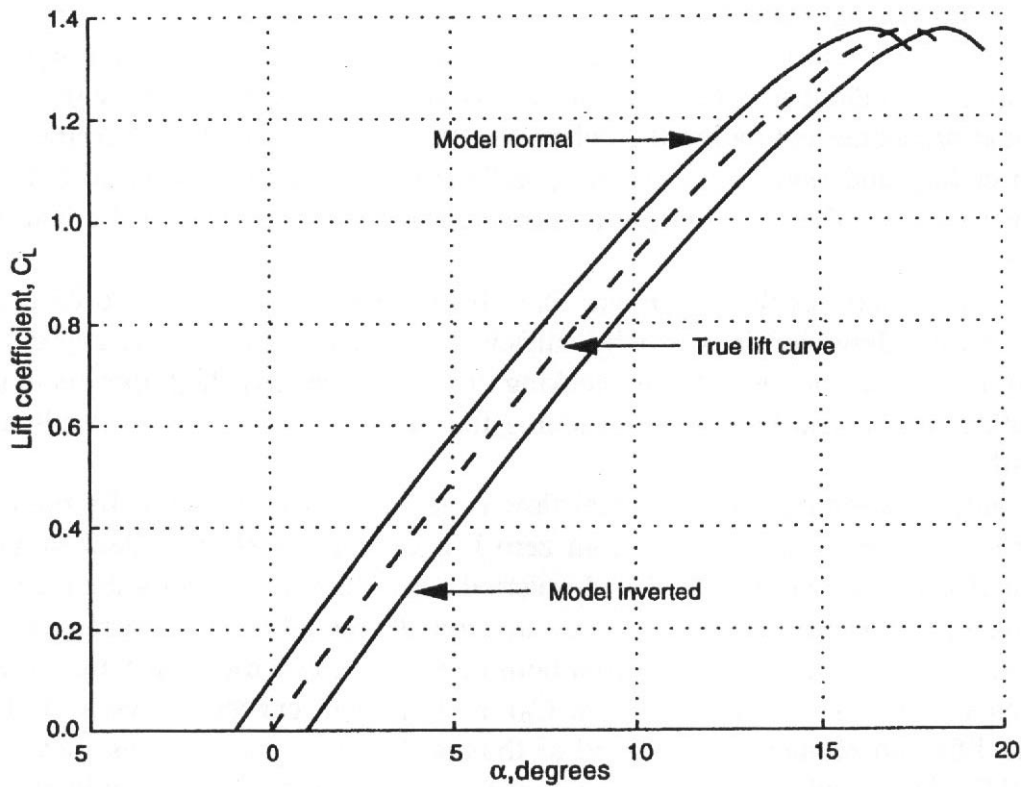
FIGURE 7.21   Upright and inverted C_L versus a curves.

wind, for a component of the lift is decreasing the drag when the lift is positive and increasing it when the lift is negative. See Figures 7.22 and 7.23.

The same procedure outlined above for a wing must be followed for each complete model. Upright or normal runs with the image system in place **are** followed by model inverted runs with the image system in place. These runs yield the true angle of zero lift and alignment correction. Additional runs needed for tare and interference evaluation are discussed in the next section.

The tunnel time required for this balance alignment plus the additional time for tare and interference runs can be quite large. Also, many wind tunnel models are not designed so that they can be run both upright and inverted. Thus, in many wind tunnel tests these values are taken from data obtained from a calibration wing or model, and the **upflow** values **are** determined over the range of dynamic pressure used in the tunnel. If flow angle and velocity variations in the airstream are large, the above alignment would apply only to wings whose span and chord approximate the test wing.

It is impracticable to align the balance for each model, and hence the misalignment correction is applied in the data reduction as follows. Suppose that the polars of the normal and inverted runs appear as in Figure 7.22. With the wing in the normal position the balance reads

$$C_{D,\text{indicated}} = C_{D,\text{true}} - C_{L,\text{indicated}}(\tan \alpha_{\text{up}}) \qquad (7.16)$$
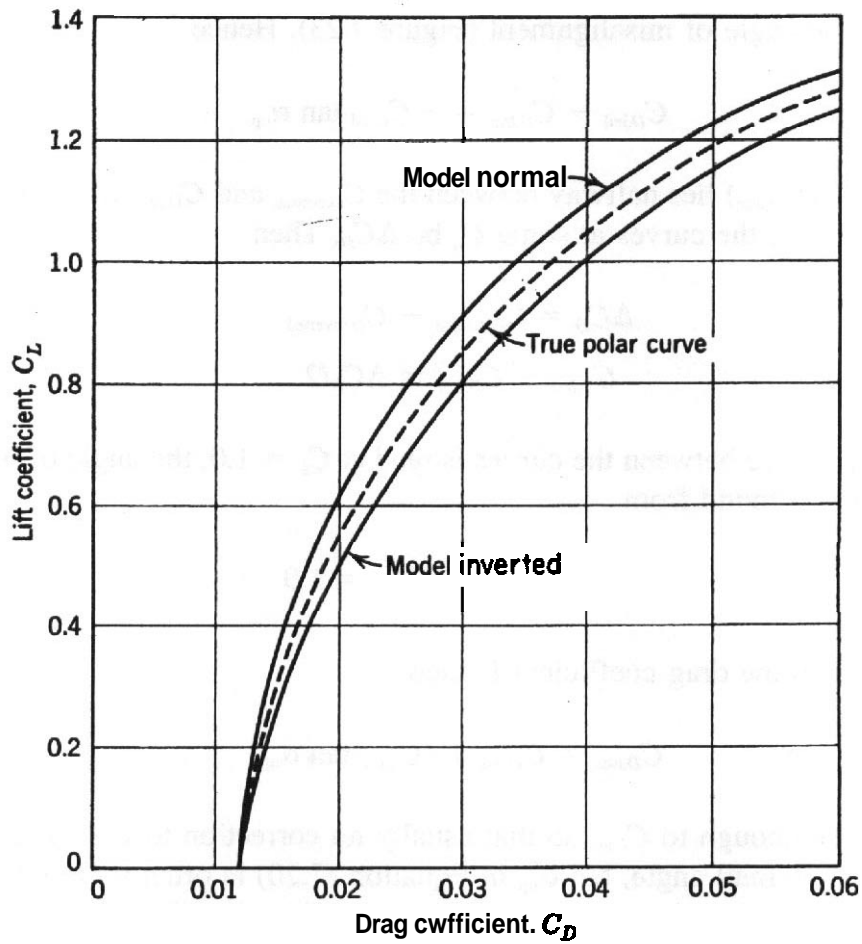
FIGURE 7.22   Drag polar, C_L versus C_D.
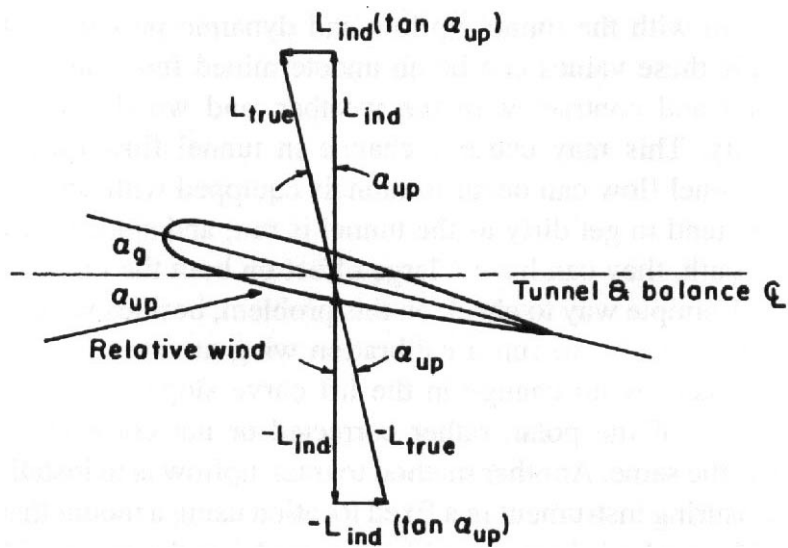
FIGURE 7.23   Influence of alignment, projection of lift in drag direction.

where α_{up} is the angle of misalignment (Figure *7.23*). Hence

$$C_{D,\text{ind}} - C_{D,\text{true}} = -C_{L,\text{ind}} \tan \alpha_{up} \tag{7.17}$$

The correct C_D ($C_{D,\text{true}}$) lies halfway between the $C_{D,\text{normal}}$ and $C_{D,\text{inverted}}$ curves. Let the difference between the curves at some C_L be ΔC_D. Then

$$\Delta C_D = C_{D,\text{normal}} - C_{D,\text{inverted}} \tag{7.18}$$

$$C_{D,\text{ind}} - C_{D,\text{true}} = \Delta C_D/2 \tag{7.19}$$

and, if the difference between the curves is read at $C_L = 1.0$, the angle of misalignment, α_{up} may be found from

$$\tan \alpha_{up} = (\Delta C_D/2)_{C_L} = 1.0 \tag{7.20}$$

The correction to the drag coefficient is then

$$C_{D,\text{true}} = C_{D,\text{ind}} + (C_{L,\text{ind}})\tan \alpha_{up} \tag{7.21}$$

True C_L is close enough to $C_{L,\text{ind}}$ so that usually no correction to C_L is needed.

When α is a small angle, $\tan \alpha_{up}$ in Equation *(7.20)* is often replaced with the angle in radians. Rather than calculating $\tan \alpha_{up}$ in Equation *(7.17)* at one value of C_L such as 1.0, it is better to measure ΔC_D at several values of C_L and plot ΔC_D or $\Delta C_D/2$ versus C_L. Then fair in a linear curve or use linear regression to obtain the slope or $\tan \alpha$.

Two more important points in regard to the evaluation of the alignment correction remain. First, in order to have the tare and interference effects identical for both the model normal and inverted runs, the image system must be installed and the dummy struts arranged as in Figure *7.20*.

A second problem with the tunnel upflow and dynamic pressure calibration is that in some tunnels these values can be an undetermined function of time. Some tunnels will expand and contract with the weather, and wooden tunnels can be affected by humidity. This may cause a change in tunnel flow quality. A more serious change in tunnel flow can occur in tunnels equipped with screens to reduce turbulence. Screens tend to get dirty as the tunnel is run, and since they are located in the tunnel bellmouth, they can have a large effect on both the tunnel upflow and dynamic pressure. A simple way to check on this problem, besides visually checking screens and cleaning them, is to mn a calibration wing at several check q's in an upright position. If there is no change in the lift curve slope, the q calibration is the same. No rotation of the polar, either corrected or not corrected for upflow, means the upflow is the same. Another method to track upflow is to install a yawhead or similar flow-measuring instrument in a fixed location using a mount that maintains probe alignment. The probe is best mn without a model in the tunnel. This method is not as accurate or as sensitive as the calibration wing.

The engineer who, upon finding a change in the data for a second series test of a certain model, proclaimed that $\alpha_{Z.L.}$ was "not where he left it" was not entirely without scientific backing. The method of evaluating upflow with upright and inverted runs is the same with a sting balance. The sting balance can simplify inverting the model if the sting is capable of rolling $180°$.

Although the error in angle of attack can be determined from the lift curve of Figure 7.21, the upflow angle is often so small that it is difficult to obtain from the lift curve. Usually the upflow angle is taken from Equation (7.20) or a plot of Equation (7.17) and added to the model's geometric angle of attack. For a model mounted in a normal upright condition with upflow in the tunnel

$$\alpha = \alpha_{geom} + \Delta\alpha_{up} \quad \text{(in degrees)} \tag{7.22}$$

$$\Delta C_{D,up} = \Delta\alpha_{up}C_{L_W} \tag{7.23}$$

with $\Delta\alpha$, in radians and C_{L_W} the wing lift coefficient. The above corrections to the angle of attack and the drag coefficient are not the total corrections. There are additional corrections owing to the constraint to the tunnel flow due to the walls or wall corrections (see Chapter 9).

When the variations in upflow are very large in the region of the wing as measured by a yawhead, laser, or similar instrument, the following method can be used. The upflow at several spanwise stations of the wing is multiplied by the chord at that location. The product is then plotted versus the wing span and the area under the resulting curve is divided by the wing area to yield an average value for the wing. A similar method can be used to determine an average for the wing's downwash at the tail. This method is not as accurate because it is difficult to get the same accuracy with a flow probe as is given by a good balance.

When evaluating the tunnel upflow balance misalignment, the model support tares in both upright and inverted runs must be known. The upflow for the tare and interference is obtained with model and image, as shown in Figure 7.20. This yields a tunnel upflow balance alignment without the local upflow effect of the balance fairing or wind screen. These balance alignment data are then used to evaluate the support and interference tares as detailed in the next section. When the model is then run both upright and inverted without the image system, the local upflow from the wind screens is also accounted for.

When the tunnel upflow and balance alignment value is determined, that is, tan α_{up}, the value should be checked by applying it via Equation (7.21) to both the upright and inverted runs. If tan α_{up} is correct, the upright and inverted curve should collapse and form a single or true curve as in Figure 7.22.

As can be seen, the determination of balance alignment and upflow is a time-consuming effort if it is done for each model that is tested. This is why it often is done with a calibration model.

In order to correct for misalignment of the side-force balance, two runs must be made, with both the tare and the interference dummies in place. The model in a normal position should be yawed in one direction and then inverted and then yawed

in the same direction relative to the tunnel. The correct side-force curve will be halfway between the curves made by the model normal and the model inverted. The inversion is necessary to nullify effects of the model's irregularities.

Side-force corrections as outlined are rarely made, since they entail a set of dummy supports that can be yawed; moreover, extreme accuracy in side force is not usually required. The principles of the correction, however, are important.

It should be recalled that changes in the shape of a polar curve may be due to scale effects and that comparisons of various tests of similar airfoils must be made from measurements at the same effective Reynolds number. (It has been shrewdly noted that, if the section selected is one of the more "popular" types that have been frequently tested, it is nearly always possible to find some results that will "agree" with yours.)

Evaluations of Tare and Interference

Any conventional wind tunnel setup requires that the model be supported in some manner, and, in turn, the supports will both affect the air flow about the model and have some drag themselves. The effect on the free air flow is called interference. The direct drag of the supports is called tare. Although tare drags could be eliminated entirely by shielding the supports all the way into the model (with adequate clearances, of course), the added size thus necessitated would probably increase the interference so that no net gain would be achieved and a more difficult clearance problem would be created.

Evaluation of tare and interference is a complex job, requiring thought as well as time for proper adaptation for each particular test and subsequent completion. The student invariably suggests removing the model to measure the forces on the model supports. This procedure would expose parts of the model support not ordinarily in the airstream (although the extra length could be made removable) and would fail to record either the effect of the model on the supports or the effect of the supports on the model.

Independent Tare and Interference Determination   First let us consider a rarely used method that evaluates the interference and tare drag separately. Actually the value of the sum of the two will nearly always suffice without our determining the contribution of each, but, besides being fundamental, this long method may offer suggestions for determining interference for certain radical setups. The procedure is as follows.

The model is first tested in the normal manner, the data as taken including both the tare and the interference effects. In symbolic form we have

$$D_{\text{meas}} = D_N + I_{LB/M} + I_{M/LB} + I_{LSW} + T_L \qquad (7.24)$$

where D_N is the drag of model in the normal position, $I_{LB/M}$ the interference of lower surface bayonets on the model, $I_{M/LB}$ the interference of the model on lower surface
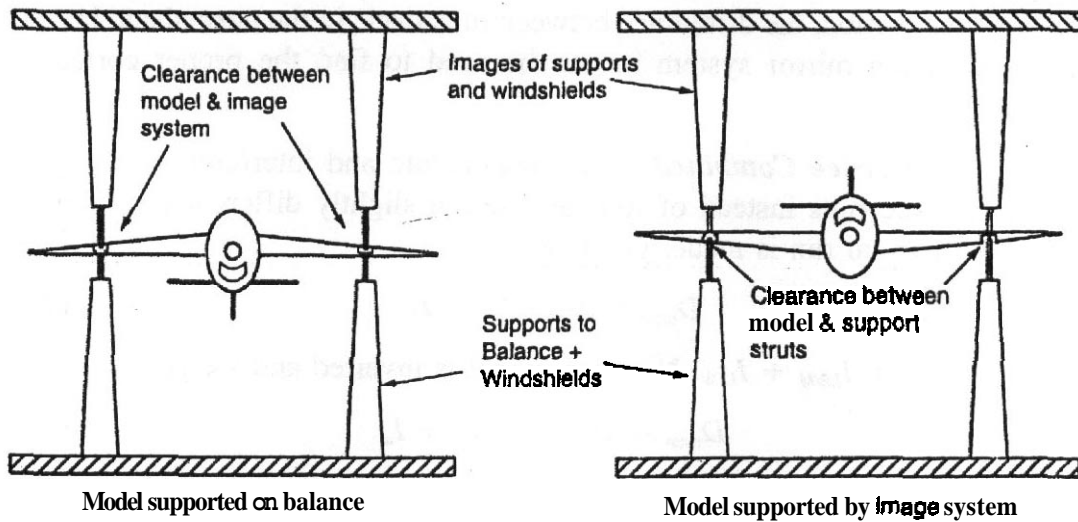
FIGURE 7.24 Mirror (or "image") method of determining the effect of the **supports** on the model.

bayonets, I_{LSW} the interference of the lower support windshield, and T_L the free-air tare drag of the lower bayonet.

Next the model is supported from the tunnel roof by the "image" or "mirror" system. The normal supports extend into the model, but a small clearance is provided (Figure 7.24). The balance then reads the drag of the exposed portions of the supports in the presence of the model. That is,

$$D_{\text{meas}} = T_L + I_{M/LB} \tag{7.25}$$

For the interference run the model is inverted and run with the mirror supports just clearing their attachment points (Figure 7.24). We then get

$$D_{\text{meas}} = D_{\text{inverted}} + T_U + I_{UB/M} + I_{USW} + I_{M/UB} I_{LB/M} + I_{LSW} \tag{7.26}$$

where D_{inverted} is the drag of the model inverted (should equal the drag of the model normal, except for misalignment) and the symbol U refers to the upper surface.

Then the mirror system is removed and a second inverted run is made. This yields

$$D_{\text{meas}} = D_{\text{inverted}} + T_U + I_{UB/M} + I_{M/UB} + I_{USW} \tag{7.27}$$

The difference between the two inverted runs is the interference of supports on the lower surface. That is, Equation (7.26) minus Equation (7.27) yields

$$I_{LB/M} + I_{LSW} \tag{7.28}$$

By subtracting Equations (7.25) and (7.28) from the first run [Eq. (7.24)], the actual model drag is determined if the balance is aligned. As explained more fully

in the previous section, the difference between runs made in the normal and inverted positions with the minor system in can be used to find the proper corrections for alignment.

Tare and Interference Combined   The support tare and interference effects can be found in three runs instead of four by using a slightly different procedure. In this case the normal run is made, yielding

$$D_{\text{meas}} = D_N + T_L + I_L \tag{7.29}$$

where $I_L = I_{M/LB} + I_{LB/M} + I_{LSW}$. Next the model is inverted and we get

$$D_{\text{meas}} = D_{\text{inverted}} + T_U + I_u \tag{7.30}$$

Then the dummy supports are installed. Instead of the clearance being between the dummy supports and the model, the exposed length of the support strut is attached to the model, and the clearance is in the dummy supports (Figure 7.20). This configuration yields

$$D_{\text{meas}} = D_{\text{inverted}} + T_L + I_L + T_U + I_U \tag{7.31}$$

The difference between Equations (7.30) and (7.31) yields the sum of the tare and interference, $T_L + I_L$. The second procedure has the advantage that the dummy supports do not have to be heavy enough to hold the model, nor do they require any mechanism for changing the angle of attack. Actual setups **are** shown in Figures 7.25 and 7.26.
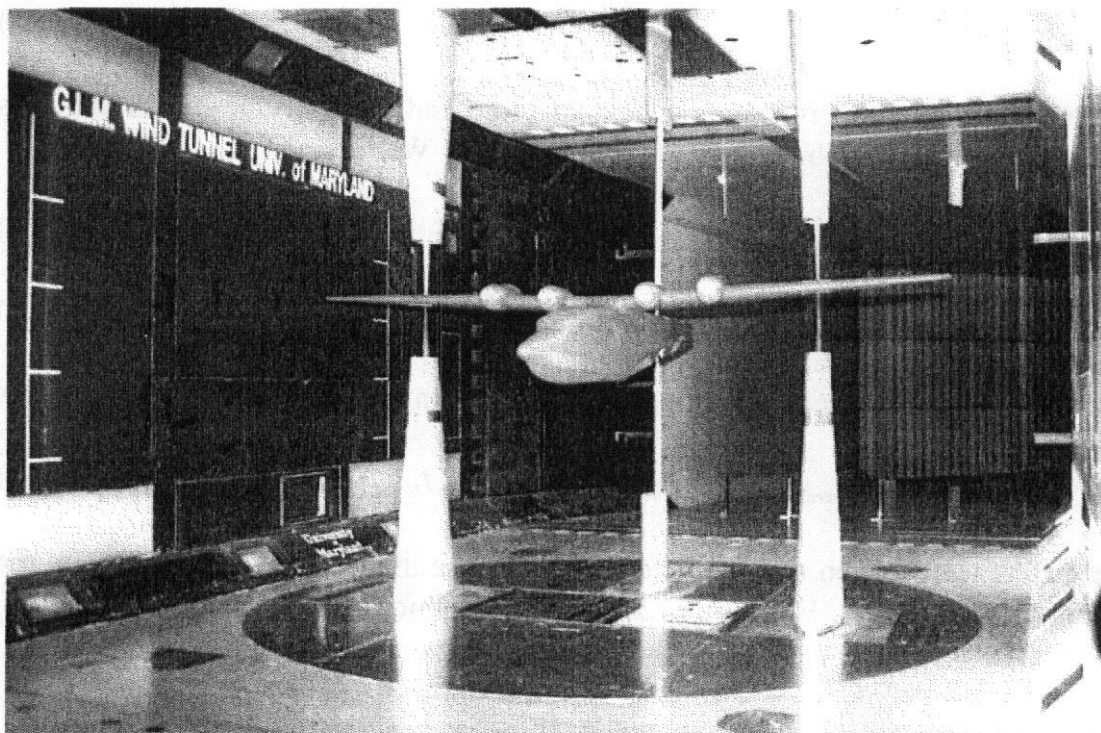
FIGURE 7.25   Three-support system **with** image system for evaluating tare and interference. (Photograph courtesy of Glenn L. Martin Wind Tunnel.)
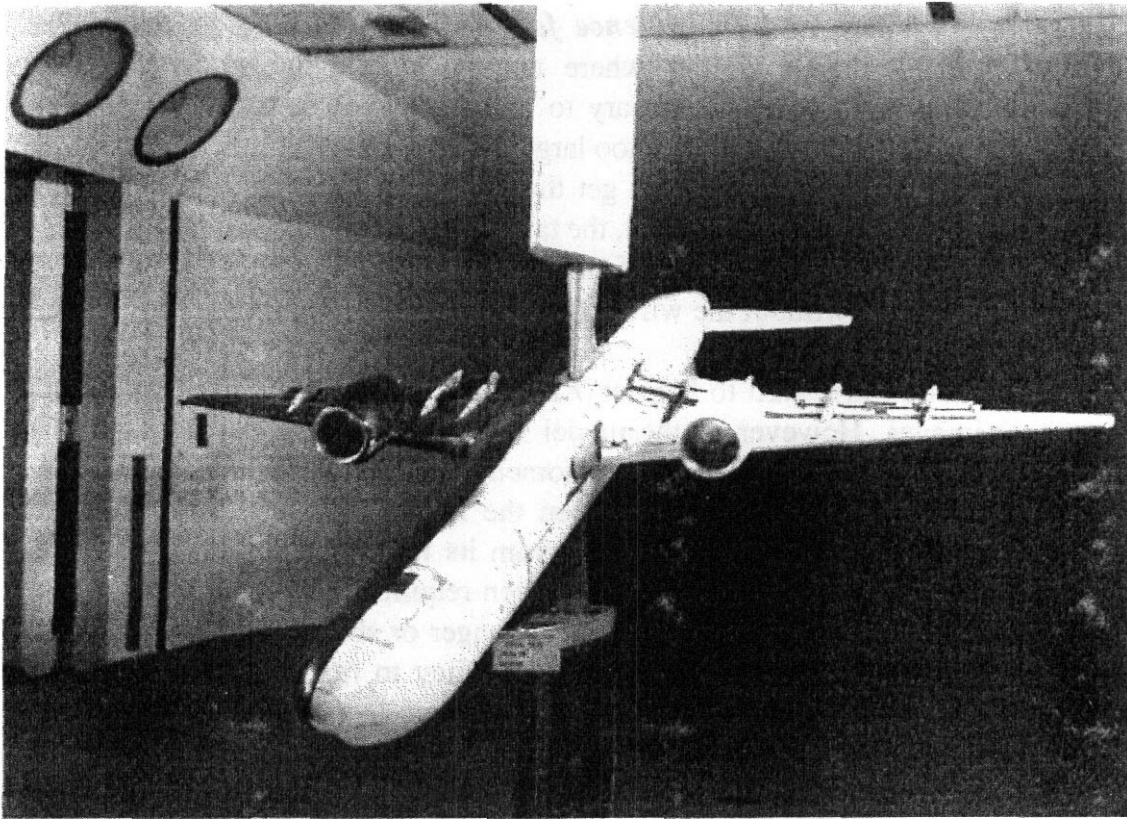
FIGURE **7.26** **Tare** and interference runs on Boeing 767 mounted on single strut and pitch arm. The model is painted light blue on right side and black on left side for flow visualization and identification purposes. (Photograph courtesy of Boeing Aerodynamic Laboratories.)

Approximate Method without an Image System A third method of evaluating the tare and interference, sometimes employed where an image system is impracticable, consists of adding extra dummy supports on the lower surface and assuming their effect to be identical with the actual supports. Sometimes there is danger of mutual interference between the dummies and the *real* supports.

Approximations of Tare and Interference from Calibration Models Doubtless the increase of runs necessary to determine the small tare and interference effects and the concern expressed about the difference between those effects on the upper and lower surfaces seem picayune. Yet their combined effect often represents from 10 to 50% of the minimum drag of the whole airplane--clearly not a negligible error.

It should be noted that the tare and interference forces vary with angle of attack and model changes. They must be repeated checked and evaluated, particularly for major changes of wing flaps and nacelle alterations close to the support attachment. With many models every configuration must have its own support interference evaluated—a long and tiresome test procedure.

Because the evaluation of tare and interference requires large amounts of time, they often are approximated by evaluating them on a calibration model, and these values are then applied as approximate tares to other models.

Considerations of Tare and Interference for Various Mounting Systems   For models of propeller-driven aircraft where the model is powered by variable-frequency electric motors, it is necessary to bring both power and water-cooling lines into the model. These usually are too large to be contained inside the mounting strut. If a special fairing is required to get the wires, for example, into the model or if they are taped to the mounting strut, the tares for these items must be evaluated. The easiest method is to make a set of pitch and yaw runs with the same model configuration with and without the wires. The difference between these runs is then added to the standard strut tares.

A note of caution in regard to Figures 7.20 and 7.24: The images are supposed to be mirror images. However, if the model struts enter the model fuselage, the trunnion, which usually is on the balance moment center and the tunnel centerline, is not at the centerline of the model. When the model is inverted, the exposed portion of the image strut and the distance from its fairing to the model must be exactly the same as the upright model. This often requires the length of the image fairing exposed to the tunnel flow to be either longer or shorter than the standard, or lower, fairing. Thus, it generally is a good policy to make the image fairing longer than the normal fairing and let it extend through the tunnel ceiling.

In the three-run method of taking tare and interference there is a possibility of air flowing in and out of the gap between the mounting strut and the fairing if the standard struts do not have a seal at their tops. To get the correct tare and interference, the image system must duplicate exactly the geometry in this region.

For a support system that uses two supports on the wing and a tail support, an alternate method is sometimes used. The reason for this alternate treatment is that the length of the tail support varies as angle of attack is changed. This factor so complicates the dummy arrangements that a system is usually employed that does not require a complete dummy tail support.

The procedure is as follows: Consider the second method of evaluating the tare and interference. When the image system is brought down to the inverted model, a short support is added to the then upper surface of the model where the tail support would attach in a normal run. The piece attached corresponds in length to the minimum exposed portion of the tail support and increases the drag of the model by the interference and tare drag of a tail support on the model's lower surface. For angles of attack other than that corresponding to minimum length of exposed tail support, the drag of the extra exposed tail support length must be evaluated and subtracted.

A rear-support windshield that moves with the rear support to keep a constant amount of strut in the airstream could be employed as long as the added interference of the moving shield is evaluated by a moving-shield dummy setup.

The evaluation of the tare, interference, and alignment of a wing-alone test follows the procedure outlined above, except that further complication is introduced by the presence of a sting that must be added to the wing to connect it to the rear strut of the support system. The tare and interference caused by the sting may be found by adding a second sting during the image tests. As may be noted in Figure 7.27, the attachment of the sting to the rear support includes a portion of the strut above the connection, and the dummy sting has a section of support strut added
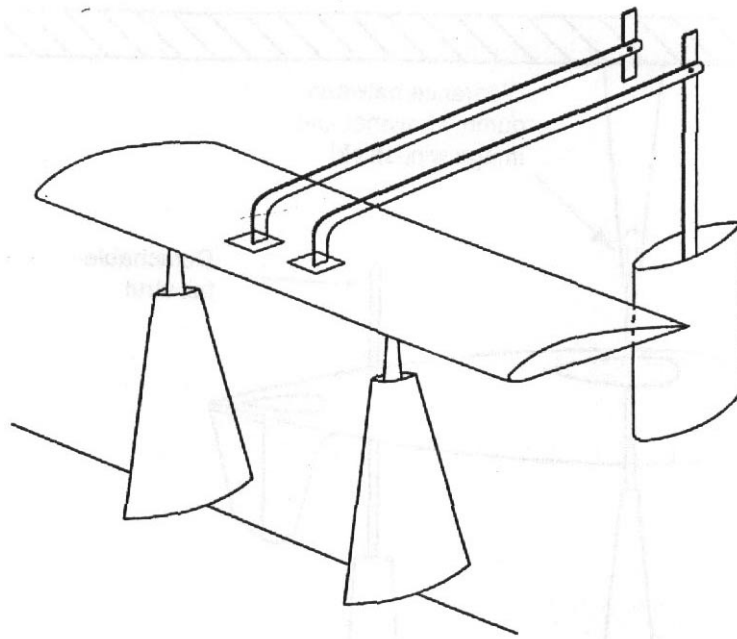
FIGURE 7.27   **Setup** for determining **tare** and interference of sting.

both above and below its connection point. This complication is needed to account for the interference of the strut on the sting as follows: When the wing is held at a high angle of attack, there will be an obtuse angle below the sting. When the wing is inverted and held at a high angle relative to the wind, there will be an acute angle below the sting, for the rear strut will then be extended to its full length. To eliminate this difference between the normal and inverted tests, the support strut is extended above the sting attachment point, so that the sum of the angles between the sting and the support is always 180°. The image sting has the same arrangement. Note that although the angles between the sting and the rear support vary with the angle of attack, the image sting is always at right angles to its short rear-support strut. Furthermore, the image rear-support strut does not remain vertical but changes its angle with the wing. The error incurred by failing to have the sting image system simulate the exact interference and rear-strut angle is believed to be negligible.

Tare and interference for the tail strut alone may be evaluated, as shown in Figure 7.28. For asting mount Figure 7.29 shows the arrangement. The setup for determining the tare **and** interference for a fork support is shown in Figure 7.30. Here the model is supported externally and a small clearance is left where the struts come into the wing. This measures the drag of the fork plus the effect of the wing on the fork but not the effect of the fork on the wing, which experience has shown to be small. Hence, the tares are used as approximate tares where the desire to save tunnel time precludes taking the usual tare and interference runs.

Figure 7.31 shows the results of a wing-alone test for a NACA 0015 wing of aspect ratio (AR) 6.0. The wing in this particular test was small, and the corrections for tare, interference, and alignment are correspondingly large, but the variation of the corrections is typical. The following points are of interest:

Clearance between
dummy bayonet and
image windshield

Detachable
tail strut
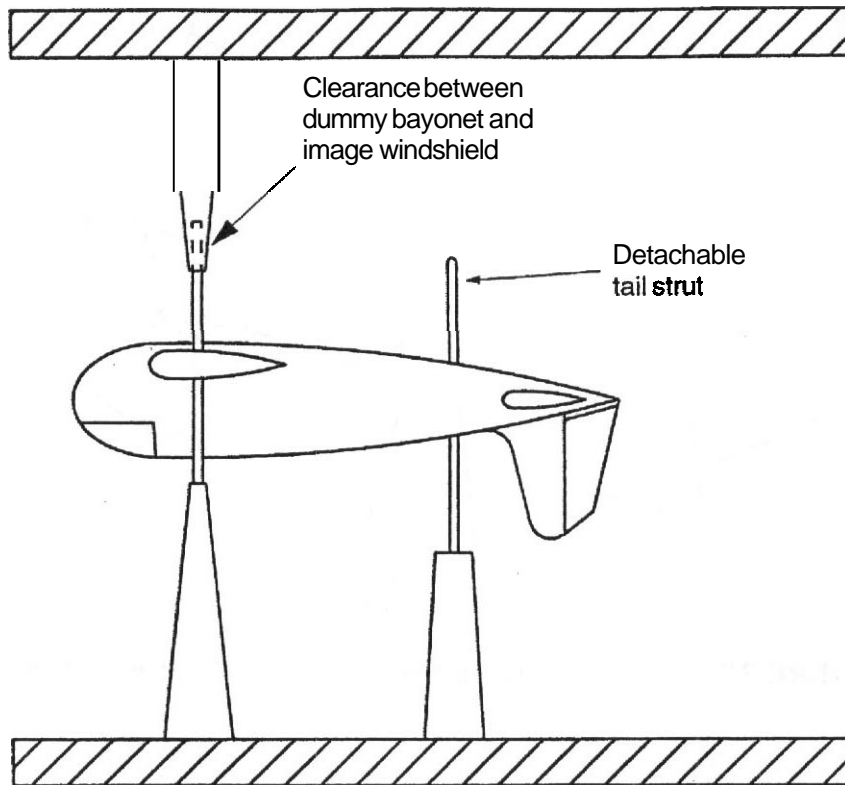
FIGURE 7.28   Setup for determining tare and interference of the tail support.
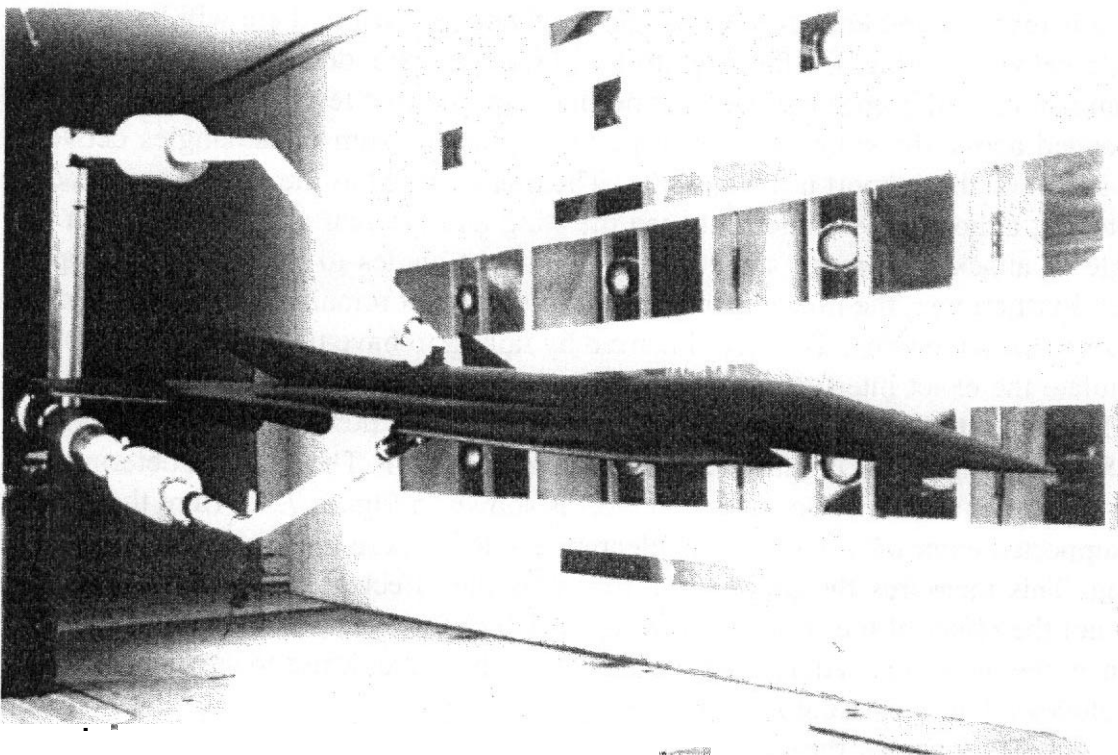
FIGURE 7.29   Tare and interference: supersonic transport with surface sting support in NASA Langley 4 × 7-m tunnel. (Photograph courtesy of NASA Langley and Dynamic Engineering, Inc.)
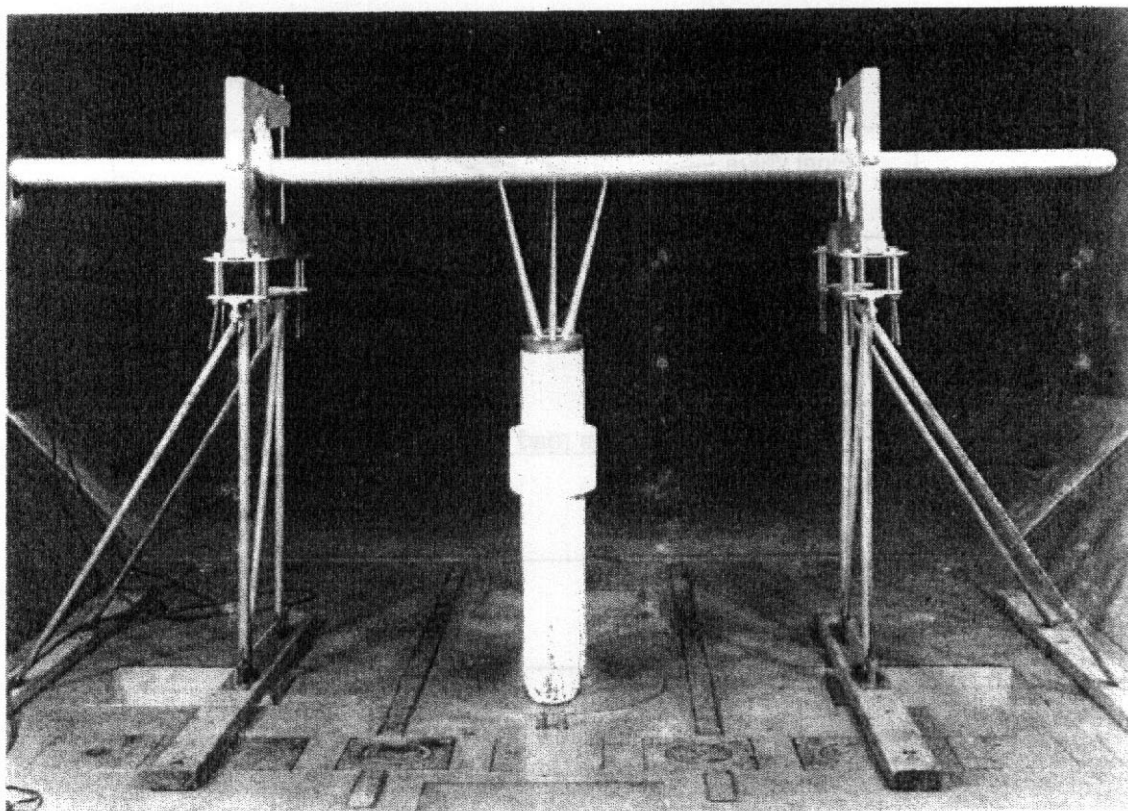
FIGURE 7.30   Tare and interference determination for a fork-type support. (Courtesy University of Washington Aeronautical Laboratory.)

1. The correction for tare and interference decreases as C_L (and a) increases.
2. The incidence strut drag decreases with increasing a. (The amount of strut exposed decreases with a.)
3. The alignment correction increases with C_L.

A large amount of interference may arise from air that bleeds through the windshields that surround the support struts to protect them from the windstream. These struts frequently attach at points of low pressure on the model, and if the shield is brought close to the model, a considerable flow may be induced that will run along the model. This flow may stall the entire underside of the model and produce results that are not only wrong but also unsteady and difficult to evaluate. It is therefore frequently advantageous to terminate the windshields well below the model and let the test be subjected to added but well-defined tare drag and to provide seals to stop the bleed flow. See Figure 7.32.

Subsonic testing of military aircraft is often done over angle-of-attack ranges from $0°$ to $90°$ and missiles from $0°$ to 180". When the model is a slender body and is mounted on a swept strut parallel to the body axis and free stream, the strut will be similar to a splitter plate behind a cylinder. A splitter plate behind a cylinder can inhibit the vortex formation and reduce the wake pressure. When this occurs with a wind tunnel model, there is an improper flow simulation. The effect of the
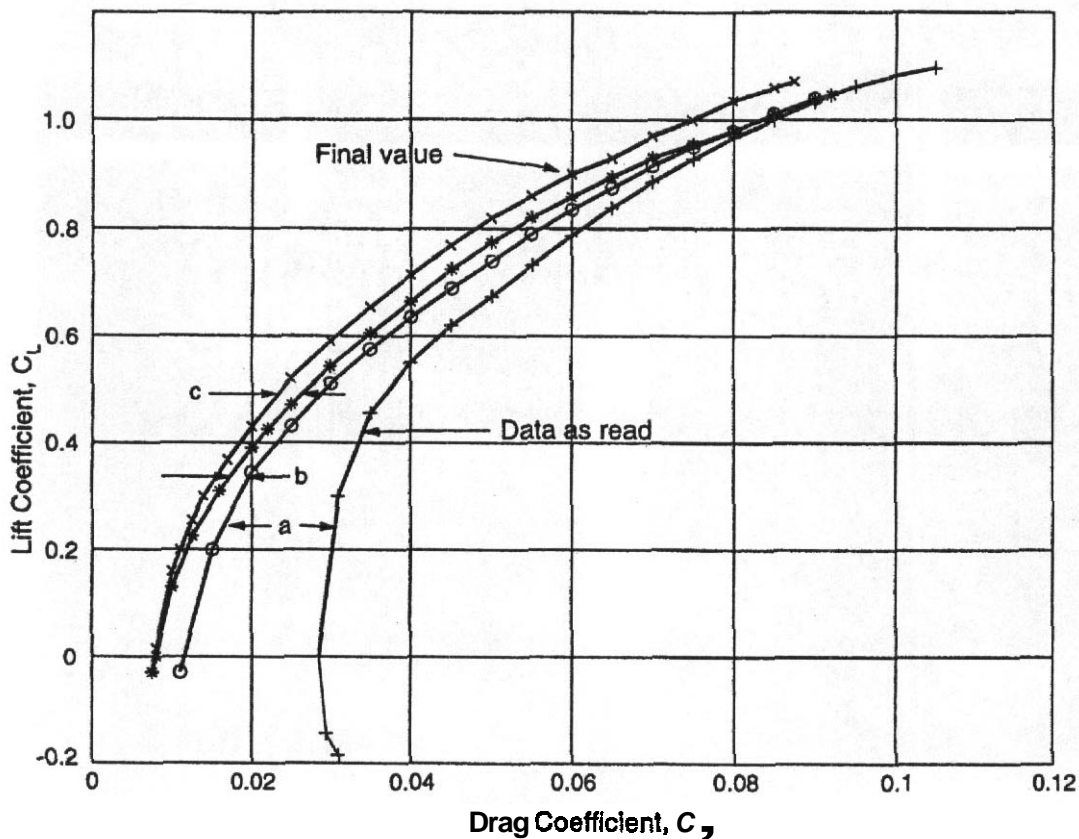
FIGURE 7 3 1   Corrections for a wing-alone test: a, sting and support tare and interference; b, drag of exposed incidence strut; c, alignment.

splitter plate on a cylinder is a function of the plate size and location relative to the cylinder and Reynolds number."

The problem of properly taking and evaluating support tares and interferences for models at a high angle of attack is difficult. The models are generally mounted on stings with internal balances making the use of mirror images difficult. If the model is supported by auxiliary supports, there can be mutual interferences between the support, the model, and the normal sting. Auxiliary supports may require a second internal balance, adding possible complexity to the model. And finally, there is the complexity caused by the large range of angles that must be covered.
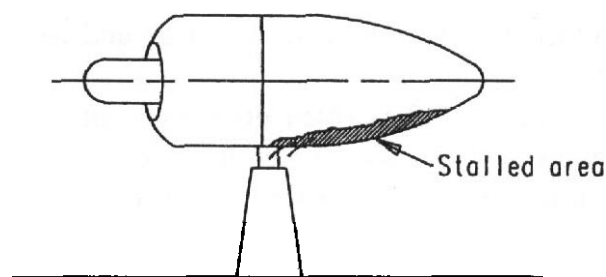
FIGURE 7.32   Effect of bleeding.

A number of reasonably common mounting arrangements are discussed in the next section.

Complete Aircraft and Submarine Mounting

Every tunnel program has its own set of objectives that must be used to guide the choice of mounting arrangement. There is always some tare and/or interference. The inevitable trade-offs that are made between tare magnitude and interference are somewhat different for the various mounting schemes.

Single-Strut Mounting   This arrangement is by far the simplest. Only a single windshield is needed, and it need not move as the model is rotated in yaw. An example is shown in Figure **7.33.** The single strut is satisfactory for models and nacelles and may be used in conjunction with wingtip supports to evaluate tare and interference. The single strut usually mounts in the body of the model. The lateral spacing of the trunnion pins must be as large as possible to carry the rolling moments and to prolong the life of the trunnion pin bushings when the model has asymmetric stall (this structure is buried in the model body). When the strut is made with a relatively large cross-sectional area, it is fairly rigid in torsion (yaw) and a fair lead may be incorporated in its leading edge for wires for instrumentation, power to drive the horizontal tail, hinge moment data, and the like. Because the wires are internal to the strut, additional tare and interference runs are not required for such
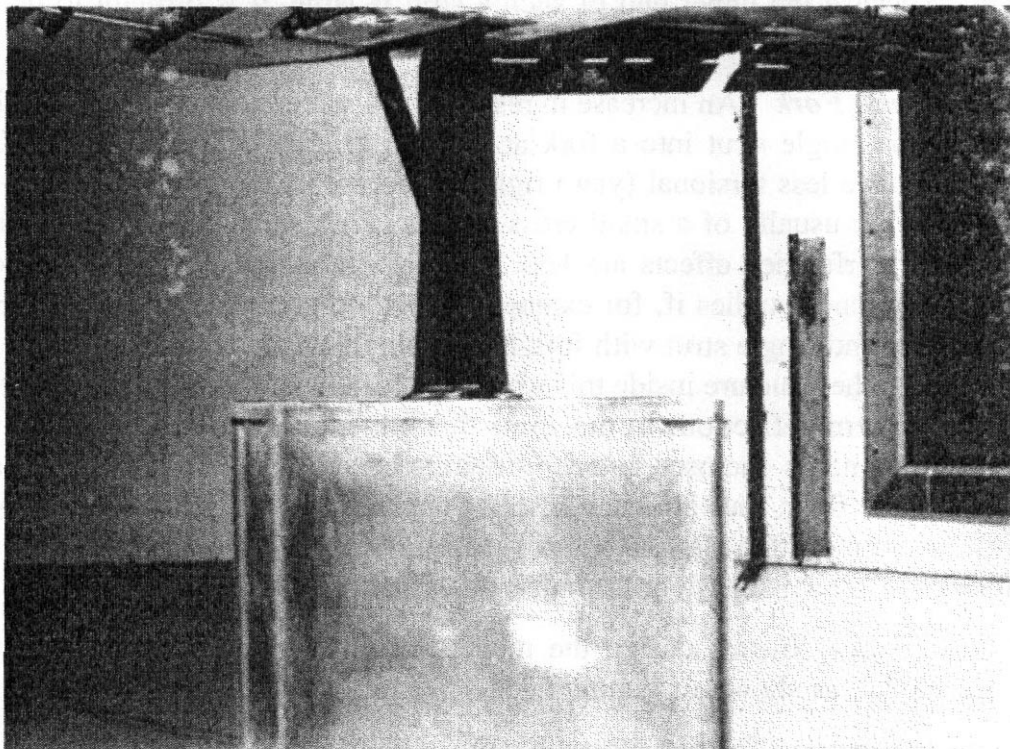
FIGURE 7.33   Single strut with pitch arm. Both strut and pitch arm rotate in yaw. (Photograph courtesy of University of Washington Aeronautical Laboratory.)
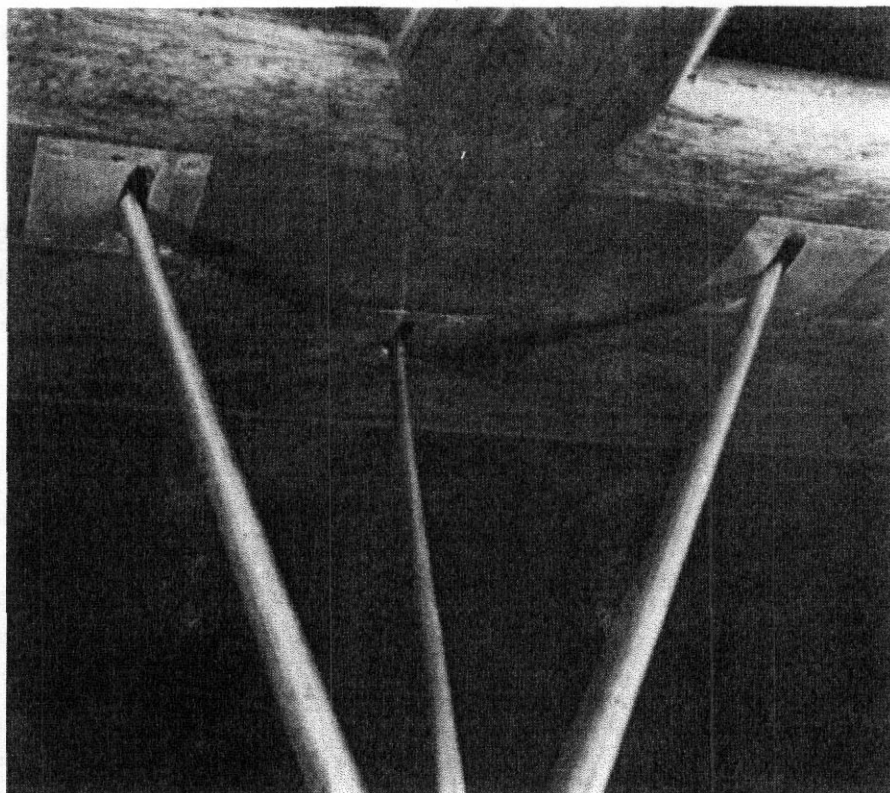
FIGURE 7.34   Fork-and-pitch-arm-type mounting strut. Both fork and pitch arm rotate in **yaw.** (Photograph courtesy of University of Washington Aeronautical Laboratory.)

wires, and because the upper end of such a strut is large, it is difficult to use for wing-alone tests.

Single Strut with Fork   **An** increase in resistance to roll deflections may be gained by splitting the single strut into a fork at the top, as shown in Figure 7.34. This method may have less torsional (yaw) rigidity, as the forward struts that carry the trunnion pins are usually of a small cross section. With small-cross-section struts, the tare and interference effects are less. This system usually requires additional tare and interference studies if, for example, wires are taken into the model. Both the single strut and single strut with fork have a single windshield that is not a part of the balance. The structure inside this windshield can be quite robust, thus limiting the support system deflections to the struts that are exposed to the airstream. The balance fairing and its enclosed balance structure can be designed to be removable below the tunnel floor, thus allowing a stiff, nonpitching strut to be attached to the balance. This strut with a flat plate that yaws can be installed flush with a splitter plate above the wind tunnel floor for half models and building/structural shape tests.

Single Strut Only   In this design the model pitching and/or yaw mechanism is inside the model, as shown in Figure 7.35.

Two-Strut Mounting   **The** two-strut mounting systems surpass the single-strut system for rigidity in both torsion (yaw) and roll but add the complication that the windshields must be moved and rotated **as** the model is yawed. Figure 7.36 shows
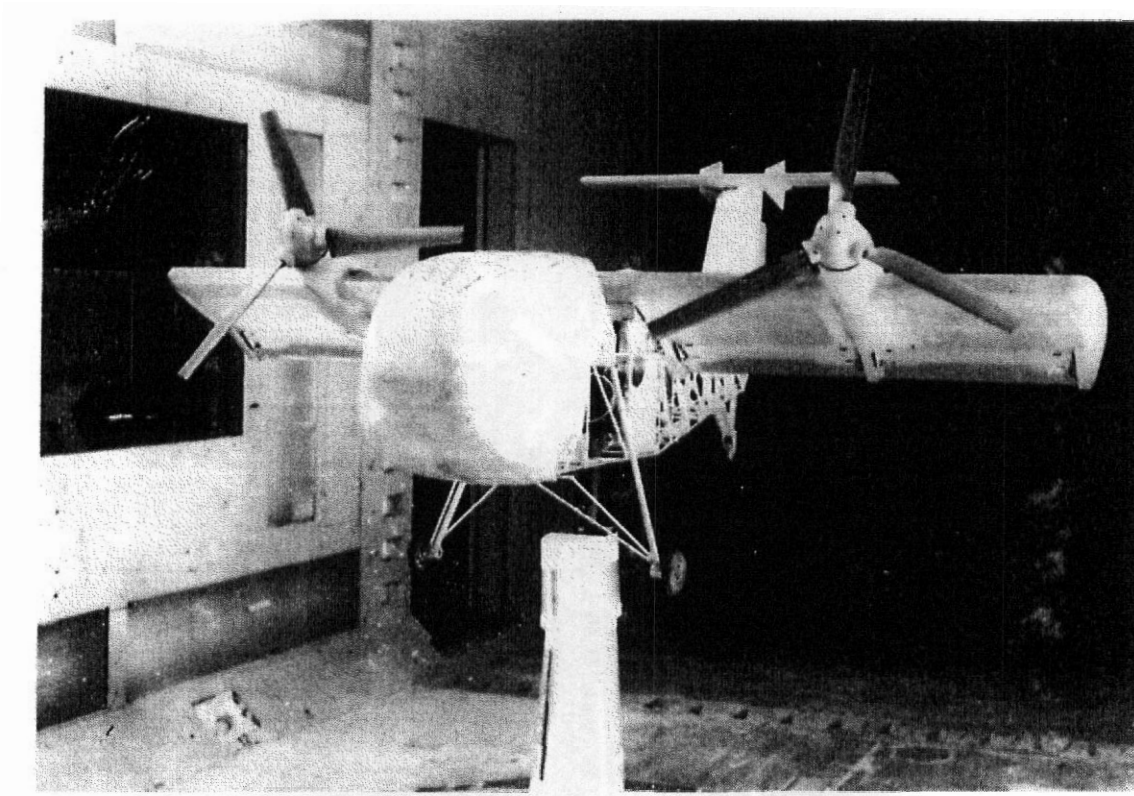
FIGURE 7.35 Single strut with pitch and yaw mechanism inside model. (Photograph courtesy of Glenn L. Martin Wind Tunnel.)
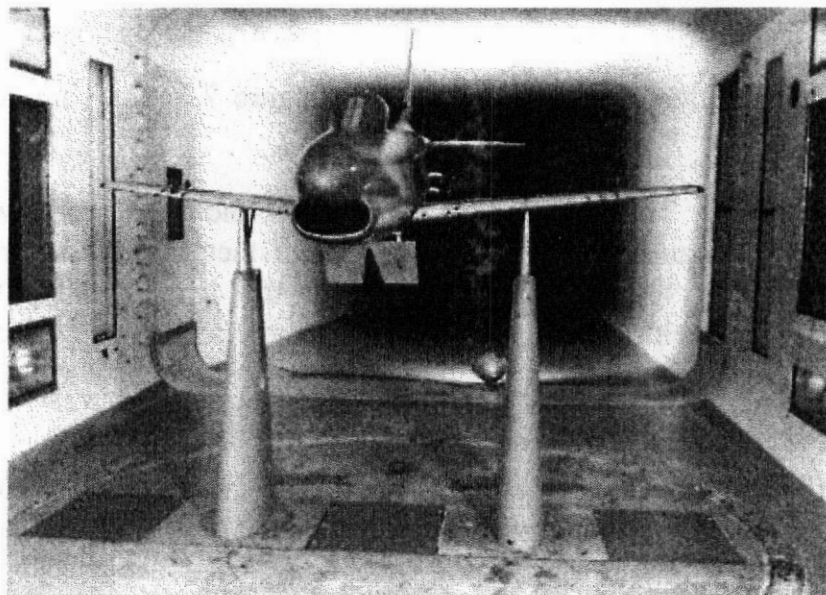
FIGURE 7.36 F-86D on two-strut support. (Courtesy of the Boeing Co.)

FIGURE 737 Two-strut **tandem. (Photograph courtesy of Texas** A&M **University Low** Speed Wind Tunnel.)

a setup with the mounting struts side by side; in Figure 7.37 they are employed in tandem.

Three-Point Mounting   The conditions of rigidity, tare, and interference evaluation and ease of varying the angle of attack **are** all met satisfactorily by the three-point supporting system. This system is more complex in that it requires that two and sometimes three windshields be arranged to yaw with the model, as can be seen in Figure 7.38. The rear strut introduces side forces that complicate the yawing moment measurements of a yawed model.

Wingtip Mounting   When it becomes necessary to determine the pressure distribution of regions close to the mounting struts, the models **are** sometimes mounted from the wingtips, leaving the fuselage and nacelles in air unobstructed by support fittings. Models of larger scale may be tested with wingtip mounting, and valid comparisons can be obtained of the effect of component parts. An example of a wingtip-mounted installation is shown in Figure 7.39.

Mounting from the Tunnel Roof   A few balances mounted above the tunnel support the model in an inverted position for "normal" running, as illustrated in Figure 7.40.
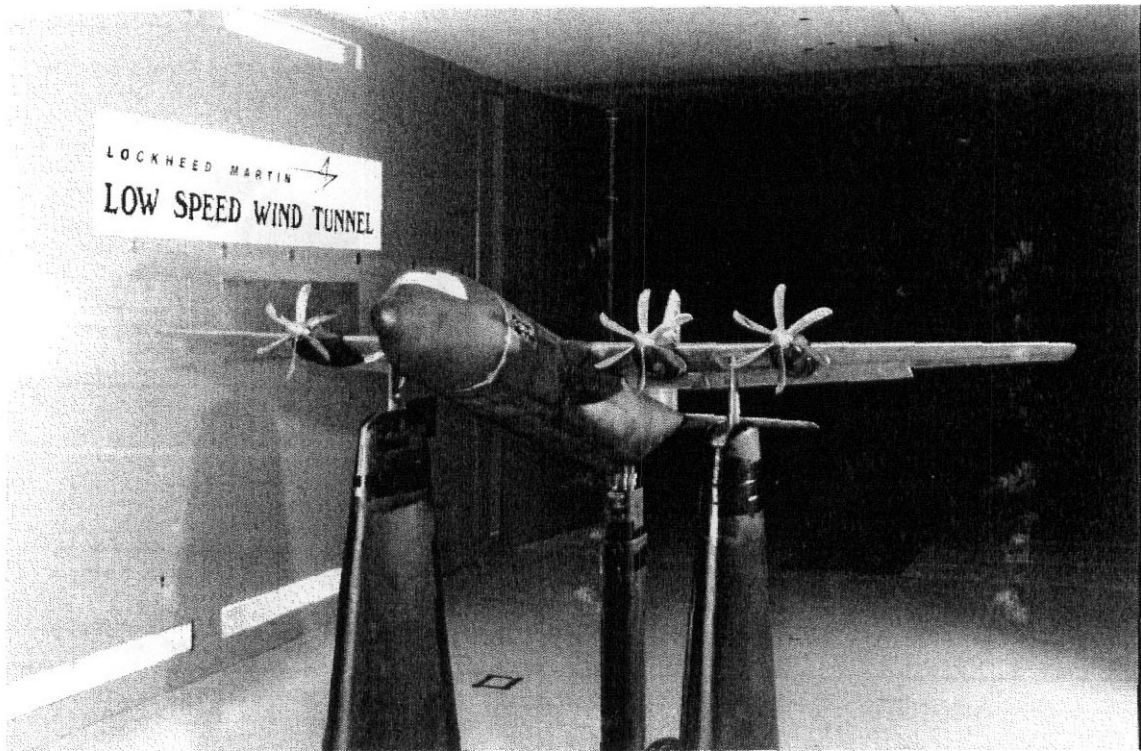
FIGURE 7.38 C-130J on three-strut support. (.Courtesy of the Boeing Co.)

This arrangement seems to be a holdover from early wire balances that supported the model similarly so that the lift forces would put tension in the wires. No particular advantage seems to accrue from inverted testing. On the contrary, such a balance position hinders the use of a crane to install models, and the terminology of testing "normal" and "inverted" becomes itself inverted compared to the more common arrangements.
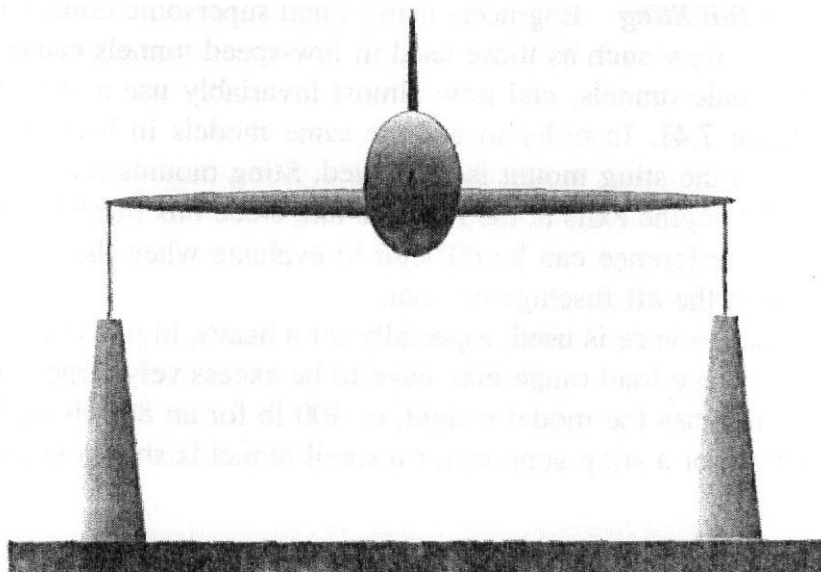
FIGURE 7.39 Tip mount providing cleaner flow near wing mot.
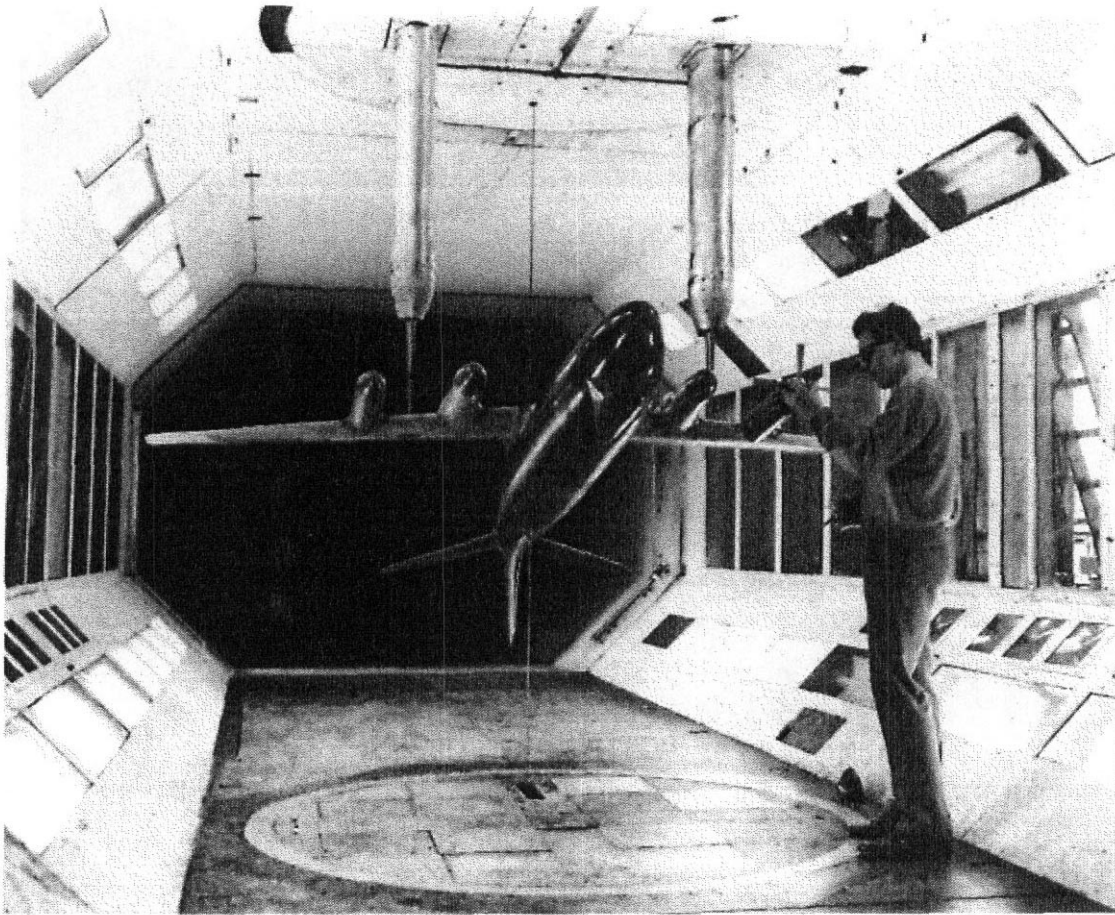
FIGURE 7.40   Ceiling-supported model. Inverted testing is quite common in Europe. (Photograph courtesy of British Aerospace Defense.)

There also can be extra costs associated with this method in obtaining a sufficiently rigid structure above the tunnel on which to mount the balance.

Mounting from a* Tail *Sting Engineers using small supersonic tunnels found that struts normal to the flow such as those used in low-speed tunnels cause excessive blocking in supersonic tunnels, and now almost invariably use a sting mount, as illustrated in Figure 7.41. In order to use the same models in low-speed tunnels (which are cheaper) the sting mount is employed. Sting mounts are fine for those airplanes having jet engine exits at the fuselage tail, since this furnishes a place for a sting. Tare and interference can be difficult to evaluate when the sting diameter requires a change in the aft fuselage contour.

When an internal balance is used, especially for a heavy, high-Reynolds-number model, the axial balance load range may have to be excessively large, since it will have to carry sin a times the model weight, or 400 lb for an 800-lb model at $a =$ 30°. A drive system for a sting support for a small tunnel is shown in Figure 7.42.

Reflection Plane and Similar Arrangements

These are used to reduce model cost or obtain a modest increase in Reynolds number.
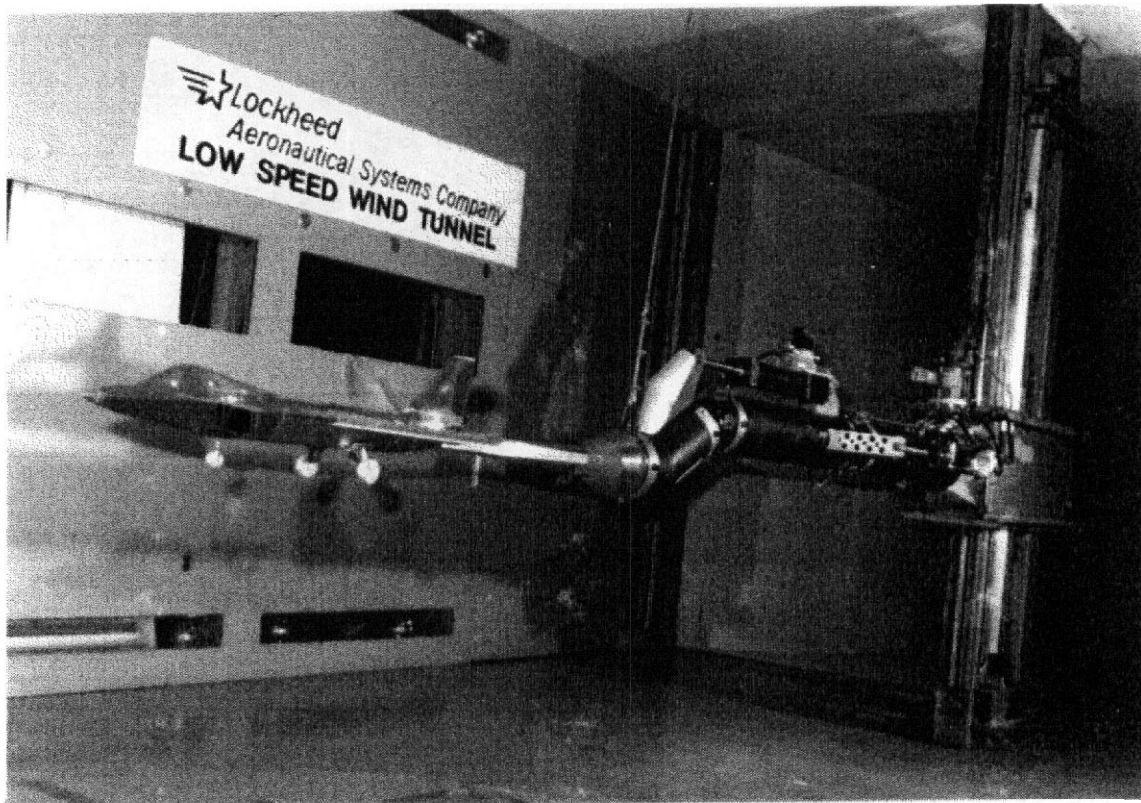
FIGURE 7.41   F-22 model on high angle of attack sting system. (Courtesy of Lockheed Martin Co.)
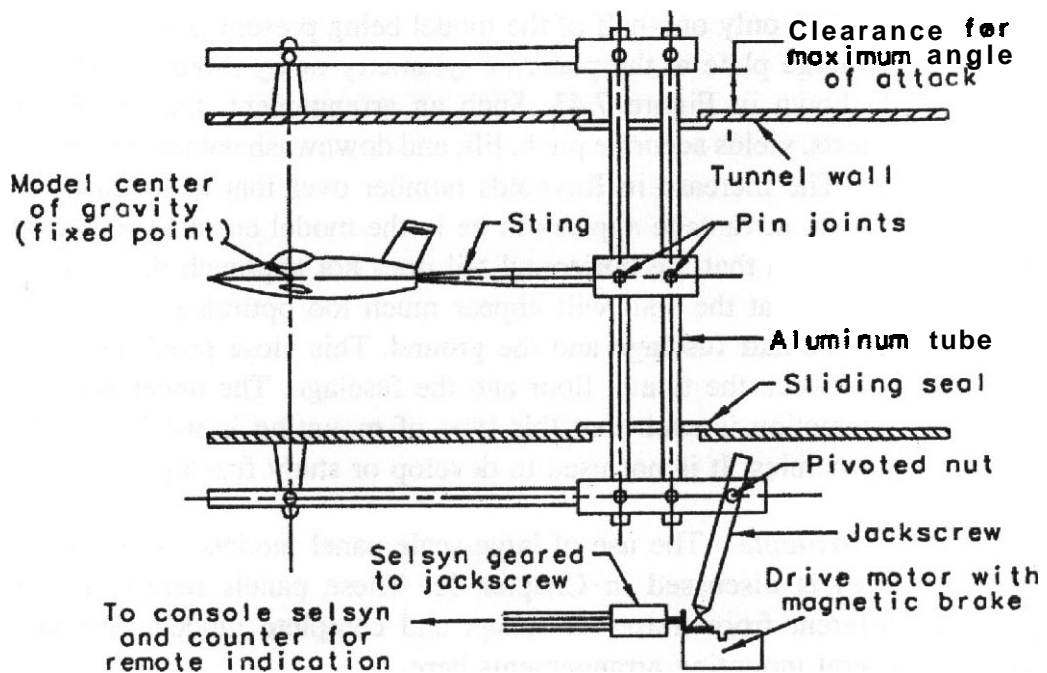
FIGURE 7.42   Parallelogram linkage for angle-of-attack control used in 40 × 40-in. low-speed tunnel.
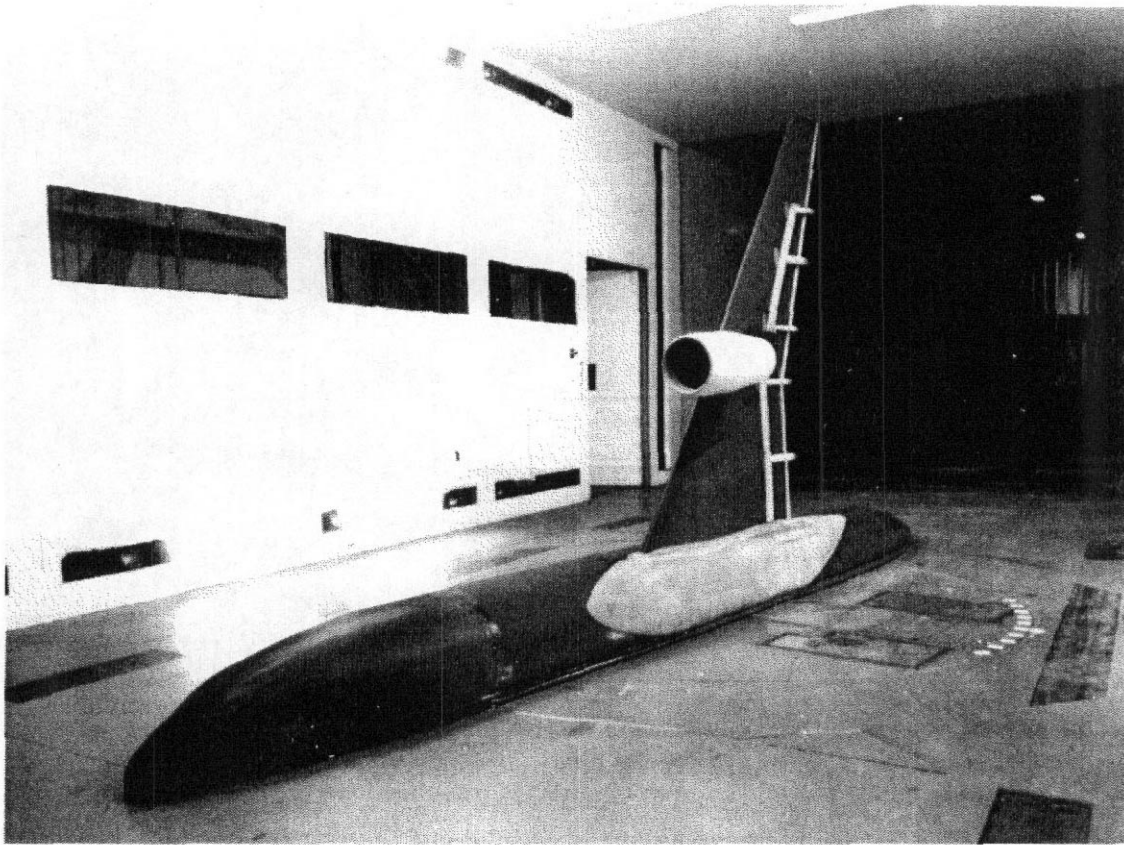
FIGURE 7.43 L-1011 reflection plane model setup. (Courtesy of San Diego Aerospace Museum.)

Half Models The largest scale models may be tested by having them split down the plane of symmetry, only one-half of the model being present. Asymmetric flow is prevented by a large plate at the plane of symmetry or by mounting the model on the floor, as shown in Figure 7.43. Such an arrangement, though obviously unsuited for yaw tests, yields accurate pitch, lift, and downwash data at the maximum Reynolds number. The increase in Reynolds number over that of a full model is about 20%. The main advantage appears to be in the model construction costs.

Care should be taken that the horizontal tail does not approach the tunnel wall too closely or stability at the stall will appear much too optimistic. Some gap is provided between the half fuselage and the ground. This close proximity leads to flow interaction between the tunnel floor and the fuselage. The uncertainty in the details of this interaction is such that this type of mounting is used primarily to study wing aerodynamics. It is not used to develop or study fuselage shapes.

Mounting on a Turntable The use of large-scale panel models for investigation of control surfaces is discussed in Chapter 11. These panels require mounting arrangements different from those for wings and complete models. We include discussion of several mounting arrangements here.

When the model is mounted on a turntable flush with the tunnel wall, the forces and moment on the turntable are included in the data and are difficult to separate.
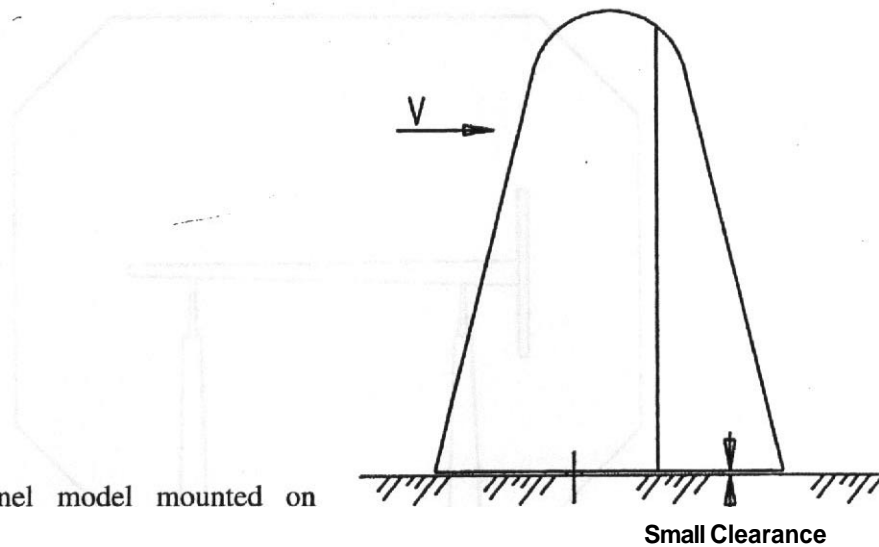
FIGURE 7.44 Panel model mounted on short strut.

Small Clearance

Fortunately, for the type of tests usually sought with this arrangement, the absolute value of the drag is not needed, and the effect of the endplate on lift is negligible.

Mounting on a Short Strut   Mounting the panel model on a short strut, as shown in Figure 7.44, has the advantage of decreasing the tare drag of the setup, but it is hard to evaluate the effect of the slot. Theoretical considerations indicate that a slot of 0.001 of the complete span, not panel span, will decrease the effective aspect ratio enough to increase the induced drag by 31%; a slot of 0.01 span will cause an increase of 47%. The effect of viscosity (not included in the above figures) will tend to decrease the error listed above, but the degree of viscous effect has not been clearly established. If the slot can be held to less than 0.005 span, its effect will probably be negligible; few engineers believe that 0.02 span is acceptable.

Mounting as a Wing with an Endplate   Moutning the panel as a wing with a small endplate to assist in keeping the spanwise lift distribution as it should be is shown in Figure 7.45. No endplate of reasonable size will prevent tip flow; hence the snapwise load distribution with this mounting will be greatly in error.

The last paragraphs draw attention to the advantage of having a yoke-type balance frame, whether or not the balance is a yoke balance. The presence of lateral brace members to which bracing wires may be attached is a great convenience. Such members are obviously necessary for wingtip mounting.

Some balances have a ring that completely encircles the tunnel jet. Though the ring offers a number of brace points, the part of the ring above the test section interferes with the installation of the image system.

7.6   INTERNAL BALANCES

Internal balances are used extensively for complete model work and even more extensively for measuring loads on parts of models. A six-component internal balance
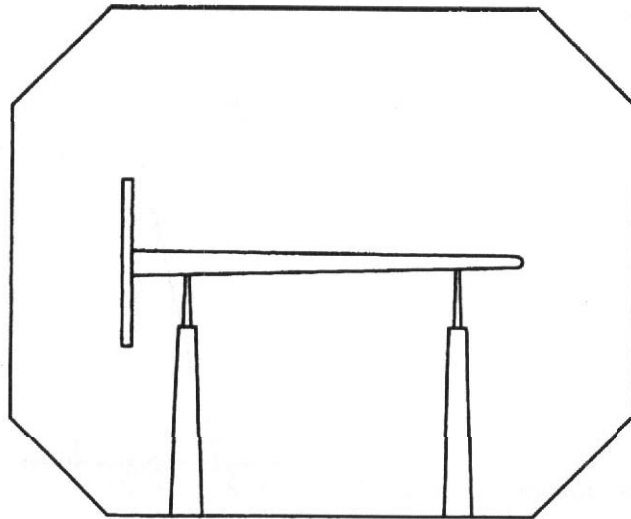
FIGURE 7.45   Panel mounted as a wing with endplate.

must address all the problems faced by a six-component external balance, but it must accomplish its purpose within a tightly specified and highly restricted volume and shape. Even the best internal balance cannot match the overall dynamic range and component independence of most external balances. But the option of matching the properties of an internal balance closely to a specific need greatly expands the options available when planning an experimental investigation.

The two transducer types that are most widely used for internal balances are strain gages and piezoelectric elements. Of these two, strain gages far outnumber piezoelectric devices. The reason for this is that although piezoelectric devices are extremely stiff and have outstanding frequency response, they do not measure steady loads well. In practice, the terms internal balance and *internal* strain gage balance are effectively synonomous.

Basic Aspects

There are two basic types of elements in an internal balance: force elements and moment elements. In any six-component system there will be three force units and three moment units.

Force-measuring elements employ either a cantilever beam or a column arrangement. An eccentric column provides greater sensitivity but also allows more deflection, as does a single cantilever. The choice might well depend on the particular balance size and arrangement needed for a specific model. The axial force "cage" shown in Figure 7.46*a* is one of the most common types. This unit can be made very sensitive by sizing the flexures, but since the model is attached to the cage, it is subjected to the relatively large normal forces. One might thus expect (see Figures 7.46*b* and 7.47) an obvious interaction to occur because of the deflection of the cage flexures. A unit designed at David Taylor Model Basin (DTMB), shown in Figure 7.46*c*, has reduced this kind of interaction to a minimum. All forces except
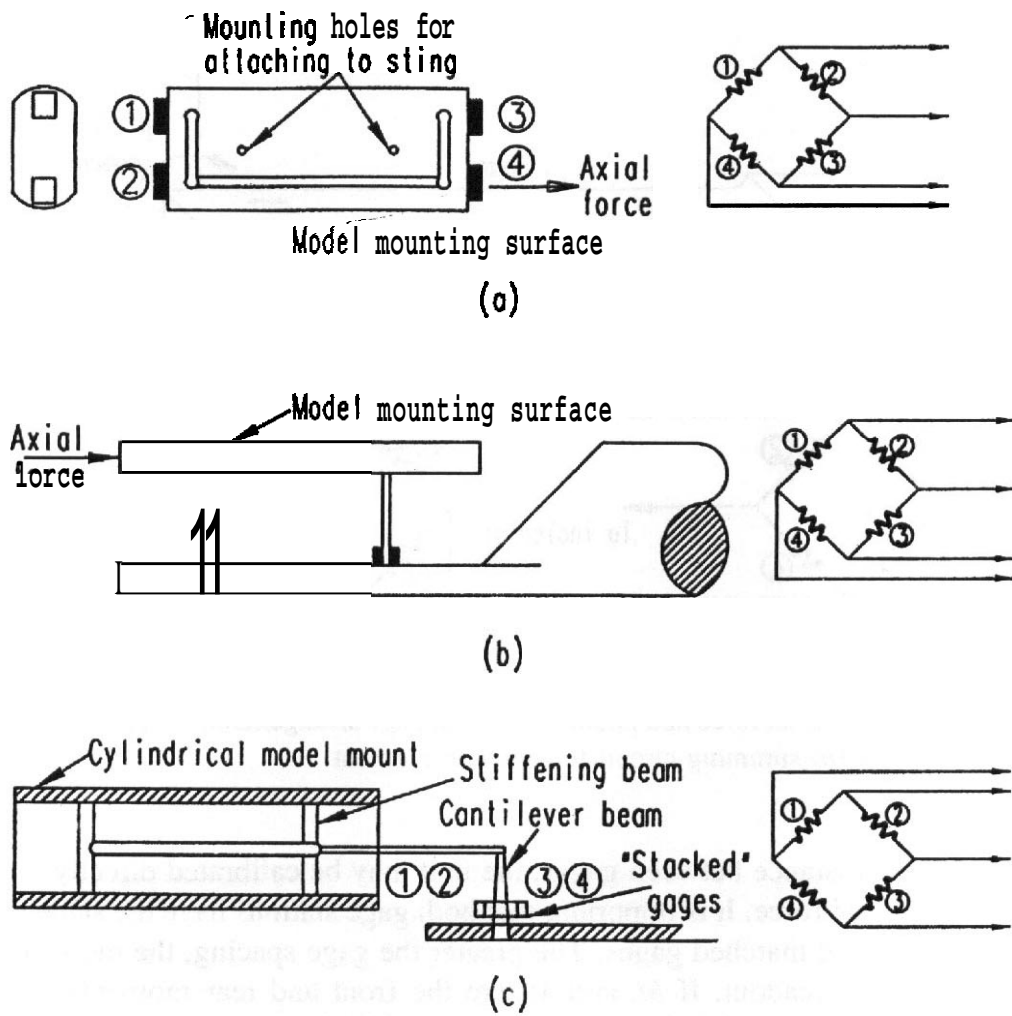
FIGURE 7.46   Axial force gages.

axial load are carried by the webs as shear or direct tension or compression. A rod transmits the axial force to a cantilever beam mounting the gages.

The arrangement for normal force readout is shown typically in Figure 7.48. In this case, the wiring is arranged so that the difference between two moments is read electrically. Since the normal force is equal to the difference of the two moments
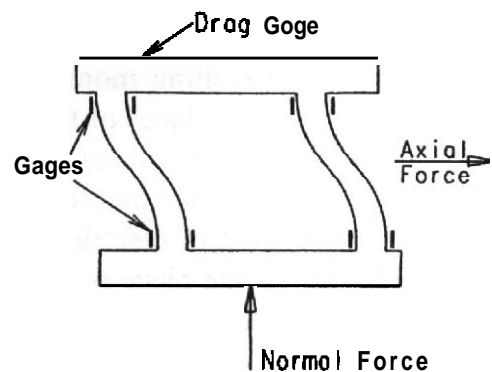
FIGURE 7.47   Normal force interaction on axial force.
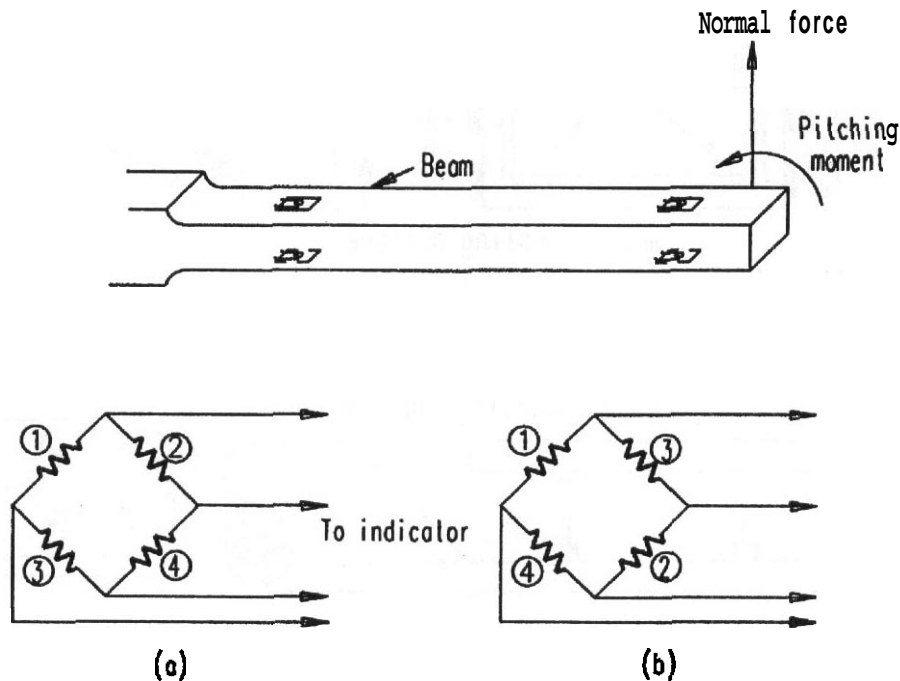
FIGURE 7.48   Normal force and pitching moment gage arrangement: (a) differential circuit for normal force; (b) summing circuit for pitching moment.

divided by the distance between gages, the unit may be calibrated directly in terms of applied normal force. It is important that both gage stations have the same section properties, I/y, and matched gages. The greater the gage spacing, the more accurate the normal force readout. If M_f and M_r are the front and rear moments, then the normal force N is given by $(M_r - M_f)/d$, where d is the spacing between gages. It is noted that the same arrangement may be used to measure side force.

Pitching or yawing moments may be measured by the same gage arrangement discussed above except, as shown in Figure 7.48, the bridge is connected as a summing circuit. The differential circuit employed for normal force will also yield the moment if the moment reference point is between the two gage stations, for, then,

$$M_{ref} = M_f + \frac{x_{ref}}{d}(M_r - M_f)$$

where x_{ref} is measured from the front gage station. Another way is indicated in Figure 7.49, where the pitch gages are "stacked" and located between the normal force gages. For rolling moment a torque tube or a double-beam type with gages mounted on the side faces of the beams can be utilized. There are many mechanical variations in internal balance design, but the basic arrangement of strain gages attached to flexures is common to all.

With the advent of electric-discharge-milling capability many internal balances are made out of one piece of material. This eliminates problems with hysteresis in mechanically attached joints. If the balance is made of separate parts and fastened together, great care must be used to avoid slippage, which leads to hysteresis, and
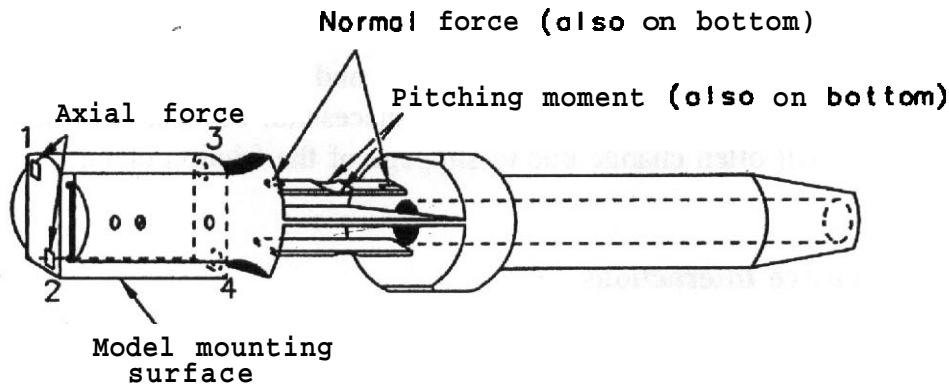
FIGURE 7.49 Three-component strain gage balance (NASA design).

in obtaining the desired alignment. Internal balances have also been made success-
fully of built-up parts welded together with an electron-beam-welding process.[12]

The choice of material is a matter of engineering judgment, and both aluminum
and steel are used. A common steel that has been used is AISI 4340M. The heat
treatment of this steel requires quenching; thus there can be distortion of machined
parts, including breaking of the parts due to thermal shock. For this steel it is
better to machine after heat treatment. If vacuum melt 4340M is used, the physical
properties remain the same but fatigue life is increased. Two other steels that do
not require quenching in the heat treating (they are cooled in the furnace) are 17-
4PH, a stainless steel, and the maraging family of steels. Both of these present no
matching problems and will not warp when heat treated. The purpose of heat treating
the steels is to raise the yield point and increase the fatigue life.

Since the flexures in a balance are designed on the basis of bending strain,
advantages in some designs may be achieved by the use of aluminum alloys. The
cost of the balance material is of little relative importance when compared to the
design and fabrication costs as well as the tunnel downtime due to a balance failure.
Basically, the choice of material and method of fabrication is a matter of good
engineering judgment.

In addition to three- and six-component balances used to measure the overall
aerodynamic characteristics of models, many special balances normally using strain
gages are built. These can include wing and tail root bending moments; loads on
wheels, doors, and nacelles; and the most common control surface hinge moments.
Perry[18] has presented the fundamentals of transducer design and given some de-
sign guidelines.

Control surface hinge moment balances can be built in many ways. One method
is to build gaged brackets that bolt to the main surfaces and the control surface.
Each bracket is bent to set the control at the desired angle. Each bracket must be
calibrated. This method is useful on models that have limited space. Another method
is to use a precision-sealed ball bearing in the outboard hinge. The inboard end of
the control surface has a strain gage beam rigidly attached to a pin. This pin slides
into a close fitting hole in a metal control surface. To set control surface angles, a
hole is drilled through the control surface for a roll pin and the pin is attached to

the hinge moment balance (one hole for each control surface angle). The use of a beam that is rigidly attached to the main surface and uses a friction clamp to hold a hinge pin on the control surface is not too successful, because the angle of the control surface will often change due to slippage of the friction clamp.

Sources of Balance Interactions

No balance is capable of perfectly measuring the loads that it was intended to measure. By this is meant that the lift load component can only make a change in the lift-load-sensing element, with no change in the other five components due to lift load. There are two general sources of errors in balances. The first arises from misalignment of the balance parts and is caused by manufacturing tolerances in both the parts and their assembly. These are linear or first degree. The second arises from the elastic deformation of the various parts. These are second degree and nonlinear, There could be higher order terms due to plastic deformation of balance parts, but in this case the parts have improper dimensions and there is an error in the balance design.

Initially we shall not consider problems in the balance-sensing elements such as temperature effects on strain gages or possible effects from the electronics used to obtain signals from the balance.

The purpose of calibrating a balance is to arrive at a set of equations that can be used to determine the loads applied by the model through the output signals. These are called the balance interaction equations. In the past external balances were adjusted to make the interactions as small as possible. When these small interactions were nonlinear, they were replaced by linear approximations. This was done to minimize the personnel and time required to obtain the model forces.

With the advent of dedicated computers it is possible and highly desirable to be more sophisticated in applying corrections to the raw balance sensor outputs. Balances are designed and built to meet various test requirements. But all balances show certain mechanical similarities. For any balance sensor to be able to produce an output requires a deflection in the balance. This deflection must be an elastic deflection so that the sensors' output is repeatable.

Curry[14] illustrates the source of errors in a balance by considering a load sensor (Fig. 7.50) that is intended to measure axial force. The effect of the normal force N, the pitching moment M, and the axial force A on the load sensor is determined. The sensor will have an output A', and this is to be measured along the load axis.

Now if there is an angular displacement β between the measuring axis and the load axis, components of the applied normal force will appear along the measuring axis. Thus the sensor output A' becomes

$$A' = A \cos \beta + N \sin \beta \tag{7.32}$$

Balance design criteria dictate that the balance be rigid to support the model and that the parts be built to close tolerances to minimize misalignments. Thus β can
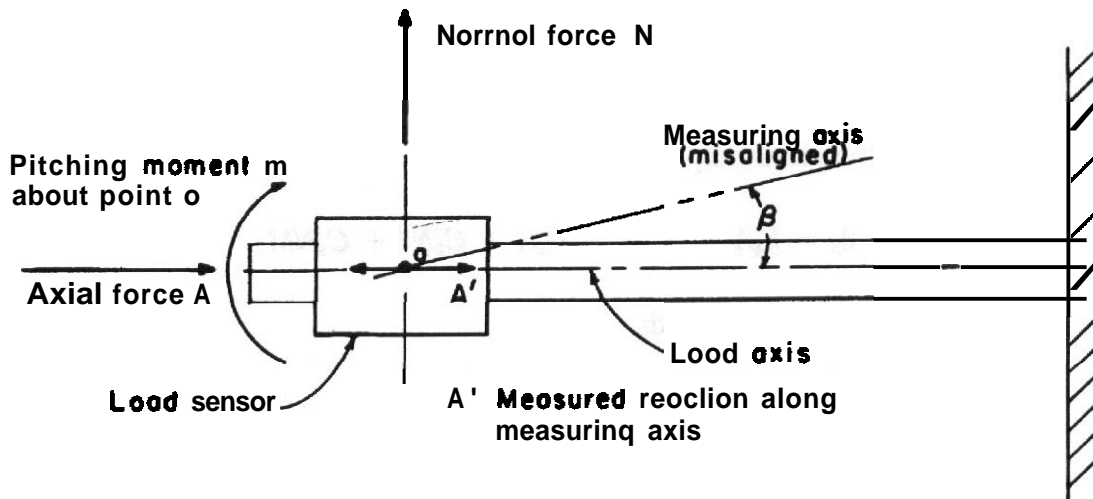
FIGURE 7.50   Schematic of axial balance load sensor.

be considered to be a small angle. If β is in radians, then $\cos \beta = 1$, $\sin \beta = \beta$, and Equation (4.1) becomes

$$A' \approx A + N\beta \tag{7.33}$$

Now assume that due to manufacturing tolerances there is a small initial misalignment of the measuring axis relative to the load axis. This misalignment is constant, and the angle will be β_0.

When the normal force acting through the center of the sensor is applied, the sensor and its support will deflect as a cantilever beam with an end load. This results in a misalignment due to normal force β_1. The application of a pitching moment about the point may cause the beam to deflect in a different mode, causing an angular displacement β_2. The deflection curve of the deflected beam and sensor are, of course, different with these two loads.

Thus β_1 and β_2 are independent of each other and are only functions of the normal force and the pitching moment. Since β_0 is constant and β_1 and β_2 will vary with the loads, they can be written as

$$\beta_0 = C_1 \qquad \beta_1 = C_2 N \qquad \beta_2 = C_3 M$$

The total angular displacement will be the sum of the misalignment and the deflections due to loads:

$$\beta = \beta_0 + \beta_1 + \beta_2 = C_1 + C_2 N + C_3 M \tag{7.34}$$

Substituting Equation (4.3) into Equation (4.2) yields

$$A' = A + C_1 N + C_2 N^2 + C_3 NM \tag{7.35}$$

The sensor output A' is thus a function of the axial load, the initial misalignment

(the first-degree term), and displacements due to the other loads (second-degree terms).

If the axial force sensitivity constant is defined as k_A (output units per unit of axial force), then the axial output $\theta_A = k_A A'$. Thus Equation *(4.4)* becomes

$$\theta_A = k_A A' = k_A(A + C_1 N + C_2 N^2 + C_3 NM) \tag{7.36}$$

Solving for the axial load yields

$$A = \frac{\theta_A}{k_A} - (C_1 N + C_2 N^2 + C_3 NM) \tag{7.37}$$

The terms in parentheses are the balance interactions. The term θ_A/k_A is the sensitivity term and is usually called raw data, the uncorrected output from the axial force sensor. The linear term $C_1 N$ is the initial angular displacement and is generally due to tolerances in manufacture and assembly. The second-order, or quadratic, terms $C_2 N^2$ and $C_3 NM$ are due to elastic deformation. The interactions are not dependent on the component sensitivities but are only functions of balance geometry and material properties. They are functions of the modulus of elasticity, which in turn is a function of temperature. Strain gages also are affected by temperature. This implies that the balance sensitivity as well as the interactions will be dependent on temperature.

The presence of the second-order interactions means that the raw data values depend on both the applied load and the initial load. See Figure 7.51.

In a multicomponent balance each of the measuring components may be considered to have six degrees of freedom in overall deflections. Each degree
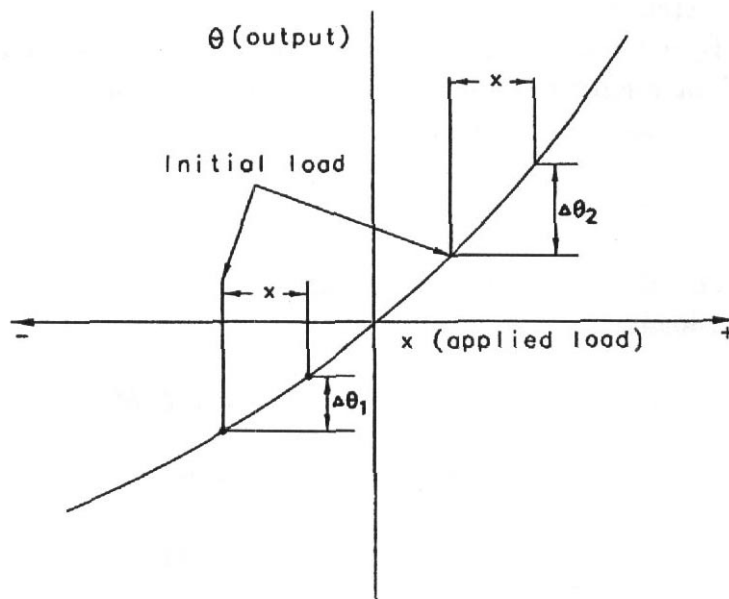
FIGURE 7.51 Nonlinear balance load sensor output.

of freedom may be influenced by more than one applied load component (as A' was influenced by N and M). In addition to overall deflections, deflections within the supporting members and flexures that comprise the internal configuration of the sensing element also contribute to the interactions. These deflections should be considered in a more comprehensive analysis that would include the creation of **a** detailed finite element model of the balance. In analyzing the deflections and their resulting interaction terms, one source of deflection and the resulting interaction terms may be considered at a time since superposition applies. **A** six-component balance has **27** interactions.

When using a six-component balance, all six components must be recorded since the balance interaction equations for each component contains terms from all six components. If the lateral components are not recorded, there will be errors in the longitudinal components and vice versa.

Calibration of Internal Balances

The calibration procedure serves several purposes, including

1. to proof load the balance;
2. to determine balance coefficients;
3. to determine deflections as a function of load;
4. to check repeatability over short time intervals;
5. to check stability over longer time intervals;
6. to determine sensitivity or minimum load for response; and
7. to determine hysteresis.

Processes   Multicomponent internal or sting balances are generally calibrated outside the tunnel. The calibrations require a rather elaborate calibration rig, an example of which is shown in Figure **7.52.** The system provides capability for the balance to be rotated through 360" and pitched in the vertical plane. The pitching motion is used to keep the applied load system aligned to the model attachment portion of the balance, just as the model will be when the system is loaded in the tunnel. This means the model attachment portion is kept horizontal for all loading conditions since this system uses weights and gravity to apply the loads. It also allows the balance and sting deflection to be measured. The provision for rolling the system allows positive and negative loads in lift and side force to be applied with hanging weights. Such a rig usually has positive stops at 0°, 90°, 180°, and **270"** to facilitate these loads. Loads can also be applied at other roll angles, as models on sting balances are often rolled rather than yawed. Calibration bars are used to apply the loads. These bars are indexed so that various values of moments can be applied while holding the normal or side force constant.
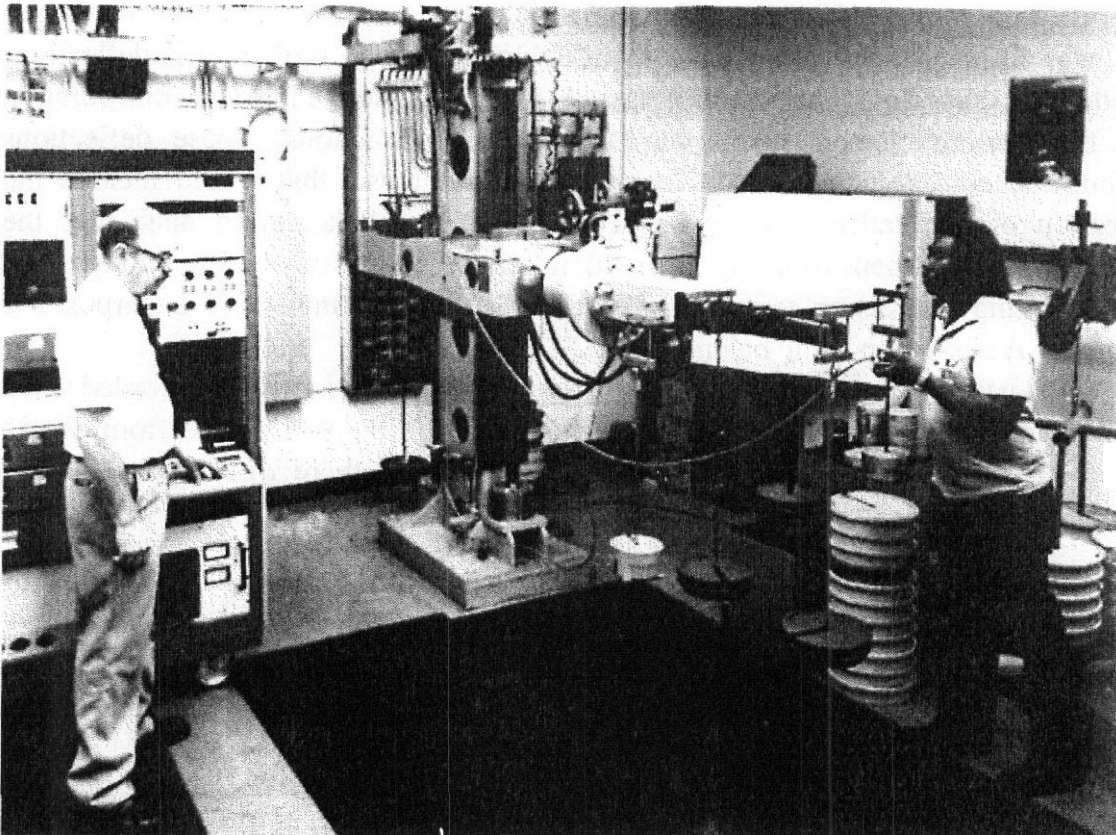
FIGURE 7.52 Calibration mount for internal strain gage or sting balances. This balance is being subjected to combined loads of lift, rolling moment, and pitching moment to determine second-order interactions. (Photograph courtesy of Boeing Aerodynamics Laboratories.)

The orientation of the loads applied to the balance must be positively and precisely correlated to the model orientation when the model is attached to the balance. This alignment is usually accomplished by pins, keys, or splines rather than through any system of adjustments so that the accuracy of reproducibility is close to machine tool limits.

At zero load the calibration bar is leveled. As loads are applied at each load station the bar is again leveled and the deflection of the sting and calibration bar is recorded along with the balance outputs. The deflection measurements are. used to correct indicated angles of attack during the test.

A large number of load combinations is required in order to obtain the balance coefficients and estimate their reliability. The time required to do a complete six-component balance calibration with manually applied loads runs into weeks with several people involved. There are at least two fully robotic balance calibration systems available commercially. These systems can carry out a complete six-component calibration in a few hours with a much smaller number of people required. It appears likely that calibration will become a service provided commercially rather than a process that is supported internally in a large number of tunnel-related laboratories.

Mathematical Problem of Balance Calibration and Utilization   A six-component balance subjected to a load F provides a corresponding output **O** where each of these vectors has six elements. The relation between these can be expressed formally as

$$\mathbf{O} = \mathbf{f(F)} \tag{7.38}$$

and the inverse relation as

$$\mathbf{F} = \mathbf{g(O)} \tag{7.39}$$

The common practice is to remove offsets and assume a second-order functional approximation for these relations. The resulting form is

$$O_i = \sum_{j=1}^{6} a_{ij}F_j + \sum_{j=k}^{6}\sum_{k=1}^{6} a_{ijk}F_jF_k + \varepsilon_i \tag{7.40}$$

$$F_i = \sum_{j=1}^{6} \Gamma_{ij}O_j + \sum_{j=k}^{6}\sum_{k=1}^{6} \Gamma_{ijk}O_jO_k + \gamma_i \tag{7.41}$$

The last terms in these equations are the residuals. Minimizing these terms can provide the basis for choosing the coefficients of the above second-order approximations. To develop these in more detail, we can represent Equations (7.40) and (7.41) in matrix form by

$$\mathbf{O} = [A]\mathbf{\Phi} + \varepsilon \tag{7.42}$$

$$\mathbf{F} = [\Gamma]\mathbf{\Omega} + \gamma \tag{7.43}$$

where $\mathbf{\Phi}$ and $\mathbf{\Omega}$ are 27-element vectors consisting of the six components, the squares of the six components, and the 15 cross products of the six components taken two at a time of **F** and **O**. The terms [**A**] and [**Γ**] are 6-row-by-27-column matrices containing all the coefficients indicated by Equations (7.40) and (7.41). If we remove ε and γ from Equations (7.42) and (7.43), respectively, and then transpose, we obtain the equations

$$\mathbf{O}^{\mathrm{T}} = \mathbf{\Phi}^{\mathrm{T}}[A]^{\mathrm{T}} \tag{7.44}$$

$$\mathbf{F}^{T} = \mathbf{\Omega}^{T}[\Gamma]^{T} \tag{7.45}$$

If 27 loading conditions are chosen and executed, this will result in 27 sets of (**O**, **F**, $\mathbf{\Phi}$, $\mathbf{\Omega}$) that can be used to assemble the equations

$$[\mathbf{O}^{\mathrm{T}}]_l = [\mathbf{\Phi}^{\mathrm{T}}]_l[A] \tag{7.46}$$

$$[\mathbf{F}^{T}]_l = [\mathbf{\Omega}^{T}][\Gamma]^{T} \tag{7.47}$$

where $[O^T]_l$ and $[F^T]_l$ are 6-column-by-27-row matrices. Here, $[\Phi^T]_l$ and $[\Omega^T]_l$ are 27 × 27 matrices entirely determined by the loading combinations chosen. In principle, we can solve for the coefficient matrices by inverting the loading matrix and the output matrix and premultiplying, to obtain

$$[A]^T = [\Phi^T]_l^{-1} [O^T]_l \tag{7.48}$$

$$[\Gamma]^T = [\Omega^T]_l^{-1} [F^T]_l \tag{7.49}$$

For systems of this size and complexity, this direct attack may, but quite likely will not, give good results since numerical conditioning problems **are** common. In any case, it is possible to obtain more useful information by techniques such as response surface methods from experimental statistics. Draper and Smith[15] and many others may be consulted. Among many effects that must be carefully evaluated is hysteresis. This requires repeated loading sequences in which the loads are increasing and decreasing. The required number of loading combinations in practice will be many times the 27, which is the minimum number to populate the basic matrices above.

Temperature Sensitivity and Other Items   Apparent strain caused by changes in the balance temperature at zero load (zero lift) can be caused by temperature gradients across the balance structure and by the average temperature level of the sensing elements. The zero shift due to temperature can be reduced by use of factory-compensated gages; use of bridges with four active arms and thermal-sensing-compensating wire in the bridge circuit; and finally insulating, heating, or cooling the balance to minimize both temperature excursions and gradients, if possible.

The following should be kept in mind. To the extent that the data readout system may be considered as having infinite impedance, with no shunting paths in balancing circuits, the interactions may be considered independent of the data systems. If, however, the balance is calibrated on a data system that does not have infinite impedance, then the data system used during test work must have the same impedance **as** the calibration data system. Also, the effects of shunting paths across arms of the bridges or across "half bridges" will modify the individual arm or half-bridge sensitivity to the quantities they sense. Thus the interaction quantities that these elements sense may fail to cancel to the same extent that they would with either no shunting paths or different shunting paths, which will produce differences in the interactions as indicated by the output data.

REFERENCES AND NOTES

1. AIAA, "Recommended Practice for Atmospheric and Space Flight Vehicle Coordinate Systems," ANSI/AIAA R-004, **1992.**
2. Etkin, B., and Reid, L., *Dynamics of Flight, Stability and Control, 3rd* ed., Wiley, New York, **1996.**

3. SAE, "Vehicle Aerodynamics Terminology, Recommended Practice," SAE J1594, June 1987.

4. Milliken, W. F., and Milliken, D. L., "Race Car Vehicle Dynamics," SAE, Warrendale, PA, 1995.

5. Lewis, E. V., Ed., *Principles of Naval Architecture,* 2nd rev., Vols. 1–3, Society of Naval Architects and Marine Engineers, Jersey City, NJ, 1988.

6. Moritz, H., "Geodetic Reference System," *Bull. Géodésigne,* 62, 348–356, 1988.

7. Bray, A., Barbato, G., and Levi, R., *Theory and Practice of Force Measurement,* Academic, London, 1990.

8. This is the most frequently used arrangement for aircraft and external balances. Others are discussed subsequently.

9. There are many others.

10. Gratzer, L. B., "Optimum Design of Flexure Pivots," Report 390, University of Washington Aeronautical Laboratory, Seattle, WA, 1953.

11. Mouch, T. N., and Nelson, R. C., "The Influence of Aerodynamic Interference on High Angle of Attack Wind Tunnel Testing," AIAA Paper 78-827, presented at the AIAA Twelfth Aerodynamic Testing Conference, 1982.

12. Ewald, B., "The Development of Electron Beam Welded One Piece Strain Gage Balances," AIAA Paper 78-803," in *Proceedings of the Tenth AIAA Aerodynamic Testing Conference, AIAA,* Washington, DC, 1978, pp. 253–257.

13. Perry, C. C., Ed., *Modem Strain Gage Transducers, Their Design and Construction,* Series in Epsilonics, MicroMeasurements, Inc., Raleigh, NC, Ll–IV.2, 1981–1984.

14. Curry, T. M., "Multi-Component Force Data Reduction Equation," in *Proceedings of Technical Committee on Strain Gages, Third SESA International Congress on Experimental Stress Analysis,* Chapter 7, University Park, PA, May 1971.

15. Draper, N. R., and Smith, H., *Applied Regression Analysis,* Wiley, New York, 1966.

8 Use of Wind Tunnel Data: Scale Effects

One of the top airplane designers of the World War II era in Great Britain has been credited with the statement that he "could go on designing airplanes all day long if he had not also to build them and make them fly," and his point is surely well taken. Data may *easily* "be taken all day long$^\vee$—as long as they are not used to design airplanes or other vehicles or full-scale devices that cannot be tested directly at operating Reynolds numbers.

All discrepancies that arise because of the use of models for experimental data gathering rather than actual articles might properly be considered "scale effects." However, the common use of the term *scale effects* refers to differences that arise when the fluid dynamic dimensionless parameters, primarily Reynolds number for "low-speed" flows, are not the same in the experiments and in actual operations. Most test articles have some geometric differences as compared to the actual operating articles. Differences arising from these typical geometric differences are simply referred to as geometric effects. In the case of automobile aerodynamic experiments, some of the largest issues arise from the fact that test articles are commonly extremely different in geometric detail from actual vehicles.

The very subject of extrapolating wind tunnel data to full scale will probably elicit a grim smile from many aeronautical engineers who have had the responsibility. The aerodynamicist disparages the wind tunnel engineer; the wind tunnel engineer thinks the aerodynamicist wants too much; and if any poor soul is assigned the combination of jobs, well, one is reminded of the classic humorous tale of crossing a hound dog and a rabbit wherein the offspring ran itself to death. Yet, it is essential that each of the persons engaged in various aspects of aerodynamic development grasp the fundamental contribution of each approach to seeking the necessary facts.

A reasonable indication of reality lies in the fact that wind tunnels are very rarely called upon to test exactly scaled operational models. Though this offers a magnificent "out" to the wind tunnel engineer, it is not meant that way. Reynolds number effects on small items are too great even if they could be accurately constructed; hence the small excrescences are mostly left off the models. In many cases the aerodynamicist who plans on adding these items selects the lowest possible drag estimates, with the net result that he or she underestimates their interference and overestimates the performance of the vehicle. The cure for this situation is to consolidate these items and minimize their effect. Room for improvement can surely exist when examples can be cited of airplanes that have no less than 22 separate air intakes and dozens of removable inspection panels.

There is very limited correlation between flight test and wind tunnel data outside company files. This lack is attributed to the dual reasons that after flight test there is rarely time to back up and correlate with the wind tunnel and that, even where it is done, the success or failure of the methods used is generally considered company proprietary for the very good reason that the information is expensive to obtain. There **are** only a handful of papers in available literature with detailed information and actual data from correlations of wind tunnel and flight results.

Any flight test and wind tunnel correlation suffers from a great number of unknowns. The tunnel data suffer from inexact or unknown Reynolds number extrapolation, possible uncertainties in corrections to the data such as tare and interference and wall effects, errors in duplicating the power on effects with fixed-pitch propellers, simulation of flow around or through jet engine nacelles, omission of manufacturing irregularities and small excrescences, and insufficient deflections of the model under load. Some models **are** built to simulate a 1g load. The flight test **data** suffer from pilot techniques, accelerations due to gusts, errors in average center-of-gravity locations, determination of true air speed, and unknowns of propeller efficiencies, jet engine operational characteristics, and other power plant effects. Considering the impressive room for disagreements, the generally good agreement found in the few available reports is remarkable.

The situation in other fields, including automobile aerodynamics, yacht hydrodynamics and aerodynamics, and submarine hydrodynamics, is essentially parallel to that in aeronautics.

There is a positive aspect that should not be missed: Much design work is considered successful if improvements **are** achieved, regardless of whether the methods available, be they computational, analytical, or experimental, provide absolute accuracy in predicting all performance quantities of interest. Accurate quantitative predictions of the actual device performance is, of course, always the most desirable achievement.

We will take up, in turn, each of the important aerodynamic quantities usually measured in the tunnel and say what we can about their use. The boundary layer is the key. The understanding of scale effects is essentially the understanding of boundary layer properties and behavior as they **are** affected by differences in the model and full-scale articles. Wakes **are** also important, although wakes can be considered to be the children or descendants of boundary layers in the context of vehicle aerodynamics and hydrodynamics.

8.1   BOUNDARY LAYER

Due to viscosity, the air or water in contact with the body surface has the same velocity as the body surface. There is a region of generally high velocity gradient that is typically small in extent relative to body dimensions over which the air velocity transitions from the velocity of the body to essentially "free stream," or more accurately to a velocity that would exist in a potential flow around a body similar to the actual body over parts where there is no separation. The region in

which this velocity change takes place is called the **boundary** *layer*, and the velocity gradients in the boundary layer very largely determine whether the drag of a body is x or 10x. The various properties of boundary layers are very important in determining scale effects. Critical aspects are locations at which the boundary layer transitions from laminar to turbulent and where separation occurs. There are many papers and books on boundary layer theory to which reference may be made for details. **Examples** are Schlichting[1] and Young.[2]

It was discovered during early research in aerodynamics that a turbulent boundary layer has much greater associated skin friction drag than does a laminar boundary layer. Consider as illustrative the drag on a flat plate aligned with the free stream. Take the reference area as the planform area, base the Reynolds number on the chord or streamwise dimension, and account for the fact that both sides experience skin friction so that the wetted area is twice the reference area. The contributions to total drag coefficient from skin friction drag for laminar and turbulent boundary layers are given by

$$C_{D,\text{laminar}} = \frac{2.656}{\sqrt{R_{ec}}} \tag{8.1}$$

$$C_{D,\text{turbulent}} = \frac{0.148}{R_{ec}^{0.2}} \tag{8.2}$$

These are plotted in Figure 8.1 along with a drag curve of a *23012* airfoil.

The boundary layer thickness, defined as the distance from the surface to the point where the velocity in the boundary layer is *0.99* times the velocity just outside
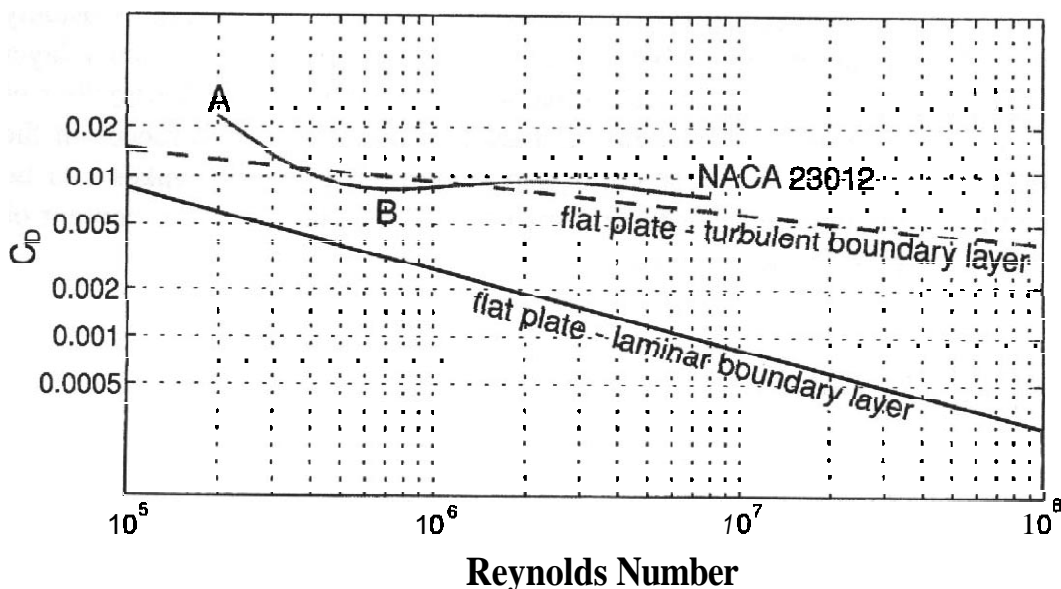
FIGURE 8.1 $C_{D0,\text{min}}$ versus R_{ec}. (From Jacobs, E. **N.**, "The Variation of **Airfoil** Section Characteristics with Reynolds Number," NACA TR 586, 1937.)

the boundary layer, is another property of interest and is given approximately by

$$\delta_{\text{laminar}} = 5.2\sqrt{l^2/R_{el}} \tag{8.3}$$

$$\delta_{\text{turbulent}} = 0.37l/(R_{el})^{1/5} \tag{8.4}$$

where l is the distance from the body leading edge and R_{el} is the Reynolds number based on l and free-stream velocity.

Several important features of boundary layer behavior should be kept in mind. First, both boundary layer drag and thickness are functions of Reynolds number. Second, laminar boundary layers have far less drag but also far less energy with which to surmount roughness or comers, so laminar layers "separate" from a surface much more easily than do turbulent layers. Third, the maintenance of a laminar boundary layer becomes more difficult as the Reynolds number (its length) increases. Fourth, a laminar boundary layer is encouraged by a pressure falling in the direction of flow. This is referred to as a "favorable gradient" whereas the situation when the pressure is rising in the direction of the flow is referred to as having an "adverse gradient." Fifth, the location of the "transition" from laminar to turbulent flow is a topic of ongoing research. And this location is usually estimated from a variety of sources of information ranging from available methods of transition prediction to experience-based rules of thumb. This is true for all currently available computational methods as well as wind tunnel experiments.

Modem airfoil design procedures can produce favorable pressure gradients over a large portion of the chord. The extent of laminar flow can be increased by very smooth surfaces and by either removing the boundary layer by suction or energizing it by surface blowing. In the light of these actions we may examine how a flow can be changed widely under conditions of changing Reynolds number.

Assume that the wing shown in Figure *8.2* is in a stream of such turbulence that flow along a surface with constant pressure (perhaps a flat pate parallel to the free stream) will result in a boundary layer that changes from laminar to turbulent at a Reynolds number of 1×10^6, and further assume a model size and velocity such that the Reynolds number based on airfoil chord length shown in Figure **8.2a** is 1×10^6. We note two items: First, the laminar boundary layer is unable to negotiate the curve of the airfoil and considerable separation is indicated; and, second, transition takes place ***before*** the Reynolds number reaches 1×10^6 since the flow downstream of the maximum thickness is passing into an adverse pressure gradient that discourages the continuation of the laminar boundary layer. Here, then, is a case where we may consider there to be too much laminar flow because it leads to a relatively high resultant drag. The behavior described corresponds to point **A** in Figure 8.1 and the way the boundary layer behaves on a *23012* airfoil at a Reynolds number of 300,000. The additional drag due to separation is a result of higher pressure drag **as** compared to skin friction drag.

Returning to Figure **8.2b**, which corresponds to a higher Reynolds number, we see that the transition point has moved forward according to the third cited feature of boundary layer behavior and now we have the maximum laminar flow and
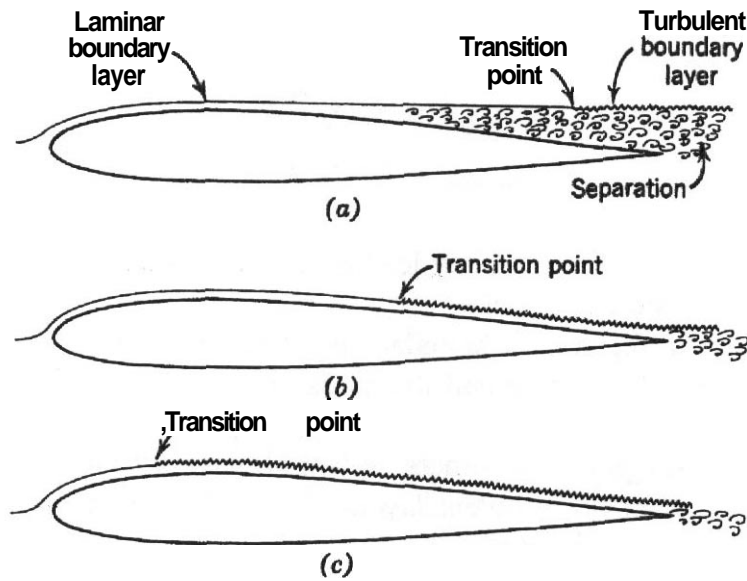
FIGURE 8.2 Effect of increasing Reynolds number on boundary layer flow.

minimum drag. This corresponds to point B in Figure 8.1 and a 23012 airfoil at a Reynolds number of 650,000.

The still higher Reynolds number illustrated in Figure 8.2c fails to show a decrease of drag, even though both laminar and turbulent drag decrease with increasing Reynolds number, since there has been a great increase in the region of turbulent flow. This corresponds to point C in Figure 8.1 ($R_{ec} = 1.2 \times 10^6$).

A further increase in Reynolds number yields a reduction in drag coefficient, although the transition has now reached the minimum pressure point and its further forward motion is resisted by the falling pressure (favorable gradient) from the leading edge to that point.

Since the details of the pressure pattern of every airfoil is unique, and since the same may be said of every airplane or other vehicle design, it is apparent that tests made in the Reynolds number range where laminar separation occurs on the test model will be exceedingly difficult to extrapolate accurately to Reynolds numbers much larger than the test Reynolds number.

The effects can be profound on essentially all qualities of interest—forces, moments affecting stability, hinge moments, and so on. Obviously, it is highly desirable either to provide wind tunnel Reynolds numbers equal to operating values, which is seldom feasible, or to somehow make the model boundary layer behave more like that of the full-scale vehicle at operating Reynolds numbers. The two features that are most critical are the locations of boundary layer transition from laminar to turbulent and the locations of separation.

The location of transition is dependent on a number of factors. Among them are the Reynolds number, the surface details, the pressure gradient, and the turbulence level in the external stream. Generally speaking, the higher the Reynolds number, the sooner the transition on a given shape. The problem commonly faced, therefore, is how to cause transition to occur earlier on a model than it would if no attention

were given to this issue. The most common tool used for this purpose is a boundary layer trip device.

The locations of separation are more difficult to manipulate with success since the most common situation is that separation occurs sooner at lower Reynolds numbers typical of tunnel tests than at typical operating Reynolds numbers. It is easy to cause separation earlier-than its natural tendency but difficult to delay it. There are, therefore., no standard practices for dealing with "scaling" of separation points. Some situations, such as in wind tunnel tests of buildings, in which model and full-scale geometries have sufficiently sharp comers, produce separation at essentially fixed locations independent of Reynolds number. These are easy cases with which to deal since there is little or no effect of scale on separation locations. When separation occurs on curved surfaces, as on the upper surfaces of wings near stall, then the separation location is almost always strongly affected by Reynolds number and therefore exhibits a strong scale effect.

8.2 TRIP STRIP

A trip strip is an artificial roughness added to the model to fix the location of transition from a laminar to turbulent boundary layer on the model. The trip strip can also, in some situations, prevent a separation of the laminar boundary layer near a leading edge of a curved surface. If, however, the trip strip either protrudes too high above the surface or has too great an amount of roughness, it can produce effects other than just fixing the transition location. If the elements of the trip device are too large, then there may be additive drag directly on the elements themselves and/or the newly turbulent boundary layer may be robbed of sufficient energy that early separation will occur downstream of or even at the trip device. These are undesirable effects.

We give accounts of a number of ways trip ships have been created.

1. Grit. The traditional trip strip based on NACA/NASA[3] reports is a finite-width strip of grit. When properly applied, the grit gives a three-dimensional hip that simulates the way natural transition occurs, which is always over some stream-wise extent rather than very suddenly. The two commercially available materials that are commonly used are carborundum and ballotine microbeads or balls. They both are available in graded sizes with nominal diameters (see Table 8.1). The width of the trip strip is usually 0.125–0.250 in. Masking tape is used to lay out the trip strips and then one paints or sprays on shellac, lacquer, artist's clear acrylic, or superhold hair spray. The hair spray has the advantage of being soluble in water and thus can be removed without harm to the model finish. After spraying or painting, the grit is dusted or blown on the wet adhesive. The grit is difficult to apply to vertical and lower surfaces, but this can be done by bending a card into a V and with skill blowing the grit onto the surface. It is difficult to obtain a repeatable, uniform, relatively sparse distribution of the grit. If the grit is dense packed, the trip willapproach a two-dimensional trip, which is undesirable. Also, during the

TABLE **8.1.** Commercial Carborundum Grit Numbers and Corresponding
Particle 'Diameters"

Grit Number	Nominal Grit Size (in.)	Grit Number	Nominal Grit Size (in.)
10	0.0937	60	0.0117
12	0.0787	70	0.0098
14	0.0661	80	0.0083
16	0.0555	90	0.0070
20	0.0469	100	0.0059
24	0.0331	120	0.0049
30	0.0280	150	0.0041
36	0.0232	180	0.0035
46	0.0165	220	0.0029
54	0.0138		

course of a test the grit breaks away from the adhesive. Both of these problems can lead to lack of repeatability of data from run to run during a test and from test to test. The resulting data variability is most severe in drag. Sample boards and photographs of grit density can be helpful in improving repeatability. This method has been the most widely used historically but has increasingly been replaced by methods that provide more precision in repeatability as instrumentation systems have improved.

2. Two-Dimensional Tape. These consist of 0.125-in. printed circuit drafting tape or chart tape. The trip strip is built up with multiple layers of the tape. The surface must be clean and oil free to obtain good adherence of the first layer of tape. If layers of multiple-color tape are used, it is easy to detect a layer that has blown off the model. The tape requires the height of the trip strip to vary in discrete steps due to the tape thickness. The two-dimensional tape acts on the boundary layer in a different manner than the three-dimensional grit, and thus its simulation is not as good as a more distributed roughness such as grit.

3. Wire, Thread, or String. This is similar to the two-dimensional tape but the thread or string is glued down in the same manner as the grit, by spraying the surface with an adhesive and stretching and pressing the thread onto the surface. This method is not often used, although the use of wire in this manner was one of the earliest methods.

4. Three-Dirnentional Pinked Tape. Tape is cut in two using dressmaker's pinking shears. This leaves two pieces of tape with triangular edges. The tape is applied to the model with the $90°$ points pointing forward. Layers of tape can be built up to give various heights and the points staggered in the span direction to give a more representative transition than straight two-dimensional tape.

5. Triangles. Tape and pinking shears are used to make small triangles that are applied to the model. Multiple layers can be used to increase the thickness. This method is slow to apply.

6. *Epoxy Dots.* A vinyl tape with backing is run through a modified computer-paper-tape[4] machine. This produces holes of 0.050 in. diameter, 0.100 in. center to center. The tape less backing is then applied to the model surface. An epoxy compound is forced into the holes. When the epoxy sets, a series of dots above the surface with heights equal to the tape thickness form the trip strip. The tape can be obtained in different thicknesses-or multiple layers can be used. See Figures 5.14, 5.15, and **8.3** for a model with natural transition and with fixed transition using the dot-type trip strip.

The epoxy dot method has become the method of choice in many laboratories. It provides good control and repeatability while appearing to induce transition at a controlled location that is very similar to natural transition.

7. *Other.* The exposed portion of streamlined mounting struts may be "staked" by the use of center punches to yield a permanent transition strip. Round struts have been knurled to yield the same results.
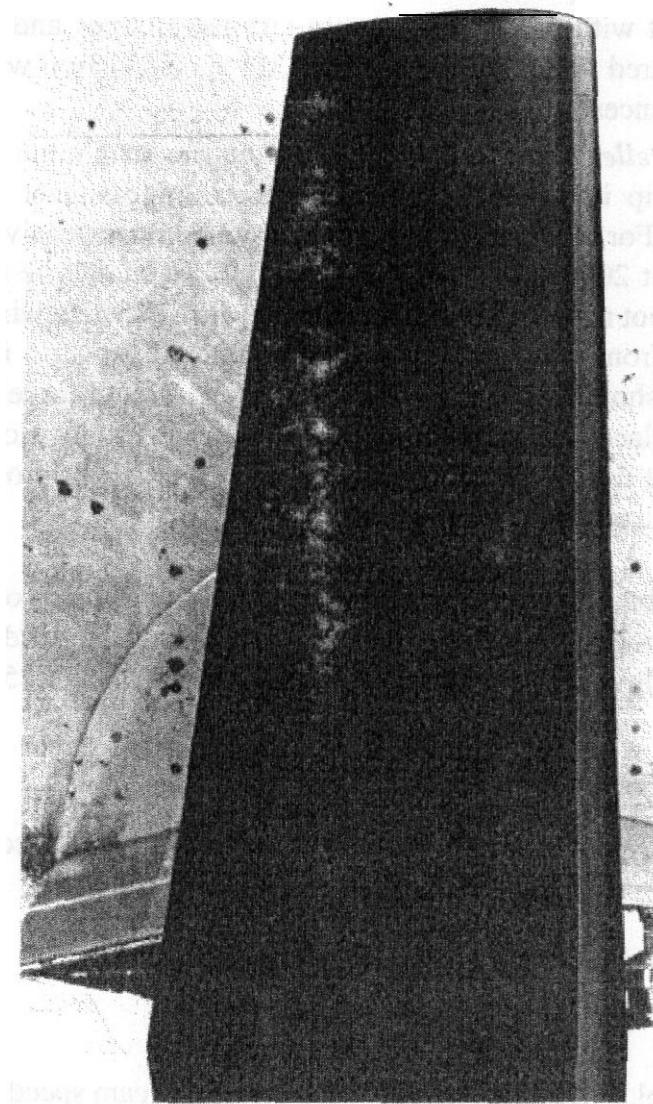
FIGURE 8.3   Fixed transition at 8% chord using 0.007-in.-high epoxy disks: $C_L = 0.28$, $R_{ec} = 1.26 \times 10^6$ (based on average chord). (Photograph courtesy of University of Washington Aeronautical Laboratory.)

Location

The trip strip is intended to simulate the boundary layer transition on the full-scale device. Obviously it is desirable to use the best available methods to predict the location of transition for any particular test article. The following gives general guidance:

1. *Lifting Surfaces.* Lifting surfaces include wings, horizontal and vertical tails, and auxiliary fins such as winglets. The trip strip is applied to both sides of the surface. For NACA four- and five-digit airfoils and conventional wing construction, the full-scale transition will occur at approximately 10% of the chord at cruise lift coefficients. For the newer laminar flow airfoils and smooth composite skin, full-scale transition can be as far aft as 60% of the chord, although this will move forward on the upper surface as the angle of attack is increased beyond cruise values. If the transition is fixed near the leading edge for composite skin laminar airfoils, there will be larger changes in the lift, drag, and pitching moment. For general-aviation-type aircraft with production quality airfoils, Holmes and Obara[5] present a summary of measured transition in flight and some comparison with tunnel tests, plus extensive references.

2. *Fuselage, Nacelles.* For fuselages that have the maximum thickness well forward, the trip strip is often located where the local diameter is one-half the maximum diameter. For a low-drag body, one designed for extensive laminar flow, the trip strip is put at 20–30% of the body length. Care should be taken to ensure that laminar flow is not reestablished aft of the trip strip. Where a windshield, inlets, or blisters protrude from the main contour, an additional trip strip is often used to prevent the reestablishment of laminar flow. For flow through nacelles, a trip strip inside the nacelle is placed about 5% aft of the hi-light, and usually flow visualization is used to ensure that the boundary layer is tripped. The trip strip on the outside is also about 5–10% aft of the hi-light.

In applications where there is a possibility of reestablishment of laminar flow, flow visualization such as sublimation or oil flow should be used to ensure that there is no laminar flow aft of the trip strip. See Figures 5.14, 5.15, and 8.3.

Height of the Trip Strip

Braslow and Knox[6] give means of estimating the heights to be used for trip strips. The height of the trip strip can be chosen from the following:

$$h = \frac{12K}{R_{\text{eft}}} \tag{8.5}$$

Here R_{eft} is the Reynolds number per foot based on free-stream speed; K is a constant (actually a Reynolds number) based on grit roughness. The value of K is 600 for Reynolds numbers greater than 100,000 based on free-stream speed and distance from the leading edge to the trip strip. This is the minimum Reynolds number for
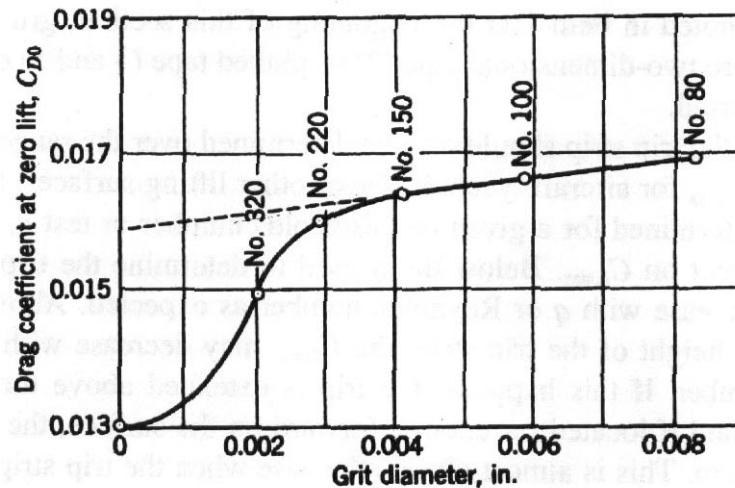
FIGURE 8.4   Results of a transition study using a series of grit sizes. (Redrawn from data courtesy of Verdian-Calspan Operations.)

transition based on roughness. According to **Braslow** and **Knox,**[6] if the Reynolds number based on distance to the trip strip is less than 100,000, the value of K increases to about 1000 at very small Reynolds number. The height h is in inches.

The use of Equation **(8.5)** yields trip strip heights that can be used for stability and control tests but does not yield enough information for performance tests, that is, drag due to the trip strip. When drag data are required, a trip strip height buildup should be run.

Results of a study made to determine the required grit size are presented in Figure **8.4.** With increases in grit size to about 0.003 in., the drag coefficient increases quite rapidly. This is interpreted as an indication that a completely turbulent boundary layer has not been established downstream of the transition trip. Above a grit size of 0.004 in., the rise of drag with grit size is considerably smaller and is constant. This indicates that transition is complete and the increasing drag is a pressure drag on the transition strip. In this case, the grit size that should be used for testing is indicated to be between 0.003 and 0.004 in. To correct the measured wind tunnel drag for the effect of the trip strip, the data for fully established transition are extrapolated back to zero trip strip height, as indicated by the dashed line in Figure **8.4.** The drag correction is then the delta between the model drag with trip strip and the zero-height-extrapolated drag value. This delta then corrects for the pressure drag caused by the trip strip, while the trip strip itself ensures that the laminar-to-turbulent transition is at the proper location. If the tunnel test is run at various q's and the drag correction is required at all of them, then the trip strip height should be determined for each q. The largest height of the hip strip will be determined by the lowest dynamic pressure. The lowest height is determined by the highest q. If this is used, then there is a risk that the boundary layer will not be tripped at the low q. This implies that in the most complete test plans the trip strip height will be changed with each q; thus it becomes of paramount importance that the trip strip application is repeatable and easy to apply. This influences the type of trip strip

that is used. As noted in item 1 at the beginning of this section, grit may be hard to repeat, therefore two-dimensional tape (2) or pinked tape (4 and 5) or epoxy dots (6) may be preferred.

The height of the trip strip should also be determined over the range of C_L's from cruise through $C_{L,\max}$ for aircraft, yacht keels, or other lifting surfaces. Since the trip strip height is determined for a given test Reynolds number or test q, there will be the following effect on $C_{L,\max}$. Below the **q** used to determine the trip strip height, the $C_{L,\max}$ will increase with q or Reynolds number as expected. Above the q used to determine the height of the trip strip, the $C_{L,\max}$ may decrease with increasing q or Reynolds number. If this happens, the trip is extended above the edge of the boundary layer, and if located far enough forward on the surface, the hip strip has become a stall strip. This is almost always the case when the trip strip is at 5–10% of the chord, as required by the NACA four- and five-digit series airfoils. The trip strip acting as stall strip is usually not a problem with laminar flow airfoils with the trip at 30% chord or greater. It may be the best policy to make the runs for the variation of $C_{L,\max}$ with Reynolds number without trip strips. If leading-edge laminar separation is suspected, it can be checked by flow visualization.

Transition or trip strips are not needed on all models. If the model shape is such that it precludes the formation of laminar flow, then trip strips are not required. This is often the case with many architectural models of buildings, bridges, open lattice towers, trees, shingled roofs, and the like. If there is a question about laminar flow and transition, the effect of trip strips can be measured, but care must be taken to ensure that the trip smp does not cause premature separation. Again, flow visualization will be useful as a positive check.

The effect of various fractions of laminar and turbulent flow on drag coefficient can be estimated by use of Equations (8.1) and (8.2) with appropriate weighting factors. Figure 8.5 shows the drag coefficients corresponding to various amounts of laminar and turbulent boundary layers at various Reynolds numbers estimated in this way. Zero form drag is assumed. In this chart are shown the theoretical minimum wing drag of 100% laminar flow and the decrease in drag coefficient due to extension of the laminar layer. For example, extension of the laminar layer from 20 to 60% at $R_{ec} = 2 \times 10^6$ reduces the drag coefficient from 0.0073 to 0.0048. In fact, it is just this extension of laminar flow that reduces the profile drag of the laminar flow airfoils.

Some general observations concerning scale effect on minimum drag for these sections are in order because of their greater extent of laminar flow. Over the lower range of Reynolds numbers (up to $R_{ec} = 9 \times 10^6$) a gradual decrease in minimum drag occurs. This reaction is attributed to the thinning of the boundary layer. At the higher Reynolds numbers the drag increases steadily, at least up to $R_{ec} = 25 \times 10^6$, because of the forward movement of transition. Of course, again airfoil geometry (camber, thickness, thickness form) influences the general behavior, but the scale effect is due primarily to the relative strengths of the two competing/interacting boundary layers. Comparison tests of two difference airfoils of different families can be most deceiving if the evaluation is done at low Reynolds numbers. For example, the 65_3-418 airfoil displays much larger profile drag than the 0012 section
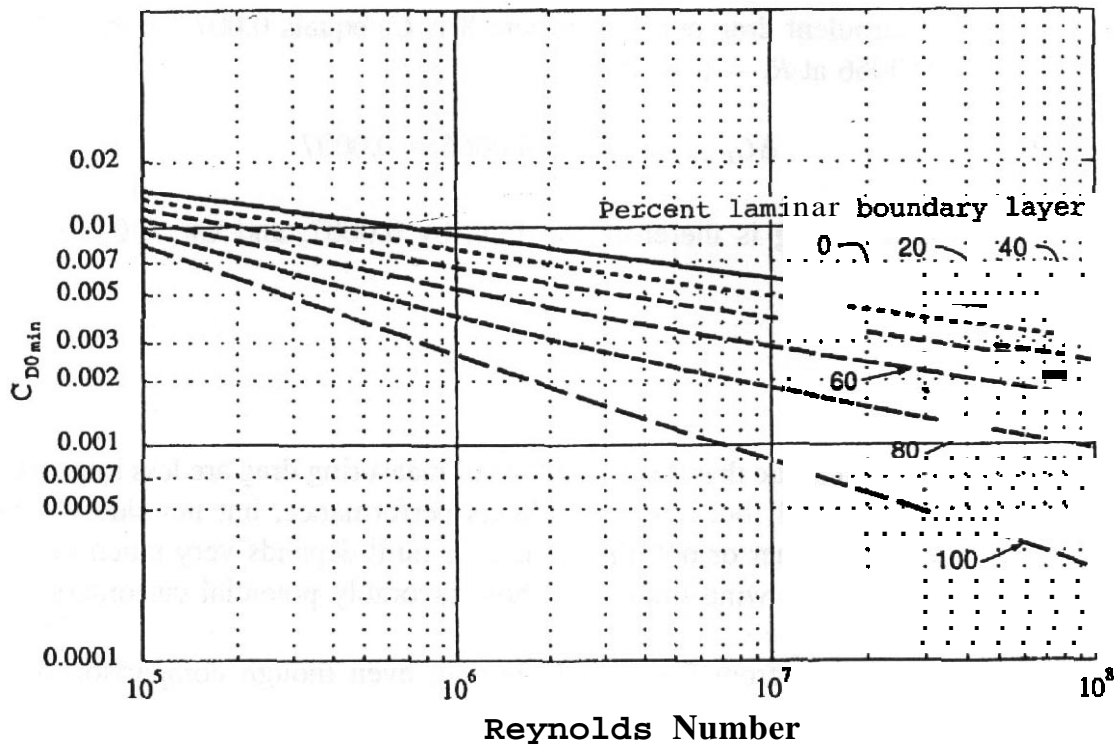
FIGURE 8.5 $C_{D0,min}$ versus R_{ec} for various percentages of laminar flow. Zero form drag assumed.

at low Reynolds numbers, whereas a full-scale conditions just the opposite is true. The six-series section has extensive laminar separation in the low Reynolds number range; the 0012 has far less separation at the lower Reynolds numbers and hence has lower drag.

In extrapolating drag coefficients, it is necessary to make due allowance that the Reynolds number of the tunnel data is the "effective" Reynolds number. This procedure is necessary because the part of the drag associated with skin friction decreases with increasing Reynolds number. Thus for a given effective Reynolds number the friction coefficients are larger than at a numerically equal Reynolds number in a very low turbulence stream. The difference between measured drag and the actual drag at the equivalent free-air Reynolds number may be read from the turbulent drag curve of Figure 8.1. An example is given.

Example 8.1   The drag of a wing is measured at a test Reynolds number of 3×10^6 and a turbulence factor of 2.0. The measured drag coefficient is 0.0082. Find the equivalent free-air drag coefficient.

1. As $R_{eff} = TF \times R_e$,

$$R_{eff} = 2.0 \ (3 \times 10^6) = (6 \times 10^6)$$

2. From the turbulent drag curve of Figure 8.1, C_D equals 0.0073 at $R_e = 3 \times 10^6$ and 0.0066 at $R_e = 6 \times 10^6$:

$$\Delta C_D = 0.0073 - 0.0066 = 0.0007$$

3. The measured drag is therefore too high by 0.0007, and $C_D = 0.0082 - 0.0007 = 0.0075$.

8.3 DRAG

Although some might argue that the difficulties of measuring drag are less important than stability and control (because drag affects performance, but not safety), the simple truth is that whether or not a plane is ever built depends very much on the drag data obtained in the wind tunnel and how favorably potential customers can be led to receive it.

The first conclusion (from Figure 8.1) is that, even though comparison tests between objects may be made with fair accuracy, a test Reynolds number of 1.5 $\times$ 10^6–2.5 $\times$ 10^6 would be needed if extrapolation is intended. An ameliorating condition is that, if a low Reynolds number separation exists and is cured by some change, the probability that it will arise at a higher Reynolds number is extremely small.

If an effort is made to maintain a true profile on the full-scale airplane, tunnel wing drag extrapolated to the net Reynolds number (by the aid of Figure 8.5) should be only slightly optimistic owing to the drag of the flap and aileron cutouts, control surface inspection doors, and pitot tubes, antennas, other excrescences, and the like that are not represented on the model.

The effects on the minimum drag of a complete airplane are more difficult to handle. There are truly an immense number of small items on a full-scale aircraft that cannot he represented at model scale. Whether they undercompensate or overcompensate for the drag reduction expected from higher Reynolds number is anyone's guess. Frequently the engineer assumes that the two exactly compensate, but he or she would hate to guarantee better than ± 0.0010 in C_D, except in cases where the company has extensive flight experience with a series of evolutionary airplanes so that the tunnel results can be viewed essentially as incremental data for design changes. This is also true for other methods, including computational aerodynamics.

Similarly, the rate of change of drag with lift, usually considered as the change in span efficiency factor e, should not change for straight wings.' For instance (Figure 8.6), it has been observed that, when C_L^2 for a given airplane is plotted against the total drag coefficient C_{DT}, the graph is nearly a straight line. Furthermore, since we may write

$$e = \frac{1}{(dC_D/dC_L^2)\pi \, AR} \tag{8.6}$$

where AR = aspect ratio, it becomes apparent that the slope of the line dC_D/dC_L^2
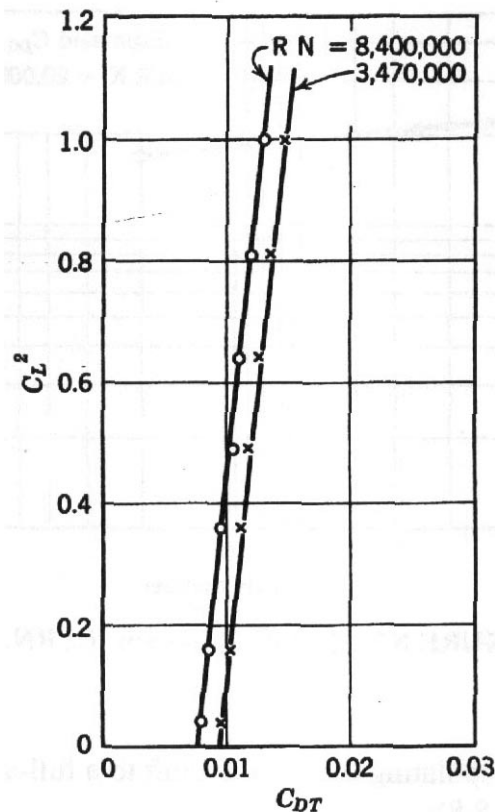
FIGURE 8.6   Plot of C_L^2 versus C_{DT} for a NACA 23012 at two Reynolds numbers.

may be used to find e. Fortunately the slope of this line is practically independent of Reynolds number, and a wind tunnel test may hence be used to determine full-scale e. A plot of the drag polar for the 23012 airfoil at two Reynolds numbers is given in Figure 8.6.

As we have noted, the determination of the amount the C_L^2-versus-C_{DT} curve is moved over (i.e., the scale effect on $C_{D0,\min(\text{aircraft})}$) with increasing Reynolds number is not so simple; in fact, no direct rule is known. If similar tests have been completed in the past and flight tests made, perhaps the comparison will yield the ΔC_D necessary. For an entirely new aircraft, the minimum drag may be measured at several speeds, and a plot of $C_{D0,\min}$ versus log R_e may be made. The straight line that usually results from such a plot may be extrapolated to find the approximate full-scale $C_{D0,\min}$, as indicated in Figure 8.7.

Another method, particularly for components, consists of converting the tunnel test point to a skin friction coefficient by the equation

$$C_f = C_{D0} \times \left(\frac{S}{\text{wetted area}} \right)$$

and spotting this point on a plot of C_f versus R_e. The point is then extrapolated along the turbulent skin friction curve to the full-scale Reynolds number. The resulting skin friction coefficient is then converted to a ΔC_{D0}.

Estimated $C_{D0\,min}$
at R N = 20,000,000
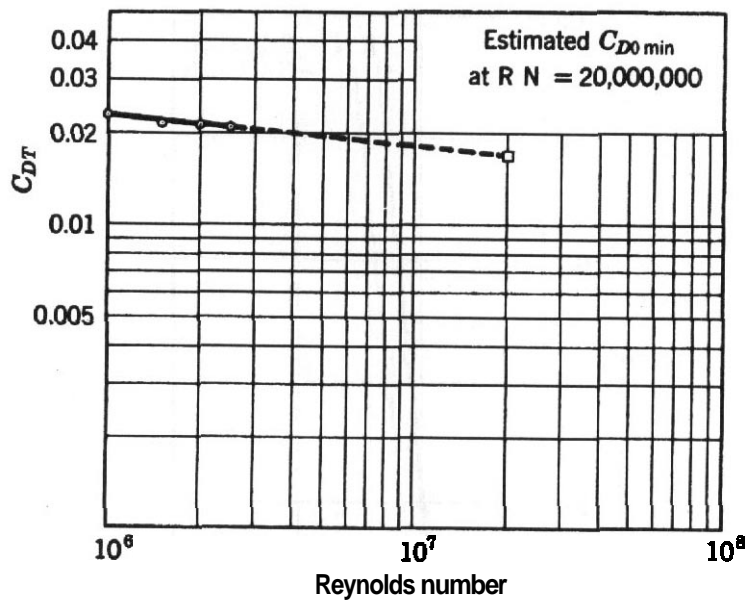
FIGURE 8.7 Plot of C_{DT} versus log RN.

A third method of extrapolating the total aircraft to a full-scale Reynolds number is as follows (see Figure 8.8):

1. Plot C_D-versus-C_L tunnel data.
2. Subtract $C_{Di} = C_L^2/\pi$ AR.
3. Estimate $C_{L,max}$ (full scale) from Figure 8.9, taken from Jacobs[8] or other sources, and extend C_{D0} until it is horizontal at $C_{L,max}$. The increased curvature of the C_{D0} curve should be moved to an increased C_L in a manner similar to that described in Section 8.4.
4. Decrease $C_{D0,min(tunnel)}$ by the C_D change in wing drag from the tunnel Reynolds number to full scale. See Figure 8.1. (This is the controversial step. Some engineers make no change to tunnel $C_{D0,min}$ because manufacturingirregularities on the actual aircraft may increase the drag as much as increased Reynolds number decreases it.)
5. Add C_{Di} back in to get the final extrapolated drag curve. In this step use values of C_L up to $C_{L,max}$ (full scale).

Special attention should be paid to the extrapolation of C_D at $C_{L,max}$. In many cases the engineer neglects the drag increase that accompanies the increase of $C_{L,max}$ with Reynolds number, and predicted glide angles near $C_{L,max}$ are then considerably above the attained values.

The methods outlined above for getting full-scale values from tunnel data are successful only when applied by experienced aerodynamicists and are most successful when applied by aerodynamicists experienced with the entire development process of a particular company.
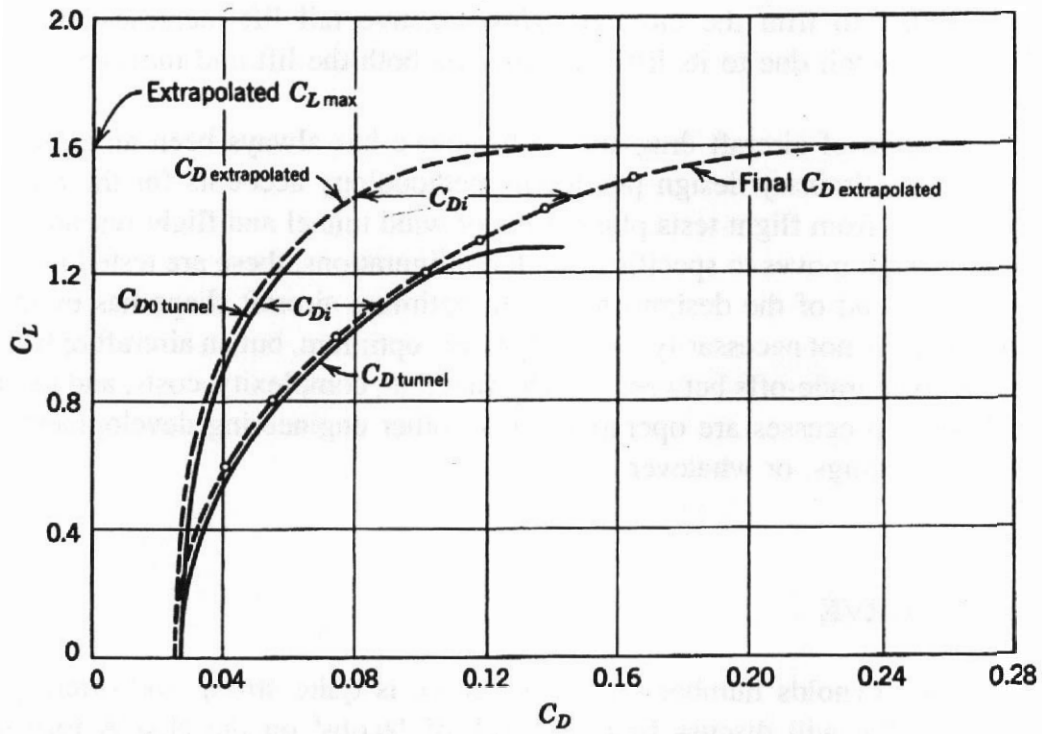
FIGURE 8.8   Extrapolating airplane drag curve to full-scale Reynolds number.

In closing we may state that, though the low-drag "bucket" found in the tunnel may be a bit optimistic, the shape of the drag curve up until $C_{L,\max}$ effects predominate seems to follow closely the drag obtained in flight.

If comparisons are to be made between tunnel and flight test data, the tunnel data must be corrected for trim drag. For a tail-aft aircraft there is usually a **down-**
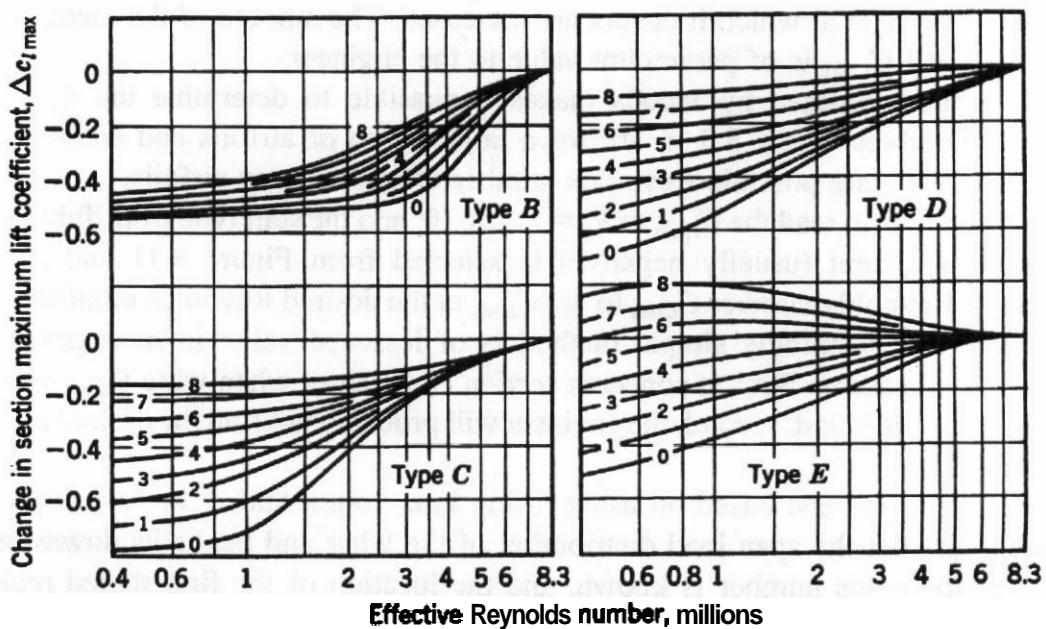
FIGURE 8.9   Effect of Reynolds number on $C_{L,\max}$.

load on the tail to trim the airplane. This negative tail lift increases the drag of the horizontal tail due to its lift and increases both the lift and induced drag of the wing.

The prediction of aircraft drag and performance has always been an empirical process. The preliminary design prediction methodology accounts for the drag of existing designs from flight tests plus results of wind tunnel and flight research. As the aircraft design moves to specific aircraft configurations, these are tested in wind tunnels. At the end of the design process an optimum aircraft shape has evolved. This final shape is not necessarily an aerodynamic optimum, but an aircraft optimum that has involved trade-offs between weight, function, complexity, costs, and performance. Similar processes are operative for all other engineering developments of cars, boats, buildings, or whatever.

8.4 LIFT CURVE

The effect of Reynolds number on the lift curve is quite strong and often quite unpredictable. We will discuss first the work of Jacobs[8] on the NACA forward-thickness airfoils and then some other profiles.

Forward-Thickness Airfoils

Jacobs[S] indicates that variations in lift curve slope with changes in Reynolds number are very small, but in general the lift curve will be more linear as the Reynolds number increases. The slope will increase slightly? and the stall will become more abrupt. (See Figure 8.10.) Lift curves already linear at the lower Reynolds numbers will have the linear range of angle of attack extended at higher ones. It follows that $C_{L,\max}$ and the angle at which it occurs are increased. The amount of the increase of both angle and $C_{L,\max}$ is of paramount value to the engineer.

The method outlined by Jacobs makes it possible to determine the $C_{L,\max}$ at Reynolds numbers below 8.3×10^6 for a large group of airfoils and enables the engineer to estimate possible Reynolds number effects on new airfoils.

The method is to read the $C_{L,\max}$ at $R_e = 8.3 \times 10^6$ and the stall type from Table **8.2.** Then the increment (usually negative) is selected from Figure 8.11 and added to the high-Reynolds-number $C_{L,\max}$ to get $C_{L,\max}$ at the desired Reynolds number. Unfortunately' this seemingly simple method is of lessened value in most practical cases for two reasons: First, it concerns *section* $c_{l,\max}$ values when wing $C_{L,\max}$ values are usually needed; and, second, the engineer will probably not find the desired airfoil in Table **8.2.**

Many methods exist based on using lifting line, vortex lattice, or surface panel models to predict the span load distribution of the wing and hence its downwash. The local Reynolds number is known, and the location of the first stalled region and wing $C_{L,\max}$ can be estimated. The success of these methods depends on knowing the effect of Reynolds number on the wing airfoil sections.
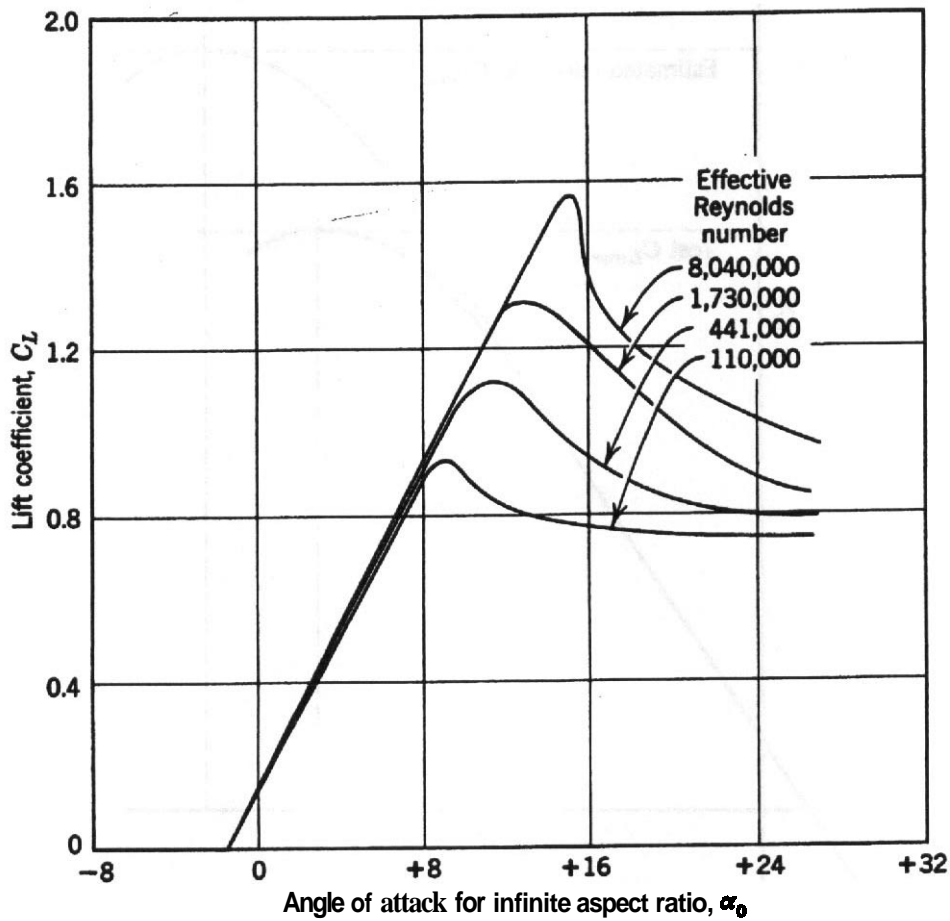
FIGURE 8.10   Effect of Reynolds number on the lift curve.

TABLE 8.2. Stall Types for Selected Airfoils

Airfoil NACA	Stall Type	Airfoil NACA	Stall Type
0006	A	4412	C_4
0009	B_0	4415	D_4
0012	C_0	4418	E_4
0015	D_0	4421	E_5
0018	E_0	23006	A
0021	E_1	23009	C_2
0025	E_2	23012	D_2
0030	—	23015	D_2
2212	C_3	23018	E_2
2409	B_2	23021	E_2
2412	C_2	43012	D_4
2415	D_2	43015	D_4
2418	E_2	43018	E_4
4406	A_3	63012	D_6
4409	B_4	63018	E_7
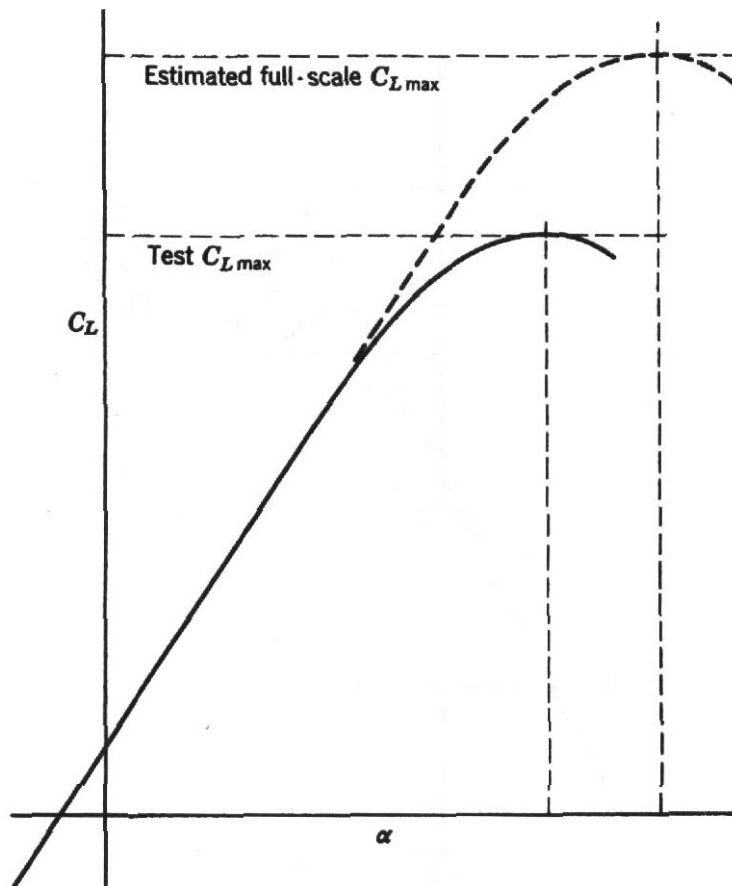
FIGURE 8.11   Estimating full-scale $C_{L,max}$.

The way around the problem is largely empirical. Some engineers have had sufficient experience correlating tunnel data with flight tests so that they feel qualified to estimate $C_{L,max}$ due to Reynolds number. Most of their estimations run around $\Delta C_{L,max} = 0.15$ for the range from a tunnel test at $R_e = 1.5 \times 10^6$ to full-scale Reynolds number $= 6 \times 10^6$.

For large jet-transport aircraft with leading-edge and multielement trailing-edge flaps, the extrapolation to much higher Reynolds number in the range of 60×10^6 at the wing root for a B-747-type aircraft is much more difficult. Such an extrapolation requires an experienced aerodynamicist and flight test data. The method is as follows (refer to Figure 8.11):

1. The linear part of the lift curve from tunnel data is extended with the same slope.
2. Through the value of $C_{L,max}$ (full scale) as estimated, a horizontal line is drawn.
3. The curved portion of the test lift curve is then raised until it has the proper value of $C_{L,max}$ and shifted laterally until it joins the linear part of the constructed full-scale lift curve.

The net result is a full-scale lift curve having the proper value of zero lift, slope, and $C_{L,max}$ but probably having an angle of maximum lift that is too great and a stall

that is too gentle. These two deficiencies are not serious, however, and the engineer has at least something with which to work.

Since the speed of the airplane is reduced for landing, it is sometimes possible to obtain tests at the landing Reynolds number in a tunnel of moderate capacity.

Maximum-lift coefficients measured in different wind tunnels agree much better when based on "effective" Reynolds numbers than when based on the test Reynolds number. Increased Reynolds numbers obtained by added turbulence are often satisfactory for maximum-lift measurements.

Hills[10] found agreement on $C_{L,\text{max}}$ within ± 0.1 when data from 1.5×10^6 were extrapolated to 26×10^6 by Jacobs's method.

Low-Drag Airfoils

The effect of scale of the lift characteristics of the six series of laminar flow airfoils has not been as thoroughly investigated as for the other airfoils previously discussed. And there are now a very large number of custom-designed airfoils using modem airfoil programs. Fortunately some data on Reynolds number effects are available in Loftin and Bursnall[11] for a number of six series sections up to $R_e = 25 \times 10^6$. Although the effects vary with form, thickness, and camber, some general remarks can be made. The angle of zero lift and the lift curve slope are virtually unaffected by scale, but the effects on maximum lift follow one of two general tends depending on the airfoil thickness ratio. For thickness ratios of 12% or less there is little effect over the lower Reynolds number range (up to $R_e = 6 \times 10^6$). Increasing Reynolds number beyond this area produces a rapid increase in $C_{L,\text{max}}$ to a more or less constant value, which then decreases slowly on up to around $R_e = 25 \times 10^6$. Turbulent separation beginning at the trailing edge seems to be responsible for this.

For the thick sections the trend is toward a continual increase in $C_{L,\text{max}}$ with increasing R_e. The large-scale effect exhibited by an 18% thick airfoil seems to be related to the rapidly changing condition of the boundary layer at the leading edge. New airfoils tested at fairly low Reynolds numbers present a difficult task of estimating behavior at much greater Reynolds numbers.

8.5   FLAP CHARACTERISTICS

We are usually justified in expecting a little more from a flap full scale than is found in a tunnel at low Reynolds numbers, provided that the basic airfoil does not suffer extreme effects itself. In a number of examples flight turned up about 0.2 more flap lift coefficient increment than did the tunnel. Figure 8.12 illustrates a tunnel range in which the flap increment was unaffected by scale.

With the current computational ability to design airfoil sections via computer with the desired pressure distributions for cruise flight and then using leading- and trailing-edge flaps for high lift, the problem of extrapolation wind tunnel data for R_e effects is quite difficult. See Figure 8.13 for the effect of scale on the F-111A flaps down.
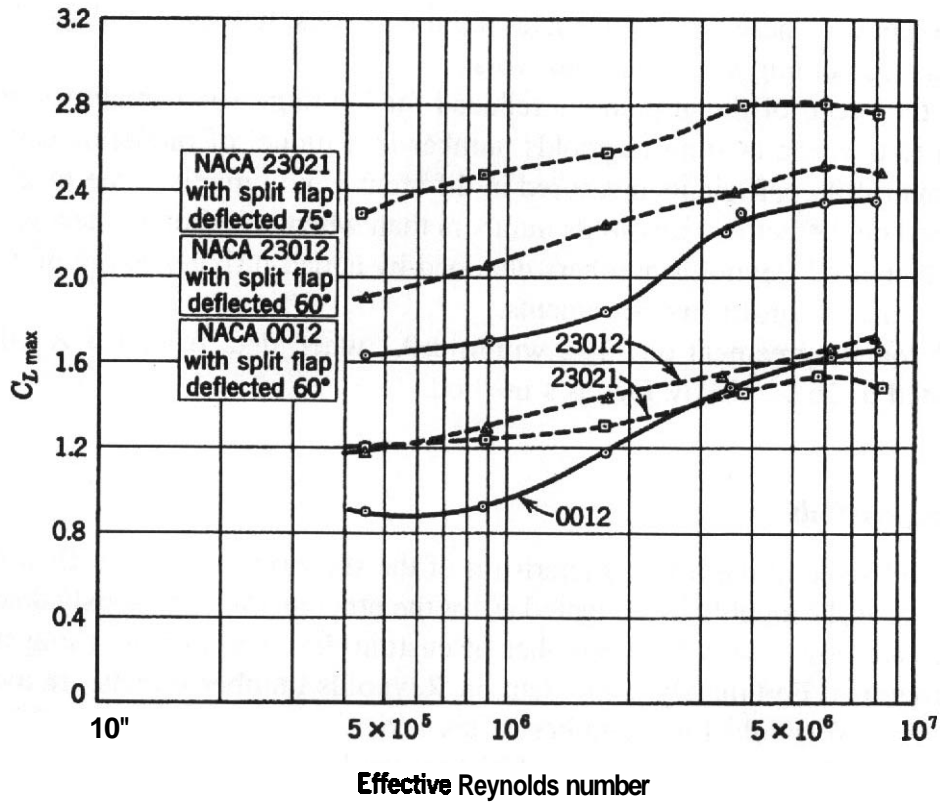
FIGURE 8.12 Effect of Reynolds number on $C_{L,\max}$, flaps down.
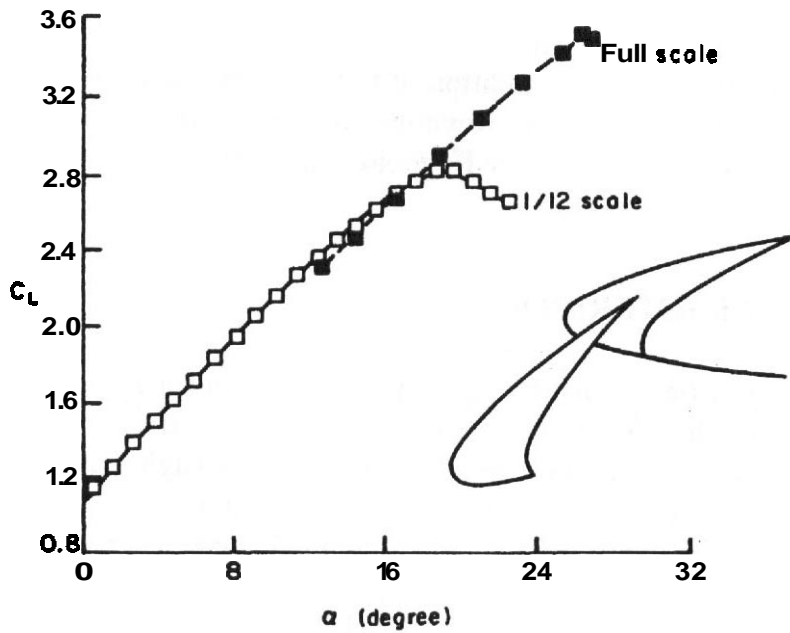
FIGURE 8.13 Effect of scale on the lift characteristics of the F-111 aircraft. (Courtesy of NASA Ames.)
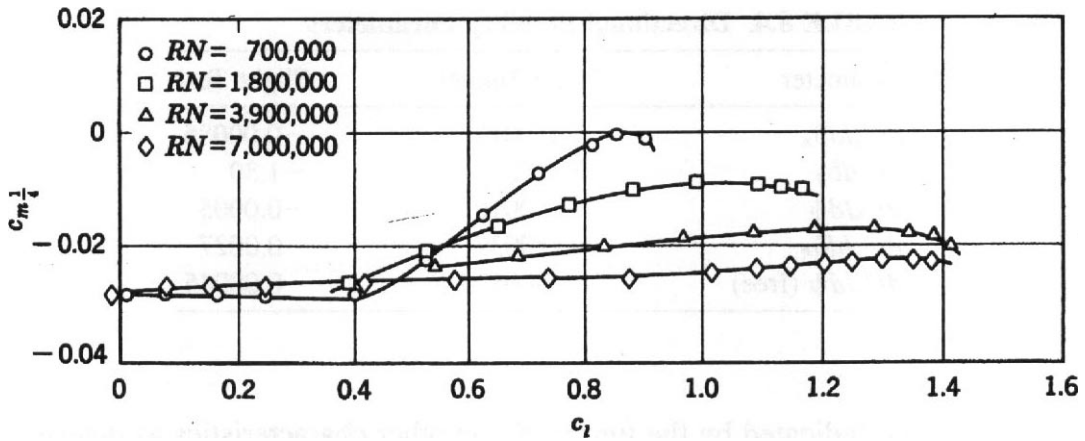
FIGURE 8.14   Effect of Reynolds Number on a 662-215 (a = 0.6) Airfoil.

8.6   PITCHING MOMENT

The static longitudinal stability of airplanes having airfoils with forward thickness (such as the 23012) seems to change little from typical tunnel Reynolds numbers of around 10^6 up to flight values of around 20×10^6. Usually the tunnel–flight discrepancy is in the direction of slightly more stability of the airplane than was predicted in the tunnel.

But the extrapolation of pitching moments when the airfoil thickness is well rearward (such as in the 65 and 66 series airfoils) is far more difficult to handle. The pitching moment variation of the 66,2-215 (a = 0.6) airfoil is shown in Figure 8.14 from tests made in the British compressed-air tunnel and is reported by Hills.[10] Obviously, the extrapolation of even the data made at 1.8 $\times$ 10^6 would be a very difficult job. Nor were trip strips of much value here. Satisfactory tests were accomplished only by going to high Reynolds numbers.

8.7   LONGITUDINAL STABILITY AND CONTROL

In general the longitudinal characteristics will not be seriously different from those indicated by tunnel tests. Frequently one finds the model neutral point a little farther forward than full scale when power is off and in pretty fair agreement with power on for propeller-powered aircraft. The elevator needed to trim rarely varies more

TABLE 8.3. Hinge Moment and Downwash Data Comparisons

Parameter[a]	Wind Tunnel	Flight Test
$dC_h/d\alpha$ ($\delta_E = 0°$)	−0.0014	−0.0011
$dC_h/d\delta$	−0.0044	−0.0044
$d\epsilon/d\alpha$	0.45	0.41

[a]C_h = hinge moment coefficient, δ = control deflection.

TABLE 8.4. Directional Stability Parameters

Parameter	Wind Tunnel	Flight Test
$dC_n/d\delta_R$	−0.00126	−0.00085
$d\psi/d\delta_R$	−0.787	−1.39
$dC_h/d\psi$	−0.0010	−0.0005
$dC_h/d\delta_R$	−0.0037	−0.0027
$dC_n/d\psi$ (free)	−0.00125	−0.00045

than $2°$ from that indicated by the tunnel. Some other characteristics as determined by wind tunnel and flight tests of a two-engined propeller-driven aircraft may be of interest, even though they cannot be taken as typical; they are given in Table 8.3.

8.8   DIRECTIONAL STABILITY AND CONTROL

The directional stability in flight in a number of instances has been seriously less than indicated in the wind tunnel, necessitating a redesign of the vertical tail. The reasons for this difference are not fully understood. In a number of airplanes the rudder was not powerful enough to yaw the aircraft into rudderlock on the model, but did so in flight. Catastrophes have been avoided only because rudderlock flight tests are always made quite gradually and with full cautions as appropriate when anticipating possible trouble. The comparative values in Table 8.4 are from wind tunnel and flight tests of two-engine propeller-driven aircraft.

8.9   LATERAL STABILITY AND CONTROL

The agreement between flight and tunnel tests on the lateral parameters seems to be generally satisfactory. The disagreement between tunnel and flight for aileron power is expected from considerations of cable stretch and wing flexibility. The values listed in Table 8.5 are from wind tunnel and flight tests of a two-engine propeller-driven aircraft. Of course, though they are normal values, they cannot be taken as typical for all airplanes.

TABLE 8.5. Lateral Stability Parameters

Slope	Wind Tunnel	Flight Test
$dC_l/d\delta_a$	0.00175	0.00144
$C_{l,max}/\delta_a$	0.023/18°	0.022/20°
$dC_l/d\psi$	0.00128	0.00076
dC_l/dC_n	−0.688	−1.69

8.10   CORRELATION OF WIND TUNNEL TO FLIGHT DATA

This is an area where most of the data are kept by companies as closely guarded secrets.

When comparisons are made between tunnel and flight data, it must be kept in mind that there **are** uncertainties in the data obtained by each method. In flight test the data are taken at full-scale Reynolds numbers and the aircraft's roughness and excrescence effects are properly included. The full-scale drag effects of control surface and flap gap leakage, air conditioning, cabin pressurization, heat exchanger, thrust reversers, engine-nozzle modifications, and so on, can best be evaluated by flight test. The limitations in flight test are the inability of doing an airplane buildup. It is difficult to fly an aircraft tail on and tail off to obtain the horizontal tail effect. (Although some control engineers seem to think all they need to do is manipulate the controller gains or put in a neural net and let it "learn.") In flight test the total drag of the complete aircraft is obtained from which only general conclusions can be drawn. Quite often there is not sufficient data to assess the effect of variations in Reynolds number. Thus Reynolds number effect can be concealed in the parasite drag or drag rise due to the Mach number. This may require the analysis to use an assumed effect of Reynolds number. For analysis it is desirable to separate the drag polar into the following parts:

1. $C_{DP,\text{min}}$, due to friction, pressure, interferences, excrescences, and roughness;
2. ΔC_{DP}, the variation of C_{DP} with C_L due to friction, pressure, nonelliptic span load, vortex, and so on;
3. C_{Di}, induced drag variation with C_L^2 and aspect ratio, due to span load or vortex lift; and
4. ΔC_{Dm}, the drag due to compressible waves and shock-wave-induced separation.

If this separation of the various parts of the total drag is to be obtained, a large number of flight test data points are required and very complete wind tunnel data are needed as a guide to the analysis.

In analysis of flight test data it is not correct to assign all of the drag variation with lift to the wing, as the drag of the fuselage and other parts of the aircraft also vary with lift. Trim drag from the lift and drag of the horizontal tail must be accounted for when trying to determine the drag of the wing. The negative lift of the tail increases the wing lift required for level flight and therefore the induced drag of the wing. The tail itself also has a parasite and induced drag that must be taken into account. The tail operates in the wing downwash so its lift is usually not perpendicular to the flight path. Drag data from flight tests **are** only as accurate as the installed thrust (either jets or propellers) can be measured or predicted.

An additional problem with flight test data is that it often is acquired while the aircraft is accelerating. For example, $C_{L,\text{max}}$ is obtained with the aircraft either decelerating at about 1–3 knots/sec and/or sinking. This makes the $C_{L,\text{max}}$ from flight test higher than the true $C_{L,\text{max}}$ by 0.2 or so. It is difficult both to obtain and analyze data taken from flight tests.

The use of wind tunnel tests to predict airplane drag has the following advantages. A specific aircraft configuration can be studied one component at a time over the lift coefficient and Mach number range. This allows trim drag, interference, nonelliptic span load, pitch up on swept wings, and the like to be studied in detail. As deltas in many cases are not affected by Reynolds number, new designs or aerodynamic features can be compared against model standards whose full-scale values are known.

There can be problems with wind tunnel data when corrections such as support and interference tares, blockage corrections, and wall corrections are not properly applied.

Two-dimensional pressure drag can be extrapolated to full-scale Reynolds number using the skin friction laws of **Schlichting**[12] and Squire and **Young**[13] when the experimental pressure distribution of the airfoil is used to compute the local velocities. See also **Jones**[14] and **Bicknell**.[15]

Depending on the size of the program, there may only be a small number of tunnel entries (in some cases only one) during the design stage. When this occurs, there is a strong chance that the tunnel results have been used to modify the design and that the model and aircraft are no longer similar, making comparison difficult, if not possible.

With **V/STOL** vehicles it is difficult to obtain steady-state data, especially in transition between vertical and horizontal flight. In the wind tunnel the data are often steady state, assuming that it is taken outside of the flow breakdown region. This requires extreme care in attempting to match tunnel and flight data.

Neal[16] makes a comparison using both flight test data and wind tunnel test data from the NASA Ames 40 X 80-ft tunnel of a Learjet Model 23 using a 0.15 scale model and the second airplane built. Based on mean aerodynamic chord, the 0.15 model was tested at $R_e = 1.4 \times 10^6$. The airplane in the 40 X 80-ft tunnel was tested at R_e values of 4.1×10^6 and 8.4×10^6. The flight test data were taken at $R_e = 8.6 \times 10^6$. The data correlation between the 40 X 80-ft tunnel and flight test was good. The variation in $C_{L,max}$ with R_e was similar to NACA series 6 airfoils. The $\Delta C_{L,max}$ from the 0.15 scale to full scale was 0.32, both for flaps up and $40X^o$ flaps. Other than an anomaly in α_{L0} between the 0.15 and full scale, the lift curve was similar to Figure 8.10. The 0.15 scale model had a higher drag level and the polar was rotated. There were also slight changes in C_{m0} flaps up tail on, but not for tail off, and slight changes in the slope of C_m versus C_L.

Although the most comprehensive information on wind tunnel to full-scale correlation is certainly held as proprietary, there are many useful reports available. Examples include reports and papers by **Millikan**,[17] and **Hockman**,[18] **Linden**,[19] **McKinney**,[20] **Stalford**,[21] **Moul**,[22] **Stenge**,[23] Paterson," **MacWilkinson**,[25] and **Rooney**[26] and their co-authors.

REFERENCES AND NOTES

1. Schlichting, H., *Boundary Layer Theory,* 7th ed., McGraw-Hill, New York, 1979.
2. Young, A. D., *Boundary Layers,* AIAA education series, AIAA, Washington, DC, 1989.

3. Braslow, A. L., Hicks, R. M., and Harris, R. V., "Use of Grit Type Boundary Layer Transition Trips on Wind Tunnel Models," NASA TN D-3579, 1966.

4. For those readers who may not have been around then, there were several means of recording machine readable data for computers in the period 1950–1980. One was paper tape, in which patterns of holes were punched.

5. Holmes, B. J., and Obara, C. J., "Observations and Implications of Natural Laminar Flow on Practical Airplane Surface," ICAS-82-5.1.1., in *Proceedings of the Thirteenth Congress of International Council of the Aeronautical Sciences,* Vol. 1, AIAA, New York, 1982, pp. 168–181.

6. Braslow, A. L., and Knox, E. C., "Simplified Method for Determination of Critical Height of Distributed Roughness Particles for Boundary Layer Transition at Mach Numbers from 0 to 5, NASA TN 4363, Sept. 1958.

7. The parameter *e* for swept wings is not as tractable as for straight wings. Sometimes the tip stall is reduced by a higher Reynolds number in a manner that increases e, and other times *e* is reduced.

8. Jacobs, E. N., "The Variation of Airfoil Section Characteristics with Reynolds Number, NACA TR 586, 1937.

9. At very low values of the Reynolds number, about 150,000, the lift curve again steepens, and $dC_L/d\alpha$ may then exceed 2π/radian (see chapter on small wind tunnels).

10. Hills, R., "Use of Wind Tunnel Model Data in Aerodynamic Design," *J. Roy. Aero. Soc., 155,* 1–26, Jan. 1951.

11. Loftin, L. K., Jr., and Bursnall, W. J., "The Effects of Variations in Reynolds Number between 3.0×10^6 and 25.0×10^6 upon the Aerodynamic Characteristics of a Number of NACA 6-Series Airfoil Sections," NACA TN 1773, Dec. 1948 (also reissued as TR 964).

12. Schlichting, H., *Boundary Layer Theory,* McGraw-Hill, New York, 1960, pp. 620–625.

13. Squire, H. B., and Young, A. D., "The Calculation of the Profile Drag of Aerofoils," ARC R&M 1838, 1938.

14. Jones, B. M., "Flight Experiments on the Boundary Layer," *J. Aeronaut. Sci., 5,* 81–101, 1938.

15. Bicknell, J., "Determination of the Profile Drag of an Airplane Wing in Flight at High Reynolds Numbers," NACA TR 667, 1939.

16. Neal, R. D., "Correlation of Small-Scale and Full-Scale Wind Tunnel Data with Flight Test Data on the Lear Jet Model 23," Paper 700237, SAE National Business Aircraft Meetings, 1970.

17. Millikan, C. B., Smith, J. E., and Bell, R. W., "High Speed Testing in the Southern California Cooperative Wind Tunnel," *J. Aeronaut. Sci., 15,* 69–88, Feb. 1948.

18. Hockman, M. T., and Eisiminger, R. E., "The Correlation of Wind-Tunnel and Flight Test Stability and Control Data for an SB2C-1 Airplane," *J. Aeronaut. Sci., 15,* 5–17, Jan. 1948.

19. Linden, J. E., and Obrimski, F. J., "Some Procedure for Use in Performance Prediction of Proposed Aircraft Designs," SAE Preprint 650800, Oct. 1965.

20. McKinney, L. W., and Baals, D. D., Eds., "Wind-Tunnel/Flight Correlation—1981," NASA CP 2225, 1982.

21. Stalford, H. L., "High-Alpha Aerodynamic Model Identification of T-2C Aircraft Using EBM Method," *J. Aircraft,* 18, 801–809, 1981.

22. Moul, T. M., and Taylor, L. W., Jr., "Determination of an Angle-of-Attack Sensor Correction for a Light Airplane," *J. Aircraft,* 18, **838–843, 1981.**

23. Stengel, R. F., and Nixon, W. B., "Stalling Characteristics of a General Aviation Aircraft," *J. Aircraft,* **19, 425–437, 1981.**

24. Paterson, J. H., MacWilkinson, D. G., and Blackerby, W. T., "A Survey of Drag Prediction Techniques Applicable to Subsonic and Transonic Aircraft Design," AGARD CP **124, 1973.**

25. MacWilkinson, D. G., Blackerby, W. T., and Paterson, J. H., "Correlation of Full Scale Drag Prediction with Flight Measurements on the C141A Aircraft—Phase II, Wind Tunnel Test, Analysis, and Prediction Techniques. Vol. I—Drag Predictions, Wind Tunnel Data Analysis and Correlation," NASA CR **2333,** Feb. **1974.**

26. Rooney, E. C., "Development of Techniques to Measure In-Flight Drag of a U.S. Navy Fighter Airplane and Correlation of Flight Measured Drag with Wind Tunnel Data," AGARD CP **124,** Oct. **1973.**

9 Boundary Corrections I: Basics and Two-Dimensional Cases

The flow conditions in a wind tunnel are quite obviously not completely the same as in an unbounded airstream or in "free air" in the case of aircraft or in an environment with only one plane boundary, as may be supposed for ground vehicles. There is no difference traceable to having the model at rest and the air moving relative to the local earth reference. However, the distances of some or all of the stream boundaries from the article under test are usually less than the corresponding distances for actual operations. This is the most fundamental of the effects that must be evaluated. In addition the wind tunnel stream may not have the same distribution of flow properties in space and time, even within its more limited extent. A uniform stream is the most commonly envisioned operational condition that is to be approximated by a wind tunnel simulation. Relatively small deviations can have significant effects on resulting surface stress distributions and corresponding total forces. An example of a nonuniform stream condition is the presence of a longitudinal static pressure gradient in the test section with a corresponding variation in the speed of flow. Another example is the existence at the lateral boundaries of either solid walls plus boundary layers or relatively still air plus shear layers, which do not exist in actual operations.

The material in this and the next two chapters is focused on vehicle-type applications. Environmental or wind engineering applications may differ due to the fact that substantial spatial and time variations in the flows are intentionally introduced.

We introduce terminology that has evolved over decades and reflects the effects of the finite stream. We endeavor, in subsequent sections, to provide more detailed descriptions and models of various effects. The presence of lateral flow boundaries a finite distance from the body under investigation produces several effects that are interdependent but to a first approximation have been traditionally considered separately. We define the following terms:

Horizontal Buoyancy   This refers to a variation of static pressure along the test section when no model is present. It is nonzero in many wind tunnels. It produces a drag force analogous to the hydrostatic force on objects in a stationary fluid in a uniform gravitational field. It may produce a significant effect in the thrust direction for some short-section free-jet configurations. This should not be confused with the static pressure variation along the test section that is induced by the presence of a test article. There is a possible interaction of the two gradients in some cases of sufficiently large test articles.

This interaction is the subject of ongoing discourse among practicing professionals. This effect may be considered as a nonunifonnity of flow in the streamwise direction but is induced by the lateral boundaries.

Solid Blockage   **The** ratio of the "frontal area" of an article to the stream cross-sectional area is effectively zero in most actual operations. In wind tunnel tests, this ratio reflects the relative size of the test article and the test section. It is usually chosen in the range of 0.01–0.10 with 0.05 being typical. **An** effect of this ratio being finite is that the surface stresses are larger than for the corresponding free-air condition in the case of a closed test section and smaller for an open jet. The effect is greater at a given value of the ratio for the closed test section than for the open jet. This effect is represented by considering the "blockage" to produce an effective change in oncoming flow speed or dynamic pressure. This representation to a first order assumes no change in the distribution of the surface stresses as a result of the finite area ratio. This assumption is obviously not valid for "large" values of the blockage.

Wake Blockage   This effect is a result of the finite size of a body wake and is somewhat similar to solid blockage. It is more complicated because the size of the wake is itself a function of the body shape and the ratio of the wake area to the tunnel area. The magnitude of the correction for wake blockage increases with an increase of wake size, which corresponds to an increase in drag. In a closed test section wake blockage increases the measured drag. Wake blockage is frequently considered negligible with an open test section, since the airstream is then free to expand. Actually it is more free to expand than in an infinite stream.

Streamline Curvature   This refers to an alteration to the curvature of the streamlines of the flow about a body in a wind tunnel as compared to the corresponding curvature in an infinite stream. For a wing the moment coefficient, lift, and angle of attack are increased in a closed wind tunnel and decreased in an open jet. Note that this recognizes an alteration of the pattern of surface stresses on a test article associated with the finite distances to boundaries. This effect will produce hinge moments that are too large in a closed test section and too small in an open one.

Normal Downwash Change   This refers to the component of induced flow in the lift direction at the test article. It is changed due to the finite distances to the boundaries. **A** closed jet makes the lift too large and the drag too small at a given geometric angle of attack corresponding to a smaller **downwash** at the test article than in an unbounded stream. An open jet has the opposite effect.

Spanwise Downwash Distortion   This refers to an alteration to the local angle of attack along the span of a lifting wing. In a closed test section the angles of attack near the **wingtips** of a model with large span are increased, making tip stall start at a lower geometric angle of attack. The effect of an open jet is the opposite (tip stall begins at a higher geometric angle of attack), and in both cases the effect is diminished to the point of negligibility by keeping model span less than 0.8 tunnel width, at least for high-aspect-ratio wings.

This is fundamentally a three-dimensional effect and will not be present in two-dimensional applications.

Tail Downwash Change   This refers to an alteration to the normal downwash (and other components of induced flow) behind the wing so that the measured tailsetting and static stability require adjustment. In a closed jet the wing wake location is higher than in free air and the model is more stable. The opposite is true in an open jet. This stability effect is large. This is fundamentally a three-dimensional effect associated with the trailing vortex system.

Asymmetric Downwash Distortion   This refers to an alteration to the normal flow about an asymmetrically loaded wing such that the boundary effects become asymmetric and the observed rolling and yawing moments require adjustment. This is a three-dimensional effect.

Propeller Induction Attenuation   This refers to an alteration to the flow into a thrusting propeller such that a given thrust occurs at a speed lower than it would in free air. The opposite is true when an open jet is employed. The effect is opposite when the propeller is braking. This effect is frequently considered negligible when a free jet is employed.

Fortunately, there are few tests for which all the above corrections must be applied. The classical application of all of these effects is in a linear manner. They are each estimated and the final adjustment is a superposition of the individual effects.

It is important to understand that the effects being considered so far are consequences of the fact that a wind tunnel test section is finite in size. Other effects must also be considered and evaluated. These include flow nonuniformities such as flow angularity and spatial variations in dynamic pressure. In addition the contributions to measurements due to tare and interference must be evaluated. All of these are treated elsewhere. It is necessary that the influence of those effects has been removed insofar as possible or practical before wall effects are considered.

We consider the basic formulation of treatments of wall effects in this chapter and more details with results for two-dimensional cases. Three-dimensional cases, which are the majority in practice, are considered in more detail in Chapter 10. Some additional applications are considered in Chapter 11.

9.1   DESCRIPTIONS OF WIND TUNNEL FLOW

Flows in Closed and Open Test Sections

We describe generally occurring features of flow states in closed test sections and open jet test sections with streamlined bodies and bluff bodies present. Figure 9.1 shows sketches of closed test sections with a streamlined and a bluff body. There is much less volume of rotational flow created by the streamlined body than the bluff body. However, the situations shown always have a clear separation between the highly rotational flow originating from the test article's boundary layers and
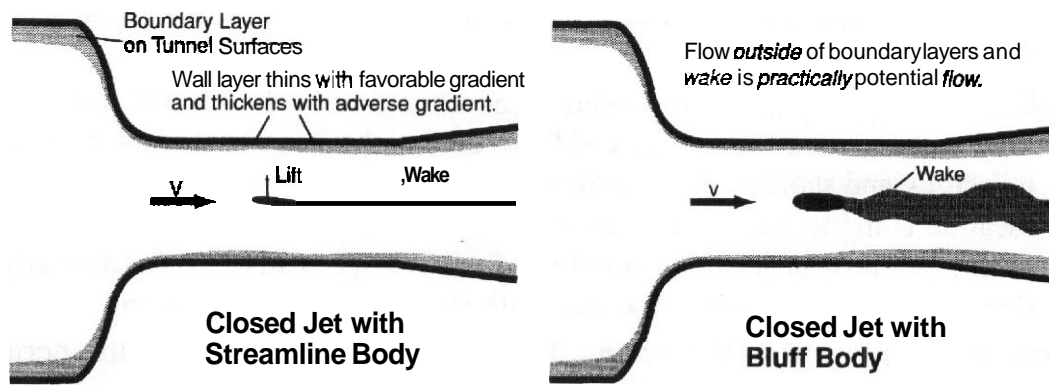
FIGURE 9.1   Closed test-section cases.

wake and the boundary layers on the tunnel surfaces. This ignores the fact that there will usually be some support structure that extends from a tunnel surface and also has boundary layers and a wake. When test articles **are** mounted on a tunnel surface, then there is a direct interaction of the tunnel surface boundary layer and the test article boundary layer.

The sketches actually overemphasize the influence of the bodies by showing the bodies and rotational flow regions larger in proportion to the tunnel size than is usually the case in practice.

Figure 9.2 shows sketches of an open jet tunnel with a streamlined and a bluff body. Here there is a free shear layer at the boundary of the test-section flow instead of a wall boundary layer. This generally results in a higher level of unsteadiness than is the case for closed test sections.

All currently used wall correction methods make use of the existence of the essentially **inviscid** flow region that separates the rotational flow generated along the tunnel boundaries and the rotational flow generated by the test article. The classical methods ignore the boundary layers and shear layers along the tunnel boundaries. In addition, most wall correction methods have been developed using the assumption that the test-section length is sufficient so that the entrance and exit flows can be considered to be parallel to the test-section boundaries.
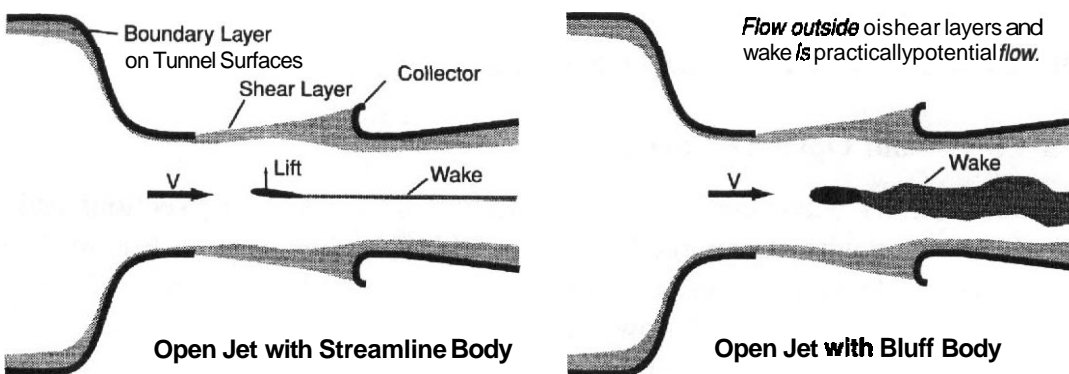
FIGURE *9.2*   Open jet test-section cases.
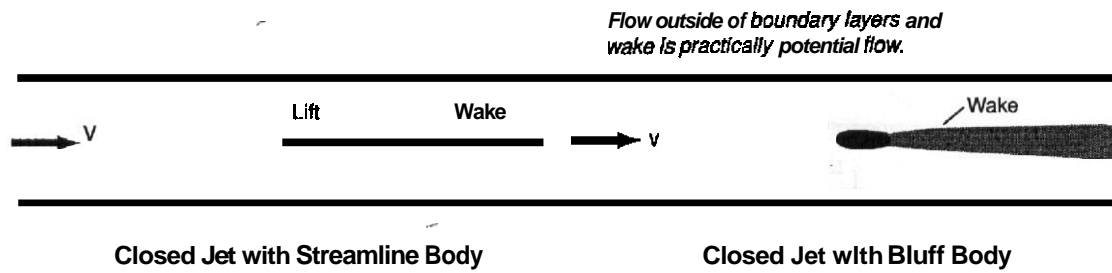
FIGURE 9 3 Working models for closed test section.

Flow Models for Closed and Open Sections

The working models for developing wall corrections are then as indicated in Figures **9.3** and **9.4.** For the closed test-section case, the flow is considered **inviscid** throughout with the test article and its wake represented by an equivalent body. The tunnel walls are parallel and extend to infinity upstream and downstream. For the open test section, the flow is considered **inviscid** throughout and with the test article and its wake represented by an equivalent body. The stream **boundaries are** constant-pressure streamlines with the pressure equal to the ambient pressure outside the stream.

Idealized Example

We show in this section a model of a body plus wake that is constructed by use of the classical **singularities,** doublets, sources, and sinks. The resulting body is an idealized version of a circular cylinder with a wake somewhat like that which exists at **supercritical** Reynolds numbers. We anticipate the discussion of the method of images in the next section. The equation for the stream function of a doublet aligned parallel to the **x** axis located at (x_d, z_d) with strength $2\pi U_0 a^2$ plus a stream with speed U_0 can be written as Equation **(9.1).** The length scales are normalized to h, which we will consider to be half of the tunnel height. The equation for the **x** component of velocity is given by Equation **(9.2):**

$$\frac{\psi}{U_0 h} = (z - z_d)\left(1 - \frac{a^2}{(x - x_c)^2 + (z - z_d)^2}\right) \tag{9.1}$$

$$\frac{u}{U_0 a^2} = \frac{(x - x_d)^2 - (z - z_d)^2}{[(x - x_d)^2 + (z - z_d)^2]^2} \tag{9.2}$$

The equations for the other basic solutions are similar and can be found in standard aerodynamic texts. We show here a simple but instructive set of plots. We have constructed the streamlines for a cylinder with radius equal 0.2 in unconstrained flow and in a tunnel with height equal 2.0. The streamline patterns are shown in Figures 9.5 and **9.6.** We then add a simulated wake by placing a source at the origin

Zero Thickness Shear Layers Separating Tunnel Flow from
Quiescent Air are therefore Lines of Constant Pressure

Open Jet with Streamline Body   **Open Jet with Bluff Body**
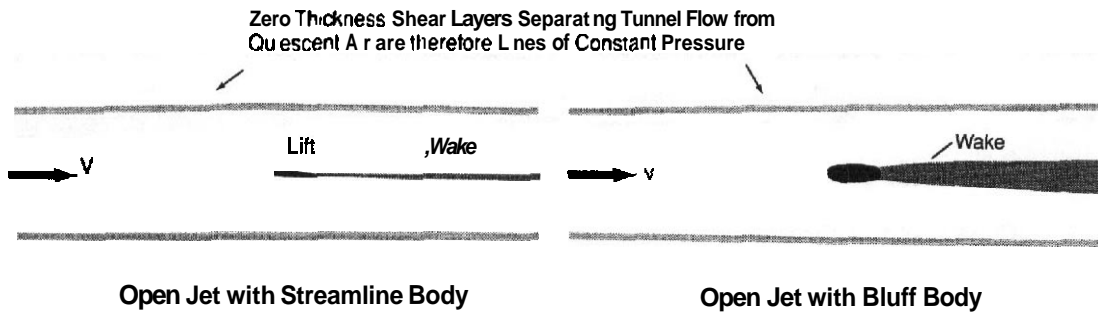
FIGURE 9.4   Working models for open test section.
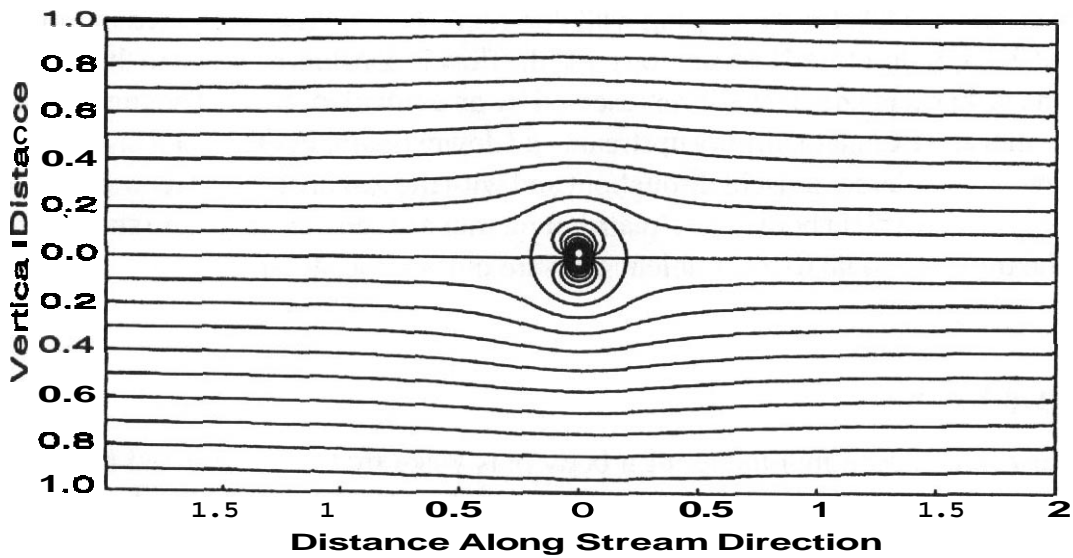
FIGURE 9.5   Streamlines for cylinder in free air.
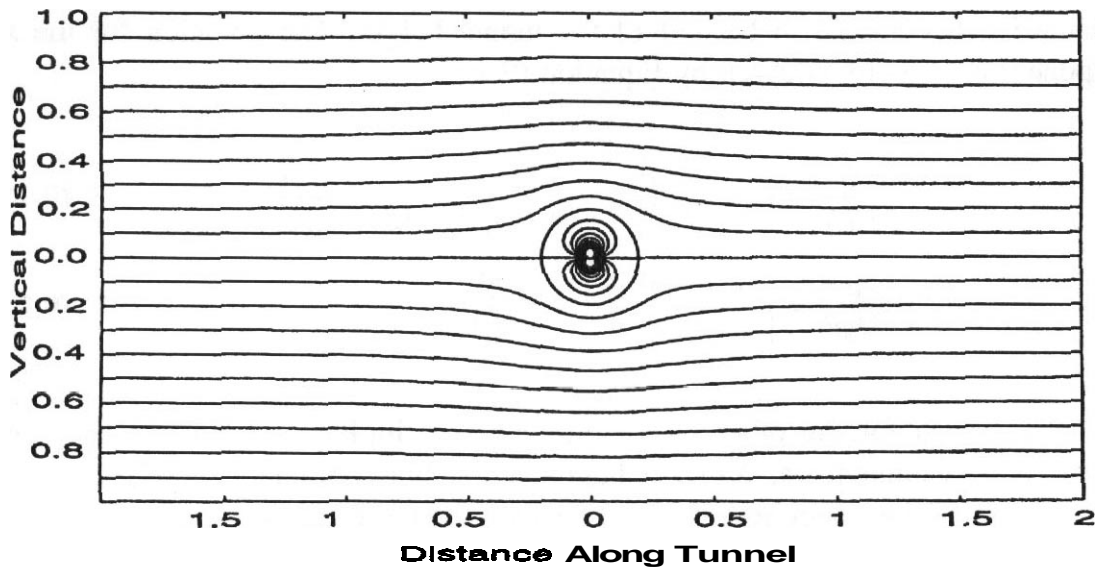
FIGURE 9.6   Streamlines for cylinder constrained by tunnel.
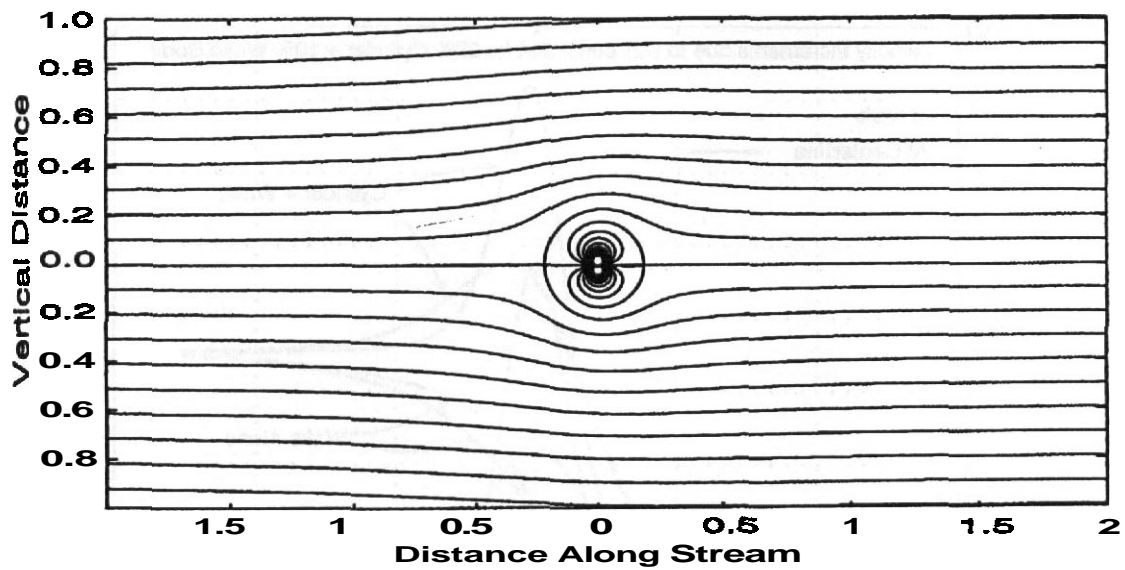
FIGURE 9.7   Streamlines for cylinder plus wake in free air.

with strength such that the eventual half body will have a half height of 0.1 and show the streamlines in Figures 9.7 and 9.8. The differences may not be dramatic to the untrained eye, but these are very significant differences to a wind tunnel engineer. The size of the blockage shown is beyond the limits used for high-accuracy work and has been chosen so that the differences are visible on plots of this size. The streamwise velocity increments induced by the constraint of the walls for the cylinder, the wake body, and the combination are shown in Figure 9.9. There are several things to notice from this figure. First is that the velocity increments are quite large relative to the accuracy of measurements that are typically sought
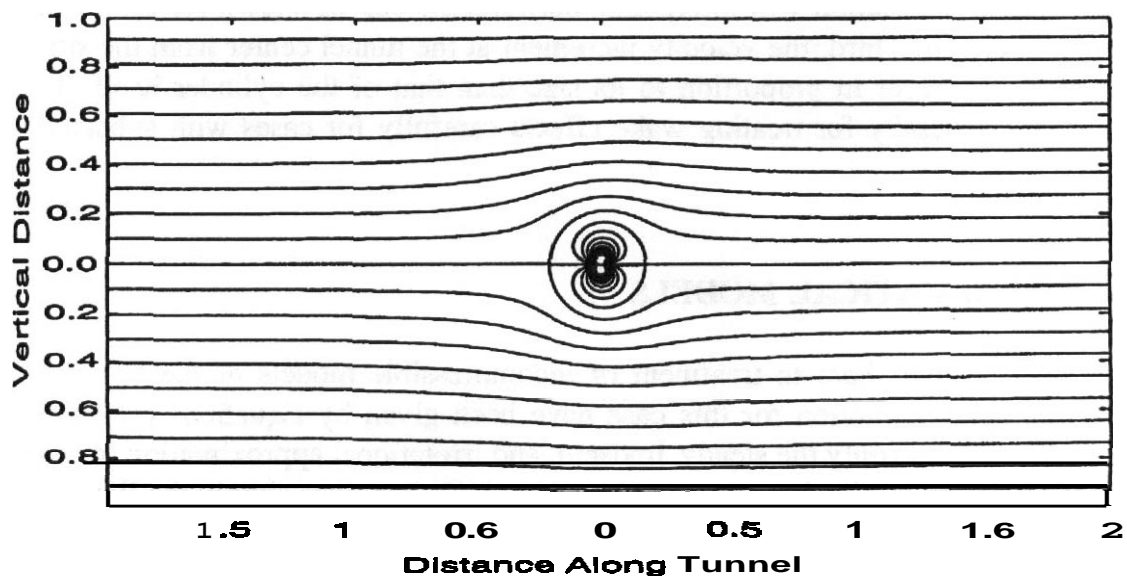
FIGURE 9.8   Streamlines for cylinder plus wake constrained by tunnel.
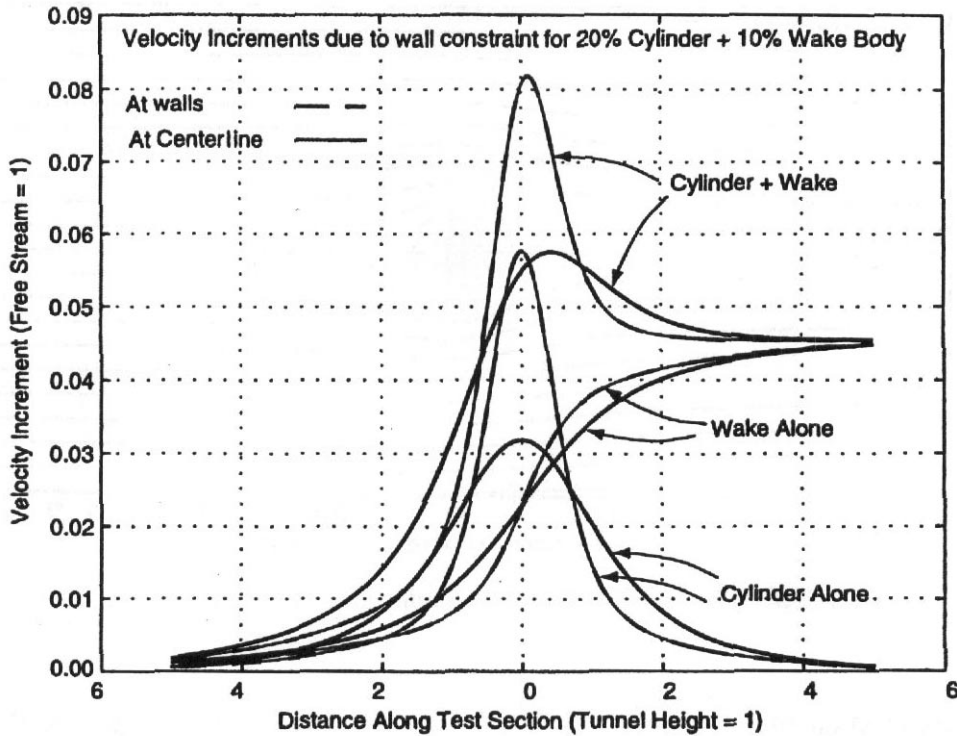
FIGURE 9.9 Streamwise velocity increments due to tunnel constraint.

in aerodynamic design work. For the combination above, the velocity increment at the centerline is about 5.5%, corresponding to a dynamic pressure increment of about 11%. These will be approximately proportional to the blockage value so a blockage of 5%, which will be more typical, will produce velocity and dynamic pressure increments of about 1.3 and 2.6%, respectively. Second, the velocity increment due to constraint varies throughout the tunnel volume. The variation at a given streamwise station will interpolate between the curves shown for the centerline and the wall. Third, the velocity increment at the tunnel center from the simulated wake is larger in proportion to its size than that of the cylinder itself. This indicates a necessity for treating wake effects carefully for cases with substantial separated flow.

9.2 MATHEMATICAL MODELS

We limit ourselves here to treatment of incompressible models of the flow. The fluid equations of motion for this case have been given by Equations (1.41) and (1.42). We will use only the steady, inviscid, and irrotational approximation for wall correction determination here, so the Equation (1.42) becomes simply the Bernoulli equation as developed and given by Equation (1.43). We rewrite it here as

$$p + \tfrac{1}{2}\rho V^2 = p_\infty + \tfrac{1}{2}\rho V_\infty^2 = p_{tot} \tag{9.3}$$

We also recall the introduction of a velocity potential ϕ in Equation (1.41) and the resulting expression of the continuity equation. This produced Laplace's equation:

$$\nabla^2\phi = 0 \qquad\qquad (9.4)$$

The flow in the wind tunnel outside the rotational region enveloping the model is well approximated by solutions of this equation with appropriate boundary conditions on the various surfaces. Laplace's equation is perhaps the most studied partial differential equation in the history of applied mathematics. One of the most useful treatments continues to be by Kellogg,[1] who thoroughly develops the fundamentals although he focuses on gravitational field and electric field applications. Milne-Thomson[2] and Lamb[3] focus completely on fluid dynamic applications. These classical works give treatments for relatively simple geometries.

The two most extensively applied methods for relatively simple geometries are complex variable methods for two-dimensional treatments and modeling using superpositions of singularities to construct flow fields of interest. A special case of the latter is the method of images, which is useful when there are planes or other surfaces through which there is to be no flow. This can often be obtained by positioning singularities in periodic patterns relative to the surfaces. The method of images has been extensively applied to wind tunnel wall correction studies. We will present some results in the following sections.

Complex geometries require computationally intensive methods and have been treated in detail since the advent of digital computers. Finite difference methods along with all of the techniques that have been developed in the voluminous work on computational fluid dynamics in the last 30 years can in principle be used to solve Laplace's equation. These techniques generally fail to take advantage of the known special properties of the solutions of the equation and are more computationally intensive than necessary. The most effective methods for complex geometries are based on superposition of singularities, as was done in the classical work for simpler geometries. The use of currently available computers allows models to be made up of thousands of singularities. Katz and Plotkin[4] give extensive treatment of these methods for various geometries when there is no external boundary. The addition of the wind tunnel walls or the edge of the free jet can be treated using methods described there. There are several extensively developed "panel codes" that have been widely used in the aeronautics community. These include PMARC, VSAERO, and PANAIR.

A few paragraphs above we glibly declared that Laplace's equation "with appropriate boundary conditions" describes important regions of flow in the wind tunnel. The determination of appropriate boundary conditions is not easy. It is a continuation of the problem that has always faced aerodynamicists upon recognizing that the Navier–Stokes equations are the equations that it would be most advantageous to use and solve but also recognizing that obtaining the full solution of the Navier–Stokes equations is beyond our resources. We utilize solutions of Laplace's equation as approximations to the unavailable solutions to the Navier–Stokes equations. It is

known that there are many solutions to Laplace's equation that do not approximate real flows. The real flows **are** presumed to be solutions to the Navier–Stokes equations. It is by specifying the boundary conditions that particular solutions of Laplace's equation are selected. The most famous such specification is the Kutta or **Kutta**–Joukowsky condition for airfoils. In our application to wind tunnel wall corrections, we must select the region of flow to which Laplace's equation will be considered a good model by specifying the boundary of the region and the mathematical boundary conditions on all surfaces that enclose the region.

The same problem has been faced in classical aerodynamics studies. When the entire flow is very streamlined and there is very little flow separation, taking the region to be the entire volume outside the solid surfaces and applying a boundary condition of no flow through the solid surfaces along with auxiliary specifications such as the Kutta condition will work quite well. As the regions of separation and thick boundary layers increase in volume, the problem becomes more difficult. It is necessary to arrive at estimates of "effective" surfaces defining the volumes in which Laplace's equation is to be used to model the flows. There are important precedents in the developments of iterative methods in which potential flow methods are used to compute pressure distributions, followed by use of boundary layer codes to compute boundary layers, followed by recomputation of the potential flow using new surfaces based on the addition of boundary layer displacement thickness to the underlying geometric surface, and so on. The problem treatment becomes more difficult when there are large regions of separated flow.

It is necessary to invoke some experimentally based information to assist in obtaining the solutions to any aerodynamic problem whether it is in the wind tunnel or otherwise. This is true even for the most ambitious of the current efforts to utilize large-eddy simulation techniques to reach useful computational solutions of the Navier–Stokes equations. In the case of wind tunnel applications, there is the advantage that there will be experimental data on the specific items under study. The type of data available will vary with the objectives of the experiments. Total force data will be most common. Flow visualization data, pressure data, and flow field measurements are, of course, common. And increasingly pressure measurements on the wind tunnel surfaces are being included for the specific purpose of applying them to wall correction estimates. In varying ways the experimental measurements are applied to determine the region in which Laplace's equation will he expected to be a good model for the flow.

We can identify two aspects to our problem of applying Laplace's equation. First we must be able to obtain solutions for given boundary conditions on the bounding surfaces of a well-specified region. Second we must be able to find effective surfaces that bound the region in which Laplace's equation will be considered to be a useful model of the flow. The direct application of standard iterative methods using boundary layer computations still represents more computational effort than is typically available for wind tunnel wall correction determination, as does the **application** of full-blown **Navier–Stokes** computations. Fortunately, direct use of experimental data obtained during the tests provides important assistance in this effort.

Method of Images

When there is sufficient symmetry and the detail required is not too great, the classical method of images can be applied. This is the way wall corrections have been evaluated for decades. We describe some aspects of this method here.

It is well known that the flow pattern about a wing may be closely simulated mathematically by replacing it with a vortex system composed of a lifting line vortex and a pair of trailing vortices. For detailed near-flow-field simulation the lifting line approximation can be replaced by a vortex lattice. Similarily, a solid body may be represented by a source–sink system, and a wake may be represented by a source. Thus the entire airplane or component may be simulated by "artificial" means to almost any degree of accuracy desired, depending, of course, on the complexity of calculations that can be tolerated. Fortunately, a very simple first-order setup suffices for a rather good approximation.

Students of fluid theory are well acquainted with the simulation of a boundary near a source, sink, doublet, or vortex by the addition of a second source, sink, doublet, or vortex "behind" the boundary to be represented. Solid boundaries are formed by the addition of an image system that produces a zero streamline matching the solid boundary. An open boundary requires an image system that produces a zero velocity potential line that matches the boundary in question. After the image system is established, its effect on the model is the same as that of the boundary it represents.

We may see how to make up an image system by considering the following case for a vortex in a closed rectangular tunnel; and we note herewith that it is usually necessary to satisfy the conditions only in the plane of the lifting line. A three-dimensional image system is necessary to get the boundary-induced upwash aft of the wing, the streamline curvature effect, or the corrections for a wing with a lot of sweepback.

Consider a single vortex A that we wish to contain within the solid walls 1 and 2 (Figure 9.10). To simulate wall 1, we need a vortex B of sign opposite to that of A, and for wall 2 a vortex C of the same sign as B. Now, however, vortex B needs a vortex B' to balance it from wall 2, and vortex C needs a vortex C' to balance it from wall 1, and so on out to infinity with vortices of alternating sign.

The containment of a wing or vortex pair similarly becomes that shown in Figure 9.11a for vertical walls and in Figure 9.11b for horizontal walls.

The image system for a closed rectangular test section thus becomes a doubly infinite system of vortices. Figure 9.12 shows the image system needed for a wing in a closed rectangular tunnel when the three-dimensional quantities are required.

We may, through elementary vortex theory and logic, develop the form that corrections for boundary-induced upwash will take for an arbitrarily shaped test section. The only mathematical tools needed are the expression for the induced velocity w due to a vortex of strength Γ at a distance r. This is for a semi-infinite vortex, that is, starting at the lifting line and trailing to infinity in one direction:

$$w = \frac{\Gamma}{4\pi r} \tag{9.5}$$
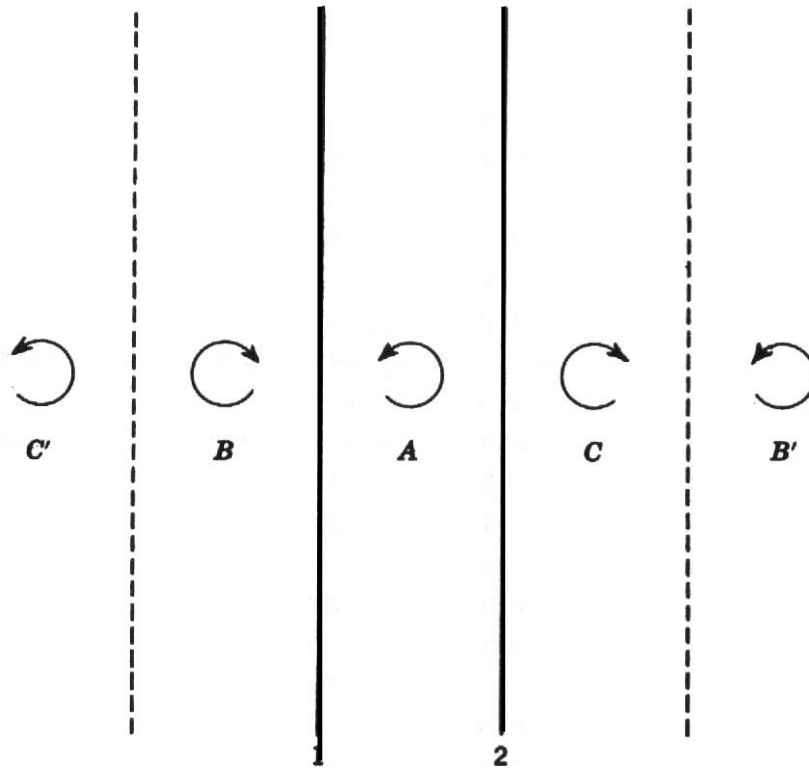
FIGURE 9.10   Vortex arrangement for simulation of vertical boundaries.

The relation between lift and circulation for a uniformly loaded wing is

$$\Gamma = \left(\frac{SV}{2b}\right)C_L \tag{9.6}$$

Combining the two, we get

$$w = \left(\frac{SV}{8\pi rb}\right)C_L \tag{9.7}$$

Now r represents the vortex spacing in the image system, which we may express as some constant times a tunnel dimension, say the tunnel height h, and the model wing span may be expressed in terms of the tunnel width B. The induced angle at the centerline of the test section is then

$$\Delta(\Delta\alpha_i) = \frac{w}{V}\frac{S}{V8\pi k(b/B)(hB)}C_L$$
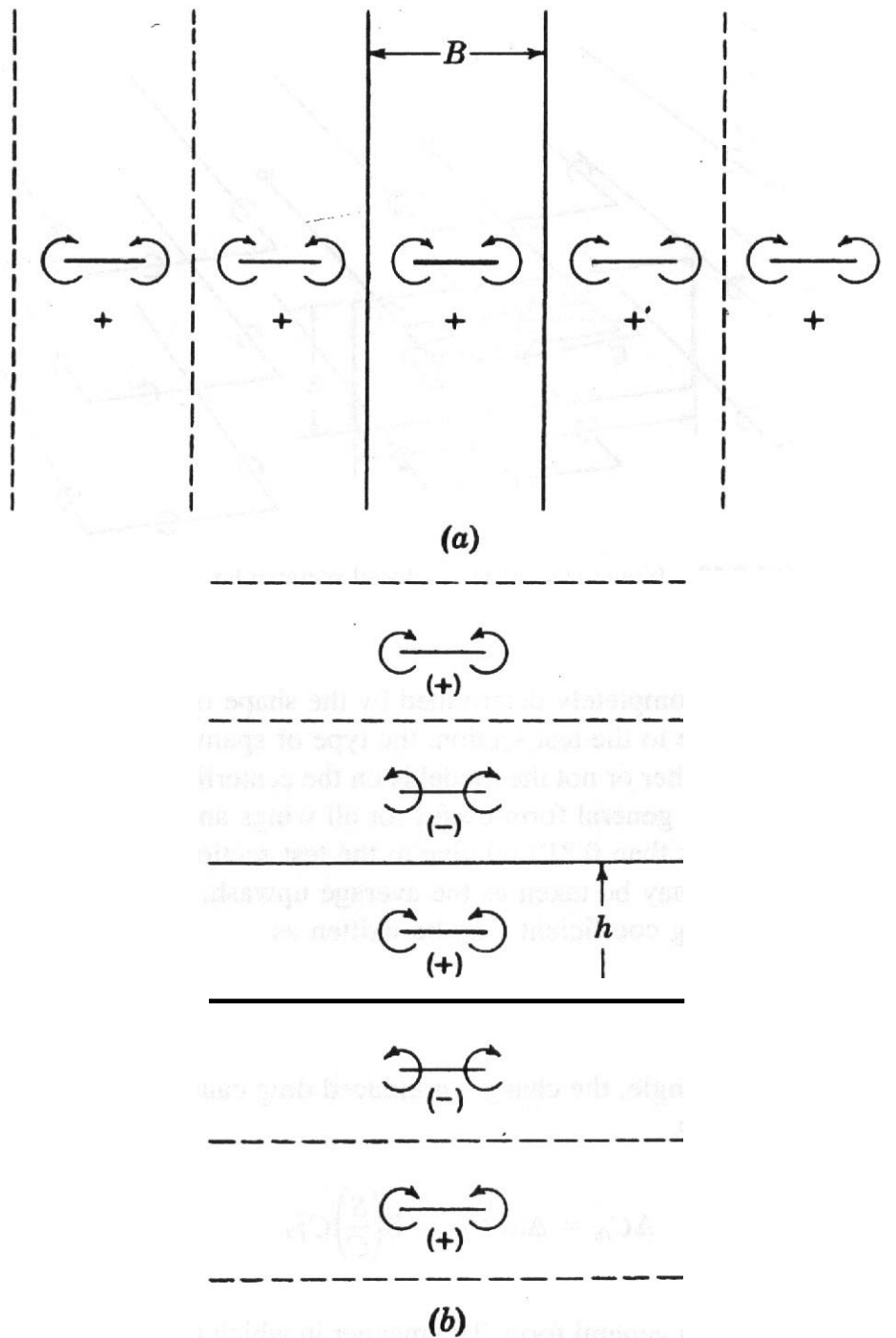
FIGURE 9.11   Vortex pair arrangement for simulation of (a) vertical boundaries and (b) horizontal boundaries.

for any one image, and, summing the whole field, setting $B/8\pi kb = \delta$, and noting that hB is the test-section area C, we have

$$\Delta\alpha_i = \delta\left(\frac{S}{C}\right)C_{LW}(57.3) \qquad (9.8)$$

for the complete system. This equation is in degrees; the subscript W denotes that the correction is based on the wing lift.
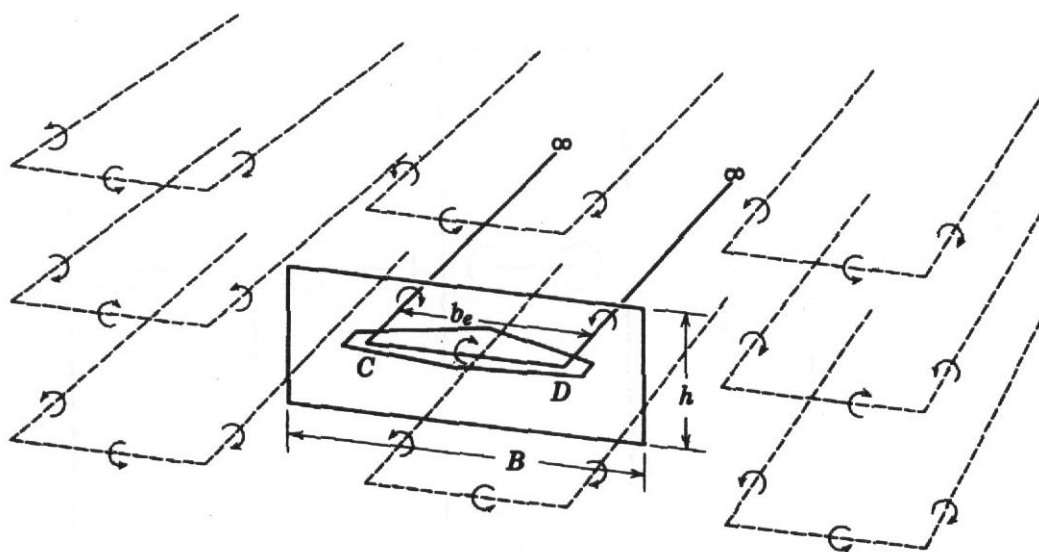
FIGURE 9.12   Image system for a closed rectangular test section.

It develops that 8 is completely determined by the shape of the test section, the size of the model relative to the test section, the type of **spanwise** load distribution over the model, and whether or not the model is on the centerline of the test section. Equation (9.8) is hence a general form useful for all wings and test section as long as the wing is small (less than $0.8B$) relative to the test section so that the **upwash** at the tunnel centerline may be taken as the average **upwash**.

Since the induced drag coefficient may be written as

$$C_{Di} = \alpha_i C_L$$

where α_i is the induced angle, the change in induced drag caused by the **boundary-** induced **upwash** becomes

$$\Delta C_{Di} = \Delta \alpha_i \, C_{LW} = \delta \left(\frac{S}{C} \right) C_{LW}^2 \tag{9.9}$$

Equation (9.9) is also a general **form.** The manner in which the **downwash** affects larger models and how it must be handled for the special cases of **asymmetrical** loadings is covered later.

Panel Methods

We use the term panel here generically to include all methods in which the solutions are developed by using a superposition of **singularities** or fundamental solutions and the boundary conditions are satisfied on a finite number of points on the selected surfaces (usually the tunnel walls). An early implementation of this type of method was given by **Joppa**.[5] There have been a number of computations over the years reporting the use of contemporary design panel codes for configurations in wind

tunnels. Generally; however, these have not found their way into routine use by wind tunnel engineers for wall corrections. Their cost in resources has remained too high for the additional increments in effectiveness that they promise, and they must still be augmented by experimental data in ways that are not standard when they are used by the design aerodynamicists.

We will present some examples of application of these panel methods in later sections.

Measured Variable Methods

The use of measured variables to augment purely theoretical approaches has been done in several ways and continues to evolve. The preceding treatments involve a variety of parameters that must be determined. The usual basis is on geometry plus idealized models of the flow. An example is the span of the trailing vortices used in the calculation of downwash effects. A closely related assumption is the trajectory of the trailing-vortex system. Both of these could in principle be obtained from flow measurements and results from the observations could then be used in the flow models for wall correction assessment.

The most important methods using measured variables are represented by the work of Maskell,[6] Hackett and Wilsden,[7] and Ashill and Keating.[8] Maskell's result makes use of the measured drag coefficient for improved blockage corrections. Hackett and Wilsden introduced the method now known as the "wall signature" method, in which pressures measured at the walls are used to construct a relatively simple singularity set to represent the test article and then calculate the wall effects based on that singularity set. The method given by Ashill and Keating is called the two-variable method. This method provides a calculation of wall effects without the necessity for knowing the geometry of the test article. That this is an area continuing to be developed can be seen by reference to recent publications by Hackett[9] in which there is an improvement of the method of applying Maskell's[6] earlier development along with a challenge to some aspects of blockage methods included in the classical methods described in this book as well as to other publications by Ashill, Jordan, and Simmons[10] as well as Rueger, Crites, and Weirich[11] and others.

Pressure Signature or "Hacket–Wilsden" Method   In *1974* Hackett and Boles[12] showed that tunnel wall static pressures may be used to infer wake geometry and hence wake blockage. Hackett and Wilsden[13] and Hackett, Wilsden, and Lilley[14] followed in 1975 with an extension involving a row of pressures along the center of the tunnel side wall, which gave the axial distributions of both solid and wake blockages. These "wall pressure signatures" were analyzed using chart look-up methods that give a hands-on feel for the physics involved. In the interests of greater flexibility (shorter test sections, more complex "signatures"), influence matrix methods were then introduced.[15] This version also included means for estimating tunnel-induced upwash. The method applied to a jet in cross-flow has also been reported.[16]
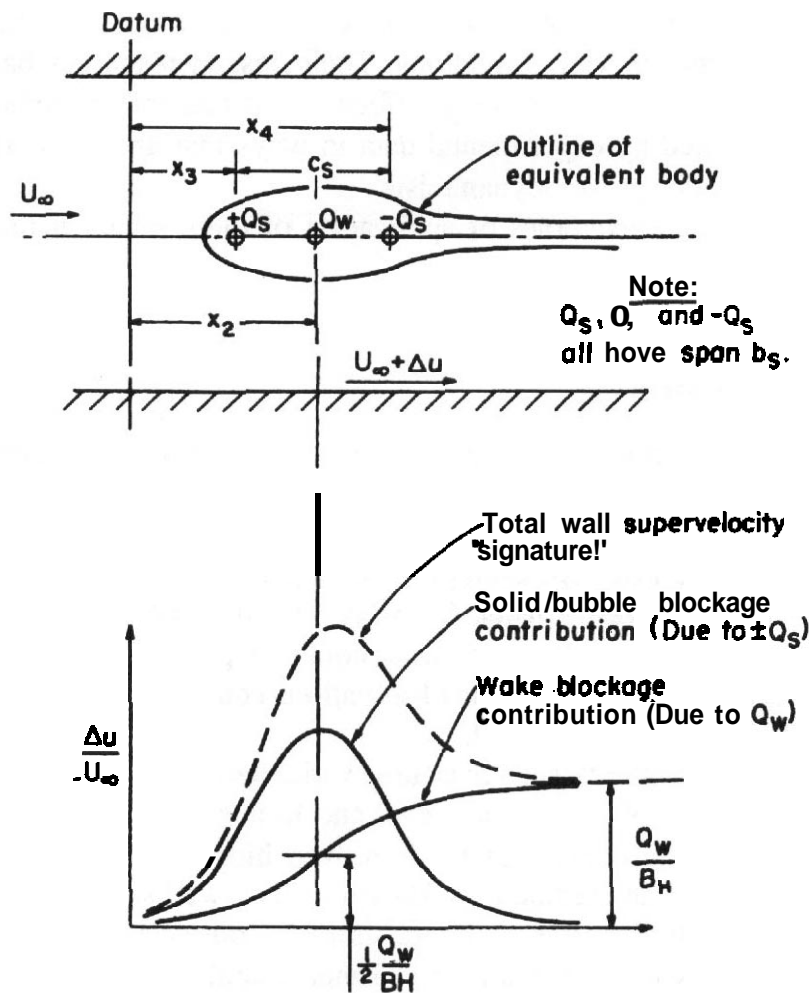
FIGURE 9.13 Nomenclature for Hackett's blockage correction.

The "chart" method[14] provides a good illustration of the approach. For a model on the tunnel centerline, pressures are measured along the side wall from ahead of the model to a point downstream, yielding a pressure distribution similar to that shown in Figure 9.13 with the velocity peak just aft of the model. For analysis, the profile is divided into a part due to solid and bubble blockage (symmetric) and a part due to wake blockage (antisymmetric). The wake blockage source strength Q_w comes from the wake signature analysis. Initially the wake source is placed at a streamwise location X_2 coincident with the model midlength. The solid blockage parameters, the source–sink strength Q_c, and the spacing c_s are obtained from a chart look-up procedure.[13,14] When the wake blockage signature is measured in a sufficiently long test section, the velocity ratio goes from zero upstream of the model to a constant value downstream determined by the wake size. To achieve this, the test-section length should be about 1.5 times its effective diameter with the model at 0.5 diameters from the nozzle. For shorter tunnels neither the upstream zero value nor the downstream constant value will be reached. However, versions of the method[15] are able to handle this situation.

A least-squares curve fit of a parabola is applied to the upper part of the symmetric curve. If the pressure peak does not match X_2 assumed initially, the wake is moved and another iteration is made. The use of a parabolic fit and forcing the wake source to be midway between the solid source–sink pair provide consistency of application. Once the wake source and the peak are aligned, parameters defining the symmetric, solid blockage curve are used with charts to obtain the source–sink spacing c_s and the strength Q. The three source strengths and their locations are used to build up an interference velocity $\Delta u/U$, or blockage "epsilon," by adding the three component parts on the centerline. Again, a chart is used for these calculations. Charts for a rectangular tunnel of $W/H = 1.43$ and a program listing for the method are given by Hackett, Wilsden, and Lilley.[14]

As the previously described method was somewhat slow for "on-line," real-time calculations, an improved method was developed.[15] Beside the blockage correction from the source–sink model, an angle-of-attack correction using vortices was added. This method also handles swept wings and jets in a cross-flow and uses a skewed-line singularity algorithm for sources, doublets, and horseshoe vortices. The method uses influence matrices at user-specified locations for line-source elements and horseshoe vortices and uses measured wall conditions to solve for their strengths. The source matrices are the sum of two other matrices corresponding to the direct influence of the line sources and a matching but opposite sign source situated far downstream to satisfy continuity. The side-wall pressures are still used for blockage corrections.

The ceiling and floor pressures at the same longitudinal distance in the tunnel are used to obtain the lift interference. The vortex-induced effects include vertical velocities at the side walls, which, in extreme high-lift/large-model cases, will affect wall pressures and hence appear to represent a blockage dependent on lift. For this reason, the lifting solution is done first and is available for an optional computation, which removes this spurious effect. The corrected side-wall data then reflect the true blockage.

The effects on the measured pressures of model offset from the tunnel center, sweep, and angle of attack we discussed. To minimize computer storage and run time requirements, the equations for singularity strength are solved for overspecified boundary conditions using a least-squares algorithm. This has the additional benefit of smoothing the curve fit through the tunnel wall data. These procedures are described, as are the equations for the source and vortex strengths.

The matrix method of calculating the blockage correction is capable of being run on a computer in real time. For powered tests it is desirable to run at constant values of jet momentum coefficient, or tip speed ratio for rotors. The tunnel dynamic pressure with blockage corrections can be determined "on-line" and adjusted to obtain constant normalized values.

The blockage corrections,[14] together with Glauert's angle-of-attack corrections, were applied to four floor-mounted wings. These have ratios of wing area to tunnel cross-sectional area from 1.67 to 16.7%. The data agreement was quite good for lift and fairly good for induced drag. The same report also shows good correlation on sphere drag above and below the critical Reynolds number. The measured pres-

sures in the tunnel were predicted and compared to measured results for Reynolds numbers above the critical value, and good agreement was achieved past the major diameter. Similar correlation of measured pressures corrected for blockage was achieved for three geometrically similar idealized automobile models in the 16.25 X 23.25-ft Lockheed tunnel.

Pozzorini[17] reports on the application of the pressure signature method to extreme attitude experiments.

Two-Variable, or "Ashill–Keating," Method We contemplate here a situation like that indicated by Figure 9.3 with a possibly large region of rotational flow following interaction with the model but with the rotational flow not making contact with the walls in the vicinity of the model. We follow the development of Ashill and Keating.[8] Take the streamwise direction as the x direction. Then there is a region of flow within the tunnel for which the perturbation potential ϕ defined by the relation

$$\phi = \Phi - U_\infty x \tag{9.10}$$

satisfies Laplace's equation. Here, U_∞ is the stream speed in the tunnel far upstream of the model and Φ is the total velocity potential. The region of applicability is bounded by a surface, S_1, that just encloses the rotational region of flow surrounding the model and trailing downstream and a second surface, S_2, that essentially coincides with the tunnel walls for a solid-wall wind tunnel. Let v represent the volume bounded by S_1 and S_2. Application of Green's identity[18] shows that the perturbation potential within v is expressible as

$$\phi = -\frac{1}{4\pi} \int_{(S_1 + S_2)} \left(\frac{1}{r}\nabla\phi - \phi\nabla\frac{1}{r}\right) \cdot \mathbf{n}\, dS \tag{9.11}$$

The unit normal is taken positive into the region v. If the surfaces S_1 and S_2 were given geometric surfaces, panel method codes could be used to calculate the potential throughout the region, v, and the flow field. For a solid-wall wind tunnel we do know the surface S_2 except for the perturbation due to boundary layers, which we will neglect here. We are particularly interested in cases for which the surfaces S_1 is not known due to significant flow separation and the fact that the wake would in any case be convected in an unknown manner. Nevertheless, suppose we did know the surface S_1. In that case, Equation (9.11) with the integral extending only over the surface S_1 would define the flow field external to the surface S_1 in the absence of the tunnel walls. This is referred to as the "unconstrained" flow and is indicated by the equation

$$\phi_u = -\frac{1}{4\pi} \int_{(S_1)} \left(\frac{1}{r}\nabla\phi - \phi\nabla\frac{1}{r}\right) \cdot \mathbf{n}\, dS \tag{9.12}$$

Comparing these two equations and defining $\Delta\phi = \phi - \phi_u$ provides

$$\Delta\phi = -\frac{1}{4\pi} \int_{(S_2)} \left(\frac{1}{r}\nabla\phi - \phi\nabla\frac{1}{r} \right) \cdot \mathbf{n}\, dS \qquad (9.13)$$

as the potential increment due to the presence of the tunnel walls with two important caveats. These are that the surface S_1 is the same shape with and without the walls and that the distribution of **singularities** on S_1 representing the flows in the two cases are the same. Practice has shown that the method works quite well even when at least one of these conditions is not well approximated. On a solid wall the first term in the integrand of Equation (9.13) is zero, so the resulting equation is

$$\Delta\phi = \frac{1}{4\pi} \int_{(S_2)} \phi\nabla\frac{1}{r} \cdot \mathbf{n}\, dS \qquad (9.14)$$

This equation indicates that the perturbation potential is a function of quantities of the tunnel wall. These quantities can be inferred from pressure measurements on the wall, and the equation can then be used to calculate the distribution of the velocity induced by the presence of the wall throughout the regions of interest. Practice has shown that on the order of 100–200 wall pressures in a typical **low-speed** wind **tunnel** can give good results for this method. Its great advantage is that no mathematical model of the test article need be created. The wall pressure measurements are sufficient. There continues to be an active development of these methods.

9 3   RELATED DEVELOPMENTS

We have focused entirely on low-speed applications using the definition of sufficiently low Mach number so that compressibility is not a substantial influence. However, there has been a large body of work on wind tunnel wall effects catalyzed by the severe problems encountered in the conduct of experiments in the **transonic-**speed range. This work has produced both adaptive-wall wind tunnels and porous or slotted-wall wind tunnels along with extensive analysis aimed at determining how to configure **variable-geometry** walls for best advantage and how to assess residual interferences from partially open or not completely adapted walls. The analyses start from considerations very like those introduced in the preceding sections. Useful summaries and references to the literature are given by **Wolf**[19] and by Lewis and **Goodyer.**[20]

A considerable effort at collecting material defining the current state of the art in the field has gone into the new **AGARDograph** 336.[21] Both low-speed and transonic developments are included in its scope.

Minimum- or Zero-Correction Tunnels

There are three approaches to achieve either zero or small wall corrections for larger or V/STOL models with their high lifts. These are an active-wall tunnel where blowing and suction through porous tunnel walls is used, an adaptive-wall tunnel where the solid tunnel walls are deflected, and ventilated or slotted tunnels. In the first two schemes the purpose is to cause the tunnel walls to form a streamline at the walls that has the same shape at the walls as would occur in free air. Similar concepts have been studied and applied for automotive testing with the purpose of reducing the blockage effect to allow the testing of large models in a given size tunnel. The active-wall tunnel will be discussed first.

After demonstrating that the tunnel walls could be represented by vortex lattices (see the discussion of Joppa's vortex-lattice method in Section 10.8), Bernstein and Joppa carried this work forward to the concept of a tunnel using active walls to reduce the wall effects for STOL vehicles[22] using the basic assumption that the tunnel walls are in the far flow field and thus potential flow will give an accurate description of the model's flow. Note that this is the assumption underlying all of the methods of computing wall corrections. Since the detailed flow at the model is not required, the model can be represented by a simple horseshoe vortex. Then, near the walls a control surface is constructed. As solutions to potential flow problems are unique, and if at all points on the control surface the flow is identical to free air, then the model will be in free air. Since the control surface represents free air, it can be replaced with a stream tube, and therefore only the normal velocity to the control surface needs to be controlled and made equal to zero. The tunnel operates in the following manner:

With the model at some attitude and tunnel velocity the model lift is measured. Then, with the simple flow model, the flow conditions at the wall are calculated. This calculated flow is used to control flow into or out of the tunnel, which then changes the model lift. The new lift is measured and the process repeated until the walls (control surface) coincide with the free air at the tunnel walls for the measured lift. In an ideal case where injection is continuously distributed, both the mass flow and momentum across the control surface will be matched, yielding a perfect simulation. For a practicable application the flow injection cannot be controlled to yield a continuous distribution. For a given wall porosity a large number of small jets were used to match the mass flow and momentum. But both mass flow and momentum could not be simultaneously matched.

To prove this concept, tests were made with a two-dimensional wing. Free-air conditions were assumed to be met when the tunnel height was 12 times the wing chord. The active-wall tunnel used a tunnel height of twice the chord. This was done by the use of inserts that extended 4.5 chord lengths ahead of and behind the model and contained 24 plenums to control the flow through the ceiling and floor. Tests were made with both 5 and 31% porosity and using injection rates from matching mass flow to matching momentum.

Two-dimensional testing with large wing chords to tunnel heights results in the model acting like one with increased camber (see the discussion of streamline

curvature later in this chapter). This increase in camber increases with angle of attack and results in a steeper lift curve slope that yields a higher lift coefficient for a given angle of attack. The active walls will reduce lift at a fixed angle of attack.

With these data, Joppa shows that matching mass with a large momentum mismatch overcorrects the data, and for momentum match with mass mismatch the data are undercorrected. This occurred for both porosities but with a much closer match to the free-air curve for 31% porosity when compared to the 5% porosity. The experiments by Joppa demonstrate that the active-wall concept works in both theory and practice if both mass flow and momentum can be matched and that only the flow normal to the tunnel walls need be controlled using the model's measured lift.

The second approach is the adaptive wall, in which the contour of the walls is made to conform to a free-airstream tube. For a two-dimensional airfoil the tunnel has a flexible ceiling and floor. With the model installed the wall pressures are measured and compared with a calculated pressure distribution at the walls for an unlimited flow field external to the tunnel. The wall shape is altered until the two pressure fields agree within limits. If the agreement is perfect, then the tunnel flow is the same as free air. There are two approaches to calculating the unlimited flow field. One used by Ganzer[23] uses wall pressures and wall contour to calculate the unlimited flow field. This method requires no knowledge of the model and its local flow field. The second method[74] uses a doublet to represent the model.

For two-dimensional wings both Ganzer[23] and Goodyer[25] have shown that the method works in general, although there are some difficulties when either shocks or large pressure gradients are present. Goodyer also demonstrated that the method works for the blockage of a nonlifting body (cylinder) up to a blockage ratio of 29.27%.

Reference to more recent work has already been given.

A small tunnel with variable contour side walls and ceiling and a fixed floor was used by Whitfield et al.[26] to investigate the blockage for automobile tests. As the tunnel floor represents the road, it was kept fixed. There were three flexible strips in the walls and six in the ceiling. These strips slide on fixed wiper plates that extended into the tunnel when the strips deflected away from the model. Three similar representative models of automobiles were used to produce blockage ratios of 10, 20, and 30%, and tests were made at $0°$ and $10°$ yaw. Static pressures were measured on the model and the walls and ceilings. The model pressures for the three blockage ratios agreed for the contoured walls, and their levels were different than straight walls for 10 and 20% blockage. The wipers did not appear to have any effect on the data, but this may not be true for a lifting model with a deflected wake.

Sears[27] has proposed an adaptive-wall tunnel that prevents the wake of a V/STOL model from impinging on the tunnel walls.

Slotted Tunnels

In transonic testing slotted or porous test-section walls with a surrounding plenum have long been used to prevent the test section from choking at high Mach numbers. There also have been several low-speed tunnels built for V/STOL testing that have

slotted walls. This results in mixed tunnel boundary, part solid and part open. The mixed-wall boundary conditions have made it difficult to determine the proper wall corrections for this type of test section. Work continues on two and three dimensions for both blockage and deflected wakes.

It might be well to review the potential theory methods of determining wall and blockage factors for corrections. These are

1. the image method,
2. panel methods,
3. the wall perturbation method, and
4. methods using measured wall pressures or other variables.

For slotted- or porous-wall tunnels the image method is not applicable since the walls are no longer planes or surfaces of symmetry. The image system has been used for tunnels that have either an open or a closed test section. Vortex-lattice methods are used for closed test-sections. For slotted tunnels, a vortex lattice is used for the solid portion of the walls and source panels for the open portion. Inflow or outflow from the plenum determines the sign. Linear small-perturbation theory was used by Ganzer and Igeta[24] for the adaptive-wall tunnel. The wall static pressures are used in the adaptive-wall methods also, as well as for blockage corrections with fixed solid walls.

Based on the reversal of sign of the wall correction factor between open and closed test sections, it has been reasoned that a ventilated test section could reduce both the magnitude and inhomogeneity of the wall corrections for large models and high lift coefficients.

There is a large amount of work using different approaches for low-speed and transonic tunnels in attempting to calculate wall corrections for slotted tunnels. The basic problem is in predicting how the tunnel air on the suction side of the model flows into and out of the plenum through longitudinal slots or porous walls. But at the time this edition was written there is still no completely accepted methodology for correcting force and moment coefficients for lifting models in this type of tunnel. It may well be that the problem is to match both the mass flow and momentum through the walls simultaneously, as noted by Bemstein and Joppa.[22]

The use of slotted walls and ceiling with a solid floor for automobiles has also been investigated.[28] Again, the purpose is to increase the allowable blockage ratio. In this work the model was at zero yaw and its location within a test section, equal to twice the automobile length, had to be empirically determined. The reentry of plenum air into the diffuser had to be carefully controlled. The slotted tunnel was able to test up to a 21.4% blockage ratio.

9.4   BODIES SPANNING THE TUNNEL

In order to study effects primarily concerned with airfoils sections, it is customary to build models of constant chord that completely span the test section from wall

to wall or floor to ceiling. The trailing vortices are then practically eliminated, and the image system for a small *wing* consists of a vertical row of vortices (having alternately plus and minus signs) above and below the model. Usually, however, when two-dimensional tests are made, the models are made of large chord to obtain the highest Reynolds number possible, and the wing must be represented by a distribution of vortices instead of a single one. The effect of the floor and ceiling of the tunnel is to restrain the naturally free air curvature of the flow so that the model acts like one with extra camber.

The effects of the walls on the model thickness and wake are subject to solid and wake blockage, as well as buoyancy if the tunnel has a longitudinal static pressure gradient. These effects will be considered separately.

The wall corrections for two-dimensional testing have been discussed by Allen and Vincenti.[29] We generally follow their treatment. Since the trailing vortices that escape in the boundary layer are quite weak, no downwash corrections are needed.

Often the end plates in the wall are equipped with various schemes to remove or thin the boundary layer and to avoid separation on the side walls for models with high-lift flaps. Terminating the flaps short of the wall will produce a pair of shed vortices and destroys the concept of a two-dimensional wing with a uniform span load.

Buoyancy

Almost all wind tunnels with closed throats have a variation in static pressure along the axis of the test section resulting from the thickening of the boundary layer as it progresses toward the exit cone and to the resultant effective diminution of the jet area. Some tunnels have slightly expanding test sections to minimize this effect. It follows that the pressure is usually progressively more negative as the exit cone is approached, and there is hence a tendency for the model to be "drawn" downstream.

Glauert[30] found that the magnitude of the gradient may be expressed as a nondimensional factor k defined by

$$\frac{dp}{dl} = \frac{-k(\rho/2)\ V^2}{B}$$

where l is jet length (ft), p is pressure (lb/ft^2), and B is jet width (ft). An ideal tool for this measurement is a long static tube. The factor k has been observed in the range 0.016-0.040 for a closed square jet of width B but should be experimentally measured for a given tunnel.

The amount of "horizontal buoyancy" is usually insignificant for wings, but for fuselages and nacelles it is larger and becomes important. For large torpedolike bodies, it can be of the order of the minimum drag in some tunnels.

Corrections may be calculated as follows. Suppose that the static pressure variation along a jet is shown in Figure 9.14 and that the model to be tested has the cross-sectional area S, as shown in Figure 9.15. It will be seen that the variation of static pressure from, say, station 2 to station 3 is $p_2 - p_3$ and that this pressure
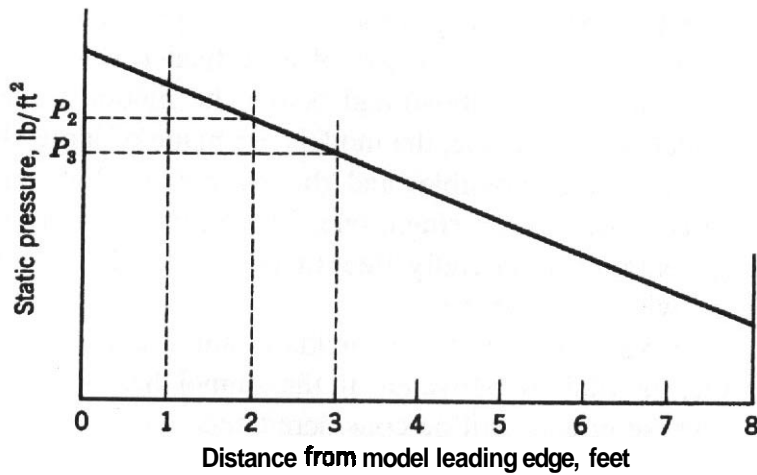
FIGURE 9.14   Static pressure gradient.

differential acts on the average area $\frac{1}{2}(S_2 + S_3)$. The resulting force for that segment of the fuselage is therefore

$$\Delta D_B = (p_2 - p_3)[\tfrac{1}{2}(S_2 + S_3)]$$

The expression for the total buoyancy drag is therefore given by

$$D_B = \int_0^l S(x)p'(x)\, dx \tag{9.15}$$

where

$$p'(x) \equiv \frac{dp}{dx} \tag{9.16}$$

This equation can be evaluated by plotting local static pressure against body
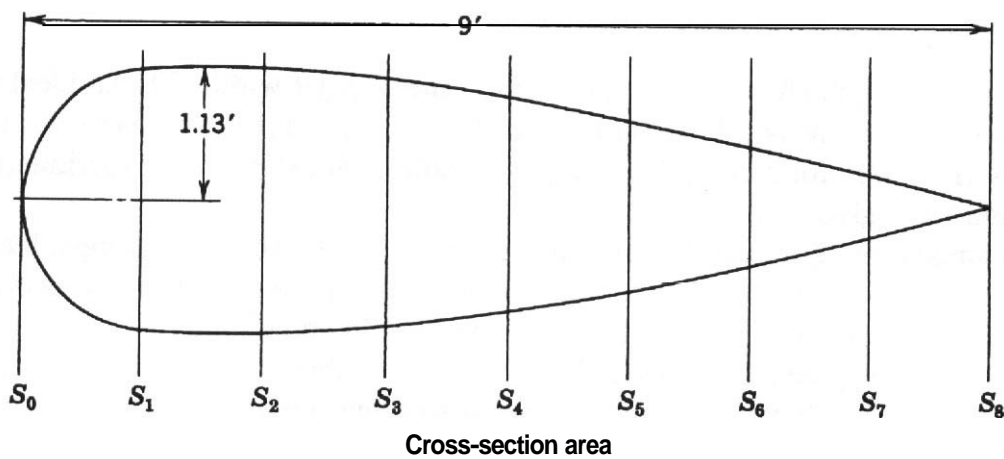
FIGURE 9.15   Cross-sectional variation along streamwise direction.

section area, the buoyancy then becoming the area under the curve, or by plotting the local static pressure coefficient against body section area divided by wing area to get the buoyancy drag coefficient directly.

For the case where the longitudinal static pressure gradient is a constant, that is, $p(x)$ is a straight line, the equation becomes

$$D_B = p' \int_0^1 S(x)\, dx = p' \times \text{Vol} \tag{9.17}$$

where $S(x)$ is the fuselage cross-sectional area at station x, x is the distance from the fuselage nose and p' is the slope of the longitudinal static pressure curve.

The existence of a falling static pressure curve implies that the test section is getting effectively smaller; in other words, the streamlines are being squeezed by the contracting tube. Adding the squeezing effect to the pressure-gradient effect, Glauert[31] found that the total drag increment for a constant gradient (for a two-dimensional body) is

$$D_B = \tfrac{1}{2}\pi\lambda_2 t^2 p' \quad \text{lb/ft span}$$

where t is body thickness and λ_2 is the body shape factor from Figure 9.16.
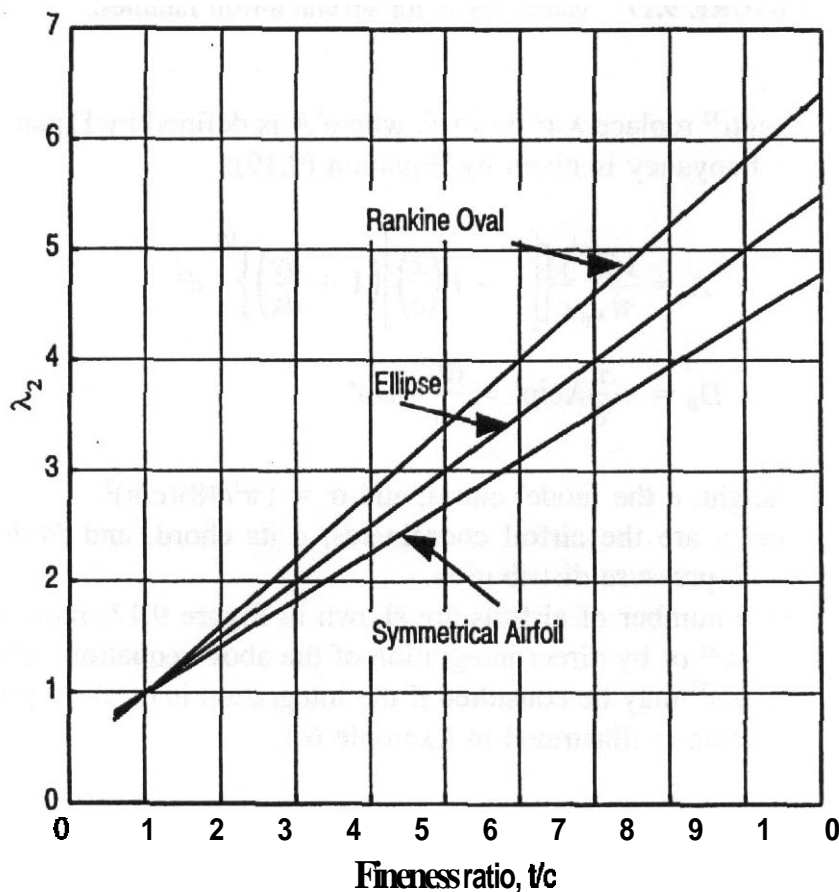
FIGURE 9.16   Shape factors for selected forms.
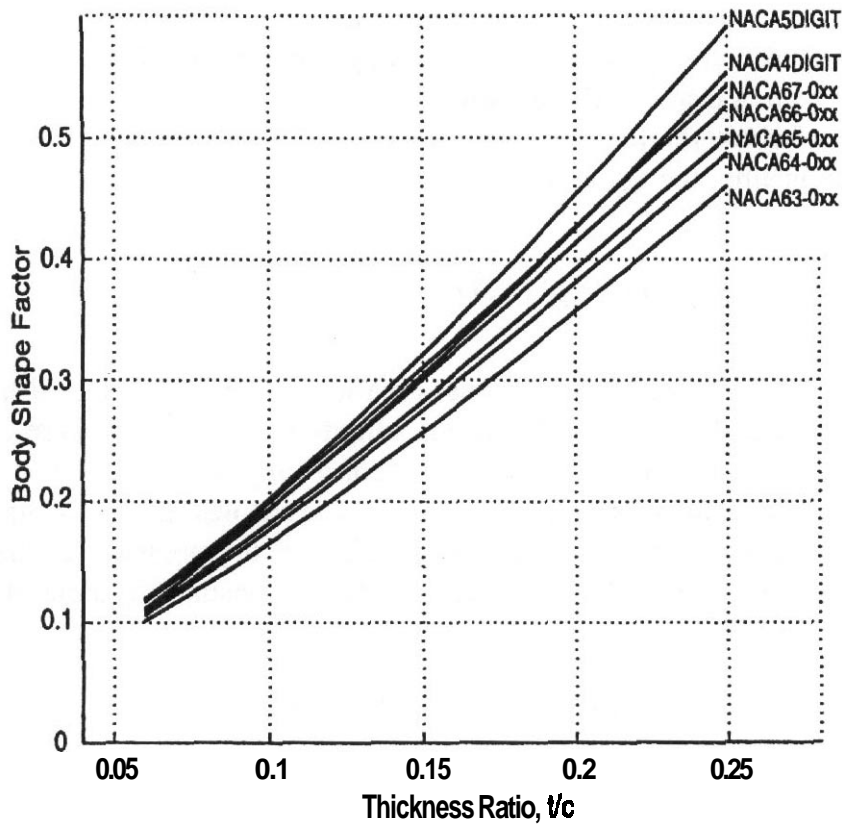
FIGURE 9.17   Values for A for several airfoil families.

Allen and Vincenti[32] replace $h_2 t^2$ by $\frac{1}{4} \Lambda c^2$, where A is defined by Equation (9.18) and the drag from buoyancy is given by Equation (9.19):

$$\Lambda = \frac{16}{\pi} \int_0^l \frac{y}{c} \left\{ \left[1 - P\left(\frac{x}{c}\right) \right] \left(1 + \frac{dy}{dx} \right) \right\}^{1/2} d\frac{x}{c} \tag{9.18}$$

$$D_B = -\frac{\pi}{8} \Lambda c^2 p' = \frac{6h^2}{\pi} \Lambda \sigma p' \tag{9.19}$$

Here h is tunnel height, c the model chord, and $\sigma = (\pi^2/48)(c/h)^2$.

The terms x and y are the airfoil coordinates, c its chord, and $P(x/c)$ its no-camber, symmetrical, pressure distribution.

Values of A for a number of airfoils are shown in Figure 9.17; more are given by Allen and Vincenti[32] or by direct integration of the above equation. Abbott, Von Doenhoff, and Strivers[33] may be consulted if the integration is used. Application of the buoyancy correction is illustrated in Example 6.1.

Solid Blockage

The presence of the tunnel walls confining the flow around a model in the test section reduces the area through which the air must flow as compared to free-air

conditions and hence, by continuity and Bernoulli's equation, increases the velocity of the air as it flows in the vicinity of the model. This increase of velocity, which is approximated as constant over the model for customary model sizes, is called *solid blockage.* Its effect is a function of model thickness, thickness distribution, and model size and is independent of the camber. The solid-blockage velocity increment at the model is much less (about one-fourth) than the increment one obtains from the direct area reduction, since it is the streamlines far away from the model that are most displaced. The average velocity in the lateral plane of the model *is* proportionately increased.

To understand the mathematical approach, consider solid blockage for a right circular cylinder in a two-dimensional tunnel. The cylinder, which may be simulated by a doublet of strength $\mu = 2\pi V a^2$, where a is cylinder radius, is "contained by an infinite vertical series of doublets of the same strength as the one simulating the model. Pope[34] (pp. 46, 73) or Katz and Plotkin[4] may be consulted. The axial velocity due to the first doublet is

$$\Delta V = \frac{\mu}{2\pi h^2}$$

so that

$$\frac{\Delta V}{V_u} = \frac{a^2}{h^2}$$

where V_u is uncorrected velocity.

Since the velocity produced by a doublet varies inversely with the square of the distance from the doublet, the two-sided infinite series may be summed as

$$\varepsilon_{sb} = \left(\frac{\Delta V}{V_u}\right)_{total} = 2\sum_{1}^{\widetilde{\infty}} \frac{1}{n^2} \frac{a^2}{h^2}$$

$$= \frac{\pi^2}{3} \frac{a^2}{h^2}$$

It is seen that a large 2-ft-diameter cylinder in a tunnel 10 ft high would act as though the clear jet speed were increased by 3.3%.

The preceding development was anticipated by our presentation of an idealized example. See Figures 9.5–9.9.

Now, the blockage due to a given airfoil of thickness t may be represented as that due to an "equivalent" cylinder of diameter $t\sqrt{\lambda_2}$, and with this approach the solid blockage for any two-dimensional body may be found from simple doublet summation. Glauert[31] wrote the solid-blockage velocity increment as

$$\varepsilon_{sb} = \frac{\pi^2}{3} \frac{\lambda_2}{4} \frac{t^2}{h^2} = 0.822\lambda_2\frac{t^2}{h^2} \tag{9.20}$$

Values of λ_2 may be found in Figure 9.16. For an open jet the constant becomes -0.411.

Allen and Vincenti[32] rewrite Equation (9.20) by introducing a as in Equation (9.19), and $\Lambda = 4\lambda_2 t^2/c^2$. Their result is then

$$\varepsilon_{sb} = \Lambda\sigma \tag{9.21}$$

where A and a have the same values as in Equation (9.19). The manner of using this increment will be held until a later time.

A simpler form for the solid-blockage correction for two-dimensional tunnels has been given by Thom.[35] It has the merit of showing the parameters upon which the correction depends a little more clearly than (9.21). Thom's solid-blockage correction is

$$\varepsilon^{sb} = \frac{K_1(\text{model volume})}{C^{3/2}} \tag{9.22}$$

where K_1 equals 0.74 for a wing spanning the tunnel breadth and 0.52 for one spanning the tunnel height in the case of 7 × 10-type tunnels. (A good approximation for airfoil model volume is 0.7 × model thickness × model chord × model span.) Klunker and Harder[36] give corrections for very large models.

The term C above is the tunnel test-section area, which, if a little greater accuracy is desired, may be properly taken as the geometric area less the boundary layer displacement thickness taken around the perimeter. Usually, the approximation that the displacement thickness is one-sixth of the boundary layer thickness works well, since it is inevitable that the boundary layer is turbulent. (For the laminar case, as a matter of interest, one-third would be a good approximation for the displacement thickness.) It is not possible to give an approximation for the displacement thickness in a wind tunnel, since it varies with roughness, cracks, leaks, Reynolds number, and Mach number. Thus, the thickness will have to be measured using a boundary layer mouse, hot wire, total probe, and the like.

The boundary layer displacement thickness, when it is desired, may be calculated from

$$\delta^* = \int_0^Y \frac{u}{V_0}dy$$

where u is the local velocity in the boundary layer at a height y above the surface, Y is the boundary layer thickness, and V_0 is the free-stream velocity.

Several wind tunnels of the 7 × 10 ft general size seem to have boundary layer displacement thicknesses near the center of the test section of about $\frac{1}{2}-\frac{3}{4}$ in.
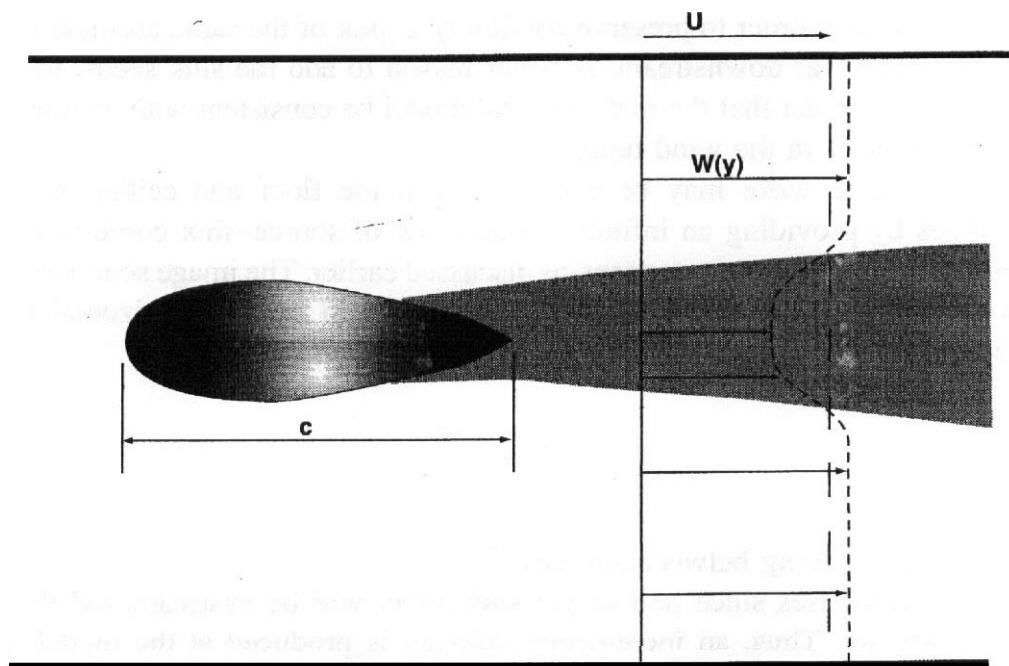
FIGURE 9.18   Schematic of blockage conditions.

The above method has the advantage that it can be applied with very little computational effort. While it makes the tunnel walls streamlines, it does not accurately make the model surface a streamline. This can be achieved with greater accuracy by using a panel code. This option is becoming easier and easier to implement as routinely available computer power increases.

Wake Blockage

Any real body without suction-type boundary layer control will generate a wake that will have a mean velocity lower than the free stream. According to the law of continuity, the velocity outside the wake in a closed tunnel must be higher than the free stream in order that a constant volume of fluid may pass through each cross section (Figure 9.18). The higher velocity in the main stream has, by Bernoulli's principle, a lowered pressure, and this lowered pressure, arising as the boundary layer (which later becomes the wake) grows on the model, puts the model in a pressure gradient, and results in a velocity increment at the model.

To compute this wake effect, we must first mathematically simulate the wake and the tunnel boundaries. The wake simulation is fairly simple. In the two-dimensional case a line source at the wing trailing edge emitting, say, "blue" fluid will result in a "blue" region similar to a wake. This is the reason we introduced a "wake body" in our earlier idealized example. Since the only drag existent is represented by this wake, the proper quantity Q to be emitted may be determined by

$$D = \rho Q V$$

It is said that in order to preserve continuity, a sink of the same absolute strength should be added far downstream. A better reason to add the sink seems to be that it is required in order that the mathematical model be consistent with an unchanged approach velocity in the wind tunnel.

The simulated wake may be contained with the floor and ceiling remaining streamlines by providing an infinite vertical row of source–sink combinations according to the image system concept, as discussed earlier. The image sources produce no axial velocity at the model, but the image sinks will induce a horizontal velocity in the amount

$$\Delta V = \frac{Q/h}{2}$$

where h is the spacing between sources.

The factor $\frac{1}{2}$ arises since half of the sink effect will be upstream and the other half downstream. Thus, an incremental velocity is produced at the model by the walls that should be added to the tunnel-clear results to allow for "wake blockage." A useful form of the above statement is

$$\varepsilon_{wb} = \frac{\Delta V}{V_u} = \tau c_{du}$$

where

$$\tau = \frac{c/h}{4}$$

Thorn's paper[35] yields the same relation for two-dimensional wake blockage.

Maskell[37] has examined the effect of the flow outside the wake and how its higher speed results in a reduced pressure over the rearward portion of the model. For the two-dimensional case this equals the wake image effect, and he suggests that the correction be

$$\varepsilon_{wb} = \frac{\Delta V}{V_u} = \frac{c/h}{2} c_{du} \tag{9.23}$$

We see here the direct introduction of a "measured variable," the uncorrected drag coefficient c_{du}. The wake gradient effect, from Allen and Vincenti,[32] is

$$\Delta C_{d,wb} = \Lambda \sigma \tag{9.24}$$

and is usually quite small.

Wake blockage may be neglected for the rare case of a two-dimensional test section with open top and bottom. Upon evaluation it would be opposite in sign to

the correction for closed sections. Also, recent work by Mercker and Wiederman[38] stimulated by ground vehicle applications has shown that the length of open test sections may become important and may introduce corrections of significance that are not indicated by the model of an infinite-length open jet section.

Streamline Curvature

The presence of ceiling and floor prevents the normal curvature of the free air that occurs about any lifting body, and—relative to the straightened flow—the body appears to have more camber (around 1% for customary sizes) than it actually has. Accordingly, the airfoil in a closed wind tunnel has more lift and moment about the quarter chord[39] at a given angle of attack than it would in free air, and the angle of attack is too large as well. This effect is not limited to cambered airfoils, since, using the vortex analogy, any lifting body produces a general curvature in the airstream.

We may gain an insight into the streamline curvature effect, and calculate values as well, by assuming that the airfoil in question is small and may be approximated by a single vortex at its quarter-chord point. The image system necessary to contain this vortex between floor and ceiling consists of a vertical row of vortices above and below the real vortex. The image system extends to infinity both above and below and has alternating signs. Let us start by considering the first image pair as shown in Figure 9.19. It is apparent that they induce no horizontal velocity since
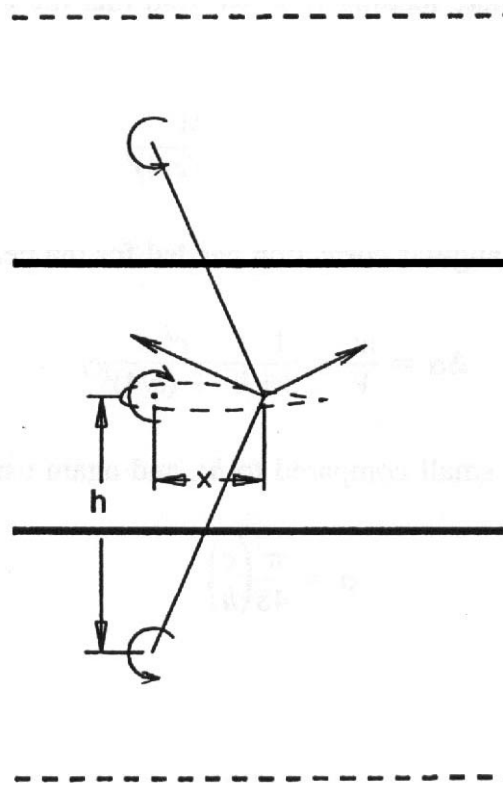
FIGURE 9.19   First pair of image vortices for a lifting surface.

the horizontal components cancel, but, as will also he seen, the vertical components add.

From simple vortex theory, the vertical velocity at a distance x from the lifting line will be

$$w_v = \frac{\Gamma}{2\pi} \frac{1}{\sqrt{h^2 + x^2}} \frac{x}{\sqrt{h^2 + x^2}} = \frac{\Gamma}{2\pi} \frac{x}{h^2 + x^2}$$

Substitution of reasonable values for x and h into the above equation reveals that the boundary-induced **upwash** angle varies almost linearly along the chord, and hence the stream curvature is essentially circular.

The chordwise load for an airfoil with circular camber may be considered to be a flat plate loading plus an elliptically shaped loading. (See p. 110 of Pope[34].) The magnitude of the flat plate load is determined from the product of the slope of the lift curve $(2\pi/\text{rad})$ and the boundary-induced increase in the angle of the tangent at the half-chord point because for circular camber the curve at this point is parallel to the line connecting the ends of the **camberline.** The load is properly computed as an **angle-of-attack** correction.

The elliptical loading is determined by the product of the slope of the lift curve and the angular difference between the zero-lift line (i.e., the slope of the curve at the **three-quarter** chord point) and the chord line (the angle at the half chord). The lift, pitching moment, and hinge moment corrections are due to this elliptic component of the load.

Considering the flat-plate loading first, we find that the **upwash** induced at the half chord by the two images closest to the real airfoil is

$$w_v = 2 \frac{\Gamma}{2\pi} \frac{c/4}{h^2 + (c/4)^2}$$

Since $\Gamma = cc_i V/2$, the angular correction needed for the nearest images becomes

$$\Delta\alpha = \frac{w_v}{V} = \frac{1}{8\pi} \frac{c^2}{h^2 + (c/4)^2} c_l$$

Assuming that $(\tfrac{1}{4}c)^2$ is small compared to h^2, and again using

$$\sigma = \frac{\pi^2}{48}\left(\frac{c}{h}\right)^2$$

we get

$$\Delta\sigma = \left(\frac{6\sigma}{\pi^2}\right)c_l$$

The second pair of vortices being twice as far away will be roughly one-fourth as effective, and the third pair one-ninth, so that for the images above and below the real wing, we have

$$\Delta\alpha_{sc} = \frac{6\sigma}{\pi^3}\left(1 - \frac{1}{4} + \frac{1}{9} - \frac{1}{16}\cdots\right)c_l$$

$$= \frac{6}{\pi^3}\frac{\pi^2}{12}\sigma c_l$$

since the alternating series shown above equals $\frac{1}{12}$ when summed to infinity. The additive lift correction is

$$\Delta c_{l,sc} = -2\pi\left(\frac{\pi}{2}\right)\sigma c_l = \sigma c_l \qquad (9.25)$$

and the additive moment correction is

$$\Delta c_{m\frac{1}{4},sc} = \frac{-\sigma}{4}\Delta c_{l,sc} \qquad (9.26)$$

Allen and Vincenti[32] spread the vorticity out along the airfoil chord instead of concentrating it at the quarter chord. The lift and moment values of the simple analysis remain the same, but the angle-of-attack correction becomes

$$\Delta\alpha_{sc} = \frac{57.3\sigma}{2\pi}(c_{lu} + 4c_{m\frac{1}{4}u}) \qquad (9.27)$$

If the chord is kept less than 0.7 tunnel height (and it usually is), wall effects on the **distribution** of lift may be neglected.

Since there is no drag in theoretical two-dimensional flow, there is no streamline curvature correction for drag.

Summary: Two-Dimensional Corrections

The complete low-speed wall effects for two-dimensional wind tunnel testing are summarized here for convenience. The data with the subscript u are uncorrected data based on clear stream q, with the exception of drag, which must have the buoyancy due to a longitudinal static pressure gradient removed before final correction.

Velocity [from (9.21) and (9.23)] is given as

$$V = V_u(1 + \varepsilon) \qquad (9.28)$$

where $\varepsilon = \varepsilon_{sb} + \varepsilon_{wb}$.

Dynamic pressure [from expanding (9.28) and dropping higher order terms] is

$$4 = q_u(1 + 2\varepsilon) \tag{9.29}$$

The Reynolds number [from (9.28)] is

$$R = R_u(1 + \varepsilon) \tag{9.30}$$

For a, c_l, and $c_{m\frac{1}{4}}$ [from (9.25)–(9.27)] we have

$$\alpha = \alpha_u + \frac{57.3\sigma}{2\pi}(c_{lu} + 4c_{m\frac{1}{4}u}) \tag{9.31}$$

$$c_l = c_{lu}(1 - \sigma - 2\varepsilon) \tag{9.32}$$

$$c_{m\frac{1}{4}} = c_{m\frac{1}{4}u}(1 - 2\varepsilon) + \frac{1}{4}\sigma c_l \tag{9.33}$$

For c_{d0} (from the dynamic pressure effect plus the wake gradient term) we get

$$c_{d0} = c_{d0u}(1 - 3\varepsilon_{sb} - 2\varepsilon_{wb}) \tag{9.34}$$

For the above,

$$\sigma = \frac{\pi^2}{48}\left(\frac{c}{h}\right)^2$$

The case of the free two-dimensional jet (floor and ceiling off but wingtip walls in place) requires an additional factor that accounts for the downward deflection of the airstream as follows (both flow curvature and downwash deflection are included):

$$\Delta\alpha = -\left[\frac{1}{4}\left(\frac{c}{h}\right)c_l + \frac{\pi}{24}\left(\frac{c}{h}\right)^2(c_l)\right](57.3) \tag{9.35}$$

$$\Delta c_{d0} = \frac{1}{4}\left(\frac{c}{h}\right)c_l^2 \tag{9.36}$$

$$\Delta c_{m\frac{1}{4}} = -\frac{\pi^2}{96}\left(\frac{c}{h}\right)^2 c_l \tag{9.37}$$

These values should be added to the observed data.

It is noted that a drag correction is present here and further that these corrections are extremely large. Since the jet is free to expand, blockage corrections are not necessary.

The case where a wing completely spans a free jet without lateral restraining wall is not of much value in practice. Such a setup is rarely used except in small tunnels for preliminary tests. The spillage around the wingtip makes the wing less effective, so that the coefficients as obtained should he increased. In this case the two-dimensional

airfoil is in reality a very low aspect ratio wing. One test (unpublished) indicates that for clh = 0.2 the measured lift was 18% lower than the expected two-dimensional values.

Example 9.1   Find the corrected data for the following two-dimensional test: model 65-209 airfoil; test speed 100 mph; test section 2 X 7 ft; model chord 2.5 ft, standard sea level air; $\alpha_u = 4.0''$; lift 61.30 lb; drag 7.54 lb; moment about quarter chord −7.98 ft-lb; tunnel longitudinal static pressure gradient −0.02 lb/ft²/ft. Neglect area reduction by boundary layer.

From Figure 9.17, A = 0.163, and from (9.19) and following, $\sigma = 0.0262$ and the buoyancy is

$$\Delta D_B = -\frac{6(7)^2}{\pi}(0.163)(0.0262)(-0.02)$$

$$= 0.008 \text{ lb}$$

The uncorrected coefficients are

$$c_{lu} = \frac{61.30}{25.58 \times 5.0} = 0.48$$

$$c_{d0u} = \frac{7.54 - 0.008}{25.58 \times 5.0} = 0.00589$$

$$c_{m\frac{1}{4}u} = -\frac{7.98}{25.58 \times 5.0 \times 2.5} = -0.025$$

The corrected coefficients are

$$\alpha = 4.0° + \frac{(57.3)(0.0262)}{2\pi}[0.48 + 4(-0.025)] = 4.09°$$

$$c_l = 0.48[1 - 0.0262 - 2(0.163)(0.0262) - 2(0.0893)(0.00589)]$$

$$= 0.472$$

$$c_{d0} = 0.00589[1 - 3(0.163)(0.0262) - 2(0.0893)(0.00589)]$$

$$= 0.00577$$

$$c_{m\frac{1}{4}} = (-0.025)[1 - 2(0.163)(0.0262) - 2(0.0893)(0.00589)]$$

$$+ (0.0262)(0.472/4)$$

$$= -0.0216$$

Experimental Verification, Two-Dimensional Corrections

By testing models of several sizes at the same Reynolds number, data were obtained that have yielded an excellent check on the wall corrections presented. These, from Allen and Vincenti,[32] are shown in Figure 9.20 uncorrected and in Figure 9.21 corrected. It is seen that the method given brings the data into agreement.
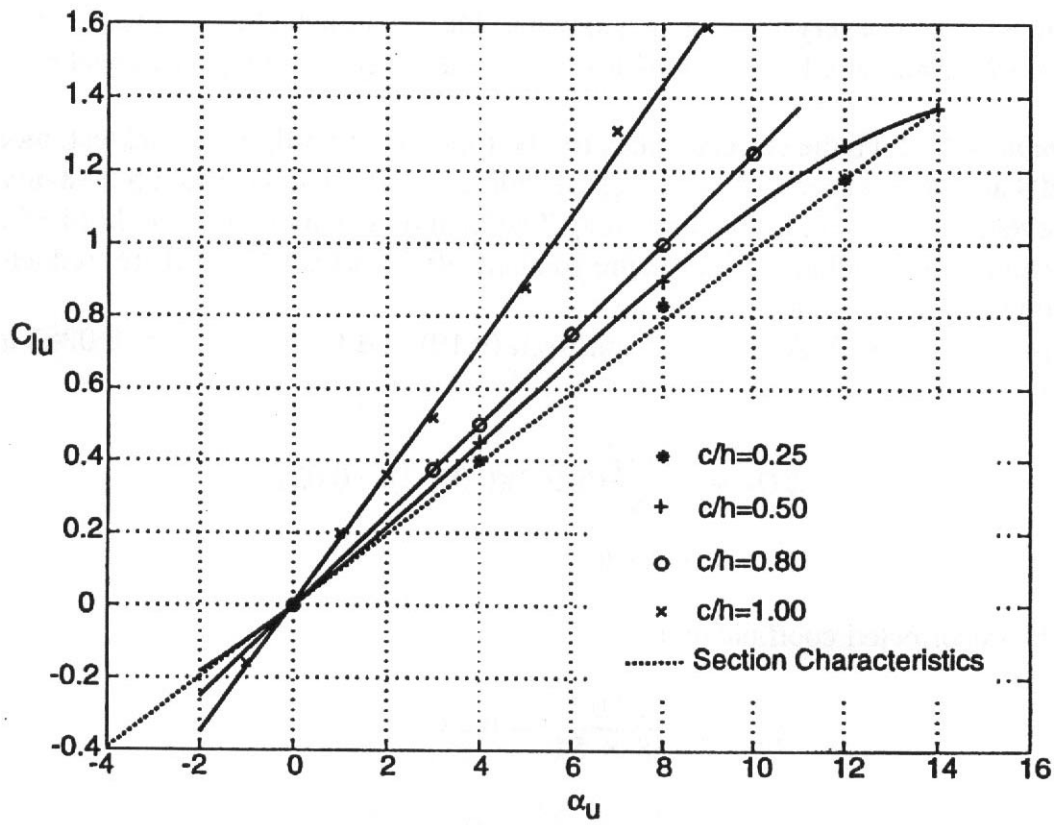
FIGURE 9.20   Lift characteristics for NACA 0012 airfoil section uncorrected for tunnel-wall interference.
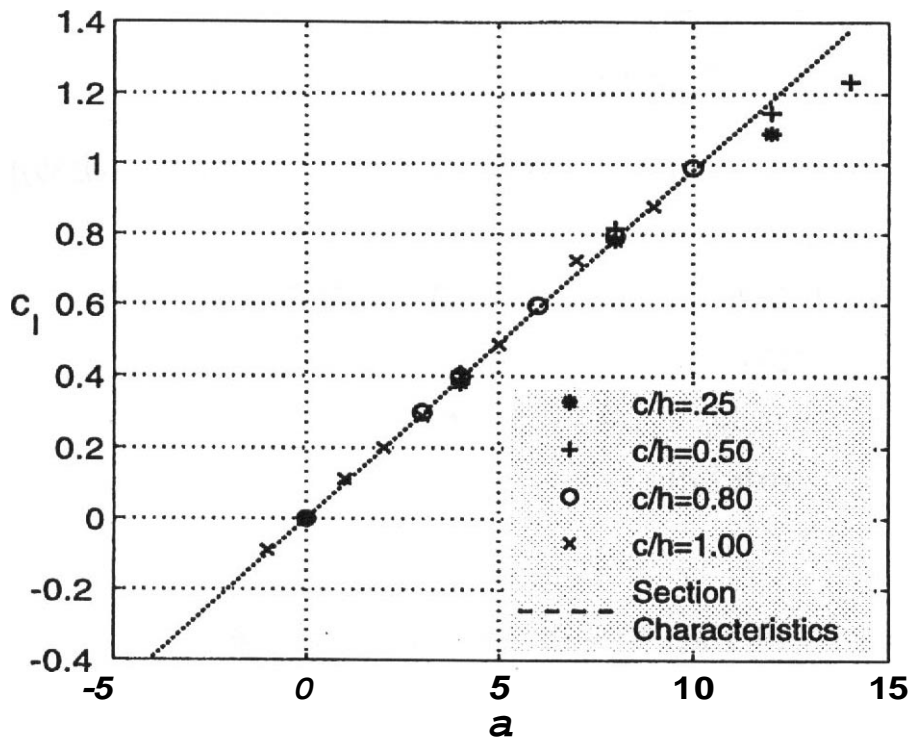
FIGURE 9.21   Data of Figure 9.19 corrected for tunnel-wall interference.

REFERENCES AND NOTES

1. Kellogg, O. D., *Foundations of Potential Theory,* Dover Publications, New York, 1953.

2. Milne-Thomson, L. M., *Theoretical Hydrodynamics,* Dover Publications, New York, 1996 (first edition published by Macmillan & Co., 1938).

3. Lamb, H., *Hydrodynamics,* 6th ed., Cambridge University Press, Cambridge, 1932 (first edition published 1879).

4. Katz, J., and Plotkin, A., *Low Speed Aerodynamics, from Wing Theory to Panel Methods,* McGraw-Hill, New York, 1991.

5. Joppa, R. G., "Wind Tunnel Interference Factors for High-Lift Wings in Closed Wind Tunnels," NASA CR 2191, 1973.

6. Maskell, E. C., "A Theory of the Blockage Effects on Bluff Bodies and Stalled Wings in a Closed Wind Tunnel," ARC R&M 3400, 1965.

7. Hackett, J. E., and Wilsden, D. J., "Determination of Low Speed Wake Blockage from Wall Static Pressure Measurements," AGARD CP 174, Paper 23, Oct. 1975.

8. Ashill, P. R., and Keating, R. F. A., "Calculation of Tunnel Wall Interference from Wall Pressure Measurements," *Aeronaut. J.,* 9 5 36–52, Jan. 1988.

9. Hackett, J. E., "Tunnel Induced Gradients and Their Effect on Drag," *AIAA J.,* **34**(12), 1172–1183, 1996.

10. Ashill, P. R., Jordan, R., and Simmons, M. J., "Recent Experience in the Prediction and Assessment of Wind Tunnel Wall Interference," Paper 21, in *Proceedings Wind Tunnels and Wind Tunnel Test Techniques,* Royal Aeronautical Society, Cambridge, United Kingdom, 1997.

11. Rueger, M., Crites, R., and Weirich, R., "Comparison of Conventional and Emerging ("Measured Variable") Wall Correction Techniques for Tactical Aircraft in Subsonic Wind Tunnels," AIAA Paper 95-0108, presented at the Thirty-Third Aerospace Sciences Meeting and Exhibit, Reno, NV, Jan. 1995.

12. Hackett, J. E., and Boles, R. A., "Highlight Testing in Closed Wind Tunnels," *J. Aircraft,* 12, 1976 (see also AIAA Paper 74-641, July 1974).

13. Hackett, J. E., and Wilsden, D. J., "Determination of Low Speed Wake Blockage Corrections via Tunnel Wall Static Pressure Measurements," AGARD CP 174, Paper 23, Oct. 1975.

14. Hackett, J. E., Wilsden, D. J., and Lilley, D. E., "Estimation of Tunnel Blockage from Wall Pressure Signatures: A Review and Data Correlation," NASA CR 152,241, Mar. 1979.

15. Hackett, J. E., Sampath, S., and Phillips, C. G., "Determination of Wind Tunnel Constraints by a Unified Wall Pressure Signature Method. Part I: Applications to Winged Configurations," NASA CR 166,186, June 1981.

16. Hackett, J. E., Sampath, S., Phillips, C. G., and White, R. B., "Determination of Wind Tunnel Constraint Effects by a Unified Wall Pressure Signature Method. Part II: Application to Jet-in-Crossflow Cases," NASA CR 166,187, Nov. 1981.

17. Pozzorini, R., 'Wind Tunnel Corrections by the Unified Hackett Method: Selected Results for Extreme Attitude Model Tests," Paper 16, in *Proceedings of Wind Tunnels and Wind Tunnel Test Techniques,* Royal Aeronautical Society, Cambridge, United Kingdom 1997.

18. Katz, J., and Plotkin, A., *Low-Speed Aerodynamics, from Wing Theory to Panel Methods,* McGraw-Hill, New York, 1991, Chapter 3.

19. Wolf, S. W. D., "Adaptive Wall Technology for Minimization of Wind Tunnel Boundary Interferences—A Review," in *Proceedings of International Conference on Adaptive Wall Wind Tunnel Research and Wall Interference Correction,* Xian, China, June 1991, Northwestern Polytechnical University.

20. Lewis, M. C., and Goodyer, M. J., "Two Dimensional Wall Adaptation for Three Dimensional Flows," in *Proceedings of International Conference on Adaptive Wall Wind Tunnel Research and Wall Interference Correction,* Xian, China, June 1991, Northwestern Polytechnical University.

21. Ewald, B., Ed., "Wind Tunnel Wall Corrections," AGARDograph 336, 1998.

22. Bernstein, S., and Joppa, R. G., "Development of Minimum Correction Wind Tunnels," *AIAA J. Aircraft,* 13, 243–247, 1976.

23. Ganzer, U., "Wind Tunnel Corrections for High Angle of Attack Models," Paper 4, AGARD Report 692, Munich, 1981.

24. Ganzer, U., and Igeta, Y., "Transonic Tests in a Wind Tunnel with Adapted Walls," ICAS-82-5.4.5, in *Proceedings of the Thirteenth Congress of the International Council of the Aeronautical Sciences,* Vol. 1, AIAA, New York, 1982, pp. 752–760.

25. Goodyer, M., "Wind Tunnel Corrections for High Angle of Attack Models," Paper 7, AGARD Report 692, Munich, 1981.

26. Whitfield, J. D., Jacocks, J. L., Dietz, W. E., and Pate, S. R., "Demonstration of the Adaptive Wall Concept Applied to an Automotive Wind Tunnel," Paper 82-0584, paper presented at the Twelfth AIAA Aerodynamic Testing Conference, Williamsburg, VA, 1982.

27. Sears, W. R., "Wind Tunnel Testing of V/STOL Configurations at High Lift," ICAS-82-5.4.1, in *Proceedings of the Thirteenth Congress of the International Council of the Aeronautical Sciences,* Vol. 1, A M , New York, 1982, pp. 720–730.

28. Raimondo, S., and Clark, P. J. F., "Slotted Wall Test Section for Automotive Aerodynamic Test Facilities," Paper 82-0585, presented at the Twelfth AIAA Aerodynamic Testing Conference, Williamsburg, VA, 1982.

29. Allen, H. J., and Vincenti, W. G., "Wall Interference in a Two-Dimensional-Flow Wind Tunnel with Consideration of the Effect of Compressibility," NACA TR 782, 1944.

30. Glauert, H., "Wind Tunnel Interference on Wings, Bodies, and Airscrews," ARC R&M 1566, 1933.

31. Glauert, H., "Wind Tunnel Interference on Wings, Bodies, and Airscrews, ARC R&M 1566, 1933.

32. Allen, H. J., and Vincenti, W. G, 'Wall Interference in a Two-Dimensional-Flow Wind Tunnel with Consideration of the Effect of Compressibility," NACA TR 782, 1944.

33. Abbott, I. H., Von Doenhoff, A. E., and Strivers, L. S., Jr., "Summary of Airfoil Data," NACA TR 824, 1948.

34. Pope, A., *Basic Wing and Airfoil Theory,* McGraw-Hill, New York, 1951.

35. Thorn, A., "Blockage Corrections in a High Speed Wind Tunnel," ARC R&M 2033, 1943.

36. Klunker, E. B., and Harder, K. C., "On the Second-Order Tunnel Wall Constriction Correction in Two-Dimensional Compressible Flow," TN 2350, 1951.

37. Maskell, E. C., "A Theory of the Blockage Effects on Bluff Bodies and Stalled Wings in a Closed Wind Tunnel," ARC R&M 3400, 1965.

38. Mercker, E., and Wiedemann, J., "On the Correction of Interference Effects in Open Jet Wind Tunnels," SAE Paper 960671, 1996.

39. The moment about the half chord is independent of the camber and has no curvature effect.

10 Boundary Corrections 11: Three-Dimensional Flow

The concepts on which wall corrections are founded are exactly the same for two-dimensional and three-dimensional treatments. The geometry of the models, the wind tunnels, and the flow fields are of course more complex in the three-dimensional treatment.

We reiterate a key aspect of the discussion in Chapter 9: All wall correction methods are based on the idea that the highly rotational flow regions generated on the one hand by close contact with the walls and on the other hand by close contact with the test article are separated by a significant volume of fluid for which Laplace's equation is a useful model of the behavior.

10.1 BUOYANCY

The philosophy behind the buoyancy correction has been covered in Chapter 9. For the three-dimensional case the total correction (pressure gradient and streamline squeezing effect) has been given by Glauert[1] as

$$AD, = -\frac{\pi}{4}\lambda_3 t^3 \frac{dp}{dl}$$ (10.1)

where λ_3 is the body shape factor for three-dimensional bodies from Figure 10.1 and t is the body maximum thickness.

Example 10.1   Calculate the drag due to buoyancy for the model of Figure 9.15 when tested in a closed round tunnel of 9 ft diameter at 100 mph. The static pressure gradient is 0.026 lb/ft^2/ft.

  1. The volume of the body is 16.62 ft^3. Neglecting the virtual mass,

$$\Delta D_B = \frac{dp}{dl}(\text{volume}) = (0.026)(16.62) = 0.43 \text{ lb}$$
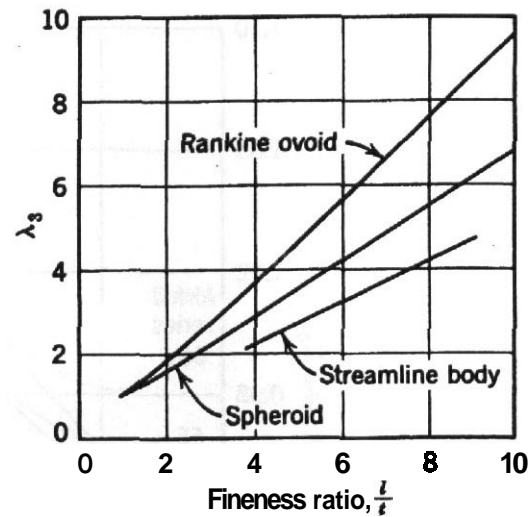
FIGURE 10.1   Values of λ_3.

2. From Figure **10.1**, for $l/t = 3.98$, $\lambda_3 = 2.2$ (estimated), $t = 2.26$ ft,

$$\Delta D_B = -\frac{\pi}{4}\lambda_3 t^3 \frac{dp}{dl}$$

$$= -\frac{\pi}{4}(2.2)(2.26)^3(-0.026)$$

$$= 0.519 \text{ lb}$$

As seen from Example 10.1, approximating the integral too grossly may change the buoyancy drag as much as 20%, but this in turn would be about 1% of the total model drag for models of ordinary dimensions.

10.2   SOLID BLOCKAGE

The solid-blockage corrections for three-dimensional flow follow the same philosophy described in Chapter 9 for two dimensions. According to Herriot,[2] the body is again represented by a source–sink distribution and is contained in the tunnel walls by an infinite distribution of images.

Summing the effect of the images, we have, for the solid-blockage velocity effect for a wing,

$$\varepsilon_{sb,W} = \frac{\Delta V}{V_u} = \frac{K_1 \tau_1 (\text{wing volume})}{C^{3/2}} \tag{10.2}$$

where K_1 is the body shape factor from Figure 10.2, τ_1 is a factor depending on the tunnel test-section shape and the model span-to-tunnel-width ratio, from Figure **10.3**.
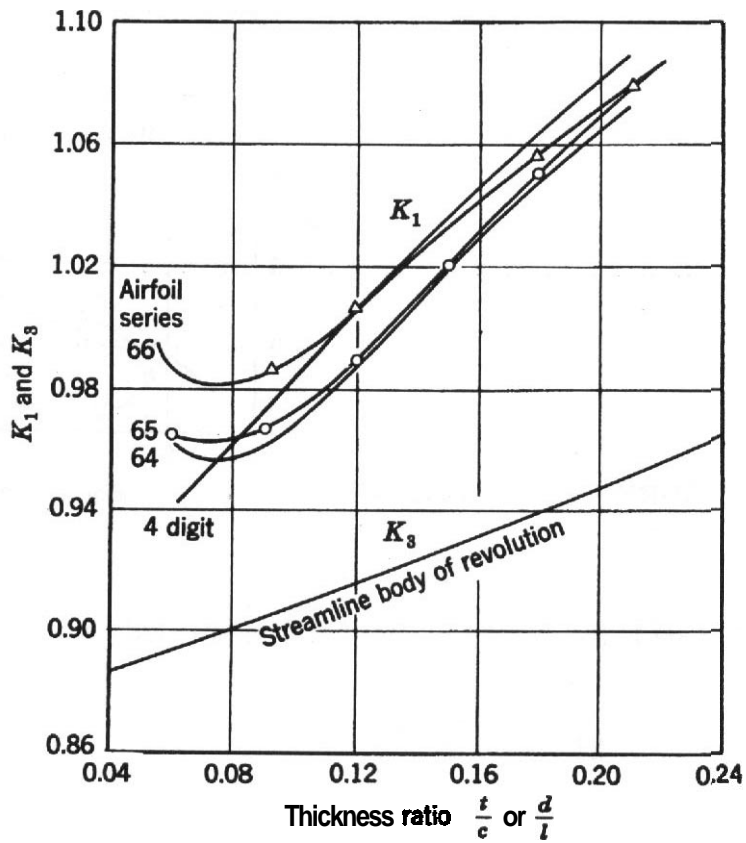
FIGURE 10.2 Values of K_1 and K_3 for a number of bodies.
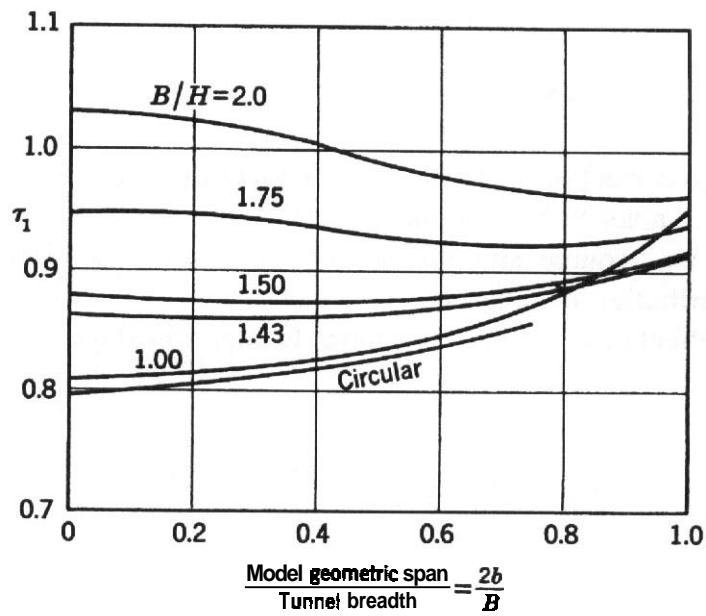
FIGURE 10.3 Values of τ_1 for a number of tunnel types. Use $b/B = 0$ for bodies of revolution.

For bodies of revolution a similar approach results in

$$\varepsilon_{sb,B} = \frac{\Delta V}{V_u} = \frac{K_3 \tau_1 (\text{body volume})}{C^{3/2}} \tag{10.3}$$

where K_3 is the body shape factor from Figure 10.2; τ_1 is a factor depending on the tunnel test-section shape and the model span- (assumed *zero*) to-tunnel-width ratio from Figure 10.3.

Thom's short-form[3] equation for solid blockage for a three-dimensional body is

$$\frac{\Delta V_{sb}}{V_u} = \varepsilon_{sb} = \frac{K(\text{model volume})}{C^{3/2}} \tag{10.4}$$

where K equals 0.90 for a three-dimensional wing and 0.96 for a body of revolution. (A good approximation for the volume of a streamline body of revolution is $0.45ld^2$, where l is length and d is maximum diameter.)

Solid blockage for a wing–body combination is simply the sum of each component as determined from the above relations.

The velocity ratio method yields the result that the velocity increment at the wall of a round closed wind tunnel is 2.2 times that at the tunnel centerline for bodies of revolution and about 2.0 for typical airplane models.

For open jets the solid blockage may be taken as one-fourth the above values. Normally this results in a quantity that is negligible.

103 WAKE BLOCKAGE

Maskell's Method

Although for many years wind tunnel engineers were satisfied with wake blockage corrections based on the single theory of simulating the wake by a source at the wing trailing edge (Thom[3] and others), Maskell[4] has reported the necessity of considering the momentum effects outside the wake when separated flow occurs. These effects are produced by lateral-wall constraint on the wake and result in lower wake pressure and hence lower model base pressures than would occur in free air.

There are three important contributions in Maskell's paper: First, wake blockage yields results similar to those on the same model in a higher speed airstream (i.e., the wake does not vary significantly along or across the model); second, the natural tendency for the wake to tend toward axial symmetry (even for wings of aspect ratio 10) permits a single correction for essentially all three-dimensional models (see Figure 10.4); third, the wake induces a pressure gradient in the streamwise direction which produces a drag increment on the body. The complete wake blockage results for three-dimensional models are presented below.

The correction for wake blockage for streamline flow follows the logic of the two-dimensional case in that the wake is simulated by a source of strength $Q =$
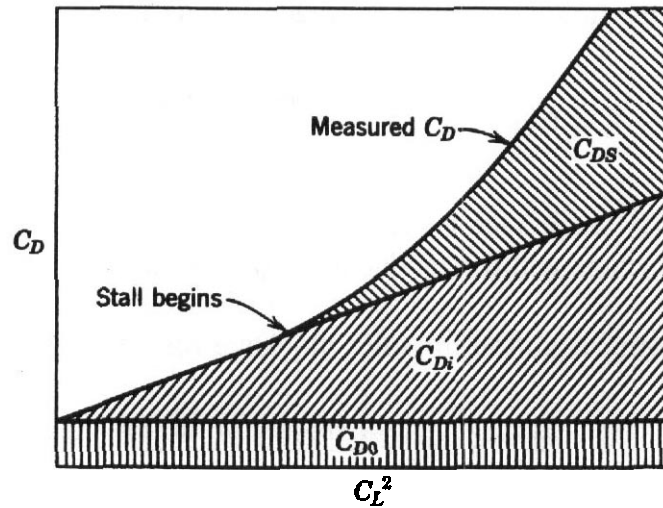
FIGURE 10.4   Drag analysis for **a lifting wing.**

$D/\rho V$, which is matched for continuity by adding a downstream sink of the same strength. However, for the three-dimensional case the image system consists of a doubly infinite source–sink system spaced a tunnel height apart vertically and a tunnel width apart horizontally in a manner similar to the doubly infinite sequence shown by Figure 9.12 for horseshoe vortices. The axial velocity induced at the model by the image source system is again zero, and that due to the image sink system is

$$\Delta V = \frac{Q}{2Bh}$$

The incremental velocity is then

$$\varepsilon_{wb} = \frac{\Delta V}{V_u} = \frac{S}{4C}C_{Du} \tag{10.5}$$

or

$$\frac{q_{wb}}{q_u} = 1 + \frac{S}{2C}C_{Du} \tag{10.6}$$

The increase of drag due to the pressure gradient may be subtracted by removing the wing wake pressure drag,

$$\Delta C_{Dw} = \frac{K_1\tau_1(\text{wing volume})}{C^{3/2}}C_{Du} \tag{10.7}$$

and the body wake pressure drag,

$$\Delta C_{DB} = \frac{K_3\tau_1(\text{body volume})}{C^{3/2}}C_{D0u} \tag{10.8}$$

The values of K_1, K_3, and τ_1 are again from Figures 10.2 and 10.3. The values from (10.7) and (10.8) are usually negligible.

The wake blockage for separated flow is as follows: Through considerations mentioned above, Maskell added a term to account for the increased velocity outside the wake and its consequently lowered pressure. Dividing the total drag coefficient into a constant amount C_{D0}, one proportional to C_L^2, and one due to separated flow C_{Ds} (see Figure 10.4), he obtains the total wake blockage corrections $\varepsilon_{wb,t}$ as

$$\varepsilon_{wb,t} = \frac{S}{4C}C_{D0} + \frac{5S}{4C}(C_{Du} - C_{Di} - C_{D0}) \tag{10.9}$$

$$\frac{q_c}{q_u} = 1 + \frac{S}{2C}C_{D0} + \frac{5S}{2C}(C_{Du} - C_{Di} - C_{D0}) \tag{10.10}$$

For angles below separated flow, the last term, which is equal to C_{Ds}, vanishes.

Maskell[4] should be consulted for bluff models that have a substantial separated wake at $\alpha = 0$, for a correction based on base pressure then becomes necessary.

Figure 10.5 shows the variation of the "constant" from over 2.5 for high-aspect-ratio models down to approximately 1.0 for two-dimensional models.

In Maskell's correction the basic problem is obtaining the values for C_{D0} and C_{Du}. Two approaches will be outlined. The first approach is to plot C_{Lu}^2 versus C_{Du}. The minimum value of C_{Du} is picked as C_{D0} and the slope of the linear portion of the curve is used to calculate C_{Di}. For flap-down models the intercept of the linear portion of C_{Lu}^2 versus C_{Du} when extended to the C_{Du} axis may have a negative value; this is accounted for in the following equations as ΔC_{Du}, which is either zero or a negative number:

$$C_{Di} = C_{Lu}^2 \left[\frac{dC_{Du}}{dC_{Lu}^2}\right] + \Delta C_{Du} - C_{D0} \tag{10.11}$$
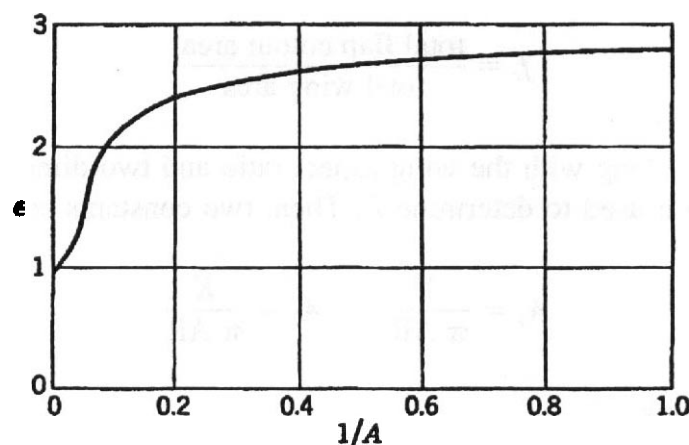
FIGURE 10.5   Variation of blockage factor with aspect ratio for nonlifting rectangular plates.

A second approach for C_{Di} and C_{D0} is based on Young[s] in which is found the following equation:

$$C_{Di} = \frac{C_L^2}{\pi \, AR} + \frac{K(\Delta C_L^2)}{\pi \, AR} \tag{10.12}$$

where C_L is the lift of the **unflapped** wing, ΔC_L is the lift increment due to flaps, AR is the aspect ratio, and K is obtained from **Young**.[6] It is a function of flap span, flap cutout, wing span, wing aspect ratio, and the two-dimensional lift curve slope in radians. The values of K are based on the following assumptions:

1. an unswept wing with an elliptical load distribution or **taper** ratio of $2:1$;
2. one set of flaps per semispan;
3. one cutout inboard of the flaps;
4. a constant ratio of local flap chord to local wing chord along the wing span; and
5. effect of the flaps that is considered to be the equivalent of a constant change in geometric incidence along the flap span, resulting in a local lift increment due to the flap independent of the local wing incidence.

A net flap span ratio is defined for multiple flaps as

$$f_n = \sum \frac{\text{flap spans}}{\text{wing span}} \tag{10.13}$$

The overall flap span ratio is defined as

$$f_t = \frac{\text{total flap span}}{\text{wing span}} \tag{10.14}$$

The total flap span is from the outboard end of the outboard flap on the left wing to the same point on the right wing. The flap cutout ratio is

$$f_c = \frac{\text{total flap cutout area}}{\text{total wing area}} \tag{10.15}$$

These three ratios along with the wing aspect ratio and two-dimensional lift curve slope in radians are used to determine K. Then, two constants are defined:

$$A_1 = \frac{1}{\pi \, AR} \qquad A_2 = \frac{K}{\pi \, AR} \tag{10.16}$$

Thus Young[7] obtains

$$C_{Di} = A_1 C_L^2 - A_2(\Delta C_L^2) \tag{10.17}$$

and C_{D0} is found as

$$C_{D0} = C_{D,\alpha=0} - (A_1 + A_2)C^2_{L,\alpha=0} \qquad (10.18)$$

The subscript $a = 0$ means the value of lift and drag at $\alpha = \psi = 0$ is used. It is assumed that there is no separated flow at these angles. The value of C_{D0} is defined as $C_{D,\alpha=0}$ minus the terms dependent on the wing lift plus the flap increment. The test values for C_D and C_L may or may not be corrected for tare and interference.

The induced drag is then

$$C_{Di} = A_1 C^2_{Lu} + A_2(C^2_{L,\alpha=0}) \qquad (10.19)$$

This is the same lift increment as used in Equation (10.17). Finally,

$$C_{DS} = C_{Du} - C_{D0} - C_{Di} \qquad (10.20)$$

If C_{DS} is a negative number due to data scatter, it is set to zero.

This method allows Maskell's correction to be calculated in real time if desired. Care should be taken on models with leading-edge flaps if they are separated at $a = 0$.

There also is some controversy about the $\frac{5}{4}$ factor in the velocity correction equation. Maskell determined this factor from nonlifting flat plates perpendicular to the airstream. This then yields a separation bubble across the whole span of the plate. Wings of aspect ratio 5 and greater do not initially stall across the whole span. Thus, Maskell's factor may be too large. Another approach to Maskell's correction is given by Vassaire.[8]

Approximate Blockage Corrections

The total solid and wake blockage corrections may be summed according to

$$\varepsilon_t = \varepsilon_{sb} + \varepsilon_{wb,t} \qquad (10.21)$$

When all is lost as far as finding blockage corrections for some unusual shape that needs to be tested in a tunnel, the authors suggest

$$\varepsilon_t = \frac{1}{4}\frac{\text{model frontal area}}{\text{test-section area}} \qquad (10.22)$$

Blockage applies to everything in the test section, of course, and hence corrections to the free-air conditions must allow for the windshields and struts or other items necessary in the test section during a test. If the image system method of evaluating tare and interference is used, the blockage contribution of the mounting system is automatically evaluated. That is, putting the image system in increases the model drag by the tare and interference plus the wake and solid blockage of the image windshields and support struts. When T and I are subtracted, the windshield effects go with them.

On the other hand, when for some reason an image system is not to be used, ε_t should be taken as

$$\varepsilon_t = \varepsilon_{model+struts} + \varepsilon_{windshields}$$

A maximum ratio of model frontal area to test-section cross-sectional area of 7.5% should probably be used unless errors of several percent can be accepted.

The windshield term will he a constant that can be evaluated with the help of Equations (10.2) and (10.5). For tests without yaw, the strut blockage may be included in the windshield term. An alternative method is to make a pitot-static survey with the windshields in, and use its values for, "free stream," allowing for model blockage only in the work-up.

Blockage in open test sections is of opposite sign and smaller than for a closed tunnel.

Measured Variable Methods

Until the mid-1970s blockage corrections had been primarily based on simple potential flow solutions that yielded solid blockage based on geometric considerations. These corrections account only for the local flow acceleration around the model. In wind tunnel tests there is also a viscous wake for unseparated flow and finally a separated wake that includes the viscous wake. The later two blockages were more difficult to calculate. In 1957 Hensel[9] developed a method based on measuring a wall pressure opposite the model and using doublets to model the flow. Maskell's method: which appeared in 1965, is an empirical relation based on the measured drag and a less empirical variant using base pressure. For rectangular plates Maskell demonstrated that the drag coefficient is related to the base pressure, which is a function of plate aspect ratio. The separation of profile drag, both viscous and separated, from induced drag for complete models or the selection of suitable base pressure sometimes is somewhat ambiguous when attempting to use Maskell's method.

Hackett–Wilsden and Ashill–Keating Methods   The Hackett–Wilsden and Ashill–Keating methods have been discussed in the preceding chapter. These methods encompass both solid and wake blockage but generally are most useful when significant and difficult-to-predict wake effects are present.

10.4   STREAMLINE CURVATURE

The corrections for streamline curvature for three-dimensional studies follow the same philosophy as those for the two-dimensional case in that they are concerned with the variation of the boundary-induced upwash along the chord. Once again the variation turns out to be essentially a linear increase in angle so that the streamline curvature effect may be treated as the loading on a circular-arc airfoil. Similarly, the loading is treated as a flat-plate effect based on the flow angle change between the quarter and half chord and an elliptic load based on the flow angle change between half and three-quarter chord. But for the three-dimensional case the image system is vastly different from the simple system for two dimensions.

The three-dimensional image system is shown in Figure 9.12. It consists of the real wing horseshoe system with its bound vortex C_D and trailing vortices C_∞ and D_∞ plus the doubly infinite series that by symmetry make the walls, floor, and ceiling stream surfaces. The induced flow of the doubly infinite image system at the lifting line of the real wing is the main boundary upwash effect, and it may be found in the familiar δ values for any particular condition. Here, as mentioned previously, we are interested in the *change* of upwash along the chord and, in some cases, along the span as well.

The amount of correction needed is most easily handled as a "τ_2" effect (see Section 10.8), where the "tail length" is, as in the two-dimensional discussion, one-quarter of the wing chord length. The τ_2 factor represents the increase of boundary-induced upwash at a point P behind the wing quarter chord in terms of the amount *at* the quarter chord. The total angle effect is then

$$\Delta\alpha_{\text{total}} = \Delta\alpha + \tau_2\,\Delta\alpha \tag{10.23}$$

where $\Delta\alpha$ is the effective correction required for upwash at quarter chord and τ_2 is the streamline curvature effect on the angle. Values of τ_2 may be found from figures in Section 10.8 using $\frac{1}{4}c$ as the tail length needed to determine τ_2.

Another form of the same correction may be derived by assuming that the τ_2 curves are linear for the short "tail length" of the wing streamline curvature corrections. We then have

$$\Delta\alpha_{sc} = \tau_2\,\delta\left(\frac{S}{C}\right)C_{LW}$$

$$= \frac{c}{4B}\frac{d\tau_2}{d(l_t/B)}\delta\frac{S}{C}C_{LW}(57.3)$$

For a particular tunnel, both B and $d\tau_2/[d(l_t/B)]$ will be known, so that

$$\Delta\alpha_{sc} = kc(\Delta\alpha)(57.3) \quad \text{deg}$$

and once k is determined, no charts are needed to find Δa, for various models. The additive lift correction is given as

$$\Delta C_{L,\text{sc}} = -\Delta\alpha_{\text{sc}} \cdot a$$

where a is the wing lift curve slope. The additive correction to the moment coefficient is derived as

$$\Delta C_{m,\text{sc}} = -0.25\ \Delta C_{L,\text{sc}} \tag{10.24}$$

It should be noted that many tunnel engineers prefer to apply the correction entirely to the angle rather than to the angle and the lift. To make the correction to the angle only, τ_2 should be determined by using $\frac{1}{2}c$ as a tail length instead of $\frac{1}{4}c$. The moment correction will then be

$$\Delta C_{m,\text{sc}} = +0.125\ \Delta\alpha_{\text{sc}(2)} \cdot a \tag{10.25}$$

10.5   GENERAL DOWNWASH CORRECTIONS

Very early in the century experimenters using open throat wind tunnels found their tunnels giving very pessimistic results. The measured minimum drag and rate of change of drag with lift were too large, and the slope of the lift curve was too small. The minimum-drag effect was largely due to the very low Reynolds numbers then found in the low-speed tunnels, but the other two effects were due to the tunnel boundaries. The discovery of a way to represent the walls mathematically for some significant cases allowed a calculation of their effect. We will now present the theory and numerical values of the correction factors needed when a three-dimensional tunnel is used.

Consider the free-air streamlines caused by a pair of trailing vortices such as are made by a uniformly loaded wing (Figure 10.6). These streamlines extend to infinity in free air, but when the wing is enclosed in a round duct, they become contained, the wall itself becoming a streamline through which no fluid can pass. As in the two-dimensional case, the problem becomes one of finding the mathematical device that will simulate the walls by making a streamline that coincides with the walls. If we let the wing be small relative to the tunnel size, the problem becomes the simplest of all boundary problems; a streamline with the same radius as the tunnel test section is created by a pair of vortices placed a distance $x = 2R^2/b$ on each side of the tunnel (Figure 10.7). They must have the same strength as the wing vortices.

These two image vortices violate Helmholtz's vortex theorem; that is, a vortex cannot end in the fluid but must go the fluid boundary or form a closed loop. But
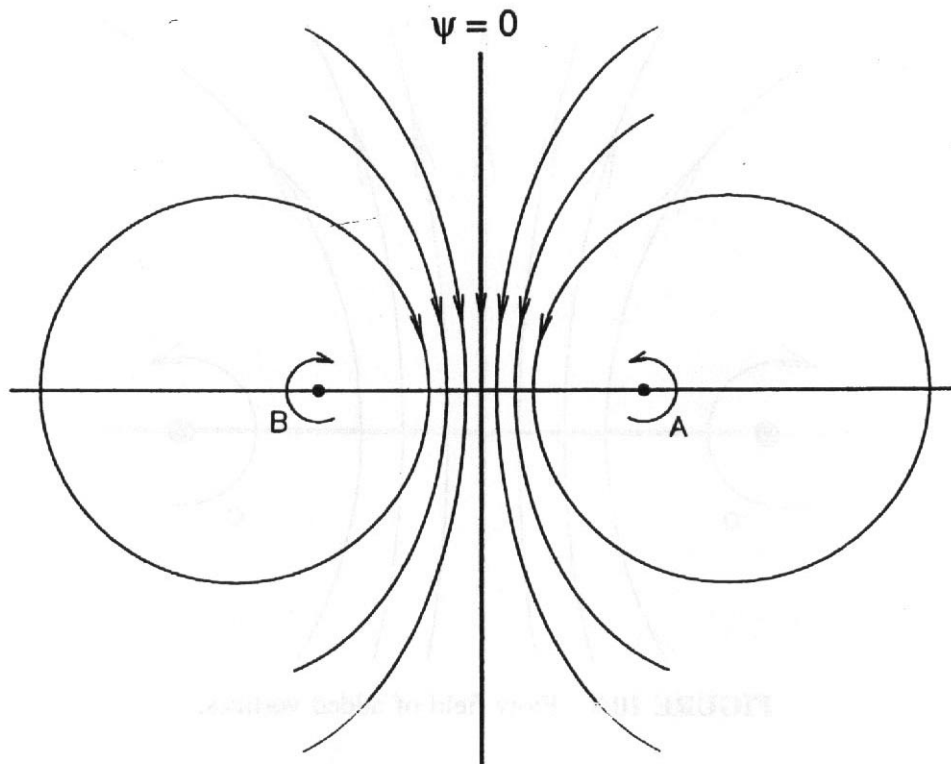
FIGURE 10.6   Flow field of trailing vortices.

like **Prandtl's** momentum theory for the induced angle of attack and drag of a finite wing, they give the correct answers.

The streamlines due to the added vortices are shown in Figure 10.8. It will take but a moment for the student to **trace** Figure 10.6 on Figure 10.8 and to see for himself or herself how the $\psi = 0$ streamline coincides with the tunnel wall. Writing
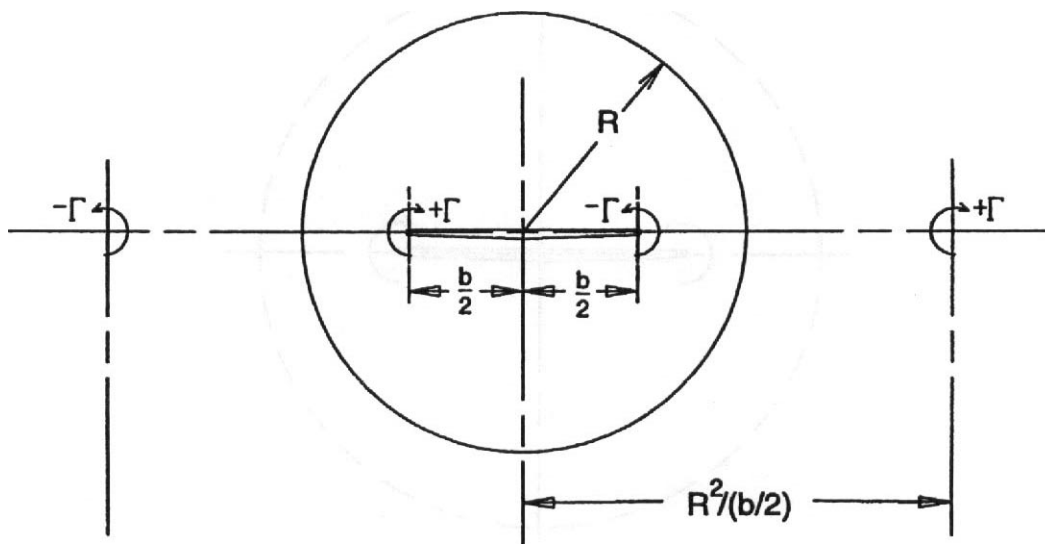
FIGURE 10.7   Locations **of added** "image" **vortices, closed round jet.**
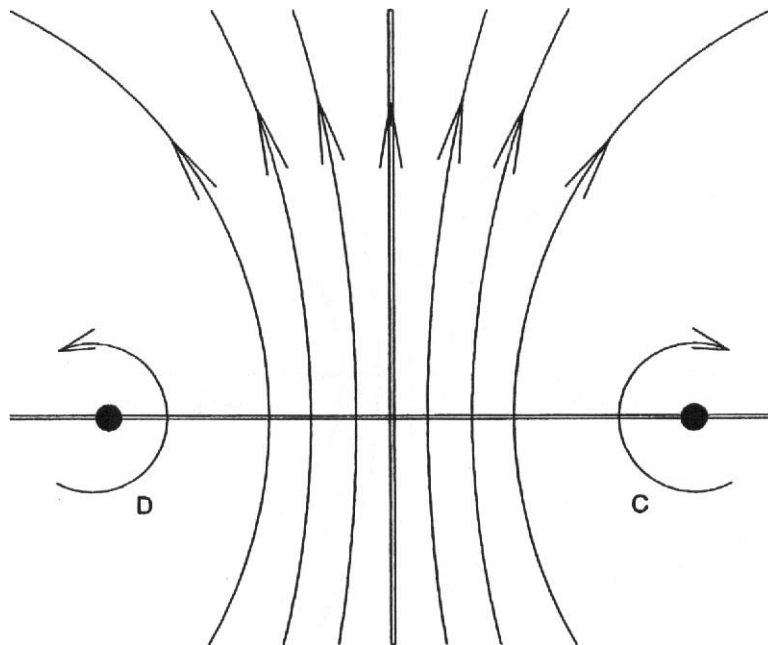
FIGURE 10.8 Flow field of added vortices.

the stream function for the four trailing vortices, summing them, and setting the sum to zero (Figure 10.9) will show that the spacing of the images must be at the distance shown in Figure 10.7.

Another way to look at the effect of the added vortices is to consider their velocity field at the wing, as shown in Figure 10.10. The upflow tends to offset the downflow caused by the wing trailing vortices, and the wing then has too little induced angle
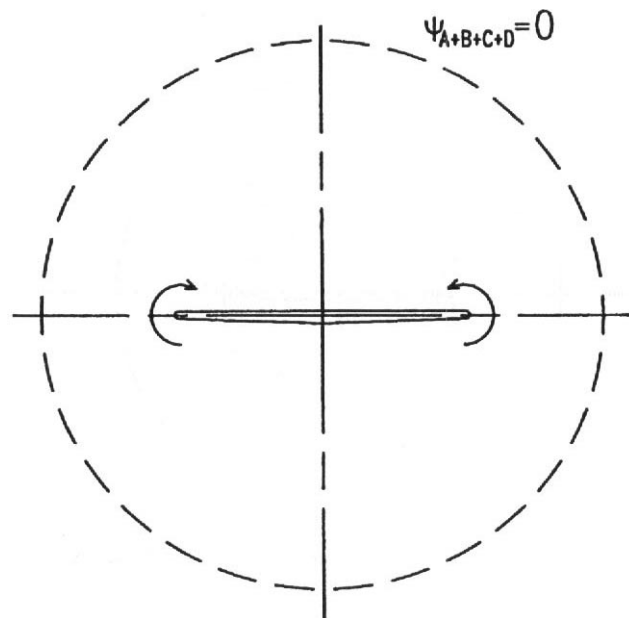
FIGURE 10.9 Total flow field of both bound and added vortices; $\psi = 0$.
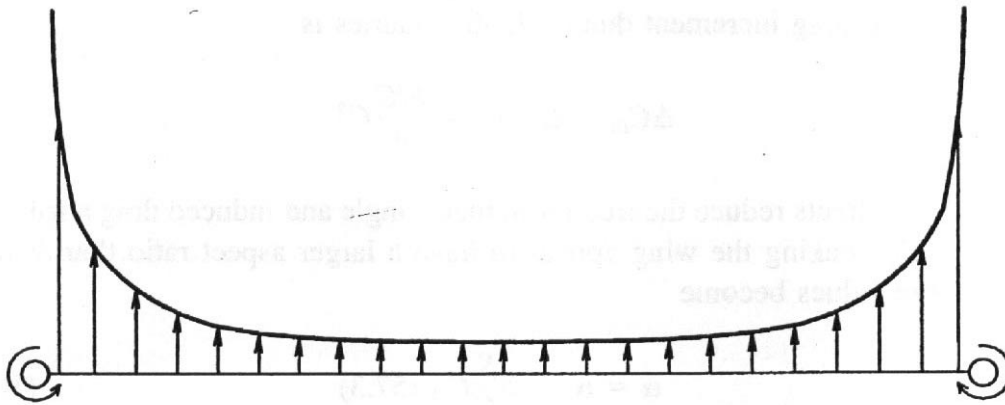
FIGURE 10.10 Distribution of upwash due to added vortices.

and too little induced drag. The exact amount may be found as follows: The lift of a uniformly loaded wing may be written as

$$L = \frac{\rho}{2}SV^2C_L = \rho V \Gamma b$$

so that the circulation is

$$\Gamma = \frac{SVC_L}{2b}$$

The upwash at a distance r from a semi-infinite vortex is

$$w = \frac{\Gamma}{4\pi r}$$

and for two vortices at a distance $R^2/(b/2)$ this becomes

$$w = \frac{\Gamma b}{8\pi R^2}$$

Substituting for Γ we get

$$w = \frac{SV/\pi R^2}{8}C_L$$

and the induced angle due to the boundaries (let the tunnel cross-sectional area be C) is

$$\Delta\alpha_i = \frac{w}{V} = \frac{S/C}{8}C_L$$

The induced drag increment due to the boundaries is

$$\Delta C_{Di} = \Delta\alpha_i\, C_L = \frac{S/C}{8} C_L^2$$

Both these effects reduce the free-air induced angle and induced drag attributable to a given C_L, making the wing appear to have a larger aspect ratio than it really has. The true values become

$$\alpha = \alpha_u + \delta\frac{S}{C} C_{LW}(57.3) \tag{10.26}$$

$$C_D = C_{Du} + \delta\frac{S}{C} C_{Lw}^2 \tag{10.27}$$

where $\delta = 0.125$ for a round closed test section when the wing is small and has uniform loading. The subscript W is added to emphasize that corrections are based on wing lift only.

But wings are seldom small and never have uniform loading. We shall have to reexamine these assumptions and see whether they induce serious errors. An examination of Figure **10.10** will give an insight into the statement that the wing span should be less than **0.8** of the tunnel width.

The factor 6 is a function of the span load distribution, the ratio of model span to tunnel width, the shape of the test section, and whether or not the wing is on the tunnel centerline. The factor 6 may be found for almost all conditions somewhere in this chapter, and **(10.26)** and **(10.27)** are general; once 6 is found, it may be used to find the boundary effects. For most tunnels, however, only the 6's for uniform loading had been provided. This seems odd until one realizes that the shed vortices rapidly roll up into a single pair of vortices that closely approximate the trailing vortex pattern of uniform loading. They then have a vortex span b_v (which is given for a large selection of wings in Figure 10.11), and it is proper to use the uniform loading correction. However, since b_v is developed somewhat downstream, it is suggested that it is more reasonable to take an effective vortex span

$$b_e = \frac{b + b_v}{2} \tag{10.28}$$

for use at the wing. (See **Swanson** and **Toll**.[16]) The values of δ for elliptic loading are rarely used.

Thus, in summary, to find 6 for a given wing, find b_e from **(10.28)** and use the proper δ for uniform loading. For wings not covered in Figure **10.11,** the approximation

$$b_e = 0.9b$$

will not result in a serious error. If elliptic loading corrections are to be used, the geometric span b should be used in computing k, the span-to-tunnel-width ratio.
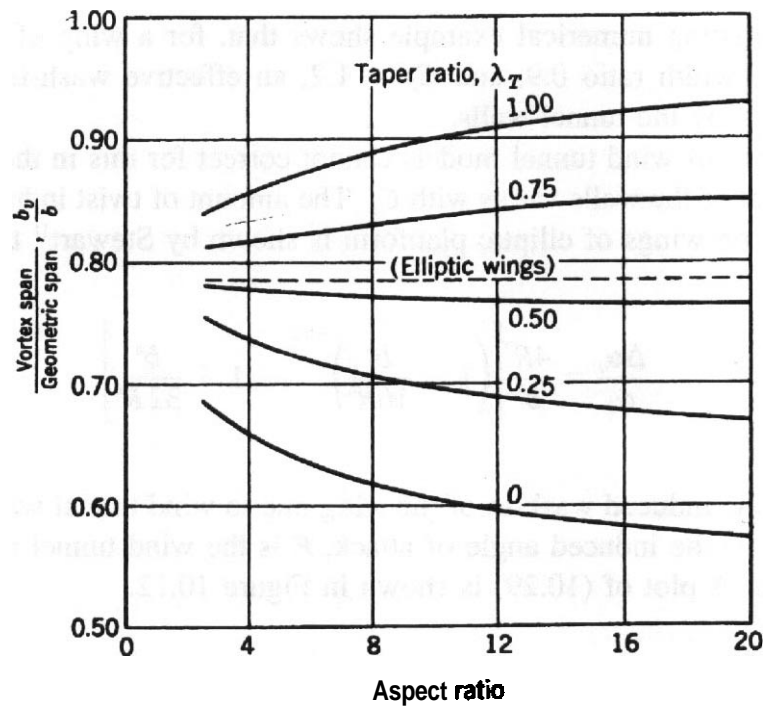
FIGURE 10.11   Values of vortex span for elliptic, rectangular, and tapered wings.

The theory for open test sections will not be outlined other than to mention that the condition for a free boundary is that no pressures can be supported ($\phi = 0$, where ϕ is the velocity potential). For open jets, δ normally has a negative sign. Values of δ for open jets are given in the following sections.

The special effects of very large models are covered in the next two sections. This problem is presumably taken care of in the initial design of the model for a given tunnel. But if the model initially has the maximum permissible span, and then during its life the airplane is stretched, the wing loading increases to a point that more area is needed. A simple solution is to add an extension to the wing tip. This increases both the area and the aspect ratio, but it can be disastrous for the wind tunnel model.

10.6   LIFT DISTRIBUTION INTERFERENCE

Round Jets

The variation of spanwise distribution due to the walls of a closed throat wind tunnel is small unless the wing has a large span. If this condition exists, the data become discouraging, tip stall starting earlier and being more severe than it actually would be in free air.

Lift distribution interference in a round closed tunnel is discussed by Stewart,'' who finds that ratios of span to tunnel width greater than 0.8 will indicate early tip

stall. An interesting numerical example shows that, for a wing of aspect ratio 7, span-to-tunnel-width ratio 0.9, and $C_L = 1.2$, an effective wash-in amounting to $1.44°$ is caused by the tunnel walls.

The designer of wind tunnel models cannot correct for this in the model design since the effect of the walls varies with C_L. The amount of twist induced by a round closed tunnel on wings of elliptic planform is shown by Stewart[11] to be

$$\frac{\Delta\alpha_i}{\alpha_i} = \frac{4R^2}{b^2}\left[\left(1 - \frac{b^4}{16R^4}\right)^{-1/2} - 1 - \frac{b^4}{32R^4}\right] \tag{10.29}$$

where $\Delta\alpha_i$ is the induced wash-in of the wing due to wind tunnel wall interference, $\alpha_i = C_L/\pi AR$ is the induced angle of attack, R is the wind tunnel radius, and b is the wing span. A plot of (10.29) is shown in Figure 10.12.

Elliptic Jets

Gavin and Hensel[12] have discussed the effect of the tunnel walls on the spanwise distribution of lift for closed elliptic jets with wings of aspect ratio 8.0. Though the
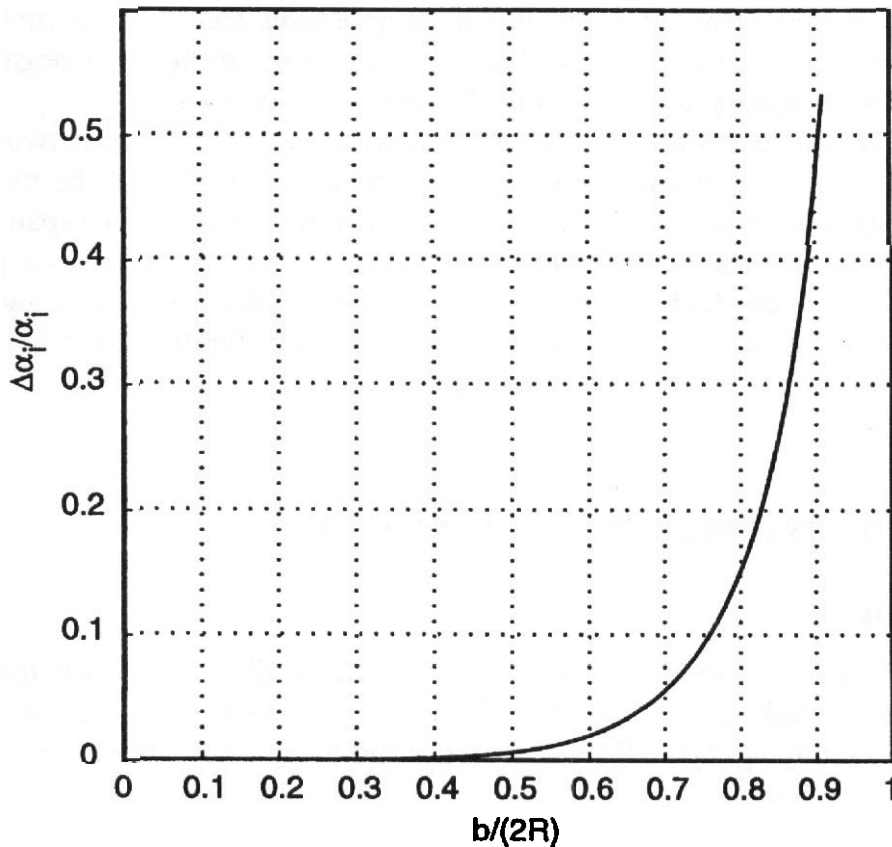
FIGURE 10.12   Wall-induced aerodynamic twist.

example discussed is very limited, further calculations using their method are possible. Their calculations may be summarized as follows:

1. At high lift coefficients when the wing tips lie outside the focal points of the elliptic jet, the variation of the induced angle of attack along the span is no longer negligible. This amounts to apparent wash-in, which becomes severe as the wing tip approaches the stall. As a result, when the wing span approaches the tunnel major diameter, determinations of stall characteristics in the tunnel are conservative; that is, the wing tips will stall at higher angles in free air.

2. Other things being constant, tunnel wall interference is less for lift distributions in which the lift is concentrated toward the centerline. That is, for untwisted wings, those with high taper ratios have tunnel-induced upwash of smaller magnitude than wings with low taper ratios.

3. Tunnel wall interference is less for wings of high aspect ratio, other conditions being held constant.

4. For wings with normal lift distributions, the mean upwash factor is a minimum when the wing tips are approximately at the tunnel foci.

10.7   DOWNWASH CORRECTIONS

Circular Jets

The corrections for uniform loading in a circular jet have been completed by Kondo,[13] and those for elliptic loading by Glauert[14] following a method proposed by Rosenhead.[15] They are both based on the ratio of span to tunnel diameter k = $b/2R$, actual values being presented in Figure 10.13. Glauert's data have been corrected to more modem units.

Owing to model length or mounting, it is sometimes necessary to place the model with its wing not on the jet centerline. This places the trailing vortices closer to one wall than to the other, altering the flow pattern and hence the proper value of 6. This condition has been examined by Silverstein,[16] who finds the values of δ with a displaced wing of uniform loading in a round jet to be as shown in Figure 10.14. The nomenclature is described in Figure 10.15.

Rectangular Jets

Van Schliestett[17] has discussed basic rectangular jet corrections for very small wings, correcting a mathematical error that appears in TR 461.[18] His results are given in Figure 10.16.

The boundary corrections for wings of moderate span compared to the tunnel width have been worked out for uniform loading by Terazawa[19] and for elliptic
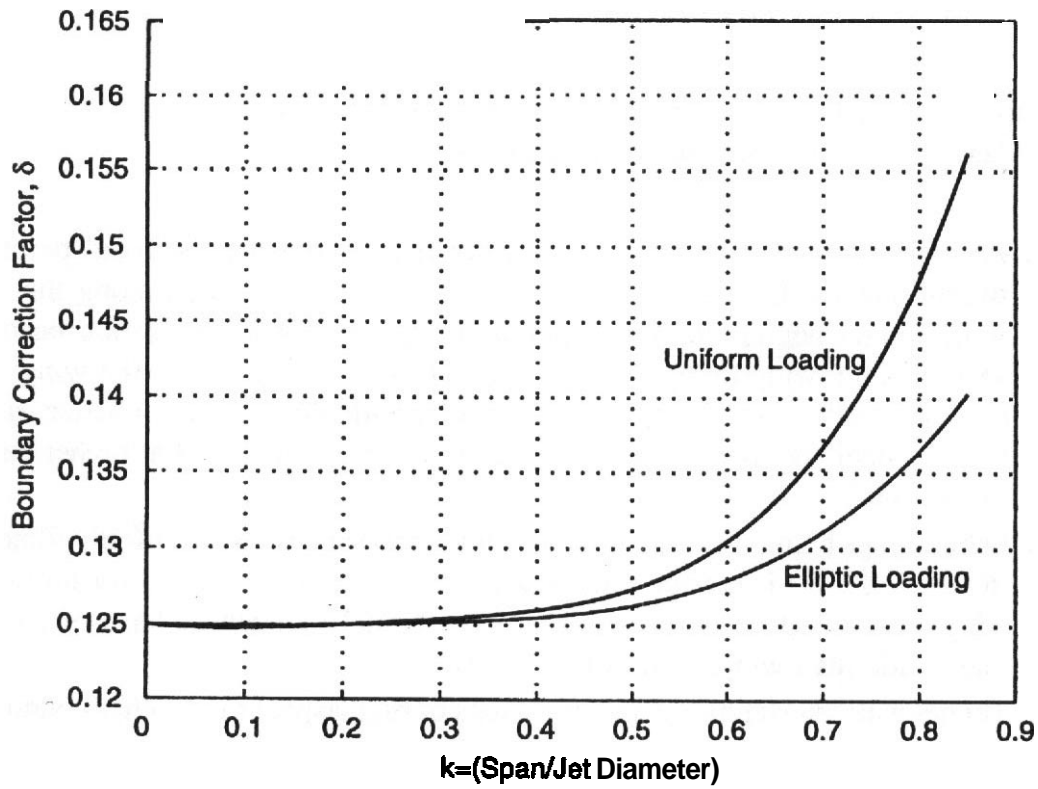
FIGURE 10.13 Values of **S** for a wing with elliptic loading and for one with uniform loading in a closed round jet. For an open round jet the sign of δ is negative.
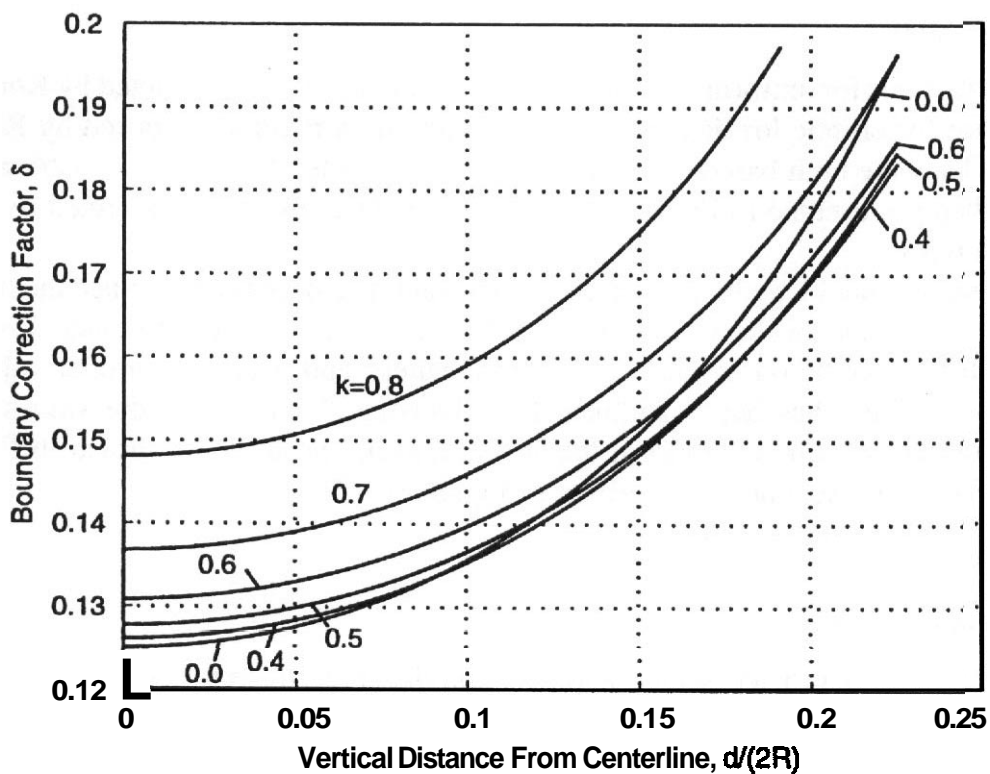
FIGURE 10.14 Values of δ when a wing with uniform loading is displaced above or below the centerline of a closed round jet; δ is negative for the open jet.
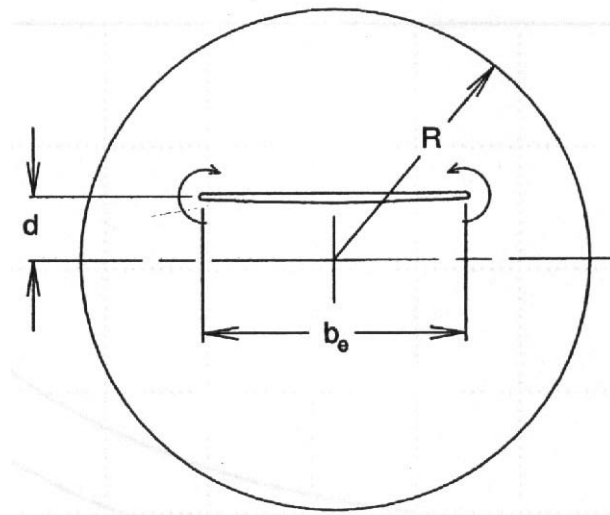
FIGURE 10.15   Nomenature for wing in round tunnel.
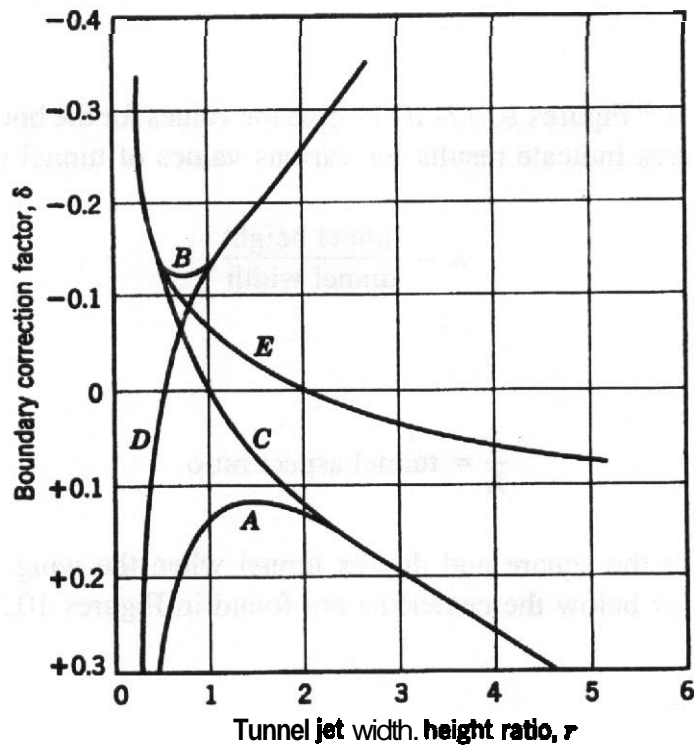
FIGURE 10.16   Values of δ for open and closed rectangular jets, very small wings only;
A, closed tunnel; B, free jet; C, jet with horizontal boundaries only; D, jet with vertical
boundaries only; E, jet with horizontal boundary.
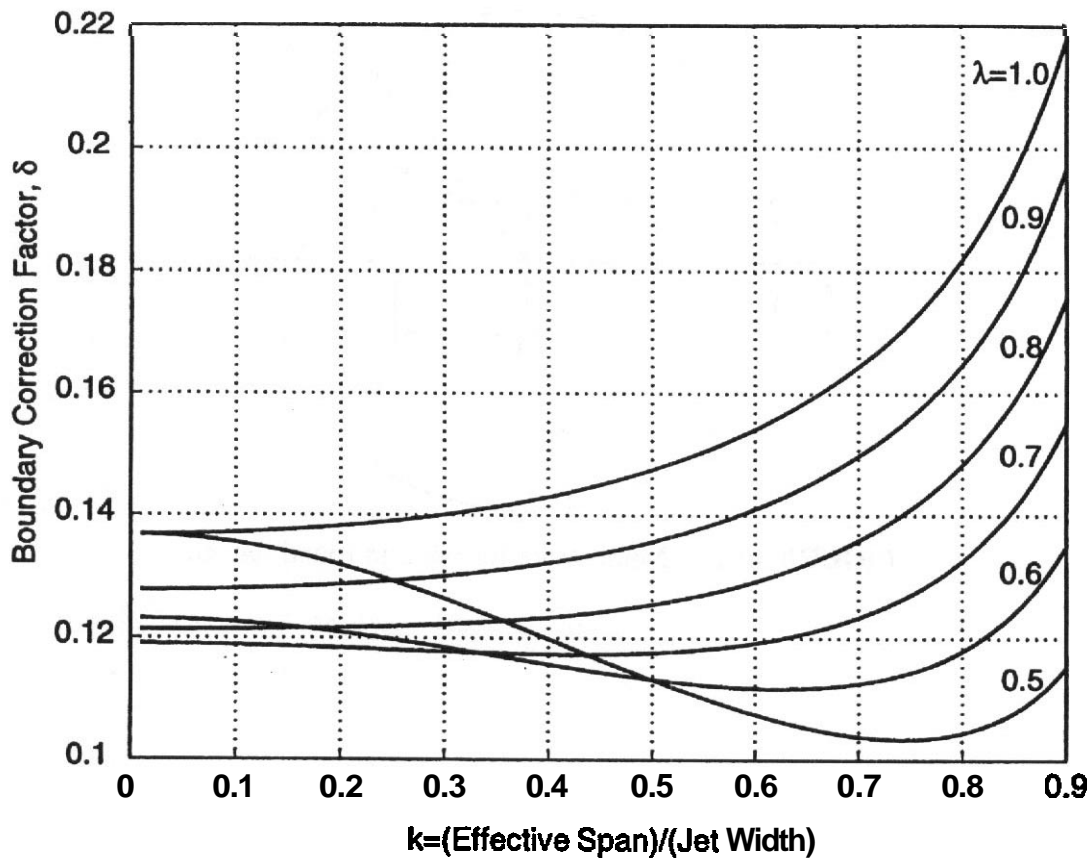
FIGURE 10.17   Values of δ for a wing with uniform loading in a closed rectangular tunnel.

loading by Glauert.[20] Figures **10.17–10.19**give the values for the boundary correction factor δ. The curves indicate results for various values of tunnel aspect ratio:

$$A = \frac{\text{tunnel height}}{\text{tunnel width}}$$

that is,

$$\frac{1}{\lambda} = \text{tunnel aspect ratio}$$

Values of δ for the square and duplex tunnel when the wing of uniform span loading is above or below the centerline are found in Figures **10.20–10.23.**

Circular-Arc Jets

The testing of panels as discussed under "Aileron Panels, Rudders, and Elevators in Section **13.2** requires special correction that mathematically simulates the tunnel boundaries and the image wing that theoretically exists on the other side on the
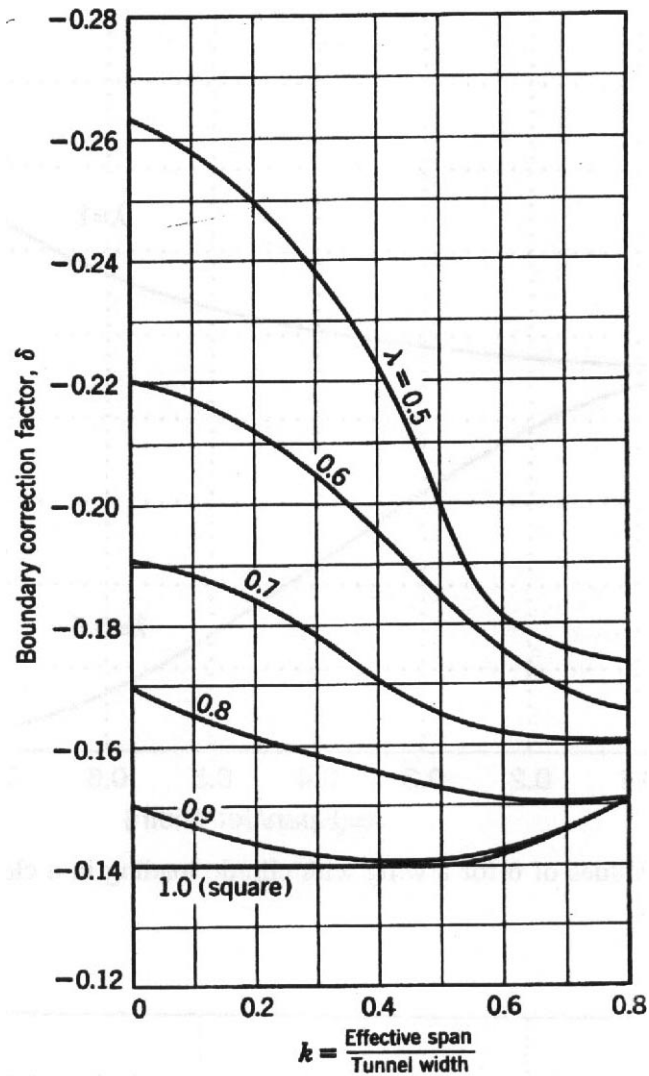
FIGURE 10.18   Values of δ for a wing with uniform loading in an open rectangular jet.

mounting plate. This condition has been considered by Kondo[13] for a test section whose original shape was round before the addition of the mounting plate (Figure **10.24).**

The variables are the wing area *S,* the area of the *original circle before the plate was added S_0,* the ratio of tunnel radius to tunnel weight

$$\lambda = \frac{h}{B} \tag{10.30}$$

and the ratio of span to tunnel height

$$k = \frac{b_e}{B} \tag{10.31}$$
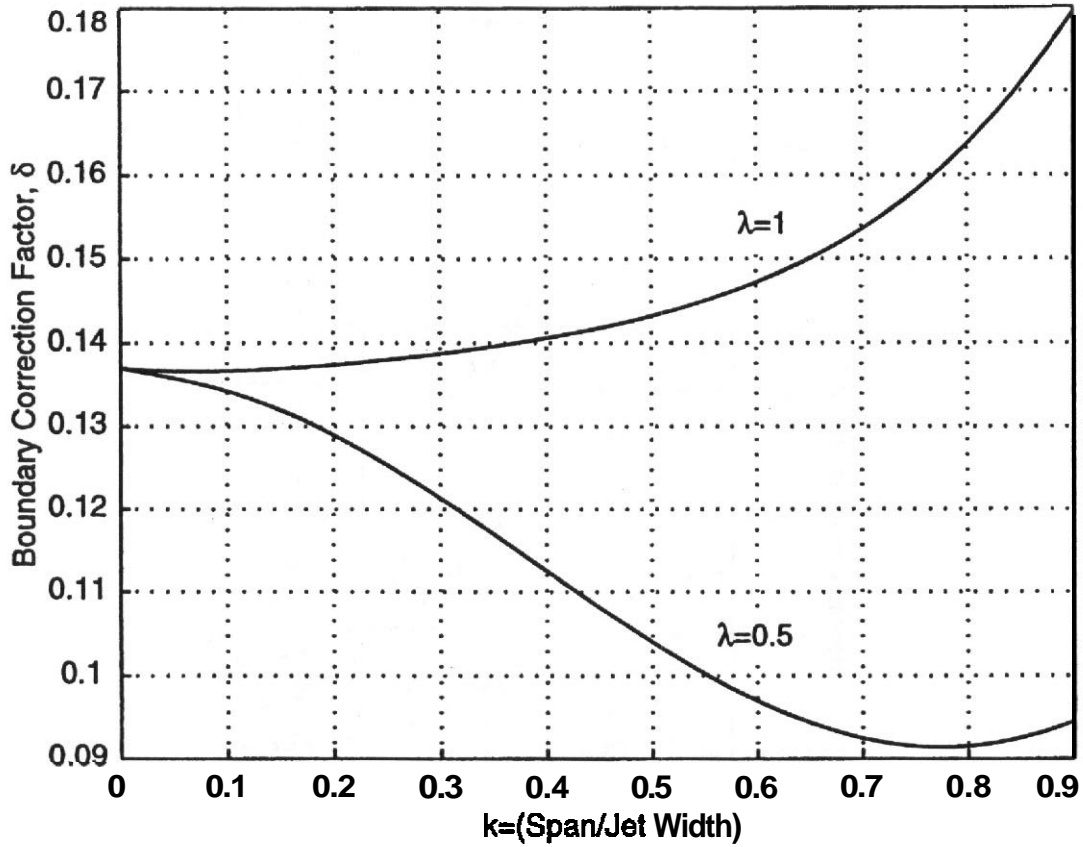
FIGURE 10.19   Values of δ for a wing with elliptic loading in a closed rectangular jet.
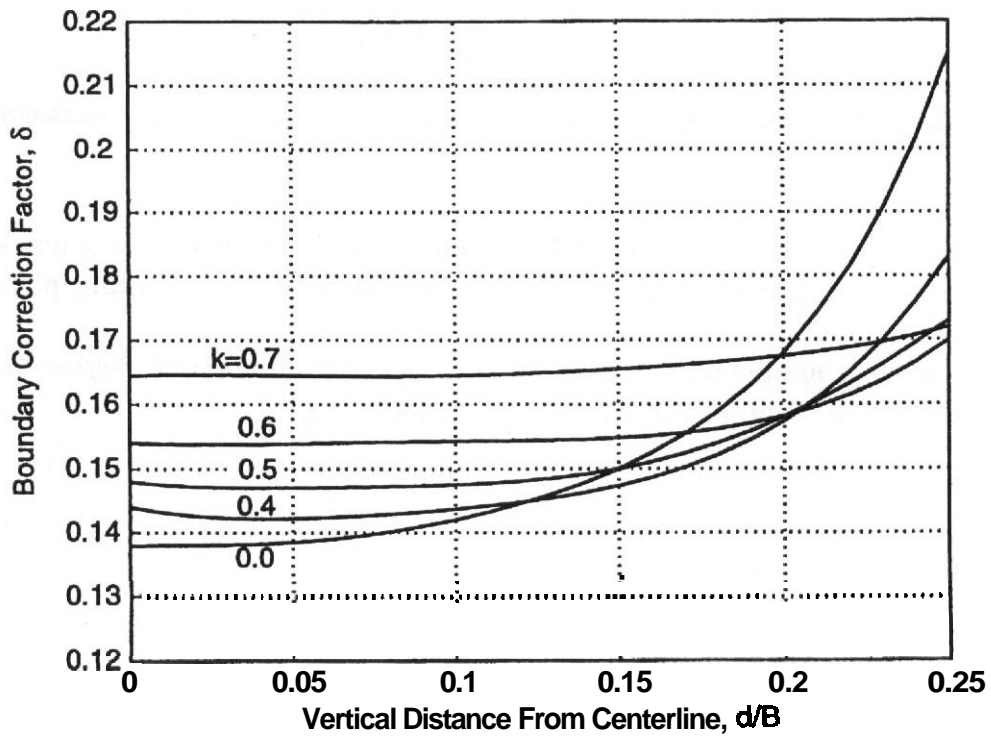
FIGURE 10.20   Values of δ when a wing with uniform loading is displaced above or below the centerline of a closed square jet.
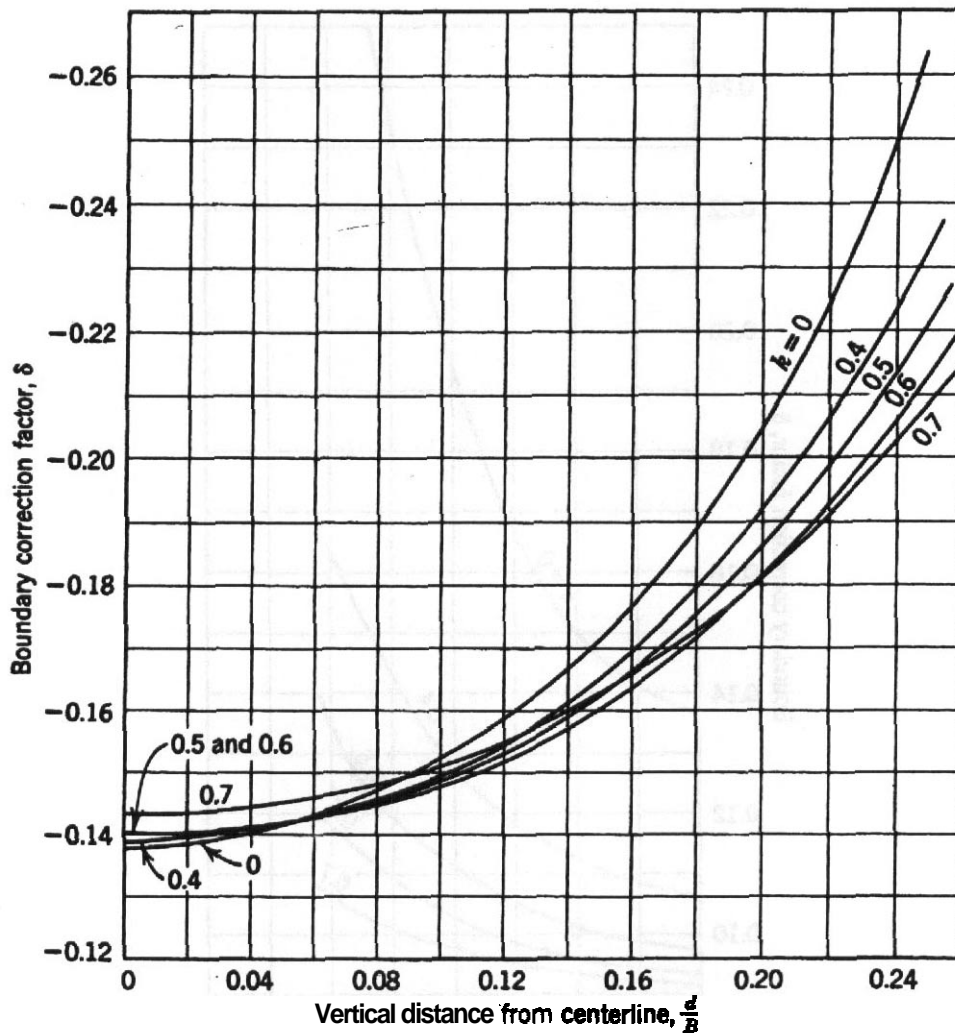
FIGURE 10 21   Values of δ when a wing with uniform loading is displaced above or below the centerline of an open square jet.

The additive corrections as usual take the form

$$\Delta\alpha = \delta\left(\frac{S}{C}\right)C_{LW}(57.3) \qquad \Delta C_D = \delta\left(\frac{S}{C}\right)C_{LW}^2$$

but a word of caution is necessary. The reference is somewhat confusing in the definition of "wing area" and "tunnel area." The wing area to be used is the *actual wing area including the image area,* and the tunnel area is the area of the original circle not *including the image circle.*

Values of δ for various values of k and **A** may be found in Figure 10.25 for closed-arc jets and in Figure 10.26 for open circular-arc jets.

It will be noted that these corrections are not strictly applicable to aileron tests, since in practice the "image" wing would have the control surface deflected oppositely. Further corrections for circular-arc jets are given by Sivells and Salmi.[21]
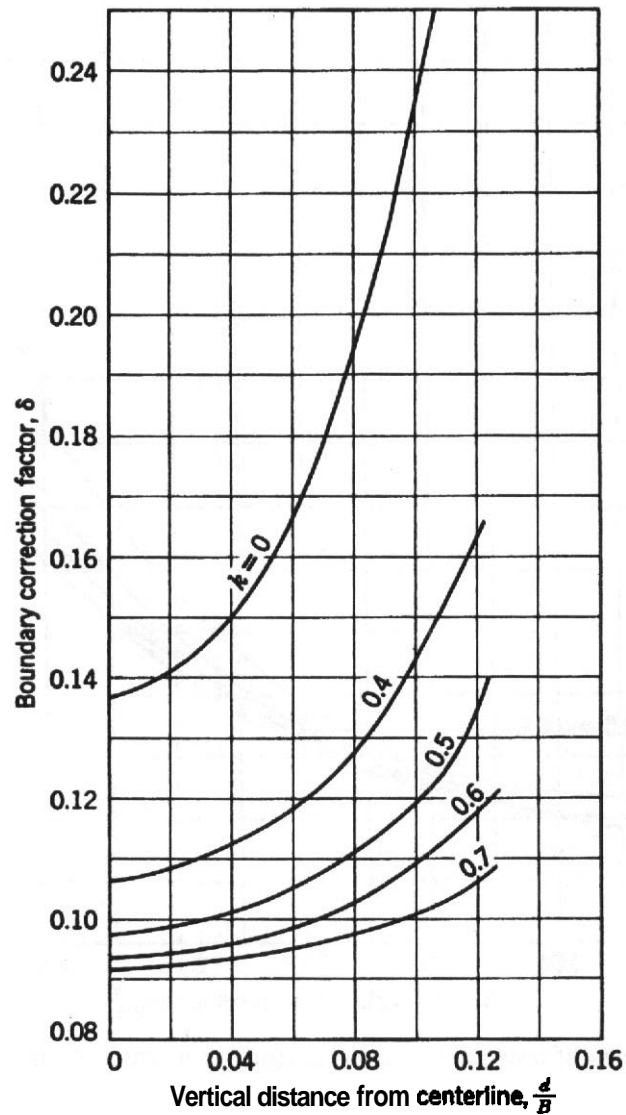
FIGURE 10.22   Values of δ when a wing with uniform loading is displaced above or below the centerline of a closed 2 : 1 rectangular jet.

Elliptic Jets

The corrections for wings with uniform loading in an elliptic jet have been completed by **Sanuki** and **Tani**[22] and those for elliptic loading by **Rosenhead.**[23]

Sanuki and Tani[22] base their values for δ (uniform loading) on the ratio of the minor to the major axis of the jet λ and the ratio of the span to the major axis k (Figure 10.27).

$$\lambda = \frac{h}{B} \tag{10.32}$$

$$k = \frac{b_e}{B} \tag{10.33}$$
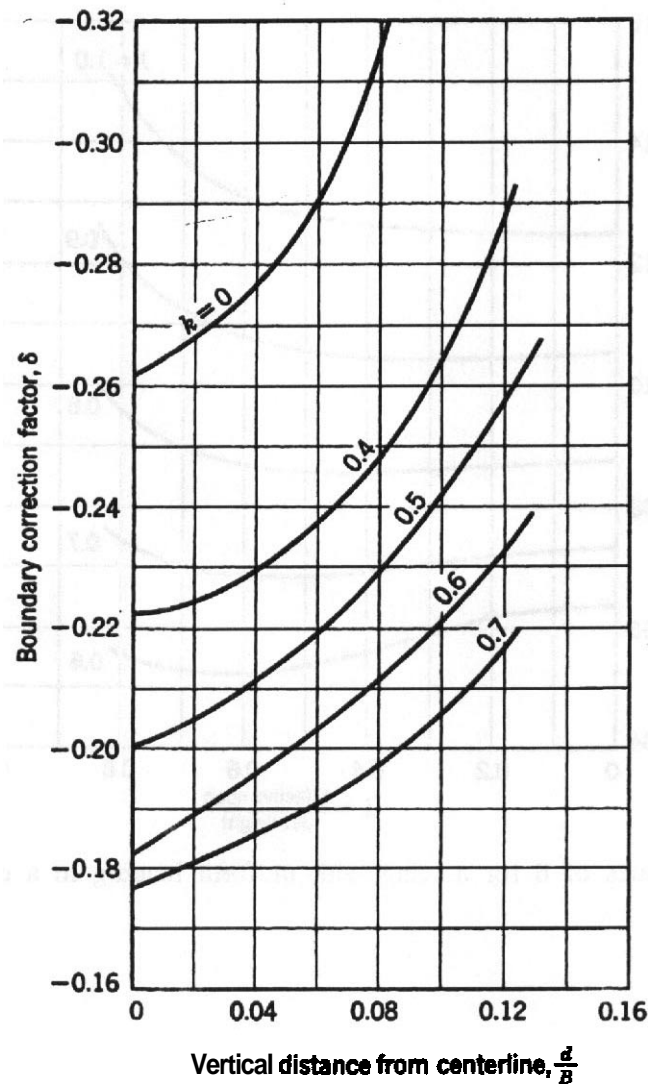
FIGURE 10.23   Values of δ when a wing with uniform loading is displaced above or below the centerline of an open 2 : 1 rectangular jet.
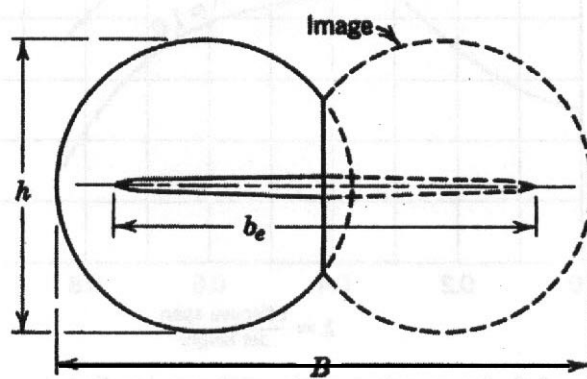
FIGURE 10.24   A model b_e in a tunnel whose boundaries are circular arcs.
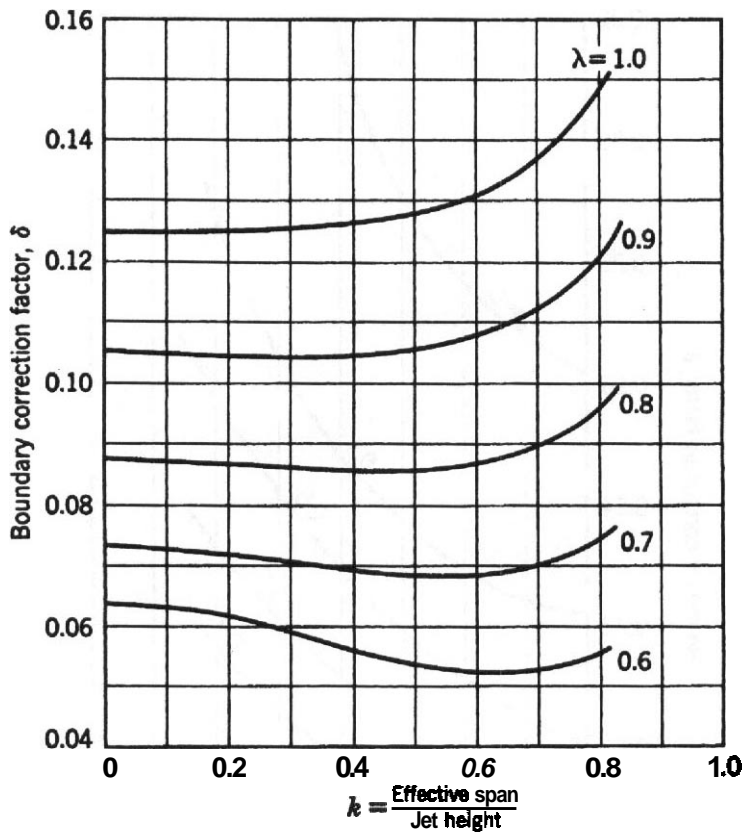
FIGURE 10.25 Values of 6 for a wing with uniform loading in a closed circular-arc wind tunnel.
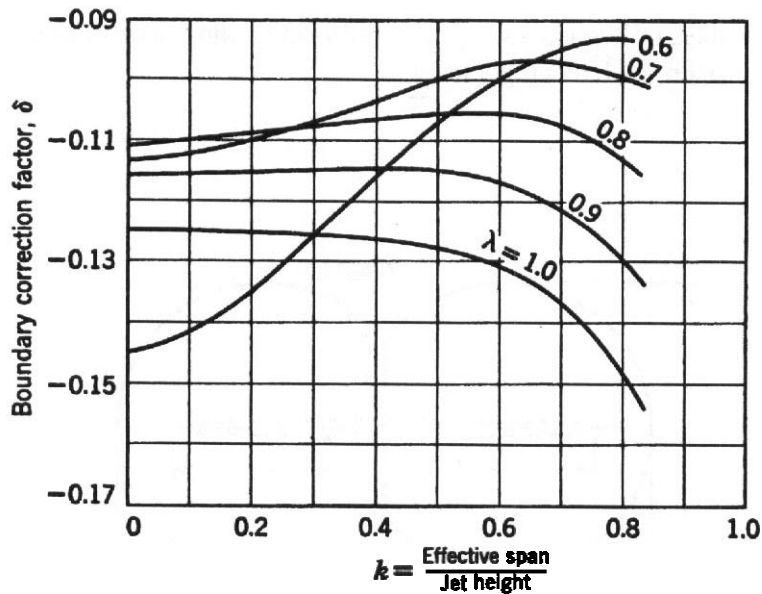
FIGURE 10.26 Values of 6 for a wing with uniform loading in an open circular-arc wind tunnel.
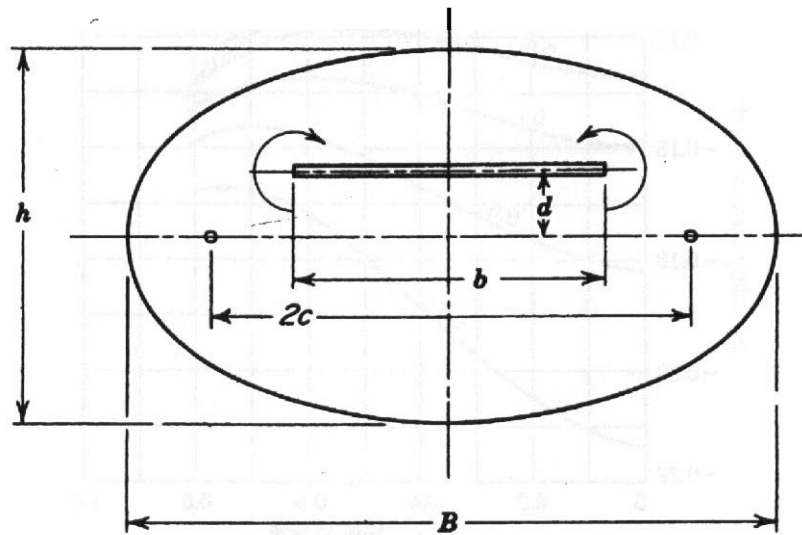
FIGURE 10.27   Nomenclature for wing in an elliptical test section.

Values of δ are shown in Figures 10.28 and 10.29.

The values for the wing not on the tunnel centerline (uniform loading) may be found in Figures 10.30 and 10.31; nomenclature is given in Figure 10.27.

Rosenhead[23] bases his values for 6 (elliptic loading) on the ratio of the axis containing the wing to the other axis of the jet, and for λ on the ratio of the span to the focal length blc. For presentation here, however, the latter has been reconverted to the ratio of span to tunnel width $k = b_e/B$ (Figure 10.27). The values of δ are shown in Figures 10.32 and 10.33.

Additional corrections for wings with uniform loading in $1 : \sqrt{2}$ partly open elliptic test sections have been given by Riegels." In view of the improbability of
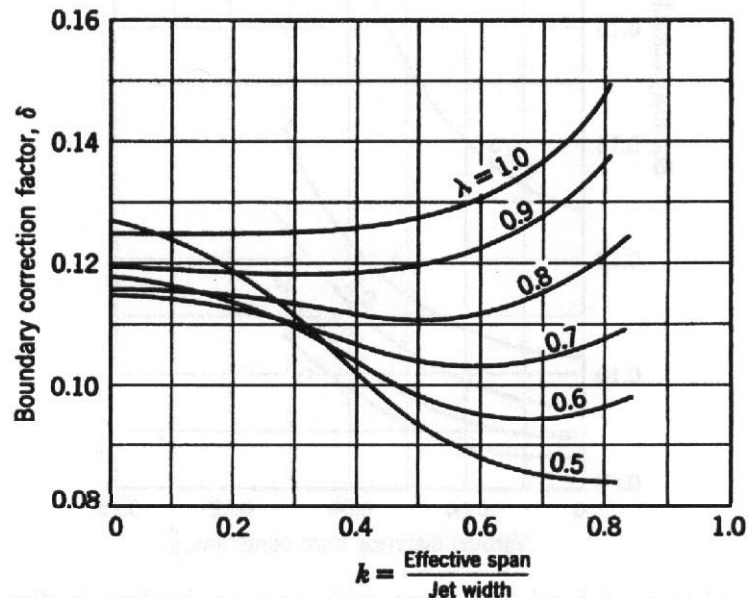
FIGURE 10.28   Values of δ for a wing with uniform loading in a closed elliptic jet.
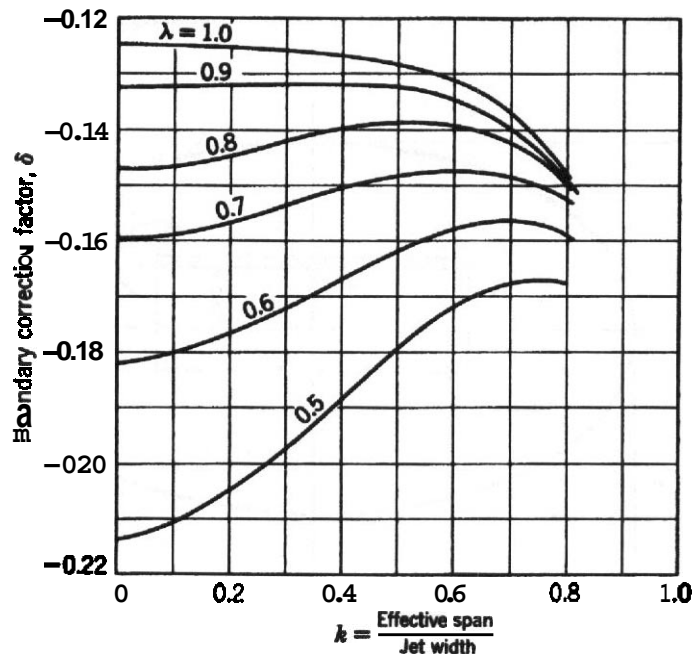
FIGURE 10.29   Values of δ for a wing with uniform loading in an open elliptic jet.
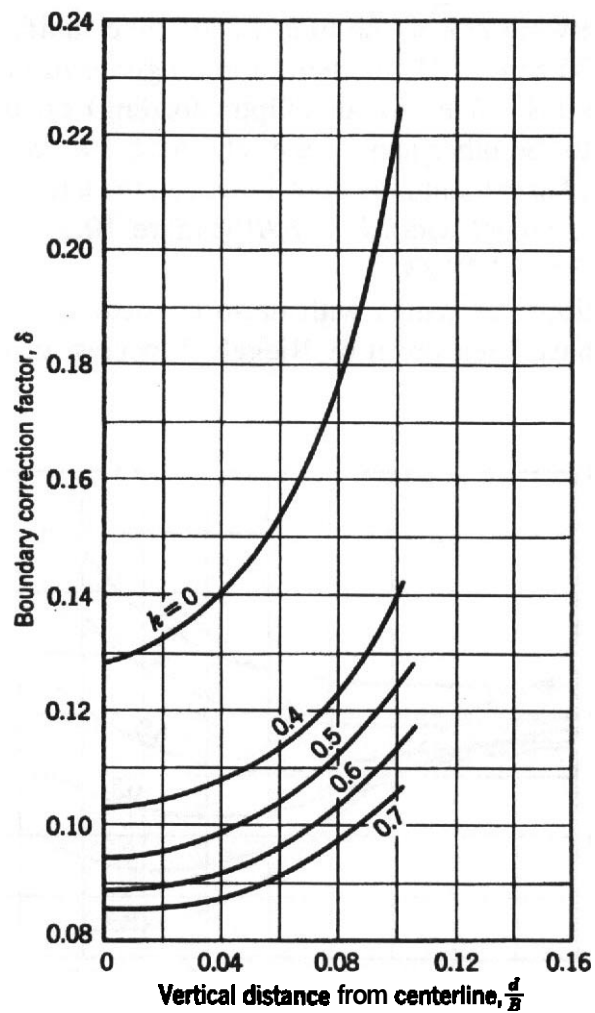
FIGURE 1030   Values of δ when a wing with uniform loading is displaced from the centerline of a closed 2 : 1 elliptic jet.
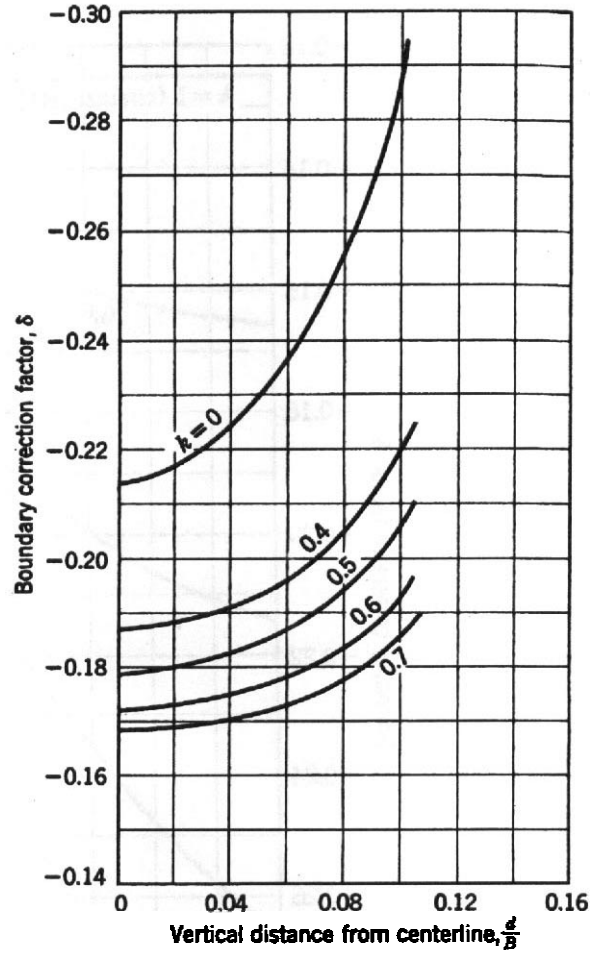
FIGURE 10.31   Values of δ when a wing with uniform loading is displaced above or below the centerline of an open 2 : 1 elliptic jet.
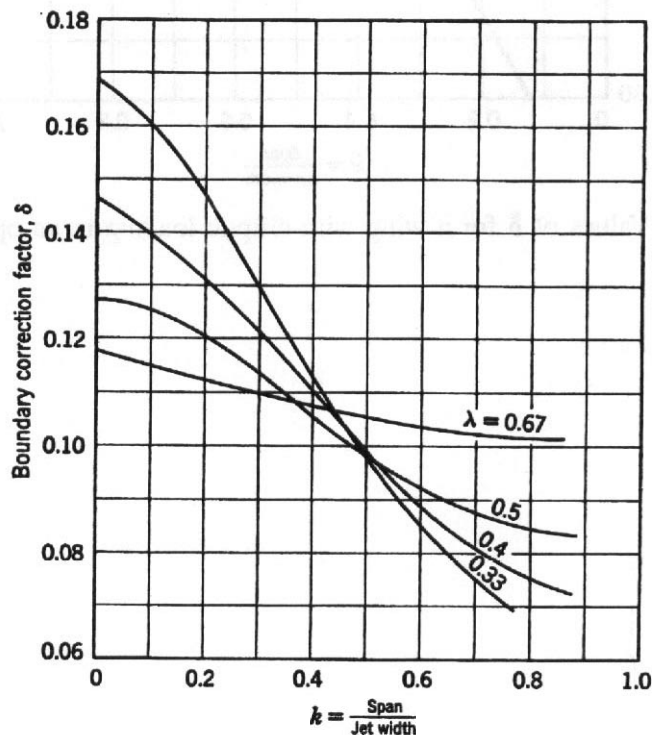
FIGURE 10.32   Values of δ for a wing with elliptic loading in a closed elliptic jet.
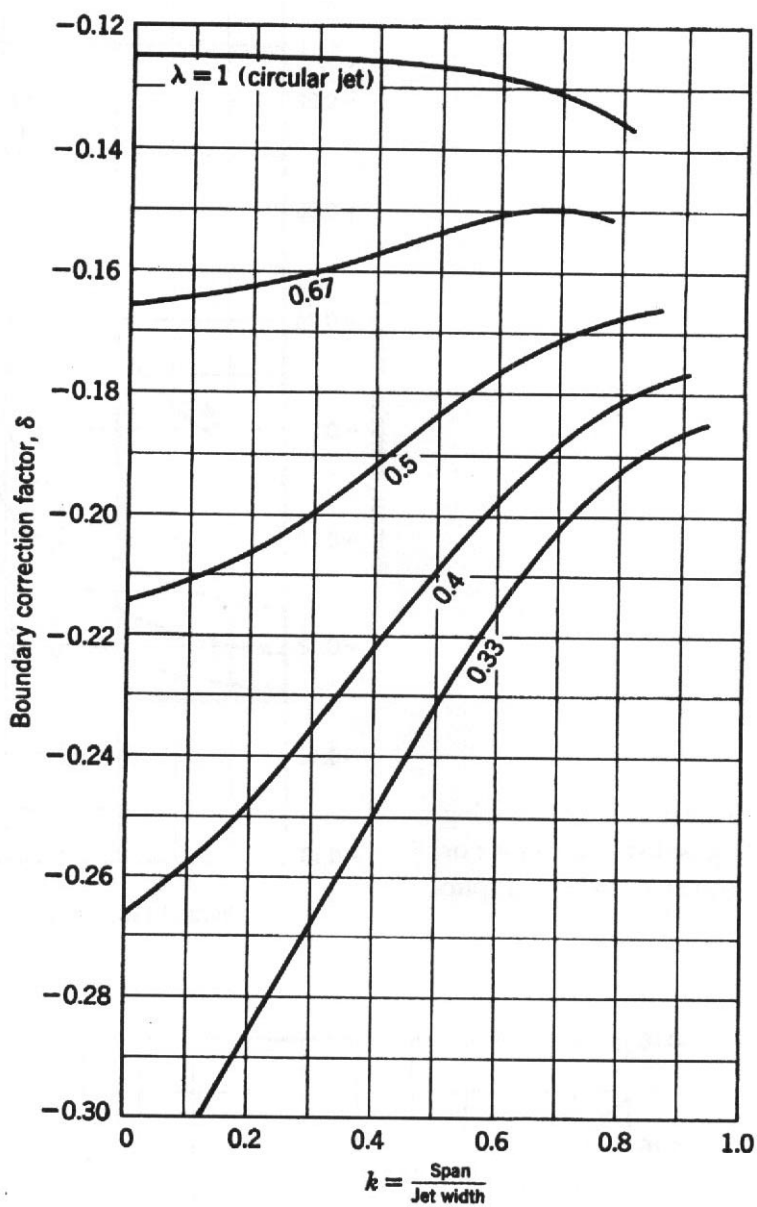
FIGURE 10.33   Values of δ for a wing with elliptic loading in an open elliptic jet,
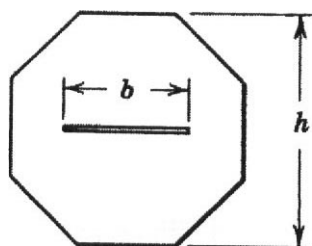
FIGURE 10.34   Wing in an octagonal jet.
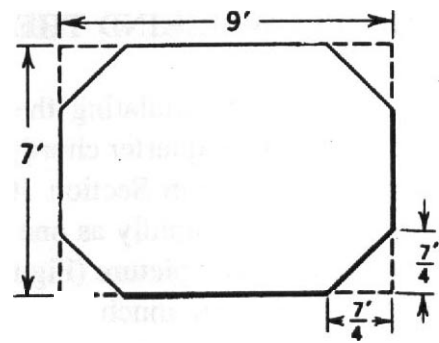
FIGURE 10.35   Tempering comers to form an octagonal test section.

using these values, they are not presented, although their existence and derivation are of interest.

Octagonal Jets

Wings with elliptic loading in octagonal test sections have been considered by Batchelor[25] and Gent.[26] The conclusion is that, for regular octagonal test sections (Figure 10.34), the corrections for circular sections may be used, the maximum error being 1.5% in δ or well under 0.2% in C_D for the most critical case.

The octagonal test section formed by tempering the comers of a rectangular jet has been discussed only for the case where a 7 X 9-ft rectangular jet is reduced by 45° flat fillets whose vertical height reduced the amount of side wall exposed by one-half (Figure 10.35). The effect of these fillets is to make the basic rectangular jet more nearly approach the elliptic jet. The wind tunnel boundary factor is hence reduced.

The correction factors for both the 7 X 9-ft rectangular and the octagonal test section are shown in Figure 10.36. As may be surmised, the corrections of the octagonal jet are essentially those of an elliptic jet of the same height–width ratio.
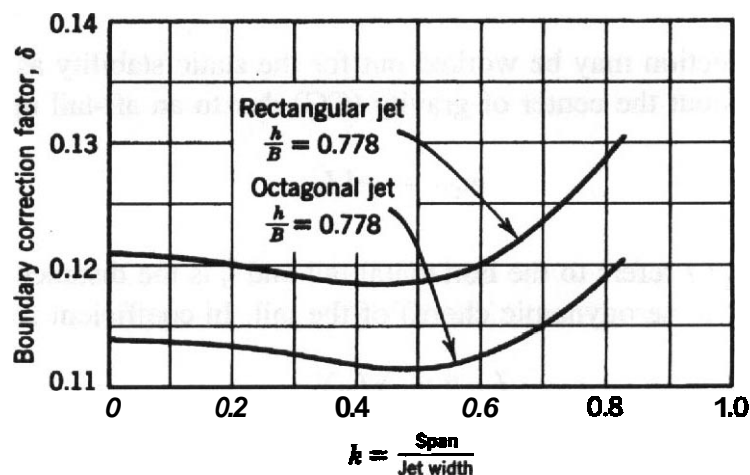
FIGURE 10.36   Values of δ for wings with elliptic loading in octagonal and rectangular test sections with tempered comers.

10.8   FLOW BEHIND THE WING

The method of simulating the boundaries by an image system in a plane taken through the wing quarter chord perpendicular to the axis of symmetry of the airplane has been covered in Section *10.5.* However, the amount of velocity induced by a vortex increases rapidly as one moves from the end of the vortex, so that, from the three-dimensional picture (Figure **9.12**), the amount of **upwash** at the tail of a model in a tunnel is very much more than that at the wing. Thus, for instance, at a time when the walls are reducing the wing angle of attack by $2°$, they could conceivably be reducing the tail angle of attack by $3°$. This large discrepancy, proportional to the lift coefficient, makes complete models in a closed test section appear very much more stable than they would in free air, while in an open jet the opposite effect is true.

This problem has been discussed by Lotz,[27] and the **boundary-induced upwash** velocity at a distance l_t behind the quarter-chord line has been presented as

$$w_k = \delta \frac{S}{C} C_{LW}(1 + \tau_2)V \tag{10.34}$$

where w_k is the **upwash** velocity in the plane of symmetry at distance l_t behind the quarter chord (w_k does not vary greatly along the span), C the jet **cross-sectional** area, V the tunnel velocity, and τ_2 the **downwash** correction factor.

Values of τ_2 for a number of tunnels are given in Figures *10.37–10.42,* and values of δ for the relevant model may be found in the preceding sections.

Some doubt exists about the validity of the **downwash** corrections for open throat wind tunnels as regard the values behind the lifting line since they were derived for an infinitely long test section and not for one about one diameter long, as is typical for actual tunnels. This finite length does change δ and τ_2, but, for wing corrections and corrections for streamline curvature, the change is not serious. For stability corrections for complete models in open test sections it would be in order to consult Silverstein and **Katzoff**[28] if the tail length is more than $0.4B$, where B is the tunnel width.

A parallel correction may be worked out for the static stability as follows:
The moment about the center of gravity *(CG)* due to an **aft-tail** upload is

$$m_{CG_t} = -l_t L_t \tag{10.35}$$

where the subscript *t* refers to the horizontal tail and l_t is the distance from the *C G* to the $\frac{1}{4}$ *MAC* (mean aerodynamic chord) of the tail. In coefficient form

$$C_{m,CG_t} = -\left(\frac{S_t l_t}{S\,MAC}\right)\left(\frac{q_t}{q}\right)C_{L_t} = -\overline{V}\eta_t a_t \alpha_t \tag{10.36}$$

$$\left(\frac{dC_{m,CG}}{d\alpha}\right)_t = -a_t\overline{V}\eta_t \tag{10.37}$$
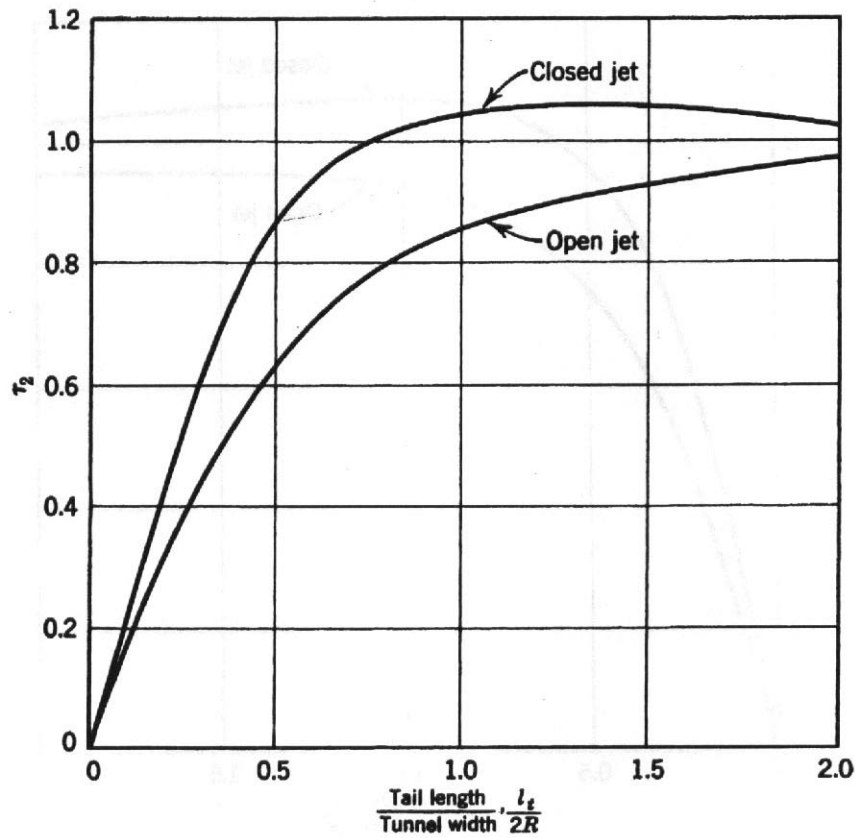
FIGURE 10.37   Values of τ_2 for open and closed circular jets.

By making two tail-on runs at different horizontal tail incidence angles ($i_t = a_t$), this term can be evaluated. Then

$$\Delta C_{m,\text{CG}_t} = \left(\frac{dC_{m,\text{CG}}}{d\alpha_t}\right)\Delta\alpha_t \tag{10.38}$$

From (10.34) the additional correction to the tail angle of attack is

$$\Delta\alpha_t = \frac{w_k}{V} = \delta\tau_2\left(\frac{S}{C}\right)C_{LW}(57.3) \tag{10.39}$$

Hence

$$\Delta C_{m,\text{CG}_t} = \left(\frac{dC_{m,\text{CG}}}{d\alpha}\right)_t \delta\tau_2\left(\frac{S}{C}\right)C_{LW}(57.3) \tag{10.40}$$

$$C_{m,\text{CG}} = C_{m,\text{CG}_u} - \Delta C_{m,\text{CG}_t} \tag{10.41}$$

The subscript W is added to emphasize that the correction is based on the wing lift, as are the corrections to angle of attack and the drag coefficient equations [(9.8), (9.9) and (10.26), (10.27)].
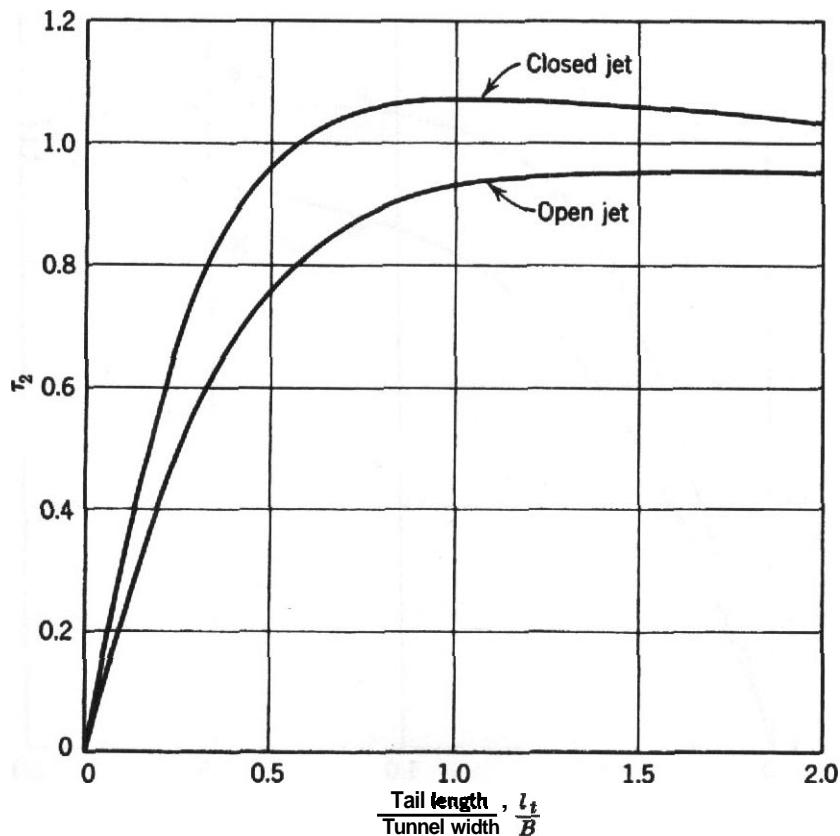
FIGURE 10.38 Values of τ_2 for open and closed elliptic jets.

To properly evaluate the correction to the pitching moment [(10.37)] requires a minimum of three runs: two tail-on runs at different tail incidence angles and a tail-off run. Basically what is being measured is the q at the tail. In many cases, for aircraft with both leading- and trailing-edge flaps a plot of $a_t \overline{V} \eta_t$ versus a will show an increasing value at low a's, a constant value in midrange a's followed by a decrease at higher α's. The low values at low a's are caused by the typical leading-edge flap stall at low a's, while the decrease at high a's near $C_{L,\max}$ is the trailing-edge flaps stalling. This effect is a function of the vertical location of the horizontal tail and the downwash of the wing. A note of caution: When evaluating $a_t \overline{V} \eta_t$ for models with remotely pitchable tails, these runs should be made at moderate tail angles to avoid a stalled tail. Because these runs are required to correctly reduce the data, models should be designed to allow the tail incidence angle to be changed easily and its angle accurately determined and accurately reset. Many experiments have produced ambiguous results because of inability to set and reset angles of surfaces and complete models with sufficient accuracy and precision.

The third run yields the basic information that is required to apply wall corrections. This is the wing lift coefficient and should be evaluated any time a model change is made to the wing. This is the basis for the suggestions by wind tunnel engineers that tests to determine optimum flap settings be done tail-off. The problem with this is that flaps produce large negative pitching moments, and these in turn can require large downloads by the tail to balance the airplane, which may negate the
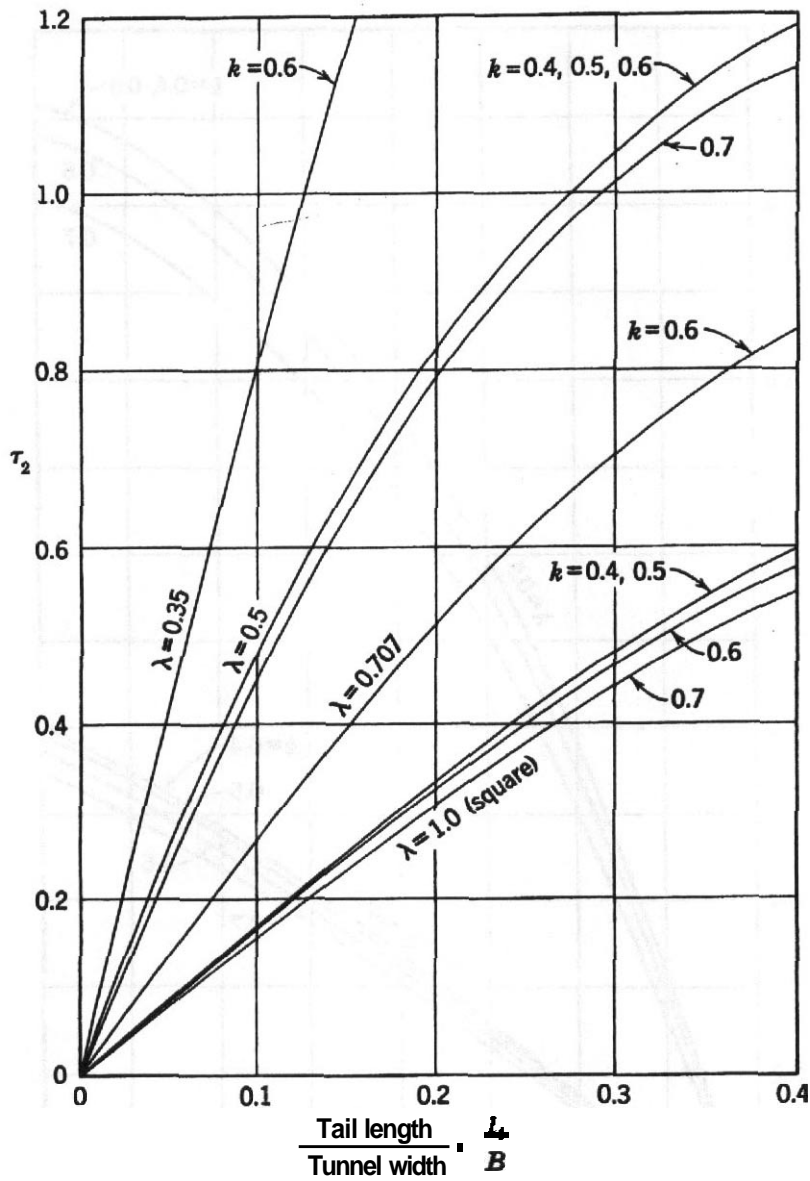
FIGURE 1039 Values of τ_2 for several closed rectangular wind tunnels, wing on tunnel centerline, and horizontal tail on wing centerline. Values for $\lambda = 0.35$ are by extrapolation.

gain in $C_{L,max}$ due to the flaps. There is no easy solution to this problem except to require that the model be designed so that the time required to put the tail on and off is minimal. Care should be taken with changes to the inboard portion of the wing because any change in **downwash** can effect the tail both through the $d\varepsilon/d\alpha$ term (Figures 13.36 and 13.38) in the stability equation and the q at the tail.

The changes in pitching moment curve slope due to wall corrections can be quite large but their validity has been amply demonstrated by flight tests.

If it is impossible to evaluate $(q_t/q)(dC_L/d\alpha_t)$, the relation

$$\frac{q_t}{q}\frac{dC_{Lt}}{d\alpha_t} = \frac{0.1\ \mathrm{AR}}{\mathrm{AR}_t + 2}(0.8) \tag{10.42}$$
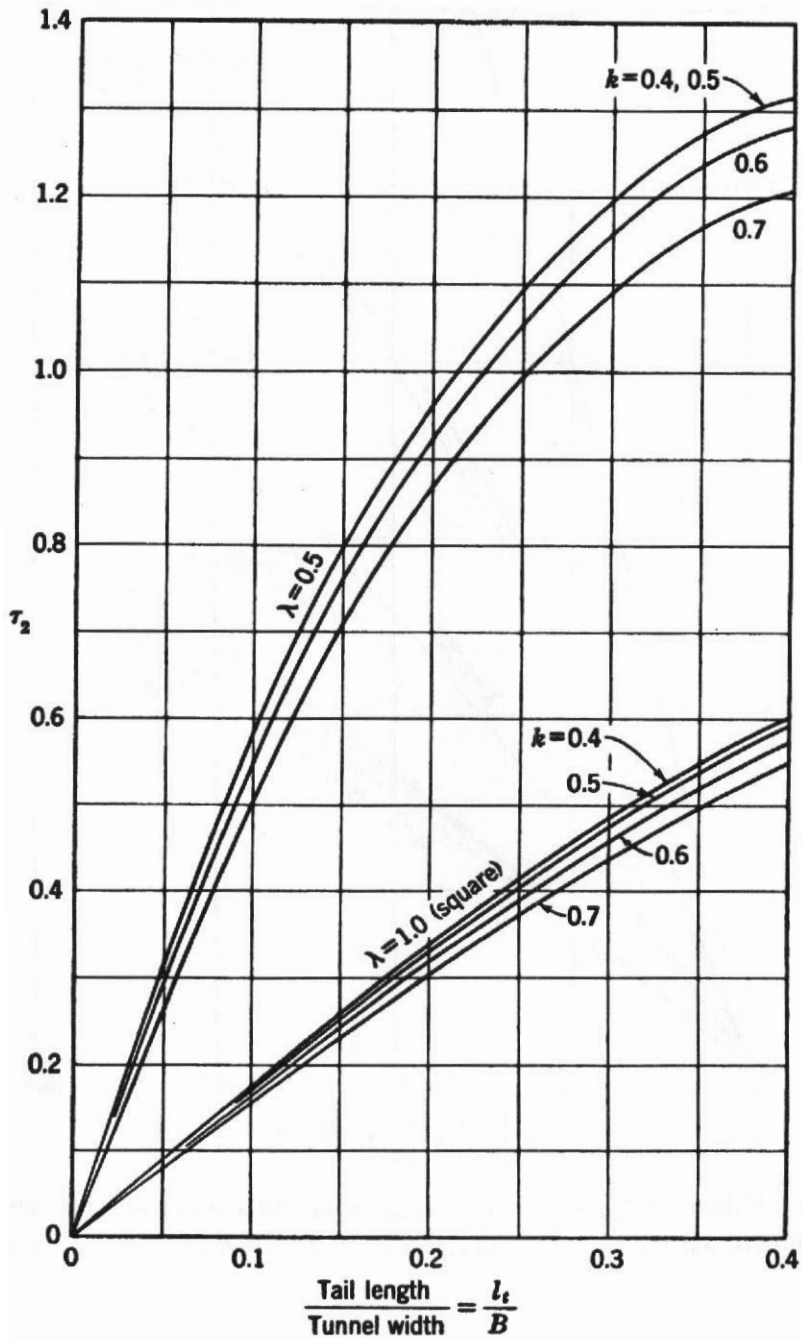
FIGURE 10.40   Values of τ_2 for two closed rectangular wind tunnels, wing on tunnel centerline, but horizontal tail $0.1b_e$ above or below wing centerline.

may be used. This is an approximate lift curve slope formula reduced by the factor 0.8. It is common to hear the factor 0.8 spoken of as a loss in dynamic pressure. Though there is some loss in average dynamic pressure over the horizontal tail produced by the fuselage boundary layer, it is far less than 20%, and the correction is more properly thought of as the result of the blanketing of the horizontal tail by the fuselage and its boundary layer and the resultant loss in lift across the fuselage, than as a loss in average dynamic pressure.
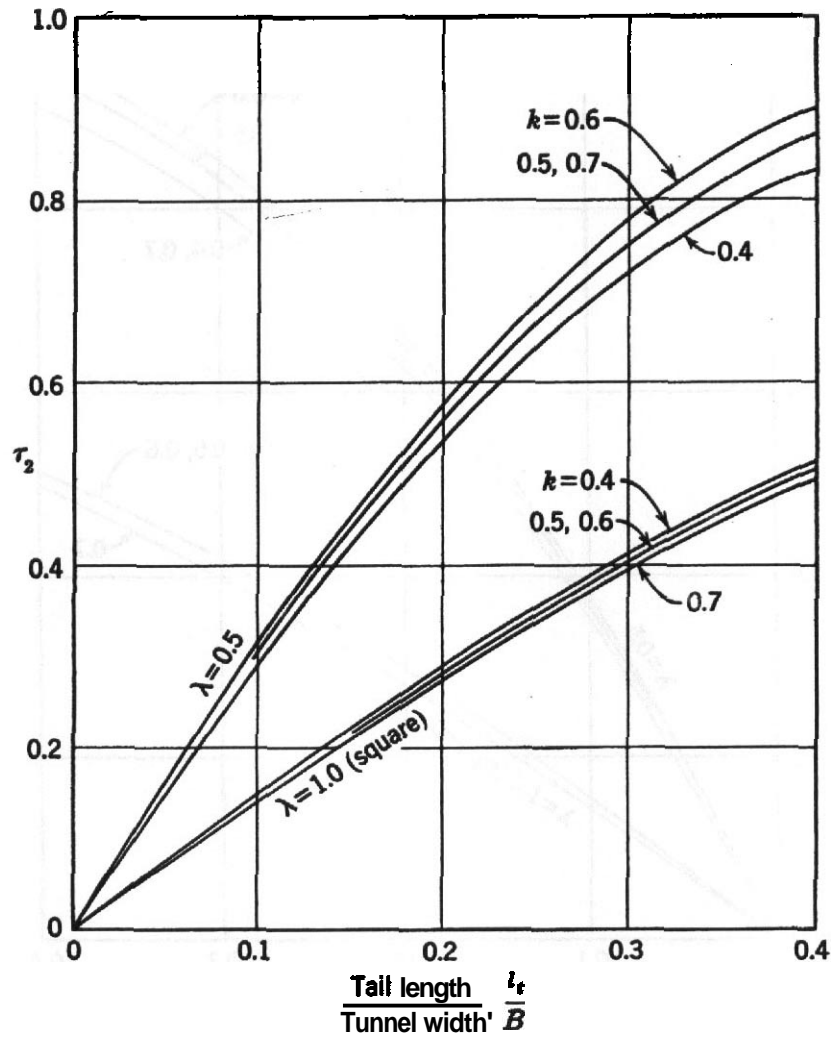
FIGURE 10.41   Values of τ_2 for two open throat rectangular wind tunnels, wing on tunnel centerline, horizontal tail on wing centerline.

Nonrectangular Tunnels

Over the years solid-wall tunnels have been built with a large variety of shapes other than rectangular. These shapes have included round, circular arcs, elliptic, regular octagonal, regular hexagonal, flat top and bottom with semicircular ends, and rectangular with comer fillets. The representation of these shapes by images outside of the walls have never been exactly correct. The curves that yield the wall correction factors from previous editions have been retained in this edition because the errors for moderate-size models and lifts are not too large and are further reduced by the wing-to-tunnel cross-sectional-area ratio, which is a small number. However, with the almost universal availability of high-performance computers the wall correction factors for these tunnels can be determined by vortex lattices in the walls, as discussed in Joppa's corrections, without the vortex wake relocation, if desired, or by other computational methods now widely available. The same techniques can be expanded to handle swept surfaces as well. All of these methods **are** being overtaken by those based on information from wall pressure measurements.
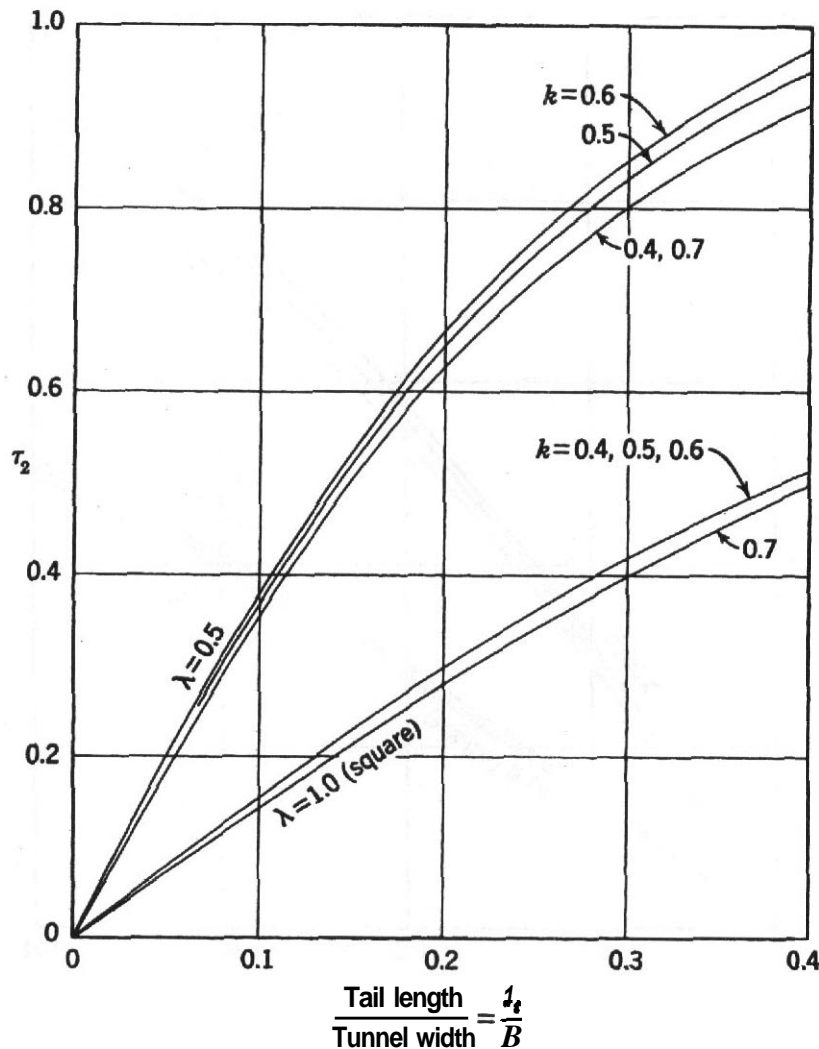
FIGURE 10.42   Values of τ_2 for two open throat rectangular wind tunnels, wing on tunnel centerline, but horizontal tail $0.1b_e$ above or below wing centerline.

Heyson's Method: V/STOL Aircraft

Glauert's classical wall corrections for wings assumed that all of the wing's lift is due to circulation and that the vortex wake trails straight aft in the plane of the lifting line and the free stream, which yields a vertical interference at the model. This assumption is not valid for V/STOL or powered lift systems, where the downwash at low forward speeds will produce a wake angle approaching the 90° required in hover. Heyson[29] at NASA Langley began his work on the wall correction problem with rotors.

Expanding this beginning, Heyson[30] considered a broader class of problems. He represented the wake by a semi-infinite string of point doublets with axes tilted relative to the model's lift and drag. This wake proceeds linearly to the tunnel floor and then aft along the floor. Then images and superposition are used to find the effect at the model. Heyson's method yields both vertical and horizontal interferences rather than the vertical interference only as given by Glauert. The two methods agree on interference factors for a wake trailing straight aft.

Heyson[30] calculated interference factors at selected points in the tunnel for a point or vanishingly small model. He demonstrated how doublet strings may be distributed along a wing or a rotor and showed the results for a tunnel with a width-to-height ratio of **2.**

Heyson[31] extended the use of superposition using digital computers to obtain interference factors for swept and nonswept wings, tails aft of wings, single rotors with tail, and tandem rotors. This work gives numerical results of the affect of many variables on the correction factors. Fortran programs are reported[31]

Heyson[33] further extended his work to a general theory of wall interference in closed rectangular test sections plus ground effects. In his work large wake deflections are addressed, in both vertical and lateral directions. This work includes a program to determine interference factors at a point (vanishing small model) and a discussion of the program and flow charts for the program. Owing to both lateral and vertical wake deflections, there are nine interference velocities. As lateral directional testing is concerned with moments, the gradient of the interference velocities are needed, which yields 27 velocity gradients. Rather than develop actual correction formulas for all possible models, the paper discusses tunnel wall effects as a problem in similitude.

The following discussions of **Heyson's** corrections will be limited to the plane of symmetry of the aircraft and will follow **TR R-124**[30] and **TR R-302.**[31] These corrections use a linear wake that is deflected downward. The angle of the wake deflection is a function of the lifting systems' lift and induced drag. The four wall interference factors are a function of the wake's deflection. Hence a new set of factors is needed at each test point. In the classical corrections, the wall correction factor is constant for a given tunnel and model. **Heyson's** works have copious numbers of figures, which could be used to calculate the wall effects. However, the task of determining the wake skew angle, reading eight interference factors for the wing and tail as minimum, calculating the interference velocities, and applying them to the data would be time consuming with a large chance for error. Thus the use of **Heyson's** methods implicitly assumes that a digital computer will be used.

To calculate the interference factors at any point in the tunnel, say the centerline of the wing, first requires the wake skew angle χ. This is the angle from the vertical to the wake and is the complement of the momentum downwash angle. The skew angle can be obtained from charts in **TR R-124**[30] and **TN D-814**[34] or calculated as outlined in **TR R-124.**[30]

The interference factors are based on χ effective, not the momentum value of χ. In forward flight the wake of a lifting system changes form and angular deflection as it moves aft of the model. The wakes for wings, rotors, and jets eventually evolve into a pair of trailing vortices. As these vortices roll up, they do not move downward as rapidly as the central portion of the wake; almost all the momentum transfer induced by the lift appears in the central portion of the wake. This region is constrained to be bounded within the trailing vortex pair after roll up.

The actual downward deflection of the wake vorticity in the rolled up wake is approximately one-half that predicted by momentum. This was first pointed out by Heyson and Grunwald.[35] This paper established the criteria of an effective skew

angle that is used to determine the interference factors. The following definitions for downward deflection angle or wake skew angle were chosen[36] to handle the hover case (although testing in a tunnel may be questionable):

$$\tan 0, = \frac{4}{\pi^2}\tan \theta \qquad (10.43)$$

or

$$\tan \chi_e = \frac{\pi^2}{4}\tan \chi \qquad (10.44)$$

where $0 = 90° - \chi$. Note:

1. Effective angles are used only for obtaining interference factors.
2. Induced velocities are obtained directly from momentum theory.

The second statement is required to avoid an imbalance between the forces and the induced velocities engendered by the forces.

The theory in TR R-124[30] and TR R-302[31] and the programs in TM X-1740[32] yield four interference factors that are used to determine the interference velocities at the chosen point:

$$\Delta w_L = \delta_{w,L}\frac{A_m}{A_T}w_0 \qquad (10.45)$$

$$\Delta u_L = \delta_{u,L}\frac{A_m}{A_T}w_0 \qquad (10.46)$$

$$\Delta w_D = \delta_{w,D}\frac{A_m}{A_T}u_0 \qquad (10.47)$$

$$\Delta u_D = \delta_{u,D}\frac{A_m}{A_T}u_0 \qquad (10.48)$$

where the 8 factors are similar to the wall correction factor *6* in Glauert's work; A, and A_T are the momentum areas of the lifting system and tunnel cross-sectional area; w_0 and u_0 are the momentum theory values of the vertical and longitudinal velocities at the lifting system due to the lifting system only; Δw_L and Δw_D *are* the boundary-induced vertical interference velocities (positive upward) resulting from lift L and induced drag D_i; and Δu_L and Δu_D are the boundary-induced longitudinal interference velocities (positive to the rear) from lift and induced drag.

The interference factors $\delta_{w,L}$, $\delta_{u,L}$, $\delta_{w,D}$, and $\delta_{u,D}$ are functions of the tunnel geometry, height of the model in the tunnel, span loading, angle of attack, and wing sweep of the model. We will follow TR R-124[30] and apply the corrections to a vanishingly small or point model.
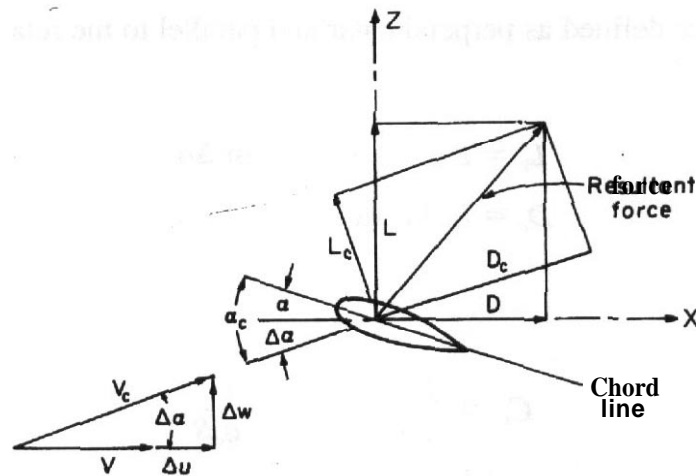
FIGURE 10.43   Nomenclature for Heyson's wall corrections.

The four interference velocities **are** combined to yield the total interference at the model:

$$\Delta w = \Delta w_L + \Delta w_D \tag{10.49}$$

$$\Delta u = \Delta u_L + \Delta u_D \tag{10.50}$$

The corrections **are** applied to the data as follows: The subscript c refers to values corrected for interference. Figure **10.43** illustrates the corrections of angles, velocities, and forces:

$$\alpha_c = \alpha + \Delta\alpha \tag{10.51}$$

$$\Delta\alpha = \tan^{-1}\frac{\Delta w}{V + \Delta u} = \tan^{-1}\frac{\Delta w/V}{1 + \Delta u/V} \tag{10.52}$$

Note that **Heyson** does not use the small-angle assumption of classical **wall** corrections:

$$V_c = \sqrt{(V + \Delta u)^2 + \Delta w^2} \tag{10.53}$$

or, in *terms* of q or dynamic pressure,

$$\frac{q_c}{q} = \left(1 + \frac{\Delta u}{V}\right)^2 + \left(\frac{\Delta w}{V}\right)^2 \tag{10.54}$$

as lift and drag are defined as perpendicular and parallel to the relative wind or the corrected velocity:

$$L_c = L \cos \Delta a - D \sin \Delta a \qquad (10.55)$$

$$D_c = L \sin \Delta a + D \cos \Delta \alpha \qquad (10.56)$$

and finally,

$$C_{L_c} = \frac{L_c}{q_c S} \qquad C_{D_c} = \frac{D_c}{q_c S} \qquad (10.57)$$

See TR R-302[31] for the interference distribution over swept and nonswept wings, rotors, and the like and interference at the tail. The tail corrections, as with classical wall corrections, are based on the difference between the wall-induced angle of attack at the wing and wall-induced angle of attack at the tail. This is equivalent to a change in tail incidence and, of course, varies with the forces on the wing or lifting system. Heyson[37] discusses two methods of correcting the tail pitching moment. The first accounts for the difference in pitching moment caused by the tail in the tunnel and the moments if the tail had the same wall interference as the wing. The second takes the difference in wall-induced angles of attack at the wing and tail and rotates the tail incidence by this moment.

In TR R-302[31] there is a detailed discussion of the effect of model size (wing and rotor), wing sweep, and location of a swept wing's pivot on the interference factor $\delta_{w,L}$. It should be realized that although the factor $\delta_{w,L}$ will vary, the induced velocity Δw_L is also influenced by the model and tunnel momentum areas [(10.45)].

There are extensive comparisons in TR R-302[31] and TN D-6416[36] between Heyson's theory and the conventional corrections after Glauert. The correlation between the two methods is quite good at zero-induced drag. At high lift coefficients (low skew angles) Heyson's theory indicates vertical interference factors greater than conventional theory. For an effective skew angle between 75° and 90° the magnitude of $\delta_{w,L}$ remains about constant at values equivalent to the conventional corrections. An effective skew angle of 75" is equivalent to a momentum skew of 57" or a momentum downwash angle of about 33°.

If a swept wing's aerodynamic center and pivot point coincide at the center of the tunnel, then the average $\delta_{w,L}$ shows little or no change up to an angle of attack of 20" for effective skew angles greater than 65° for a 45° swept wing. If the pivot is moved to the apex of the lifting line, there is little effect on $\delta_{w,L}$ at effective skew angles above 75° (momentum downwash 33°) for a wing with 45" sweep.

Heyson's corrections would be useful for the occasional odd model, once the programs are installed and checked, with the assumption that the available computer is of adequate size to carry out the calculations in a reasonable time.

One more point must be considered when testing models at low skew angles or large momentum downwash angles. Flow breakdown caused by an interaction between the model wake and the tunnel floor will result in a tunnel flow that does

not reasonably approximate the uniform flow of level flight. This limit occurs approximately when $X_f/b = 1.25$ where $X_f =$ h tan χ, h is the height above the floor, and χ is the momentum skew angle.

Joppa's Vortex-Lattice Method.

Another approach to wall corrections for wings developing high lift was put forward by Joppa.[38-40] Computer programs are included.[40] Joppa's work, like Heyson's, became practicable with the advent of sufficiently fast digital computers. Rather than allowing the wake or vortex to trail straight aft as in classical wall corrections, or assuming a deflected linear wake, Joppa took the following approach.

The wing vortex wake in the tunnel follows a different trajectory in the tunnel than in free air. Joppa calculated the wake trajectory and its flow field in free air by assuming a simple lift system represented by a horseshoe vortex. This lifting system then has its trajectory and flow field calculated in a wind tunnel at the same remote velocity and circulation strength. The differences are then interpreted in terms of wall interference.

The free-air trajectory is found using vortex segments that are about 0.10 of the vortex span. The wing is taken as having a uniform load with a bound vortex on the $c/4$ and a vortex span of $(\pi/4)b$. This is the usual representation of an elliptical load. The first trailing segment lies in the wing from the bound vortex to the trailing edge. The angle of the first downstream trailing vortex is determined by adding the induced angle of attack and the effective angle of attack at the plane of symmetry. The direction of each downstream segment in turn is calculated by the sum of velocities due to all other elements at its upstream end. This determines the coordinates of the downstream end; the following downstream segment is then translated to that point, keeping it attached. Then the process is repeated and the vortex trajectory is moved into place by sweeping along its length by successive iterations. As the vortex curves down, it also curves inward at first, reducing the vortex span. The final trajectory is determined by first calculating the downward deflections and then a second pass for the horizontal or inward deflection. This double iteration is necessary to avoid an instability in the path after a few iterations. The path converges in three or four double passes before the instability develops. It is interesting to note that a curved vortex line is itself physically unstable.

These techniques are included in the more recent panel codes such as PMARC, VSAERO, and PANAIR. They are referred to as "free wake" options or "wake relaxation" options. It is almost always required that the aerodynamicist provide good intelligence, as the codes frequently provide nonsensical results if they converge at all when these options are applied.

The tunnel walls could have been represented by curved image vortex systems as in the conventional method, but this method only works for rectangular tunnels. To make the method applicable to any tunnel shape the tunnel walls are represented by vortex lattices. The strength of each element of the lattice is determined by simultaneously requiring the normal component of velocity to vanish at the center of each lattice. This satisfies the boundary condition of no flow through the tunnel

walls at the control point. By this method the geometry of the image flow field does not change during each iteration and the large matrix of coefficients need only be inverted once. For each vortex ring an equation at its control point is written where the strength of the ring Γ_i is the unknown. To keep the number of equations to a tractable level, some judgment must be used.

When the equations for Γ_i are solved and Γ_i is known, the wall-induced velocity at any point in the test section can be calculated. The interference is expressed as an angle, which is the arc tangent of the vertical-induced velocity and tunnel velocity.

For a round tunnel Prandtl used two images (Figure 10.7) to represent the wall. This gives the upwash at the wing lifting line. But as the effect of the lifting line was not taken into account, it will not yield the downstream variation in wall-induced upwash. In fact, the use of two semi-infinite vortices to represent the walls violates Helmholtz's vortex theorems. However, at the wing it does give the correct answer. Joppa's method can represent a round tunnel by approximating it as a multisided polygon. Joppa[40] compares his work with a nondeflected vortex wake with approximate results from Silverstein[16] and Lotz.[27] Joppa's value of δ lies very close to halfway between the approximate methods.

The solution for the wake trajectory in the tunnel is an iterative combination of the free-air-trajectory solution and vortex-lattice wall solution. The wake solution method for free air is used with the velocities from the wall for an undeflected wake added to those of the wing in free air. When the wake trajectory is found, a second solution for the Γ_i's in the wall is found for this wake. Then the cycle is repeated. As there is no strong interaction in the two systems for normal models and tunnels, only two to three cycles are required. When the solution is complete for the same tunnel velocity and wing circulation, they yield the following:

1. complete velocity field in free **air,**
2. complete velocity field in tunnel, and
3. the separate contribution to item 2 of the wing and tunnel walls.

The interference velocities are the difference between the velocity in free air and the tunnel at a given point. Joppa[40] only presented results for the vertical velocity components because he limited the work to moderate wake deflections that yield small longitudinal components. The vertical interference velocity is felt as an angle-of-attack change. Thus

$$\Delta\alpha = \tan^{-1}\left(\frac{V_y}{V_x}\right)_T - \tan^{-1}\left(\frac{V_y}{V_x}\right)_{FA} \tag{10.58}$$

where subscript y is vertical and x is horizontal, with T the tunnel and FA the free air. As the calculations are made for the same circulation and free-stream velocity values in the tunnel and free air, then

$$\Delta\alpha = \delta\frac{2\Gamma b}{CV} \tag{10.59}$$

where C is the tunnel cross-sectional area. And thus

$$\delta = \left(\frac{CV}{2\Gamma b}\right)\left[\tan^{-1}\left(\frac{V_y}{V_x}\right)_T - \tan^{-1}\left(\frac{V_y}{V_x}\right)_{FA}\right] \tag{10.60}$$

Joppa's results are based on circulation lift only and are for a wing of low aspect ratio to achieve high values of C_L/AR and relatively large wake deflection angles.

The effect of the tunnel's relocation of the vortex wake on the pitching moment correction is quite sensitive to the location of the tail relative to the wing.

The energy wake is also relocated in the tunnel, and this affects the dynamic pressure at the tail. The dynamic pressure of the tail may be less than free stream owing to wakes from wing flaps or greater than free-air stream due to propulsion devices. The values of $dC_m/d\alpha_t$ should, because of these uncertainties, be measured.

If both the vortex wake and the energy wake shift the same amount in the tunnel when testing in the STOL flight range, Joppa proposes that the tail on the model be made vertically movable. Then, prior to the test the vortex wake shift for each value of wing circulation is calculated. Then stability testing would be done at several tail heights. This would produce a family of pitching moment curves, each one of which would be valid for a given wing lift coefficient. The final moment curve would be a composite curve from these curves. This would reduce the energy wake shift correction to zero due to the relocation of the tail. The only correction then required would be due to wall-induced effects.

10.9   SUMMARY: CLOSED TEST SECTION

In this section the complete data reduction process for an experimental evaluation of a complete airplane configuration will be summarized. This will include materials from previous chapters as well as the present one. The process can be done by hand (pocket calculator) as well as by digital computer, and once through by hand for any wind tunnel engineer is highly recommended:

1. *Keeping Track of* the Data. A typical pitch run can have 20 or more a's at which data are taken. In the data reduction there are either tables or curves that must be used to obtain required values; thus there has to be a common variable to keep track of the data.

Quite often when data are acquired by a computer, the computer software will assign a sequential number (often referred to as a record number) to acquired data. (This is analogous to the old IBM card number. Those were important in case the card deck was dropped!) This is not a good variable to use to keep track of the data for the following reasons. During a test the values of a or ψ used may not be the same for all runs, nor is it reasonable to require that they be the same. The number of angles may be reduced to save running time, they may be increased to define a curve better, or some angles may be repeated when checking for bad points.

Based on the above discussion, the only way to keep track of the model attitude when acquiring data is to use a measured value from the model. Thus, the measured a and ψ or β or roll angle from the model positioning mechanism should be used. Modern database software has made this much more manageable in the last few years. It allows quicker and more flexible access for cross plotting of data from virtually any combination of parameters manipulated during an experiment.

2. Assumptions. It is assumed that the model angles and the balance forces and moments are in engineering units, that is, angles in degrees and forces and moments in pounds and inch-pounds (or SI units). This means that the measured quantities have been converted from bits or voltages to engineering units through the applicable calibrations and unit conversions.

The discussions that follow will assume that an external balance is used to avoid taking into account all of the possible variations that exist for stings and internal balances. Since the discussion is general in nature, it can easily be adapted for other model support and balance systems.

3. *True Balance Loads.* The loads read out of the balance are corrected to the true loads applied to the balance by the balance calibration equations (see Chapter 7). These are the values required in all subsequent calculations. They will be designated by subscript u, for example, L_u. The balance calibration is applied to all loads, both aerodynamic and tares.

4. *Applying Mechanical Calibrations to α and ψ.* If the measured values are not the actual model geometric angles, the calibrations from the indicated angle should be applied to the geometric angle. This most often occurs for a due to location of the trunnion and the pitch arm.

If corrections are required for balance and model support deflections, these are also applied. Generally these deflections are obtained by applying known loads to the balance support system and model, so the loads from 3 are used. The true geometric angle will be designated by the subscript g, that is, a_g, ψ_g.

5. *Basic Corrections to Dynamic Pressure.* Most tunnels are run by an indicated dynamic pressure obtained from two measured pressures. The indicated dynamic pressure is then corrected for the tunnel dynamic pressure calibration (see Chapter 6). This dynamic pressure will be designated q_A.

If the data system measures the error in the operator's maintaining the desired dynamic pressure, this value will be added to q_A as a Δq_{op} value.

Thus, at any data point the dynamic pressure approaching the model is $q_A +$ Δq_{op}. This is not standard practice today since many tunnels have control systems for maintaining the tunnel speed. These, however, are not perfect and must be monitored. There is still almost always a need to monitor and record both a target dynamic pressure and the measured dynamic pressure corresponding to each set of balance, pressure, or other data that are acquired.

6. *Summary of Corrections.* At this stage of the data reduction process there is a table for each run of the "true" test values for model geometric angles, dynamic pressure, and balance loads. The following corrections will be due to the tunnel walls.

7. Blockage Corrections. Solid blockage ε_{sb} is a function of the model volume and the tunnel size. As indicated under Solid Blockage in Section 9.4, it usually is in two parts: one for the wing and a second for the body, both of which are summed to yield ε_{sb}. If possible, these values should be determined prior to the start of the test.

Wake blockage ε_{wb} (see under Wake Blockage in Section 9.4): If the wake pressure drag blockage equations [(10.7) and (10.8)] are to be used, they should be determined prior to the tests. These values are quite small for most models and are often neglected.

Maskell's corrections for a separated wake are often applied and to an extent include the wake pressure drag blockage terms. Maskell's **correction** is in two parts [Eq. (10.9)]. The first is based on the parasite drag C_{D0} and the second on the separated wake. The first part includes parts of Eqs. (10.7) and (10.8) and both corrections should not be applied. From unseparated flow, $C_{Du} = C_{Di} + C_{D0}$, and for separated flow, $C_{Du} > C_{Di} + C_{D0}$. Owing to data scatter, using a computer to reduce data usually requires a statement that if $C_{Du} - C_{Di} - C_{D0}$ is negative, it should be set to zero. Hackett's blockage must be determined by the wall pressures (see the discussion of Hackett–Wilsden and Ashill–Keating methods in Section 10.3). The final blockage correction is given as

$$\varepsilon_T = \varepsilon_{sb} + \varepsilon_{wb} \tag{10.61}$$

$$q_C = q_A (1 + \varepsilon_T)^2 \tag{10.62}$$

$$V_C = V_A (1 + \varepsilon_T) \tag{10.63}$$

It should also be noted that the blockage corrections are required to produce the correct dynamic pressure that is used to calculate all coefficients, including pressure and hinge moment. Thus, when blockage corrections are used, the force data must be acquired and reduced before the pressure coefficients, hinge moments, and so on, are reduced.

The dynamic pressure is now fully corrected unless Heyson's wall corrections are used. In Heyson's corrections there is an additional correction to dynamic pressure due to the large wake deflections (see under Heyson's Method: V/STOL Aircraft in Section 10.8).

8. Support Tares and Interferences. In tests where only incremental values are of primary interest either the support tare and interferences values are not applied or a general set that do not take into account the interference of the supports on the model are applied. As the general tares are taken from another model, and as the mounting struts for an external balance enter the wing, these tares are best applied as a function of C_{LW} rather than a. This is because of possible differences in α_{L0} and the reference plane used to measure a. The tares for the appropriate q_I or q_A should be used. This is done to save test time and costs incurred in evaluating all required support tares and interferences for each model and its various configurations.

If the tares are taken with the model being tested, the appropriate tares for the model configuration at the correct α_I or a, and q_I or q_A are used (Chapter 7).

The tares are subtracted from the balance force data of item 3.

9. Weight Tares. The weight tares are a result of the model center of gravity not being on the balance moment center. Thus when the model is pitched, there will be a pitching moment versus α_I due to the weight. When the model is yawed, there will be both a pitching and a rolling moment due to weight. Similar tares will arise with a sting and internal balance. The tare values are subtracted from the balance data. The weight tares are a function of model configuration; thus the correct tare must be applied to the correct run.

If additional tares are required, such as internal nacelle forces, they also must be applied at this point. There is no order of preference in the order of subtracting support, weight tares, and other tares.

At this point the data have the correct geometric angles, correct dynamic pressure, and correct aerodynamic forces on the balance (corrected for support, weight, and other tares).

10. Moment Transfer. Now the balance forces and moments are transferred to the desired center-of-gravity location on the aircraft. These calculations only affect the three moments: pitch, yaw, and roll. The equations required are a function of the type of balance, which determines the relationship between the balance moment center, the model trunnion, and the location of the desired center of gravity. Thus, it is difficult to write the actual equations for all cases. As an example, if the balance moment center and the model trunnion coincide, then the following information is required. The three distances from the moment center to the center of gravity along the three orthogonal tunnel centerlines passing through the balance moment center act on each combination of model α and ψ. The three lengths will change as the model is pitched and yawed since the desired center of gravity moves relative to the balance moment center. Because the equations are a function of geometry, they must be worked out for each tunnel and model. The pitching moment is affected by lift and drag, the yawing moment by drag and side force, and the rolling moment by lift and side force.

The customer or the model builder must furnish the distances between the trunnion and the desired center-of-gravity locations. The tunnel group knows the relationship between the trunnion and balance moment center.

Extreme care must be taken to make sure that all tare values (e.g., support weight) have been applied before the balance data are transferred from the balance moment center to the desired center of gravity. Many of these tares involve lift, drag, and side force that are used in the moment transfer.

11. *Uncorrected Coefficients.* The table of data from item 9 above is now reduced to coefficient form using the corrected dynamic pressure q_C. The dynamic pressure due to wake blockage and operator error will vary with α_g or ψ_g. The value associated with the angles under consideration is used. The lift coefficient as well as yawing moment, rolling moment, and side force have no further corrections and thus are final corrected values. The drag, pitching moment, and angle of attack need further corrections.

12. *Wall Corrections.* The wall correction theories of Glauert, Heyson, and Joppa are based on the forces generated by the model lifting system. The spanwise lift

distribution either can be taken as uniform or can be distributed in an elliptical or other load for the wing. Which spanwise lift load is used depends on how the lifting surface was mathematically represented. In general, Glauert and Joppa use a uniform load with a reduction in vortex span and the same circulation at the centerline as an elliptical load. Heyson's later work distributes the point doublets along the span and thus allows easily for either a uniform or elliptical load for wings and a uniform or triangular load for rotors or any other desired loading. If desired, the load can be distributed along the span in Joppa's and Glauert's methods also.

For an airplane model this means that the wall corrections are based on using wing lift only. Thus, runs should be made with the wing only for wing and wing-plus-flap combinations. For some models this is not possible because the model was not designed to be tested with the wing alone. The reasoning behind this is that the fuselage is always there and thus should be considered as a unit with the wing. Also, the amount of time required to assemble/disassemble the model for wing-alone runs may be prohibitive. In these cases runs are made with the horizontal tail off (tail-off runs) to obtain the required data for wall corrections. The following discussion will use the conventional, or Glauert-type, corrections, where the assumed vortex wake trails straight aft of the wing. In this case the correction factor at the wing is a constant. The plots in Chapter 6 are for this case. If either Heyson's or Joppa's method are used, the wall correction factors would be calculated based on the tail-off data for each angle of attack, or C_L.

Angle-of-Attack Correction

$$\alpha_C = \alpha_g + \Delta\alpha_{up} + \Delta\alpha_w \tag{10.64}$$

where α_C is the corrected angle of attack, a, the geometric angle of attack (see item 4), $\Delta\alpha_{up}$ the tunnel upflow as determined in Section 4.16 by either probes or a calibration wing or as a part of evaluating the tare and interference, where

$$\Delta a, = \frac{\delta S}{C C_{LW}}(57.3) \tag{10.65}$$

δ being the wall correction factor and a function of the model-span-to-tunnel-width ratio [see Eq. (6.55)], span load, location in the tunnel, and tunnel shape and C_{LW} the wing or tail-off lift coefficient for the model wing configuration used in the run.

Drag Coefficient

$$C_{DC} = C_{Du} + \Delta C_{D,up} + \Delta C_{Dw} \tag{10.66}$$

where C_{Du} is from item 11.

$$C_{D,up} = C_{LW} \Delta\alpha_{up} \tag{10.67}$$

where $\Delta\alpha_{up}$ is in radians.

$$\Delta C_{Dw} = \frac{\delta S}{C C_{LW}^2} \tag{10.68}$$

Pitching Moment Coefficient

$$C_{m,CG_C} = C_{m,CG_u} - \Delta C_{m,CG_t} \tag{10.69}$$

$$\Delta C_{m,CG_t} = \left(\frac{\partial C_{m,CG}}{\partial\delta_s}\right) \delta\tau_2\left(\frac{S}{C}\right)C_{LW}(57.3) \tag{10.70}$$

where $\partial C_{m,CG}/\partial\delta_s$ is the rate of change of the pitching moment coefficient with stabilizer deflection, which is proportional to the change in angle of attack for the tail. It is $-a$, $\overline{V}\eta_t$ [see Eq. (10.37)] and is obtained by making at least two, but preferably three, tail-on runs at different stabilizer angles. Care must be taken in evaluating $\partial C_{m,CG}/\partial\delta_s$ to make sure that the tail lift is in the linear portion of its $C_{L-\alpha}$ curve, that is, the tail is not stalled. Measuring $\partial C_{m,CG}/\partial\delta_s$ avoids any error in assuming values for a, and η_t. For a model with leading- and trailing-edge flaps the value may vary with a . At low a's, when the leading edge is separated, it will have a lower value than the nonstalled region, and again, at high α's, when the trailing-edge flaps stall, the value will again decrease. In some cases the aerodynamic engineer prefers to use the variable value. The parameter τ_2 is the additional correction factor for differences in upwash from the tunnel walls at the tail and wing (see Section 10.8). Again, this term is a function of model geometry and size, tunnel geometry and size, and location of the tail relative to the wing. The important parameters are tail-length-to-tunnel-width ratio and vertical location of the tail relative to the wing. If desired, the value of τ_2 can be varied to account for the vertical motion of the tail relative to the wings as the model is pitched.

The three wall corrections are usually worked up in the form of K_1C_{LW} for a, $K_2C_{LW}^2$ for drag, and K_3C_{LW} for pitching moment. These constants from Equations (10.65), (10.66), and (10.68) are stored versus the geometric angle of attack. There will be a set of these corrections for all combinations of the wing, flaps, spoilers, and so on, that are in the experimental run matrix. The correct set of wall corrections must be specified for each run.

13. Summary of *Data Corrections.* At *this* point the data have been corrected for angle calibrations, deflections, dynamic pressure calibration, operator error and blockage, forces and moments for balance calibration, operator error and blockage, forces and moments for balance calibration, support and interference tares, weight tares, and finally tunnel boundaries. The data are at the desired center-of-gravity position or positions on the wind axes for an external balance.

14. Transfer to Other Axes. There *are* three axes systems that are used; these are wind, body, and stability axes. The axes can pass through either the balance moment center or the desired model center of gravity. The axes are defined as follows:

a. *Wind Axes.* The lift, drag, and cross-wind force are parallel to the test-section centerlines. This axis system is used to define the lift as perpendicular to the remote

velocity, the drag as parallel to the velocity, and the cross-wind force as perpendicular to the plane of lift and drag. The moments are about the three axes.

b. Body Axes. This axis system is attached to and moves with the model. The lift is replaced with normal force, drag with axial, or chordwise, force, and cross wind with side force.

c. *Stability Axes.* In this axis system the vertical axis, or lift, is perpendicular to the remote velocity, and the drag and side force yaw with the model (the yaw axis is not pitched with the model).

It is very useful for wind tunnel engineers to be familiar with the ways the various axis systems are used for flight mechanics and performance studies. Etkin and Reid[4'] can be consulted for more details.

Most external balances measure about the wind axis and most internal balances measure about the body axis. Thus it becomes necessary to transfer from one axis system to another, depending upon how the data are intended to be analyzed. Since the data have already been transferred to the desired center of gravity (item 10), the following equations can be used to transfer the data to the desired axes.

The transformations from wind axes to stability axes are

$$
\begin{aligned}
C_{L,SA} &= C_L \\
C_{D,SA} &= C_D\cos\psi - C_Y\sin\psi \\
C_{m,SA} &= C_m\cos\psi + \frac{b}{c}\, C_l\sin\psi \\
C_{l,SA} &= C_l\cos\psi + \left(\frac{c}{b}\right)C_m\sin\psi \\
C_{n,SA} &= C_n \\
C_{Y,SA} &= C_Y\cos\psi + C_D\sin\psi
\end{aligned}
\tag{10.71}
$$

where subscript SA designates stability axis.

The transformations from wind axes to body axes are

$$
\begin{aligned}
C_{NB} &= C_L\cos a + C_D\cos\psi\,\sin a - C_Y\sin\psi\,\sin a \\
C_{AB} &= C_D\cos\psi\,\cos a - C_L\sin a - C_Y\sin\psi\,\cos a \\
C_{mb} &= C_m\cos\psi - \left(\frac{b}{c}\right)C_l\sin\psi \\
C_{lB} &= C_l\cos\psi\,\cos a + \left(\frac{c}{b}\right)C_m\sin\psi\,\cos a - C_n\sin a \\
C_{nB} &= C_n\cos\alpha + C_l\cos\psi\,\sin a + C_m\sin\psi\,\sin a \\
C_{YB} &= C_Y\cos\psi + C_D\sin\psi
\end{aligned}
\tag{10.72}
$$

The a is the geometric angle of attack and is not corrected for the tunnel upflow and walls. The subscripts are body axis B, normal force N, axial force aerodynamic, wing span b, and mean A, chord c.

The transformations from body axes to wind axes are

$$C_{LW} = -C_A \sin \alpha + C_N \cos \alpha$$

$$C_{DW} = C_A \cos a \cos \psi + C_Y \sin \psi + C_N \sin a \cos \psi$$

$$C_{mW} = C_m \cos \psi + \left(\frac{b}{c}\right) C_l \cos a \sin \psi + \left(\frac{b}{c}\right) C_n \sin a \sin \psi$$

$$(10.73)$$

$$C_{lW} = C_l \cos a \cos \psi - \left(\frac{c}{b}\right) C_m \sin \psi + C_n \sin a \sin \psi$$

$$C_{nW} = C_n \cos \alpha - C_l \sin \alpha$$

$$C_{YW} = -C_A \cos a \sin \psi + C_Y \cos \psi - C_N \sin a \sin \psi$$

The subscript W means wind axes.

15. Final Comments. **Although** the calculations in the data reduction process are simple, a single run of 20 or 30 angles requires a large number of calculations. The number of calculations will be even larger if **Heyson's** or Joppa's wall correction theories are used, because they require the wall interference factors to be calculated at each test point.

Furthermore, the support **tare** and interference values, weight tares, other tares such as internal nacelle drag, and wall corrections are all functions of the model configurations on a given test run. Thus, before a run is reduced, the proper set of these corrections must be selected and the computer instructed to select the correct set. Under pressure to get the data out quickly, mistakes can be made. Therefore, at the end of the test these items must be checked on a run-by-run basis and any error corrected. Because of this, some tunnel operators will only release preliminary data during a test. This check on the data reduction process should be made before any computer readable set of data is released. If the data for support tares and other tares are taken during the test, considerable time will be required to work up and check these tares. Thus the data reduction of the final data will also be delayed.

The data reduction process has many constants that are functions of model size, such as wing area and moment transfer dimensions. Therefore, early in the test both a pitch and yaw run should be reduced using a pocket calculator (check point) to make sure that all the constants **are** installed correctly in the main computer program. The check point must be done independently of the computer program and use the original sources of model and tunnel values. If the two results do not agree, the **error** must be found and corrected. It is amazing how many constants can have numbers transposed or entered in the wrong field. It also should be noted that wall corrections usually are not applied to tests with ground planes because you desire the effect of the ground or lower boundary. Usually the dynamic pressure calibration and the **upflow** change when the ground plane is installed.

Although each detail of the data reduction process is straightforward, the chance for errors is large, so extreme care must be taken in carrying out the process. A good data reduction person must be a good bookkeeper.

Example 10.2 Summary of Three-Dimensional Corrections (Closed Test Section)   The model and tunnel dimensions are as follows:

The tunnel is **8** ft × **12 ft** with four fillets **1.5** ft high. Thus the actual cross-sectional area is **91.5** ft^Z. The model dimensions are as follows:

Wing: area = **7.1997** ft^2, MAC = **12.8933** in., span = **88.182** in., AR = **7.50,**
0.25 MAC is at model station (MS) = **49.980,** waterline (WL) = **10.379,**
taper ratio = **0.30.**

Horizontal Tail: area = **2.149** ft^2, MAC = **9.3346** in., span = **35.184** in., AR
= **4.0, 0.25** MAC is at MS = **90.240, WL** = **16.902** at **a** = 0°, δ_s = 0".

Model Trunnion: MS = **53.480. WL** = 10.494.

The body has an overall length of **90.96** in., a maximum width of **8.88** in., and depth of **9.48** in. The maximum circumference is **29.5** in. for an effective diameter of **9.39** in. The wing volume is **0.6291** ft^3 and the body volume is **2.472** ft^3. The angle of attack is measured from the chord line of the wing MAC.

The data in Table **10.1** have been corrected for balance load interactions (item **3),** and the mechanical calibrations have been applied to the angle of attack **a.** There were no corrections applied for balance and model deflections.

Support tares and interference (item 8) will not be applied as the test was run for comparative data.

Blockage corrections (item **7)** are in two parts: a solid blockage due to the model volume and a wake blockage due to the wakes shed from the model. The solid blockage is from Eq. **(10.2)** for the wing and Eq. **(10.3)** for the body (see Section **10.2).**

The wing thickness ratio on the average is **14%** and the airfoil is similar to a **65** series; thus K_1 from Figure **10.2** is **1.006.** The ratio of model span to tunnel breadth is **0.61;** for the tunnel **B/H** = **1.50;** thus τ_1 = **0.88.** The wing volume is **0.629** ft^3 and the tunnel cross-sectional area is **91.5** ft^2.

Thus

$$\varepsilon_{sb_w} = \frac{(1.006)(0.88)(0.629)}{91.5^{1.5}} = 0.0006363$$

For the body, with an effective diameter of **9.39** in. and length of **90.96** in., d/l = **0.1032.** From Figure **10.2,** K_3 = **0.91.** The volume of the body is **2.472** ft^3.
Therefore

$$\varepsilon_{sb_B} = \frac{(0.91)(0.88)(2.472)}{91.5^{1.5}} = 0.002236$$

Then the total solid blockage, ε_{sb_t} = **0.002872.**

TABLE 10.1. Data Table

α_i	α_g	L_u	D_u	M_u	$-M_w$	$M_u - M_w$	M_{ac}	C_{LC}	C_{Du}	C_{MAC_u}
					Tail Off					
2	2.48	356.0	41.18	−366.2	−28.4	−394.6	−1642.8	1.39914	0.16184	−0.50076
4	4.94	421.8	47.53	−80.2	−56.8	−137.0	−1622.2	1.65775	0.18680	−0.49428
6	7.41	482.4	54.39	183.4	−85.3	+98.1	−1601.8	1.89592	0.21376	−0.48793
					Tail On, $\delta_t = 0°$					
2	2.48	339.2	41.16	245.9	−36.5	209.4	−980.0	1.33258	0.16170	−0.29873
4	4.94	411.9	47.41	292.6	−70.0	222.6	−1228.0	1.16818	0.18625	−0.37417
6	7.41	481.6	54.89	346.2	−107.7	244.5	−1436.3	1.89200	0.21564	−0.43752
					Tail On, $\delta_t = -5°$					
2	2.48	328.1	41.39	1020.6	−36.5	984.1	−131.4	1.24934	0.16256	−0.04005
4	4.94	389.8	47.07	1064.1	−70.0	994.1	−379.0	1.53094	0.18487	−0.11548
6	7.41	456.8	53.64	1190.4	−101.7	1007.1	−602.1	1.79329	0.21067	−0.18341

TABLE 10.2   Results for Wake Blockage

Configuration	C_{DP_e}	$1/\pi ARe$	$\dfrac{S}{4C}C_{D0}$	$\dfrac{5S/4C}{(C_{Du} - C_{D0} - C_{Di})}$	ϵ_{wb_t}
Tail off	0.10068	0.031411	0.001980	0.00	0.001980
$\delta_s = 0°$	0.11108	0.028890	0.002185	0.00	0.002185
$\delta_s = -5"$	0.11820	0.028785	0.002325	0.00	0.002325

Maskell's wake blockage (Section 10.3) will be applied by calculating the equivalent parasite drag and $1/\pi ARe$ (Chapter 13) for each of the three runs. The results are given in Table 10.2, where $q_C = q_A(1 + \epsilon_t)^2 = 35.00(1 + \epsilon_t)^2$, and the corrected dynamic pressures for each model configuration are in Table 10.3 (q_A from tunnel calibration).

The weight tares (item 9) to the pitching moment versus the angle of attack are listed and applied in Table 10.1, in which tare values are corrected for balance interactions.

Moment transfers (item 10) will be transferred from the balance moment center that coincides with the trunnion to the 25% chord of the mean aerodynamic chord using the dimensions given in Table 10.4, taken from the model drawings at $a = 0°$. The 25% MAC is **0.115** in. below and 3.50 in. forward of the trunnion. The slant distance from the trunnion to the center of gravity is 3.502 in. (this distance will be called a). The angle γ is positive clockwise from the tunnel centerline to the desired center of gravity. Thus,

$$\gamma = 360 - \tan^{-1}\frac{0.115}{3.50} = 360° - 1.88° \quad \text{(or } 358.12")$$

The horizontal transfer distance is $s = -a\cos(\gamma + a)$ and the vertical transfer distance is $t = a\sin(\gamma + a)$.

Applying the moment transfers to the lift and drag values gives the moment about the aerodynamic center of the wing's MAC in Table 10.1, $M_{ac} = M_u - M_w - sL_u - tD_u$.

Using the dynamic pressure corrected for blockage, wing area, and mean aerodynamic chord, the coefficients uncorrected for tunnel upflow and wall corrections are obtained (item 11). It should be noted that the lift coefficient is fully corrected (Table 10.1).

TABLE 10.3.   Corrected Dynamic Pressure

Configuration	ϵ_{sb_t}	ϵ_{wb_t}	$1 + \epsilon_t$	q_C
Tail off	0.002872	0.001980	1.004852	35.3405
$\delta_s = 0°$	0.002872	0.002185	1.005057	35.3549
$\delta_s = 0°$	0.002872	0.002325	1.005197	35.3647

TABLE 10.4. Dimensions **Table**

	Trunnion	**25%** MAC (wing)
Model station	53.480	49.980
Model waterline	10.494	10.379

For wall corrections (item **12**), using Equation **(10.28)** to find the effective vortex span for the wing aspect ratio of **7.5** and taper ratio of **0.3**, $b_v/b = $ **0.72** from Figure **10.11,** and thus $b_e = 0.86(b) = $ **75.84,** and $b_e/b = $ **0.53** $=$ **k.** From Figure **10.17,** $\delta = $ **0.108:**

$$\Delta\alpha_w = \delta\left(\frac{S}{C}\right)(57.3)C_{LW} = 0.4869C_{LW} \tag{10.74}$$

$$\Delta C_{Dw} = \delta\left(\frac{S}{C}\right)C_{LW}^2 = 0.008499C_{LW}^2 \tag{10.75}$$

The values of $\Delta\alpha_w$ and ΔC_{Dw} are based on the wing or tail-off lift coefficient and are listed in Table **10.5** versus the indicated angle of attack. In the same table the corrections due to tunnel upflow are also given.

The correction to tail-on pitching moment is

$$\Delta C_{m,CG_t} = \frac{\partial C_m}{\partial\delta_s}\left(\frac{S}{C}\right)\delta\tau_2(57.3)C_{LW} \tag{10.76}$$

The average value of $\partial C_m/\partial\delta_s$ from the data is **−0.05143.**

The AC of the tail is **6.52** in. above the wing AC at $a = $ **0°**; thus $h_t/b_e = $ **0.086.** The tail moment arm (between ACs) is **40.26;** therefore $l_t/B = $ **0.280.**

An examination of Figures **10.17** and **10.19** shows a large difference in the shape of the curve at $a = $ **1.0** and $a = $ **0.5.** Figure **10.40** for the tail above and below the wing only has $a = $ **0.5, 1.0.** Linear interpolations will lead to error. Using Figure **10.39** for the wing and tail on the tunnel centerline, with data for $\alpha = $ **1.0, 0.207,**

TABLE 105. **Wall** Corrections

α_i	$\Delta\alpha_w$	ΔC_{Dw}	$\Delta\alpha_{up}$	$\Delta C_{D,up}$	$\Delta\alpha_T$	ΔC_{DT}	ΔC_m
2	0.68	0.01664	−0.012	−0.00029	0.67	0.01635	−0.02488
4	0.81	0.02336	−0.012	−0.00035	0.80	0.02301	−0.02947
6	0.92	0.03055	−0.012	−0.00040	0.91	0.03015	−0.03371

0.5, an increment can be obtained from $\alpha = 1.0, \ldots, 0.67$. This increment is then applied to the data of Figure 10.40 from $a = 1.0$ to yield a τ_2 of 0.71, as

$$\Delta C_{m,CG_t} = \frac{\partial C_m}{\partial \delta_s}\left(\frac{S}{C}\right)\delta\tau_2(57.3)C_{LW}$$

$$\Delta C_{m,CG_t} = -0.05143\left(\frac{7.1997}{91.5}\right)(0.108)(0.71)(57.3C_{LW})$$

$$\Delta C_{m,CG_t} = -0.01778C_{LW}$$

Using charts for a $\lambda = 0.67$ tunnel, $6 = 0.108$ and $\tau_2 = 0.75$. Thus the approximations were fairly close. Note that most wind tunnels have calculated both 6 and τ_2 for various model sizes (values are in Table 10.5).

If a measured value is not available for $\partial C_m/\partial \delta_s$, it can be estimated as follows:

$$\frac{\delta C_m}{\partial s,} = -a_t\overline{V}\eta t$$

From Equation (10.42), $a_t\eta_t = 0.0533$. This is based on the assumption that the two-dimensional lift curve slope is 0.100 per degree:

$$\overline{V} = \frac{l_t S_t}{S_W\, \mathrm{MAC}} = \frac{(40.260)(2.149)}{(7.1997)(12.8933)} = 0.93229$$

$$\frac{\partial C_m}{\partial \delta_s} = -0.04969$$

This is within 3.7% of the measured value. It is, however, preferable to measure $\partial C_m/\partial \delta_s$, thus requiring no assumptions on a, and q_t.

The use of total model lift (wing plus tail) rather than the wing lift will lead to the following values for $a, = 2.0°, \delta_s = -5.0°$:

$$\Delta\alpha = 0.62 \qquad \Delta C_D = 0.01395 \qquad \Delta C_m = -0.02300$$

This is a **decrease** in a of 0.05" and C_D of 0.00240 and an increase in C_m of 0.00188.

In percent the errors are a $= -1.65$, $C_D = -1.3\%$, and $C_{MAC} = -15.8\%$. The C_{MAC} value is large because C_{MAC} is a small number. However, the error is a function of the tail lift and would be greater for larger negative stabilizer angles or negative elevator angles. Because the wall corrections are functions of the wing circulation, it is not rational to use the total model lift.

At this point, if desired, the data can be transferred to the body or stability axis (item **8**). In this example the pitching moment was calculated about the aerodynamic center of the wing's mean aerodynamic chord. However, in most wind tunnel tests the moments are also taken about forward and aft center-of-gravity positions that

TABLE 10.6. Final Valves

α_i	α_C	C_{LC}	C_{DC}	C_{MAC_C}
		Tail Off		
2	3.15	1.39914	0.17819	−0.50076
4	5.74	1.65775	0.20981	−0.49428
6	8.32	1.89592	0.24391	−0.48793
		Tail On, $\delta_t = 0°$		
2	3.15	1.33258	0.17805	−0.27385
4	5.74	1.61818	0.20926	−0.34700
6	8.32	1.89200	0.24579	−0.40381
		Tail On, $\delta_s = -5''$		
2	**3.15**	**1.24934**	**0.17891**	**−0.01517**
4	**5.74**	**1.53094**	**0.20788**	**−0.08600**
6	8.32	1.79329	0.24082	−0.14970

correspond to the desired limits for center-of-gravity travel. Table 10.6 gives the final corrected coefficients.

10.10   SUMMARY: OPEN JET

The air stream in an open test section is free to expand; therefore, the wake and solid-blockage effects are small but not zero. As suggested in Section 10.3, the solid blockage may be taken as one-fourth that of a closed tunnel. An examination of figures in this chapter for boundary correction factors (6 at the wing and τ_2 at the tail) shows that the numerical values are different for open and closed tunnels of similar geometry. The boundary correction factor at the wing (δ) is negative for open tunnels and positive for closed tunnels. Other than the blockage correction and the sign change of the boundary correction factor, the same methods can be used as for a closed tunnel.

   A word of caution: Many open test-section tunnels with external balances have a splitter plate to shield the balance from the airstream. In this case the tunnel may have one solid boundary, depending on the splitter plate location. This type of mixed boundary is discussed by Heyson.[42,43]

REFERENCES AND NOTES

1. Glauert, H., "Wind Tunnel Interference on Wings, Bodies, and Airscrews," ARC R&M 1566. 1933.

2. Hemott, J. G., "Blockage Corrections for Three Dimensional-Flow Closed-Throat Wind Tunnels with Consideration of the Effect of Compressibility," NACA TR 995, 1950.

3. Thom, A., "Blockage Corrections in a High Speed Wind Tunnel," ARC R&M 2033, 1943.

4. Maskell, E. C., "A Theory of the Blockage Effects on Bluff Bodies and Stalled Wings in a Closed Wind Tunnel," ARC R&M 3400, 1965.

5. Young, A. D., "The Induced Drag of Flapped Elliptic Wings with Cut Out and with Flaps that Extend the Local Chord," ARC R&M 2544, 1942 (see Equation 6.25).

6. See Young's Figures 18, 19, and 20.

7. See Young's Equation 25.

8. Vassaire, J. C., "Correction de Blocage dans les Essais en Soufflerie, Effects de deCollements," AGARD CP-102, Paper 9, 1972.

9. Hensel, R. W., "Rectangular Wind Tunnel Blocking Corrections Using the Velocity Ratio Method," NACA TN 2372, 1951.

10. Swanson, R. S., and Toll, T. A., "Jet Boundary Corrections for Reflection Plane Models in Rectangular Wind Tunnels," NACA TR 770, 1943.

11. Stewart, H. J., "The Effect of Wind-Tunnel-Wall Interference on the Stalling Characteristic of Wings," J. Aeronaut. Sci.. 8, 426–428, 1941.

12. Gavin, J. R., and Hensel, R. W., "Elliptic Tunnel Wall Corrections," J. Aeronaut. Sci., 9, 533–537, Dec. 1942.

13. Kondo, K., 'The Wall Interference of Wind Tunnels with Boundaries of Circular Arcs," Air Research Institute, University of Tokyo, 126, 1935.

14. Glauert, H., 'The Interference of the Characteristics of an Airfoil in a Wind Tunnel of Circular Section," ARC R&M 1453, 1931.

15. Rosenhead, L., "Uniform and Elliptic Loading in Circular and Rectangular Tunnels," Pmc. Roy. Soc., Series A, Vol. 129, 1930, p. 135.

16. Silverstein, A., "Wind Tunnel Interference with Particular References to Off-Center Positions of the Wing and to the Downwash at the Tail," NACA TR 547, 1935.

17. Van Schliestett, G., "Experimental Verification of Theodorsen's Theoretical Jet-Boundary Correction Factors," NACA TN 506, 1934.

18. Theodorsen, T., "Interference on an Airfoil of Finite Span in an Open Rectangular Wind Tunnel, NACA TR 461, 1931.

19. Terazawa, K., "On the Interference of Wind Tunnel Walls on the Aerodynamic Characteristics of a Wing," Air Research Institute, University of Tokyo, 44, 1932.

20. Glauert, H., "The Interference on the Characteristics of an Airfoil in a Wind Tunnel of Rectangular Section," ARC R&M 1459, 1932.

21. Sivells, J. C., and Salmi, R. M., "Jet Boundary Corrections for Complete and Semispan Swept Wings in Closed Circular Wind Tunnels," NACA TN 2454, 1951.

22. Sanuki, M., and Tani, I., "The Wall Interference of a Wind Tunnel of Elliptic Cross-Section," Pmc. Phys. Math. Soc. Jpn., 14, 592–603, 1932.

23. Rosenhead, L., 'The Airfoil in a Wind Tunnel of Elliptic Cross-Section," Proc. Roy. Soc., Series A, Vol. 140, 1933, p. 579.

24. Riegels, F., "Correction Factors for Wind Tunnels of Elliptic Section with Partly Open and Partly Closed Test Section," NACA TM 1310, 1951.

25. Batchelor, G. K., "Interference in a Wind Tunnel of Octagonal Section," Australian Committee for Aeronautics (CSIR) 1, Jan. 1944.

26. Gent, B. L., "Interference in a Wind Tunnel of Rectangular Octagonal Section," Australian Committee for Aeronautics (CSIR) 2, Jan. 1944.

27. Lotz, I., "Correction of Downwash in Wind Tunnels of Circular and Elliptic Sections," NACA TM 801, 1936.

28. Silverstein, A., and Katzoff, S., "Experimental Investigations of Wind-Tunnel Interference on the Downwash Behind an Airfoil," NACA TR 609, 1937.

29. Heyson, H. H., "Jet Boundary Correction for Lifting Rotors Centered in a Rectangular Wind Tunnel," NASA TR R-71, 1960.

30. Heyson, H. H., "Linearized Theory of Wind Tunnel Jet Boundary Corrections and Ground Effect for VTOUSTOL Aircraft," NASA TR R-124, 1962.

31. Heyson, H. H., "Use of Superposition in Digital Computers to Obtain Wind Tunnel Interference Factors for Arbitrary Configurations, with Particular Reference to V/STOL Models," NASA TR R-302, 1969.

32. Heyson, H. H., "Fortran Programs for Calculating Wind Tunnel Boundary Interference," NASA TM X-1740, 1969.

33. Heyson, H. H., "General Theory of Wall Interference for Static Stability Tests in Closed Rectangular Test Sections and in Ground Effects," NASA TR R-364, 1971.

34. Heyson, H. H., "Nomographic Solution of the Momentum Equation for VTOL-STOL Aircraft," NASA TN D-814, 1961.

35. Heyson, H. H., and Grunwald, K. J., "Wind Tunnel Boundary Interference for V/STOL Testing," Paper 24, NASA SP 116, pp. 409–434.

36. Heyson, H. H., "Rapid Estimation of Wind-Tunnel Corrections with Application to Wind Tunnels and Model Design," NASA TN D-6416, 1971.

37. Heyson, H. H., "Equations for the Application of Wind Tunnel Wall Corrections to Pitching Moments Caused by the Tail of an Aircraft Model," NASA TN D-3738, 1966.

38. Joppa, R. G., "A Method of Calculating Wind Tunnel Interference Factors for Tunnels of Arbitrary Cross Section, Report 67-1, University of Washington, Department of Aerospace Engineering, 1967 (see also NASA CR 845, 1967).

39. Joppa, R. G., "Wall Interference Effects in Wind Tunnel Testing of STOL Aircraft, AZAA *J. Aircraft,* 6, 209–214, 1969.

40. Joppa, R. G., 'Wind Tunnel Interference Factors for High Lift Wings in Closed Wind Tunnels," NASA CR 2191 1973.

41. Etkin, B., and Reid, L. D., *Dynamics of Flight, Stability and Control,* 3rd ed., John Wiley & Sons, New York, 1996.

42. Heyson, H. H., "Linearized Theory of Wind Tunnel Jet Boundary Corrections and Ground Effect for VTOUSTOL Aircraft," NASA TR R-124, 1962.

43. Heyson, H. H., "General Theory of Wall Interference for Static Stability Tests in Closed Rectangular Test Sections and in Ground Effect," NASA TR R-364, 1971.

11 Boundary Corrections III: Additional Applications

The principles and many practical manifestations of boundary corrections have been discussed in the previous two chapters. A number of additional applications are discussed in this chapter.

11.1 REFLECTION PLANE MODELS

The main purpose for choosing reflection plane models is to get the largest model size and hence the largest experimental Reynolds number. In turn, the large model size may require special attention to wall corrections. Another effect is that the reflection plane "reflects," and under some conditions (e.g., aileron down, for which the normal situation would be antisymmetric, or a vertical tail for which there is no "reflection" in the normal configuration), the reflection is not exactly the condition that is desired.

Experiments using reflection plane models are conveniently divided into four classes:

1. small symmetrical models (less than $0.6h$) such as halves of flapped wings or horizontal tails,
2. small unsymmetrical models such as aileron panels,
3. small vertical tail models where a reflection is not desired, and
4. large reflection plane models of all kinds.

The first three will be discussed in the following, but reference to the work of Swanson and Toll[1] or Heyson[2-5] is suggested for guidance on experiments using large reflection plane models. Heyson[5] gives methods for handling a skewed wake, both vertically and laterally. These techniques could therefore handle a horizontal and vertical tail with both rudder and elevator deflections.

Small Symmetrical Models

The data for a small reflection plane model that is half of a symmetrical model may be corrected by treating the upwash and blockage as though the entire model were

428
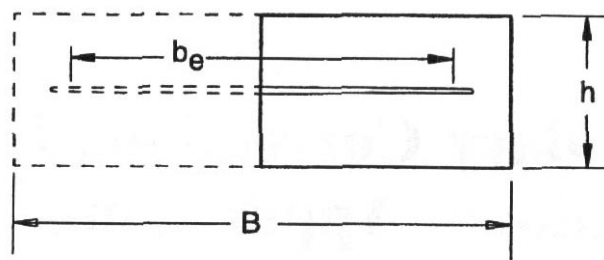
FIGURE 11.1   Nomenclature for a reflection plane model.

in a tunnel of double the width, as indicated in Figure 11.1. The values of δ for such a setup are shown in Figure 10.17, and those for a circular-arc tunnel are in Figure 10.25. One normally gets a slightly lower lift curve slope and slightly higher induced drag than in the complete-model, complete-tunnel case, owing to some streamwise vortex shedding in the root boundary layer. When panel area and MAC are used, the final data are directly applicable to the airplane if the split is along the plane of symmetry with an added amount of span to allow for the boundary layer displacement thickness. Chapter 13 should also be consulted.

Small Unsymmetrical Models

When the model is of a part that is unsymmetrical in the actual flight vehicle (e.g., aileron deflected), additional troubles accrue since the reflection will act as though it is symmetrical. In this case the tunnel data include a small carryover from the reflection and will show from one-tenth to one-fourth more increment of lift, drag, pitching moment, yawing moment, and rolling moment than would occur for the actual asymmetric flight article. Tunnel data for aileron effectiveness is frequently higher than is obtained in practice because of failure to simulate aileron cable stretch and wing twist. This can be corrected by comparing the span loading with ailerons at zero and deflected and subtracting the carryover due to the reflected panel.

The only time this effect can be misleading in comparing different ailerons on the same basic panel is when one aileron has more span than another. As indicated in Figure 11.2, the reflection effects increase with span and the aileron of greatest span yields the data most erroneously high.

Difficulties arising from the doubled increment of lift, drag, and moment have been covered in Chapter 13, which may be consulted for proper interpretation of the results.

Small Vertical Tail Models

Small vertical tail models present a number of additional difficulties since the degree of endplating given by the fuselage and horizontal tail is very difficult to predict. One approach is to consider the vertical tail a completely reflected symmetrical semispan wing and, after determination of the slope of the vertical tail lift curve from the complete model tests, to reduce the panel test data to conform. Normally
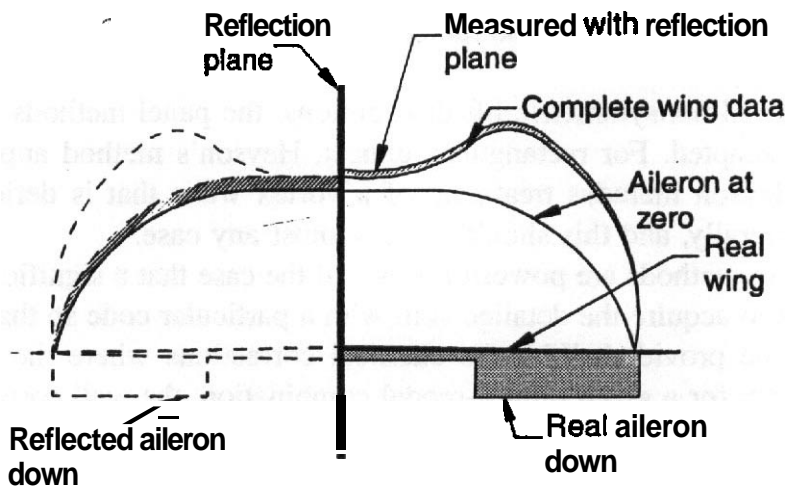
FIGURE 11.2   Effect of reflection plane on panel with aileron down.

the vertical tail drag is of so little interest that no increase of panel drag to allow for the reduced aspect ratio is required.

Another approach, and perhaps the best one, is to determine the slope of the lift curve of the vertical tail from complete model tests and use the hinge moment data from panel tests at the same lift coefficient. This neglects the difference of span loading for panel and actual vertical tail installation. Still another alternative is to build a complete tail assembly model. Here the model is large enough for high Reynolds numbers, and actual endplating is well simulated. The effects of sidewash must be obtained from the complete model tests and incorporated into the data, as must be done for any isolated tail representation. The tail assembly model should have a fuselage stub nose at least one MAC ahead of the tail quarter chord.

Large Models

The analysis for large models is complicated fundamentally because the boundary-induced upwash cannot be considered constant along either the chord or the span. It is therefore necessary to take greater care with the upwash corrections and work out the spatial dependences. Variation of the blockage along the model almost never is large enough to require detailed evaluation.

Besides streamline curvature effects, variation of boundary-induced upwash along the span of the model tends to load up the tips. Some test section shapes intensify this effect more than others.

11.2   SWEPT WINGS: NONUNIFORM LIFT

Corrections for swept wings can be determined for any shape tunnel test section by use of panel methods or by the earlier Joppa's method. Heyson's method is applicable for rectangular tunnels. When the aerodynamic center of the wing and the pivot point coincide and are near the tunnel centerline for a swept wing, the

change in the vertical wall correction factor from a swept wing for moderate downwash angles is very small.

For arbitrary and nonsymmetric lift distributions, the panel methods or Joppa's method can be adapted. For rectangular tunnels, Heyson's method appears to be easier to use. Heyson includes treatment of a vortex wake that is deflected both vertically and laterally, and this should cover almost any case.

Although these methods are powerful, it is still the case that a significant investment is required to acquire the detailed skill with a particular code so that complex corrections can be provided. With the classical corrections where the correction factor is a constant for a given tunnel–model combination, the wall corrections are of the form of a constant times the wing or tail-off lift coefficient. Panel methods as well as Heyson's method and Joppa' method, on the other hand, require calculations of the wall correction factors based on the wing lift for each test point. These values would be used for tail-on runs, as are conventional corrections, using a table look-up for the same model attitude and power setting. The panel methods can in principle use the complete configuration.

For a research test the likely increased time to reduce the data may not be critical. However, for a developmental test where the results of one run are often used to determine the next run, a long time to reduce data may be unacceptable.

The panel methods and the vortex lattice method of Joppa appear adaptable to slotted tunnels. This is an area that still requires significant research to improve techniques.

11.3   CONTROL SURFACE HINGE MOMENTS

It is apparent that the small size of such surfaces on complete models makes hinge moment corrections likely to be in the same range as measurement uncertainty. Large models, such as those used for reflection plane tests, have their hinge moments increased by solid jet boundaries in a manner similar to the increase of pitching moment. The increase of hinge moment due to the walls in some such cases can be of the order of 8% for a 30% flap on large reflection plane models.

Hinge moment data must be reduced with the dynamic pressure as corrected for both solid and wake blockage, as is true for pressure coefficients.

11.4   GROUND PROXIMITY EFFECTS FOR AIRCRAFT

When an aircraft operates within a semispan or less from the ground, its downwash pattern is altered and decreased by the ground. The ground can be considered to be a reflection plane and treated in the same way as wall effects have been treated. This results in a decrease in the downwash, a corresponding increase in the lift curve slope, a decrease in induced drag, and an increase in the slope of the pitching moment curve. The latter results in an increase in elevator angle to trim the airplane. The flight condition at design forward center-of-gravity position and $C_{L,\max}$ usually

determines the elevator power required. This condition is simulated in a wind tunnel by placing a ground board or ground plane under the model or by lowering the model to the proximity of the floor. The ground plane spans the tunnel, and for an external balance it must be adjustable in height. The supports under the board must have minimum blockage and in larger tunnels will have to support personnel working on the model. For a sting support, a sting that can change the model height at constant angle of attack is very convenient.

Turner[6] determined a limit for testing with a conventional ground board. The limit was for models with full-span high-lift configurations. Data are given for models with aspect ratios from 6 to **10** using tilt wings, jet flaps, and double-slotted flaps. The limit is a function of the ratio of the height above the ground plane to model span versus C_L. When $C_L > 20$ Wb, a moving-belt ground plane should be used. As with all such limits the line represented by the equation represents a gray area near which the results should be carefully evaluated. The limit in this case is similar to flow breakdown for V/STOL models (see Section **11.7).** The downwash from the model approaching the floor or ground at an angle approaching **90"** produces a stagnation point on the ground plane. A portion of the flow then moves upstream. The presence of the ground plane's boundary layer leads to this event at higher clearance values than when there is no ground plane boundary layer present. A necklace vortex is formed on the ground plane similar to that formed when a flow encounters protuberance from a surface. There is a resulting tunnel flow distortion. The rule of thumb for V/STOL models with distributed lift is almost exactly the same. The effect on tunnel data that is most easily detected is a decrease in the lift curve slope when testing the fixed ground planes.

Some tunnels are equipped with a moving-belt ground plane. These usually require sting balances. The boundary layer is usually sucked off at the leading edge of the belt. Thus, if the belt moves at the test speed, there is no boundary layer on the belt as with a fixed ground plane. The speed of a moving belt appears to be limited by belt slippage around the drive roller. These units are expensive, and it is difficult to make the belt track. The sting must have adjustable, but positive, limits to the model a range and the sting lower height. The ground plane should extend, as a minimum, from the nose of the model to aft of the tail.

A second approach to removing the boundary layer in fixed ground planes can be achieved either by suction through floor perforations or by blowing through slots to create a thin jet parallel to the floor to replace the momentum lost in the boundary layer. The thickness of the boundary layer on a ground board can also be controlled to some extent by a flap on the trailing edge. This can introduce other distortions through the creation of circulation around the ground board.

Often both the upflow at the wing and the dynamic pressure will be a function of ground board height. The data are usually corrected for blockage and, if required, buoyancy, which is almost certain to be changed upon the installation of a ground board. The tunnel wall or boundary corrections usually are not applied since the model is very close to the floor. If boundary corrections are required, they only include the two walls and the ceiling. Note that if "corrections" to all four boundaries are applied, the ground effect will be removed and results for free air are recovered.

   The large General Motors automotive tunnel, where cars are tested on the floor, uses suction at the leading edge of the test section to remove the boundary layer. This air then enters the tunnel behind the test section to maintain continuity. The Glenn L. Martin Wind Tunnel at the University of Maryland uses this system. The development of moving belts has been advanced in recent years by the need for better simulation of moving ground in race car development. See Chapter 14.

11.5 DOWNWASH CORRECTIONS: POWERED MODELS

The slipstream behind a tractor propeller will increase the local dynamic pressure over that portion of the wing that is immersed in the slipstream. Depending on airplane geometry, the propeller may also change the local angle of attack of the wing. Generally lift will be increased but the amount depends on the balance between the increase in dynamic pressure and the possibly decreased local angle of attack. For other than some V/STOL aircraft these effects are assigned to power effects and the power-off values of δ and τ_2 are used. However, $a_t \overline{V} \eta_t$ must be evaluated if the tail is in the slipstream. This term may be a function of thrust coefficient T_C. See the next two sections for V/STOL corrections when the propellers are tilted to provide direct lift.

   For an aircraft where the whole span of the wing is immersed in the propeller slipstream there are likely to be substantial wall effects. Use of a panel code such as PMARC can be considered for evaluating wall effects. This is a type of experiment for which the measured variable methods are the best available choices.

   It may also be possible for some analysts to mathematically model the wing propellers and their slipstream, then use the method of images to calculate the effect of the tunnel walls. In the determination of the moment correction, $a_t \overline{V} \eta_t$ data must be obtained with power on as the term is likely to be a function of T_C.

11.6 BOUNDARY CORRECTION: PROPELLERS

Glauert[7] has examined the problem of experiments on propellers in a wind tunnel and suggests that the propeller diameter be kept "small" relative to the jet diameter and that an open throat tunnel be employed. Under these conditions no boundary corrections were considered to be needed.

   For various practical reasons it is frequently not possible to adhere to the above stipulations. An approach to the wall corrections for propeller experiments in a closed throat tunnel may be made as follows. See Figure 11.3 for nomenclature.

   In a closed jet the propeller slipstream under conditions of positive thrust will have a velocity u greater than the velocity V in the jet without the propeller. Since the same volume of air that passes section x ahead of the propeller must pass section y behind it, it follows that the velocity w outside the slipstream will be less than V. In free air, w would, of course, equal V. The lower velocity air outside the slipstream has a static pressure that is increased relative to the "free"-stream tunnel flow
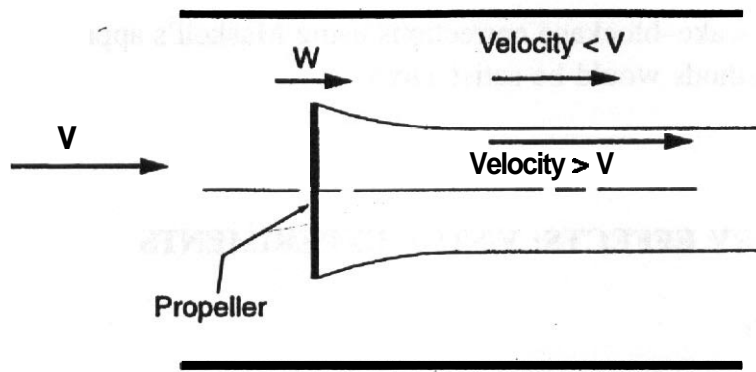
FIGURE 11.3   Nomenclature for a propeller in a closed test section.

approaching ahead of the propeller, and it follows that the slipstream also has too high a static pressure. This reacts back to the propeller so that it develops thrust that is greater than would be developed in an **unrestricted** flow of the same speed with the same propeller rotation rate and blade angle. Or it can also be said that the thrust developed would be equal to that which would be expected at a lower speed V' in free air. The test should therefore be run at a speed above V' in order to develop the forces corresponding to speed V' in unrestricted flow.

The amount of correction for this "continuity" effect may be found from

$$\frac{V'}{V} = 1 - \frac{\tau_4 \alpha_1}{2\sqrt{1 + 2\tau_4}} \tag{11.1}$$

where $\tau_4 = T/pAV'$, $\alpha_1 = A/C$, A is the propeller disk area, C is the jet cross-sectional **area,** and T is thrust.

Values of V'/V **are** shown in Figure 11.4. It is apparent that Equation **(11.1)** becomes invalid for negative thrust leading to τ_4 approaching -0.5 since the correction becomes infinite for that value $(C_D = 1.0$ or $T_c = -0.392)$. Although we are not aware of any particular data sources from studies of the problem, it could be
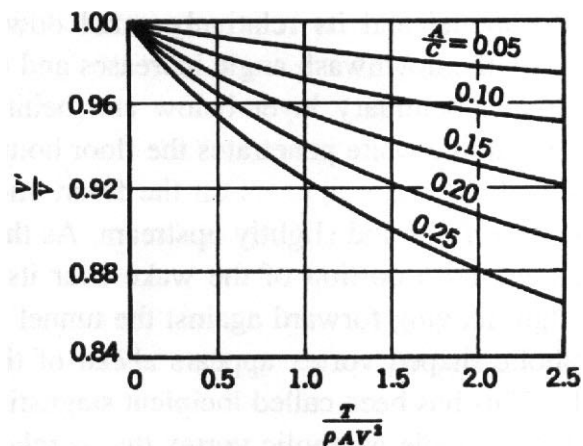
FIGURE 11.4   Speed correction for thrust-
ing propeller.

expected that the wake–blockage corrections using Maskell's approach or the measured variable methods would be satisfactory.

11.7   BOUNDARY EFFECTS: V/STOL EXPERIMENTS

Flow Breakdown

The basic concept for all V/STOL aircraft is to create lift by using a propulsion device to produce downward-directed momentum. Momentum is of course a product of a mass and a velocity. For a given value of momentum there is a hyperbolic relationship between the mass involved and the velocity. The two extremes can be considered. First there can be a large mass and small velocity (small Δv) such as is the case for helicopter rotors; second, there can be a small mass and a large velocity (large Δv) such as is the case for a jet engine. The wake produced by the first is "soft" and can be deflected by the tunnel flow, while the second is stiff (it goes where you point it) and will be deflected much less by the tunnel flow in the transition region. The powered lift system can either be distributed across the span, as for a rotor or spanwise jet flap, or it can be a point, as for powered lift jets or lift fans.

As a V/STOL model goes through transition slowing from level flight to hover, the downwash angle (measured from free stream to the centerline of the wake) will change from a small angle in level flight to $90°$ at hover. As the wake angle changes, so will the forward velocity, from some relatively large value to zero at hover. When the transition flight region from forward flight to hover is simulated in a wind tunnel, the model and tunnel combination will encounter a phenomenon called flow breakdown as the lift flow begins to impinge on the floor of the tunnel in the vicinity of the test article. The resulting flow patterns are not similar to those that occur in an unrestricted flow. The point at which flow breakdown occurs imposes a limit on the minimum forward speed that can be simulated in a wind tunnel experiment.

Rae[8] has provided a treatment of the flow breakdown phenomena. Consider a model in a tunnel at a given lift. At high tunnel speed the flow is relatively undisturbed by the model and its relatively small downwash angle. As the tunnel speed is reduced, the downwash angle increases and the model wake begins to interact with the tunnel boundary layer below and behind the model. As the tunnel speed is decreased, the wake penetrates the floor boundary layer, a stagnation point near the center of the wake appears on the floor, and portions of the wake move laterally across the floor and slightly upstream. As this condition is approached, the flow is unstable and a portion of the wake near its leading edge will intermittently snap through, moving forward against the tunnel flow. When the wake snaps through, a parabolic-shaped vortex appears ahead of the rotor curving aft toward the tunnel walls. This has been called incipient stagnation. A further reduction in tunnel speed leads to a stable parabolic vortex that is relatively small and well aft of the model.
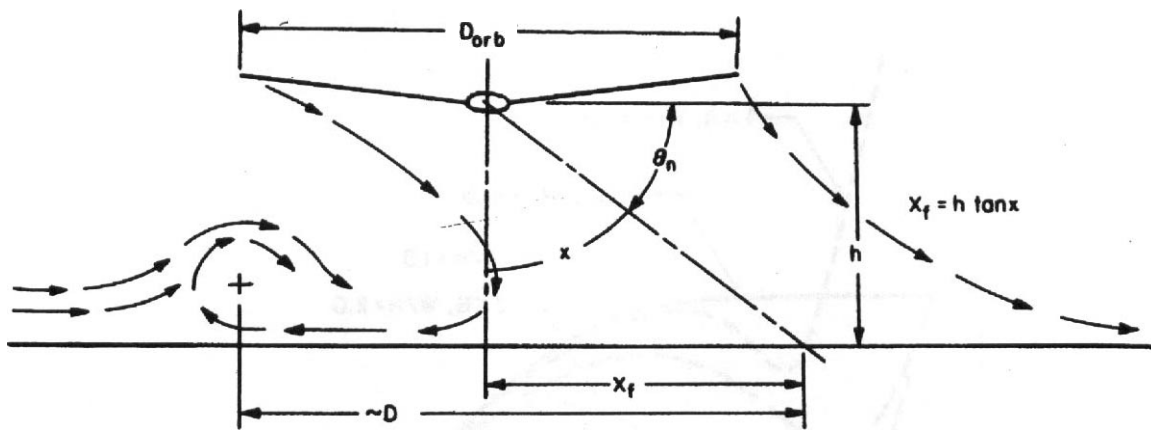
FIGURE 11.5   Nomenclature sketch of rotor wake in flow breakdown showing floor vortex.

Figure 11.5 shows a sketch of a cut through the midplane of the tunnel for this type of flow structure. This flow has two well-defined stagnations: one near the center of the wake and the second forward of the wake centered near the core of the parabolic or necklace vortex. As the tunnel speed is further reduced, the forward stagnation points move further forward and the vortex becomes larger. At some point, as the speed is reduced, the flow is not representative of free-air flow, and the data cannot be corrected. This point is called flow breakdown. It should be noted that the vortex at low forward speeds trails across the floor up the tunnel wall and across the ceiling as it moves aft.

Rae[8] used plywood and plexiglass boxes open at the ends in the tunnel flow direction to simulate different-size tunnels for a single-size model. Each of the inserts must have its flow calibrated for dynamic pressure and upflow as described by Ganzer and Rae[9] and by Lee.[10] As the same model is used in the main test section and the inserts at the same conditions, then both the Reynolds number and Mach number are matched. Using this technique for a tunnel width-to-height ratio of 1.5, a rotor with three disk loadings run at the same rpm and tip speed ratios gave the following results. The flow breakdown occurred at different tip speed ratios (tunnel speed), but the momentum downwash angle for a given rotor insert combination was constant. Thus flow breakdown is only a function of the momentum downwash angle for a given ratio of model area to tunnel cross-sectional area. As expected, the smaller the model-to-tunnel-area ratio, the larger the allowable downwash. Downwash for a given model-to-tunnel-area ratio varies with the test-section width-to-height ratio. Comer fillets and curved end walls reduce the allowable downwash for a given W/H. Furthermore, the allowable downwash at the location of the tail is less than at the rotor or wing. As suggested by Heyson,[11,12] the flow breakdown limit for a model with distributed lift can be estimated in terms of X_f/b, where X_f is the distance aft of the model at which a theoretically straight wake impinges on the floor and b is the full model span, or rotor diameter:

$$\frac{S_f}{b} = \frac{h \tan \chi}{b}$$

Here χ is the wake skew angle and $\chi = 90° - \Theta_n$, where Θ_n is the momentum
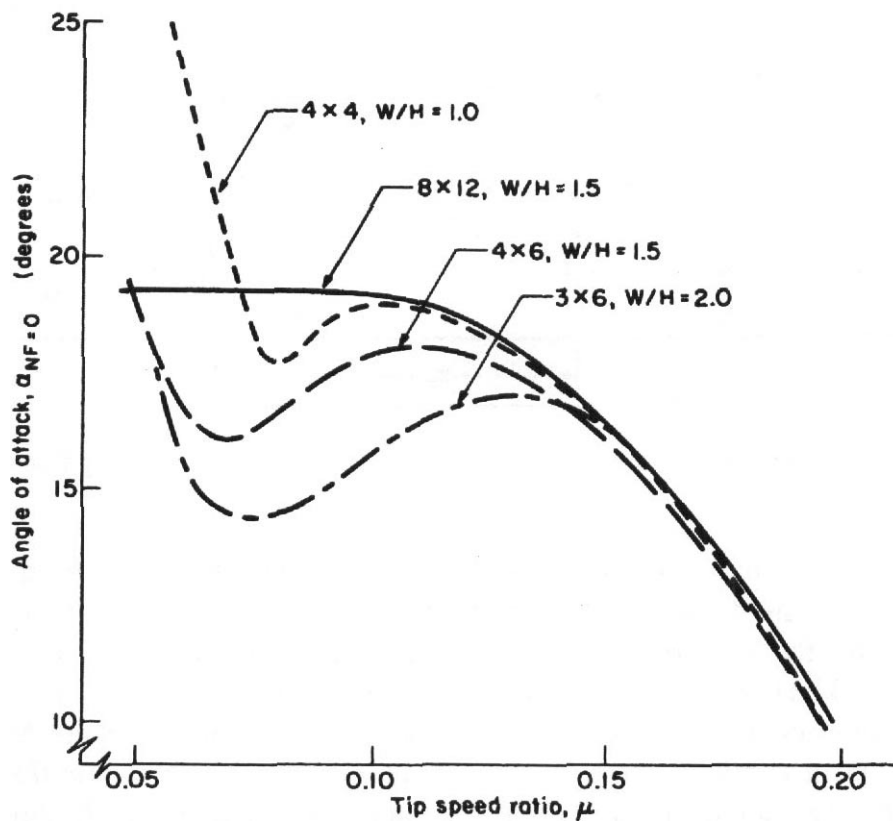
FIGURE 11.6   Effect of flow breakdown on tail mounted behind a rotor in various size tunnels.

downwash angle as defined in Figure 11.5 and the values of Θ_n can be obtained by consulting Heyson.[13,14]

The flow breakdown limit is more severe at the tail of a model than at a wing. In Figure 11.6 (from Rae and Shindo[15]) data are shown from a tail with a 1-ft span one diameter aft of a 2-ft-diameter propeller used to simulate a rotor. The tail was isolated from the propeller, had its own internal balance, and could be pitched independently of the propeller. The data, as expected, show an increase in the zero lift angle of attack with decreasing propeller tip speed ratio (propeller run at fixed rpm). As the tip speed ratio is reduced, the flow angle aft of the propeller increases very rapidly and then flattens out, as shown by the 8 X 12-ft data, where there is no flow breakdown and the data are close to free-air data. In the inserts the flow angle follows the same trend to a maximum value and then decreases due to tunnel wall effects. As flow breakdown is approached, the flow angle suddenly increases again due to the vortexlike flow below the model.

To illustrate the effect of wall corrections on pitching moment data in the form of the zero lift angle of the tail for the 4 × 6-ft insert and the 8 X 12-ft test section of Figure 11.6, the data with Heyson's corrections are shown in Figure 11.7. The data for the propeller in the 4 × 6-ft insert were corrected to free air, and these were used as test points for data in the 8 × 12-ft test section. It should be noted that the wall corrections change both the tip speed ratio and the tip plane path or shaft angle. The data in Figure 11.7 show the delta in the tail angle of attack
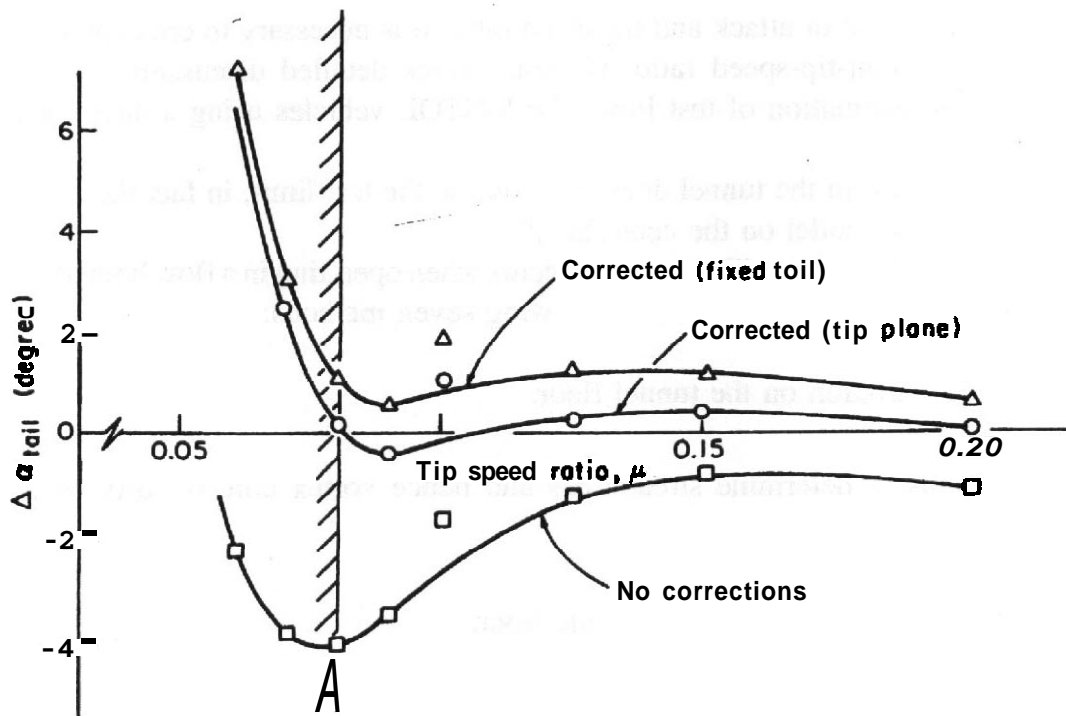
FIGURE 11.7   Tail angle of attack corrected for wall effects above and below flow breakdown.

(8 **X** 12 ft to 4 **X** 6 ft) with no wall corrections, data corrected for a fixed tail location. These data arose because the tail was attached to the propeller fairing; hence it was at a fixed vertical location. Because the rotor was run at $-3°$ shaft angle, the tail was below the tip plane path. Correcting the 4 × 6-ft insert data rotated the shaft angle and thus the tail should have been rotated to maintain its relation to the tip plane path. This mislocation of the tail was corrected by the methods of **Heyson** and **Katzoff**[16] and **Jewell** and **Heyson**[17] to find the change in flow angle at the tail due to vertical displacement, yielding the curve labeled "corrected tip plane."

The curve labeled corrected tip plane demonstrates that **Heyson's** theory will correct the tail angle of attack, and hence pitching moment, quite well as long as data are not taken below the flow breakdown point (hatched vertical line). Below the limit the wall corrections overcorrect the data by large amounts. At a tip speed ratio of 0.06, the overcorrection is 7" out of $22°$ for the **8** × 12-ft tunnel, a 32% error. This error increases very rapidly, which implies that the test limit must be known and approached with caution.

The application of **Heyson's** corrections to the angle of attack, lift, and drag of both rigid and hinged rotors will correct the data only above the flow breakdown limit. The rigid rotor (propeller) was corrected by assuming a uniform load distribution." The hinged rotor was corrected by using (a) a uniform load (9 doublets) and (b) a triangular load (20 **doublets**).[18] Both loadings gave similar results. The data can be corrected only above the flow breakdown. As **Heyson's** corrections

changeboth the angle of attack and tip speed ratio, it is necessary to cross-plot data to obtain a constant-tip-speed ratio. Heyson[11] gives detailed discussions of wall corrections and estimation of test limits for V/STOL vehicles using a distributed-lift system.

Raising the rotor in the tunnel does not increase the test limit; in fact the lowest limit was with the model on the centerline.[19]

The location of the vortexlikecore that occurs when operating in a flow breakdown mode can be detected by at least the following seven methods:

1. pressure variation on the tunnel floor,
2. smoke,
3. tuft wands to determine streamlines and hence vortex core or tufts on the walls and floor,
4. vortex meters,
5. variation of total pressure above the floor,
6. a laser, and
7. a PIV.

The path of the vortexlike floor was traced by methods 1, 2, and 5 and the results agree quite well. An example of the static pressure method is also shown in Figure 11.8. This is a useful method since it could be installed in the tunnel floor permanently. The core of the vortexlikeflow is located at the minimum pressure coefficient. As the tip speed ratio decreases, the downwash angle increases and the vortexlike core moves forward in the tunnel.

The presence and locations of the floor vortex can also be determined by tufts on the tunnel floor and walls. This method does not locate the core, but it is a reliable indication of flow breakdown.

The problem of flow breakdown is much more complicated when a discrete or point-type powered lift system, as produced by jets or lift fans, is used. The first problem with these configurations is the wide range of locations at which the engine can be located on the aircraft.

Tyler and Williamson[20,21] studied flow breakdown for lift jets in the Canadian National Research Council (NRC) V/STOL propulsion tunnel. Since they were using lift jets, they defined incipient stagnation as a conservative but safe minimum tunnel speed. This is the highest tunnel velocity for the formation of the floor vortex. By defining a thrust coefficient as

$$C_T = \frac{F}{q_\infty h^2}$$

where h is the height of the nozzle exit above the floor, the limit was established based on incipient stagnation as $C_T = 0.62$ for both a single jet and a pair arranged in tandem over a tilt range of $-5°$ to $+20°$. When two jets were side by side, the limit was $C_T = 0.90$. The nozzle spacing for the two jets was 4.3 times their jet
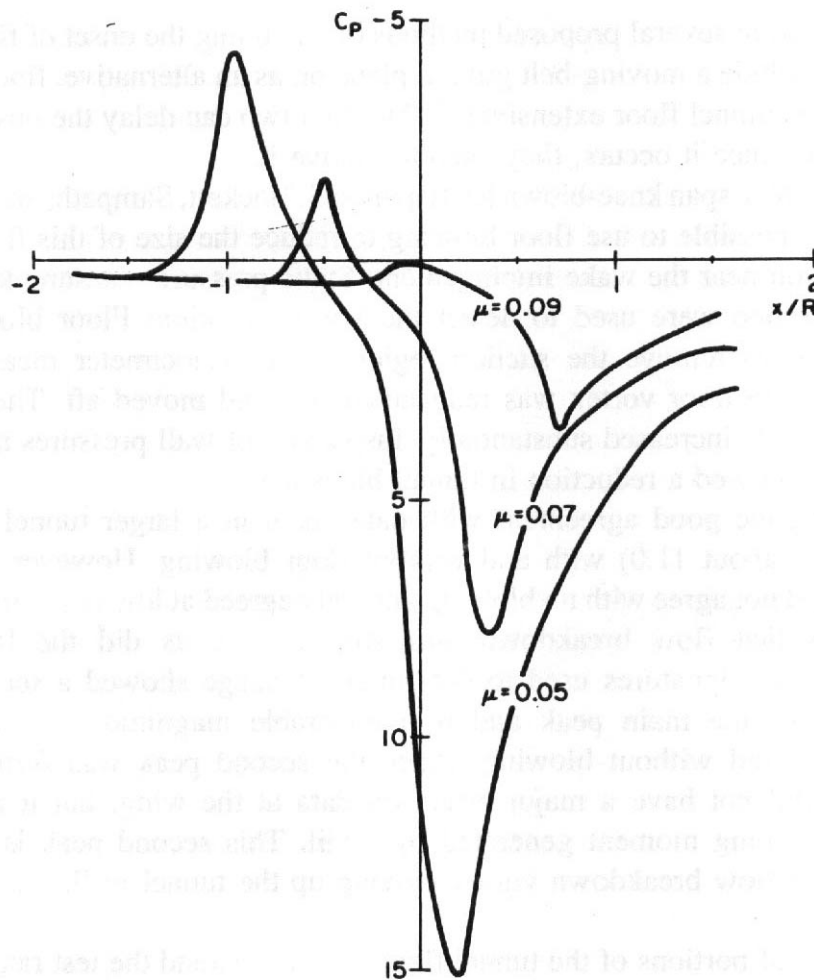
FIGURE 11.8   Variation of tunnel floor static pressure under a rotor; $\mu = 0.09$ is above flow breakdown, while $\mu = 0.07$ **and** $\mu = 0.05$ are below breakdown. Positive C_P's are wake center stagnation; negative C_P's flow breakdown vortex core.

diameter. They concluded that a tandem pair was the same as a single jet of the same total nozzle area centered between the pair.

Studies were made of local flow in the plane of the nozzle exit. It was concluded that the tunnel velocity could be reduced so very little below incipient stagnation that incipient stagnation should be taken as the lower test limit. It should be noted that the thrust per unit area for lift jets and lift fans is much larger by orders of magnitude than a rotor or other distributed-powered lift system.

A small amount of data for a representative nonswept wing model with two nonmetric lift jet engines forward of the wing are reported by Shindo and Rae." The model had a 3-ft span and was tested in an insert, the large tunnel, and over a ground plane at the same location as the insert floor. Changes in the aerodynamic characteristics of the model were measured. These data are only applicable to the configuration that was tested. The data showed that the flow breakdown occurs at higher ratios of free stream to jet velocity in the insert due to the side walls than for the ground plane. The flow breakdown point was within 5% of Tyler and Williamson's[21] values.

There have been several proposed methods of extending the onset of flow breakdown. These include a moving-belt ground plane or, as an alternative, floor blowing and opening the tunnel floor extensively.[23] The first two can delay the onset of flow breakdown, but once it occurs, they cannot remove it.

In tests on a **46%** span knee-blown jet-flap model, Hackett, Sampath, and Phillips[74] found that it is possible to use floor blowing to reduce the size of this floor vortex to a small region near the wake impingement. Static pressure measurements along the floor centerline were used to detect the vortex location: Floor blowing was increased so as to remove the suction region. Laser velocimeter measurements confirmed that the floor vortex was reduced in size and moved aft. The angle of attack at the model increased substantially. Inspection of wall pressures and subsequent analysis showed a reduction in tunnel blockage.

The model gave good agreement with data taken in a larger tunnel at model C_μ's of 4.0 (C_L about 11.0) with and without floor blowing. However, at higher C_μ's the data did not agree with no blowing and only agreed at low a's with blowing. This indicates that flow breakdown was still present, as did the laser data. The wall pressure signatures used to determine blockage showed a second pressure peak **aft** of the main peak and of comparable magnitude at model C_μ's above **4.0** with and without blowing. Since the second peak was further aft in the tunnel, it did not have a major effect on data at the wing, but it may have an effect on pitching moment generated by a tail. This second peak is probably the result of the flow breakdown vortex moving up the tunnel walls, as discussed by Rae?

The removal of portions of the tunnel floor can also extend the test range. Using a rotor in Hansford[23] found the allowable downwash before flow breakdown was extended from 45° to 75°. When removing the floor of a tunnel to allow the sharply deflected wake to escape the tunnel, there is the concern of the loss of tunnel air. In this test series there were no indications of the wake reentering the tunnel through the floor. The mass of air lost by venting was recovered through a breather ring aft of the test section. Pitch and yaw flow angles measured at the start of the test section were more uniform with the tunnel vented at low advance ratios. When tests are made with a vented tunnel, the effect of venting on the tunnel flow should be determined, as well as tracing the exiting air to ensure that a portion does not return through the vent.

REFERENCES AND NOTES

1. Swanson, R. S., and Toll, T. A., "Jet Boundary Corrections for Reflection Plane Models in Rectangular Wind Tunnels," NACA TR 770, 1943.

2. Heyson, H. H., "Linearized Theory of Wind Tunnel Jet Boundaries Corrections and Ground Effect for VTOUSTOL Aircraft," NASA TR R-124, 1962.

3. Heyson, H. H., "Use of Superposition in Digital Computers to Obtain Wind Tunnel Interference Factors for Arbitrary Configurations, with Particular Reference to V/STOL Models," NASA TR R-302, 1969.

4. Heyson, H. H., "Fortran Programs for Calculating Wind Tunnel Boundary Interference," NASA TM X-1740, 1969.

5. Heyson, H. H., "General Theory of Wall Interference for Static Stability Tests in Closed Rectangular Test Sections and in Ground Effects," NASA TR R-364, 1971.

6. Turner, D. K., "Requirements for Moving Belt in Ground Effect Experiments," Paper 25 in Proceedings of Conference on VTOUSTOL Aircraft, NASA SP 116, 1966, pp. 409–434.

7. Glauert, H., "Wind Tunnel Interference on Wings, Bodies, and Airscrews," ARC R&M 1566, 1933.

8. Rae, W. H., "Limits on Minimum Speed V/STOL Wind Tunnel Tests," *AIAA J. Aircraft*, **4,** 249–254, 1967.

9. Ganzer, V. M., and Rae, W. H., "An Experimental Investigation of the Effect of Wind Tunnel Walls on the Aerodynamic Performance of a Helicopter Rotor," NASA TN D–415, 1960.

10. Lee, J. L., "An Experimental Investigation of the Use of Test Section Inserts as a Device to Verify Theoretical Wall Corrections for a Lifting Rotor Centered in a Closed Rectangular Test Section," M.S. Thesis, University of Washington, Dept. of Aeronautics and Astronautics, 1964.

11. Heyson, H. H., "Rapid Estimation of Wind Tunnel Corrections with Application to Wind Tunnels and Model Design," NASA TN D-6416, 1971.

12. Heyson, H. H., "Wind Tunnel Wall Effects at Extreme Force Coefficients," in *Proceedings of the International Congress on Subsonic Aerodynamics,* New York Academy of Sciences, New York, 1967.

13. Heyson, H. H., "Linearized Theory of Wind Tunnel Jet Boundaries Corrections and Ground Effect for VTOUSTOL Aircraft," NASA TR R-124, 1962.

14. Heyson, H. H., "Nomographic Solution of the Momentum Equation for VTOUSTOL Aircraft," NASA TN D-814, 1961.

15. Rae, W. H., and Shindo, S., "Comments on V/STOL Wind Tunnel Data at Low Forward Speeds," in Proceedings, 3rd CAL/AVLABS Symposium, Aerodynamics of Rotary Wing and V/STOL Aircraft, Vol. II, Cornel Aeronautical Laboratory, Buffalo, NY, 1969.

16. Heyson, H. H., and Katzoff, S., "Induced Velocities Near a Lifting Rotor with Nonuniform Disk Loading," NACA Report 1319, 1956.

17. Jewell, J. W., and Heyson, H. H., "Charts of the Induced Velocities Near a Lifting Rotor," NASA TM 4-15-596, 1959.

18. Rae, W. H., and Shindo, S., "An Experimental Investigation of Wind Tunnel Wall Corrections and Test Limits for V/STOL Vehicles," Final Report DA-ARO-31-124-G809, U.S. Army Research Office, Durham, NC, 1973.

19. Shindo, S., and Rae, W. H., "Low Speed Test Limit of V/STOL Model Located Vertically Off Center," *AIAA J. Aircraft, 15,* 253–254, 1978.

20. Tyler, R. A., and Williamson, R. G., "Wind Tunnel Testing of V/STOL Engine Models— Some Observed Flow Interaction and Tunnel Effects," AGARD CP 91-71, Dec. 1971.

21. Tyler, R. A., and Williamson, R. G., "Experience with the NRC 10 ft. by 20 ft. V/STOL Propulsion Tunnel —Some Practical Aspects of V/STOL Engine Model Testing," *Can. Aeronaut. Space J., 18,* 191–199, 1972.

22. Shindo, S., and Rae, W. H., "Recent Research on V/STOL Test Limits at the University of Washington Aeronautical Laboratory," NASA CR **3237, 1980.**

23. Hansford, R. **E.,** "The Removal of Wind Tunnel Panels to Prevent Flow Breakdown at Low Speeds," **Aeronaut.** *J.,* 75, **475479, 1975.**   .

24. Hackett, J. E., Sampath, S., and Phillips, C. G., "Determination of Wind Tunnel Constraints by a Unified Wall Pressure Signature Method. Part I: Applications to Winged Configurations," NASA CR **166,186,** June 1981.

12 Additional Considerations for Aerodynamic Experiments

The conduct of aerodynamic experiments in a broad sense is the subject of this book. The various chapters address a number of aspects essential to successful aerodynamic investigations but there are some others that we feel need to be addressed but that **are** not accommodated elsewhere. These include basic guidelines for design of experiments, methods for assessing data quality, model design and construction, and general comments on arrangements for use of facilities.

12.1 WIND TUNNEL EXPERIMENTS

There is an extensive literature on design of experiments that can provide valuable guidance for design and conduct of wind tunnel experiments just as for other areas of study and development. Montgomery[1] and Dietrich[2] are primary sources for the discussion that follows and can be consulted along with the bibliographies they contain for much more extensive coverage of these issues.

A block diagram representation of a wind tunnel experiment is shown in Figure 12.1. The elements of the input vector **are** variables such **as** angle of model pitch, roll, or yaw and the pressure drop across the tunnel nozzle. The elements of the controllable vector will be variables such as model size, tunnel size, model materials, model construction process, time of conduct of the experiment, model nominal configuration, and choice of mounting arrangements. Some variables may appear in either the input vector or the controllable factor vector depending on immediate purpose. The elements of the output vector will be responses such **as** force and moment components as indicated by the balance, pressure readings from the pressure-measuring system, still or video images of smoke or other flow visualization methods, and noise measured from microphone arrays. Elements of the uncontrollable factors vector will include such variables as turbulence level of the incoming stream, temperature in many facilities, relative humidity, model deformation under load, and surface deterioration with time.

In any particular case, a parameter may not be controllable, even though it may in principle be controllable. Examples are tunnel size and incoming stream temperature. The scope of the parameters that **are** "controllable" depends on the resources available to the experiment planner. A group of students at a particular university will have to plan their experiments within the limitations of the facilities immediately available. A chief engineer of a large aerospace company or automobile

444
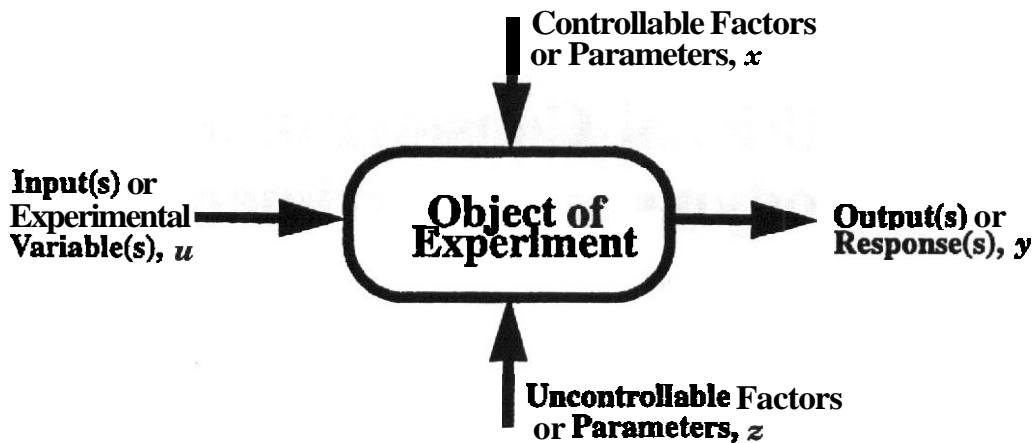
FIGURE 12.1   Conceptual model of an experimental setup.

company may have the possibility to conduct experiments at any facility on earth and may even be able to do experiments at several facilities in the development cycle for a major new vehicle.

We consider the output to be a functional of the input, controllable, and uncontrollable factors. All variables represent vector quantities in the nongeometric mathematical sense. The symbol t represents time:

$$y = f[u(t), x(t), z(t)] \tag{12.1}$$

12.2   UNCERTAINTY OF MEASUREMENTS

An underlying axiom in the conduct of experiments is that no measurement can be known to provide an exactly true result.

Consideration of this axiom quickly leads to a conclusion that the utility of any measurement depends strongly on an assessment of its accuracy in some meaningful way. Assessment of the accuracy of any given measurement is quite difficult. It requires careful consideration of all aspects of the particular experiment being contemplated or analyzed.

Types of Uncertainty

The uncertainty associated with any measurement is conceived to be made up of a variety of "components." A particular contributing component is generally considered to be a member of one of two types: "random" or "systematic." These classifications are also referred to as "precision" and "bias" components of measurement error. We will use the terms random and systematic as being more descriptive in our view. These terms will now be discussed.

An idealized view of the two types of error components is the following. Random components upon repetitive observations produce varying values that are distributed
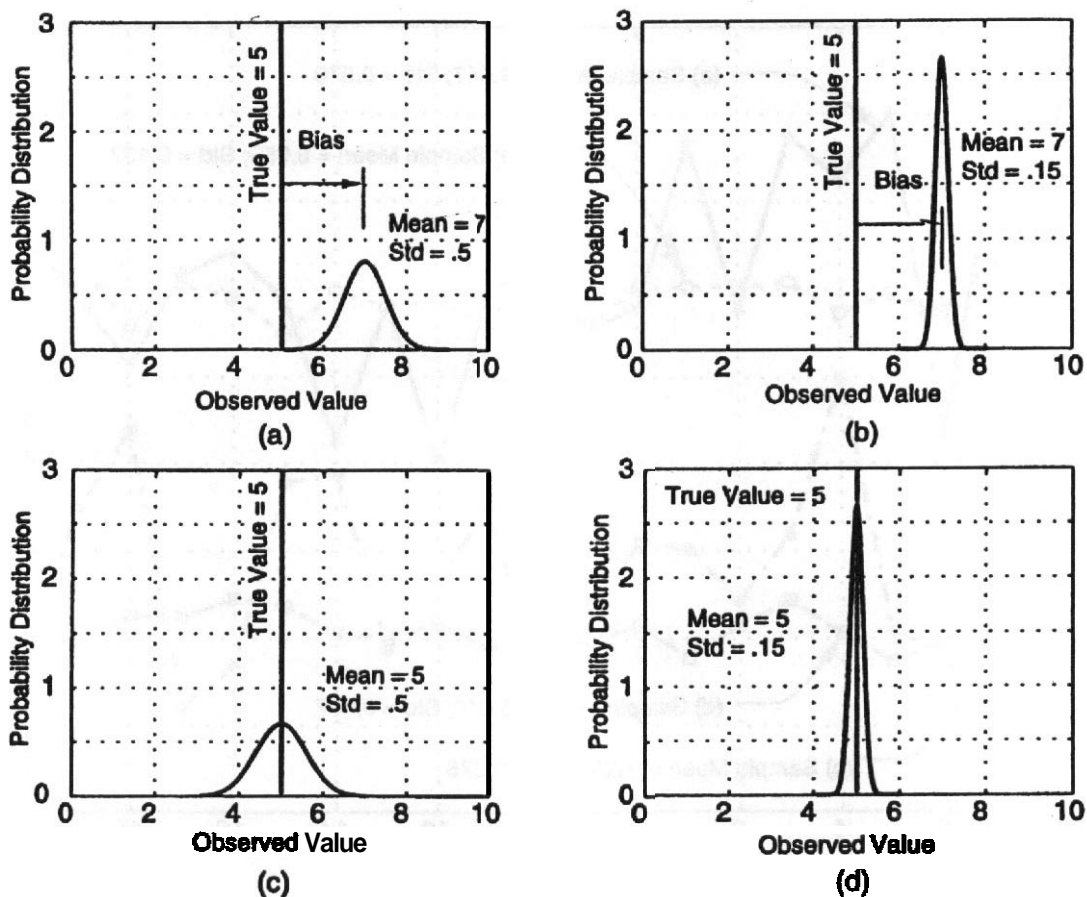
FIGURE 12.2   Representation of distribution of measurements.

in some fashion about the unknowable true value, but if an accurate average of the population could be obtained, it would provide the unknowable true value. Systematic components upon repetitive observations produce the same values, but those values differ from the unknowable true value. A schematic representation is typically given in Figure 12.2. The plots are probability distributions for the observations. Plots (a) and *(b)* have a systematic or bias error equal to 2 while the systematic error shown by plots *(c)* and *(d)* is zero. The cases indicated by *(b)* and (d) are said to be more precise than *(a)* and *(c)*. The practical impact of this is that the number of observations for cases like (b) and *(d)* to achieve a given precision of the mean will be fewer than for cases like *(a)* and *(c)*. Note that none of the values shown on the plots of Figure 12.2 are known or can be known exactly for any experimental data population. In Figure 12.3 we give a plot of four sets of 20 data points that correspond to a typical realization of each of the cases of Figures 12.2*a–d*, where we have assumed that the probability distributions are of the Gaussian class. The points are connected by lines to give an easier visual identification of the sets, not to indicate a time history. Each point is an average over some time interval. Compare the sample means and standard deviations to the indicated values for the populations from which they have been obtained. We will develop ideas about these aspects further in the next section.
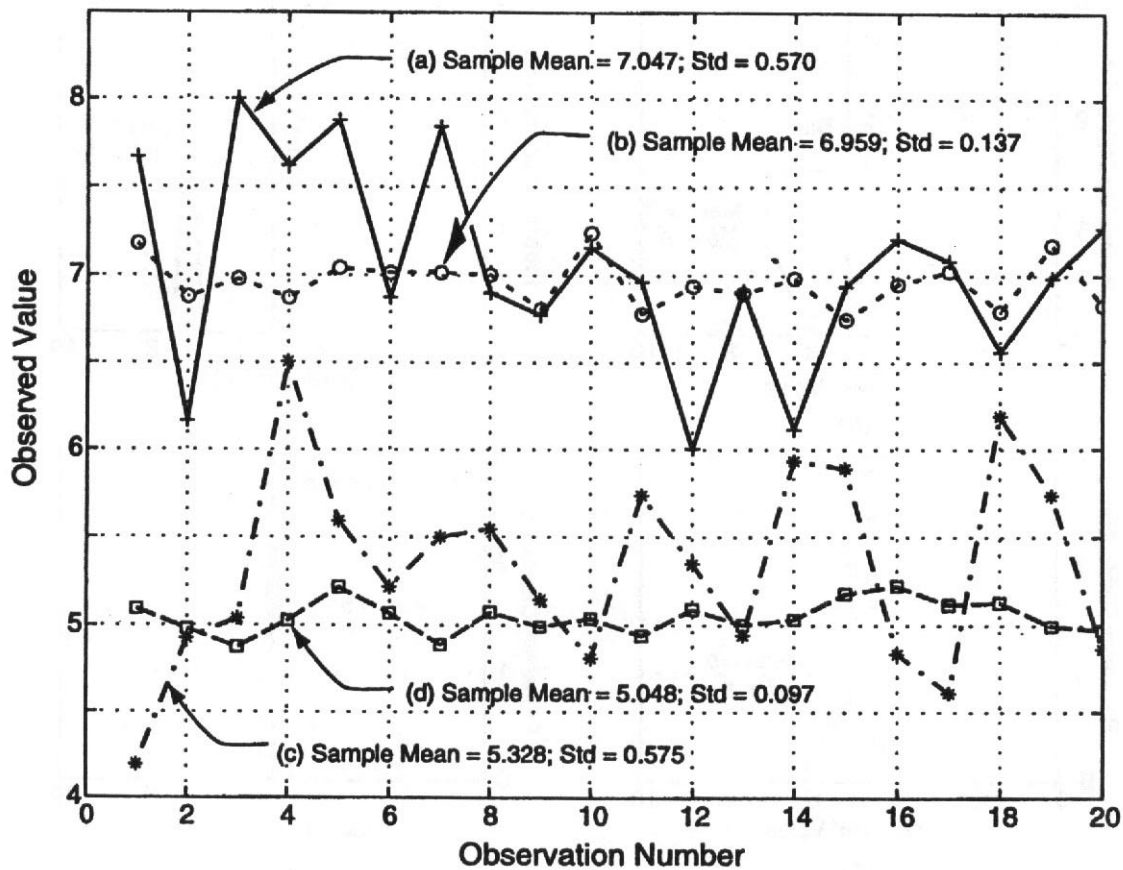
FIGURE 12.3   Sample data sets with 20 observations per set.

The systematic or bias error contributions **are** the sources that are most difficult to deal with in a wholly satisfactory way. It is common to consider all components that **are** not random to be bias error components. There is a sense in which bias errors are simply additional random errors of a nature such that there is no practical possibility of obtaining a significant number of empirical observations that represent a significant sample of the relevant population of observations. For example, the deviation of as-built geometry of models from the specifications will produce some changes in the aerodynamic characteristics. To obtain a direct empirical evaluation of the effects of such deviations would require the construction and testing of many models that **are** made identical to the extent that the design and manufacturing processes allow. Since the cost of a single model is often the greatest single outlay in an aerodynamic experiment, it is not feasible to make 10 or more. There are many examples that are logically equivalent to this. Some other way must be used to estimate the effects of such deviations.

Random (or Precision) Components

A random uncertainty is present when repeated measurements of a particular physical quantity, that to the best approximation is held constant, produce differing results. The quantity itself may actually be varying or the differing results may be due to

characteristics of the measuring system or to variations in the environment. Sorting out which of these is responsible and to what degree is always a goal, but there is always a residual variation that must simply be observed and characterized to the degree that possible repetitions allow. The key feature of a random sequence of measurements is that it is not possible to anticipate the size of each succeeding measurement with respect to the immediately preceding one. With sufficient data, a pattern with respect to frequency of occurrence can be determined. This pattern is called the probability distribution. The most commonly considered probability distributions are the normal, or Gaussian, distribution and associated distributions that arise from sampling of Gaussian populations. The previously cited sources can be consulted for extensive discussions.

The predictability of random measurements is that with known probability distributions the probability that a measurement will fall within specified limits can be given or the proportion of measurement results that will fall within a specified range can be given.

The treatment of uncertainty of random components is rather well specified by the many works on statistical methods. The systematic components are actually more troublesome.

Probability Distributions   The quantities measured in an experiment and any derived result that thereby becomes a function of the measured quantities are considered to be ***random variables.*** They are quantities for which exact values that will occur in any future experiment cannot be predicted. Their variability can in principle be given in terms of probability density functions. The expected value of any function of a random variable can be obtained by integrating over all values the product of the function and the probability density function of the random variable. Most common examples are the expressions for the mean and variance of a random variable y with probability density function $f(y)$, mean μ, and variance σ^2 as given by Equations (12.2) and (12.3):

$$\mu = \int_{-\infty}^{\infty} y f(y) \, dy \tag{12.2}$$

$$\sigma^2 = \int_{-\infty}^{\infty} (y - \mu)^2 f(y) \, dy \tag{12.3}$$

A probability distribution function has the property that its integral over the infinite range is unity. We introduce four probability density functions here. They are the normal, or Gaussian, distribution, the t distribution, the chi-square distribution, and the uniform distribution. There are others of great importance even to our subject, but we refer readers to the references for discussions of those. We use the symbol μ for mean value and the symbol a for standard deviation in the following.

1. ***Normal or Gaussian Probability Distribution.*** The normal probability distribution is given by Equation (12.4). It has two parameters, the mean and the standard deviation:

$$f_n(y) = \frac{1}{\sigma\sqrt{2\pi}} \exp\left(\frac{-(y-\mu)^2}{2\sigma^2}\right) \qquad -\infty < y < \infty \qquad (12.4)$$

2. ***Uniform Probability Distribution.*** The uniform distribution is given by Equation (12.5). It also has two parameters, the mean and the half range:

$$f_u(y) = \begin{cases} 0 & y < \mu - a \\ \dfrac{1}{2a} & \mu - a \le y \le \mu + a \\ 0 & y > \mu + a \end{cases} \qquad (12.5)$$

The standard deviation for the uniform distribution is related to the range by the equation

$$\sigma = \frac{a}{\sqrt{3}} \qquad (12.6)$$

3. ***Chi-square Probability Distribution.*** The chi-square distribution is the probability density function for the sum of the squares of k random variables each of which is normally distributed with mean equal to zero and variance equal to one. The following relations give the chi-square distribution function. The symbol $\Gamma(u)$ indicates the gamma function with argument u. The chi-square distribution has one parameter, k, which is the number of terms in the summation and is called the degrees of freedom:

$$\chi_k = \sum_{i=1}^{k} y_i^2 \qquad (12.7)$$

where

$$f_n(y_i) = \frac{1}{\sqrt{2\pi}} \exp\left(\frac{-y_i^2}{2}\right) \qquad -\infty < y_i < \infty \qquad (12.8)$$

$$f_{\chi^2}(\chi, k) = \frac{1}{2^{k/2}\Gamma(k/2)}\chi^{k/2-1}e^{\chi/2} \qquad \chi > 0 \qquad (12.9)$$

The chi-square distribution is obviously one sided as a sum of squares is necessarily greater than or equal to zero. The mean $\mu = k$, and the standard deviation $\sigma =$

$\sqrt{2k}$. We introduce the chi-square distribution here only because of its role as a constituent in the formation of the t distribution, which is described next. For specific applications of the chi-square distribution see the references.

4. *The Student t Probability Distribution.* The *t* distribution is the probability distribution of a quotient formed by a numerator that is a normally distributed random variable with mean equal to zero and variance equal to one with a denominator that is the square root of a random variable with a chi-square distribution. It is given by Equation (12.10). There is one parameter, *k*, called the degrees of freedom, as it is inherited from the constituent chi-square distribution:

$$f_{tk}(y) = \frac{\Gamma[(k+1)/2]}{\sqrt{k\pi}(y^2/k + 1)^{(k+1)/2}\,\Gamma(k/2)} \qquad -\infty < y < \infty \qquad (12.10)$$

The mean of the *t* distribution is zero and its standard deviation $\sigma = \sqrt{k/(k-2)}$ for k > 2. Although it is not obvious from the functional form, the t distribution approaches the normal distribution as the number of degrees of freedom increases. It is essentially indistinguishable from the normal distribution for k > 100. The graph of Figure 12.4 shows the t distribution for four values of k. This curve for k = 100 also serves to illustrate the normal distribution. We note that the computation of these functions with available tools such as MATLAB® and a Pentium® PC is straightforward.
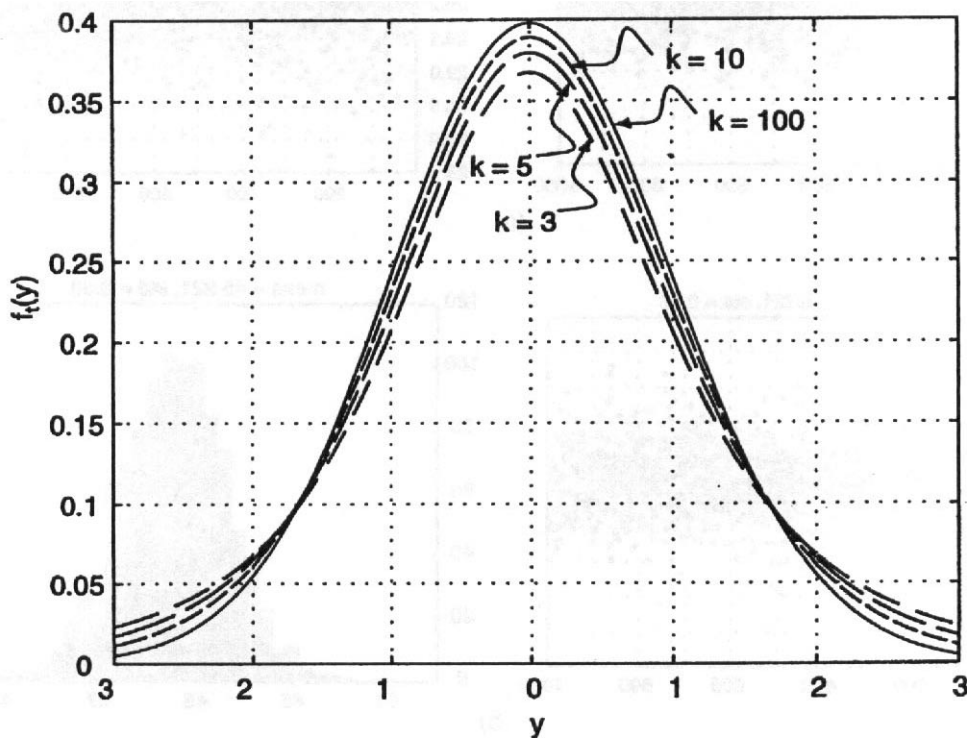
FIGURE 12.4   Student t distribution.

Estimating the Mean from Measurements Suppose we have a set of data that are the repetitive measurements for a particular quantity. To be concrete, let's consider a set of measurements from the drag component of an external wind tunnel balance. Figure 12.5 shows three scatter plots and a typical histogram for 1000 values taken at a rate of eight samples per second for three different types of objects in a wind tunnel. Note the differing ranges on the vertical scales of the scatter plots that are labeled in pounds. The distribution appears within the bounds that can be considered normal, although no consistency checks have been conducted. We assume that the populations from which these observations have been made are normally distributed. The values of the means and standard deviations shown are for the sets of 1000 observations. An important question is the degree to which the average of any number of randomly drawn points approximates the mean of the population. We assume we have only the data and general knowledge of how the experiment was arranged. The objective is to **arrange** the experiment so that it is as repeatable as possible within our resources. The relationship between the confidence limits for the mean μ and the confidence probability β_{cp} as estimated from n observations is obtained in the following way.
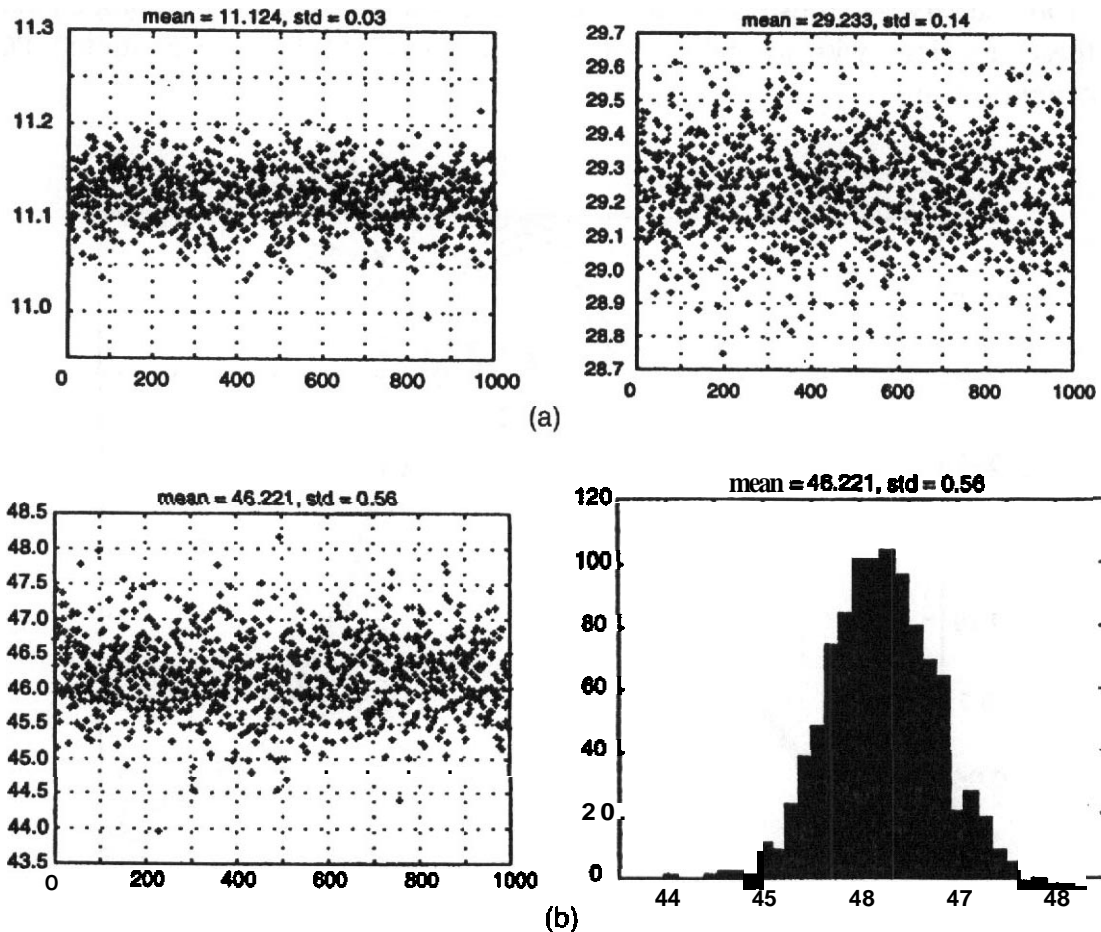
FIGURE 12.5   Scatter plots and typical histogram for external balance data.

First compute the sample mean $\bar{x}$ and the sample standard deviation s, as indicated by the equation

$$\bar{x} = \frac{1}{n}\sum_{i=1}^{n} x_i \quad \text{and} \quad s = \sqrt{\sum_{i=1}^{n} \frac{(x_i - \bar{x})^2}{n-1}} \tag{12.11}$$

The probability statement is given by the equation

$$\text{Probability } \{\bar{x} - k_3 s < \mu < \bar{x} + k_3 s\} = \beta_{cp} \tag{12.12}$$

or alternatively

$$\text{Probability } \{\bar{x} - \Delta x < \mu < \bar{x} + \Delta x\} = \beta_{cp} \tag{12.13}$$

This statement gives a relationship between the "confidence interval" $\pm\Delta x$ and the "confidence probability" β_{cp}. The coefficient k_3 is called the confidence factor. Obviously it is the factor relating the sample standard deviation to the confidence interval. Since the observations are assumed to have been drawn from a normally distributed population, the probability distribution function needededis the t distribution of Equation (12.10) with $k = n - 1$ degrees of freedom. The equation describing the needed relationship is

$$\beta_{cp} = \int_{-\Delta x\sqrt{n}/s}^{\Delta x\sqrt{n}/s} f_{tk}(y) \, dy \tag{12.14}$$

This equation provides the functional relationship between the confidence probability and the confidence interval for given number of samples and sample standard deviation.

Table 12.1 gives values for $k_3 = \Delta x/s$ for several confidence probabilities. This table can be computed with a very few lines of code using MATLAB or some similarly capable tool.

For our three sets of data, we will apply the above relations using the confidence probability of 0.95 to obtain the corresponding confidence intervals on the mean and see how it depends on the number of sample observations used in the calculation. We have computed the means, the standard deviations, and the confidence limits for each of the three sets of data for n ranging from 8 to 1000. Our sense is that taking less than eight observations in these types of situation is not often a good choice. The results are shown in Figures 12.6–12.8.

The differences in the standard deviations of the above data sets are due to differing time dependence of the aerodynamic forces on the three different objects. There is interaction with the balance, and it must be kept in mind that balances are

TABLE 12.1. Confidence Factors $k_3 = \Delta x/s$ for Three Confidence Probabilities and a Range of Number of Observations n

n	Confidence Probabilities, β_{cp}			n	Confidence Probabilities, β_{cp}		
	.95	.99	.999		.95	.99	.999
2	8.9846	45.0121	450.156	37	0.3334	0.4471	0.5889
3	2.4841	5.7301	18.2434	41	0.3156	0.4224	0.5546
4	1.5912	2.9204	6.4623	49	0.2872	0.3832	0.5007
5	1.2417	2.0590	3.8506	57	0.2653	0.3532	0.4600
6	1.0494	1.6462	2.8039	65	0.2478	0.3293	0.4278
7	0.9248	1.4013	2.2521	73	0.2333	0.3097	0.4015
8	0.8360	1.2372	1.9119	89	0.2107	0.2791	0.3609
9	0.7687	1.1185	1.6804	105	0.1935	0.2561	0.3305
10	0.7154	1.0277	1.5126	121	0.1800	0.2379	0.3067
11	0.6718	0.9556	1.3831	137	0.1690	0.2232	0.2874
12	0.6354	0.8966	1.2807	169	0.1519	0.2004	0.2576
13	0.6043	0.8472	1.1974	201	0.1391	0.1834	0.2356
14	0.5774	0.8051	1.1279	233	0.1291	0.1701	0.2183
15	0.5538	0.7686	1.0689	265	0.1210	0.1594	0.2044
16	0.5329	0.7367	1.0180	329	0.1085	0.1428	0.1831
17	0.5142	0.7084	0.9737	393	0.0992	0.1306	0.1672
19	0.4820	0.6604	0.8996	457	0.0919	0.1210	0.1549
21	0.4552	0.6209	0.8400	521	0.0861	0.1133	0.1450
23	0.4324	0.5878	0.7907	649	0.0771	0.1014	0.1298
25	0.4128	0.5594	0.7490	777	0.0704	0.0926	0.1185
29	0.3804	0.5131	0.6822	905	0.0652	0.0858	0.1097
33	0.3546	0.4767	0.6305	1033	0.0611	0.0803	0.1027

dynamic systems with their own transfer functions. For objects that exhibit periodic shedding at frequencies that can drive the balance, the histogram will differ considerably from a normal form. In such cases, a dynamic analysis needs to be conducted and any sinusoidal time series removed from the data to obtain residuals that are more nearly normally distributed.

Example 12.1 The desired uncertainty in the mean is 0.02 lb at the 95% confidence level. How many samples must be taken in each of the above cases?

The confidence factors for the three cases are: 0.666, 0.143, and 0.036. From the table, it is seen that 12 samples will be sufficient for the first cases, 200 will be required for the second case, and the third case would require several thousand samples. This last case is likely impractical.

It can be seen from the above data that substantial reduction in the confidence limits for the mean can be obtained by including a sufficient number of observations in a data set. Taking larger data sets increases costs and must be evaluated against
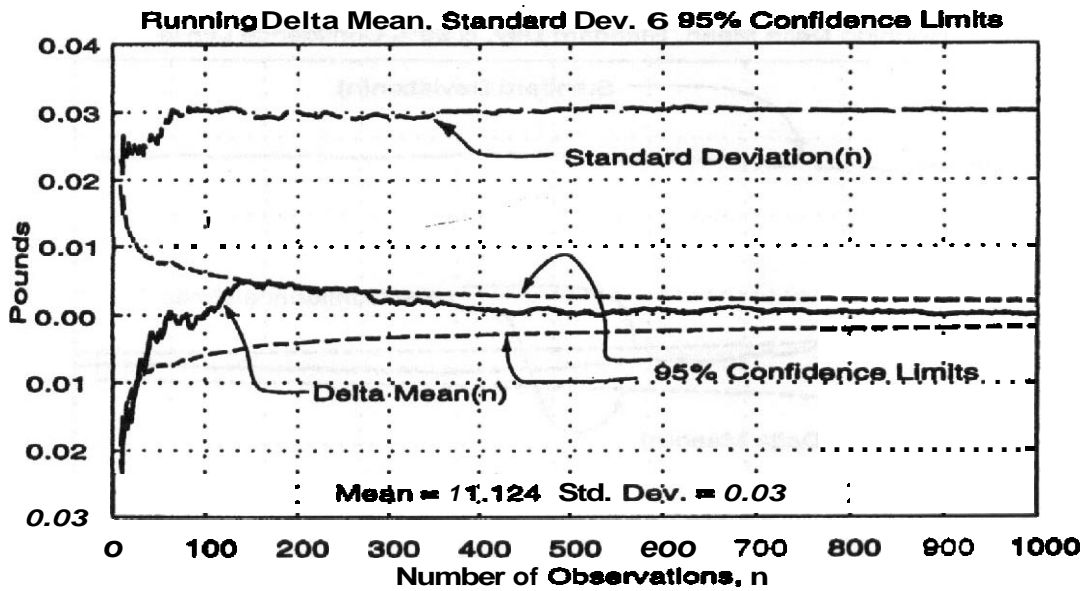
FIGURE 12.6   Confidence limits on the mean for $n = 8, \ldots, 1000$, overall mean 11.124, standard deviation 0.03, $\beta_{cp} = 0.95$.

the economic benefits expected from the decreased confidence limits for given confidence probability or increased confidence probability for given confidence limits.

Systematic (or Bias) Components

When a set of observations or measurements of a physical quantity is obtained, any random variations are obvious and require treatment, as we have already discussed.
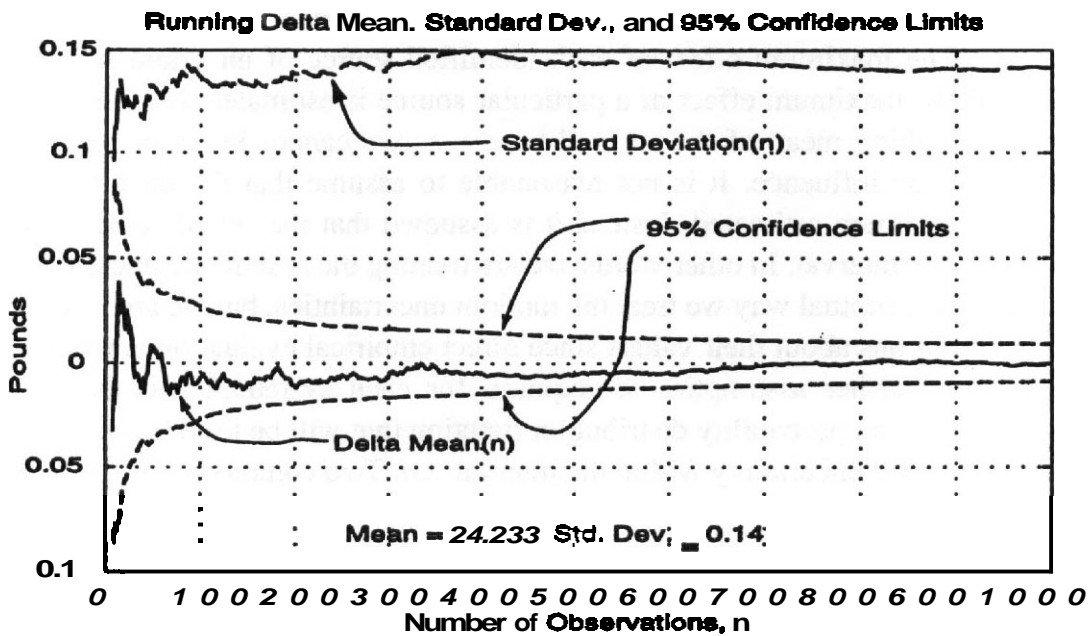
FIGURE 12.7   Confidence limits on the mean for n = 8 to 1000, overall mean 29.233, standard deviation 0.14, $\beta_{cp} = 0.95$.

Running Delta Mean. Standard Dev. & 95% Confidence Limits
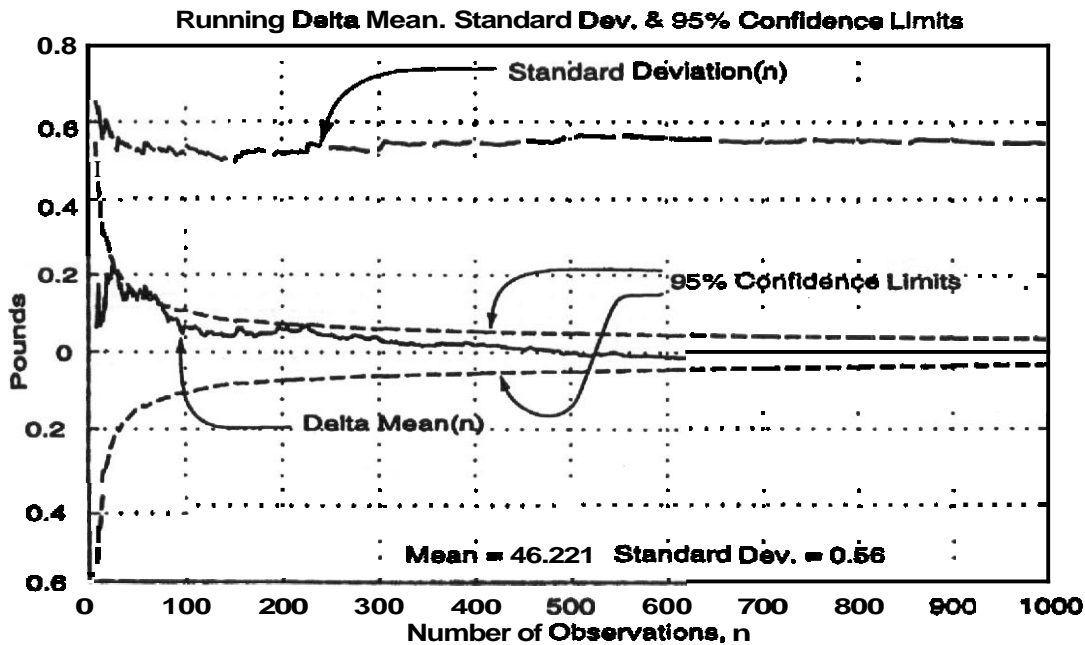
FIGURE 12.8 Confidence limits on the mean for $n = 8, \ldots, 1000$, overall mean **46.221,** standard deviation 0.56, $\beta_{cp} = \mathbf{0.95.}$

In addition it is reasonable to assume that the results **are** being influenced by a constant amount by the environment [uncontrolled and unrecorded changes indicated as $z(t)$ in Figure 12.11 or by the instrument calibration constants differing from their true values. The determination of the constants would not have been exact and the instrument properties almost certainly have changed somewhat since the last calibration.

We must conduct an analysis of each set of measurements and make an assessment using all applicable knowledge in our possession of the influences likely to affect the outcomes. The maximum effect of each identified source of uncertainty must be assessed. If the maximum effect of a particular source is estimated as a, then its effect on the resulting mean of the set will be $\pm a$ as we cannot know in general the direction of the influence. It is not reasonable to assume that the uncertainty always is the maximum estimated. Instead it is assumed that the actual value may lie anywhere in the interval. In other words, we are treating the systematic uncertainties in the same conceptual way we treat the random uncertainties, but we are forced to invoke assumptions about their values since direct empirical evaluation is simply not available. A further assumption is required for each systematic component uncertainty. This is the probability distribution function that will be used to describe the distribution of the uncertainty within the interval $\pm a$. Two common assumptions are Gaussian or uniform. Assuming a uniform distribution is more conservative or pessimistic.

The systematic errors **are** therefore to be treated as a number of variables, each with an assumed probability distribution and each with an estimated maximum influence on the mean of a set of measurements. The fact that each time we combine their influence the effect is the same shift in the mean is of no statistical significance.

We cannot know the Value of the shift so we must treat it according to the estimated maximum value and the assumed probability distribution. When effects of various components of uncertainty are combined, it is common to assume they are independent in the statistical sense. There are, however, a number of instances in which this assumption is clearly not valid and different sources are said to be correlated. We will discuss correlated error Sources in the sequel.

Combined (or Total) Uncertainty

For a single variable that has what we shall term direct uncertainty components of both systematic, U_s, and random, U_r, types, the combined uncertainty is given by the Pythagorean relation

$$U = \sqrt{U_s^2 + U_r^2} \tag{12.15}$$

In addition to this type of single-variable combination, there are always requirements to determine uncertainties of quantities related to uncertain variables through functional expressions. The expressions relating dimensional forces and moments, dynamic pressure, and reference lengths to the force and moment coefficients are the most common examples in aerodynamic experiments. The generic relation has been indicated in Figure 12.1 and Equation (12.1). The different classifications of the arguments of the functional f are mathematically irrelevant so we will use the simpler but still general representation with the single vector argument x for this discussion. We will also consider f to be a function of x rather than a functional of $x(t)$ for the present discussion. There are many cases in aerodynamic experiments in which this assumption is not valid. Examples abound in which hysteresis effects are evident. Putting those aside for the moment, we consider outputs y related to inputs, controllable factors, and uncontrollable factors, all represented by x:

$$y = f(x) \tag{12.16}$$

The elements of **x** are random variables with uncertainties that may have both random (precision) and systematic (bias) contributions to their uncertainties. The task here is to obtain the uncertainty in y when the function f and uncertainties in x are given. It is typically assumed that the uncertainties are of magnitudes such that the first-order terms in a Taylor series expansion of the function f provide a sufficient approximation of the changes in y corresponding to changes in x. An equation for the Taylor series to first order is Equation (12.17), where the mean of f and $\tilde{x}$ are zero:

$$\bar{y} + \tilde{y} = f(\bar{x}) + \left[\frac{\partial f}{\partial x} \right]_{\bar{x}} \tilde{x} \tag{12.17}$$

Then

$$\bar{y} = \left[\frac{\partial f}{\partial x} \right]_{\bar{x}} \tilde{x} \tag{12.18}$$

The bracketed quantity is the Jacobian matrix. The expected values of the squares of the elements of **vector** $\bar{y}$ are by definition the standard deviations of the elements of y. These **are** the quantities we need to determine the uncertainties in the means (the elements of $\bar{y}$) using the relations developed earlier. **We now** need to obtain **the relation**ship between the squares of the elements of $\bar{y}$ and the elements of f. Obtaining the results in matrix form is convenient both in the ease of manipulation of the symbolic result and because the results can be considered pseudocode for writing a program in a system such as MATLAB. The needed result is obtained by **forming the** outer product of $\bar{y}$ and its transpose, $\bar{y}^T$, and then taking the expected value of the matrix. The diagonal terms are the standard deviations of the elements and the off-diagonal terms are the cross correlations of the elements. Following this procedure yields

$$\bar{y}\bar{y}^T = \left[\frac{\partial f}{\partial x} \right]_{\bar{x}} \tilde{x} \left[\left[\frac{\partial f}{\partial x} \right]_{\bar{x}} \tilde{x} \right]^T = \left[\frac{\partial f}{\partial x} \right]_{\bar{x}} [\tilde{x}\tilde{x}^T] \left[\frac{\partial f}{\partial x} \right]_{\bar{x}}^T \tag{12.19}$$

The elements of the Jacobian matrix are derivatives of the function f evaluated at the mean value $\bar{x}$. Equation (12.19), upon taking the expected values of both sides, provides the relationship between the correlation matrix for the output vector, $\langle [\bar{y}\bar{y}^T] \rangle$, and the correlation matrix for the input vector, $\langle [\tilde{x}\tilde{x}^T] \rangle$. The angular brackets indicate the expected-value operation.

Expressing the uncertainty as the sum of random and systematic contributions, $\tilde{x} = \tilde{x}_r + \tilde{x}_s$, and foregoing the explicit matrix brackets yield

$$\langle \tilde{x}\tilde{x}^T \rangle = \langle \tilde{x}_r\tilde{x}_r^T \rangle + \langle \tilde{x}_r\tilde{x}_s^T \rangle + \langle \tilde{x}_s\tilde{x}_r^T \rangle + \langle \tilde{x}_s\tilde{x}_s^T \rangle \tag{12.20}$$

A correlation matrix is diagonal if the elements of the vector are independent random variables. This is assumed to be the case for the random contribution so the first term on the right-hand side of Equation (12.20) is a diagonal matrix. The random and the systematic contributions are also assumed to be independent random variables, so the second and third terms are zero. There may be some correlated elements in the systematic contributions, so the fourth term may not be diagonal. Off-diagonal terms may be positive or negative and of course combine according to Equation (12.19), so these terms may increase or decrease the variances in the elements of the output vector. Using the notation $[f_x]$ for the Jacobian matrix, Equation (12.21) is obtained for the total uncertainty of the output when the functional relation and the uncertainty of the input **are** known:

$$\langle \bar{y}\bar{y}^T \rangle = [f_x][\langle \tilde{x}_r\tilde{x}_r^T \rangle + \langle \tilde{x}_s\tilde{x}_s^T \rangle][f_x]^T \tag{12.21}$$
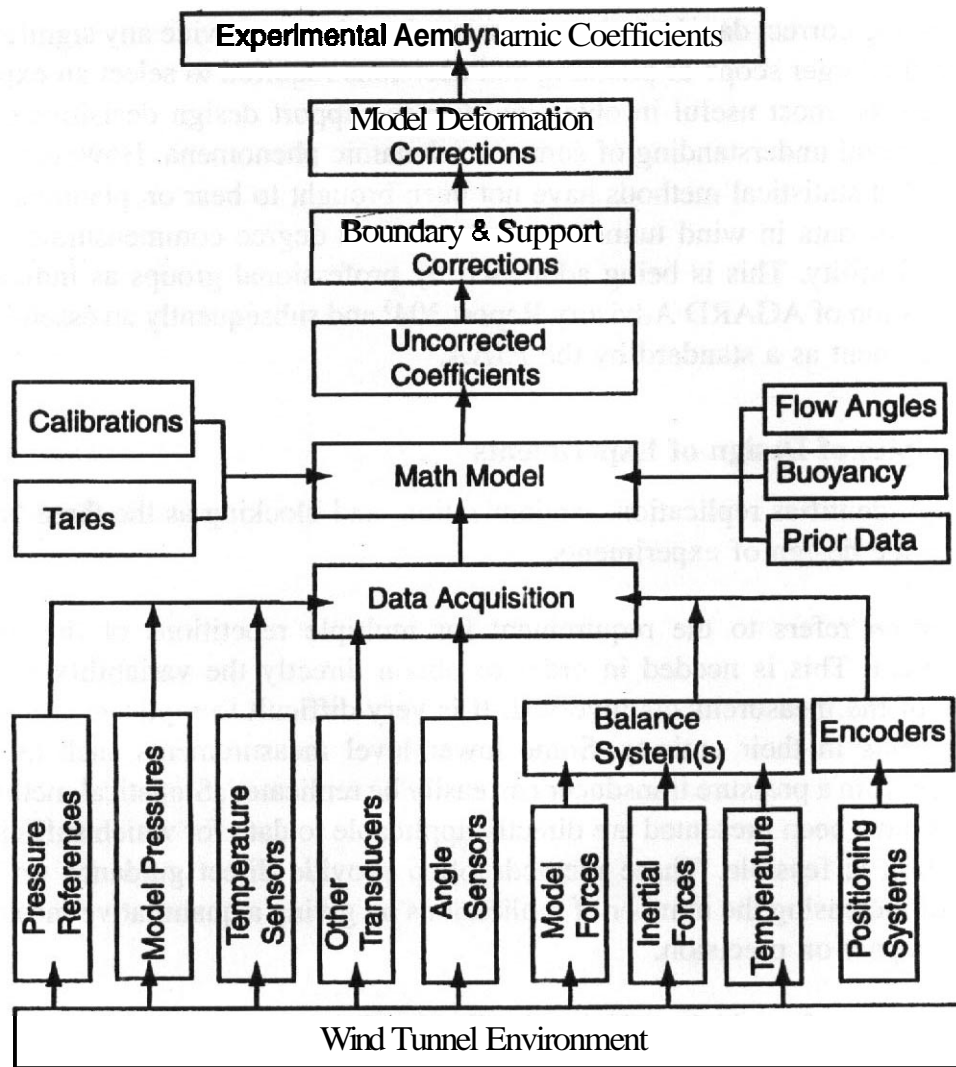
FIGURE 12.9   Representative data flow.

Applying this result to a wind tunnel experiment can require extensive time and effort. **AGARD AR 304**[3] contains an extensive example of an application to a force and a pressure test. We include in Figure 12.9 a diagram of data flow that is representative of a wind tunnel test.

12.3 ASPECTS OF DESIGN OF EXPERIMENTS

Statistical methods provide very useful tools in efforts to provide quantitative statements of measurement accuracy. In order to realize the best advantages, the design and conduct of the experiment must be done in concert with the choice of the methods chosen for analysis and interpretation of the resulting data. Here we are focusing on the issues related to utility of statistical methods rather than the issues of a general aerodynamic nature that are addressed throughout this book and in other related literature. It is to be kept clearly in mind that statistical methods are

useful in making correct data interpretations, but they do not provide any significant guidance in the larger scope of planning and decisions required to select an experiment that will be most useful in obtaining data to support design decisions or in improving general understanding of some aerodynamic phenomena. However, it is our opinion that statistical methods have not been brought to bear on planning and interpretation of data in wind tunnel experiments to a degree commensurate with their potential utility. This is being addressed by professional groups as indicated by the publication of AGARD Advisory Report 304[3] and subsequently an essentially identical document as a standard by the AIAA.[4]

Some Principles of Design of Experiments

Montgomery'[1] identifies replication, randomization, and blocking as the three basic principles in the design of experiments.

> ***Replication*** refers to the requirement for multiple repetitions of the basic experiment. This is needed in order to obtain directly the variability in the results of the measurements involved. It is very difficult to replicate complex experiments in their entirety. Some lower level measurements such as the readings from a pressure transducer can easily be replicated. Statistical methods such as have been presented are directly applicable to data for which sufficient replication is feasible. These methods often provide direct guidance on the value of increasing the number of replications by giving a quantitative measure of the impact on precision.

> For aspects for which sufficient replication is not possible, judgment and prior experience provide the tools that must be applied. This is the case for the systematic or bias contributions that must almost always be evaluated without the benefit of significant replication.

> · ***Randomization*** refers to the goal of producing replications of conditions for which the resulting experimental observations are independently distributed random variables. A result of effective randomization can be to average out the effects of uncontrollable factors. Just as replication is often not possible for complex experiments, randomization will also be compromised. However, there are common examples of aerodynamic experiments in which the order in which conditions are set can have an effect on the resulting data. The facts that call for randomization insofar as is feasible need to be kept in mind during the planning and execution of experiments.

> ***Blocking*** is in a sense a counter to randomization that is applied when the experimental conditions can be manipulated to isolate a particular effect. This is in fact a primary practice in wind tunnel experiments. Many incremental effects are measured such as tail-on and tail-off measurements for airplanes or mirrors on and mirrors off for automobiles. It is recognized that these increments will be more precise if these subparts are added and removed while

the main parts remain installed in the experimental setup. These are examples of "blocking" that provide data on incremental effects that are more precise than would be obtained if the complete model with and without the subelements is removed and reinstalled in the wind tunnel.

The three concepts of replication, randomization, and blocking are important principles that should be kept clearly in mind during the design of an experiment and the associated data analysis.

We have collected here a bare minimum of results and suggest that most readers will need a ready reference on probability, statistics, and design of experiments. We have treated only the most common case that arises in wind tunnel experiments, which is the estimation of confidence interval–confidence probability pairs for a particular measurement. We do not address the broader issue of the application of principles of design of experiments to planning wind tunnel programs that encompasses selection of configuration modifications. This is, however, an area that can likely benefit from a more formal application of the methods for design of experiments.

Guidelines for Wind Tunnel Experiments

This is a rather commonsense listing of requirements for initiating and executing a successful aerodynamic experiment. Failure to include some of the necessary steps, however, is too common.

1. Clearly state the problem being addressed and define the purpose of the experiment. This rather obvious point is often overlooked because the initiators may begin with a small homogeneous group for whom the purposes are indeed clearly known. But successful completion will often require contributions from a number of people for whom a particular experiment is only one of many important activities. A clear statement of the problem being addressed will often be critical in obtaining efficient application of their professional knowledge and skills or in avoiding a serious misunderstanding about what will be needed. This clear statement of the problem should be provided to all persons involved in the planning and execution of the experiment in sufficient time so that they can be mentally and physically prepared. The day before an experiment is to begin is too late to give a software engineer the specifications for the data gathering even if someone else has said, "Oh we'll just use the same program we used last month."

   The expected results from an experiment must have associated expected accuracy and precision that are the minimum goals in order that the objectives can be met. These accuracy and precision requirements should be a part of the problem statement. Maximum advantage must be taken of results from previous experiments, theories, and computations as they are available in the professional literature or from corporate records.

   Keep in mind that learning from experiments, as with other approaches,

is iterative. Usually, a series of experiments that build on each other rather than one all-encompassing experiment is a more effective use of resources.

2. Identify the outcomes needed, including the ranges of values of parameters that wilt provide the information to resolve the problem. This will imply a range of operating states and configuration geometries. There will be required accuracies and precisions associated with each variable or parameter that should be identified.

3. Identify feasible model provisions and compatible facilities. This will require conceptual and preliminary design of the models and fixtures. It will require identifying any wind tunnel boundary corrections to be applied along with tare, interference, and other data corrections. It will require assessment of the impact of these choices individually and in sum on the accuracy and precision of the outputs. Keep in mind that statistical significance and practical significance of the accuracy and precision of any outcome are entirely different issues. Each is to be considered in its own sphere of importance.

4. Prepare run schedules and configuration change implications. Embedded in these decisions will be the degree to which replication, randomization, and blocking can contribute to the enrichment of the data to be obtained.

   Compare the resources needed and resources available. Iterate steps 1–4 until a match is obtained.

   Prepare a clear guide for the conduct of the experiment. Make sure all persons involved understand the required actions and procedures. Make sure all persons, materials, models, instrumentation, and software will be available at the time and place for executing the experiment.

5. Initiate the experiment. Provide for monitoring of all processes and data gathering. Include process evaluation of achieved accuracies and precisions of measurements.

6. Conduct data analyses to provide quantitative evaluation of the achieved accuracies and precisions. This information should be provided to the aerodynamicists and other project personnel as a part of the data package so that the product decisions can include appropriate consideration of outcome uncertainties.

We include here as Figure 12.10 another block diagram adapted from AGARD AR 304[3] that depicts a planning process for an experiment with emphasis on the inclusion of uncertainty evaluation.

12.4 MODEL DESIGN AND CONSTRUCTION

General Considerations

The type and the construction of the wind tunnel model are dictated by the purposes of the experiment and the tunnel in which the experiment is to be conducted. After the obvious and paramount necessity of safety considerations for the personnel
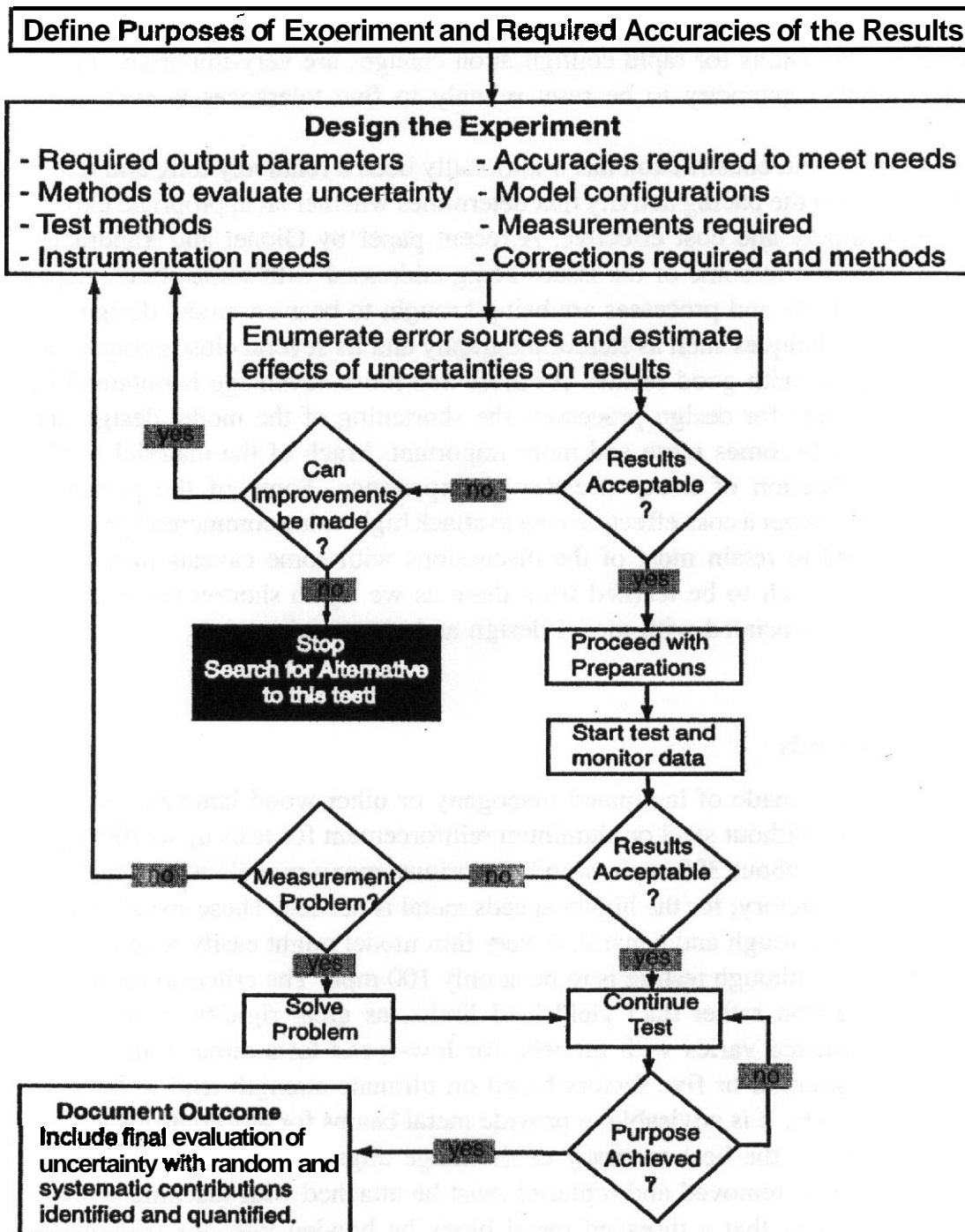
FIGURE 12.10   Experiment planning and execution process diagram.

and the facilities comes sufficient accuracy, accessibility, and maintenance. All are essential. Sufficient accuracy almost always translates to extreme requirements. Working conditions in a wind tunnel are at best very trying. The temperature may vary from **30°F** in winter to **140°F** in summer. The model is usually so placed that accessibility is at a premium and repair facilities may or may not be available. All these factors demand that changes be as simple as possible and the model with all

its parts and additions be thoroughly tested outside the tunnel before tests are commenced. Provisions for rapid configuration changes are very important. Provisions for variable geometry to be reset reliably to fine tolerances is even more important.

Model design and construction has traditionally been a relatively long and tedius process. It is often the pacing activity that determines whether an appropriate experiment can be timely and cost effective. A recent paper by Gionet and Yandrasits[S] has drawn attention to some of the issues being addressed with some effect. Rapid prototyping methods and processes are being brought to bear on model design and construction. Techniques such as stereolithography and its several close competitors have been applied with good results. As more and more advantage is obtained by reducing cycle time for design processes, the shortening of the model design and fabrication cycle becomes more and more important. Much of the material in this chapter is a reflection of many decades of experience. Some of the particular processes are no longer a cost-effective way to attack high-value commercial projects. We have decided to retain most of the discussions with some caveats introduced because there is much to be learned from them as we try to shorten the time and reduce the costs associated with model design and construction.

Choice of Materials

In general, models made of laminated mahogany or other wood laminates will be adequately strong without steel or aluminum reinforcement for tests up to 100 mph. Above that, and to about 300 mph, wood or various epoxy models with steel load members are satisfactory; for the higher speeds metal is needed. These speed criteria are, of course, very rough and general. A very thin model might easily require solid steel construction although testing is to be at only 100 mph. The criterion for model strength is deflection rather than yield load limits, as great rigidity is desirable. Although the practice varies with tunnels, for low-speed tests either four factors based on yield strength or five factors based on ultimate strength tend to be used for margins of safety. It is advisable to provide metal beams for any control surfaces in order to maintain the best accuracy of the hinge alignment. All parts of wood models that must be removed and replaced must be attached with machine screws. This usually requires that a threaded metal block be bonded into one part of the model and the other part have a metal block for the screw head. Wood screws are intended to be used only once. Care must be taken in design and construction to ensure that the parts fit together with a method such as alignment pins to ensure proper and repeatable alignment.

Historically, shops attached to wind tunnels would prepare the laminated mahogany blocks. Today it is more effective to purchase commercially available laminated die materials when a woodlike mated is the best choice. These materials are not only more cost effective at the outset but also more dimensionally stable than the results achieved without the capability to completely saturate the wood with sealer or glue.

Some of the new plastics, epoxy resins, fiberglass, and carbon filter are often very useful in model building. Where weight is a problem (as on flutter models) fiberglass can be used for external stores, slipper tanks, and the like. Even the low-melting-point alloys can be used in many ways. For example, fillets can be made of Cerrobend, which works easily and takes a good polish.

Fabrication

Basically, the choice of model construction methods is a function of the available shop facilities and skills. For projects built by students, wood (including die makers' laminates) is an excellent choice, while for a large corporation that has computer-aided design (CAD) available, the loft lines from the CAD system can be transformed into a set of instructions for numerically controlled machine tools, as illustrated in Figure 12.11. In this case, depending on loads, steel or aluminum is ideal for lifting surfaces and flow-through jet nacelles. The fuselage can be built on a steel–aluminum spar with aluminum bulkheads that are threaded to take thick (0.125–0.250-in.) fiberglass-epoxy pieces of shell that form the body.

Wings and tails can also be built of large flat plates (spar) of aluminum–steel to which epoxy or wood is bounded and contoured. For sharp trailing edges and for plastic contour material the leading edge should also possibly be metal. In any case, the model designer must design the model to fit the capabilities of the people and shop that will produce the model.
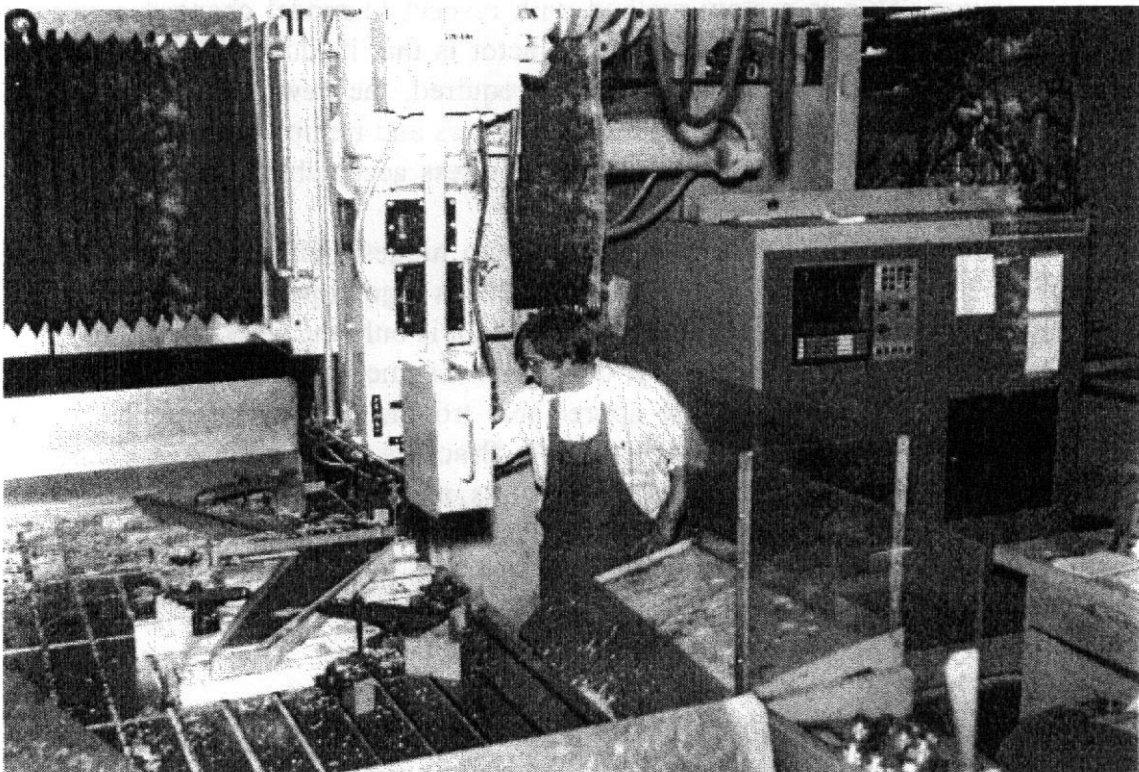
FIGURE 12.11   Contouring a swept wing with a numerically controlled milling machine. (Photograph courtesy of Boeing Aerodynamic Laboratories.)

A simple way to build a model to be used for configuration trade-off studies is to build the load-carrying capability into the model out of metal. Styrofoam is bonded to these metal spars and cut to contour with a hot wire. The styrofoam is then covered with thin fiberglass or Mylar sheets (about **2** mils) to provide a smooth contour. The fiberglass and styrofoam are not considered to be load bearing, as in sandwich construction used for radio-controlled models. In general, these are one-shot models and do not lend themselves to major modifications, but their cost is relatively low.

Usually models have many component parts, each to be made separately. If models are to be made of wood that is not impregnated with a stabilizer, it is advisable to make each part oversize by **0.0625** or **0.125** in. and allow some additional seasoning. This permits any strains in the laminated block to relieve themselves by warping. The last fraction of an inch is then worked down to female templates by files, scrappers, and sandpaper. The day should be so planned that time remains to spray at least one coat of clear lacquer after the piece is done to seal it and prevent warping due to changes in moisture content. This is not the type of process that is often a good choice in a commercial project today. But it can be a good learning process for student teams and may be the way for an amateur team to produce a quality model.

Hinged surfaces present a problem for the model designer largely because the smallest hinge possible to construct is far too large in scale. In view of the hopelessness of accurate reproduction, the designer just does the best he or she can. Several basic types of hinges are in general use. The first is a set of brackets for each angle setting. This is a slow method with respect to model changes, and it slows model construction as well. **A** serious factor is that if, during the program, test results indicate that additional angles are required, the new brackets usually require shop work above the level of tunnel engineers and tie up the tunnel during fitting **as** well. This type of approach has become less acceptable **as** design cycle time has become more of an issue.

A second method is to furnish the surfaces with hinges and to use an exterior sector with drilled holes for each angle setting. This is a good positive method that at least yields the same setting for repeat points, and it is only the work of a moment if additional settings become necessary. One must assume, of course, that such a sector in the "breeze" will not cause appreciable trouble. However, brackets for control surfaces give a repeatable angle setting. Brackets, often with fairings, are about the only way to attach leading-edge slats, slots, and trailing-edge slotted flaps, especially if they have a Fowler-type action. **A** third method is to furnish hinges and an interior setting lock. We have had too many of these slip and broken too many to be enthusiastic about this type except when it is designed by someone with much experience. The engineer using this type of hinge should check the setting at the *end* of each run.

A fourth method for metal control surfaces is to use hinges near the tip. The inboard end has a reamed hole that slides over a large pin. For each angle a hole is drilled and reamed through the control surface and the large pin. The holes are spaced spanwise. The surface angle is then held with a straight or roll pin.

Model makers still-differ in their opinions of suitable finishes. For wood models, the choice is usually between three types, all quick drying: shellac, clear lacquer, or pigmented lacquer. Shellac and the clear lacquers seem to yield a slightly thinner coat (0.002–0.005 in.) than the pigmented lacquer (0.003–0.008 in.). On the other hand, many model makers believe that the smoothest finish is obtained only with the pigmented lacquer. Regardless of the choice, an adjustment in the templates should be made to allow room for the finish. Finishes put on and sanded back to zero thickness are not believed to offer sufficient protection and moisture seal.

For metal or plastic models, either sprayed enamel or lacquer can be used. Usually a primer coat is applied first. This is necessary for a metal model to obtain proper bond, and then pigmented finish coats are added. Generally a flat finish rather than high gloss is preferred to avoid highlights in both configuration and flow visualization photographs. Tough and somewhat thick aircraft epoxy paints should be avoided. They can only be removed by sanding in many cases, and often a model must be refinished when it is used for more than one test. It is amazing how chipped and pocked a model becomes during a test. One source of the nicks is razor blades used to cut tape for sealing joints or applying tufts on the model surface. The tape should be cut away from the model surface.

Dimensional Tolerances and Fine Details

An aircraft model for a 7 × 10-ft tunnel (i.e., with a span of 6–8 ft) should have the wing contour accurate to 0.005 in. to the true contour and the fuselage to within 0.01 in. No perceptible ridges or joints should be permitted. If a metal model is to be employed, a surface finish of rms 10 (25 microinches) may be attained by using No. 600 wet emery paper. If this discussion of model accuracy and finish seems nonsensical in the light of the common additions of roughness to trip the boundary layer, it is not quite as bad as it seems. The drag of a turbulent boundary layer on a smooth surface is both different and more repeatable than that on a questionable surface, and the smoothness behind intentional roughness thus makes sense. Dimensions may seem harder to justify, except to note the large difference in pitching moment associated with small changes in camber or camber distribution. It is in fact easy to see the extreme sensitivity to small geometry changes in critical areas by using one of the currently available good airfoil design computer programs.

Air passages, radiator openings, and cooling entrances may be simulated by an indenture of the entry without any completed flow passages. Such passages, if completed, could have Reynolds numbers too low for satisfactory testing. A parallel situation exits for all small excrescences: antennae, bomb racks, pitot-static tubes, and the like. They too would show such scale effect that their true effect could not be measured, and hence they are left off. Quite often jet engine nacelles are of the flow-through type. In some cases the nacelles are equipped with four or more static orifices. The nacelles are calibrated so that the internal aerodynamic forces can be calculated from the static pressures and can then be subtracted from the force data or a nacelle wake rake is used to obtain nacelle forces.

Pressure Models

Pressure models for tests of the type described in Chapter 14 require additional care in design and construction. Pressure taps on the wing are located at least at 0.125, 2.5, 5.0, 10.0, 15.0, 20.0, 30.0, 40, 50, 60, 70, 80, 95, and 100% of the chord on both upper and lower surfaces at several spanwise stations. This obviously necessitates a large number of tubes, which should be brought out from the model under circumstances least influencing the flow. There are never enough pressure taps, which is a major impetus for the evolving pressure-sensitive paint described in Chapter 4. Figure 12.12 shows how much space inside a model is required for routing tubes. Remember the surface accuracies that must be maintained along with this type of accessibility.

The design of the pressure orifices themselves is very important. If static-pressure orifices are kept small (say about $\frac{1}{32}$ in. in diameter), negligible difference is found between drilling them perpendicular to the surface or perpendicular to the chord. But it is certain that they must be absolutely flush. A metal tube in a wood model has a tendency to form a slight ridge as the softer wood is finished around it. Some designers use metal strips at the section where the orifices are to be, thus avoiding the difficulties of finishing dissimilar materials. An artifice practiced by the Canadian National Research Council seems a satisfactory arrangement. This embraces a solid
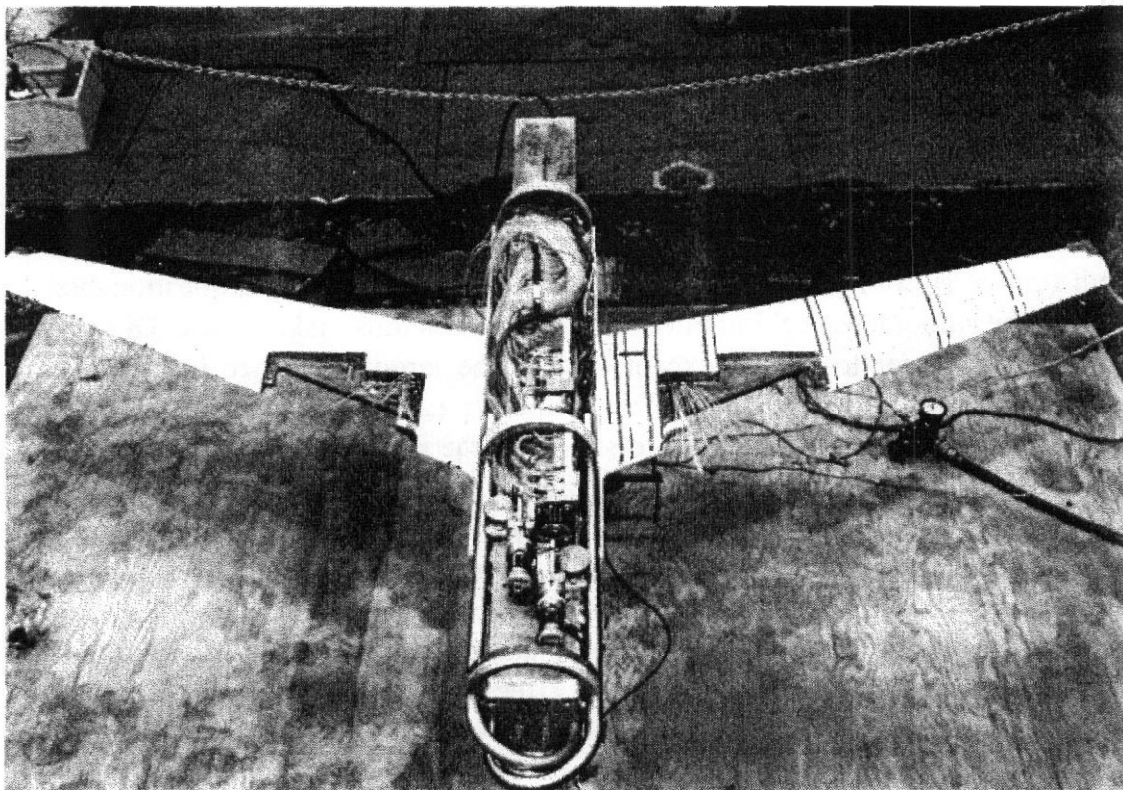
FIGURE 12.12 Model with scanivalves and tubing for surface pressures in aft body and high-pressure air lines for nacelles in forward body. (Photograph courtesy of Boeing Aerodynamic Laboratories.)

transparent plastic plug leading down to the buried metal tubes. After the airfoil is shaped, holes are drilled down to the tubes through the plastic.

Since the plastic offers finishing characteristics similar to those of wood, remarkable smoothness is attained. If the wings of the model are exceedingly thin, it is sometimes advantageous to put the upper surface orifices on one wing and those for the lower surface on the other. Wings of metal and epoxy over metal usually have milled slots cut into the wing. Thin-wall stainless steel tubing is then laid in the slots and brought to the model surface. The slots are then fillet with epoxy and tubes and epoxy returned to contour. On steel wings soft solder can be used to fill slots. Often it is desirable to cut a large chordwise slot for tubes about 0.5 in. from the chord line of the pressure taps. Then the individual tubes are brought from thin slots to the larger slot. This larger slot then intersects a spanwise slot that it used to get the tubes into the fuselage.

When sanding or filling surfaces with pressure orifices, care must be taken to avoid plugging the tubes. One way this can be accomplished is to blow dry compressed air through all of the tubes when sanding or filing.

Though many satisfactory pressure models have been built using copper tubing, scanivalve or manometer fill time can usually be saved by going to annealed stainless steel tubing since, for a given (and usually critical) outside diameter, its inside diameter is a maximum. The stainless steel tubing is less likely to kink than copper, but it is harder to solder without an acid treatment.

Manometer fill times, which run as much as 2 min under some circumstances, may be estimated with good accuracy from the data given by Sinclair and Robins[6] and an early NOL memo.' This is no longer of such interest for long tubing runs since almost all pressure instrumentation is inside the model, which provides short tube lengths. The time lags are still of importance precisely because the data systems are very fast and quite capable of recording data before the pressure equalizes over even a short piece of tubing.

Since automatic data acquisition equipment has become generally available, two trends have occurred with pressure or load models. First, the number of pressure ports has increased. Second, pressures are recorded by the use of electronically scanned transducers. Since the electrical cables required are much smaller than a plastic tube for each port, the massive problem of getting tubes out of the model is gone. At the same time, data accuracy requirements are being pushed to more extreme limits so even small disturbances are sometimes critical.

Model Handling and Material for Quick Filling

Though perhaps not a wind tunnel model design criterion per se, the fact remains that wind tunnel models have to be moved about, and, depending on their size, this may become a ticklish problem. Most tunnels have a lifting crane for moving the model into the test section, and in turn whenever possible model designers should provide an attachment near the center of gravity of the model. Some tunnels provide canvas sandbags for supporting the model when it is resting on the floor or a table.

TABLE 12.2. Recipe for a Good Filler Wax

Tunnel wax formula	
Beeswax:	about 80% by weight
Venice turpentine:	about 20% by weight
Powdered rosin:	about $\frac{1}{2}$% by weight

Bring turpentine to a boil, add **the rosin, and stir. Add the beeswax in small chunks and allow to melt. Stir thoroughly. Remove from the heat** and **pour into trays for cwling.**

Many engineers and technicians have sustained cuts from sharp model parts due to inadequate provisions for handling.

Some sort of modeling-clay-type material is frequently needed for filling cracks, covering screw holes, and making minor contour changes. Children's modeling clay or, better, sculptors' Plastalina No. 4 will suffice for low-speed work. When extra strength or high temperatures must be considered, a stiff wax made according to the formula given in Table 12.2 will be found excellent. The acetone and pyroxylin putties **are** also very good, although they require a few minutes drying time. Automotive car body fillers made of a two-part epoxy **are** excellent for filling holes. They cure rapidly and are easy to shape. If the filler covers a screw or bolt, paper or tape should be put into the hole first. It is a difficult job to dig filler out of the head of a screw. A heated Allen wrench can be used to clean the filler from the head socket, but it is best not to fill the head socket. These fillers do not work too well for removable fillets as they tend to be brittle and will break very easily when the cross section is thin.

12.5   PLANNING THE EXPERIMENT

A wind tunnel experiment should be run only if (1) some new knowledge is desired and (2) the experiment as planned has a reasonable chance of obtaining the knowledge sought with the necessary accuracy. In view of the cost of models and tunnel time, it should be determined that the "new knowledge" does not already exist. In many cases—too many cases—a good library search could have saved time and money.

It is hard to write specific rules for setting up an experiment and taking data, since there are such a multitude of types. However, the following procedures do stand as accepted and respected. If some seem obvious to the experienced engineer, we hasten to add that at one time or another we have seen all the rules stated below completely disregarded. This list includes a number of items that are specific to aircraft tests, but any good engineer can adapt it to his or her own application.

1. Check all calibration curves of new equipment before, during, and after a test. Always calibrate for the full-load range, and always use a number of loads—not a single load with the assumption that the calibration is linear.

2. Take enough points so that the loss of any one point will not hurt the fairing of the curve.

3. Always repeat the wind-off zero and the wind-on first point at the end of the run. Have acceptable balance "drift" limits up before the program starts (0.1 or 0.2% maximum reading is a reasonable drift allowance).

4. Take points on base runs at every degree plus $0.5°$ readings at the stall or other points of interest. Take routine runs with $2°$ plus readings and $1°$ increments at the stall.

5. Check all models against their templates and check the templates. Do not hesitate to cancel a program and pay the cancellation fee if the model is not within acceptable limits. If you do this, the *new* person responsible for model fidelity will have future models right.

6. Be very careful when you shorten a program by omitting "irrelevant" components and continue to monitor irrelevant components as a test progresses. For instance, changes that primarily affect only the pitching moment might lead one to monitor only the pitch balance. If there is trouble with the lift balance, this omission would make it impossible to plot the data completely since the angle-of-attack correction is affected by the lift, and if later a change to a new center of gravity seems desirable, the drag values must be available and their accuracy known to be adequate. Similarly reading less than six components in the interest of saving time on yaw runs can lead to serious work-up troubles of a similar nature.

7. Plan model variations of wide enough scope to bracket needed data so that interpolation rather than extrapolation is possible.

8. Whenever possible find out how others do the type of test you contemplate and profit from their experience.

9. Be clear in all instruction and data presentation. Never use the word *pressure* when it might be confused with *static pressure* or *total pressure.* Always use a subscript for pitching and yawing moments to indicate the axis about which they are measured, and specify the desired center-of-gravity location. Also, if multiple entries are made with a model, make sure that the statement "the same as the last test" is really true before you use it. This caveat also applies to "repeat" runs within an experiment.

12.6   ARRANGING FOR USE OF FACILITIES

Each tunnel has a somewhat different procedure for use, and no exact rules can be written to cover them all. Nevertheless, a description of a tunnel procurement may be useful in giving a general familiarity with the system. The following description is of course not accurate in total for any specific program. The elements, however, must be included as any project unfolds. The description can be used by new engineers or prospective users to develop some reasonable anticipation of what to expect.

Most of the large wind tunnels may be scheduled months in advance, and hence an inventor seeking to prove some new idea may be very disappointed in the delay he or she may find necessary. Aircraft companies avoid this problem by maintaining their own facilities and having priority even if some other user has a scheduled entry. During heavy development times they will regularly schedule entries of 100 hr duration every few weeks. Then, as their time approaches, they select from needed experiments the one with the greatest urgency. As an entry time approaches, the following procedure is common:

1. About 2 months before a planned experiment, the tunnel manager is informed of the tunnel configuration desired: for example, external balance, swept strut, and two-dimensional test section. If the desired setup does not meld with the other programs scheduled about that time, a shift of a week or so may be necessary to avoid excessive tunnel changes.

2. Three weeks before the scheduled beginning of the experiment complete model drawings, stress analysis, desired tunnel operating conditions, and a preliminary run list **are** sent to the tunnel manager.

3. Two weeks before the experiment a meeting is arranged between the engineers who will directly oversee the conduct of the experiment for both the tunnel and the airplane company. At this meeting any points not apparent in the pretest information may be ironed out. Agreement on the special equipment needed is reached: pressure measurements (number of tubes and expected pressure ranges) and cameras, both still and motion picture. All constants required for data reduction should be provided, including model reference dimensions such as wing **area,** span, mean aerodynamic chord, transfer dimensions for center-of-gravity positions desired, and reference for angle of attack. The realistic definition of desired accuracy should include forces and moments, angle settings, pressures, and model location; the acceptance of reduced accuracy where it actually is **sufficient** may result in considerable savings in time and money. A list of plots needed and the form of the tables of data **are** presented for both printed and other media. Agreement is reached on a date for the presentation of preliminary data and for the final report.

4. One week before the scheduled start the company representatives **arrive** with the model and commence as much of the setup and weight tares **as** feasible outside the tunnel. There may still remain some questions about the program, which must be settled before running. The representatives must do a certain amount of legwork to ascertain that all the items previously agreed upon have actually been accomplished.

5. During the last **day** before the test, company representatives remain on 1-hr alert, ready to move into the tunnel and start their test.

REFERENCES AND NOTES

1. Montgomery, D. C., *Design and Analysis of Experiments, 3rd ed.,* John Wiley & Sons, New York 1991.

2. Dietrich, C. E, *Uncertainty, Calibration, and Probability,* 2nd ed., Adam Hilger, Philadelphia, 1991.

3. AGARD Fluid Dynamics Panel Working Group 15, "Quality Assessment for Wind Tunnel Testing," AGARD Advisory Report 304, 1994.

4. AIAA, "Assessment of Wind Tunnel Data Uncertainty," AIAA Standard S-071-1995, 1995.

5. Gionet, C., and Yandrasits, F., "Developments in Model Design and Manufacturing Techniques, Six Day Model," Paper 9, presented at Wind Tunnels and Wind Tunnel Test Techniques, The Royal Aeronautical Society, Cambridge, United Kingdom, April 14–16, 1997.

6. Sinclari, A. R., and Robins, A. W., "A Method for the Determination of the Time Lag in Pressure Measuring Systems Incorporating Capillaries," NACA TN 2793, 1952.

7. Naval Ordnance Laboratory (NOL), "Time Lags Due to Compressible Poiseuille Flow Resistance in Pressure Measuring Systems," NOL Memo 10,677, 1950.

13 Aircraft and Aircraft Components

13.1 GENERAL TEST PROCEDURE

Depending on the innovations incorporated and the terms of the development contract or program, a new model airplane may require from one to six models (or more) and up to six different wind tunnels. A typical program is as follows: After the preliminary layout of the proposed new airplane has been made, a "complete" model is designed and constructed. This first model,' usually of 6–16% scale, is a breakdown model; that is, the different configurations of the airplane may be built up progressively through additions to the wing alone, making possible the evaluation of the relative effect of each component. Testing this model requires measurement of all six forces and moments: lift, drag, and side force and rolling, yawing, and pitching moments. The important criteria of maximum lift (stalling speed), minimum drag (high speed), and static stability are evaluated. The breakdown model aids in determining the exterior configuration of the airplane so that the specialized models can be designed. An example of a breakdown model is shown in Figure 13.1.

The breakdown model is useful for much more than simply satisfying the aerodynamicist's curiosity about the contributions of each component. One instance comes to mind where much of the breakdown was omitted. ("We can only fly the whole airplane"). When the performance fell far short of that predicted, and after the tunnel and tunnel crew had been duly excoriated, a breakdown model disclosed that the horizontal-jet pod supports were lifting "nearly as much as the wing" and in the opposite direction!

The second model (after the first breakdown model there is no specific order for the additional ones) may be a small-scale spin model for determining the spin-recovery characteristics in a spin tunnel. Here the model is put into a tailspin in the vertical airstream of the tunnel, and a remotely operated mechanism moves the control surfaces as desired to bring the plane out of the spin. Motion pictures of the recovery can be examined to see whether the procedure is satisfactory (see Chapter 18).

A third model, also light and fragile, may be flown in a free-flight tunnel such as the Langley V/STOL tunnel where motion pictures record its stability and maneuverability.

A fourth model, so constructed that its structural rigidity is carefully related to the full-scale airplane, may be tested for critical flutter speed (see Chapter 18).
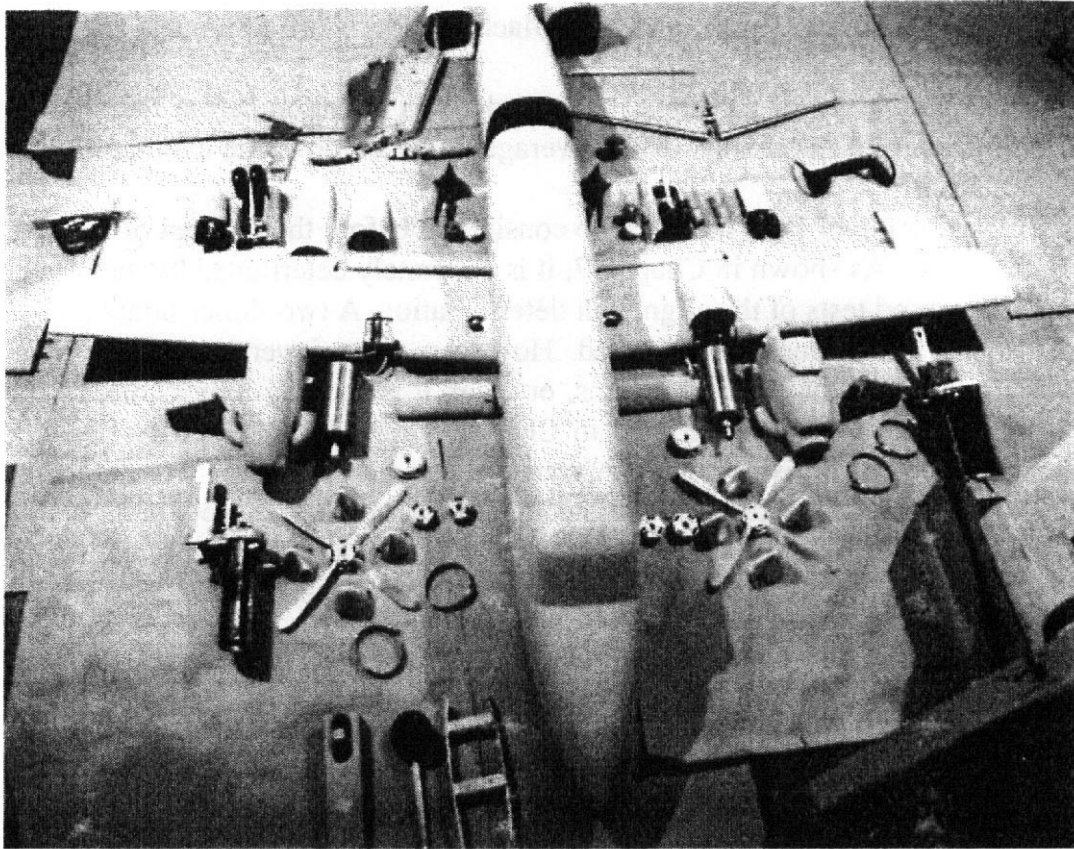
FIGURE 13.1   Breakdown of wind tunnel model of Beech 1900 turboprop airliner. (Photograph courtesy of Raytheon.)

If the design appears satisfactory or can be made so after these preliminary tests, larger models of component parts may be tested. Aileron panels and tail surfaces to perhaps 40% scale may be tested, and nacelles to a similar scale for propeller aircraft may be investigated for cooling and drag.

Compressibility effects are investigated with high-speed models in high-speed tunnels. Sometimes additional section tests of the airfoils to be used are made in a two-dimensional tunnel, and if the design is entirely untested, pressure distributions over the flap, flap vanes, and the like may be taken to determine loads for the structural design.

Finally, for smaller aircraft, when the first actual airplane is finished, it can be tested in a full-scale tunnel for aerodynamic "clean-up" changes. Here also the manufacturing irregularities can be examined and improvements suggested. Military airplanes can be subjected to simulated battle damage so that studies can be made of possible catastrophic effects.

The costs of such development programs are not small, of course. Yet, compared to the cost of building the actual airplane, testing it, and changing it, the model-testing cost is miniscule. Rarely would a single concern have the entire facilities required for a complete testing program. The customary solution is for the complete model and the control surface panels to be tested in the company's own wind tunnel,

leaving the spin, stability, flutter, and high-Mach-number work to tunnels specially designed for them.

The basic parameters of the tunnel that need direct attention before the wind is turned on include considerations of the average angle of flow, the average q, and the balance loads.

The average angle of flow need not be considered before the full test of a three-dimensional wing. As shown in Chapter 7, it is accurately determined by the model normal and inverted tests of the alignment determination. A two-dimensional model should also be run normal and inverted. However, when inversion is not to be employed for any of a number of reasons, or when it is actually impossible, as for a panel model, the procedure outlined in Chapter 7 may be followed for finding the average angle for a given model. A rough check may be made from the first run by comparing the expected and obtained angles of zero lift. Indeed, particularly for the panels, much advantage accrues in the analysis of later data from assuming the models to be absolutely accurate and hence making expected and obtained angles of zero lift identical, which is the usual procedure.

The average dynamic pressure must be calculated for each model of different planform by a method like that for obtaining the average angle. That is, the product of local q (from the dynamic pressure survey of the test section) and the model chord at the same station is plotted against the model span. If the area under the qc-versus-span curve is then divided by the total wing area, the resulting quotient is the average dynamic pressure. This average dynamic pressure is *not* used to find the various coefficients until it is increased by the blocking factor obtained from methods of Chapter 10.

Last, but not least, a check of expected loads should be made to ascertain that ample provision has been made to run the entire program at one speed. Changing the tunnel speed during a program adds one more effect to the data unless, of course, Reynolds number effects are required:

1. After the first run has been made, check it thoroughly against expected results. If possible, arrange the setup so that the first run is simple enough for comparison with previous tests. Items to be checked include α_{ZL}, $dC_L/d\alpha$, $C_{L,\max}$, $C_{D0,\min}$, and C_{m0}.

2. Determine the testing accuracy as follows:
   a. Run a test twice without any change in it. This checks the reproducible accuracy of the balance and the speed control.
   b. Reset and repeat a run made previously after there have been several intervening runs. This determines the reproducible accuracy of setting the flaps, tabs, and the like, as well as the accuracy of the balance and speed control.

3. Keep a running plot of all data as they come out. Any uncertain points can be substantiated immediately by taking readings at small increments above and below the uncertain ones. Many tunnels have the capability of plotting the data on a point-by-point basis as they are acquired. These data may or may not have all of the required data reduction steps; however, they show

any bad data points, unexpected results, and usually give A's that can be used to plan the next run.

4. Occasionally repeat a basic run. This will indicate any gradual model warpage or other alternations occurring with time. It must be realized that the surface condition is gradually degraded in a long test and a repetition of baseline configuration monitors this-effect.

5. Always repeat the first reading at the end of each run. This will indicate any control surface slippage, for example. Inspect the model frequently, checking all control settings, and wherever possible make angular measurements of controls, with the inevitable slack taken out in the loaded direction.

   Besides checking the control settings one must check that the setting quadrants are right. An example comes to mind of a model whose stabilizer quadrant markings were an even $10°$ off. Fortunately the model had been run before and the wide difference in trim conditions started a search for trouble. One can imagine much difficulty arising later if a test pilot is told to set the stabilizers $10°$ wrong for the first flight!

6. Make every data sheet self-contained. Avoid using expressions such as "Same as run 6," for this necessitates looking up run 6. Every data sheet must contain the model designation, configuration, test speed, date, tunnel temperature, and pressure. Further data, such as effective Reynolds number and model dimensions, are valuable. In tunnels with computerized data systems these directives apply to the manner of presentation of data.

7. Keep an accurate log of everything that happens. When analyzing the data, the exact point at which changes were made will be of paramount importance.

8. Always keep a run list in chronological order; never assign a number like run 3b just because the later run is a check of run 3.

The size and design of the tunnel determine the size of the model that can be accommodated and, sometimes, other important criteria such as model weight or power arrangements. Occasionally a gasoline engine can be operated in the tunnel.' The tunnel itself also determines the complexity of the model and hence its cost. The cost of a model is a function of both size and complexity. A simple wing for student experiments built by the students will be minimal, usually just material cost. The cost of a complete low-speed tunnel model shows in both the model designer's time and shop time. Models with complex leading- and trailing-edge flaps to be tested at several angles, gaps, and overlaps are very expensive. The same is true of a powered or jet lift V/STOL model. A good policy is to try to keep the model as simple as possible with careful consideration of its intended use. For example, incorporation of movable control surfaces early in the preliminary design of an aircraft may not be necessary, but the model should be designed so that these features may be added as required in later tests. There is a strong tendency to grossly underestimate the time required to build a complete airplane model at the first attempt. The amount of remotely operated model equipment is a function of the number of tests to he made and the type of tunnels in which the model will be used.

13.2 COMPONENTS

The testing of larger scale models of parts of an airplane offers many advantages provided that the data can be properly applied to the airplane. Nacelles, tail surfaces, dive brakes, and ailerons are parts belonging in this group.

To take a concrete example, models of 8-ft span are about the maximum usually tested in a 10-ft tunnel. If the full-scale aircraft has a wing span of 80 ft, the largest model that can be tested will be $\frac{1}{10}$ scale. This reduction in size makes it nearly impossible to reproduce small items accurately; their Reynolds number will be very small; and it will be exceedingly difficult to measure the hinge moments of control surfaces. A 30% model of the vertical tail could be tested as well as a 30% aileron model, but, if such large-scale panel models are to be employed, they must, of course, be tested under flow conditions that simulate those on the complete airplane. Mounting the panel like a complete wing (Figure 7.45) permits an endflow about the inboard tip that does not actually exist on the real airplane. Such flow may easily invalidate the test results, and unfortunately even the addition of an endplate will not provide sufficient sealing to produce complete flow conditions. It also can be difficult to account for the forces and moments of the endplates when balance data are taken.

Two arrangements are satisfactory: mounting the panel on a turntable or mounting it with a small gap (less than 0.005 span) between its inboard end and the tunnel floor. Illustrations are given in Figures 7.44 and 13.2. Either of these arrangements will seal the inboard end of the panel and subject it to nearly the same flow conditions as would occur on the actual aircraft. Usually the effective aspect ratio then developed will be about $0.95(2b)^2/(2S_p)$, where b is the panel span and S_p is the panel area.

An important and sometimes insoluble problem may arise for aileron panels from sweptback wings. Here the flow over the aileron is affected very strongly by the remainder of the wing and cannot be simulated by any simple reflection plane. It is therefore suggested that a thorough study of spanwise loadings be made and adequate correlation ensured before attempting panel tests of such ailerons. A full half-span model is satisfactory.

A minor point in panel testing of the type shown in Figures 7.44 and 13.2 is that, though the hinge moments should be reduced to coefficient form by using the tunnel dynamic pressure, the force coefficients should be based on tunnel dynamic pressure corrected to allow for the diminished velocity in the boundary layer. The corrected q is usually about 99% of the centerline q. If the boundary layer velocity profile is known, it can be used to adjust the q.

Minimum confusion in applying the test data will result if the panel is selected so that positive tunnel directions are positive airplane directions. Thus a left panel should be mounted on a right wall[3] and a right panel on a left wall. Floor-mounted models should be left airplane panels. In the selection of the panel span the inboard juncture of aileron or flaps should not occur at the floor but a few inches above it.

Owing to asymmetry, much of the panel data will require that the loads from the panel with flap or aileron zero be subtracted from those with surface deflected in order to determine the contribution of the control. Obviously, since the surface zero data are to be repeatedly used, only very good data should be used for the
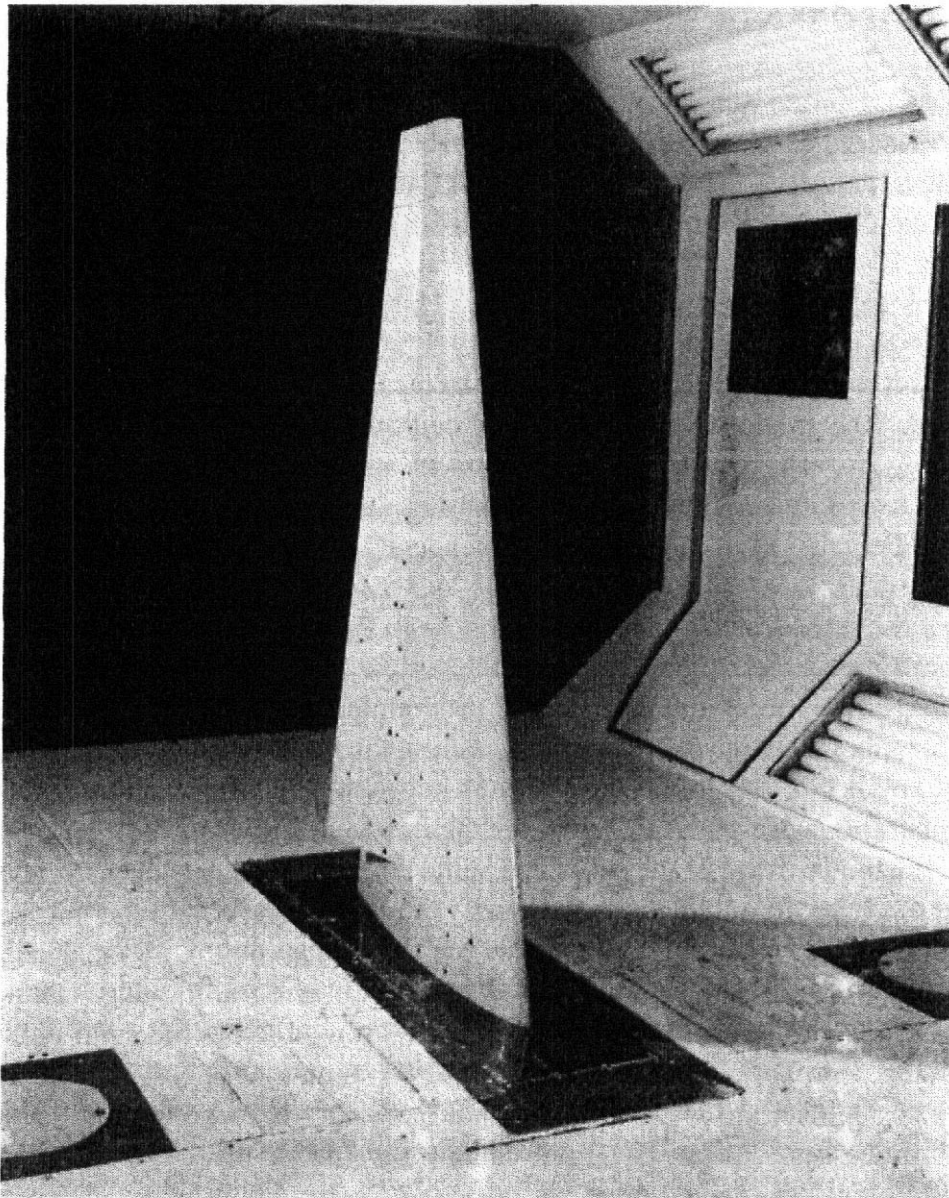
FIGURE 13.2   Reflection-plane tail test. (Courtesy of San Diego Aerospace Museum.)

base run, but good data **are** not always obtainable. For instance, the deflection of the surface will cause a change of lift and hence a change in wall correction angle. The proper basic coefficient should be obtained from curves of surface zero data plotted against corrected angle of attack. The problem is further confused by the fact that the surface deflected may allow greater angles of attack than the surface zero **run** and no basic data can exist for the entire range.

Details of the calculations necessary for refemng panel tests of ailerons, rudders, and elevators to the complete aircraft **are** given in later sections.

Three-Dimensional Wings

The first wind tunnel tests ever made were concerned with the behavior of wings (Figure 13.3). The wing is still the most critical item in the success of any aircraft.
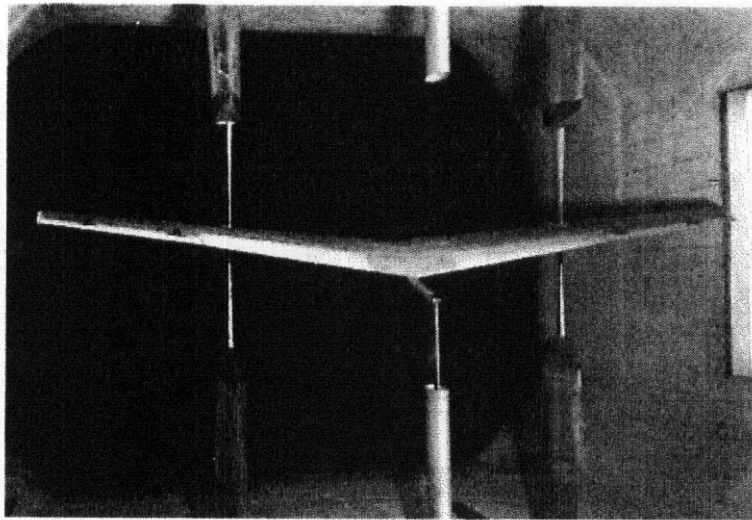
FIGURE **13.3** Three-dimensional wing being tested with image system in. Omission of the image pitch strut reduces the total drag of the system with little error in data. (Courtesy Wichita State University.)

Computers have given the aerodynamicist powerful tools in wing design. Airfoils can be designed to yield a desired chordwise pressure distribution. Vortex lattice methods can determine the distribution of loads along the span. The variables in wing design are airfoil section, taper, twist, and sweep. The wing is usually designed for minimum drag at cruise lift coefficients. To obtain takeoff and landing performance the camber is increased to obtain large values of maximum lift and acceptable stall patterns by use of leading-edge flaps, slots, droop, and trailing-edge flaps. This large number of variables requires extensive wind tunnel experiments to obtain an optimum wing. Computational methods using Euler equations or Reynolds averaged Navier–Stokes solvers are widely pursued but have not yet made large inroads into designers' processes. Their efficiency cannot yet match the experimental tools available.

Some aerodynamicists prefer to run the wing and fuselage rather than the wing alone. The argument for this choice is based on the possible effect of the fuselage on the wing stall pattern and the fact that the aircraft will fly with a fuselage.

A tunnel installation for a wing experiment is shown in Figure **13.3.** This installation makes use of a widely used fixture known as a trunnion (shown in Figure 13.4). It provides an attachment for a dummy bayonet. Two sealing blocks are needed for both upper and lower surfaces, one with a slot to allow a strut to pass and one solid to be used when the dummy system is not employed. (Recall that during the process of testing the model may be mounted both normal and inverted, with and without the image system.) The second set of blocks may be omitted and the slot sealed with tape, clay, tunnel wax, or epoxy-filling compounds. The material used depends on the desired surface condition. Tape may not follow the contour, clay and wax are soft, and the epoxy filler can be difficult to remove.

Tests of a wing should be run at as high a Reynolds number as possible to aid extrapolation to flight Reynolds number. The achievement of large test Reynolds numbers is constrained by tunnel size and aircraft size. As a rule of thumb, the
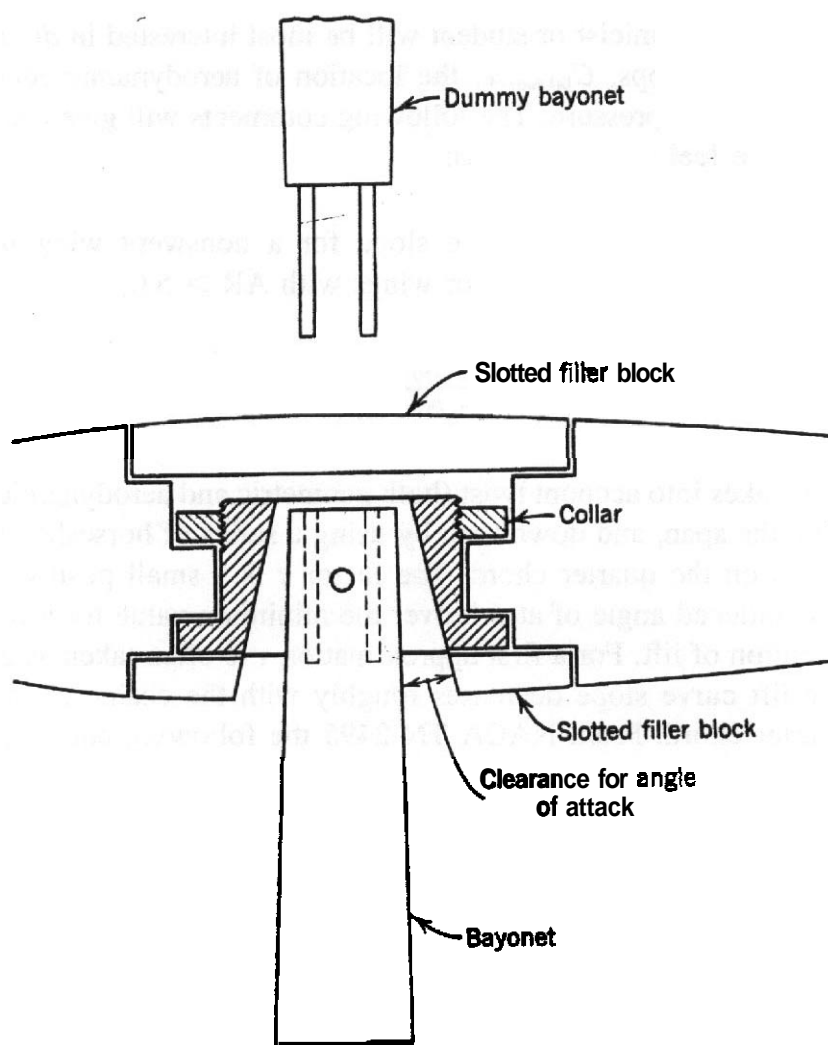
FIGURE **13.4** Trunnion model attachment fitting.

model span should be less than 0.8 of the tunnel width. This constraint on model span determines the maximum model scale. The wing aspect ratio will then determine the model chord. The Reynolds number may be increased by increasing the velocity of the test, but test velocity may be constrained by both the balance load limits and the fact that the lift curve slope is a function of Mach number. To see the latter, as a first approximation using the Prandtl–Glauert correction to a two-dimensional lift curve slope yields

$$a_0 = \frac{a_{0,M=0}}{\sqrt{1 - M^2}} \tag{13.1}$$

A test Mach number of 0.20 will yield a change in the incompressible lift curve slope of 2%. Therefore, tests in which the maximum lift is desired should be run at speeds near the full-scale takeoff or landing speed.

As tare and interference drag can be as large as the wing minimum drag, flaps up, the tare and interference must be carefully evaluated.

In general the aerodynamicist or student will be most interested in $dC_L/d\alpha$, α_{ZL}, $C_{L,max}$ and how stall develops, $C_{D0,min}$, e, the location of aerodynamic center, C_{mac}, and possibly the center of pressure. The following comments will give a student or tunnel engineer some feel for these items:

(a) $dC_L/d\alpha$. The theoretical lift curve slope for a nonswept wing based on Glauert's solution for the span load is, for wings with AR > 5.0,

$$a = \frac{a_0}{1 + (57.3a_0/\pi \, AR)(1 + \tau)} \tag{13.2}$$

Glauert's solution takes into account twist (both geometric and aerodynamic), chord distribution along the span, and downwash by using a series of horseshoe vortices, the bound vortices on the quarter chord. The factor τ is a small positive number that increases the induced angle of attack over the minimum value for a wing with an elliptic distribution of lift. For a first approximation τ is often taken as zero. For swept wings the lift curve slope decreases roughly with the cosine of the sweep angle of the quarter chord. From NACA TN 2495 the following equation, which agrees with experimental data, may be used:

$$a = 0.95\left(\frac{a_0}{1 + (57.3a_0/\pi \, AR)}\right)\sqrt{\frac{\cos\Lambda c}{4}} \tag{13.3}$$

Quite often swept wings, especially those with leading- and trailing-edge flaps, do not have a linear lift curve.

There are more elaborate methods for predicting the lift curve slope and wing performance using vortex lattice methods that will distribute the load both spanwise and chordwise, but they are beyond the scope of this book. The equations given here are intended to be used to check wind tunnel results to determine if they are approximately correct. If results of a more elaborate analysis are available, they should be used.

(b) $C_{L,max}$. The maximum lift coefficient for airfoils varies from 0.6 for very thin profiles to about 1.7 for highly cambered thick profiles. In general it increases with Reynolds number (see Section 7.4). The wing maximum lift coefficient usually runs from 85 to 90% of the airfoil values and is never more than the airfoil values. Swept wings show a loss considerably more than the above values.

Besides determining the value of $C_{L,max}$, the shape of the stall portion of the stall region is important. In general, it is desired to have a gentle stall. This means that the curve should be gently curved near a maximum value without abrupt drops in values of C_L just past the maximum value.

The location of the start of the stall is also important. It is desirable that the stall start inboard of the ailerons so that lateral control can be maintained. A stall that starts at the root of the wing may cause excessive tail buffet. To study the stall

pattern, flow visualization techniques such as oil flow and tufts are used (described in Chapter 5).

(c) α_{ZL}. The angle of zero lift in degrees is roughly equal to the amount of camber in percent for airfoils and untwisted wings of constant section. It requires a considerable amount of calculation to determine α_{ZL} for a twisted wing.

(d) $C_{D0,min}$. The minimum coefficient of drag decreases with increasing Reynolds number (see Chapter 8) and usually has a value between 0.0050 and 0.0085 in the tunnel after the tare and interference have been subtracted. The values given may be higher for wings equipped with lower surface trailing-edge fairing for flap tracks (Fowler action flaps) or hard points for external stores.

The value of $C_{D,P,min}$ is sensitive to the transition point between laminar and turbulent flow. The location of transition can be determined by the flow visualization methods of Chapter 5. Often it is desired to fix the transition by boundary layer trips. These are at various locations on the model and they will increase $C_{D,P,min}$. The effect of trip strips on $C_{D,P}$ can be determined (see Chapter 8).

(e) The C_L-versus-C_D curve or drag polar below the start of flow separation is often approximated by Equation (13.4). This curve fit is used for two purposes. First, it can simplify performance calculations in cruise and climb. Second, by dividing the drag into parasite and induced parts, the effects of configuration changes can be more easily monitored:

$$C_D = C_{D,P,e} + \frac{C_L^2}{\pi \, AR \, e}$$ (13.4)

where $C_{D,P,e}$ is the equivalent parasite drag coefficient and e is Oswald's efficiency factor. For a wing only it accounts for a drag increase due to nonelliptic span loading. For a whole model it accounts for the change in span loading caused by, for example, the fuselage and nacelles and the increase in tail drag with C_L.

The values are determined by a plot of C_L^2 versus C_D, as shown in Figure 13.5. Over a range of C_L approximately between 0.2 and 0.8–1.0 the curve is linear. At low values of C_L it is curved, and at large values of C_L separation causes the curve to deviate from a linear relationship. Often the curve is slightly nonlinear for swept wings and judgment will have to be used. The value of $C_{D,P,e}$ is less than $C_{D,P,min}$. Equation (13.4) is of the form

$$C_D = C_{D,P,e} + KC_L^2$$

where

$$K = \frac{1}{\pi \, AR \, e}$$ (13.5)

Thus the slope K is used to determine e and the intercept on the C_D axis to determine $C_{D,P,e}$.
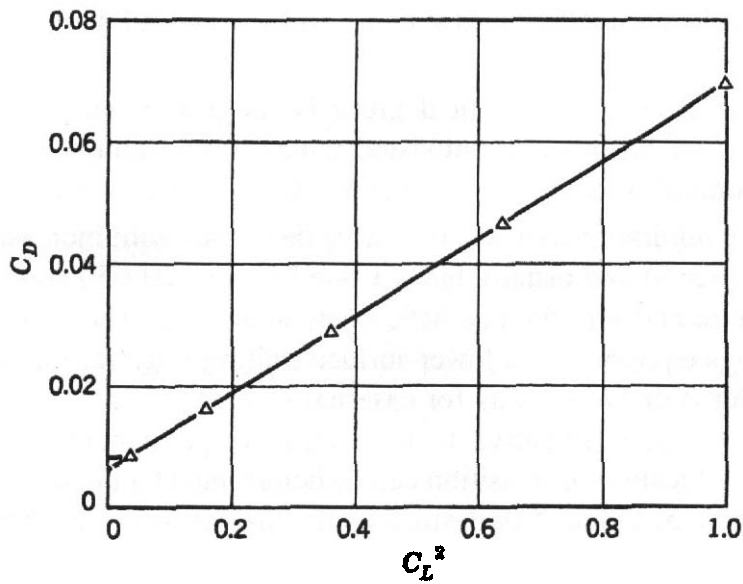
FIGURE 13.5 C_D versus C_L^2 for a NACA 23012 wing.

Often during wind tunnel experiments on either wings or complete aircraft it is desirable to find the effect of configuration changes on the level of parasite drag. This is done by setting $e = 1.0$ in Equation (13.4) and then calculating the induced drag coefficient. This value is subtracted from the measured C_D to yield an approximate C_{D0}, which is plotted versus C_L.

Example 13.1 Values of C_L and C_D are given in Table 13.1. Find Oswald's efficiency factor e if AR $= 7.0$.

From *a* plot of C_D versus C_L^2 the slope $K = 0.05173$; $C_{D,P,e} = 0.0081$, $C_{D,P,\text{min}} = 0.0090$, and $e = 0.879$.

(f) Location of the aerodynamic center may be computed as follows[4]: Consider a wing mounted so that the axis of rotation is at some point behind and below the

TABLE 13.1. Wing Data

α	C_L	C_D
−3.93	0.0688	0.0090
−1.82	0.2411	0.0111
+0.28	0.4309	0.0177
2.39	0.6123	0.0277
4.48	0.7932	0.0406
6.57	0.9712	0.0583
8.65	1.1296	0.0777
10.74	1.2665	0.0987
12.80	1.3734	0.1244
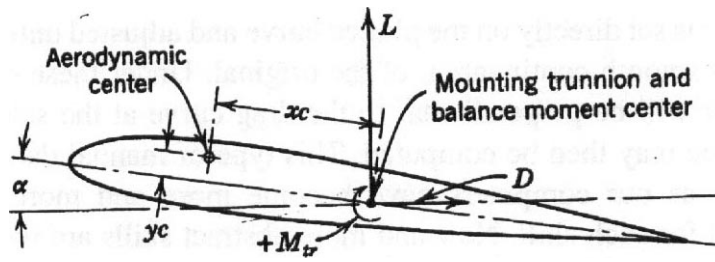
FIGURE 13.6   Force system, Example 5.1.

probable location of the aerodynamic center (see Figure *13.6).* (The aerodynamic center is defined as the point about which the moment coefficient is constant.) Let the distance along the chord from the trunnion to the aerodynamic center be x, and let the distance above the trunnion by y. Both *x* and y are measured in fractions of the MAC.[5]

It will be seen that

$$M_{ac} = M_{tr} - xc(L \cos a + D \sin a) - yc(D \cos a - L \sin a) \qquad (13.6)$$

where M_{tr} is the moment measured about the mounting trunnion. Hence

$$C_{m,ac} = C_{m,tr} - x(C_L \cos \alpha + C_D \sin \alpha) - y(C_D \cos \alpha - C_L \sin \alpha) \qquad (13.7)$$

Applying the condition that $C_{m,ac}$ does not vary with C_L, we get

$$\frac{dC_{m,ac}}{dC_L} = 0 = \frac{dC_{m,tr}}{dC_L}$$

$$- \left[\left(1 + C_D \frac{d\alpha}{dC_L} \right) \cos \alpha + \left(\frac{dC_D}{dC_L} - C_L \frac{d\alpha}{dC_L} \right) \sin \alpha \right] x \qquad (13.8)$$

$$- \left[\left(\frac{dC_D}{dC_L} - C_L \frac{d\alpha}{dC_L} \right) \cos \alpha - \left(1 + C_D \frac{d\alpha}{dC_L} \right) \sin \alpha \right] y$$

The data may easily be used to find C_L, C_D, *a*, *and the slopes* $dC_{m,tr}/dC_L$ and $d\alpha/dC_L$ since they are straight lines. The determination of dC_D/dC_L is difficult, for it is a curve.

If the wing efficiency factor has been determined, dC_D/dC_L may be found directly from

$$C_D = C_{D0,min} + \frac{C_L^2}{\pi \, AR \, e} \qquad \frac{dC_D}{dC_L} = \frac{2C_L}{\pi \, AR \, e} \qquad (13.9)$$

If information for the above equation is not available, the slope of the drag curve at the proper point may be obtained by the familiar mirror method. In this method

a small hand mirror is set directly on the plotted curve and adjusted until the reflected curve appears as a smooth continuation of the original. Under these conditions the plane of the mirror will be perpendicular to the drag curve at the selected C_L, and the drag curve slope may then be computed. This type of manual data analysis has become a lost art as our computers have become more and more capable and decreased the need for such skill. New and more abstract skills are required to stay on top of the processes that are entrusted to our machines.

Equation (13.8), having two unknowns, requires the substitution of two points and then the simultaneous solution of the resulting equations. The approximation of measuring dC_D/dC_L may be eliminated for one of these points by selecting for the point the angle at which C_D is a minimum. At this point, obviously $dC_D/dC_L = 0$.

Example 13.2 Find the aerodynamic center of an airfoil whose tests yield the data in Table 13.2. The mounting trunnion is at the 49% chord point and 17.9% below the chord line.

Plots of the data yield $dC_{m,tr}/d_C = 0.254$:

$$\frac{dC_L}{d\alpha} = 0.1025 \text{ per degree} = 5.873 \text{ per radian}$$

At a $= 2.3°$, $C_L = 0.34$, $C_{D0,min} = 0.0087$, and $dC_D/dC_L = 0$. At a $= 8.8°$, $C_L = 1.00$, $C_D = 0.0210$. By the mirror method $dC_D/dC_L = 0.048$.

Substituting into Equation (13.8), the equations simplify to

$$0.99916x + 0.01765y = 0.254 \qquad 0.97300x + 0.06216y = 0.254$$

$$x = 0.2516 = 0.252 \qquad y = 0.1475 = 0.148$$

The aerodynamic center is $0.490 - 0.252 = 0.238$, or 23.8% of chord or 1.2% chord ahead of the quarter chord, and $-0.179 + 0.148 = -3.1\%$ below the chord line.

In order to simplify the process of locating the aerodynamic center, the assumption is sometimes made that the moment is due entirely to the lift and that the aerodynamic

TABLE 13.2. Airfoil Data: Example 13.2

α	C_L	C_D	$C_{m,tr}$
-2	-0.086	0.0120	-0.023
0	0.111	0.0095	0.024
2	0.326	0.0087	0.079
4	0.531	0.0096	0.131
6	0.737	0.0138	0.183
8	0.943	0.0195	0.231
10	1.118	0.0267	0.281
12	1.260	0.0369	0.317
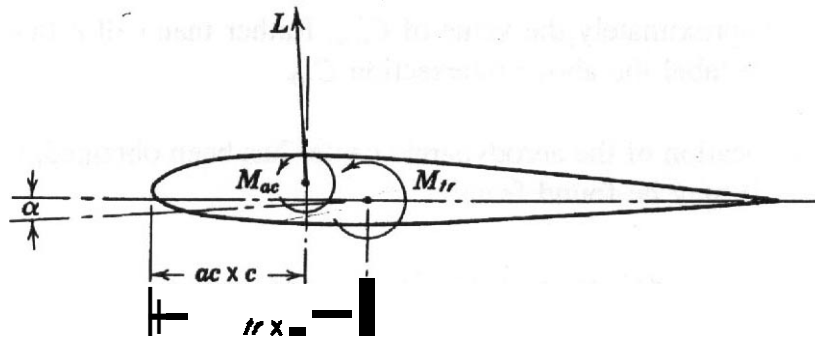
FIGURE 13.7   Force system, Example 13.2.

center is on the chord line (see Figure 13.7). Since the lift and drag act through the aerodynamic center, the moment about the trunnion is (Figure 13.7)

$$M_{tr} = M_{ac} + L(tr - ac)c \tag{13.10}$$

where M_{ac} is the moment about the aerodynamic center and tr the chordwise location of the balance trunnion.

Rewriting Equation (13.10) in coefficient form, we have

$$C_{m,tr} = C_{m,ac} + C_L(tr - ac) \tag{13.11}$$

and differentiating and transposing $(dC_{m,ac}/dC_L = 0)$ yield

$$ac = tr - \frac{dC_{m,tr}}{dC_L} \tag{13.12}$$

The aerodynamic center is theoretically a small amount behind the quarter chord. In practice, it is found ahead of the quarter chord for the older profiles and behind for many new profiles.

Example 13.3   Calculate the location of the aerodynamic center for the data of Example 5.2 using Equation (13.11).

1. From a plot of $C_{m,tr}$ versus C_L,

$$\frac{dC_{m,tr}}{dC_L} = 0.254$$

2. Substituting the trunnion location and $dC_{m,tr}/dC_L$ in Equation (13.12), we have ac $= 0.49 - 0.236$. This compares with 0.238 by the method of Equation (13.8).

   Equation (13.11) indicates that when $C_L = 0$, $C_{m,ac} = C_{m,tr}$. In other words, the value of the moment coefficient at the point where the curve strikes the

C_m axis is approximately the value of $C_{m,ac}$. Rather than call it that, the usual practice is to label the above intersection C_{m0}.

(g) After the location of the aerodynamic center has been obtained, the moment coefficient about it may be found from

$$C_{m,ac} = C_{m,tr} - x(C_L \cos \alpha + C_D \sin a) - y(C_D \cos a + C_L \sin a)$$

The value of $C_{m,ac}$ varies with the amount and shape of the camber line. For wings using symmetrical airfoils, it is zero; for nonswept wings, the value is -0.10 or less. For swept wings it becomes larger and more negative and is a function of sweep and aspect ratio. For wings with flaps on the trailing edge the values of -1.0 can be exceeded. It should be noted that large negative values of $C_{m,ac}$ can often reduce the airplane $C_{L,max}$ at some center-of-gravity positions due to large downloads on the trail.

Example 13.4 Calculate the $C_{m,ac}$ for Example **13.2.**
Substituting each point into Equation **(13.7)** we have the data shown in Table **13.3.**
It is not unusual to find some small spread in the values of $C_{m,ac}$, although strictly speaking the definition states that it must be constant. The small nonlinearity in the values of $C_{m,ac}$ is due to the vertical displacement terms of the aerodynamic center in Equation **(13.7).** This can easily be verified by plotting the x and y displacement terms versus C_L or a. It is a surprising fact that the location of the aerodynamic center is practically unchanged by flaps. The explanation lies in the manner in which the moment is generated:

$$C_{m\ total} = C_{m\ due\ to\ changing\ \alpha} + C_{m\ due\ to\ camber}$$

As indicated by theory, the C_m due to changing a is constant about the quarter chord. The C_m due to camber is a constant about the half chord. Hence adding

TABLE 13.3. Calculated Moment Coefficients

α	$C_{m,ac}$
-2	-0.0026
0	-0.0053
2	-0.0026
4	0.0016
6	0.0076
8	0.0118
10	0.0383
12	0.0383
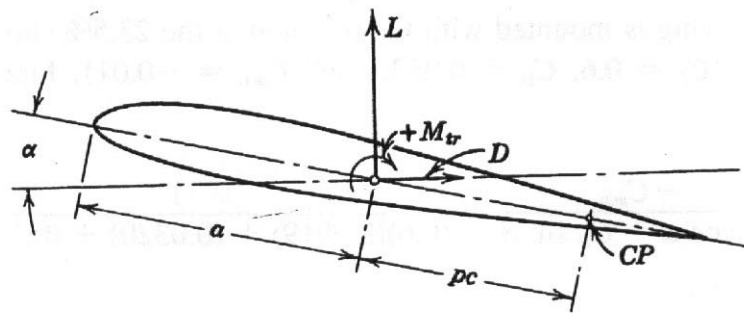
FIGURE 13.8   Force system, Example 5.3.

camber in the form of flaps merely increases the values of $C_{m,ac}$ without changing the location of the aerodynamic center as determined by changing a.

(h) The center of pressure is defined as that point on the chord of an airfoil through which the resultant force acts. Though its usefulness has declined with the introduction of the concept of the aerodynamic center, it must occasionally be determined from force tests. The procedure is as follows: The forces measured appear as a lift force L, a drag force D, and a moment about the mounting trunnion M_{tr} (see Figure 13.8). At the point through which the resultant force acts, the moment vanishes. Hence

$$M_{CP} = 0 = M_{tr} + L(p \cos a) + D(p \sin \alpha)$$

where p is the distance from the trunnion to the center of pressure, positive to the rear of the trunnion.

We then have

$$-C_{m,tr} = C_L\left(\frac{p}{c}\right)\cos \alpha + C_D\left(\frac{p}{c}\right)\sin a = 0$$

and

$$\frac{p}{c} = \frac{-C_{m,tr}}{C_L \cos a + C_D \sin a} \tag{13.13}$$

The location of the center pressure from the wing leading edge is then

$$CP = \frac{p}{c} + \frac{tr}{c} \tag{13.14}$$

Example 13.5 **A** wing is mounted with the trunnion at the 23.5% chord point. **At** a = 7.3, we have C_L = 0.6, C_D = 0.0320, and $C_{m,tr}$ = −0.011. Find the center of pressure:

$$\frac{p}{c} = \frac{-C_{m,tr}}{C_L \cos \alpha + C_D \sin a} = \frac{0.011}{(0.6)(0.9919) + (0.0320) + (0.127)}$$

$$= 0.0184$$

$$CP = 0.0184 + 0.235 = 0.253 = 25.3\%$$

Two-Dimensional Wings

Alternations to airfoils sections are frequently investigated in two-dimensional tunnels wherein a short constant chord section of a wing completely spans the jet width, as shown in Figure 13.9, simulating infinite aspect ratio. The jet is usually $2\frac{1}{2}$–4 times higher than it is wide. In some tunnels of this type the drag is read by the momentum survey method and the lift by the pressure on the tunnel walls. The pitching moment may also be **read** from the pressure on the tunnel walls, but in many cases the wing is mounted on trunnions and the moment is read with a simple beam balance. The proportionately large drag of two endplates prohibits accurate drag measurements by the usual force tests and complicates the endplate seal.

Since the models customarily used in two-dimensional tunnels are larger in proportion to jet size than others, corrections for constriction, buoyancy, and camber
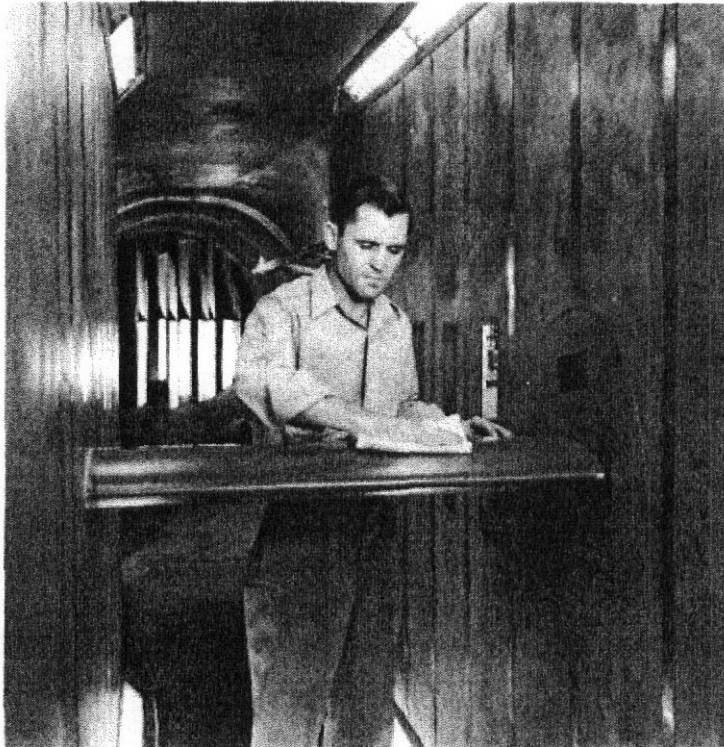
FIGURE **13.9** Airfoil model in two-dimensional tunnel. (Photograph **courtesy** of NASA.)

must be considered (Chapter 9). Excessive errors due to wall effect will arise in $c_{l,\max}$ if the model chord exceeds $0.4h$ and in $c_{d0,\min}$ if it exceeds $0.7h$, were h is the tunnel height.

The information obtained from two-dimensional tests will be reducible to section coefficients c_l, c_{d0}, and $c_{m\frac{1}{4}}$. These coefficients (unlike wing coefficients C_L, C_D, and $c_{m\frac{1}{4}}$, which are an average of conditions including varying Reynolds number and effective angles of attack across the span) consider only a section under constant load and hence constant effective angle of attack. It is customary to consider the minimum profile drag coefficient C_{D0} as equivalent to c_{d0} when both are at the same Reynolds number. Likewise, it is assumed that $C_{m,ac} = c_{m,ac}$.

The location of the aerodynamic center and the center of pressure may be calculated as discussed above. The lift coefficients c_l and C_L may also be considered equal except at their maximum, where the spanwise lift distribution usually results in a diminution in lift of at least 10–15% for straight wings. Expressed symbolically,

$$C_{L,\max} = 0.90 c_{l,\max} \quad \text{(approximately)} \tag{13.15}$$

Two-dimensional testing is used to obtain data for aerodynamic comparison of various airfoil shapes. Comparisons would include $c_{l,\max}$ and the shape of the lift curve at maximum lift, minimum drag, and the variation of c_d and $c_{m,ac}$ with c_l or a. The lift curve slope usually decreases from the two-dimensional value to a three-dimensional wing and is slightly affected by Reynolds number and increases with Mach number for Mach numbers less than 1. There is some question about the validity of two-dimensional drag data.

Low-Aspect-Ratio Wings

The advantages of using a low aspect ratio for supersonic airplanes are quite impressive, and not infrequently the tunnel engineer finds himself or herself testing such configurations for low-speed characteristics.

Low-aspect-ratio lift curves may look quite different from those at high aspect ratio. Below AR = 2.0 the curve is usually concave upward (see Figures 13.10 and 13.11). The lift curve slope at zero lift may be approximately by

$$\frac{dC_L}{d\alpha} = 0.008 + 0.018 \text{ AR}) \quad \text{(per degree)} \tag{13.16}$$

below AR = 3.0. Between AR = 3.0 and AR = 5.0 the following equation may be used:

$$\frac{dC_L}{d\alpha} = 0.1 \frac{\text{AR}}{\text{AR} + 2}$$

For greater aspect ratio, Equation (13.2) should be employed.
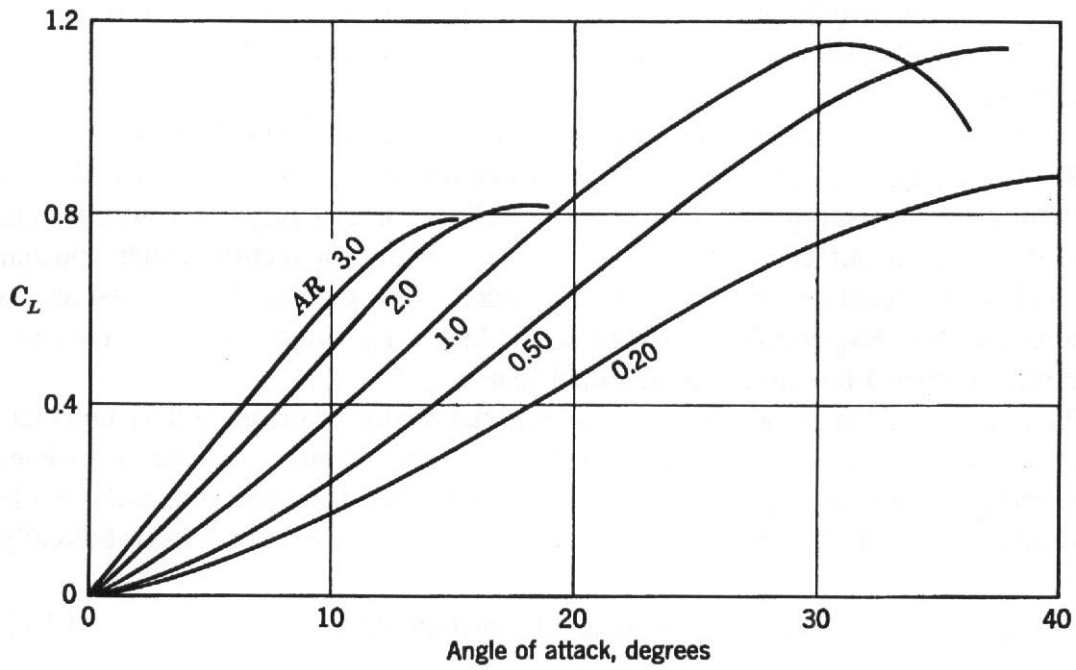
FIGURE 13.10   Lift of rectangular flat plates.
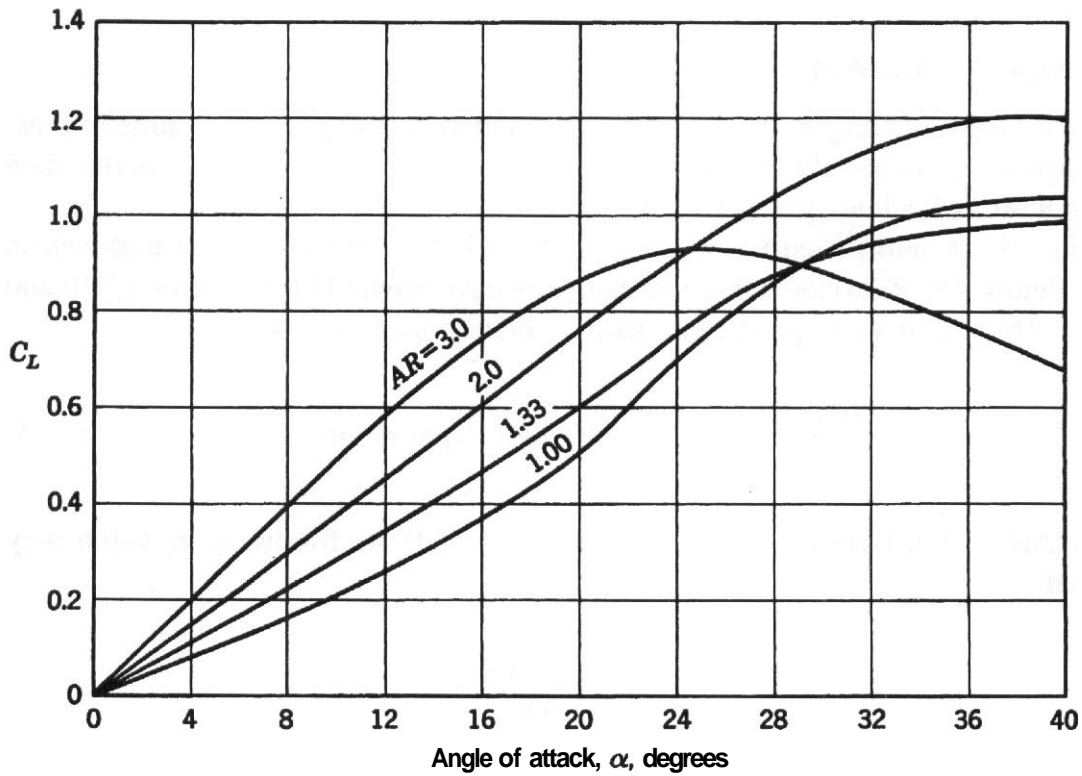
FIGURE 13.11   Lift coefficients for delta wings of various aspect ratio, NACA 0012 profile.

Aileron Panels

The airplane designer is interested in three items connected with proposed ailerons. First is the rolling moment he or she is seeking. The other two, the yawing moment and the hinge moment, represent the price that must be paid. In addition, the tunnel engineer is concerned with referring the data to the complete airplane. The problem first apparent is that the panel model will not have the same lift curve slope as the complete wing. Actually, however, this is of small import as long as the roll due to a given aileron deflection is at a known wing lift coefficient. This, it will be shown, requires that the complete wing be previously tested and its lift curve known and available. The procedure for then referring the aileron panel angles of attack to the complete wing is as follows:

1. From the estimated performance of the airplane, note the speeds that correspond to various important flight conditions, such as minimum control speed and climb speed. Calculate the complete wing lift coefficients that correspond to these speeds.

2. Plot the span loading curve, which is usually known before the test (for a nonswept wing, Schrenk's method can be used for an approximation). The total under this curve, A_T divided by the total wing area, S_T is a measure of the wing lift coefficient. Likewise, that part of the span loading curve above the panel span, A_P, when divided by the area of the wing panel, S_P, is a measure of the panel lift coefficient. The ratio of these two ratios, then, is the ratio of the complete wing lift coefficient C_{Lw} to the panel lift coefficient C_{Lp}. That is,

$$\frac{C_{Lw}}{C_{Lp}} = \frac{A_T/S_T}{A_p/S_p} \tag{13.17}$$

Equation (13.16) may be used to find the panel lift coefficients that correspond to the selected wing lift coefficients.

3. Test a panel with aileron zero and obtain a plot of C_{Lp} versus α_u, where α is the angle of attack uncorrected for tunnel wall effect.

4. From 3, read the uncorrected angles that should be set to read the desired panel lift coefficients. The tunnel operator may then set these uncorrected angles with arbitrary aileron deflections and maintain a proper panel model to complete model correlation.

The span loading as required above may be simply found by a method proposed by Schrenk[6] or by one proposed by Pearson.[7] Schrenk's method for untwisted wings without flaps is as follows:

1 Plot the wing chord against the span. If the airfoil section varies, then a weighted chord

$$c_l = \frac{ca_0}{\overline{a_0}} \qquad (13.18)$$

should be used. The term with a bar over it is the average section slope, given by

$$\overline{a_0} = \frac{2}{S} \int_0^{b/2} a_0 c \, dy \qquad (13.19)$$

2. On the same graph, plot a quarter ellipse whose area is equal to half the wing area and whose span equals the wing span.
3. The span loading will be represented by a line midway between 1 and 2. (See Figure 13.12.)

The data for an aileron test require some special consideration for three reasons: the structural problems due to cable stretch and wing twist; the simulation of a symmetrical case as a result of the carryover arising from the wall reflection (see Chapters 9 and 10); and the doubled force increments arising from the same source. Cable stretch and wing twist are problems that must be evaluated by the structural engineers for a particular airplane. Assuming that the carryover is small, one is fully justified in using the measure force data (corrected for wall effects and blockage) for computing the rolling and yawing moments about the aircraft centerline. But if one is interested in the complete wing lift, drag, and pitching moment, the measured data, including as they do the **full** reflection, are too large. In other words a 50-lb lift increment ($\Delta C_L = 0.1$, say) for one aileron down is not a **100-lb** increment
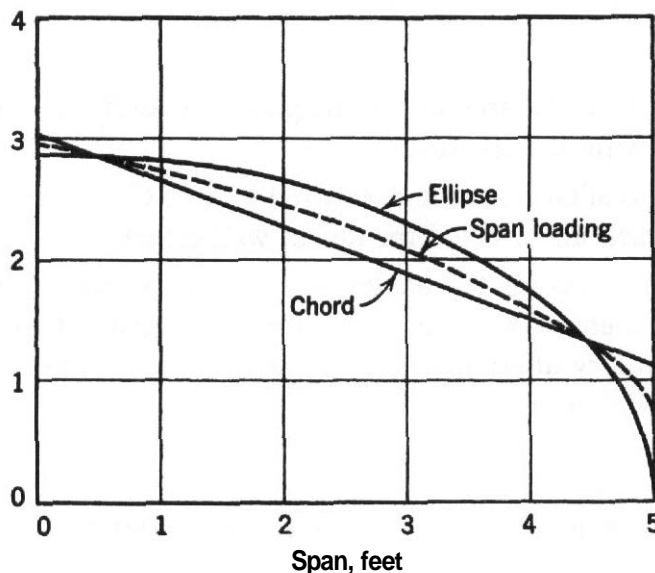
FIGURE 13.12 Interpolation for span loading.

($\Delta C_L = 0.1$) when the whole wing is considered, since the image aileron should not be down. Thus, letting a subscript d mean aileron down, and 0 mean control neutral, wing data for an asymmetrical model may be found from

$$C_L = \tfrac{1}{2}(C_{L0} + C_{Ld}) \tag{13.20}$$

$$C_D = \tfrac{1}{2}(C_{D0} + C_{Dd}) \tag{13.21}$$

$$C_m = \tfrac{1}{2}(C_{m0} + C_{md}) \tag{13.22}$$

The roll and yaw data may be **treated** as outlined below.

In testing one panel of a wing, it is seen that a yawing and rolling moment about the aircraft centerline is produced that in actuality would be canceled by the panel on the other side. Thus it is necessary to subtract the moments due to the panel with aileron zero from the moments with the aileron deflected. The subtraction also acts to remove the tare effects of the turntable, the net result being the yawing and rolling moments due to the deflection of the aileron only. The only requirement is that the test conditions must simulate the proper **spanwise** loading over the aileron.

In working up the data, the coefficients must be corrected to complete wing areas and spans so that the results will be usable. The definitions are as follows (the subscript p indicates "panel"):

$$C_{Lp} = \frac{L_p}{qS_p} \qquad \text{panel lift coefficient}$$

$$C_{D'p} = \frac{D'}{qS_P} \qquad \text{panel drag coefficient including mounting plate drag}$$

$$C_{np} = \frac{YM_p}{qS_w b_w} \qquad \text{panel yawing moment coefficient}$$

$$C_{lp} = \frac{RM_p}{qS_w b_w} \qquad \text{panel rolling moment coefficient about balance rolling axis, based on wing area and span}$$

To get the rolling moment at the aircraft centerline, we have (see Figure 13.13)

$$RM_a = RM_p + La'$$
$$C_{l'a} = C_{lp} + C_{Lp}\frac{S_p}{S_w}\frac{a'}{b_w} \tag{13.23}$$

where a' is the distance from the balance rolling moment axis to airplane centerline (the subscript a indicates "aircraft").

However, this represents the moment of one panel plus the aileron about the aircraft centerline; to find the part due to the aileron only, we subtract the rolling
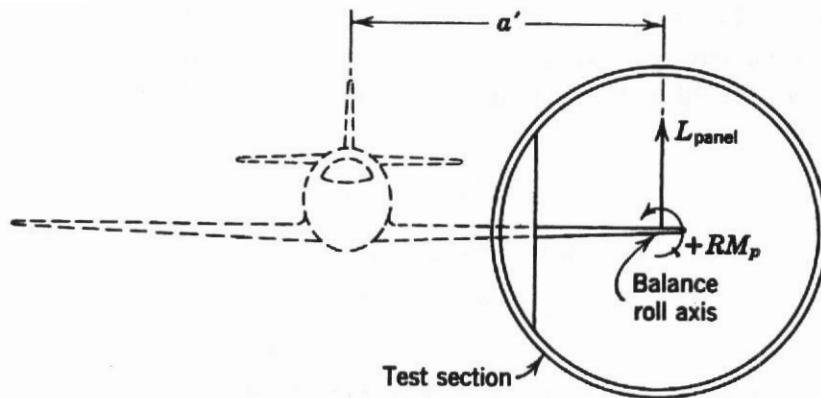
FIGURE 13.13   Panel rolling moment and its relation to the rest of the airplane (front view).

moment coefficient of the panel with aileron zero, C_{l0}. Hence the rolling moment coefficient of one aileron[S] about the airplane centerline is

$$C_l = C_{lp} + C_{Lp}\frac{S_p}{S_w}\frac{a'}{b_w} - C_{l0} \qquad (13.24)$$

By a similar process, the yawing moment coefficient due to one aileron[a] is (see Figure **13.14**)

$$C_n = C_{np} - C_{D'p}\frac{S_p}{S_w}\frac{a'}{b_w} - C_{n0} \qquad (13.25)$$

where $C_{np} = YM_p/qS_wb_w$, b' is the distance of the balance yaw axis to the aircraft and C_{n0} is the yawing moment coefficient of one panel about the aircraft centerline, aileron zero.
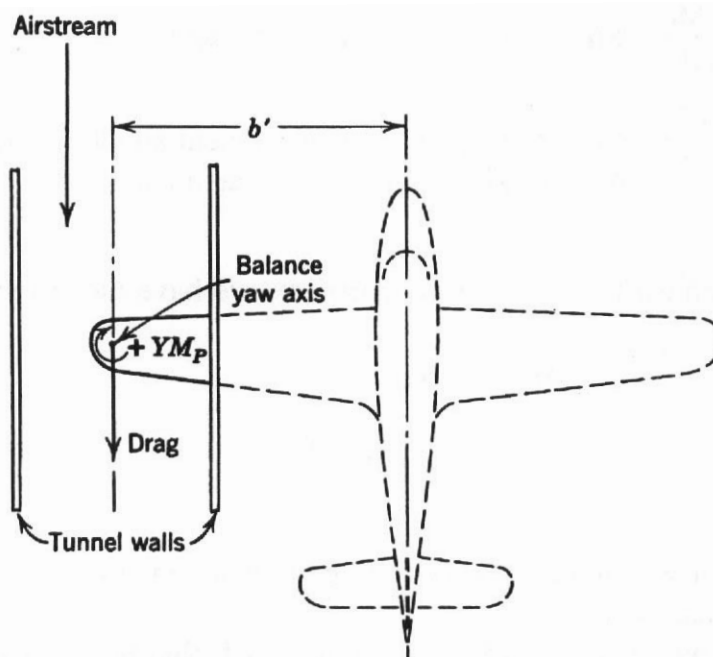
FIGURE 13.14   Panel yawing moment and its relation to the rest of the airplane (plan view).
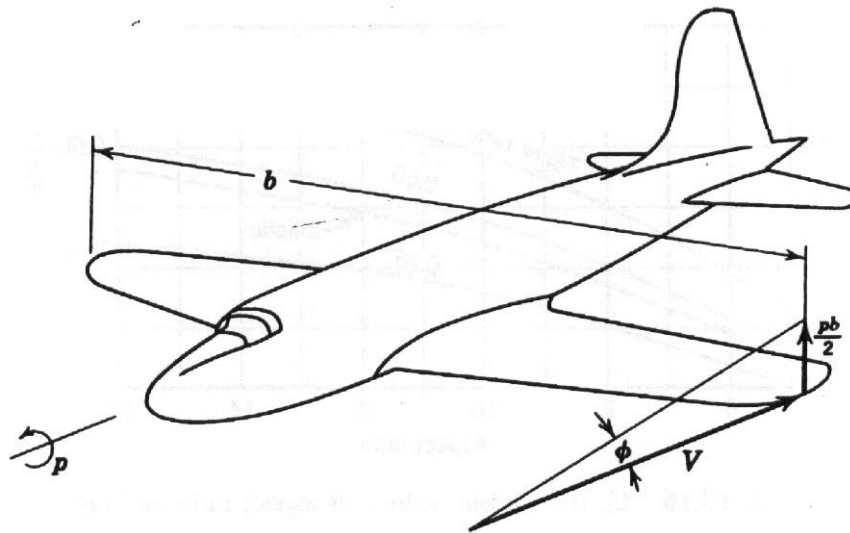
FIGURE 13.15   Roll rate–helix angle relation.

For structural purposes or a check of the spanwise load calculations, the lateral center of pressure may be found by dividing the semispan rolling moment about the airplane axis of symmetry by the lift.

Although not directly apparent, the rolling moment coefficient also determines the helix angle (see Figure 13.15).

At a given rate of steady roll the rolling moment is opposed by an equal and opposite damping moment. In the usual symbols, the rolling moment

$$\text{RM} = \frac{\rho}{2} SV^2 C_l b = \text{DM}$$

where DM is the damping moment. Dividing through by the helix angle, $pb/2V$ (p is the rolling velocity in radians per second),

$$\text{DM} = \frac{pb}{2V}\frac{\rho}{2}SV^2 b\frac{C_l}{pb/2V} = \frac{\rho}{2}SVp\frac{b^2}{2}\frac{dC_l}{d(pb/2V)}$$

The term $d(C_l)/d(pb/2V)$ is called the damping-in-roll coefficient (frequently written C_{lp}) and is a function of wing taper and aspect ratio, both of which are constant for a given airplane. For unswept wings, values of C_{lp} may be found from Figure 13.16. The helix angle is then[9]

$$\frac{pb}{2V} = \frac{C_l}{C_{lp}} \tag{13.26}$$

and the rolling velocity is

$$p = \frac{2V}{b}\frac{C_l}{C_{lp}} \tag{13.27}$$
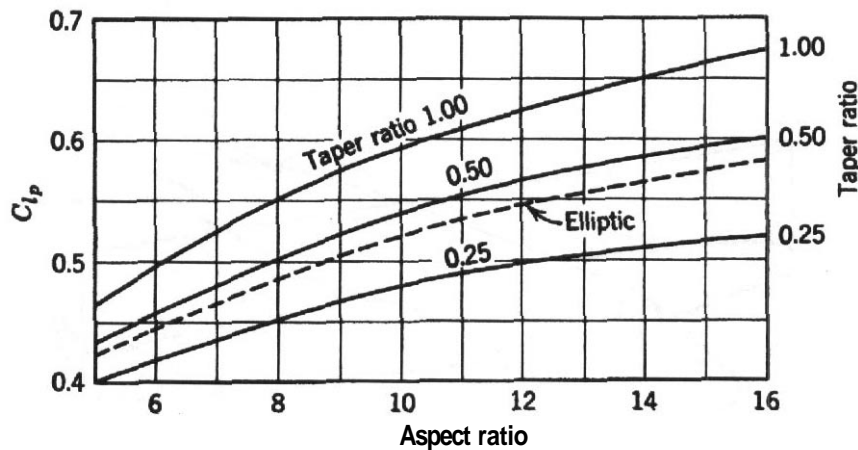
FIGURE 13.16 C_{lp} **for various values of aspect** ratio **and taper.**

The maximum rolling velocity for airplanes with reversible controls is usually limited by stick force considerations rather than by the airplane's actual ability to roll. Power-driven controls as well as aerodynamic balances to decrease the hinge moments are used to increase the rolling velocity; however, wing twist will decrease rolling velocity.

Example 13.6   Data from a test run at $q = 25.6$ lb/ft^2 on a wing panel of 12 ft^2 yields $C_L = 0.789$, $C_D = 0.0599$ at $\alpha = 5.44°$, left aileron down 15". (Data have been corrected for tunnel wall effect.) Here $C_{lp} = -0.0102$, $C_{np} = -0.0010$. Find the rolling and yawing moments about the aircraft centerline if the distance from the balance roll axis to the aircraft centerline is 8 ft. The rolling moment for aileron zero is $C_{l0} = 0.0191$, and the yawing moment is $C_{n0} = -0.0028$. Also, $S_w = 70$ ft^2, $b_w = 25$ ft:

$$C_l = C_{lp} + C_{Lp}\frac{Sp}{S_w}\frac{a'}{b_w} - C_{lp0}$$

$$= -0.0102 + 0.789\frac{12}{70}\frac{8}{25} - 0.0191$$

$$= -0.0102 + 0.0433 - 0.0191 = 0.0140$$

$$C_n = C_{np} + C_{D'p}\frac{S_p}{S_w}\frac{b'}{b_w} - C_{np0}$$

$$= -0.0010 - 0.0599\frac{12}{70}\frac{8}{25} + 0.0028$$

$$= -0.0015$$

Example 13.7   Assume that sufficient control force exists to develop the above C_l at 150 mph. Calculate the helix angle and rate of roll. The wing taper ratio is 2:1 (A $= 0.50$) and the model is **40%** scale.

1. $AR = b^2/S = 25^2/70 = 8.93$. From Figure 13.16 at $AR = 8.93$ and $\lambda = 0.50,$

$$C_{lp} = 0.520$$

$$\frac{pb}{2V} = \frac{C_l}{C_{lp}} = \frac{0.014}{0.520} = 0.0269 \text{ rad}$$

2.

$$p = \frac{pb}{2V} \frac{2V}{b} 57.3$$

$$= 0.0269 \frac{(2)(150)(1.47)}{25/0.40} 57.3$$

$$= 10.9 \text{ deg/s}$$

Typical data that might be expected from tests of an aileron are shown in Figures 13.17–13.19. The roll-versus-yaw plot is particularly useful when figuring ratios for differential ailerons.

Perhaps at this point it would be fitting to discuss the lateral axis more fully in order to explain the reaction obtained before and during a roll. Consider the case when the ailerons are deflected but no roll has yet had time to develop or perhaps an asymmetrical span loading is being resisted. The down aileron creates more lift and induced drag and usually more profile drag, whereas the opposite effect is noted for the up aileron. The net result is a yawing moment opposite in sign to the rolling
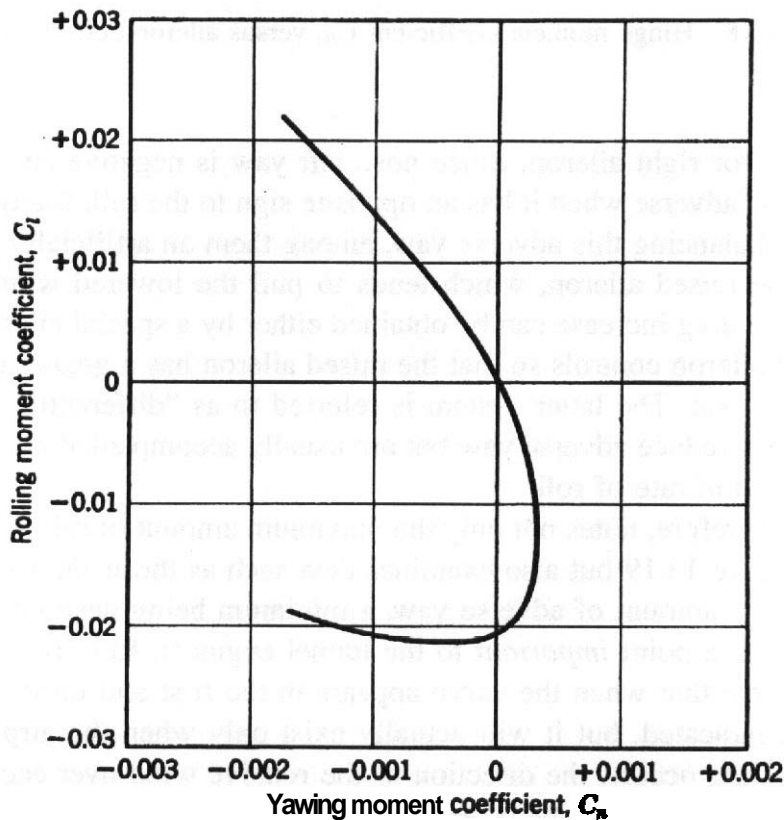
FIGURE 13.17   Aileron adverse yaw.
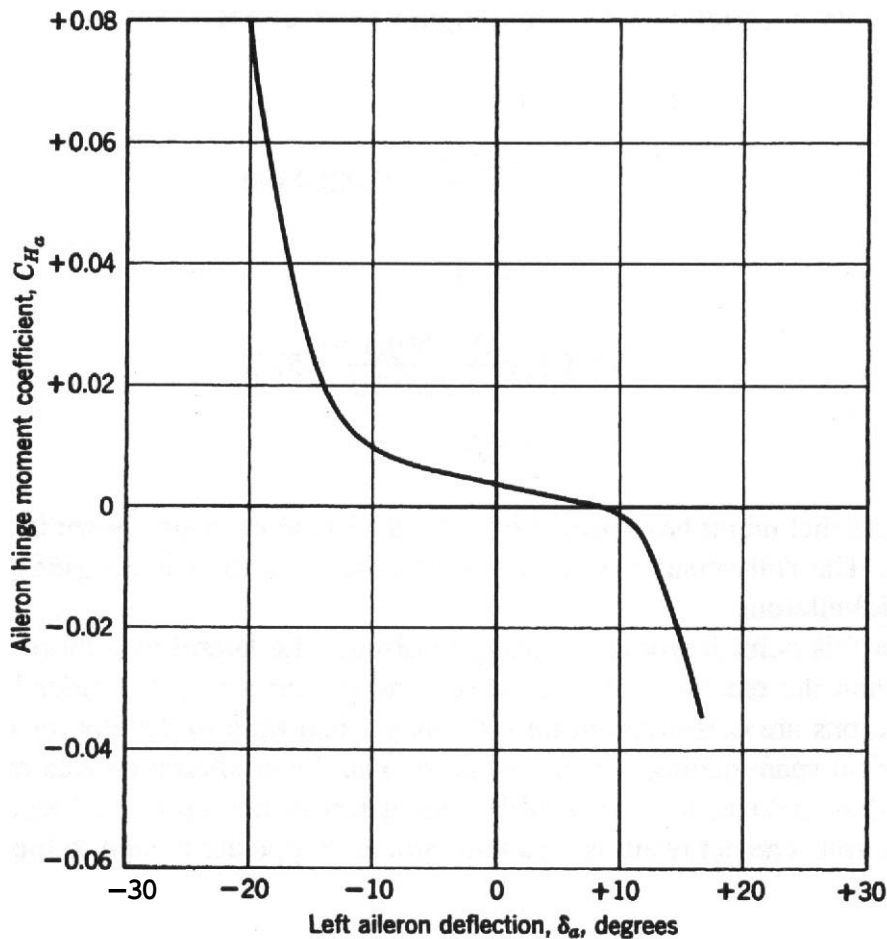
FIGURE 13.18 Hinge moment coefficient C_{Ha} versus aileron deflection δ_a.

moment: left yaw for right aileron. Since nose left yaw is negative and right roll positive, the yaw is adverse when it has an opposite sign to the roll. Many methods are suggested for balancing this adverse yaw, among them an artificially increased profile drag of the raised aileron, which tends to pull the lowered wing into the turn. Such a profile drag increase can be obtained either by a special aileron design or by gearing the aileron controls so that the raised aileron has a greater deflection than the depressed one. The latter system is referred to as "differential ailerons." Differential ailerons reduce adverse yaw but are usually accompanied by an overall reduction in maximum rate of roll.

The designer, therefore, notes not only the maximum amount of roll ($C_{l,max}$) from graphs such as Figure 13.19 but also examines data such as those shown in Figure 13.17 to observe the amount of adverse yaw, a minimum being desirable.

Now we come to a point important to the tunnel engineer. Referring to Figure 13.17 again, we note that when the curve appears in the first and third quadrants, favorable yaw is indicated, but it will actually exist only when the airplane does not roll. When rolling occurs, the direction of the relative wind over each wing is so altered that a strong adverse yaw is developed, and the results of the static tunnel test may be entirely erroneous.
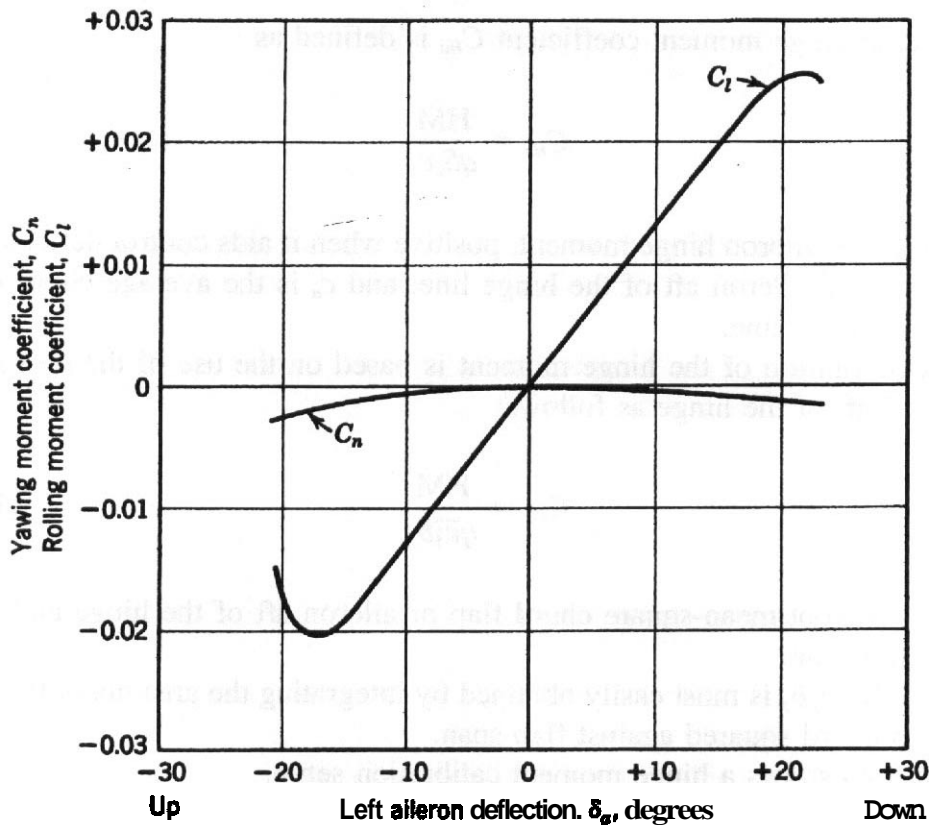
FIGURE 13.19   Left aileron power.

Under most conditions, the air loads on the ailerons oppose their deflection, producing a moment that must be supplied by the pilot or by some outside means. Methods employed to help the pilots include powered "boosters" and mass and aerodynamic balance. The mass balances may only balance the weight of the surface or they may be arranged to provide an inertia force while the ship is rotating. The aerodynamic balances control surface areas of various cross-sectional shapes ahead of the hinge and area disposition such as horns, shielded horns, and internal, medium, and sharp nose aerodynamic balance. They may also include various devices aft of the hinge line, such as balance tabs, spring tabs, and beveled trailing edges.

Aerodynamic balances are simpler and lighter than mass balances or power boost and hence are to be preferred as long as icing need not be considered for general-aviation-type aircraft. Large aircraft and fighters almost always need power boost. Unfortunately, most aerodynamic balances are effective for only a portion of the aileron travel, as may be seen by the extent of the decreased slope in Figure 13.18. A measure of balance superiority is then the range of decreased hinge moments as well as the slope of the balanced part of the curve. Complete aileron data must, of course, include the effect of the other aileron as well as the amount of the differential decided upon.

The aileron hinge moment coefficient C_{Ha} is defined as

$$C_{Ha} = \frac{HM}{qS_a c_a} \tag{13.28}$$

where HM is the aileron hinge moment, positive when it aids control deflection; S_a is the area of the aileron aft of the hinge line; and c_a is the average chord of the aileron aft of hinge line.

Another definition of the hinge moment is based on the use of the **root-mean-square** chord aft of the hinge as follows:

$$C_{Ha} = \frac{HM}{q\bar{c}_f^2 b_f} \tag{13.29}$$

where $\bar{c}_f$ is the root-mean-square chord flap or aileron aft of the hinge and b_f the flap or aileron span.

The quantity $\bar{c}_f^2 b_f$ is most easily obtained by integrating the area under the curve of local flap chord squared against flap span.

Figure 13.20 shows a hinge moment calibration setup.

The variance of definitions again demonstrates the necessity of clear and complete definitions of every item in the wind tunnel report.

Complete consideration of hinge moments must include the gearing ratio of the controls. Depending on the purpose of the aircraft, various limiting conditions are imposed by both the military and the Federal Aviation Administration (FAA).
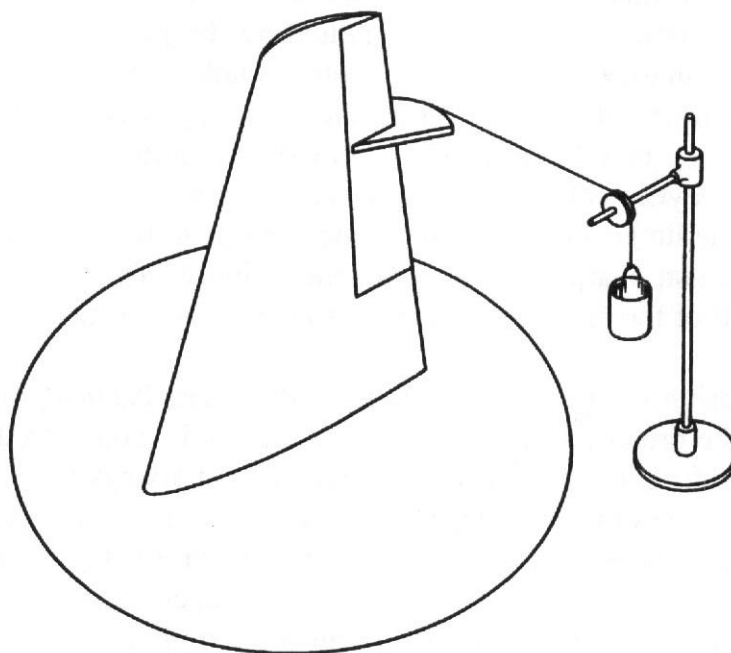
FIGURE 13.20 Setup for calibrating hinge moment strain gages on a panel model. For quick checks a good spring scale is convenient.

Example 13.8   An-airplane has the specifications given in Table 13.4.

Calculate the wheel force (one hand) necessary to deflect the ailerons $10°$ at 262 mph indicated air speed.

For the total hinge moment coefficient resulting from both ailerons, we have

$$C_{Ha} = 0.0188 - (-0.0089) = 0.0277$$

$$M_{ail} = qS_ac_aC_{Ha} = (175.2)(17.43)(1.426)(0.0277)$$

$$= 120.5 \text{ lb-ft}$$

$$\text{Wheel moment} = \frac{120.5}{3.33} = 36.2 \text{ lb-ft}$$

$$\text{Wheel force} = \frac{36.2}{0.625} = 58.0 \text{ lb}$$

Rudders

The rudder produces a side force that in turn produces a yawing moment about the center of gravity of the airplane. This may or may not produce yaw, for the lateral loading may be asymmetrical and the rudder employed only to maintain a straight course. Some drag, a small moment about the quarter-chord line of the tail itself, some roll, and a rudder hinge moment will also be created. The fact that the drag moment is stabilizing is no argument in favor of a large vertical tail drag, since, in maintaining a straight course with asymmetrical loading, drag is decidedly harmful.

The designer of a vertical tail seeks the following:

1. A large side force with minimum drag.
2. The steepest slope to the side force curve so that small yaw produces large stabilizing forces.
3. The smallest hinge moment consistent with positive control feel. The maximum pedal force is defined by the FAA and the military.
4. Proper rudder balance so that under no conditions will the pilot be unable to return the rudder to neutral, and preferably it should not even tend to overbalance.

TABLE 13.4. Airplane Properties: Example 13.8

W = 40,000 lb	At −10" aileron, C_{Ha} = 0.0188
S = 755 ff	b = 71.5 ft
S_{ail} = 17.43 ft²	Aileron chord aft of hinge = 1.426 ft
Wheel radius = 0.625 ft	$\dfrac{\text{Wheel throw}}{\text{Aileron deflection}} = 3.33$
Aileron differential = 1:1	
At +10" aileron	
C_{Ha} = −0.0089	

5. A zero trail angle[10] so that control-free stability is the same as control-fixed stability. It will be seen that the zero trail angle permits smaller pedal forces and rudder movements to return a yawed aircraft to zero.

6. The largest yawing moments about the airplane's center of gravity. This moment is due almost entirely to the side force. The proportions due to the yawing moment of the vertical tail about its own quarter chord and the yawing moment of the vertical tail surface due to its drag are quite small but not always insignificant.

The rudder calculations, unlike the aileron panel tests, will require the absolute value of the drag coefficient. [See Equation (13.30).] This is not easily obtained with a panel test, but in view of the small contribution of the drag effect, an approximation may be made by reading the section drags with a wake survey rake at stations along the vertical tail with the rudder angle zero and by summing them to get the total drag coefficient. This may be subtracted from the minimum drag as read by the balance to get the drag of the endplate. The method as outlined makes the very questionable assumption that the tare drag is unaffected by rudder angle, which is justified only by the peculiar conditions of this setup in which tare accuracy is not vital.

The sign convention for control surfaces and tabs is as follows: A positive angular deflection yields a positive force on the main surface. A positive hinge moment produces a positive deflection.

The rudder setup for finding n (and hence C_n) is shown in Figure 13.21. The contributing parts are (1) the moment due to the vertical tail side forces, (2) the moment due to the vertical tail drag, and (3) the moment due to the vertical tail moment about its own quarter chord.

In symbols these factors become

$$n_{cg} = (n_v)_v - Y_v l_v \cos \psi - D_v l_v \sin \psi$$

$$= q S_v \bar{c}_v C_{n\frac{1}{4}v} - q S_v C_{Yv} \cos \psi \cdot l_v - q S_v C_{Dv} \sin \psi \cdot l_v \qquad (13.30)$$

$$C_{ncg} = \frac{S_v \bar{c}_v}{Sb} C_{n\frac{1}{4}v} - \frac{S_v l_v}{Sb} C_{Yv} \cos \psi - \frac{S_v l_v}{bS} C_{Dv} \sin \psi$$

where n_{cg} = yawing moment of vertical tail about center of gravity
S_v = vertical tail area
$C_{n\frac{1}{4}v}$ = vertical tail moment coefficient about its own quarter chord
$\bar{c}_v$ = mean aerodynamic chord of vertical tail
S = wing area
b = wing span
l_v = tail length (distance from tail quarter chord to center of gravity)
C_{Yv} = Y_v/qS_v
ψ = angle of yaw
$(n_v)_v$ = moment of vertical tail about its own quarter chord
D_v = drag of vertical tail
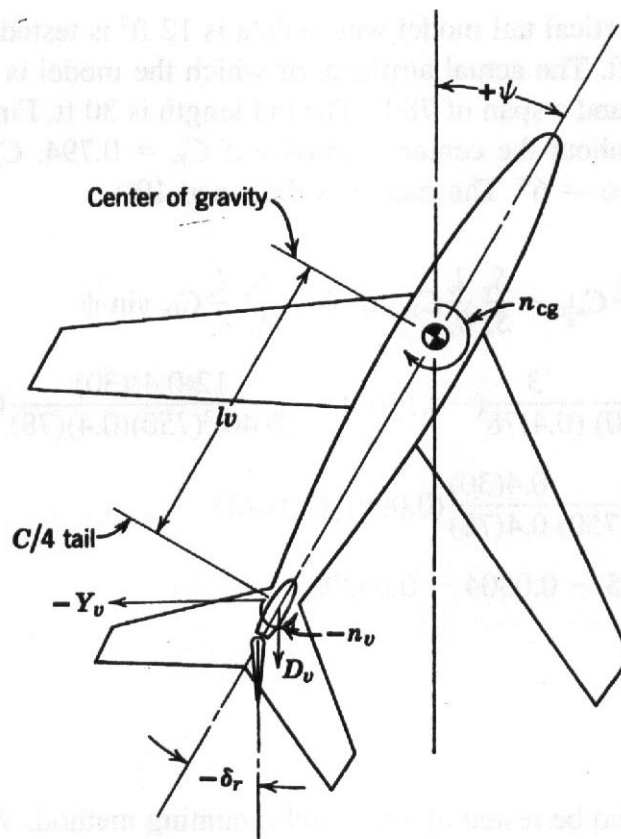
FIGURE 13.21   Plan view of yawed airplane.

Sometimes it is desired to estimate the tail contribution to yawing moment; in this case some simplification of Equation (13.30) is possible. The tail drag term and the tail moment about its own quarter chord are small, and for moderate yaw angles cos $\psi \approx 1.0$. Letting $S_v l_v / S_b$ equal the tail volume coefficient $\overline{V}_v$ and putting $C_{Y_v} = C_{Lv} = a_v \psi$, we have

$$C_{n,\text{cg}} = -a_v \psi \overline{V}_v$$

where $a_v = dC_{Lv}/d\alpha_v$.

This equation does not include the sidewash effect discussed in the next paragraph; it also assumes that the ratio of dynamic pressures q_v/q is unity.

It was mentioned earlier that span loading must be considered in order to apply data properly from an aileron panel test to the complete airplane. In the next section on elevators attention is drawn to the proper method of applying the data from an isolated horizontal tail. The vertical tail is less affected by the remainder of the airplane, but some sidewasb does exist when the airplane is yawed. Hence 15° yaw by no means results in a vertical tail angle of attack of 15°. Proper evaluation of the sidewash can be made by equipping the complete model with a vertical tail whose incidence is variable and by going through a procedure similar to that outlined for the horizontal tail in Section 13.3.

Example 13.9   A vertical tail model whose area is 12 ft^2 is tested at 100 mph. The model MAC $\doteq$ 3.0 ft. The actual airplane, of which the model is 40% scale, has a wing area of 750 ft^2 and a span of 78 ft. The tail length is 30 ft. Find the tail yawing moment coefficient about the center of gravity if C_{Y_v} = 0.794, C_{D_v} = 0.0991, and $C_{n\frac{1}{4}v}$ = −0.1067 for ψ = 6". The rudder is deflected 10°:

$$C_{n,\mathrm{cg}} = \frac{S_v}{S_w}\frac{(\mathrm{MAC})_v}{b_w}C_{n\frac{1}{4}v} - \frac{S_v}{S_w}\frac{l_v}{b_w}C_{Y_v}\cos\psi - \frac{S_v}{S_w}\frac{l_v}{b_w}C_{D_v}\sin\psi$$

$$= \frac{12}{(0.40)^2(750)}\frac{3}{(0.4)78}(-0.1067) - \frac{12(0.4)(30)}{(0.40)^2(750)(0.4)(78)}0.794(0.9945)$$

$$- \frac{12}{(0.40)^2(750)}\frac{0.4(30)}{0.4(78)}(0.0991)(0.1045)$$

$$= -0.001025 - 0.0304 - 0.00398$$

$$= -0.0354$$

Elevators

The elevators may also be tested by the panel mounting method. With this arrangement, one-half the horizontal tail is usually mounted as shown in Figure 13.2 and the results are doubled to get the data for the entire tail.

It will be noted that for airplanes of conventional dimensions, the pitching moment of the horizontal tail about its own quarter chord and the pitching moment about the airplane center of gravity produced by the horizontal tail drag are negligible when compared to the moment produced by the tail lifting force. Hence it will probably be necessary only to measure the lift of the panel model along with the elevator hinge moments to evaluate the desired qualities. Occasionally it will be desirable to compare two different methods of trimming to determine which has less drag for a given lift. Then, of course, drag measurements will be necessary.

The tail lift curve slope as determined from the panel model may require adjustment in order to apply the test results. Example data are shown in Figure 13.22. For example, suppose that the complete model has been tested at a constant angle of attack with varying settings of the stabilizer. The pitching moment about the airplane center of gravity due to the horizontal tail,

$$M_t = -l_t q_t S_t C_{Lt} \tag{13.31}$$

may be measured, and with the known tail area S_t and tail length l_t the value of C_{Lt} may be determined. In these calculations it is probably better to use $q_t = q_{\mathrm{freestream}}$ than the very questionable $q_t = 0.8q_{\mathrm{freestream}}$ sometimes arbitrarily employed. From the calculated C_{Lt} and known stabilizer angles the slope of the tail lift curve on the airplane $(dC_{Lt}/d\alpha_t)$ may be established. It then remains to diminish the panel lift curve slope by the factor $(dC_{Lt}/d\alpha_t)_{\mathrm{airplane}}$ divided by $(dC_{Lt}/d\alpha_t)_{\mathrm{panel}}$.
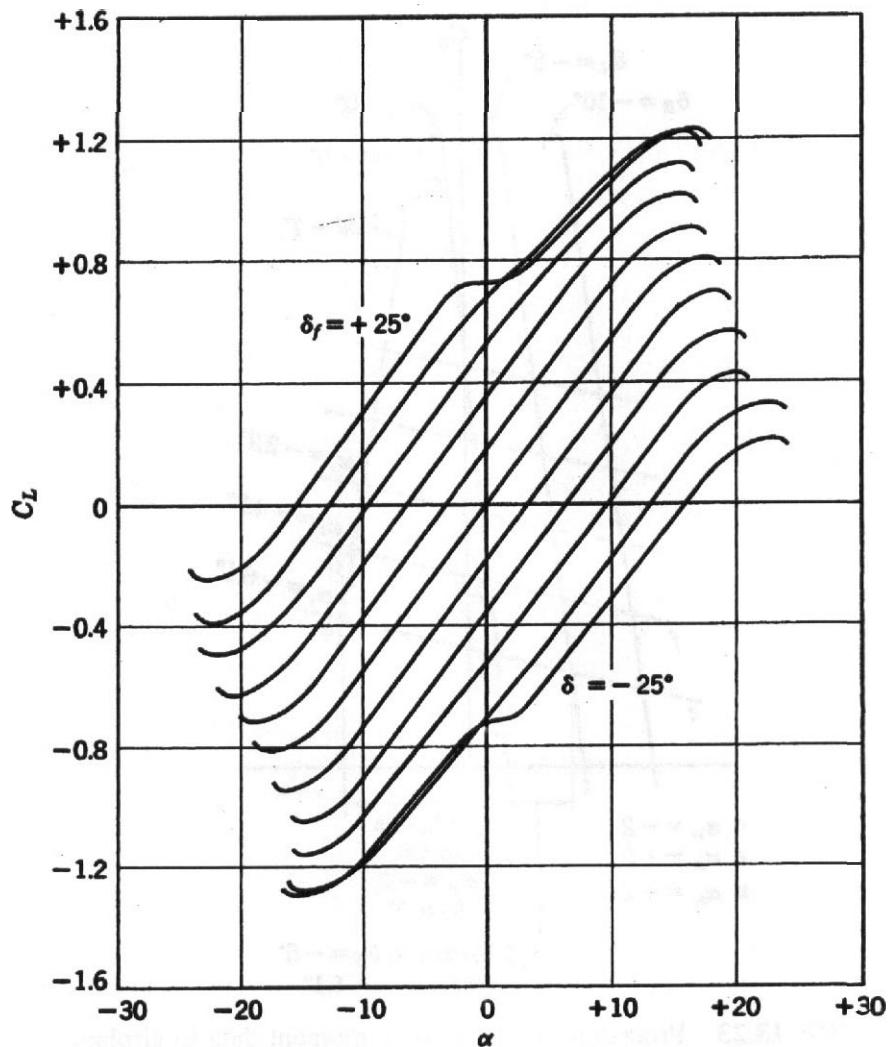
FIGURE 13.22   Typical panel lift curves. The breaks in the curves for large flap deflections occur when the flap stalls.

The procedure followed to align the hinge moment data to the airplane may be traced through Figure **13.23.**

Let us suppose that the power-off moment curves of our example airplane are as shown in Figure **13.23** for the model with tail and without tail, some center-of-gravity location" being specified. If lines abc, *def*, . . . are drawn between points of equal angle-of-attack values, the difference between the model plus tail (M **+** T) and M − T curves is the contribution of the horizontal tail with elevator zero at the specified α_w. The moment due to the tail $\Delta C_{mt} = q_t(C_{Lt})S_t l_t$ and values of C_{Lt} are readily determined. From the previously prepared tail lift curve we find the tail angles of attack that correspond to the C_{Lt} values, and so label the lines abc, *def*, . . . as $a_t = -6.1, -4.2, \ldots$ This procedure furnishes the relation between the panel tests and the complete airplane, since values of hinge moment and tail lift coefficient for various angles of attack are available from the panel tests.

To carry this chart to completion, the values of ΔC_m for various elevator deflections are calculated from the C_{Lt} values corresponding *to* the tail angles of attack, and
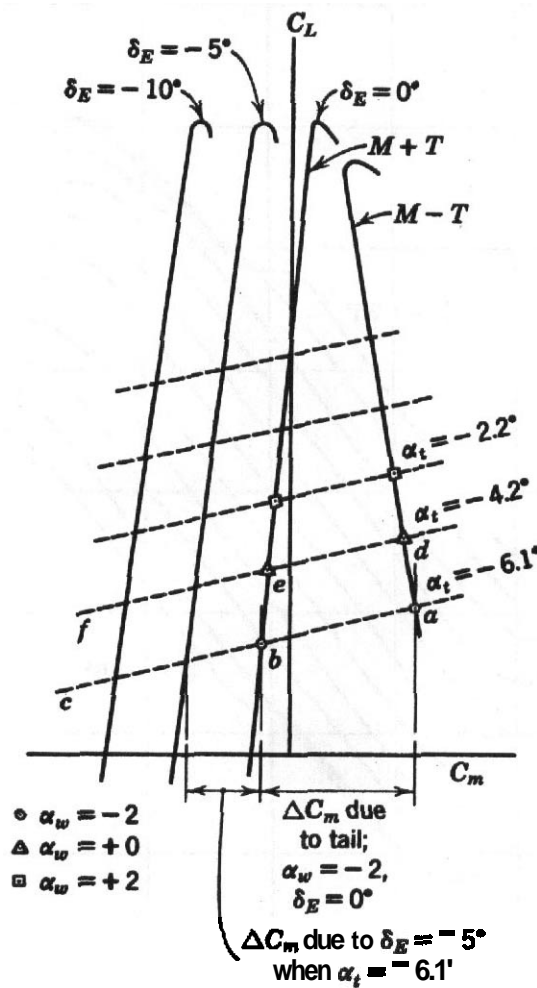
FIGURE 13.23   Procedure to align hinge moment data to airplane.

curves of constant elevator deflections may be drawn in. The complete chart may then be used to read the amount of elevator needed to trim at any C_L or the amount of moment available for maneuvering with a specified stick load. The maneuvering investigation requires the hinge moment data and the mechanical advantage, as follows:

1. Assume the chart to indicate that an elevator deflection of $-15°$ is required to trim at $C_L = 1.9$ and $\alpha_{tail} = +12$. From the airplane geometry and $C_L = 1.9$, the value of q may be found from $q = W/SC_L$.

2. From the chart of hinge moment versus α_{tail} we read (say) for $a = +12$ and $6, = -15°$ a $C_{He} = 0.0640$.

3. From airplane geometry and q (step 1) the elevator hinge moment is calculated from $\mathrm{HM}_e = qS_e c_e \cdot C_{He}$.

4. From the curve of mechanical advantage versus δ_e and the known linkage lengths, the stick force may then be found.

In this manner the various flight conditions may be investigated and desirable balance changes evaluated. Note that the limit to forward center-of-gravity travel

is a function of elevator power, which is a function of elevator deflection and size. The elevator power must be sufficient to balance the airplane at maximum lift ($C_{m,CG} = 0$). The critical condition is gear and landing flaps down in ground effect.

Fuselages, Nacelles, and Bodies-of Revolution

Tests of fuselage alone are rarely made, for the interference effect of the wing on the fuselage is of such prime importance and magnitude that tests of a fuselage without the presence of the wing are of very questionable value. When a fuselage alone is tested, the boundary effects are usually important. Blockage corrections are commonly moderate to large.

Nacelle tests are much more valuable than fuselage tests because usually entirely different items are being investigated. Generally the nacelle tests are concerned only with cooling pressure drops and cooling drags and not with the total nacelle drag, which would be largely dependent on the wing–nacelle interference.

If a power-driven propeller is to be utilized in the setup, careful consideration should be given to the control and measurement of the rpm. For nacelles simulating modem high-power units, the loss of a single rpm can represent a large thrust decrement and, in turn, can invalidate any drag measurements that may be made. It is usually advantageous to fix the rpm by means of a synchronous driving motor and to vary the tunnel speed and propeller blade angle to get various flight conditions. Such an arrangement corresponds to the customary constant-speed setup of most airplanes.

The usual nacelle is of such dimensions that buoyancy, constriction, and propeller corrections are important. For clarity, let us assume that a model is to be tested at 100 mph. The constriction effect of the closed jet increases the velocity over the model so that the results are similar to those encountered in free air at a slightly higher speed, say 102 mph. The effect on the propeller is opposite, however, yielding the results expected in free air at 96 mph. It is therefore necessary to increase the tunnel speed to approximately 104 mph, at which time the propeller slipstream is the same as in free air at 100 mph. The propeller coefficients are then based on 100 mph. The buoyancy effect is assumed to be the same as expected at 100 mph without the propeller.

Drag coefficients for a nacelle may be based either on nacelle frontal area or other reference area. The choice should be clearly stated. The quantity of cooling air per second Q is usually defined by

$$Q = KS\sqrt{2\,\Delta p/\rho} \qquad (13.32)$$

where K is the engine conductivity; S the nacelle or engine frontal area (ft^2); Δp the baffle pressure drop (lb/ft^2); and ρ the air density (slugs/ft^3).

Bodies of revolution or fuselages are best tested on their sides using a single strut and yawing the model to simulate angles of attack. This procedure both reduces the tare and interference and makes their determination easier. For accurate angle

determination the torsional deflection of the strut under torque load should be calibrated and corrected in the data work-up.

Propellers

Propellers are frequently investigated in wind tunnels either alone or in conjunction with a fuselage or nacelle. If an entire model is tested, the propeller diameter will be small compared to the tunnel jet diameter, and the corrections to be described will become small also. For tests in which propeller characteristics are to be determined, the propeller diameter may well be 60% of the jet diameter, and the corrections are not only large but unfortunately not as accurate as those for wings. An approach to the problem has been made by Glauert, as discussed in Chapter 11.

Numerous coefficients have been advanced for presenting propeller data, each type perhaps being advantageous for particular applications. One of the more popular forms is

$$C_P = \frac{P}{\rho n^3 d^5} = \text{power coefficient} \tag{13.33}$$

$$C_T = \frac{T}{\rho n^2 d^4} = \text{thrust coefficient} \tag{13.34}$$

where P is power input (ft-lblsec); n is in revolutions per second (rps); d is propeller diameter (ft); and T is thrust (lb). The "variable" of propeller testing is usually the advance ratio $J = V/nd$, where V, n, and d are in units such that J is dimensionless. In English units V is in feet per second, d in feet, and n in revolutions per second. Following the discussions of Chapter 1 on nondimensional properties indicates that the thrust and power coefficients are expected to be functions of advance ratio J, Reynolds number, and Mach number. The dominant independent variable is the advance ratio. Mach number comes next if it approaches 1, and finally is Reynolds number. Small scales are not used for propeller development due to the Reynolds number dependence. However, there are a good number of propeller-driven unmanned air vehicles that use relatively small propellers that can therefore be evaluated directly in a number of wind tunnels.

Plots of C_P and C_T against J for a typical propeller are shown in Figure 13.24.

Emergency Power Wind Turbines

The need for a power source to operate when a jet engine airplane has a high-altitude flame-out has reactivated the interest shown many years ago in wind-driven generators or hydraulic pumps, and not infrequently the tunnel engineer is called upon to evaluate a particular generator by an operational test. When this is so, the special precautions that are paid to models such as rotors, propellers, and the like, whose possibility of failure is higher than that of rigid models, should be applied.

Corrections to the data from a windmill test are subject to boundary corrections, as outlined in Chapter 11, specifically wake blockage, and propeller corrections
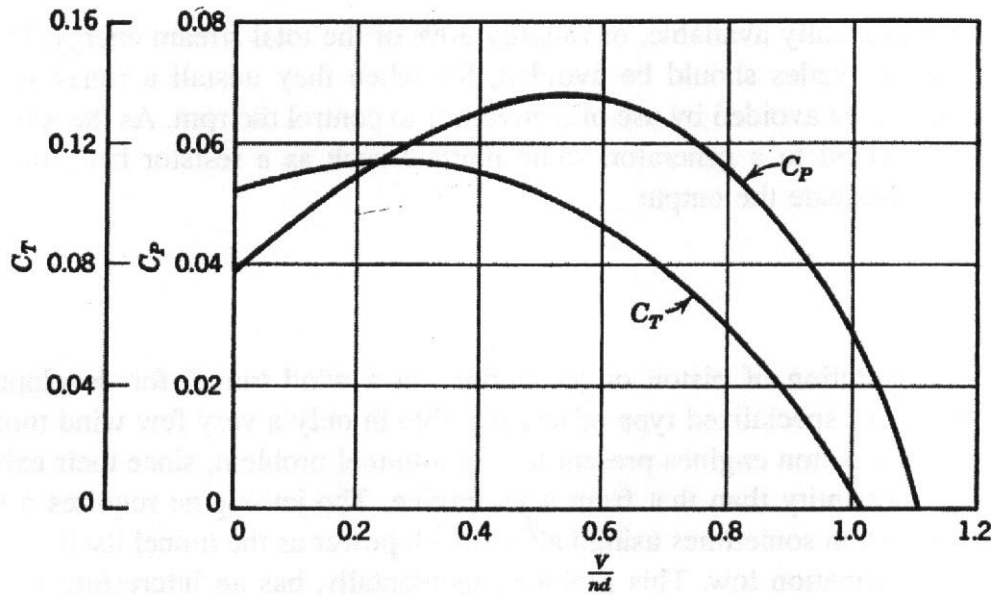
FIGURE 13.24   Typical propeller data.

with a negative sign. However, the emergency power generator is frequently so small relative to the tunnel and the interest in very accurate data as compared to proof testing is commonly so slight that corrections may be neglected. This is not true of windmills intended to be used for ground power generation.

It is of interest to look into the mechanism of a windmill from the theoretical side in order to gain an understanding of how it works. Of course the device takes energy from the air, but surprisingly the total free-stream energy passing through a stream tube with cross-sectional area equal to that of the windmill is not available to the windmill. The slowing of the stream resulting from the interaction with the windmill makes a portion of the air go around the windmill instead of through it.

Looking at the problem from a momentum standpoint, we **find** that if the velocity at the windmill is $V(1 - a)$, the final velocity will be $V(1 - 2a)$, and letting the windmill radius be R, we have for the power out

$$P_0 = V(1 - a)[\rho\pi R^2 V(1 - a) \cdot V - \rho\pi R^2 V(1 - a) \cdot V(1 - 2a)]$$

$$= 2\pi\rho R^2 V^3 a(1 - a)^2 \tag{13.35}$$

Differentiating and solving, we find the maximum power out occurs when $a = \frac{1}{3}$. Substituting this value and comparing the maximum power out with the total in a free stream of the same radius P_S, we have

$$\frac{P_0}{P_S} = \frac{0.296\rho\pi R^2 V^3}{0.5\rho\pi R^2 V^3} = 0.594 \tag{13.36}$$

or even with blades that have no drag the windmill could only extract **59.4%** of the stream energy. A good figure in estimating windmill sizes seems to be about **one-**

half that theoretically available, or roughly 30% of the total stream energy. During testing, stalled blades should be avoided, for when they unstall a runaway may occur. This can be avoided by use of a governor to control the rpm. As the windmill is often connected to a generator, some method such as a resistor bank must be provided to dissipate the output.

Engines

The actual operation of piston or jet engines in a wind tunnel for development reasons is a very specialized type of test possible in only a very few wind tunnels. Of the two, the piston engines present less of a tunnel problem, since their exhaust is smaller in quantity than that from a jet engine. The jet engine requires a huge scavenging system sometimes using half as much power as the tunnel itself in order to keep contamination low. This problem, incidentally, has an interesting facet in high-speed work, where the presence of rather small amounts of exhaust changes the values of γ and hence confuses the operating Mach number. In some low-speed tunnels the air exchangers can handle the exhaust problem.

If an engine is run in the tunnel with minimal air exchange, extreme care must be taken to protect personnel from high concentrations of carbon monoxide. After the test run the tunnel should be opened up and run to vent the CO before personnel enter the test section.

Stores

The word "stores" is a catch-all for all types of jettisonable fuel tanks, bomb shapes, and other capacity devices. In general, they are designed for minimum drag while on the aircraft and adequate stability after jettison. Tests run with the stores alone largely seek solutions for the stability problems; their cargo is typically of uniform density and their centers of gravity correspondingly from 40 to 55% of their length from their nose.

Necessary wall corrections for the tests include wake and solid blockage. The lift is ordinarily so small that downwash corrections are not needed. Tests consist of angle-of-attack runs up to very large angles (say $50°$ or perhaps 60"). These sorts of angles in slight hurt the impact circle of probable error and are to be avoided, but stability must still exist if a bad pitch-off produces them. The shape should be tested with the fins in both the ✚ (horizontal–vertical) and ✕ (rotated 45") positions.

The best drag data possible are not good enough for serious bomb work, nor is it possible to correlate tunnel data with flight, simply because the flying bomb is always rolling and sometimes pitching. Tare and interference tests of a store shape are illustrated in Figure 13.25.

A few words about free-spinning rocket or bomb models might be added here of interest to wind tunnel engineers. A little thought will reveal that with a model at high angle of attack the downward-moving fin will stall first, and the lift on the upward-moving fin then becomes a "driver." The result can be a great and sudden
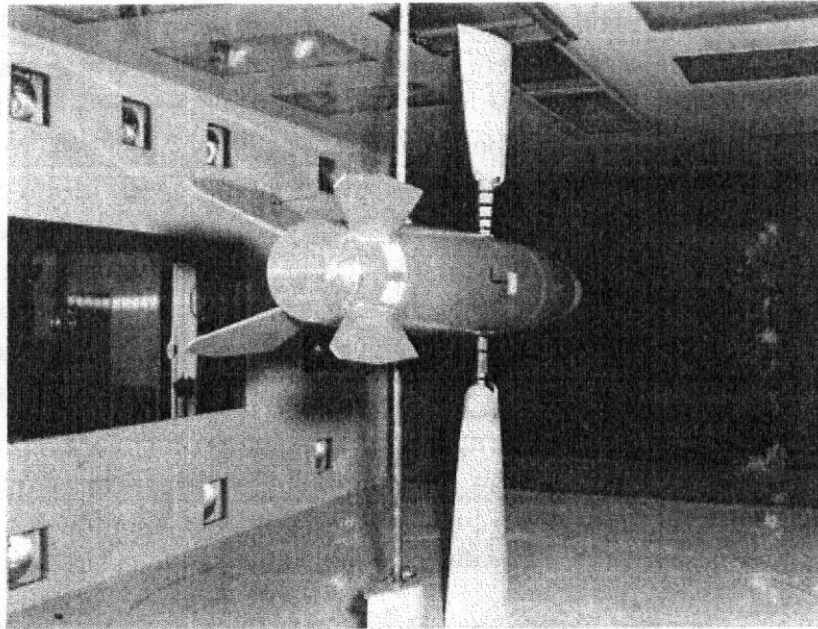
FIGURE 13.25   Testing using a single- or double-support strut. Both the single- and double-support struts are quite weak in torsion (yaw), and any models tested with them should not have natural frequencies close to those of the tunnel. Seven-by-ten tunnels of the type shown often have low-speed oscillations around 1 Hz, and lateral restraint wires may have to be added if the model natural frequency is in the range. The model shown is installed with an image system. (Courtesy Sandia National Laboratories.)

increase in rpm—in one instance an increase from 300 to 2000 rpm in a very few seconds. Don't leave, just shut down the tunnel.

Loads: Doors, Landing Gear, and Others

Local loads on landing gear doors, bomb bay doors, flaps, nacelles, and so on, are best obtained by the use of strain gage balances designed for the expected loads. When the distribution of air loads is desired on the wing, fuselage, and tail, a choice from among the available pressure-measuring systems must be made. Pressure-sensitive paint has become a reasonable candidate for high-value projects.

The data are usually presented in the form of a pressure coefficient versus model location. These data can then be integrated to obtain, for example, local lift coefficients on a wing or tail and plotted versus span for span load. In most cases the purpose of the test is to obtain aerodynamic loads for structural design.

Invariably, in a large pressure test there will be plugged and leaking ports assuming traditional methods are being used. These problems are supposed to be caught in the model checkout, but some will still show up in the final data. Because of bad port problems there is a tendency to label any port that appears to fall outside the expected curve as a bad port. This can be dangerous, especially on leading-edge flaps. In one case on a leading-edge flap several ports at the same chordwise location very close to the leading edge showed very large negative C_p's. When looking at

one chordwise pressure station, one might assume that the port was bad. But it is hard to believe that at the same percent chord at several spanwise stations the same model port is bad in exactly the same way. Another anecdote that leads to caution in data interpretation was passed along recently. A number of pressure ports are included on a model coated with pressure-sensitive paint to provide in situ calibration data. A small model of a fuselage plus delta wing was run at a moderate angle of attack. One port near the intersection of the fuselage and leading edge provided such a low pressure ($C_p \approx -6$) that either the port or the transducer was considered to be malfunctioning-. However, when the paint system was put into action, not only was the pressure confirmed but an even lower value was obtained a small distance away.

133' COMPLETE CONFIGURATIONS

An experiment in which six-component balance data for a complete configuration is to be measured is the most difficult of all wind tunnel experiments: More variables are under consideration than in other experiments, and the individual parts of the experimental matrix are more complicated. For instance, each data run requires up to *three* additional runs to evaluate the tare, interference, and alignment *(see* Chapter 7).

Because tare and interference runs are extremely time consuming, they are often either replaced with a set of support tares taken from a calibration model or not applied at all to the data. When no tares are applied, the data are compared with a base airplane configuration and are incremented from the baseline data. This is usually done only when the firm conducting the test has had a lot of experience with a particular tunnel, model-mounting system, and probably some associated flight test work. Although experiments using a complete model are difficult, they are the most common type of aircraft program. Usually there are several wind tunnel entries of the model as the airplane design develops.

Experiments to determine optimum leading- and trailing-edge flap configurations and angles can be quite long owing to the large number of variables, which include pitch-up on swept wings. The effect of control surface deflections both in pitch and yaw are checked not only for cruise but also for takeoff and landing flap settings, in and out of ground effect. The effect of power for prop-driven airplanes or high-bypass turbine engines merely adds to the complexity of the experiment with various power settings and engine-out simulations for multiengined aircraft required.

The data are usually corrected for the effect of tunnel walls, tunnel upflow, and tunnel blockage (Chapter 10). The use of trip strips on the model is discussed in Chapter 6. Powered lift simulation limits for V/STOL-type aircraft are discussed in Chapter 11.

Before a brief discussion of the required runs for the model of a general-aviation-type aircraft is given, a brief discussion of how an experiment is run is in order. Before a wind tunnel run sequence is begun with a model, the angle of attack is usually calibrated. This is done by the use of an inclinometer. The model reference

plane is set to zero angle of attack (the fuselage reference line and chord plane of the mean aerodynamic chord are usually used as references). Then the model is pitched through the desired angle-of-attack range, and the relation between alpha indicated and alpha measured or geometric is determined. The next calibration is a weight tare. The model center of gravity does not coincide with the balance moment center and thus there is a change in pitching moment measured with angle of attack. This must be subtracted from the data as it is not an aerodynamic moment. In yaw there is both a rolling and a pitching moment. If a sting balance is used, the model is rolled rather than yawed, and if the model center of gravity is on the model centerline, there is no weight tare. Many weight tares will be taken during a test since they are a function of the model center-of-gravity location and hence model configuration.

In a low-speed wind tunnel with unpowered models there is usually one wind-on run made per model configuration. If the model is powered, several runs at different power settings may be made per model configuration without stopping the tunnel. Because of one run per setup, it is desirable to have a method of displaying the test results as they are obtained. The best form of data visibility is as presented in Figure 13.26. For pitch runs C_L–α, C_L–C_D, C_L–C_m, and sometimes C_l–α are required. For yaw runs it is C_N–ψ, C_l–ψ, C_Y–ψ, or sometimes side slip angle β is used instead of yaw angle ψ.

These plots serve three purposes:

1. They will show any points that do not fit the curves (so-called bad points). When these occur, the test point is repeated (a check point). Note: The check
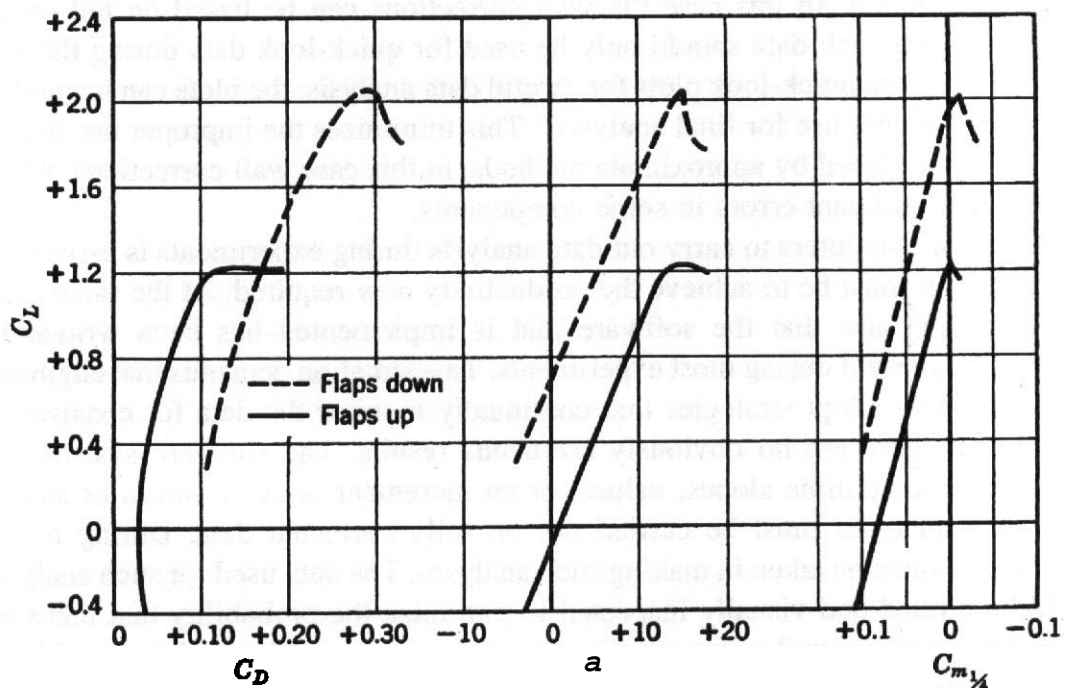
FIGURE 13.26   Typical curves of lift, drag, and pitching moment, flaps up and down.

point should not be approached from a stalled condition owing to the possibility of hysteresis in stalled regions. If the check point fits the curve, it replaces the initial point. If the check point repeats the initial point, additional test points **are** then taken to define the curve in this region.

2. Sometimes in the stall region the angle increments **are** too large to define the curve. When this happens, additional points are taken to define the curves.

3. The plots are often used to make comparisons between model configurations and to check values and slopes.

The plots can be obtained in two ways. First, for small student-type tunnels without computerized data systems, the uncorrected (raw) balance data in engineering units can be plotted by hand. This task argues for an external balance of the pyramid type where the forces and moments can be obtained without excessive calculations, rather than platform- or sting-type balances.

For tunnels equipped with computerized data systems where the data are both recorded and reduced by a computer, the type of balance is not critical. As it is desirable to see the data in coefficient form as close to real time as possible, the speed of the data reduction process in the computer will determine the number of corrections applied to the data. Balance corrections, if small, blockage, and mounting tare corrections may be omitted to save time. Angle calibrations, weight tares, and wall corrections should be applied. In most cases the wall corrections will be approximate wall corrections. The wall corrections to α, C_D, and C_m are all based on wing-alone or tail-off lift coefficients. The pitching moment correction is also a function of the location of the wing wake system relative to the horizontal tail and is measured during the test. It is not always practicable, owing to the time required, to change the model to make the tail-off and the two runs required for pitching moment correction. In this case the wall corrections can be based on tail-on lift coefficients, but such data should only be used for quick-look data during the test. To avoid using the quick-look plots for careful data analysis, the plots can be marked "Raw data-do not use for final analysis." This minimizes the improper use of data that has been reduced by approximate methods, in this case wall corrections, which can lead to significant errors in some components.

The use of computers to carry out data analysis during experiments is essentially universal, as it must be to achieve the productivity now required. At the same time, it is often the case that the software that is implemented has been written by someone not present during most experiments. This situation demands that engineers conducting tests adopt strategies that continually monitor the data for consistency and see that there **are** no obviously erroneous results. The software systems are often used to determine slopes, values, or an increment or A in values or slopes. These data analyses must be **carried** out on fully corrected data. During a test, extreme care must be taken in making such analyses. The data used for such analyses should be plotted and visually inspected to minimize the probability that there are bad points or other unpleasant surprises in the data used. These plots should use the same fairing or fitting routines that will be used for the final data reduction. This is especially critical when the software is used to take increments or A's

TABLE 13.5. **Test** Program for **Unswept** Configuration without Power

Runs	Model Configuration	Data Sought	Each Run Consists of:
1–4	W	Tare, interference, and alignment; final polar plot	Polars, model normal and inverted, dummy struts in, dummy struts out
5–6	W	Wing lateral stability for future correlation	Yaw $\pm 30°$ at $C_L = 0.3, 1.0$
7–10	WB	Tare, interference, and alignment, final polar plot	Polars, model normal and inverted, dummies in, dummies out
11–12	WB	Wing and body lateral stability for future correlation	Yaw $\pm 30°$ at $C_L = 0.3, 1.0$
13	WBH	Polar plot, effect of horizontal tail	Polar
14–15	WBH	Lateral stability for evaluating vertical tail and correlation	Yaw 230" at $C_L = 0.3, 1.0$
16	WBHV	Polar plot; effect of vertical tail	Polar
17–18	WBHV	Directional stability	Yaw at $\pm 30°$ at $C_L = 0.3, 1.0$
19–23	WBHV	Tail setting and downwash	Polar with tail incidence $-4, -3, -2, -1, 1$
24–25	WBHV	Effect of yaw on static longitudinal stability	Polar with $\psi = 5°, 10°$
26–43	WBHV	Rudder equilibrium and power	Yaw 230" at $C_L = 0.3, 1.0$; rudder at $2°, 5°, 10°, -2°, -5°, -10°, -15°, -20°, -25°$
44–63	WBHV	Aileron power	Yaw $\pm 30°$ at $C_L = 0.3, 1.0$ with aileron $-25°, -20°, -15°, -10°, -5°, 5°, 10°, 15°, 20°, 25"$
64–72	WBHV	Elevator power	Polars with elevators from $-25"$ to $15°$, $\psi = 0$
73–89	WBHVF	Effect of flaps on elevator and trim	Polars with elevators from $-25°$ to $15°$, $\psi = 0$, for takeoff and landing flaps
90–95	WBHVF	Effect of flaps on lateral stability	Yaw at $\pm 30°$ at $\alpha = 3°, 10°$, for takeoff and landing flaps
96–104	WBHVF	Effect of flaps on lateral control	Polars with flaps $55°$, $\psi = 0$, ailerons at $-25°$ to $20°$

TABLE 13.5. *(Continued)*

Runs	Model Configuration	Data Sought	Each Run Consists of:
105	WBHFG	Effect of gear down	Polars with landing flaps, $\psi = 0$ model inverted to reduce interference between supports and gear, and vertical tail removed to avoid physical interference with tail strut.
106	WBHFG	Effect of gear down on lateral stability	Yaw $\pm 30°$ with $a = 3°$, $10°$, flaps $55°$; model inverted

Note: W = wing; B = fuselage; H = horizontal tail; V = vertical tail; G = gear; F = flaps; "tare" = dummy shuts installed; polar plot = C_L vs. a, C_D, and C_m from α_{ZL} through stall; "correlation" = data to assist in laying future designs; polar run = L, D, M, from a through stall.

between two runs. When slopes are required, care must be taken in the routine used and the range of values over which the slope is required. As an example, if one is trying to find $C_{D,P,e}$ and Oswald's efficiency factor e (Example 13.1) and one uses a linear regression curve fit over the C_L range from $0°$ to $3°$ or $4°$ past stall, one will not get the correct values for either term. The values of $C_{D,P,e}$ and e are based on the linear portion of the C_L^2–C_D curve and not the whole curve. Thus the software must be given the lower and upper limits of C_L to be used.

At the time of publication of the second edition of this book, it was argued that many of the answers being sought in a wind tunnel experiment could be obtained as quickly by manual means given automatic plots as by software algorithms. This was a commentary on the state of affairs of software, computer hardware, and a considerable cadre of already very experienced aerodynamicists accustomed to manual extraction of information from plots. There will be few instances today where that argument is true. The software is more sophisticated, the computers are faster, and the typical users are more skilled at using the computing machinery than in doing manual data extraction. No less attention to detail in monitoring outputs, however, can be tolerated as an experiment progresses. The engineer has to think of what he or she is trying to do and assure himself or herself that the program will yield the correct desired results. Unfortunately, the computer and its software are not inherently concerned with whether or not the results are correct.

A list of the runs usually employed for an unswept and unpowered model is provided in Table 13.5. The numerical values in this table are, of course, only approximate, exact values being dictated by the particular design in question. Additional runs would be needed to check fillets, alternative tail surfaces, ground effect, and so on. Attention is drawn to items in Table 13.5 marked "correlation." In many instances correlation runs are added to evaluate separate effects of configurations that would never be flown. For example, a two-engine model usually has a run

made without nacelles. The data from this run compared with those from the run with them in place aid in identifying the effect of the nacelles on the airplane's efficiency, drag, and lift. After several models have been tested, the effects of a "good" nacelle become known, and when a "poor" one turns up, it is so identified and attention is directed toward improving it. A standard procedure is to list the important performance parameters in tabular form, noting the change in each as each component is added to the wing. Studies made of such tables can be informative indeed.

A configuration with sweep requires more stall studies than are shown in this program of runs, particularly for longitudinal, lateral, and directional stability.

Comments on the customary curves and information desired follow.

Lift Curve, Flaps Up

Items of interest on the flap-up lift curve include the value of $C_{L,\max}$ for determining flap-up stalling speed and minimum radius of turn, the shape of the curve at the stall (it should be moderately smooth, but may not be), the angle of zero lift, the slope of the lift curve $dC_L/d\alpha$, and the value of negative $C_{L,\max}$. At the Reynolds numbers usually encountered in the wind tunnel, $C_{L,\max}$ will be from 0.6 to 1.7, $dC_L/d\alpha$ for nonswept wings from Equation (13.2), and swept wings from Equation (13.3). Construction of the power-off trim lift curve is shown in Figure 13.27. A similar method can be used for trim drag.

Lift Curve, Flaps Down

This curve will have very nearly the same slope as the flap-up curve and the same location of the aerodynamic center. The value of flap-down $C_{L,\max}$ is important for determining the increment due to the flap $\Delta C_{L,\max}$, for this apparently does not change with Reynolds number and may be used to determine full-scale $C_{L,\max}$, flaps down (see Chapter 6), which is needed for landing and takeoff runs. The value of $C_{L,\max}$, flaps down, will vary from 1.2 to 3.5, the higher value being sought after but rarely attained. Trailing-edge flaps increase a for zero lift, increase the $C_{L,\max}$, and reduce the *a* for stall. They often will change the shape of the C_L–α curve near stall. Leading-edge flaps, slats, slots, and Krueger flaps tend to extend the lift curve to higher a stall and greater values of $C_L$max. The basic purpose of flaps is to reduce the wing area through increased $C_{L,\max}$ and thus reduce the parasite drag in cruise. To be usable, the $C_{L,\max}$ must be for trimmed flight. Thus, flap systems that generate large negative pitching moments may require a large tail to develop adequate downloads for trim, which reduces the total $C_{L,\max}$ (wing and tail).

The angle of 0.9 $C_{L,\max}$ is of interest for landing-gear-length considerations. It will probably be from $\frac{1}{2}°$ to $3°$ less for flaps down than for flaps up if the flaps cover the inboard wing area and from $5°$ to $8°$ less if they cover the entire span. Again the sharpness of the stall is of interest, since large lift coefficients that are perilously close to a violent stall cannot safely be utilized to their full value. There is usually little need to take the flap-down lift curve as low as the angle of zero lift. The stall
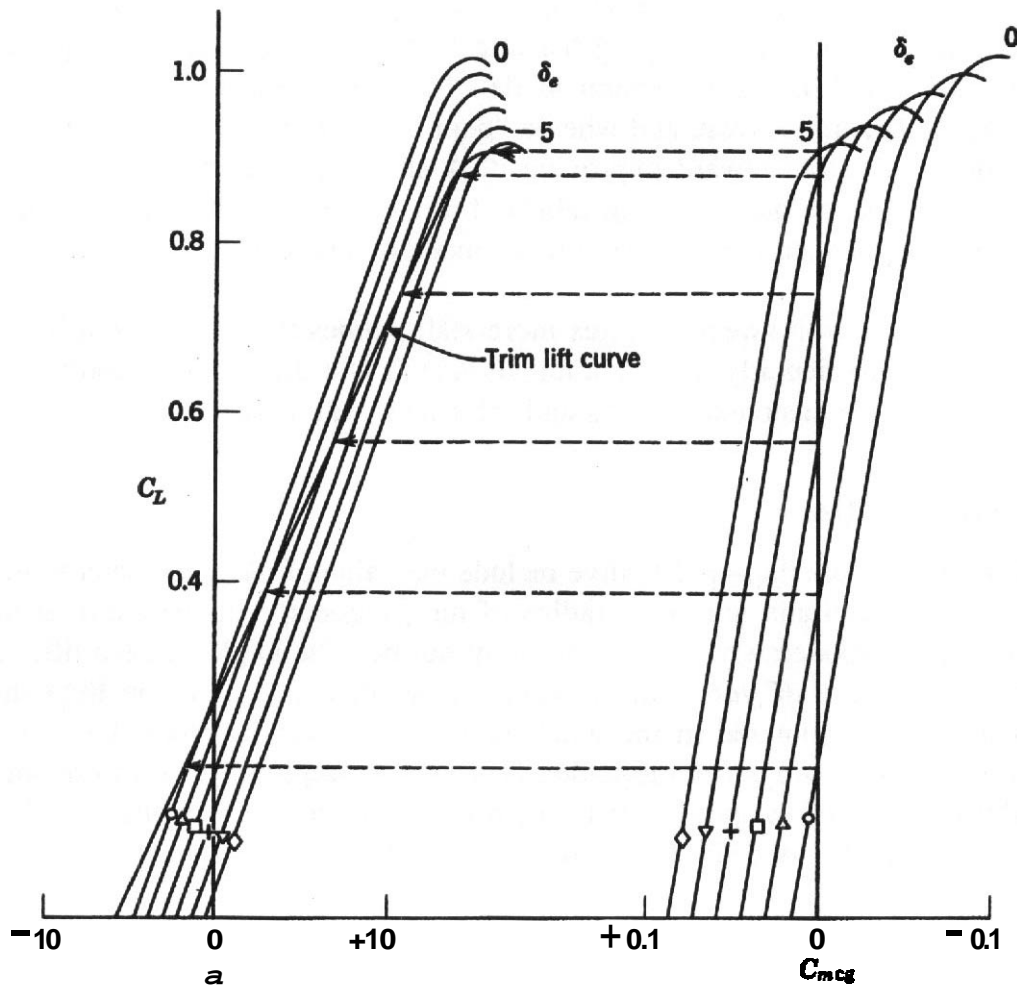
FIGURE 13.27   *Construction of the trim lift curve.*

should be read in very small steps so that its shape is accurately determined. To increase the span of the wing affected by flaps and hence the maximum lift, the ailerons are sometimes drooped (Figure **13.28**).Spoilers on top of the wing can be used for roll control, to decrease lift usually in landing approach, and, when on the ground, to increase drag and kill lift, putting more weight on the wheels to increase the effective use of the brakes. If such devices are used, the number of runs in a wind tunnel increases as their effectiveness is determined.

Here are some hints about testing for $C_{L,\max}$:

1. If possible, plan $C_{L,\max}$ tests at flight Mach number since for many airfoils the local velocity over the leading edge becomes sonic when $M_{\text{freestream}}$ equals 0.1 or **0.2.**
2. Low-aspect-ratio wings with sweep have a leading-edge vortex and are not usually sensitive to Reynolds number unless the leading-edge radius is large; **RN = 2 X 10^6** is usually adequate.
3. High-aspect-ratio wings are quite sensitive to Reynolds number.
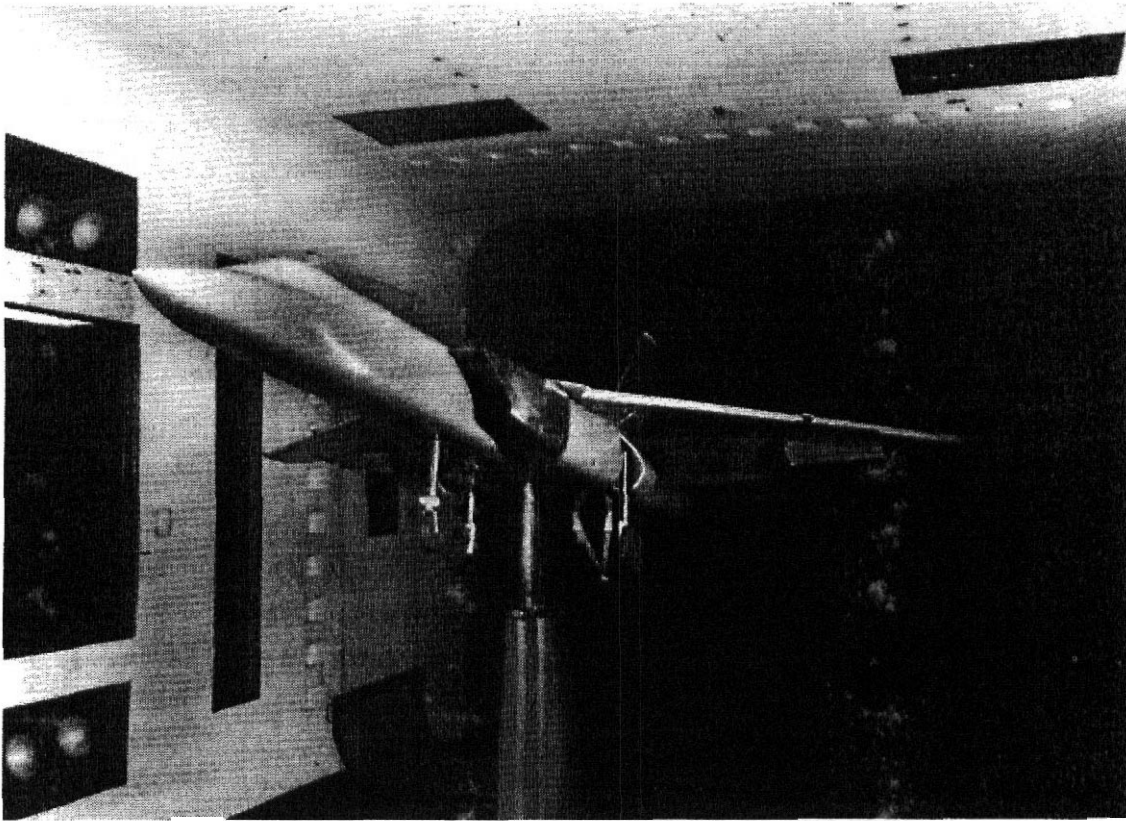
FIGURE **13.28**   Testing for $C_{L,\max}$. (Courtesy of the Boeing Co.)

4. Multielement high lift wing systems are Reynolds number sensitive. This is a major reason for recent demand for very high Reynolds number testing facilities.

5. In studying $C_{L,\max}$, the model should be as close to trim as possible. On low-aspect-ratio models with short tails, the tail effectiveness varies with angle of attack as the local dynamic pressure changes.

6. The addition of nacelles usually reduces $C_{L,\max}$.

7. For swept-wing models attention must also be paid to pitch-up (reversal of the slope of the C_m curve) in the C_L–C_m curve as it can limit the usable C_L.

Data from tests of a model of a twin-jet penetration fighter are presented in Table 13.6. As is shown, it is customary to list both the fundamental data and the progressive increments, the increments drawing attention to both good and bad items more directly than the total numbers. The data as shown are for an untrimmed model, and the increase of lift curve and maximum lift with the addition of the horizontal tail will become a decrease when trim is considered. A pair of nacelles usually reduces the lift curve slope about 0.02. The angle for $0.9C_{L,\max}$ (which is of interest in designing the landing gear) should not be taken too seriously until good ground board tests are completed.

TABLE 13.6. Lift Curve Data from Tests of a Twin Jet Fighter

Configuration	α_{ZL}	$\Delta\alpha_{ZL}$	$C_{L\alpha}$	ΔC_L	$C_{L,max}$	$\Delta C_{L,max}$
W	−0.3	—	0.0612	—	1.115	—
WB	+0.2	0.5	0.0650	0.038	1.115	0.0
WBC	+1.0	0.8	0.0650	0.0	1.115	0.0
WBCHV	+0.9	−0.1	0.0709	0.059	1.197	+0.082
WBCHVF$_{20}$[a]	−1.2	−2.1	0.0700	−0.009	1.34	+0.143
WBCHVF$_{50}$	−4.2	−3.0	0.0700	0.0	1.37	+0.03
WBCHVG[b]	+0.9	0.0	0.0700	0.0	1.197	0.0
WBCHVGF$_{20}$	−1.2	−2.1	0.0700	0.0	1.34	+0.143
WBCHVGF$_{50}$	−4.2	−3.0	0.0700	0.0	1.37	+0.03

"Nose flap 30° with all T.E. flap deflections.
[b]Compared with WBCHV.

Drag Curves, Flaps Up and Down

The designer is particularly interested in $C_{D,min}$ because of its effect on aircraft performance. To ensure accuracy in this range, the readings should be made every degree near $C_{D,min}$. Aircraft $C_{D,min}$ will vary widely with the type of airplane and wing loading, a value of 0.0120 not unreasonable for a clean fighter.

The airplane drag coefficient C_D at $C_{L,max}$ is needed for takeoff and landing calculations. Varying widely, depending on type of airplane and amount of flap, this coefficient may range from 0.1000 to 0.5000.

The shape of the drag curve is important for climb and cruising, a minimum change with C_L being desirable.

Drag data for a twin-jet fighter are shown in Table 13.6. Of interest here is the decrease of effective induced drag when flaps are down. The increments of drag due to, for example, gear, flaps, and tip tanks are presented on a basis of wing area for consideration on the particular airplane at hand. It is also common to see them quoted on their own frontal area so that their losses may be compared from airplane to airplane.

Pitching Moment Curve

The slope of the pitching moment curve must be negative for stability, of course, although definite values for the desired slope are not agreed upon. Goett[12] gives an excellent discussion of wind tunnel procedure for finding the critical stability and control characteristics for single- and twin-engine propeller-driven aircraft.

Quite often in reducing data the moments are calculated referenced to a nominal center-of-gravity location (usually near 25% MAC) and at desired forward and aft center-of-gravity limits. The forward and aft center-of-gravity limits usually allow for the destabilizing effects of power and possibly free controls depending on the aircraft's control system. It is often necessary to test for power effects on propeller aircraft with low-power loadings.

Sometimes the stability is stated in terms of the added rearward travel possible before reaching neutral stability. For extensive discussion of these issues see the excellent text by Etkin and Reid.[13] This might be 0.1 MAC, meaning that the aircraft will still be stable if the center of gravity is moved one-tenth chord aft of the normal rearward location. It should further be stated whether this is for a control-free or control-fixed condition.

The forward center-of-gravity location is not as restricted for many modem high-performance aircraft equipped with *unit horizontal tail* or *stabilators* that are power operated. The stick force is not a function of center of gravity, since it is artificial and can be programmed as desired by the control system designers. There is no distinction between stick-fixed and stick-free stability for these irreversible control systems for which no "floating" is possible.

In general, the pitching moment curves are used to determine if the airplane has positive static stability throughout the desired center-of-gravity range at all flight conditions (cruise, takeoff, landing). The airplane's controls must be able to trim the aircraft under the same range of conditions. The aft center-of-gravity limit is a function of stability (slope) and determines the tail area for a given tail length while the forward center-of-gravity limit is a function of control, $C_{m,CG} = 0$, usually in landing configuration near the ground, and determines the required elevator size and travel. For swept-wing aircraft special attention is paid to pitch up as it will Limit the usable C_L. Static stability does not guarantee dynamic stability, but usually it is a prerequisite unless there is to be a full-time active control system.

The lift, drag, and moment data are usually presented on one sheet (see Figure 13.26). The reversal of the moment positive and negative values makes the moment curve appear "normal" when viewed with the page on end.

Longitudinal stability data for two airplanes are listed in Tables 13.7 and 13.8. Of interest is the customary destabilizing effect of the fuselage and of course the large stabilizing effect of the horizontal tail. For performance calculations trimmed values of C_L and C_D are often desired. These can be constructed as described in Figure 13.27.

TABLE 13.7. Longitudinal Stability Data for Single-Engine Propeller Airplane with Power Off

Configuration	C_{m0}	ΔC_{m0}	$C_{L,\text{trim}}$	$\frac{dC_m}{dC_L}$	AC
W	−0.021	—	0.50	0.042	25.8
WB	−0.036	−0.015	0.40	0.091	20.9
WBH	0.062	0.098	0.53	−0.120	42.0
WBHV	0.032	−0.029	0.25	−0.130	43.0
WBHVF$_{30}$	0.102	0.070	0.86	−0.118	41.8
WBHVF$_{55}$	0.167	0.065	1.22	−0.138	43.8

Note: **Moment reference at 30.0% MAC, 0.4%above MAC.**

TABLE 13.8. Longitudinal Stability Data for Twin Engine Propeller Airplane with Power Off

Configuration	C_{m0}	ΔC_{m0}	dC_m/dC_L
W	−0.007	—	0.017
WB	−0.015	−0.008	0.025
WBN	−0.020	−0.005	0.085
WBHV	0.024	0.044	−0.102

Note: Moment reference at 30% MAC, on MAC.

With automated systems another approach can be used effectively. The horizontal tail can be pitched remotely until the C_m about the desired center-of-gravity reference location is zero and then all needed data are recorded. This procedure becomes very valuable for aircraft that have very wide ranging pitch control capability. Trim points can be located as indicated here; then a small range of pitch angles about the trim points can be taken to get the slope of the pitch curves near the trim points.

Stabilizer effectiveness $(dC_m/d\delta_s)$ is obtained by holding a_{rr} constant, varying the tail incidence, and measuring the resulting pitching moment data. This slope should be evaluated early in the experimental program, since it is needed for the tail-on wall corrections (see Chapter 10).

Elevator or Stabilizer Power Curve

The plot of ΔC_m against elevator deflection or stabilizer incidence is made at several values of the lift coefficient. It indicates the amount of elevator or stabilizer deflection needed to produce a certain moment coefficient. An example is given in Figure 13.29. Usually the plot is nearly a straight line from +15° to −20" deflection with a slope of about −0.02 for elevators and about twice that for the complete tail.

A further study of the elevator may be made from a plot of $C_{m,CG}$ versus C_L for several elevator angles, as shown in Figure 13.30. The intersections of the curves with the axis indicate trim condition. This plot may also be made against a. The plot for an airplane with a unit horizontal tail would be similar. For propeller-driven aircraft, runs with propellers, windmilling, or at idle power, flaps and gear down are often required.

It is also necessary to determine whether the elevator balance is sufficient to keep the control forces small enough that maximum-load factors may be developed. The control force criterion is usually critical in landing or accelerated flight, flaps and gear up, props windmilling.

Aileron Power Curves

The aileron criteria are usually determined at zero yaw and may be considered from the plots of C_l versus C_n (Figure 13.17), and C_l and C_n versus δ_a (Figure 13.19), and C_{Ha} versus δ_a (Figure 13.18). The important qualities of good ailerons are high
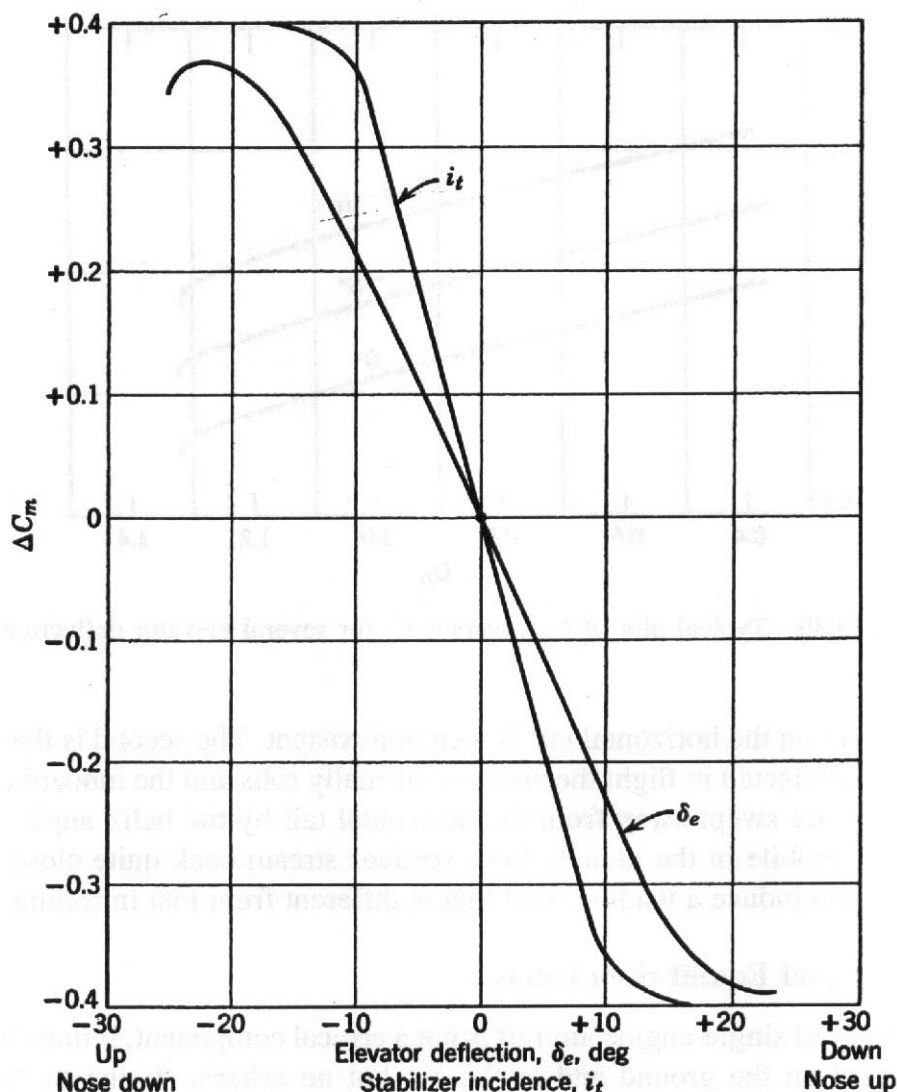
FIGURE 13.29   Typical plot of change in moment coefficient with elevator and stabilizer deflection.

rolling moment and low hinge moments (the latter can also be obtained from panel models). The maximum rate of roll and the maximum helix angle are determined from $C_{l,\max}$, with a $C_{l,\max}$ of 0.03 being satisfactory for one aileron.

The above information is obtained from runs at the proper angles of attack with $\psi = 0$. The rolling moments are measured for various aileron deflections and the helix angles computed. (See runs 44-63 in Table 13.5.)

When taking aileron or rudder data, a small amount of rolling and yawing moment and side force is usually found even when the controls are neutral and there is zero yaw. This delta is due to asymmetrical flow in the tunnel, model asymmetry, or some hysteresis due to small separation areas. Both the appearance and the usefulness of the data are improved if aileron and rudder moments at zero yaw are subtracted from the data.

It is a nice refinement to run aileron tests with the horizontal tail off for two reasons. The first (and minor one) is that it saves effort in data reduction since
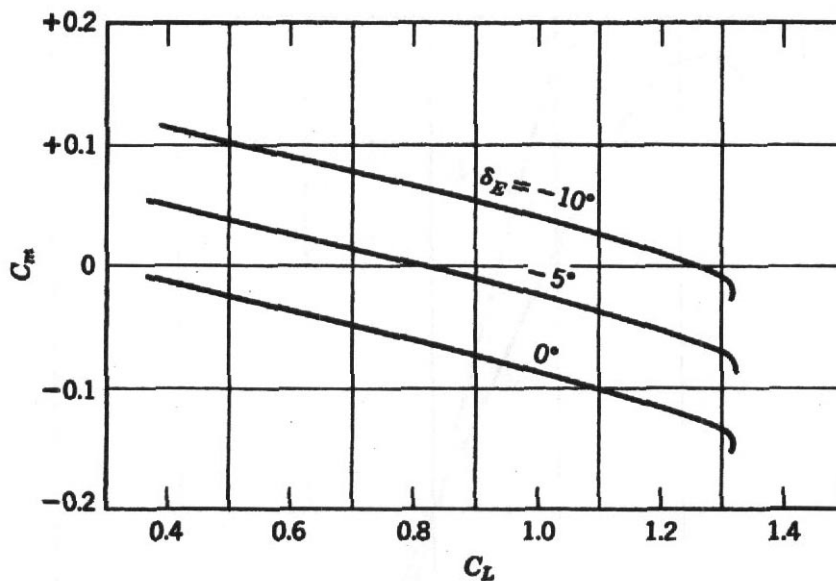
FIGURE 13.30   Typical plot of $C_{m,CG}$ versus C_L for several elevator deflections.

tunnel wall effect on the horizontal tail is then nonexistent. The second is that when the ailerons are deflected in flight the airplane normally rolls and the inboard aileron trailing vortices are swept away from the horizontal tail by the helix angle. When the model is immobile in the tunnel, these vortices stream back quite close to the horizontal tail and induce a loading on it that is different from that in rolling flight.

Rudder Power and Equilibrium Curves

The rudder for most single-engine aircraft is not a critical component. It must furnish adequate control on the ground and in the air, but no criteria similar to "rate of roll" or "pounds of stick force per g" have been established. The problem of the propeller-driven high-powered single-engine aircraft becomes difficult under the high-power, low-air-speed (wave-off) condition. Here it is not unusual to require full rudder to overcome torque to maintain straight flight. The criteria become more those of hinge moments than those usually obtainable from the complete model. Particular attention must be paid to avoiding overbalance at high rudder deflections.

The modem high-performance multiengine airplane must possess sufficient directional stability to prevent it from reaching excessive angles of yaw or developing rudder forces that tend to keep the plane yawing. Furthermore, it must also be able to be balanced directionally at the best climb speed with asymmetric power (one engine out, the other at full power for a two-engine airplane) as specified by the FAA and the military.

The most critical condition for the criterion of decreasing rudder pedal force occurs at high thrust coefficient, flaps and gear down, at large angles of side slip. For propeller aircraft depending on propeller rotations the side-slip angle may be critical to the right or left, and test runs must be made accordingly.

The asymmetric power[14] condition requires yaw runs at the attitude corresponding to $1.2V_{stall}$ gear down, flaps at takeoff setting, takeoff power on right engine, left engine windmilling.

Usually the rudder information is grouped into two curves. The first, rudder equilibrium, is a plot of rudder deflection against angle of yaw, or in other words, δ_r for $C_n = 0$. This need be taken for yaw in only one direction, for it will be similar in the other direction. The slope $d\psi/d\delta_r$ can be about -1.2 for maneuverable airplanes on down to -0.5 for the more stable types. An example curve is shown in Figure 13.31.

The second curve, rudder power, is a plot of C_n versus δ_r. A slope of $dC_n/d\delta_r = -0.001$ is reasonable but varies with airplane specifications; one usual criterion is "one degree slip per degree rudder deflection"; that is,

$$\frac{dC_n/d\delta_r}{dc_n/d\psi} = \frac{d\psi}{d\delta_r} = 1.00$$

Again the curve need be plotted only for either plus or minus rudder. An example curve is shown in Figure 13.32.

The effect of yaw on the characteristics of an airplane is shown in Figure 13.33.

Comparison of Lateral to Directional Stability

Information about the roll axis is needed to determine whether sufficient dihedral is incorporated in the design to provide lateral stability at the most critical condition.
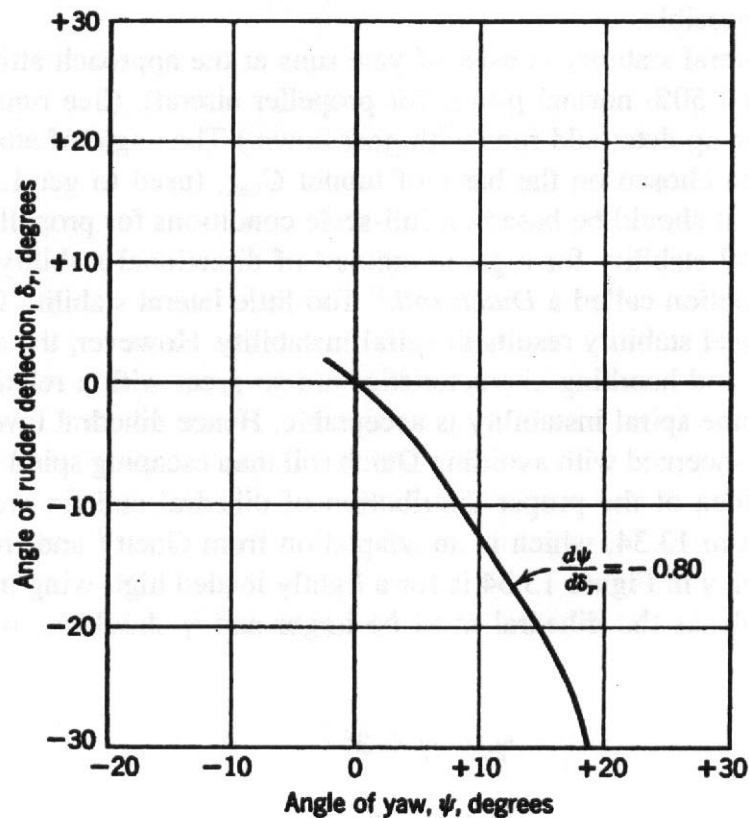
FIGURE 13.31   Rudder equilibrium.
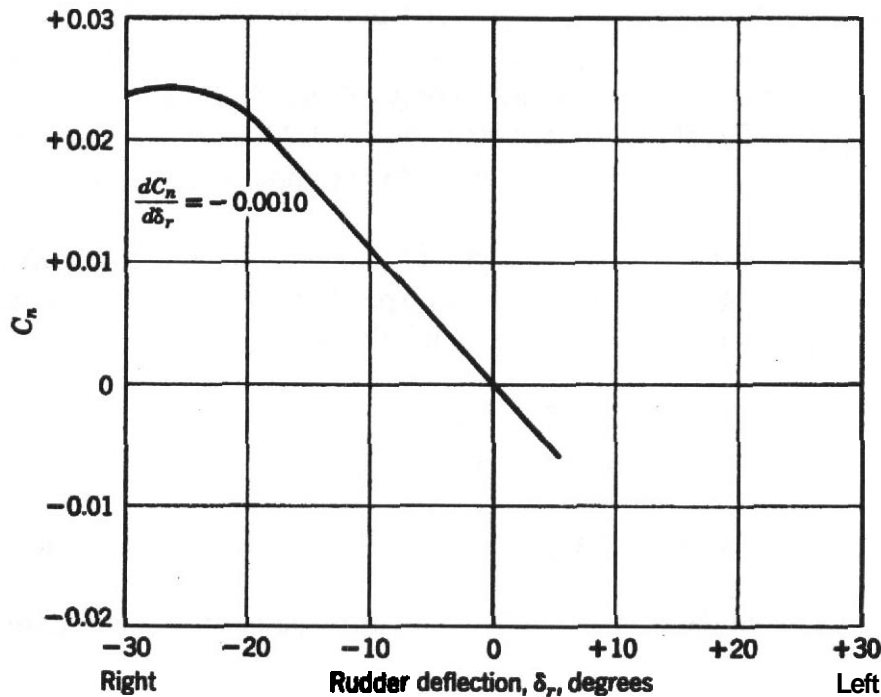
FIGURE 13.32   Rudder power.

This will be, for most propeller aircraft, the approach with flaps down and power on, where power and flaps combine to reduce the dihedral effect. The ailerons should be free if possible.

The tests for lateral stability consist of yaw runs at the approach attitude, flaps and gear down, and 50% normal power for propeller aircraft. (See runs 90–95 in Table 13.5 for gear-up data; add runs with gear down.) The angle of attack for the approach should be chosen on the basis of tunnel $C_{L,\max}$ (used to get $1.2V_{\text{stall}}$), but the thrust coefficient should be based on full-scale conditions for propeller aircraft.

Too much lateral stability for a given amount of directional stability results in an objectionable motion called a Dutch *roll*.[13] Too little lateral stability for a given amount of directional stability results in spiral instability. However, the advantages in general control and handling characteristics are so great with a relatively large vertical tail that some spiral instability is acceptable. Hence dihedral investigations are usually more concerned with avoiding Dutch roll than escaping spiral instability.

A very rough idea of the proper distribution of dihedral and fin area may be obtained from Figure 13.34, which is an adaptation from Goett[12] and from Figure 13.35. The value of γ in Figure 13.34 is for a lightly loaded high-wing monoplane. For low-wing airplanes the dihedral must be larger and γ should be replaced by γ_L, where

$$\gamma_L = \gamma + 3°$$

The 3° difference between high and low wing configurations is due to fuselage cross-flow effects. The effective dihedral, not the strict geometric dihedral, is
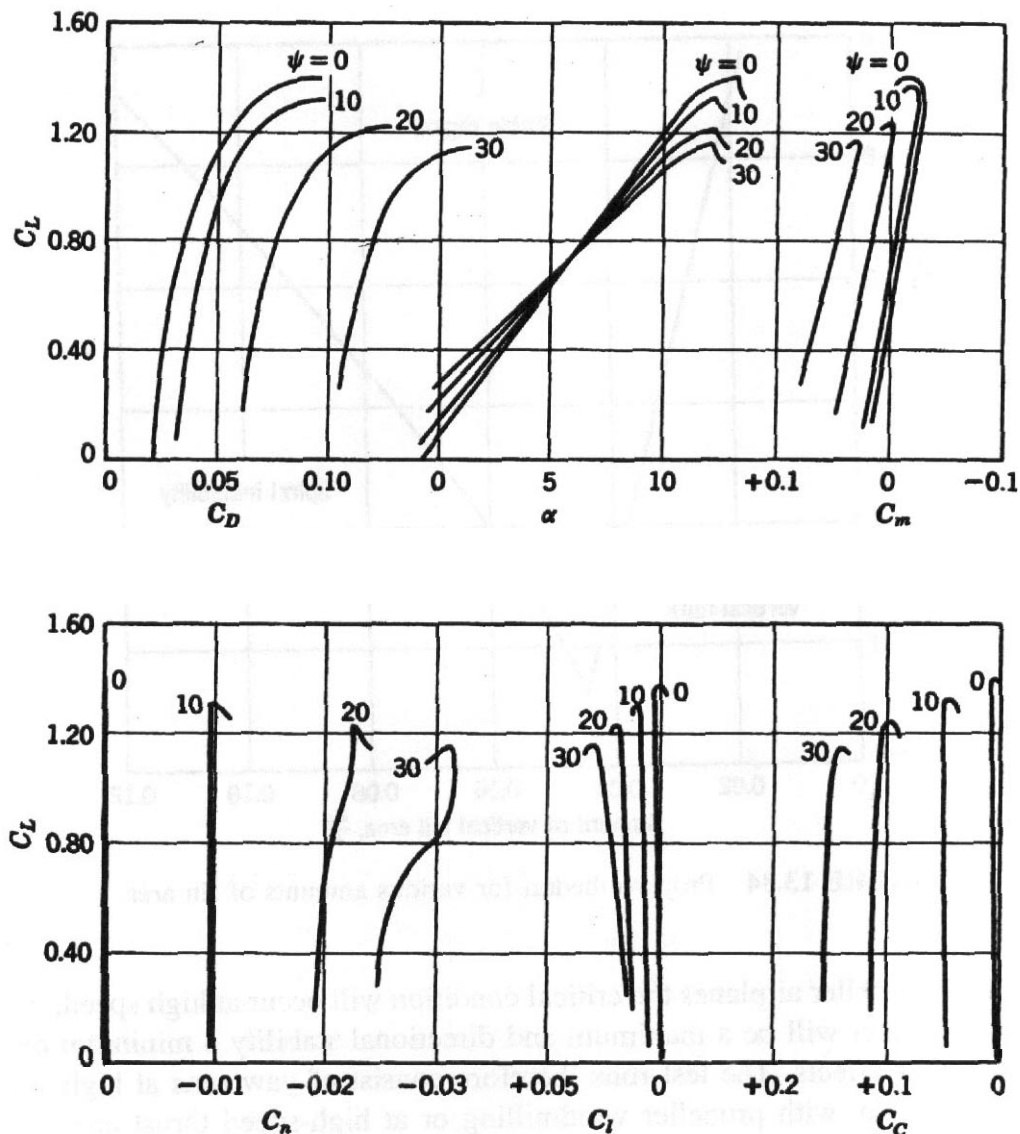
FIGURE 13.33   Effect of model **yaw** on basic **characteristics.**

the important value. The effective dihedral is obtained by using the following rule: $dC_l/d\psi = 0.0002$ is equivalent to $1°$ effective dihedral. Wing sweep also can have a pronounced effect on the effective dihedral; highly swept-back wings display too much dihedral at moderate lift coefficients and are normally constructed with no geometric dihedral.

Since a geometric wing dihedral alone does not indicate the overall effective dihedral, which includes vertical tail, wingtip shape, sidewash, and power effects for propeller aircraft, a more quantitative indication of the effect of combinations of directional stability and effective dihedral is shown in Figure 13.35. As shown, excessive dihedral coupled with weak weathercocking leads to the oscillatory or Dutch roll boundary. Excessive directional stability leads to the spiral divergence boundary. The complete wind tunnel model yields the total stability and dihedral including all interference effects.
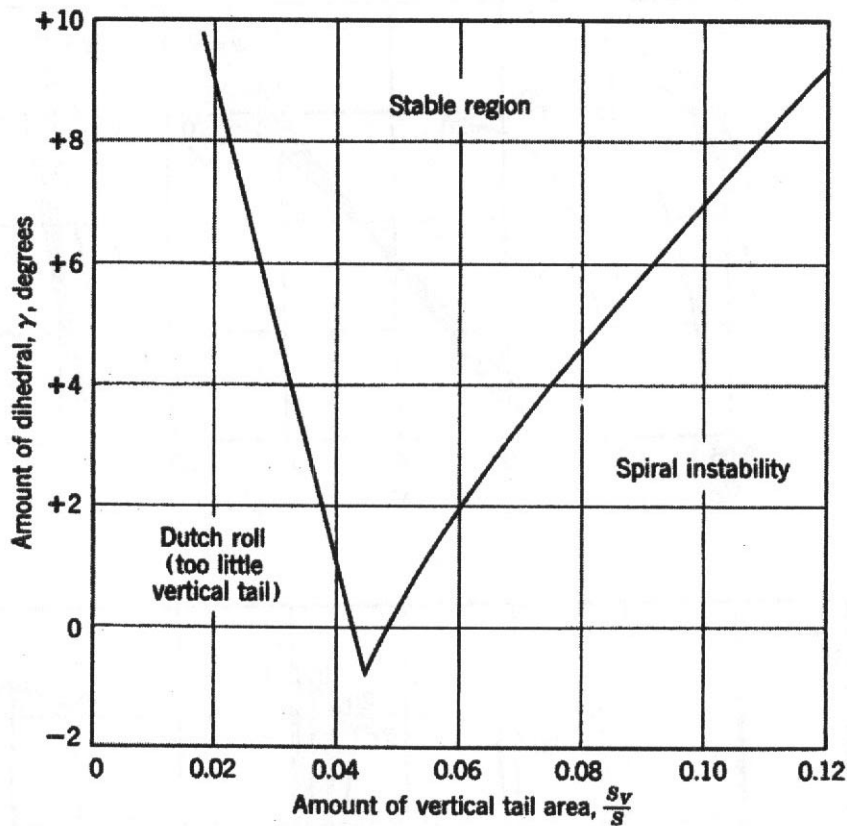
FIGURE 13.34   Proper dihedral for various amounts of fin area,

For most propeller airplanes the critical condition will occur at high speed, where the dihedral effect will be a maximum and directional stability a minimum owing to small power effects. The test runs therefore consist of yaw runs at high speed, flaps and gear up, with propeller windmilling or at high-speed thrust coefficient. Experience indicates that a value of roll to yaw that can be expected to give what pilots call satisfactory stability is

$$\frac{dC_l/d\psi}{dC_n/d\psi} \cong -0.8 \qquad (13.37)$$

Data for one experiment are given in Table **13.9**.

Lateral wind tunnel data is usually plotted as C_L, C_D, C_m, C_n, C_l, C_C, or C_Y versus ψ (yaw angle) or β (side-slip angle). A typical example is shown in Figure **13.36.** The generally preferred axis system is the stability axis system.

As discussed in Chapter 7, most external balances measure forces and moment directly in wind axis components, an axis system aligned with the tunnel centerline, while internal balances measure in body axis components, which pitch, roll, and yaw with the airplane model. In lateral stability it is desirable to use stability axes that yaw with the model but do not pitch. The equations to transfer from wind axes to body or stability axes and for body to wind axes are given in Chapter 7.

When yaw runs are presented on stability axes the cross-wind force is replaced with the side force C_Y and the drag C_D is along the airplane centerline. No particular
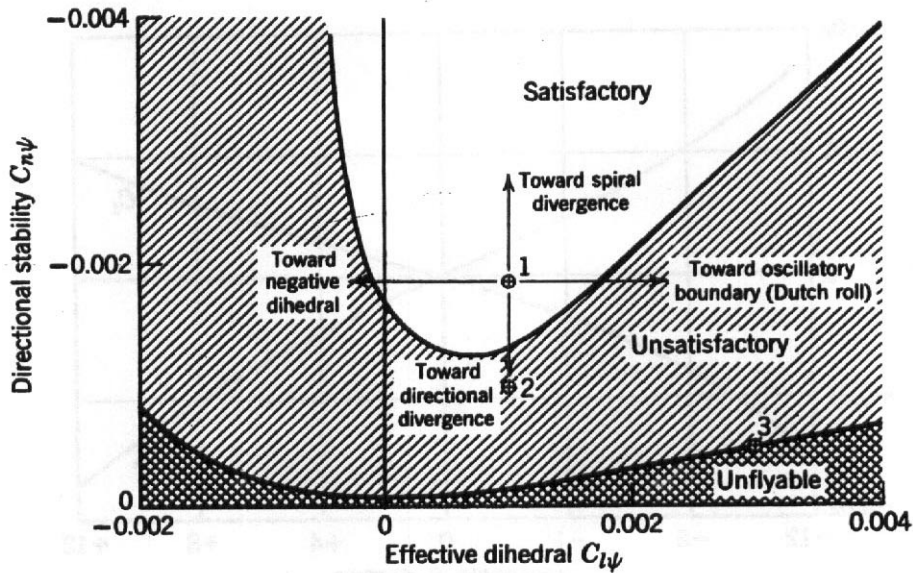
FIGURE 1335   **Free-flight** tunnel results showing good and bad combinations of $C_{n\psi}$ and $C_{n\psi}$.

slope or values of C_Y are required. The only use of C_Y is to calculate the side force for asymmetrical flight and hence the necessary angle of **bank** to counteract said side force with a tangent component of lift. The side force needed to overcome the torque reaction at low speed while maintaining straight flight may also be evaluated for propeller-powered aircraft.

Tailsetting and Average Downwash Angle

To avoid the drag of cruising with elevators deflected and the loss of maximum ΔC_m due to the elevator if a partial elevator is needed for trim, it is usually desirable

TABLE 13.9. Directional Stability **for a** Single-Engine Airplane at **Low** and High Andes **of** Attack

Configuration	α	$C_{n\psi}$	$\Delta C_{n\psi}$	$C_{l\psi}$	$\Delta C_{l\psi}$	dC_l/dC_n
W	2.5"	−0.00012	—	0.00056	—	—
	11.1"	−0.00014	—	0.00037	—	—
WB	2.5"	0.00118	0.00130	0.00058	0.00020	—
	11.1"	0.00082	0.00096	0.00037	—	—
WBH	2.5"	0.00063	−0.00055	0.00070	0.00012	—
	11.1"	0.00027	−0.00055	0.00087	0.00050	—
WBHV	2.5"	−0.00165	−0.00228	0.00210	0.00050	−0.727
	11.1"	−0.00186	−0.00213	0.00087	—	−0.467
WBHVF$_{45}$	2.5"	−0.00230	—	0.00040	—	−0.174
	11.1"	−0.00250	—	0.00012	—	−0.480
WBHVF$_{55}$	2.5"	−0.00230	—	0.00040	—	−0.174
	11.1°	−0.00250	—	—	—	—
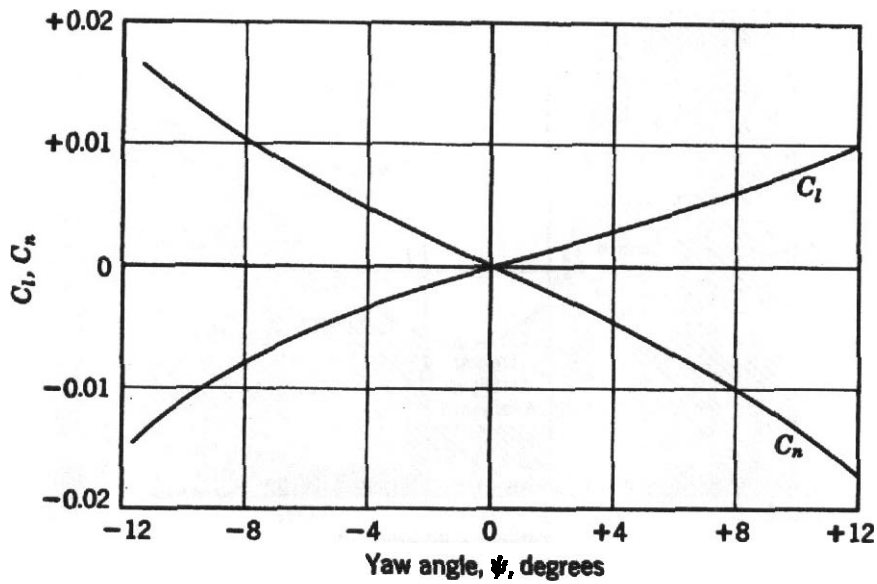
FIGURE 13.36   Typical yaw characteristics.

to set the stabilizer incidence so that the aircraft is trimmed at cruising with $\delta_e =$ 0. For stability considerations as well as correlation for future designs, it is necessary to know the angle of downwash at the tail for each wing angle of attack. The procedure is as follows:

1. Run the model with the horizontal tail removed, obtaining a tail-off stability curve similar to that shown in Figure 13.37.

2. Next run the model with the horizontal tail on, using tail incidence i,, at angles of, say, $-8°$, $-4°$, $0°$, $4°$, and $8°$. Curves as indicated in Figure 13.37 will be obtained.
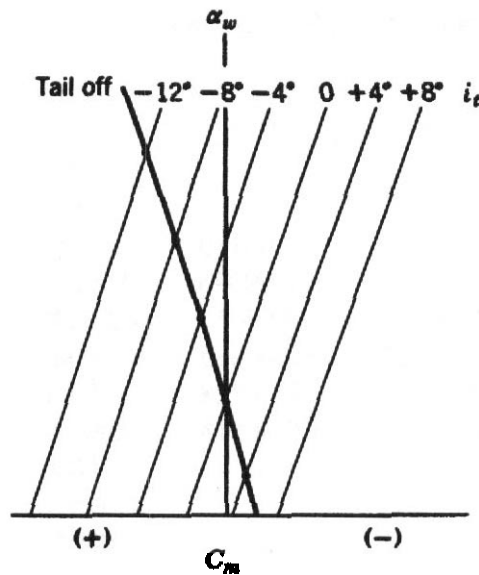
FIGURE 13.37   Pitch moment, tail off and tail on, at various values of tail incidence.
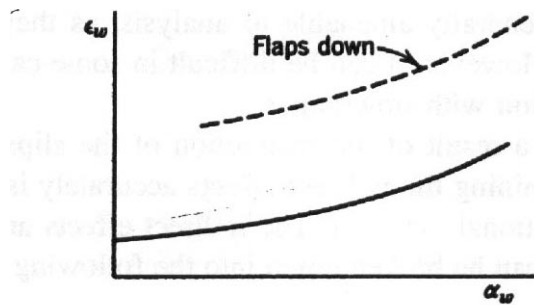
FIGURE 13.38   Downwash at tail, flaps up and flaps down.

Now the intersections of the horizontal tail-on curve with the tail-off curve are points where, for a given wing angle of attack α_w, the tail-on pitching moment equals the tail-off pitching moment; that is, the tail is at zero lift, and hence

$$\alpha_t = \alpha_w + i_t - \varepsilon_w = 0 \tag{13.38}$$

where ε_w is the downwash angle at the tail and α_t, the tail angle of attack.

Since α_t and i_t are known for the points of intersection, ε_w may be determined from Equation (13.38), and a plot of ε_w against α_w or C_L may be made. This plot and the usual effect of flaps on downwash are shown in Figure 13.38. Not infrequently the curve of ε_w against α_w is a straight line.

Methods shortcutting the above lengthy procedure have been devised based on the assumption that the wing downwash is zero at zero lift. However, when a wing is twisted, the total lift is zero, but it is not zero at all spanwise stations. Thus, the wing is usually producing a downwash in the region of the tail. The shortcut is only true for a nontwisted wing. In general, it is better not to use such methods as they eventually lead to errors.

13.4   POWER EFFECTS OF PROPELLER AIRCRAFT

The effect of the propeller on stability and control can be broken down into direct and indirect effects. The direct effects are as follows:

1. Pitching and yawing moments that arise from the thrust line do not pass through the center of gravity.
2. The propeller normal force in the plane of rotation produces pitching or yawing moments. This contribution can be large even at zero thrust coefficients and adversely affects longitudinal and lateral stability.
3. The torque reaction to the propeller.
4. For multiengined aircraft there is a yawing and rolling moment for the engine-out condition. This usually is the critical design condition for sizing the rudder.

The direct effects are generally amenable to analysis, as they involve a force (thrust) and moment arm. However, it can be difficult in some cases to obtain data for the normal force variation with flow angle.

The indirect effects are a result of the interaction of the slipstream with other parts of the aircraft. Determining the indirect effects accurately is very difficult by analytical or even computational methods. The indirect effects are sensitive to the airplane configuration and can be broken down into the following broad categories:

1. effect of slipstream on the moments of the wing, nacelles, and fuselage;
2. effect of slipstream on the wing's lift coefficient due to higher local dynamic pressure over portions of the wing;
3. effect of slipstream on downwash and cross-flow at the tail; and
4. effect of slipstream on the dynamic pressure at the tail.

The effect of slipstream on the fuselage and nacelle moments is usually small compared to other power effects and is difficult to analyze. The slipstream effect on the wing's pitching moment with the flaps down can be large. The same is true for the wing's lift, both with the flaps up and down, which affects stalling speeds power on and off. The partial immersion of the wing in the slipstream will alter the downwash and thus change the angle of attack of the horizontal tail. The normal force at the propeller will also change the downwash at the tail. The rotational component of the slipstream will change the angle-of-attack distribution across the horizontal tail as well as the vertical tail. The critical condition is at high power and low speed. And, finally, the increased velocity of the slipstream will change the tail's contribution to stability. Just how much the downwash due to the propeller, rotation effect, and velocity increase affects the tail's contribution is a function of how much or how little of the tail is immersed in the slipstream. In general, the propeller downwash is destabilizing even at zero thrust.

The displacement of the slipstream in side slip results in one flap being immersed in the slipstream to a greater extent than the other, which reduces the dihedral effect, and this effect is maximized at low speeds and high thrust. From the foregoing discussion, it can be seen that the effect of power tends to be destabilizing both longitudinally and laterally, with the critical conditions generally occurring at high thrust and low speed with the flaps down. For multiengined aircraft, the magnitude of the power effects are also a function of the propeller's direction(s) of rotation, that is, for example, both right handed or one right and one left.

Effect of Power

To illustrate the effect of power, let us look at a single-engine tractor with a wing loading of **39** lb/ft^2 and a power loading of 7 lb/hp. The thrust line of this airplane was very close to the center of gravity. Figure 13.39 shows pitching moment as a function of lift coefficient for several power settings for both flaps down and flaps up. As can be seen from the plots, there is a large change in the longitudinal stability
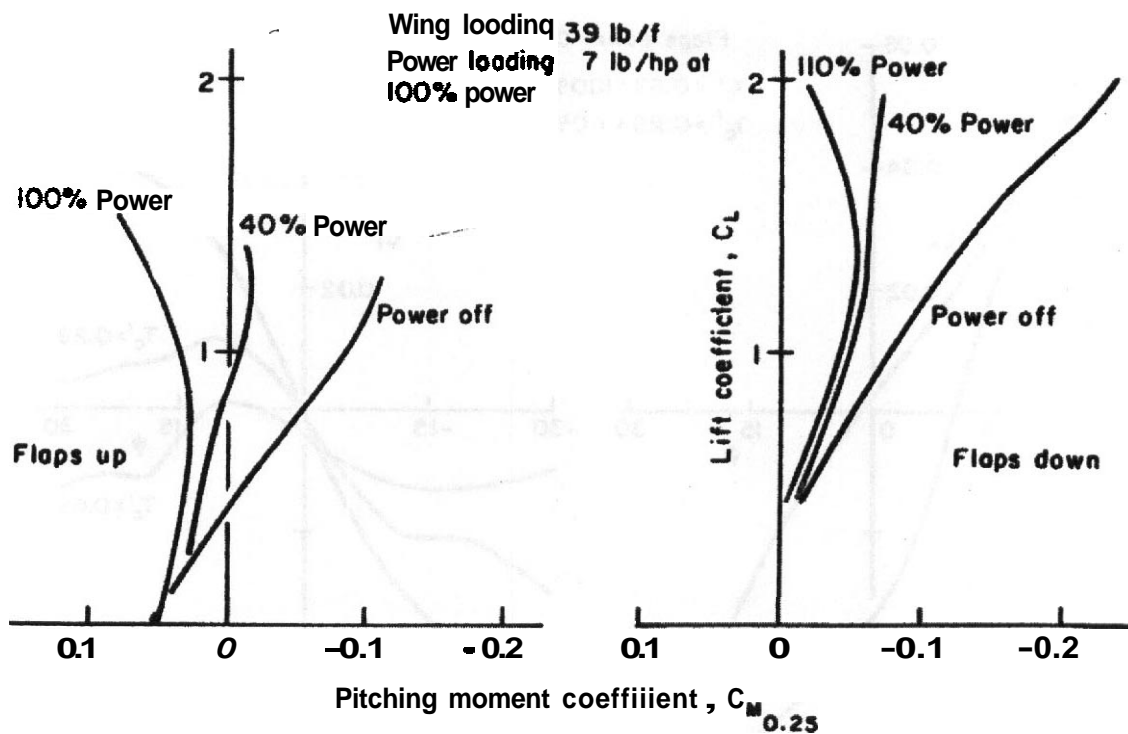
FIGURE 13.39   Effect of power on longitudinal stability.

between power off and 100% power, with both flaps up and down. For this airplane with the flaps up there is about an 80% reduction in the moment curve slope from power off to 100% power and a 50% reduction with the flaps down.

Figure 13.40 shows the effect of power on the lateral characteristics with the flaps down. The effect of the partial immersion of the flaps in the slipstream can be seen in the rolling moment plot. These figures show that the effect of power can be dramatic in a high-performance airplane. Fortunately, the above effects may be evaluated in the wind tunnel, and the aircraft may be revised and/or the flight test pilot forewarned.

Propeller Characteristics   The simulation of the propeller slipstream for a constant-speed propeller requires matching both the axial and rotational velocity ratios. To match these ratios over the entire range of lift coefficients would require an adjustable pitch propeller. However, a satisfactory approximation of the slipstream may be accomplished with a single setting of a fixed-pitch model propeller over a large part of the lift coefficient range where power effects are of importance. From momentum theory, it can be found that the axial velocity ratio can be matched with a propeller of scale diameter. The rotational velocity can be matched by using a geometrically similar propeller operating at the proper advance ratio. Typical fixed-pitch model propellers have aluminum or steel blades with steel hubs and allow the blades to be set over a wide range of pitch angles. In other words the blade angles are adjustable between runs but not during a run as for full-scale constant-speed propellers.
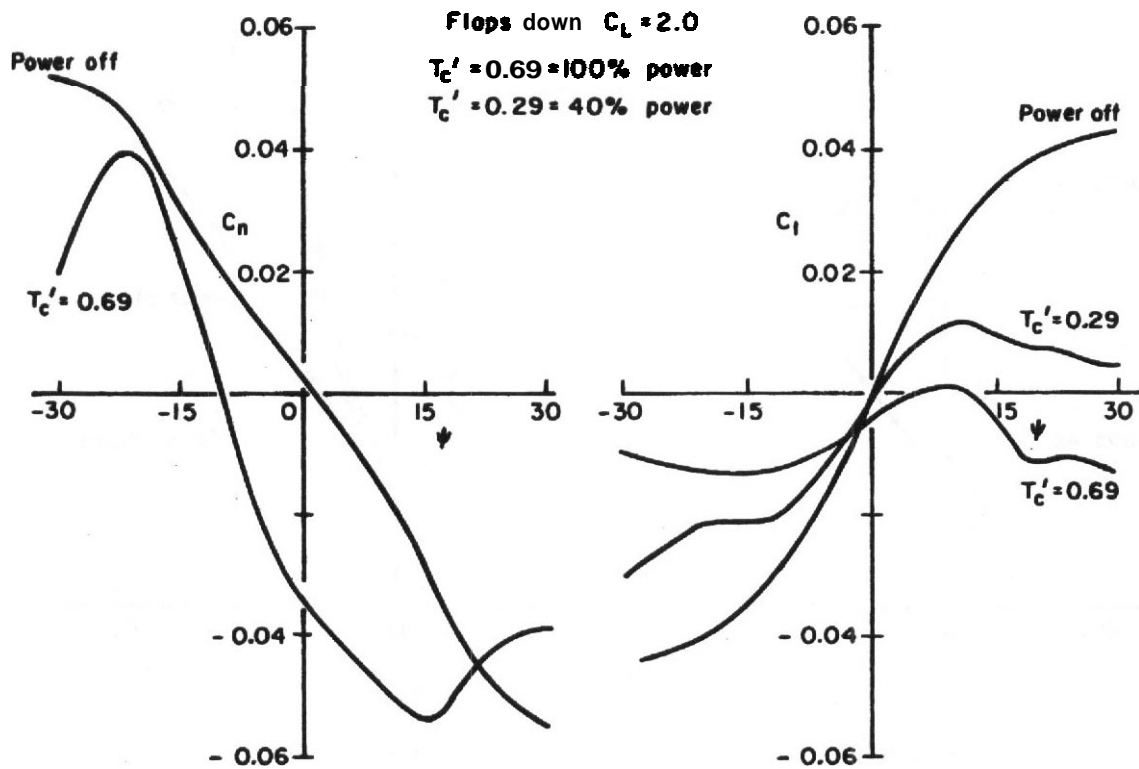
FIGURE 13.40 Effect of power on lateral stability.

We have briefly discussed propeller evaluations earlier (see under Propellers in Section 13.2).

The relationships between model and full-scale propellers are obtained as follows. Thrust and torque coefficients are defined by the equations

$$T_c = \frac{T}{\rho V^2 d^2} \tag{13.39}$$

$$Q_c = \frac{Q}{\rho V^2 d^3} \tag{13.40}$$

where T and Q are thrust and torque, respectively, and d is the propeller diameter. The advance ratio J is defined as

$$J = \frac{V}{nd} \tag{13.41}$$

A propeller of a given shape moving along its axis will have the thrust and torque coefficients as functions of advance ratio, Reynolds number, and Mach number according to the considerations discussed in Chapter 1. In other words, we will have $T_c = f(J, R_e, M)$ and $Q_c = g(J, R_n, M)$. So long as the Mach number stays comfortably subsonic, the dominant dimensionless parameter is the advance ratio J. The Reynolds number for the scale model cannot be matched to the full-scale value.

Using subscript S for full-scale airplane and subscript M for model, we have, for similarity,

$$\frac{V_s}{n_S d_S} = \frac{V_M}{n_M d_M} \tag{13.42}$$

Also

$$T_{cM} = \frac{T_M}{\rho V_M^2 d_M^2} \quad \text{and} \quad T_{cS} = \frac{T_S}{\rho V_S^2 d_S^2} \tag{13.43}$$

Dividing produces

$$\frac{T_{cM}}{T_{cS}} = \frac{T_M}{\rho V_M^2 d_M^2} \frac{\rho V_S^2 d_S^2}{T_S} \tag{13.44}$$

Substituting from Equation (13.42) and clearing, we obtain

$$\frac{T_{cM}}{T_{cS}} = \frac{T_M}{T_S} \frac{n_S^2 d_S^4}{n_M^2 d_M^4} \tag{13.45}$$

and it can be shown that the thrusts are

$$T_S = \rho n_S^2 d_S^4 C_{TS} \quad \text{and} \quad T_M = \rho n_M^2 d_M^4 C_{TM} \tag{13.46}$$

and that, for a given V/nd, if the two propellers are geometrically similar, $C_{TS} = C_{TM}$ with scale effect omitted. Hence

$$\frac{T_M}{T_S} = \frac{n_M^2 d_M^4}{n_S^2 d_S^4} \quad \text{and} \quad \frac{T_{cM}}{T_{cS}} = 1 \tag{13.47}$$

or, if the model is tested at $T_{cM} = T_{cS}$, similarity of thrust will be preserved. In a similar manner, Q_{cM} should equal Q_{cS}.

The motors used to drive the propeller are usually of small diameter and high-power output. They are generally water-cooled, variable-frequency, alternating-current motors. These motors operate at frequencies up to 400 Hz with maximum voltages of 240 or 480 V. Maximum rpm varies between 12,000 and 24,000 rpm. Motors have either a two- or four-pole tachometer. The rpm is best measured by counting the tachometer frequency and dividing by 60 or 30 to get the rpm. The motors also have one or two built-in thermocouples to monitor their temperature. One limitation on the choice of a motor is the physical size of the model into which it must fit. Another consideration in selecting a motor is that usually maximum power can only be held for 1 or 2 min before overheating: thus the motor should be selected to avoid continuous operation near maximum power. This problem can be reduced by operating at a lower wind tunnel velocity.

A **variable-speed** alternator is used to supply power to the motors. It must have a variable-frequency range commensurate with the motor rpm requirements. Since the motors require a specified volts-per-cycle input to minimize current and thus heating, the power source must match the motor's specified volts-per-cycle range.

The wire bundle providing power and water to the model motors should be brought into the model on a lower surface. The bundle should have some sort of fairing around it to make the model support tares more repeatable.

Selecting the motor is dependent on test velocity and vice versa. Knowing full-scale flight conditions and power setting to be simulated, model power may be calculated by the equation

$$P_M = P\left(\frac{\sigma_M}{\sigma}\right)\lambda^2\gamma^3 \tag{13.48}$$

where λ is the model scale, y the model test velocity per full-scale velocity, and σ the density ratio. Knowing the model scale, a plot can be constructed of required power versus lift coefficient, as sketched in Figure 13.41 for a range of dynamic pressures. Lines of constant rpm may also be plotted. Limits on rpm are defined by the motor characteristics and considerations of tip losses if the model propeller tip speed is higher than full-scale tip speed.

Model Propeller Calibration

With the tunnel test velocity determined, the selection of an appropriate blade angle can be accomplished. This required the full-scale information shown in Figure 13.42:

1. a plot of T_c' versus C_L for the power setting to be simulated, $T_c' = C_{D,\text{power-off}} - C_{D,\text{power-on}}$;
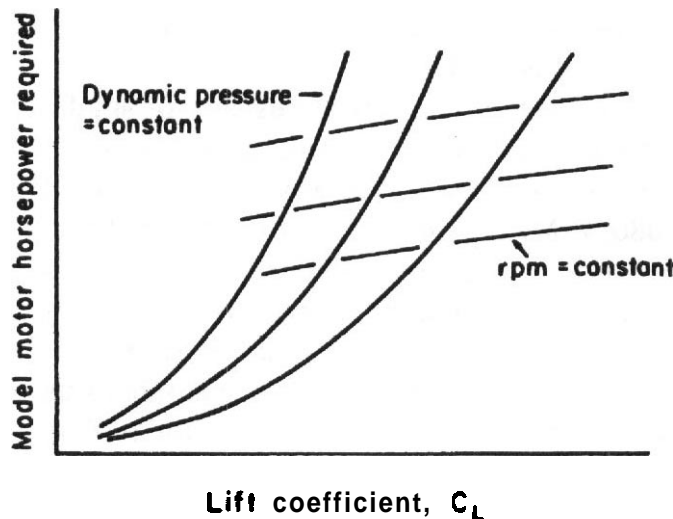
FIGURE 13.41   Model motor power requirements.
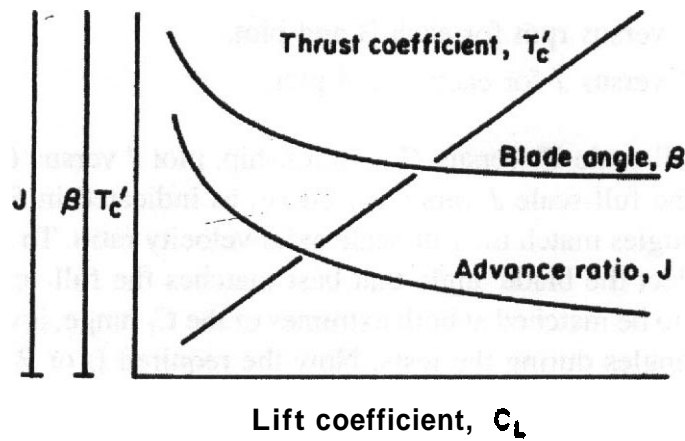
FIGURE 13.42   Full-scale airplane propeller characteristics.

2. a plot of **J** versus C_L (**J** = advance ratio = V/nd, **n** = **rpm**);
3. a plot of **β** versus C_L; and
4. the range of lift coefficients that are to be simulated.

Then, with the model in the tunnel at the minimum drag point, runs are made at several values of **β**, which cover the range of full-scale **β's** over the desired C_L range. A run is also made with the propeller off, and the difference in drag between power off and power on determines T_c'. Thus, for each **β** selected a run should be made through the **rpm** range of the motor and drag, test-section static temperature, and pressure for each motor rpm should be recorded. These data are indicated in Figure 13.43:
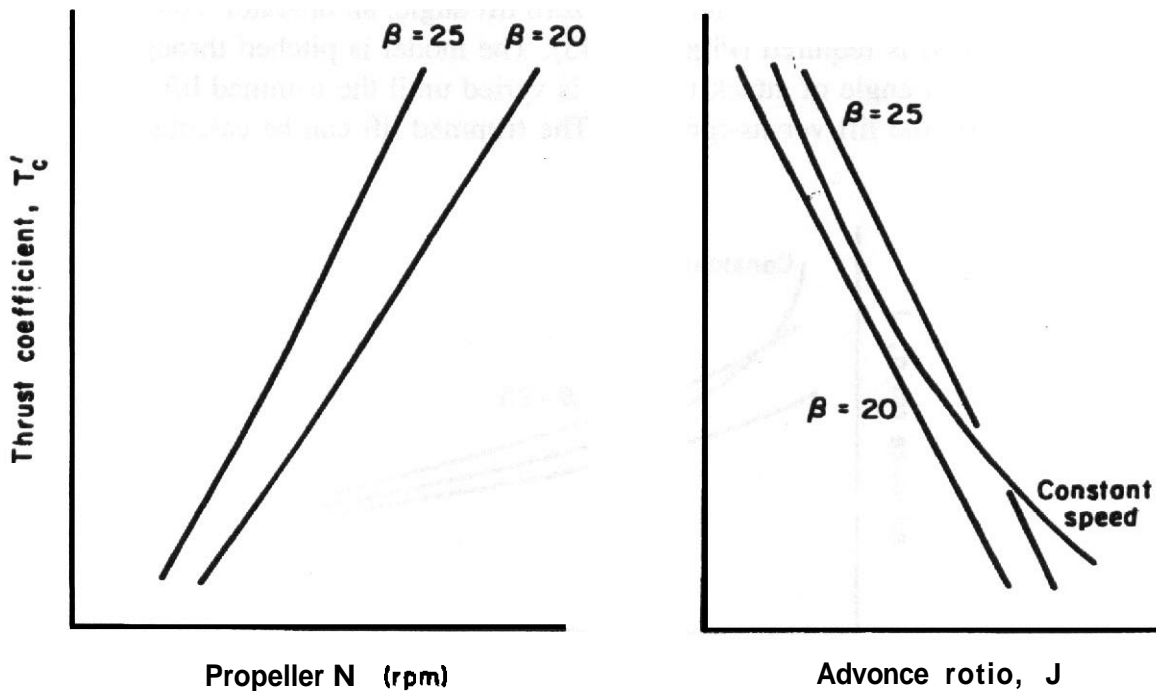
FIGURE 13.43   Model propeller blade angle selection.

1. Calculate T_c'' versus rprn for each β and plot.
2. Calculate T_c' versus J for each β and plot.

To match the full-scale T_c'-versus-C_L relationship, plot J versus C_L for each β on the plot that has the full-scale J versus C_L curve, as indicated in Figure 13.44. As plotted, all blade angles match the full-scale axial velocity ratio. To match rotational velocity ratios, select the blade angle that best matches the full-scale curve. If the rotational effect is to be matched at both extremes of the C_L range, it will be necessary to use two blade angles during the tests. Now the required β or β's for the model propeller as well as the relationship between T_c' and rpm for those β's are known. If the static temperature and pressure vary from values used in calibration, the test rpn is adjusted to hold the advance ratio at the same value used in calibration.

Experimental Methods for Powered Models

Two different methods are commonly used for powered experiments. The first is to test at a constant thrust coefficient, that is, constant rpm. The Tf-versus-rpm plot of Figure 13.42 is used to select the proper rpm. A series of runs are made at different T_c' values. The data may be used directly for yaw runs and calculation involving no air speed charges, such as short period motions. The data may be cross-plotted to match the full-scale airplane T_c'-versus-C_L relationship for information when the airplane velocity does change. The second method involves testing at constant power. The rpm is varied to match the T_c'-versus-C_L relationship of the full-scale airplane. A plot of model lift versus rpn as indicated in Figure 13.45 is required and is obtained from the T_c'-versus-C_L and T_c'-versus-rpm plots as given in Figure 13.42.

For each configuration that changes the zero lift angle, an operator's plot of rprn versus a indicated is required (Figure 13.45). The model is pitched through the a range, and at each angle of attack the rprn is varied until the trimmed lift and rprn match a point on the lift-versus-rpm plot. The trimmed lift can be calculated from
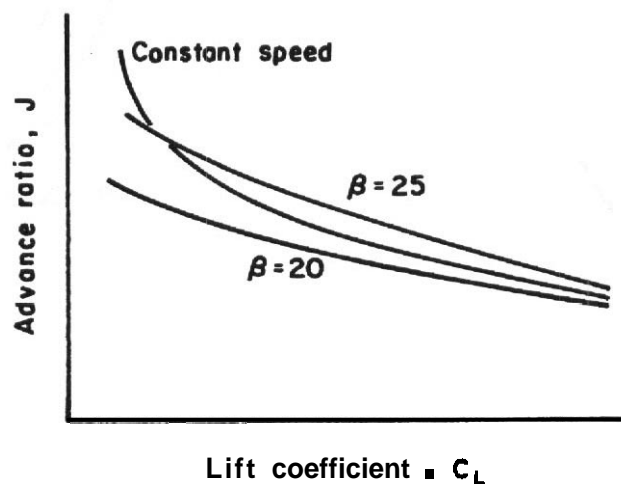
FIGURE 13.44   Model propeller final selected blade angle,
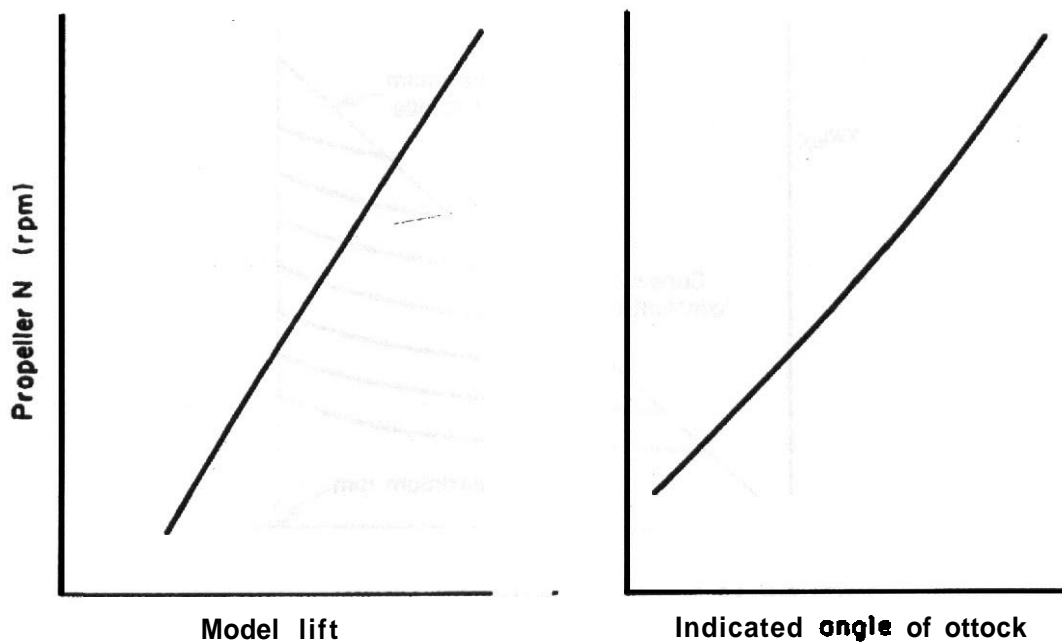
FIGURE 13.45   Model power operating charts.

the balance pitching moment and lift readings. Additional runs with the same configuration but with different tail angles, for example, can use the same operator's plot. The data generated can be used directly in calculations where the airplane velocity is variable. For calculations involving other T_c'-versus-C_L relationships, additional constant power runs at different powers must be made to allow cross-plotting the data. As can be seen, the second method is more time consuming than the first. In practice a combination of the two methods is often used. Various $T_c' =$ constant runs are made that allow the construction of different T_c'-versus-C_L relationships. Constant-power runs at the maximum engine power may be made to give a closer definition of the curves than would be obtained by cross-plotting the $T_c' =$ constant data. It should be noted that if the airplane power is increased, the constant-power runs yield no data that can be extrapolated for the new engine.

If it is desired to match both the axial velocities of T_c' and rotational velocities Q_c, the model propeller must be exactly geometrically similar to the full scale and the test run at the same J's. If there is room in the model, the motor and propeller can be mounted on a strain gage balance that will measure the torque and yield Q_c. If a torque balance cannot be installed in the model, the following procedure can be used: Set the motor in a dynamometer and obtain curves for bhp for various values of rpm and input kilowatts. The results will yield a plot similar to Figure 13.46. When making the calibration, monitor the motor temperature to not exceed limits or stall the motor as there is great risk of burning up the windings. It also should be noted that most AC voltmeters and ammeters are intended for 60 Hz. They may not be accurate at other frequencies.

As outlined before, when the model is in the tunnel to calibrate Tf-versus-rpm, also measure Q_c from the torque balance or the input kilowatts. Then for several values of β plot T_c' versus Q_c, as shown in Figure 13.47. The curve for the actual
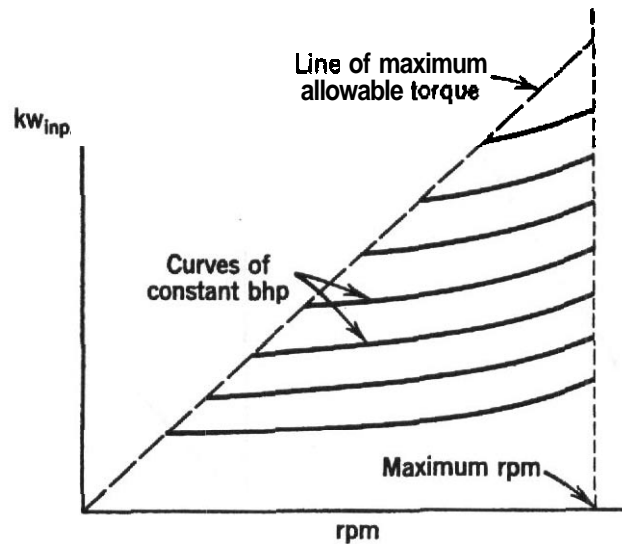
FIGURE 13.46 Model motor dynamometer chart.

propeller is put on the same plot. From this plot select a model β that most closely matches the full-scale propeller. If the full-scale propeller is a constant-speed propeller, it may be necessary to pick two model β's to match high and low speeds or J's as before.

The test is then mn as described before in the constant-power method. Either Q_c from the torque balance of input kilowatts should be recorded with the data. If desired, constant T_c' runs can be made for cross-plotting.

Table 13.10 lists power and sizes of some electric motors used for this purpose and photographs are shown in Figures 13.48 and 13.49.

Because of the small size of hydraulic motors and the high rpm they develop, they are now being used in many instances for V/STOL propeller drive systems. Typically, pressures of 600 to 5000 psi are needed to meet the power requirements. Some performance curves for a typical hydraulic motor are shown in Figure
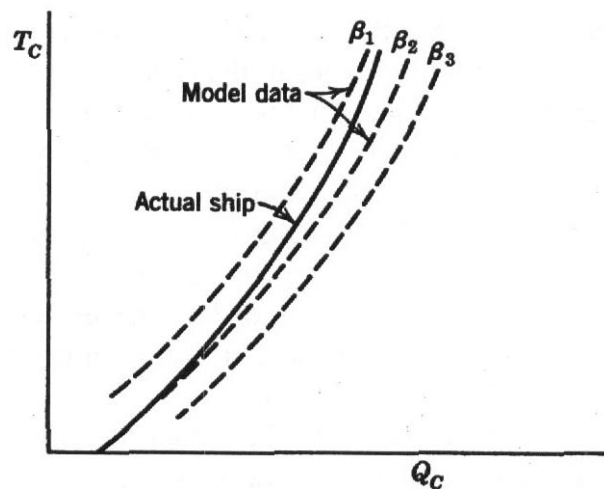
FIGURE 13.47 Model and full-scale propeller performance.

TABLE 13.10. Dimensions of Some Wind Tunnel Electric Model Motors

Horsepower	Diameter (in.)	Length (in.)	rpm
6.4	2.16	12.00	12,000
9	2.2	7.5	27,000
20	3.2	7.0	18,000
35	4	10.0	18,000
52	4	17	11,500
75	4.5	12	18,000
130	8	16	5,400
150	7.5	14	8,000
200	10	33	5,000
1000	28	38	2,100

13.50. Also available are some air-driven turbines that can be used to drive propellers. When considering such a device, it should be borne in mind that the required rpm for propeller windmilling cases is usually much less than the free wheeling rpm of the propeller. Thus, the turbine must be capable of holding such rpm.

The problem of "jumping the balance" with water lines, power leads, and so on, is quite simple as once the desired water flow rate is established (and not changed)
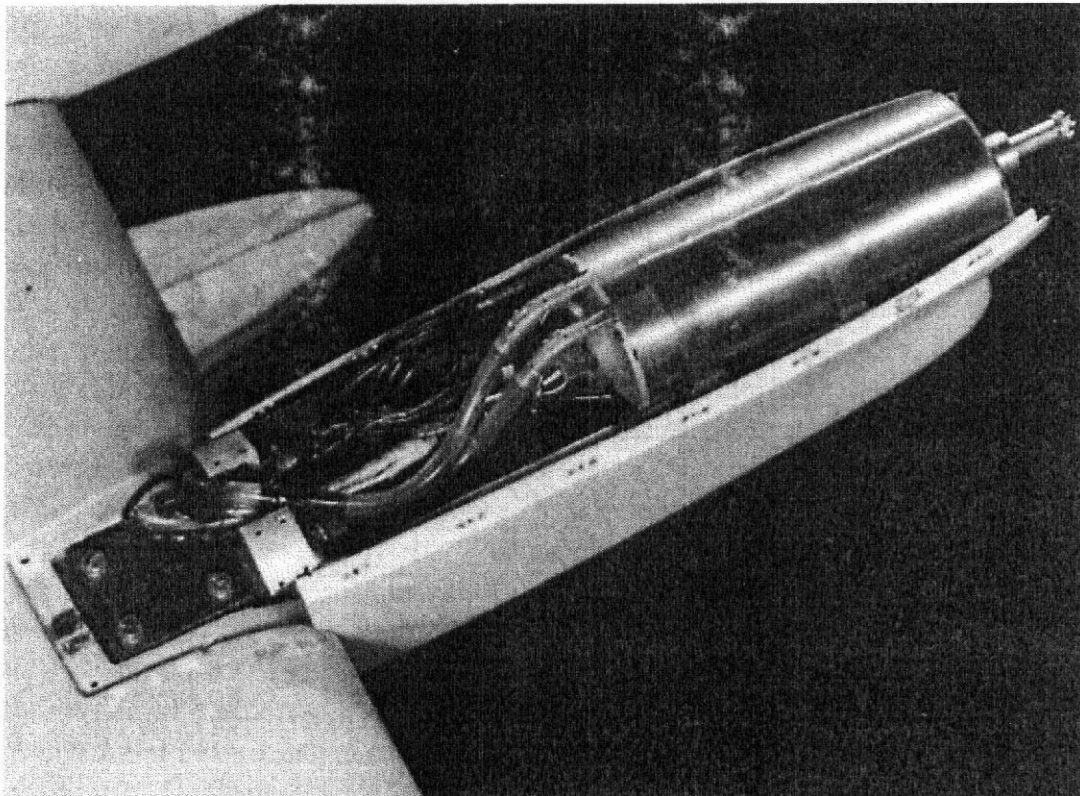
FIGURE 13.48   Water-cooled AC motor in nacelle. (Photograph courtesy of Raytheon.)
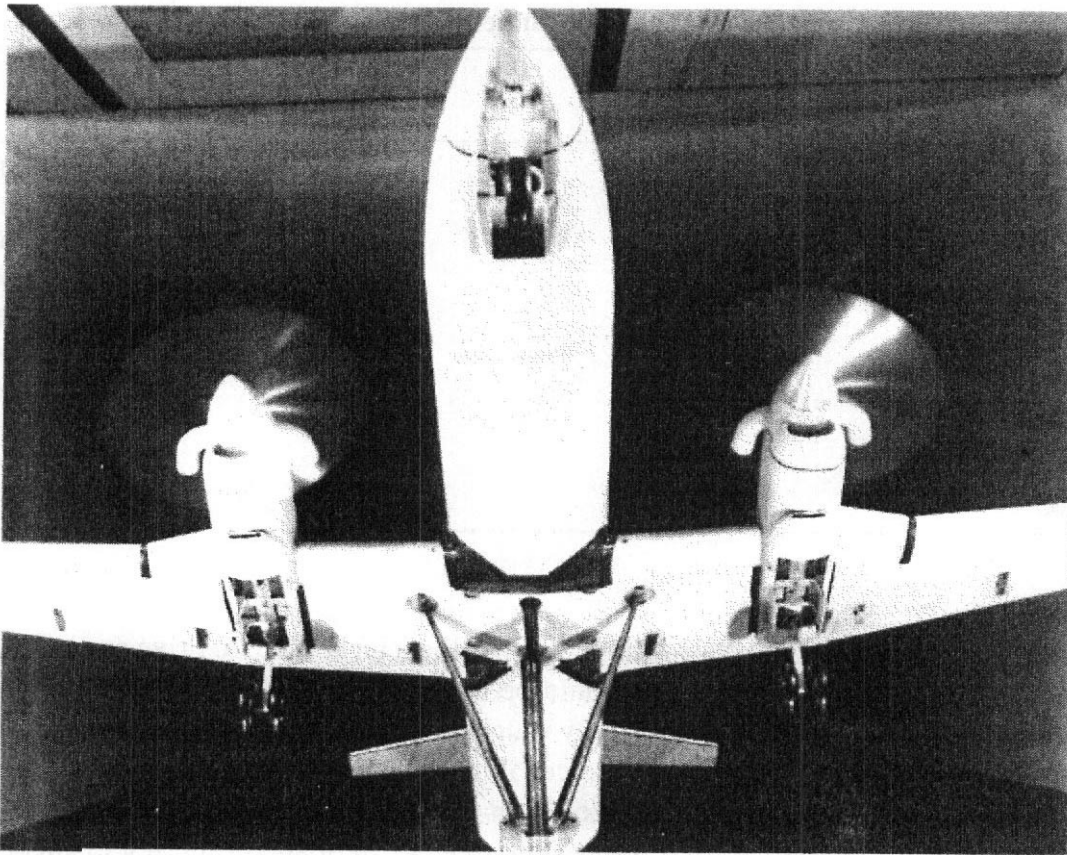
FIGURE 13.49 A powered model. The power and water leads leave the model between the mounting forks and enter the balance fairing through streamline tubing. (Photograph courtesy of Raytheon.)
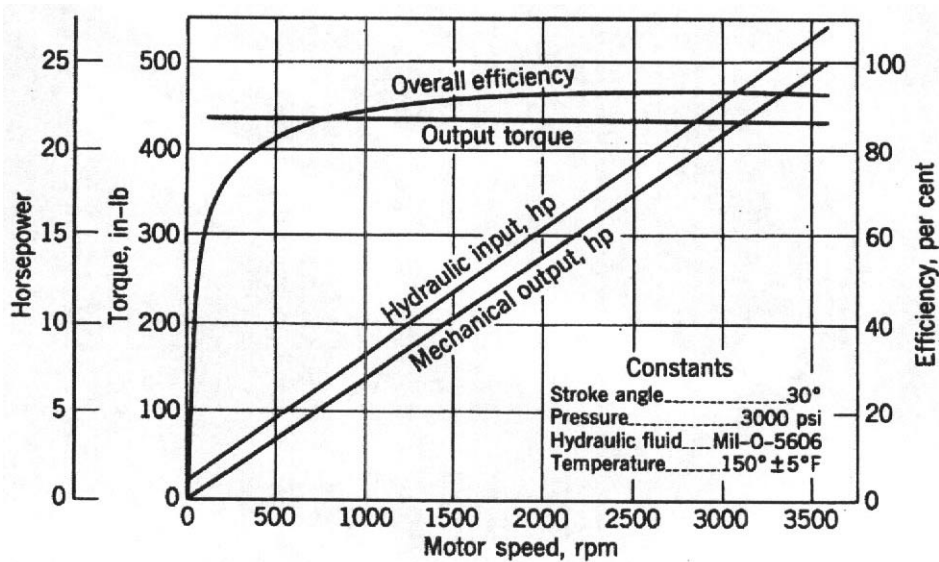
FIGURE 13.50 Hydraulic motor characteristic performance curves (intermittent hp **34.9** at 4850 **rpm).** (Courtesy Vickers Inc.)

the load put on the balance is constant and not a function of the model power. The problem of jumping the balance with hydraulic or compressed air is not that simple since both the pressure and mass flow will vary with the required power; thus balance loads also vary in both forces and moments. These balance loads as functions of pressure and mass flow must be determined and subtracted from the data. See Section 13.5 for a possible method of jumping the balance with hydraulic pressure lines.

13.5   POWER EFFECTS OF JET AIRCRAFT

The need for power-on tests is far less acute for a jet-engine airplane than for a propeller-driven one. The effect of the thrust moment is easily calculable, and there is no large slipstream of high rotation that strikes the fuselage and tail with a wide variety of effects. Indeed, the sting mounting usually employed helps simulate the jet stream for the single-engine airplane. However, as the engine bypass ratios increase, the nacelle inlet lip normal force may become more important for engines mounted close to the wing. This is destabilizing and may require power testing in takeoff and landing configurations.

There are two methods of simulating a jet engine in power-off testing. The first is to fair in the inlet and exhaust with smooth fairings. With engines mounted close, but external to the body, or close to the wings, this approach may significantly distort the flow over the nacelle and adjacent areas. The same may be true on aircraft with engines buried in the fuselage with inlets near the leading edge of the wing root. The method may be acceptable for single engines on a sting mount with inlet in the fuselage nose.

The second approach is to use flow-through nacelles, which can be of two types. The first is a simple flow-through nacelle. The internal drag is either ignored or it is estimated or measured and subtracted from the data. The second type has an internal cowl or plug that is used to provide a correct inlet condition corresponding to a specific flight condition. The internal drag of these can also be estimated or measured and subtracted from the data.

Sketches indicating the three types of nacelles are shown in Figure 13.51.

A blowing nacelle is used when a thrust producing jet is required. The inlet is covered by a faired dome that is used for a high-pressure plenum. By the use of choke plates and screens the flow is more uniformly distributed as it is exhausted from the nacelle. Often a blowing nacelle has two independently measured and regulated flows to represent both the fan air and primary air.

The use of a flow-through nacelle for inlet flow simulation and the fan cowl geometry effects and blown nacelles for the jet effect will simulate the engine airframe interactions successfully if the following three conditions can be satisfied:

1. There must be no coupling in the near-field flow between the inlet and exhaust flow fields.
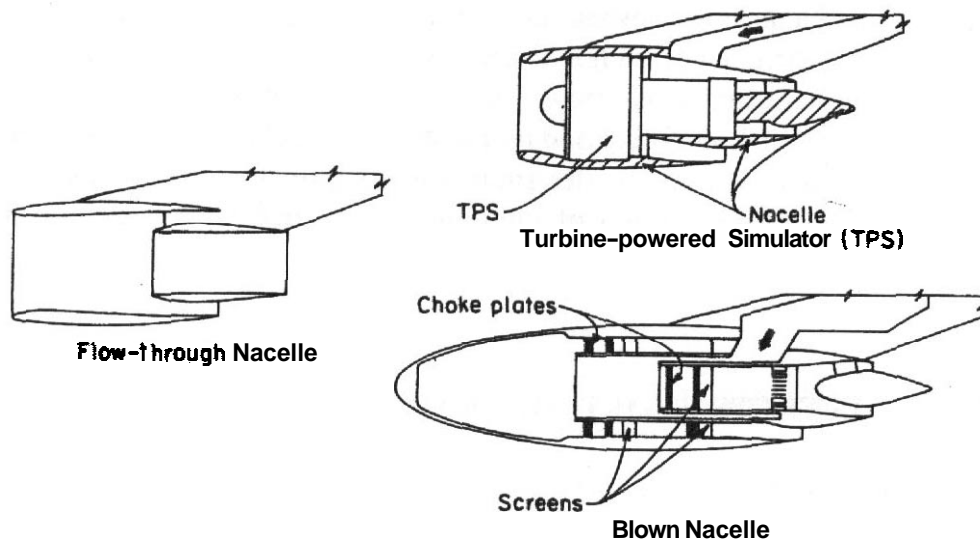
FIGURE 13.51   Three ways to simulate jet-engine nacelles.

2. The ram condition plume of the blown nacelle must accurately represent the plume exiting from the flow-through nacelle.

3. The potential flow field that is displaced by the domed inlet must not significantly alter the adjacent aerodynamic flow field.

The difficulty of always meeting these three assumptions can be avoided by using a turbine-powered simulator (TPS), which is sketched in Figure 13.51, and a model in a tunnel with TPS units is shown in Figure 13.52. These provide a practical model equivalent of a real engine in a real airplane. The TPS uses high-pressure air to drive a turbine that drives a fan stage that compresses the inlet air. The
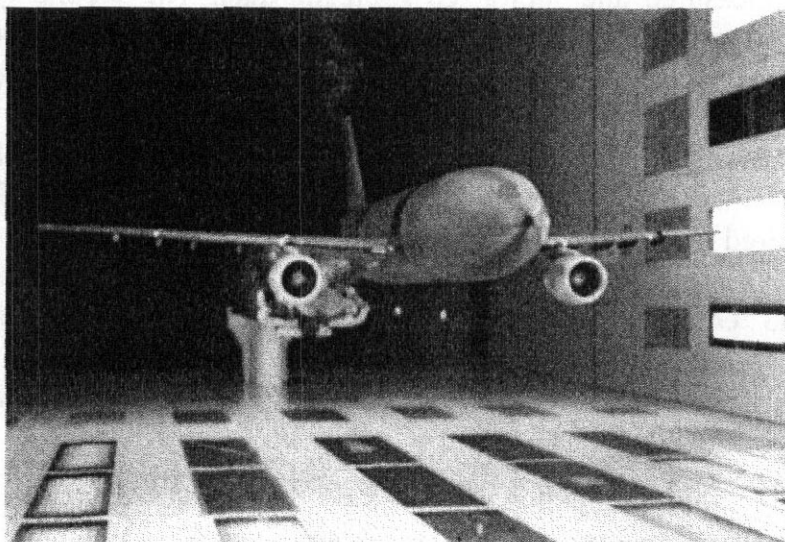
FIGURE 13.52   A sting-mounted model near the tunnel floor with two TPSs. The sting support is capable of vertical translation. (Photograph courtesy of DNW.)

inlet air is exhausted through a fan nozzle and the turbine air through a primary nozzle. The TPS will simulate 80–90% of the inlet flow, the pressure ratios of the fan and the core jets, and the fan temperature, but the core temperature is very low. The error in core temperature does not significantly affect an accurate representation of the thrust and exhaust flow. This is because in high-bypass engines the core flow is a small part of the total flow and is surrounded by the large fan flow. To accurately duplicate the full-scale engine airframe, the TPS must be calibrated.

The simulation of jet engines puts two requirements on the wind tunnel facility: a large air supply and some method of jumping either an external or an internal balance with this air. Since the blown nacelles or similar ejectors to simulate an engine exhaust usually require large masses of air when compared to a TPS, they will define the air supply system. Furthermore, to keep the size of the air lines into the model reasonable, as required by support tares, the air must be delivered to the model at high pressure. The mass flow is, of course, also a function of the tunnel and hence the model size. For tunnels of the size used for development testing, this leads to an air supply that can deliver on the order of 20 lb/sec at 1000 psig or more.

There are many schemes in existence for getting air of this mass flow and pressure across balances. These methods can be adapted for hydraulic fluid if a hydraulic motor is used to drive a propeller. When faced with this problem for an external balance, the easiest solution appears to be the use of loops of high-pressure hose.

This is not a correct approach, as can be seen when one realizes that most dial-type pressure gages use a Bourdon tube, a curved tube closed at one end used to measure pressure by gearing the pointer to the tube and using the tendency to the tube to straighten out under pressure to drive the pointer. A curved piece of hydraulic tubing or hose will do the same thing and load the tunnel balance when the curve is between the balance and a connection to the tunnel structure.

Ideally the air should pass along the vertical centerline of an external balance so that it can enter a large high-pressure plenum in the fuselage. From the model plenum the air flow is controlled by small, electrically driven ball valves or their equivalent as it is routed to its desired use. For an internal balance the air will usually pass through the sting and then through the internal balance to a plenum. A note of caution: high-pressure piping falls under piping or boiler codes. This means that all welds usually must be made by a certified welder; welds may or may not require x-ray tests and pipes and welds must pass hydrostatic tests before they can be used.

One highly successful method jumping an external balance is to use an L-shaped air line. Starting from the compressor side, at some point near the balance the pipe is firmly attached to the structure of the building. From this point the bottom of the L runs toward the balance. Very close to the ground connection there is a gimbal made out of X flexures. Within the gimbal there is a bellows with a liner (to prevent the air from vibrating the bellows). The pipe then makes a 90° bend up to the balance. In this leg there are two gimbals with bellows. The lengths of the pipe are critical as the gimbals should have very little deflection when the system is at rest. With adequate pipe length any small motions due to the healing/cooling of, for

example, pipe will be taken up in the three gimbals (Figure 13.53). The effect of pressure in the pipe can be calibrated by caping the test-section end and pressurizing the pipe. *Note:* This will also require a valve to release the pressure. The effect of mass flow can be achieved by the use of a zero-thrust nozzle. This is T-shaped pipe with two calibrated sharp-edge orifice plates at the end or the top of the T. This is attached to the air line at the model trunnion. The mass flow can be changed by changing orifice plates.

To jump an internal balance with compressed air requires the balance to be designed for this purpose. The air is delivered through a sting system that is nonmetric. The six-component balance has a central air duct that matches the sting. The
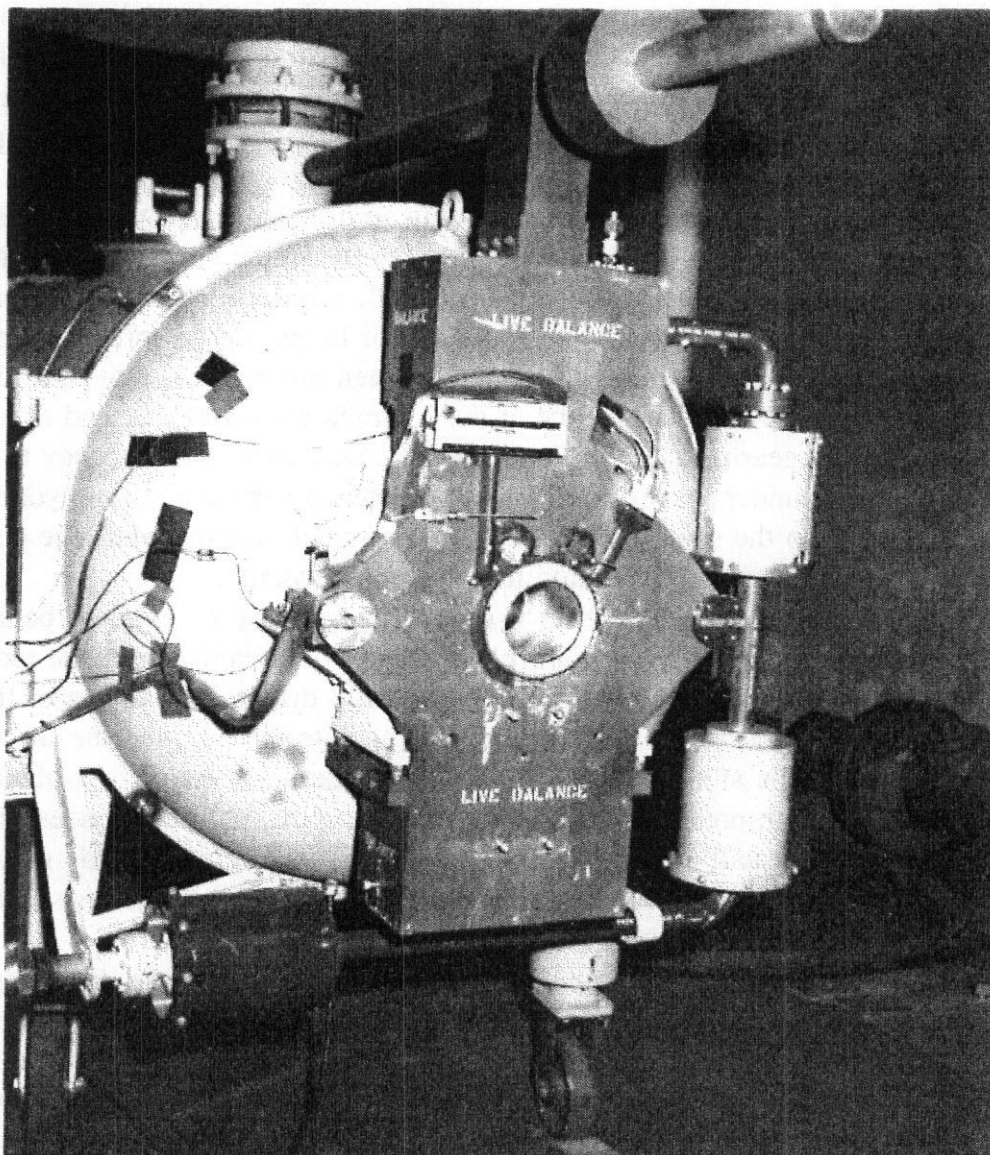
FIGURE 13.53 Calibration stand for model jet engines. Two six-component balances are at the top and bottom with the nacelle inlet in the center. The high-pressure air enters from the lower left through a shielded gimbal. Two other gimbals are in the vertical leg of the L. (Photograph courtesy of Boeing Aerodynamic Laboratories.)

air duct has opposing bellow seals and is sealed at the model end. Holes in the circumference pass the air to a chamber that encloses the bellows and from this chamber to the model plenum. The balance is calibrated with the balance pressurized at the expected running pressures to account for small interactions and sensitivity changes due to the air pressure. Momentum tares are evaluated by calibration with a zero-thrust nozzle. An example of a scheme for jumping air across an internal-type balance is shown in Figure 13.54.

What is required to get high-pressure air to the model has been outlined. But before we turn to equipment to calibrate the jet engine simulators, a word of caution about high-pressure air systems. Air or any other gas in large quantities at high pressure represents a large amount of stored energy, and it must be treated with respect. The air controls in the model and most of the other controls in the system are remotely operated by either electrical or pneumatic methods.

To protect people working on the model, there must be some interlock system to prevent the model from inadvertently being charged with high-pressure air. Any place in the system where air can be trapped must have bleed valves and a pressure gage to ensure that there is no high-pressure air when disassembling. An example is the piping across the balance when checking pressure tares. When removing flanges, each bolt should be slightly backed off one after the other. The bolts should never be completely removed one at a time. People have been killed when removing a cap on a high-pressure pipe when pressurized. The load on the cap can exceed the strength of the bolt and the cap can blow off. When going from a pipe designed for high pressure to one designed for a lower pressure through a pressure-reducing valve, blow-out or rupture disks are required to protect the lower pressure pipe in
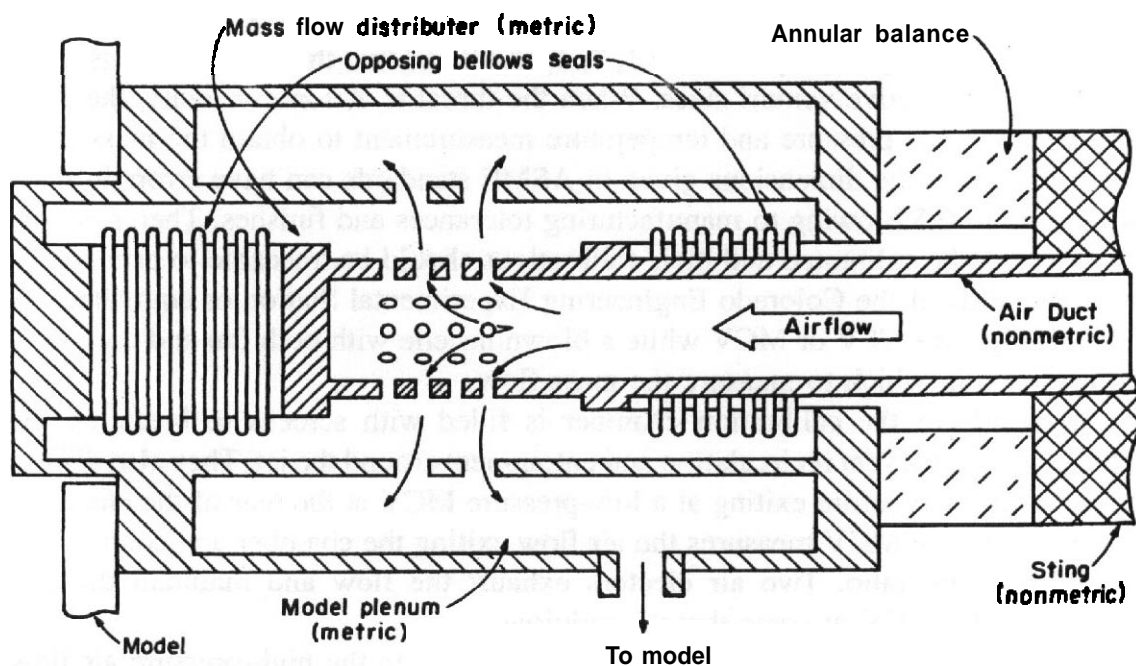
FIGURE 13.54   Schematic of jumping air across an internal (sting) balance. The forces on the two bellows cancel out, leaving small air line tares.

case of a valve failure. Any high-pressure-air system should be designed by an engineering firm experienced in high-pressure piping. Do not try to cheat the safety system by replacing a rupture disk that continually ruptures with one of a higher rating or bypass the safety system. Also, extreme care must be taken with **positive-** displacement pumps to prevent "dead heading" the pump. The pressure will build up at an alarming rate. Do not clean pipe connections with a petroleum product or an in-line explosion may occur due to dieseling. Treat all high-pressure-air systems as if they are a loaded and fused bomb--they are.

The problems of getting the air across the balance and into the model have been discussed, and now the requirements for calibrating a flow-through nacelle, a blown nacelle, or a TPS will be discussed.

If the requirements for the nacelle drag in a flow-through, or the thrust of a blown nacelle or TPS, are not stringent, they can be obtained by momentum methods using a wake rake. This method is theoretically correct, but it is difficult to get the correct momentum when integrating the rake output owing to distorted velocity profiles.

A better way to calibrate these devices is to use a special calibration stand that will cover the full range of flight operations (Figure 13.53). One such device is a chamber 4 ft in diameter by 12 ft long. At the forward end two six-component balances support a force-balance assembly to which either a TPS, blown, or flow-through nacelle is mounted. The inlet of the TPS or flow-through nacelle is open to the ambient pressure of the room and the exhaust confined to the chamber. A bellows seals the air passage around the nacelle and force due to pressure is canceled by compensating bellows. Thus the balance measures the nacelle thrust. Air is jumped across the balance by the same method used for the tunnel external balance. The air flow required to drive the blowing nacelle or TPS is measured by either a calibrated single critical flow venturi (CFV) or a set of CFVs that operate in parallel in any combination desired, called multiple critical venturis (MCVs). These have throat areas ranging in proportion to 1, 2, 4, and 8 and two throats at 16. This gives a total of 47 effective venturi sizes. When the throat is at sonic velocity, the CFV only requires one pressure and temperature measurement to obtain the mass flow. Venturis built to the dimensions given in ASME standards can have errors in mass flow of up to 0.5% owing to manufacturing tolerances and finishes. Therefore, the CFVs should be calibrated and their calibrations should be traceable to primary air flow standards of the Colorado Engineering Experimental Station or equivalent. A TPS requires one CFV or MCV while a blown nacelle with both fan and core flow requires two in which to measure the mass flow.

The inside of the calibration chamber is filled with screens to break up the exhaust jet and prevent recirculation and entrapment around the jet. They also diffuse and mix the flow before exiting at a low-pressure MCV at the rear of the chamber. The low-pressure MCV measures the air flow exiting the chamber and controls the nacelle pressure ratio. Two air ejectors exhaust the flow and maintain the low pressure at the MCV at sonic throat conditions.

For a TPS the fan air flow is the difference between the high-pressure air flow into the nacelle and the low-pressure MCV at the end of the chamber. Fromm[15,16] and Harper" give descriptions of the problems of model testing of powered nacelles.

Flow-through nacelles are calibrated for internal drag by using the difference between ideal thrust and the measured thrust. Flow-through nacelles often have trip strips just inside the inlet lip. The location of the trip strip is often determined by flow visualization to ensure the desired turbulent boundary layer within the duct. The nacelle has four or more internal static ports. The average of these pressures is used to determine the mass flow via the nacelle calibration when running the test. From the test mass flow the nacelle drag is determined via the nacelle calibration.

13.6   V/STOL VEHICLES

Aircraft can be characterized by their mode of takeoff and landing. There are large numbers of aircraft that use conventional takeoff and landing (CTOL) techniques. These aircraft require relatively long runways. A second mode is vertical takeoff and landing (VTOL), such as helicopters and the Harrier AV-8. The third mode is short takeoff and landing (STOL). The required length of runway can very from 500 to 2500 ft depending on the size and weight of the aircraft. The STOL field length is the hardest to define and, perhaps, as one wag put it, "the STOL field length is the length required by our aircraft." The VTOL and S M L type. are often called V/STOL aircraft. Over the years there have been a multitude of V/STOL vehicle configurations proposed, studied, and built.[18,19]

There is a distinguishing aspect to wind tunnel experiments supporting development of V/STOL aircraft: The generation of lift to support the weight of the aircraft at lower speeds than for conventional vehicles means that the wake, whether from an engine or from extremely high lift wing designs, moves downward at a higher angle relative to the free stream. This can reach conditions that require special methods to evaluate the interference on the flow from tunnel boundaries.

Helicopters

The helicopter is the most successful and widely used V/STOL vehicle, both commercially and military. It can take off vertically or with a short ground run if heavily loaded; it can hover; and it can maneuver in any direction. Outside the military the helicopter is used more for emergency transport, law enforcement, and industrial purposes rather than as public transport, such as airlines, owing to its relatively high operating costs. The high-speed performance of a helicopter tends to be limited by rotor tip losses due to compressibility and retreating blade stall plus the decreasing ability of the rotor to produce propulsive thrust as speed increases. Various schemes have been proposed and explored to overcome the helicopter's speed limits, such as wings to unload the rotor at high speed, additional sources of thrust other than the rotor, folding and storing rotors, and so on. None of them provide more than marginal improvement.

Helicopter rotors in forward flight are inherently producers of unsteady forces, moments, and air flow no matter what reference frame is adopted. These unsteady phenomena are an ongoing source of study because they have unwelcome conse-

quences, including producing vibratory inputs to the aircraft structure and producing excessive noise. Efforts to reduce these unwelcome side effects constitute much of the ongoing research activity in the helicopter field and lead to many experiments, some of them in wind tunnels, and show rotor models in use for experiments in wind tunnels. (See Figures 13.55 and 13.56.)

Tilt Rotor

This configuration obtains the vertical takeoff capability of a helicopter by having rotors whose axes can be oriented from horizontal to a little past vertical. The difference between a rotor and a propeller is generally that a rotor is designed for lower disc loading and the blade pitch can be varied as a function of the azimuth angle. A propeller is usually designed for higher disc loading, and while the blade pitch may be variable, all the blades have the same pitch at any moment in time. An example of a tilt rotor configuration is the Bell-Boeing Osprey.

Vectored Thrust

This category has rotatable jet nozzles, entire engines, or ducted fans. Sometimes this is considered to include both jet-powered and tilt propeller or tilt rotor vehicles.
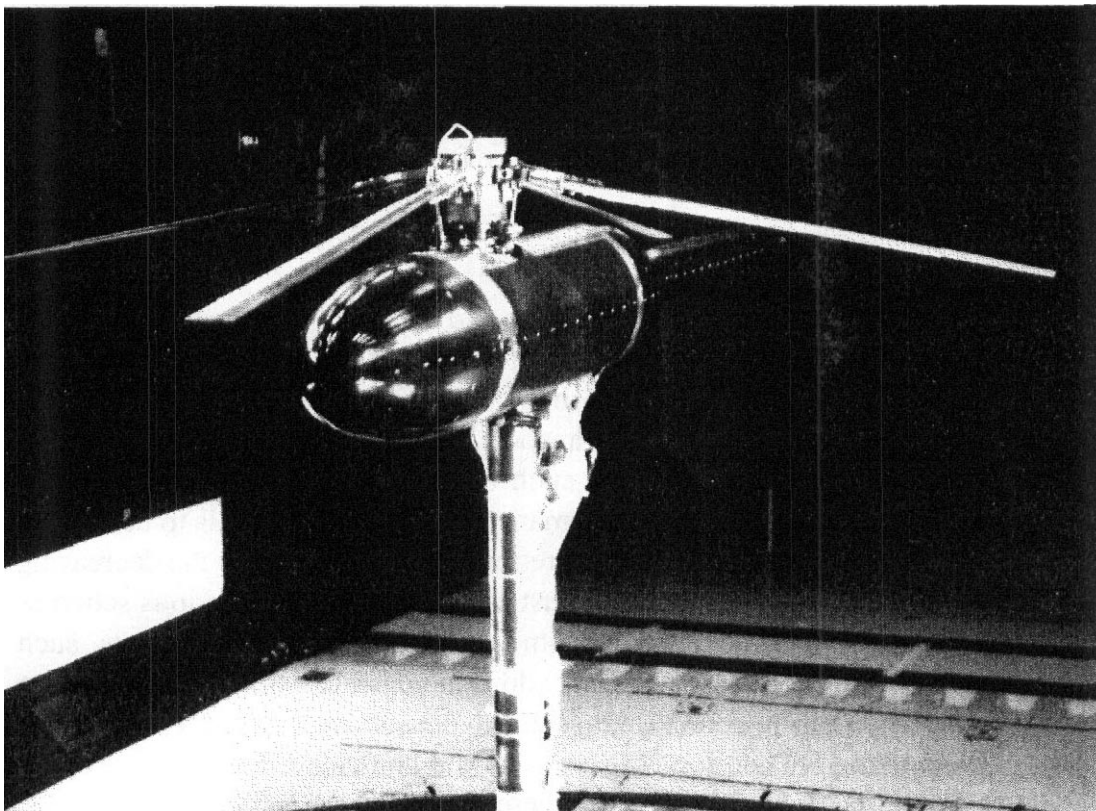
FIGURE **13.55** Rotor test **rig** with generic fuselage. (Photograph courtesy of Glenn L. Martin Wind Tunnel.)
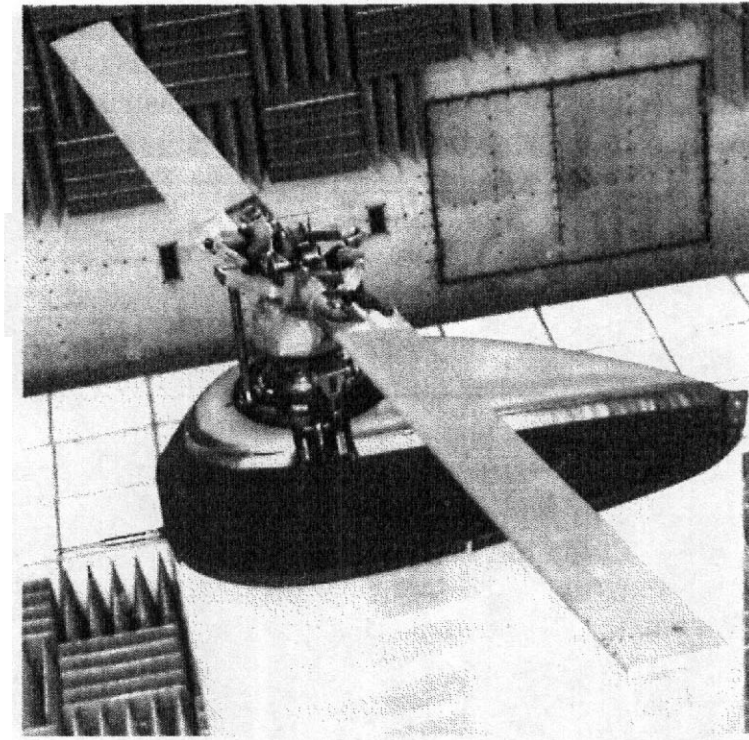
FIGURE 13.56 Two-blade helicopter rotor in DNW open test section for aeroacoustic testing. (Photograph courtesy of U.S. **Army** Aeroflightdynamics Directorate, Ames Research Center.)

These types of vehicles provide the wind tunnel engineer with another challenge. There will be high-speed concentrated jets issuing from the thrusters perpendicular or nearly perpendicular to the airstream and the airstream speeds of interest will extend down to zero. This introduces an entirely separate class of flow problems and corresponding tunnel boundary interactions that must be evaluated as part of any good experimental program. An example of this class of vehicle is shown in Figure 13.57.

Others

Tilt Wing This configuration obtains the high lift for vertical takeoff by rotating the wing, engines, and propellers about a spanwise axis a little more than $90°$. The propeller is in a horizontal plane for takeoff and landing and a vertical plane for forward flight. A large portion of the wing is immersed in the slipstream(s). This type of interaction between wings and propulsive flows continues to be a subject of research. An example from a development experiment for this class of configuration is shown in Figure 5.13.

Deflected Slipstream The propeller slipstream is deflected through a large angle by the use of specially modified wing flaps or other very high lift wing modifications. When the aircraft is powered by jet engines, this method of powered lift is often called either upper surface blowing or lower surface blowing. In supper surface
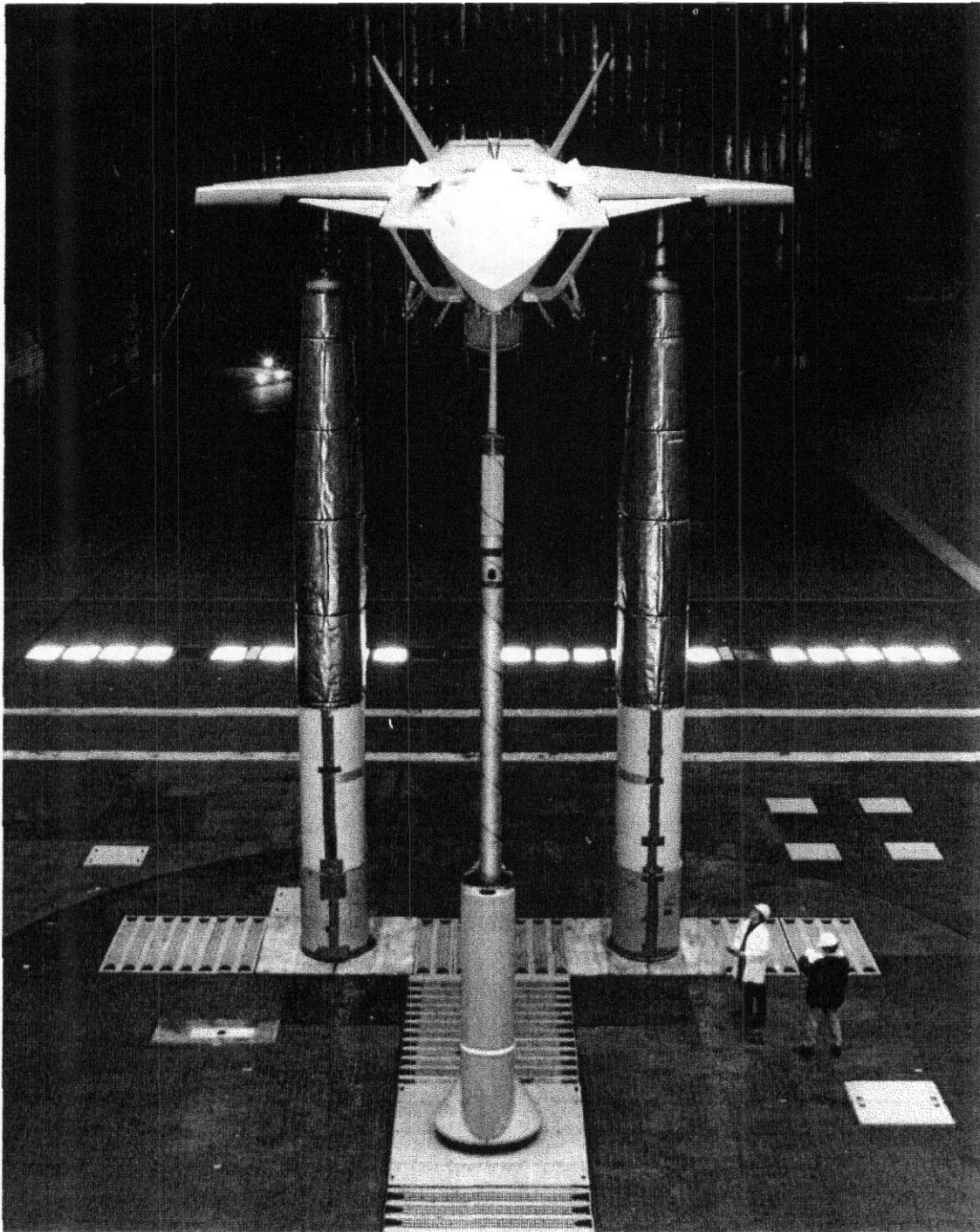
FIGURE 13.57 Powered lift model in NASA Ames 80 × 120-ft tunnel. (Photograph courtesy of NASA Ames.)

blowing the engine's jet blows across the upper surface of the wing and flap. The flow follows the wing-flap due to the Coanda effect and the high energy in the boundary layer prevents separation. The wing also reduces the noise on the ground. On lower surface blowing the engine exhaust is below the wing and impinges on the lower flaps to deflect the flow (Fig. 13.58). **An** example of this class of vehicle is shown in Figure 13.58.
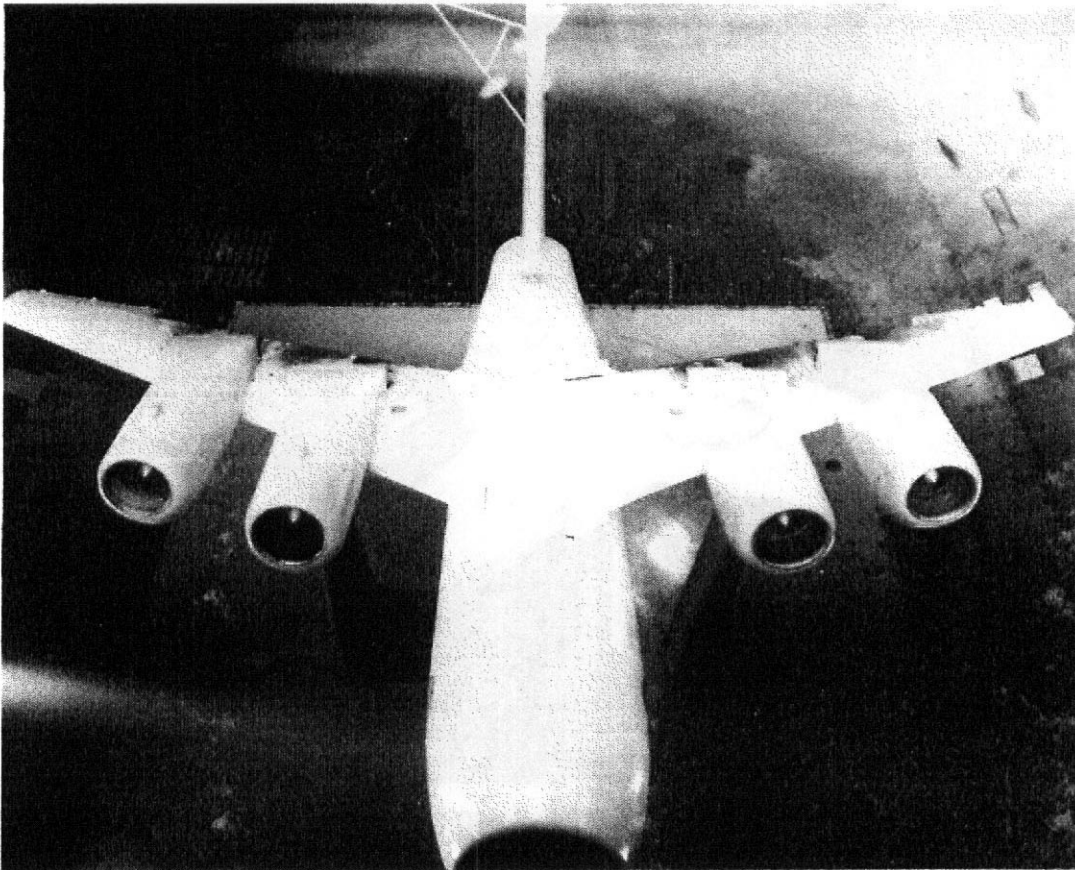
FIGURE 13.58 Vector slipstream by upper surface blowing of jet engine exhausts in NASA Ames 40 × 80-ft tunnel. (Photograph courtesy of NASA Ames.)

Jet Flaps High-pressure air is ducted along the wing span and is blown over the wing or parts of the wing in several ways. At the trailing edge of the wing either the air is blown over the upper surface of the flap using the Coanda effect over a curved surface at the trailing edge or the jet nozzle is built to deflect the jet wake. In either case the thin jet is turned downward. When the flap is blown, the high-energy air delays separation. The air can also be ejected at the leading edge to delay separation of the wing, and this can be used alone or in combination with the two trailing-edge blowing methods. When the amount of air on a blown or jet flap is greater than that required to prevent separation, additional circulation lift is produced, which is greater than that predicted by either jet reaction or potential flow.

Fan in *Wing* A large fan is buried within the wing airfoil contour. In hover the wing acts as a duct, improving the static thrust of the fan. In forward flight at low speed the fan aids the wing lift. The fan is primarily used for vertical lift and transition, and jet engines or other propulsion methods are used for thrust in forward flight. A development model is shown in Figure 13.59.

Autogyros The autogyro uses an unpowered rotor (same as a helicopter in autorotation) to provide lift. The thrust for forward flight is usually supplied by a piston engine propeller combination.
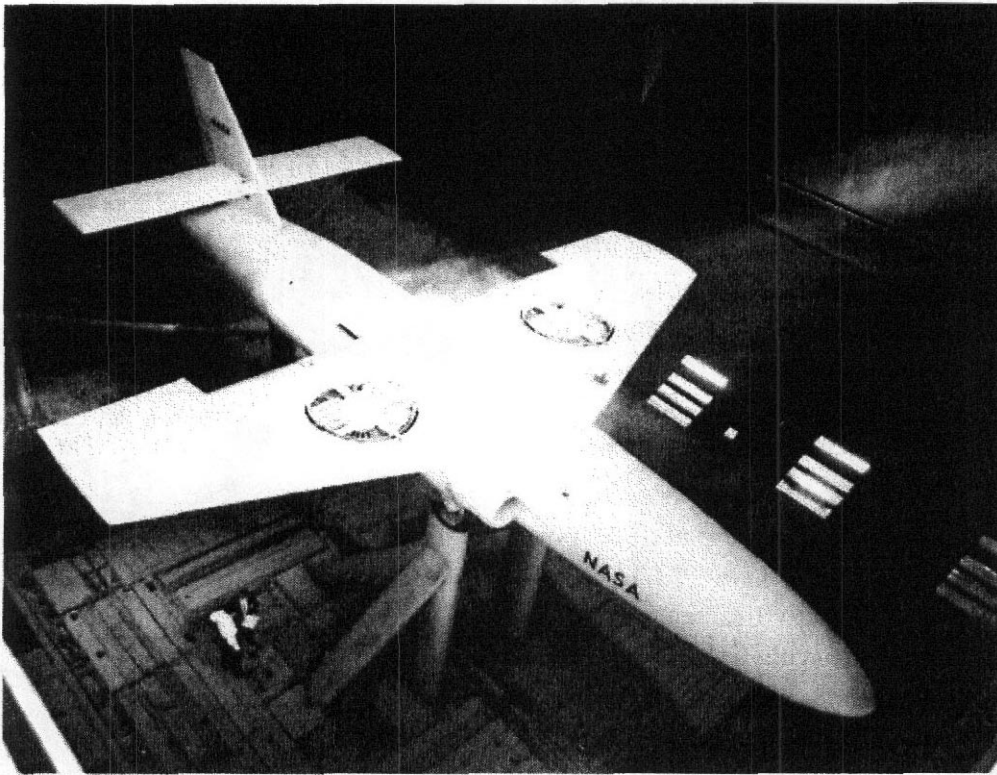
FIGURE 13.59   Fan-in-wing model in NASA Ames 40 X 80-ft tunnel. (Photograph courtesy of NASA Ames.)

This list of types of V/STOL aircraft is not intended to be all inclusive, and aircraft using combinations of powered lift systems have been proposed.

At low flight velocities used in V/STOL operations, the wing lift can be produced in three ways:

1. *Basic lift of a wing or unpowered lift.* This lift is due to circulation and is independent of thrust.

2. *Lift due to defected thrust by any of several methods as describedpreviously.* This lift varies linearly with thrust.

3. *Additional circulation lift due to either jet exhaust or a propeller slipstream moving over the wing.* This lift is a function of the increased velocity and the increase in the effective chord of the flap used to deflect the air downward. The increase in effective flap chord is due to high-speed air being approximately parallel and in the same plane as the flap. This lift varies in a nonlinear manner with thrust, as the rate of increase in lift decreases with increasing thrust.

The basic concept in all V/STOL aircraft is to create lift by using power to produce a downward directed momentum. For the purpose of discussion of wind tunnel tests of V/STOL aircraft, the powered lift can be divided into two broad categories. The first is a distributed power lift such as produced by a helicopter

rotor or a blown flip. The second is point power lift similar to the vectored thrust from a jet engine.

Experimental Issues

Wind tunnel experiments on V/STOL vehicles, including isolated rotors, have much in common with experiments that require powered models of a conventional configuration. Among the more important issues is how to keep the size of the matrix of runs within bounds and yet obtain the most important data. A common approach is to obtain data for conditions known to be at and near feasible flight trim conditions rather than just incrementing all the experimental variables through a predetermined list of values.

To illustrate the situation, consider a development program for a tilt wing aircraft. It is desired to measure the six component balance data as functions of a, β, i_w, J, τ_b, δ_a, δ_r, δ_e, and R. Table 13.11 identifies the meaning of the symbols. Consider also what may seem the reasonable proposition that 10 values per variable are desired to obtain well-defined functions over the ranges of interest. This would require 10^9 (that is, one billion) data points. Suppose we could average recording a data point every 3.6 sec or 1000 points per hour. We would need 10^6 h to conduct the experiment. Even if we immediately conceded and reduced the Reynolds number variation to a single value, we would still need 100,000 h. This has to be reduced drastically in order to be feasible. It is done by finding the combinations that correspond to trimmed flight conditions and taking measurements only in a small band about the trimmed flight states. This requires that the run schedule be carefully considered in advance and that data be reduced in real time and used to update to choices of conditions to be included in the run program.

If the purpose of the test is to obtain basic data, then a different procedure is followed. Usually the purpose of these research tests is to determine the effect of one parameter on the other parameters. As an example, for a pure jet flap on a wing one might desire the effect of varying the jet momentum coefficient on lift, drag, and pitching moment from zero lift to maximum lift. Thus pitch runs would be made at various momentum coefficients with all the other variables held constant.

TABLE 13.11.   Experimental Variables

Symbol	Variable
α	Angle of attack of aircraft
β	Side slip of aircraft
i_w	Angle of incidence of wing relative to fuselage reference line
J	Propeller advance ratio
θ_b	Pitch angle of propellers
δ_a	Angle of ailerons
δ_r	Angle of rudder
δ_e	Angle of elevator
R_e	Reynolds number

V/STOL Instrumentation

As can be seen from the description of the various methods of producing powered lift, the simulation will be accomplished in the wind tunnel by two general methods. The first is by rotational devices such as a helicopter rotor, propeller, ducted fan, or fan in wing. The second is usually by compressed air to simulate jets and blown flaps. The rotational devices can be powered by electric motors, hydraulic motors, or air motors. The rotation devices can also be used to simulate a jet exhaust similar to a turbine power simulator. When the power is an electric motor, the problem of jumping from ground to the balance is relatively easy even for a water-cooled motor. However, when either compressed air or hydraulic power is used, the problem of jumping the balance is more complex as there can be loads applied to the balance that vary with both pressure and mass flow. V/STOL models almost always require much more instrumentation within the model than a standard nonpowered force model.

Measuring rpm   If the model has rotating machinery, such as a helicopter rotor, lift fan, or propeller, the rpm must be controlled to match tip speed ratios on rotors, advance ratio on propellers, and thrust on lift fans. There are two types of optical systems that can be used. The first is a transmissive sensor, a light on one side of a disk with a hole in it and a light detector on the other side of the disk. For one hole in the disk one pulse per revolution is obtained. The second is a reflective sensor where a light shines on the shaft that has a painted mark that reflects light to the detector, yielding a one-per-revolution pulse for a single mark. Both of the above units may have to be shielded from ambient light. A third method is an AC generator where a magnet is rotated with the shaft inside a coil producing a sine wave whose frequency varies with shaft rpm. All three of these methods can use a counter that will measure pulses or frequency per second, which can be converted to rpm. The output of the counter must be visual for the operator. Many counters have binary outputs that can be adapted for input to a data system. A fourth way to measure rpm is to use a DC generator whose output voltage is proportional to an rpm that can be calibrated. This is the least accurate. A digital voltmeter could be used for visual output and data system input or the voltage itself could be used.

The rpm of rotors and propellers can be checked by the use of commercial strobotachometers. These use a xenon flash tube that is flashed at various frequencies that are set on the dial in terms of rpm. When a marked blade is rotating at the same rpm, it is stopped by the light. These units must be used with care, for if the desired rpm is 2000, the blade will appear to stop also at 4000 and 1000 or other even multiples of the blade speed. This problem is further complicated when multiple blades are in use. The use of a strobotachometer when there are multiple blades requires distinctive markings on the blades that can reliably be discerned under the illumination of the flashing light.

Compressed Air   When compressed *air* is used for simulating, for example, vectored thrust, the mass flow must be measured accurately and controlled reliably. This usually requires calibration of the nozzle by one of two methods. The first is to

calibrate the nozzle in a calibration facility so that the thrust, mass flow, and so on, are known by measuring pressure and temperature for desired thrusts. The second method is to use a pitot rake to calibrate the thrust. This is a simpler method, but not as accurate as the first.

Rotors   It is common that during rotor experiments both the lead–lag angle and the flapping angle versus azimuth position are required. These are sometimes measured by strain gage beams calibrated for angle versus strain. During experiments on rotors and propellers, stresses or moments on the blades may be desired, and these too are usually measured by strain gages. Such measurements give insight into blade twist and vibration frequencies when operating. As these measurements are taken on rotating devices, the signals are transmitted through slip rings. Much, if not all, of the data from rotating blades are needed as a function of blade position, which requires a continuous trace of the data signal or more likely a high-speed digitization system. Until recently the most convenient method of acquiring the data was on an FM tape deck. An event marker was put on one of the tape channels to be used to determine the blade azimuth position. Today, a high-speed digitizer is more accurate, more convenient, and less costly than an FM instrument grade tape recorder.

Vectored Thrust   When the lift is produced by jet engines, it may be desired to separate the wing lift from the thrust lift to determine the interference between the component parts. This necessitates the model being designed so that the loads on the engine can be measured separately from those of the model. For example, the first, often an external, balance can be used to measure the power and aerodynamic forces and moments while the model is attached to the power section by a second balance that measures the aerodynamic forces and moments. The difference between the two balances is the power effects plus the interferences.

The other approach is to have the first balance measure the aerodynamic forces and moments plus interference and the second balance measure the power effects. The second method is often more difficult because of the tares on the air lines due to pressure and mass flow.

Balances for rotors must be even more carefully designed than some other balances or selected to avoid resonances between the balance and the rotor. The excitation frequencies from the rotor are multiples of the rotor speed. For existing external balances it is necessary to avoid operating in regions of balance-rotor resonance.

Tare and Interference   Tare and interference measurements for V/STOL models are the same as for conventional models with the following exceptions. If the model uses compressed air, the pressure and mass flow tares must be evaluated. The second problem is with helicopter rotors, because it is difficult to use an image system from the ceiling. Generally, for rotors only the tare of the model supports themselves is evaluated. This method neglects the effect of the rotor wake on the support system. The tares are taken with the rotor blades removed, and the forces, moments, and

driving torque are recorded at the various air speeds. If the rotor is mounted to a fuselage, the tares and interference of the fuselage are handled the same as any model.

Model Sizing The determination of model size for a given tunnel for a **V/STOL** model that must be tested in the transition flight range is complicated. As discussed in Chapter 11, there is a lower speed test limit that is a function of the model area and tunnel cross-sectional area for models with distributed lift. This limit requires a small model in a big tunnel. A small model at low velocity means low Reynolds numbers. If care is not taken, the Reynolds number may get in the range of 200,000 or less. **At** this low Reynolds number the aerodynamic properties of conventional airfoils may be quite different than at $RN = 6 \times 10^6$ (see Chapter 8). It should be noted that the full-scale aircraft also may be operating at low Reynolds numbers in transition. Because of the Reynolds number issue and **difficulty** in model construction, most of the tunnels built in the 1960s for **V/STOL** are large.

There is no known easy way out of the dilemma of small models relative to tunnel size. If the model is not to be tested toward the hover end of transition, the size can be increased. But for models with large **downwash** angles and large wing-span-to-tunnel-width ratios, the distribution of the tunnel interference may become nonuniform.

The Rotor Model The design of a model rotor presents some **difficulties** not encountered with most other wind tunnel models of airplanes. The hub and hinge design and construction can usually be worked out in a satisfactory manner, but some inherent difficulties arise with the rotor blade representation. It is common practice in rotor design to have the blade statically balanced about its quarter-chord line. Such a balance rules out the homogeneous blade and requires either a built-up blade or a solid wood blade with a metal leading edge. Most model blades are now of built-up-type construction, even for quite small models.

The actual blade dynamically flabs and twists during flight, and when it is possible, usually when larger models are employed, a model will be designed so that its dynamic characteristics match those of the full-scale craft, and realistic **aeroelastic** deformations and vibratory stresses are obtained. The performance of a rotor is helped aerodynamically by root cutaway, inverse taper, and twist, and the model designer may be expected to produce such designs despite their difficulty.

The model should be equipped with adequate flat surfaces for leveling and angle measurements, some type of hinge lock to be used during balancing, and an ample supply of spare parts as rotor models are never examples of great reliability.

Hinged Rotor Operation There **are** certain operational procedures that must be followed with rotors equipped with flapping hinges operating in a horizontal plane:

1. The motor is brought up to operating speed with the tunnel off. As the rotor starts to rotate, there is very little centrifugal force on the blade. If the tunnel is running, the advancing blade will flap up to very large angles, owing to

its large lift, and the blade will not track, leading to relatively large oscillating loads.

2. When the rotor is at the desired rpm, the tunnel is brought up to desired speed.

3. When shutting down at the end of a run, the tunnel is brought down to zero or a very low speed and-then the rotor rpm is reduced. When large blade angles are used, this procedure may not be possible because of either limits on the power of the rotor drive or blade strength being marginal to carry the large static thrust or flow recirculation between the rotor and tunnel floor. For these conditions it may be possible to tilt the rotor forward, start the tunnel, and gradually increase the speed. The rotor will autorotate, and as the rpm builds up, rotor power may be added. Extreme care must be taken when operating in an autorotation mode to avoid excessive rotor rpm. When conditions are at large collective pitch angles with the rotor shaft tilted aft to the flow, the rotor can also enter an autorotating mode. This can be detected by a reduction in rotor torque, with the torque sign changing as the rotor begins to autorotate. Again, extreme care must be observed when the rotor is powered by an electric motor to avoid large increases in rpm due to the rotor driving the motor. The increase in rprn is usually very dramatic if such an increase occurs; control can be obtained by cutting the tunnel and pitching the rotor forward.

Flow Visualization for Rotors: Propellers   Small tufts can be attached to the blades; the centrifugal force does not seem to seriously affect the tufts. The minitufts described in Chapter 5, which are fluorescent and viewed under ultraviolet light, are ideal for this application. When an event-marked signal (used to determine blade position) is available, it can be used to trigger the flash stopping the blade at the desired azimuth position.

A smoke generator can also be used to visualize the flow through the rotor—propeller disk.

13.7   REENTRY LANDING CRAFT

Low-speed tests of reentry landers are made to determine the performance, stability, and control during the approach and landing of the spacecraft. The low-speed test program for these vehicles is the same in principle as for an unpowered airplane. Low-speed evaluations of any supersonic configuration are likely to require higher angles of attack than are needed for configurations that are designed for lower speed flight.

REFERENCES AND NOTES

1. High-speed tests for transonic airplanes may precede the low-speed tests.
2. Lockspeiser, B., "Ventilation of 24 ft Wind Tunnel," ARC R&M 1372, 1930.

3. Not upside-down on a left wall.

4. A second method of calculating the location of the aerodynamic center is given in the appendix of "The Measurement of the Damping in Roll on a JN4h in Flight," NACA TR 627, 1923.

5. The mean aerodynamic chord may be found from either

$$\text{MAC} = \frac{2}{3}\left(C_T + C_R - \frac{C_T C_R}{C_T + C_R}\right)$$

where C_T is the wing tip chord and C_R the wing root chord for straight tapered wings, or

$$\text{MAC} = \frac{2}{S}\int_0^{b/2} c^2 \, dy$$

for other platforms.

6. Schrenk, O. A., "A Simple Approximation Method for Obtaining the Spanwise Lift Distribution," NACA TM 948, 1940.

7. Pearson, H. A., "Span Load Distribution for Tapered Wings with Partial-Span Flaps," NACA TR 585, 1937.

8. Panel rolling (C_{lp}) and yawing moment (C_{np}) coefficients; do not confuse with damping-in-roll $dC_l/d(pb/2V)$ or damping-in-yaw $dC_n/d(rb/2V)$.

9. Equation (13.26) applies only to roll without yaw or sideslip and can be misleading at high angles of attack, where adverse yaw in flight may be appreciable.

10. For zero trail angle the rudder is so balanced that it remains at a zero deflection even when the airplane is yawed.

11. If another location is desired for the center of gravity, the curves may be rotated about zero lift by the relation

$$\Delta \frac{dC_m}{dC_L} = \frac{\% \text{ MAC change}}{100} = \text{Acg}$$

12. Goett, H. H., "Tunnel Procedure for Determining Critical Stability," NACA TR-781,1943.

13. Etkin, B. E., and Reid, L. D., *Dynamics of* Flight, Stability and *Control,* John Wiley & Sons, New York, 1996.

14. This is the critical condition for multiengine types.

15. Fromm, E. H., "The Boeing Flight Simulation Chamber for Static Calibrations of Engine Simulators," paper presented at the Forty-Fifth Meeting of the Supersonic Tunnel Association, Sandia National Laboratories, Albuquerque, NM, April, 1976.

16. Fromm, E. H., 'Wind Tunnel Testing of Integrated Aerodynamic and Propulsion Effects," paper presented at the Forty-Eighth Meeting of the Supersonic Tunnel Association, Toulouse, France, Sept., 1977.

17. Harper, M., "The Propulsion Simulator Calibration Laboratory at Ames Research Center," AIAA Paper 82-0574, 1982.

18. Kohlman, D., *Introduction to V/STOL Airplanes*, Iowa State University Press, Ames, Iowa, 1987.

19. Campbell, J. P., *Vertical Takeoff and Landing Aircraft*, MacMillan, New York, 1962.

14 Ground Vehicles

In the last few decades the wind tunnel has become a primary tool in ground vehicle design programs. Various needs for understanding and dealing with phenomena related to air flow have significantly increased the wind tunnel testing time required in support of design decisions for trains, busses, individual passenger vehicles, motorcycles, trucks, and racing cars of all types.

There has been a corresponding increase in the number of wind tunnels specially built or adapted for the study of aerodynamics of ground vehicles. Many of these wind tunnels have been constructed for companies in the automobile industry. Most are focused on production car development, with a smaller number focused on racing car development. Wind tunnels developed for automobiles are for the most part very useful for other forms of ground transportation too, which of course promotes the increase of wind tunnel testing in the development of these other vehicles. Hucho[1] et al. provide a comprehensive treatment of aerodynamic considerations in the design and development of automobiles and trucks, including aspects of wind tunnels that are particularly adapted to ground vehicle test purposes. In Volkert and Kohl,[2] and Nilssor and Berndtsson,[3] and Ogata et al.[4] three very different examples of wind tunnels specifically designed and built for automotive development activities are presented.

So, what are the main uses of a wind tunnel in the design program of a ground vehicle? The most prominent uses are presented in the following sections as well as a few comments on significance for selected types of vehicles.

Aerodynamic Forces and Moments

Among the most important results obtained from wind tunnel experiments supporting design programs are the aerodynamic forces and moments acting on the test vehicle in a controlled and repeatable environment. Force and moment measurements are important for all ground vehicles. For some the principal interest is on drag because of its reflection on energy requirements. For others, such as performance cars, racing cars, and motorcycles, the moments, lift, and side force are at least as important as drag because of their impact on controllability and safety.

The drag and lift forces generated on a high-speed train, for instance, are fundamental in determining its safety, the maximum cruise speed, and all the consequent issues (e.g., the time of travel and the fuel efficiency) that eventually affect ticket prices. In the case of motorcycles the moments and forces generated in straight-line motion and upon exposure to side winds have a dominant effect on the performance of the vehicle and the safety of the rider. Drag is often the component that receives

the greatest attención as it has a dominant effect on fuel consumption at a given speed and on the top speed attainable.

The lift force is of extreme importance in determining controllability for performance cars and race cars, becoming more critical as the speed increases. Lift is often considered in terms of front lift and rear lift. This is equivalent to considering total lift and pitching moment. Other aerodynamic force and moment components also play major roles in the controllability of ground vehicles at high speeds. Side force, yawing moment, and rolling moment under side-wind conditions or due to passing of another vehicle are important determinants of the safety and comfort of a passenger vehicle or the capability of a race car in competition.

Cooling Flows: Power Plant and Brakes

For vehicles where the power plant is tightly enclosed, careful study of the cooling system performance is an important part of development commonly done in the wind tunnel. Many companies have wind tunnels that, in the automobile industry, are called "environmental wind tunnels" that are solely devoted to cooling system development. There are a few facilities that are used for both cooling system development and external aerodynamic development. Wind tunnel experiments with the engine operating under load, with controlled airstream temperature, and with radiation allow for parametric studies to be done that can provide the parameter effects on cooling system performance. This provides direct evidence for choosing system parameters and greatly reduces the amount of road tests required. Road tests are still very important, but a road test following a well-designed wind tunnel experiment can be focused on optimization of a few configurations chosen from the many that may have been investigated in the wind tunnel experiment. Most important is that data will be available from the controlled wind tunnel environment that will allow a more thorough analysis to be conducted.

In the case of busses and trains the propulsion units are usually much bigger and hence the heat source is increased. The concern then becomes not only that the heat be dissipated but also that heat be kept away from the passenger compartment. Air flow plays a significant part in the arrangement.

Brakes as well as the propulsion unit generate a large amount of heat that must be dissipated. In fact, the brakes must commonly absorb energy more rapidly than the motor installed in a given vehicle can produce it. The efforts to minimize overall drag has in some cases resulted in too severe reduction in the air flow to the brakes. This has a negative effect on performance and on the life times of brake system components. There have been a number of instances in which this was not recognized until after vehicles were in production. It is now common practice to evaluate the air flow to the brake systems. There is still substantial uncertainty about the minimum specifications, so this is an area in which there is a requirement for ongoing research.

Heating, Ventilation, and Air Conditioning (HVAC)

The requirements for a more or less comfortable climate vary greatly with the type of vehicle. A summary of requirements and systems is given by Hucho.[5] The

significant contributions of wind tunnel experiments to HVAC are in two parts. First, the selection of locations for supply inlets and outlets is critically influenced by the external pressure distribution, which is a primary topic of wind tunnel investigations. Second, the likelihood of spray or dirt ingestion at various candidate ventilation intake locations is very important and can be evaluated in wind tunnel experiments.

Wind Noise

For comfort, for compliance with environmental legislation, and increasingly for marketing reasons much effort is dedicated to reducing the noise sources in ground vehicles. For many vehicle classes, low noise is perceived to indicate high quality. Several wind tunnels in the automobile industry, as well as a number in the aircraft industry, have been designed or modified to have low background noise and outfitted with aeroacoustic instruments for measuring noise sources and for evaluating the noise reaching the driver's and passengers' ears.

Many techniques have been adapted in recent years from general acoustics to apply to aeroacoustics of automobiles and other ground vehicles. The principal noise sources have typically been classified into three parts: (1) engine and drive-train, (2) tires, and (3) aerodynamic or wind. For decades, the first two were of such intensity that the third was not a serious factor in the perceived noise of either occupants of vehicles or persons in the drive-by environment. Advances in the last two decades have reached a point where the third is now an important element in the perceived noise of both occupants and persons in the drive-by environment. The wind tunnel is currently the best available tool for aeroacoustic development. As aeroacoustics becomes more important in ground vehicle design, the same happens with the wind tunnel, although this new requirement demands considerable additional facility development, instrumentation, and personnel capability.

Wipers, Washers, and Related Surface Flows

A final set of applications of the wind tunnel are experiments on the effect of aerodynamics when the vehicle is under hard weather conditions that involve sprays, mists, and accumulation of dirt. salt. or other contaminants on the vehicle itself or the reduction of visibility for nearby vehicles. In a number of automobile wind tunnels it is possible to simulate rain, snow, and dirt propagation situations. Studies are done to optimize the design of the wind shield and head light wipers, rear-view mirrors, and other details of the geometry in order to minimize the negative effects of particle deposition on the vehicle's surfaces. Once again road testing is not eliminated but complemented by the information from the wind tunnel experiments.

In the following parts of this chapter the role of the wind tunnel in the development of ground vehicles is illuminated by giving some details of selected cases. Ground vehicles are categorized into three groups: production cars, racing cars, and other vehicles. First concepts and techniques are introduced, and then selected results obtained by the engineering community and published in technical papers are given.

14.1 PRODUCTION AUTOMOBILES

Wind Tunnel Role in Production Car Design

The aerodynamic evaluation that influences the shape of a new vehicle is only one of many different areas that must be-considered and carefully evaluated in a design program for a new automobile. The aerodynamic development enters from the earliest stages, just after the concept is conceived, and continues up to full production level. Although aerodynamics is only one of the very many aspects of the development, it is one of a few that is required all along the life of the project. Computational simulations and road testing have an important role in modem car aerodynamic design programs, but windtunnelmeasurementscontinue to be the most common and extensively used approach. This is because wind tunnel measurements are highly efficient and highly productive for ground vehicle simulations. Full-scale Reynolds numbers can usually be attained, and the low dynamic pressures compared to those needed in aircraft experiments result in much less severe structural demands on the models.

In aircraft development once a target mission is defined, achievement of aerodynamic targets usually becomes one of the most important tasks of the design phase. In the automobile industry this is almost never the case. The degree to which aerodynamic development influences the shape of the final product depends on several factors, not all of them directly related to automotive technology. Some of the most important factors are as follows:

- The relevance of aerodynamic characteristics is variable for different classes of vehicle. For instance, a two-seater, high-speed sports car and a six-seater minivan will have significantly different requirements. In the first the drag and lift forces that are generated are critical, especially at higher speeds. In the second, more functional aspects of aerodynamics, such as interior cabin cooling, dirt deposit on the windows and aerodynamically generated noise become more important.
- The importance of fuel efficiency varies from market to market. In most European and some Asian markets fuel efficiency is critical due to high taxation on fuel. In these markets aerodynamic drag reduction becomes critical for the success of the product.
- In many countries information on aerodynamical characteristics has become part of the marketing of the product. It is then mandatory, especially in the sedan market, that the new products present competitive aerodynamic characteristics. It often appears that this is important even if an objective analysis of cost of ownership for a particular vehicle class shows that fuel costs are far below cost of capital investment, depreciation, and maintenance.
- Government regulations regarding fuel efficiency are often significant.

Based on these and other factors, the role of wind tunnel experiments will be more or less relevant. However in the last three decades, with market demand for higher fuel efficiency in Europe and Asia due to pump prices and an oil crisis and

concerns with fuel waste, air pollution, and global warming in the United States, aerodynamic development and the associated wind tunnel experiments have become more and more a standard part of the automobile design arena. The scope of the role is expected to continue increasing, although the specific manifestation will certainly continue to change as it evolves. Wind noise, for example, will likely play a larger role in the development process.

The description of the role of the wind tunnel in a new automobile design program presented here is for a typical passenger vehicle. The degree to which the results from the various stages of the experiments will affect choices of design features will depend on the vehicle mission. Virtually all aspects that have to do with any sort of air flow in a new vehicle require at some point the use of a full-scale, scale, or climatic wind tunnel.

Preliminary Shape or Theme Development Stage In the theme development stage wind tunnel experiments are done to compare aerodynamic performance of proposed designs and variations. In some cases actual parametric studies are performed even before the design comes into play. A basic shape and set of dimensions are determined based on the proposed vehicle type and the external shape is optimized.

Hucho[6] has described two strategies for aerodynamic development: *detail optimization* and *shape optimization.* Detail optimization is a process in which an initial vehicle geometry is assumed given to the aerodynamicist. It would typically be a product of a design studio or perhaps it might be an existing vehicle. A set of parameters such as those indicated in Figure 14.1 **are** selected and varied independently and in combination with schematic results for a single indicator of goodness, also shown in Figure 14.1. The results are used to select the set of parameters by the project team based on these and competing issues in the design evaluation.

Shape optimization is a process in which the initial shape is chosen from basic aerodynamic considerations and then modified in steps to reach a result that is judged a desirable vehicle shape given all the other constraints. We give a schematic indication of this process in Figure 14.2, again with drag coefficient as the single measure of desirability. An image of the starting shape for this sequence is shown in Figure 14.3.

Traditionally scale models are preferred, cheaper, and quicker to produce; they **are** a good compromise between accuracy and testing time. Security issues are very
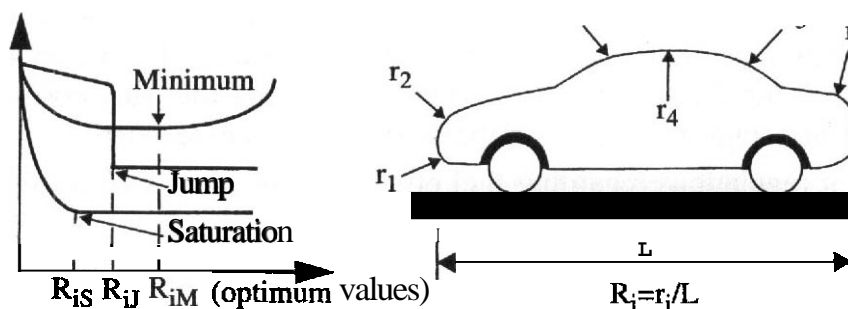
FIGURE **14.1** Schematic of drag vs. geometry relation.
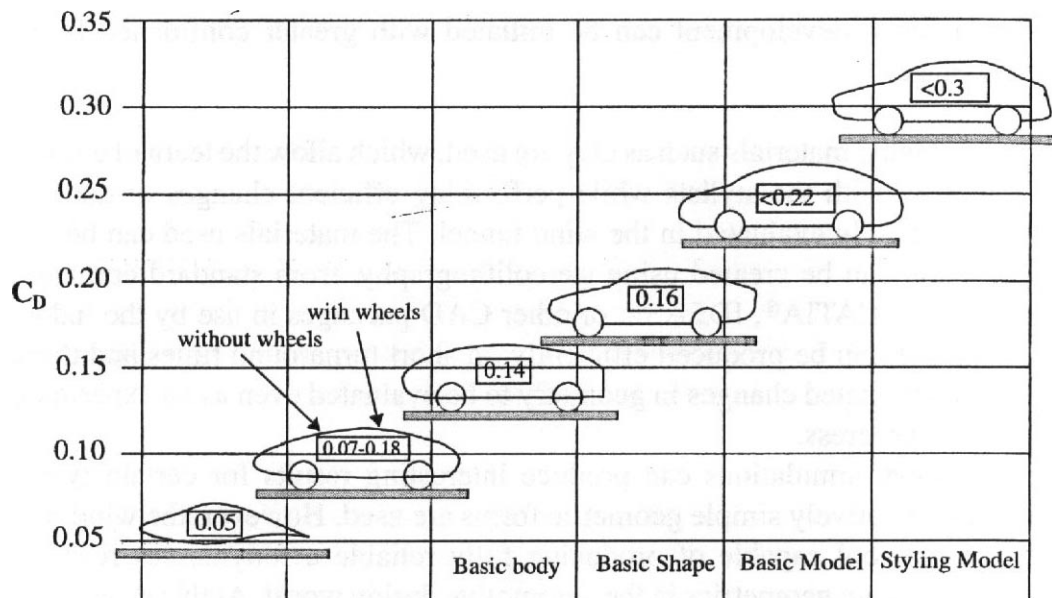
FIGURE 14.2   Schematic: shape optimization process.

important in this stage, and the easy handling of a scaled model—less prone to attracting attention—is an advantage. Some car companies have opted to work with full-scale models from the start. Some of the advantages of this option are as follows:

- Geometric tolerances are more easily met for small trim elements.
- Existing car platforms can be used as the underpinning for the clay models allowing for early optimization to be made with cooling air flow and underbody details, sometimes with less additional cost.
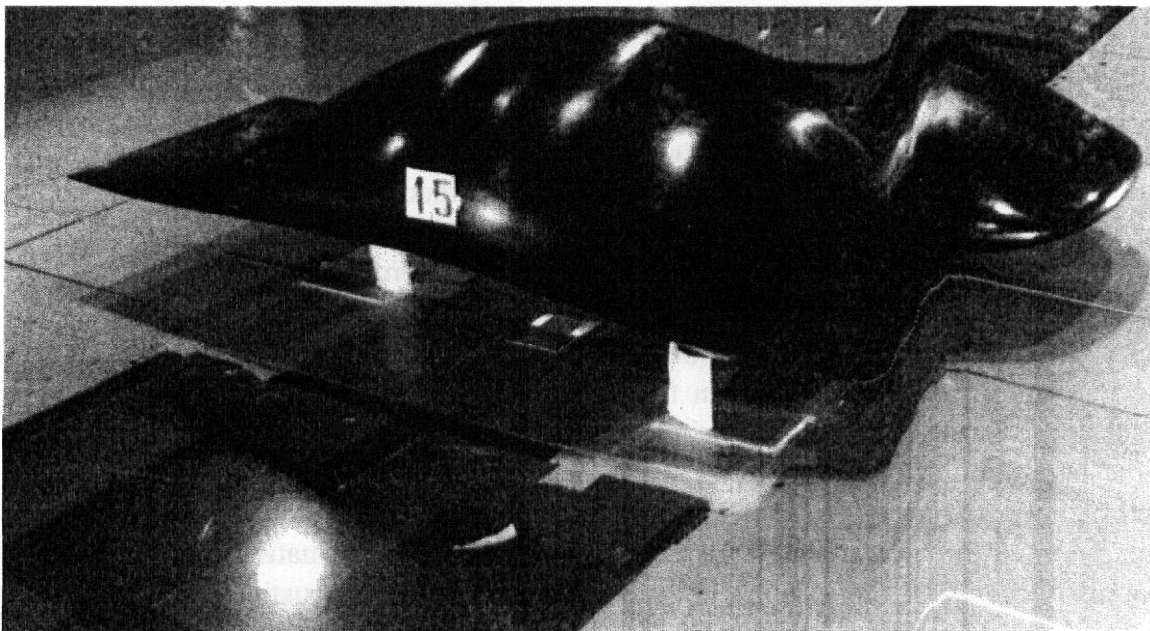
FIGURE 14.3   Body shape with low drag in proximity to the ground, $C_d = 0.049$. (Photograph courtesy of Pininfarina.)

Aeroacoustic development can be initiated with greater confidence from an early stage.

Easily moldable materials such as clay are used, which allow the team of engineers to work closely with the stylists while performing efficient changes to the model that **are** immediately evaluated in the wind tunnel. The materials used can be easily milled, or parts can be created using **stereolithography,** from standard commercial software such as **CATIA®, IDEAS®,** or other CAD packages in use by the industry. Accurate shapes can be produced efficiently on short turnaround times and thereby allow for unanticipated changes in geometry to be evaluated even as an experimental program is in progress.

Computational simulations can produce interesting results for certain types of vehicles when relatively simple geometric forms are used. However, the wind **tunnel** is still the only tool capable of producing fully reliable aerodynamics results for reasonably complete geometries in the automotive design world. At this stage evaluation of drag tendencies and discovery of possible large separation regions **are** what is most relevant. The detail in these early models is still far from full production, and lift values are so dependent on that detail that they are usually of little value here. This happens either because the shape is a first iteration in detail of what the actual product will be or because the power train and other components that are relevant for the lift forces **are** simply not ready at this stage. Flow surveys can be used for detection of separation regions and other features of the flow that might be dictated by the generic shape under study. In some cases the need for this type of investigation is largely superseded by extensive experience of the aerodynamics groups in auto companies over the last 20 years. There are seldom surprises regarding generic shape classes. An early test may be required if the shape being contemplated is known to be near a boundary that separates two flow topologies.

"Tuning" after Main Shape or "Theme" Is Frozen After the main shape is frozen, smaller details are yet to be optimized. Clay models **are** used either in scaled version or in full scale. Changes studied are mostly to the shape of bumpers, **rear**-view mirrors, air cooling inlets, back shape, lights, hood details, radii of curves, wheel well flows, and other details. The work performed in this phase is represented in Figure 14.1.

This is also the time when changes are performed in order to optimize geometries that have to do with the interaction between aerodynamics and the functionality of the vehicle. Examples are the optimization of external mirrors and the A pillar in order to minimize dirt deposit on the side windows under heavy rain and snow conditions. Other examples are windshield wipers and headlight wipers under the same harsh conditions. Surface pressure measurements are often done to support optimization of air intakes for engine and **brake** cooling. If the experiments are being done at full scale, aeroacoustics measurements and evaluation of alternatives can also occur. Explorations are under way to support aeroacoustics measurements at small scale but for the moment full scale is considered mandatory for confident evaluation. Lift and side forces **are** evaluated in order to check if the values obtained are in the expected range or if some drastic changes to the shape have to be

implemented. The underbody flow detail can be quite close to production at this stage and hence studied and optimized here. Flow surveys are commonly carried out near air inlets and other critical points to identify any possible separation regions, circulation regions, and other flow patterns that are not desirable.

- --

Accessory Refinement, Mockups, First Prototypes   At this stage the design is totally frozen barring discovery of a totally disastrous characteristic that has somehow survived the earlier development process. Wind tunnel experiments continue to be conducted, however, in order to optimize more functional aspects of the vehicle that are very dependent on aerodynamic features. Examples **are** the cooling air flow, air conditioning, passenger cooling flow, windshield and headlight wipers, dirt deposit on the side windows and rear windows, and aeroacoustics, especially at higher speeds.

This phase of the development is usually parallel with the development of the first full-scale running prototypes, and information is exchanged between wind tunnel testing and road testing in order to guarantee that the development will be as cost and time efficient as possible. Often full-scale engine running tests are conducted in a properly equipped wind tunnel with higher air temperatures in order to access the performance of different cooling systems. Some of this testing may occur with a running engine only or both with a running engine and running wheels if the tunnel is fitted with rollers. In either case special arrangements must be available to handle the exhaust gases. It often happens in a new car design that the combination of front-end design, engine cooling requirements, and proposed cooling system is not feasible. Finding out about this during road testing involving several people in a desert proving ground can be very expensive and even dangerous. The wind tunnel then becomes a fundamental validation tool for the cooling system.

Aeroacoustics is another concern at this stage. Either on the outside or on the inside of the vehicle numerous measurements are carried and results are analyzed. Changes are then implemented accordingly. Although data may have been obtained in a previous stage it is here that the validation of the measurements is done. The wind tunnel is again crucial, especially if it allows testing at higher speeds (where aerodynamically generated noise is more relevant) and if it is designed for acoustic measurements.

Cross-wind sensitivity is another aspect that concerns the engineers responsible for the aerodynamic development of a new automobile. Although the wind tunnel is not the best simulator of cross winds (due to the random nature of the direction and intensity of natural winds), it is the only available way to evaluate the aerodynamic forces and moments generated at yaw in a steady wind condition. There have been extensive correlations of the response of various vehicles to natural and artificial side gusts with the aerodynamic properties measured in the wind tunnel. This allows a reasonably confident prediction of the cross-wind response of a vehicle once the wind tunnel measurements and sufficient detail of the suspension systems **are** in hand.

Final Trimming, Prototypes, and Production Cars   In this period that spans from the finished prototypes and beginning of production to the end of the life of the vehicle the wind tunnel becomes an evaluation tool for smaller details. These details have to do with "cosmetic" changes dictated by marketing, performance requirements, or functionality. During the lift of a vehicle a number of exterior gadgets and/or appendages are designed and their properties must be tested. Examples are special aerodynamic mirrors, lower ground clearance, different bumpers, wings or spoilers, skirts, aerowheels, different racks for skis or other purposes, and trailer configurations. These and other possible appendages and resulting configurations are tested for stability, drag and lift, moments, cross-wind stability, and acoustic effects. Some of these can be developed with justification as component tests with a partial body to "host" the component.

Convertibles

The requirements and constraints for convertibles are somewhat different. Although the design process is essentially similar, there are some new aspects that are not present for standard cars. The aerodynamic evaluation and development for a convertible must be done for at least two configurations, top down and top up. Additional configurations of differing arrangements of the side glasses may also be included as these variations are more likely to produce larger perturbations on the aerodynamic properties than comparable variations in window positions for standard vehicles.

The aerodynamic properties that are considered desirable are essentially the same for a convertible and a sedan. But the achievable properties are generally in the direction considered to be less desirable relative to sedans of similar themes. The conduct of force and moment measurements for a convertible is the same in detail as for sedans. Essentially different measurements are required to determine the actual shape that will be realized by the soft top at various speed and cross-wind conditions. This leads to a need to evaluate alternative fabrics, frames, and attachment arrangements.

The essentially open environment is checked carefully for flow properties near the head locations of driver and passengers. Flow velocities near zero are sought. The acoustic environment is also checked at the head locations. Details of the windshield shape and edge treatment are critical determinants of both flow and acoustic environment. Cogotti[7] has given a discussion of experimental techniques used in the development of convertibles.

14.2   RACING VEHICLES

Wind Tunnel Role in Race Car Design

Although the aerodynamic development of race cars shares many of the tools and processes used in the aerodynamic development of production cars, the objectives of the testing are often very different. In racing the aerodynamics are a dominant

factor in determining the success of a vehicle. Hence the effort and relevance put into aerodynamic development is very large, as almost any measurable improvement may prove critical on the track or course.

There are many different classes of auto racing, but only some motivate extensive aerodynamic development work. Some examples are the formula racing championships Formula One,[8] CART,[9] and IRL,[10] the endurance and high-speed GT racing, the NASCAR[11] racing in the United States, and the manufacturer-sponsored tourism races in Europe. The differences between the vehicles in the various classes are significant enough to justify different goals in the development and testing programs. In fact, the aerodynamics for each class must be tailored for specific tracks and courses. However, the common aerodynamic goals are straightforward and common to all of them. They are to provide the driver with the possibility for the minimum lap times and the best control to ultimately beat the competition. This sometimes requires minimum drag, but it usually requires more attention to maximizing down force with proper balance between front and rear wheels while also obtaining a relatively low drag. Every class of racing has design rules that constrain the allowable shapes available to the aerodynamicist.

In order to achieve these goals, effective aerodynamic development programs include extensive track testing. This validates and extends the results learned in the wind tunnel while integrating the knowledge with the driver and other members of the development team. In the off season during a major part of the development, and even during the season when changes to the vehicle are to be evaluated, wind tunnel experiments **are** of fundamental importance.

Aerodynamic development of race cars is in general limited by existing regulations dictating dimensions, weights, materials, and shapes of the allowable changes to the vehicle or some of its aerodynamic appendages. Due to the complexity of the flow and the importance of even the smallest incremental improvements, the development relies heavily on experimentation. The design engineer is responsible for planning and conducting series of experiments with proposed designs and configurations before and during the season.

Race car aerodynamic development can be considered to be in two phases that repeat for each racing season, as discussed next.

Preliminary Development   In this stage an array of different configurations, car setups, **and** design possibilities are evaluated. Extensive experiments are planned and executed. Preliminary conclusions are reached as to what setups and configurations **are** optimum for different situations. Wind tunnel experiments and road trials are performed. Wind tunnel experiments have an important role in the comparison of various options under consideration and the subsequent selection of the most promising configurations. This phase has the obvious advantage of test condition repeatability.

This stage is often done with scale models. The scale models used for race vehicle development are much more detailed than the clay models used for early production car development. The race car models are usually made with the proper

shell structure, allowing internal flows to be properly simulated, and are sufficiently strong to allow running at the highest available tunnel speeds.

Optimization during Racing Season During the season a number of changes may be prompted by either less than optimum results or changes in regulations. Changes in regulations commonly come about from safety issues or from a circumstance arising in which some major sponsors feel their entries have been disadvantaged in some way. The wind tunnel becomes again instrumental in the evaluation of different options for aerodynamic solutions.

The prevailing practices with regard to the choice of scale models, full-scale models, or actual vehicles differ somewhat among the various race series. Most NASCAR teams, for example, carry out a considerable amount of full-scale wind tunnel work with the actual vehicles. Some of them conduct scale wind tunnel experiments as well. Few if any NASCAR teams do very extensive development using scale models. The situation is quite different for Formula One teams where a large fraction of the development effort is often done with scale models.

An advantage of using models for aerodynamic experiments is that the work can proceed without having an actual vehicle at a wind tunnel. This allows a greater possibility for parallel activities to proceed. Race car wind tunnel experiments are usually done in a facility equipped with a moving ground. Stationary ground experiments can be useful for some race car aerodynamic development, but this should be carefully considered. In closed wheel vehicles sensitivity of lift forces and even drag forces to ground clearance and ground effects can be high. And in open wheel vehicles there is a dominant effect of the wheels on the aerodynamics.

Wind Tunnel Methods for Racing Vehicles

The most significant racing vehicle types can be categorized in three groups: open wheel race cars (Figure 14.4), Le Mans/GT-type racing vehicles (Figure 14.5), and production cars transformed for racing (Figure 14.6).

For all three types the ground effects are very important so that accurate simulation of near-ground flow is necessary. For the open wheel vehicles, the wheel rotation has effects that are greater on the overall aerodynamics than is the case for the covered wheel vehicles. For the open wheel vehicles, wind tunnel experiments not only must provide proper ground simulation but also must include wheel rotation as well.

We discuss ground simulation methods in Section 14.4. The principles of ground simulation are the same regardless of the type of vehicle being developed. However, the need for the more sophisticated methods are greater as the ground clearance decreases and the speed of vehicle operation increases. The requirements to conduct valid and productive experiments on racing vehicles, therefore, are the most demanding.

As a rule of thumb wind tunnel results are very useful for the track or road. Even if the wind tunnel experiments are just a simulation, this is by far the most used approach in aerodynamic development of race cars. In general, good results
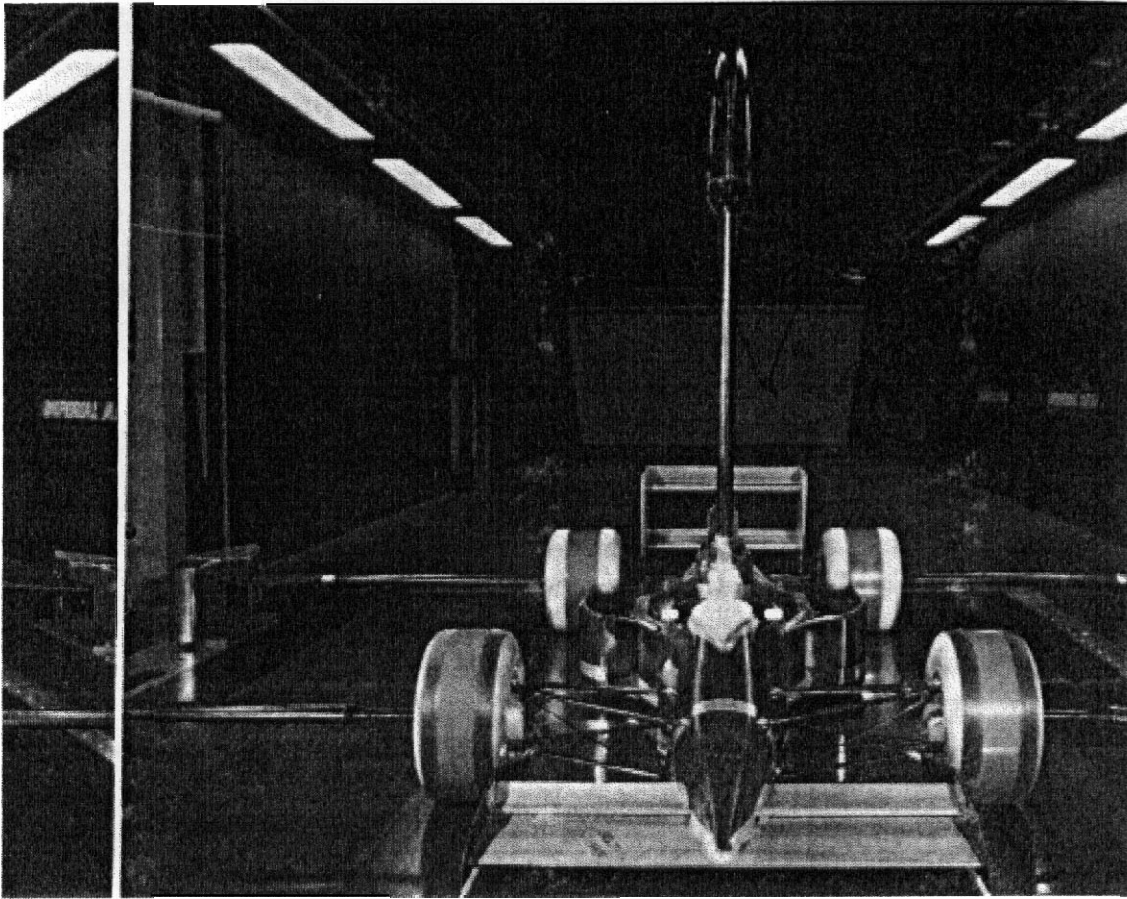
FIGURE 14.4   An open wheel race car in a wind tunnel. (From Katz, Joseph A., *Race Car Aerodynamics,* Bentley Publishers, Cambridge, MA 02138. © Bentley Publishers.)
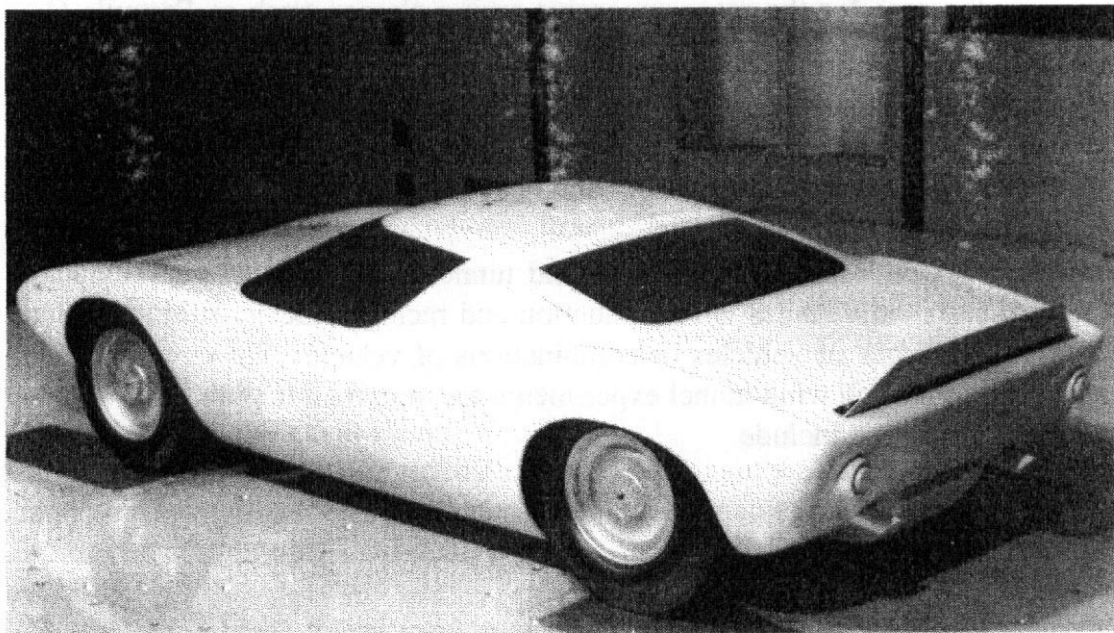
FIGURE 145   A LeMans/GT-type race car in a wind tunnel. (Photo courtesy of Glenn L. Martin Wind Tunnel.)
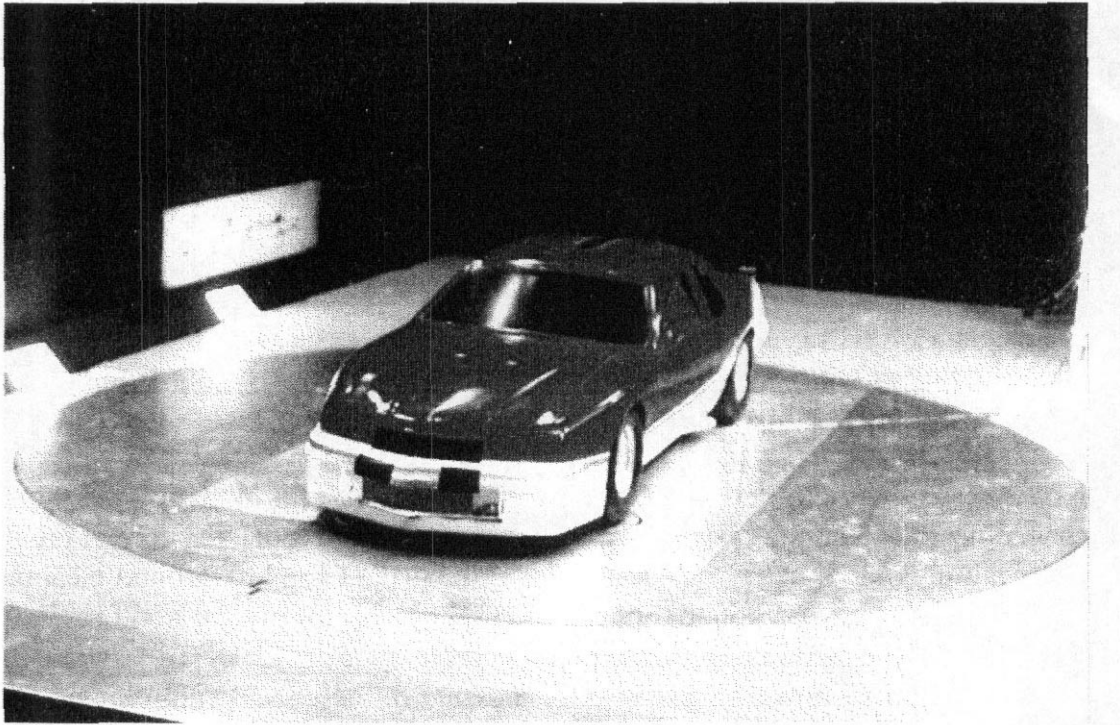
FIGURE 14.6   A NASCAR race car model in a wind tunnel. (Photo courtesy of Glenn L. Martin Wind Tunnel.)

in the wind tunnel correspond to good results on the track and only relatively fine tuning of the vehicle suspension settings in combination with the aerodynamic settings is necessary following the wind tunnel work. More and more racing car manufacturers have developed their own full-time dedicated wind tunnel. This is particularly the case for the more expensive racing classes, such as Formula One and CART.

14.3   TRUCKS, MOTORCYCLES, AND OTHER VEHICLES

By far the most widespread use of the wind tunnel as a tool in the aerodynamic development of road vehicles is in production and racing vehicles. However, there are a few more types of vehicles or combinations of vehicles that require special attention and for which wind tunnel experiments are important in their development or certification. These include

- trucks,
  motorcycles,
- tractor-trailer configurations,
  groups of vehicles, and
  trains.

The systems employed in the wind tunnel testing of these vehicles are in all cases similar to the ones applied to the passenger or racing automobiles. However, due to the specific requirements of the development, emphasis on different aspects of the testing changes with the type of vehicle tested.

A brief discussion of such requirements follows.

Trucks

For road-going cargo trucks there are primary concerns with comfort, safety, fuel efficiency, and practicality.

Typically the ground clearance of a road-going truck is very large compared to the thickness of a controlled boundary layer on the floor of a modem wind tunnel. Hence, unless the testing is carried with a very small scale model, the correct ground flow conditions have been considered less critical than for low-ground-clearance vehicles. Usually a good boundary layer suction system allows for good results to be obtained when developing this type of vehicle even in scale. There are some reasons for caution, however, because these vehicles are considerably longer with respect to their width than automobiles. This means that there is a longer relative distance over which the truck body flow field will interact with the floor or near road fluid. Since the rear of these vehicles is a part that continues to attract attention for possible drag reduction, the ground simulation should not be dismissed as an important aspect.

These vehicles are to be driven for many hours, often in very adverse weather conditions. It is then essential that the windshield, side windows, and rear-view mirrors be kept as free from deposits as possible. Be it from dust, snow, rain, or other undesirable particles. Great effort is then put into the development of the flow around the driver cabin in order to minimize these effects.

Another aspect that is of great relevance for this type of vehicle is the fuel efficiency. Typically these vehicles displace a very large weight, and considerable amounts of power and fuel are required to maintain a high average speed on the freeway. Due to practical considerations having to do with the need to maximize cargo space for the minimum wheel base, an optimum aerodynamic shape is not acceptable. Hence trucks generally have blunter shapes with sharper edges generating substantial base pressure deficits and high shape drag. In the development stages the usage of aerodynamic appendices and small changes that do not interfere with the practicality aspects can significantly reduce drag and improve fuel efficiency. Such improvements eventually reflect in the final price of the goods transported and are critical.

Another important aspect for truck aerodynamics is safety. Two major concerns during development are to control the value of lift forces generated at higher speeds, their distribution between the axles, and to make sure that the vehicle handles well when exposed to side winds. Numerous side-wind sweeps are carried for different configurations and details, such as radius of edges, deflectors, and other appendices. Details are optimized in order to guarantee the highest degree of safety.

Another important aspect is the cooling system. The power units in these vehicles are larger and operate continuously much closer to capacity than automobile engines. They produce an enormous amount of heat. The cooling system must then be carefully designed not only to ensure proper cooling of the engine compartment but also to do so in the efficient way possible.

Finally, due to the size of these vehicles and to the fact that most automotive wind tunnels are designed with small vehicles in mind, there are few wind tunnels in the world that will support full-scale truck testing. For this reason and for financial reasons scale testing is most commonly used. In development that does not include force measurements, however, some tests may be done at full scale even with the resulting higher blockage, taking advantage of the full-scale detailing level. This is typically done for the optimization of the window surfaces and mirrors for evaluation of deposits.

Tractor-Trailers and Groups of Vehicles

An aspect related to road vehicle safety and fuel efficiency is the interaction between the flow around different vehicles traveling in proximity or different parts of a compound vehicle. The wind tunnel becomes again fundamental for it allows the study of complex interaction features of these three-dimensional flows in a controlled environment.

At the same time, the test requirements become more demanding and more difficult to satisfy. This is because the scale of the models that can be used becomes more constrained for the given test facilities as the lengths of the vehicle combinations increase. The level of the experimental detail and sophistication for groups of vehicles is typically much less than is common for single-vehicle development. An example is given by the paper of Zabat et al.[12]

Trains

Aerodynamics of trains has become of greater importance as maximum speed has increased. The efficiency of rail vehicles supported by steel wheels on steel rails is very high compared to any other land mode of transportation. Aerodynamic resistance becomes the largest energy absorber other than grade climbing for long runs. Overcoming the aerodynamic resistance represents a larger and larger fraction of the overall power requirement as the speed increases. For the highest speed trains, for example the Japanese Shinkansen and the French TGV, aerodynamically generated noise becomes an important environmental issue.

The importance of aerodynamics and the utility of wind tunnel methods in addressing them is indicated by the large investment by the Japanese Railway Technical Research Institute[13] in a new wind tunnel capable of air speeds up to 300 km/h in a test section 5 X 3 X 20 m equipped with a moving-belt ground simulator 2.7 X 6 m capable of speeds of 60 m/s. The tunnel test sections can be arranged in several configurations. One is an open jet with a large anechoic chamber. The background noise level is reported to be 75 dbA at a jet speed of 300 km/h. A smaller test section

for use with model-scale trains and full-scale pantographs, a known source of noise, provides speeds to 400 km/h. The new wind tunnel opened in 1996.

We mention two examples of studies on aerodynamics of trains. The first study is on the limits of speeds in cross-wind operations.

The aerodynamic characteristics of the vehicle due to cross winds depends not only on the shape of the vehicle:-but also on that of the infrastructure (e.g., a bridge or an embankment along which the train is passing). A wind tunnel test was conducted using a model train on a particular trestle arrangement. The measured lift, side-force, and rolling moment coefficients and corresponding critical wind speeds are shown in Figure 14.7. The critical wind speed is that environmental wind speed that can cause overturning as a function of wind approach angle and vehicle speed.

The second study involves the search for a tonal noise of irritating amplitude during passing. A class of shinkansen train exhibited such an annoying pure-tone sound as it passed. The source was identified using trackside microphone arrays as a ventilating fan and louver combination. Examination of alternative configurations in a wind tunnel experiment using half-scale models showed that the source was a plate louver with circular holes for ventilating air passage. Alternative hole shapes that do not produce tonal sound radiation were identified and adopted.

Motorcycles

Aerodynamic experiments on motorcycles are conducted for the same reasons as for automobiles. However, a special emphasis must be put on the safety when the vehicle is exposed to side winds or to ensure high lift forces are not generated at high speed. In racing motorcycles low lift and drag forces are fundamental for the
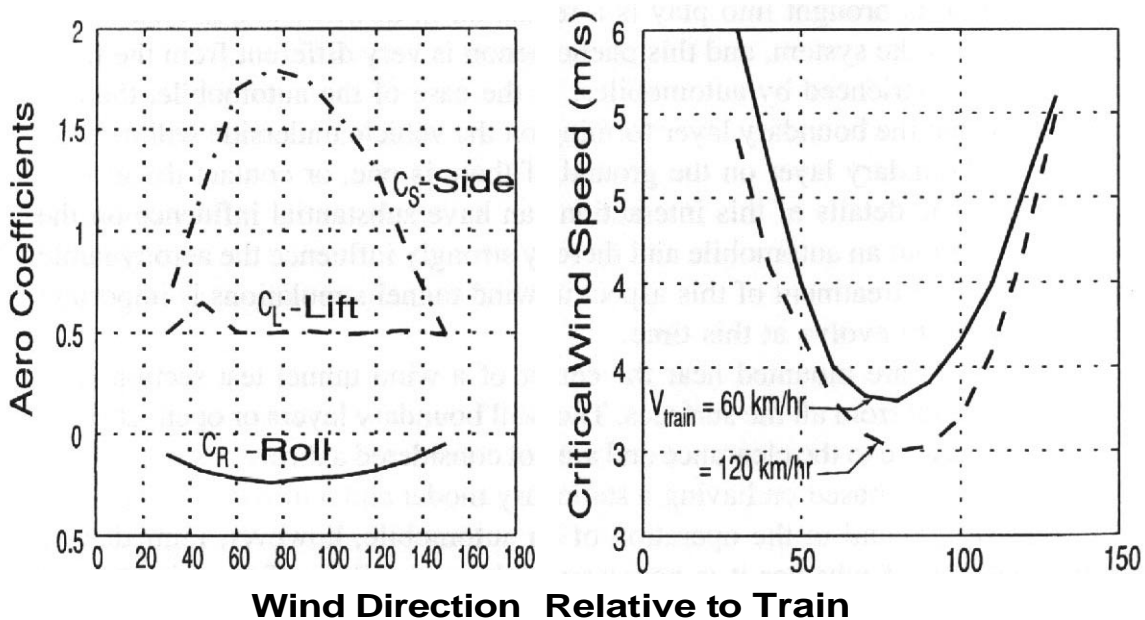
FIGURE 14.7   Aerodynamic forces and moments on first train car and corresponding critical wind speeds.

performance on a straight line and wind tunnel testing is instrumental in reaching competitive results. A particular aspect is that in this type of vehicle the driver is exposed to the flow, which makes the aerodynamic development more challenging. The aerodynamic characteristics of the rider–machine assembly must be investigated and tailored for a range of different vehicle–rider positions.

14.4   SYSTEMS FOR GROUND VEHICLE EXPERIMENTS

Methods that have been developed for measuring the aerodynamic characteristics of ground vehicles in wind tunnels and some indications of their genesis are presented next. Examples and discussion of actual implementation and some results of specific investigations are included.

Ground Influence and Treatment in Wind Tunnels

Background   Automobiles, trucks, motorcycles, and so on, move in close proximity to the road. Clearance from the surface varies with the intended use of the vehicle, with a value of 5–6 in. being common for passenger cars in a typical load condition. This may represent about 10% of the height of the vehicle and perhaps 3% of the length of the vehicle. The clearance for racing vehicles is typically as small as the rules and racing surface regularity will allow. Zero clearance around the edges through use of flexible material has been used in a few cases. This contrasts with the wing of an airplane that, even in landing, seldom comes closer than about half its streamwise length to the ground and still has clearance that is 5–10 times its vertical thickness. The clearance for a wing may be a fraction of its span, which is the dimension that is used to judge when a wing is "in ground effect," but the phenomenon that is brought into play is a reduction in downwash associated with a trailing vortex wake system, and this phenomenon is very different from the main ground effects experienced by automobiles. In the case of the automobile, there is the possibility that the boundary layer forming on the vehicle underside will directly mingle with a boundary layer on the ground, if there is one, or contact the ground if there is not. The details of this interaction can have substantial influence on the flow under and about an automobile and thereby strongly influence the aerodynamic characteristics. The treatment of this aspect in wind tunnel simulations is important and is continuing to evolve at this time.

Aircraft models are mounted near the center of a wind tunnel test section with very large clearance from all the surfaces. The wall boundary layers or open jet shear layers are thin relative to the clearance and are not considered a direct compromise of the simulation that is based on having a stationary model and a moving stream. The proximity of the ground in the operation of an automobile, however, immediately raises the question of whether it is necessary to have the floor of the wind tunnel moving at the same speed as the air to achieve a useful simulation. If it were technically simple to provide such a system, then it is certain that moving-ground systems would have been in wide use many years ago. Klemin[14] reported on a
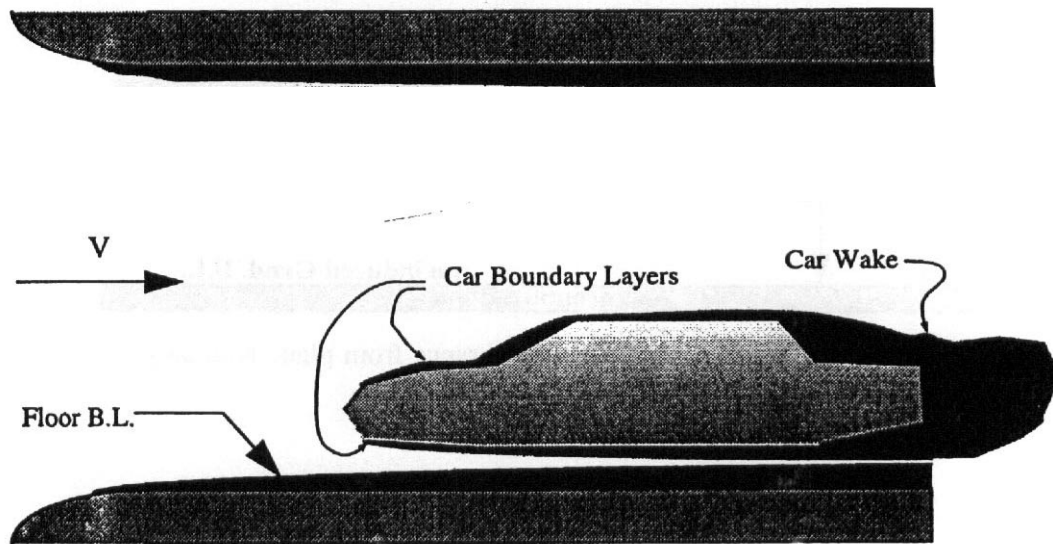
FIGURE 14.8 Schematic of a car in a wind tunnel.

moving-ground simulation more than 60 years ago. However, it is technically difficult and adds considerably to the costs of experiments. So a large majority of wind tunnel measurements of automobile aerodynamic characteristics have been done with stationary surfaces representing the ground. We will describe the most common methods that have been used and later will give some results of experiments designed to evaluate some of the methods.

The situation is indicated in Figure 14.8, which represents a cut through the center plane of a car. A very much simplified schematic representation of boundary layers on the tunnel ceiling and floor and on the car is given. A car on the road, ignoring ambient winds and gusts, would have boundary layers develop along its surfaces very similar to those on the model in the wind tunnel, but there would be only induced boundary layers on the road rather than a developed boundary layer as exists on the floor in a fixed surface wind tunnel,

It turns out that the influence of the car body under typical conditions in a wind tunnel actually reduces the thickness of the floor boundary layer in the vicinity of the car as compared to the boundary layer thickness on the tunnel floor in the absence of the car.

Fundamental Flow Features Consider a body moving through a semi-infinite fluid at various distances from a plane boundary. Assume the fluid far from the body is at rest relative to the plane boundary. Sketches indicating some primary characteristics are shown in Figures 14.9–14.12. The regions that are shaded are regions in which the vorticity is significantly different from zero. Nonshaded regions are parts of the flow that are essentially irrotational and behave nearly as ideal flow. These sketches are based on Wiedemann,[15] as is the approach given in this section.

Figures 14.9–14.12 represent the situation when a body is moving through a fluid that is stationary relative to the "ground" plane. This would also be the case
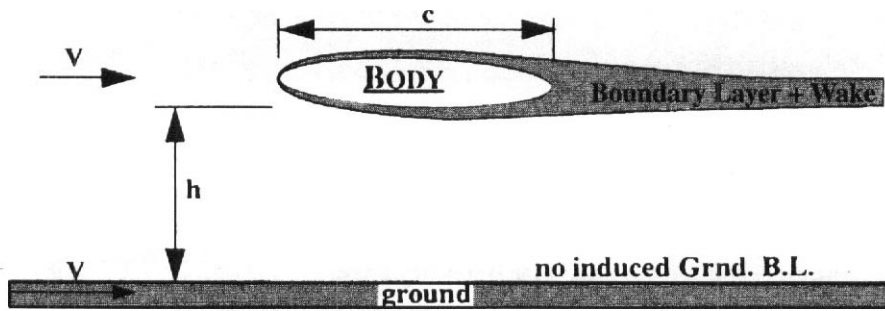
FIGURE 14.9   Body with large clearance from plane boundary.
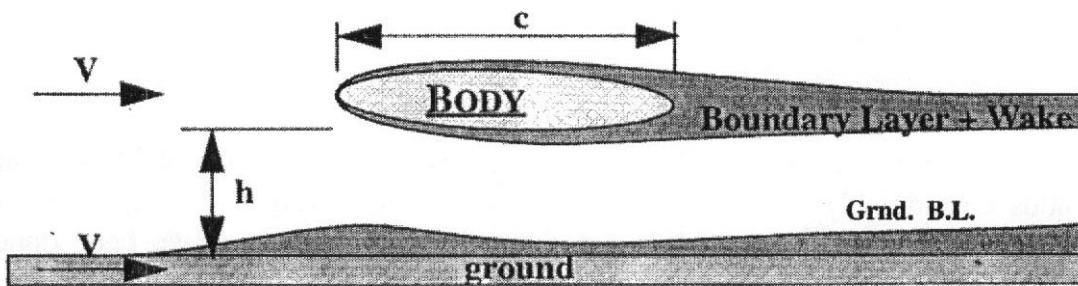
FIGURE 14.10   Body with medium clearance from plane boundary.
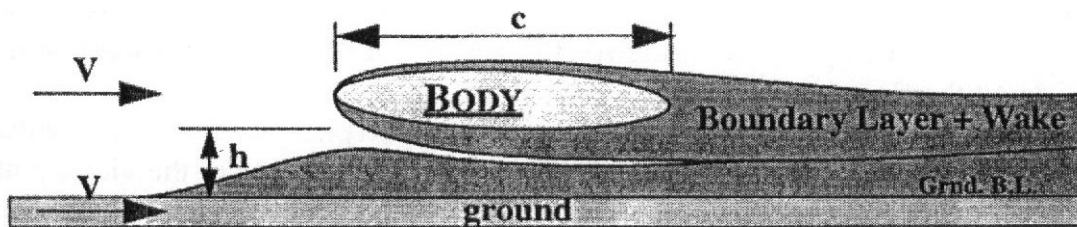
FIGURE 14.11   Body with small clearance from plane boundary.
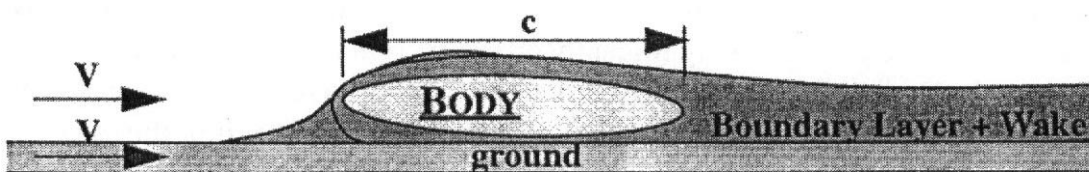
FIGURE 14.12   Body with very small clearance from plane boundary.

in a wind tunnel with a perfect moving ground with the speed synchronized with the stream speed. Following Wiedemann,[15] we describe the four cases shown.

- Large Clearance (Figure 14.9). The presence of the ground affects the effectively inviscid velocity distribution at the body. There is a small influence on the development of the boundary layer on the body. The induced flow near the ground is sufficiently small so that no significant boundary layer is developed. Medium Clearance (Figure 14.10). The presence of the wall is significant on the body and the presence of the body induces a significant boundary layer on the ground. There is a definite region of effectively irrotational flow between the boundary layer on the body and the ground boundary layer.
- Small Clearance (Figure 14.11). There is strong interaction on both boundary layers, and there is little mixing of rotational fluid or merging of the body boundary layer with the ground boundary layer within the streamwise extent of the body. There is no potential core separating the two boundary layers over much of the body length.
- Very Small Clearance (Figure 14.12). This is a limiting situation in which the viscous forces dominate the motion between the body and the ground. The convective terms of the Navier–Stokes equations become very small and the flow is essentially creeping flow.

The clearance of existing automobiles puts them in the middle two classes. Production vehicles fall mostly into the medium-clearance category while racing vehicles fall mostly into the small-clearance category.

Systems Used for Ground Simulation

Basic Fixed-Floor Wind *Tunnel*   It is obvious that in the case of a fixed-wall wind tunnel, there is already a floor boundary layer of some thickness determined by the particular local situation. Also, it is reasonable to consider a classification of flow analogous to that indicated in Figures 14.9–14.12 as the clearance is varied. The situation with a fixed-floor wind tunnel is indicated in Figure 14.13 for a representative height. There are clearly similar variations in the relative boundary layer thicknesses and some height at which the floor and body boundary layers begin to intermingle within the vicinity of the body. It is evident that critical
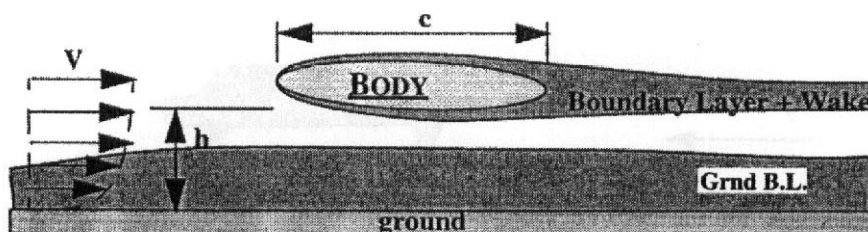
FIGURE 14.13   Body in fixed ground wind tunnel with exaggerated floor boundary layer.

parameters will be the ratio of clearance (h) to body size (c) and the ratio of clearance to floor boundary layer thickness as represented by displacement thickness or momentum thickness. When the incoming floor boundary layer is thick relative to the clearance, it has considerable potential to modify the flow about the body. In the first place, there is low-energy fluid that can be entrained more easily into the boundary layer of the body and the wake of the body. Second, the displacement thickness of the floor boundary layer will be modified by the presence of the pressure field of the body, which will induce a flow angularity that will vary with the streamwise coordinate. Historically, many measurements have been done with untreated fixed-floor systems. These measurements must be interpreted carefully. Data obtained with these systems have proved very useful in cases where the users have extensive data sets, including on road results for validity checking and where relative performance of alternative designs is directly evaluated. This is not a currently recommended practice.

Symmetry   The idea is to use two models with exactly the same shape inverted relative to one another so that there is a plane of geometric symmetry representing the ground (see Figure 14.14). For geometries and Reynolds numbers that lead to steady flow, this is a valid method of simulating a moving ground for large to medium clearances. However, there are two limitations. Fist, there are few, if any, cases of interest for which the flow is actually steady and for which the symmetric geometry can be known a priori to produce symmetric flow at all times. The mean flow may or may not be symmetric, although it is still common to encounter the erroneous assumption that symmetric geometry always yields symmetric flow. Second, if the clearance is such that there would be an induced ground boundary layer, this technique will not reproduce that effect. This technique has been applied in a few research studies but is not used in automobile development programs. In addition to the fundamental problem mentioned, the model costs are doubled for each experiment.

Elevated Ground Plane   A relatively thin plate, referred to as a **"ground plane,"** is mounted parallel to the floor of the wind tunnel and above the thickness of the floor boundary layer and extending entirely across the wind tunnel. The length required depends on the models to be tested but is commonly made the length of the test section. In some cases the length has actually exceeded the test-section length. The typical height will be three to five times the thickness of the floor boundary layer. A new and therefore thinner boundary layer begins along the up-

FIGURE 14.14   Symmetric models to obtain ground plane representation with no ground plane boundary layer.

stream edge of the plate. This technique is fairly simple and inexpensive but it presents some disadvantages, the most obvious, of course, being that the boundary layer is not removed but rather replaced. The new, thinner boundary layer may still affect some tests. Also some flow perturbations may result either from the introduction of the plate in the test section that changes the flow or by perturbations at the leading edge being carried downstream. A major difficulty is that the arrangement provides a split flow, below and above the plate, that is influenced by the characteristics of the test article. This makes accurate determination of the effective test speed significantly more difficult. Some installations included flaplike segments at the downstream end that were used to adjust the flow split above and below the plate. The support of the vehicle can be troublesome, especially if full-scale vehicles are to be tested. This type of mounting system was widely used into the 1970s but is little used today.

Raised Floor: Suction at Leading Edge   This system is used at the General Motors Full Scale Wind Tunnel and at the Glenn L. Martin Wind Tunnel among others. The arrangement is indicated in Figure 14.15. A blower is used to take the low-energy air from the tunnel floor boundary layer at the leading edge of the test section and reinject it at the downstream end of the test section. The effect is very similar to the elevated ground plane. There are two strong advantages. First there is positive control of the incoming flow through the easily adjusted suction blower setting. It is adjusted to make the floor and ceiling pressures at the entrance of the test section equal. Second the effective area of the test section is affected very little as the typical raised floor height is about equal to or somewhat less than the boundary layer thickness at the entrance of the test section.

Suction through Perforated Floor   This is the classic boundary control method that has been studied for decades as applied to airplane wings and other devices. It appears in two distinct forms for the current application.

The first form is the use of suction applied to a floor segment upstream of the model. This suction reduces the thickness of the boundary layer with the resulting boundary layer dependent on the amount of suction applied. The boundary layer begins to grow again at the downstream end of the suction segment. The result can be similar to the raised-floor method. The setting of the suction level can be more problematical, however, since the geometry does not provide a sharply delineated place where the streamlines are to be parallel. There is a delicate compromise
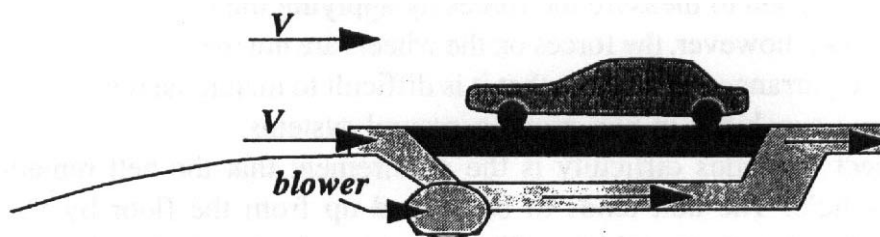
FIGURE 14.15   Tunnel boundary layer removal system.

between the amount of suction that yields optimum positive results and the effect that suction may have on the angularity of the flow. Usually smaller amounts of suction are used in conjunction with other techniques.

The second form is the provision of widely distributed perforations that allow suction throughout the test section, including under and beyond the model. This type of system can prevent a growing boundary layer, but practical limitations mean that it cannot duplicate the moving-ground case with precision. There is a necessary compromise associated with balancing induced flow angularity and boundary layer thickness allowed.

There are two wind tunnels at the Porsche[16] development center that use this type of system. Results have been studied and compared to measurements on the road and using other methods.[17,18]

Tangential Blowing   Fluid is injected parallel to the free stream through a thin slot along the floor and upstream of the model. The resulting flow is a case of a "wall jet" that energizes the boundary layer and allows the displacement and momentum thicknesses to be reduced or even made negative over some region. The displacement or momentum thickness, for example, could be made zero at the location of the front of the test article. There will, of course, be the typical thickening of the boundary layer with distance downstream, which will produce effective flow angularity. Mercker and Wiedemann[19] give a discussion of tangential blowing fundamentals as applied to ground simulation. Hackett et al.[20] conclude that tangential blowing provides drag results that are quite close to those for moving ground but that flow details and therefore other measures can differ considerably between tangential blowing and moving-ground conditions.

Moving Ground   A rolling belt is installed as the effective floor of the wind tunnel and ideally is run so that the belt speed matches the air speed in the test section. Conceptually one can exactly simulate the road condition; in a reference fixed to the vehicle we now have air and road movement. This method is considered to be the standard of comparison. It best simulates the real operating conditions. Disadvantages are of two principal types. First is the complexity and cost of the implementation of the belt itself. There are no belt systems today that match tunnel speeds of $200+$ mph $(100+$ m/s), although some are approaching this speed. Second the test article cannot just rest on balance pads but has instead to be held from the top or the sides. Either the balance is inserted into the vehicle or a fairly delicate system must be designed to measure the forces by applying the balance to the wheel axes. In this last case, however, the forces on the wheels are not measured. These more difficult measuring arrangements mean that it is difficult to match the repeatability of the data-gathering capability in non-moving-ground systems.

Another aspect that adds difficulty is the requirement that the belt remain flat under the test article. The belt tends to be sucked up from the floor by the low pressures present under many vehicles. This must be counteracted with a suction on the underside of the belt.

This system is very powerful. However, the setup and conduct of experiments involving a moving ground is considerably more time consuming, complicated, and expensive. It continues to be applied primarily to racing vehicles and to comparative tests for other vehicles rather than to production programs. There are indications that this may change in the near future.

Combinations Two or more of the above methods can be beneficially combined:

- Raised Floor and Tangential Blowing. If a tangential blowing slot is placed just downstream of the front of a raised floor, the wall jet does not have to overcome the velocity deficit that exists in the typical incoming boundary layer. This provides better control of the profile downstream of the blowing slot.
- Raised Floor, Tangential Blowing, and Moving Ground. This combination can provide a very good initial profile on the beginning of the moving belt. Other combinations such as concentrated suction upstream of a moving belt can also provide good initial profiles that are then maintained by the moving-ground system.

Wheel Rotation

Most experiments on ground vehicle aerodynamics that have been done in the past have been done with nonrotating wheels. This is true for experiments that have used actual vehicles in full-scale wind tunnels as well as for experiments that have used models. This is an obvious inconsistency with the real vehicles in actual operating conditions. The fact that many of these experiments have provided useful data is simply a result of the fact that most attention has been focused on the upper body external aerodynamics. And much of the focus has been on the single force component, drag. As attention is moving to the details of underbody flow, cooling flows, and the interplay of internal flows with external flows, provision of wheel rotation is becoming more important.

As with moving-ground simulation, which has long been recognized as required for technically precise reproduction of on-road conditions, so have rotating wheels. But provision of rotating wheels is also a technically complicating and costly addition that has not proven necessary for much of the historical progress in ground vehicle aerodynamics. But it is necessary element when complete simulation is required. One is faced with several significant decisions in the implementation of a system with wheel rotation. Several options are now described.

Rotating Wheels with Fixed Ground Systems using a fixed ground almost always support the vehicle on the wheels either by having them resting on a pad that in turn rests on the balance or by mounting a set of posts directly into the bottom of the wheels. If the wheels are to be rotated and the remainder of the system remains a fixed-ground type, this can be done by placing rollers under the floor with a relatively small exposure through the floor that supports the vehicle wheels. Figure 14.16 is a sketch indicating this arrangement. The motor-driven rollers are mounted
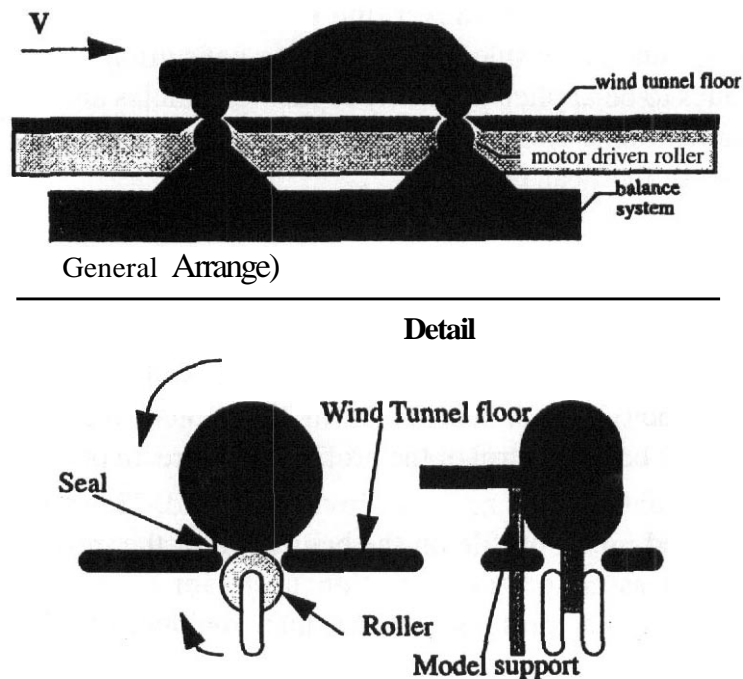
FIGURE 14.16 Rotating-wheel arrangement with fixed ground.

on the balance system so the highly reliable and precise external balance remains the primary data source. There must be a clearance between the wind tunnel floor system and the roller system.

A second system is to support the vehicle by posts at some convenient locations and drive wheel rotation through motors contained within the vehicle. Common post locations are just behind the wheels or just inside the wheels. This arrangement requires there to be a clearance between the bottoms of the wheels and the floor. Since this clearance is required to be very small to minimize the flow through the gap, maintaining it precisely can be difficult.

The various treatments available to improve ground simulation for fixed-ground systems can be combined with these wheel rotation systems.

Rotating Wheels with Moving Ground As previously indicated, the test article with a full moving ground must be suspended above the moving belt. The two options frequently used are suspension from above or from the side. In a few instances, a sting from the rear has been employed. This is an undesirable arrangement because the base pressure is greatly affected by a sting from the rear and base pressure is among the most important variables to be determined by an experiment on a bluff body. Adding rotating wheels to this arrangement can be done by addition of a drive mechanism inside the test article if clearance from the moving-ground surface is to be maintained as it must if the balance is to record total aerodynamic forces on the vehicle including the rotating wheels.

Several variations have been used. The wheels can be actually separated from the vehicle body and supported in position from the sides but resting on the moving belt so that the belt drives the rotation of the wheels. The body then is supported

from above with the forces on the body being measured. This introduces the difficult technical issue of infemng the effective net forces on the body plus rotating wheels. There is not sufficient data in the public domain to do this with confidence.

Multiple-belt systems can be conceived with possibility of supports from narrow between-belt sections. Such systems have not been implemented except for very small scale pilots. An example of such a system was used by Hacked et al.[21]

Combinations   A hybrid system that provides many benefits but still falls short of total simulation fidelity is to provide a moving-ground belt between the wheels and to place the wheels on rollers that rest on an external balance. Such a system is described by Coggotti.''

Choice of Scale for Experimental Studies

This is an issue with very different aspects for developers of ground vehicles as compared to the aerospace industry or marine vehicle industry. The proper perspective is obtained by revisiting the basic equations of fluid dynamics, which are reviewed in Chapter 1. The nondimensional form of the equations contains the two similarity parameters, R_e and M. We consider Mach number to be low enough in the present applications so that the incompressible limit is a valid approximation. This is not true, of course, for many aerospace applications. This is almost exactly true for marine vehicles. The Reynolds number is our most important consideration. In the case of aerospace vehicles, there **are** few cases in which a model-scale experiment can produce an operational Reynolds number. And there **are** even fewer cases in which a full-scale vehicle can be ground tested to operational speeds. So methods of extrapolation are very important. The situation is similar for marine vehicles.

For ground vehicles, there are a considerable number of wind tunnels that can accommodate full-size actual vehicles at operational speeds, and it is possible to obtain operational Reynolds numbers on models of scales from 1 : 1 down to around 1 : 3 in even more wind tunnels. Our equations inform us that we will obtain precisely the same fluid dynamic results so long as the Reynolds number is held constant, for any scale whatsoever, if and only if the geometric boundary conditions are precisely similar. To reiterate this point: What drives the choice of scale for an experiment? We assume that the ovemding requirement is technical. The choice must be technically correct. And among available technically correct options, it is likely that the most cost-effective option will be preferred. As indicated above, it is possible to achieve equivalent fluid dynamic results for a range of scales so long as the test articles have the requisite geometric precision. The costs can be considered to be the sum of the cost of the wind tunnel and the cost of the test article. The larger the wind tunnel the greater the cost of wind tunnel time. The cost of a test article, however, can vary widely depending on many aspects, with size being only one factor. Therefore, various projects will have a variety of optimal choices for the size of the test articles.

In many car companies the aerodynamic development of a new vehicle has historically encompassed a period of scale model testing. This usually happens in an early design phase when clay models have almost universally been used in both studio design studies and aerodynamic development. The most common scales have been .375 and .400, although tests have been carried at many other scales. The use of scaled models at this stage offers several benefits. They **are** usually somewhat cheaper to produce than a full-scale clay, especially if they are essentially copies of a studio clay. The evaluation experiments can be done in a smaller and therefore less expensive wind tunnel. Handling and transport are less costly for models as compared to full scale. Use of scaled models is hence very attractive because it is cost effective. This is partly because there is not a requirement to reproduce the precise geometry of a production vehicle. This requirement is to discern the incremental effects of theme choices rather than to produce exact scale results.

As further refinement in the effects of details is sought, the cost of modeling becomes higher. However, the development of fast prototyping techniques such as stereolithography has provided a quick and effective way to produce accurate parts for any of the typical scales that are used.

Ground Simulation   The boundary layer thicknesses in wind tunnels that are geometrically similar are proportional to the sizes of the wind tunnels. This means that systems for ground simulation also scale in the same way. In the case that model-scale experiments are to be conducted in the same tunnel as full-scale experiments, it is necessary to have ground simulation equipment in both scales. However, that is not too common, especially for passenger car development, and a compromise is sometimes reached with some boundary layer thickness decreasing technique. These systems are usually optimized for the full-scale experiments. Hence when a scaled model is evaluated, the ratio of boundary layer thickness to ground clearance of the test body is much higher than for **full** scale. This can have great impact on the results since a very relevant **part** of the body (the underside and wheels) will be exposed to a lower kinetic energy flow.

Detailing   The single most important factor in obtaining good results from comparative and repetitive aerodynamic experiments on vehicles is the accuracy of geometry of the test article. This should be obvious since the flow structures, pressure losses, and all other aspects of the flow around and about a car body are highly dependent on details of the geometry.

Road Tests versus Wind Tunnel Tests

When on a road an automobile often experiences a reality that has little to do with the steady, controlled, and homogeneous flow to which it is exposed in a wind tunnel. When on the road wind gusts with variable direction and intensity are common, as are wakes from passing vehicles and obstructions from different bodies. Variations in air temperature, sun radiation, and road temperature are also common, as are winter conditions with extremely wet or icy road and rain and snowfall.

Although rain is fairly easy to simulate in a wind tunnel, many other factors cannot and are not simulated. Road testing is fundamental in automobile development programs. The two forms of testing, while different in nature, are complementary.

Wind tunnel testing is safe when it comes to concealing a new product; changes can be performed to the vehicle or model quickly and in house, which makes them less expensive. Most importantly the conditions in the wind tunnel are controlled and predictable. Repeatability is high so comparison tests are in order. If the company owns its own tunnel, then there is the added advantage of convenience. Many people will have access to the test without leaving their work place. Of course wind tunnels, especially in full scale, are very expensive to build and operate, and road testing is still required.

Road testing is a mandatory part of a development program. It is the only way to really test a proposed vehicle's performance, and millions of miles of road testing are necessary during development. In aerodynamics, however, these tests are relevant, concerning side-wind stability and the study of deposits on windows, tail lights, and other parts of the vehicle that may affect safety. It does present engineers with a real-life test. However, it is usually expensive to relocate a team of engineers and test drivers along with test vehicles, there are safety concerns when the project is classified, and the repeatability of the conditions is very difficult to achieve.

An interesting study concerning the effects of turbulence experienced by road vehicles in road conditions was conducted by Watkins et al.[23] In their study a moving vehicle was fitted with hot-wire anemometry and a survey of the turbulence intensity under normal weather conditions (winds up to 10 m/s) and under extreme winds was conducted. The study revealed that for normal operating conditions the vehicle was exposed to a longitudinal and lateral turbulence intensity of 2.5–5%. For the case of strong winds it ranged from 2 to 10%. Spectral analysis showed that the energy peak was centered at about 1 Hz and ranged from 0.25 to 2.5 Hz. The study suggests that some wind tunnel testing should be conducted with higher turbulence levels in the flow, namely, yaw tests, since strong side flow on the road is highly turbulent. For more details the reader is encouraged to read the original paper.

Ground Effects in Race Cars

One of the greatest concerns of race car aerodynamicists is with the lift forces generated. As described above, the effect of lifting devices in near-floor situations changes dramatically and can induce significant increases in lift forces. As a consequence this concept is applied successfully to the design of race cars by applying wings near the ground or by shaping the underbody of the car in order to take advantage of the ground effect.

Both cases are particularly relevant for wind tunnel testing. The sensitivity of the aerodynamics of vehicles that depend on ground effects significantly increases the need for an accurate ground simulation in testing.

The introduction of a sloped underbody in a race car together with a restricting surface on the sides of the body transforms the region between the car and the road into a channel. The side restricting surface can be composed of either skirts of

flexible material or solid walls when the underbody is shaped as to include ducts. The resulting effect is much like in a venturi type duct and hence these ground effects are commonly referred to as **venturi** effects (see Figure 14.17).

The idea is that the air that flows through the underbody region is accelerated up to a certain point and then slowed down through an expansion region where the flow is allowed to recuperate pressure to the ambient value. Since we are dealing with incompressible flow, the region with high-speed air flow will have a lower pressure and down force is generated.

The air speed and associated pressure decrease **are** critical for the lift forces generated. It is then fundamental that for race cars that depend heavily on ground effects a moving-belt facility be used.

This is a simple conceptual description of the phenomenon and the plots in Figure 14.18 help illustrate the effect. The reader is referred to a more in-depth discussion on race car aerodynamics for more details.

Automotive Aeroacoustics

Introduction The following description is generic and the concepts described are valid for trains, motorcycles, and other ground vehicles for which wind-generated noise is relevant. The examples of application are however centered on the automobile.
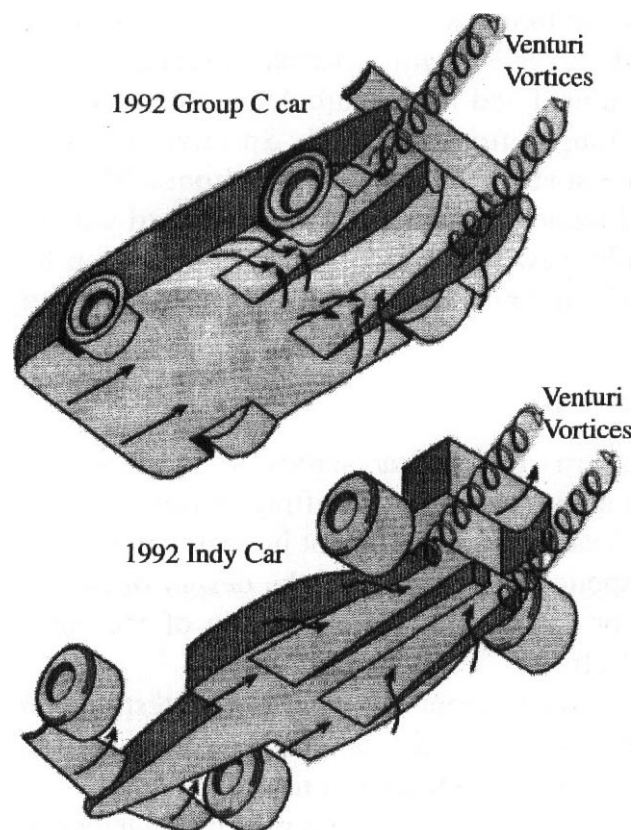
FIGURE 14.17 Venturi effect bodies: ducted flow; Side skirted body. (From Katz, Joseph A., Race Car *Aerodynamics*, Bentley Publishers, Cambridge, MA 02138. © Bentley Publishers.)
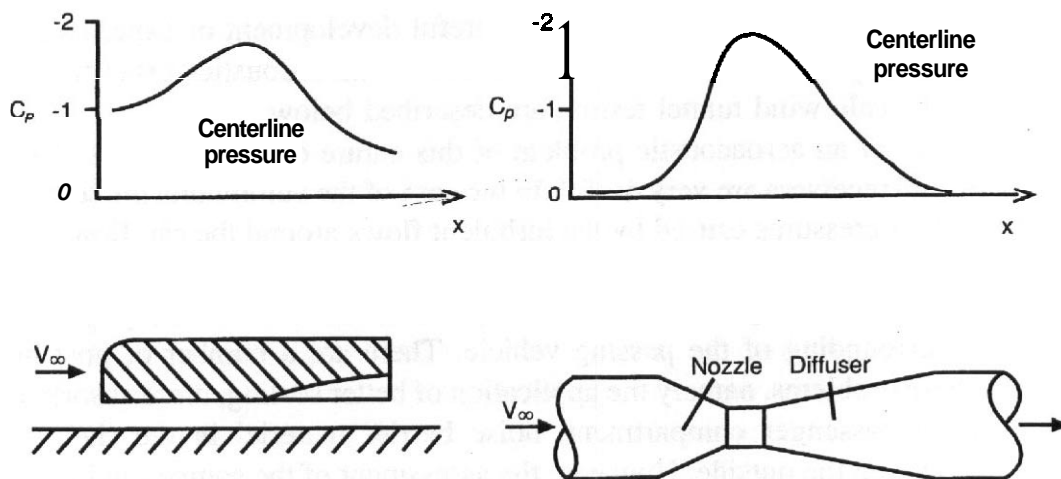
FIGURE 14.18   Pressure coefficient: analogy between race car and duct. (From Katz, Joseph A., *Race Car Aerodynamics,* Bentley Publishers, Cambridge, MA 02138. © Bentley Publishers.)

In the last 15 years the automotive design process has seen a rise in the importance of aerodynamic design accompanying a general trend of increase of high-technology input into the automobile. Gradually quieter and more efficient engines, transmission, and tires together with an increase in the average travel velocity of the automobile have created a need for understanding and predicting the effects of aeroacoustics in an early stage of product development. This need for development has propelled a number of experimental and computational approaches that are useful for the automotive design process.

Automobile noise can be categorized as interior and exterior noise, the interior noise being of more relevance to the internal occupants of the vehicle and the exterior noise being of relevance for standing observers. The exterior noise is also related to some environmental concerns.

The purpose of this part of the text is to present a summary of the problems involved in the aerodynamically generated noise in the automobile, how the minimization of these problems is tackled in the design of new products, and the role of the wind tunnel in this process. Note, however, that this text is only introductory to the subject of automotive aeroacoustics, and further references should be consulted for a more in-depth discussion.

In a car with an aerodynamically perfected external shape and details the customer will expect low levels of wind noise at high speeds. This is not always the case. In fact, the evolution of drag and lift coefficients in the last 20 years has made cars more efficient and stable but there is no guarantee that the aerodynamic optimization of the shape will yield low wind noise levels. There is a large number of details that, if not attended to, will create different sources of noise that will disturb the user and surrounding environment. Finding those details and dealing with them in an efficient and cost-effective manner are the job of the automotive aeroacoustician.

Approach to Automotive Aeroacoustics   Since there is no established similarity rule for the measurement of noise as there is for force measurements, the experimental work carried in this field is mostly composed of full-scale wind tunnel testing.

Full-scale wind tunnel time is expensive and careful development of experimental methods is necessary. Some state-of-the-art automotive aeroacoustics experimental methods for full-scale wind tunnel testing **are** described below.

In the analysis of an aeroacoustic problem of this nature clear definitions of the sources, path, and receivers are very useful. In the case of the automobile the sources are the fluctuating pressures caused by the turbulent flows around the car, flow over surface gaps, and protrusions and outright leaks. The paths **are** the body shell of the car and the surrounding static fluid, and the receivers are the occupants and others in the surrounding of the passing vehicle. There are a number of possible solutions to these problems, namely the application of better sealing, more absorbing materials in the passenger compartment, noise barrier material in the shell, or improved air flow on the outside. However, the assessment of the sources and needs of the users are quite a challenge.

Hypothetically we could solve the equations of fluid flow for the turbulent flow on the outside and use established theories of solid mechanics, acoustics, and vibration to calculate the acoustics inside the passenger compartment. Of course this is not possible, for closed-form analytical solutions are not available and computational models are only useful to a certain extent due to lack of accuracy. Nevertheless, the use of approximate models is of some importance. The models can range from fairly elaborate ones making an attempt to solve for the full flow numerically to those where the near-field flow is solved numerically and a **Kirchhoff** method is used to find the far field, or even, in what is the most important approach, approximating the near field flow with sound and then using some variation on Lighthill's acoustic analogy to find the radiated sound. This is the approach that is generally followed here.

The commonly used sound radiation models are the monopole, the dipole, and the quadrupole.

The monopole source effect, from an unsteady introduction of volume into the surrounding fluid, is the most efficient noise generator at low Mach numbers (typical of automobile flows). The next most efficient generator of sound at low Mach numbers is the dipole source, related to the unsteady application of forces on the fluid. Finally the least relevant source for automobile flows is the quadrupole, which results from internal stresses and turbulence inside the flow.

The monopole, or unsteady volumetric addition, source is relevant for automobiles, and a good example is the exhaust pipe volume addition. This (as well as the engine intake manifolds) is considered a primary monopole source and can be very effective in producing noise. Primary sources are dealt with in a high-priority basis during the development process so that a well-designed car will have these sources well minimized. However, secondary types of monopole sources can be very annoying and are not as carefully evaluated in many cases. Such is the case of leaks in the sealings of doors or unsteady addition of volume to the passenger compartment through some leak path.

The dipole type of source results from unsteady pressures acting upon a rigid surface. Hence the separated turbulent flow impinging on a surface can be considered a dipole type of source. These types of sources are very characteristic due to the

large number of regions around an automobile where the flow is separated. Another type of dipole source results from the unsteady forces generated due to the von Karman vortex shedding in the wake of the antenna.

The quadrupole source is caused by collisions of fluid elements and is typical of the turbulent shear layer of a jet. We will soon show that the ratio of quadrupole source strength to dipole source strength is very small for automotive flows. Since dipole sources are invariably present in automotive aerodynamic noise, quadrupole-type sources can usually be ignored since they are comparatively very weak.

Velocity Dependence and Scaling of Automotive Noise   For the case of compact sources (the size of the source is small compared to the wavelength of the perturbation) we have that, for a monopole source,

$$p = \frac{\rho}{4\Pi r} \frac{\partial}{\partial t} \dot{Q}$$

and for a typical velocity V and a length L the volume flow $\dot{Q}$ is proportional to VL^2.

Approximating the derivative with *an* order-of-magnitude approach $\partial/\partial t \sim V/L$ and introducing the intensity given by $I = p^2/2\rho c$, we get

$$I_{\text{monopole}} \sim \frac{p}{r^2 c} L^2 V^4$$

For a dipole source we have

$$p = \frac{1}{4\pi r \rho c} \frac{\partial F}{\partial t} \cos q$$

The force is proportional to $\rho U^2 L^2$, so we find, for the intensity,

$$I_{\text{dipole}} \sim \frac{\rho}{r^2 c^3} L^2 V^6$$

Finally for a quadruple source, which can be thought of as equal and opposite dipole sources, the intensity can be shown to be

$$I_{\text{quadropole}} \sim \frac{\rho}{r^2 c^5} L^2 V^8$$

If we divide these intensities, we find the ratio of the strengths. We find that the dipole source strength divided by the monopole source strength is proportional to the square of the Mach number. Similarly, the quadrupole source strength divided by the dipole source strength is proportional to the square of the Mach number. From this we find that for low-Mach-number flows if monopoles are present they

will be the primary noise source. If not the monopoles, then the dipoles will be preponderant if present and quadrupoles will be relevant only if no monopoles or dipoles are present.

A key factor regarding automobile aeroacoustic noise is the dependence of the sound pressure level (SPL) on velocity for different types of sources. It is known that the SPL of a simple monopole source is proportional to the fourth power of the velocity. Also it is known that for the dipole source the dependence is on the sixth power of the velocity. For the quadrupole it is the eight power. Since automobile aerodynamic noise is typically a combination of monopoles and dipoles, the dependence on velocity will be somewhere between the fourth and the sixth power of velocity (this fact has been confirmed experimentally). It is then obvious why aerodynamic noise becomes very relevant as velocities increase. Another important conclusion is that when making aeroacoustic measurements the velocity must be very closely controlled to ensure repeatability. This can be done in most modem wind tunnels but is nearly impossible on the road due to unstable winds that change the effective flow velocity. For this reason, noise measurements on the road are not used for development purposes and wind tunnel testing is of fundamental importance.

Another effect of velocity is on the propagation of sound originated by separated flow phenomena or other dipole-type sources. The analysis can be carried with velocity or with the pressure coefficient. It can be shown that for a dipole type source we have

$$\left(\frac{V}{V_\infty}\right)^6 = (1 - C_P)^3$$

where V is the local velocity, V_∞ the free-stream velocity, and C_P the local pressure coefficient. Let us compare several regions subject to similar turbulent flow structures. If the pressure coefficient is -1 in one region and zero in another, the region with lower C_P will generate a SPL that is 9 dB larger than for the other region, according to the sixth-power rule. If $C_P = -2$, which is not uncommon around the A-Pillar, the difference will be 14 dB. Moreover, at the stagnation point where $C_P = 1$ no sound will be generated.

In a similar fashion, flow affected by an upstream separation region will generate less sound if its velocity is decreased. An example is the flow underneath the car that is slowed down further downstream as it passes through all kinds of protuberances. Even a reduction to three-quarters of the upstream velocity results in a decrease of 7.5 dB in radiated sound for a component in the flow.

One of the main outcomes of this analysis to aeroacoustically efficient vehicle design is that the placement of geometrical characteristics that cause separation should be done in regions of lower speeds and higher pressures. Special care must be taken with add-on objects that are exposed to high velocities like antennas or rear-view mirrors.

Estimates of Typical Frequencies   Some interesting information is obtained when one tries to estimate the frequencies involved in automotive aeroacoustics phenomena. For many noise sources the Strouhal number is of the order of unity. The Strouhal number relates the frequency of a sound source to the length and velocity scales associated with that source. The Strouhal number is defined as $S_t = fL/D$, where f is the frequency in hertz, L the length scale of the source, and V the velocity scale of the source. If we consider the whole car, we have that with a velocity of 30 m/s and a length of about 5 m we find that the frequency of the large-scale separation in the rear-wake region is of the order of 6 Hz. If we consider the wheel housings and underbody areas with length scales ranging from 10 to 50 cm, the resulting frequencies are 60–300 Hz. If we consider details on the exterior of the body ranging from 10 to 100 mm, the resulting frequencies are of the order of 300–3000 Hz. Also it is known that the Strouhal number for a circular cylinder in the flow regime in study is approximately 0.2. Thus, given a flow velocity of 30 m/s, a 4-mm-diameter radio antenna will produce a tonal noise at approximately 1500 Hz.

Automobile Aeroacoustic Sources   Aerodynamic noise contributors can typically be grouped into three categories:

  aerodynamic noise due to the basic shape of the vehicle and exterior components such as outside rear-view mirrors, antennae, and others;

  noise due to flow over surface gaps such as around the doors; and

  noise due to leaks through seals.

Separated-Flow Regions   Most of the aerodynamic drag in automobiles is due to the large low-pressure separated region in the base of the body. However, this is not the most annoying source of dipole-type noise from the flow because the frequency of the sound is very low. Smaller features can cause more annoying sounds, such as the external rear-view mirrors. The wake flow of the mirror has some energy and is impinging on the front side windows. These windows are usually made of glass and placed close to the passenger's ears. This can often be the most annoying source of sound in an automobile. Some of the most relevant effects are presented below in more detail.

The rear-view mirrors are placed in a very high turbulence and velocity flow and their design is an important part of the aerodynamic development of a new vehicle. The design accounts for the drag and lift forces produced and for the deposition of deposits on the side windows. The noise generated is then one of many parameters that have to be optimized along with the styling constraints, which can be stringent. However, and generally speaking, the rounding of the trailing edges of the mirror will have a positive effect in decreasing the noise generated in that region. In fact, any change that affects the size and direction of the wake can be very relevant.

Another cause of high wind noise due to separation is the windshield wipers. The flow over the hood of most cars today has little or no flow separation, which

results in a high velocity impinging flow on the wipers. The result is again a **high-** frequency noise close to the ears of the passengers. Solutions to this problem usually encompass a kick-up of the flow before it reaches the wipers or simply hiding the wipers in a recessed cavity below the hood.

Yet another common source of annoying noise is the radio antennae. The process of von Karman vortex shedding that occurs is a well-known periodical phenomenon that occurs when a circular cylinder is exposed to flow at high enough Reynolds number. This results in a tonal noise that some manufacturers have tried to diminish by tripping the flow in order to prevent the formation of the von Karman street. Some solutions include wrapping a helical stake around the shaft of the antennae (much like in industrial chimneys), including part of the antennae in a sleeve or boot, or varying the diameter of the antennae in a stepped fashion.

Finally the existence of roof racks or other objects of that nature will cause flow separation and/or tonal noise of the type generated by a cylindrical antenna. These objects are of a very practical nature, and usually the solution to decreasing the noise generated is to trip the flow to separate before reaching these objects. But a specific solution depends on the geometry of the protuberance involved.

Note that even if the automobile was completely streamlined and no flow separation would occur there would still be noise, for the flow has a Reynolds number in the order of 10^6 or 10^7 and the boundary layer that would develop along the surface would be turbulent and would generate noise.

Cavity Noise   Two types of noises originate from flow through a cavity: through the big cavities (e.g., open windows and sunroofs) and through the small cavities (door and panel gaps).

The flow through large cavities can generate trailing-edge noise or leading-edge noise. A critical and very undesirable situation occurs when a disturbance is created at the leading edge. This disturbance is then convected to the trailing edge and an acoustic wave is produced. Under the right condition this acoustic wave is propagated upstream and triggers another disturbance at the leading edge, and the process continues to get stronger and stronger. This acoustic wave can then trigger a standing wave in the passenger compartment that is felt as a strong low-frequency throb. This can be extremely annoying. The usual way of dealing with this problem in sunroofs is by tripping a kick-up of the flow at the leading edge. Regarding side windows such solutions are not as easy to implement so the initial design must take this effect into account. The positioning of the rear-view mirrors or partially limiting the opening of the rear windows can help minimize the problem.

The flow through small cavities can potentially be very annoying since the resulting sound is usually a high-frequency tonal sound. Also many modem cars have rear-view mirrors that are designed to fold in case of a collision, and there are additional gaps in these regions, which can be very effective in noise generation since they are exposed to a very high speed turbulent flow. The solution to this type of problem is usually the introduction of additional acoustic sealing in the exposed cavities.

Leaks   A leak is a monopole type of source and hence it is not uncommon for a source of this type to dominate the noise generation. A leaking seal, for instance, can increase interior noise by as much as 10 dB. Common places for leaks are the window seals, the movable window seals, and the Axed side-window seals. The existence of a leak can increase the interior sound level by both the very monopole characteristics of unsteady mass injection and by allowing sound propagation without interference of the structure of the car, which would normally introduce a significant transmission loss.

The two types of noise source mechanisms are represented in Figure 14.19. In the first case there is path for flow to go through the sealing region and there will be mass injection. If the mass injection is unsteady, we will have a monopole type of source. However, even if the injection is steady, the flow will separate and be turbulent in region 3 giving rise to dipole type of sources in the separation region and quadruple type inside the turbulent flow. In the second case sound is transmitted through a seal even if there is no flow. If there is a high enough pressure $P(t)$ on the outside that will move the seal back and forth, noise will be transmitted. This movement will be resisted by the seals' stiffness, mass, and damping. The best solution (as expected from analogy with the wall case) is found to be to have multiple seals rather than to try to increase the mass or stiffness of a single seal. It is experimentally found that doubling the stiffness or mass of a seal will give a 3-dB increase in attenuation whereas using a double seal can double this attenuation.

Underbody and Wheels   The extremely turbulent and separated flow between a car and the ground as well as around the wheels is responsible for noise generation that is then transmitted through the lower parts of a car or even propagated around the transmitted through side panels. However, due to the complexity of the flow
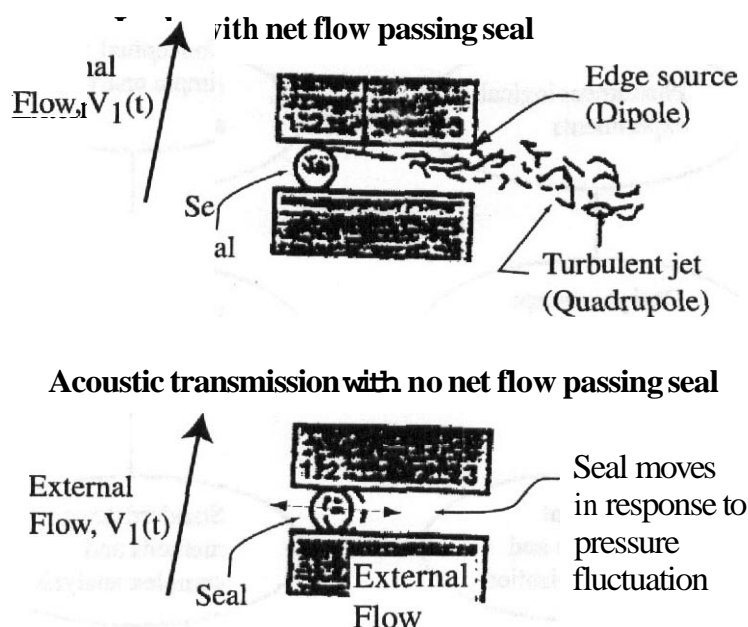
FIGURE 14.19   Scheme of typical leak system.

involved, there is not much information available or many studies carried on in this area.

Analogy with Aircraft Noise   Many aspects of aircraft noise are still completely understood. This is even more so in automotive aeroacoustics. Figure 14.20 shows schematically the various stages of development of experiment and analysis. Automotive aemacoustics is still operating in stages 1 and 2.

Exploratory experiments to pin down noise sources are being conducted that are looking at very idealized models of these sources and in more advanced cases doing phenomenological experiments on particular identified generic source types and looking at the first concepts and analyses for predicting and reducing the noise from them. We are still far from having design concept verification experiments or specific design ideas and analyses used, even on a development basis. We have quite a long way to go before we will be doing developmental tests for these problems.

Experimental Methods   Measurement of automobile aerodynamic noise is usually performed by placing the vehicle in a wind tunnel and placing a number of microphones at the passengers' head positions. Then the wind tunnel is run at moderate speeds and the microphones are used to get a time average of the SPL in the

Experiment and Analysis
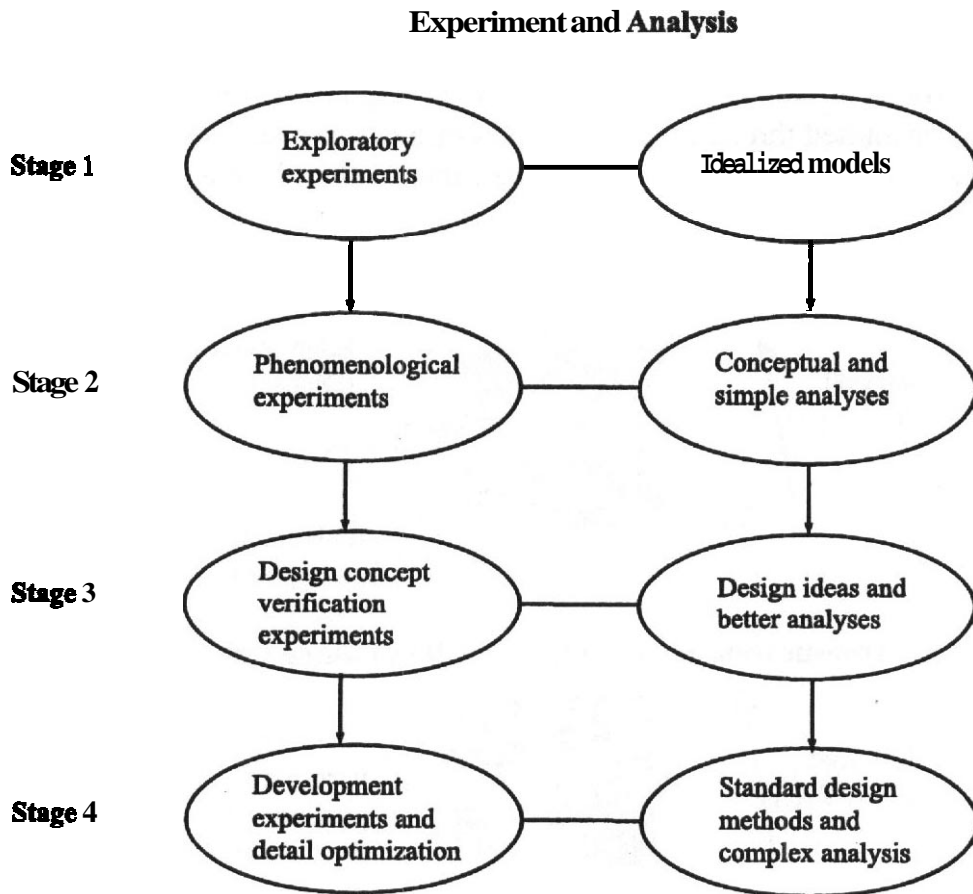
FIGURE 14.20   Experiment and analysis scheme.

automobile interior. Typically, the signal is averaged over a period of 60 s or so. Once a baseline level for the automobile aerodynamic noise interior SPL has been measured, one can use trial-and-error techniques to see which specific components and regions contribute more to the total SPL. This procedure can be quite time consuming but the results are usually good.

Instead of a simple microphone, an artificial head is commonly used. The artificial dummy is shaped after a human body and different microphones are placed in the artificial ears. The artificial head then gives results that agree better with what a human occupant will hear. One can then analyze the signal on-line or record it for playback. The playback possibility allows for a panel of listeners to subjectively evaluate different aerodynamic noises helping the design engineers correlate the objective values with the subjective human perception of the noise.

Role of Psychoacoustics   Psychoacoustics is the study of the human response to acoustic stimuli.

Sound quality applies psychoacoustic principles to the study of how humans perceive sounds from various sound sources such as automobiles. The application of sound quality to automobiles is as follows. The first step is to obtain sound recordings preferentially with an artificial head setting of microphones. The second step is to conduct subjective evaluations of the perception of these sounds by a panel of listeners. The subjective evaluation step is crucial for without good subjective data the correlation with the objective data will be poor and hence little is gained from the experimental measurements. The third step is the objective characterization of the sounds in study. Psychoacoustics metrics such as loudness, sharpness, and roughness as well as narrow-band spectra, one-third-octave spectra, and other measurements are introduced and can help in categorizing the subjective data. The final step in the process is to correlate the subjective impressions with the characteristics of the sound that underlie these impressions. If a strong correlation is achieved, the design process can be much improved if sources can be related to effects.

Quieter Wind Tunnels   The reduction of wind tunnel background noise is one of the single most important actions that can be taken to improve the results obtained from automotive aeroacoustic measurements. There are several wind tunnels in operation today that are specially fitted for aeroacoustic developments. Examples of tunnels especially designed for this purpose are the DNW wind tunnel in Holland, the BMW Technik and AUDI acoustic wind tunnels in Germany, and the Nissan and Honda acoustic wind tunnels in Japan. Examples of tunnels that were not originally designed for acoustic work but that have recently been retrofitted to lower background noise are the IVK wind tunnel of the University of Stuttgart in Germany, the Lockheed low-speed wind tunnel in Marietta, Georgia, and the Pininfarina wind tunnel in Italy.

There are number of actions that can be taken to decrease the background noise level. As one would expect, one major source of noise is the fan. Replacing the fan with a low rotation speed design can decrease the noise level considerably. Another important step is the treatment of the walls of the wind tunnel circuit with absorption

material. The IVK tunnel uses a newly developed (and very expensive) treatment on the walls that is very effective. In the design stage of a wind tunnel an open section type of tunnel is attractive because the limiting walls are outside of the flow, which allows for a very efficient wall treatment to be used.

Exterior Automobile Aerodynamic Noise Measurements   A major application of exterior noise measurements data is the prediction of the effect of that noise on outside observers. However, there are other reasons why these measurements are important in an attempt to work on interior acoustics problems. These are the so-called indirect measurements. While the correlation between the exterior radiated noise and the interior SPL may not be 100%, the exterior measurements can indicate important qualitative changes. An immediate application is the use of microphones to evaluate the acoustic behavior of exterior rear-view mirrors in an early stage of development when clay models are being used. Outside microphones can be placed in the flow, in which case a nose cone must be inserted to allow the flow to pass smoothly over the microphone, minimizing the self noise caused by separation phenomena in the microphone itself. Or they can be placed outside the flow (in an open test-section wind tunnel), in which case the self noise is eliminated but a correction for the effect of the shear layer must he introduced.

Imaging and Source Localization   Localization of sources is usually accomplished using arrays of microphones or special-purpose microphones in reflectors called "directional microphones." In the next paragraphs these techniques are described in greater detail.

Microphone Arrays   Arrays of microphones together with the appropriate software for signal processing are a unique tool for locating and identifying individual sound sources on either stationary or moving bodies. A great deal of experience in using microphone arrays has been gained during studies of sound sources on high-speed trains, aircraft engines, and engine jets as well as in making directional measurements of noise emission by industrial machinery and processes over large distances. Arrays of flush-mounted microphones may be used to measure and evaluate surface pressure fields on surfaces exposed to flow. Finally, array technology is also used to locate and identify sound sources on motor vehicles. Two data reduction techniques are commonly used: (1) evaluation in the time domain by summing the microphone signals and the synthetic antenna and (2) spatial transformation of sound fields (STSF) based on Fourier transforms of the correlation function of the array elements. These two processes are described next.

Microphone Array: Time Domain Measuring Principle   The principle is here explained by refemng to a linear array of equally spaced microphones. Signals from the microphones are digitized in real time and recorded for subsequent analysis. The analysis is carried out by accounting for the propagation times for sound waves from any selected point to reach each of the microphones. This procedure is repeated

for each source position of interest. The signals from each microphone are summed according to

$$p(t) = \sum_{i=1}^{N} p_i(t + t_{pi}) g_i h_i$$

where N is the number of **microphones,** $p_i(t + t_{pi})$ is the sound pressure at microphone i at time t $+$ t_{pi} (t being the time at which sound is emitted at the focal point and t_{pi} the propagation time from the focal point to the microphone position), g_i is a weighting factor, and h_i is the amplitude correction for microphone i.

Spatial Transformation of Sound Fields   Spatial transformation of sound fields is a Fourier-transform-related technique that enables a description of the sound field of a source to be obtained within a given solid angle. It involves a scan using an array of transducers (typically eight) over a planar surface close to the source of investigation. From the cross spectra measured during the scan a representation of the sound field is extracted. Any power descriptor of the near field (intensity, sound pressure, etc.) can be **investigated by** means of near-field acoustic holography (NAH) while the more distant field can be determined by application of Helmholtz's integral equation.

In the automotive industry, **STSF** has been implemented in testing a variety of sources such as engines in test cells, whole vehicles, or gear boxes. It was not initially used in wind tunnels due to microphone self-induced noise problems and wind tunnel background noise. However, it is currently beginning to be used by some automotive companies in their wind tunnels.

Acoustic Mirrors   One of the systems developed for sound source location is the acoustic mirror telescope. Two versions are commonly used: one for static tests and wind tunnel tests and one for full-scale measurements of sound sources of vehicles passing by the mirror. Figure 14.21 illustrates the principle of the acoustic mirror telescope.

The concave mirror shown on the left side is a section of an ellipsoid of revolution. It has two focal points that are marked by a small circle. A microphone is positioned at the focal point close to the mirror. Sound waves emanating from a source at the
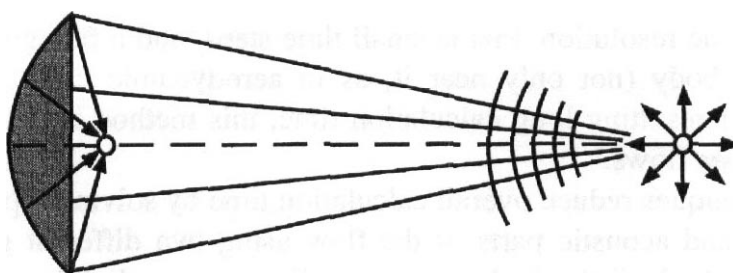
FIGURE 14.21   Acoustic mirror.

other focal point are focused upon the microphone by reflection at the elliptical mirror surface. The intensity produced by this source is hence greatly enhanced as compared to its free-field value. Sound waves radiated from other locations are concentrated by the mirror upon other image points. The elliptical contour is chosen instead of a spherical or parabolic shape because it produces the best imaging effect in the vicinity of the focal points. In contrast to one-dimensional microphone arrays the acoustic mirror can resolve sound sources not only in one direction but in all directions normal to its axis. The spatial resolution of the acoustic mirror is limited only by diffraction of the sound waves at the edge of the mirror. When the acoustic mirror is used in wind tunnel tests, some additional corrections have to be applied to measure data. The apparent source position is downstream of the actual position because of the convection of the sound waves by the wind tunnel flow. Also, in the case of an open section wind tunnel, the turbulent free shear layer will cause an additional scattering of the sound waves. In this case the width of the image of a point source of sound increases with increasing flow velocity.

Computational Approaches to Aeroacoustics   A complementary approach to solving for the aeroacoustic field around the automobile is a computational approach. Computational aeroacoustics techniques for aerodynamic noise prediction can be grouped into four main approaches: direct solution of the Navier–Stokes equation, perturbation techniques, **Lighthill's** acoustic analogy, and **Kirchhoff's** methbd.

The **first** method makes use of **Navier–Stokes** equations to describe noise **production** and propagation. In this way, the methodologies used in fluid dynamics can also be used in aeroacoustics, but there are some important aspects to be considered:

(a) The time dimension must be introduced.

(b) Pressure fluctuations are five orders of magnitude smaller than mean values.

(c) Interesting frequencies are higher than unsteady aerodynamic frequencies.

(d) Long-time solution is required to obtain a correct spectrum.

In view of these aspects, a computational fluid dynamics (CFD) technique for noise prediction and propagation should satisfy the following requisites:

· high accuracy numerical schemes both in time and space,
  low numerical dissipation and diffusion, and
· nonreflective boundary conditions.

Moreover long-time resolution, that is small time steps, and a fine grid over the volume around the body (not only near it, as in aerodynamic calculations) are required. Because of resulting long calculation time, this method is only used for low-Reynolds-number flows.

Perturbation techniques reduce overall calculation time by solving separately for the incompressible and acoustic parts of the flow using two different grids. This method is based on the hypothesis that viscous effects are negligible with respect to acoustic fluctuations.

Methods based on acoustic analogy theory also allow the splitting of the problem into two parts: prediction of the sources and subsequent sound propagation using Ffowcs-Williams–Hawkings equation valid for cases with solid walls similar to the ones encountered in the automotive field. The advantage is that Ffowcs-Williams–Hawkings equation is an explicit equation that does not require iterative solvers. The main problem is the prediction of noise sources. Sometimes they can be analytically calculated, as in the case of open rotors. But other times they have to be calculated by means of suitable CFD techniques. However, in this case a sufficient number of grid points for CFD simulation is only needed near the body and dissipation and diffusion problems are less important.

Methods based on Kirchhoff's theory are similar to the previous ones, but sound sources have to be placed and computed on a virtual surface around the body. The advantage is that there are only surface integrals. However, in the case of low Mach numbers (typical of automotive flows) the volume integrals in the Ffowcs-Williams–Hawkings equation can be neglected. Moreover, Kirchhoff's methods require derivatives of fluid dynamics quantities on the virtual surface.

Aeroacoustics in the Automotive Field In automotive applications the fact that the flow velocity is very small compared to the velocity of sound allows a simplification of the inhomogeneous term Q_a representing aerodynamic noise sources in the aeroacoustic wave equation:

$$\frac{1}{c_0^2}\frac{\partial^2}{\partial t^2}p' - \nabla^2 p' = Q_a(\mathbf{x}, t)$$

In order to understand what kind of simplifications are allowed, we need to analyze the source terms included. We previously described monopole, dipole, and quadrupole sound radiation models. These pressure fluctuations are solutions of Ffowcs-Williams–Hawkings equation (inhomogeneous wave equation in the presence of solid surfaces) and can be written as

$$p'(\mathbf{x}, t) = \begin{cases} \dfrac{1}{4\pi}\dfrac{\partial^2}{\partial x_i\, \partial x_j}\displaystyle\int_V \left[\dfrac{T_{ij}}{R|1 - M\cos\theta|}\right]_{\iota=\iota_e} d\mathbf{y} & \text{(quadrupole)} \\[2ex] -\dfrac{1}{4\pi}\dfrac{\partial}{\partial t}\displaystyle\int_S \left[\dfrac{\rho_0 V_i n_i}{R|1 - M\cos\theta|}\right]_{\iota=\iota_e} dS & \text{(monopole)} \\[2ex] +\dfrac{1}{4\pi}\dfrac{\partial}{\partial x_i}\displaystyle\int_S \left[\dfrac{(p - \quad)\;}{R|1 - M\cos\theta|}\right]_{\iota=\iota_e} dS & \text{(dipole)} \end{cases}$$

where x_i are the observer coordinates, y_i the source coordinates, ι the emission time, ι_e the retarded time, T_{ij} Lighthill's stress tensor, R the distance between the source and the observer, M the Mach number, θ the angle between R and the velocity V, ρ_0 and p_0 the density and pressure of the undisturbed medium, V_i the velocity components, and n_i the components of the local normal to the body.

The analysis of relative magnitude performed above is again useful. In the presence of dipole or monopole sources the quadrupoles are negligible and the volume integrals vanish. Also, the dipole sources are obtained from the calculation of the pressure fluctuations at the wall $p - p_0$. This means that we can couple a CFD technique with an acoustic analogy for vehicle external noise prediction. This process is described next.

The simplifications above directed the approach to the acoustic analogy. The approach is as follows: Through a suitable CFD solver aeroacoustics sources are calculated and through the **Ffowcs-Williams–Hawkings** equation noise around the body is calculated. Only dipole sources are considered, for the unsteady mass addition term regards sources that are expected to be well dealt with in the design process and hence can be neglected.

In the first phase of the process a CFD solver is used to output the pressure fluctuations at each grid point over the body surfaces that are representative of equivalent aeroacoustic dipole sources. In the second phase, the **Ffowcs-Williams–Hawkings** equation is solved neglecting the quadrupole term. The following conditions must be satisfied:

- low Mach number,
  viscous distribution negligible with respect to pressure,
- the body moving in a steady medium, and
- the observer located outside the source region (i.e., **boundary** layers, separated flow, or wakes).

The observer should also move at the same speed as the body since we wish to reproduce the conditions of a wind tunnel test. The acoustic solver reads in wall pressure histories from the CFD solver and computes acoustic pressure fluctuations at each observer location. Pressure–time histories output by the acoustic solver are then translated into frequency domain through fast Fourier transforms (FFTs) in order to get dominating frequencies and sound pressure levels. An example of such a calculation is given by Kumarasamy, Korpus, and Barlow.[24]

Much is yet to be done in the field of experimental and computational aeroacoustics. The current stage of development is far from being very useful in terms of a rational design methodology, but in the next years greater developments are expected as the interest in the field grows and so do the human and material resources devoted to it. However, for now the wind tunnel remains as the most important tool to evaluate and improve the aeroacoustic field around an automobile.

Other Issues

Other issues that must be kept in mind when it comes to wind tunnel testing have to do with phenomenon that exists on a real road condition but is not simulated in the wind tunnel. On the road a vehicle encounters a highly distorted flow with rotation that is unsteady and turbulent. The scales of turbulence are often of the dimension of the vehicle itself. Passing vehicles and wind gusts induce vibrations

and aerodynamic forces that are not experienced in a wind tunnel. Le Good et al.[25] present an interesting comparison between aerodynamic coefficients obtained from road testing and wind tunnel testing. A coastdown methodology was used; for details on the methodology and on the configurations used the reader is referred to the original paper. However, it is relevant to point out that in general the drag values generated from the coastdown methodology were higher than the ones obtained in the wind tunnel. Also it was apparent from the results that drag variation from small configuration changes were essentially the same for the two techniques. Eaker[26] presents a similar study using an improved coastdown methodology and arrives at different results. The coastdown and wind tunnel drag values are found to be in great accordance. This improved coastdown method is however much more time and work consuming, reducing its efficiency. The results from the standard coastdown technique produce significant differences from the wind tunnel measurements, just as in the study by Le Good et al.[25]

Climatic factors such as radiation from the sun and the consequent heating up of the road surface, radiation from the road surface and conditions of snow and rain that change the flow around the body, and possible irregularities on the road that add vibrations to the car that are not simulated in a wind tunnel, all make road testing extremely important in the design program. The wind tunnel data is only a part of what is necessary to make decisions in the design process.

Yet another commonly overlooked aspect of wind tunnel testing of automobiles is the effect of the longitudinal position of the vehicle in the test section. Garry et al.[27] performed a study involving flat plates and automobile shapes in three different wind tunnels. The effect of longitudinal position changes was studied. It was found that the drag decreased as the bodies were moved back closer to the diffuser. This effect is most probably due to the change in base pressure as the body is moved further toward the diffuser region. The authors suggest that this effect may contribute to some of the lack of correlation between different tunnels. In particular, lower drag was measured in shorter, open jet wind tunnels when compared to longer, closed section tunnels.

Advanced Experimental Techniques

A number of experimental techniques can be categorized as advanced techniques because they are not extensively used in automotive aerodynamics. This is because of both cost and setup difficulties but most of all because the results obtained are usually not good enough to justify the effort required to obtain them. It is believed, however, that as the technological level of automobile aerodynamics laboratories increases some of these techniques will become common and will be widely used. Examples are laser Doppler anemometry, pressure-sensitive paint, and particle image velocimetry. Durst et al.[28] present a good discussion and results of an experimental campaign using laser-based anemometry, flow visualization, and frontal area measurement. The reader is referred to more specialized publications on these techniques.

REFERENCES AND NOTES

1. Hucho, W. H., Ed., *Aerodynamics of Road Vehicles, from Fluid Mechanics to Vehicle Engineering, 4th ed., SAE* International, Warrendale, PA, 1998.

2. Volkert, R., and Kohl, W., "The New Ford Aerodynamic Wind Tunnel in Europe," SAE Paper 870248, Feb. 1987.

3. Nilsson, L., and Berndtsson, A., "The New Volvo Multipurpose Wind Tunnel," SAE Paper 870249, Feb. 1987.

4. Ogata, N., Lida, N., and Fujii, Y., "Nissan's Low-Noise Full Scale Wind Tunnel," SAE Paper 870250, Feb. 1987.

5. Hucho, W. H., Ed., Aerodynamics of Road Vehicles, Butterworths, London, 1987, Chapter 10.

6. Ibid., Chapter 4.

7. Cogotti, A., "Experimental Techniques for the Aerodynamic Development of Convertible Cars," SAE Paper 920347, Feb. 1992.

8. Federation Internationale de L'automobile, 8 Place de La Concorde, 75008 Paris, France, URL: www.fia.com

9. Championship Auto Racing Teams, Inc., 755 West Big Beaver Road, Suite 800, Troy, MI 48084, URL: www.cart.com

10. lndy Racing League, 4565 W. 16th Street, Indianapolis, IN 46222, URL: **www.indyracingleague.com**

11. National Association for Stock Car Auto Racing, Dayton Beach, FL, URL: www.nascar.com

12. Zabat, M., Stabile, N., Frascaroli, S., and Browand, F., "Drag Forces Experienced by 2, 3, and 4 Vehicle Platoons at Close Spacings," SAE Paper 950632, Feb. 1995.

13. See web site http://www.rtri.or.jp.

14. Klemin, A., "A Belt Method of Representing the Ground," *J. Aeronaut. Sci.,* 1, 198–199, 1934.

15. Wiedemann, J., "Some Basic Investigations into the Principles of Ground Simulation Techniques in Automotive Wind Tunnels," SAE Paper 890369, International Congress and Exposition, Detroit, MI, Mar. 1989.

16. Vagt, J. D., and Wolff, B., "Special Design Features and Their Influences on Flow Quality: Test Results from Porsche's New Wind Tunnel," paper presented at AutoTech 1987, London, Dec. 1987.

17. Eckert, W., Singer, N., and Vagt, J. D., "The Porsche Wind Tunnel Floor-Boundary Layer Control—A Comparison with Road Data and Results from Moving Belt," SAE Paper 920346, Feb. 1992.

18. Carr, G. W., and Eckert, W., "A Further Evaluation of the Ground-Plane Suction Method for Ground Simulation in Automotive Wind Tunnels," SAE Paper 940418, Feb. 1994.

19. Mercker, E., and Wiedemann, J., "Comparison of Different Ground Simulation Techniques for Use in Automotive Wind Tunnels," SAE Paper 900321, Feb. 1990.

20. Hackett, J. E., Baker, J. B., Williams, J. E., and Wallis, S. B., "On the Influence of Ground Movement and Wheel Rotation in Tests on Modem Car Shapes," SAE Paper 870245, Feb. 1987.

21. Hackett, J. E., Williams, J. E., Baker, J. B., and Wallis, S. B., "On the Influence of Ground Movement and Wheel Rotation in Tests on Modem Car Shapes," SAE Paper 870245, Feb. 1987.

22. Coggotti, A., "Ground Effect Simulation for Full Scale Cars in the Pininfarina Wind Tunnel," SAE Paper 950996, 1995.

23. Watkins, S., and Saunders, J. W, "Turbulence Experienced by Road Vehicles under Normal Driving Conditions," SAE Paper 950997, Feb. 1995.

24. Kumarasamy,S., Korpus, R., and Barlow, J., "Computation of Noise Due to the Flow Over a Circular Cylinder," Proceedings of Second Computational Aeroacoustics Workshop on Benchmark Problems, NASA Conference Publication 3352, Langley Research Center, Hampton, VA, June 1997.

25. Le Good, G., Howell, J., Passmore, M., and Garry, K., "On-Road Aerodynamic Drag Measurements Compared with Wind Tunnel Data," SAE Paper 950627, Feb. 1995.

26. Eaker, G., "Wind Tunnel to Road Aerodynamic Drag Correlation," SAE Paper 880250, Feb. 1988.

27. Garry, K., Wallis, S., Cooper, K., Fediw, A., and Wildsen, D., "The Effect on Aerodynamic Drag of the Longitudinal Position of a Road Vehicle Model in a Wind Tunnel Test Section," Proceedings of SAE International Congress and Exposition, Detroit, MI, Feb. 1994.

28. Durst, F., Buchheim, R., Beeck, M., Hentschel, W., Piatek, R., and Schwabe, D., "Advanced Experimental Techniques and Their Application to Automotive Aerodynamics," SAE Paper 870244, Feb. 1987.

15 Marine Vehicles

At first thought, it may seem that wind tunnel work for marine vehicles would be primarily focused on sail rigs for sailing boats. These are the subjects of wind tunnel tests, but the majority of wind tunnel tests for marine vehicles address hydrodynamic questions. Chapter 1 can be consulted for basic data on water and air. The Navier–Stokes equations are considered an accurate mathematical model for the behavior of both air and water. The density of water remains essentially constant until the pressure drops sufficiently low so that cavitation will occur. Air is compressible, of course, but the behavior is very little affected for Mach numbers below about 0.3, as discussed in Chapter 1. So air flow at low Mach number gives a completely satisfactory model of the behavior of water flow. Tests conducted in wind tunnels are often easier and more productive than equivalent tests in water facilities.

The boundary conditions for the flow problem of interest must be modeled properly, as is the case for any engineering test. This rules out wind tunnel tests for situations where free-surface effects play a dominant role. These are the domain of towing tanks. However, underwater portions of surface ships such as the append-ages of sailing boats as well as hydrodynamics and hydroacoustics of submarines are common subjects for wind tunnel experiments to support design decisions. Wind tunnel experiments can also be useful for studying wind loading that acts on the portion of surface ships that is above the water.

This chapter will survey the most frequent wind tunnel experiments for marine vehicles at a level appropriate for the conceptual design of the test apparatus and experimental programs. While the experiments are in themselves somewhat unique, the experimental procedures follow the same logic as those for purely atmospheric vehicles. Experience has shown that these procedures, when modified appropriately and interpreted correctly, can generate a wealth of valuable information for the design and analysis of marine vehicles.

15.1 SURFACE VESSELS: ABOVE THE WATER

Most marine vehicles operate at the interface of the air and water; consequently, wind tunnel experiments for marine vehicles involve examining phenomena both above and below the surface. Those occurring above the water, with the exception of those generated by sails, will be the subject of this section. A discussion of experiments on sails is given in Section 15.4.

Ship Wind Loads

Wind acting on the topsides and superstructure of ships can generate considerable loads that frequently must be accounted for in the design process. When the ship is intact, these forces affect the sizing of propulsion machinery and maneuvering thrusters and mooring and berthing arrangements. In the case of precision-maneuvered ships, such as minesweepers, buoy tenders, or mineral exploration drillships, identifying and counteracting these forces and the forces created by water currents and waves can determine the selection of the propulsion machinery and related controls. When a ship is damaged, these forces can determine the very survival of the ship and its crew. While hull subdivision enables ships to sustain flooding of significant portions of their volume, the ship is almost always left in a state of diminished stability. So the immediate problem of sinking is replaced by the only slightly less catastrophic possibility of capsizing. An excellent technical discussion of ship maneuvering and stability issues is presented by Lewis.' This reference also defines the terminology used in this and other sections.

A good overview of published results for wind loads is presented by McTaggart and Savage.[2] There is a fair amount of published data for typical intact merchant ship forms exposed to beam winds but not much published data for damaged or heeled ship forms or data for ship forms at other heading angles.

Like the wind ashore, the wind sweeps over the ocean in a thick boundary layer. This boundary layer creates a velocity distribution with respect to height above the surface that obeys the approximate relationship?

$$\frac{U(z)}{U(10 \text{ m})} = \left(\frac{z}{10 \text{ m}}\right)^{\alpha} \tag{15.1}$$

Where $U(z)$ is the wind velocity at height z meters above the ocean surface, $U(10$ m) is the wind velocity at 10 m above the ocean surface, and a is a constant that varies between 0.118 and 0.125 depending on the local wind characteristics. The best value for most locations is 0.125.

This velocity distribution needs to be modeled in a wind tunnel experiment. The most common solution is to introduce blockage in the airstream upstream from the model, which will create a similar velocity distribution in the test section. This technique is identical to that used in experiments on buildings and other ground structures exposed to similar conditions. There is a variation in the planetary boundary layer profiles for marine conditions, open plains, urban cityscapes, and so on. The distribution of velocity and turbulence levels in the vicinity of the model should be measured prior to testing to ensure they match full scale to the degree required for the objectives of the experiments. The topic of atmospheric boundary layer simulation is discussed in Chapter 16.

A ship model can create significant blockage, particularly when tested in beam winds. The chapter on blockage corrections should be consulted for guidelines regarding blockage. As a rule of thumb, the model size should be such that when the model is at $90°$ yaw the bow and stem remain no less than half a ship length

from the tunnel walls. This leads to a guide that the model length is to be no greater than half the tunnel floor width.

Some elements of the superstructures of ships have shapes for which the flow can be very Reynolds number dependent. We have discussed this issue in Chapter 8 in a broader context. There are typically elements with curved surfaces including circular cylinders (e.g., cylindrical exhaust stacks or hemispherical cargo tanks) for which the separation locations vary significantly with Reynolds number. Since most ship model experiments are necessarily done at relatively small scale, the Reynolds numbers achieved in the wind tunnel experiments are much smaller than full-scale values. Attempts must be made to obtain separation locations on the elements that are representative of full-scale behavior. Among these means are increasing roughness of portions of the model with sand or the like, attaching trip wires or other devices to fix separation points, or distorting the model scale. Each test program should include a preliminary set of runs to identify portions of the model that have these strongly Reynolds dependent characteristics and insure that they are modeled adequately to meet the test objectives. This is typically a greater issue for ship studies than is the case for buildings only because typical building geometries are more angular, and, therefore, practically fix the separation locations independent of Reynolds number.

Experiments of this type are ideally suited for the floor of the wind tunnel test section. The model should be mounted in such a manner that the forces experienced by the floor surrounding the model are not measured and in such a way that no air can pass between the floor of the test section and the bottom of the model. If several combinations of list, sinkage, and trim are being investigated, several models will be required. In some instances as shown by Deakin[4] and SNAME[3] the model of the hull is mounted in water or some other viscous liquid that will not transfer wind loads to the model. The test rig described by Deakin is discussed in more detail in the section on sail testing. A typical mounting arrangement for a ship in the intact condition is shown in Figure 15.1.

It is important to ensure that the critical conditions for the ship are included in an experimental program. For example, in the case of an intact ship the draft and consequently the exposed freeboard of a ship can change by as much as 30 ft or more, depending on whether the ship is in a loaded or an unloaded condition. This can represent as much as 50% of the freeboard. If the experimental program is intended to obtain information to use for sizing a bow thruster or determining the wind loads on a mooring buoy or anchor chains, then the maximum freeboard (minimum draft) condition should be included in the configuration matrix. However, if the data are being generated for a computer simulation of the ship transiting a canal in a loaded condition, then the minimum freeboard (maximum draft) condition will be more important. Care should be exercised when simulating damaged ships as well. A damaged or foundering ship can assume an almost infinite combination of sinkage, list, and trim angles and the experimental matrix of configurations should include those that are expected to be the "worst case" for the problem being investigated.

In crowded navy anchorages, groups of ships are frequently moored together rather than individually. This has led to the conduct of wind tunnel simulations
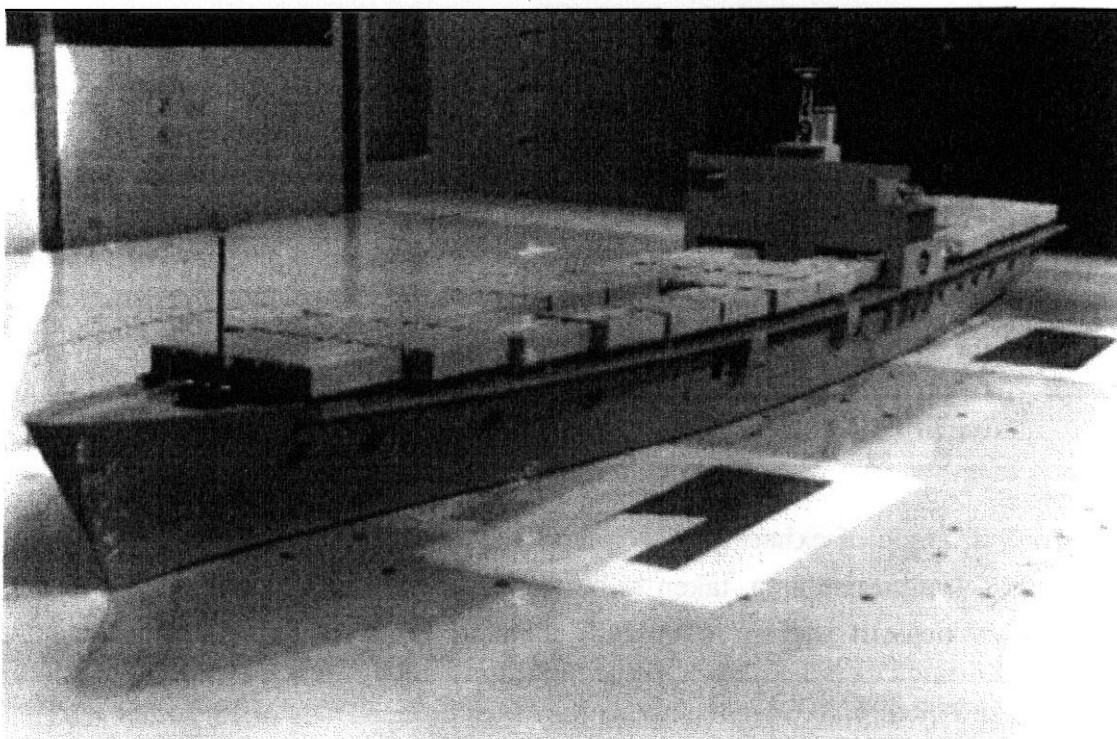
FIGURE 15.1   Ship model for determining wind loads. (Photograph courtesy of the Glenn L. Martin Wind Tunnel.)

of groups of moored ships? The models in these experiments were individually instrumented for longitudinal and lateral forces and yaw moments.

Stack Gas Dispersion

With the exception of nuclear reactors, all ship main propulsion machinery requires air for combustion and releases exhaust gases into the atmosphere. The exhaust gases are usually at higher temperature and can contain corrosive combustion by-products such as sulfuric acid that need to be dispersed clear of the ship. These stack gases can affect operation of the ship by, for example, obscuring vision or asphyxiating the crew. Wind tunnel experiments are frequently used to investigate these design issues.

The simulated intake and exhaust ducts need to obey certain scaling laws for the tests to be meaningful. Consider the condition when the vessel is underway moving forward with the velocity vector in the plane of symmetry for the vessel. This situation is shown in Figure 15.2. If viscous forces are neglected, the variables involved in the flow dynamics are as follows:

ρ_a = density of ambient air

ρ_p = density of exhaust gas

V = speed of vessel relative to ambient air

W = speed of exhaust gas relative to vessel
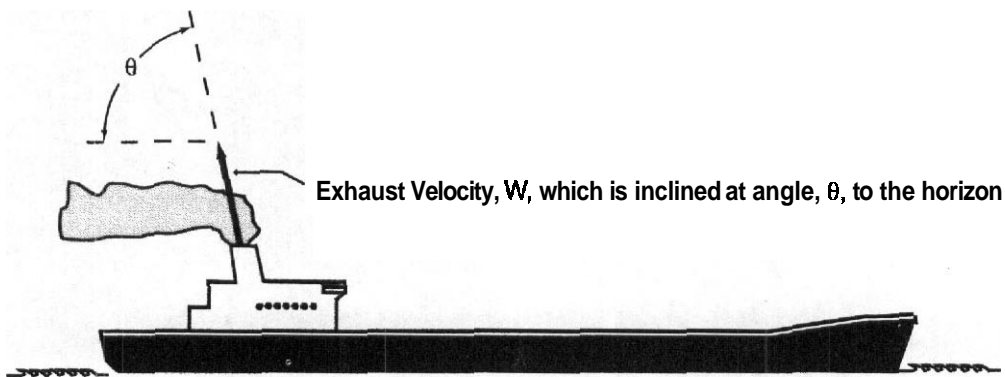
FIGURE 15.2   Illustration for considering plume dynamics.

θ = initial angle of exhaust gas velocity (W) relative to the vessel speed V.

A = vessel reference area, taken to be frontal area

D= initial exhaust stream "diameter" equal to $\sqrt{4A_p/\pi}$, where A is the exhaust area

g = local gravitational field acceleration

If the geometry of the vessel is assumed to be fixed, and nondimensional groups are formed, the following similarity parameters are found:

1. θ, initial angle to the mean flow direction
2. $\rho_a V^2/\rho_p W^2$, initial plume momentum = P_{mv}
3. $\rho_p WD^2/\rho_a VA$, plume mass flow rate = P_{mdot}
4. $\Delta\rho g D/\rho_a W^2$, plume buoyancy = P_{buoy}, and $\Delta p = \rho_a - \rho_p$

Note that we are assuming relative insensitivity to Reynolds number. The Reynolds number would be an additional parameter if viscosity were included in our list of variables.

To obtain dynamic similarity in two flows, say the full-scale and the wind tunnel model-scale flows, the values of the above groups need to be the same for the two flows. This is not practical in most cases, so we must choose the groups that are most important for the particular situation under consideration.

In many cases the nondimensional group called "plume buoyancy" in the preceding discussion is found to be quite small for the full-scale ship. This indicates that the buoyancy forces are small with respect to the momentum forces and thus will have a minimal effect on the near-field dynamics of the plume/vessel flow interaction although buoyancy will have a significant effect on the eventual plume motion far from the vessel. Under these circumstances the plume buoyancy may be ignored and only the plume momentum and plume mass flow need be considered further. Of the two, plume momentum is usually the most significant similarity parameter and efforts should concentrate on matching this.

The baseline model setup for these studies is similar to that used for studying ship wind loads. The model is mounted on the floor of the test section such that it

can be rotated to study all wind incidence angles. Since forces and moments do not have to be measured, the model does not need to be attached to the balance. Appropriate air pumps must be fitted to provide the scaled volume of intake and exhaust air at the appropriate positions on the ship.

Investigating the dispersion of stack gases can be done in several ways. The simplest method is to introduce smoke into the modeled stack gas flow and photograph the smoke plume. Another approach is to heat the stack gas and survey the temperature at various points on the model.[6] Chapter 5 can be consulted for additional information regarding flow visualization.

Passenger Comfort on Recreational Yachts

A related problem is wind invasion on the external passenger spaces of ships and recreational yachts. Examples of these spaces include flybridges on a motor yacht or outdoor recreational areas on a cruise ship. These spaces are usually protected from excessive wind by carefully shaped superstructures, coamings, railings, and windbreaks surrounding the area affected.

Model arrangements for studies of this type of flow are similar to those described in the previous section. A model of the ship is placed in the wind tunnel and smoke or some other flow visualization tool is used to investigate the intrusion of wind upon the passenger spaces. Quantitative measurements may be done with omnidirectional flow probes such as spherical pressure probes or multielement hot-film probes. The model must be constructed so that a variety of configuration options can be explored to provide the best environment possible. If aerodynamic drag is judged to be important, the model will be connected to the balance so that the impact of modifications on both wind intrusion and overall drag can be assessed simultaneously.

Ship Flow Fields: Effects on Aircraft

Aircraft are frequently called upon to operate in the vicinity of ships. Examples of such applications include airplanes landing on the flight decks of aircraft carriers and helicopters returning to their hangars aboard destroyers after completing antisubmarine warfare operations. These operations usually result in the aircraft operating, to some degree, in the air wake of the ship and its superstructure. The safety of these flight operations requires that these effects are carefully studied. While these studies have been performed by full-scale wake surveys aboard the ships themselves,' they are frequently the subject of wind tunnel tests.[7,8]

These tests are performed for two main reasons: to explore ship configuration issues during design and to establish operational limits for existing ship designs. Less frequently these tests are used to collect data for aircraft simulation studies and for calibrating shipboard anemometers.

Tests for aircraft interaction fall into two groups: flow visualization and measurement of velocity and turbulence levels in regions of concern. The models used are similar to those described in the sections on stack gas dispersion and ship wind

loads. A model of the superstructure above the waterline is usually mounted on the floor of the test section with sufficient upwind blockage to simulate Earth's boundary layer, as discussed in the section on ship wind loads. Attention should be paid to turbulence levels in the simulated atmospheric boundary layer to ensure that full-scale conditions are reasonably reproduced. The influence of propulsion machinery intake/exhaust should be modeled in accordance with the guidelines presented earlier regarding stack gas dispersion. The model should be arranged so that all wind speeds and wind angles of incidence under consideration can be measured. In the case of an aircraft carrier this may be considerably simplified because they are usually turned into the wind for aircraft launch and retrieval. This may not be the case for helicopter operations, however, so the purpose of the test data needs to be carefully considered before finalizing the test plan.

Visualization of the flow can be achieved with yam tufts, smoke, or helium bubbles as described in previous sections. The velocity and turbulence surveys can be performed with hot-wire anemometer probes or other means as discussed in other sections of this book.

If the tests are being performed as a part of a design study rather than to characterize an existing ship, the model should be arranged so that configuration changes can be made quickly. For example, a study designed to eliminate the influence of vortices developed by the flight deck on an aircraft carrier may require many subtle configuration changes to achieve adequate performance. The model should accommodate these changes with a minimum of fuss and effort during the test program.

Sometimes, such as in the studies by Cahill and Biskaduros,[8] motions of the ship have been included. In these studies, time domain predictions of typical ship motions in the sea state corresponding to the wind velocity under study were used to actuate the model during the flow field visualization. Excellent photographic results of the resulting flow field are reported.

Figure 15.3 shows a picture of smoke being used for visualization of the flow over the deck of a ship. In this case there is an upflow at the front of the ship that produces a leading-edge separation and a wakelike flow encompassing the entire deck area.

15.2   SURFACE VESSELS: BELOW THE WATER

This section discusses experiments to investigate flow below the water line on surface ships. One motivation for these tests is that wind tunnels can frequently achieve Reynolds numbers much closer to full scale than can be obtained in a tow tank. Thus these experiments frequently focus on the viscous aspects of the flow about the hull and appendages.

A discussion of experiments related to underwater sailing yacht appendages is contained in Section 15.4.
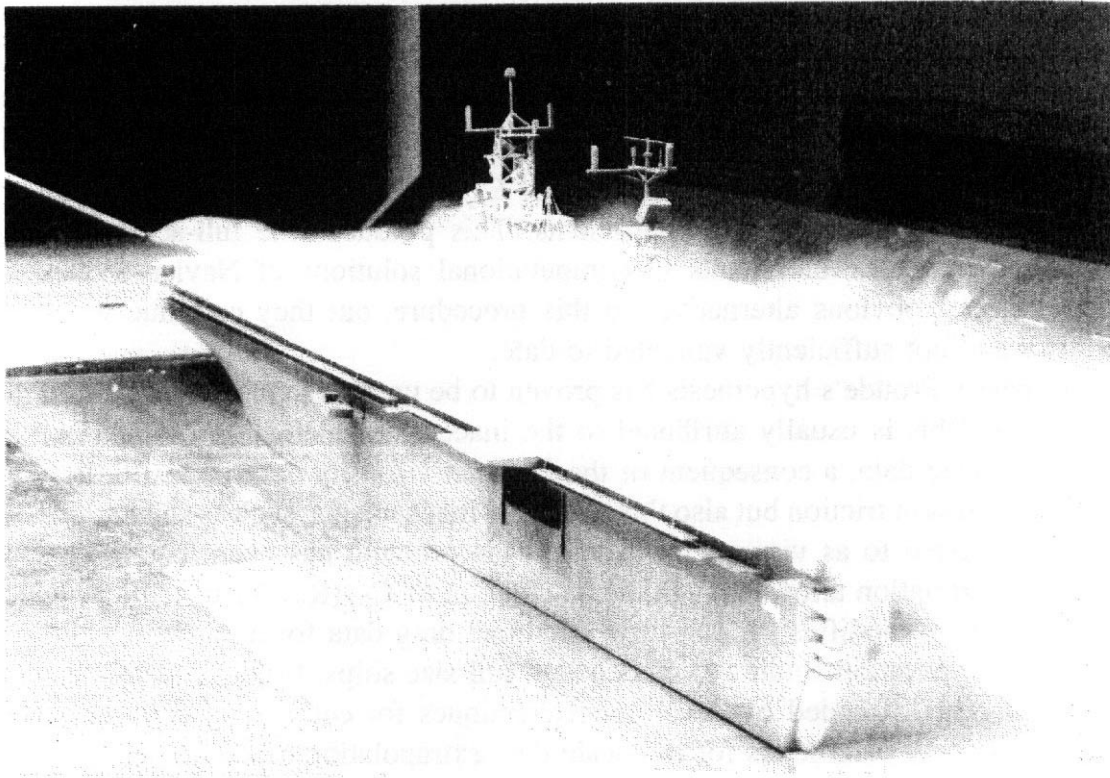
FIGURE 15.3   Visualization of the flow over a ship aircraft deck.

Viscous Hull Resistance

Dimensional analysis of the ship powering problem reveals that two similarity parameters must be matched to perform meaningful scale model tests, the Reynolds number and the Froude number? The Reynolds number has been discussed previously. The Froude number is given by

$$F = \frac{V}{\sqrt{gL}} \tag{15.2}$$

where the terms on the right-hand side are the ship velocity, length, and acceleration due to gravity in consistent units.

The need to match both Reynolds and Froude numbers creates a significant difficulty. If water is used as the fluid medium for the model experiments and if there is a significant scale ratio between the model and the full-size vessel, it is impossible to match both similarity parameters. The historic solution to this dilemma is known as Froude's hypothesis. Froude's hypothesis involves assuming that the drag coefficient of the ship is made up of two components: a frictional drag coefficient that is dependent solely on the Reynolds number and a residual drag coefficient that is dependent solely on the Froude number? This assumption yields

$$C_D(\mathrm{Re}, F) \cong C_{D,f}(\mathrm{Re}) + C_{D,r}(F) \tag{15.3}$$

The frictional drag coefficient $C_{D,f}(\mathrm{Re})$ is commonly estimated from data for flat

plates using the speeds of the ship and model and their wetted surface areas. The experimental procedure this assumption suggests is as follows. The ship model is tested at Froude numbers that match the range of full-scale Froude numbers of interest. Then the values of $C_{D_f}(\text{Re})$ for the model are calculated and subtracted from the drag coefficients. Finally the values of $C_{D_f}(\text{Re})$ for the full-scale ship are calculated and added to the drag coefficients. This produces the full-scale drag coefficients. Current developments in computational solutions of Navier–Stokes equations suggest obvious alternatives to this procedure, but they continue to be quite costly and not sufficiently validated to date.

Unfortunately Froude's hypothesis has proven to be unsatisfactory under certain circumstances. This is usually attributed to the inaccurate calculation of $C_{D_f}(\text{Re})$ based on flat-plate data, a consequent of the fact that viscosity contributes to drag not only through skin friction but also through other mechanisms, such as separation, collectively referred to as viscous form drag. This problem has been handled by including a "correlation allowance" in the calculation of $C_{D_f}(\text{Re})$ for the full-scale ship that, in effect, modifies the flat-plate frictional drag data for a particular hull type based on correlation studies of models and full-size ships. In recent years this approach has been extended by developing techniques for calculating correlation allowance or similar parameters for full-scale data extrapolation based on very low speed model tests where the wave-making component (the Froude scaled portion of resistance) is negligible.' This approach has led to the use of increasingly large models for ship tow tank studies.

This subject has received considerable attention, and efforts to improve viscous drag estimates have involved studying them directly in a wind tunnel.[10] The total viscous drag can be measured at Reynolds numbers approaching full scale by direct force and moment measurement. The viscous skin drag and viscous form drag can then be separated by making careful measurements of the boundary layer velocity profile and integrating the results c .r the surface of the body. Direct measurement of the viscous pressure drag can also be made by measuring the pressure distribution over the model surface and likewise integrating these pressures over the body surface.

A reflection plane model as described in the section on propulsion system testing is usually used for these investigations. The model is mounted on a strut with suitable tare and interference corrections calculated with an image system. The boundary layer surveys can be performed with Preston tubes, pitot tubes, hot wires, laser velocimeters, or other suitable arrangements.

Propulsion System and Powering Requirements

Wind tunnels are used to study the environment in which the ship propeller operates. This is usually done by preparing a model of the underwater portion of the ship with control surfaces, shafts, shaft supports, and any other underwater appendages and performing a wake survey in the volume to be occupied by the propeller. In one study wind tunnel experiments have been demonstrated to provide data that more closely agree with full-scale measurements than data measured by more traditional means in a tow tank." This is a result of the ability to more closely approximate

full-scale Reynolds numbers in the wind tunnel experiments and the strong dependence of the flow in the plane of the propeller disc on viscous effects.

The ship models can be one of two types. The first approach is to model the underwater portion of the hull and mount it inverted on the floor of the wind tunnel. The second method is to mount two models of the underwater portion of the hull against one another in a "clamshell" arrangement along the waterline and mount the whole arrangement on a strut. The floor method has the advantage of allowing a larger model for a given tunnel blockage but it has the disadvantage of placing the hull in the test-section floor boundary layer. This can be alleviated to some degree by using a raised floor or a boundary layer control on the tunnel floor to provide a thinned boundary layer. This boundary layer was useful when modeling flows that occur in the atmospheric boundary layer but is not needed when modeling flows below the waterline. Means of controlling the floor boundary layer are discussed at some length in Chapter 14 in connection with simulation requirements for ground vehicles. An example of the reflection plane or clamshell arrangement is shown in Figure 15.4.

Careful attention must be paid to boundary layer thickness on the model itself to achieve accurate modeling of the flow, as has already been mentioned. The model-scale boundary layers will be too thick and will need to be thinned. Suction may be used to reduce the thickness of the boundary layer. The survey of the wake can be performed in accordance with methods indicated in Chapter 4.

In some cases the performance of the propeller must be evaluated. In this case the propeller must be operated over the same range of advance coefficient as will
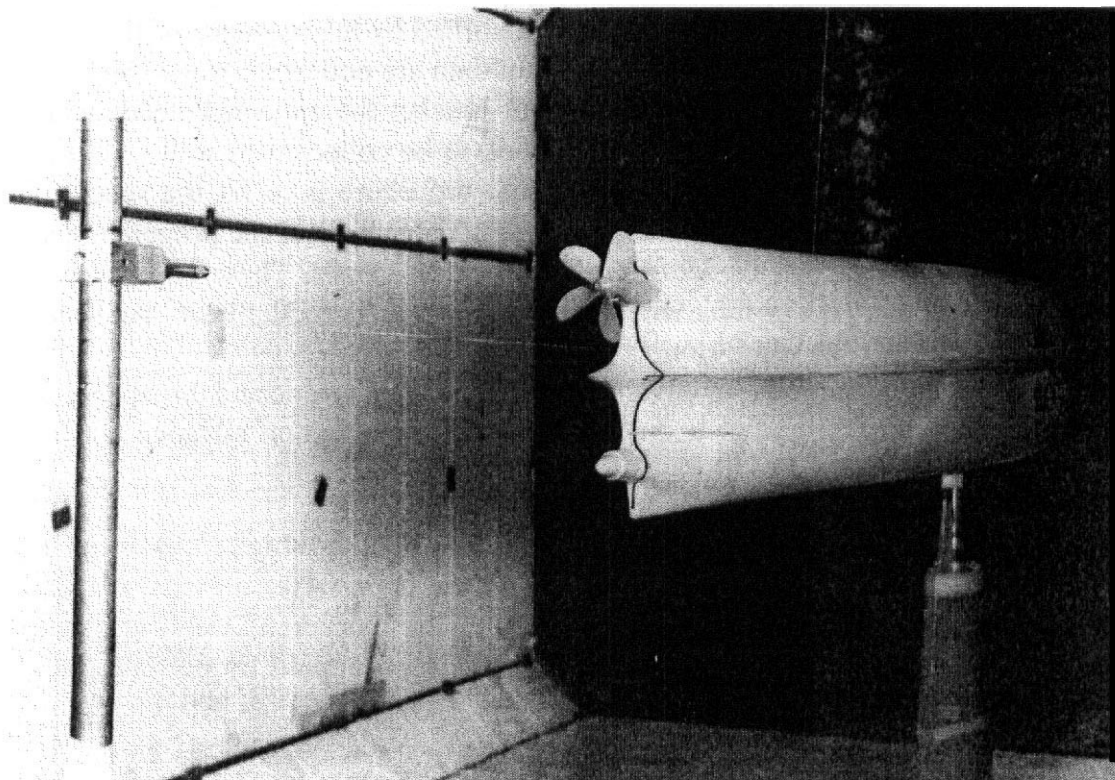
FIGURE 15.4 Reflection plane model of the underwater portion of a ship hull.

occur in full scale. Propeller modeling was discussed in Chapter 13 in the context of propeller-driven aircraft. The modeling issues are the same here although the design choices will be very different.

We include here a discussion of ship powering from the point of view of a naval architect responsible for the entire program of experiments, including tow tank work and wind tunnel work, as appropriate. This will provide wind tunnel engineers a broader perspective when they are involved in some portion of such programs.

Ship and submarine powering performance is usually determined from a series of model experiments. The first two are the unpowered hull resistance experiments and the open water propeller experiments. The results from these two experiments **are** used to determine several interaction coefficients in the captive model self propulsion experiments.'

Unpowered hull resistance experiments can be performed in a model basin by using Froude's hypothesis as outlined earlier in this chapter. In this approach a full-scale drag coefficient as a function of Froude number is determined by testing the model at a full-scale Froude number, subtracting the contribution of viscous friction at model scale, and then adding in the contribution of viscous friction at full scale. Wind tunnel experiments may be useful to help in obtaining the viscous friction for the full-scale hull. If the body is to be completely submerged, as in the case of a submarine, Froude scaling is no longer required and the model tests may be performed in a wind tunnel, as discussed later in this chapter and the resulting drag coefficients used directly. Ship model basin test and data reduction techniques **are** discussed in more detail in Lewis.'

The open water propeller experiments determine the thrust and torque coefficients as a function of advance coefficient. These experiments **are** done in a condition where flow into and out of the propeller is undisturbed by the presence of the hull, rudder, or shaft support structure. At a minimum data are collected over a range of advance coefficients and thrust coefficients that bracket the expected steady-state powering condition of the ship. Torque data need to be collected as well to aid in **the** selection of propulsion machinery. The usual procedure is to fix the speed of advance, collect measurements for a range of rotational speeds of the propeller, and repeat this sequence for the needed range of advance speeds. These experiments are traditionally done in a tow tank with a device called a "propeller boat" but seem also to have been done in wind tunnels.[12,13]

Several different definitions for advance coefficients and torque and thrust coefficients can be used for propeller testing. The two most common advance **coeffi-cients are**

$$J = \frac{V_a}{nD} \tag{15.4}$$

that corresponds to aeronautical usage as introduced in Chapter 13, and

$$\nu = \frac{nD}{\sqrt{V_a^2 + n^2D^2}} \tag{15.5}$$

where D is the propeller diameter, V_a is the speed of advance, and n is the propeller speed, which by convention, is expressed in revolutions per second. In each case the advance coefficient is directly related to the angle of attack a particular blade element is experiencing. The first form of the advance coefficient, verify J, is most common, particularly in studies concerned only with the steady-state powering condition. The second form, v, is used where dynamic conditions are to be investigated since $J = \infty$ if n = 0. This situation might be encountered in a condition of interest if the shaft was stopped but the ship was still moving.

The two most common forms of the thrust coefficient are given by the expressions

$$K_T = \frac{T}{\rho D^4 n^2} \tag{15.6}$$

and

$$C_T = \frac{T}{\rho D^2 (V_a^2 + n^2 D^2)} \tag{15.7}$$

and the two most common forms of the torque coefficient are given by

$$K_Q = \frac{Q}{\rho D^5 n^2} \tag{15.8}$$

and

$$C_Q = \frac{Q}{\rho D^3 (V_a^2 + n^2 D^2)} \tag{15.9}$$

where T and Q are the propeller thrust and torque. The coefficients K_T and K_Q are used most frequently with advance coefficient **J** as the independent variable while C_T and C_Q are used most frequently with advance coefficient v. Sample plots of ship propeller thrust and torque coefficient in both forms are shown in Figure 15.5 and Figure **15.6.**

Once the hull resistance and propeller tests are completed, the interaction coefficients for the hull and propeller can be determined from the model self-propulsion test. In this test the ship model is fitted with model propellers that are powered and connected to a thrust and torque dynamometer and means for powering the propeller. The model is then attached to the carriage and the model is towed at a fixed speed V corresponding to a full-scale Froude number of interest. In sequential runs while the ship Froude number remains constant, the propeller speed is varied over a range of values that result in slightly positive and slightly negative drag force as measured on the carriage. Propeller torque Q and thrust T are also recorded.

The data are reduced for a particular operating point as follows. First the powered model hull drag and propeller thrust are plotted as functions of propeller speed.
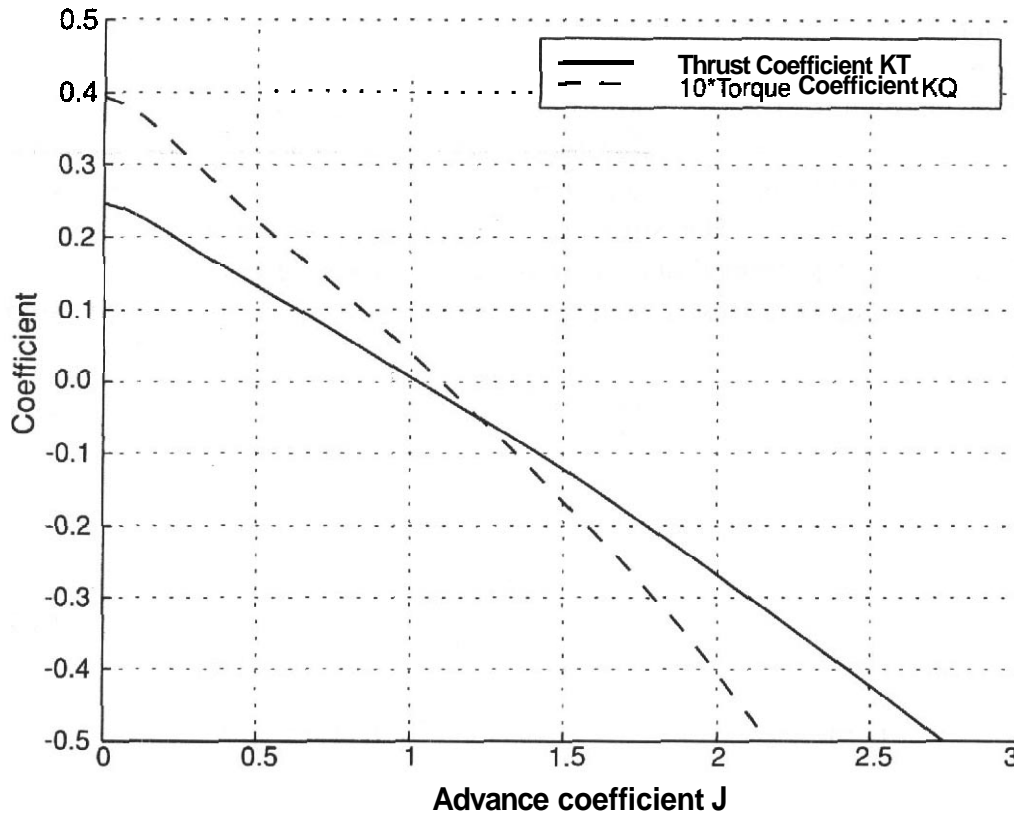
FIGURE 15.5   Typical propeller thrust and torque coefficients, first form.

The propeller speed at which the hull drag curve crosses over from negative to positive values is known as the self-propulsion point. The propeller speed that corresponds to this can be called n_{sp}. The propeller thrust corresponding to n_{sp} can be called the self-propulsion thrust. T_{sp}. These values are shown graphically in Figure 15.7.

The first interaction coefficient, the thrust deduction fraction, can now be calculated. It is defined as the ratio between the bare hull resistance at a particular speed and the measured propeller thrust required to drive the ship at that speed:

$$\text{tdf} = \frac{R_{\text{bare hull}}}{T} \tag{15.10}$$

Values are usually around 0.85–0.95 because it requires more propeller thrust to drive the hull at a given speed than it takes to simply pull the ship through the water. Physically this is because the flow into and out of the propeller increases the speed of the water over the bottom of the ship, thus increasing its effective resistance. In many references a thrust deduction factor is defined that is similar to the one shown in (15.10) and given by

$$\tilde{\text{tdf}} = \frac{T - R_{\text{bare hull}}}{T} \tag{15.11}$$
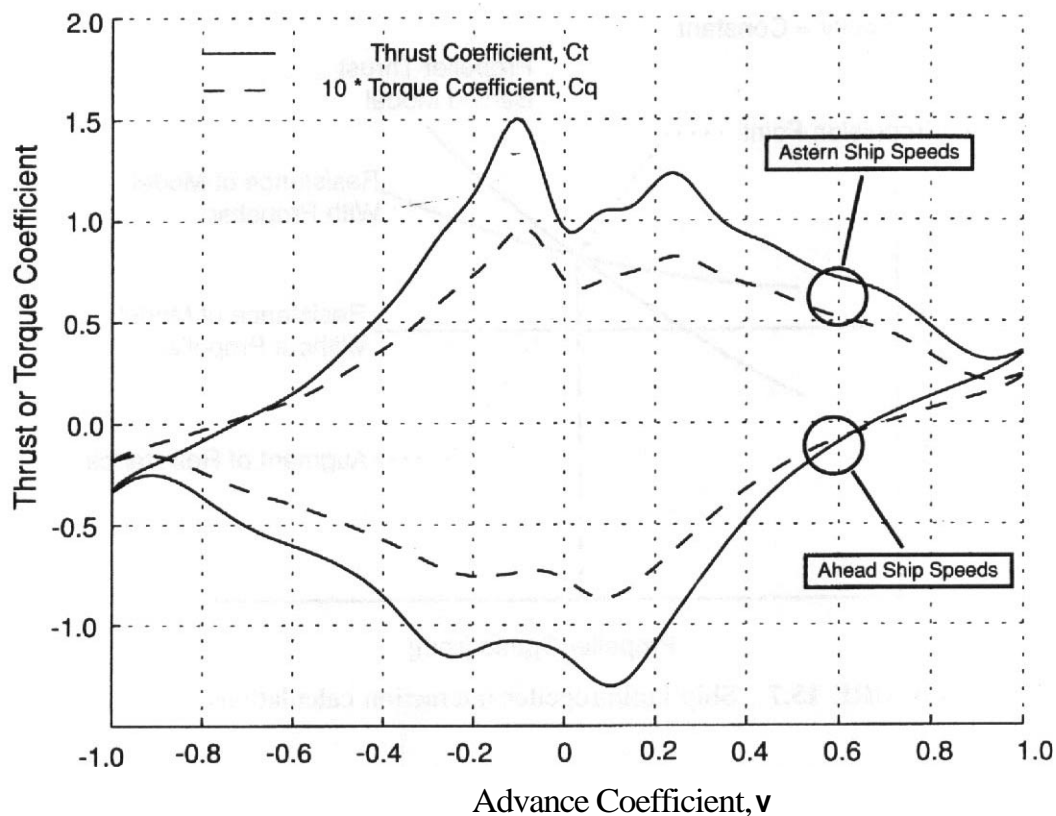
FIGURE 15.6   Typical propeller thrust and torque coefficients, second form.

Now, notice that all the information is available to calculate the thrust coefficient for the propeller at the self-propulsion point $K_{T,\text{sp}}$. We can use this information to calculate the effective "average" speed of advance by using the open water propeller data. In the open water tests we determined the functional relationship $K_T = f(J)$. This function can be inverted to provide $J = f^{-1}(K_T)$. If we enter this function with our value of $K_{T,\text{sp}}$ we can find the effective advance coefficient as $J_{\text{sp}} = f^{-1}(K_{T,\text{sp}})$. Now the effective speed of advance can be found from J_{sp} from the definition of the advance coefficient as $V_{aT} = J_{\text{sp}} n D$. This is known as the speed of advance by thrust identity. It can be used to calculate the Taylor wake fraction by thrust identity, our second hull–propeller interaction coefficient, from the relation

$$w_T = \frac{V_{aT}}{V} \tag{15.12}$$

This procedure can be duplicated with the torque coefficient for the propeller at the self-propulsion point $K_{Q,\text{sp}}$. The analysis proceeds in an identical manner and yields our third hull–propeller interaction coefficient, the Taylor wake fraction by torque identity:

$$w_Q = \frac{V_{aQ}}{V} \tag{15.13}$$

Test Section Velocity = Constant

**Propeller Thrust
Behind Model**

Model Self-Propulsion Point ....·.
sion Point ····:.

**Resistance of Model
With Propeller**

**Resistance of Model
Without Propeller**

······**Augment of Resistance**

Resistance or Thrust [lbf]

Propeller Speed [rpm]
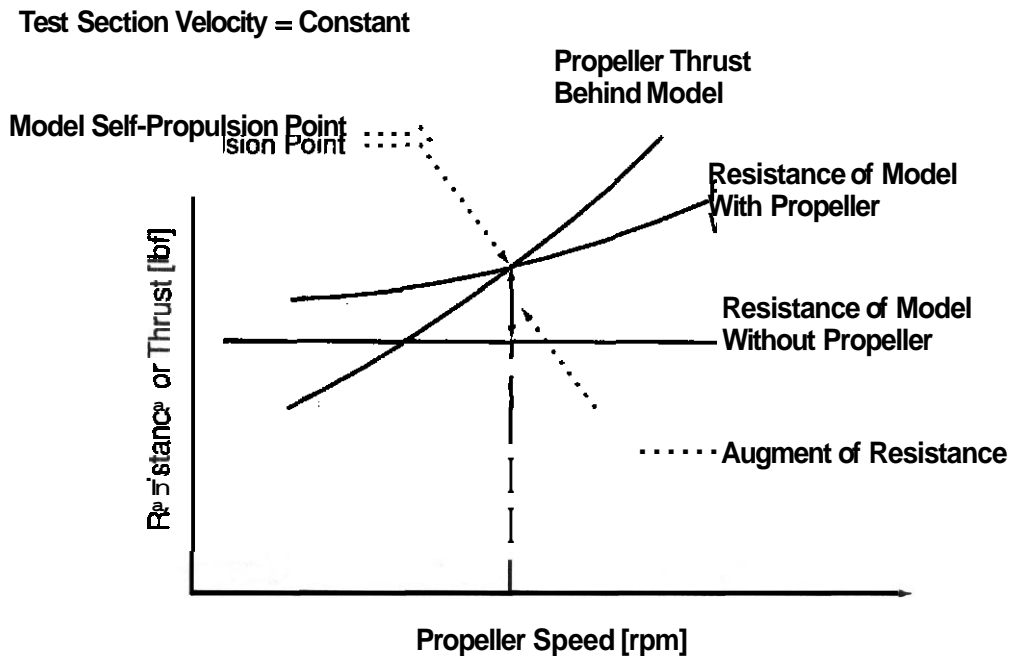
FIGURE 15.7 Ship hull/propeller interaction calculations.

The final steady-state powering estimates are prepared by using the bare hull resistance data, the open water propeller data, and the interaction coefficients from the self-propulsion tests.

Stabilizing and Control Surface Design

Ship control surfaces are generally required for two purposes; steering the ship and active roll abatement. Both types have been the subject of wind tunnel studies. In fact, the basic design data that naval architects frequently use of designing these systems were obtained from wind tunnel experiments.' Performing scale model experiments on submerged foils in a wind tunnel is preferable to using a water tunnel or a towing tank because the wind tunnel can come closer to matching the full-scale Reynolds number and thus provide more complete modeling of the viscous effects. This is true primarily because one cannot simply increase model speed by the inverse of the scale ratio to maintain Reynolds number when testing scale underwater foils in water because cavitation conditions limit the maximum speed that can be used. Cavitation limits will be discussed later. Mach effects limit the speeds that can be used in wind tunnels, but it turns out that this is a less severe restriction than the cavitation limit in a water facility.

The models of the foils to be evaluated are usually mounted on the floor of the wind tunnel test section. The control surfaces on a ship are influenced by the state of the boundary layer on the hull as it approaches the foil. It may be considered desirable to model the expected boundary layer properties. If this is needed, the thickness of the boundary layer in the vicinity of the proposed location of the foil can be estimated and simulated using upwind floor treatment. The achieved boundary

layer must be carefully documented. The model must be operable over a range of angles of attack. In some cases operation of the foil in a reversed flow (i.e., leading with the trailing edge) should be explored. This corresponds to the condition where the ship is operating in reverse. Since the rudder shaft, for example, is usually located near the quarter-chord point of the foil and since backing speeds of a ship can be a significant percentage of the maximum forward speed, it is possible that the worst case torsional loading of the rudder shaft may be in the astern condition. The best evidence of this is the fact that the limiting astern speed on many ships is determined during sea trials and corresponds to the speed at which the steering machinery loses control of the rudder.

Cavitation occurs when the pressure at a point in the flow field drops below the vapor pressure of the fluid. At this point the fluid element "flashes" into vapor until the pressure increases to a value greater than the vapor pressure. The condition for cavitation can then be stated by the expression

$$P_{\text{local}} < P_{\text{vapor}} \tag{15.14}$$

The vapor pressure for seawater is given in Table 15.1.'

Cavitation on control surfaces cannot be simulated in the wind tunnel. The occurrence of cavitation can be estimated, however, by measuring surface pressure distribution with pressure taps or pressure-sensitive paint and then using the resulting data for calculating pressure coefficients. The pressure coefficient data can then be used to calculate the local pressure (in psi) at a point on the actual control surface from the definition of pressure coefficient and from basic hydrostatic relations as

$$P_{\text{local}} = C_{p,\text{local}} q_\infty + p_{\text{atm}} + \rho g h \tag{15.15}$$

where p_{atm} is the atmospheric pressure and h is the water depth at the point in question. The dynamic pressure used in this calculation should be the equivalent speed used to nondimensionalize the data. For example, suppose the control surface is tested in a simulated boundary layer in the wind tunnel and the air speed at the outboard tip of the control surface is used to nondimensionalize the wind tunnel pressure measurements. Then the velocity at the tip of the control surface in the actual installation should be used to dimensionalize the data to check for cavita-

TABLE 15.1. Seawater Vapor Pressure

Temperature		Vapor Pressure	
°F	°C	psi	kpa
32	0	0.09	0.621
59	15	0.25	1.724
212	100	14.70	101.325

tion. This velocity is probably not the same as the speed of the ship owing to the ship's boundary layer and the acceleration of fluid flow into and out of the propeller disk.

Wind tunnels have also been used to explore the performance of control surfaces as mounted on the hull of the ship.[14] For these simulations a model of the underwater portion of the ship is prepared and mounted on the floor of the wind tunnel. The control surface(s) and other necessary appendages, such as propeller shafting and shafting support structure, are mounted on the hull. The control surface can be mounted with its own strain gauge balance to determine fin forces. Interference effects can also be studied by tracking the trajectory of the tip vortices with neutrally buoyant soap bubbles or smoke. Since these tests are performed on models of the entire ship, the full-scale Reynolds number can be duplicated only rarely. Since much of the control surface span is likely to be operating in the hull boundary layer, it is likely that boundary layer control on the model hull will be needed in order to duplicate the expected boundary layer on the full-scale ship. The boundary layer thickness can be estimated by first using a potential flow analysis to obtain surface streamlines and then using a two-dimensional boundary layer method from a standard reference, for example, Young,[15] to compute predicted boundary layer development.

If the interference tests concern the propeller, then the propeller needs to be modeled as well. Propeller modeling was discussed in the previous section on ship powering. The key result was that the advance coefficient is the most important similarity parameter to match for propellers when performing wind tunnel experiments.

Acoustic Sources

Measurement of the strength of underwater acoustic sources is another marine topic that can be studied in the wind tunnel. Aboard most ships underwater noise is generated by four mechanisms: machinery vibration conveyed to the hull structure, flow of water past the hull, propeller operation in an unsteady flow environment, and cavitation. Of these four, wind tunnels can be used to study the second and third.

Much of the work on evaluation of acoustic sources on surface ships is classified and has been performed in purpose built facilities at government laboratories. A description by Leggat et al.,[14] of one such experiment does appear in the open literature. Figure 15.8 shows the experimental arrangement.

The goal was to study the noise generated by a propeller on the back of a frigate, particularly the higher blade rate harmonics. An upside-down model of the ship's underbody was mounted on the floor of the test section. The hull was fitted with antiroll fins, bilge keels, shafts, struts, propellers, and the rudder. The model was arranged so the propellers were powered. The model was fabricated in such a way that the appendages could be modified. The influences of propeller tip to hull clearance, propeller blade type, propeller strut type, axial clearance from the propeller, propeller-to-rudder clearance, shaft angle, and hull boundary layer thickness at
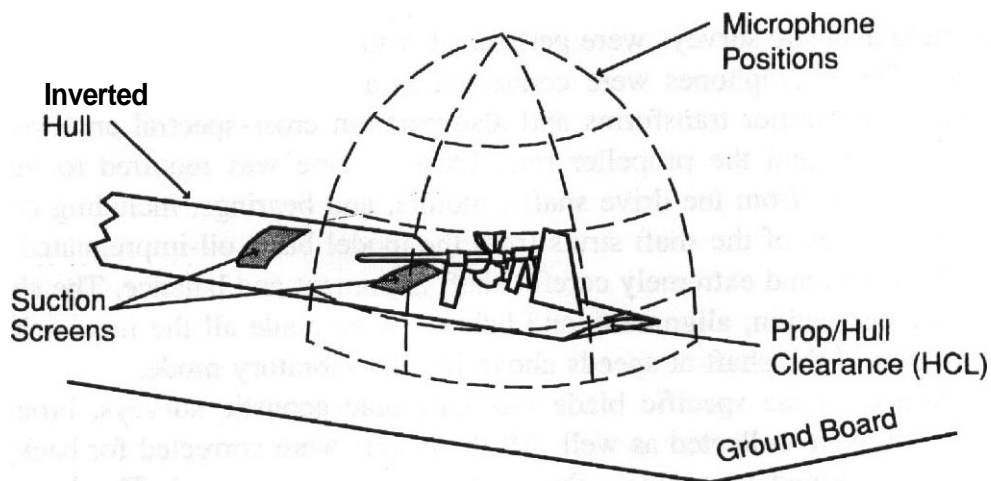
FIGURE 15.8   Arrangement for measuring acoustic radiation from a propeller.

the propeller plane on the strength of the blade rate harmonic noise levels were investigated.

Propeller noise is critically dependent on the flow field in which the propeller operates. Nonuniformities in this flow field can cause local cavitation and pressure pulses, that can in turn create noise. As a consequence, correctly simulating the flow field in the vicinity of the propeller disc was a high priority. Since the full-scale Reynolds number could not be achieved, suction boundary layer control was introduced upstream of the propeller blades to control the boundary layer thickness. The upper limit on the test-section velocity was the compressibility limit on the propeller.

The goal of the test was to obtain good measurements of the first seven or eight harmonics of the blade rate. This required the shaft speed to be held steady within 1% for 30 sec. Extracting the blade rate harmonic noise levels from the acoustic signal was facilitated by generating a shaft rate pulse sequence that was recorded along with the acoustic data. The cross-power spectrum of the shaft rate pulses and the microphone signal produced data at integer multiples of shaft frequency. By this means the signal processing was tightly coupled to the constantly varying actual shaft rpm. This approach allowed resolution out to eight times the blade rate frequency.

The rigid plane that supported the model (the test-section floor) provided an incorrect acoustic boundary condition. The result was increased reflected noise from the hard wall rather than the pressure relief that would have occurred from a free surface. Published techniques[14] for correcting these effects are beyond the scope of this book.

The acoustic tests were preceded by a hot-wire survey of the boundary layer to adjust the suction control and to assess the turbulence levels. This was done to quantify the magnitude of the change in the angle of attack experienced by a typical propeller blade while rotating in the stem wake. These variations are the important flow field quality for determining acoustic energy levels.

Far-field acoustic surveys were performed with microphones supported near the propeller. The microphones were connected to a spectral analyzer that could do 512-point fast Fourier transforms and also perform cross-spectral analysis of the acoustic signals and the propeller rate. Extreme care was required to minimize mechanical noise from the drive shafts, motors, and bearings, including complete vibration isolation of the shaft struts from the model base, oil-impregnated bronze journal bearings, and extremely careful shaft alignment and balance. The shaft and propeller construction, alignment, and balance were made all the more critical by the operation of the shaft at speeds above its first vibratory mode.

In addition to the specific blade rate harmonic acoustic surveys, broad band acoustic data were collected as well. All the results were corrected for background noise and combined to evaluate the configurations considered. The background noise corrections were generated with the tunnel on, the model propeller drive system turned off, and the boundary layer control and shaft drive system turned on.

15.3   UNDERWATER VEHICLES

This section discusses wind tunnel experiments to support design decisions for underwater vehicles. These experimental programs can be quite effective when the operational domain of interest is sufficiently far from the free surface. These experiments **are** in many respects similar to conventional aircraft experiments, so much useful information can be gleaned from preceding chapters. The design constraints are almost always different, however, and this leads to differing selections of geometries, and therefore differences in the details of the experimental requirements.

Forces, Moments, and Control Surface Effectiveness

Stability and control of underwater vehicles is an issue that generally requires more attention than the stability and control of marine surface vehicles. There are two reasons for this. First, underwater vehicles have more degrees of freedom in which to maneuver. Second, underwater vehicles are frequently unstable. As a consequence, the formulation of the maneuvering and control analysis is frequently more sophisticated than comparable analyses for surface ships. The analyses typically include all six degrees of freedom and explicitly consider coupling relationships that are usually simplified or ignored in the case of surface ships. As a result the characterization of the forces and moments experienced by the body, as it maneuvers, needs to be more complete and more accurate.

The static hydrodynamic characteristics of underwater vehicles **are** frequently determined in a wind tunnel. Since most underwater vehicles operate far from the free surface, Froude scaling (discussed in an earlier section) is no longer relevant and the single most important similarity parameter is the Reynolds number. Wind tunnel experiments have an advantage over those performed in a tow tank because Reynolds number that are much closer to full-scale values are achievable in a wind tunnel. These test programs **are** also frequently more productive than tow tank tests

since model attitude, control surface deflection, and model configuration changes can usually be made much faster in a wind tunnel.

Numerous examples of wind tunnel experiments to characterize static forces and moments of underwater vehicles appear in the literature (see, e.g., Watt, Nguyen, Cooper, and Tanguay,[12] Fidler and Smith,[16] Goodman,'' and Barlow, Harris, and Ranzenbach[18]). These studies typically explore the forces and moments of the bare body and the effectiveness of various control fin configurations and deflections.

The model construction, mounting, and data corrections required for these experiments are similar in all respects to those for aircraft studies. The main difference is that underwater vehicles generate most of their lift from buoyancy forces on the body so the lifting surfaces appended to the body are exclusively for control of the body. They tend to be much smaller than aircraft wings, so interference effects tend to be of much greater importance. If the control surfaces are located near the propeller, then the model should include the propeller. The propeller should be operated at the correct advance coefficient.

A generic torpedo-like body that was used in the study by Barlow, Harris, and Ranzenbach[18] is shown in Figure 15.9. This test used a single strut mount. Standard image strut tare and interference corrections, as outlined in Chapter 9, were used.

The control surfaces on the model shown in Figure 15.9 are obviously very short in span compared to any airplane. It is common for specifications to call for control surfaces to have spans that do not extend beyond the maximum diameter of the main body. This inevitably leads to the possibility of a serious deficiency in the
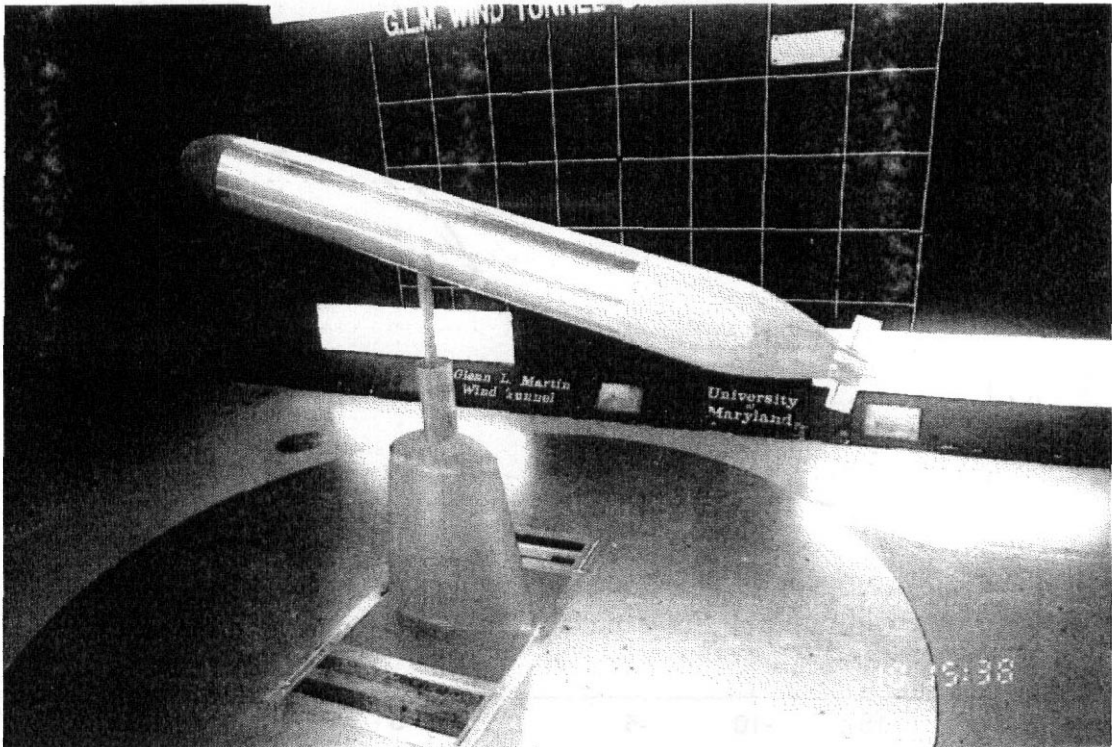
FIGURE 15.9   Generic submarine like body on single strut mount. (Photograph courtesy of the Glenn L. Martin Wind Tunnel.)

force-generating capability of the surfaces, and a need to carefully evaluate the effects of body shape ahead of the surfaces, the foil cross sections, and the effect of propulsion-system-induced flows. All of the issues discussed previously concerning Reynolds number effects apply to this type of experiment.

We show in Figure 15.10 the effect of varying the span of stabilizing surfaces on the pitch moment coefficient of the body–fin combination shown in Figure 15.9.

Another issue of importance in the design of underwater vehicle control surfaces is the effect of gaps at the inboard end of a movable control surface. Figure 15.11 shows a setup in a wind tunnel for investigating this effect.

Researchers have also conducted experiments to determine dynamic effects for underwater vehicles.[19] These studies are difficult to perform, however, because the frequencies at which the body needs to be manipulated are very high. At the same time, the low density of air makes the magnitude of the forces due to unsteady motion quite small and therefore difficult to separate from the inertial dynamic forces associated with the body motion.

Propulsion System and Powering Requirements

Surveys of the propeller environment, like those discussed in the section on surface ships, can be performed on underwater vehicles as well. Sample results are contained in reports by, for example, Ohman and Nguyen[20] and Fry.[21]
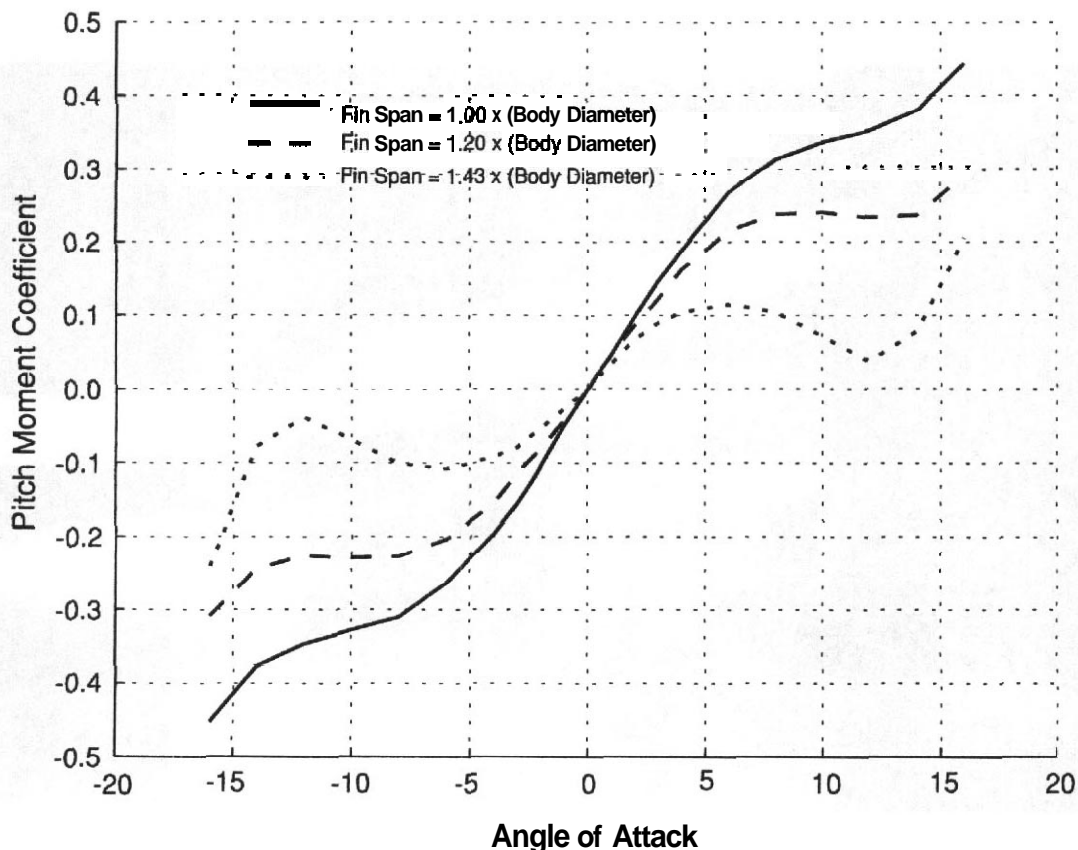
FIGURE 15.10 Effect of varying span of fins on stability of vehicle.
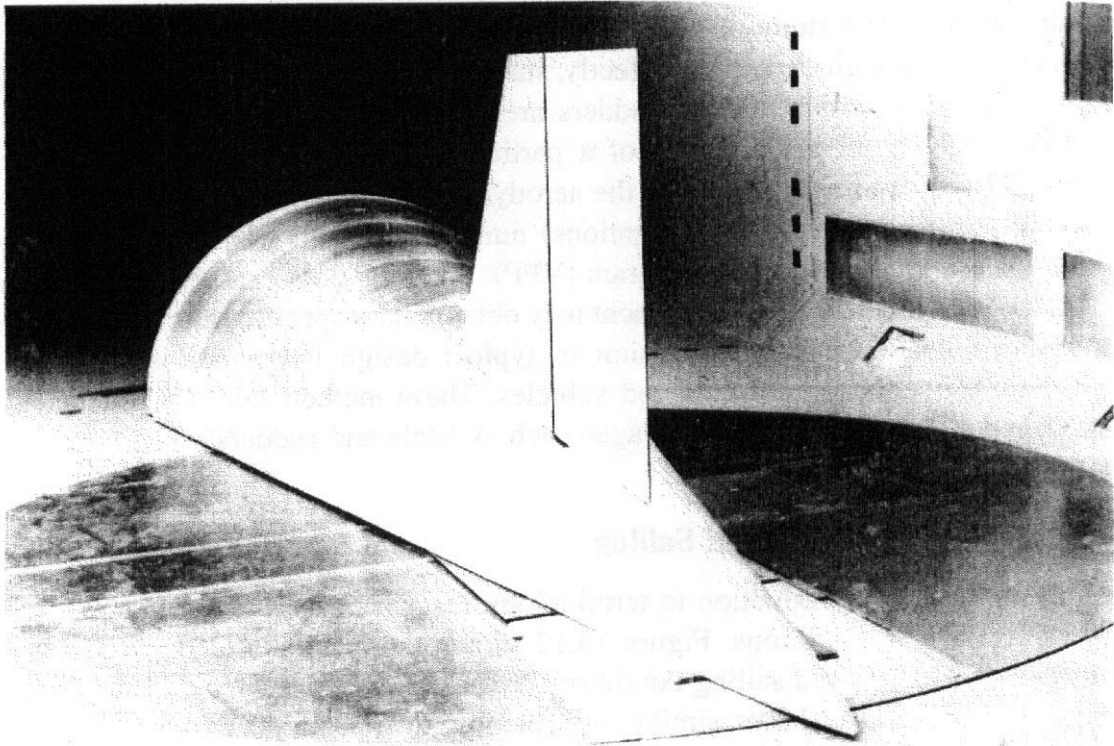
FIGURE 15.11 A wind tunnel installation for investigating the effect of gap on control surface effectiveness. (Photograph courtesy of the Glenn L. Martin Wind Tunnel.)

The material in the previous section on surface ship powering should also be consulted for a background discussion of the underwater vehicle powering problem. This discussion applies to underwater vehicles as well, except that Froude scaling is not required so that the body and propeller can be tested at the same time. Powering experiments are mentioned in publications by Watt, Nguyen, Cooper and Tanguay.[12] Here the authors point out that the very high propeller speeds (e.g., 10,000 rpm) required to match full scale advance coefficient make it difficult to measure accurately the propeller torque and thrust.

Acoustic Sources

The study of hydroacoustics has led to special facilities such as the anechoic facility described in Section 2.7. See the earlier section on acoustic sources for surface ships for a discussion of experimental technique.

15.4 SAILING VESSELS

While wind tunnels may appear to be an ideal environment for studying sailboat design issues, meaningful experimental investigations are difficult. Part of the problem rests in the fact that no single experimental facility is completely equipped to simultaneously consider the influence of the interacting aerodynamic and hydrody-

namic systems. The study of hull behavior is the natural domain of towing tanks. Sails are best, though to date imperfectly, studied in the wind tunnel, and the strictly underwater parts like keels and rudders are studied in both tow tanks and wind tunnels. The overall performance of a particular design can only be determined accurately by blending the data for the aerodynamic and hydrodynamic subsystems (and supporting numerical investigations) numerically with what has come to be known as a velocity prediction program (VPP). The VPP does exactly what its name suggests, it predicts the velocity a yacht may obtain under specific sailing conditions.

This section presents a discussion of typical design issues and related wind tunnel experiments for sail powered vehicles. These include sail experiments and experiments on underwater appendages such as keels and rudders.

Basic Aerohydrodynamics of Sailing

We present a brief introduction to terminology for sail boats in upwind conditions and in downwind conditions. Figure 15.12 shows a typical sloop rigged sail boat under way in an upwind sailing condition. Names of major elements of the rig are shown. Figure 15.13 shows similar information for a sail boat in a downward configuration. We will refer collectively to the rudders and keels as underwater appendages. The main sail and the jib will be referred to as upwind sails while the main sail and spinnaker will be referred to as offwind sails.

A sense of the complexity of the coupled aero and hydrodynamic forces can be gained from studying Figure 15.14. In the horizontal plane the driving force and the resistance must cancel each other, as must the aerodynamic and hydrodynamic
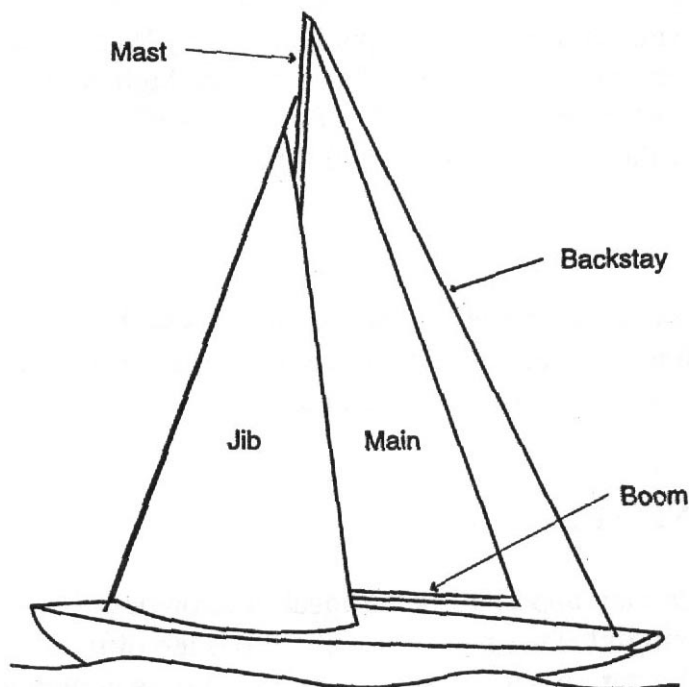
FIGURE 15.12   Sloop rigged sail boat in upwind configuration.
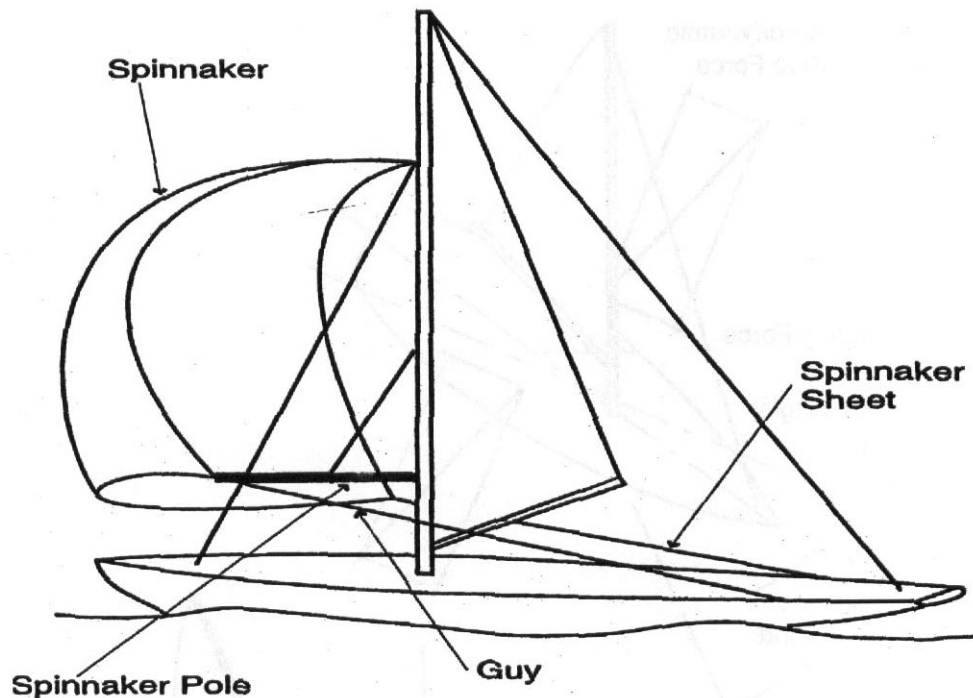
FIGURE 15.13   Sailboat in downwind configuration.

side force. In the vertical plane the weight and vertical component of the aerodynamic force must be offset by the buoyancy and the vertical hydrodynamic forces. A similar balance involving the moments must be achieved as well. The attitude of the boat is determined by these forces, but the forces are in turn determined by the attitude. Just where the optimum point of operation for the boat lies has been determined primarily by experience in competition rather than by analysis.

The complexity of the task performed by the VPP can also be appreciated by considering the polar plot of the sailing vessel's performance. This plot shows the sailboat velocity as the radial component and the heading of the boat relative to the true wind direction as the angle. The polar plot is prepared by selecting a wind strength and heading and then optimizing the sail trim until the maximum driving force is obtained in the desired direction. An example of a polar plot is shown in Figure 15.15. One result from the polar plot shown is that the fastest way to sail directly away from the wind when the wind speed is 7 knots (shown as a $180°$ true wind angle on the diagram) is to sail with a true wind angle of approximately $140°–150°$, zig-zagging back and forth. This somewhat counterintuitive result is quite realistic with real boats and shows how optimization of the rig and hull for sailing away from the wind may actually involve optimization of the boat velocity while sailing in a different direction!

Since progress toward a design objective can only be truly determined in the VPP, it is difficult at times to optimize the design of a component during a model test. For example, the viscous drag of a keel might be reduced by decreasing the volume of a torpedo-shaped lead weight attached to the bottom of it, but doing so
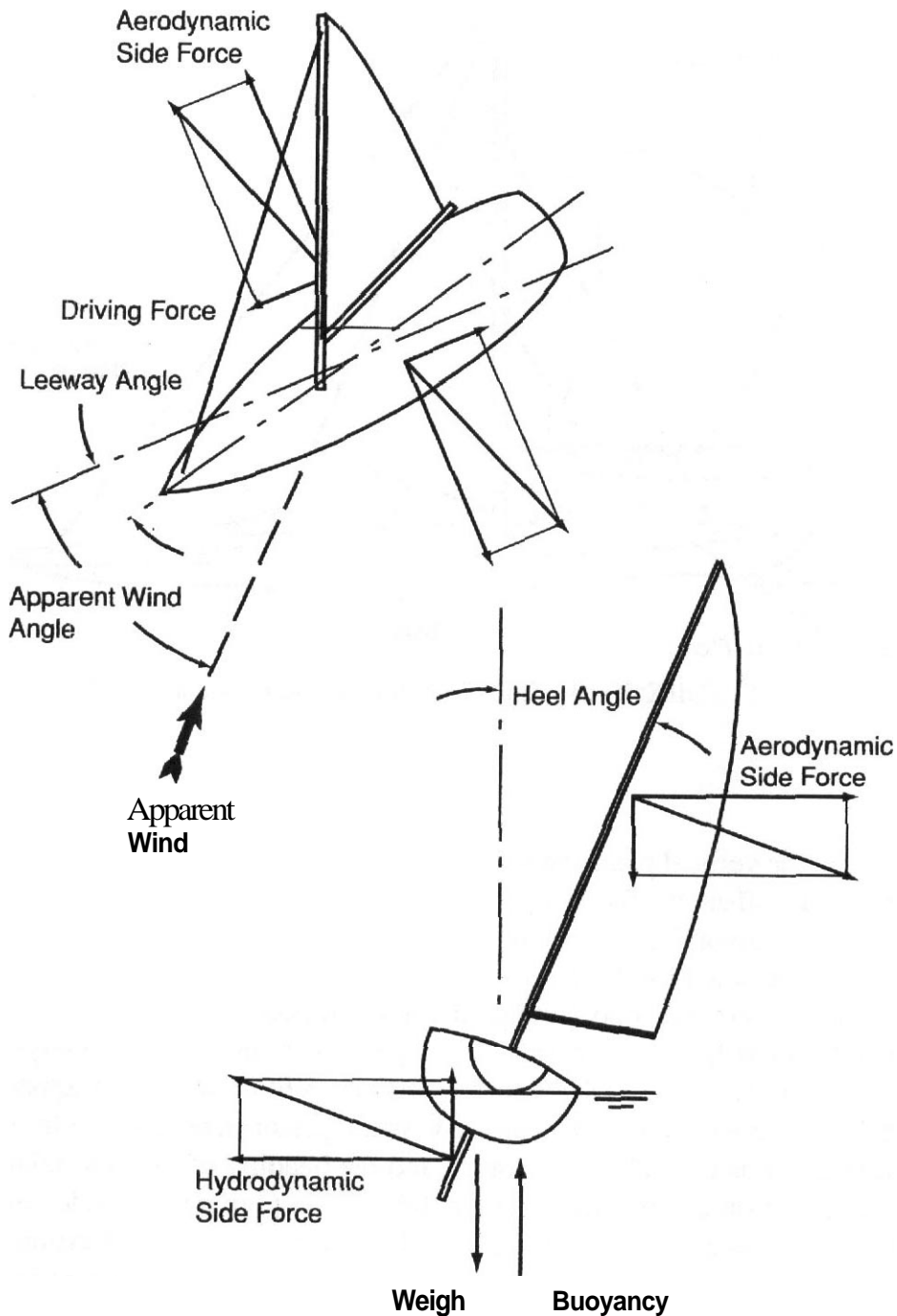
FIGURE 15.14 Force systems acting on a sail boat.

will decrease the righting moment and hence the stability of the sailboat, thus allowing it to carry less sail and reduce driving force. Where is the optimal point in this particular design trade-off? Only the VPP can tell. And the VPP itself is always evolving as predictive techniques improve. The consequence of this is that a significant amount of planning must go into any optimization study and development of the wind tunnel test plan to make efficient use of time available for the experiments.
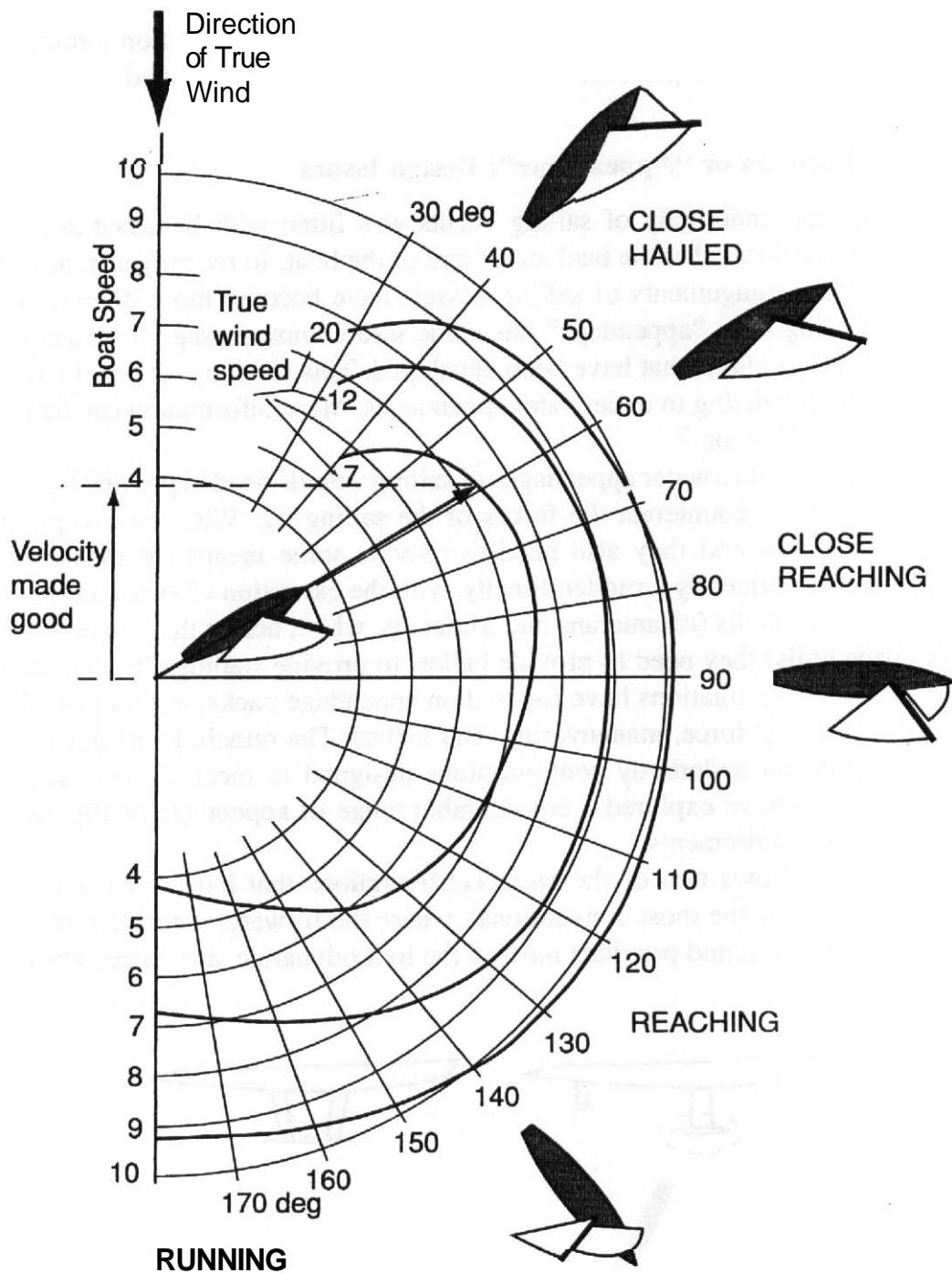
FIGURE 15.15   Trimmed polar velocity plot.

This design exercise is further complicated by the fact that sailboat competitions are almost always constrained by rating rules. Thus the problem is not only to build a fast boat but to not incur unreasonable rating penalties in the process.

One should bear in mind during the remainder of this section that yacht races are frequently decided by only a few seconds after hours of racing. As a consequence small differences in resistance can have enormous effect on the performance of the yacht in question. Thus testing yacht components is one of the most demanding

applications for a wind tunnel. This is parallel to other competition vehicles for which even the smallest performance increment is diligently pursued.

Keels and Rudders or "Appendages": Design Issues

Traditionally the underbody of sailing yachts was fitted with ballasted keels and movable rudders located at the back or aft end of the boat. In recent years, however, the underwater arrangements of sailing vessels have become more diverse so the all-encompassing term "appendage" has come into common usage to describe the variety of configurations that have been developed. This section will briefly discuss the design issues relating to underwater appendages. More information can be found in Larsson and Eliasson.[22]

In all cases the underwater appendages of sailing vessels need to provide hydrodynamic side force to counteract the forces of the sailing rig. With the exception of sailboards (windsurfers) they also need to provide some means for maneuvering the vessel, most frequently a rudder. Finally, with the exception of small unballasted dinghies and multihulls (catamarans and trimarans, which derive their stability from widely space hulls) they need to provide ballast to provide stability. To date almost all wind tunnel investigations have focused on appendage packages that provide all three functions: side force, maneuvering, and ballast. The remainder of this section will concentrate on underbody configurations designed to meet all three requirements. Designers have explored a considerable range of appendage configurations to satisfy these requirements.

Figure 15.16 shows two of the basic configurations that have been built. The first configuration is the most conventional, where the forward appendage is a keel that carries the ballast and provides most of the hydrodynamic side force. The other
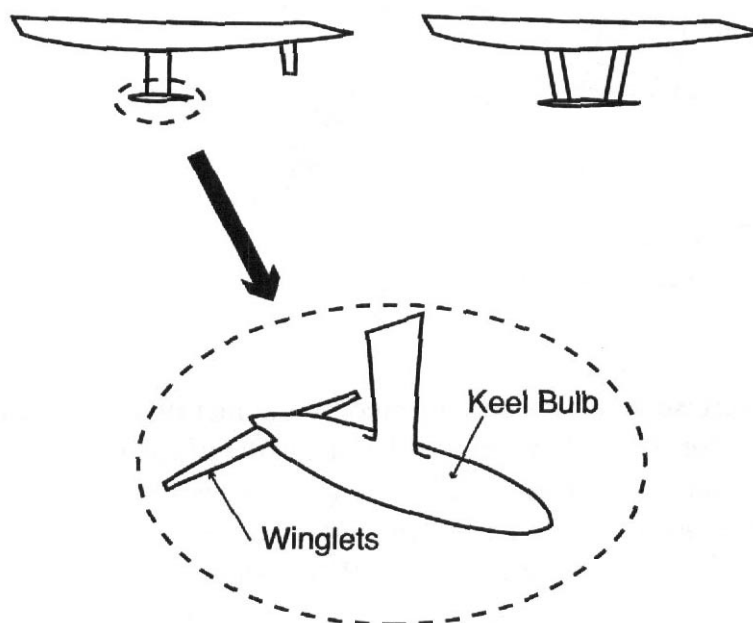
FIGURE 15.16   Yacht keels with ballast bulbs and winglets.

configuration shown attempts to combine the functions of the rudder and keel into two equally sized appendages plus a torpedo for ballast between the two foils. Both of these appendage configurations employ torpedo or bulb shaped ballast packages at their lowest extremes.

Consideration of the force diagrams given in Figure 15.14 shows that the appendage system must provide hydrodynamic side force and trim in yawing moment. This can be seen to be analogous to the lift and pitching moment for an airplane. There will be induced drag based on the same physics as for the airplane. The methods to minimize induced drag will therefore be the same for the two applications. The most potent way to reduce induced drag is to increase span. This is more often possible for airplane designers than for designers of sail boat keels. Efforts to reduce induced drag have also led designers to affix "winglets" to the ends of the keels or to provide special shaping of the keel bulbs to control spanwise flow and reduce the intensity of the tip vortices, as shown in Figure 15.16.

Winglets have also been attached to the ends of the rudders in the conventionally arranged appendages in an effort to both control induced drag and decrease seaway-induced pitching motions. These rudder winglets have also been shown to contribute to driving force when the boat pitches.

Limits on the lengths of appendages are necessary in order to allow operation in shallow water. Since both induced drag and stability are improved by increased draft, the practical necessity of reasonable draft limits has caused rating rules to penalize designs that have excessive draft. Also, appendages must be strong enough to support the loads they experience and also need to be strong enough to survive grounding damage. If the keel is not fitted with a bulb, the volume of the keel section needs to be thick enough to carry required ballast.

Rudders need to be of adequate size to control the vessel and thick enough to withstand the hydrodynamic loads they generate. They need to be thick enough to allow a rudder shaft of sufficient strength to connect the rudder to the hull and must mesh with the hull surface with clearances that allow adequate rotation. Rudders usually need not be as tolerant of grounding damage as keels because they are usually shorter than keels and therefore are protected when grounding.

These design issues are discussed in more detail in Larsson and Eliasson.[22]

Wind Tunnel Arrangements for Appendage Testing

Yacht appendages are usually deeply submerged where free-surface effects usually are not important so their steady-state operation can be studied in wind tunnels. Certain appendage configurations, however, are designed to yield benefits only in the actual unsteady operation of a yacht in a seaway. The principal example of this is winglets attached to the rudder that are intended partially to reduce the induced drag of the rudder but also to alleviate pitch motions. In addition there is some thought that these winglets can also generate thrust when subjected to unsteady flow due to the Katzmayer effect, as discussed in Sclavounos and Huang.[23] In these cases the aerodynamic coefficients as a function of pitch and yaw should be

determined and the resulting data used to study their effectiveness in a simulation of a yacht in an unsteady condition.

Appendages are tested in two ways: reflection plan models and floor mounting. We will discuss each method in turn in the following sections. In both cases only one appendage is usually tested at a time. But novel configurations, particularly those that may have interacting vortex systems, may require interaction studies in which models of all the interacting appendages are mounted on the model.

In both test types foil pressure measurements can be used to predict the onset of cavitation, but usually yacht appendages are designed so that the loading is well below that required to produce cavitation.

Wake surveys and flow visualization studies can be used in either modeling approach to investigate the vortex systems for each appendage and to help reduce the strength of these systems.

Reflection Plane Models   *In* the reflection plane method a model of the appendages and hull below the waterline and its image is constructed, as shown in Figure 15.17. This method has the advantage of including the interaction between the hull and the appendages in the study. It also allows heel and side slip to be studied since the model can be prepared for a condition where the boat is heeled. This is a fundamentally different flow regime than can usually be studied with a floor model
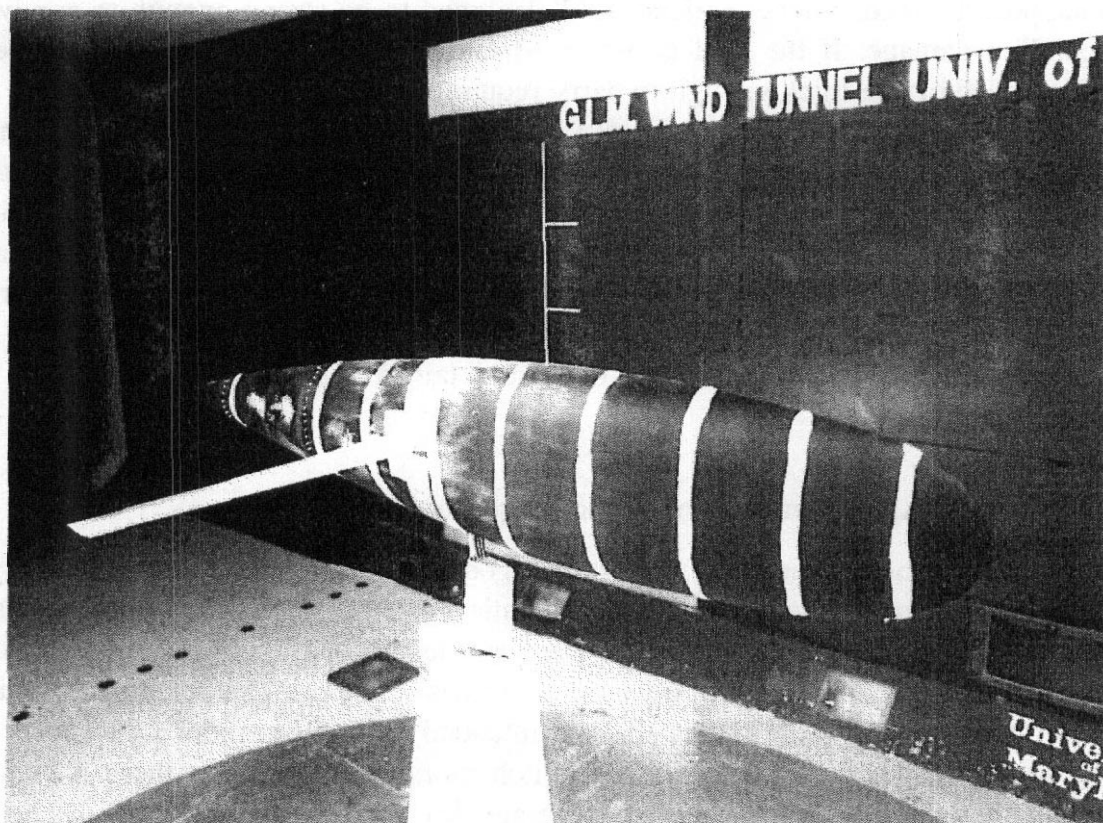
FIGURE 15.17   Relfection plane model with oil stripes applied prior to oil flow **visualiza-**tion **run.**

because the rotation that occurs when side slip is investigated will be about a different axis with respect to the appendage than with the floor model.

An example of a reflection plane model test is given in Draijer and Menkveld.[10] This study, mentioned earlier, was intended to clarify issues related to viscous drag estimation for towing tank investigations of sailing yachts.

These tests are good for examining interference effects and the total side force developed by the hull–appendage system. This can be particularly useful in cases where the distinction between the hull and appendages is blurred by the details of the shape. In most modem underbody configurations, though, the detailed design of the appendage should use the larger foils found in floor-mounted models, particularly when bulblwinglet details are being investigated.

The aero-zeroing of the model in the pitch plane should use yacht side force rather than yacht pitching moment since side force is the quantity of greatest interest.

Floor-Mounting Arrangements   In this arrangement a model of the foil is mounted upside down on the floor of the wind tunnel. A portion of the hull and/or other foils should be included if interaction is considered important. The foil should be free to pivot to examine different side-slip angles. This arrangement is similar in most respects to arrangements for control surface testing for surface ships and submersibles. The chief difference is that the yacht can be both yawed and rolled in a way that puts the yacht appendage into a flow regime that is different from that experienced by a ship control surface.

The chief advantage of this technique is that the model of the appendage can be bigger for a given test-section size so the resolution of the resistance measurements and flow visualization studies can be greater. A picture of such an appendage test is shown in Figure 15.18. An example of floor mounting a keel model, which included the underwater part of the hull, is described by Flay and McMillan.[24]

Sails and Sail Rigs: Design Issues

Sail design involves two issues: the shaping of the sail to provide "optimum" aerodynamic performance and the structural design of the sail. The structural issues are of themselves extremely complex but are beyond the scope of this discussion, except as to how the structural deformation of the sails affects aerodynamic properties. What follows is a discussion of the purely aerodynamic design of sails.

A conventional sail is a flexible membrane made of some combination of woven fibers and homogeneous plastic films supported by flexible spars and wires. The shape of the sail is influenced by several factors. First, shape is introduced into the sailcloth itself by making the sail out of panels of cloth. The panels are cut with a curved edge, or "bmadseam," so that when the panels are stitched together a three-dimensional shape is introduced. This process is shown in Figure 15.19.

Next, shape is introduced by placing, or "flying," a sail on the spars and/or wires meant to support it, as shown in Figure 15.20. This process is similar to introducing shape into the sail by broadseaming except now a degree of control is retained because by altering the shape of the spar (by carefully bending the mast in different
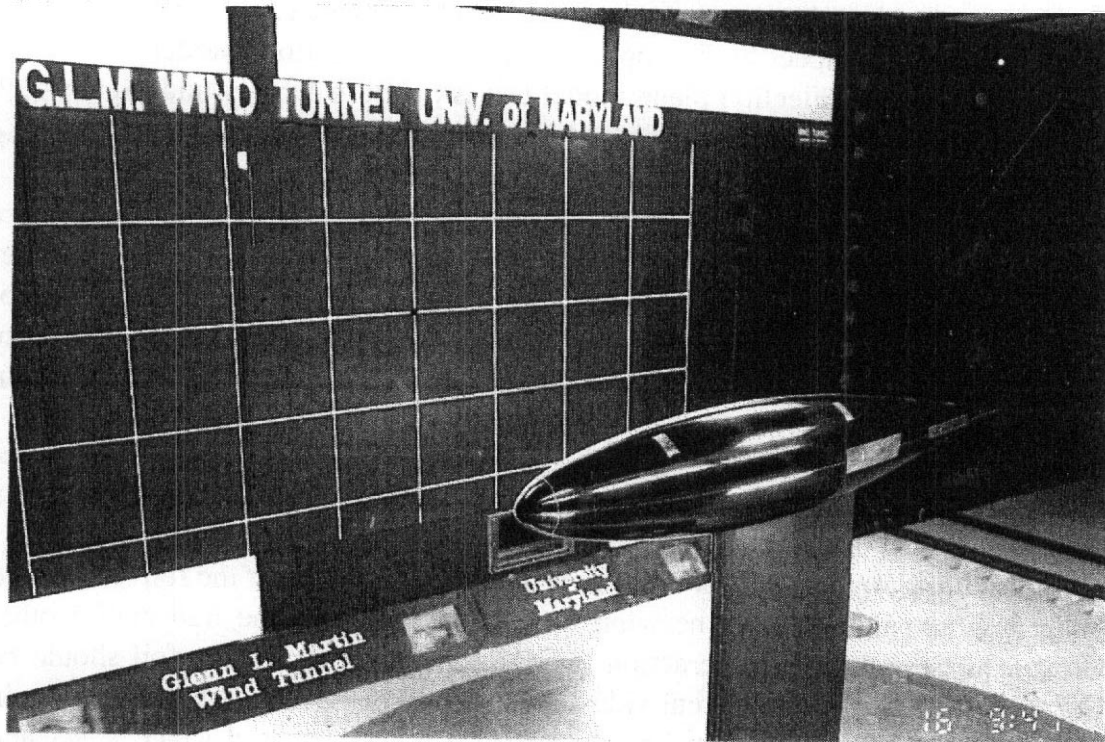
FIGURE 15.18   Floor-mounting yacht keel arrangement.

Broadsearn

Panels are cut with a curved edge
or broadseam

When the sail is assembled,
broadseaming gives the sail a
"builtin" shape.
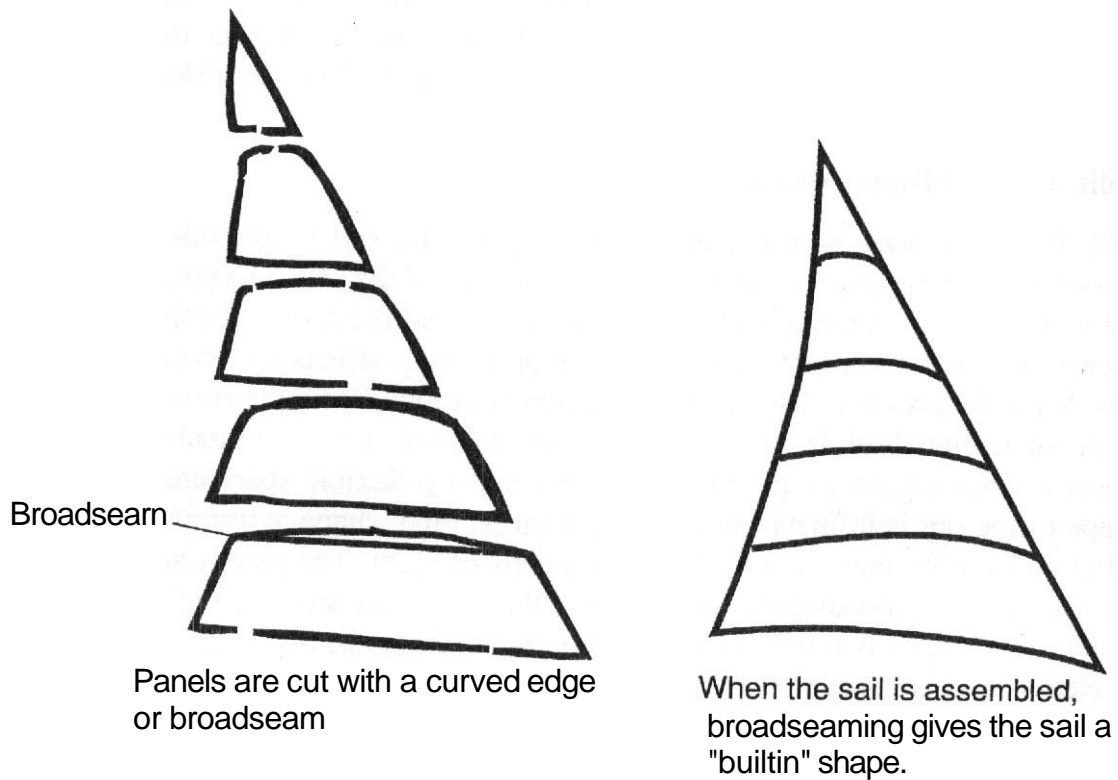
FIGURE 15.19   Introducing sail shape by broadseam.

Foot Curve
Extra Material is added to
lull and foot.

When flown, extra material
helps to determine **flying** shape
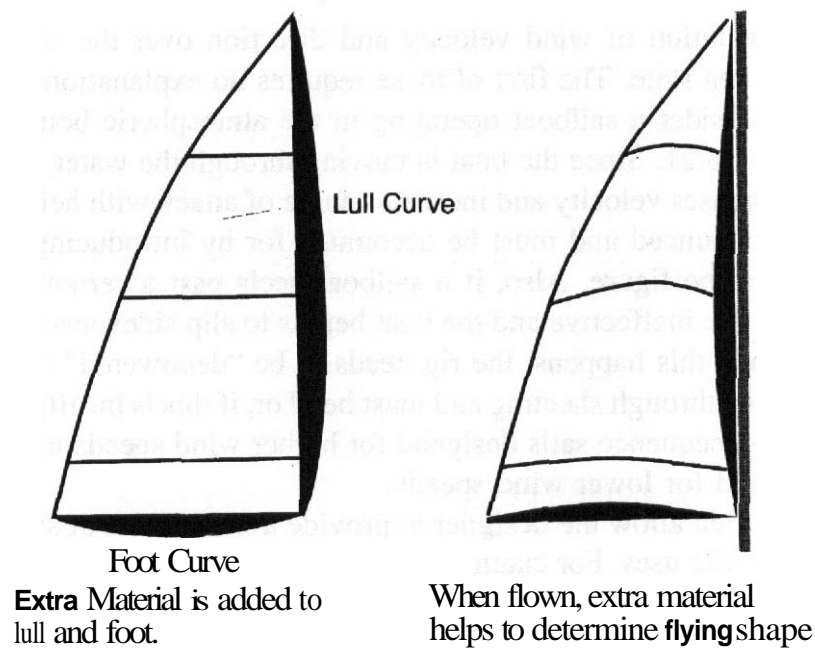
FIGURE 15.20   Introducing shape by mounting hardware.

ways) the shape of the sail can be controlled. However, this only works with certain sails. The main is highly influenced in this manner, and all sorts of mechanisms are fitted to boats to either passively or actively control the amount and distribution of mast bend. The jib is not much influenced by mast bend, but it is greatly influenced by what is called "headstay sag." This is the degree of deflection in the catenary curve of the headstay that supports the leading edge of the jib and is determined primarily by the amount of tension on the headstay. The attempt to decouple headstay tension from mast bend or at least achieving correct mast bend and headstay sag simultaneously is one of the main goals of the design of the mast and staying arrangement. The spinnaker is relatively unaffected by mast bend.

The "sheeting" of a sail also influences its shape. In the case of a mainsail the sheeting influences the position of the boom. The sheeting is usually accomplished by the mainsheet, which primarily controls the angle of the boom with the centerline of the yacht and the boom vang, which controls the angle the boom makes with the deck. Both controls critically influence sail shape. For example, the mainsheet primarily controls the angle of attack that the sail as a whole has with the wind while the vang influences the distribution as a function of distance along the mast. Jibs are likewise influenced by the sheeting, although in this case the position of the sheet lead is normally all that can be adjusted. Usually the fore and aft location of the lead determines twist distribution and the athwartship location of the lead determines the final angle of attack.

The spinnaker is usually flown almost completely free of the supporting rigging so mast bend has little influence on sail shape. The shape of the spinnaker is entirely controlled by the construction of the sail and by the sheeting of the sail, which is determined by the location of the spinnaker pole and the sheet lead.

The desired shape for a sail depends on many considerations too numerous to list here, but there are three basic considerations, the direction that the boat is sailing,

the uneven distribution of wind velocity and direction over the sailplan, and the wind speed and sea state. The first of these requires no explanation but the second and third do. Consider a sailboat operating in the atmospheric boundary layer, as shown in Figure 15.21. Since the boat is moving through the water, the air flowing into the sails increases velocity and increases angle of attack with height. This effect can be quite pronounced and must be accounted for by introducing twist into the sail, as shown in the figure. Also, if a sailboat heels past a certain point the hull appendages become ineffective and the boat begins to slip sideways to an unreasonable degree. When this happens, the rig needs to be "depowered" by reducing the camber of the sails through sheeting and mast bend or, if this is insufficient, reducing sail area. As a consequence sails designed for higher wind speeds tend to be flatter than sails designed for lower wind speeds.

Rating rules often allow the designer to provide a wide range of sails of different planform for specific uses. For example, some boats carry multiple jibs and spinnakers of widely different sizes for the broad range of conditions that may be encountered. Decisions regarding the size and distribution of inventories of sails are an
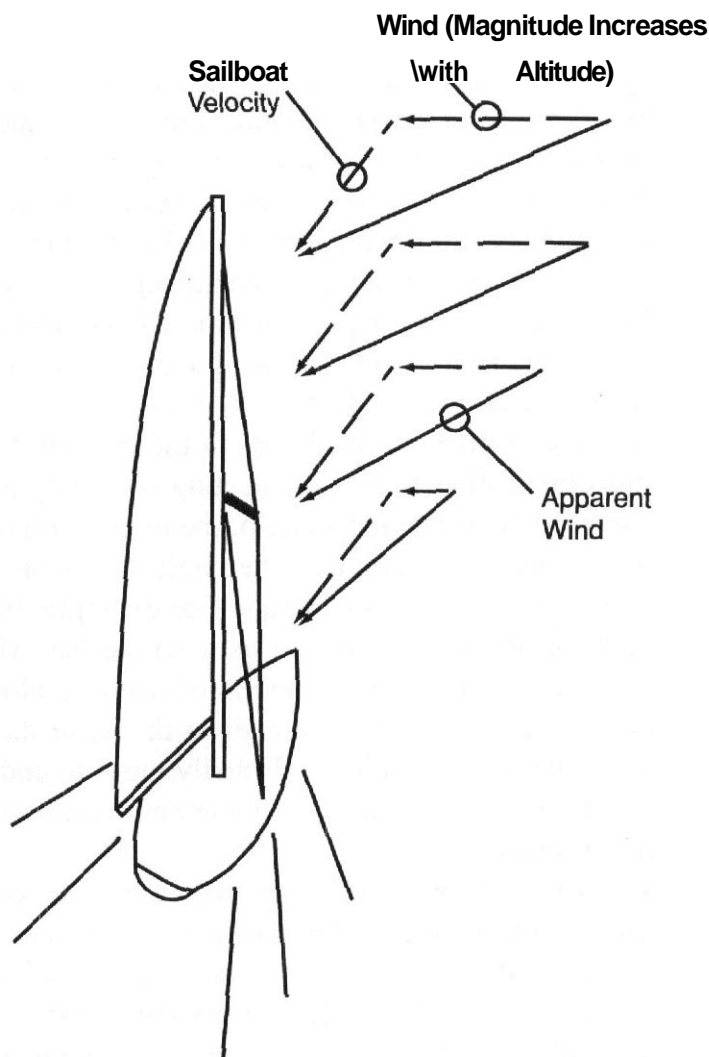
FIGURE 15.21 **Sailboat operating in an atmospheric boundary layer.**

ideal subject for wind tunnel investigation. For example, if you are going to carry five spinnakers for offwind sailing at apparent wind angles ranging from 85" to 180° over a wind speed range of 5–50 knots, what are the best five sails to carry? By testing candidate sails over the range of apparent wind angles and plotting the driving force as a function of heading angle, a well-rounded set of sails can be chosen.

Other issues related to sail design include effective "endplating" of the bottom end of a sail against the deck to reduce the strength of the vortex formed along the foot of the sail and the interference of the mast on the flow over the main. Excellent discussions regarding the design of sails can be found in books by Marchaj[25] and Whidden[26] and references contained therein.

Wind Tunnel Arrangements for Sail Testing

As of this date the "perfect" wind tunnel test of sailboat sails has not been performed. The impediments have been many and include the following:

> difficulty in modeling the atmospheric velocity gradient and the resulting variation in angle of incidence along the spanwise position of the sail,

- inability to match full-scale Reynolds number without destroying the sails,
- difficulty in reproducing full-scale sail shape and cloth properties (porosity, finish, etc.) and mast/rigging flexibility, and
- difficulty in measuring the miniscule differences in force that separate a good sail shape from a great one.

All is not lost, however. Even though sail performance tests in a wind tunnel are not completely accurate representations of the full-scale phenomenon, wind tunnels can be useful for studying the aerodynamic forces at work and relating these forces to design parameters. These tests therefore can be a useful component in a sail development program but cannot completely replace on-water evaluation of the designs.

Researchers have attempted to surmount the problems mentioned above. The atmospheric velocity gradient can be simulated by introducing blockage upstream of the test section, as discussed earlier in this chapter. The best modeling of this aspect of the flow is achieved in facilities that have a long flat floor upwind of the model to allow the boundary layer to develop to a sufficient thickness.

Modeling the variation in the angle of incidence is a bit more difficult, however. Recently researchers in New Zealand have attempted to simulate twist by introducing helically curved vanes upwind of the test section. Results of this effort have been published.[27,28,29]

Matching, or at least approaching, the full-scale Reynolds number is only possible when the model-scale ratio is small or the sails are made from some rigid material, the so-called tin sail. Solid sails can survive higher test-section velocities but do not allow the careful trimming of sails required to extract peak performance. It also negates whatever influence cloth properties have on the test results.

Reproducing sail shape and cloth characteristics can be achieved with careful model construction. Marchaj[18] quotes a sailmaker's recommendation that the luff (leading-edge) dimension of a conventional sail be a minimum of 7 ft long for accurate modeling of a sail. The rigging details of the boat model and the rig can be modeled to whatever accuracy is required by careful construction.

The portion of the boat's hull that is above the waterline should be carefully modeled. Flow below the model should be eliminated. It should also be arranged in such a way that it can be heeled to whatever degree is required to meet the test objectives. The support structure on the floor around the model should not be attached to the tunnel balance, if at all possible, but if it is, a correction scheme should be introduced to correct the data. Errors of this kind will have a great influence on the calculation of the heeling moment.

Meeting all these mounting requirements is not an easy thing. An effective solution is the sailboat-mounting arrangement used by the Wolfson Unit of the University of Southampton and described in Deakin[4] and illustrated in Figure 15.22.

This test rig suspends a model of the hull and rig in a pool of water that is approximately coincident with the floor of the wind tunnel. The model is restrained by passing a bar through a hole in the hull. This bar is then attached to force blocks and the bow of the boat is supported by a rod attached to a force block as well. By having a model with several holes drilled through the hull, a variety of heel angles can be investigated with the same model. The forces are resolved as illustrated in Figure 15.22.
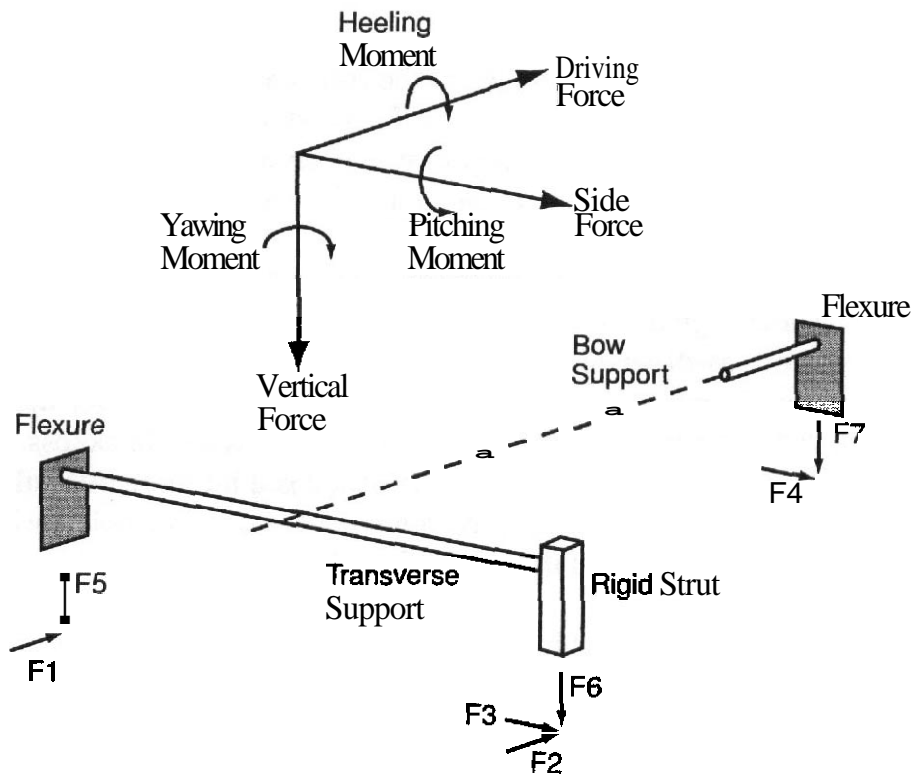
FIGURE 15.22 The Wolfson unit sail model test rig.

The test instrumentation should be arranged so the forces and moments developed by the sails can be monitored in real time while the test proceeds. Ideally the forces should be resolved into body frame axes so the driving force, heeling moment, and side-force coefficients are displayed to aid the adjustment, or "trimming," process of the sails. Sails are sensitive to slight adjustments to the sail shape and position so when the model is moved to a new heading angle the sails need to be adjusted in accordance with the trimming objectives of the test. These trimming objectives need to be carefully formulated and are discussed in the sections that follow on specific types of sail tests.

The trimming of the sails needs to be done by a person who has significant experience performing this task on a full-size racing sailboat. There is simply no substitute for this critical role in the test program since the setting of the sails involves so many variables that the only way to make any practical progress through a test matrix is to hand trim, or "eyeball," many of these adjustments. Fortunately, since most sail test programs involve the cooperation of a sail loft, experienced personnel are usually available for this purpose.

Once the sail is eyeball trimmed, people should be cleared from the test section and the force coefficients should be allowed to settle. This can take 10–30 sec depending on the size of the wind tunnel, the size of the model, and the number of people who were in the test section. At this point the force, moment, and attitude data should be recorded.

Next the "optimality" of trim should be checked. Different investigators have used different techniques for this. At a minimum (assuming that automated yaw control is available) the model should be yawed over a range of values to see if the trimming objectives are improved. Another approach is to outfit the model with remote control of the sails so that they can be adjusted without anybody entering the test section and disturbing the flow conditions. Thus fine tuning of the sail trim can be performed by watching the force coefficient displays. A picture of a model outfitted with remote-control winches is shown in Figure 15.23.

Deakin[4] reports that gusts were simulated at the Southampton tunnel by manipulating overlapping vertical blinds located downstream of the test section. In these tests a ballasted model of the boat was floated in a pool of water and located in the tank so that it was free to roll and sway but was restrained in surge. The heel angle was recorded with a roll gyro and the velocity shear was modeled. The gusts increased wind speed by 40% over a few seconds by first closing and then opening the blinds.

Blockage corrections will likely be required for both the drag force and the apparent wind angle (from distortion of the downwash by the tunnel walls). These topics are discussed in Chapters 9, 10, and 11. In addition, a review of techniques for downwind sail tests is given by Mairs and Ranzenbach.[30]

The performance of sails decreases with use. The porosity, stress–strain characteristics, and surface finish of the cloth all degrade and the unstressed dimensions of the cloth panels distort and alter the shape of the unloaded sail. For this reason a careful log should be kept of the amount of test time each sail has experienced. Degradation should be checked during any test involving detailed analysis of sail performance by checking the repeatability of the measurements for some portion
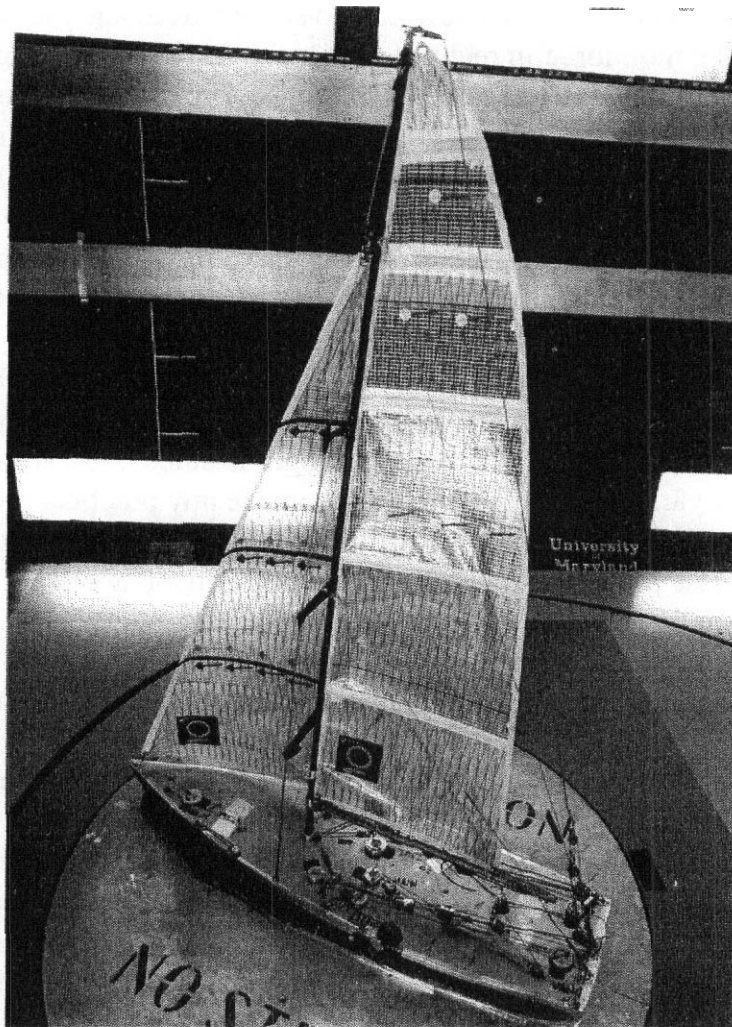
FIGURE 15.23   Picture of a sail test model fitted with remote-control winches. (Photograph courtesy of Glenn L. Martin Wind Tunnel.)

of the inventory to be tested. For comparison tests each sail being compared should have the same amount of use as the others in a test matrix.

Upwind Sails   The trimming objectives for upwind sails should consider the relationship between driving force and heeling moment. For example, consider two trim conditions having equal driving forces but unequal heeling moments. The trim condition with the lower heeling moment will be preferable. As the wind speed increases on an actual boat, the rig is progressively "depowered" to reduce heeling moment (at the expense of driving force) to keep the boat under control. Thus the trim condition that would be ideal for one wind speed would not be ideal for another speed. Finding this ideal trim is generally not possible without loading the results of the wind tunnel investigation into the VPP program described earlier. Only then can the critical relationship between rig forces and hull stability and hydrodynamic forces be established and studied. The result of this is that the wind tunnel data set will ideally consider both a range of heel angles for the model and a range of tuning objectives in the test program.

These data are best generated by performing several tunings at each heel angle and hull centerline angle of incidence to the free stream. The first tuning will attempt to maximize driving force without regard to driving force. The procedure for this should be as described above. An approximate eyeball tuning should be done with final tuning by remote control and then yaw the model over some small range to establish how "good" the trim is. The second and following trims should repeat this procedure with a decreasing upper limit on the heel moment. This will allow the VPP to select the optimally depowered rig for the conditions being examined.

The tuning process for upwind sails can include mast bend, forestay tension, jib sheet lead position, mainsheet tension, and boom vang tension. This process should not overlook the critical influence of mast bend and forestay sag on the set shape of the sail. Also pay close attention to mounting arrangements that influence the size of the gap between the foot of the main and jib and the deck. The size of this gap influences the strength of the vortex developed at the foot of the sail. If this gap is completely eliminated, the foot vortex system will disappear and the efficiency of the rig will increase.

The model should be heeled for most upwind sail tests. If only one heel is to be explored, it should be in the 20°–30° range. The only exception to this would be the case where the rig is intended for a vessel capable of creating an unusual righting moment to counteract the heeling moment. Examples of vessels of this type include catamarans or other multihull vessels or a dinghy where crew weight can be used to augment stability. A photograph of a typical upwind sail test is shown in Figure 15.24.

If the details of the sail shape are a part of the investigation, the shape of sails should be recorded as the test matrix proceeds. This is best accomplished by fitting the sails with "draft stripes" and the photographing the sail from a position as directly in line with the mast as practical. These photographic images can then be digitized and compared with other trim conditions or even used as a geometry baseline for correlation studies with numerical predictions of sail performance. An example of such a photograph is shown in Figure 15.25.

Upwind sails are not usually as sensitive to Reynolds number effects since the flow is not dominated by separation phenomena to the extent that offwind sails are. A rough measure of the influence of separation on the flow can be determined by a method suggested in a recent report by the United States Sailing Association.[31] Recall that Prandlt's classical lifting Line theory predicts that the induced drag of a three-dimensional airfoil can be calculated as

$$C_{D,i} = \frac{C_L^2}{\pi e \, \text{AR}} \tag{15.16}$$

where e is the span efficiency factor and AR is the aspect ratio of the foil. All the terms in the denominator are a constant for a particular airfoil, so the result is that the induced drag coefficient is proportional to the square of the lift coefficient. Since this technique uses inviscid flow assumptions, the validity of the ideal flow assumptions can be tested by plotting C_L^2 for the different trim conditions at a given angle of attack as a function of C_D. If the plot is linear, then the drag is primarily
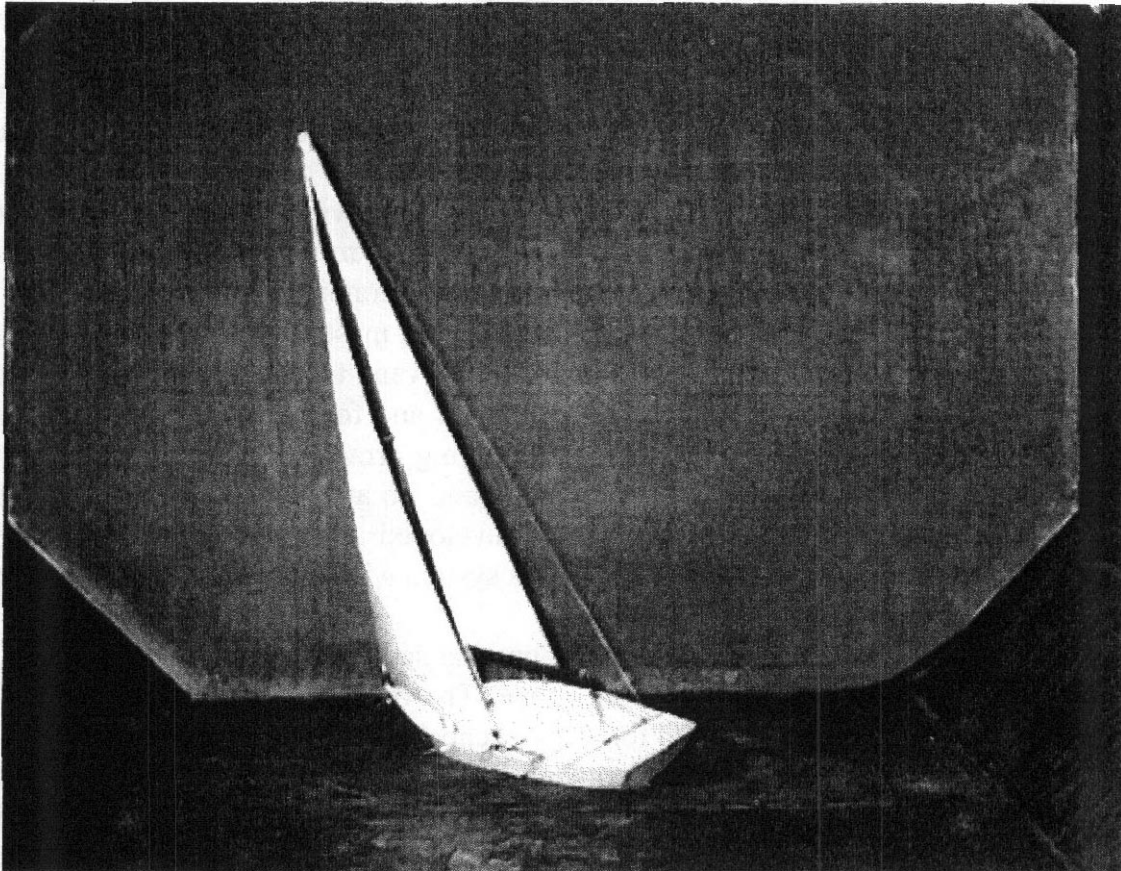
FIGURE 15.24 Typical upwind sail test.

induced. To isolate the aerodynamic drag contributions of the sails, the tare drag of the rig without the sails should be subtracted from the data generated with the sails set before making these calculations.

Downwind Sails Downwind sail experiments are similar to upwind sail experiments in most respects, but there are significant differences. Most of these differences can be traced to the fact that upwind sails are primarily lifting surfaces with mostly attached flow. The experiments are, therefore, similar to those carried out for evaluating wings and appendages. Downwind sails, on the other hand, have large regions of separation, which is characteristic of bluff bodies, but in some configurations retain substantial characteristics of lifting systems. A useful comparison is to stalled wings. The forces on objects in such flows are known to be much stronger functions of Reynolds number than the forces in flows that are almost completely attached. Since most experiments on downwind sails are necessarily performed at Reynolds numbers significantly below full scale, care should be exercised in interpreting the results.

The need to have the Reynolds number as large as practical for downwind sail experiments leads to relatively large models and corresponding requirement for significant blockage corrections. Methods for blockage corrections are given in
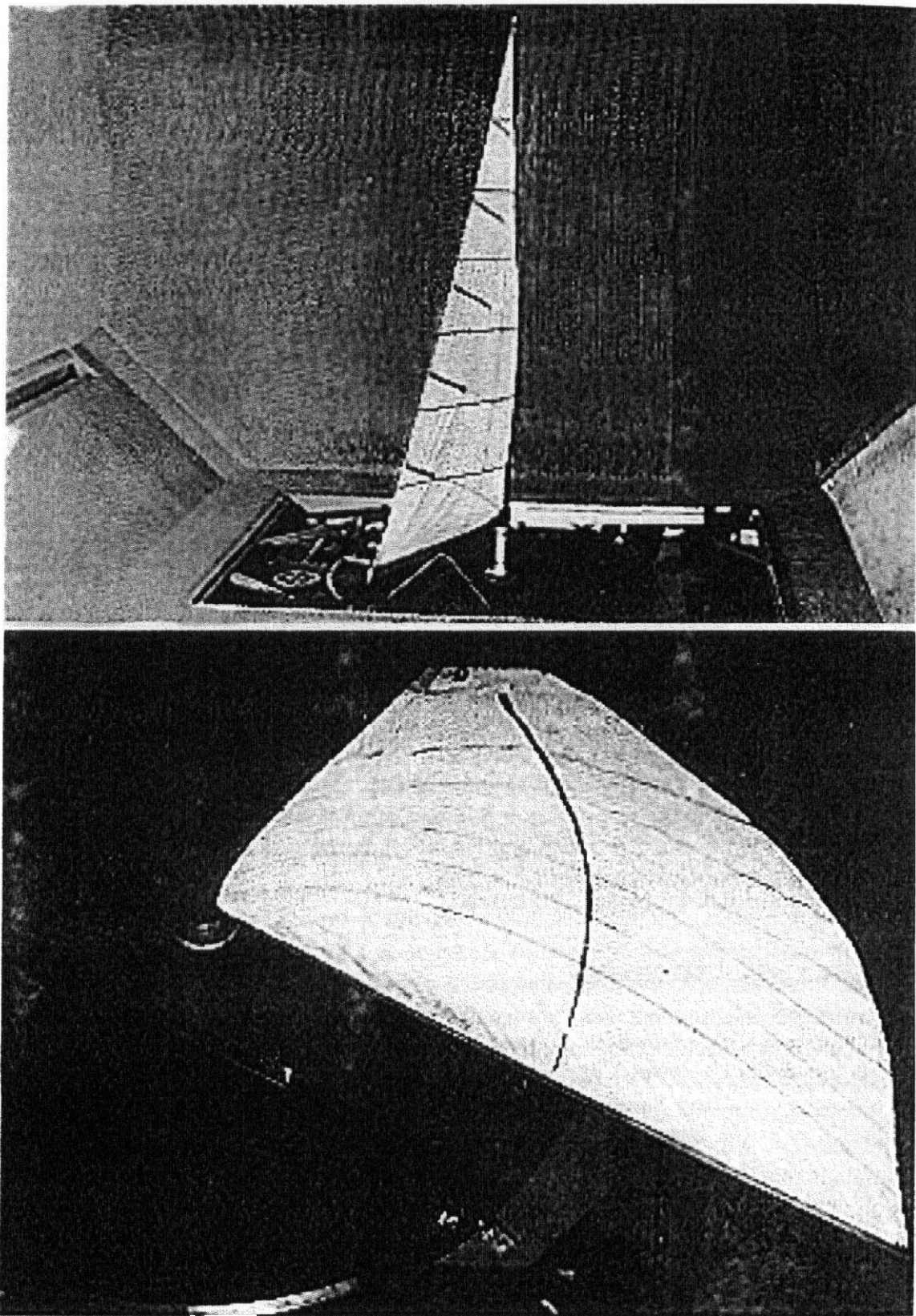
FIGURE 15.25   Recording upwind sail shape with draft stripes.
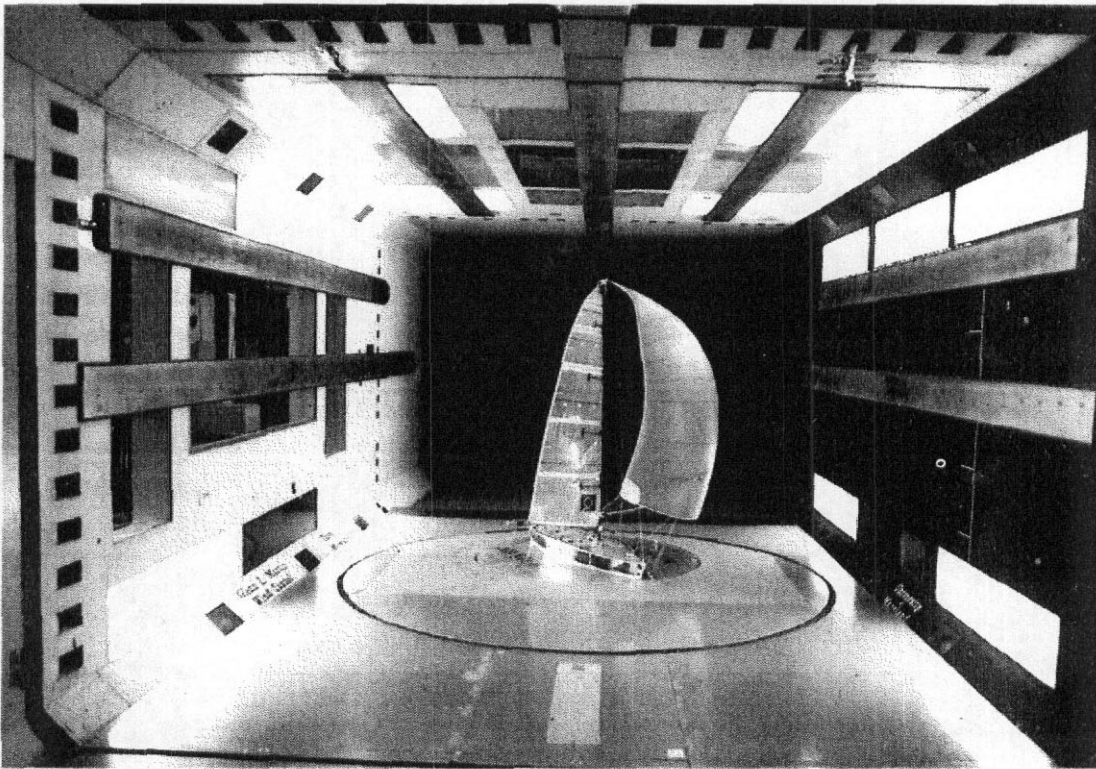
FIGURE 15.26   Wind tunnel offwind sail test rig. (Photograph courtesy of the Glenn L. Martin Wind Tunnel.)

Chapters 9, 10, and 11. Mairs and Ranzenbach,[30] as mentioned earlier, present a detailed review of blockage correction schemes appropriate for downwind sail tests.

Figure 15.26 shows a downwind sail test being performed in the Glenn L. Martin Wind Tunnel at the University of Maryland.

REFERENCES AND NOTES

1. Lewis, E. V., Ed., *Principles of Naval Architecture,* Society of Naval Architects and Marine Engineers, Jersey City, NJ, 1988.

2. McTaggart, K., and Savage, M., "Wind Heeling Loads on a Naval Frigate," paper presented at the International Conference on Stability of Ships and Ocean Vehicles, Melbourne, FL, Nov. 1994.

3. SNAME, "Guidelines for Wind Tunnel Testing of Mobile Offshore Structures," SNAME T&R Bulletin 5-4, Society of Naval Architects and Marine Engineers, 1988.

4. Deakin, B., "Model Test Techniques Developed to Investigate the Wind Heeling Characteristics of Sailing Vessels and Their Response to Gusts," paper presented at the tenth Chesapeake Sailing Yacht Symposium, Society of Naval Architects and Marine Engineers, Annapolis, MD, 1991.

5. Long, M. E., "Wind-Tunnel Tests on Multiple Ship Moorings, Part 3. Determination of Air Loads on Multiple Ship Moorings for Destroyers, Submarines, Liberty Ships, and Escort Carriers," David Taylor Model Basin Report 830, Bethesda, MD, July 1952.

6. Marquand, C. J., "Aerodynamic Model Study of Marine Gas Turbine Exhaust Cooling," *J. Ship Res., 22,* 123–129, June 1978.

7. Shultz, M., "Air Wake Survey of Full-scale CVA(N)-65," David W. Taylor Model Basin Aerodynamic Laboratory, Bethesda, MD, January 1963; Cantone, A., "Smoke Tunnel Studies on Wind Velocities over the Deck of an Aircraft Carrier," Naval Air Engineering Laboratory Report NAEL-ENG-7140, Lakehurst, NJ, March 1964.

8. Cook, M. L., "A Wind Tunnel Air Wake Survey of an 11144 Scale Model Aircraft Carrier with Deck and Island Modifications,"David W. Taylor Model Basin Aerodynamic Laboratory Report 1805, Bethesda, MD, 1968; Also see Naval Postgraduate School Masters Theses: Cahill, T. A., "Visualization of the Flow Field Around an Oscillating Model of the USS Enterprise (CVN-65) in a Simulated Atmospheric Boundary Layer," Monterey, CA, 1988; Biskaduros, J. L., "Flow Visualization of the Airwake of an Oscillating Generic Ship Model," Monterey, CA, 1987; Bolinger, W. K., "Visualization of the Flow Field Around a Generic Destroyer Model in a Simulated Turbulent Atmospheric Boundary Layer," Monterey, CA, 1987; and Anderson, G. A., "Mapping the Airwake of a Model DO-943 Along Specific Helicopter Flight Paths," Monterey, CA, 1989.

9. Newman, J., *Marine Hydrodynamics,* MIT Press, Cambridge, MA, 1977.

10. Joubert, P. N., and Matheson, N., "Wind Tunnel Tests of Two Lucy Ashton Reflex Geosims," *J. Ship Res., 14,* 241–276, Dec. 1970; Draijer, W. and Menkveld, H. J., "Measurement of the Resistance of a Yacht Model in a Wind Tunnel for High Reynolds Number," paper presented at Symposium Yachtarchitecture, Schiphol-Oust, Holland, Nov. 1975.

11. Hurwitz, R. B., and Jenkins, D. S., "Analysis of Wake Survey and Boundary Layer Measurements for the RV ATHENA Represented by Model 5366 in the Anechoic Wind Tunnel," David Taylor Naval Ship Research and Development Center/Ship Performance Department, DTNSRDC/SPD Report 0833-02, July 1980.

12. Wan, G. D., Nguyen, V. O., Cooper, K. R., and Tanguay, B., "Wind Tunnel Investigations of Submarine Hydrodynamics," *Can. Aeronaut. Space J., 39,* 119–126, Sept. 1993.

13. Molland, A. F., and Turnock, S. R., "Wind Tunnel Test Results of a Model Ship Propeller Based on a Modified Wageningen B4.40," University of Southampton, Department of Ship Science Report No. 43, Highfield, Southampton, U.K., Dec. 1990.

14. Leggat, L. J., Mackay, M., Cooper, K. R., Williams, C. D., and Johnston, G. W., "Canadian Wind Tunnel Research for Naval Hydrodynamics," in *Advanced Hydrodynamic Testing Facilities,* Proceedings of the Twenty-Second Defence Research Group Seminar on Advanced Hydrodynamic Testing Facilities, NATO, The Hague, The Netherlands, 1982.

15. Young, A. D., *Boundary Layers,* AIAA, Washington, DC, 1989.

16. Fidler, J. E., and Smith, C. A., "Methods for Predicting Submersible Hydrodynamic Characteristics," Naval Coastal System Laboratory Report NCSC TM-238-78, Panama City, FL, July 1978.

17. Goodman, A., "Experimental and Theoretical Investigation of Factors Affecting Fin-Body Interference," Hydronautics, Inc. Report TR-7927-1, Silver Springs, MD, 1980.

18. Barlow, J. B., Harris, D., and Ranzenbach, R., "Time Domain Simulation of Underwater Vehicles," paper presented at MAN '98, International Symposium and Workshop on Force Acting on a Manoeuvring Vessel, Dijon, France, Sept. 1988.

19. Wetzel, T. G., and Simpson, R. L., "Unsteady Flow Over a 6:1 Prolate Spheroid," Virginia Polytechnic Institute and State University Report VPI-AOE-232, Blacksburg, VA, 1993.

20. Ohman, L. H., and Nguyen, V. D., "Applications of the Five-Hole Probe Technique for Flow Field Surveys at the Institute for Aerospace Research," Institute for Aerospace Research, Ottawa, Ontario, 1994.

21. Fry, D. J., "Hull/Appendage/Propeller Interaction Experiment," David Taylor Research Center/Ship Hydrodynamics Department, Report DTRC/SHD-1288-01, Bethesda, MD, 1966.

22. Larsson, L., and Eliasson, K., Principle of Yacht Design, International Marine Publishers, Camden, ME, 1994.

23. Sclavonnos, P., and Huang, Y., "Rudder Winglets on Sailing Yachts," Marine Technology, SNAME, July 1997.

24. Flay, R. G. J., and McMillan, D. C., "A Wind Tunnel Investigation of Yacht Hydrodynamic Side Force and Drag," *J. Ship **Res., 00,** 000–000, Dec.* 1993.

25. Marchaj, C. A., *Aero-Hydrodynamics of Sailing,* Dodd, Mead & Company, New York, 1979. Also see the related material in *Sail Performance* (McGraw-Hill, 1990) by the same author.

26. Whidden, T., and Levitt, M., The *An and Science of Sails,* St. Martin's Press, New York, 1990.

27. Flay, R. G., and Vuletich, I. J., "Development of a Wind Tunnel Test Facility for Yacht Aerodynamic Studies," *J. Wind Eng. Ind. Aerodyn., 58,* 231–258, Dec. 1995.

28. Flay, R. G., Locke, N. J., and Mallinson, G. D., "Model Tests of Twisted Flow Wind Tunnel Designs for Testing Yacht Sails," *J. Wind Eng. Ind. Aerodyn., 63,* 155–170, 1996.

29. Flay, R. G., "A Twisted Flow Wind Tunnel for Testing Yacht Sails," *J. Wind Eng. 2nd. Aerodyn., 63,* 171–184, 1996.

30. Mairs, C. M., and Ranzenbach, R. C., "Experimental Determination of Sail Performance and Blockage Corrections," paper presented at the Thirteenth Chesapeake Sailing Yacht Symposium, Soc. of Naval Architects and Marine Engineers, Annapolis, MD, 1997.

31. United States Sailing Association, 'Wind Tunnel Tests of Sailing Yacht Rig Aerodynamics," U.S. Sailing Report No. 1234, July 1995.

16 Wind Engineering

Wind tunnel evaluations of components, individual structures, and groups of structures all are routinely used to obtain data to support design decisions that often are intended to ensure structural integrity but also may be aimed at issues of utility in addition to safety. Pedestrian-level wind conditions are often a substantial concern. Patterns of deposit for drifting snow or debris are frequent subjects of investigations. Local concentrations and dispersion patterns of pollutants are also topics of wind tunnel simulations.

A number of applications that come from the field of wind engineering are discussed in Chapter 2. See Section 2.10 for discussions complementary to the material in this chapter.

Extreme cases that call for special attention are perhaps the easiest to identify. Very tall structures that are relatively elastic clearly may experience sufficient wind-induced response so that the wind effects will impose significant requirements on the structural specifications. Buildings whose profiles are extraordinary are clear candidates for analysis and possible wind tunnel simulation to determine if some building surface loads may exceed typical local code expectations. Special attention is warranted if a structure has the potential for significant dynamic motions. Tall, slender buildings, long-span bridges, marine platforms, extensive cable-suspended flexible roofs, and transmission line cables with their towers are typical examples. The most widely publicized wind-induced structural failure is almost surely the Tacoma Narrows Bridge, which under the influence of a moderate and steady wind developed a large-amplitude oscillation leading to total separation of the bridge decking from the suspension system. A substantial part of the failure process was captured on motion picture film. The film provides dramatic evidence of the potential power of the interaction of a relatively moderate wind that excites dynamic modes of a susceptible structure.

Problems often arise in situations that appear rather common so a review of potential for wind-related design issues is strongly recommended for all structures. For some areas that have relatively frequent tropical storms, this is now a requirement of local regulations.

Compared to vehicle aerodynamics, wind engineering is a relatively young technical field that has seen strong activity for the last 30 years or so. Two sources of information on the field and its ongoing development are the *Journal of Wind Engineering and Industrial Aerodynamics* published by Elsevier Scientific Publishing Co. and the proceedings of a remarkable series of international conferences on wind engineering that have been held at four-year intervals at sites around the world since the inaugural at the National Physical Laboratory, Teddington, England, in

1963. The tenth in the series is planned to be held at the Danish Maritime Institute, Copenhagen, Denmark, in June 1999.' A reference of particular value to our immediate interests is the proceedings of a conference specifically focused on wind tunnel modeling.[2]

Wind tunnel simulations are intended to give information on wind effects on structures under particular wind conditions, that is, particular wind speed and wind direction relative to the structure and its surroundings. In the case of wind engineering studies, there are implied features of the incoming stream that are typically characterized for general topographic features but may be dependent on direction even for a particular geographic site. This would be true, for example, for a structure located on a shore where significant features of the incoming wind may differ when coming from the water side as compared to coming from the land side. The data from the wind tunnel for specific speeds and directions are used with historic data on local wind conditions to make predictions for the effects on the actual full-scale structures.

The most conservative approach to choosing design requirements is to take the worst-case climatic wind speed to be expected based on the historic record combined with the worst-case loading indicated from the wind tunnel simulations without regard to wind direction in either the historic record or the wind tunnel simulation. As experience has accumulated over the last three decades, it has become more acceptable to consider in a more realistic fashion the details of both directional effects from the wind tunnel results and the local climate in determining design requirements.

The climatic wind conditions at a particular site are obviously critical, but also obviously predictable only in a statistical way and with considerable uncertainty for any given period of time. The most extreme events are of greatest significance in the design requirements and at the same time are the most uncertain. Choices are necessary in relating the wind tunnel simulation to reported climatic wind speeds, even though much of the historic data may be from less than ideal (incompletely defined) instrument locations. Typical choices for reference wind speed and direction are the conditions above the model boundary layer in the wind tunnel, which are considered to be comparable to the hourly mean wind speed at gradient height. In some situations, a profile in the wind tunnel may extend over such a large fraction of the tunnel height that there may not be a reasonable approximation to a "free stream." In such cases the wind speed at the top of the structure may be used as the reference to be considered as similar to the hourly mean at the height of the actual structure at its intended location.

16.1   MODELING THE ATMOSPHERIC SURFACE WIND

High wind speeds correspond to atmospheric boundary layers with neutral thermal stratification. These are the conditions of greatest interest with regard to structural wind loading. This is not the case of severest conditions for dispersion of pollutants that may occur for relatively low wind speeds and thermal inversion conditions.

It is necessary to create flows representative of the atmospheric boundary layer over a number of different types of terrain. The properties of the flow are typically

described by the vertical distribution of the mean speed, $\overline{w}(h)$, the values of turbulence intensity for the three flow components, and the integral scales for each component. It is generally considered most important to reproduce the vertical distribution of mean speed plus the intensity and scale of the longitudinal component of turbulence. Some cases in which the object under study is long and slender may require that the component of turbulence normal to the mean wind and the long axis of the object be modeled with reasonable fidelity.

It happens that the time variation of the atmospheric wind as represented by the power spectral density has a low region in the range from a few minutes to a few hours. Figure 16.1, based on Lumley,[3] shows this characteristic. This feature separates what can be considered as "turbulence" to the right of the low region and variations of mean wind speed to the left of the low region. Changes in the simulated mean wind speed are obtained by varying the wind tunnel flow rate. Changes in the turbulence and profile properties are obtained by changes in roughness elements upstream of the test object. Changes in simulated wind direction are obtained by rotating the test object in the wind tunnel.

If the actual boundary layer is known at the location of a proposed site, the same boundary layer should be simulated. If not, the maximum speed at 30 ft altitude may be measured or estimated and the boundary layer is structured according to

$$\frac{u}{u_{ref}} = \left(\frac{z}{z_{ref}}\right)^{\alpha} \tag{16.1}$$

where u is the mean velocity at height z and u_{ref} the mean velocity at reference height.

The boundary layer shape exponent α varies according to the terrain. Wind speed increases with height, while turbulence is greatest near the ground. Several boundary layer profiles are shown in Figure 16.2.
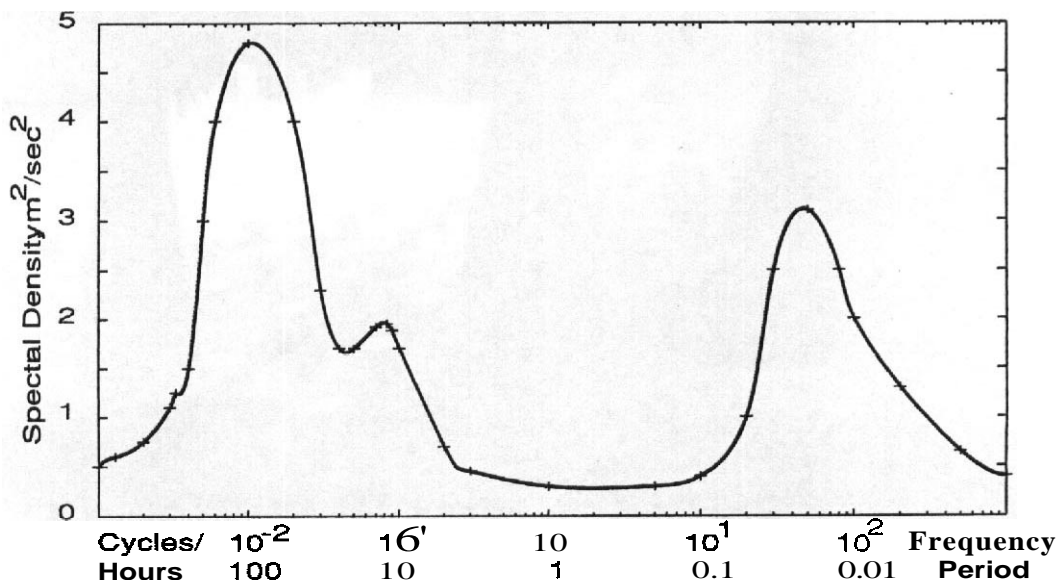
FIGURE 16.1   Approximate spectrum of wind speed near the ground.
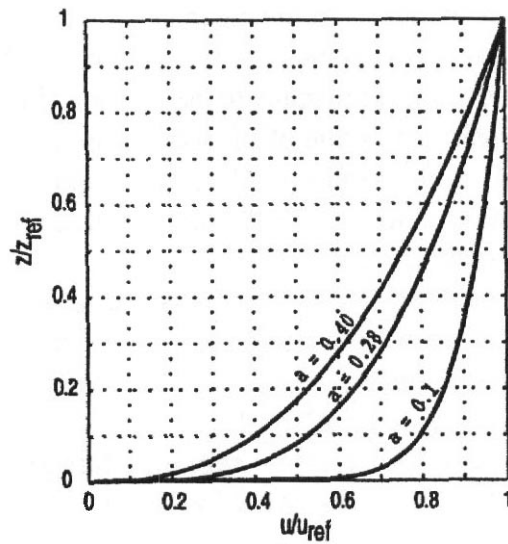
FIGURE 16.2 **Boundary layer shapes and exponents.**

The dynamic pressure used for reducing the forces and moments to coefficient form may be taken as an average value over the model, the value noted at the middle of the model, or free stream q. It must, in any case, be clearly and unequivo-cally defined or the data are useless. Figure 16.3 shows a set of strakes and floor roughness needed to produce atmosphericlike boundary layers.
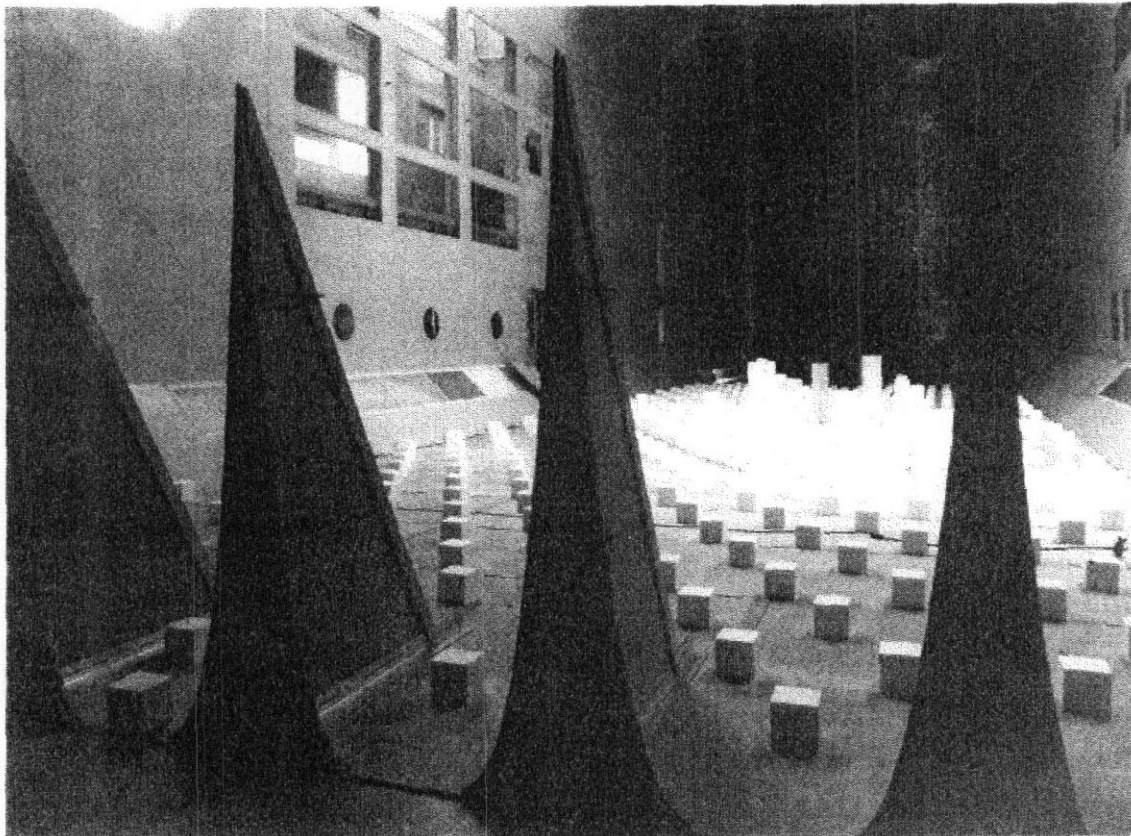
FIGURE 16.3 Closeup of high-drag strakes needed to produce atmosphericlike boundary layer flows. (Courtesy of Institute for Aerospace Research, NRC)

Figure 16.4 and 16.5 show a plan view and a photograph of wind tunnels used in wind engineering studies. These tunnels have the characteristically long test sections that allow easier manipulation of the properties of the incoming profiles and turbulence features.

Geometric Scale

Geometric scale is influenced by the wind modeling as well as the overall size of the wind tunnel. It is desirable to obtain equality of the ratios of building size to roughness length of terrain, boundary layer thickness, and integral scale of the longitudinal component of turbulence. The integral scale of turbulence is the most difficult to manipulate.

Blockage of the tunnel cross section is generally held below 10% and is preferably held to about 5%. Typical scales used are in the range of 1 : 300 to 1 : 600 for large buildings and down to 1 : 100 or less for smaller structures for which surface layer simulation only is required. An example installation is shown in Figure 16.6.

Speed Scale **and** Reynolds Number

The wind tunnel simulation is almost always at very much smaller than full-scale Reynolds number. The simulations are useful representations of the full-scale flows for two reasons. First, the influence of high turbulence intensity is to reduce the Reynolds number dependence. Second, the typical shapes of buildings, bridges, and the like yield flows that are less dependent on Reynolds number than typical vehicle shapes. Reynolds number effects are strongest when the locations of transition and separation vary with Reynolds number. If there is no laminar flow due to high free-stream turbulence and the shapes are so sharp that all separation locations are geometrically determined, then there will be little dependence on Reynolds number. If rounded shapes are part of a structure, then some schemes such as roughening of the surface are sometimes used.

Given that Reynolds number is not a factor in choosing speed and that rigid models are in use, then speed can be chosen primarily for the best performance of
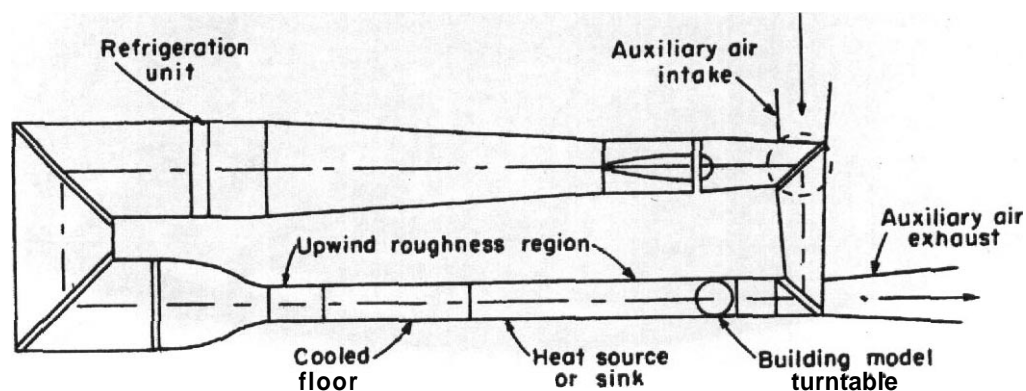
FIGURE 16.4   Layout of meteorological wind tunnel at the Wind Engineering Laboratory at Colorado State University.
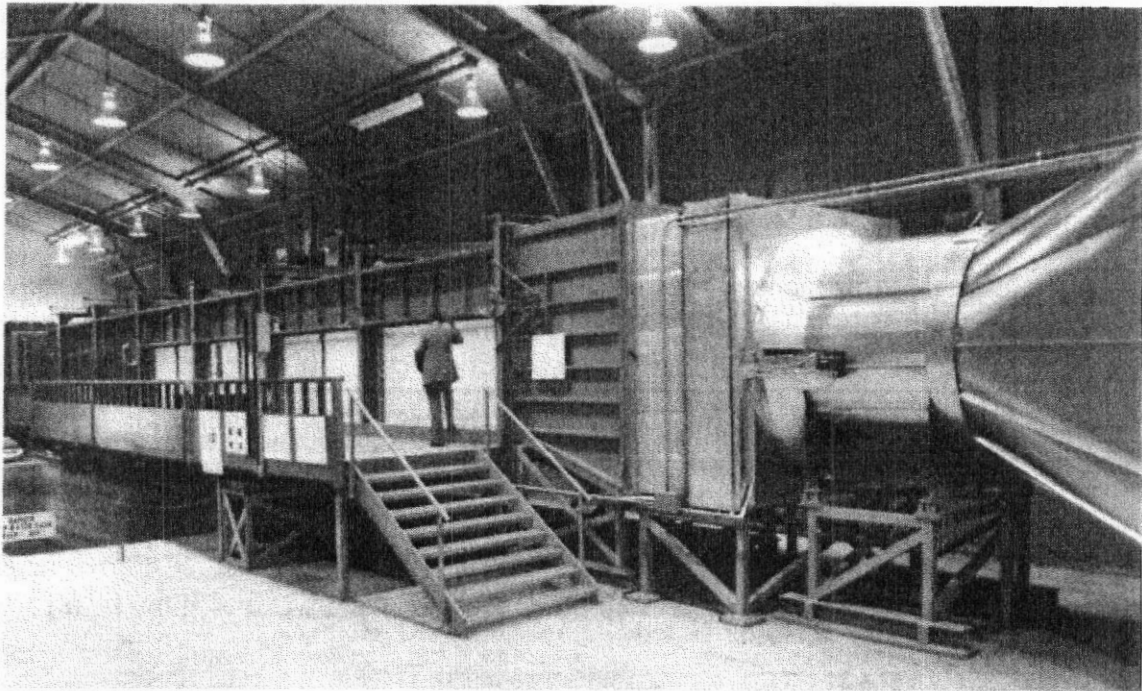
FIGURE 16.5   Atmospheric simulation tunnel at Verdian-Calspan Operations.
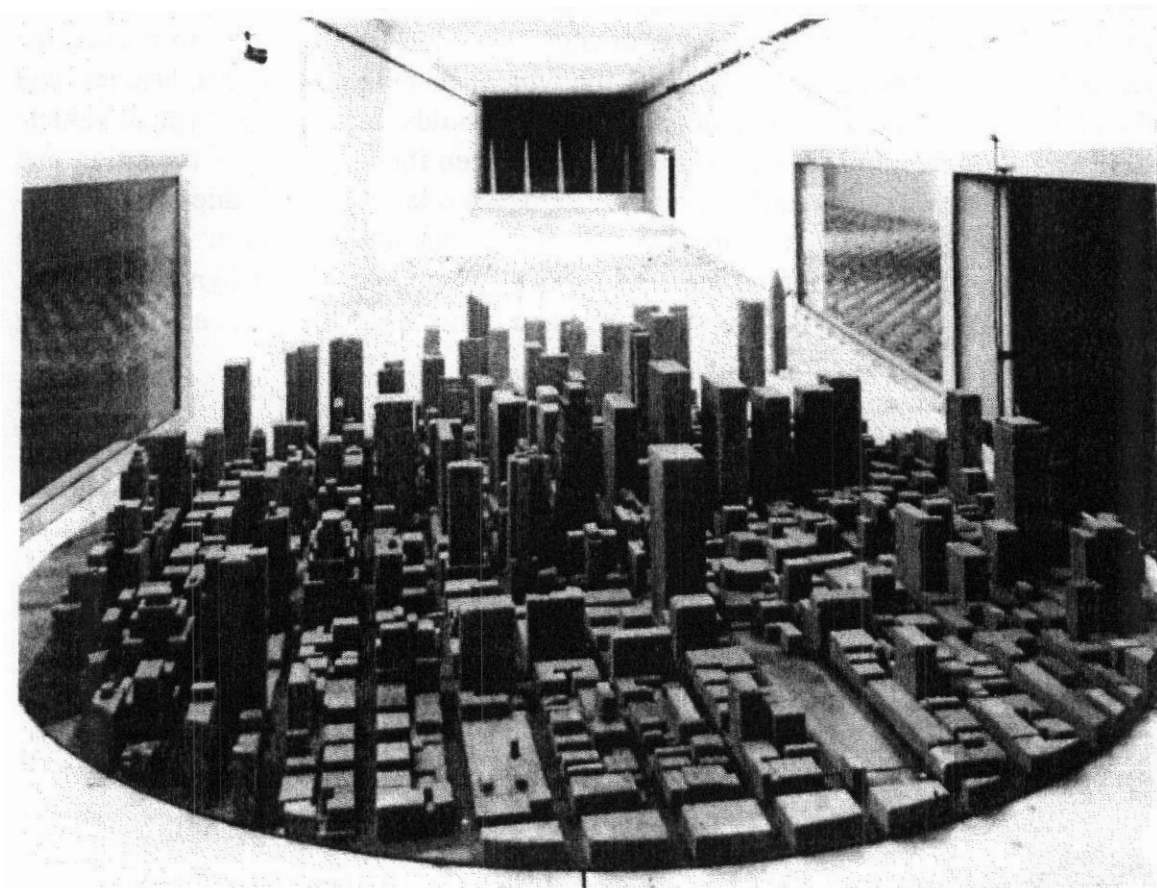
FIGURE 16.6   The **strakes,** floor roughness, and upstream buildings needed to simulate the proper conditions for studying the wind pressures and pedestrian-level velocities for the Equitable Center West, New York. Scale is 1 : 400. (Courtesy Cermak, Peterka Petersen, Inc.)

the instrumentation that is used. If the model used is elastic, then dynamic parameters influence the choice of flow speed. This will be discussed later.

Terrain Effects

Information on flow characteristics over a variety of terrain is available to use in setting up flows. However, particular local topography must always be considered to determine if it will produce effects that are unique and important. Topographic models in scales ranging from 1 : 1000 to 1 : 5000 can be used for evaluation of effects on the flow field. The information from such a simulation can then be used in setting up a flow model at a larger scale for building or other structure simulations. Figure 16.7 shows a tunnel crew preparing a terrain simulation.

Effects of Nearby Buildings and Topography

Significant neighboring buildings, structures, and topographic features should be modeled if only with block-type representation. This typically includes significant features out to 1000–2000 ft from the main structure of interest. Figure 16.8 shows a building with adjacent buildings simulated by blocks. The flow is influenced in this case by having the stagnation point much higher than would be the case in a more open environment.

FIGURE 16.7   Laying in contoured terrain. (Courtesy Verdian-Calspan Operations.)
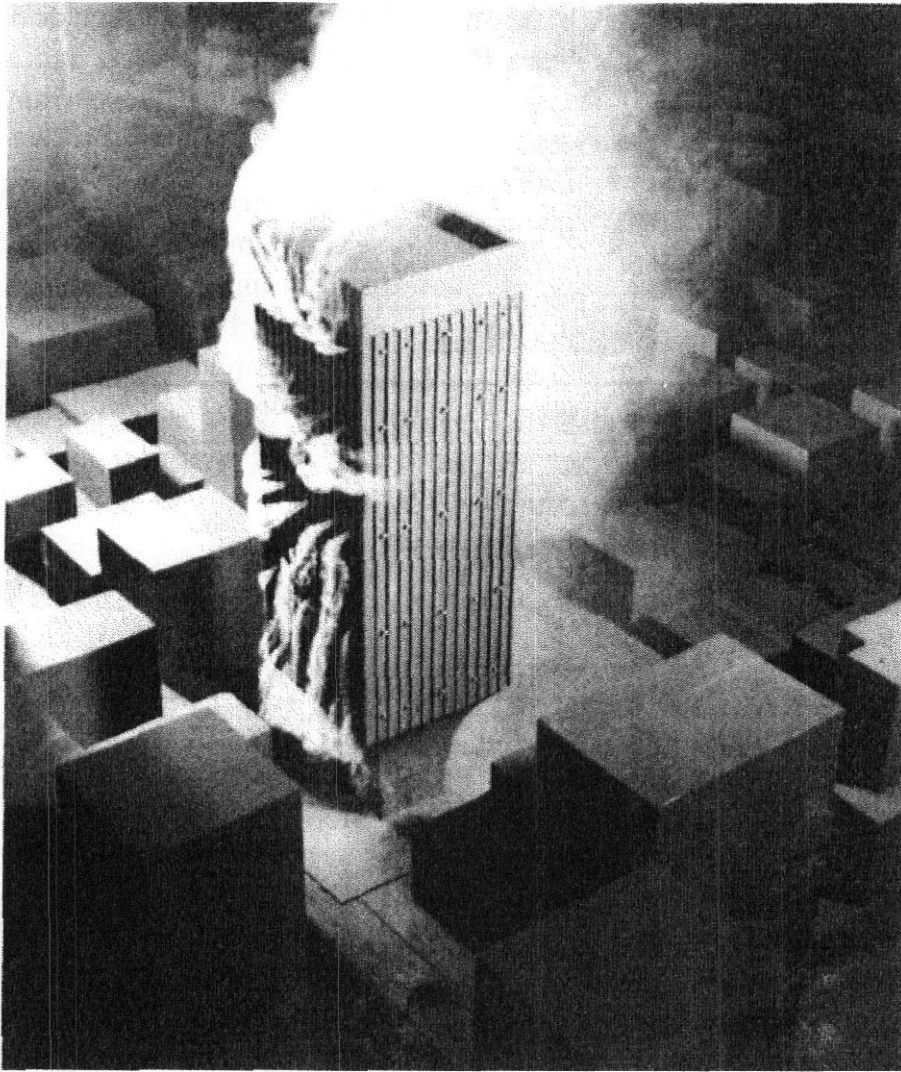
FIGURE 16.8   Smoke visualization showing the location of stagnation point in the presence of adjacent buildings.

16.2   LOCAL PRESSURES AND PANEL LOADS

Since the environment provided by the simulation of the turbulent atmospheric boundary layer is obviously unsteady, there is an immediate requirement to assess the degree to which unsteady treatment of fluid flow phenomena is required. Cases that involve the dynamics of larger sections of the structure, if it is elastic, may require unsteady treatment. For local pressures measured on a rigid model to predict local panel loads, a quasi-static treatment is valid. The structural responses of these small subsystems are faster than the energy containing frequencies of the atmospheric fluctuations. Appropriate data can be obtained by simulations at one wind speed.

The instrumentation, however, must have sufficiently high bandwidth capability to accurately track the time-varying pressures resulting from the incoming turbulence structures. Significant tubing lengths are difficult to avoid, so care must be taken in assessing the effects on the measurements.

The purposes of local pressure measurements usually include the prediction of wind loads on windows, wall elements, and so on. It is necessary to carry out preliminary assessments to anticipate the regions most likely to encounter peak effects. Even with cogent preassessment it is typical to require 400–800 pressure taps on a substantial building. To keep overall time requirements in acceptable ranges, the usual azimuthal program will be to collect data at 10° increments. Additional azimuthal points are usually needed for directions near those that exhibit the most critical behavior.

Panel wind loads are obtained by integration of the pressures over the areas of interest. Various means of implementing such integrations using pheumatic averaging have been applied. These have the advantage of requiring fewer transducer readings, but they must be carefully analyzed and validated for each implementation. Current instrumentation and computing equipment is quite capable of doing almost any required computation for these purposes in very little time.

Internal Pressures

The action of wind affects the internal pressures as well as the external pressure distribution of buildings and other partially sealed enclosures. The wind-induced load on any wall, window, or membrane subjected to the internal pressure on one side and the local external pressure on the other is of course the integral of the difference in these pressures. The external pressure distributions are obtained from the direct simulation and measurement as discussed above. The correct internal pressure depends on a number of parameters that describe the restrictions on flow between the exterior and interior of the structure and the flow within the structure.

Internal pressure caused by action of the wind depends on the external pressure distribution along with the distribution of porosity of the envelope of the structure and on the characteristics of internal flow passages. In a few cases, the internal pressures may be influenced by dynamic properties of the envelope materials and the internal flow volumes. Two obvious limiting cases can be identified: the unlikely, but possible, event that the envelope is impermeable in the one case at the stagnation point, or point of highest external pressure, or in the second case at the point of minimum external pressure. These two conditions define the largest interior-to-exterior loads and exterior-to-interior loads, respectively, that could exist. Using these for design specifications is conservative, but considerable information on interior details and their effects on flow resistances is needed to develop detailed models that could be used for developing design specifications that are less conservative.

16.3   LOADS ON COMPLETE STRUCTURES

Loads on complete structures that are effectively rigid can in principle be obtained by integrating surface pressures. This is effective for obtaining upper and lower limits, but accurate time-varying total loads are a challenge to obtain by surface

pressure integrations. Unlike integrating over relatively small panels, integrating over an entire structure while maintaining reasonable time accuracy requires very extensive, effectively simultaneous sampling of pressures. It can be done in principle, but often it may be preferable to construct a rigid model mounted on a very stiff and sensitive balance. This can be done, of course, for either a complete structure or a part of the structure on which total, perhaps time-varying, loads are needed.

A full-scale structure for which such a measurement will be of interest will have some potential resonant response. The model structure and wind speed in the simulation must be chosen to have a model-scale resonant frequency that is high enough so that the measured characteristics are not affected by any resonant behavior of the model. The model-scale frequency f_m, which corresponds to the full-scale frequency f_{fs}, is given by

$$f_m = f_{fs} \frac{L_{fs} V_m}{L_m V_{fs}} \tag{16.2}$$

Here L_{fs}/L_m is the full-to-model-size ratio, usually quite large, and V_m/V_{fs} is the ratio of wind speed set in the wind tunnel to the full-scale wind speed of interest. This ratio is typically of order 1. This indicates that the model resonant frequency must be quite high, which leads to a requirement for light, rigid models mounted on piezoelectric-type balance elements.

Concepts from structural dynamics that provide definitions for structural modes and generalized forces are used with the techniques of measurement mentioned above to predict full-scale motions.

16.4   STRUCTURES EXHIBITING ELASTIC MOTION

Some structures undergo dynamic deformations of sufficient magnitude so that the motion itself modifies the aerodynamic forces. They tend to be slender and relatively flexible. The simulations for these types of structures are termed aeroelastic simulations. We have not treated such cases for vehicles but will do so in Chapter 18.

Aeroelastic models are governed by a combination of the equations of motion for fluid dynamics and the equations of motion for elastic structures. A derivation similar to that in Chapter 1 wherein the Navier–Stokes equations were nondimensionalized can be carried out to obtain the dimensionless parameters that govern dynamic similarity. An excellent presentation is given by Bisplinghoff, Ashley, and Halfman.[4]

We will give an outline for a structure that can be modeled as a slender beam. Figure 16.9 is a representation of a cantilever-beam-like structure subjected to a transverse load from a wind profile in one direction. The equation of motion for a slender beam is given by the equation

$$[EI(y)w''(y,\,t)]'' + m(y)\ddot{w}(y,\,t) = \tfrac{1}{2}\rho V^2(y,\,t)Ac(y)C_d(y) \tag{16.3}$$
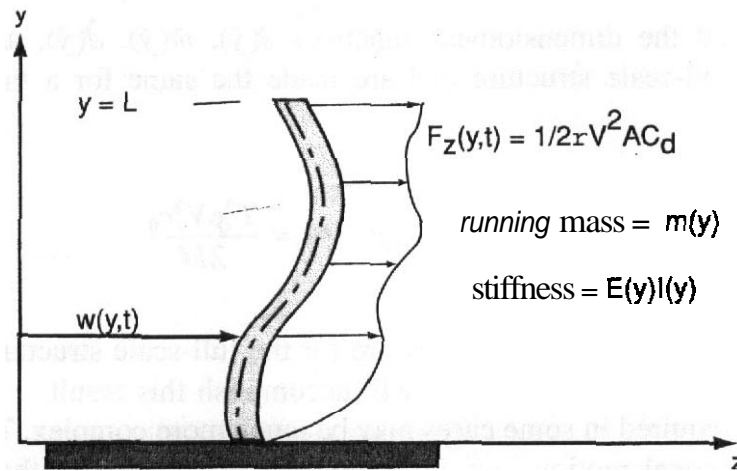
FIGURE 16.9   Cantilever beam subjected to dynamic transverse load.

To nondimensionalize this equation, the following relations are introduced:

$$y = L\hat{y} \qquad t = T_1\hat{t} \qquad m(y) = \frac{M}{L}\hat{m}(\hat{y}) \tag{16.4}$$

where L is the beam length, M is the total mass, and T_1 is an appropriate time scale. It may be the period of the first normal mode or it might be an aerodynamic time interval, *L/V:*

$$w(y, t) = L\hat{w}(\hat{y}, \hat{t}) \qquad EI(y) = EI_0\hat{s}(\hat{y}) \tag{16.5}$$

where EI_0 is the value at $y = 0$ and $\hat{s}(\hat{y})$ is the dimensionless function describing the stiffness:

$$V(y, t) = V_r\hat{v}(\hat{y}, \hat{t}) \qquad c(y)C_d(y) = c_0\hat{d}(\hat{y}) \tag{16.6}$$

where V_r is the reference speed, perhaps at $y = L$, c_0 is **a** representative length dimension of the cross section at the base, and the functions give the shapes of the variations that must be consistent. This last relation implies an assumption of Reynolds number independence. The equation of motion now appears in the form of Equation (16.8):

$$\frac{EI_0}{L^3}[\hat{s}(\hat{y})\hat{w}''(\hat{y}, \hat{t})]'' + \frac{M}{T_1^2}\hat{m}(\hat{y})\ddot{w}(\hat{y}, \hat{t}) = \frac{1}{2}\rho V_r^2 c_0\hat{d}(\hat{y})\hat{v}^2(\hat{y}, \hat{t}) \tag{16.7}$$

or

$$\frac{T_1^2EI_0}{M L^3}[\hat{s}(\hat{y})\hat{w}''(\hat{y}, \hat{t})]'' + \hat{m}(\hat{y})\ddot{w}(\hat{y}, \hat{t}) = \frac{1}{2}\frac{T_1^2\rho V_r^2 c_0}{M}\hat{d}(\hat{y})\hat{v}^2(\hat{y}, \hat{t}) \tag{16.8}$$

Supposing that the dimensionless functions $\hat{s}(\hat{y})$, $\hat{m}(\hat{y})$, $\hat{d}(\hat{y})$, and $\hat{v}(\hat{y}, \hat{t})$ are known for the full-scale structure and are made the same for a model, then the two coefficients

$$C_1 = \frac{T_1^2 EI_0}{M\,L^3} \quad \text{and} \quad C_2 = \frac{T_1^2 \rho V_r^2 c_0}{2M}$$

must be the same for the model as they are for the full-scale structure. It turns out that there may be several choices that will accomplish this result.

The analysis required in some cases may be much more complex. Two directions of sway and torsional motion may be important, in which case the equations of motion are more complex than those for the unidirectional motion for a slender beam as given above.

In some limited number of cases, a model that is geometrically scaled internally and externally can provide a dynamically similar representation of the full scale insofar as structural dynamics is concerned. The Reynolds number, however, will not be near the full-scale value, so appeal is necessary to the same range of arguments that have been made previously that indicate much smaller Reynolds numbers are satisfactory for a majority of cases. These models are referred to as "replica" models. Such models are possible for large-scale ratios only if the full-scale structure is shell-like, having its elastic stiffness obtained from mass concentrated near the surfaces.

Most aeroelastic models are "equivalent" models that have appropriate distributions of mass and stiffness to reproduce the structural modal properties of the full-scale structure but are very different in structural detail. A segment of a structure may be modeled in a two-dimensional fashion for some highly slender shapes such
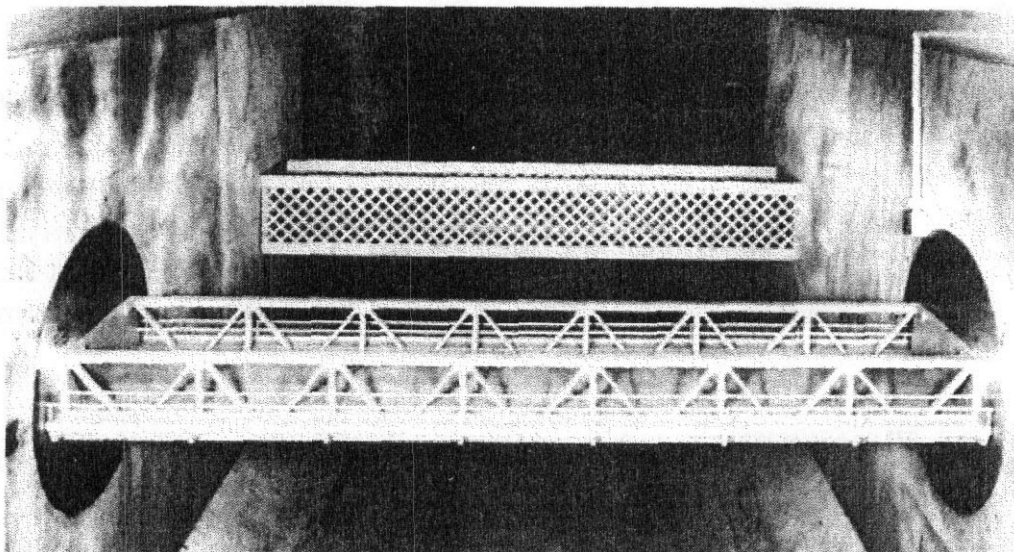
FIGURE 16.10 Wind tunnel model installation for studying buffeting. The model in the foreground is in the wake of the sectional model of a railway bridge upstream. (Courtesy National Physical Laboratory.)
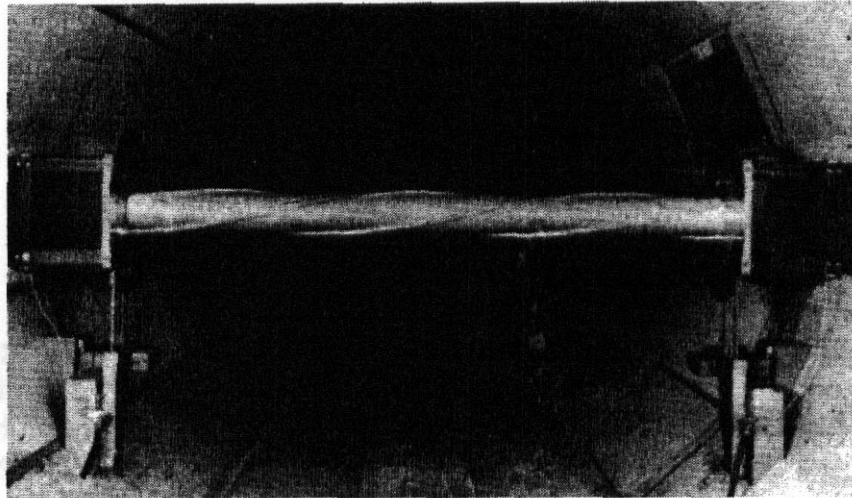
FIGURE 16.11   A sectional model of a circular cylinder with so-called three start helical strakes. (Courtesy National Physical Laboratory.)

as bridge decks or tall towers. The sections are then mounted elastically in the wind tunnel in a manner that represents the constraints of the adjacent structure.

Some structures that often require aeroelastic modeling are long-span bridges, flexible-roof systems, tall buildings, cooling towers, transmission towers and cables, masts, and chimneys.

Figures 16.10 and 16.11 show example tunnel installations of sectional models.

REFERENCES AND NOTES

1. http://www.danmar.dk/icwe99/.

2. Wind Tunnel Modeling for Civil Engineering, *Proceedings of the International Workshop on Wind Tunnel Modeling Criteria and Techniques in Civil Engineering Applications,* Simio, E., Ed., National Institute for Standards and Technology, Gaithersburg, MD, 1982.

3. Lumley, J. L., and Panofsky, H. A., *The Structure of Atmospheric Turbulence,* Interscience, New York, 1964.

4. Bisplinghoff, R., Ashley, H., and Halfman, R., "Aeroelasticity," in *Aeroelastic Model Theory,* Addison-Wesley, Reading, MA, 1955, Chapter 11.

17 Small Wind Tunnels

In order to avoid the impression that useful wind tunnels must have a large jet and a speed of 200 mph or more, it seems pertinent to discuss some uses of smaller tunnels. A 30-in. tunnel was used by Van Schliestett[1] in the study of boundary correction factors, and a still smaller tunnel was used by Spaulding and Memam[2] in their outstanding calibrations of pitot-static tubes. Other examples could be given of successful programs carried out in small tunnels.

The fundamental advantage of a small wind tunnel is the economics of operation. Small tunnels cost less to build and less to run.

A further advantage of a small tunnel is that smaller models, down to a point, require less time to build, can be constructed in simpler shops, and are therefore less expensive. Small size may be a disadvantage, it is true, but those who have built models with overall length or width of 6 or more feet (2 m) are well aware of the time and cost of such models.

The key to successful experiments made in a small tunnel is to have a clear understanding of the likely role of Reynolds number on the objects of the experiments. Although it has been said that there are cases in which Reynolds number has no effect, this is not exactly true. It is a matter of whether the relevant effect of Reynolds number is in fact obtainable in a small tunnel.

Small wind tunnels are routinely used for instruction in methods of experimentation. This is done very well even if the data from the experiments are not useful for prediction of behavior of similarly shaped devices at much larger Reynolds number, There are many objects that are sufficiently small so that the aerodynamic properties are directly measurable at the appropriate Reynolds numbers in small wind tunnels. Examples are various instrumentation devices, sports objects that are hand thrown, and small- to moderate-size model airplanes.

We have given a discussion of scale effects in Chapter 8, which should be consulted in conjunction with the material here.

17.1 TESTS LEAST AFFECTED BY REYNOLDS NUMBER

A small tunnel can be very useful in the study of flow patterns and how those patterns are affected by parametric variations in some geometric parameters. These studies can be made with, for example, smoke, tufts or china clay, lamp black, and fluorescent oil, as discussed in Chapter 5, although great care should be taken with regard to the possibility that any attachment to the surfaces may create a significant perturbation to the flow. Care must be exercised in recording the details of the

resulting patterns whether it be done by artistic sketching, by photographic, or by cinematographic means. Studies of this type can give insight into separation on wings, fuselages, near intersections, sails, or other shapes such as automobiles.

Pressure distribution measurements on airfoils can be instructive even at relatively low Reynolds numbers. For a given airfoil shape the distribution does not change drastically with Reynolds number so long as the angle of attack is well below stall. The induced drag increment due to planform selection is well represented at low Reynolds numbers. In this case the drag due to lift must be separated from the parasite drag.

The aforementioned pitot-static calibration is an example of an instrument calibration that is a perfect candidate for a small tunnel.

Many experiments concerning wind tunnel wall corrections are suitable for the small tunnel. These tend to be little affected by Reynolds number.

The progress or sequence of the stall over a wing may be unchanged by Reynolds number, although the entire stall is unusually delayed by higher Reynolds numbers.

Key indicators of Reynolds number effects are the locations of transition of the boundary layers from laminar to turbulent and the behavior of lines of separation as model attitude is changed. If both of these are fixed by a natural aspect of the shape or by specific manipulation, then the flow is unlikely to change significantly with Reynolds number.

So-called qualitative tests are candidates for small wind tunnels. Qualitative tests are expected to lead either to an indication of feasibility or an indication of nonfeasibility, which in turn will imply either more testing or abandonment of the project.

17.2   THE SMALL WIND TUNNEL FOR INSTRUCTION

A small tunnel is invaluable for instructional purposes. Almost no type of experiment is performed in a large tunnel that cannot be duplicated in a small tunnel, the possible exception being on models with turbine thrust simulators. For instructional purposes plastic model kits can often be reinforced and used as a low-cost way of obtaining the rather complex geometry of a complete vehicle.

Many schools have a small wind tunnel, along the lines of that shown in Figure 17.1. The jet size is from 12 to 30 in. square and the dimension are such that a space 14 X 30 ft is sufficient for the tunnel and motor. Ten to 25 hp will provide 100–150 mph in the test section.

Walls for the test section may be made so that they may be wholly or partially removed, thus making it possible to perform tests with an open or closed jet and to study asymmetrical boundaries. Open test sections cannot be used for nonreturn tunnels without a plenum around the test section.

Many of these smaller tunnels are three-component balances rather than a six-component balances. This allows the measurement of the longitudinal components without the complexity associated with full six-component measurements. The neces-
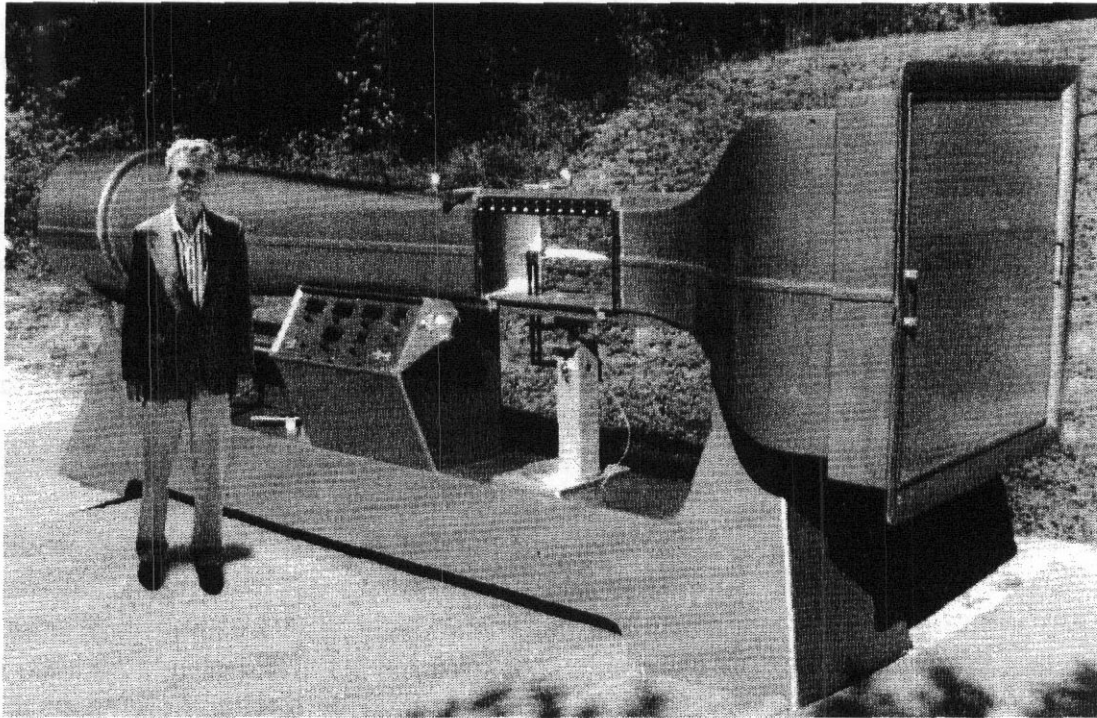
FIGURE 17.1 The late Professor Wiley Sherwood and an instructional wind tunnel of his design. (More than 450 wind tunnels were constructed under his direction.) (Photograph Courtesy of Aerolab, Inc., Laurel, MD.)

sity for completing an experiment in the typical laboratory period of 3–4 hr precludes as complete a test as might be desired.

A significant number of high schools have developed special science programs that include some introduction to aerodynamics. In a small number of cases a small wind tunnel has been acquired.

We have provided synopses of a selection of experiments suitable for instructional purposes. Some of these, as indicated, provide an opportunity to introduce the student to some of the more sophisticated instrumentation that is frequently used. Most of these can be completed in about 3 hr provided the participants have prepared themselves by studying appropriate material prior to arriving at the laboratory. The following descriptions assume that a closed test section will be used. Some modifications will be required if a blower tunnel or an open jet is used.

Experiment 1: Tunnel Calibration and Flow Quality

Objectives

a. Calibrate the test section speed against the nozzle pressure drop.
b. 'Evaluate the uniformity of the time mean flow in the test section.
c. Determine the turbulence factor in the center of the test section.

Tunnel Condition

· Empty test section.

Apparatus

Pitot-static tube, yawhead, turbulence sphere, two micromanometers, meter stick, and traverse device to position flow probes throughout test section. (We give the simplest types of apparatus. Electronic systems can always be substituted for the more basic devices.)

Measurements

a. Place pitot-static tube at the center of the test section. Attach one microma-nometer for measuring nozzle pressure drop, Ah, and the other to measure the total minus static from the pitot-static tube, q. Vary the tunnel speed control and record the pressures. Plot q versus Ah and determine the slope of the best straight-line fit. This is the tunnel calibration constant.

b1. Measure the dynamic pressure at 11 equally spaced points across the jet at the mid height. Repeat this at 11 equally spaced heights if time permits. Plot variation from the centerline value in percent. Prepare a contour plot if area data are obtained.

b2. Repeat b1 with the q measurement replaced by the flow angle measurement.

c. Put the turbulence sphere at the test section center. Determine the turbulence factor by the method described in Chapter 6.

Experiment 2: Balance Alignment and Aspect Ratio

Objectives

a. Obtain lift, drag, and pitch moment measurements for wings at two aspect ratios.

b. Find alignment correction.

c. Apply boundary corrections and obtain corrected lift, drag, and pitch moment coefficients.

Tunnel Condition

Balance in.

Apparatus

Two wings with the same airfoil section profiles and chord but different aspect ratios: 4 and 6 are good choices.

Measurements

a. Install wing of $AR = 6$. Read L, D, and M at $2°$ increments from below zero lift to past the stall. Angles should be set by a method that provides setting with precision of at least $0.1°$.

b. Invert model and repeat.

c. Repeat both steps above for wing of $AR = 4$.

d. Plot all data uncorrected. Make alignment and boundary corrections and plot corrected results. (Final data here include tare and interference effects, but with models of about 3-in. chord the evaluation of these effects is extremely difficult.) Note on plots α_{ZL}, $dC_L/d\alpha$ $C_{L,max}$, $C_{D0,min}$, C_{m0}, and ac.

Experiment 3: Tailsetting and Downwash

Objectives

a. Find downwash at tail as a function of angle of attack.

b. Find lift, drag, and pitch moment as functions of angle of attack and tail incidence.

c. Find tail incidence for pitch trim at $C_L = 0.2$ and the corresponding downwash and angle of attack at the tail.

Tunnel Condition

Balance in.

Apparatus

Airplane model with horizontal tail having variable incidence.

Measurements

a. Measure lift, drag, and pitch moment for angles of attack from zero lift to beyond stall with tail off.

b. Repeat with tail on and elevator at zero setting for at least three tail incidences between $\pm 8°$.

c. Plot angle of attack versus moment coefficient and downwash at the tail versus angle of attack. Determine tail incidence to provide zero pitch moment when lift coefficient is 0.2. Determine the angle of attack of the tail in this condition. Note that a moment reference corresponding to a representative center-of-mass location must be chosen. This is not generally the same as the resolving center of the balance, so the necessary moment transfers must be compared.

Experiment 4: Static Stability and Control

Objectives

a. Determine the allowable center-of-mass range that corresponds to positive static stability and possible trim with given elevators.

Tunnel Condition

- Balance in.

Apparatus

- Model with removable tail and movable elevators.

Measurements

a. Measure lift, drag, and pitch moment for angles of attack from zero lift to beyond stall with the tail off.
b. Repeat with the tail on for elevator settings of at least 0, −5, −10 and −15°.
c. Plot C_m against C_L for each elevator setting and C_m against δ_e. Find dC_m/dC_L. Also plot C_L against a.

If a sting-type balance is available, this is a good experiment for which to use it. A separate experiment would be the calibration of the sting-type balance.

Experiment 5: Profile Drag by Momentum Theory

Objectives

a. Obtain airfoil drag by measuring wake momentum deficit.

Tunnel Condition

- Constant chord wing installed that extends the width of the tunnel.

Apparatus

- Twelve-inch chord airfoil, wake survey rake and multiple tube manometer, or pitot or pitot plus static that can traverse wake, scanivalve, or pressure transducer plus associated electronics can be used in place of the manometer. Back-lighted manometers can be photographed and have the advantage of showing students the shape of the wake plus ensure that the entire wake is obtained.

Measurements

a. Set tunnel speed in the range of 80–100% of maximum. Obtain total pressure from rake or traverse $0.7c$ behind airfoil trailing edge for angles of attack from $-3°$ to $6°$. Integrate the momentum deficit for each condition to obtain c_{d0}. Plot c_{d0} against a.

b. Set angle of attack at zero. Measure wake pressures for a range of tunnel speed, taking at least three speeds from the maximum down to a value determined by the capability of the measuring devices to resolve the pressure differences. Plot c_{d0} against Reynolds number.

Experiment 6: Pressure Distribution

Objectives

a. Obtain pressure distributions on a typical airfoil over a range of angles of attack.

b. Integrate pressure distributions to obtain lift and drag contributions from pressure.

Tunnel Condition

Closed jet, balance out.

Apparatus

- Pressure tapped wing. It would be very good if it is the same wing as used for experiment 5. Multiple-tube manometer or scanivalve-type pressure transducer and associated electronics.

Measurements

a. With tunnel set at desired dynamic pressure obtain pressures for several angles of attack from zero lift through and beyond stall. Plot c_n, c_c, and $c_{m,ac}$ versus a. If run in conjunction with experiment 5, plot c, versus c_d.

Experiment 7: Dynamic Stability

Objectives

a. Obtain short-period made characteristics for a particular configuration.

Tunnel Condition

Model on hinge or pivot allowing free oscillation. No balance required.

Apparatus

- A model that can be a wing or a missile body with fins or a complete configuration. The mounting must allow for free rotation about an axis that corresponds to a typical center-of-mass location. A method of recording the time history of the model pitch is required. It is good if the actual mass distribution of the model can be varied. An optical method of timing the oscillations is a good option.

Measurements

a. Measure the moment of inertia of the model about the axis of oscillation.
b. Set the axis location. At a series of speeds, say 40, 60, and 80 mph, disturb model and record the time history of the pitch. Extract the frequency of the oscillations and the damping of the motion treated as a second-order system. Plot period against velocity. Compute the stability derivatives $C_{m\alpha}$ and $C_{mq} + C_{m\dot{\alpha}}$ from the time histories and the moment of inertia.
c. Set the axis at a new location and repeat.

Experiment 8: The Boundary Layer

Objectives

a. To directly measure boundary layer at various stations on an airfoil and deduce the location of transition.

Tunnel Condition

- Constant chord extending the width of the tunnel. No balance required.

Apparatus

- Twelve- to 15-in. chord NACA 0012 wing (used because of large amount of data on this airfoil), boundary layer mouse plus manometer or scanivalve and associated electronics, or traversible hot-wire or thin-film gage or very small pitot.

Measurements

a. Place mouse and pitot at 5, 10, 15, 20, 25, 30, and 35% chord and record dynamic pressures at 0.03, 0.06, 0.09, 0.12 in. from surface.
b. Determine transition region by plotting velocity profiles and velocity at constant height. If time permits, it is good to repeat for a range of speeds, that is, Reynolds numbers. Flow visualization can be used to check transition point.

17.3 LOW-REYNOLDS-NUMBER TESTING

Small tunnels provide conditions corresponding to relatively low Reynolds numbers, and it is fitting to have a good understanding of flow at these values in order to avoid the pitfalls into which many engineers have fallen. Indeed, a remarkable correlation exists at any time between the current capabilities of wind tunnels and the type of airfoils designers select. At Reynolds numbers of about 50,000 a thin wing with 4–6% camber appears best and was used in early aircraft such as the Brequet and many World War I fighters. At Reynolds numbers around 1.5 $\times$ 10^6 the Clark Y performs quite well, as do other sections with perhaps 4% camber and 12% thickness. They in turn were used on the *Spirit of St. Louis* and many other airplanes of the period 1925–1935. At 4 $\times$ 106–8 $\times$ 106 the symmetrical sections of slightly higher thickness show up well, and we find those on many aircraft of 1935–1940. Later, of course, the tunnels with lower turbulence became available, and they in turn greatly influenced design from 1940 to 1950 until high subsonic effects began to crowd out other problems.

The point is to draw attention to the fact that most "modem" airfoils will yield embarrassingly poor results at low Reynolds numbers, and teachers, students, or others trying either NACA 0015 or 65 series wings at RN = 150,000 will find themselves with extremely wiggly lift curves and drag curves for symmetrical wings showing less drag at 5° angle of attack than at zero—an unexpected, if not "impossible," state of affairs.

Hysteresislike Effects

Mueller and co-workers [*][*] give results of extensive studies of flow over two-dimensional airfoils at Reynolds numbers as low as 40,000 based on chord. We show data for Reynolds numbers of 130,000 and 400,000 in Figures 17.2 and 17.3. At RN = 40,000 the lift curve for a NACA 66_3-018 from negative to positive stall is in three distinct pieces. Two parts are near the stall, and at a = $\pm 8°$, there is a linear region with very low slope. Mueller and Batill[3] show smoke photographs taken at a = 0° that indicate laminar separations on both the top and bottom of the airfoil at 65% chord with periodic vortex shedding. As shown in Figure 17.4, at a = +6° the flow attached to the lower surface but separates at 10–15% chord on the upper surface. At α = 8° there is a laminar separation bubble on the upper surface that acts similarly to a trip strip inducing transition with turbulent reattachment and a large increase in lift. The lift increase is limited, however, by a trailing-edge separation. This trailing-edge separation moves forward with a, causing the typical $c_{l,\max}$ shape of the lift curve. At RN = 40,000 drag was not measured due to the small forces.

At RN = 130,000 the airfoil shows a complete reversal of the lift curve slope at a = 0°, and the drag is lower at 6° than at 0D. The addition of a trip strip near the leading edge gave more normal curves for lift and drag. At a Reynolds number of 400,000 the lift curve and drag curve were typical of low-Reynolds-number performance. Lift and drag data for the same NACA 66,-108 airfoil are given by Mueller and Batill[3] for additional Reynolds numbers. Smoke-wire flow visualization
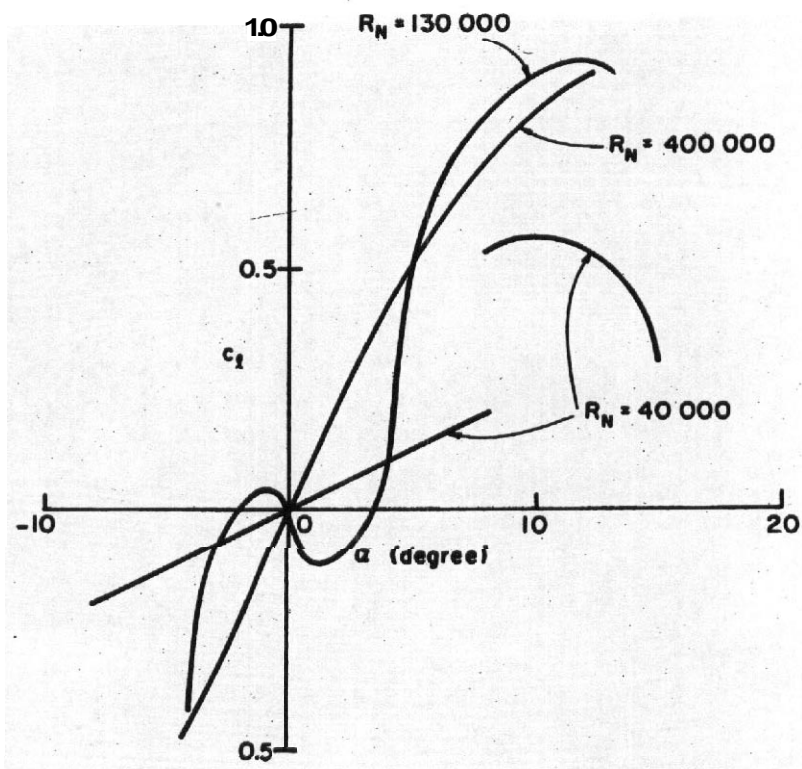
FIGURE 17.2 Lift curves for a smooth NACA 66₃-018 airfoil at three low Reynolds numbers. (Adapted from Mueller et al.[3] Copyright © 1982 AIAA. Reprinted with permission.)
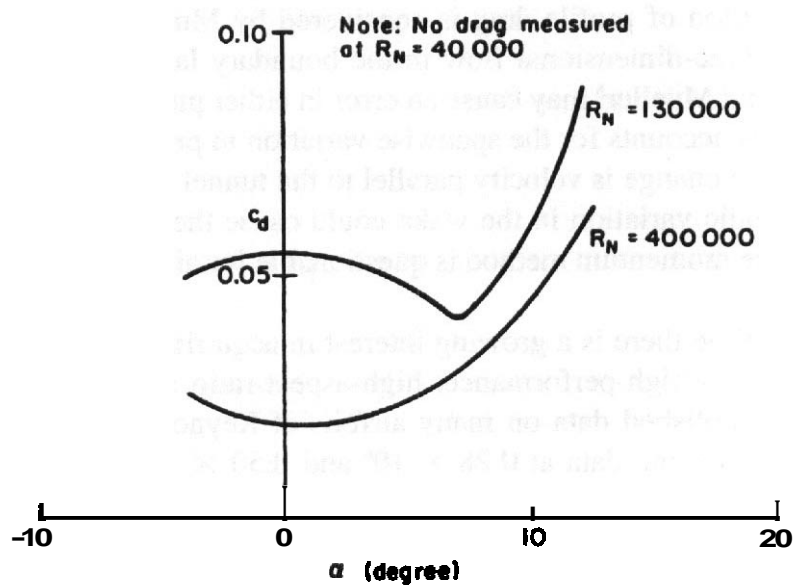
FIGURE 17.3 Drag curves for a smooth NACA 66₃-018 airfoil at two low Reynolds numbers. (Adapted from Mueller et al.[3] Copyright © 1982 AIAA. Reprinted with permission.)
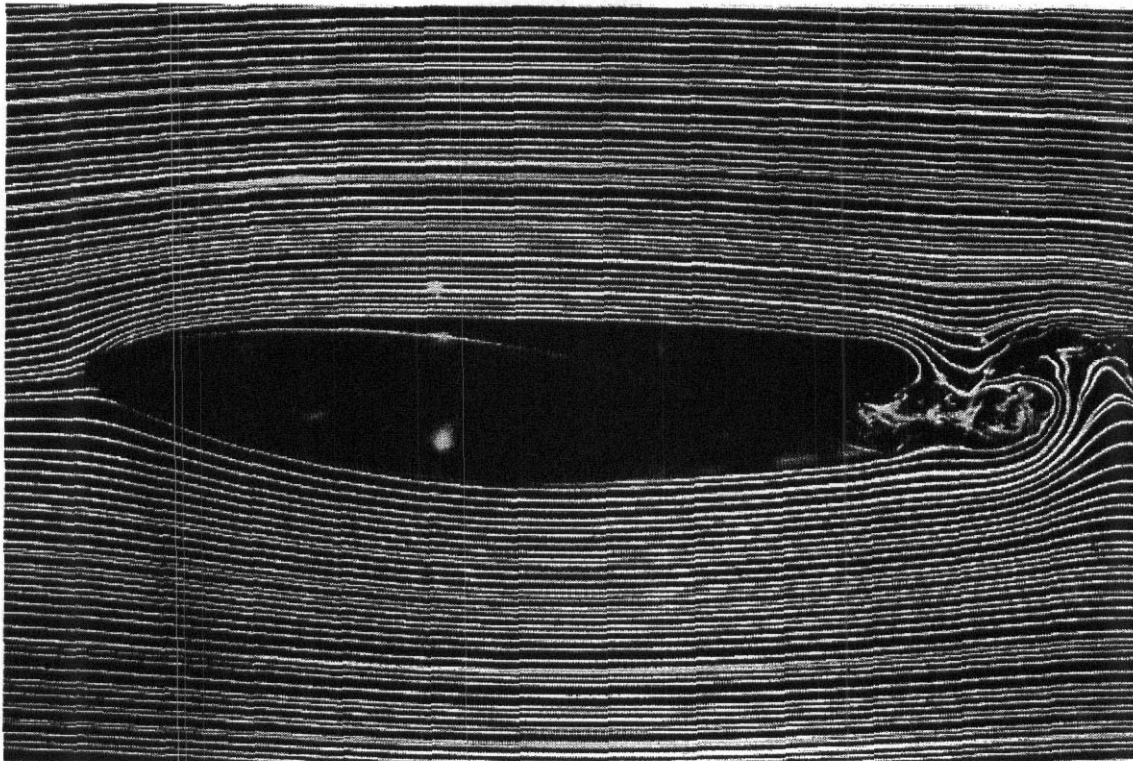
**FIGURE 17.4   Smoke-wire flow visualization for a smooth NACA 66,-018 airfoil at 6°
angle of attack, RN = 40,000. (Adapted from Mueller et al.[3] Copyright © 1982 AIAA.
Reprinted with permission.)**

at RN = 55,000 for the NACA 66,-018 airfoil shown by Batill and Mueller' gives
an insight into the surface flow at low Reynolds numbers. This work provides an
indication that it is wise to be cautious about assumptions regarding low-Reynolds-
number flows.

Spanwise variation of profile drag is considered by Mueller and Jansen? They
suggest that the three-dimensional flow in the boundary layer at RN = 55,000 as
shown by Batill and Mueller[5] may cause an error in either pitot or hot-wire measure-
ments and that this accounts for the spanwise variation in profile drag. The momen-
tum is based on the change is velocity parallel to the tunnel centerline, and the shed
vortices and periodic variation in the wake could cause the error, It has been long
considered that the momentum method is questionable for airfoils where separations
are present.

At the present time there is a growing interest in acquiring data at low Reynolds
numbers. For use on high-performance, high-aspect-ratio sailplanes, Althaus and
Wortmann[6] have published data on many airfoils at Reynolds numbers from 1 ×
10^6 to 3 × 10^6 with some data at 0.28 × 10^6 and 0.50 × 10^6. Other uses of low-
Reynolds-number airfoil data would possibly be general-aviation, remotely piloted
vehicles, fan blades, wind turbines, and model airplanes. The data discussed above
have been taken in Eiffel-type tunnels with very large contractions with many
screens, prior to the contraction, which leads to very low values of turbulence. The
tunnel has 12 antiturbulence screens followed by a 24 : 1 contraction. The turbulent

intensity is less than 0.1%. Research of this nature is a case where the power consumed by screens is acceptable as they provide the needed laminar flow.

Uncertainties in Measurements

Batill and Mueller[5] use the method of Kline and McClintock[7] to determine the uncertainties in the data. This method uses a careful specification of the uncertainties associated with primary experimental measurements such as pressure, temperature, and so on, and the accuracy of the instruments used.

The uncertainty of c_l is W_c and is a function of the uncertainty of the measurements. For a force coefficient measured by a balance,

$$\text{Force} = \mathbf{F} = \boldsymbol{BE} = c_f(\tfrac{1}{2}\rho_\infty V_\infty^2) S \tag{17.1}$$

where BE is the output voltage E times a calibration constant to put it into engineering units. The c_f is any aerodynamic coefficient, such as c_l, c_d, and so on,

$$c_l = \frac{BE}{q_\infty S} \tag{17.2}$$

and the force uncertainty is

$$W_{c_f} = \left[\left(\frac{\partial c_f}{\partial B} W_B \right)^2 + \left(\frac{\partial c_f}{\partial E} W_E \right)^2 + \left(\frac{\partial c_f}{\partial S} W_S \right)^2 + \left(\frac{\partial c_f}{\partial V_\infty} W_{V_\infty} \right)^2 + \left(\frac{\partial c_f}{\partial \rho_\infty} W_{\rho_\infty} \right)^2 \right]^{1/2} \tag{17.3}$$

This may be simplified by dividing c_f:

$$\frac{W_{c_f}}{c_f} = \left[\left(\frac{W_B}{B} \right)^2 + \left(\frac{W_E}{E} \right)^2 + \left(\frac{W_S}{S} \right)^2 + \left(\frac{\partial W_{V_\infty}}{V_\infty} \right)^2 + \left(\frac{W_{\rho_\infty}}{\rho_\infty} \right)^2 \right]^{1/2} \tag{17.4}$$

Now assuming that the tunnel test section is vented to the atmosphere, the equation of state yields

$$\rho_\infty = \frac{P_{\text{atm}}}{RT_{\text{atm}}} \tag{17.5}$$

Thus

$$\frac{W_{\rho_\infty}}{\rho_\infty} = \left[\left(\frac{W_{P_{\text{atm}}}}{P_{\text{atm}}} \right)^2 + \left(\frac{W_{T_{\text{atm}}}}{T_{\text{atm}}} \right)^2 \right]^{1/2} \tag{17.6}$$

Since $q_\infty = \frac{1}{2}\rho_\infty V_\infty^2$,

$$\frac{W_{V_\infty}}{V_\infty} = \left[\left(\frac{W_{T_{atm}}}{2T_{atm}}\right)^2 + \left(\frac{W_{q_\infty}}{q_\infty}\right)^2 + \left(\frac{W_{P_{atm}}}{P_{atm}}\right)^2\right]^{1/2} \tag{17.7}$$

and

$$V_\infty = \left(\frac{2q_\infty}{\rho_\infty}\right)^{1/2} = \sqrt{\frac{2q_\infty R T_{atm}}{P_{atm}}} = K\sqrt{\frac{q_\infty T_{atm}}{P_{atm}}} \tag{17.8}$$

As a good example consider the determination of the lift coefficient by integration of pressures along the chord:

$$c_l = \sum_{i=1}^{n}(C_{P_{l_i}} - C_{P_{u_i}})\left(\frac{\Delta x}{c}\right)_i \tag{17.9}$$

In this case the uncertainties are the result of the length along the chord increment and the pressures. As $W_{\Delta P} = W_q$ is some value in percent,

$$W_{C_P} = \left[\left(\frac{\partial C_P}{\partial \Delta P}W_{\Delta P}\right)^2 + \left(\frac{\partial C_P}{\partial q_\infty}W_{\Delta q_\infty}\right)^2\right]^{1/2} \tag{17.10}$$

where

$$\frac{\partial C_P}{\partial \Delta P} = \frac{1}{q_\infty} \quad \text{and} \quad \frac{\partial C_P}{\partial q_\infty} = \frac{1}{q_\infty^2} \tag{17.11}$$

The average uncertainty of the pressure coefficient is used to determine the uncertainty of the lift coefficient:

$$W_{c_l} = \left[\left(\frac{\partial c_l}{\partial C_{P_u}}\overline{W_{C_{P_u}}}\right)^2 + \left(\frac{\partial c_l}{\partial C_{P_l}}\overline{W_{C_{P_l}}}\right)^2 + \left(\frac{\partial c_l}{\partial \Delta x/c}W_{\Delta x/c}\right)^2\right]^{1/2} \tag{17.12}$$

This is a straightforward method applicable to cases where single samples of the measurement are taken, as is often the case in wind tunnel tests.

The above analysis for lift coefficient by the integration of pressures requires that $P, - P_\infty$ for the C_P and the tunnel q_∞ be measured simultaneously. The same is true for data with the force balance. The simultaneous measurement of tunnel q is

required to avoid the problem of time-dependent fluctuations in tunnel speed, which are very difficult to control at the low speeds required for very low Reynolds numbers. Almost all wind tunnels give difficulty in holding air speed precisely when run at low speeds owing to the inertia of both the drive system and the air.

To summarize the problems with acquiring accurate data at very low Reynolds numbers below 100,000–150,000: First, the tunnel must have very low turbulence to promote laminar boundary layers on the model. This is necessary since the data are dependent on the behavior of the laminar boundary. The low turbulence requires large contraction ratios and damping screens before the contraction.

Second, since the test speeds are low, there is almost always present time-dependent excursions in tunnel velocity about the average, which requires the data and tunnel q to be taken simultaneously. This generally requires a computer-controlled electronic data system.

Third is the problem of balance zero shifts or drift.

The use of electronic data systems usually requires amplification with response down to DC. The low-signal level due to small forces and pressures requires high gains. Thus the amplification must be of high quality (cost). The drift with time must be closely monitored. The signal conditioners or power supplies must be of the low noise type. And finally, owing to low transducer output voltages, care must be taken with shielding to avoid deficient signal-to-noise ratio. One-millivolt noise on a 1000-mV signal is quite different than a 1-mV noise on a 3-mV signal.

When balances are used, they will have a relatively low spring rate or stiffness to generate an adequate signal from the low applied loads. To measure lift and drag, Mueller and Batill[3] used a strain gage balance with two flexures: one for small loads and a second, stiffer, flexure that was engaged for larger loads. As the material frequency is proportional to the square root of the spring stiffness over mass, the natural frequency of the balance plus model will be very low. This may require the judicious use of electronic filtering of the balance output signal or a low-frequency cutoff. There also is the possibility of the model–balance having a large enough amplitude vibration that can lead to either a broken flexure in the balance or an inability to prevent the balance–model fouling with adjacent parts that have very small clearances.

For other exploratory tests of aircraft models at low Reynolds numbers (below 150,000 based on chord), it may be possible to apply a grit strip or other type of trip strip to fix transition as on large models and avoid the laminar bubble at the leading edge of the lifting surface that was encountered by Mueller and Jansen.[4] The model may have a slightly higher drag and lower minimum lift. However, these results should be acceptable when used for trends and increments. Similar acceptable results should be obtained on automobiles and trucks as long as the desired results are not sensitive to the Reynolds number.

Also, small tunnels can, of course, be used for any test of exploratory nature when the model is not sensitive to laminar and turbulent boundary layers and the transition. It may well be that in many cases the problem of building the model,

especially in the case of structures such as transmission towers, cranes, and so on, will be the limiting factor.

REFERENCES AND NOTES

1. Van Schliestett, B., "Experimental Verification of Theordorsen's Theoretical Jet Boundary Correction Factors," **NACA** TN 506, 1934.
2. Spaulding, E. R., and Merriam, K. G., "Comparative Tests of Pitot-Static Tubes," **NACA** TN 546, 1935.
3. Mueller, T. J., and Batill, S. M., "Experimental Studies of Separation on a Two Dimensional Airfoil at Low Reynolds Numbers," AIAA J., 20, 457–463, 1982.
4. Mueller, T. J., and Jansen, B. J., Jr., "Aerodynamic Measurements at Low Reynolds Numbers," Paper 82-0598, presented at the Twelfth AIAA Aerodynamic Testing Conference, Williamsburg, VA, 1982.
5. Batill, S. M., and Mueller, T. J., "Visualization of Transition in the Flow over an Airfoil Using the Smoke-Wire Technique," AIAA J., 19, 340–345, 1981.
6. Althaus, D., and Wortmann, F. X., *Stuttgarter Profilkatalog I*, F. Vieweg & Sohn, Braunschweig, West Germany, 1981.
7. Kline, S. J., and McClintock, F. A., "Describing Uncertainties in Single-Sample Experiments," *Mech.* Eng., 3–8, 1953.

18 Dynamic Tests

18.1 SPIN CHARACTERISTICS AND SPIN RECOVERY

The study of spin and spin recovery is covered in three broad areas: (1) entry into stall and loss of control, (2) poststall entry into a spin, and (3) spin and recovery.

A complete spin program will require models and tests in each of these areas. However, in many cases it may only be necessary to demonstrate that it is possible to consistently recover from a spin. Thus spin and recovery tests are often made first in a spin tunnel.

Chambers' gives an outline of a design procedure for predicting spins. This procedure requires several types of wind tunnel tests in addition to spin tunnel tests. These include static six-component full model tests at $C_{L,\max}$ and beyond at various side-slip angles accounting for Reynolds number effects at stall and poststall regions.

There are two types of dynamic tests made using balances. The first is a forced oscillation test with the model using an internal balance mounted on an oscillating sting, as described by Orlik-Ruckemann.[2] The results from this test yield combined derivatives that are used to analyze the airplane's motion in stall departure. The second dynamic test uses a rotary balance. The Langley Research Center spin tunnel's rotary balance allows the model to be tested through a $\pm 15°$ side slip and $8°–90°$ angle-of-attack range. Usually the balance moment center and the desired aircraft center of gravity coincide. The balance moment center is either on the spin axis or at a desired offset from the same axis. The model can be rotated either right or left up to 90 rpm. By use of the tunnel air speed and rotational speed steady spins can be simulated. Figure 18.1 shows a model installed in the Langley spin tunnel. Tares in the form of inertial forces and moments over the range of attitudes and rotational speeds at zero tunnel speed are taken and subtracted from the wind-on test data. Tares are taken by surrounding the model with a covered bird cage structure that encloses the model but does not touch it. This allows the air immediately surrounding the model to rotate with the model. The result of the rotary balance tests are used in inertial/aerodynamic computer programs like those reported by Barlow and Tischler[3,4] or Bihrle and Barnhart[5] to predict possible spin modes. Component buildup testing can be performed on the rotary balance to show the influence of the various components on spin characteristics as described by Bihrle and Bowman.[6] It also should be noted that the rotary balance when not rotating can be used for measurement of static data at high angles of attack. Some horizontal tunnels as well as vertical spin tunnels are equipped with rotary balances.

680
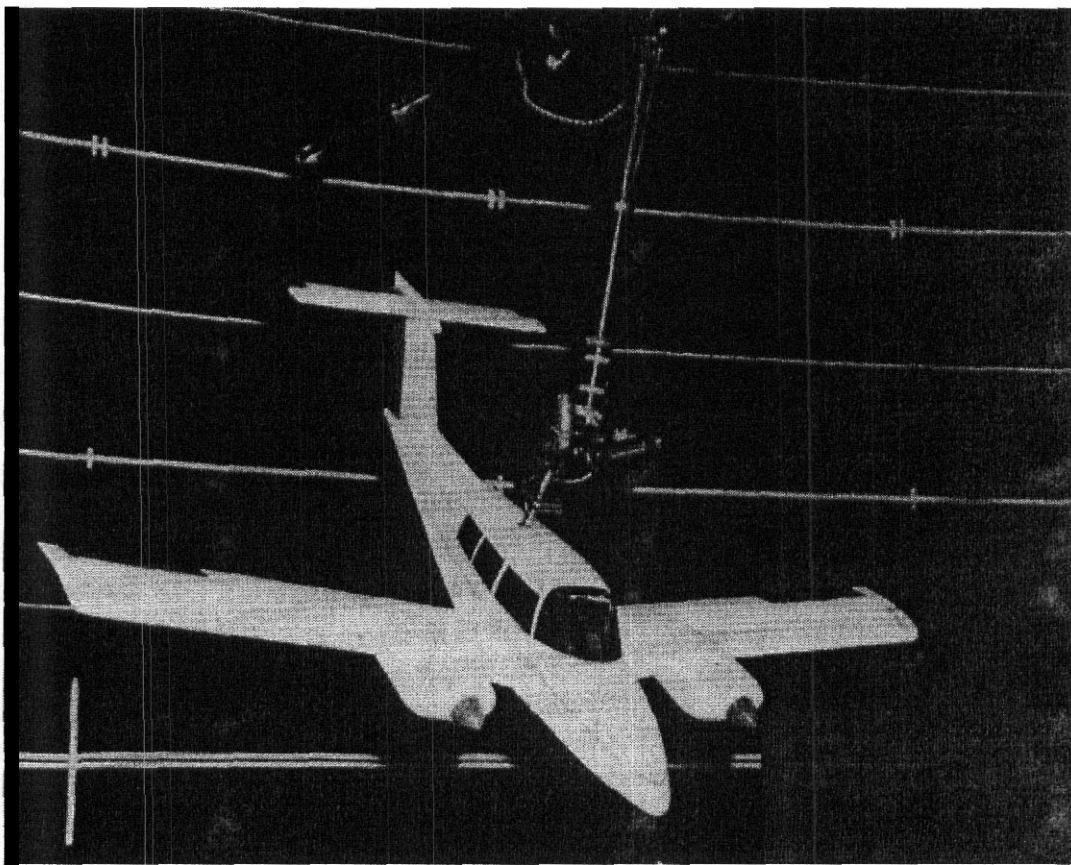
FIGURE 18.1 Beech Model 76 on rotary balance in NASA Langley 20-ft vertical spin tunnel. Model is 0.18 : 1 scale. (Photograph courtesy of Raytheon.)

The Langley 30 × 60 tunnel has been used with free-flight models for studies through stall and loss of control. This facility uses a computer to implement flight control laws and provide control inputs along with those of the human pilot. Due to model support cables, departure from stall into a full spin cannot be simulated in this facility.

NASA also uses free-flight models dropped from a helicopter to study spin entry characteristics. The results from these experiments help predict the airplane's susceptibility to spin entry and the dominant spin modes. Radio-controlled model airplanes are also used to investigate spin behavior as reported by Holcomb?

In addition to rotary balance measurements, spin and recovery characteristics are investigated in the spin tunnel using free-flying models. The dynamically scaled model is hand launched into the tunnel at various pitch attitudes with prerotation. The tunnel air speed is adjusted to balance the model's sink rate, thus holding the model level at the viewing window. The spin and recovery are recorded with a movie camera or video tape recorder. The angle of attack, bank angle, spin rate, and turns for recovery following a remotely initiated control input are extracted from the images. The tunnel speed yields the rate of descent. The recovery from the spin is initiated by remote control to set the model's aerodynamic controls to a predetermined position. The models are often built out of balsa wood or

thin fiberglass, because both weight and moments of inertia must be properly scaled.

Required scaling laws are discussed by Wolowicz, Bowman, and Gilbert.[8] The scale factors between the model and full scale, where M is the model, A is the full-scale aircraft, and N is the model scale (e.g., $\frac{1}{16}$ scale), are

$$\text{Length } L_M = L_A N \tag{18.1}$$

$$\text{Area } S_M = S_A N^2 \tag{18.2}$$

$$\text{Weight } W_M = W_A N^3 \left(\frac{M}{A}\right) \tag{18.3}$$

$$\text{Moment of inertia } I_M = I_A N^5 \left(\frac{\rho M}{\rho A}\right) \tag{18.4}$$

$$\text{Velocity } V_M = V_A \sqrt{N} \tag{18.5}$$

$$\text{Spin rate } \Omega_M = \frac{\Omega_A}{\sqrt{N}} \tag{18.6}$$

Figure 18.2 shows a model being hand launched into the Langley spin tunnel.
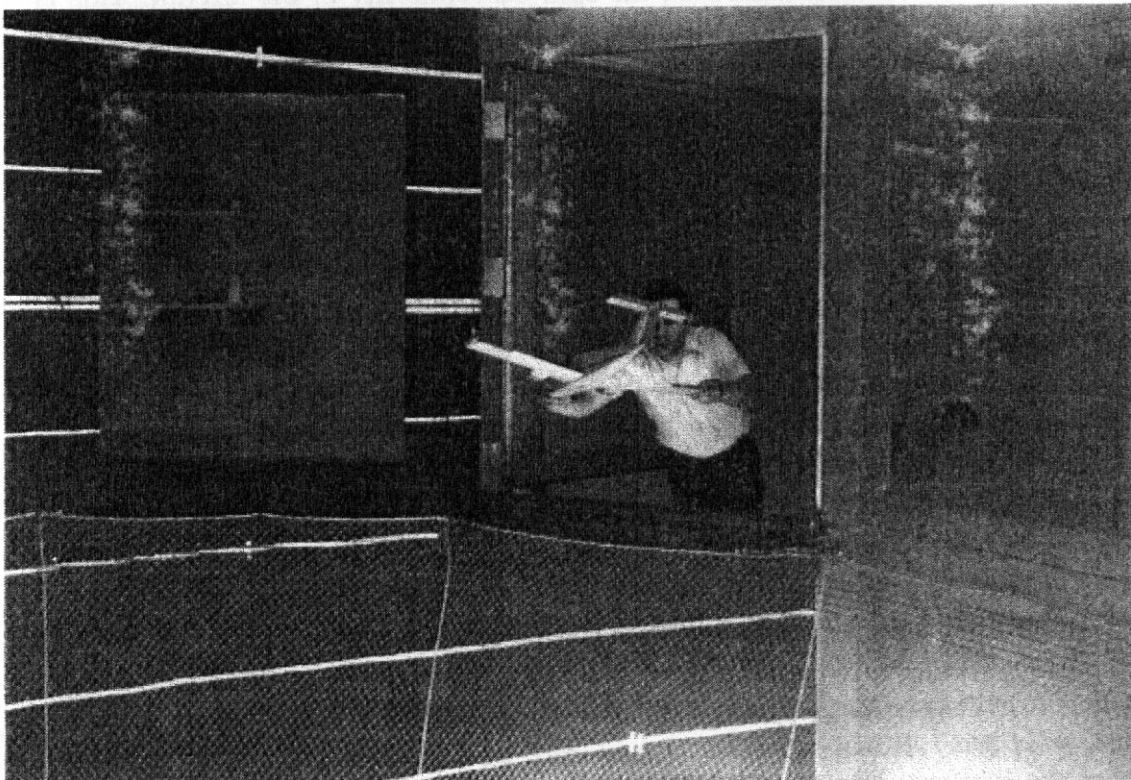
FIGURE 18.2 Beech Model 76 being launched in NASA Langley 20-ft vertical spin tunnel. Model scale is 0.07 : 1. (Photograph courtesy of Raytheon.)

Free-flying experiments in the spin tunnel can determine (1) spin modes and recovery characteristics, (2) effects of mass distribution and center of gravity, (3) the effect of external stores, (4) the type and size of required spin recovery chute to be installed on flight test airplanes, and (5) exit trajectory of air crew if ejection is necessary. It is necessary to determine both the spin and spin recovery in both right and left spins for all combinations of rudder, elevator, and ailerons. This requires a large matrix of experimental runs as indicated by Tumlinson, Holcomb, and Gregg,[9] who report approximately 500 spin simulations made in one aircraft study.

The data are in the form of film and observation notes. The film have historically been analyzed in a cross-hair-equipped film viewing machine using a protractor to yield both fuselage and spin axis angles to a precision of $\pm 1°$ or better. Image processing software with the increased power of computer equipment is a more effective method.

The angle conventions may be of interest. The fuselage angle (8) is measured from the horizontal and is negative nose down. The spin axis angle (8) is measured from the horizontal and is positive left wing up. The angle of attack is

$$\alpha = 90° - (-\theta) \tag{18.7}$$

The number of turns for recovery from the images can be determined to one-quarter turn using typical frame rates. The spin rate (Ω) can be determined to $\pm 2\%$.

The free-flight method in the spin tunnel only simulates developed spins and recovery; it yields no information on the spin susceptibility of the aircraft. This is obtained from the other methods discussed above. If the model experiments reveal two or more spin modes, it is almost impossible to predict which mode, if any, will be predominant or most likely to occur in actual flight.

18.2   DYNAMIC AEROELASTIC EXPERIMENTS

The constant search by designers for ways to achieve thinner wings that can support external stores, engine pods, and the like always keeps airplane designs near the edge of acceptability in terms of structural deformation and possible dynamic instabilities. Since the deflections of the aircraft structure will influence the dynamic behavior and flutter characteristics, experimental evaluation of flexible models in wind tunnels is necessary to determine these "elastic" effects.

Essentially, two basic types of aeroelastic models have evolved, the dynamic stability model, and the flutter model. As pointed out by Bisplinghoff, Ashley, and Halfman[10] in their classic treatment of this subject, dynamic stability experiments are focused primarily on dynamic behavior dominated by rigid-body modes of motion. *On* the other hand, flutter experiments are focused on the elastic modes.

Elastic models may be used in steady-state testing to determine the effect of deflection on static stability by mounting the model on the balance support system. It is important, however, to duplicate to scale the deformations of the full-scale vehicle and to be sure that the support system allows the model to deform elastically.

Figure 18.3 illustrates the effect of deflection on the static stability curve; the dashed curve is the effective stability curve, since the aircraft does not fly at constant q over the C_L range.

Most model suspension rigs allow freedom in pitch, vertical translation, and yaw with limited roll and fore and aft freedom. Such a system will not allow a determination of the long-period, or phugoid, motion because the tunnel operates at constant speed whereas wide changes in velocity occur during the phugoid on the full-scale vehicle.

The model may be "kicked" into a displaced attitude and released; the ensuing motion defines the short-period oscillation that occurs at constant speed. Camera and video studies, along with direct displacement transducers or similar instrumentation, may be used to record the motion. Frequency and damping characteristic values can be obtained.

Flutter experiments are designed to find a number of parameters, typically including

1. critical flutter speed,
2. flutter frequency(s),
3. flutter mode(s) symmetrical or antisymmetrical),
4. fuselage coupling, and
5. wing-empennage interaction.

In most cases where complete models are used in the experiments, it is common practice to use a vertical rod mount. This system, an example of which is shown in Figure 18.4, provides relatively free motion in pitch, roll, yaw, and vertical translation. Fore and aft as well as spanwise motions are considerably restrained.

A second method is to constrain the model by a cable bridle that holds the model centered in the tunnel, as illustrated in Figure 18.5.

Experiments using components such as wing panels to investigate aileron flutter and empennage models to investigate stabilizer, elevator, or rudder flutter are fre-
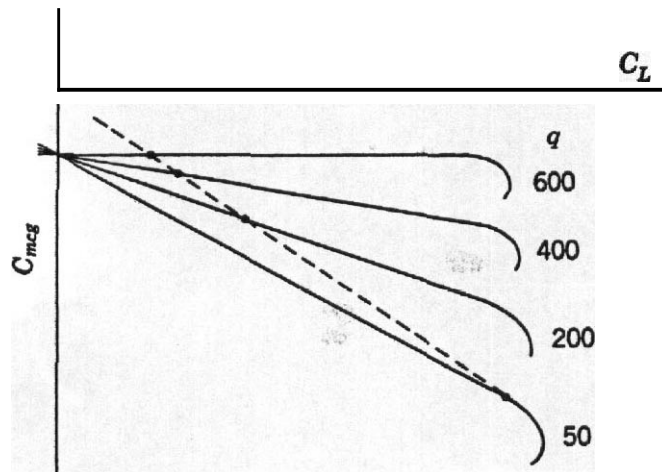
FIGURE 18.3 Effect of a swept-wing aircraft elastic deformation on longitudinal static stability.
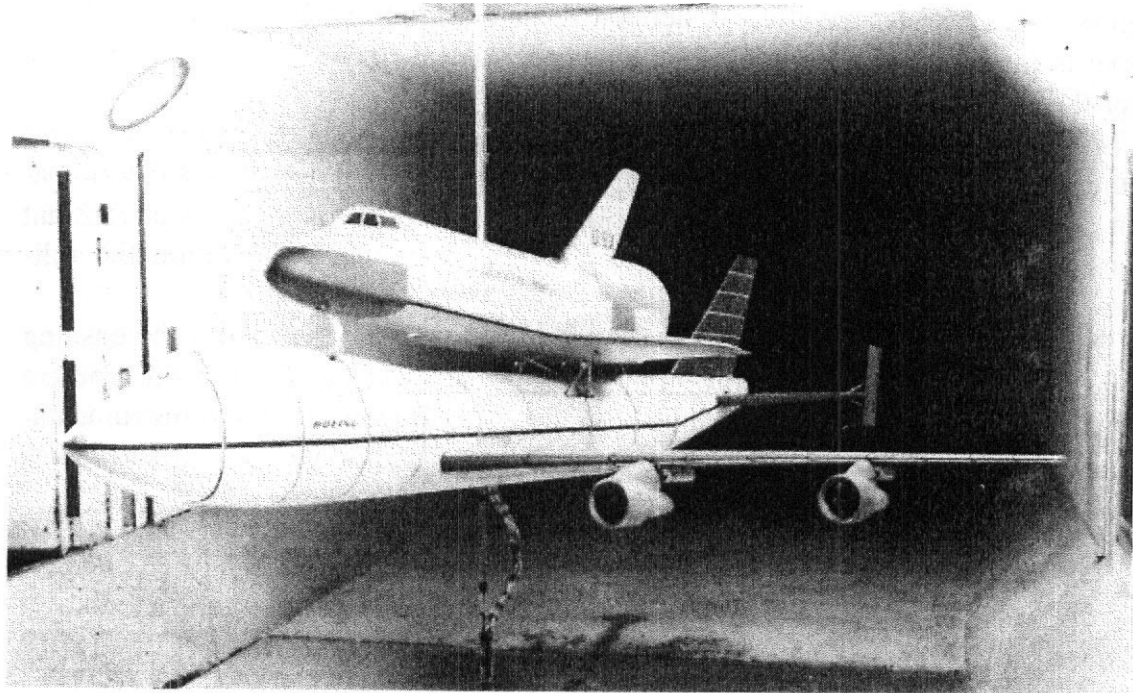
FIGURE 18.4 Boeing 747/Space Shuttle flutter model on vertical rod mount. (Photograph courtesy of Boeing Aerodynamic Laboratories.)

quently undertaken to obtain individual component flutter characteristics. Figure 18.6 shows a large-scale empennage flutter model mounted in the tunnel.

It is interesting to note that high-speed motion cameras and video recorders are among the most useful devices in flutter experiments because the mode shape is readily seen in the image sequences. Accelerometers, strain gages, and so on.
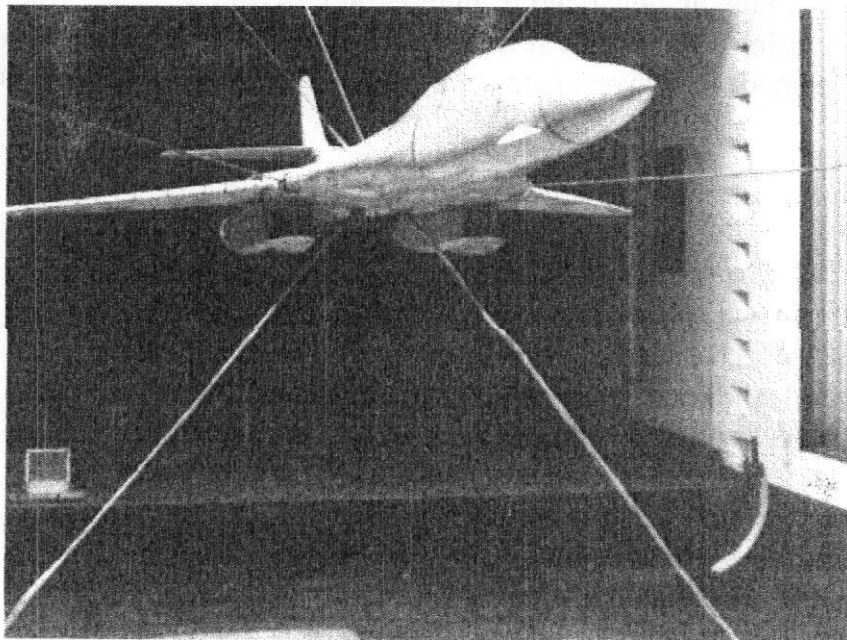
FIGURE 18.5 Rockwell B-1 flutter model on cable mount. (Photograph courtesy of the Boeing Co.)

FIGURE 18.6 DC-10 tail flutter model with double-hinged rudder. (Photograph courtesy of NASA Langley and McDonnell-Douglas Corporation.)

mounted on the wing spars or other parts of the main structure provide data from which flutter frequency is readily deduced.

The experimental procedure is to approach the expected critical flutter speed slowly. At each new speed setting, the model can be excited by means of a "jerk wire" or some other impulsive disturbance. Tracings of instrumentation output must be monitored. As critical speed is approached, the time to damp increases and can easily be detected if strip-chart-like displays are used. Finally, when the strip display indicates divergence, the cameras are turned on if movie cameras are in use and the run is terminated by cutting the tunnel. Some tunnels have a device called a "q stopper" that drops speed rapidly and thus reduces probability of model destruction. This consists of two splitter plates on the ceiling and floor. The splitter plates are equipped with spring-loaded flaps with snubbers at the end of their travel. When rapid speed reduction is needed, such as during model flutter, the flaps are automatically deployed toward the tunnel centerline. This reduces the speed quickly by dramatically increasing the drag in the test section near the model and forces some of the high-energy air to pass between the splitter plates and the ceiling and floor.

There is always a risk during a flutter event of getting such a severe model flutter that the model is either partially or totally destroyed. The loss of a model or parts can also damage the wind tunnel propellers if adequate safety catch screens are not in place. The true air speed is of direct interest in flutter experiments, rather than

dynamic pressure. The stream temperature is therefore a more important parameter than is the case for many force and pressure experiments.

The primary purpose of a flutter experiment is to ensure that the airplane will not encounter flutter within its flight envelope at any one of its possible loadings. The loading requirement means that the distribution of fuel must be considered in cases of aircraft with wet wings. On some military aircraft with soft wings, external stores must also be considered.

Principal results from flutter experiments are the true air speed for flutter **as** a function of altitude. Obviously a design should have flutter speeds that are higher than design speed at any given altitude.

Flutter Model Scaling and Design

Flutter models must be dynamically scaled as well as having the proper external geometric shape. The geometric scale ratio is usually fixed by consideration of wind tunnel size and other applicable limitations. The maximum model span that the tunnel can accommodate should not exceed 0.8 of the tunnel width, as discussed in Chapter 10. This sets the model to full-scale span ratio b_M/b_A. The subscripts refer to model- and full-scale airplane. The quantity b could be any linear dimension, although wing span appears most convenient. The model mass distribution and both bending and torsional stiffnesses must be made to follow the scaling laws. The requirement on mass is indicated by the requirement that

$$\frac{(m/\pi\rho b^2)_M}{(m/\pi\rho b^2)_A} = 1 \tag{18.8}$$

or

$$\frac{m_M}{m_A} = \frac{\rho_M b_M^2}{\rho_A b_A^2} \tag{18.9}$$

where m is the mass per foot, ρ_M the tunnel operating airstream density, and ρ_A the atmospheric density for full-scale aircraft. The total mass or weight ratio then becomes

$$\frac{M_M}{M_A} = \frac{\rho_M}{\rho_A}\left(\frac{b_M}{b_A}\right) \tag{18.10}$$

The frequency ratio that should be preserved is

$$\frac{(V/b\omega)_M}{(V/b\omega)_A} = 1 \tag{18.11}$$

or

$$\left(\frac{V}{b\omega}\right)_M = \left(\frac{V}{b\omega}\right)_A$$

Other relations important for flutter models are as follows:

1. the velocity ratio:

$$\frac{V_M}{V_A} = \sqrt{\frac{b_M}{b_A}} \tag{18.12}$$

2. the "static" moment scale ratio:

$$\frac{S_M}{S_A} = \frac{\rho_M}{\rho_A}\left(\frac{b_M}{b_A}\right)^4 \tag{18.13}$$

3. the mass moment of inertia ratio:

$$\frac{I_M}{I_A} = \frac{\rho_M}{\rho_A}\left(\frac{b_M}{b_A}\right)^5 \tag{18.14}$$

4. the stiffness ratio:

$$\frac{\text{Model stiffness}}{\text{Airplane stiffness}} = \frac{\rho_M}{\rho_A}\left(\frac{V_M}{V_A}\right)^2\left(\frac{b_M}{b_A}\right)^4 \tag{18.15}$$

The foregoing ratios are used to guide model design. Then the completed model is given vibration tests to determine the true frequency.

Actual scale reproduction of the airplane structure is not practical. The model designer seeks a simplified structure that will give the right bending and torsional stiffness while allowing a provision of proper mass distribution. For low-speed models, a single spar as shown in Figure 18.7 can frequently be used to obtain the moments of inertia for both vertical and fore and aft bending. It is customary to have all the stiffness in the spar with the covering providing only the aerodynamic shape. To accomplish this, the wing, fuselage, or tail external shape is made in sections. The gaps between the sections can be covered with thin rubber dental dam, or better, filled with a thin soft foam rubber. The filler should not increase the stiffness of the structure especially for aerodynamic surfaces such as the wing and tail.

After the spar is fabricated, the stiffness can be checked by static deflection tests. For these tests, the spar can be mounted as a cantilever beam. An accelerometer that can measure angles can be attached to the spar, the spar can be loaded, and the slope of the elastic curve determined by the accelerometer output.
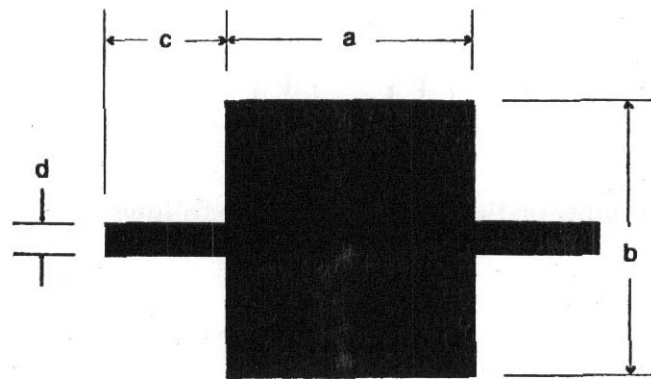
FIGURE 18.7   Typical spar cross section for low-speed flutter model. Dimensions a and b determined by I_h and J required. Dimension c determined **by** I_f required. Dimension d set at $0.1b$; I, and I, are moments of inertia in vertical and fore and aft bending.

From beam deflection analysis the relationship between deflection and stiffness properties is known to be

$$\frac{d^2y}{dx^2} = \frac{M}{EI} \tag{18.16}$$

With $dy/dx = \Theta$, we obtain

$$\frac{M}{EI} dx = d\Theta \tag{18.17}$$

and since the spar stations **are** finite distances apart, the equation

$$_n\Delta\Theta_{(n+1)} = \int_n^{n+1} \frac{M}{EI} dx \tag{18.18}$$

applies. Therefore to obtain the average value of M/EI between stations, it is only necessary to subtract successive values of the measured deflections to get

$$_n\Delta\Theta_{(n+1)} = \Theta_{(n+1)} - \Theta_n \tag{18.19}$$

Since $\Delta\Theta$ is equal to the area of the M/EI curve between stations, the average value of M/EI is obtained by dividing $\Delta\Theta$ by the distance between stations. Finally, $1/EI$ is obtained by dividing out the known applied bending moment. The values for bending stiffness in the other plane and for the torsional stiffness can be found by a similar procedure. All quantities must be compared to the airplane design data to check the fidelity of the model spar design and fabrication.

TABLE 18.1. Typical Flutter Model Scale Ratios for a Four-Engine Turbofan Cargo Plane

Ratio	Symbol	Numerical Value
Geometry	b_M/b_A	$1/24^a$
Density	ρ_M/ρ_A	$1/.44^b$
Velocity	V_M/V_A	$1/7.5$
Frequency	$\dfrac{(V/b_\omega)_M}{(V/b_\omega)_A}$	3.20
Deflection	$\dfrac{\delta_A/\delta_M}{b_A/b_M}$	2.34
Weight	W_M/W_A	1/9,600
Static moment	S_M/S_A	1/230,000
Weight moment of inertia	I_M/I_A	*115,529,600*
Stiffness	EI_M/EI_A or GJ_M/GJ_A	1/12,960,000

"Dictated by size of tunnel to be used.
*Dictated by tunnel and flight conditions.

The low-speed flutter model usually does not have either the right scaled weight (gravitational force) or the right deflection ratio. The ratio of gravitational force to aerodynamic force is

$$\frac{m}{\rho b^2} = \frac{g}{V^2/b} \tag{18.20}$$

The ratio $g/(V^2/b)$ is seldom scaled properly, so that some additional vertical force must be applied if the model is to fly at the proper lift coefficient. The ratio of the deflection (due to a scaled load) of an aeroelastic model to that of the full-scale airplane should be consistent with

$$\frac{\delta_A b_M}{\delta_M b_A} = 1.0 \tag{18.21}$$

This unit value is seldom achieved, but fortunately the product in Equation (18.21) may go as high as 3.0 without introducing appreciable error. Some typical values of the various ratios introduced in this section are listed in Table 18.1. A partially completed flutter model is shown in Figure 18.8.

-18.3   STORE RELEASE OR JETTISON EXPERIMENTS

It is often necessary to determine the release characteristics of tip tanks, underwing stores, bombs, or other devices. Although it is simple and direct to state that we will design the model and experiment process to duplicate the ratio of inertia forces
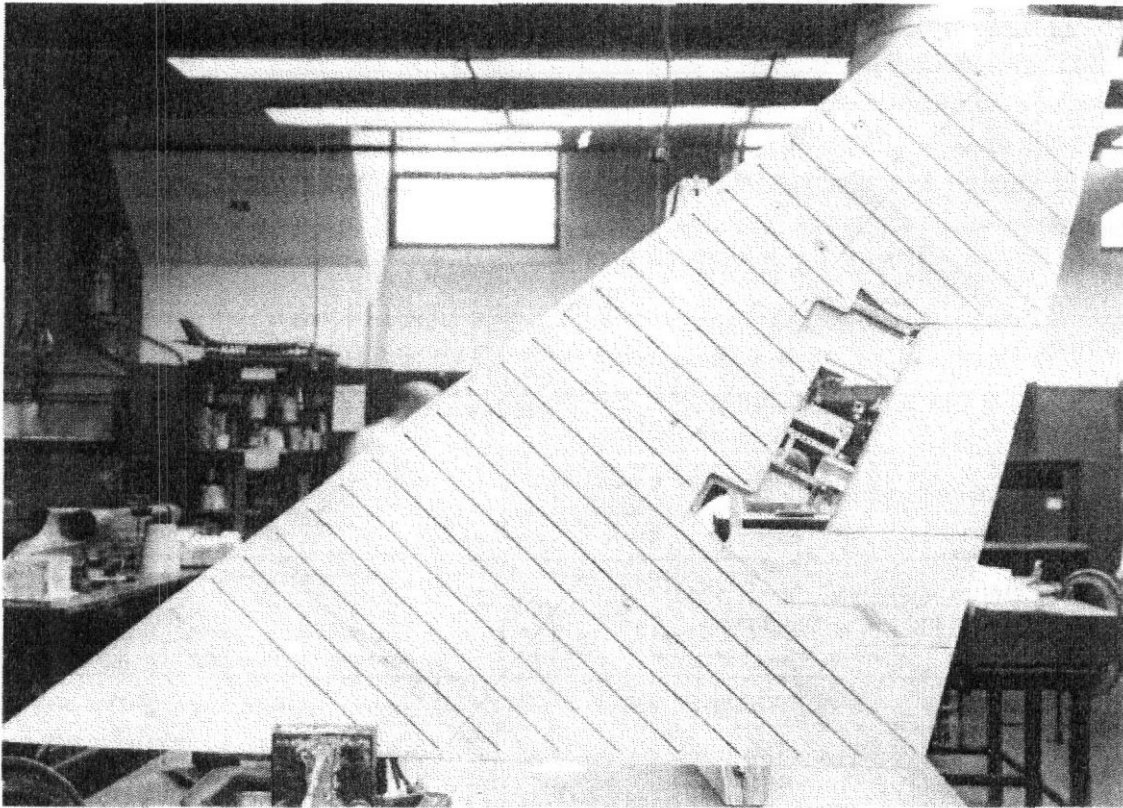
FIGURE 18.8 A nearly completed flutter model. The dark lines are joints rather than glue locations. (Courtesy of the Boeing Co.)

to gravity forces (i.e., we will duplicate the Froude number), it is probably more instructive to go through the mental gymnastics of a hypothetical case.

Assume a store **16** ft long and a $\frac{1}{10}$-scale model **1.6** ft long. Further assume that whenever the full-scale store falls a length, it is pulled back half a length by aerodynamic drag and pitches $10°$. The linear acceleration is hence **16** ft/sec², and the rotational acceleration **20** deg/sec². Obviously we would like the model to pitch $10°$ while it is pulled back half a length also, so that the trajectory is similar to the full-scale condition.

The first thing we note is that while the full-scale stores takes **1** sec to fall a length and pitch $10°$, the model must do the same in **0.316** sec. Since half the model length is **0.8** ft, the linear acceleration needed for the model is again **16** ft/sec². But the angular acceleration turns out to be 200 deg/sec², or, in other words, the angular acceleration is increased by the scale factor λ (which is equal to l_{FS}/l_M; see below).

The aerodynamic force that produces the linear displacement is proportional to the body area and hence decreases as λ^2, and if we follow the dimensionally sound procedure of reducing the model weight by λ^3, the linear acceleration will be increased by λ. We get around this by reducing the test air speed by $\sqrt{\lambda}$.

The torque is largely due to the force on the fin area (down by A^2), the dynamic pressure (down by λ), and the length of the lever arm (down by A). In order to get λ times the full-scale pitch acceleration, we must reduce the model moment of

inertia by X^S. Note that we more or less arbitrarily reduced the full-scale weight by λ^3. This is the relation that will exist if the model has the same average density as the full-scale article. This is not necessary. If we had used λ^2 and let $B_M = V_{FS}$, the moment of inertia would have come down by λ^4. This type of "heavy scaling" is useful at high Mach number and is discussed by Reed and Curry."

Hence we have (using W for weight, I for moment of inertia, l for typical length, and subscripts M and FS for model and full scale)

$$W_M = W_{FS}\frac{\rho_M}{\rho_{FS}}\left(\frac{l_M}{l_{FS}}\right)^3 \qquad (18.22)$$

$$I_M = L_{FS}\left(\frac{l_M}{l_{FS}}\right)^5 \qquad (18.23)$$

$$V_M = V_{FS}\left(\frac{l_M}{l_{FS}}\right)^{1/2} \qquad (18.24)$$
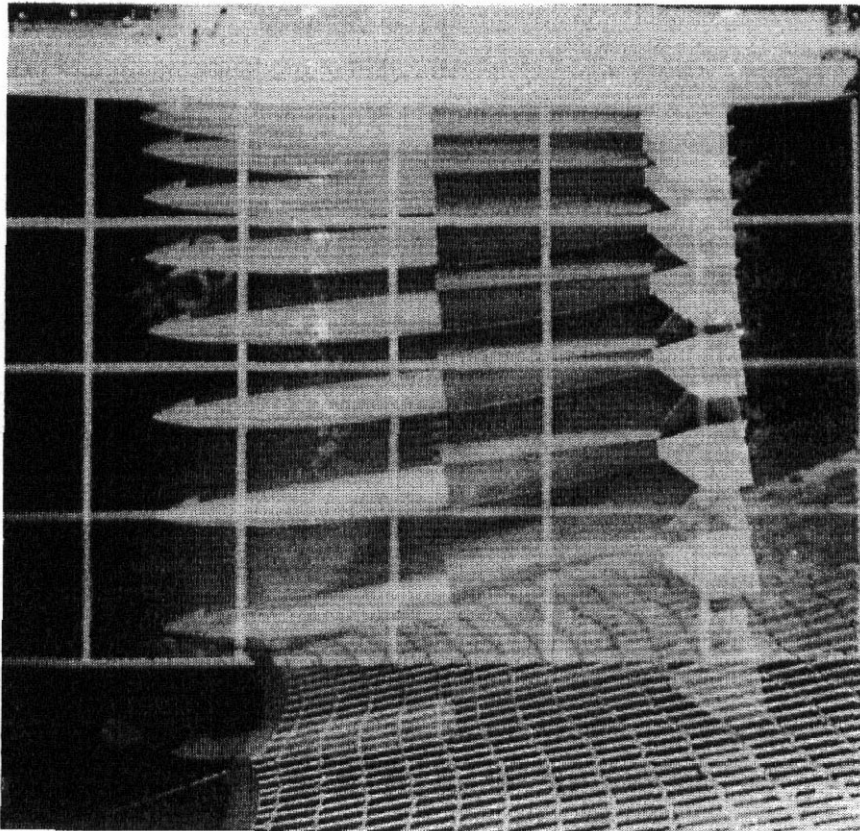
FIGURE 18.9 Multiple-flash pictures of the release and separation of a bomb shape. In multiple-flash pictures the static items (the airplanes fuselage and the catch-net in the above photograph) will always appear brighter than the moving model, since their image is reinforced by each flash. (Courtesy Sandia National Laboratories.)

Poor releases (wild pitching or hitting the airplane with the store) are almost invariably cured by jettison guns and may be cured by store tilt, flaps on the airplane fuselage near the store fins, flaps on the store-mounting pylon, or toed-in stores. Stores have sometimes remained "with the airplane" after being mechanically re-leased. There have been a few reports of a belly carried bomb crawling up the side of the fuselage so the pilot was looking out the side of the cockpit at his "dropped" and presumably fused bomb. Drop data may be obtained in the form of high-speed video, movies, or multiple-flash stills. An example of multiple-flash stop motion recording is shown in Figure 18.9. Motion sequences may be analyzed and the results given in conventional plots, as shown in Figure 18.10. When cameras or
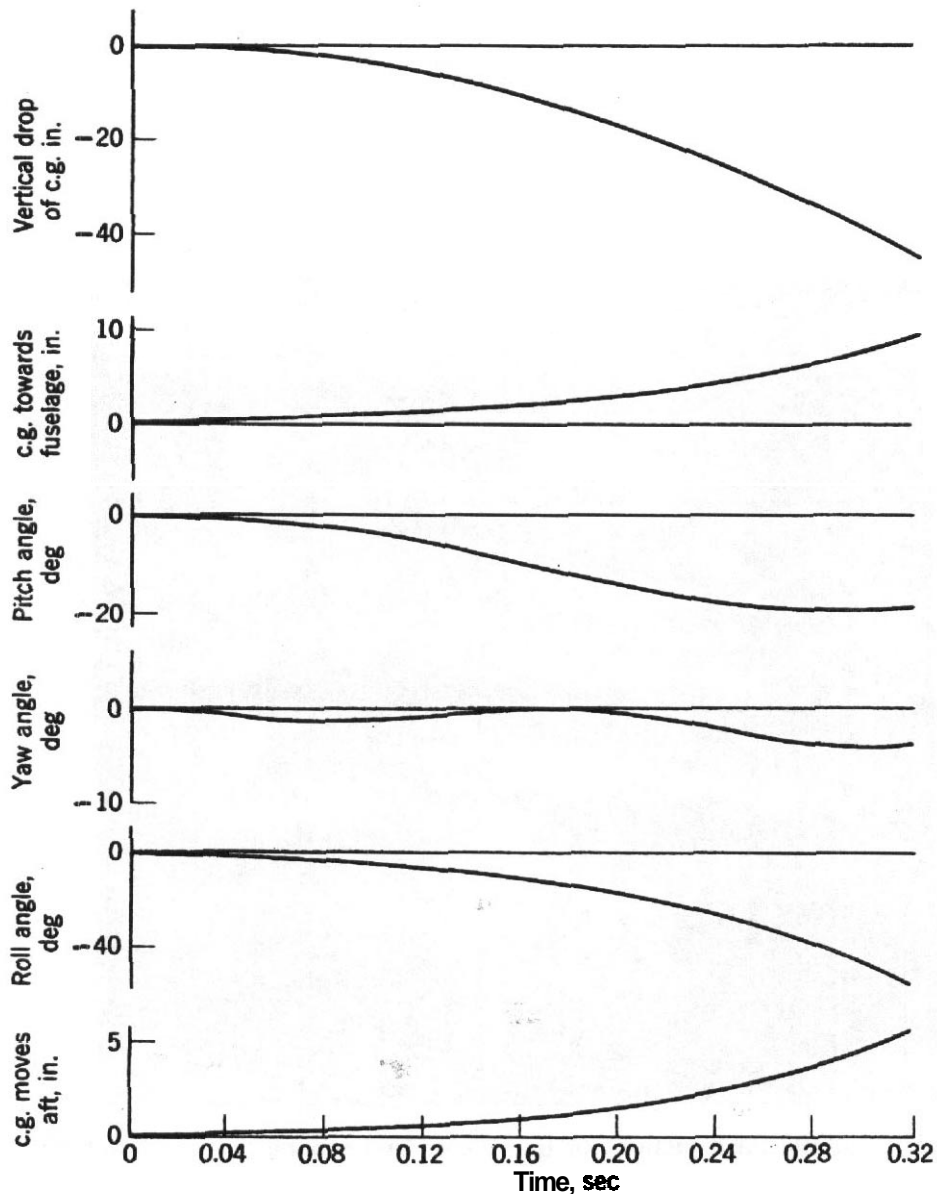
FIGURE 18.10   Presentation of store drop data (CG = center of gravity). Other configura-tions may typically be plotted on the same sheet to aid in selecting the best configuration.

high-speed video is used, both side and top cameras are. needed. Extra windows in the tunnel may often be needed.

A more elaborate approach to the separation problem that avoids the difficulty of matching model- and full-scale moments of inertia is briefly as follows: The store model is mounted on an internal balance on a sting. The balance output in terms of angles, forces, and moments is fed into a six-degree-of-freedom simulation program. The motion consistent with the measured forces and inertial properties is determined and the sting is directed to move accordingly. This process is repeated in short steps and yields the path of the store as it leaves the aircraft. This method does not require the safety net with its large drag penalty, nor does it run the risk of the breakup of the model and possible damage to the tunnel's propellers. It is, however, quite expensive to develop and validate.

18.4   PARABRAKE EVALUATIONS

The use of drag chutes to provide "air braking" is quite common and the wind tunnel may be used to determine the drag characteristics of such devices. The chute may be packed in the model tail section and opened remotely during the test. Figure 18.11 shows a drag chute deployed during a tunnel test of a turboprop cargo-troop transport plane. Troublesome oscillations of the chute occurred during this test program, probably as a result of too short a bridle and too short suspension lines on the chute. Wake from the airplane also likely contributed.

18.5   CAVITY RESONANCE

One of the newer problems that besets modern high-speed aircraft is cavity resonance, a high-intensity vibration of wheel wells, bomb bays, or cockpits that arises when their covers are removed and the high-speed airstream moves by (and into) the opening.

This phenomenon has been localized by means of tunnel experiments and overcome in some cases by means of Helmholtz resonators, that is, tuned chambers that are. opened into the offending cavity. The procedure for a tunnel experiment is to open the various cavities one at a time and to pick up their natural frequencies with a pressure pickup fed into a frequency analyzer possibly in parallel with a scope and a real-time recorder. Resonance, if any, will occur close to the same speed at which it will occur on the airplane but at a frequency increased by the scale factor. If space is available for Helmholtz resonators, they may be tried; if not, scoops or lips may be added to the cavities intuitively until the intensity is down. This is an area of continuing research effort and is being attacked by computational methods of computational aeroacoustics. It is far from being mastered in a general context.

A second approach, if the natural frequency has already been determined by flight test, is to mount the model or some subpart on strain gages selected so that their spring constant and the mass of the model or subsystem provides the natural
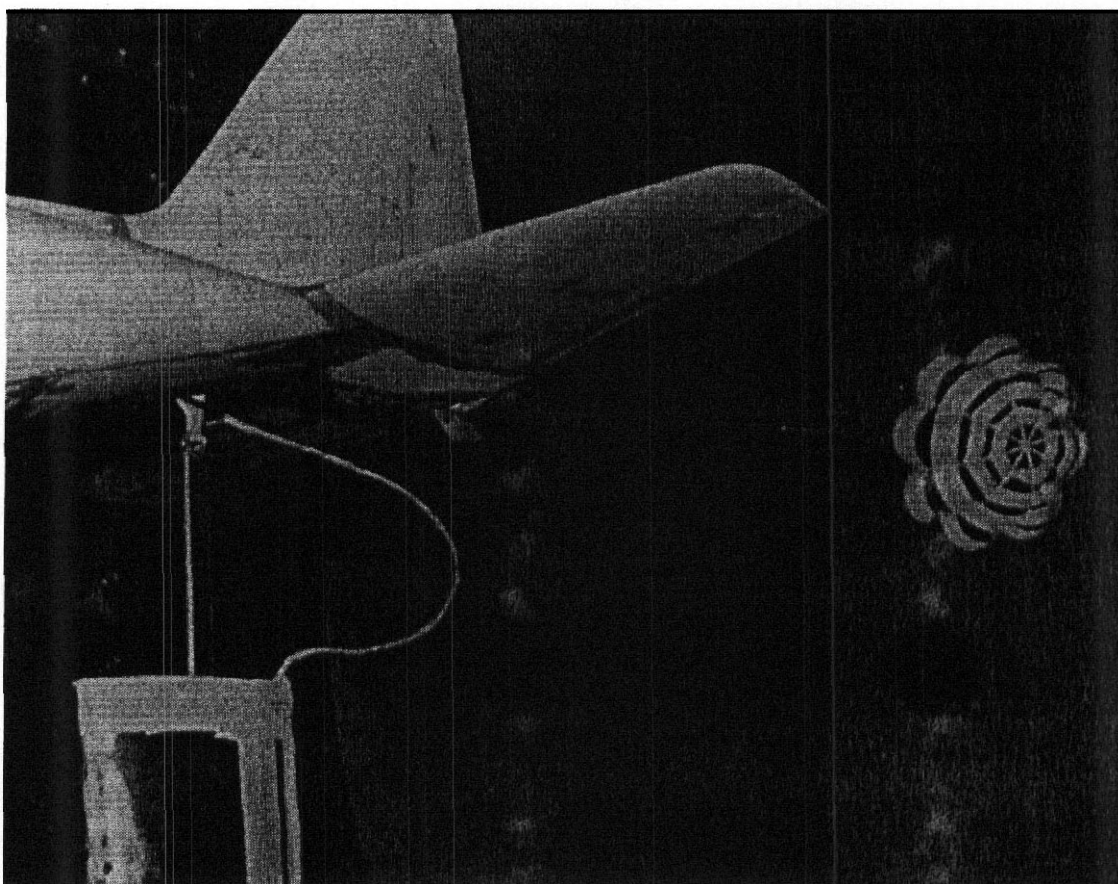
FIGURE 18.11   Model parabrake deployed behind a cargo transport model. The nailing loop from the windshield contains wires to the solenoid-operated chute compartment doors. (Courtesy Lockheed Georgia Co.)

frequency value already known. Baseline data will provide signal levels that can be used to judge the effectiveness of proposed changes.

REFERENCES AND NOTES

-1. Chambers, J. R., "Overview of Stall/Spin Technology," Paper 80-1580, presented at the AIAA Atmospheric Flight Mechanics Conference, Danvers, MA, 1980.

2. Orlik-Ruckermann, K. J., "Techniques for Dynamic Stability Testing in Wind Tunnels, in Dynamic Stability Parameters," AGARD CR-235, May 1978.

3. Barlow, J. B., and Tischler, M. B., "Dynamic Analysis of the Flat Spin Mode of a General Aviation Aircraft," *AIAA J. Aircraft*, 19(13), 198–210, 1982.

4. Barlow, J. B., and Tischler, M. B., "Determination of the Spin and Recovery Characteristics of a General Aviation Design," *AIAA J. Aircraft*, 18(4), 238–244, 1981.

5. Bihrle, W., and Barnhart, B., "Spin Prediction Techniques," *AIAA J. Aircraft*, 20, 97–101, 1983.

6. Bihrle, W., and Bowman, J. S., "Influence of Wing, Fuselage, and Tail Design on Rotational Flow Aerodynamics Beyond Maximum Lift," *AIAA J. Aircraft*, 18, 920–925, 1981.

7. Holcomb, M. L., "The Beech Model 77 'Skipper' Spin Program," Paper 79-1835, presented at the AIAA Aircraft Systems and Technology Meeting, New York, NY, 1979.

8. Wolowicz, C. H., Bowman, J. S., and Gilbert, W. P., "Similitude Requirements and Scaling Relationships as Applied to Model Testing," NASA Technical Paper 1435, Aug. 1979.

9. Tumlinson, R. R., Holcomb, M. L., and Gregg, V. D., "Spin Research on a Twin Engine Aircraft," Paper 81-1667, presented at the AIAA Aircraft Systems and Technology Conference, Dayton, OH, 1981.

10. Bidplinghoff, R. L., Ashley, H., and Halfman, R. L., *Aeroelasticity,* Addison-Wesley, Reading, MA, 1957.

11. Reed, J. F., and Curry, W. H., "A Wind Tunnel Investigation of the Supersonic Characteristics of Three Low Fineness Ratio Stores Internally Carried in a Simulated F-105 Bomb Bay," Sandia Corporation SCTM 30-56-51, 1956.

APPENDIX 1
Subsonic Aerodynamic
Testing Association (SATA)

The Subsonic Aerodynamic Testing Association was formed to provide a worldwide organization for operators of subsonic aerodynamic facilities. The first meeting was convened at the University of Maryland in March, 1965. The objectives of the SATA are to provide a means of interchange of ideas, techniques, and solutions of problems associated with subsonic aerodynamic experimental facilities and experiments. General areas of interest include:

- Physical measurement, instrumentation, handling and reduction of data. Design, performance, and economics of test facilities.
- Facility operation and maintenance

Current members of SATA are listed below. Descriptions of the facilities of the members and contact information can be found through the world wide web site, http://www.niar.twsu.edu/sata/sata.htm.

Members of SATA (1998)	Joined
Agency for the Assessment and Application of Technology (Indonesia)	1997
Agusta Helicopters	1991
Bihrle Applied Research	1993
Boeing Philadelphia	1965
Boeing Seattle	1965
Boeing St. Louis	1965
British Aerospace Airbus	1971
Calspan Buffalo	1967
Centro Tecnico Aerospacial/IAE/ASA-L Brazil	1977
Chrysler Corp.	1970
Cox and Company	1997
CSIR−Aerotek (South Africa)	1988
Daimler-Benz Aerospace Airbus	1993
Daimler-Benz AG	1980
Danish Maritime Institute	1996
Darmstadt University of Technology	1986

DERA Bedford	1994
DERA Farnborough	1969
Dresden University of Technology	1993
DNW (The Netherlands)	1978
FFA Sweden	1976
Ford Motor Company–Design Center	1979
Ford Motor Company–Product Development	1965
Georgia Institute of Technology	1965
General Motors Design	1965
General Motors Research	1985
Industrie Pininfarina SPA (Italy)	1979
Israel Aircraft Industries	1990
KAWADA Industries (Japan)	1994
Korea Aerospace Research Institute	1996
Lockheed Martin Aeronautical Systems Co (Georgia)	1965
Massachusetts Institute of Technology	1965
Micro Craft San Diego	1994
NASA Ames	1965
NASA Langley	1965
NASA Lewis	1981
National Research Council of Canada	1965
Naval Surface Warfare Center (Bethesda)	1965
Nihon University (Japan)	1989
Nissan Motor Company	1989
Northrop Advanced Systems	1988
Northrop Grumman	1967
Ohio State University	1995
Old Dominion University	1997
ONERA France	1983
Pennsylvania State University	1973
Porsche AG	1986
Royal Melbourne Institute of Technology (Australia)	1993
Sandia National Laboratories	1994
Sverdrup Technology-AEDC Group	1965
Swift Aero	1995
Swiss Aircraft and Systems Company	1995
Technion-Israel Institute of Technology	1984
Texas A & M University	1965
United Technologies Research Center	1965
University of Kansas	1994
University of Maryland	1965
University of Notre Dame	1979
University of Washington	1965
US Air Force Academy	1980
US Air Force Wright Laboratories	1965

US Naval Academy	1979
Virginia Polytechnic Institute and State University	1989
Volkwagenwerks AG	1976
Volve Car Corporation	1974
Wichita State University	1965
Windkanal Dresden–Klotzsche	1993

APPENDIX 2
Numerical Constants and
Units Conversions

USEFUL NUMERICAL CONSTANTS

Gas constant for air = 287 J/(kg°K) = 1716 ft-lb/(slug°R)
Acceleration of gravity = 32.174 ft/sec^2 = 9.8066 m/s^2

Standard **Sea** Level Conditions

Pressure = 14.7 lb/in.^{2} = 29.92 in. Hg = 2116.2 lb/ft^2 = 101,325 N/m^2
Density = 0.002378 slug/ft^3 = 1.225 kg/m^3
Temperature = **518.69°R** = **288.16°K** = 59°F = 15°C
Viscosity = 3.7373 X 10^{-7} lb-s/ft^2 = 1.7894 X 10^{-5} N-s/m^2
Speed of sound = 1116 ft/s = 340.2 m/s

UNIT CONVERSIONS

Length	Speed
1 inch = 2.54 centimeters	1 ft/sec = 0.6818 mph = 0.5921 knots
1 mile = 5280 feet = 1609.3 meters	1 knot = 1.152 mph = 1.8536 km/hr
1 foot = 0.3048 meter	1 m/s = 3.281 ft/s
1 nautical mile = 6080 feet	1 mph = 1.6093 km/hr

Volume	Power
1 ft^3 = 7.48 gallons = 28.326 liters	1 hp = 550 ft-lb/s = 0.7457 kw
1 imperial gallon = 1.201 gallon	

Force	Pressure
1 lb = 4.4482 N	1 lb/ft^2 = 47.880 N/m^2
	1 lb/in.^{2} = 6894.8 N/m^2
	1 in. H$_2$O = 5.204 lb/ft^2
	= 0.07355 in. Hg

Work or Energy
1 ft-lb = 1.3558 joules
1 BTU = 1055.1 joules

INDEX